Edited by
Wilfried Andrä and Hannes Nowak

WILEY-VCH

Magnetism in Medicine

A Handbook

Second, Completely Revised and Enlarged Edition

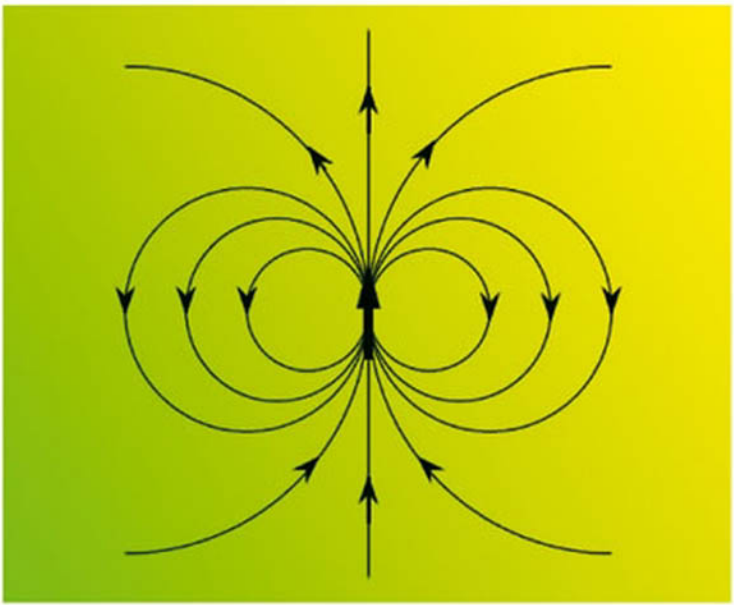

Magnetism in Medicine

Edited by
Wilfried Andrä and
Hannes Nowak

1807–2007 Knowledge for Generations

Each generation has its unique needs and aspirations. When Charles Wiley first opened his small printing shop in lower Manhattan in 1807, it was a generation of boundless potential searching for an identity. And we were there, helping to define a new American literary tradition. Over half a century later, in the midst of the Second Industrial Revolution, it was a generation focused on building the future. Once again, we were there, supplying the critical scientific, technical, and engineering knowledge that helped frame the world. Throughout the 20th Century, and into the new millennium, nations began to reach out beyond their own borders and a new international community was born. Wiley was there, expanding its operations around the world to enable a global exchange of ideas, opinions, and know-how.

For 200 years, Wiley has been an integral part of each generation's journey, enabling the flow of information and understanding necessary to meet their needs and fulfill their aspirations. Today, bold new technologies are changing the way we live and learn. Wiley will be there, providing you the must-have knowledge you need to imagine new worlds, new possibilities, and new opportunities.

Generations come and go, but you can always count on Wiley to provide you the knowledge you need, when and where you need it!

William J. Pesce
President and Chief Executive Officer

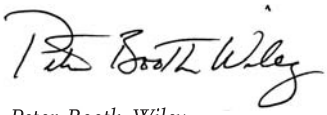

Peter Booth Wiley
Chairman of the Board

Magnetism in Medicine

A Handbook

Edited by
Wilfried Andrä and Hannes Nowak

Second, Completely Revised and Extended Edition

WILEY-VCH Verlag GmbH & Co. KGaA

The Editors

Prof. Dr. Wilfried Andrä
Kernbergstrasse 39
07749 Jena
Germany

Dr. Hannes Nowak
Biomagnetic Center
Department of Neurology
Friedrich Schiller University
Erlanger Allee 101
07747 Jena
Germany

Library of Congress Card No.: applied for
British Library Cataloguing-in-Publication Data
A catalogue record for this book is available from the British Library.

Bibliographic information published by the Deutsche Nationalbibliothek
The Deutsche Nationalbibliothek lists this publication in the Deutsche National-bibliografie; detailed bibliographic data are available in the Internet at http://dnb.d-nb.de

Printed in the Federal Republic of Germany
Printed on acid-free paper

Typesetting Asco Typesetters, Hong Kong
Printing betz-druck GmbH, Darmstadt
Binding Litges & Dopf Buchbinderei GmbH, Heppenheim

ISBN 978-3-527-40558-9

Contents

Preface

Magnetism often has a slight overtone of being mysterious. This is probably caused by the surprisingly strong forces between magnets which everybody can experience with magnetic toys, magnet boards, or similar objects. A strange effect is the unique ability of magnetic fields to penetrate many substances without any attenuation. Though the physical basis of magnetism is well explored, the outsider usually does not know very much about the details and sometimes tends to overestimate the real possibilities provided by magnetism. Nevertheless, the limits of applications have not yet been reached. Considerable progress has taken place in medicine during recent years, and there is no reason to assume that this development has already come to an end.

Progress in medicine has often been initiated by the discoveries and results of research studies conducted among the various disciplines of natural science. One of the most famous examples to date is the discovery of a certain type of electromagnetic radiation, the X-ray, by Wilhelm Conrad Röntgen in 1895. In this case, the importance of the discovery with respect to medical applications was recognized immediately. Development was started and propelled by fruitful cooperation between both physicians and physicists. This teamwork is still very strong, and has led recently to the introduction of what is called electron beam tomography (EBT). In other cases – for example, that of nuclear magnetic resonance – the time taken between its discovery and subsequent application in medicine was longer. Sometimes, a new method has become established in clinical practice only after having passed through a long period of *in-vitro* investigations and preclinical trials. However, there are applications – for example, in biomagnetism – which could not be developed before other crucial parts (in this case the superconducting quantum interference device, SQUID, as a sensitive magnetic field detector) had been invented and further developed.

This cooperation between physicians, scientists, and engineers has proved itself in the past to be effective. It is a necessary condition for the continuing development of new methods or more sophisticated techniques and instruments. This is of particular relevance for the application of magnetism in medicine. Knowledge in this field is comparatively poor, even in the case of physicists. Specialists working in different fields of science and technology are, as a rule, not familiar with relevant problems in medicine, and as a consequence possible new ideas or solutions

to problems cannot be found until partners from different fields have been introduced to the physical and medical basis of this interdisciplinary topic.

One fundamental intention of this book is, therefore, to impart information about both the state of the art as well as the need for further progress with magnetism in medicine. This can only be done, within the ambit of this book, by means of reference to typical examples. A complete review of all existing contributions in this field would result in an edition of several volumes. We hope that the examples presented are suitable both for initiating cooperation between specialists already working on specific topics, and to encourage a response from newcomers who might contribute original ideas. In our opinion, the successful development of important methods such as functional magnetic resonance imaging (fMRI) and magnetic source imaging (MSI) in recent years is proof enough of the fact that even high-level technologies, which are already in existence, can be essentially improved and expanded as soon as interdisciplinary teams are involved. Moreover, there are also topics for which a level of knowledge has not yet been attained that would enable a "chain reaction" to start and thus accelerate further development. Here, in the language of physicists, a "critical mass" of interdisciplinary cooperating specialists has probably not been achieved.

During the years since the first edition of this book was published, many new developments have been made in the areas of medical research and clinical practice. Therefore, all contributions to the Second Edition have been updated, with most articles having been completely rewritten. Several new topics have been added, including: safety aspects of magnetic fields; fetal magnetography; new MRI techniques for cardiovascular imaging; clinical applications at ultra-high fields; interventional magnetic resonance imaging; concepts, systems, applications and new approaches in diagnostic and therapeutic MR mammography; monitoring of magnetic markers; remote-controlled drug delivery; and magnetic drug targeting.

The editors wish to express their thanks to all authors for their kind cooperation. Our special thanks is given to Mario Liehr and Jürgen Reichenbach for their valuable cooperation in the editorial work. We are also grateful to the Biomagnetic Center at the Department of Neurology, University of Jena for kind support in the preparation of this book.

Jena, September 2006

Wilfried Andrä
Hannes Nowak

List of Contributors

Christoph Alexiou
HNO-Klinik der Universität
Erlangen–Nürnberg
Waldstrasse 1
91054 Erlangen
Germany

Wilfried Andrä
Kernbergstrasse 39
07749 Jena
Germany

Michael Apel
Miltenyi Biotec GmbH
Friedrich-Ebert-Strasse 68
51429 Bergisch Gladbach
Germany

Peter Bachert
Arbeitsgruppe In-vivo-NMR-Spektroskopie
Abteilung Medizinische Physik in der Radiologie (E020)
German Cancer Research Center
Im Neuenheimer Feld 280
69120 Heidelberg
Germany

Roland Bammer
Department of Radiology
Lucas MRS Imaging Center
Stanford University Medical School
1201 Welch Road
Stanford, CA 94305
USA

Dimitri Berkov
INNOVENT e.V. Jena
Prüssingstrasse 27b
07745 Jena
Germany

Jürgen H. Bernhardt
Neureuther Strasse 19
80799 München
Germany

Gunnar Brix
Bundesamt für Strahlenschutz
Abteilung für Medizinische Strahlenhygiene und Dosimetrie
Ingolstädter Landstrasse 1
85764 Oberschleißheim
Germany

John D.M. Campbell
Miltenyi Biotec Ltd.
Almac House
Church Lane, Bisley
Surrey GU24 9DR
United Kingdom

Donald W. Chakeres
Department of Radiology
College of Medicine and Public Health
Ohio State University Hospital
The Ohio State University
630 Means Hall
1654 Upham Drive
Columbus, OH 43210
USA

Michael Eiselt
Institute of Pathophysiology
Friedrich Schiller University
Nonnenplan 2
07743 Jena
Germany

David E. Farrell
Department of Physics
Case Western Reserve University
Cleveland, OH 44106
USA

Roland Fischer
Institut für Medizinische Biochemie
und Molekularbiologie II
Zentrum für Experimentelle Medizin
Universitätsklinikum Hamburg-
Eppendorf
Martinistrasse 52
20246 Hamburg
Germany

Minoru Fujiki
Neurosurgery
Department of Neurosurgical Science
Faculty of Medicine
Oita University
Japan

Peter Görnert
Innovent e.V.
Prüssingstrasse 27 B
07745 Jena
Germany

Urs Häfeli
Division of Pharmaceutics and
Biopharmaceutics
Faculty of Pharmaceutical Sciences
The University of British Columbia
2146 East Mall
Vancouver, B.C. V6T 1Z3
Canada

Birgit Hailer
Innere Midizin II
Philippusstift Essen
Hülsmannstrasse 17
45355 Essen
Germany

Jens Haueisen
Institute of Biomedical Engineering
and Informatics
TU Ilmenau
Gustav-Kirchhoff-Strasse 2
98693 Ilmenau
Germany

Uwe A.O. Heinlein
Miltenyi Biotec GmbH
Friedrich-Ebert-Strasse 68
51429 Bergisch Gladbach
Germany

Rudolf Hergt
Institut für Physikalische
Hochtechnologie e.V. Jena
Albert-Einstein-Strasse 9
07745 Jena
Germany

Karl-Heinz Herrmann
Institute of Diagnostic and
Interventional Radiology
Medical Physics
Friedrich Schiller University
Philosophenweg 3
07743 Jena
Germany

Jürgen Hennig
University Hospital Freiburg
Department of Radiology
Medical Physics
Hugstetter Strasse 55
79106 Freiburg
Germany

Clemens Janz
Zartener Strasse 29
79199 Kirchzarten
Germany

Roland Jurgons
HNO-Klinik der Universität
Erlangen–Nürnberg
Waldstrasse 1
91054 Erlangen
Germany

Werner A. Kaiser
Institute of Diagnostic and
Interventional Radiology
Friedrich Schiller University
Erlanger Allee 101
07747 Jena
Germany

Thomas R. Knösche
Max Planck Institute for Human
Cognitive and Brain Sciences
Muldentalweg 9
04828 Bennewitz
Germany

Olaf Kosch
PTB Berlin, FB 8.2 Biosignale
Abbestrasse 2–12
10587 Berlin
Germany

Andrew C. Larson
Department of Radiology
Northwestern University
Feinberg School of Medicine
448 E. Ontario Suite 700
Chicago, IL 60611
USA

Jonathan S. Lewin
The Russell H. Morgan Department of
Radiology and Radiological Science
School of Medicine
Johns Hopkins University
600 North Wolfe Street
Baltimore, MD 21287
USA

Debiao Li
Radiology and Biomedical Engineering
Cardiovascular MR Research
Northwestern University
448 E. Ontario Suite 700
Chicago, IL 60611
USA

Stefan Miltenyi
Miltenyi Biotec GmbH
Friedrich-Ebert-Strasse 68
51429 Bergisch Gladbach
Germany

Michael E. Moseley
Department of Radiology
Lucas MRS Imaging Center
Stanford University Medical School
Stanford, CA 94305
USA

Nobukazu Nakasato
Department of Neurosurgery
Kohnan Hospital
4-20-1 Nagamachi-Minami
Taihaku-ku
Sendai 982-8523
Japan

Hannes Nowak
Biomagnetic Center
Department of Neurology
Friedrich Schiller University
Erlanger Allee 101
07747 Jena
Germany

Arnulf Oppelt
Schwedenstrasse 25
91080 Spardorf
Germany

Stefan O. R. Pfleiderer
Institute of Diagnostic and
Interventional Radiology
Friedrich Schiller University
Erlanger Allee 101
07747 Jena
Germany

Jürgen R. Reichenbach
Institute of Diagnostic and
Interventional Radiology
Medical Physics
Friedrich Schiller University
Philosophenweg 3
07743 Jena
Germany

Hendryk Richert
INNOVENT e.V.
Prüssingstrasse 27b
07745 Jena
Germany

Joachim Röther
Department of Neurology
Academic Teaching Hospital
Hannover Medical School
Friedrichstrasse 17
32427 Minden
Germany

Ekkehard Schleussner
Department of Obstetrics
Friedrich Schiller University
Bachstrasse 18
07743 Jena
Germany

Petra Schmalbrock
The Ohio State University
Department of Radiology
653 Means Hall
1654 Upham Drive
Columbus, OH 43210
USA

Jürgen Schmitz
Miltenyi Biotec GmbH
Friedrich-Ebert-Strasse 68
51429 Bergisch Gladbach
Germany

Uwe Schneider
Department of Obstetrics and
Gynaecology
Friedrich Schiller University
University Hospital
Bachstrasse 18
07743 Jena
Germany

Axel Schreiber
Siemens AG Medical Solutions
Marketing Magnetic Resonance
Karl-Schall-Strasse 6
91052 Erlangen
Germany

Oliver Speck
Universitätsklinikum Freiburg
Abt. Röntgendiagnostik, Medizin,
Physik
Hugstetter Strasse 55
79106 Freiburg
Germany

Gerhard Stroink
Department of Physics
Dahousie University
Halifax, Nova Scotia B3H 3J5
Canada

Shoogo Ueno
Department of Biomedical Engineering
Graduate School of Medicine
University of Tokyo
7-3-1 Hongo, Bunkyo-ku
Tokyo 113-0033
Japan

Peter Van Leeuwen
Entwicklungs- und Forschungszentrum für Mikrotherapie
Universitätdsstrasse 42
44799 Bochum
Germany

Clifford R. Weiss
The Russell H. Morgan Department of Radiology and Radiological Science
School of Medicine
Johns Hopkins University
600 North Wolfe Street
Baltimore, MD 21287
USA

Christoph Werner
Scharnhorststrasse 2
07743 Jena
Germany

1
Introduction

1.1
The History of Magnetism in Medicine

Urs Häfeli

1.1.1
Origins

Although magnetic effects such as the ''northern lights'' in the northern hemisphere have been observed for thousands of years, it was not until the discovery of iron smelting, at around 1200 BC, that a body of knowledge on magnetism began to develop. The first effects of magnetism were observed when the smelted iron was brought close to the iron oxide in the chemical form of $FeO{\cdot}Fe_2O_3$ (Fe_3O_4), a natural iron ore which came to be known as lodestone or magnetite.

The origin of the term ''magnetite'' is unclear, but two explanations appear most frequently in the literature. In one of these, magnetite was named after the Greek shepherd Magnes, who discovered it when the nails on the soles of his shoes adhered to the ore. In the other explanation, magnetite was named after the ancient county of Magnesia in Asia Minor, where it was found in abundance.

The first treatise on magnetized needles and their properties (see Fig. 1.1) was presented by Petrus Peregrinus in 1289 (Peregrinus, 1269). This treatise clearly documented a number of magnetic properties including that: (1) magnetic forces act at a distance; (2) magnetic forces attract only magnetic materials; (3) like poles repel and unlike poles attract; and (4) north poles point north, and south poles south. Equipped with this knowledge, the medieval Europeans navigated the globe, discovering and conquering countries as they went.

Peregrinus, however, failed to note that the Earth itself is a magnet. Yet it was not until 1600 that this discovery was finally made by William Gilbert, a physician of Queen Elizabeth I. In order to arrive at this conclusion, Gilbert performed numerous experiments that separated hearsay from truth, documenting them in his book *De magnete* along with a summary of the knowledge of the time about magnetism and electricity (Gilbert, 1600). Gilbert's systematic and scientific treatise is considered by many to be one of the first great works in science (Butterfield, 1991) (see Fig. 1.2).

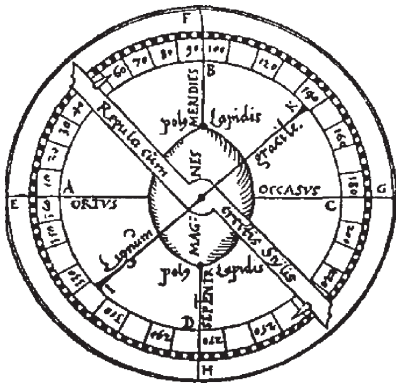

Fig. 1.1. One of Petrus Peregrinus' inventions is this "Astrolabium", an oval lodestone mounted inside a wooden box. The four points of the compass and 360 subunits were painted on the inside of the box. This instrument was placed in a bowl of water to determine the azimuth of the sun, for example, and the angle was read after the astrolabium had stopped moving.

1.1.2 First Medical Uses of Magnets

Thales of Miletus, the first Greek speculative scientist and astronomer (ca. 624–547 BC) was also the first to make a connection between man and magnet. He believed that the soul somehow produced motion and concluded that, as a magnet also produces motion in that it moves iron, it must also possess a soul. It is likely that this belief led to the many claims throughout history of the miraculous healing properties of the lodestone.

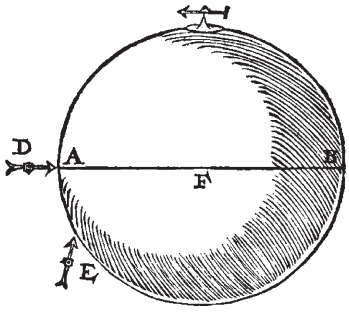

Fig. 1.2. The terrella (spherical lodestone), and the location of its poles from Gilbert's book *De Magnete*. The magnetic versorium (compass needle) on top of the sphere is pointing along a meridian circle; the versorium at D points directly to the center of the sphere and hence to the pole A, in contrast to the versorium at E.

Medical references to magnetism were made by Hippocrates of Cos (ca. 460–360 BC), who used the styptic iron oxides magnetite and hematite to stop bleeding and to control hemorrhage (Mitchell, 1932). Unraveling the true early medical applications of magnetite as described by Hippocrates and his scholars is, unfortunately, complicated by the two meanings of the same term. In particular, magnetite overlaps with the older term ''magnesite'', a magnesium carbonate with laxative properties.

In the first century, Pliny the Elder (23–79 AD), a Roman scholar, collected and condensed the entire knowledge of the time into a thirty-seven-volume encyclopedia, which was used for the next 1700 years. Amid its wealth of information lies a description of the treatment of burns with pulverized magnets. Pliny, however, failed to discriminate fact from fiction, and included much folklore and superstition in his writings. He also theorized that ''sympathies and antipathies'' were the cause of magnetic phenomena, a viewpoint which was shared by Galen of Pergamum (129–199 AD). Galen compared the lodestone to cathartic drugs which attract certain ''qualities'' such as bile and phlegm, to drugs which remove thorns and arrow-points or draw out animal and arrow-tip poisons, and to ''corn'', which is better able to draw water into itself than the sun's heat is to draw water out of it (Brock, 1916). The same attracting properties of lodestone were advocated by Dioscorides of Anazarbos in the first century in his encyclopedia of medical matter. He recommended their external use for ''drawing out gross humors'' (Gunther, 1934).

When magnetite was applied externally, this was either as the unbroken lodestone or in pulverized form, compounded with other ingredients, under the name of Emplastrum Magneticum. The usual practice seems to have been to bind the lodestone or magnetic plaster directly to the affected body part. This technique was thought to be efficacious in treating diseases such as arthritis, gout, poisoning, or baldness. Lodestones were even thought to have strong aphrodisiac potency (Mourino, 1991).

Although most ancient medical uses of magnetite were external, it was also promoted for internal applications by the Egyptian physician and philosopher Avicenna (980–1037 AD). Avicenna recommended using the magnet in doses of one grain as an antidote for the accidental swallowing of poisonous iron (rust). The pulverized magnet was often taken with milk, and the magnetite was believed to render the poisonous iron inert by attracting it and speeding up its excretion through the intestine. This remedy may have worked as a consequence not only of its intended mechanism but also because it induced vomiting (Stecher, 1995). Albertus Magnus (1200–1280), in his book *Mineralia*, recommended the same milk/magnetite mixture for the treatment of edema (Magnus, 1890).

1.1.3
Use of Attracting Forces of Magnets in Medicine

The earliest known account of the surgical use of lodestone is believed to be found in the writings of Sucruta, a Hindu surgeon who lived around 600 BC (Hirschberg,

1899). Sucruta wrote in his book *Ayur-Veda* that the magnet which is in Sanskrit called "Ayas Kanta" – the "one loved by iron" – can be used to extract an iron arrow tip. Sucruta specified that the extraction works best if "... the piece of iron is embedded parallel to the fibers of the tissue, does not contain any ears (barbs), and the opening is wide".

Sucruta's applications were not explored again for almost 2000 years. Gilbertus Anglicus wrote around 1290 in his earliest medical work that "... certain surgeons apply adamant or magnet, if iron is concealed in the flesh" (Anglicus, 1290). This concept was described in a publication from 1640 which suggested that iron in the form of iron filings should be fed to a patient with a hernia (Kirches, 1640). The appropriate placing of an externally attached magnet was then expected to attract the iron, thus drawing in and restoring the protruding intestine. The successful employment of this treatment was reported some years later by surgeon Ambrose Parè, a claim which he asked doubters to take at face value "... on the faith of a surgeon" (Johnston, 1678)!

Other accounts of successful magnetic extractions also appeared, including the description by G. Bartisch. In 1583, he wrote: "A good cream, in case iron, steel or stone had leaped into your eyes, is made from 3 lots of rabbit fat, 1 lot of wax, 1 quint of yellow agstone and 1/2 a quint of lodestone. Such a cream, if applied over your eyes in form of a plaster, helps." Hirschberg, who cited this description (Hirschberg, 1899), added: "Of course, it doesn't help at all!" A similar dose of skepticism may be appropriate in the case reported by Andry and Thouret (Andry, 1779) who reported that around 1635 surgeons succeeded in bringing the point of a knife that had been swallowed accidentally to the integuments with the aid of the emplastrum magneticum. The point was then surgically removed from that location.

Gilbert cited such claims at the end of the 16th century, and categorically denied them: Lodestone ground into a plaster would not be strong enough to extract large iron objects; the same plaster applied to the head could not cure headaches; if lodestone were used with incantations it would not cure insanity; magnets applied to the head would not cause unchaste wives to fall out of bed; and lodestones would draw neither the pain out of gout nor poisons from other parts of the body (Butterfield, 1991). Gilbert believed that the only effect of this plaster was to heal ruptured tissues by drying them out. What magnetite (or iron) was good for, Gilbert maintained, was chlorosis, as patients with this disease were thought to benefit from small doses of iron filings mixed with strong vinegar. Gilbert found that this mixture also helped older patients with splenomegaly, chronic malaria and anemia – diseases not uncommon in the East Anglian swamps of England at that time.

More believable accounts of the applications of magnetic forces – at least in terms of present-day standards – began to appear in the 17th century. For example, Andreas Frisii described a case in which a needle accidentally lodged in the side of a person's throat was removed by a traveling mountebank, as "... fools rush in where wise men fear to tread" (Frisii, 1670):

"When the master permitted the use of water from the spa because of health reasons, a careless maid swallowed a needle which got stuck in the inside of her throat and thus talking became difficult for her. Without doing more damage, the needle moved on to the tonsils and remained visibly stuck there for a total of nine years. Although she could feel the needle, there was no inflammation, but the maid was still afraid of a future disaster. The metal occupied several surgeons, but none of them dared in fear of an even larger misfortune, to pull out the needle by hand. Then, in the 23rd year (= 1623), a man, of the kind who still heal certain diseases even though they do not know much about medicine, appeared. They dare to promise everything to everybody, but nonetheless, their experimental knowledge is quite extensive. The one I am speaking about promised easy relief without complaints and pain. She believed it, and he began, after making an incision with a smooth knife, to pull the skin apart and place the lodestone (not the powder, as was commonly done) directly on the wound. After the ninth day the needle adhered to the stone, and the woman was relieved."

In subsequent years, medical applications of magnets came to include the removal of iron particles embedded in the eye (Quinan, 1886). The magnets used were native, or later, artificial or electromagnets. In 1627, Wilhelm Fabricius of Hildanus (1560–1634), a German physician who practiced medicine in Bern, Switzerland, documented the first case of an iron splinter being extracted from a patient's eye chamber. The following is a translation of the physician's original Latin description, titled "Of a slag splinter stuck in the cornea and its ingenious healing" (Hildanus, 1627):

"A certain farmer from the valley St. Michelis, as they call it, near the Lake of Bienne, named Benedictus Barquin, bought steel from the trader, wanted to choose the best, and therefore beat, as it is commonly done, piece against piece. A splinter from one of them flew into the part of the cornea where the iris is visible, and this not without great pain. The relatives tried to help for several days without any result, and thus pain and inflammation increased. So he finally came on March 5th to see me in Bern. First through sensible nutrition, then through purging of the body using drugs as well as through bleeding (that is to say he had a bloodshot eye), I tried to pull out the splinter, first with instruments and then in other ways. But the splinter was so small, that it wasn't possible to pull it out. Therefore I followed another route and decided to pull out the splinter with the help of a small bag, as I described it earlier in Cent. 4, Observ. 17. But again, I lost oil and work, and my wife came upon by far the most advisable remedy. While I was holding open the eyelid with both hands, she approached the eye with a lodestone, as near as he could endure. We had to repeat this several times (it was necessary to do it like that, since he could not stand the light for long anymore). Finally, the splinter jumped, visible for us all, onto the magnet."

Over the following 300 years, increasingly complex procedures for removing metallic objects from the eye were performed and reported. The second successful case report after Fabricius was described in 1684 in a letter published by the "experienced oculist", Dr. Turberville of Salisbury, England (Turberville, 1684). The physician stated that "A person in Salisbury had a piece of iron, or steel, stuck in the

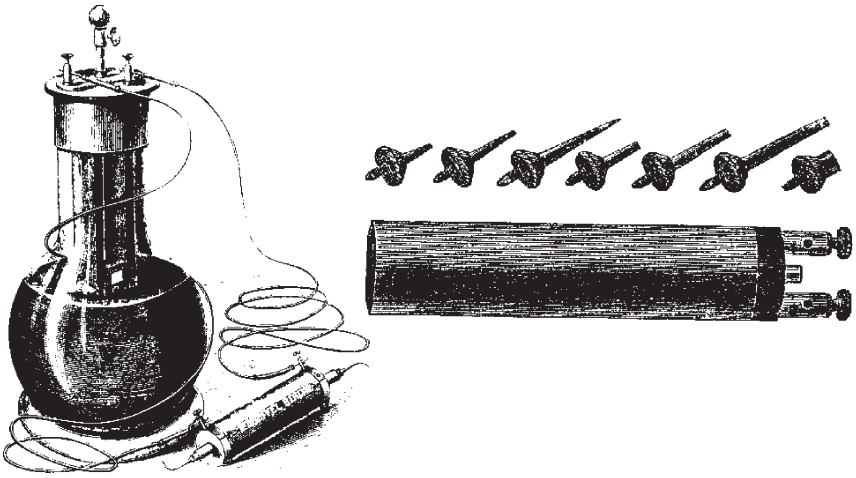

Fig. 1.3. Hand-held electromagnets used for the removal of magnetic objects from the eye. Left: The original Hirschberg magnet. Right: A further development of Dr. Hubbell. The needle-like tip is placed, preferably through the entry wound, as close as possible to the foreign iron or steel particle. The magnet is then turned on and the foreign body pulled out.

iris of the eye, which I endeavored to push out with a small spatula, but could not. But on applying a lodestone, it immediately jumped out.'' Again more than 80 years later, the use of lodestone for eye surgery was reported by Dr. Morgagni in a case involving the cornea (Morgagni, 1761). A more spectacular case involving the removal of iron fragments from behind the iris was reported by Dr. Nicolaus Meyer of Minden, Germany, in 1842. According to Hirschberg, one of the great experts in the field, this was the first case on record for the removal of pieces of iron from the interior of the eye (Hirschberg, 1883). The first case in America, was performed by Dr. Alex. H. Bayly of Cambridge, Maryland (Bayly, 1886). The magnet used in this case was an ''artificial'' or horse-shoe magnet.

Since 1879, the use of magnets has become the established procedure for the removal of magnetic objects from the interior of the eye (Tost, 1992). In that year, Dr. Julius Hirschberg reported the first ophthalmic use of electromagnets (Hirschberg, 1880). His magnet had the shape of an ''electric handmagnet'' and was used like forceps, in close proximity to the foreign metallic objects (see Fig. 1.3). Further developments in electromagnets by the Swiss ophthalmologist Otto Haab led to extractions in which the magnet was placed at greater distance from the eye (Haab, 1892). He used Rühmkorff's apparatus, a 130-kg heavy electromagnet with a small pointed horizontal protruding tip, designed at the Federal Institute of Technology in Zurich. The patient sat in front of the tip with their head fixed in a 90° cone. The cone was then moved by the physician into the extraction position. This magnet produced forces of 11.3 mT ($\sim 10^5$ dyne) at a distance of 5 mm from the tip. Due to the size of this magnet, it was later termed ''the giant magnet'' (Fig. 1.4).

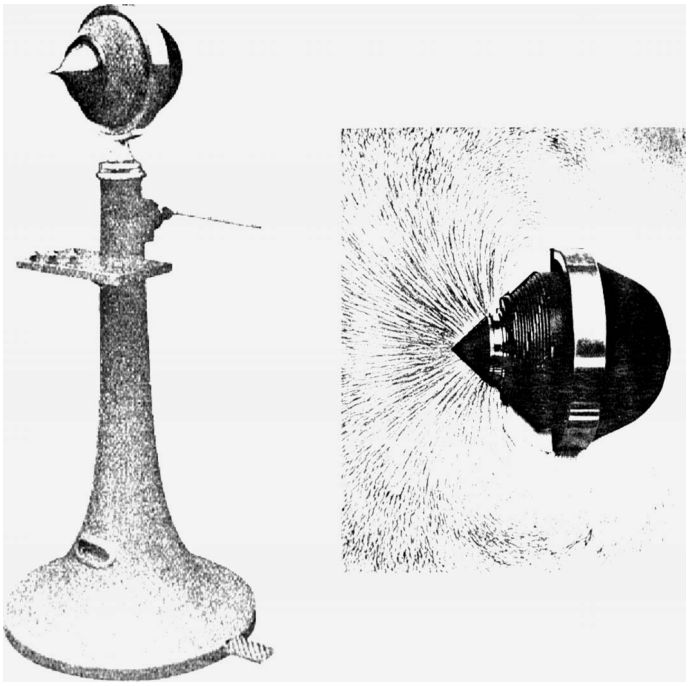

Fig. 1.4. Dr. Haab's giant magnet for the removal of iron or steel foreign bodies from a patient's eyes. The magnetic field lines around the tip of the instrument are shown to the right.

Haab and Hirschberg's different approaches to the removal of magnetic objects from the eye resulted in a 22-year-long (from 1892 to 1914) scientific battle waged through letters and articles. Their views differed with respect to the type of magnet to use, the position of the patient, and the route of removal of the foreign objects. Haab favored the direct removal of small objects through the front of the eye, "der vordere Weg", while Hirschberg preferred removal through the back of the eye, "der hintere Weg". Both methods were known to be associated with peeling of the iris, a serious side effect, although it was not until 1970 that both techniques were shown to be equally risky (Springer, 1970). It is no longer necessary to establish the superiority of either method since the use of magnets to remove objects from the eyes is currently declining, due to advancements in modern eye surgery.

Magnets have been employed to remove iron or steel objects not only from the eyes, but also from other body parts. Swallowed pins and nails are commonly extracted magnetically from the stomachs of unlucky children, and shrapnel drawn from the surface wounds of war, bomb or crime victims. The extraction of a safety pin from a child's stomach is illustrated in Figure 1.5 (Luborsky et al., 1964).

Another interesting approach to render ingested and potentially dangerous metallic objects harmless is seen in the application of magnets in veterinary medicine. Grazing cows often swallow sharp steel objects such as the barbs from barbed wire,

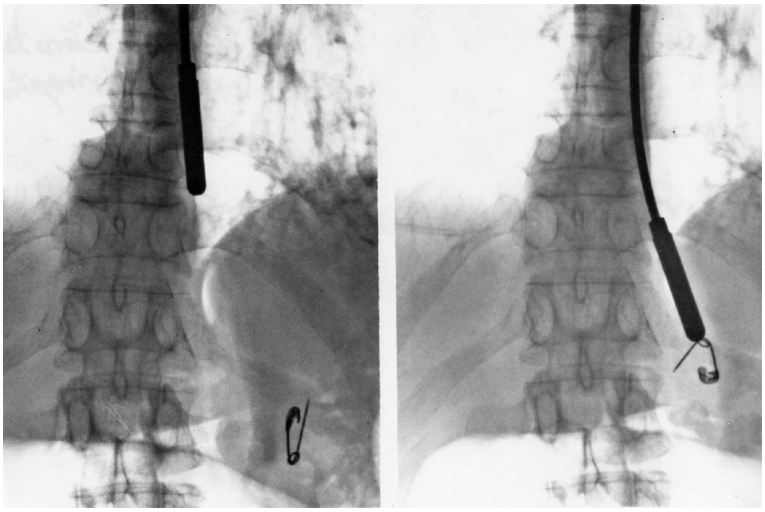

Fig. 1.5. Removal of an open safety pin from a patient's stomach. A probe is "swallowed" by the patient (left) and maneuvered by the physician until the tip is near the rounded end of the pin. When the tip of the probe is magnetized, it attracts the pin (right). With the pin in position, the point is less likely to do damage to the digestive tract as it is pulled out. (Photograph courtesy of F.E. Luborsky; Luborsky et al., 1964).

or pieces of wire from bales of hay. In order to prevent these sharp objects from damaging the stomach and intestinal walls, the cows are forced to swallow a "cow magnet", a 7 cm-long and 1 cm-diameter rod Alnico magnet covered with an anti-corrosive plastic coating. The cow magnet remains in one of the cow's stomachs, where it attracts any steel or iron objects that pass by, rendering them non-dangerous and preventing the so-called "hardware disease". The magnets can be easily retrieved when the cow is slaughtered, and do not appear to have any adverse side effects (Livingston, 1996).

1.1.4
Treatment of Nervous Diseases and Mesmerism

The first person to mention the topical application of a magnet in nervous diseases was Aetius of Amida (550–600 AD), who recommended this approach primarily for the treatment of hysteria, and also for gout, spasm, and other painful diseases. Some five centuries later, abbess Hildegard of Bingen (1098–1179) – who was said to have received the words for her books directly from God – described the use of plants and minerals (stones) for medical purposes and devoted a whole chapter to the lodestone. Her method of using the lodestone was somewhat new, in that the magnet had to be held in the patient's mouth to remedy fits of anger or rage, to make fasting bearable, and to keep lies and maliciousness at bay (Riethe, 1961).

Several hundred years later, the Swiss Theophrastus Bombast von Hohenheim (1493–1541), a doctor and alchemist, reasoned that since magnets have the mysterious power of attracting iron, they should also be able to attract diseases from the body. He was often criticized for his beliefs and was mockingly called "Paracelsus", which means "greater than Celsus" (Celsus was a famous Roman doctor who lived around 25 BC to 50 AD); he finally adopted the name Philippus Aureolus Paracelsus. In his work, *Volumen Medicinae Paramirum*, Paracelsus described exact procedures to transplant diseases from the body into the earth by using a magnet. The choice of magnetic pole was important for these procedures. In his treatment of epilepsy – a disease in which there is "... more nervous fluid in the brain", "... the repulsing pole of a magnet" was "... applied to the head and the spine", and "... the attracting pole to the abdominal region". Paracelsus further extended the use of magnets to leucorrhea, diarrhea and hemorrhages, for which his procedures were often successful. However, the effectiveness of his methods could probably be attributed more to the amazing powers of human imagination than to magnetism.

Reports from England during the 1740s regarding the production of strong artificial (not lodestone) magnets led to renewed interest in the use of strong magnets for healing purposes. It is unclear who was responsible for the introduction of steel magnets, but evidence points to it being either Gowin Knight, a physician; John Canton, a schoolmaster and amateur physicist; or John Michell, an astronomer. The term "horse-shoe magnet", however, came from Michell. One of the people who experimented with the new magnets was Father Maximilian Höll (1720–1792), a Jesuit priest and astronomer at the University of Vienna. In 1774, Höll became friends with the then 40-year-old physician Franz Anton Mesmer, to whom he gave some of these magnets. By applying them to his patients – who mainly had symptoms of hysterical or psychosomatic origin – Mesmer achieved many seemingly miraculous cures.

Mesmer first conjectured that the magnets worked by redirecting the flow of the universal "fluidum" from the atmosphere or the stars to the patients' bodies. He soon discovered, however, that magnets could be replaced by nonmagnetic objects such as paper, wood, stone, and even humans and animals. This led Mesmer to coin the term "animal magnetism" for the fundamental biophysical force he considered responsible for the free flow of fluidum. Disease originated from an "obstructed" flow, which could be overcome by "mesmerizing" the body's own magnetic poles and inducing a "crisis", often in the form of convulsions. The patients' health and "harmony" could thus be restored (Mourino, 1991). A graphic account of the treatment of Mesmer's first patient was given by Macklis (1993).

Mesmer's theories and, probably even more so, his rapidly gained fame soon enraged the medical faculty of Vienna. In 1777, they used the case of Maria Theresia von Paradies as the reason to expel him both from the fraternity of medicine and from the city of Vienna. Maria Theresia was a blind child piano prodigy who regained her sight after being treated by Mesmer. Unfortunately, she simultaneously lost her equilibrium as well as her musical talents. Her parents were angered and demanded that Mesmer stop the treatment. The child's reaction to the suspension of treatment was spectacular, in that she dropped immediately to the floor in convulsions, blind once again.

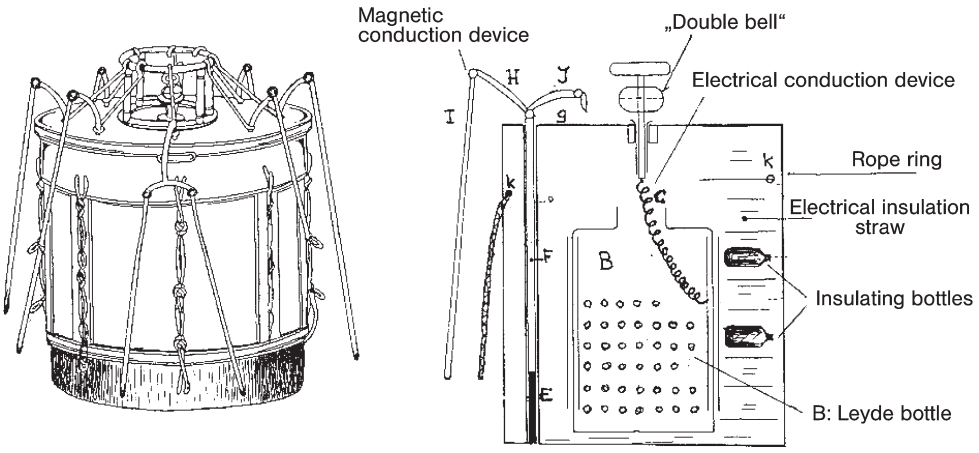

Fig. 1.6. Mesmer's tub, the first medical device from 1780 designed for the biomagnetic treatment of men and women. (Illustration courtesy of Dr. A. Dittmar, Lyon).

Evicted from Vienna, Mesmer went to Paris, where his theories of "animal magnetism" were eagerly embraced. He used his many talents in a curative, psychological way (Darnton, 1972), and his clinic soon became famous for spectacular spiritualistic sessions. In one of his best-known treatments, patients bathed in magnetized water in an oval vessel called the "Baquet de Mesmer" (Mesmer's tub) (see Figs. 1.6 and 1.7).

With time Mesmer's theories evolved from his initial teachings, developing into an empirical psychological healing science, a mix of hypnotism and psychotherapy, imaginative and psychosomatic medicine. Taken up by many healers and quacks, Mesmer's ideas were promoted in many books, and periodicals were soon crowded with reports of the successful treatment of nervous maladies. King Louis XIV of France was skeptical about these reports of animal magnetism and requested an investigation from Benjamin Franklin and Antoine Lavoisier. After having performed 16 different experiments – many of them in a blinded setup – the two scientists showed in 1784 conclusively that magnetism had nothing to do with the reported healings (Shermer, 1997). Many of the beneficial effects attributed to the use of magnets in the treatment of nervous diseases were evidently due to the increased suggestibility of the subjects to whom this novel remedy was applied. In such cases, with the necessary amount of faith, almost anything is a remedy.

Even today, magnets continue to be advertised as health-promoting, and are sold in amazing numbers and in many different forms and shapes for all purposes. Recent advertisements, for example, claim that magnetic bracelets cure headaches, and that magnetic mattresses, shoe inserts, and belts have beneficial health effects by influencing the body's magnetic field. The use of supermagnets (neodymium-iron-boron magnets) is advocated as a pseudo-scientific cancer cure. Some of these interesting claims are described in more detail by Livingston (1996).

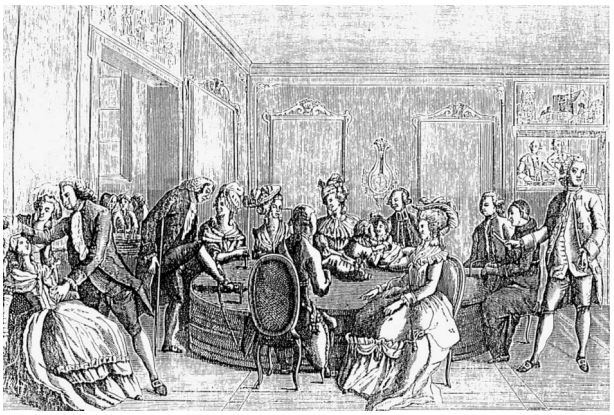

Fig. 1.7. Mesmer's tubs existed in different sizes, with large versions in great demand by the high society and the court of King Louis XVI from France during the 18th century. (Illustration from an engraving from 1779, collection of M. Gaston Tissandier; courtesy of the Lyon Historic Museum of Medicine, University Claude Bernard, Lyon).

1.1.5 Other Medical Uses of Magnets and Magnetism

During the past 20 years, the medical use of magnets has spread to fields as diverse as dentistry, cardiology, neurosurgery, oncology, and radiology, to mention only a few. The scientific advancements that made these new applications possible include the evolution and miniaturization of electromagnets, the development of superconducting electromagnets at Bell Laboratories in 1961, and the introduction of strong permanent magnets made of samarium-cobalt between 1960 and 1970 (McCaig and Clegg, 1987) and of neodymium-iron-boron (NdFeB) in 1983 (Kirchmayr, 1996; Goll and Kronmüller, 2000).

The new, much stronger magnetic materials allowed the construction of miniaturized magnets and electromagnetic coils, the smallest of which is so tiny that it could fit into the tip of a vascular catheter (Hilal et al., 1974). These small catheters permitted intravascular guidance from outside of the body with a strong magnetic field, and have been used clinically both for monitoring intracranial electroencephalograms and for producing electrothrombosis of inoperable arterial aneurysms. Furthermore, with the help of such a catheter, a discrete embolus or an intravascular adhesive can be deposited for the selective occlusion of vascular lesions. In 1979, a magnetically fixable catheter that electrically stimulated the heart was clinically tested in patients with bradycardic arrhythmia, providing temporary pacemaker therapy (Paliege et al., 1979). The design included an electrode almost identical to those of the stimulation catheters, except that its 18 mm-long and 0.9 mm-diameter tip was made from soft iron coated with gold rather than from platinum or iridium-coated NiCr-steel. It was thus ferromagnetic. Using this catheter together with an external magnet, a stable stimulation position was reached in the

Fig. 1.8. (a) The Niobe® system, a magnetic navigation system built by Stereotaxis Inc., St. Louis, Missouri, USA. The system is based on two large permanent magnets that, upon proper rotation and movement, are able to precisely direct a magnet-tipped guide wire (b) or electrophysiology mapping catheter (c) within the patient's vascular system. This system was approved by the FDA in the USA in 2003 for multiple interventional cardiology and electrophysiology procedures.

right auricle of 17 out of 19 patients, and in the right ventricle of 28 out of 32 patients. A more recent report described the successful diagnosis of a complex congenital heart disease through the use of a catheter magnetically guided through a neonate's heart (Ram and Meyer, 1991). As the distance from a baby's heart to the skin above is relatively small, an appropriately placed magnet was able to direct the magnetic catheter tip into the right ventricle, thus allowing for the injection of a contrast agent.

The magnetic guidance of catheters and similar devices in adults requires the use of higher magnetic fields and field gradients than those employed with children. One system which attains the required fields is the magnetic-implant guidance system developed for stereotactic neurosurgery (McNeil et al., 1995a,b). This system made use of very strong superconducting magnets to deliver a small magnetic NdFeB capsule within the brain with an accuracy of 2 mm. The capsule was moved by six independently controlled superconducting coils mounted in a helmet, and described to be used, in the future, to deliver radioactivity, heat, or chemotherapeutic drugs to a tumor in the brain.

During the early 2000s, the company Stereotaxis Inc., in St. Louis, Missouri, USA, further developed this system by replacing the superconducting electromagnets with easier to maintain NdFeB permanent magnets. In this new setup, the magnets are placed in a housing a few meters away from the surgical table. When the patient is ready to undergo the navigation of surgical guidewires and catheters (Fig. 1.8b and c), the two magnets in their housing are rotated into place for magnetic navigation (Fig. 1.8a). The magnetic force vector established under computer

Fig. 1.9. Using an alternating magnetic field of 100 kHz, the magnetic field applicator MFH 300F (MagForce Applications GmbH, Berlin, Germany) is able to induce hyperthermia in tumors containing magnetic nanoparticles. Clinical trials are currently being performed (Jordan et al., 2001; Gneveckow et al., 2005).

and joy stick control by the surgeon then guides a catheter with a magnetic tip to chosen positions in the heart or coronary vasculature. For this purpose, the two magnets can be rotated independently and turned from one side to the other inside their housing, thus establishing precise force vectors with a 360-degree control over the catheter tip and an accuracy within 1 mm. With this system, the company hopes to improve on cardiovascular care through the performance of more complex intravascular procedures. Since 2003, when the FDA approved the Niobe® System, multiple interventional cardiology and electrophysiology procedures can now be performed. These include the placement of a catheter against the wall of a beating heart in order to record its electrical activity and to identify heart tissue that is the source of the arrhythmia. Future applications currently being investigated by Stereotaxis Inc. include the ablation of atrial fibrillation, the repair of chronic total occlusion, the placement of percutaneous cardiac bypass grafts, the repair of mitral valves, and the drug delivery of angiogenic factors to diseased areas in the heart.

Rather than using the magnetic field of a magnet to move ferromagnetic substances to a target location, a patient's own blood flow can accomplish this task. An externally applied magnet which produces a strong local magnetic field can then be employed to stop these magnetic substances at or in the target organ (e.g., a tumor). The magnetic substances – preferentially in the form of nanospheres or microspheres – thus become concentrated in the target area. The spheres, which can be filled with either chemo- or radiotherapeutic drugs, then

produce their effects either by releasing the drug or by blocking the vessels and capillaries (embolization) (Poznansky and Juliano, 1984).

In addition to the embolization effect, the application of selective radiofrequency heating (similar to a microwave) to the area containing the magnetic microspheres can increase the tumor cell killing even further. First results of this approach using ferrosilicone were reported in 1976 by Rand et al. The systemic toxicity of this method is very low (Barry et al., 1981); furthermore, it can be combined with chemoembolization, as carried out by Sako for the treatment of liver tumors (Sako et al., 1985).

Developments by Jordan and Chan led to the current "magnetic fluid hyperthermia" (MFH) application of single domain, dextran-coated magnetite nanoparticles in tumors (Chan et al., 1993; Jordan et al., 1993). Since 2003, Jordan has been conducting a clinical Phase II trial of a combined magnetic hyperthermia and radiation therapy (Jordan et al., 2001; Gneveckow et al., 2005) using the magnetic field applicator MFH 300F built by his company MagForce Applications GmbH in Berlin, Germany (Gneveckow et al., 2004). The magnetic field applicator (Fig. 1.9) runs at 100 kHz and produces a magnetic field strength of up to 18 kA m^{-1} in a cylindrical treatment area of 20 cm diameter. The first clinical results were presented in 2004 at the 5th International Conference on the Scientific and Clinical Applications in Lyon, France. Eight patients had been treated for cervix ($n = 2$), rectal, and prostate ($n = 2$) carcinoma, chondrosarcoma, rhabdomyosarcoma, and liver metastasis. The magnetic particles were injected locally directly into the tumors. The treatment, which increased the tumor temperature to 43–50 °C, took 60 min per session and was repeated from two to eleven times. No additional applications of magnetic particles were necessary after the initial injection. The magnetic fluid hyperthermia was very well tolerated, and none of the patients stopped the treatment. There was no pain and no burns, but some discomfort was felt due to excessive tumor heating (transpiration, heat sensation). Of the eight patients, six showed local control with no recurrent growth of the tumor, while the other two showed complete remission (at 9 and 14 months after treatment, respectively). These results are very promising, however, and this topic will be discussed further in Chapter 4, Section 4.6.

In the field of dentistry, magnets are most commonly applied to aid in the retention of oral and maxillo-facial prostheses. The first treatment in orthodontics was reported in Holland in 1953 by Dr. Crefcoeur (Duterloo, 1995), since when magnets have been used for the treatment of unerupted teeth and tooth movement, as well as for the expansion, fixed retention, and correction of an anterior open bite. It seems that a prolonged constant force exerted by implanted rare-earth magnets provides effective tooth movement (Daskalogiannakis et al., 1996).

Other retention applications include the use of small rare-earth magnets to keep eyelids closed during sleep in patients suffering from facial paralysis or, conversely, to keep lids open during waking hours in patients with drooping eyelids, such as those with muscular dystrophy.

Magnetic intrauterine devices (IUD) for use in contraception have recently been developed (Livesay, 1987). The nonmagnetic versions of such devices often have a

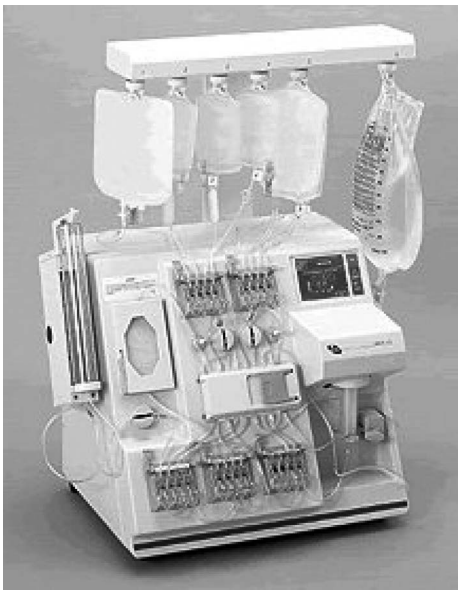

Fig. 1.10. The Isolex® 300i Magnetic Cell Selection System is the only FDA-approved product in the USA specifically for removing tumor cells in stem cell transplants.

string which extends from the uterus into the vagina; this is used by the gynecologist to remove the device. However, some studies have suggested that this string provides an entry path for bacteria and other organisms, and increases the chances of uterine infections. The addition of a small rare-earth magnet to the IUD allows for the string to be omitted. The IUD's correct position can be detected magnetically from the outside and removed using an extractor.

A recent *ex-vivo* application of magnetism in medicine is the purification of bone marrow from tumor cells with magnetic microspheres. In this procedure, the bone marrow is extracted from the patient prior to the use of conventional cancer therapy. Following high-dose treatment with radiotherapy and/or chemotherapy, the patient is rescued with an autologous bone marrow transplantation. In order to ensure that the patient's own bone marrow is free of cancer cells at the time of transplantation, a purification procedure is performed. This procedure, which was developed during the early 1980s and uses monoclonal anti-tumor antibodies conjugated to magnetic polystyrene microspheres, has now become standard (Treleaven et al., 1984; Treleaven, 1988). An initial purification system based on this technique, the Isolex 300i from Baxter (Fig. 1.10), was approved by the FDA and introduced into general therapy in 1999.

The medical use of magnets is not confined to treatment approaches, but also extends to the most powerful modern diagnostic methods such as positron emission tomography (PET) and magnetic resonance imaging (MRI). In PET, magnets

are used in a cyclotron to produce short-lived radioisotopes such as ^{15}O. These radioisotopes, when injected into a patient and imaged with the PET system, allow determination of the biodistribution and biochemical functioning of different organs and tissues. In contrast, MRI utilizes the magnetic properties of the elements, and is used extensively for three-dimensional, noninvasive scans of the patient's body; indeed, it is currently the most important diagnostic method available. The history, principle and applications of MRI are covered extensively in Chapter 3.

1.1.6
The Influence of Magnetic Fields on Man

The human body is composed of atoms of different elements surrounded by water molecules. These atoms react to magnetic and electric forces and fields, and this may lead to, for example, a net-nuclear magnetization of a person when placed in a clinical MRI machine. It is therefore easy to imagine that magnetic and electromagnetic forces could alter physiologic functions, induce effects, or influence the organism in either a positive or negative way. Although the extent and importance of these phenomena has been under investigation for the past 100 years, the effects observed have generally been minimal and seldom statistically significant. A report of the American National Research Council which examined more than 500 studies spanning 17 years of research concluded, in 1996, that "No conclusive evidence shows that exposures to residential electric and magnetic fields produce cancer, adverse neurobehavioral effects, or reproductive and developmental effects" (National Research Council, 1997). A more succinct overview, but with the same conclusions, was provided by Tenforde (2003).

When investigating magnetic effects on humans, two different magnetic field "types" are generally distinguished: (1) a static magnetic field, which exists around a large magnet; and (2) a magnetic field that is pulsed at frequencies higher than 10 Hz, often abbreviated as EMF (electromagnetic fields). The study of these effects is termed "biomagnetism", some sub-fields of which are highly controversial, while others have already been established in medical applications (see Chapter 2).

Most scientists agree that static magnetic fields of up to 10 Tesla have no obvious effects on long-term plant growth, mouse development, body temperature, or brain activity (Barnothy et al., 1956; Barnothy and Barnothy, 1958; Maret et al., 1986). Such conclusions echo findings made more than a century ago, at which time, Mr. Kennelly – the chief electrician at the Edison Laboratory – wrote, after exposing a volunteer to 27 000 times the magnetic field of the Earth, that, "... the human organism is in no wise appreciably affected by the most powerful magnets known to modern science; neither direct nor reversed magnetism exerts any perceptible influence upon the iron contained in the blood, upon the circulation, upon ciliary or protoplasmic movements, upon sensory or motor nerves, or upon the brain." (Peterson and Kenelly, 1892) (Fig. 1.11).

The lack of any apparent effects of strong magnetic fields on humans placed near powerful magnets does not imply that there are no effects at all. It would

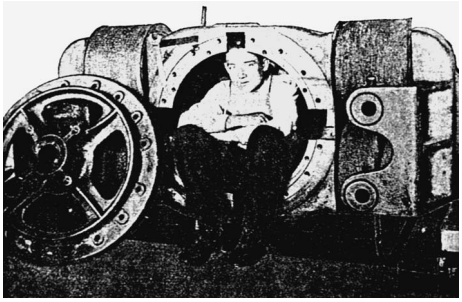

Fig. 1.11. Field magnet used in the studies of magnetic effects on dogs at the Edison laboratory (humans were not mentioned in the original legend!). The powerful attraction of bolts and chains is noticeable. The circular door at the side was made from brass.

also be foolish to conclude that humans have no magnetosensitive organs. During the past years, evidence has been mounting that not only do pigeons (Keeton, 1971), bees (Kirschvink et al., 1992a) and fin whales (Walker et al., 1992) possess magnetic receptors, but humans might also (Kirschvink et al., 1992b). Chains of magnetite particles similar to those known from magnetic bacteria and algae have been found – chains which supposedly are either a part of, or form the magnetosensitive organ itself. Several research investigations have been conducted in an attempt to show that humans have a ''magnetic sense''. One study reported an experiment in which students were driven around blind-folded and then asked to point in the direction of their dormitories. Those students who used only their natural ''magnetic sense'' had a higher success rate than those whose ''magnetic sense'' had been deceived by the field of a magnet attached to their heads (Baker, 1989). Clearly, further research is needed in this area as the results are often contradictory and suggest several interpretations.

Research indicates that humans are sensitive to small changes in magnetic field gradients, but not to the overall magnetic field (Rocard, 1964). Evidence supporting this has come from studies of the dowser reflex. A dowser, a person holding firmly onto a divining rod (see Fig. 1.12) will, under certain physical conditions, experience a force which results in an involuntary upward or downward movement of their rod. To skeptics the movement appears illusory, to believers it appears magical, but the effect has been consistently reported over the past 70 years by a number of authors. In the most-often performed experiment, a group of dowsers was made to walk along the same stretch of street. At points within 1 or 2 m of each other, they all had their divining rods pulled down to the earth.

Magnetic field measurements have shown that the dowser reflex occurs when the dowser passes through a region where the Earth's magnetic field is not entirely uniform. This field anomaly produces a magnetic field gradient, which must exceed 0.1 mOe m^{-1} (8 mA m^{-2}) to be detected. The speed with which the dowser

Fig. 1.12. Dowser holding a divining rod while searching for underground water. (Illustration from Abbé de Vallemont's *Treatise on the divining rod*, Paris, 1693).

passes through this field gradient also influences their magnetic reception. The dowser must pass through a 0.1 mOe m^{-1} field gradient within at least 1 s in order to detect it. Furthermore, the detection level can be increased by adding up the small differences in field gradients. Higher magnetic field gradients, however, lead to saturation and can only be detected by moving faster. Of additional interest is Rocard's notion that although most people are sensitive, a good dowser has a more accurate and rapid reflex than the bad dowser.

Physiological explanations of the dowser reflex have included the physiological induction of magnetic moments, electromagnetic currents, and nuclear magnetic resonance. None of these possibilities has, however, been able to account convincingly for the phenomenon, and thus the search for an explanation continues.

Electromagnetic machines produce fields and field gradients which are constantly changing and which have been found to influence humans. The earliest experiments to test the effects of these fields using humans were performed at the end of the 19th century. D'Arsonval's experiments were among the most spectacular (Rowbottom and Susskind, 1984). In one of these experiments, a person was completely enclosed in a large solenoid resembling a cage, and insulated from all contact with it (Fig. 1.13). Owing to the high-frequency oscillating magnetic field within the solenoid, strong currents were induced within the subject's body, and

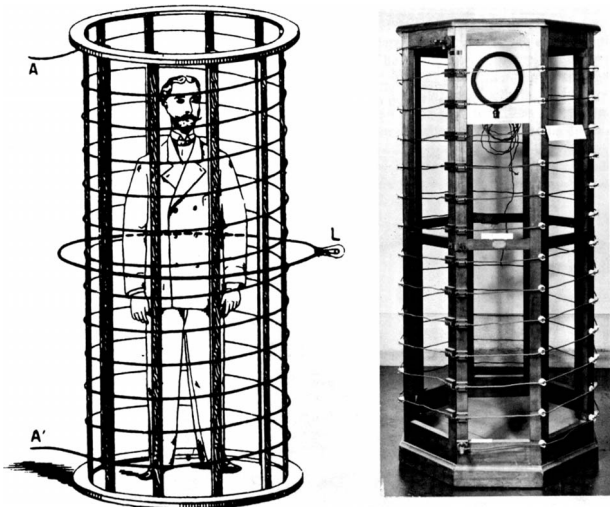

Fig. 1.13. D'Arsonval's great solenoid or cage for auto-conduction in which the person is insulated from all contact with current-carrying wire. The photograph shows the cage actually used by D'Arsonval in 1893 for his experiments.

although neither pain nor any other sensation was felt, a lamp held in the person's hands became incandescent during the procedure. D'Arsonval called this method of applying high-frequency currents to man "autoconduction".

As the 20th century began, the serious investigation of the physiologic consequences of electromagnetic fields became tainted by association with quack science and the pseudo-technology of electromedicine. Dr. Albert Adams (1863–1924), one of the controversial therapists applying electromedicine, was named "Dean of 20th century charlatans" by the American Medical Association. Adams postulated that each organ system and each patient were tuned to a characteristic electromagnetic wavelength. It should therefore have been possible to diagnose medical conditions and to deliver therapy to individuals hundred of miles away simply by using a properly tuned, radio-based device. This therapy was called "physiologic frequency manipulation", and it aroused public interest in bioelectricity and electromagnetic physiologic effects. The science community gradually lost interest in bioelectricity, but before its fall from grace, the groundwork was laid for such major clinical applications as electroconvulsive therapy, cardioversion, and transcutaneous nerve stimulation, all of which are discussed in greater detail in Chapter 4.

Between 1930 and 1960, the physiological and biological effects of electromagnetic fields were studied only minimally. Research accomplished by the small group of investigators who continued working in this area was reviewed comprehensively by Barnothy during the late 1960s (Barnothy, 1964, 1969). Although the design of many of those studies performed up to this time was flawed, some of their results have been confirmed by more stringent research. For example, results

recently endorsed in a report by the National Research Council (1997) support previous findings that electromagnetic fields induce changes in the brain's electroencephalographic (EEG) activity (Bell et al., 1991), produce measurable changes in polypeptide synthesis in salivary glands (Goodman and Henderson, 1988), and are able to influence the levels of calcium and melatonin in cells exposed to high-level fields (Graham et al., 1996). Additionally, recent double-blind studies have confirmed the effects of low-frequency pulsed electromagnetic fields greater than 0.5 mT on growth induction in bone. Indeed, their use is now the treatment of choice for certain recalcitrant problems of the musculoskeletal system, including salvage of surgically resistant nonunions in children and adults and chronic refractory tendinitis (Bassett, 1989).

Available data indicate that humans are susceptible to alternating electromagnetic fields. Epidemiological studies even suggest health effects attributable to relatively small magnetic fields such as those found underneath a high-voltage line (Jauchem, 1995). The report of the National Research Council, for example, acknowledged a 1.5-fold higher incidence of childhood leukemia in homes situated close to high-voltage power lines, though the examined studies failed to show a statistically significant association between exposures and disease (National Research Council, 1997). Unless new theories for these effects are proposed on the grounds of molecular mechanisms, it will be very difficult to either prove or disprove any association between disease and the small magnetic fields produced near electric devices, machines and power lines. Even the electromagnetic fields in heavily industrialized regions amount only to a few tenths of one mTesla, which is less than 1% of the ambient terrestrial magnetic field. Most experts would not anticipate any serious effects related to these additional magnetic fields.

Current laboratory investigations employ more sophisticated techniques, more sensitive instruments and more refined statistical methods than ever before. When combined with our deeper understanding of magnetic resonance patterns in tissues (see Chapter 3), this vastly improved instrumentation should provide a strong base from which to improve our understanding of the electromagnetic field effects at the cellular and molecular levels. In time, this will likely lead to the introduction of new, magnetism-based medical techniques for diagnosis and therapy.

References

Andry, Thouret (1779). Observationes et recherches sur l'usage de l'aimant en Medicine. *Trans. de la Societe royale de medecine*, **tom iii**, 53.

Anglicus, G. (1290). Compendium Medicinae tam Morborium universalium quam particularum.

Baker, R.R. (1989). *Human Navigation and Magnetoreception*. Manchester University Press, Manchester.

Barnothy, M.F. (1964, 1969). *Biological effects of magnetic fields*. 1 and 2 Vols. Plenum Press, New York.

Barnothy, J.M. and Barnothy, M.F. (1958). Biological effect of a magnetic field and the radiation syndrome. *Nature*, **181**, 1785–1786.

Barnothy, J.M., Barnothy, M.F., and Boszormenyi-Nagy, I. (1956). Influence of magnetic field upon the leucocytes of the mouse. *Nature*, **177**, 577–578.

Barry, J.W., Bookstein, J.J., and Alksne, J.F. (1981). Ferromagnetic embolization. *Radiology*, **138**, 341–349.

Bassett, C.A. (1989). Fundamental and practical aspects of therapeutic uses of pulsed electromagnetic fields (PEMFs). *CRC Crit. Rev. Biomed. Eng.*, **17**, 451–529.

Bayly, A.H. (1886). *Md. Med. J.*, Feb. 13.

Bell, G.B., Marino, A.A., Chesson, A.L., and Struve, F.A. (1991). Human sensitivity to weak magnetic fields. *The Lancet*, **338**, 1521–1522.

Brock, A.J. (1916). *Galen on the natural faculties.* English translation edn. William Heinemann, London.

Butterfield, J. (1991). Dr. Gilbert's magnetism. *The Lancet*, **338**, 1576–1579.

Chan, D.C.F., Kirpotin, D.B., and Bunn, P.A. (1993). Synthesis and evaluation of colloidal magnetic iron oxides for the site-specific radiofrequency-induced hyperthermia of cancer. *J. Magn. Magn. Mater.*, **122**, 374–378.

Darnton, R. (1972). F.A. Mesmer. In: *Dictionary of Scientific Biography.* Scribner, New York, pp. 325–328.

Daskalogiannakis, J. and McLachlan, K.R. (1996). Canine retraction with rare earth magnets: An investigation into the validity of the constant force hypothesis. *Am. J. Orthod. Dentofacial Orthop.*, **109**, 489–495.

Duterloo, H.S. (1995). Historic publication on the first use of magnets in orthodontics. *Am. J. Orthod. Dentofacial Orthop.*, **108**, 15A–16A.

Frisii, A. (1670). *The Kerckringii Spicilegium Anatomicum.* Amsterdam.

Gilbert, W. (1600). *De Magnete, Magneticisque, Corporibus, et de Magno Magnete Tellure; Physiologica Nova (On the lodestone, magnetic bodies, and on the great magnet the earth)*. Dover (Paperback republication, 1991, Translation: Mottelay, P.F.), New York.

Gneveckow, U., Jordan, A., Scholz, R., Bruss, V., Waldofner, N., Ricke, J., Feussner, A., Hildebrandt, B., Rau, B., and Wust, P. (2004). Description and characterization of the novel hyperthermia- and thermoablation-system MFH 300F for clinical magnetic fluid hyperthermia. *Med. Phys.*, **31**, 1444–1451.

Gneveckow, U., Jordan, A., Scholz, R., Eckelt, L., Maier-Hauff, K., Johannsen, M., and Wust, P. (2005). Magnetic force nanotherapy: with nanoparticles against cancer. Experiences from three clinical trials. *Biomedizinische Technik*, **50** (Suppl. 1), 92–93.

Goll, D. and Kronmüller, H. (2000). High-performance permanent magnets. *Naturwissenschaften*, **87**, 423–438.

Goodman, R. and Henderson, A.S. (1988). Exposure of salivary gland cells to low-frequency electromagnetic fields alters polypeptide synthesis. *Proc. Natl. Acad. Sci. USA*, **85**, 3928–3932.

Graham, C., Cook, M.R., Riffle, D.W., Gerkovich, M.M. and Cohen, H.D. (1996). Nocturnal melatonin levels in human volunteers exposed to intermittent 60 Hz magnetic fields. *Bioelectromagnetics*, **17**, 263–273.

Gunther, R.T. (1934). *The Greek herbal of Dioscorides.* University Press, Oxford.

Haab, O. (1892). Die Verwendung sehr starker Magnete zur Entfernung von Eisensplittern aus dem Auge. *Ber. dtsch. ophthal. Ges.*, **22**, 163–172.

Hilal, S.K., Michelsen, W.J., Driller, J., and Leonard, E. (1974). Magnetically guided devices for vascular exploration and treatment. *Radiology*, **113**, 529–540.

Hildanus, G.F. (1627). Observationum and Curationum Chirurgicarum Centuria V. Frankfurt.

Hirschberg, J. (1880). *British Medical Journal*, 776.

Hirschberg, J. (1883). Ueber die Magnet Extraction von Eisensplittern aus den Augeninnern. *Berlin Klin. Wochenschrift*, Jan., No. 5.

Hirschberg, J. (1899). *Geschichte der Augenheilkunde.* 12 Vols., 2nd edn. Engelmann, Leipzig.

Jauchem, J.R. (1995). Alleged health effects of electromagnetic fields: the misconceptions continue. *J. Microw. Power Electromagn. Energy*, **30**, 165–177.

Johnston (1678). Translation of Ambrose Parè's work.

Jordan, A., Wust, P., Fahling, H., John, W., Hinz, A., and Felix, R. (1993). Inductive heating of ferrimagnetic particles and magnetic fluids: physical evaluation of their potential for hyperthermia. *Int. J. Hyperthermia*, **9**, 51–68.

Jordan, A., Scholz, R., Maier-Hauff, K., Johannsen, M., Wust, P., Nadobny, J., Schirra, H., Schmidt, H., Deger, S., Loening, S.A., Lanksch, W., and Felix, R. (2001). Presentation of a new magnetic field therapy system for the treatment of human solid tumors with magnetic fluid hyperthermia. *J. Magn. Magn. Mater.*, **225**, 118–126.

Keeton, W.T. (1971). Magnetic interference with pigeons homing. *Proc. Natl. Acad. Sci. USA*, **68**, 102–106.

Kirches (1640). Ars Magnesia.

Kirchmayr, H.R. (1996). Permanent magnets and hard magnetic materials. *J. Phys. D: Appl. Phys.*, **29**, 2763–2778.

Kirschvink, J.L., Kuwajima, T., Ueno, S., Kirschvink, S.J., Diaz-Ricci, J., Morales, A., Barwig, S., and Quinn, K.J. (1992a). Discrimination of low-frequency magnetic fields by honeybees: Biophysics and experimental tests. *Soc. Gen. Physiol. Ser.*, **47**, 225–240.

Kirschvink, J.L., Kobayashi-Kirschvink, A., and Woodford, B.J. (1992b). Magnetite biomineralization in the human brain. *Proc. Natl. Acad. Sci. USA*, **89**, 7683–7687.

Livesay, B.R., et al. (1987). Proceedings, 9th International Conference on rare earth magnets and their applications.

Livingston, J.D. (1996). *Driving force: The natural magic of magnets*. 1st edn. Harvard University Press, Cambridge, US.

Luborsky, F.E., Drummond, B.J., and Penta, A.Q. (1964). Recent advances in the removal of magnetic foreign bodies from the esophagus, stomach and duodenum with controllable permanent magnets. *Am. J. Roentg. Rad. Ther. Nucl. Med.*, **92**, 1021–1025.

Macklis, R.M. (1993). Magnetic healing, quackery, and the debate about the health effects of electromagnetic fields. *Ann. Intern. Med.*, **118**, 376–383.

Magnus, A. (1890). *Opera Omnia*, **V**, August Borgnet, Paris.

Maret, G., Kiepenheuer, J., and Boccara, N. (1986). *Biophysical effects of steady magnetic fields*. Springer Verlag, Berlin.

McCaig, M. and Clegg, A.G. (1987). *Permanent magnets*. Pentech Press, London.

McNeil, R.G., Ritter, R.C., Wang, B., Lawson, M.A., Gillies, G.T., Wika, K.G., Quate, E.G., Howard, M.A., and Grady, M.S. (1995a). Characteristics of an improved magnetic-implant guidance system. *IEEE Trans. Biomed. Eng.*, **42**, 802–808.

McNeil, R.G., Ritter, R.C., Wang, B., Lawson, M.A., Gillies, G.T., Wika, K.G., Quate, E.G., Howard, M.A. and Grady, M.S. (1995b). Functional design features and initial performance characteristics of a magnetic-implant guidance system for stereotactic neurosurgery. *IEEE Trans. Biomed. Eng.*, **42**, 793–801.

Mitchell, A.C. (1932). Chapters in the history of terrestrial magnetism. *Terrestrial Magnetism and Atmospheric Electricity*, **37**, 326, 347.

Morgagni, J.B. (1761). De Sedibas et acausis morborum per anatomen indagatis. Lib. 1, Let. xiii., c. 21–22.

Mourino, M.R. (1991). From Thales to Lauterbur, or from the lodestone to MRI: Magnetism and Medicine. *Radiology*, **180**, 593–612.

National Research Council (1997). *Possible Health Effects from Exposure to Residential Electric and Magnetic Fields*. National Academy Press, Washington.

Paliege, R., Volkmann, H., and Andrä, W. (1979). Magnetische Lagefixierung einschwemmbarer Elektrodenkatheter zur temporären Schrittmachertherapie. *Deutsches Gesundheitswesen*, **34**, 2514–2518.

Peregrinus, P. (1269). *Epistola Petri Peregrini de Maricourt ad Sygerum de Foucaucourt, Militem, De Magnete*. Privately published, Italy.

Peterson, F. and Kennelly, A.E. (1892). Some physiological experiments with magnets at the Edison Laboratory. *N. Y. Med. J.*, **56**, 729–732.

Poznansky, M.J. and Juliano, R.L. (1984). Biological approaches to the controlled delivery of drugs: a critical review. *Pharmacol. Rev.*, **36**, 277–336.

Quinan, J.R. (1886). The use of the magnet in medicine. *Md. Med. J.*, **5** (Jan), 460–465.

Ram, W. and Meyer, H. (1991). Heart catheterization in a neonate by interacting magnetic fields: a new and simple method of catheter guidance. *Cathet. Cardiovasc. Diagn.*, **22**, 317–319.

Rand, R.W., Snyder, M., Elliott, D., and Snow, H. (1976). Selective radiofrequency heating of ferrosilicone occluded tissue: a preliminary report. *Bull. Los Angeles Neurol. Soc.*, **41**, 154–159.

Riethe, P. (1961). *Hildegard von Bingen: Naturkunde*. Salzburg.

Rocard, Y. (1964). Actions of a very weak magnetic gradient: The reflex of the dowser. In: Barnothy, M.F. (Ed.), *Biological Effects of Magnetic Fields*. Plenum Press, New York, pp. 279–286.

Rowbottom, M. and Susskind, C. (1984). *Electricity and medicine: History of their interaction*. 1st edn. San Francisco Press, San Francisco.

Sako, M., Hirota, S., and Ohtsuki, S. (1985). Clinical evaluation of ferromagnetic microembolization for the treatment of hepatocellular carcinoma. *Ann. Radiol.*, **29**, 200–204.

Shermer, M. (1997). Mesmerized by magnetism. *Sci. Am.*, **287**, 41.

Springer, S. (1970). *Beitrag zur Frage der Magnetoperation am Auge unter besonderer Berücksichtigung des methodischen Vorgehens*. Med. Fak. University Halle, Germany.

Stecher, G.T. (1995). *Magnetismus im Mittelalter: Von den Fähigkeiten und der Verwendung des Magneten in Dichtung, Alltag und Wissenschaft*. Kümmerle Verlag, Göppingen.

Tenforde, T.S. (2003). The wonders of magnetism. *Bioelectromagnetics*, **24**, 3–11.

Tost, M. (1992). 100 Jahre Riesenmagnet. *Aktuelle Augenheilkunde*, **17**, 158–160.

Treleaven, J.G. (1988). Bone marrow purging: an appraisal of immunological and non-immunological methods. *Adv. Drug Del. Rev.*, **2/3**, 253–269.

Treleaven, J.G., Gibson, F.M., Ugelstad, J., Rembaum, A., Philip, T., Caine, G.D., and Kemshead, J.T. (1984). Removal of neuroblastoma cells from bone marrow with monoclonal antibodies conjugated to magnetic microspheres. *The Lancet*, **14**, 70–73.

Turberville (1684). Two letters from that experienced oculist, Dr. Turberville, of Salisbury, to Mr. Wm. Musgrave, S.P.S. of Oxon, containing several remarkable cases in physic, relating chiefly to the eyes. *Philosophical Transactions*, **XIV**, No. 164.

Walker, M.M., Kirschvink, J.L., Ahmed, G., and Dizon, A.E. (1992). Evidence that fin whales respond to the geomagnetic field during migration. *J. Exp. Biol.*, **171**, 67–78.

1.2
Basic Physical Principles

Dmitri Berkov

1.2.1
Introduction

"Everything should be done as simple as possible, but not simpler"
(A. Einstein)

"Yes, I knew once," said Rabbit, "but I forgot."
(A.A. Milne, *Winnie the Pooh*)

In this chapter, an attempt will be made to provide an introduction to magnetic phenomena on a reasonable level. But what level do we consider to be reasonable? Clearly, we cannot expect a specialist in medical sciences to have a deep knowledge of the quantum mechanics required for a real understanding of most magnetic phenomena. Yet, at the same time, we cannot hope to explain something really interesting in terms of school-level mathematics and physics (note the quotation by Einstein, above). So, it was decided to introduce most magnetic phenomena using classical electrodynamics starting from Maxwell Equations, and to refer to quantum mechanics only if absolutely necessary – and even in such cases, the text is restricted to a qualitative description of a problem.

On the other hand, this chapter is not intended to serve as a detailed introduction to the classical field theory in general, and magnetism in particular. In fact, this chapter is best suited for those, "who knew it once, but then forgot". For this reason, we expect from the reader: (1) basic skills in the classical theory of fields (mainly definitions and basic properties of gradient, divergence and rotor operators); and (2) physical knowledge on the basic-school-textbook level (force and torque, its relation to the potential energy, concepts of electric and magnetic fields, electric charges and current). We have always tried to derive desired results from the first principles (as far as it is possible in terms of classical physics), but the reader interested only in the final results can simply skip the intermediate transformations. For those, who, in contrast, are interested in more detailed consideration, we cite the corresponding sources at the end of this section.

1.2.2
The Electromagnetic Field Concept and Maxwell Equations

We start with the Maxwell Equations, which form the basis of classical electrodynamics. These equations were derived more than a century ago using experimental facts and theoretical ideas known at that time. Their importance for the subsequent development of physics in general – and studies of electromagnetic phenomena in particular – cannot be overestimated. The prediction of electromagnetic waves based on these equations is only one impressive example. Below, we shall see that virtually all (classical) electromagnetic phenomena can be derived from the four Maxwell Equations. Readers are referred to Feynmann et al. (1963) for a more detailed, yet simple-to-understand consideration of these equations. For a more "theoretical" introduction, the reader is referred to Landau and Lifshitz (1975b).

1.2.2.1
Maxwell Equations in a General Case of Time-Dependent Fields

Let us denote the electric and magnetic fields in a vacuum as $\mathbf{e}$ and $\mathbf{h}$, respectively (small letters are used to distinguish these fields from the corresponding macroscopically averaged fields in condensed matter in Section 1.2.3). We will also use the electric charge and current densities, ρ and $\mathbf{j}$, so that the total charge in the "physically infinitely small" volume dV is $\rho\, dV$ and the total current through the small surface dS is $\mathbf{j}\mathbf{n}\, dS$, where $\mathbf{n}$ is a unit vector normal to this surface. In this notation, the Maxwell Equations in the so-called differential form are (c is the speed of light)

$$\text{rot}\,\mathbf{e} = -\frac{1}{c}\frac{\partial \mathbf{h}}{\partial t} \tag{1.1}$$

$$\text{rot}\,\mathbf{h} = \frac{1}{c}\frac{\partial \mathbf{e}}{\partial t} + \frac{4\pi}{c}\mathbf{j} \tag{1.2}$$

$$\text{div}\,\mathbf{e} = 4\pi\rho \tag{1.3}$$

$$\text{div}\,\mathbf{h} = 0 \tag{1.4}$$

The "differential form" means that Eqs. (1.1) to (1.4) provide the relationship between time-dependent magnetic and electric fields and their time derivatives at one and the same spatial point. Before proceeding with the explanation of the physical sense of Eqs. (1.1–1.4) (and to make this explanation more transparent), the Maxwell Equations should be derived in the integral form.

Considering an open surface S bounded by a contour L and, integrating Eqs. (1.1) and (1.2) over this surface, we obtain

$$\int_s \mathrm{rot}\,\mathbf{e}\,d\mathbf{S} = -\frac{1}{c}\int_s \frac{\partial \mathbf{h}}{\partial t}\,d\mathbf{S} \tag{1.5}$$

$$\int_s \mathrm{rot}\,\mathbf{h}\,d\mathbf{S} = \frac{1}{c}\int_s \frac{\partial \mathbf{e}}{\partial t}\,d\mathbf{S} + 4\pi\int_s \mathbf{j}\,d\mathbf{S} \tag{1.6}$$

According to the Stokes theorem, integrals of the field rotors over the surface S on the left-hand sides can be transformed into the integrals of the fields itself along the surface-bounding contour L. On the right, we can interchange time derivatives and integrations, thus obtaining time derivatives of the total field fluxes Φ through the surface S:

$$\int_s \frac{\partial \mathbf{h}}{\partial t}\,d\mathbf{S} = \frac{\partial}{\partial t}\int_s \mathbf{h}\,d\mathbf{S} = \frac{\partial \mathbf{\Phi}_h}{\partial t} \tag{1.7}$$

and the same for the corresponding term in Eq. (1.6).

Finally, in Eq. (1.6) the integral of the current density over the surface S is clearly the total current through this surface J_S. Summarizing all that, we obtain the first two Maxwell Equations in the integral form

$$\oint_L \mathbf{e}\,d\mathbf{l} = -\frac{1}{c}\frac{\partial \Phi_h}{\partial t} \tag{1.8}$$

$$\oint_L \mathbf{h}\,d\mathbf{l} = \frac{1}{c}\frac{\partial \Phi_e}{\partial t} + \frac{4\pi}{c}J_S \tag{1.9}$$

To obtain the last two required equations, Eqs. (1.3) and (1.4) are integrated over a volume V surrounded by a (closed) surface S, to obtain

$$\int_V \mathrm{div}\,\mathbf{e}\,d\mathbf{V} = 4\pi\int_V \rho\,d\mathbf{V} \tag{1.10}$$

$$\int_V \mathrm{div}\,\mathbf{h}\,d\mathbf{V} = 0 \tag{1.11}$$

The integral of the charge density over the volume V on the right-hand side of Eq. (1.10) is the total electrical charge Q inside this volume. Volume integrals of the field divergences on the left-hand sides can be transformed using the Gauss theorem into the integrals of the fields itself over the surrounding surface S, which provides the integral form of the other two Maxwell Equations

$$\oint_S \mathbf{e}\,d\mathbf{S} = 4\pi Q \tag{1.12}$$

$$\oint_S \mathbf{h}\,d\mathbf{S} = 0 \tag{1.13}$$

Now, we consider the physical sense of these equations. We shall immediately see, that these equations themselves (not to mention their consequences) already contain many fundamental properties of electric and magnetic fields.

The first Maxwell Equation in its differential form (Eq. 1.1) states, first of all, that the electric field can be induced by a changing magnetic field (such that $\partial \mathbf{h}/\partial t \neq 0$). Another property of the electromagnetic field which can be seen from Eq. (1.1) is that in the absence of an electric field (so that rot $\mathbf{e} = 0$) the magnetic field can be only stationary: $\partial \mathbf{h}/\partial t = 0$, or $\mathbf{h} = \mathit{Const}$.

Considering this equation in its integral form (Eq. 1.8), we note that the integral of the electric field over the closed contour is, by definition, the electromotive force along this contour. So this equation is nothing else but the generalized Faraday law: the electromotive force along a closed contour is proportional to the time derivative of the magnetic field flux through this contour.

According to the second Maxwell Equation (1.2), a magnetic field can be created either by a time-dependent electric field [fully analogous to Eq. (1.1)] or by an electric current, the density of which is also present on the right-hand side of the equation. Moreover, this equation implies that any current creates a magnetic field, because if $\mathbf{j} \neq 0$ then rot $\mathbf{h} \neq 0$ which is possible only when the magnetic field itself $\mathbf{h} \neq 0$. We also point out the importance of the opposite signs before the field time derivatives in Eqs. (1.1) and (1.2): the consequence is the existence of electromagnetic waves (Landau and Lifshitz, 1975b).

The integral Eq. (1.9) connects the circulation of the magnetic field over some closed contour with the time derivative of the electric field flux and the total current through the surface bounded by this contour.

The second two Maxwell Equations are also of primary importance. Equation (1.3) is the mathematical expression of the fundamental physical fact that electric charges are sources of the electric field. According to its integral form (Eq. 1.12), the total flux of the electric field through some closed surface is proportional to the total charge inside this surface. The immediate consequence of this equation is the Coulomb law (see next paragraph).

The last equation (Eq. 1.4) can be understood if we compare it with the corresponding equation for the electric field (Eq. 1.3): zero on the right-hand side of Eq. (1.4) means that there are no sources of the magnetic field, there exist no magnetic charges. Consequently the flux of the magnetic field through any closed surface is exactly zero (see Eq. 1.13).

1.2.2.2
Constant (Time-Independent) Fields: Electro- and Magnetostatics

We will very often encounter a situation where nothing (at least on the macroscopic size and time scales) in the system under consideration changes with time. In this case, the electric and magnetic fields produced by such a system are also constant, corresponding time derivatives in the Maxwell Equations vanish, and we arrive at two pairs of decoupled equations which describe electrostatic

$$\text{rot}\,\mathbf{e} = 0 \tag{1.14}$$

$$\text{div}\,\mathbf{e} = 4\pi\rho \tag{1.15}$$

and the corresponding magnetostatic

$$\text{rot}\,\mathbf{h} = \frac{4\pi}{c}\mathbf{j} \tag{1.16}$$

$$\text{div}\,\mathbf{h} = 0 \tag{1.17}$$

phenomena. Indeed, it can be seen immediately from these four equations that in a stationary case there is no connection between magnetic and electric field – a circumstance that has allowed studying magnetism and electricity separately over centuries.

Equation (1.15) immediately leads to the basic law of the electrostatics – the Coulomb law. To see this, let us consider the integral form of this equation (Eq. 1.12). If we place a point charge Q in a center of a spherical surface (with the radius R), then according to Eq. (1.12) the total flux of the electric field through this surface is $\Phi_E = 4\pi Q$. On the other hand, for the charge in a center of a sphere the field $\mathbf{e}$ at each point of the spherical surface is directed perpendicular to this surface (from the symmetry reasons), so that the total flux is given simply by the product of the field magnitude and the surface area: $\Phi_E = 4\pi R^2|\mathbf{e}|$. Comparing it with the previous expression $\Phi_E = 4\pi Q$, we immediately obtain the desired result $|\mathbf{e}| = Q/R^2$.

In a similar fashion, the first equation of magnetostatics (Eq. 1.16) leads to the Biot–Savart law. Namely, in the integral form, Eq. (1.16) reads

$$\oint_L \mathbf{h}\, d\mathbf{l} = \frac{4\pi}{c} J_S \tag{1.18}$$

(compare with Eq. 1.9), where J_S is the total current through the surface S bounded by a contour L. Let us consider a long straight wire carrying a full current J and a circular contour (radius R) around this wire so that the contour plane is perpendicular to the wire and the wire passes through the center of the circle. In this case, according to Eq. (1.18), the circulation of the magnetic field around this contour is $C_H = 4\pi J/c$. And again, from symmetry considerations the field is directed along the circle at each point of it, so that the circulation is the product of the field magnitude and the contour length (i.e., $C_H = 2\pi Rh$). Comparing these two expressions for the field circulation, we obtain the magnetic field of a straight current $h = (2/c)J/R$ – the Biot–Savart law in its simplest form.

1.2.2.3
Electric and Magnetic Potentials: Concept of a Dipole

Maxwell Equations for electro- and magnetostatics have another very important property – they allow the introduction of the so-called scalar (electric) and vector (magnetic) potentials, which greatly simplifies the solution of many practical prob-

lems. In this paragraph, we introduce these important concepts following mainly the route suggested by Landau and Lifshitz (1975b).

In order to introduce a scalar potential for the electric field, we need Eq. (1.14): rot $\mathbf{e} = 0$. According to this equation, we can always find a function ϕ from which the electric field can be evaluated as $\mathbf{E} = -\text{grad}\,\phi$ (a minus sign is chosen for convenience reasons) because for any "good" function $\text{rot}\,\text{grad}\,\phi \equiv 0$. This function ϕ is called the "scalar electric potential", and is very convenient to use because it contains all information about the electrostatic field $\mathbf{e}$. Moreover, being a scalar function, it is much easier to handle than a general vector field. The potential introduced above is not uniquely defined: $\phi' = \phi + C$, where C is an arbitrary constant, gives the same electric field as ϕ, because $\text{grad}\,C \equiv 0$. This additional constant does not really matter, because it is the field itself which has a real physical meaning (because it determines a force acting on the charges); we only need one additional condition to determine this arbitrary constant C. Usually (for finite systems), the constant is chosen so that ϕ tends to zero at the infinity.

The equation for the evaluation of ϕ also follows from the Maxwell Equations. Substituting the relation $\mathbf{e} = -\text{grad}\,\phi$ into the second Maxwell Equation (1.15), we immediately obtain

$$\Delta\phi = -4\pi\rho \tag{1.19}$$

where we have introduced the Laplace operator $\Delta(*) = \text{div}\,\text{grad}(*)$, ($(*)$ represents any function one wants the operator to operate on). This so-called Poisson Equation for the function ϕ allows us to evaluate the electric potential, when the charge distribution in our system and boundary conditions are given. Its solution for the finite system and zero boundary conditions at infinity (i.e., $\phi \to 0$ when we go away from our system) is known: the potential at the point r_0 is

$$\phi(\mathbf{r}_0) = \int_V \frac{\rho(\mathbf{r})}{|\mathbf{r}_0 - \mathbf{r}|} dV \tag{1.20}$$

where the integral is taken over the whole system volume. For a system of discrete charges, Eq. (1.20) transforms into

$$\phi(\mathbf{r}_0) = \sum_i \frac{q_i}{|\mathbf{r}_0 - \mathbf{r}_i|} \tag{1.21}$$

which is the obvious generalization of the Coulomb potential for a single charge.

Equation (1.21) allows us to introduce in a natural way a very important concept of electrostatics – the concept of a dipole moment. Let us choose the origin of our coordinate system inside the system of charges under study and evaluate the scalar potential far away from this system so that for any charge $r_0 \gg r_i$. In this case, we can use the first-order Taylor expansion for a function of many variables $f(\mathbf{r}_0 - \mathbf{r}_i) \approx f(\mathbf{r}_0) - \mathbf{r}_i\,\text{grad}\,f(\mathbf{r}_0)$ to approximate $1/|r_0 - r_i|$: here $f(r_0) = 1/r_0$ and its gradient $\text{grad}(1/r_0) = -\mathbf{r}_0/r_0^3$. So for the potential at a large distance we obtain

$$\phi(\mathbf{r}_0) \approx \frac{1}{r_0}\sum_i q_i + \left(\sum_i q_i \mathbf{r}_i\right)\frac{\mathbf{r}_0}{r_0^3} = \frac{Q}{r_0} + \frac{\mathbf{d}\mathbf{r}_0}{r_0^3} = \phi_p + \phi_{\text{dip}} \tag{1.22}$$

where the total system charge $Q = \sum_i q_i$ and its *dipole moment*

$$\mathbf{d} = \sum_i q_i \mathbf{r}_i \tag{1.23}$$

have been introduced. The first term (ϕ_p) in Eq. (1.22) is simply the Coulomb potential of the point charge Q. It decreases with the distance as r_0^{-1}, and thus dominates the potential for charged systems. This means that if the total system charge is not zero, then the only system parameter which is important to evaluate the field far enough from the system is the magnitude of this charge (and not its distribution inside the system).

However, for a vast majority of physical systems the total charge is exactly zero – otherwise huge Coulomb forces would make our world extremely unstable. For this reason, the first term in Eq. (1.22) is mostly zero and the electric potential of the system at the large distances is dominated by the second term ϕ_{dip}. The only system characteristic which this term depends on is its dipole moment defined by Eq. (1.23). The reason why this moment of the charge distribution is called a ''dipole'' moment is as follows: the simplest system with zero net charge which possesses this moment consists of two charges with the same value and opposite sign – ''two poles''. Such a system itself is also called an electric dipole.

The electric field of a dipole at the distances much larger than its size is (see Fig. 1.14)

$$\mathbf{e}_{\text{dip}} = -\nabla\phi_{\text{dip}} = \frac{3\mathbf{r}_0(\mathbf{d}\mathbf{r}_0)}{r_0^5} - \frac{\mathbf{d}}{r_0^3} = \frac{3\hat{\mathbf{r}}_r(\mathbf{d}\hat{\mathbf{r}}_r) - \mathbf{d}}{r_0^3} \tag{1.24}$$

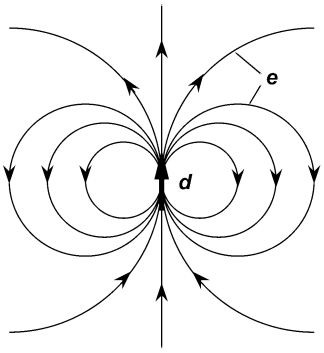

Fig. 1.14. The electric field of a dipole.

Here, ∇ denotes as usual the gradient operator and $\hat{\mathbf{r}}_r = \mathbf{r}_0/r_0$ is the unit vector in the direction of r_0; sometimes one refers to the expression (1.24) as to the field of a "point dipole".

In order to introduce analogous concepts for the magnetic field we need much more effort, and the experience gained by considering the electric field will be very useful (this is the main reason why we spent so much time describing the electric potential and dipole). The main reason why we cannot simply repeat the procedure used above for the magnetic field is evident from Maxwell Equation (1.16): in general, rot $\mathbf{h} \neq 0$, and hence the introduction of a scalar magnetic potential is impossible. However, we can use another Maxwell Equation div $\mathbf{h} = 0$ (1.17), which implies that it is always possible to define such a vector function A that the magnetic field can be evaluated as $\mathbf{h} = \text{rot}\,\mathbf{A}$, because for any vector field $\text{div}\,\text{rot}(*) \equiv 0$. This new vector function is called the magnetic vector potential.

To determine which equation should be used to evaluate A (we are seeking a magnetic version of the Poisson Equation (1.19) for the electric potential), let us substitute the definition $\mathbf{h} = \text{rot}\,\mathbf{A}$ into Maxwell Equation (1.16):

$$\text{rot}\,\mathbf{h} = \text{rot}\,\text{rot}\,\mathbf{A} = \text{grad}\,\text{div}\,\mathbf{A} - \Delta\mathbf{A} = \frac{4\pi}{c}\mathbf{j} \tag{1.25}$$

where Δ denotes again the Laplace operator. To simplify this expression we note that (similar to the electric potential) the magnetic potential is not uniquely defined: $\mathbf{A} \to \mathbf{A} + \nabla f$, where f is an arbitrary scalar function, and gives the same magnetic field $\mathbf{h} = \text{rot}\,\mathbf{A}$ (which is of real physical interest) since $\text{rot}\,\text{grad}(*) \equiv 0$. This use of "degree of freedom" in choosing A enables us to impose one additional restriction on it. It is very convenient to postulate $\text{div}\,\mathbf{A} = 0$, so that the first term in the equation for A (Eq. 1.25) vanishes and we finally obtain

$$\Delta\mathbf{A} = -\frac{4\pi}{c}\mathbf{j} \tag{1.26}$$

This equation resembles the corresponding Eq. (1.19) for ϕ and hence its solution for the vector potential vanishing at the infinity is analogous to Eq. (1.20):

$$\mathbf{A}(\mathbf{r}_0) = \frac{1}{c}\int_V \frac{\mathbf{j}(\mathbf{r})}{|\mathbf{r}_0 - \mathbf{r}|}\,dV \tag{1.27}$$

Equation (1.27) enables us to evaluate the magnetic potential (and hence, the magnetic field) of any system with the known current distribution j.

To continue our consideration we need the following mathematical statement: the average time derivative $\overline{df(t)/dt}$ of any bounded function $f(t)$ is zero. The proof is very simple:

$$\overline{\frac{df(t)}{dt}} = \frac{1}{T_{\text{av}}}\int_0^{T_{\text{av}}} \frac{df(t)}{t}\,dt = \frac{f(T_{\text{av}}) - f(0)}{T_{\text{av}}} \tag{1.28}$$

which tends to zero when the averaging time T_{av} increases, because for bounded $f(t)$ the difference $f(T_{av}) - f(0)$ remains finite.

Now, proceeding in the same fashion as for the electric potential we can derive the magnetic potential at large distances from the finite system of currents. Let us recall the fact that if a particle with the charge q is moving with the velocity $\mathbf{v}$, then the corresponding current density is $\mathbf{j} = q\mathbf{v}$. We shall also use the notation $\bar{f}$ for the quantity f averaged over a large period of time, T_{av}. It is important to note here that T_{av} should be large compared with typical times characterizing the movement of charges in our system. For all practically interesting cases, these typical times correspond to the microscopic charge movements on the atomic scale and hence are extremely small, so that for any reasonable measurement time $T_{av}\overline{df/dt} = 0$ if f remains finite (see above).

For further consideration it is more convenient to use the discrete version of Eq. (1.27), which describes the magnetic potential created by a system of moving particles with charges q_i and velocities v_i:

$$\overline{\mathbf{A}(\mathbf{r}_0)} = \frac{1}{c}\sum_i \overline{\frac{\mathbf{j}_i}{|\mathbf{r}_0 - \mathbf{r}_i|}} = \frac{1}{c}\sum_i \overline{\frac{q_i v_i}{|\mathbf{r}_0 - \mathbf{r}_i|}} \tag{1.29}$$

For large distances $r_0 \gg r_i$, proceeding exactly as for the electric potential, and using the first-order Taylor expansion for $\bar{\mathbf{A}}$, we obtain

$$\overline{\mathbf{A}(\mathbf{r}_0)} = \frac{1}{cr_0}\sum_i \overline{q_i\mathbf{v}_i} + \frac{1}{cr_0^3}\sum_i \overline{q_i\mathbf{v}_i(\mathbf{r}_0\mathbf{r}_i)} = \frac{1}{cr_0}\sum_i \overline{\frac{dq_i\mathbf{r}_i}{dt}} + \frac{1}{cr_0^3}\sum_i \overline{q_i\mathbf{v}_i(\mathbf{r}_0\mathbf{r}_i)} \tag{1.30}$$

The first term, being the average of the time derivative of a bounded function (we study finite systems, so all r_i are finite), vanishes. In order to rewrite the second term in the desired form we use the following trick: we introduce a quantity

$$\frac{1}{2}\frac{d}{dt}\overline{\mathbf{r}_i(\mathbf{r}_i\mathbf{r}_0)} = \frac{1}{2}\overline{(\mathbf{v}_i(\mathbf{r}_i\mathbf{r}_0)} + \overline{\mathbf{r}_i(\mathbf{v}_i\mathbf{r}_0))} = 0$$

which is zero because it is again a full time-derivative of a bounded quantity. Subtracting this zero from each term of the second sum in Eq. (1.30), it can be verified, using elementary vector algebra, that $\bar{\mathbf{A}}$ can be rewritten as

$$\overline{\mathbf{A}(\mathbf{r}_0)} = \frac{1}{2cr_0^3}\sum_i \overline{q_i[\mathbf{r}_0 \times [\mathbf{r}_i \times \mathbf{v}_i]]} = \frac{[\boldsymbol{\mu} \times \mathbf{r}_0]}{r_0^3} = \overline{\mathbf{A}_{dip}} \tag{1.31}$$

where we have introduced the magnetic dipole moment of a system of moving particles (or a system of currents) as

$$\boldsymbol{\mu} = \frac{1}{2c}\sum_i \overline{q_i[\mathbf{r}_i \times \mathbf{v}_i]} = \frac{1}{2c}\sum_i \overline{[\mathbf{r}_i \times \mathbf{j}_i]} \tag{1.32}$$

For a system with a continuous current distribution the definition is

$$\boldsymbol{\mu} = \frac{1}{2c}\int_V \overline{[\mathbf{r} \times \mathbf{j}(\mathbf{r})]}\, dV \tag{1.33}$$

The similarity between the expressions for the electric (see Eq. 1.22) and magnetic potentials (Eq. 1.31) created by corresponding dipoles is obvious. However, it comes even better: the expression for the magnetic field created by a magnetic dipole

$$\mathbf{h}_{\text{dip}} = \frac{3\mathbf{r}_0(\boldsymbol{\mu}\mathbf{r}_0)}{r_0^5} - \frac{\mathbf{d}}{r_0^3} \tag{1.34}$$

is exactly the same as that for the corresponding electric field shown in Figure 1.14 (with the replacement of $\mathbf{d}$ by $\boldsymbol{\mu}$). This similarity explains the name magnetic dipole moment, because otherwise it could not be justified: there exist no magnetic charges, and hence no magnetic poles in any systems.

We point out that the concept of a magnetic dipole plays in magnetism an even more important role than its counterpart – electric dipole – in electricity, because the absence of magnetic charges makes magnetic dipoles, roughly speaking, the most "elementary" object at least in magnetostatics.

The validity of the dipolar approximation (Eq. 1.31) for the exact expression (Eq. 1.27) is based only on the assumption $r_0 \gg r_s$, where $\mathbf{r}_0$ is the distance from the measurement point to the system and $\mathbf{r}_S$ is a characteristic system size. In practice, it is usually sufficient to have $r_0 \geq 10r_s$, because the next term in the Taylor expansion of Eq. (1.27) decreases with the distance as r_0^{-3} (in contrast to r_0^{-2} for the dipole potential).

While concluding this discussion, we would like to mention for those who wish to know more about the subject, that the simplicity in performing some electro- and magnetostatic calculations is by far not the most important reason to introduce scalar and vector potentials ϕ and A. The actual reason is much deeper – these potentials are primary physical concepts and natural variables necessary for the construction of the classical field theory starting from the relativistic invariant action of a charged particle moving in an electromagnetic field (Landau and Lifshitz, 1975b).

1.2.2.4
Force, Torque and Energy in Magnetic Field

To evaluate a total average force acting in a magnetic field on a finite system of moving charges, we can use directly the expression for the Lorentz force $\mathbf{F} = (1/c)q[\mathbf{v} \times \mathbf{h}]$ acting in the magnetic field $\mathbf{h}$ on the charge q moving with the velocity $\mathbf{v}$. For a system of charges we have correspondingly

$$\bar{\mathbf{F}} = \frac{1}{c}\sum_i \overline{q_i[\mathbf{v}_i \times \mathbf{h}_i]}$$

where $\mathbf{h}_i$ is the field at the location point of the charge q_i and the averaging is performed in the same sense as in the derivation of the magnetic dipole potential above. For the homogeneous field (so that $\mathbf{h}_i = \mathbf{h}$ is the same for all particles) this expression can be "greatly simplified": taking such a field out of the sum we can rewrite the force above as

$$\bar{\mathbf{F}} = \frac{1}{c}\left[\left(\sum_i \overline{\frac{d}{dt} q_i \mathbf{r}_i}\right) \times \mathbf{h}\right] = 0$$

It is zero because every term in the sum over charges is again the average time-derivative of a finite quantity (all $\mathbf{r}_i$ are finite). This is a very important result which we would like to formulate explicitly: the total average force acting on any finite body *in a homogeneous magnetic field is zero*.

Let us consider a torque in a homogeneous field. By definition, a torque is a vector product of the particle radius-vector and the force acting on the particle $\mathbf{G} = [\mathbf{r} \times \mathbf{F}]$. Using the expression for the Lorentz force, we have for a system of charges

$$\bar{\mathbf{G}} = \sum_i \overline{[\mathbf{r}_i \times \mathbf{F}_i]} = \frac{1}{c}\sum_i q_i \overline{[\mathbf{r}_i \times [\mathbf{v}_i \times \mathbf{h}]]} = \frac{1}{c}\sum_i q_i \overline{(\mathbf{v}_i(\mathbf{r}_i\mathbf{h}) - \mathbf{h}(\mathbf{r}_i\mathbf{v}_i))} \tag{1.35}$$

The second term in the sum over particles vanishes, because $\overline{\mathbf{r}_i\mathbf{v}_i} = (1/2)\overline{d/dt(r_i^2)} = 0$ for the same reason as usual. To deal with the first term we apply the same trick as in the transition from Eq. (1.30) to Eq. (1.31): we subtract from this term a zero quantity written in the form

$$0 = \frac{1}{2}\overline{\frac{d}{dt}\mathbf{r}_i(\mathbf{r}_i\mathbf{h})} = \frac{1}{2}\overline{\mathbf{v}_i(\mathbf{r}_i\mathbf{h})} + \frac{1}{2}\overline{\mathbf{r}_i(\mathbf{v}_i\mathbf{h})}$$

After some simple vector algebra we get the desired result

$$\bar{\mathbf{G}} = -\frac{1}{2c}\sum_i q_i \overline{[\mathbf{h} \times [\mathbf{r}_i \times \mathbf{v}_i]]} = [\boldsymbol{\mu} \times \mathbf{h}] \tag{1.36}$$

where $\boldsymbol{\mu}$ is the magnetic dipole moment already familiar to us. Hence, in contrast to the force, the torque acting on a body in a homogeneous magnetic field is not zero.

The next step is the evaluation of the potential energy of a dipole in a magnetic field, whereby we can make use of the previous result for the net torque. We remind the reader that the torque projection on the axis perpendicular to an arbitrary plane (see Fig. 1.15 for the geometry) is given by $G_z = -\partial U/\partial\theta$, where U is the potential energy of the body depending on the angle θ which characterizes the rotation of the body in this plane. From Eq. (1.36) we can see that in the same geometry $G_z = -\mu h \sin\theta$, so that the potential energy can be found as

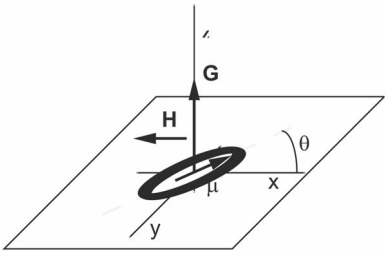

Fig. 1.15. Evaluation of the potential energy of a dipole in a magnetic field (see text for details).

$$U(\theta_0) = -\int_0^{\theta_0} N_z(\theta)\, d\theta = \int_0^{\theta_0} \mu h \sin\theta\, d\theta = -\mu h \cos\theta_0 = -\boldsymbol{\mu}\mathbf{h} \tag{1.37}$$

where by the evaluation of the integral we have omitted (as usual for the potential energy definition) a constant term ($\boldsymbol{\mu}\mathbf{h}$).

This result enables us to evaluate the energy of a magnetic dipole in a magnetic field, assuming that during the rotation in this field the magnitude of a dipole moment is held constant. This is a very important assumption because when the system is rotated in an external field, this field acts on electric charges, the movement of which provides the dipole moment of the system (see Eq. 1.32). Hence the external field, generally speaking, affects the dipole moment of the system and some additional energy source may be needed to hold it constant. A detailed discussion on this subject can be found in Feynmann et al. (1963).

Equation (1.37), or already Eq. (1.36), explains why a compass works. Indeed, a compass needle is a permanent magnet; this means (see Section 1.2.4) that it possesses a magnetic dipole moment which is constant in magnitude due to specific properties of the iron piece from which the compass needle is made. It is well known that any physical system left on its own tries to minimize its energy. And according to Eq. (1.37), the minimal energy of the magnetic dipole in an external field (which in this case is the Earth's magnetic field) is achieved when the magnetic moment points along this field. This causes the compass needle to rotate around its central point until it is directed along the Earth's magnetic field, thus pointing (approximately) in the direction of north.

With Eq. (1.37), we are now able to derive an expression for the force acting on a magnetic dipole in an inhomogeneous magnetic field (remember that in a homogeneous field such a force is zero). Using a standard connection between the force and the potential energy $\mathbf{F} = -\nabla U$, and bearing in mind that in the expression for U only the magnetic field (which is now inhomogeneous) depends on the coordinates, we obtain

$$\mathbf{F} = -\nabla U = -\nabla(\boldsymbol{\mu}\mathbf{h}) = \left(\boldsymbol{\mu}\frac{\partial \mathbf{h}}{\partial x}\right)\mathbf{i} + \left(\boldsymbol{\mu}\frac{\partial \mathbf{h}}{\partial \gamma}\right)\mathbf{j} + \left(\boldsymbol{\mu}\frac{\partial \mathbf{h}}{\partial z}\right)\mathbf{k} = (\boldsymbol{\mu}\nabla)\mathbf{h} \tag{1.38}$$

where we have used the definition of the operator $(\mathbf{a}\nabla)(*)$ to simplify the notation.

In order to understand qualitatively the consequences of Eq. (1.38), let us consider a magnetic dipole directed along the x-axis of our coordinate system, so that $\mu_x \neq 0$ and $\mu_y = \mu_z = 0$. It can be seen from Eq. (1.38) that the only term left in the expression for the force in this case is $F_x = \mu_x(\partial h_x/\partial x)$. In equilibrium, as we already know from Eq. (1.37), the moment is directed along the field, so that $\boldsymbol{\mu}_x$ and $\mathbf{h}_x$ have the same sign. If, say, $h_x > 0$, $\mu_x > 0$ and the field magnitude increases with x, then $(\partial h_x/\partial x) > 0$. In this case $F_x = \mu_x(\partial h_x/dx) > 0$, i.e., the force acting on a magnetic moment in an inhomogeneous field is directed towards the region where this field is larger (in our example in the positive direction along the x-axis). This explains, in particular, the attraction of iron bodies to a permanent magnet – such bodies either already possess a magnetic moment or it is induced by the same magnet and is directed along the external field. Hence, such bodies move towards the region where the field is stronger.

1.2.3
Magnetic Field in Condensed Matter: General Concepts

1.2.3.1
Maxwell Equations in Condensed Matter: Magnetization

For the studies of magnetic phenomena in condensed matter, the original Maxwell Equations (1.1) to (1.4) are not suitable. The reason is that fields, charges and currents appearing in these equations are exact microscopic quantities which contain in principle the whole complexity of electromagnetic processes in condensed matter: movements of single elementary particles on a microscopic space and time scale, corresponding changes of electric and magnetic field, etc. In order to obtain equations which can provide a background for the electrodynamics of condensed matter, we must average Eqs. (1.1) to (1.4) over the microscopic fluctuations mentioned above. This can be done (Landau and Lifshitz, 1975a) using the averaging over a "physically infinitely small volume", which means a volume that is: (1) sufficiently small in the sense that all macroscopic parameters of a body over this volume can be considered as constant; yet (2) at the same time is sufficiently large that it contains a large number of atoms and the averaging over such a volume eliminates fluctuations on the microscopic (atomic) level.

To study magnetic phenomena we need the averaged versions of Eqs. (1.2) and (1.4). Averaging over the "small" volume mentioned above is denoted by angular brackets: $\langle \ldots \rangle$. For historical reasons (which means as usual that (almost?) nobody knows why), the average magnetic field $\langle \mathbf{h} \rangle$ is called *magnetic induction*, and is denoted by $\mathbf{B} : \langle \mathbf{h} \rangle = \mathbf{B}$. So the averaged Eq. (1.4) has the form

$$\operatorname{div} \mathbf{B} = 0 \tag{1.39}$$

If we consider a physical system under stationary conditions (which will be the case almost always), then the average electric field in Eq. (1.2) is constant, so that its time derivative vanishes. Hence, averaging Eq. (1.2) we obtain

$$\text{rot } \mathbf{B} = \frac{4\pi}{c}\langle \mathbf{j} \rangle \tag{1.40}$$

Below, we consider a body for which the integral of the current density over its arbitrary cross-section is zero:

$$\int_S \langle \mathbf{j} \rangle \, d\mathbf{S} = 0 \tag{1.41}$$

which is always true for dielectrics and also true for conducting bodies if the total current is absent. Equation (1.41) enables us to introduce a new vector field $\mathbf{M}$, which is zero outside a body and inside it is connected with the average current density as $\langle \mathbf{j} \rangle = c \text{ rot } \mathbf{M}$ (the factor c is introduced for convenience). Indeed, integrating $\langle \mathbf{j} \rangle$ over the surface S bounded with the contour L outside a body, and applying the Stokes formula, we obtain

$$\int_S \langle \mathbf{j} \rangle \, d\mathbf{S} = c \int \text{rot } \mathbf{M} \, d\mathbf{S} = c \oint_L \mathbf{M} \, d\mathbf{l} = 0$$

because outside a body $\mathbf{M} \equiv 0$. Substituting the average current density written as $\langle \mathbf{j} \rangle = c \text{ rot } \mathbf{M}$ into Eq. (1.40), we obtain the desired result – the second Maxwell Equation for condensed matter:

$$\text{rot } \mathbf{H} = 0 \tag{1.42}$$

where we have introduced a new vector $\mathbf{H}$ as

$$\mathbf{H} = \mathbf{B} - 4\pi\mathbf{M} \tag{1.43}$$

For the same historical reasons (although it is very confusing), vector $\mathbf{H}$ is called the *magnetic field intensity*, but it should be remembered that the average value of the actual (microscopic) magnetic field intensity is denoted as $\mathbf{H}$. We realize (as do most scientists) that such a confusing notation is very annoying, but now it is too late for it to be changed, as very large numbers of books and papers would need to be rewritten, making the whole operation absolutely out of question. Fortunately, we almost never simultaneously encounter $\mathbf{h}$ and $\mathbf{H}$ (or $\mathbf{h}$ and $\mathbf{H}$) in the same problem.

The vector field $\mathbf{M}$ formally introduced above has a very important physical meaning. To determine this, we recall the definition (Eq. 1.33) of the total magnetic moment of a body and rewrite it using $\mathbf{M}$ as

$$\boldsymbol{\mu} = \frac{1}{2c}\int_V [\mathbf{r} \times \langle \mathbf{j} \rangle]\, d\mathbf{V} = \frac{1}{2}\int_V [\mathbf{r} \times \text{rot}\, \mathbf{M}]\, d\mathbf{V} \tag{1.44}$$

Here, the integration volume can be expanded to contain the body inside it because outside a body $\langle \mathbf{j} \rangle = 0$. Rewriting the last integral in Eq. (1.44) as

$$\int_V [\mathbf{r} \times \text{rot}\, \mathbf{M}]\, d\mathbf{V} = \oint_S [\mathbf{r} \times [d\mathbf{S} \times \mathbf{M}]]\, d\mathbf{V} - \int_V [[\mathbf{M} \times \nabla] \times \mathbf{r}]\, d\mathbf{V} \tag{1.45}$$

(the proof of Eq. (1.45) is a very nice exercise in vector analysis), we note that due to the mentioned expansion of the integration volume its bounding surface S is now outside the body where $\mathbf{M} = 0$ and hence the first integral in Eq. (1.45) vanishes. Finally, rewriting a double vector product in the second integral as

$$[[\mathbf{M} \times \nabla] \times \mathbf{r}] = -\mathbf{M}\, \text{div}\, \mathbf{r} + \mathbf{M} = -2\mathbf{M}$$

we obtain the desired result

$$\boldsymbol{\mu} = \frac{1}{2c}\int_V [\mathbf{r} \times \langle \mathbf{j} \rangle]\, d\mathbf{V} = \int_V \mathbf{M}\, d\mathbf{V} \tag{1.46}$$

which shows that $\mathbf{M}$ is simply the density of the magnetic moment of the body (magnetic moment per unit volume). For this reason, $\mathbf{M}$ is called the *magnetization* vector.

1.2.3.2 Classification of Materials According to their Magnetic Properties

The system of Eqs. (1.39), (1.42) and (1.43)

$$\begin{aligned} &\text{div}\, \mathbf{B} = 0 \\ &\text{rot}\, \mathbf{H} = 0 \\ &\mathbf{H} = \mathbf{B} - 4\pi\mathbf{M} \end{aligned} \tag{1.47}$$

which describes the magnetic field in a condensed matter is clearly incomplete, because we still do not know the relationship between $\mathbf{M}$ and $\mathbf{H}$ (or between $\mathbf{B}$ and $\mathbf{H}$) inside a body. This relationship depends heavily on the material from which the body under study is made. Fortunately, for an overwhelming majority of physical substances, the required relationship is very simple:

$$\mathbf{B} = \mu\mathbf{H} \quad \text{or} \quad \mathbf{M} = \chi\mathbf{H} \tag{1.48}$$

where scalar quantities μ and χ are called correspondingly magnetic permeability and susceptibility (so here μ is not the magnitude of the total magnetic moment!). From Eqs. (1.43) and (1.48), the relationship between μ and χ is $\chi = (\mu - 1)/4\pi$. In some cases (e.g., for solid monocrystalline samples), μ and χ appearing in the proportionality relationships (Eq. 1.48) are tensors of a corresponding rank. For ferromagnets, the situation is even more complicated – the relationship between **B** and **H** is nonlinear in general case and depends on the history of the sample.

The magnetic susceptibility is the most important quantity characterizing the magnetic properties of a material (Landau and Lifshitz, 1975a; Kittel, 1986). Namely, it enables us to calculate the magnetization (and hence the magnetic moment) of the body in an external field. If $\chi < 0$, then, as can be seen from Eq. (1.48), the magnetic moment induced by an external field is directed opposite to this field. Such materials are called diamagnets (e.g., inert gases, organic liquids, graphite, bismuth). According to our discussion of the force acting on a body in a nonhomogeneous magnetic field (see text following Eq. 1.38), diamagnetic bodies are repelled from the magnet.

For substances with $\chi > 0$, the induced magnetic moment caused by the external field, points in the same direction as the external field. Materials with positive but very small (for most materials $\chi \sim 10^{-6}$) susceptibility are called paramagnets (some gases, organic free radicals, most metals).

Finally, there exists a narrow class of materials for which magnetic susceptibility defined by Eq. (1.48) – when possible – is huge ($\chi \sim 10^3$, but for some specially prepared materials $\chi \sim 10^6$ can be achieved). Such substances are known as ferromagnets (iron, cobalt, nickel and their alloys, some iron and chromium oxides, etc.). It is evident that these materials are most interesting, for both theoretical studies and practical applications. We shall consider corresponding problems in the final paragraph of this section and again in Section 1.2.4. Here, it should only be mentioned that the relationships (1.48) for ferromagnets are, generally speaking, not valid – the induced magnetic moment is not simply proportional to the external field.

Diamagnetism and paramagnetism can be explained in terms of classical physics (to be more precise, in these terms we can provide explanations which appear reasonable). Let us begin with diamagnetism. The molecules of diamagnetic substances do not have their own magnetic moments; that is, they do not possess a spontaneous moment – a magnetic moment in the absence of an external field. From basic electromagnetism we are familiar with Lenz's law: when we try to change a magnetic flux through a conducting contour, then an electric current in this contour is induced in such a way, that the magnetic field created by this current opposes the change of the external magnetic flux. In other words, if we try to increase a magnetic field inside a closed contour, the magnetic moment associated with the current induced by this external field will be directed opposite to it.

From the classical point of view, electrons moving in atoms or molecules can be considered as currents. Hence, by applying a magnetic field to a body, we try to increase magnetic flux through contours formed by these currents (electron orbits).

According to Lenz's law, this increase leads to changes in corresponding currents, with the result that the magnetic moment of the body induced by this change is directed opposite to the external field, which means diamagnetism.

Molecules of paramagnetic substances already possess their own dipole moments. When we apply an external field, these moments tend to align themselves along this field, because it would minimize their magnetic energy according to Eq. (1.37). The chaotic thermal motion tries to prevent such an alignment, but an average magnetic moment nevertheless appears and points in the field direction, leading to paramagnetism ($\chi > 0$).

1.2.3.3
Mean Field Theory of Ferromagnetism

The existence of ferromagnetism is one of (not very many) the macroscopic phenomena which, in principle, cannot be explained in terms of classical physics. To demonstrate this (Kittel, 1986), it is sufficient to estimate the magnitude of interactions between atomic magnetic moments which are responsible for the ferromagnetic phenomena using the following arguments. The main manifestation of ferromagnetism is the existence of the spontaneous magnetization – that is, a ferromagnetic sample can possess a spontaneous macroscopic magnetic moment. This means that there exists some strong interaction which results in the parallel alignment of all atomic magnetic moments inside the body. The magnitude of this spontaneous magnetic moment decreases if the sample temperature increases, because the thermal movement (thermal fluctuations) acts against any order trying to destroy it. At some temperature, T_c, which depends on the material and is termed the "critical temperature" or "Curie point", the spontaneous magnetization vanishes, and for temperatures $T > T_c$ our body behaves like a paramagnet.

The interaction energy, E_{fm}, for the interaction type responsible for the ferromagnetism should be of the same order of magnitude as the thermal energy at the Curie point: $E_{\mathrm{fm}} \sim kT_c$. The only interaction known in classical physics which could cause the alignment of magnetic moments is the magneto dipole interaction between them. The interaction energy of two magnetic dipoles E_{dip} can be estimated according to Eq. (1.37) as $E_{\mathrm{dip}} \sim \mu H_{\mathrm{dip}}$, where the order of magnitude of the dipole field is (see Eq. 1.34) $H_{\mathrm{dip}} \sim \mu/r^3$, so that $E_{\mathrm{dip}} \sim \mu^2/r^3$. Substituting in this expression typical values of the atomic magnetic moment $\mu \sim \mu_B \approx 10^{-20} erg/Gauss$ (μ_B is a so-called Bohr magneton which is a very convenient unit for measuring atomic magnetic moments) and the interatomic distance ($\sim$ lattice constant in a typical crystal) $r \sim (2 \ldots 3) \cdot 10^{-8}$ cm, we obtain for the interaction energy $E_{\mathrm{fm}} = E_{\mathrm{dip}} \sim 10^{-17} erg$. The value of the Boltzmann constant is $k \approx 1.4 \cdot 10^{-16} erg/K$, so the critical temperature for a typical Ferro magnet should be $T_c = E_{\mathrm{fm}}/k \sim 0.1$ K. This value has nothing in common with the experimentally measured Curie points which, for most ferromagnets, are of the order $T_c \sim 10^3$ K (e.g., for iron, $T_c = 1043$ K). Hence, ferromagnetism cannot be explained by the magneto dipolar interaction, and in classical physics we have nothing else at our disposal.

For many decades, all attempts to develop a reasonable theory of ferromagnetism failed. The first phenomenological theory which succeeded in explaining some aspects of this phenomenon was suggested by Weiss (1907). Weiss postulated that: (1) there exists some (unknown) effective interaction field $\mathbf{H}_E$ which tends to align atomic magnetic moments parallel to each other; and (2) the magnitude of this effective field is proportional to the average magnetization: $\mathbf{H}_E = \lambda\langle\mathbf{M}\rangle$. These assumptions, together with the well-known expression (the so-called Langevin function) for the average magnetization of a system of noninteracting magnetic moments in an external field as a function of the temperature T and field $\mathbf{H}$ (Kittel, 1986) (which in Weiss' theory should be set to the sum of the external $\mathbf{H}_0$ and effective $\mathbf{H}_E$ fields), allowed Weiss to deduce the temperature dependence of the spontaneous magnetization. The result demonstrated a remarkable agreement with experimental data, which was more than acceptable for such a simple theory. However, as mentioned earlier, the existence of a ferromagnetic interaction itself was postulated by Weiss, so the nature of this interaction still required an explanation.

Such an explanation could be provided only after the appearance of quantum mechanics (for an excellent historical review, see Mattis, 1965). Here, an attempt will be made to provide a brief description of how ferromagnetism follows from its basic postulates. (Note: Should the reader feel uncomfortable when confronted with words such as "quantum", the following explanation may be missed out by simply accepting that permanent magnets do exist.)

Ferromagnetism occurs due to the collective behavior of electrons in some materials. Every electron possesses its own angular momentum $\mathbf{S}$ (called spin) which, being expressed in units of the so-called Planck constant (Feynmann et al., 1963; Landau and Lifshitz, 1971) is exactly $S = 1/2$. According to one of the basic principles of quantum mechanics – the Pauli principle – two particles with the spin $1/2$ *cannot occupy one and same quantum state* (Feynmann et al., 1963; Landau and Lifshitz, 1971) which, for our purposes, can be reformulated as "two particles having the same spin direction cannot occupy one and same space region". In other words, if the spins of two electrons do not have the same direction, then the distance between them can, in principle, be very small, but electrons with parallel spins must be "far away" from each other.

This means, in turn, that the energy of a system of two electrons with different spin directions can be very large, because two close electrons exhibit a huge electrostatic repulsion as two charges of the same sign. Moreover, the electrostatic energy of two electrons with parallel spins should be quite small because such electrons must avoid each other due to the Pauli principle (please don't ask when have the electrons read any textbook on quantum mechanics!). For this reason, the state where spins of two electrons – and their magnetic moments! – are parallel is strongly preferred from the energy point of view, because the (average) electrostatic energy in this state is much lower! And this preferred state with all electron spins parallel is exactly what we want – the ferromagnetic state, where all electron magnetic moments are aligned and hence the body possesses macroscopic spontaneous magnetization. The phenomenon just described is called the "exchange in-

teraction'', because its quantitative description is based on the so-called exchange integrals (Landau and Lifshitz, 1971). We realize that this reference does not make the things clearer, but the discussion on what these integrals are and why are they called ''exchange integrals'' is far too complicated to be presented here.

The explanation given above indeed accounts for the Curie temperatures observed experimentally. In this physical picture it is the strong Coulomb (electrostatic) interaction which is responsible for the appearance of ferromagnetism – not the weak magnetodipole forces. If we estimate T_c using the arguments given above, we simply determine the correct order of magnitude.

Of course, this is a very long way from our brief description of this basic idea to a real theory of the ferromagnetic phenomena (to see this, it is sufficient to note that if our arguments would represent the whole truth in all cases, then all substances would be ferromagnetic because there are some electrons in all materials!). But at least we have shown the beginning of the way that can lead to an explanation of ferromagnetism.

1.2.4
Magnetic Field in Condensed Matter: Special Topics

In this section, we consider some special topics dealing mainly (but not only) with ferromagnetic materials: various contributions to the magnetic energy of such materials, magnetic domains and domain walls, hysteresis phenomena, very small (so-called single-domain) ferromagnetic particles, and irreversible magnetic relaxation. Further, we briefly review the energy dissipation in alternating magnetic fields and discuss the possibility of a reconstruction of the magnetization distribution inside a body from magnetic field measurements outside it.

1.2.4.1
Magnetic Energy Contributions

There are several contributions to the total magnetic energy of the body arising from various interaction types between elementary magnetic moments (Chikazumi, 1964; Kittel, 1986; Landau and Lifshitz, 1975a). Below, we restrict ourselves to the phenomenological consideration of these contributions, and always assume (unless mentioned otherwise) that the temperature is much lower than the Curie point of the ferromagnets under study: $T \ll T_c$.

Exchange Energy

The first and most important energy contribution comes from the exchange interaction, which was introduced above as a purely quantum mechanical effect responsible for the alignment of atomic magnetic moments in a ferromagnetic body. The assumption $T \ll T_c$ means that the energy of temperature fluctuations is negligible compared with the exchange energy, so that adjacent magnetic moments are (almost) parallel. Hence, the magnitude of the magnetization $\mathbf{M}$ of the body (mag-

netic moment per unit volume) can be considered as constant $|\mathbf{M}| = M_s$; this constant is called the saturation magnetization of a ferromagnetic material. For low temperatures, only the magnetization direction can be varied inside a body under an additional condition that the distance where the magnetization direction varies considerably is much larger than the lattice constant (or mean interatomic distance for amorphous ferromagnets) of the material. The latter circumstance allows us to introduce a unit vector $\mathbf{m} = \mathbf{M}/M_s$ along the magnetization direction; its spatial distribution fully describes the magnetization structure of a ferromagnetic body.

Let us now write down the phenomenological expression for the exchange energy using simple general arguments (Landau and Lifshitz, 1975a). First, we recall that in ferromagnetic materials the exchange interaction "prefers" the parallel alignment of magnetic moments. This means that the corresponding energy is minimal for the magnetization configuration where all magnetic moments of a body are parallel to each other – the so-called homogeneous magnetization state. We set the exchange energy of such a state to zero, thus using it as a reference point. We also point out that the exchange interaction energy does not change when the magnetization configuration is rotated as a whole with respect to a ferromagnetic body.

We hope that it is clear from the consideration above that the exchange energy density (exchange energy per unit volume) e_{exch} can depend only on the spatial variation of the magnetization, thus being a function of its spatial derivatives $\partial M_i/\partial x_k$, $(i, k = 1, 2, 3)$, where M_i denotes Cartesian components of the magnetization and $x_k = x, y, z$. Moreover, e_{exch} can be a function only of a product of even numbers of such derivatives, because M_i itself and hence – $\partial M_i/\partial x_k$ – changes sign due to the time inversion operation $t \to -t$ (this is because $\mathbf{M} \sim [\mathbf{r} \times \mathbf{v}] = [\mathbf{r} \times d\mathbf{r}/dt]$, see Eq. 1.32) and the energy does not. The simplest expression which satisfies this condition and another condition mentioned above – that the exchange energy is invariant with respect to the rotation of the magnetization configuration as a whole – is

$$e_{\text{exch}} = \frac{1}{2}\sum_{i,k,l} \alpha_{ik}\left(\frac{\partial M_l}{\partial x_i}\right)\left(\frac{\partial M_l}{\partial x_k}\right) \tag{1.49}$$

Here, α_{ik} are the components of a (symmetrical) tensor of exchange coefficients which means that these components form a symmetrical 3×3 matrix. In the simplest case of a crystal with the cubic symmetry $\alpha_{ik} = \alpha\delta_{ik}$ (δ_{ik} is a Kronecker symbol: $\delta_{ik} = 1$ if $i = k$ and zero otherwise) and Eq. (1.49) takes the form

$$\begin{aligned} e_{\text{exch}} &= \frac{\alpha}{2}\sum_i \left(\frac{\partial \mathbf{M}}{\partial x_i}\right)^2 = \frac{\alpha}{2}\left[\left(\frac{\partial \mathbf{M}}{\partial x}\right)^2 + \left(\frac{\partial \mathbf{M}}{\partial y}\right)^2 + \left(\frac{\partial \mathbf{M}}{\partial z}\right)^2\right] \\ &= \frac{A}{2}\left[\left(\frac{\partial \mathbf{m}}{\partial x}\right)^2 + \left(\frac{\partial \mathbf{m}}{\partial y}\right)^2 + \left(\frac{\partial \mathbf{m}}{\partial z}\right)^2\right] \end{aligned} \tag{1.50}$$

where we have introduced a new exchange constant $A = \alpha M_s^2$ using the unit magnetization vector $\mathbf{m}$ defined above. The total exchange energy of a ferromagnetic body can be evaluated, as usual, as an integral of the corresponding density Eq. (1.49) (or Eq. 1.50) over the body volume:

$$E_{\text{exch}} = \int_V e_{\text{exch}}(\mathbf{r})\, dV = \frac{A}{2}\int_V \left[\left(\frac{\partial \mathbf{m}}{\partial x}\right)^2 + \left(\frac{\partial \mathbf{m}}{\partial y}\right)^2 + \left(\frac{\partial \mathbf{m}}{\partial z}\right)^2\right] dV \tag{1.51}$$

Magnetic Anisotropy Energy

As stated above, the exchange energy is invariant under the rotation of the magnetization configuration as a whole, which means that it does not depend on the orientation of the total magnetic moment of the body with respect to its crystallographic axes. On the other hand, there exists a well-known experimental fact that if a sample represents a single crystal, then for many ferromagnets it is much easier to magnetize it in certain directions than in some other directions. This means that there exists an energy contribution which depends heavily on the magnetization orientation relative to crystallographic axes.

This energy contribution is termed the *magnetic anisotropy energy*. Its physical origins are: (1) interaction between atomic magnetic moments with the electric field of a crystal lattice (spin-orbit); and (2) direct magnetic (spin–spin) interaction between atomic moments. For both types of interaction, the corresponding energies depend heavily on the orientation of magnetic moments relative to each other and to the crystal lattice, thus providing the desired orientation dependence of the anisotropy energy. The characteristic magnitude of this energy is usually much less than that of the exchange energy because, according to Eq. (1.32), atomic magnetic moments contain a small factor v/c, where v is the velocity of atomic electrons and c is the speed of light (a more detailed discussion of this question can be found in Landau and Lifshitz, 1975b).

To identify the nature of the anisotropy energy density, it is again sufficient to use general symmetry considerations (Landau and Lifshitz, 1975a). First, the anisotropy energy should depend on the magnetization orientation itself (and not on its spatial derivatives as the exchange energy), which means that it depends directly on the magnetization components m_i $(i = x, y, z)$. The second idea is the same as for the exchange energy – the anisotropy energy density is invariant with respect to the time inversion operation, and hence can be only an even function of such components. Considering first the simplest possible case – products of two m_i-components – we obtain the anisotropy energy density e_{an} in the form

$$e_{\text{an}} = \sum_{i,k} K_{ik} m_i m_k \tag{1.52}$$

where K_{ik} is also a symmetrical tensor.

The remainder of the information required for complete determination of the anisotropy energy density is provided by the symmetry of the crystal lattice of a ferromagnet under study. In the simplest case of a uniaxial crystal, let us choose the z-axis of our coordinate system along the main crystal symmetry axis. For such a crystal there exists only one independent component of K_{ik} for which the corresponding combination of the magnetization components is orientation-dependent (there is also another K-component corresponding to the combination of m-values, namely $m_x^2 + m_y^2 + m_z^2 = 1$ which does not depend on anything). For such crystals, the anisotropy energy density is

$$e_{\text{an}} = K(m_x^2 + m_y^2) = K \sin^2 \theta \tag{1.53}$$

where θ is the angle between the magnetization vector and the z-axis (uniaxial magnetic anisotropy). If $K > 0$, then the anisotropy energy is minimal for the magnetization along the symmetry axis ($\theta = 0$) – ''easy axis'' anisotropy. For $K < 0$, the minimal energy is achieved if the magnetization lies in the plane perpendicular to this axis – the ''easy-plane'' case.

Quite often, terms of higher orders in m_i-values are needed. In hexagonal crystals, such terms only modify Eq. (1.53) as

$$e_{\text{an}} = K_1 \sin^2 \theta + K_2 \sin^4 \theta \tag{1.54}$$

though in cubic crystals they provide the first nonvanishing contributions to the anisotropy energy density at all:

$$e_{\text{an}} = K(m_x^2 m_y^2 + m_x^2 m_z^2 + m_y^2 m_z^2) \tag{1.55}$$

This means that in cubic crystals there exist either three (for $K > 0$, energy minima for m along the cube edges, as in iron) or four ($K < 0$, minima for m along the cube space diagonals, e.g., in nickel) equivalent easy magnetization axis.

Magnetic Dipole Interaction (Demagnetizing) Energy

Another important energy contribution occurs due to the dipolar interaction of magnetic moments: any magnetic dipole creates the magnetic field (Eq. 1.34); if another dipole is placed into this field, then it possesses an energy according to Eq. (1.37). The energy of a system of two dipoles can be written either as an energy of the first dipole $\boldsymbol{\mu}_1$ in the field of the second one at the location point of the first $\mathbf{h}_{21}$, or vice versa:

$$E = -\boldsymbol{\mu}_1 \mathbf{h}_{21} = -\boldsymbol{\mu}_2 \mathbf{h}_{12} \tag{1.56}$$

Rewriting this expression in a symmetrical form

$$E = -\frac{1}{2}(\boldsymbol{\mu}_1 \mathbf{h}_{21} + \boldsymbol{\mu}_2 \mathbf{h}_{12}) \tag{1.57}$$

we can immediately generalize it to a system of many dipoles:

$$E = -\frac{1}{2}\sum_i \boldsymbol{\mu}_i \mathbf{h}_i \tag{1.58}$$

where $\mathbf{h}_i$ means the dipole field created at the location of the i-th dipole by all other dipoles.

What we need now is the continuous version of Eq. (1.58) – that is, the energy of the magnetic dipolar interaction which exists between various parts of a ferromagnetic body if the magnetization configuration of a body $\mathbf{M}(\mathbf{r})$ is known. According to the rules explained in Section 1.2.3, for the transition to the condensed matter case exact microscopic quantities appearing in Eq. (1.58) should be replaced as follows: $\mathbf{h}_i \to \mathbf{B}_i$ and $\boldsymbol{\mu}_i \to \mathbf{M}_i \Delta V_i$. Here, we have subdivided the ferromagnetic body into a (finite) number of small parts with volumes ΔV_i, so that the index i refers now not to the point dipole [as in Eq. (1.58)] but to such a small part of a body. Passing to a continuous limit, we obtain as a generalization of Eq. (1.58) an integral expression

$$E_{\text{dip}} = -\frac{1}{2}\int_V \mathbf{MB}\, dV \tag{1.59}$$

For further use it is more convenient to rewrite the equation using the field $\mathbf{H}$. Substituting the expression $\mathbf{B} = \mathbf{H} + 4\pi\mathbf{M}$ (see Eq. 1.43) into Eq. (1.59) and using the fact that in ferromagnets the absolute value of the magnetization is constant ($\mathbf{M}^2 = M_s^2 = Const$), we obtain

$$E_{\text{dip}} = -\frac{1}{2}\int_V \mathbf{MH}\, dV - 2\pi\int_V \mathbf{M}^2\, dV = -\frac{1}{2}\int_V \mathbf{MH}\, dV - 2\pi M_S^2 V$$

The last term can be omitted because for the given body it is constant, and any constant in an energy expression can be omitted (just choose this constant as a reference point). The final result then is

$$E_{\text{dip}} = -\frac{1}{2}\int_V \mathbf{MH}_{\text{dip}}\, dV \tag{1.60}$$

Here, the notation $\mathbf{H}_{\text{dip}}$ points out that the field in Eq. (1.60) is the *dipole* magnetic field created by all magnetic moments of a body. We also note that despite Eq. (1.60) appearing to be simply a continuous version of Eq. (1.58) in a general case, it is valid for ferromagnets only, because by its derivation we have substantially used the condition $\mathbf{M}^2 = M_s^2 = Const$. The similarity between Eqs. (1.58) and (1.60) arises from the confusing notation mentioned above ($\langle\mathbf{h}\rangle = \mathbf{B}$ and not H!).

The dipole energy (Eq. (1.60), often also called magnetostatic energy) is always non-negative: $E_{\text{dip}} \geq 0$. To prove this, we expand the integration in Eq. (1.60) over

the whole space (we can do this because outside a body $\mathbf{M} = 0$) and replace $\mathbf{M}$ by $\mathbf{M} = (\mathbf{B} - \mathbf{H})/4\pi$ using Eq. (1.43). Then, Eq. (1.60) takes the form

$$E_{\text{dip}} = -\frac{1}{2}\int \mathbf{MH}\, dV = -\frac{1}{8\pi}\int \mathbf{BH}\, dV + \frac{1}{8\pi}\int \mathbf{H}^2\, dV \tag{1.61}$$

Now, we need a so-called orthogonality theorem from vector analysis: a volume integral over the whole space of the product of a divergence-free and a rotor-free field is zero, if these fields are square-integrable functions (which means that integrals of their squares over the whole space are finite). Magnetic induction $\mathbf{B}$ is a divergence-free field (see Eq. 1.39), and magnetic field $\mathbf{H}$ is rotor-free (see Eq. 1.42). It is also easy to show that these fields, when created by any finite system (of permanent magnets or of electrical currents), are square-integrable. For this reason the orthogonality theorem states that the first integral in Eq. (1.61) is exactly zero, thus leading to the final result

$$E_{\text{dip}} = \frac{1}{8\pi}\int \mathbf{H}_{\text{dip}}^2\, dV \tag{1.62}$$

where the integral is taken over the whole space. From Eq. (1.62) it is evident that the magnetostatic energy is always non-negative, and is zero only if the dipolar field is absent at all. To handle the magnetostatic energy and corresponding field more easily, a useful concept of ''magnetic charges'' can be introduced in a following manner. Let us rewrite the condition of Eq. (1.39) $\operatorname{div}\mathbf{B} = 0$ using the relationship of Eq. (1.43) between $\mathbf{B}$, $\mathbf{M}$ and $\mathbf{H}$ as

$$\operatorname{div}\mathbf{H}_{\text{dip}} = -4\pi \operatorname{div}\mathbf{M}$$

Now, by formally defining a scalar quantity ρ_{mag} as

$$\rho_{\text{mag}} = -\operatorname{div}\mathbf{M} \tag{1.63}$$

we arrive at the equation

$$\operatorname{div}\mathbf{H}_{\text{dip}} = 4\pi\rho_{\text{mag}} \tag{1.64}$$

that exactly resembles the corresponding Maxwell Equation (1.3), which states (see discussion in Section 1.2.2.2) that the sources of the electric field are electric charges. This is the reason why the quantity ρ_{mag} defined by Eq. (1.63) is called the density of ''magnetic charges'', despite the fact that real magnetic charges (i.e., charges which would produce the real microscopic magnetic field $\mathbf{h}$) do not exist (see Eq. 1.4). ''Magnetic charges'' introduced above are simply a very convenient mathematical tool both for quick estimation and for detailed calculations dealing with the magnetostatic energy.

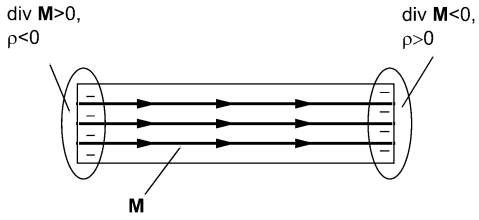

Fig. 1.16. "Magnetic charges" for a uniformly magnetized slab.

Let us present a simple example. We consider a ferromagnetic slab uniformly magnetized along its long axis, as shown in Figure 1.16. Clearly, div $\mathbf{M} = 0$ everywhere except for the regions near the ends of the slab. If we consider a small volume around, say, the slab's right-hand end, then it can be seen that there exists a total nonzero flux of the magnetization $\mathbf{M}$ *into* this volume. According to the definition of the divergence operator (which is, roughly speaking, the average flux of a vector field out of a small volume surrounding the given point divided by this volume), this means that the average divergence of $\mathbf{M}$ for the region near the right-hand slab end is negative (div $\mathbf{M} < 0$) and, according to the definition in Eq. (1.63), there is a net positive "magnetic charge" near this end. By the same token, there exists a negative magnetic charge (we omit "..." here and below, but please do remember that magnetic charges are not real physical charges!) near the left-hand end of the slab (Fig. 1.16).

It follows from Eq. (1.64) that magnetic charges are the sources of the magnetic field $\mathbf{H}$. Thus, from the arguments presented above we can conclude that the magnetic field created by a uniformly magnetized slab (which is a very good model for a bar-shaped permanent magnet) should look exactly like the electric field of a large (not point-like!) dipole because such a slab possesses two magnetic charges with equal magnitude and opposite sign on its ends. And this similarity is indeed present, which is a well-known text-book result.

Now we are also able to explain why the magnetostatic energy is often called the "demagnetizing" energy. For the simplest case of a ferromagnetic layer uniformly magnetized perpendicular to its plane (Fig. 1.17) there exist (according to the pre-

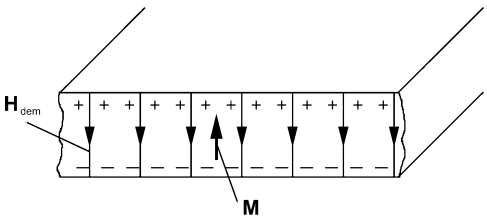

Fig. 1.17. Demagnetizing field of a layer which is uniformly magnetized perpendicular to its plane.

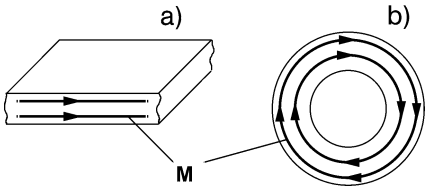

Fig. 1.18. Examples of stray-field-free magnetization configurations.

vious consideration) positive magnetic charges on its upper surface, and negative charges on its lower surface. The field induced by such a system of two charged planes is well known (it looks exactly as the electric field of a flat capacitor) – it exists only inside the layer, is homogeneous (from symmetry reasons), and is directed from positive to negative charges. This means that it is directed opposite to the magnetization thus trying to decrease it. The latter statement is true not only for the example presented above but also in a general case – the magnetic field $\mathbf{H}_{\text{dip}}$ created by some magnetization distribution tries to decrease the corresponding magnetization and hence is called the demagnetizing field [and its magnetostatic energy, Eq. (1.62) – the demagnetizing energy].

The concept of magnetic charges also enables us to determine in which cases there is no demagnetizing energy – we should simply avoid the appearance of such charges, because they create the demagnetizing field and this field always (according to Eq. 1.62) carries energy with them. Magnetic charges (Eq. 1.63) are absent if $\text{div}\,\mathbf{M} = 0$ everywhere – in other words, the charges are absent when the lines of the magnetization field are continuous. Some examples of corresponding magnetization configurations (magnetic layer and core) are shown in Figure 1.18.

1.2.4.2
Magnetic Domains and Domain Walls

Although some materials such as iron, cobalt, and nickel are ferromagnetic, macroscopic samples of, for example, nickel taken without special preparation either do not possess a spontaneous magnetization at all, or their total moment is much less than those expected for the magnetically saturated sample (where all atomic magnetic moments are aligned parallel to each other). The phenomenological explanation of this fact was provided by Weiss at the start of the 20th century in connection with his effective field theory (see above). For polycrystalline samples, Weiss' explanation can be reformulated as follows (Kittel, 1986). The effective field – and hence the directions of the spontaneous magnetization – may be different in different parts of a ferromagnetic sample (e.g., in different crystallites). Then, inside one crystallite all elementary magnetic moments would be parallel, so that a single crystallite would possess a net macroscopic magnetic moment. However, due to different (and essentially random) directions of these moments for various crystallites, the net magnetic moment of the sample would be very small, as is observed experimentally.

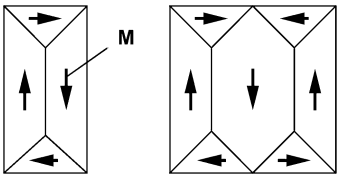

Fig. 1.19. Examples of magnetic domain configurations that do not produce any stray field.

Today, we know that such regions of a ferromagnetic sample where atomic magnetic moments are aligned parallel to each other – the *magnetic domains* – do not necessarily coincide with crystallites (in particular, a single-crystal sample may also consist of many domains). Nonetheless, the idea itself concerning the coexistence of such regions with various magnetization directions inside one sample was correct, and today we have at our disposal many methods which enable the direct observation of such domains (Chikazumi, 1964); subsequently, the so-called domain theory has become a well-established area of magnetism.

The main reason why magnetic domains do exist even in single-crystal samples is the demagnetizing energy (see Section 1.2.4.1). If all magnetic moments of a macroscopic sample were to be aligned, it would possess a huge total magnetic moment inducing a strong magnetic field. According to Eq. (1.62), a system which produces such a field would have a very large demagnetizing energy, making the corresponding fully aligned state energetically unfavorable. For this reason, in the absence of a strong external field (which would cause the alignment of all elementary moments along this field), a macroscopic ferromagnetic sample is usually divided into many domains, the magnetic moments of which are oriented in such a manner that the existence of ''magnetic poles'' or ''magnetic charges'' (which can be considered as sources of a magnetic field **H**) is avoided as far as possible (Fig. 1.19). Another important factor which determines the direction of magnetic moments inside a single domain is the magnetic anisotropy of a crystal: the magnetic moment of a domain should preferably be directed along one of the crystal anisotropy axis of a crystal lattice (to minimize the anisotropy energy).

Domains are separated from each other by boundaries called *domain walls* (Chikazumi, 1964; Kittel, 1986). The parameters of these walls (e.g., their thickness and energy) which are important in applications of magnetic materials can be calculated using the above-mentioned phenomenological domain theory. Although such calculations are far beyond the scope of this chapter, we can try to understand the main dependencies of these parameters on magnetic properties of the material, at least qualitatively.

Let us consider the simplest example of a domain wall – a wall between two domains in a uniaxial crystal where magnetization directions in these domains are opposite (along two opposite directions of the anisotropy axis) (Landau and Lifshitz, 1975a; Kittel, 1986). The transition between these two magnetization directions should be very smooth on the atomic length scale (see Fig. 1.20), because

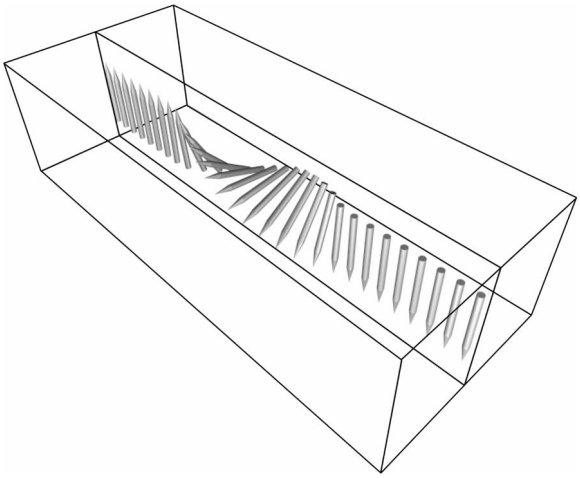

Fig. 1.20. Structure of a 180° domain wall in a uniaxial magnetic material.

abrupt changes in the magnetization direction with a large angle between magnetizations, in two adjacent atomic layers would lead to high exchange energy.

To estimate the width δ_w of this transition region (domain wall) (Landau and Lifshitz, 1975a), we first note that this width should increase with the increasing exchange constant A of the material (see Eq. 1.50) because a larger magnitude of the exchange interaction requires a smoother transition (smaller magnetization angles between two adjacent atomic layers are allowed). On the other hand, the larger the width of such a wall, the larger is its anisotropy energy, because inside a wall, the magnetic moments are not oriented along the (energetically favorable) direction of the anisotropy axes. For this reason, δ_w should decrease with an increasing anisotropy constant K (see Eqs. 1.53 and 1.55). The simplest combination of the constants A and K with the dimension of a length and with the properties just mentioned is $\delta_w \sim \sqrt{A/K}$, and this expression indeed gives the correct dependence of the domain wall width on the magnetic parameters of the material in the situation shown in Figure 1.20.

The corresponding energy dependence can be guessed using the same arguments: the domain wall energy clearly increases with both A and K, because inside a domain wall we have both energy contributions. The corresponding dimensionally correct combination (with the dimension energy per unit area) gives the desired domain wall energy dependence on the material parameters: $E_w \sim \sqrt{AK}$.

1.2.4.3
Magnetization Curves and Hysteresis Loops

If we apply an external field to a demagnetized (i.e., without a net magnetic moment) ferromagnetic sample, then a macroscopic magnetic moment $\mu = \int \mathbf{M}\, dV$ will appear in this specimen. If we increase the field magnitude, then the magni-

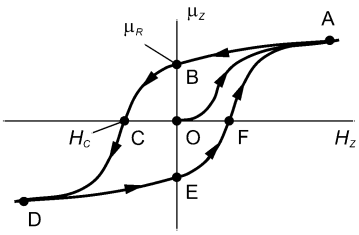

Fig. 1.21. Typical initial magnetization curve $O \rightarrow A$ and hysteresis loop. $A \rightarrow B \rightarrow C \rightarrow D \rightarrow E \rightarrow F \rightarrow A$ for ferromagnetic materials.

tude of this moment also increases until at some certain field value H_{sat}, the so-called saturated state where all microscopic moments of a sample are aligned in the field direction will be achieved. The increase of the field intensity beyond this value will clearly not result in any further moment growth. The process just described is termed the "initial magnetization process"; the corresponding dependence of the total magnetic moment projection μ_z on the field direction (which we will take as a positive direction of the z-axis) – the initial magnetization curve – is shown in Figure 1.21 as the line OA.

Within the domain picture there are two main reasons for such a continuous magnetization growth with the increasing field: (1) rotation of the magnetization inside a domain towards the external field direction; and (2) domain growth – that is, the sizes of those domains whose magnetic moments are oriented approximately along the external field will increase on the cost of less favorably oriented domains. Processes of the first type result in an increase of the anisotropy energy, because magnetic moments are forced to rotate out of the easy-axes directions (along which they were oriented in the absence of the external field). This anisotropy energy growth (see Eqs. 1.53 and 1.55) should be compensated by the decrease of the energy in the external field (Eq. 1.37), which can require quite large field magnitudes. In contrast to the magnetization rotation, the second type of process requires "only" domain wall displacements, and this can be normally be done without major effort. For this reason, the lower part of the initial magnetization curve is usually dominated by the domain growth, whereas its behavior near saturation is determined by the magnetization rotation processes.

One of the most striking phenomena in ferromagnetism is the existence of the magnetization hysteresis or the irreversibility of the magnetization processes (Chikazumi, 1964; Kittel, 1986). This means that if we decrease the field magnitude starting from the saturated sample state A (Fig. 1.21), then the field dependence of the sample magnetic moment (shown by the curve AB) does not coincide with the corresponding dependence for the increasing field (curve OA). When we decrease the field to zero, there is still some substantial net magnetic moment left – this is called the *remanent magnetic moment* μ_R. If we then reverse the field direction and again increase its magnitude, a certain (often quite large) nonzero value of this field H_c (called the coercive force) is needed to bring the net sample moment

to zero (point C in Fig. 1.21). Further increase of the field amplitude in the negative direction also leads to sample saturation in this direction (state D). Finally, by decreasing the field magnitude up to zero and then increasing it again in the positive direction, the magnetization of our sample will follow the curve $D \to E \to F \to A$. So, during a complete field cycle $H_{sat} \to -H_{sat} \to H_{sat}$ the sample magnetic moment changes along the curve $A \to B \to C \to D \to E \to F \to A$, which is called the *hysteresis loop*.

The general reason for such a hysteretic behavior is the existence of so-called metastable states – those system states that correspond to local (and not global) energy minima. Such states are separated from the global minimum and other local minima by energy barriers. If the heights of these barriers are large compared to the temperature (in other words, to the energy of thermal excitations), then the system may remain in such a metastable state for a macroscopically long time, although this particular state does not correspond to the global energy minimum achievable for the given external parameters (in our case, in the given external field).

To make this explanation more transparent, let us consider the simplest example of a single-domain uniaxial ferromagnet placed in an external field with the direction along its easy anisotropy axis. We start from a large value of this field in one direction (which we will call positive) where the sample is saturated. When we reduce the external field to zero, all atomic magnetic moments remain oriented in the same direction, because this direction corresponds to one of the two possible minima of the anisotropy energy, and hence the sample remains saturated (for simplicity, we neglect the demagnetizing field). If we now apply a relatively small external field in the opposite (negative) direction, then a global energy minimum of the system would correspond to the magnetization saturated in this negative direction (because the magnetization direction would coincide not only with one of the two easy axis directions but also with the external field). However, before we applied this small negative field the magnetization was aligned in the positive direction of the anisotropy axis. It still corresponds to a (local) energy minimum because all moments are oriented along the anisotropy axis (see Eq. (1.53) and subsequent discussion) so that in order to switch to the opposite (negative) direction, they must overcome an anisotropy energy barrier.

In this situation the sample magnetic moment will remain oriented in the positive direction until a certain negative field value is achieved where the minimum corresponding to the positive magnetization orientation vanishes. In this field, the magnetic moment will "suddenly" jump to the opposite direction and the hysteresis loop for such a sample will resemble that shown in Figure 1.22. For real systems, where different easy axes as well as structural defects and demagnetizing fields are present, the resulting hysteresis loop can be much more complicated, although the main result – the presence of hysteresis due to the existence of metastable states – remains valid.

As explained above, during the hysteresis cycle metastable states vanish (under the influence of the external field) and the system jumps into energetically lower states. Because the system energy drops after such a jump (transition), an energy

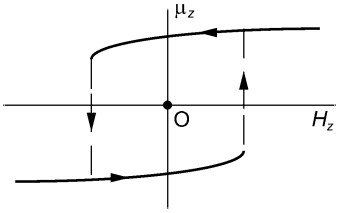

Fig. 1.22. A hysteresis loop for a Stoner–Wohlfarth particle (see text for details).

dissipation occurs when we proceed along the hysteresis loop changing the external field. The total energy loss for one complete hysteresis cycle can be calculated quite easily (Chikazumi, 1964) using general expressions for the energy of a ferromagnetic body in an external field. However, the final result can be guessed without any calculations based again on dimensionality arguments. Namely, we need some characteristics of the hysteresis loop such as that shown in Figure 1.22 which has the dimension of an energy (erg, or in magnetic quantities μH) and is dependent on the magnetization behavior during the whole remagnetization process (because energy losses can occur in principle at any point of the hysteresis loop). The simplest loop characteristic which satisfies these two conditions is its area S_{hyst} in $\mu - H$ coordinates, given by the corresponding curve integral over the complete hysteresis loop:

$$W = \oint \mu_z(H_z)\, dH_z = S_{\text{hyst}} \tag{1.65}$$

This expression, indeed, provides the correct result for the total energy W losses after one complete hysteresis cycle (such as the path $A \rightarrow B \rightarrow C \rightarrow D \rightarrow E \rightarrow F \rightarrow A$ in Fig. 1.21).

1.2.4.4
Single-Domain Particles and Superparamagnetism

Sufficiently small ferromagnetic particles possess an important property which makes them attractive for many applications: particles below a certain size are always in a so called single-domain state (Kneller, 1966; Landau and Lifshitz, 1975a). This means that the whole particle volume is occupied by a single magnetic domain – that is, all atomic magnetic moments of such a particle are aligned parallel to each other (homogeneous magnetization state).

The main reasons for the transition to a single-domain state for very small particles are: (1) the demagnetizing energy which favors closed (noncollinear) magnetization configuration decreases when the particle size decreases; whereas (2) the exchange energy of a nonhomogeneous magnetization configuration increases when the size of such a configuration (which cannot be larger than a particle size) decreases. This means that below a certain particle size, the homogeneous (single-

domain) particle magnetization state which has a relatively large demagnetizing energy but very low exchange energy is energetically more favorable than some closed (multi-domain) magnetization configuration with low demagnetizing but large exchange energy.

To estimate the critical size below which a particle should be single-domain (Landau and Lifshitz, 1975a), let us study the size dependence of the energy contributions mentioned above. The demagnetizing energy of a single-domain state can be easily estimated using Eq. (1.60). The demagnetizing field $\mathbf{H}_{\rm dem}$ inside a homogeneously magnetized spherical particle with the saturation magnetization $\mathbf{M}$ is $\mathbf{H}_{\rm dem} = -4\pi\mathbf{M}/3$ (Kittel, 1986) which, according to Eq. (1.60), leads to the demagnetizing energy of the order $E_{\rm dem} \sim M^2 V$, where V is the particle volume. The exchange energy density of a nonhomogeneous magnetization configuration inside a particle if large ($\sim M$) magnetization changes occur at the length scale of the particle size a is $e_{\rm exch} \sim \alpha M^2/a^2$ (see Eq. 1.50), so that the total exchange energy is $E_{\rm exch} \sim e_{\rm exch} V \sim (\alpha M^2/a^2) V$ (and only large magnetization rotations leading to closed magnetization configurations can provide substantial decrease of the demagnetizing energy).

The particle "prefers" a single-domain state if the corresponding demagnetizing energy is less than the exchange energy of a closed magnetization state inside a particle: $E_{\rm dem} < E_{\rm exch}$, or $M^2 V < (\alpha M^2/a^2) V$. This means that the particle is in a single-domain state if its size is less than $a_{\rm cr} \sim \sqrt{\alpha}$. For materials with a large magnetic anisotropy constant K, one should also take into account the anisotropy energy of a nonhomogeneous magnetization configuration which leads to the estimate $a_{\rm cr} \sim \sqrt{\alpha K/M^2}$. The critical sizes for common ferromagnetic materials such as Fe or Ni are $\sim$10 . . . 100 nm.

The energy calculation for a single-domain particle can be greatly simplified. First, its magnetization configuration can be described by a single vector μ of its total dipole magnetic moment the magnitude of which is simply proportional to the particle volume: $\mu = M_s V$ (M_s is the saturation magnetization of the particle material). The exchange energy (see Eq. 1.50) for the homogeneous magnetization configuration is $E_{\rm exch} = 0$. Further, for a spherical particle its demagnetizing energy does not depend on the moment orientation and hence can be omitted as any constant in the energy expression. Thus, the particle energy can be written as a sum of its magnetic moment energy in the external field $\mathbf{H}_0$ (see Eq. 1.37) and its magnetic anisotropy energy (see, e.g., Eq. 1.53):

$$E = -\mathbf{m}\mathbf{H}_0 M_s V + KV \sin^2(\mathbf{nm}) \tag{1.66}$$

Here, we have used the unit vector $\mathbf{m}$ along the particle magnetic moment and the unit vector $\mathbf{n}$ along the particle anisotropy axis.

The system of uniaxial single-domain particles each of which possesses the energy (Eq. 1.66) is known as a Stoner–Wohlfarth model (Stoner and Wohlfarth, 1948), and is widely used in fine magnetic particle theory due to its (apparently) simple properties. One of its most important features is the existence of a magnetization hysteresis in a collection of such particles (see the corresponding explana-

tion in Section 1.2.4.3). Due to the simple energy expression (Eq. 1.66) for a single particle, many magnetic characteristics of the noninteracting Stoner–Wohlfarth model such as initial susceptibility, permanent magnetization and coercive force can be computed either analytically or by very transparent numerical calculations (Kneller, 1966).

Another interesting property of fine particle systems is that, above a certain temperature T_{sp}, such a system behaves like a paramagnetic body, although T_{sp} is still much lower than the Curie point T_c for the corresponding ferromagnetic material. To understand this behavior (Kneller, 1966), let us consider a system of uniaxial particles with the energies described by Eq. (1.66).

In the absence of an external field the magnetic moment of each particle has two equivalent equilibrium positions (states) along two opposite directions of the anisotropy axis. These states are separated by the energy barrier, with height equal to the maximal possible anisotropy energy: $E_{an}^{max} = KV$. If the system temperature is sufficiently low such that the thermal activation energy kT is much less than this barrier height, then the magnetic moment of each particle will (almost) forever stay in one of these two states depending on the previous system history (i.e., in which direction a strong external field was applied, say, several years ago). However, for sufficiently high temperatures $T > T_{sp}$, thermal transitions between the two equilibrium states may occur on the observable time scale so that after some time each moment can be found with equal probabilities in one of these two states.

For such temperatures the total magnetic moment of a fine particle system in the absence of an external field is zero (as for paramagnetic and diamagnetic substances), because each moment can be oriented with equal probabilities in two opposite directions. When a small external field is applied, then the moment orientation along that direction of the anisotropy axis that has the smallest angle with this field is preferred and the system demonstrates a net average magnetization along the applied field (as usual paramagnets do). However, the magnetic susceptibility (which characterizes the system response to the applied field) for such a system of fine ferromagnetic particles is about $10^4 \ldots 10^6$ times larger than for usual paramagnetic materials because the moment of small particles which now play the role of single atoms (molecules) of a paramagnet is much larger than any atomic or molecular magnetic moment. For this reason, the behavior of a fine particle system for $T > T_{sp}$ is known as *superparamagnetism*.

To estimate the temperature of this superparamagnetic transition T_{sp} (which is also known as a blocking temperature T_{bl}), we are reminded that, according to the Arrhenius law, for a system with the temperature T the average transition time between two states separated by an energy barrier ΔE is $t_{tr} \sim \tau_0 \exp(\Delta E/kT)$, k being the Boltzmann constant, $\Delta E \sim KV$ (see above). The prefactor τ_0 should be measured experimentally, and for magnetic phenomena under study is about $\tau_0 \sim 10^{-9}$ s. To observe the superparamagnetic behavior, the observation time t_{obs} should be at least of the same order of magnitude as t_{tr}, which leads to the relationship $t_{obs} \geq \tau_0 \exp(\Delta E/kT)$. Hence, for the given observation time t_{obs} the blocking temperature can be estimated as $T_{sp} \sim KV/\ln(t_{obs}/\tau_0)$. The corresponding value,

for example for iron particles of size ~10 nm and an observation time $t_{obs} = 1$ is $T_{sp} \sim 10^2$ K.

In real fine particle systems the transition to a superparamagnetic state with increasing temperature occurs gradually due to the always-present particle size and shape distribution. These distributions lead to a spread of the energy barrier heights, and this results in different transition temperatures for different particles.

1.2.4.5 Irreversible Magnetic Relaxation

The magnetic moment of a ferromagnetic system magnetized in an external field and then left on its own often changes with time. This is one of the manifestations of the so-called "irreversible magnetic relaxation phenomena", which inevitably occur at finite temperatures in any magnetic system which is not in a thermal equilibrium state.

A typical experiment to observe irreversible magnetic relaxation is as follows: a system is magnetized in an external field so that it acquires some total magnetic moment in the direction of this field. The magnitude and (or) the direction of the applied field is then suddenly changed and the time dependence of the system magnetic moment is measured. For a wide class of magnetic systems (magnetic powders, some alloys, thin films, etc.) such measurements provide a nontrivial result: magnetization relaxation is not exponential ($\mu_z \sim \exp(-t/\tau_c)$, which one would expect for the thermal relaxation of a system over an energy barrier) but rather can be described by a linear–logarithmic dependence

$$\mu_z = \mu_0 - S \ln\left(\frac{t}{t_0}\right) \quad \text{or} \quad \frac{d\mu_z}{d(\ln t)} = -S(= Const) \tag{1.67}$$

where the coefficient S is called *magnetic viscosity*. This linear–logarithmic dependence fits in many cases experimental data measured over many time decades from seconds to years (!) quite well. Such relaxation is called "anomalous" in order to distinguish it from the simple exponential relaxation.

The first phenomenological explanation of this phenomenon for magnetic systems was provided by Street and Wooley (1949). These authors suggested that such an unusual (at that time) relaxation behavior was due to the wide distributions of the energy barrier heights in the system under study. To understand why such a distribution leads to the linear–logarithmic behavior, let us consider the simplest model, namely a system of noninteracting magnetic particles each of which has two equilibrium magnetization states separated by the energy barrier E. We assume that the height of this barrier changes from particle to particle, and that the fraction of particles dN with the energy barriers in the small interval from E to $E + dE$ is $dN = \rho(E)\, dE$ (in this case $\rho(E)$ is called the distribution density of the energy barriers).

The irreversible magnetization relaxation for particles with the given energy barrier E is given by the simple exponential Arrhenius law mentioned above: $\mu_z \sim \exp(-t/\tau_c)$. This means that for each such particle the probability $p(t)$ to jump over the barrier during the time t is given by $p(t) = 1 - \exp(-t/\tau_c)$. The relaxation time τ_c also exhibits an exponential dependence on the barrier height: $\tau_c = \tau_0 \exp(E/kT)$ where the prefactor is about $\tau_0 \sim 10^{-9}$ s (see the discussion of the superparamagnetic phenomena given above).

For the observation time t, all particles with the relaxation time $\tau_c \ll t$, had already relaxed almost surely ($t/\tau_c \gg 1$, $\exp(-t/\tau_c) \approx 0$ probability to jump $p(t) \approx 1$), so that their relaxation can no longer be observed. The particles with much larger relaxation times $t/\tau_c \ll 1$ are still not yet relaxed almost surely ($t/\tau_c \ll 1$, $\exp(-t/\tau_c) \approx 1$, probability to jump $p(t) \approx 0$), hence, their relaxation could no longer be observed either. Thus, the only particles whose relaxation we measure at the observation time t are those with the relaxation time $\tau_c (= \tau_0 \exp(E/kT)) \sim t$ – that is, with the energy barriers $E \approx E_c = kT \ln(t/\tau_0)$. Due to the very strong (exponential!) dependence of the relaxation time on the energy barrier height E, only those particles with barriers in a narrow interval $\Delta E \sim kT$ around the so-called *critical energy* $E_c(t) = kT \ln(t/\tau_0)$ make any substantial contribution to the magnetic relaxation, observed at time t (see Fig. 1.23a), where the probability to jump – that is, the probability $P(E)$ to overcome the energy barrier – is shown as a function of the barrier height E. In other words, it is a very good approximation to treat the critical energy E_c, as the boundary between the already relaxed and not yet relaxed particles (Fig. 1.23b).

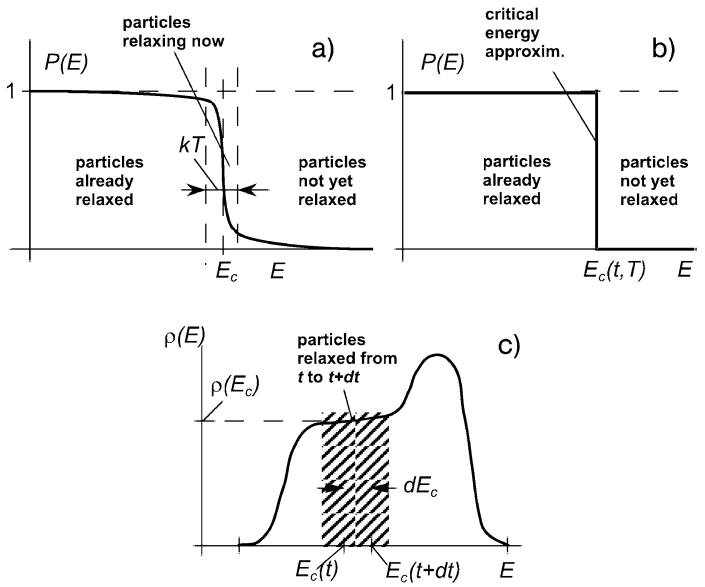

Fig. 1.23. An explanation of the linear–logarithmic time dependence of the magnetization.

The width of the energy barrier distribution $\rho(E)$ is normally much larger than the thermal energy kT. For this reason, inside the mentioned small interval $\Delta E \sim kT$ around E_c this distribution can be treated as constant. Hence, the number of relaxed particles dn (and the magnetic moment decrease $-d\mu_z$) in the time interval from t to $t + dt$ can be calculated as the product of the corresponding value $\rho(E_c)$ and the shift of the critical energy dE_c during this interval (see Fig. 1.23c; we recall that the critical energy separates relaxed and nonrelaxed particles): $d\mu_z \approx -\rho(E_c)\, dE_c(t)$. Substituting in this relationship the time dependence of the critical energy $E_c(t) = kT \ln(t/\tau_0)$, so that $dE_c(t) = kT\, dt/t$, we obtain

$$d\mu_z \approx -kT\rho(E_c)\, dt/t \quad \text{or}$$

$$t\frac{d\mu_z}{dt} = \frac{d\mu_z}{d \ln t} \approx -kT\rho(E_c) \tag{1.68}$$

which coincides with Eq. (1.67) if we set $S = kT\rho(E_c)$. This means that the magnetic viscosity is simply proportional to the value of the energy barrier distribution density for the critical energy E_c. Generally speaking, this depends on the observation time due to the time-dependence of $E_c \sim \ln t$. However, since this dependence is very weak (logarithmic), it can be neglected for nonpathological barrier densities $\rho(E)$, and this leads to the almost constant magnetic viscosity (Eq. 1.67) observed experimentally.

1.2.4.6
Reconstruction of Magnetization Distribution Inside a Body from Magnetic Field Measurements

In this last section we turn our attention to a question which, despite being somewhat aside from the main route, is extremely important for applications of magnetism in many areas, and especially in medicine. The question relates to the possibility of reconstructing the complete magnetization configuration inside a body, based on measurements of the magnetic field outside it. If this were possible, then we would obtain a powerful tool for studying areas such as current distribution inside a human brain, This in turn would lead to immense progress not only in the diagnosis of a variety of diseases but also to an understanding of how the human brain functions.

From a mathematical viewpoint, we are looking for the solution of an integral Eq. (1.27): provided that the magnetic potential $\mathbf{A}(r_0)$ outside a body is known everywhere, could we reconstruct the current distribution $\mathbf{j}(\mathbf{r})$ inside this body? This would be the same as that of reconstructing the magnetization distribution $\mathbf{M}(\mathbf{r})$ from the magnetic field measurements because $\mathbf{M}(\mathbf{r})$ can be calculated from the known current distribution using the relationship $\text{rot}\, \mathbf{M}(\mathbf{r}) = \mathbf{j}/c$ (see Section 1.2.2.3) whereby the field can be found as $\mathbf{H} = \text{rot}\, \mathbf{A}$.

The problem described above is known as an inverse problem of potential theory (Romanov, 1987) and, unfortunately, cannot be solved uniquely in general. To dem-

onstrate this fact, we consider first the corresponding problem in electrostatics, namely the reconstruction of charge distribution inside a body from electric field measurements outside it. To show the nonuniqueness of the solution we turn our attention to a simple example, the electric field outside a sphere which carries a total charge Q. It is a well-known text-book result that while the charge distribution inside the sphere remains spherically symmetrical, the field outside the sphere is given by $E(\mathbf{r}) = Q/r$. Hence, this field is exactly the same if, for example: (1) there is a point charge Q in the sphere center; or (2) if the same total charge Q is uniformly distributed on the sphere's surface. Moreover, there is no way to determine the real charge distribution in a sphere unless the field inside the sphere can be measured.

The mathematical reason why such a reconstruction fails is that outside the charged bodies the electric potential satisfies the Laplace Equation $\Delta\phi = 0$ (ϕ is a harmonic function). For such functions a so-called Dirichlet problem can be formulated: find a solution of the Laplace Equation $\Delta\phi = 0$ outside some closed region Ω that satisfies some reasonable boundary condition on the surface S of Ω ($\phi(\mathbf{r} \in S) = f(\mathbf{r})$) and vanishes at the infinity. It can be shown that the solution of this problem is unique – that is, the values of the potential $\phi(\mathbf{r})$ in the whole space outside some closed surface S can be found if we know its values on this surface $\phi(\mathbf{r} \in S)$. Hence, when measuring the potential (or the field) outside a charged body we have at our disposal actually only two-dimensional (2D) information (ϕ-values on any closed *surface* surrounding a body), which is clearly insufficient to reconstruct a three-dimensional (3D) *volume* charge distribution inside the body.

The same arguments are valid for the magnetic vector potential. Indeed, this potential satisfies the vector Poisson Equation (1.26) which outside a system of currents (or magnetic samples) transforms into the vector Laplace Equation $\Delta\mathbf{A} = 0$. Again, according to the same solution of the Dirichlet problem, the values of the vector potential in the outer space are completely determined by its values on some closed surface surrounding a system under study, so there is no way to obtain more than 2D information and hence reconstruct a (generally) 3D current or magnetization distribution inside the system.

Although this is a disappointing answer in general, there exist several particular problems for which additional information about the current (magnetization) distribution is available, such that a reconstruction becomes possible. First, in the simplest case when the magnetic field is known to be created by a single point-like dipole, it is possible to reconstruct its position and the magnitude and orientation of its magnetic moment. In principle, such a reconstruction is possible for any given finite number of dipoles, but in practice its reliability falls rapidly when this number increases.

Another tractable case is when some symmetry properties of the magnetization distribution to be reconstructed are known in advance. If, for example, we know that the magnetization inside a finite cylinder is distributed in axially symmetrical fashion and we can measure the magnetic field on some closed surface surrounding this cylinder, then the reconstruction is (in principle) possible.

In concluding this discussion, we would like to mention that, apart from the principal difficulties demonstrated above, the solution of the Fredholm integral equations of the 1st type

$$f(x) = \int K(x, y)g(y)\,dy$$

(one must solve for $g(y)$ if the left-hand function $f(x)$ and the integral kernel $K(x, y)$ are known) is the so-called ''ill-conditioned problem'' (Press et al., 1992) in the Hadamard sense. This means, that small errors in the experimental data (represented here by $f(x)$) can cause arbitrary large deviations in the solution if no special precautions (the so-called ''regularization techniques'') are taken. However, this very interesting topic cannot be discuss at this point, and interested readers are referred to literature references in Press et al. (1992).

Appendix

In this Appendix, the most important expressions from this chapter are listed in Gauss units (left column) and SI units (right column) units. If expressions in SI and Gauss systems coincide, only one formula is presented. The values of the SI constants ε_0 and μ_0 appearing in these expressions are

$$\varepsilon_0 = 10^7/(4\pi c^2 \approx 8.854 \times 10^{-12}\ \text{Farad m}^{-1}$$

$$\mu_0 = 4\pi \times 10^{-7}\ \text{Henry m}^{-1}$$

$$\text{rot}\,\mathbf{e} = -\frac{1}{c}\frac{\partial \mathbf{h}}{\partial t} \qquad \text{rot}\,\mathbf{e} = -\frac{\partial \mathbf{h}}{\partial t} \tag{A.1}$$

$$\text{rot}\,\mathbf{h} = \frac{1}{c}\frac{\partial \mathbf{e}}{\partial t} + \frac{4\pi}{c}\mathbf{j} \qquad \text{rot}\,\mathbf{h} = \mu_0\varepsilon_0\frac{\partial \mathbf{e}}{\partial t} + \mu_0\mathbf{j} \tag{A.2}$$

$$\text{div}\,\mathbf{e} = 4\pi\rho \qquad \text{div}\,\mathbf{e} = \frac{\rho}{\varepsilon_0} \tag{A.3}$$

$$\text{div}\,\mathbf{h} = 0 \tag{A.4}$$

$$\oint_L \mathbf{e}\,d\mathbf{l} = -\frac{1}{c}\frac{\partial \Phi_h}{\partial t} \qquad \oint_L \mathbf{e}\,d\mathbf{l} = -\frac{\partial \Phi_h}{\partial t} \tag{A.8}$$

$$\oint_L \mathbf{h}\,d\mathbf{l} = \frac{1}{c}\frac{\partial \Phi_e}{\partial t} + \frac{4\pi}{c}J_S \qquad \oint_L \mathbf{h}\,d\mathbf{l} = \mu_0\varepsilon_0\frac{\partial \Phi_e}{\partial t} + \mu_0 J_S \tag{A.9}$$

$$\oint_S \mathbf{e}\,d\mathbf{S} = 4\pi Q \qquad \oint_S \mathbf{e}\,d\mathbf{S} = \frac{Q}{\varepsilon_0} \tag{A.12}$$

$$\oint_S \mathbf{h}\,d\mathbf{S} = 0 \tag{A.13}$$

$$\phi(\mathbf{r}_0) = \int_V \frac{\rho(\mathbf{r})}{|\mathbf{r}_0 - \mathbf{r}|} dV \qquad \phi(\mathbf{r}_0) = \frac{1}{4\pi\varepsilon_0} \int_V \frac{\rho(\mathbf{r})}{|\mathbf{r}_0 - \mathbf{r}|} dV \tag{A.20}$$

$$\mathbf{e}_{\text{dip}} = \frac{3\mathbf{r}_0(\mathbf{d}\mathbf{r}_0)}{r_0^5} - \frac{\mathbf{d}}{r_0^3} \qquad \mathbf{e}_{\text{dip}} = \frac{1}{4\pi\varepsilon_0}\left[\frac{3\mathbf{r}_0(\mathbf{d}\mathbf{r}_0)}{r_0^5} - \frac{\mathbf{d}}{r_0^3}\right] \tag{A.24}$$

$$\mathbf{A}(\mathbf{r}_0) = \frac{1}{c}\int_V \frac{\mathbf{j}(\mathbf{r})}{|\mathbf{r}_0 - \mathbf{r}|} dV \qquad \mathbf{A}(\mathbf{r}_0) = \frac{\mu_0}{4\pi}\int_V \frac{\mathbf{j}(\mathbf{r})}{|\mathbf{r}_0 - \mathbf{r}|} dV \tag{A.27}$$

$$\mathbf{h}_{\text{dip}} = \frac{3\mathbf{r}_0(\boldsymbol{\mu}\mathbf{r}_0)}{r_0^5} - \frac{\mathbf{d}}{r_0^3} \qquad \mathbf{h}_{\text{dip}} = \frac{\mu_0}{4\pi}\left[\frac{3\mathbf{r}_0(\boldsymbol{\mu}\mathbf{r}_0)}{r_0^5} - \frac{\boldsymbol{\mu}}{r_0^3}\right] \tag{A.34}$$

$$\begin{aligned} &\operatorname{div}\mathbf{B} = 0 && \operatorname{div}\mathbf{B} = 0 \\ &\operatorname{rot}\mathbf{H} = 0 && \operatorname{rot}\mathbf{H} = 0 \end{aligned} \tag{A.47}$$

$$\begin{aligned} &\mathbf{B} = \mathbf{H} + 4\pi\mathbf{M} && \mathbf{B} = \mu_0(\mathbf{H} + \mathbf{M}) \\ &\mathbf{B} = \mu\mathbf{H} && \mathbf{B} = \mu\mu_0\mathbf{H} \\ &\mathbf{M} = \chi\mathbf{H} && \mathbf{M} = \chi\mathbf{H} \end{aligned} \tag{A.48}$$

Acknowledgments

The author is greatly indebted to Prof. A. Hubert for carefully reading the manuscript; he also thanks I. Berkov for technical assistance in preparing the manuscript.

References

Chikazumi, S. (1964). *Physics of Magnetism*. John Wiley, New York.

Feynmann, R.P., Leighton, R.B., and Sands, M. (1963). *The Feynmann Lectures in Physics*. Addison-Wesley, London.

Kittel, C. (1986). *Introduction to Solid State Physics*. John Wiley, New York.

Kneller, E. (1966). *Encyclopedia of Physics, Bd. XVIII/2 – Ferromagnetismus, Theorie der Magnetisierungskurve kleiner Kristalle*. Springer-Verlag, Berlin-Heidelberg, p. 438.

Landau, L.D. and Lifshitz, E.M. (1971). *Quantum Mechanics – Non-relativistic Theory*. Pergamon Press, Oxford.

Landau, L.D. and Lifshitz, E.M. (1975a). *Electrodynamics of Continuous Media*. Pergamon Press, Oxford.

Landau, L.D. and Lifshitz, E.M. (1975b). *The Classical Theory of Fields*. Pergamon Press, Oxford.

Mattis, D.C. (1965). *The Theory of Magnetism*. Harper & Row, New York.

Press, W.H., Teukolsky, S.A., Vetterling, W.T., and Flannery, B.P. (1992). *Numerical Recipes in Fortran: The Art of Scientific Computing*. Cambridge University Press, p. 964.

Romanov, V.G. (1987). *Inverse Problems of Mathematical Physics*. VNU, Utrecht.

Stoner, E.C. and Wohlfarth, E.P. (1948). A mechanism of magnetic hysteresis in heterogeneous alloys. *Phil. Trans. Roy. Soc.*, **A-240**, 599–642.

Street, R. and Wooley, J.C. (1949). A study of magnetic viscosity. *Proc. Phys. Soc.*, **A62**, 562–572.

Weiss, P. (1907). Hypothesis of the molecular field and ferromagnetic properties. *J. Phys. Chim. Hist. Nat.*, **6**, 661–690.

1.3
Creating and Measuring Magnetic Fields

Wilfried Andrä and Hannes Nowak

1.3.1
Introduction

The scientific treatment of magnetism in medicine is inseparably connected with both the generation of magnetic fields as well as with their measurement. However, before going into details of this topic it is necessary to provide a definition for the unit of magnetic field strength which will be used throughout the chapters of this book. Unfortunately, there is considerable confusion even in the technical literature on magnetism and, of course, also in the specialist medical literature. Very often, the terms ''magnetic field'' (H) and ''magnetic flux density'' or ''magnetic induction'' (B) are confused, though the meaning of these two terms is quite different, as explained in Section 1.2 where the relationship between H and B is provided in Eq. (1.43).

This mixing of magnetic quantities has, in general, no serious consequences for the reader, however. More important is to have simple rules of conversion in order to transform units of one system into units of another system. The two systems most often used are the ''International System of Units'' (SI) and the so-called Gaussian system or cgs system. The latter is often used in American publications, whereas in the following chapters of this book the SI system is applied according to the recommendations of the International Organization for Standardization.

In order to convert Gaussian units into SI units, the number of Gaussian units must be multiplied by conversion factors that are listed in Table 1.1. For example, 1 Gauss (G) corresponds to 10^{-4} Tesla (T).

In the following paragraph, typical values of field strength are given in SI units along with the corresponding cgs units in parentheses.

1.3.2
The Generation of Magnetic Fields

Magnetism in medicine has often to deal with magnetic fields that exist naturally. One well-known example is that of the Earth's magnetic field, H_{ea}, the actual am-

Table 1.1. The relationship between gaussian and SI units.

Quantity	Symbol	Gaussian unit	Conversion factor	SI unit
Magnetic field strength	H	Oerstedt (Oe)	$10^3/4\pi$	A m^{-1}
Magnetization	M	Gauss (G)	10^3	A m^{-1}
Magnetic T polarization	J	Gauss (G)	10^{-4}	Vs m^{-2} = T
Magnetic T induction	B	Gauss (G)	10^{-4}	Vs m^{-2} = T
Susceptibility = M/H	χ	1	4π	1
Using Gaussian units		$B = H + 4\pi M$		
Using SI units		$B = \mu o(H + M)$, with $\mu o = 4\pi 10^{-7}$ V·s A·m^{-1}		

plitude of which is about 40 A m^{-1} (0.5 Oe). In many reports the corresponding flux density $B_{ea} = \mu_0 H_{ea}$ is given ($\mu_0 = 4\pi \times 10^{-7}$ Vs Am^{-1} is the permeability of the free space) with a magnitude of about 5×10^{-5} Vs m^{-2} (0.5 G). Especially in reports dealing with very weak or very strong magnetic fields, the unit Vs m^{-2} is usually replaced by the abbreviation T (= Tesla).

A second type of magnetic field, generated by natural processes, forms the central subject of biomagnetism. The sources of these fields are small electric currents within the human body, giving rise to extremely weak magnetic fields outside the body (this subject is described in more detail in Chapter 2). The corresponding field strength is at maximum of the order of $H_{bio} \approx 10^{-4}$ A m^{-1} (1.25×10^{-6} Oe), and the flux density $B_{bio} \approx 1.25 \times 10^{-10}$ T (1.25×10^{-6} G).

Artificially produced magnetic fields are required in many medical methods. Their magnitudes range approximately from less than 1% of the Earth's magnetic field up to more than 4×10^6 A m^{-1} (5×10^4 Oe). The weak as well as the extremely strong fields are usually generated by electric currents flowing in suitably designed wires. Large-sized solenoids are used in magnetic resonance tomography (MRT). In order to produce the strong constant magnetic fields required for this technique, very high currents must flow for a very long time. This demand can be met by using superconducting wires (see Section 3.2), while in other cases the wire is replaced by copper tubes designed for effective water cooling. The field generated in the center of a long solenoid can easily be estimated using Eq. (1.69):

$$H = iN/L \tag{1.69}$$

where i is the current, N is the number of windings and L denotes the length of the coil. The field on the axis of a solenoid as shown in Figure 1.24 is exactly parallel to the coil axis, and can be calculated using the following equation:

$$H(x)/j = (1/2) \cdot \left[UP \cdot \ln \frac{R_a + \sqrt{R_a^2 + UP^2}}{R_i + \sqrt{R_i^2 + UP^2}} - UM \cdot \ln \frac{R_a + \sqrt{R_a^2 + UM^2}}{R_i + \sqrt{R_i^2 + UM^2}} \right] \tag{1.70}$$

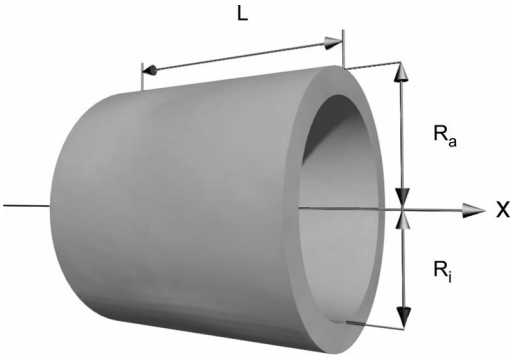

Fig. 1.24. A solenoid for the generation of magnetic fields.

with $UP = (x + L/2)$ and $UM = (x - L/2)$; x is the distance from the coil center; j is given by the Equation $j = i/F$, where i is the total current flowing through the cross-section $F = (R_a - R_i) \cdot L$ of the solenoid. The natures of R_a, R_i, and L are explained in Figure 1.24. The calculation of field strength for points outside the coil axis is more complicated and beyond the scope of this book, but interested readers are referred to specialized literature (e.g., Smythe, 1989). In general, the field can be calculated as a sum of contributions generated by circular currents of different radius and axis position (Landau and Lifschitz, 1967). The final equations are complicated, and normally the calculation of required field strengths is performed by numerical computation. Analytical formulas for long solenoids and locations near the axis have been provided by Jackson (1962). It should be pointed out that off-axis fields are in general oblique to the axis. Coils similar to that shown in Figure 1.24 are used for magnetic stereotaxis as well as for many other applications. In order to achieve different geometrical field distributions, the construction of the current-carrying wires must be correctly chosen. A typical example for such design was provided by Meeker et al. (1996) in a report detailing magnetic stereotaxis. The general considerations on the construction of air-core solenoids, including mechanical problems and problems of cooling, are treated in detail by Zijlstra (1967a).

Fields of medium strength are generated primarily by means of electromagnets, many different types of which have been described in the literature. The constructions are usually designed according to the special application with the aim to achieve the desired field strength (and also a desired field distribution) with a minimum of both electric power consumption and weight. The general advantage of electromagnets is that it is possible to concentrate the field at a certain region with the electric currents flowing in a remote region. However, the ability of magnetic materials to ''conduct'' magnetic fields in a similar way as copper conducts the electric current is restricted. The principle of an electromagnet is shown in Figure 1.25.

Some examples of electromagnets have been described in Section 1.1. One of these was the so-called ''giant magnet'' of Dr. Haab, which was designed to remove

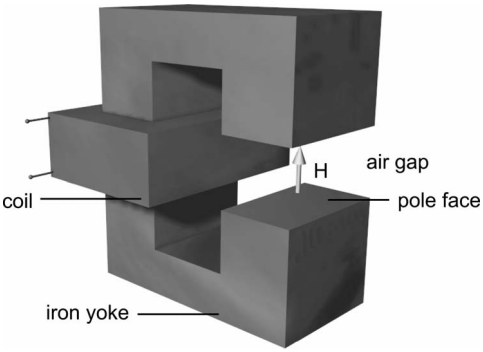

Fig. 1.25. Schematic representation of an electromagnet. The main part of the magnetic flux generated by the coil is conducted through the iron yoke to the air gap.

magnetic objects from the eye (see Fig. 1.4). Clearly, this construction appears quite different to the scheme of Figure 1.25, due mainly to the fact that in Dr. Haab's equipment the yoke is degenerated to a sphere-shaped iron body in order to produce an extremely inhomogeneous magnetic field just at the tip of the magnet. Other examples of rather large electromagnets which are more similar to Figure 1.25 are shown in Figure 3.20 (see Section 3.2). These are designed for MRT, and have flux densities of about 0.3 T and 1 T, respectively. In Figure 3.20 the magnetic core is hidden behind a casing, whereas the air gap with the bed can be distinguished. In principle, the field in the air gap can be calculated, though there is no simple relationship similar to Eq. (1.70). In the case of a comparably narrow air gap the field strength, H_{air}, can be roughly estimated by:

$$H_{\mathrm{air}} = \frac{N \cdot i - H_{\mathrm{fe}} L_{\mathrm{fe}}}{L_{\mathrm{air}}} \tag{1.71}$$

where $N \cdot i$ is the product of the current and the number of windings in the coil. L_{fe} and L_{air} are the path lengths of the field along the yoke and the air gap, respectively. The value of the field strength inside the iron yoke, H_{fe}, however, depends on several parameters, including the magnetic properties of the yoke material as a function of $N \cdot i$ and the actual geometry of the magnet. In most cases the yoke material is not strongly magnetized. Then, if L_{fe} is small compared to L_{air}, the term $H_{\mathrm{fe}} \cdot L_{\mathrm{fe}}$ in Eq. (1.71) may be neglected. More detailed calculations are complicated. In particular, the so-called demagnetizing effects give rise to serious corrections of Eq. (1.71). Demagnetizing relates to the influence of magnetic fields (caused by magnetic poles on the surfaces or inside the yoke) on the magnetization of the yoke material. In this regard, the interested reader is referred to specialist publications on magnetic problems (e.g., Kneller, 1962; Zijlstra, 1967a), wherein the general design of electromagnetic circuits is described.

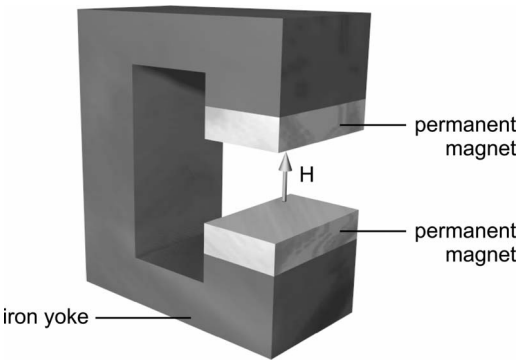

Fig. 1.26. Scheme of a permanent magnet circuit. Without the yoke there would be poles at the back sides of the permanent magnet pieces, giving rise to a stray field opposite to the main field in the air gap.

Cases also exist where permanent magnets are used, and these offer the great advantage of being independent of electric power. On the other hand, the field strength cannot be varied without complicated additional equipment. Permanent magnets might be used preferably in cases where it is not possible to connect to a mains electricity supply, for example during first aid treatment in the case of a road traffic accident (Paliege et al., 1979). More recently, a small permanent magnet was successfully used to remove intraocular ferromagnetic foreign bodies from the eye (Kuhn and Heimann, 1991). The construction of permanent magnet circuits that are properly designed for special applications depends essentially on both the magnetic material as well as the type of application. In this respect, major progress has been made in the development of permanent magnetic materials, and correspondingly the design of equipment has improved considerably during the past few decades. Further details on this subject may be found in specialized books (e.g., McCaig and Clegg, 1987). The scheme of a typical permanent magnet circuit with a yoke for flux closure is shown in Figure 1.26. For configurations similar to this figure, the upper limit of the field strength in the air gap between rectangular pole faces can be estimated by:

$$H_{\text{air}}/M_r = 8 \arctan \frac{L \cdot W}{D\sqrt{L^2 + W^2 + D^2}} \tag{1.72}$$

where D is the width of the air gap, L and W are the edge lengths of the pole face, and M_r is the magnetization of the permanent-magnet pieces.

Recently, several cases have been reported where small permanent magnets (e.g., spheres) were applied for the magnetic monitoring of capsules inside the gastrointestinal tract (see Section 4.2). One special advantage of these so-called markers is the simple mathematical formulae of the magnetic field around these magnets

which can (in a good approximation) be described as a dipole field (see Section 1.2).

1.3.3 The Measurement of Magnetic Fields

The application of magnetism to medicine covers a rather large range of fields, and as a consequence a great variety of methods has been developed suitable for the measurement of magnetic field strength. However, within the scope of this book only those methods significant to medical applications will be treated in detail. Each method offers advantages as well as drawbacks which, in general, are more or less pronounced for certain ranges of field strength. Therefore, the instruments used must be chosen according to the field range of the specific application in order to provide optimum sensitivity. Whilst a number of different definitions of the term ''sensitivity'' have been reported in the literature, within the context of this chapter the term ''detection limit'' is preferred. This denotes the lowest value of field strength which can be reliably detected. Of course the meaning of ''reliably'' must also be defined, with one condition being that the signal:noise ratio is greater than 2. A compilation of typical field ranges, together with some selected principles of measurement, is provided in Table 1.2. Many more methods and corresponding instruments – especially for applications in other technical fields – are available, though only few of these have been used for medical techniques. The reason for this is that, in many cases, the detection limit does not meet the corresponding demand, while in other cases the handling may be too complicated. On occasion, potential users may not be familiar with the respective method, and consequently only about five principles of the methods listed in Table 1.2 are usually applied in medicine.

For many years, the primary position with regard to the greatest sensitivity or lowest value of detection limit was held by the SQUID principle; this type of field sensor is described in detail in Section 2.2. More recently, the atomic magnetometer was developed with slightly higher sensitivity (Kominis et al., 2003; Schwindt et al., 2004). In addition, the optical pumped magnetometer could be used to map the human cardiomagnetic field (Bison et al., 2003). This new measuring principle is based on the detection of the so-called Larmor-spin precession of atoms which are excited by optical radiation. The sensitivity of the technique is essentially determined by the relaxation time which passes until the increased energy of the atoms is delivered to the surroundings.

The secondary position with regard to detection limit is held by three principles. The first of these, nuclear precession magnetometry, is used to detect small local variations of an otherwise strong constant magnetic field; details of the basic principle are provided in Section 3.2. The other principles are rotating-coil magnetometry, which is not used widely in medicine, and flux-gate magnetometers, which are used in different fields of application.

Table 1.2. Examples of field ranges and the corresponding measuring principles. The detection limits are given for quasistatic fields.

Field source	$\mu_0 H$ [T]	Measuring principle	Detection limit [T]
Evoked human brain activity	$\leq 10^{-13}$	Atomic magnetometer	$\leq 10^{-15}$
		SQUID	10^{-15}
		Nuclear resonance	10^{-13}
		Optical pumping	
		Torsion magnetometer	
Spontaneous currents in the human brain	10^{-12}	Nuclear precision magnetometer	$\leq 10^{-11}$
Currents of the human heart	$\leq 10^{-10}$	Flux-gate	$\leq 10^{-11}$
		Rotating coil	10^{-11}
		Magnetoresistivity	10^{-10}
Contamination of lunge and stomach	$\leq 10^{-9}$	Hall sensor	10^{-9}
Liver iron	$\leq 10^{-8}$	Magneto-optical sensor	10^{-7}
Magnetic markers	$\leq 10^{-6}$	Magnetotransistor	$\leq 10^{-5}$
Earth's magnetic field	$\geq 10^{-5}$	Magnetodiode	10^{-5}

The operating scheme of a flux-gate magnetometer is shown in Figure 1.27. The unit consists essentially of two magnetic cores (a and b) which are periodically magnetized by an alternating current i in the primary coils (1a and 1b) with a frequency ν. The periodically varying magnetization of the cores induces voltages in the two induction coils (2a and 2b). Without any external field these voltages cancel because they are electrically connected against each other. An external field H, however, leads to a different deformation of the induced voltages as functions of time in the two induction coils, thereby yielding a residual signal with the main contribution of a frequency 2ν. This can be selectively amplified, thus permitting a sensitive measurement of H (Michalowsky, 1993). Very small flux-gate sensors were developed using planar technology (Vincueria et al., 1994), providing the application of a high driving frequency ν. A flux-gate magnetometer with a low detection limit was described by Hinnrichs et al. (2000).

The principle of an anisotropic magnetoresistive (AMR) field sensor (McGuire and Potter, 1975) is illustrated in Figure 1.28. The essential feature is that the electrical resistivity of magnetic materials is influenced by scattering of electrical charge carriers caused by magnetic perturbations. This scattering depends on the

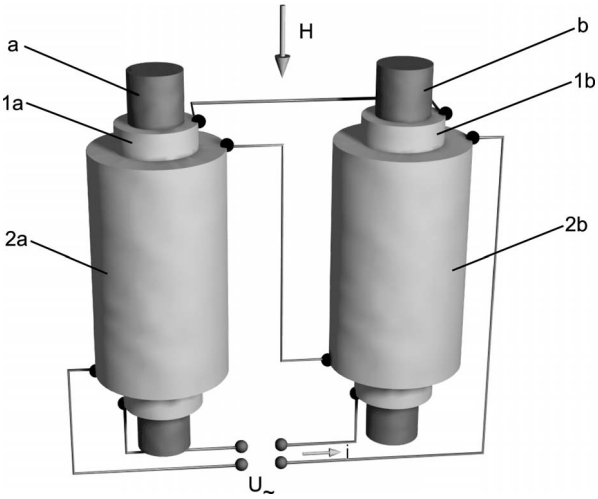

Fig. 1.27. The scheme of a flux-gate magnetometer. See text for details.

angle between the direction of current (i) and magnetization (M). In the case of AMR the magnetization is parallel to an easy axis (e.a.) inside the material, as long as no external field H is acting. Any component of H perpendicular to the easy axis induces a rotation of the magnetization out of this axis, and leads to a variation of the scattering intensity. The special oblique form of the film contacts shown in Figure 1.28 is chosen in order to assure an angle of 45° between current and magnetization for a zero external field. By using this configuration it is also possible to detect the sign of H.

Two new modifications of magnetoresistivity were investigated with the aim of developing even more sensitive field sensors. Giant magnetoresistivity (GMR) is based on the scattering of charge carriers during their transition between separated magnetic films with differently oriented magnetization (Baibich et al., 1988). Whilst AMR yields a relative alteration of the resistivity of the order of some per-

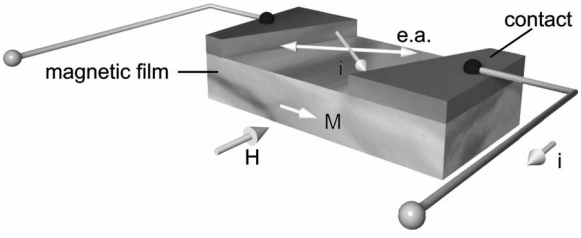

Fig. 1.28. Scheme of an anisotropic magnetoresistive element (AMR). See text for details. The easy axis (e.a.) is usually parallel to the long film edge.

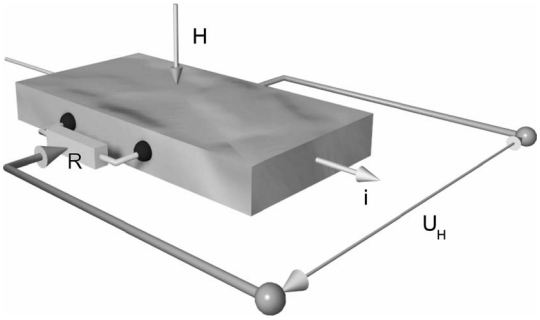

Fig. 1.29. Scheme of a Hall element. See text for details.

cent, GMR is able to change the resistivity by more than 100%. An interesting combination of GMR with a superconducting flux-to-field transformer operating at 77 K was recently described by Pannetier et al. (2004). Another effect is caused by intrinsic magnetic influence on the processes of electrical conductivity in oxide materials (von Helmolt et al., 1993). This effect has been the object of numerous investigations, and produces (relatively) a change in resistivity that is many orders of magnitude higher than that achieved with GMR. This approach is, therefore, referred to as colossal magnoresistivity (CMR). The development of suitable materials and circuits using GMR and CMR is still in progress, and consequently the ultimate detection limit for these two effects cannot yet be estimated. A combination of a superconducting flux-to-field transformer with a low-noise GMR sensor achieved a detection limit of 32×10^{-15} T $(\mathrm{Hz})^{-1/2}$ (Pannetier et al., 2004).

The next principle detailed in Table 1.2 is termed the Hall effect (Zijlstra, 1967b), the basic design of which is shown schematically in Figure 1.29. If a current (i) flowing through a conductor is exposed to an external field H, the charge carriers are deflected in a direction perpendicular to both current and H direction due to the so-called Lorentz force. As a consequence, a voltage U_H is generated which is proportional to H and can be measured by means of contacts across the current direction. In order to identify the correct perpendicular position of the voltage contacts, one contact is split into two and connected by a resistor (R), as shown in Figure 1.29.

Among several other types of magnetometer to have been devised is that of the magneto-optical sensor (see Table 1.2), which is of two basic types. The first type employs either the Faraday- or Kerr-effect, and by using optical fibers one of the most sensitive Faraday sensors achieved a noise level of 10^{-13} T/$(\mathrm{Hz})^{1/2}$ (Deeter, 1996). The second type of magneto-optical sensor transforms the distortion of magnetostrictive materials such as metallic glass, especially in combination with optical fibers, under the influence of a magnetic field. The change in optical length is measured by interference-optical means, for example with a Mach–Zehnder interferometer. Using this approach, a detection limit of 3×10^{-12} T/$(\mathrm{Hz})^{1/2}$ was realized in the low-frequency region (10 Hz) (Dagenais et al., 1988).

1.3.4 Discussion

The various methods used to generate magnetic fields appear to be essentially at their final stages, and few surprising new principles can be expected to be developed in the near future. However, gradual improvements may be introduced with regard to the generation of well-localized fields, either by means of small coils or miniaturized permanent magnets permitting magnetic manipulation in selected target regions.

Whilst methods of field measurement are still under development, the simplicity of operation, stability with respect to both temperature and time, and in some cases also the detection limit may all be improved in the near future. Another important aspect is the miniaturization of field sensors and their arrangement in the form of extended arrays suitable for the rapid measurement of field distributions and their time dependence around the entire human body or in the major organs.

References

Baibich, M.N., Broto, J.-M., Fert, A., Nguyen Van Dau, F., Petroff, F., Etienne, P., Creuzet, G., Friederichs, A., and Chazelat, J. (1988). Giant magnetoresistance of (001)Fe/(001)Cr magnetic superlattices. *Phys. Rev. Lett.*, **61**, 2472.

Bison, G., Wynands, R., and Weis, A. (2003). A laser-pumped magnetometer for the mapping of human cardiomagnetic fields. *Appl. Phys. B*, **76**, 325–328.

Dagenais, D.M., Bucholtz, F., Koo, K.P., and Dandridge, A. (1988). Demonstration of 3 pT/Hz$^{1/2}$ at 10 Hz in a fibre-optic magnetometer. *Electronics Lett.*, **24** (23), 1422–1423.

Deeter, M.N. (1996). Fiber-optic Faraday-effect magnetic-field sensor based on flux concentrators. *Appl. Optics*, **35** (1), 154–157.

Hinnrichs, C., Pels, C., and Schilling, M. (2000). Noise and linearity of a fluxgate magnetometer in racetrack geometry. *J. Appl. Phys.*, **87**, 7085–7087.

Jackson, J.D. (1962). *Classical Electrodynamics*. John Wiley & Sons, New York, Chichester, Brisbane, Toronto, Singapore.

Kneller, E. (1962). *Ferromagnetismus*. Springer-Verlag, Berlin, Göttingen, Heidelberg.

Kominis, I.K., Kornack, T.W., Allred, J.C., and Romalis, M.V. (2003). A subfemtotesla multichannel atomic magnetometer. *Nature*, **422**, 596–599.

Kuhn, F. and Heimann, K. (1991). Ein neuer Dauermagnet zur Entfernung intraokularer ferromagnetischer Fremdkörper. *Klin. Mbl. Augenheilk.*, **198**, 301.

Landau, L.D. and Lifschitz, E.H. (1967). *Elektrodynamik der Kontinua*. Akademie-Verlag, Berlin.

McCaig, M. and Clegg, A.G. (1987). *Permanent Magnets*. Pentech Press, London.

McGuire, T.R. and Potter, R.I. (1975). Anisotropic magnetoresistance in ferromagnetic 3-d alloys. *IEEE Trans. Magn.*, **11**, 1018.

Meeker, D.C., Maslen, E.H., Ritter, R.C., and Creighton, F.M. (1996). Optimal realization of arbitrary forces in a magnetic stereotaxis system. *IEEE Trans. Magn.*, **32**, 320.

Michalowsky, L. (1993). *Magnettechnik*. Fachbuchverlag, Leipzig-Köln.

Paliege, R., Volkmann, H., and Andrä, W. (1979). Magnetische Lagefixierung einschwemmbarer Elektrodenkatheter zur temporären Schrittmachertherapie. *Dt. Gesundheitswesen*, **34**, 2514.

Pannetier, M., Fermon, C., Le Goff, G., Simola, J., and Kerr, E. (2004). Femtotesla magnetic field measurement with magnetoresisitive sensors. *Science*, **304**, 1648–1650.

Schwindt, D.D., Knappe, S., Shah, V., Hollberg, L., and Kitching, J. (2004). Chip-scale atomic magnetometer. *Appl. Phys. Lett.*, **85**, 6409–6411.

Smythe, W.R. (1989). *Static and Dynamic Electricity*. Taylor and Francis.

Vincueria, L., Tudanca, M., Aroca, C., Lopez, E., Sanchez, M.C., and Sanchez, P. (1994). Flux-gate sensor based on planar technology. *IEEE Trans. Magn.*, **30**, 5042.

von Helmolt, R., Wecker, J., Holzapfel, B., Schultz, L., and Samwer, K. (1993). Giant negative magnetoresistance in perovskitelike La1/3Ba2/3MnOx ferromagnetic films. *Phys. Rev. Lett.*, **71**, 2331.

Zijlstra, H. (1967a). Experimental methods in Magnetism: 1. Generation and computation of magnetic fields. In: Wohlfarth, E.P. (Ed.), *Selected Topics in Solid State Physics IX*. North-Holland Publishing Company, Amsterdam.

Zijlstra, H. (1967b). Experimental methods in Magnetism: 2. Measurement of magnetic quantities. In: Wohlfarth, E.P. (Ed.), *Selected Topics in Solid State Physics IX*. North-Holland Publishing Company, Amsterdam.

1.4
Safety Aspects of Magnetic Fields

Jürgen H. Bernhardt and Gunnar Brix

1.4.1
Introduction

In recent years there has been an increasing awareness of the possibility of hazards to health from exposure to sources of nonionizing radiation (NIR) such as industrial low- and high-frequency devices, radar and radio equipment, as well as devices used in medicine. This in turn has led to an interest in recommendations for limiting exposures to NIR (static and low-frequency electric and magnetic fields, radiofrequency fields and microwaves).

The preparation of such recommendations necessitates a critical analysis of existing knowledge on the health effects of nonionizing electromagnetic fields. Risk evaluation and guidance on protection are performed by the International Commission on Non-Ionizing Radiation Protection (ICNIRP; see www.icnirp.org), which represents the opinions of the scientific community at large and ensures liaison with other relevant international organizations such as the International Labour Organization (ILO) and the World Health Organization (WHO).

The aims of this chapter are to summarize the risks of exposure, to assess threshold values for effects injurious to health, and to present basic restrictions and reference levels for limiting exposure at the workplace. The methods of risk evaluation as it is performed by ICNIRP will be described in Section 1.4.2, while the following sections will summarize interaction mechanisms, biological effects, results of epidemiological studies, and recommendations for limiting exposures at the workplace for static magnetic fields (Section 1.4.3), for time-varying magnetic fields (Section 1.4.4), and for radiofrequency fields (Section 1.4.5). Section 1.4.6 describes the protection of patients and volunteers undergoing magnetic resonance (MR) procedures.

1.4.2
Risk Evaluation and Guidance on Protection

The general approach to protection against NIR including electromagnetic fields (EMF) is discussed in more detail in a specific document of the ICNIRP (2002).

1.4.2.1 Evaluation Process

The evaluation process of the scientific literature performed by ICNIRP consists of three steps:

- Evaluation of single research studies in terms of their relevance to the health effects and the quality of methods used. The evaluations criteria are described in ICNIRP's statement mentioned above, and are used as guidance in this evaluation. This may result in the exclusion of some studies from the health risk assessment, or assigning different weights to studies, depending on their scientific quality.
- For each health effect evaluated, a review of all relevant information is required. At first, this review is normally performed separately for epidemiological, human laboratory, animal and *in-vitro* studies, with further separations as appropriate for the hypothesis.
- Finally, the outcomes of these steps must be combined into an overall evaluation of consistency of human, animal, and *in-vitro* data.

1.4.2.2 Development of Guidance on Protection

Guidance is based solely on scientifically established adverse health effects. Such effects are identified by the health risk assessment. In developing the guidelines, ICNIRP considers direct and indirect, acute and chronic health effects. Different adverse effects can be ranked according to the exposure level at which each becomes relevant. The critical effect is the established adverse health effect relevant at the lowest level of exposure. Protection against the critical effect means that protection is provided against all other adverse effects occurring at higher exposure levels. In principle, the ICNIRP guidelines are set to protect against critical effects, by limiting the related specific biologically effective quantity. The biologically effective quantity reflects the efficacy by which the external exposure causes a certain biological effect. This quantitative relationship between external measurable exposures and the target tissue biologically effective parameter is unique to a single-exposure condition. Reduction factors are included as a measure of caution, to account for quantitative uncertainties in the scientific database and biological variability in response. As a consequence, the guidelines will be set below the thresholds of the critical effects. There is no rigorous scientific basis for establishing reduction factors. They are not intended for compensating uncertainties in measurements performed to check compliance with exposure standards, nor do they incorporate social or political considerations, including precautionary approaches.

Restrictions on the effects of exposure based on established health effects are termed *basic restrictions*. It is the general strategy of ICNIRP to define a basic restriction in terms of the appropriate biologically effective quantity. Depending on

frequency, the physical quantities used to specify the basic restrictions on exposure to EMF are current density, specific absorption rate, and power density. Protection against adverse health effects requires that the basic restrictions are not exceeded.

Additionally, reference levels of exposure are provided for comparison with measured values of physical quantities; compliance with reference values given in the guidelines will ensure compliance with basic restrictions. In general, the reference levels are more conservative than the basic restrictions because they have been developed for situations of optimum coupling conditions between the radiation or fields and the exposed person. If measured values are higher than reference levels, it does not necessarily follow that the basic restrictions have been exceeded, but a more detailed analysis is necessary to assess compliance with the basic restrictions. In some circumstances, it may be advisable to distinguish between members of the general public and individuals exposed because of or while performing their work tasks (occupational exposure).

Whereas ICNIRP provides general practical information on measurable levels that are derived from basic restrictions on exposure, it recognizes the need for further technical advice on special exposure situations. This requires physics and engineering expertise to develop practical measures to assess and/or to enable assessment of compliance with exposure guidelines. These measures include guidance on the principles and practice of measurements, design of equipment and/or shielding to reduce exposure, and, where appropriate, setting emission limits for specific types of device (see Section 1.4.6).

The ICNIRP Guidelines (1998) have been adopted by more than 40 countries worldwide. The European Union, for example, has adopted a Directive on the minimum health and safety requirement regarding the exposure of workers to the risks arising from physical agents (electromagnetic fields), which is based largely on the ICNIRP Guidelines (EU, 2004).

1.4.3
Static and Extremely Slowly Time-Varying Magnetic Fields (0 to 1 Hz)

There are numerous sources of environmental static and extremely slowly time-varying magnetic fields – both naturally occurring and man-made – to which humans are exposed. The natural magnetic field consists of one component due to the Earth acting as a permanent magnet, and several other small components which differ in characteristics and are related to such influences as solar activity and atmospheric events. In industry, in some research institutions as well as in medicine, large-magnetic field equipment is used with stray fields in a wide circumference around the equipment.

1.4.3.1
Interaction Mechanisms and Biological Bases for Limiting Exposure

For static and extremely slowly time-varying magnetic fields there are several established physical mechanisms through which the fields interact with human beings

or living organisms. These have been reviewed by ICNIRP (1994, 2003), NRPB (2004), Schenck (2005) and Tenforde (1996, 2005). The following categories are the most important.

Magneto-Hydrodynamic Interactions

Static magnetic fields exert forces (called Lorentz forces) on moving electrolytes (ionic charge carriers), giving rise to induced electric fields and currents. To a close approximation, the Lorentz forces exerted on blood flowing through a cylindrical vessel gives rise to a voltage across the vessel. This magnetically induced voltage is commonly referred to as a "blood flow potential". Because of the angular dependence, the greatest magneto-hydrodynamic interaction between blood flow and applied magnetic field occurs when the field and flow are orthogonal, under which condition the magnitude of the induced voltage has a maximum value. Another subject of importance in the context of magnetic field safety is the magneto-hydrodynamic slowing of blood flow (see below).

Magneto-Mechanical Interactions

In a homogeneous magnetic field, certain diamagnetic and paramagnetic molecules experience a torque (or force) that tends to orientate them in a way such that the intrinsic magnetic moment is aligned parallel to the external magnetic field. Normally, intense magnetic fields exceeding 5 T are necessary to align molecular aggregates with diamagnetic anisotropy. The lowest thresholds which were reported from studies on retinal rods and sickled erythrocytes were approximately 100 mT.

Magnetic fields also produce a net force on ferromagnetic materials in the body. Some special organisms, in which magnetic particles are present (i.e., bacteria), use this mechanism for orientation within the Earth's magnetic field.

The occurrence of magnetically induced changes in enzyme structure, leading to altered metabolic reaction rates, has also been proposed. However, energy considerations suggest that at magnetic flux densities of less than 10 T, these effects will be negligible in a living person.

Electronic Interactions

Certain chemical reactions involve intermediate electron states, which could be affected by static magnetic fields producing an effect on the transition of an electron from one state to a lower state. Although such effect has the potential to lead to biological consequences, it must be stated that a magnetic field effect on chemical reaction intermediates in biological systems has not yet been demonstrated, under actual physiological conditions. It is likely that the usual lifetime of biologically relevant electron transitions is sufficiently short to ensure that magnetic field interactions exert only a small and perhaps negligible influence on the yield of chemical products. Theoretical analysis suggests that fields up to even 10 T are unlikely to affect chemical interactions.

The biological effects of exposure of animals and cells to static magnetic fields have been investigated from different endpoints, including reproduction and devel-

opment, cancer, and the nervous system. No consistent effects have been reported using fields below 2 T. The acute responses found during exposure to static fields above about 4 T are consistent with the interaction mechanisms described above (Saunders, 2005). No adverse effects on reproduction and development, or on the growth and development of tumors, have been firmly established. There is, however, little information regarding possible effects of chronic exposure.

With the advent of superconducting magnet technology, patients and volunteers can be routinely exposed to static magnetic fields of 1.5 T and more. Most of the acute effects observed at high-field MR systems are consistent with known mechanisms of interaction. Schenck et al. (1992) reported field-dependent sensations of vertigo, nausea and a metallic taste in the mouth of volunteers exposed to fields of 1.5 or 4 T. These occurred only during movement of the head. Additionally, magnetic phosphenes could be seen during eye movement in a field of at least 2 T. These effects are probably caused by electric currents induced by movement in the field.

Kinouchi et al. (1996) reported that the Lorentz force affecting blood flow generates electric potentials across blood vessels. In practice, ''flow'' potentials are readily demonstrated in volunteers exposed to static magnetic fields greater than 0.1 T. The largest flow potentials occur across the aorta after ventricular contraction, and appear superimposed on the T-wave of the electrocardiogram (Tenforde, 1992). Kinouchi et al. (1996) calculated that a static field of 5 T would induce maximum current densities around the sinoatrial node of the heart of about 100 mA m^{-2} (500 mV m^{-1} using a tissue conductivity of 0.2 S m^{-1}), which is well below the cardiac excitation threshold. Additionally, a 5–10% reduction in blood flow in the aorta was predicted to occur in static fields of 10–15 T due to magneto-hydrodynamic interactions. Kangarlu et al. (1999), however, found that volunteers exposed to an 8-T field for 1 h showed no change in heart rate or blood pressure either during or after exposure. Chakeres et al. (2003a,b) reported that exposure of 25 healthy volunteers to 8-T fields had no clinically significant effect on heart rate, respiratory rate, blood pressure, finger pulse oxygenation levels, core body temperature, and cognitive function. In order to avoid the movement-induced sensations described above, the volunteers were moved very slowly into the magnet bore. Nevertheless, nine subjects reported sensations of dizziness, while two reported a metallic taste.

1.4.3.2 Epidemiology

Epidemiological studies were performed on workers exposed to static magnetic fields of up to a few mT, and the children of such workers. The International Agency for Research on Cancer (IARC, 2002) has reviewed studies of cancer. Generally, these have not pointed to higher cancer risks, although the number of studies was small, the numbers of cancer cases were limited, and the information on individual exposure levels was poor. Some studies have investigated reproductive outcome for workers involved in the aluminum industry or in MR imaging.

Kanal et al. (1993), for example, did not identify any decreased fertility for either male or female workers. However, no studies of high quality have been carried out with workers occupationally exposed to fields greater than 1 T.

1.4.3.3
Safety Aspects and Exposure Levels

The basic restrictions for static magnetic fields are expressed in terms of the magnetic flux density in units of Tesla. For time-varying magnetic fields the basic quantity is the induced current density, expressed in units of ampere per square meter ($A\ m^{-2}$).

As stated above, biological data for static magnetic field exposure indicate that there are no significant biological effects on people at levels below about 2 T. However, in stronger magnetic fields, vertigo, nausea, a metallic taste and phosphenes can be induced during movement.

The value of 2 T is considered suitable as ceiling value for whole-body occupational exposure with a relaxation of up to 5 T for exposure of the limbs alone (ICNIRP, 1994). However, as very few long-term exposure data are available, it is considered advisable to limit the average exposure for the whole body during the entire working day to 200 mT. In addition to the basic limits, the following cautionary clauses should be taken into account:

- The magnetic field exposure of persons with conductive implants, especially when made of ferromagnetic materials, should not exceed 25 mT averaged over times shorter than 1 s.
- Workers with cardiac pacemakers and electrically active implants should not have access to areas where the magnetic flux density exceeds 0.5 mT.
- Because of existing electromagnetic compatibility problems, or field influence on magnetic data carriers, separate intervention levels may be necessary.

1.4.4
Time-Varying Magnetic Fields (1 Hz to 100 kHz)

The time-varying magnetic fields originating from man-made sources generally have much higher intensities than the naturally occurring fields (ICNIRP, 2003). This is particularly true for sources operating at the power frequencies of 50 or 60 Hz. Other man-made sources are found in research, industry (welding machines, electric furnaces and induction heating) and medicine (MRI).

1.4.4.1
Interaction Mechanisms and Biological Bases for Limiting Exposure

Time-varying magnetic fields exert a force on charged particles such as ions or asymmetrically charged molecules, which results in electric fields and circulating

electric currents in tissues in accordance with Faraday's law. At the cellular level, this interaction consists of the induction of voltages across the membranes of cells which, given sufficiently high levels, can stimulate nerve cells to conduct or muscles to contract. These interaction mechanisms occur only where high electrical field strengths of above about 5 V m^{-1} are present (Reilly, 1998).

As the membrane's electrical conductivity is smaller by approximately five orders of magnitude than that of the extracellular fluid, it forms an electrical barrier that mediates interactions of cells with extracellular electric fields. It is, therefore, now assumed that the transduction processes through which induced electric signals influence cellular properties, involve interaction at the level of the cell membrane. A growing body of evidence indicates that induced electric fields and currents circulating in the extracellular medium can alter ion-binding to membrane macromolecules, influence ion transport across the membrane, and modify ligand–receptor interactions at the cell membrane surface. These changes in membrane properties may trigger trans-membrane signaling events. A number of membrane effects and cellular manifestations occur at threshold levels for induced electric fields below 0.1 V m^{-1} (Tenforde, 1996). The most sensitive tissues are those comprising interacting networks of electrically excitable tissue, such as the central and autonomic nervous systems.

The maximal induced electric field strength is proportional to dB/dt (the rate of change of the magnetic flux density), and to a proportionality constant, which depends on the field distribution and direction, the geometry of the body, and the electric characteristics of the tissues (Bernhardt, 1988). When the frequency increases, the magnetically induced electric field and current density increase linearly as a function of frequency. The induced electric field is maximal at the surface of the body and decreases towards the center. Coupling is maximized when the magnetic field is uniform and perpendicular to the frontal cross-section of the body. While geometrically simple models are useful to illustrate fundamental aspects of magnetic field dosimetry, anatomically realistic models of man and high-resolution calculations have been used in recent years to obtain more detailed information (e.g., Dawson et al., 1997; Dimbylow, 1998). Such calculations clearly indicate that the local peak current densities are much higher than the average current densities. In a homogeneous 500-μT field of 50 Hz, the local peak current density may considerably exceed 10 mA m^{-2}, and up to 40 mA m^{-2} in some parts of the body.

The biological effects of low-frequency magnetic fields continue to be studied using a wide variety of exposure conditions, models, and biological endpoints. There is a consensus of the many national and international scientific expert groups, which have comprehensively reviewed the biological effects literature and the biological studies relevant to the assessment of possible adverse health effects of exposure to low-frequency magnetic fields. These include the IARC (2002), ICNIRP (2003) and NRPB (2004).

Studies have been carried out of direct nerve stimulation thresholds in volunteers by intense, pulsed magnetic fields, used in various specialized medical applications such as MRI (see Shellock, 2001) and transcranial magnetic stimulation

(TMS; see also Section 4.4). Threshold rates of change of MRI switched gradient magnetic fields for perception, discomfort and pain resulting from peripheral nerve stimulation has been extensively reviewed by Nyenhuis et al. (2001). Median minimum threshold rates of change of magnetic field during periods of less than 1 ms for perception were generally 15–25 T s^{-1} depending on orientation, and showed large inter-individual differences (Bourland et al., 1999). Cells of the central nervous system (CNS) are considered to be sensitive to induced electric fields that are below the stimulation threshold of nerve axons (*in-vitro* threshold of ca. 4–5 V m^{-1}; Jefferys et al., 2003). Such electric field interactions have been demonstrated in experimental studies using isolated animal brain tissue. However, the CNS *in vivo* is considered to be more sensitive to induced low-frequency electric fields and currents than *in-vitro* preparations, due to the larger number of interacting nerve cells; the data available are consistent with a threshold of 100 mV m^{-1}, which may be constant between a few hertz and a few kHz. Other excitable tissues such as the heart seem less susceptible to the direct effects of induced electric fields, but may be affected indirectly via effects on the CNS (NRPB, 2004).

The retina is considered to be a good model of the sensitivity of CNS tissue to induced electric fields. Retinal function can be affected by exposure to low-frequency magnetic fields and applied electric currents. Field thresholds in the extracellular fluid of the retina for inducing phosphenes have been estimated to lie between about 10 and 60 mV m^{-1} at 20 Hz (NRPB, 2004). However, the extrapolation of such values to other CNS tissues is complex and uncertain. The exact mechanisms underlying phosphene induction and its frequency dependence remain unknown.

1.4.4.2 Epidemiology

There is some epidemiological evidence that exposure to power frequency magnetic fields above 0.4 μT is associated with a small raised risk of leukemia in children (approximately, doubling of the relative risk). The IARC (2002) stated that their findings provided limited evidence for an excess risk in humans exposed at these field levels, and evaluated low-frequency magnetic fields as being "possibly carcinogenic to humans" (Classification 2B). However, in the absence of clear evidence of any carcinogenic effect in adults, or of a plausible explanation from experiments on animals or isolated cells, the ICNIRP (2003) has concluded that the epidemiological evidence is not strong enough to justify a firm conclusion that such fields cause leukemia in children. The IARC also considered the evidence for excess cancer risks of all other kinds, in children and adults, as a result of exposure to extremely low frequency (<300 Hz) electric and magnetic fields, to be inadequate. The findings from studies of health effects other than cancer have generally been inconsistent.

The results of epidemiological studies, either taken individually or as collectively reviewed by expert groups, cannot be used as a basis for the derivation of quantitative restrictions of exposure to low-frequency fields (ICNIRP, 2003; NRPB, 2004).

1.4.4.3
Safety Aspects and Exposure Levels

Scientific established data from which guidance can be developed concerns electric field interactions in the CNS and certain other electrically excitable tissues. A cautious approach has been used to indicate thresholds for adverse health effects. Data on other possible health effects examined lack plausibility, consistency, and coherence.

Threshold tissue electric field strengths of around 100 mV m^{-1} have been identified for effects in the CNS. Comparison of basic restrictions expressed in terms of induced electric field strength with those expressed in terms of induced current density requires computational modeling using tissue- and frequency-dependent values of the electrical conductivity.

For occupational exposure, it is concluded that a restriction of the induced electric field strength in the central, autonomic and enteric nervous systems to less than 100 mV m^{-1} is adequate to protect most adult members of the population. In the frequency range from 4 Hz to 1 kHz, the ICNIRP (1998) decided that occupational exposure should be limited to fields that induce current densities less than 10 mA m^{-2} (corresponding to a tissue field strength of about 50 mV m^{-1} using a tissue conductivity of 0.2 S m^{-1}). Below 4 Hz and above 1 kHz, the basic restriction on induced current density increases progressively, corresponding to the increase in the threshold for nerve stimulation for these frequency range (Fig. 1.30). The basic restrictions for current densities for occupational exposure are presented in Table 1.3. The current densities are given as root-mean-square (rms) values.

Where appropriate, the reference levels are obtained from the basic restrictions by mathematical modeling and by extrapolation from the results of laboratory studies at specific frequencies. They are given for the condition of maximum coupling of the field to the exposed individual, thereby providing maximum protection. The reference levels for occupational exposure (ICNIRP, 1998) are summarized in Table 1.4. The reference levels are intended to be spatially averaged values over the entire body of the exposed individual, but with the important proviso that the basic restrictions on localized exposure are not exceeded. The frequency dependence of the reference levels – shown in Figure 1.31 for the magnetic flux density – is consistent with data on both biological effects and coupling of the field.

1.4.5
Electromagnetic Fields (100 kHz to 300 GHz)

1.4.5.1
Interaction Mechanisms and Biological Bases for Limiting Exposure

There are well-documented bioeffects linked to excess temperature elevation. Such effects have been observed from exposure to radiofrequency (RF) electromagnetic fields resulting from whole-body or local heating. An important first step in assess-

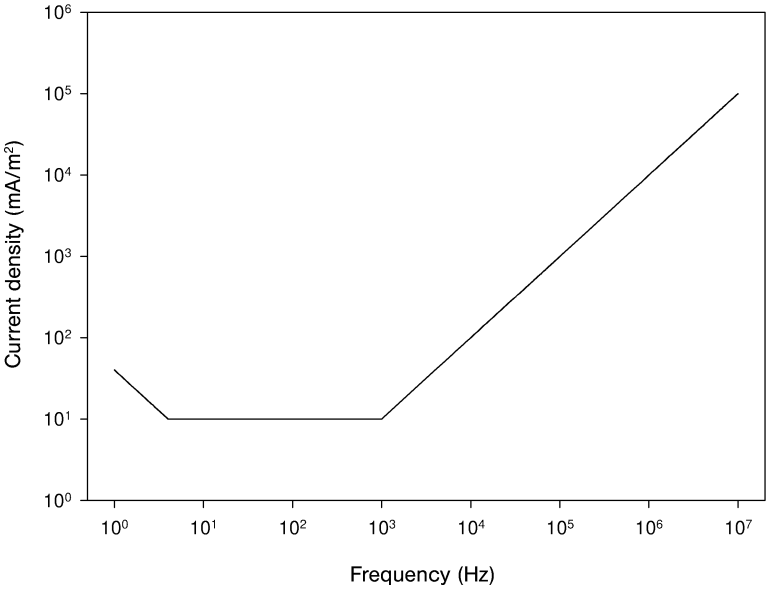

Fig. 1.30. Basic restriction for the current density for head and trunk for occupational exposure for frequencies between 1 Hz and 10 MHz. The frequency dependence reflects the frequency dependence of the thresholds of nerve- and muscle stimulation, including a safety factor. (From ICNIRP, 1998).

ing the RF exposure health risk is to define the level of energy absorption and the resulting possible temperature elevation over the entire frequency range. This database is fundamental to the establishment of exposure limits (ICNIRP, 1998). In addition, consideration must be given to long-term or chronic exposures of workers to low-level electromagnetic fields.

It is convenient to divide the RF range into different spectral regions according to the predominant or more significant mechanisms of energy absorption:

- In the sub-resonance range (0.1–10 MHz), exposure of the human body to electromagnetic fields can result in high rates of energy deposition in the hand, wrist and ankle due to current flow through small effective cross-sectional areas. In this frequency region, the biological response of humans arises not only from tissue heating but also from the stimulation of excitable tissues, such as nerve and muscles, via induced currents. Thus, the thermal mechanism dominates at higher frequencies, while induced currents become also important at lower frequencies. Therefore, in the frequency range of 0.1 to a few MHz, the significant dosimetric quantities for establishing basic exposure limits are both the internal current density and the absorbed energy.
- In the resonance range (10–300 MHz), the human body can be thought of as an absorbing antenna. A maximum absorption is reached, for plane wave exposure,

Table 1.3. Basic restriction for occupational exposure for time-varying magnetic fields for frequencies up to 300 GHz. (From ICNIRP, 1998).

Frequency range	Current-density for head and trunk [mA m^{-2}][a)]	Whole-body average SAR [W kg^{-1}]	Localized SAR (head and trunk) [W kg^{-1}]	Localized SAR (limbs) [W kg^{-1}]	Power density [W m^{-2}]
Up to 1 Hz	40				
1–4 Hz	$40/f$	–			
4 Hz to 1 kHz	10		–		
1–100 kHz	$f/100$				
100 kHz to 10 MHz	$f/100$	0.4	10	20	
10 MHz to 10 GHz		0.4	10	20	
10–300 GHz					50

[a)] Root mean square (rms) values; f indicates frequency (in Hz). All specific absorption rate (SAR) values are to be averaged over any 6-min period. Localized SAR averaging mass is any 10 g of contiguous tissue; the maximum SAR so obtained should be the value used for the estimation of exposure. There are several other clauses to be considered (see ICNIRP, 1998).

Table 1.4. Reference levels for occupational exposure to time-varying magnetic fields (unperturbed rms values).

Frequency range	Magnetic field strength *H* [A m^{-1}]	Magnetic flux density *B* [μT]	Equivalent plane wave power density S_{eq} [W m^{-2}]
Up to 1 Hz	1.63×10^5	2×10^5	
1–8 Hz	$1.63 \times 10^5/f^2$	$2 \times 10^5/f^2$	
8–25 Hz	$2 \times 10^4/f$	$2.5 \times 10^4/f$	
0.025–0.82 kHz	$20/f$	$25/f$	
0.82–65 kHz	24.4	30.7	
0.065–10 MHz	$1.6/f$	$2.0/f$	
10–400 MHz	0.16	0.2	10
400–2000 MHz	$0.008\sqrt{f}$	$0.01\sqrt{f}$	$f/40$
2–300 GHz	0.36	0.45	50

f as indicated in the frequency range column. There are several clauses to be considered (see ICNIRP, 1998).

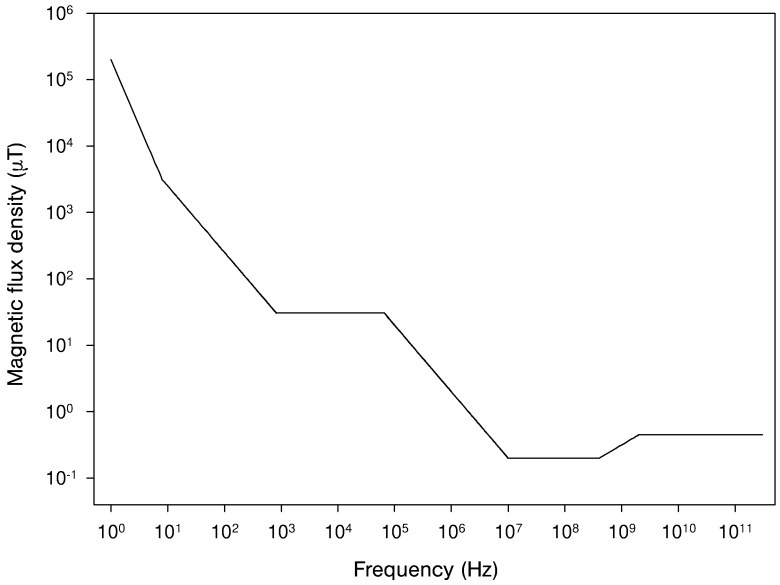

Fig. 1.31. Reference level for the magnetic flux density for occupational exposure. The frequency dependence of the reference magnetic flux density level is consistent with data on both biological effects and coupling of the field. (From ICNIRP, 1998).

in the frequency range of 30–80 MHz. At higher frequencies the wavelength becomes small compared to the body size, and so-called "hot spots" of absorption may occur in smaller parts of the body such as the head, though the total absorption will be reduced.

- Above 300 MHz, localized energy absorption can occur due to dimensional resonance phenomena or quasi-optical focusing of the incident fields. As the frequency is further increased, the depth of penetration of the incident electromagnetic energy will be reduced until most of the energy is absorbed close to the body surface at 300 GHz.

The time rate of electromagnetic energy absorption by a unit of mass of a biological system is defined as the *specific absorption rate* (SAR), the unit of which is watt per kilogram (W kg^{-1}). The SAR may be spatially averaged over the total mass of an exposed body or its parts, and may be temporally averaged over a given time of exposure or over a single pulse or modulation period of the radiation. The SAR is the significant dosimetric quantity for establishing basic exposure restrictions in the frequency range of a few MHz to a few GHz.

A review of the bioeffects literature indicates that heat-related disorders should not occur in the majority of healthy adults, provided that core temperature does not rise above 38 °C (corresponding to a temperature rise of 1 °C above baseline).

In this case it is also likely to prevent adverse effects on the performance of the most cognitive tasks. High rates of physical activity and/or warm, humid environments will reduce the additional RF heat loads that most adults can tolerate without exceeding 38 °C. An RF heat load of 0.4 W kg^{-1} averaged over the whole body should be sufficiently low that these other factors can be ignored.

It should be mentioned, however, that the individual sensitivity to heat-related stress varies among the general population. Additionally, adults taking drugs that have direct effects on the control of body temperature, or on metabolism or heat production of the body, may also be considered at greater risk.

Adverse effects on the testis should not occur, provided that temperature increases are less than 1 °C. Other tissues, such as kidney, liver and muscle, seem less sensitive. Temperature rises in the brain, retina, and spinal cord to above 38 °C, of the other tissues of the neck and trunk to above 39 °C, and of the tissues of the limbs to above 40 °C, may result in localized heat-induced damage. The lenses of the eye are particularly sensitive due to the limited ability of the eye to dissipate heat. The ability to dissipate heat from locally heated tissues depends on their temperature in relation to their surroundings and rate of blood flow through the tissue. People with cardiovascular disease, which will reduce the blood circulation, may be at increased sensitivity by RF electromagnetic fields compared with people with normal cardiovascular responses.

There are relatively few dosimetric studies linking localized temperature increases and SAR in most parts of the body. Studies indicate a range of localized temperature increases of 0.05 to 0.12 °C in the brain from a localized SAR of 1 W kg^{-1}. A number of studies have suggested that low-level RF fields may induce different subtle biological responses, particularly possible effects of pulsed fields on brain function and on changes in heat shock protein expression (NRPB, 2004). Further studies are necessary to examine these effects. However, none of these possible effects is considered sufficient to derive basic restrictions for human exposure.

1.4.5.2 Epidemiology

A large number of occupational studies have been conducted over several decades, particularly on cancer, cardiovascular disease, adverse reproductive outcome, and cataract, in relation to RF exposure. More recently, studies have been conducted on residential exposure, mainly from radio and television transmitters, and especially focusing on leukemia. There have also been studies of mobile telephone users, particularly on brain tumors and less often on other cancers and on symptoms. To date, the results of these studies have provided no consistent or convincing evidence of any causal relationship between RF exposure and adverse health effects. However, the studies have too many deficiencies to rule out an association. A key concern across all studies is the quality of assessment of RF exposure. A comprehensive review of epidemiologic studies regarding the effects of RF fields on human health has been produced by Ahlbom et al. (2004).

1.4.5.3
Safety Aspects and Exposure Limits

The basic restrictions for frequencies up to 300 GHz are presented in Table 1.3. The basic restriction for the current density is plotted in Figure 1.30 for the relevant frequency range. Reference levels for occupational exposure are presented in Table 1.4. As an example, reference levels for the magnetic flux density are plotted in Figure 1.31 for the entire frequency range. In addition, occupationally exposed workers with metallic implants and pacemaker wearers are groups at particular risk, and may not be protected by the prescribed limits.

1.4.6
Protection of Patients and Volunteers Undergoing MR Procedures

With the significant level of growth in the number of patients examined using MR technology and the rapid development of MR hardware, the consideration of possible risks and health effects associated with the use of diagnostic MR devices is gaining increasingly in importance. In Germany, for example, the annual frequency of MR examinations increased between 1996 and 2003 from 22 to 64 examinations per 1000 inhabitants.

As will be described in detail in Chapter 3, three types of magnetic fields are employed in MR imaging and spectroscopy:

- a high static magnetic field generating a macroscopic nuclear magnetization;
- rapidly alternating magnetic gradient fields for spatial encoding of the MR signal; and
- RF electromagnetic fields for excitation and preparation of the spin system.

The biophysical interaction mechanisms and biological effects of these fields are discussed in Sections 1.4.3 to 1.4.5. Supplementary information and an exhaustive bibliography concerning safety aspects of clinical MR procedures can be found in the recent literature (e.g., Ordidge et al., 2000; Shellock, 2001). The following section provides a brief summary of exposure limits and precautions to be taken in order to minimize health hazards and risks to patients and volunteers undergoing MR procedures according to:

- the technical product standard IEC 60601-2-33 issued by the International Electrotechnical Commission in 2002 (IEC, 2002); and
- the safety recommendation issued by the International Commission on Non-Ionizing Radiation Protection in 2004 (ICNIRP, 2004).

In order to reflect the uncertainty over identified deleterious effects and, moreover, to offer the necessary flexibility for the development and clinical evaluation of new MR technologies, both the IEC standard and the ICNIRP recommendation give exposure limits for three different modes of operation:

- *Normal operating mode*: Routine MR examinations that did not cause physiological stress to patients.
- *Controlled operating mode*: Specific MR examinations outside the normal operating range where discomfort and/or physiological stress may occur in some patients. A clinical decision must be taken to balance such effects against foreseen benefits; exposure must be carried out under medical supervision.
- *Experimental operating mode*: Experimental MR procedures with exposure levels outside the controlled operating range. In view of the potential risks for patients and volunteers, special ethical approval and adequate medical supervision is required.

1.4.6.1 Static Magnetic Fields

The possible health effects that might result from acute exposure to static magnetic fields were reviewed in Section 1.4.3. The basic actions are physical effects (translation and orientation), electrodynamic forces on moving electrolytes, and effects on electron spin states of chemical reaction intermediates.

Until now, most MR examinations have been made using static magnetic fields up to 3 T, although whole-body MR systems with static magnetic fields up to 8 T are already used in clinical tests. The literature does not indicate any serious adverse health effects from the exposure of healthy human subjects up to 8 T. However, it should be noted that, to date, there have been no epidemiological studies performed to assess possible long-term health effects in patients or volunteers. The greatest potential hazard comes from metallic, in particular ferromagnetic materials (such as scissors, coins, pins, oxygen cylinders) that are accelerated in the inhomogeneous magnetic field in the periphery of an MR system and quickly become dangerous projectiles. This risk can only be minimized by a strict and careful management of both patients and staff (Medical Devices Agency, 2002).

Because exposure to magnetic fields above 2 T can produce nausea and vertigo, it is recommended that examinations above this static magnetic flux density be conducted in the controlled operating mode under medical supervision. The recommended upper limit for this operating mode is 4 T, due to the limited data concerning possible effects above this static field strength. For MR examinations performed in the experimental operating mode, there is no upper limit for the magnetic flux density.

1.4.6.2 Time-Varying Magnetic Gradient Fields

The rapidly switched magnetic gradient fields used in MRI for spatial encoding induce electric fields in the human body in accordance with Faraday's law which, if of sufficient magnitude, can produce nerve and muscle stimulation (see Section 1.4.4). The induced electric field is proportional to dB/dt, the time rate of change

of the magnetic field. From a safety standpoint, the primary concern with regard to time-varying magnetic fields is cardiac fibrillation, because it is a life-threatening condition. In contrast, peripheral nerve stimulation is of practical concern because uncomfortable or intolerable stimulations would interfere with the examination (e.g., patient movements) or would even result in a termination of the examination.

Recommendations on limiting patient and volunteer exposure to time-varying magnetic fields are based primarily on the extensive investigations on peripheral nerve stimulation in humans performed at Purdue University (Schaefer et al., 2000; Nyenhuis et al., 2001). In the reported studies, data were obtained for the perception threshold, the threshold for uncomfortable stimulation, and the threshold for intolerable stimulation during exposure to gradient fields. The results indicate that the lowest percentile for intolerable stimulation is approximately 20% above the median perception threshold for peripheral nerve stimulation, which can be parameterized by the following empirical relationship:

$$\frac{dB}{dt} = 20 \cdot \left(1 + \frac{0.36}{\tau}\right) \quad (\text{in Ts}^{-1}) \tag{1.73}$$

In Eq. (1.73), τ is the effective stimulus duration (in ms) defined as the duration of the period of monotonic increasing or decreasing gradient.

The maximum recommended exposure level for time-varying magnetic fields is set equal to a dB/dt of 80% of the median perception threshold given in the relationship above for normal operation, and 100% of the median for controlled operation. As shown in Figure 1.32, the threshold for cardiac stimulation (Reilly, 1998) is well above the median perception threshold for peripheral nerve stimulation, except at very long pulse durations which are, however, not relevant for MR procedures.

1.4.6.3 Radiofrequency Electromagnetic Fields

Time-varying electromagnetic fields with frequencies above 10 MHz (RF fields), that are used in MR studies to excite and prepare the spin system, deposit energy in the human body that is mainly converted to heat. The parameter relevant for the evaluation of biological effects of RF fields is the increase in tissue temperature, which is dependent not only on localized power absorption and the duration of RF exposure, but also on heat transfer and the activation of thermoregulatory mechanisms leading to thermal equalization within the body.

As reviewed in Section 1.4.5, no adverse health effects are expected if the increase in body-core temperature does not exceed 1 °C. In the case of infants, pregnant women, elderly, and persons with cardiocirculatory impairment, however, it is desirable to limit body-core temperature increases to 0.5 °C. Additionally, local temperatures under exposure to the head, trunk, and/or extremities should be limited to the values given in Table 1.5.

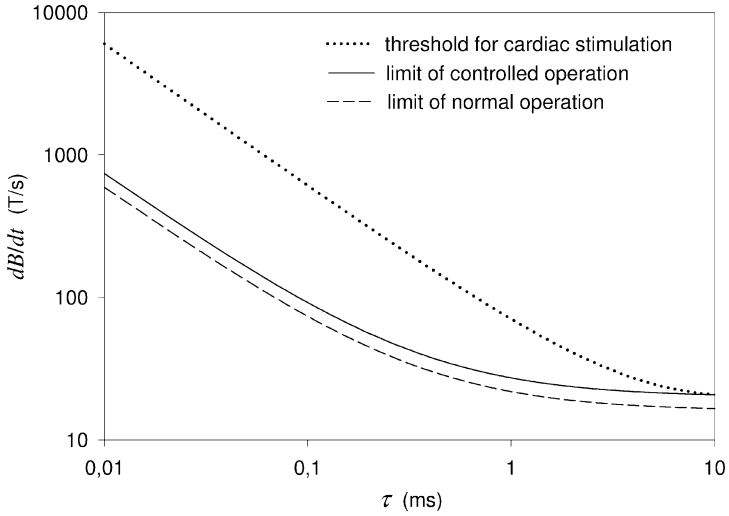

Fig. 1.32. Threshold for cardiac stimulation (Reilly, 1998) and limits for normal and controlled operation of a magnetic resonance device. Data are expressed as dB/dt as a function of the effective stimulus duration τ. The limit for the controlled operation mode is given by the median perception threshold for peripheral nerve stimulation.

Since temperature changes in the various organs and tissues of the body during an MR procedure are difficult to measure in clinical routine, RF exposure of patients is usually characterized by means of the SAR (in W kg^{-1}) As only parts of the patient's body are exposed simultaneously during an MR procedure, not only the whole-body SAR but also partial-body SARs for the head, the trunk, and the extremities should be estimated on the basis of suitable patient models (e.g., Brix et al., 2001). Based on the published experimental studies concerning temperature rise and theoretical simulations, the SAR levels summarized in Table 1.4 should not be exceeded in order to limit temperature rise to the values given in Table 1.5.

Table 1.5. Basic restrictions for body temperature rise and partial-body temperatures for volunteers and patients undergoing MR procedures.

Operating mode	Rise of body-core temperature [°C]	Spatially localized temperature limits		
		Head [°C]	Trunk [°C]	Extremities [°C]
Normal	0.5	38	39	40
Controlled	1	38	39	40
Experimental	>1	>38	>39	>40

Table 1.6. SAR levels valid for volunteers and patients undergoing MR procedures at environmental temperatures below 24 °C.

Operating mode	Averaging time: 6 min					
	Whole-body SAR [W kg^{-1}]	Partial-body SAR [W kg^{-1}]		Local SAR (averaged over 10 g tissue) [W kg^{-1}]		
	Body region					
	Whole-body	Any, except head	Head	Head	Trunk	Extremities
Normal	2	2–10[a)]	3	10	10	20
Controlled	4	4–10[a)]	3	10	10	20
Experimental	>4	>(4–10)[a)]	>3	10	>10	>20
Short-term SAR	The SAR limit over any 10-s period shall not exceed three times the corresponding average SAR limit.					

[a)] Partial-body *SARs* scale dynamically with the ratio r between the patient mass exposed and the total patient mass:
– normal operating mode: $SAR = (10 - 8 \cdot r)$ W kg^{-1}
– controlled operating mode: $SAR = (10 - 6 \cdot r)$ W kg^{-1}

With respect to the application of the SAR levels defined in Table 1.6, the following points should be taken into account:

- Partial-body SARs scale dynamically with the ratio r between the patient mass exposed and the total patient mass. For $r \rightarrow 1$, they converge against the corresponding whole-body values, for $r \rightarrow 0$ against the localized SAR level of 10 W kg^{-1} defined for occupational exposure of head and trunk (ICNIRP, 1998; cf. Table 1.3).
- The recommended SAR limits do not relate to an individual MR sequence, but rather to running SAR averages computed over each 6-min period, which is assumed to be a typical thermal equilibration time of smaller masses of tissue (Brix et al., 2002).

1.4.6.4 Contraindications

Pregnant Patients

Pregnant patients undergoing MR examinations are exposed to the combined magnetic and electromagnetic fields used in MR imaging. The few studies on pregnancy outcome in humans following MR examinations have not revealed any adverse effects, but are very limited because of the small numbers of patients involved and difficulties in the interpretation of the results. It is thus advised that

MR procedures may be used in pregnant patients only after critical risk/benefit analysis, in particular during the first trimester, to investigate important clinical problems or to manage potential complications for the patient or fetus. Moreover, it is recommended that exposure duration should be reduced to the minimum and that the exposure levels of the normal operation mode are not exceeded.

Special Safety Issues and Contraindications

MR examinations of patients who have electrically, magnetically, or mechanically activated implants (e.g., cardiac pacemakers and defibrillators, cochlear implants, electronic drug infusion pumps), as well of patients with passive implants or other objects of ferromagnetic or unknown material (e.g., aneurysm and hemostatic clips, orthopedic implants, pellets, and bullets), is contraindicated. Lists of implants and materials tested for safety or compatibility in association with MR systems have been published and updated (e.g., Shellock, 2005; www.MRIsafety.com).

References

Ahlbom, A., Green, A., Kheifets, L., Savitz, D., and Swerdlow, A. (2004). Epidemiology of health effects of Radiofrequency Exposure. *Environ. Health Perspect.*, **112**, 1741–1754.

Bernhardt, J.H. (1988). The establishment of frequency dependent limits for electric and magnetic fields and evaluation of indirect effects. *Radiat. Environm. Biophys.*, **27**, 1–27.

Bourland, J.B., Nyenhuis, J.A., and Schaefer, D.J. (1999). Physiologic effects of intense MR imaging gradient fields. *Neuroimaging Clin. North Am.*, **9**(2), 363–377.

Brix, G., Reinl, M., and Brinker, G. (2001). Sampling and evaluation of specific absorption rates during patient examinations performed on 1.5-Tesla MR systems. *Magn. Reson. Imaging*, **19**, 769–779.

Brix, G., Seebass, M., Hellwig, G., and Griebel, J. (2002). Estimation of heat transfer and temperature rise in partial-body regions during MR procedures: an analytical approach with respect to safety considerations. *Magn. Reson. Imaging*, **20**, 65–76.

Chakeres, D.W., Bornstein, R., and Kangarlu, A. (2003a). Randomised comparison of cognitive function in humans at 0 and 8 T. *J. Magn. Reson. Imaging*, **18**, 342–345.

Chakeres, D.W., Kangarlu, A., Boudoulas, H., and Young, D.C. (2003b). Effect of static magnetic field exposure of up to 8 T on sequential human vital sign measurements. *J. Magn. Reson. Imaging*, **18**, 346–352.

Dawson, T.W., Caputa, K., and Stuchly, M.A. (1997). Influence of human model resolution on computed currents induced in organs by 60 Hz magnetic fields. *Bioelectromagnetics*, **18**, 478–490.

Dimbylow, P.J. (1998). Induced current densities from low-frequency magnetic fields in a 2 mm resolution, anatomically realistic model of the body. *Phys. Med. Biol.*, **43**, 221–230.

EU (2004). Directive 2004/40/EC of the European Parliament and of the Council of 21 April 2004 on the minimum health and safety requirements regarding the exposure of workers to the risks arising from physical agents (Electromagnetic fields). (18th individual Directive within the meaning of Article 16(1) of Directive 89/391/EEC). Off. J. EU L42/38 from 30.4.2004.

IARC (2002). *Static and extremely low frequency electric and magnetic fields*. IARC Monographs on the Evaluation of Carcinogenic Risks to Humans. Vol. 80. Lyon, International Agency for Research on Cancer.

ICNIRP (1994). (International Commission on Non-ionizing Radiation Protection). Guidelines on limits of exposure to static magnetic fields. *Health Physics*, **66**, 100–106.

ICNIRP (1998). Guidelines for limiting exposure to time-varying, electric, magnetic and electromagnetic fields. *Health Physics*, **74**, 494–522.

ICNIRP (2002). General approach to protection against non-ionizing radiation protection. *Health Physics*, **74**, 494–522.

ICNIRP (2003). Matthes, R., Vecchia, P., McKinlay, A.F., Veyret, B., and Bernhardt, J.H. (Eds.) *Review of the scientific evidence on dosimetry, biological effects, epidemiological observations, and health consequences concerning exposure to static and low frequency electromagnetic fields (0–100 kHz)*. ICNIRP 13/2003, Märkl Druck München.

ICNIRP (2004). Medical magnetic resonance (MR) procedures: Protection of patients. *Health Physics*, **87**, 197–216.

International Electrotechnical Commission (2002). IEC 60601-2-33 (Second edition), *Particular requirements for the safety of magnetic resonance equipment for medical diagnosis*. IEC, Geneva.

Jefferys, J.G.R., Deans, J., Bikson, M., and Fox, J. (2003). Effects of weak electric fields on the activity of neurons and neuronal networks, In: Repacholi, M.H. and McKinlay, A.F. (Eds.), Proceedings International Workshop: Weak Electric Field Effects in the Body. *Radiat. Prot. Dosim.*, **106**, 321–324.

Kanal, E., Evans, J.A., Savitz, D.A., and Shellock, F.G. (1993). Survey of reproductive health among female MR workers. *Radiology*, **187**, 395–399.

Kangarlu, A., Burgess, R.E., Zhu, H., Nakayama, T., Hamlin, R.L., Abduljalil, A.M., and Robataille, P.M.L. (1999). Cognitive, cardiac, and physiological safety studies in ultra high field magnetic resonance imaging. *Magn. Reson. Imaging*, **17**, 1407–1416.

Kinouchi, Y., Yamaguchi, H., and Tenforde, T.S. (1996). Theoretical analysis of magnetic field interactions with aortic blood flow. *Bioelectromagnetics*, **17**, 21–32.

Medical Devices Agency (2002). *Guidelines for magnetic resonance equipment in clinical use*. http://www.medical-devices.gov.uk.

NRPB (2004). *Review of the Scientific Evidence for Limiting Exposure to Electromagnetic Fields (0–300 GHz)*. Doc. NRPB 15 (3), Chilton, Didcot, UK, 1–215.

Nyenhuis, J.A., Bourland, J.D., Kildishev, A.V., and Schaefer, D.J. (2001). Health effects and safety of intense gradient fields. In: Shellock, F.G. (Ed.), *Magnetic Resonance Procedures: Health Effects and Safety*, CRC Press, New York, pp. 31–53.

Ordidge, R., Shellock, F.G., and Kanal, E. (2000). Special issue: MR safety. *J. Magn. Reson. Imaging*, **12**.

Reilly, J.P. (1998). *Applied bioelectricity: from electrical stimulation to electro pathology*. Springer, New York.

Saunders, R. (2005). Static magnetic fields: animal studies. *Prog. Biophys. Molec. Biol.*, **87**, 225–239.

Schaefer, D.J., Bourland, J.D., and Nyenhuis, J.A. (2000). Review of patient safety in time-varying gradient fields. *J. Magn. Reson. Imaging*, **12**, 20–29.

Schenck, J.F. (2005). Physical interactions of static magnetic fields with living tissues. *Prog. Biophys. Molec. Biol.*, **87**, 185–204.

Schenck, J.F., Dumoulin, C.L., Redington, R.W., Kressel, H.Y., Elliott, R.T., and McDougall, I.L. (1992). Human exposure to 4.0 Tesla magnetic fields in a whole body scanner. *Med. Phys.*, **19**, 1089–1098.

Shellock, F.G. (2001). *Magnetic resonance procedures: health effects and safety*. Boca Raton, CRC Press.

Shellock, F.G. (2005). *Reference manual for magnetic resonance safety, implants, and devices: 2005 edition*. Biomedical Research Publishing Company, Los Angeles.

Tenforde, T.S. (1992). Interaction mechanisms and biological effects of static magnetic fields. *Automedica*, **14**, 271–293.

Tenforde, T.S. (1996). Interaction of ELF magnetic fields with living systems. In: Polk, C., Postow, E. (Eds.), *Biological effects of electromagnetic fields*. Boca Raton, FL: CRC Press, pp. 185–230.

Tenforde, T.S. (2005). Magnetically induced electric fields and currents in the circulatory system. *Prog. Biophys. Molec. Biol.*, **87**, 279–288.

2
Biomagnetism

2.1 Introduction

Hannes Nowak

Electrical activity in the living body is caused by movements of ions inside, outside and across cellular membranes. These movements of electrically charged particles, natural electrical currents, are responsible for magnetic fields measurable outside the body, which are called *biomagnetic fields* (Williamson and Kaufman, 1981). Potential differences measured on the body surface are also caused by these currents. Examples of such ion currents in humans are those from myocardial activity, which produce the electrocardiogram (ECG) and the *magnetocardiogram* (MCG) (see Section 2.3). The alpha-rhythm currents in the head produce parts of the electroencephalogram (EEG) and *magnetoencephalogram* (MEG) (see Section 2.4), and the currents from unborn child (heart or brain) generate the *fetal MCG* or *fetal MEG* (see Section 2.5).

The measurement of magnetic fields produced by the human body is termed the *biomagnetic measurement technique*, and is a completely noninvasive and contact-free method without any influence on the subject. This method is useful for obtaining both spatial (in the mm-range) and temporal (in the ms-range) information about magnetic field distribution. Based on the magnetic field measurements and the field distribution, it is possible to localize the sources of the magnetic field, which is used in *magnetic source imaging* (MSI). All tissues of the human body are practically nonmagnetic; therefore, propagation of the magnetic field is not disturbed by human tissue. This represents one principal advantage of magnetic measurement over conventional measurement of potential differences by surface electrodes (EEG, ECG), because these potential differences are strongly influenced by conductivity inhomogeneities inside the body.

Biomagnetic fields are very weak, however, and therefore very sensitive magnetic field detectors are necessary. In addition, disturbances must be reduced sufficiently in order to achieve a suitable signal-to-noise ratio. Disturbances may derive from the environment (external noise), from the measurement set-up, and even from the subject to be investigated itself.

In order to localize the sources of the biomagnetic field it is necessary to make assumptions about the structure of those sources. The simplest and most common assumption is to describe the source as a current dipole. The current dipole repre-

sents the intracellular current (also referred to as *primary current*). The extracellular currents (also called volume currents or *secondary currents*) are produced by the effects of volume conduction in the tissue surrounding the dipole.

2.2
Biomagnetic Instrumentation

Hannes Nowak

2.2.1
History

In 1820, Hans Oerstedt identified and noted down that a current flowing through a volume produces a magnetic field. Such currents also occur in the human body, producing biomagnetic fields that are detectable outside the body. One source of weak fluctuating fields is the small ion currents in living materials; these currents are produced by large masses of excitable, synchronously firing tissue, such as the heart muscles. The magnetocardiogram was first detected by Baule and McFee in 1962. These measurements (Baule and McFee, 1963) were made with a specially designed assembly of two copper pick-up coils, each with two million turns and wound on a dumbbell-shaped core (length ca. 30 cm, 9 cm diameter) of magnetic material (ferrite). The coils were connected in opposition (gradiometer) so that the induced voltage from the spatially uniform magnetic background fluctuations was almost completely cancelled. The thermal noise due to winding resistance and the noise of the preamplifier to which the pick-up coils were connected (Baule, 1965) set the fundamental limits on the use of copper coils for detecting weak magnetic fields.

A group from Moscow (Safonov et al., 1967) reported the detection of the heart's magnetic field using the same technique several years after the first Baule–McFee measurement. The Russian group used a similar gradient technique, but the subject and the detector were placed inside a shielded room with 1.5 cm-thick iron walls, which presumably reduced the background noise by a factor of about 10. A different system was developed by David Cohen, a pioneer in biomagnetism, for measuring weak magnetic fields (Cohen, 1967a). This device consisted of a small coil detector (magnetometer, air-core 200 000-turn coil 5 cm in length and 8 cm in diameter) and a magnetically shielded chamber to reduce the environmental noise by a factor of about 1000 (Cohen, 1967b). The inner size of the chamber was 2.3 m, and the chamber consisted of two cubic shells of 1.5 mm-thick ferromagnetic shielding and one layer of aluminum. With this device, Cohen first measured the magnetic fields resulting from the brain's spontaneous alpha-rhythm (Cohen, 1968). A more sensitive system was built at MIT, consisting of a shielded room

and a SQUID (*S*uperconducting *QU*antum *I*nterference *D*evice; see Section 2.2.3 for details) magnetometer, based on superconductivity (Buckel and Kleiner, 2004). The MIT shielded room had the shape of a rhombicubooctahedron, which is roughly the shape of a sphere with an inner diameter of about 2.5 m. Five layers of shielding were used: three high-μ layers and two aluminum layers (Cohen, 1970). Studies conducted by Zimmerman – who was one of the inventors of the SQUID – was the breakthrough for biomagnetism (Zimmerman et al., 1970). The "biomagnetic" method became more practical using SQUIDs, which was demonstrated first by Cohen, Edelsack and Zimmerman in 1970 (Cohen et al., 1970).

During the 1970s, biomagnetism became an independent field of research (Williamson and Kaufman, 1981). Numerous laboratories developed single-channel SQUID-devices for biomagnetic investigations, thus improving the measurement technique worldwide. Rapid development of the technology during the 1980s resulted in multichannel biomagnetometers with more than hundreds of channels. Because of different applications, multichannel biomagnetometers are today produced for MEG investigations (helmet-shaped systems), for MCG investigations (plane devices), or for fetal magnetography (adapted to the abdomen of pregnant women). For details, see Sections 2.3 (cardiomagnetism), 2.4 (neuromagnetism), and 2.5 (fetal magnetography).

The multichannel device KRENIKON® (Siemens AG, Erlangen, Germany) with 31-channels was first run in 1988 (Hoenig et al., 1989), but the commercial version with 37 channels was run in 1989 (Hoenig et al., 1991). A double-dewar MEG-system with altogether 28 simultaneously operating SQUID-channels with noise compensation and software gradiometers was developed by the Dornier company in 1990 (Becker et al., 1993; Dieckmann et al., 1996). Today, however, these systems belong to history, and the currently running commercial multichannel devices are described in Section 2.2.7. SQUIDs are described in greater detail by Clarke and Braginski (2004) and Buckel and Kleiner (2004).

In 1986, the discovery of high-temperature superconductivity (Bednorz and Müller, 1986) offered the possibility of substituting liquid nitrogen for liquid helium as a cooling medium, which is much easier to handle. Although all commercially available multichannel systems are based on low-temperature SQUIDs, some promising results have been achieved with high-temperature superconductivity (Drung et al., 1996; Kim et al., 2004).

2.2.2 Biomagnetic Fields

Biomagnetic signals are extremely weak in comparison with the Earth's magnetic field or disturbances caused by urban noise. These weak biomagnetic fields are in the order of picotesla (1 pT $= 10^{-12}$ T) and femtotesla (1 fT $= 10^{-15}$ T), at frequencies from a fraction of one Hertz to several kilohertz. The strongest fields are generated by the human heart (MCG) and by the skeletal muscles (magnetomyogram, MMG). The amplitude of the QRS-peak in the MCG is typically several tens of pT.

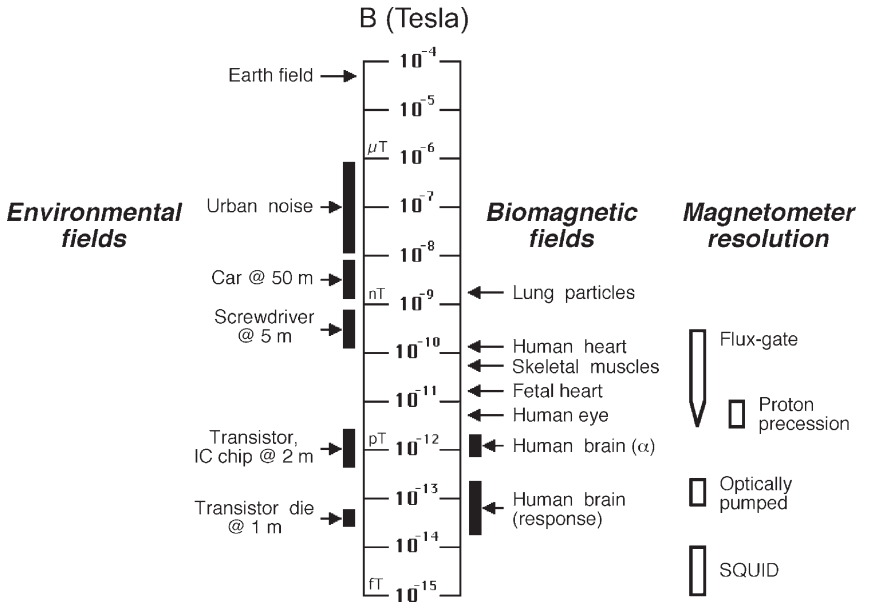

Fig. 2.1. Magnetic induction of biomagnetic fields and of environmental magnetic field disturbances as well as the magnetometer resolution. (Courtesy J. Vrba).

Neuromagnetic signals (MEG) are much weaker. The largest field intensity of a normal awake brain is due to spontaneous activity. The so-called alpha rhythm, which is observed over the posterior regions of the head, is about 1 pT in amplitude. Typical evoked fields – somatosensory, auditory or visually evoked responses – are weaker by one order of magnitude or more, their strengths being only several tens or hundreds of fT. Biomagnetic fields are also known from other electrically active organs: the eye as the magnetooculogram (MOG) and the magnetoretinogram (MRG), the stomach as the magnetogastrogram (MGG), the fetal heart and brain (fetal-magnetocardiogram: FMCG or fetal-magnetoencephalogram: FMEG, respectively), and the peripheral nerve as the magnetoneurogram (MNG).

An overview of the magnetic induction of biomagnetic fields and of ambient magnetic field disturbances, as well as the magnetometer resolution, is provided in Figure 2.1. Here, magnetic induction is expressed in Tesla (T).

The magnetic noise from the environment is four to six orders of magnitude stronger than the biomagnetic fields to be measured. Disturbances from environmental magnetic fields are caused by the Earth's magnetic field, as well as by urban noise. The magnitude of the steady Earth magnetic field is about 5×10^{-5} T (50 μT), and low-frequency variations of this field are in the order of 10^{-7} to 10^{-8} T (100 to 10 nT). The urban noise is in the same order, and caused mainly by power lines, traffic (e.g., car movements or passing trains), and by vibration.

When performing biomagnetic measurements we are faced with a twofold problem: very weak biomagnetic signals must be measured in the presence of environmental magnetic noise which is many orders of magnitude stronger than the fields to be detected. Therefore, a very sensitive sensor is needed (see Section 2.2.3, SQUID sensor) as well as the capability of reducing the ambient noise below the signal to be measured (see Sections 2.2.4 and 2.2.5 for environmental noise reduction).

2.2.3 SQUID Sensor

The most widely known characteristics of the phenomenon of superconductivity are that a superconductor loses its electric direct current (dc) resistance (zero resistance) below a certain temperature, the so-called critical temperature T_c, and that a magnetic field is expelled from the interior of a superconductor (the Meissner–Ochsenfeld effect). The microscopic theory of superconductivity published by Bardeen, Cooper and Schrieffer (BCS theory) in 1957 states that below T_c some electrons create pairs (Cooper pairs) which all belong to the same energy state, in contrast to the electrons of a normal conductor (Bardeen et al., 1957). Cooper pairs can be described by one macroscopic wave function. If two superconductors are separated by a weak link, interference phenomena of the macroscopic wave functions can be observed. Brian D. Josephson predicted this phenomenon, which must occur, in theory, between two superconductors connected by weak links, in 1962 (Josephson, 1962). This effect was later proved experimentally and is called the Josephson effect. Josephson effects are caused by coupling of the two Cooper pair systems. This coupling is realized in different ways, for example by the quantum mechanical tunneling effect through a barrier potential. In each case, the phase difference between the two Cooper pair wave functions of both superconductors determines a supercurrent across the weak link. This results, together with electron transport, in a nonlinear current–voltage characteristic which can be used for different applications in cryoelectronics. Such weak links (Josephson junctions, JJ) can be formed between two superconductors as single or multiple point contacts, microbridges, normal barrier junctions and tunnel junctions (artificial e.g., oxide barrier). Most of the applied weak links with low-T_c superconductors are tunnel junctions fabricated by thin-film technology (Clarke, 1977).

Because of the Meissner–Ochsenfeld effect, the magnetic flux Φ_{sc} caused by the external magnetic field B enclosed by a superconducting loop with the area A is kept constant (flux conservation).

$$\Phi_{sc} = B \cdot A = const. \tag{2.1}$$

This magnetic flux Φ_{sc} is quantized:

$$\Phi_{sc} = n \cdot \Phi_0 \tag{2.2}$$

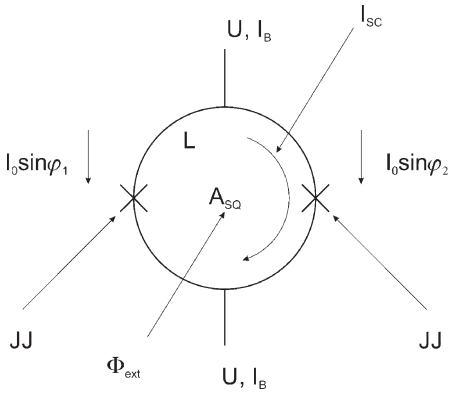

Fig. 2.2. Scheme of a dc SQUID consisting of two Josephson junctions (JJ) in a superconducting loop of inductance L and area A_{SQ}.

where n is an integer, Φ_0 is the magnetic flux quantum, $\Phi_0 = h/2e = 2.07 \cdot 10^{-15}\,Vs$, h is Planck's constant, and e is the elementary charge.

To keep the magnetic flux Φ_{sc} constant, a screening current I_{sc} is kept flowing through the superconducting circuit when the external magnetic field has changed. Both effects – the flux conservation with magnetic flux quantization and the Josephson effect – form the basis of the SQUID. Essentially, a SQUID consists of a superconducting loop incorporating one or two weak links. There are two main classes of SQUID, depending on the operating principle. The dc (direct current) SQUID consists of two weak links in the SQUID loop, while the rf (radio-frequency) SQUID has one weak link in the SQUID loop. In the following, a dc SQUID is described. If a dc bias current I_B is applied to the SQUID loop, then a voltage U can be measured. This voltage is sensitive to an external magnetic field and flux respectively. Therefore, a SQUID represents a flux to voltage converter. A schematic diagram of a dc SQUID configuration is presented in Figure 2.2.

The JJs have significantly smaller critical currents ($I_{c1}; I_{c2}$) than the remaining superconducting loop. (A superconductor loses its superconductivity above a certain current strength, the so-called critical current I_c.) A dc bias current I_B applied to the SQUID loop is divided between the two junctions, as described in Eq. (2.3).

The goal of dc SQUID preparation is to achieve two identical JJ, which is possible only in approximation. Therefore, in the presence of an external magnetic field the same phase differences (φ) do not occur at contacts 1 and 2, respectively. Under the condition of symmetrical critical currents ($I_{c1} = I_{c2} = I_0$), the bias current I_B is described by:

$$I_B = I_0 \sin \varphi_1 + I_0 \sin \varphi_2 \tag{2.3}$$

where ϕ_1 and ϕ_2 are the phase differences of the macroscopic wave functions across contacts 1 and 2, respectively. Changes of the external magnetic field B_{ext}

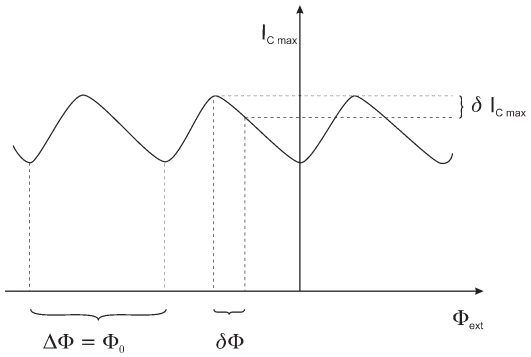

Fig. 2.3. Critical current $I_{C\,max}$ dependence on applied flux Φ_{ext}.

threading the SQUID perpendicular to the area A_{SQ} give rise to a screening current I_{sc} due to the flux conservation. I_{sc} may rise only to a critical value $(I_c - I_0)$ which mainly depends on the cross-section of the superconductor. If the geometry of the SQUID loop is chosen in such a way that the inductivity L of the loop is

$$L = \Phi_0 / I_C \tag{2.4}$$

then the current I_{sc} is changed by variation of the external magnetic field according to

$$\Phi_{ext} = B_{ext} \cdot A_{SQ} = n \cdot \Phi_0 + L \cdot I_{sc} \tag{2.5}$$

Therefore, the magnetic flux penetrating the SQUID loop must be quantitized in Φ_0. There is a periodic dependence on the critical current I_c on to the external magnetic flux Φ_{ext}.

$$I_{c_{max}}(\Phi_{ext}) = 2 \cdot I_0 \cdot |\cos(\pi \cdot \Phi_{ext}/\Phi_0)| \tag{2.6}$$

The sensitivity of a SQUID is characterized by the changing of the critical current $I_{C\,max}$ within one period, which is demonstrated in Figure 2.3.

When applying a dc bias current, the voltage U across the parallel connected junctions exhibits a sinusoidal dependence on the flux with a periodicity of the flux quantum Φ_0. The screening current and number n of flux jumping are an exact value of the external magnetic flux Φ_{ext} threading the SQUID loop. Therefore, the output voltage U is a periodical function of the external magnetic flux. This function can be linearized and read by an electronic system, the SQUID-electronics.

The SQUID operates as a zero-detector in the feedback control system. Either the flux is kept constant in the SQUID (flux-locked mode), or the screening current is kept constant (current-locked mode). The SQUID-electronics feeds back a

Table 2.1. Typical dc SQUID parameters.

Parameter	Typical value
Area of the SQUID chip	$3 \times 4\ \mathrm{mm}^2$
SQUID inductance L	ca. 45 pH
Critical current I_c	10 to 50 μA
Input inductance L_i	ca. 0.8 μH
Input current period	$0.4\ \mu\mathrm{A}/\Phi_0$
Modulation current	$20\ \mu\mathrm{A}/\Phi_0$
Output voltage	20 μV
Normal resistance	$R_\mathrm{n} = 1.0\ \Omega$
White noise	ca. 2 to 5 $\mu\Phi_0/\sqrt{\mathrm{Hz}}$
Equivalent current noise	ca. 2 $\mathrm{pA}/\sqrt{\mathrm{Hz}}$
Energy sensitivity	ca. $9 \times 10^{-31}\ \mathrm{Ws}^2$

current, which cancels changes of the input flux or current respectively, and keeps the operation at a fixed point on the $U - \Phi$ characteristic. The magnitude of the feedback current is a measure of the changes of magnetic input flux. The voltage proportional to this current is the output of the SQUID electronics. This feedback system makes it possible to detect changes in the magnetic flux down to a few $10^{-6}\Phi_0$.

Typical values of the main parameters of a dc SQUID are given in Table 2.1 for a dc SQUID UJ 111 (Josephson tunnel junction with *Nb-NbO$_x$-Pb/In/Au*) made at the University in Jena (Vodel and Mäkiniemi, 1992).

In order to keep the flux noise of a SQUID as low as possible, the inductance L of the SQUID loop must also be low. This results in an area A_SQ of the SQUID which is also very small. Therefore, a superconducting flux transformer is used to pick-up the external magnetic flux ($\Phi_\mathrm{ext} = B_\mathrm{ext} \cdot A$) by means of a large-area antenna (pick-up coil) and to transfer it to the input coil with inductance L_i of the SQUID, as shown in Figure 2.4.

Being superconducting, the flux transformer provides noiseless magnetic gain between the field detected by the pick-up coil, and that seen by the SQUID sensor.

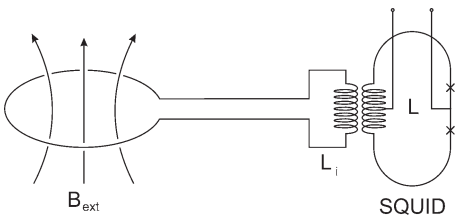

Fig. 2.4. Scheme of a flux transformer coupled to a SQUID.

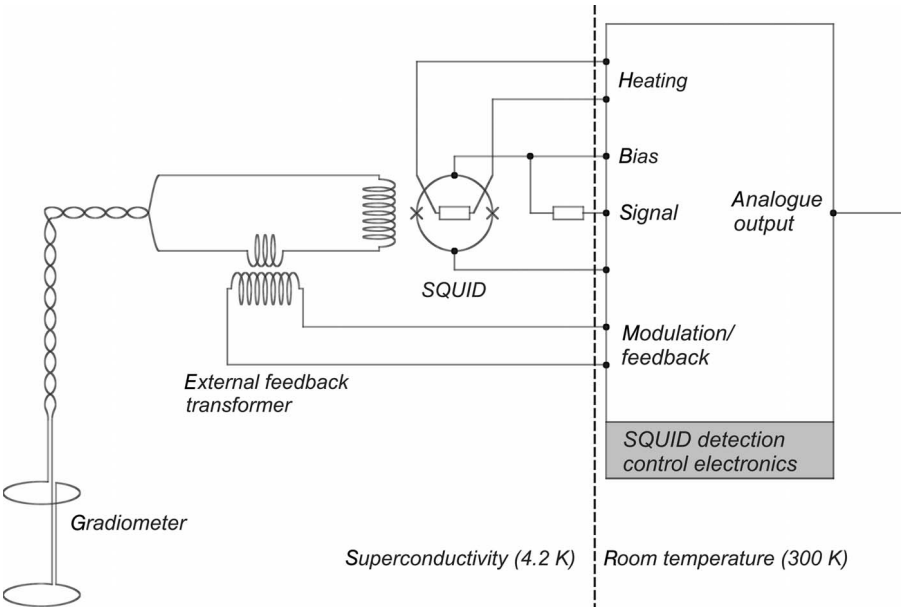

Fig. 2.5. Scheme of a low-T_c dc SQUID-system with electronics.

Superconductivity also guarantees that the magnitude of this gain is frequency-independent, down to dc.

In the case of planar thin-film SQUIDs, planar input coils are tightly and inductively coupled to the SQUID loop (Dettmann et al., 1979; Jaycox and Ketchen, 1981). Coupling factors (k^2) of about 0.8 can be achieved with planar thin-film structures.

Due to an increasing of the sensor area by a flux transformer, the sensitivity of the SQUID can be improved to several $fT/\sqrt{Hz}$. A dc SQUID readout circuit is illustrated in Figure 2.5. The flux transformer and the SQUID itself are superconductive. This low-temperature part of the system is connected to the SQUID detection control electronics.

The SQUID (Seppä, 2001; Wikswo, 2004) and the SQUID electronics (Drung, 2002, 2003) contribute in only a minor way to the total root mean square (RMS) noise value because the magnetic field noise of the surroundings of the antenna is dominant. To investigate the limitations of SQUIDs, measurements were performed with an additional magnetic (superconducting) shield for the gradiometer and a field noise of about 0.8 $fT/\sqrt{Hz}$ was achieved (Vodel and Mäkiniemi, 1992). These investigations were performed inside the Helsinki magnetically shielded room.

The field sensitivity of a biomagnetic measurement system can be expressed by flux density noise in $fT/\sqrt{Hz}$. The field sensitivity is influenced by the geometry of the detection coil. This means that the power density is proportional to the

SQUID noise, and inversely proportional to the area of the detection coil. Typical values for multichannel devices in human investigations are 5 $fT/\sqrt{Hz}$ at 1 Hz. The most sensitive multichannel biomagnetic measurement system in use has been reported by the Physikalisch-Technische Bundesanstalt-group (Drung and Koch, 1994; Drung, 1995; Burghoff et al., 2004) with a typical system white noise level of less than 2.3 $fT/\sqrt{Hz}$.

2.2.4
Shielding: Magnetically and Electrically Shielded Rooms

There are two currently applied possibilities of reducing the ambient disturbances. First, large-scale magnetic shields (this section) built up with μ-metal (MUMETALL® [μ-metal], HYPERNOM®) reduce the environmental magnetic noise (Mager, 1976). Second, special antenna configurations constructed as gradiometers (see Section 2.2.5) can reduce homogeneous magnetic disturbances sufficiently.

The shielding is based on diverting the flux by means of layers of μ-metal or by attenuation of interfering ac (alternating current) fields with conductive shells made of copper or aluminum. These methods fall under the category of *"passive shielding"*.

Effective shielding of magnetic fields (e.g., attenuation of environmental magnetic disturbances caused by energy supplies, railways, industrial installations, telecommunications, etc.) is achieved with the aid of closed metallic housings. The shielding factor (effectiveness) S is defined as the ratio of the external field H_a to the residual field in the interior of the shielding H_i

$$S = H_a/H_i \tag{2.7}$$

In many cases, the shielding attenuation (20 log S) is given as an alternative. The introduction of this logarithmic magnitude is certainly practical, because the shielding factor as a function of frequency covers several orders of magnitude (Baum and Bork, 1991).

Although multiple-shell constructions are generally used for walk-in shielded rooms (Best and Bork, 1989), there is another physical reason for selecting this design. Since ferromagnetic walls cannot be produced and assembled in one piece, attenuation covering the entire volume of the room cannot be achieved. Rooms assembled merely from pieces of ferromagnetic walls do not exhibit the rise in shielding factor expected for closed shielding at frequencies above 0 Hz. In fact, it is possible that S decreases with increasing frequency. To counteract this, the construction includes at least one conductive shell made from copper or aluminum. Furthermore, μ-metal has a higher resistance than both aluminum and copper, and therefore it is not effective for eddy current shielding. The three-shell standard magnetically shielded room (MSR) from Vacuumschmelze Hanau (AK 3b) is shown in Figure 2.6.

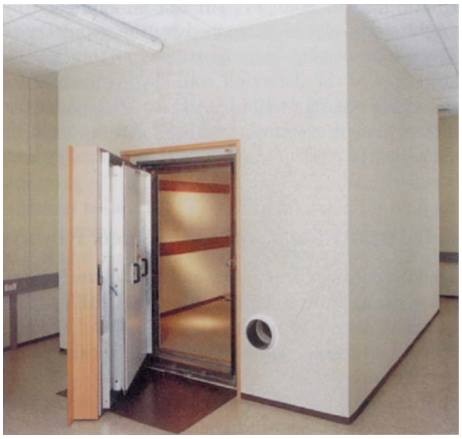

Fig. 2.6. Vacuumschmelze Hanau: magnetically shielded room AK 3b.

Various materials are employed for shell construction, the sequence being μ-metal–aluminum–μ-metal. The ferromagnetic μ-metal walls are made up of large panels produced using a special layer-building technique.

This involves crosswise overlapping of strips of μ-metal which are fixed to each other using a solvent-free bonding technique. The conductive shell of aluminum consists of elements which are edged with copper strips (copper being the contact material) screwed together to achieve an electrically conductive connection. The construction is built around a lightweight frame which allows dismantling and reassembly at an entirely different site. μ-metal may not be exposed to severe mechanical stress, and also cannot be used as flooring, even if covered with normal floor tiles. Each room has a solid floor supported by small carriers which pass through the openings provided in the base of the shielded room and extend to the foundations. The crucial property of this type of room is its shielding factor, which depends on the frequency. The magnetic field H_i resulting from an externally applied field is determined in the center of the room and related to the level H_a found at the same location without shielding.

The characteristic curves of the shielding factors S determined versus frequency f are shown in Figure 2.7. The standard μ-metal-shield corresponds with the Vacuumschmelze Hanau, magnetically shielded room AK 3b. On the basis of the value of around 65 which applies for the lowest frequencies (largely determined by the configuration of the ferromagnetic shells and the permeability of the μ-metal), the conductive shell effects arise from approximately 0.1 Hz. In this frequency range S and f are approximately proportional to each other. The shielding factor continues to increase above 10 Hz, though less steadily. In addition to Vacuumschmelze Hanau, there are other companies who offer and install magnetically shielded rooms, including IMEDCO, EUROSHIELD, AtB and Amuneal Manufacturing Corporation. Altogether, more than 80 standard magnetically shielded rooms are used in biomedical research.

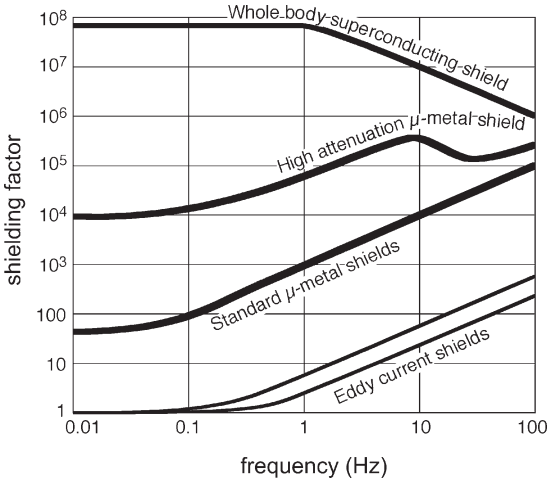

Fig. 2.7. Shielding factor of magnetically shielded rooms versus frequency. (Courtesy J. Vrba, adapted).

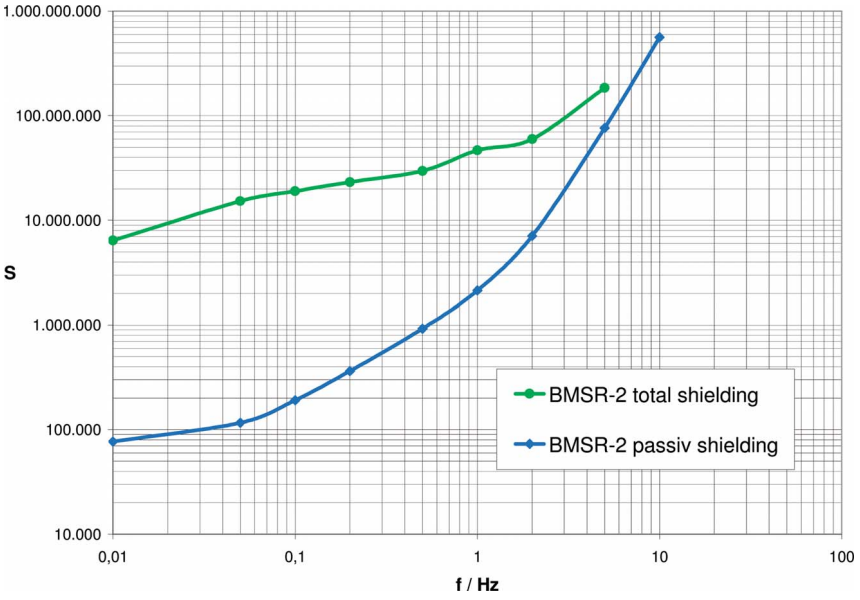

Fig. 2.8. The shielding factor versus frequency of the second Berlin Magnetically Shielded Room (BMSR-2) with eight layers (seven μ-metal-shells and one layer aluminum) and with an additional cubic rf shield with 12-m edge length housing the eight-layer shielded room. (From Bork et al., 2001; courtesy PTB).

As a result of the shielding, biomagnetic measurements can be performed inside a MSR in a normal clinical environment – that is, in buildings with a relatively high level of electromagnetic interference. Since, as a rule, the dominating interference frequency is the line frequency, a level at which the standard room (AK 3b) provides a very high shielding factor, the three-shell design can be simplified for use under less critical conditions. Conversely, to increase the magnetic shielding performance, more μ-metal-shells were used: for example, three layers in the Otaniemi MSR (Kelhä, 1981) or in Charlestown (Cohen et al., 2002). At the German National Institute of Standards (PTB) in Berlin, the high-performance Berlin Magnetically Shielded Room (BMSR) is equipped with six (Mager, 1981), and BMSR-2 with seven μ-metal-shells (Bork et al., 2001). BMSR-2 achieved a shielding factor of 75 000 in the very low-frequency range. The shielding factor increases to 10^6 (Fig. 2.8) based on eddy-current effects at a frequency of 0.5 Hz (Bork et al., 2001). Furthermore, cubic similar design was applied with three μ-metal-shells in the MIT-MSR (Cohen, 1970) and four layers in the COSMOS room (Harakawa et al., 1996).

In order to boost the clinical application of MEG, Elekta Neuromag Oy has developed a light magnetically shielded room (LMSR). The room has only one layer constructed of 14 mm-thick plates of alternating aluminum and μ-metal layers squeezed together. For noise suppression, feedback-based active compensation is utilized inside the LMSR (Simola et al., 2004). The room can be fitted to office space with standard room height. Almost no site preparation is needed prior to erecting the room.

The major advantage of passive shielding is that no power supply is required and that attenuation of the interference waves in accordance with the $S(f)$ curve is guaranteed, regardless of the time span or the 3D distribution of the interference fields. In direct contrast, we have *"active shielding"*, where magnetic coils are used to compensate interference fields (ter Brake et al., 1993). Active shielding requires magnetic field sensors, a measurement recording system, controls, a computer and an x-, y-, z-coil system with a three-channel power supply (Platzek et al., 1999). Interference fields can be reduced with this type of system; the lower the frequency, the easier this is to achieve. On the other hand, this is difficult – if not impossible – with pulses or rapidly changing amplitudes and nonstationary or very strong interference (transient phenomena). Due to the fixed construction of the coil system, optimum 3D compensation only applies to a particular interference field distribution. However, in practice interference sources occur at widely varying distances and with different current characteristics; hence, the compensation quality is not the same at all locations within the active shielding, and as a rule a homogeneous difference field distribution cannot be guaranteed. Nevertheless, in many cases active shielding can be potentially employed to supplement passive shielding, and also makes an essential contribution towards perfecting technical solutions for shielding problems (Kandori et al., 2000; Vrba, 2000; Hilgenfeld et al., 2003; Resmer et al., 2004; Taulu et al., 2004).

Superconducting magnetic shielding provides perfect shielding down to dc frequency in principle. Superconducting rings have the following property: on cooling to below the transition temperature, the magnetic flux Φ_{sc} frozen in their interior is kept constant ($d\Phi_{sc}/dt = 0$). When the external field changes this is effected by

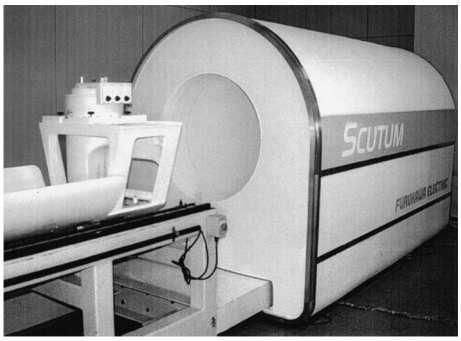

Fig. 2.9. High-temperature magnetically shielded system: SCUTUM.

macroscopic currents in the ring which provide compensation. The same reaction is found in all mathematically twofold neighboring areas of superconductors (i.e., also in hollow cylinders and similar shapes). The physical limit is governed by the critical current, and once this is exceeded then shielding becomes impossible. In spite of these extraordinarily favorable properties, low-temperature superconductors have been used as magnetic shielding in only a few special cases to date. This is primarily due to cooling with liquid helium (boiling temperature 4.2 K).

Following the sensational breakthrough based on high-temperature superconductors (HTS), superconductive shielding operated at 77 K has become conceivable – that is, with less complicated cooling technology (Ohta et al., 2004). It is therefore hardly surprising that a tremendous effort is being invested in the development of HTS shielding. In the HTS magnetically shielded system SCUTUM (Matsuba et al., 1995) shown in Figure 2.9, the shielding factor is given with about 140 dB (10^7) in the low-frequency range (0.1 to 10 Hz).

2.2.5 Gradiometers

Most biomagnetic measurement systems use gradiometers to reduce ambient magnetic noise instead of magnetometers, which measure the magnetic field itself at only one point or region. Gradiometers measure the difference in magnetic field between the coils. These gradiometers are sensitive to biomagnetic fields which are very inhomogeneous and decrease as $1/r^2$ to $1/r^3$ with the distance r between source and pick-up coil. Therefore, gradiometers are sensitive to sources placed near the pick-up coil and insensitive to relatively uniform background fields. The principle of a gradiometer is as follows: the magnetic flux to be detected penetrates two coils, which are connected in series but wound in opposite directions (as shown in Fig. 2.10 for an axial superconducting gradiometer). The distance between these two coils is the base length. The induced current caused by a homogeneous magnetic field B (ambient disturbances due to the Earth's magnetic field or power lines) will cancel out, whereas an inhomogeneous field ΔB (biomagnetic

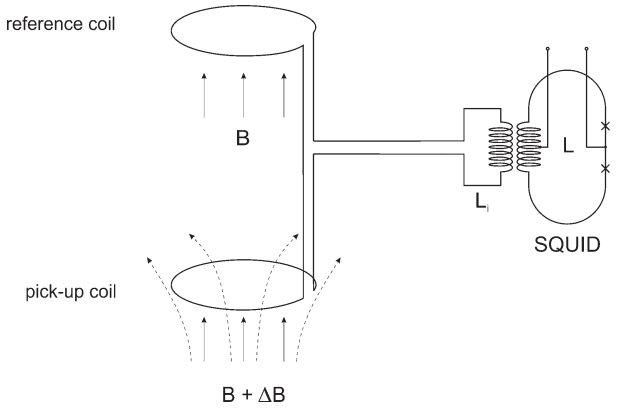

Fig. 2.10. Scheme of a first-order axial gradiometer (pick-up coil and reference coil) coupled with a SQUID; L_i: inductance of the input coil, L: inductance of the SQUID.

field) will yield different currents in each coil. Such *first-order gradiometers* do not measure the field itself, but rather the field difference between two points – that is, the field gradient. This is useful because the distance between the antenna and the source of the disturbance is large compared to that between the pick-up coil and biomagnetic field source, so the disturbing fields can be assumed to be nearly homogeneous. This principle for reducing the unwanted background disturbances from distance sources in biomagnetic studies was applied in the first biomagnetic measurements (Baule and McFee, 1963; Baule, 1965).

A *second-order gradiometer* can be built by connecting two first-order gradiometers in series. This type of antenna can suppress homogeneous fields and field gradients. Second-order gradiometers are commonly used for measuring in unshielded environments. A wire-wound gradiometer has in the best case a manufacturing accuracy of almost 10^{-3}. Such gradiometers must be balanced to increase their accuracy (Aittoniemi et al., 1978; Overweg and Walter-Peters, 1978). A noise suppression improvement of about 1000 can be achieved by mechanical balancing, which is described in more detail elsewhere (Nowak et al., 1991). Provided that the magnetic field to be measured depends only on the z-direction (axial gradiometer), the condition loop for the gradiometer can be given by

$$\sum_{i=1}^{n+1}(-1)^{i+1} n_i A_i = 0 \tag{2.8}$$

and

$$\sum_{i=2}^{n+1}(-1)^{i+1}(z_i - z_1)^k n_i A_i = 0 \tag{2.9}$$

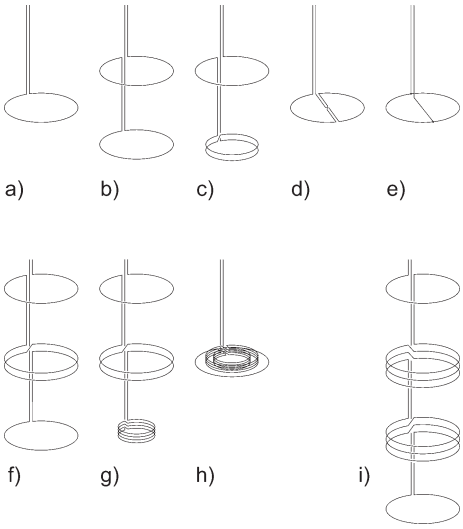

Fig. 2.11. Various antenna configurations. (a) Magnetometer; (b) symmetrical first-order gradiometer; (c) asymmetrical first-order gradiometer; (d) planar off-diagonal gradiometer in series; (e) parallel planar off-diagonal gradiometer; (f) symmetrical second-order gradiometer; (g) asymmetrical second-order gradiometer; (h) planar second-order gradiometer; (i) third-order gradiometer.

to discriminate the k'th field derivative. A_i and n_i are the area and number of turns respectively, of the single gradiometer coil. $(-1)^{i+1}$ describes the direction and the coefficient, and $(z_i - z_1)$ the distance between the compensation coil (i) and the pick-up coil. Therefore, a gradiometer with the order of n is able to compensate field derivatives to the $(n-1)$th order.

Pick-up coil configurations can be built in various designs, as shown in Figure 2.11. Magnetometers (Fig. 2.11a) are used for biomagnetic measurements mainly in a highly magnetically shielded environment, for example inside the BMSR (Koch et al., 1991) or inside an MSR with three μ-metal layers (Nowak et al., 2003). Axial first-order gradiometers measure $\Delta B_z/\Delta z$ (Fig. 2.11b and c), and axial second-order gradiometers $\Delta^2 B_z/\Delta z^2$ (Fig. 2.11f and g). Planar first-order gradiometers record $\Delta B_z/\Delta x$ and $\Delta B_z/\Delta y$ (Fig. 2.11d and e), but planar second-order gradiometers record $\Delta^2 B_z/\Delta x^2$ and $\Delta^2 B_z/\Delta y^2$ (Fig. 2.11h). Third-order gradiometers (Fig. 2.11i) were proposed and realized by CTF (Vrba et al., 1982). The relative merits of various gradiometer configurations are described by Wikswo (1995).

Software gradiometers and *electronic balancing* were first reported by Williamson (Williamson et al., 1977). Software gradiometers can be built up from hardware sensors and references, and utilize reference magnetometers (Matlashov et al., 1989; ter Brake et al., 1989; Becker et al., 1993; Drung and Koch, 1993) or reference gradiometers in some cases (Vrba et al., 1991; Tavrin et al., 1994). Direct feedback, offline subtraction or adaptive signal processing (Robinson, 1989) is also mea-

sured. Implementing the gradiometers in software seems to be the most practical method for multichannel systems because one reference system can serve a large number of sensors (see also Section 2.2.7).

The *baseline* of a gradiometer is the distance separating the coils, and must be chosen in such a way that it is long enough to reduce the effect of the biomagnetic field at the second coil to a relatively negligible level in comparison with the effect at the pick-up coil.

In multichannel systems *crosstalk* occurs between the single channels (ter Brake et al., 1986; Foley et al., 2004), because the biomagnetic field itself causes a current in the flux transformer circuit of every channel. Thus, the magnetic field arises in the vicinity of the flux transformer circuit and causes a magnetic flux in the neighboring channels. The crosstalk depends on the mutual inductance between the neighboring channels as well as on the self-inductance of the flux transformer circuit. The crosstalk coefficient is defined as the ratio between this induced magnetic flux and the original magnetic flux in the measurement channel. In order to overcome this type of mutual influence, ter Brake recommended external feedback (ter Brake et al., 1986), which makes the flux transformer circuit currentless (current-locked-mode) and which is used in most of the multichannel devices.

2.2.6 Dewar/Cryostat

Today, biomagnetic instrumentation is based on superconducting sensors which require a cooling medium. Liquid helium with a temperature of 4.2 K (−269 °C) is commonly used as a cryogenic liquid for low-temperature superconductivity. For high-temperature superconductivity, liquid nitrogen, with a temperature of 77 K, is applied as a cooling medium. Containers for cryogenic liquids are called ''dewars'' or ''cryostats'', whereby the expressions dewar and cryostat are synonyms.

The name ''dewar'' refers to vacuum-insulated containers the walls of which have a reflective coating. These were invented by Sir James Dewar as early as in 1890, based on the results produced by Weinhold in 1881 – that is, two containers with a high vacuum between them bring about a reduction of thermal exchange between the environment and the substances in the inner container. Additionally, vapor-cooled radiation shields and superinsulation must be used in order to achieve a lower boil-off rate (Zimmerman, 1983).

Superinsulation is realized by multiple layers of thin plastic foil with an evaporated aluminum film, mostly on one side. These aluminized films are placed between the inner and outer container, as well as between the radiation shields. A dewar for biomagnetic applications must be made from nonmagnetic materials, and the noise generated in the electrically conducting parts must be very low. On the other hand, the pick-up coil must be brought as close as possible to the biomagnetic source. Therefore, dewar-makers must find a compromise between thermal noise and helium boil-off rate (Hämäläinen et al., 1993). A plan of a typical liquid helium cryostat for biomagnetic measurements is shown in Figure 2.12.

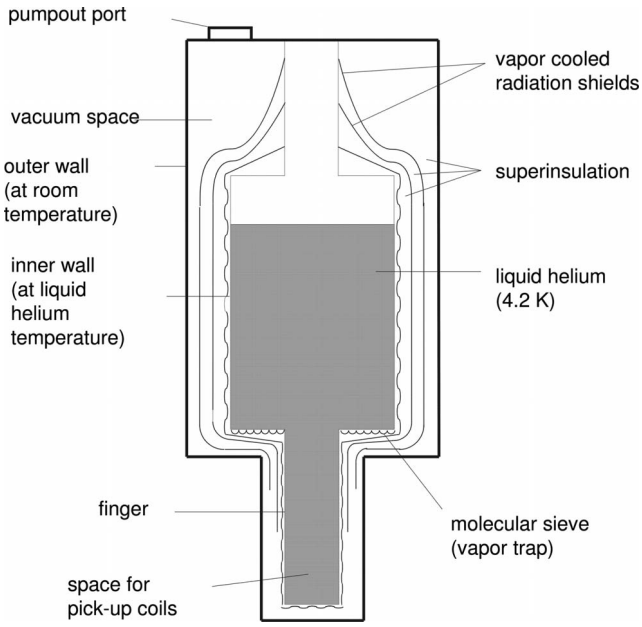

Fig. 2.12. Plan of a typical liquid helium cryostat for biomagnetic measurements.

Fiberglass and similar plastics have proven to be ideal materials for dewars used in biomagnetism because of their physical strength and low paramagnetic impurity content. Helmet-shaped dewars may also be constructed using such materials.

Placing the detection coils in the vacuum space between the inner and outer walls of the dewar can decrease the spacing of the pick-up coil from the outer bottom (Wikswo, 1988), but at the cost of a significant increase in complexity of construction (Fagaly, 1990).

2.2.7 Commercial Biomagnetic Measurement Devices

There were, and still are, several companies which offer commercial biomagnetic instrumentation either for brain, heart and/or for fetal biomagnetic investigations. Examples include: 4-D Neuroimaging (formerly BTi), located in San Diego, California, USA; VSM MedTech Ltd. (CTF Systems Inc.), located in Vancouver, British Columbia, Canada; Neuromag Ltd., located in Helsinki, Finland; Advanced Technologies Biomagnetics (AtB), located in Chieti, Italy; and CardioMag Imaging™ (CMI), located in Schenectady, New York, USA.

All these systems have been designed with the clinical user in mind. Emphasis has been placed on patient comfort and ease of use. Most of the systems are rou-

tinely operated by hospital staff with an MEG/MCG, MRI or EEG technician background. Additionally, most of the MEG-systems include a stimulus computer (with ancillary hardware) and software for auditory, visual, and tactile stimulation. The full constellation of channels (MEG, EEG, EOG/EMG and general purpose channels) can be used simultaneously and are managed by a common hardware interface/signal processing unit and acquisition workstation computer.

2.2.7.1 4-D Neuroimaging

4-D Neuroimaging (www.4dneuroimaging.com) offers six complete biomagnetometer systems under the Magnes brand name, with all types of magnetic field sensor configurations. These biomagnetometers include magnetometers (Magnes 2500 WH, Magnes 3600 WH and Magnes 1300 C) and axial gradiometers (Magnes 3600 WH, Magnes I and Magnes II).

Magnes I, which was introduced in 1989, has a single, multi-purpose sensor with 37 magnetic signal detectors arranged in a circular format and covering a circular area of 14.4 cm^2 (Benzel et al., 1993). Magnes II extends Magnes I by adding a second sensor to allow bilateral measurements with a total of 74 magnetic signal detectors. The lower sensor detection coils and SQUIDs are mounted in the vacuum space, where their operating temperature is maintained by a solid conduction thermal link to the liquid helium reservoir. The system Magnes 1300 C was designed for cardiac studies; this uses 67 magnetic detection coils (magnetometers with a diameter of 2.8 cm) in a circular arrangement (diameter 32 cm). Magnes 2500 WH features a helmet-style sensor with 148 MEG detectors and a 256-channel data acquisition system that accommodates up to 92 channels of simultaneously recorded EEG or other electrophysiological data. A detailed description of these Magnes devices is provided by Nowak (Nowak, 1998). The primary difference between the various Magnes systems is in the sensor unit (number and configuration of detectors) and associated real-time signal processing and data acquisition systems.

The *Magnes 3600 WH* is the sixth-generation MEG/EEG system in the Magnes series, and provides 248 MEG channels and 96 auxiliary channels for the simultaneous recording of EEG or other signals. The 248-MEG detector coils provide a full 248 independent measurement sites encompassing the entire brain, with an average inter-detector separation of 2.2 cm (center-to-center). The coverage provided by the 248 magnetic recording channels extends well below the temporal lobe and well anterior to the temporal pole. This extensive coverage is essential for clinical epilepsy, language and memory studies. In addition, the coverage extends well below the occipital lobe for studies involving visual stimuli and for studies of activity of the cerebellum. A 248-channel recording of a single inter-ictal epileptic spike from a patient with left posterior temporal focus recorded by Magnes 3600 WH is shown in Figure 2.13 (a).

The maximum sensitivity configuration for the Magnes 3600 WH system uses sensors configured as magnetometers, since that configuration provides the most

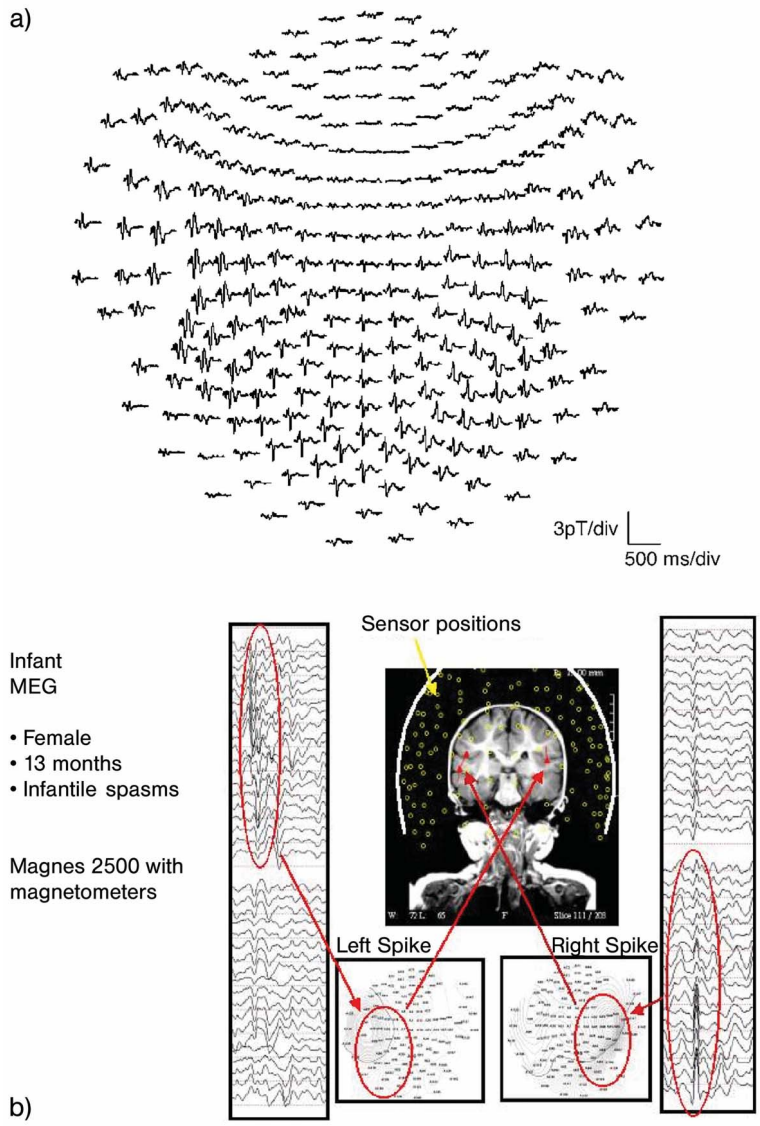

Fig. 2.13. (a) Sensor-layout display of a 248-channel recording of a single inter-ictal epileptic spike by Magnes 3600 WH. This view is from the vertex with the nose at the top. (b) Waveform, field distribution and source localization data for 13-month-old infant with infantile spasms studied with conscious sedation. The patient was positioned with her head centered in the sensor array of a Magnes 2500 WH 148-channel system. The top waveforms on each panel are from magnetometer channels over the left side of the patient's head, and the lower waveforms are from channels over the right. The sensor positions have been projected on to a single MRI slice. The interior surface of the helmet is shown.

sensitivity for detecting and localizing neuronal activity throughout the brain. However, the system can also be configured with axial gradiometers with a 5-cm baseline. A combination of magnetometers and gradiometers can also be specified. All Magnes 3600 WH systems are engineered such that the detector coils are within 16 mm of the interior helmet-shaped surface of the insulating Dewar, for maximum sensitivity.

An example for the sensitivity of the Magnes magnetometer detection array is illustrated in Figure 2.13 (b) for a Magnes 2500 WH 148-channel system. This figure shows epileptic activity recorded from both hemispheres of an infant whose head was positioned in the center of the helmet. The recordings were obtained without moving the patient's head. As can be seen, it is possible to record activity simultaneously from both sides of an infant's head, even though the closest detectors are 5 cm from the skull surface. Moreover, the magnetometers are so sensitive that detectors on the opposite side of the head record clear spike activity.

4-D has also developed a Three-Stage *Noise Suppression System* that optimizes the effectiveness of a built-in broad-baseline distributed reference array and which can quickly adapt to unexpected changes in environmental conditions. The sophisticated proprietary noise-cancellation package utilizes up to 23 reference channels. The reference channel set includes 18 magnetometers and five gradiometers located above the signal coils, as shown in Figure 2.14. The location of the reference channels is optimum: it is far enough from the signal coils to minimize the influ-

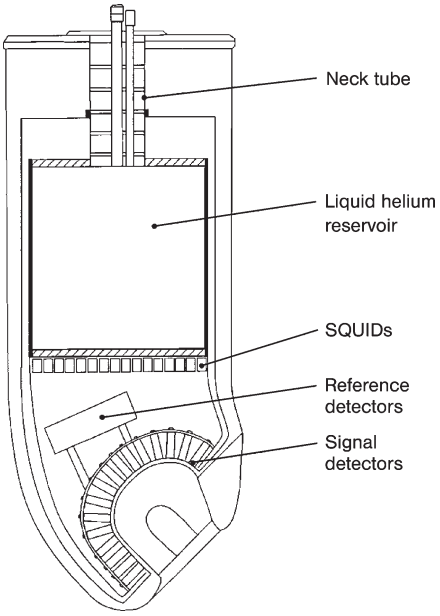

Fig. 2.14. Cutaway drawing of the Magnes dewar showing the location of the reference channels relative to the sensor coils.

ence of the signals of interest (brain activity), yet close enough to the signal coils to sample the equivalent environmental noise affecting the signal channels.

The signals from the reference channels are applied to the MEG data, both on-line and off-line, in such a way as to remove magnetic and vibrational noise while preserving signals from the brain. Typical system performance after noise reduction is a white noise frequency spectrum to below 5 $fT\sqrt{Hz}$, as shown in Figure 2.15 (c). Similar results are obtained in reducing the effects of vibration.

The proprietary design of the nonmagnetic Magnes 3600 WH *overhead gantry system* allows a comfortable access to the patient/subject and to the interior of the MSR (Fig. 2.15a). The mechanical construction isolates the system from external vibration, and the use of nonmagnetic components throughout minimizes the effects of residual vibration. The overhead gantry allows very rapid movement of the helmet away from the patient's head when a seizure occurs (this is an occasional occurrence in epilepsy evaluations).

The overhead gantry enables studies to be conducted on subjects positioned in a fully seated posture (Fig. 2.15b), fully supine (Fig. 2.15a), and any intermediate position. The supine position is optimum for clinical studies, while the seated position is optimum for studies requiring high levels of attention and behavioral responses. The position of the sensor is locked positively when in position by pneumatic locks, and is released for movement by the simple push of a button, which activates a set of redundant valves. Movement of the gantry/sensor position from the seated to supine position, and vice-versa, can be accomplished rapidly by a single operator.

Similarly, the *patient support system* is configured as a nonmagnetic bed for supine studies, and can be converted to a contoured chair configuration for studies in the seated position. The transformation from one configuration to another takes less than 1 minute by a single operator. The patient support system has a locking rail on the floor for safety during studies and precise, easy realignment of the support system when changing configurations. The support system can be easily demounted from the safety rail, allowing it to be shifted aside to permit access by gurney or wheelchair to bring in and position nonambulatory patients.

The positioning flexibility and capability for rapid configuration change of the Magnes 3600 WH are made possible by 4-D's patented *coils-in-vacuum* (CIV) technology. With CIV technology, the detector coils and SQUIDs are located within a vacuum space and cooled by thermal conduction from the nearby liquid helium reservoir (see Fig. 2.14). This design reduces both helium consumption and intrinsic noise of the system. The CIV construction allows the helmet to be aligned at an angle of 45° from the principal axis of the dewar. With this geometry, there is minimal tilting of the helium reservoir throughout the range of recording positions, from seated to horizontal. Thus, it is possible to switch the sensor rapidly from the seated to supine position and to begin recording immediately, with little of the settling time. The CIV technology makes the Magnes 3600 WH extremely stable during long recordings in the D-C mode. Furthermore, because the CIV design removes the superconducting circuitry from the liquid helium, intermaintenance periods are longer and the life of the system is prolonged.

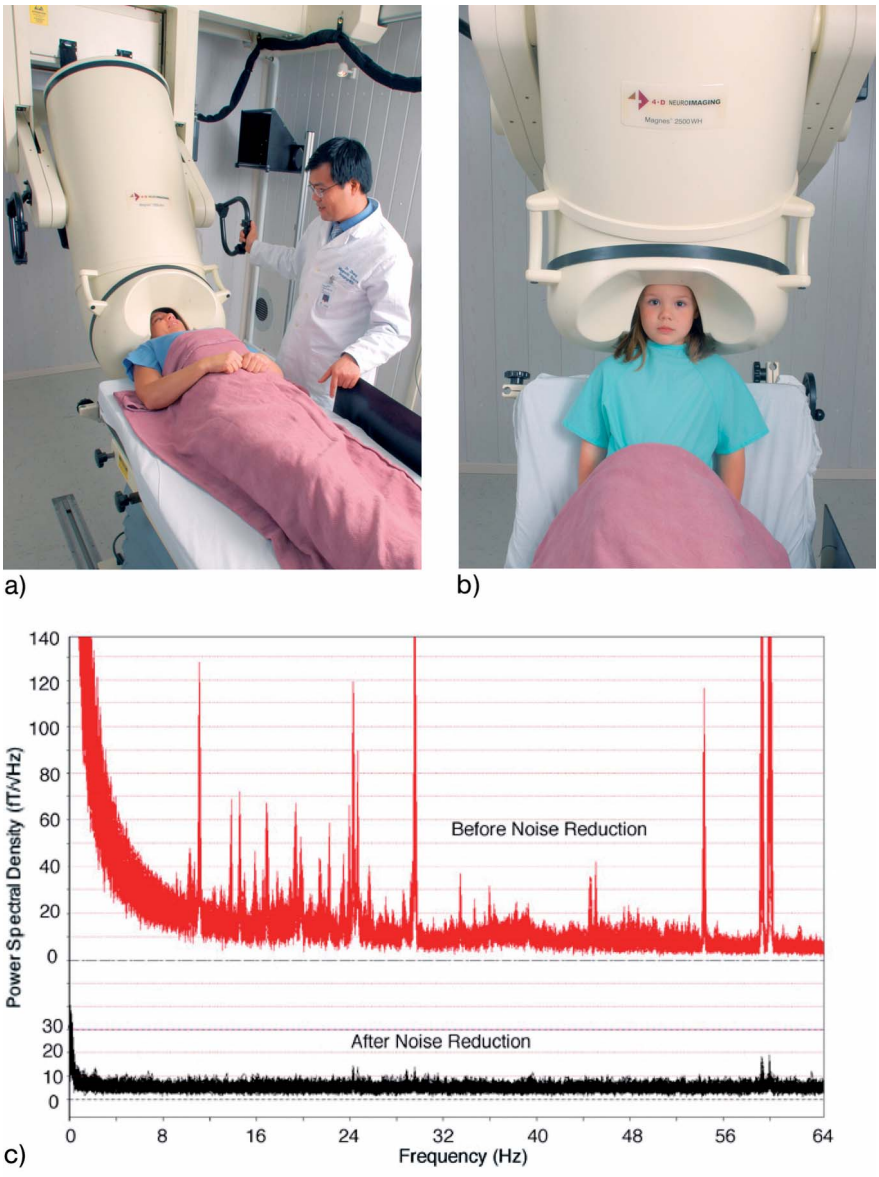

Fig. 2.15. (a) Magnes 3600 WH in position for a supine study. (b) Magnes 3600 WH in position for a seated study. (c) Typical frequency spectra (248 MEG channels overlaid) before (top) and after (bottom) noise cancellation.

An additional feature of the Magnes 3600 WH design is the provision for heating of individual SQUIDs. Its superconducting components are resistant to the effects of stray magnetic fields (flux trapping) introduced during normal operation. However, in the event that flux trapping does occur, the effects can be immediately reversed by heating individual SQUIDs, without the delay of warming and recooling the entire detector array.

The position of the patient's head within the sensor helmet can be monitored using an array of active locating coils fixed by tape or glue to the patient's scalp. The locating coil positions are registered with the *head shape digitization unit*. For maximum accuracy, up to 16 coils can be used, although the use of five coils typically produces very reliable results. The *head position* is automatically recorded at the beginning and end of a data acquisition. Software under development will allow continuous monitoring of the head position and correction of the data.

The analog-to-digital conversion of the magnetic field data is performed with a 24-bit A/D converter, providing a least significant bit step size of 1 fT, which is below the 3–4 $fT/\sqrt{Hz}$ noise level of the SQUIDs, and a *dynamic range* of greater than 16 nT. A/D conversion of the ancillary data channels, such as EEG, is performed with the same relative range, and the data are stored with the full 24-bit information.

MEG and EEG data can be obtained with sample rates up to 4 kHz for all MEG/EEG channels and up to 8 kHz for 196 MEG channels (selectable) and 48 EEG channels. All MEG and EEG channels are sampled simultaneously based on a single master clock that is distributed to all A/Ds. The MEG/EEG signals can be coupled D-C or A-C (high-pass filtered at 0.1 Hz or 1.0 Hz). The analog bandwidth is selectable from 20 to 3500 Hz. Real-time DC offset for MEG channels is standard.

In addition to the basic software package of the Magnes 3600 WH system, which includes modules for data acquisition, head shape digitization, data editing, averaging and selective averaging, data manipulation (power spectra, digital filtering, waveform addition/subtraction, baseline correction, etc.), data archiving/dearchiving, event detection, interactive dipole fitting, contour and waveform displays and utilities for system maintenance, there are the STA/R (Spatial Temporal Analysis/Review), clinical software package and the Boolean Averager/Artifact Detection package, which allows the user to process complex cognitive data quickly. In addition, 4-D supports the export of Magnes data to a variety of software packages for advanced analysis of both MEG and EEG data.

The STA/R provides an interactive interface linking the 4-D MEG signal and MEG source modeling with an anatomical reference (usually MRI) to allow users to quickly and easily visualize their data. STA/R incorporates standard 4-D software modules, adds features, and provides additional communication pathways between related applications. A typical STA/R display showing interactive real-time use of the waveform display, field mapping display and source localization tools is shown in Figure 2.16.

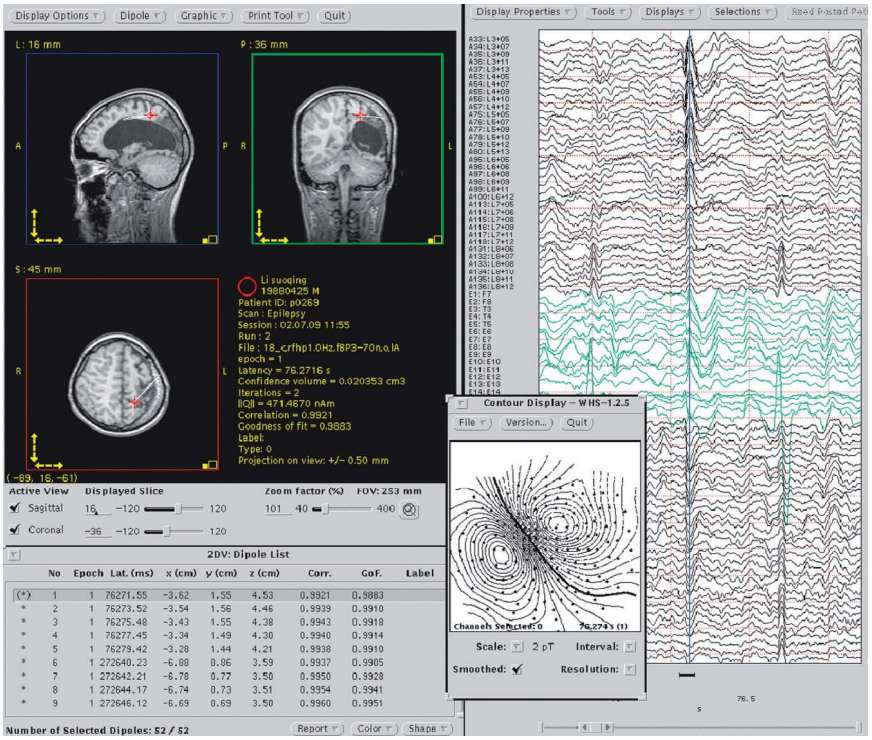

Fig. 2.16. A typical STA/R display showing interactive real-time use of the waveform display, field mapping display and source localization tools. Placing a cursor on an event, such as an epileptic spike, updates the field and the source localization displays instantaneously.

The STA/R software package is a Store Service Class Provider for DICOM v3. If the DICOM standard is not followed at the institution, 4-D's standard MRI format is also supported, and existing MRI data can be imported into STA/R.

The STA/R software provides critical real-time communication links between the MEG data and the MRI image. With these links, the user is able interactively to view waveform and field contour plots, select latencies, and view the dipole source localizations on the subject's MRI. The user can then add the resulting dipole localizations to an ongoing list. Dipoles that are selected can be sorted by user-defined criteria (e.g., correlation, source strength) and saved to a file. This feature greatly decreases the time required to review and analyze data, such as obtained during an epilepsy surgery evaluation.

Conversely, if data have already been analyzed and are submitted for review, the reviewer can select any dipole source that has been superimposed on the subject's MRI, either directly from the MR image or from the loaded list of dipoles,

Table 2.2. Installation year and location of the currently "active" sites of Magnes systems.

Year	No. of channels	Affiliation	North America	Europe	Asia
1992	37	Magnes I	–	–	Fukuoka
1993	37	Magnes I	–	Rennes	–
1994	74	Magnes II		Erlangen	
1995	74	Magnes II		Vienna	
	74	Magnes II			Obu
1996	148	Magnes 2500 WH	La Jolla		
	148	Magnes 2500 WH		Jülich	
	148	Magnes 2500 WH		Leipzig	
	148	Magnes 2500 WH	New York		
	148	Magnes 2500 WH			Kobe
	148	Magnes 2500 WH		Magdeburg	
1997	148	Magnes 2500 WH		Rouffach	
	148	Magnes 2500 WH		Konstanz	
	148	Magnes 2500 WH	Houston		
	67	Magnes 1300 C		Bochum	
1998	37	Magnes I	Denver		
	148	Magnes 2500 WH			Tokyo
1999	74	Magnes II	Madison		
	148	Magnes 2500 WH	Detroit		
	148	Magnes 2500 WH			Okayama
	67	Magnes 1300 C			Okayama
	148	Magnes 2500 WH		Madrid	
2000	148	Magnes 2500 WH			Guangzhou
2001	148	Magnes 2500 WH	Birmingham		
	248	Magnes 3600 WH	Minneapolis		
2003	248	Magnes 3600 WH	Houston[a)]		
	248	Magnes 3600 WH	Denver		
2004	248	Magnes 3600 WH	New York		
	148	Magnes 2500 WH	St. Paul		
2005	248	Magnes 3600 WH		York	
	148	Magnes 2500 WH		Barcelona	
	148	Magnes 2500 WH		Liverpool	

[a)] Upgrade from a previous Magnes system.

and then review the waveform and contour plots of the selected dipole source instantaneously. This interactive feature allows the reviewer to more efficiently scan for artifacts, thereby helping to ensure that reported sources are true physiological events.

The *Boolean Averager/Artifact Detection* package was developed specifically for use with studies of cognitive activity. The power of the Boolean Averager comes from its ability to analyze many different cognitive conditions at one time. The Boolean Averager can examine multiple complex combinations of stimuli and responses from a single run. It allows the user to test many different hypotheses with a single quick, pass through complex data. The user specifies the order and timing of both stimuli and responses required for each hypothesis, and the application then extracts the appropriate data sets, averages them if desired, and generates statistics about each condition.

The power of the Boolean Averager is greatly enhanced when used in conjunction with the Artifact Detection pre-processor. This routine identifies various artifacts such as eye-blinks and motion artifacts by using different detection algorithms, including peak-to-peak and thresholding techniques. These same algorithms can be used to identify physical events such as eye movements. Each artifact type or physical event type is identified with a unique code, which can then be used in the Boolean Averager for selection, sorting and timing.

The Magnes 3600 WH allows the widest range of applications possible to be addressed, from today's clinical applications in epilepsy, pre-surgical functional mapping, language mapping and dyslexia evaluation to the most sophisticated neuroscience research in cognitive neurophysiology, psychiatry, and psychology, including investigations of normal subjects and patient populations. Magnes 3600 WH and Magnes 2500 WH systems with magnetometer sensors have been installed in 17 urban hospital sites. An overview of 4-D Neuroimaging systems, together with installation year and location, is provide in Table 2.2.

2.2.7.2 VSM MedTech Ltd.

VSM MedTech (www.vsmmedtech.com) offers the CTF MEG™ system in configurations specifically designed for either whole-cortex or fetal MEG measurements. For cortical applications, the helmet-shaped sensor array is currently available in either a 151- or 275-axial-sensor distribution (Vrba and Robinson, 2002). All CTF MEG™ Systems are equipped with 29 reference channels dedicated to noise cancellation. Additionally, this design can be accompanied by up to 128 channels of EEG, eight channels of EOG/EMG, 16 channels of general purpose ADC, four channels of general purpose DAC, and a variety of input and output channels. The more extensive system configuration discussed below comprises a total complement of over 450 channels, all measured simultaneously.

The *sensors* manufactured by VSM MedTech are planar, DC SQUIDs based on Nb-Al-Al_2O_3-Nb JJ technology. The sensors are manufactured in a multi-step plasma-sputtering process, such that a high degree of device uniformity is main-

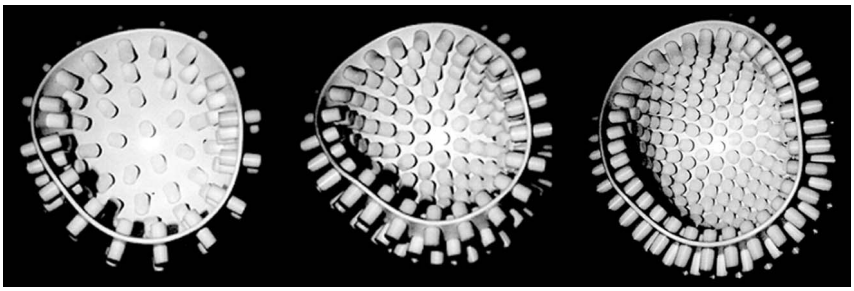

Fig. 2.17. Gradiometer distribution over the inner surface of the helmet-shaped end of the liquid helium dewar for CTF MEG™ Systems with 64 (left), 151 (center) and 275 (right) channels.

tained and immunity from flux trapping is assured. The SQUID sensors have niobium flux-transformer coupling coils and feedback coils fully integrated into their planar design. From the coupling coil, superconducting leads are brought out to tabs for connection to the pick-up coil. The pick-up coils (or flux transformers) consist of first-order axial gradiometers with a 1.8 cm diameter and 5 cm baseline. The axial gradiometers are uniformly distributed, in a closely-packed approximately hexagonal grid, over the inner surface of the helmet-shaped end of the liquid helium dewar, as shown in Figure 2.17 for the 64-, 151- and 275-channel systems, respectively. The mean sensor separation is approximately 3.1 cm for the 151-channel configuration, and approximately 2.2 cm for the 275-channel configuration. The baseline length was chosen to be the optimum compromise between noise immunity and signal pick-up, for average urban environments. Typical white-noise levels of the system are 4–7 $fT/\sqrt{Hz}$ above 1 Hz (Vrba et al., 2000).

The CTF MEG™ System includes an array of 29 reference channels located above the sensors and dedicated to *noise cancellation*. This reference array measures the magnetic vector and gradient tensor components of the background magnetic environment. This vector/tensor information is synchronously processed, in combination with the signals received from the first-order gradiometers (biomagnetic sensors), such that the synthetic equivalent of a third-order gradient response to environmental-noise sources is realized. However, by virtue of appropriate design considerations, the response of the system to the "near-field" MEG signals is closely approximated by the primary first-order hardware gradiometer. The net effect is a significant decrease in environmental noise, exceeding that provided by magnetic shielding alone, without any attenuation of the brain signals.

The execution of the third-order gradient algorithm is implemented in real-time by the system electronics, or off-line by software. However, unlike adaptive software techniques, the coefficients used by the algorithm are constant in time and are fully independent of dewar orientation and the character of magnetic-noise sources. Additionally, since the biomagnetic sensors are first-order in nature, the overall signal-acquisition process makes all three gradient orders available to the

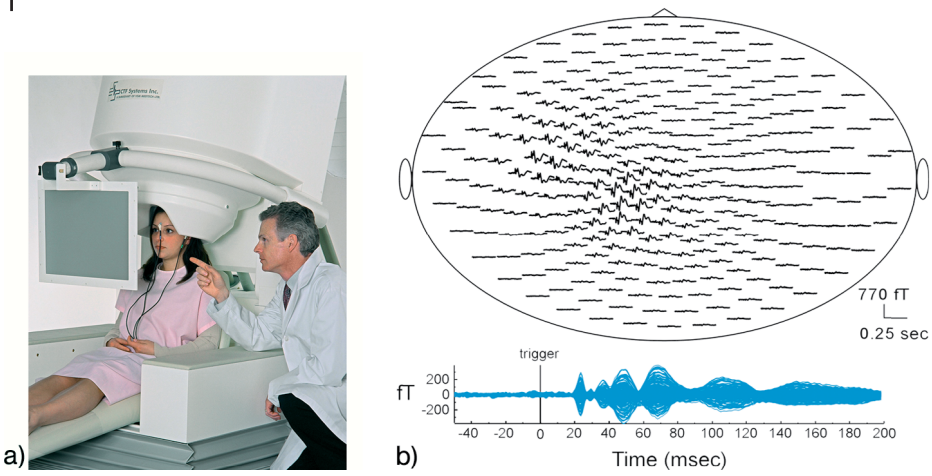

Fig. 2.18. (a) Cortical 275-channel CTF MEG™ System (VSM MedTech). (b) MEG of a somatosensory-evoked field recorded by a 275-channel cortical CTF MEG™ System (DC to 300 Hz bandwidth, 628 averages and third-order gradiometer noise cancellation).

user. Thus, depending on the user's preference, the system can be configured via software to function with either a first-, second- or third-order gradient response. This choice can be reversibly changed without increasing system white-noise levels.

The *helmet-shaped end of the liquid helium dewar* forms part of an optimized cryogenic system. The dimensions of the helmet are based on the contents of a size/shape database collected from over 20 000 adult males, assuring a 95th percentile fit to the adult male population (and thus virtually all children and adult females), including clearance for EEG electrodes. For structural integrity, the head section is constructed as one piece. For RF immunity, a shield is incorporated into the dewar's vacuum space. The vacuum gap (distance between the pick-up coils in the liquid helium and the room-temperature surface in the helmet region) is approximately 1.7 cm (Vrba et al., 1993). Additionally, the vacuum space holds a cryosorption module, maintaining operational vacuum soundness for 12 months. The cortical 275-channel CTF MEG™ system is shown in Figure 2.18 (a) (Fife et al., 2002). The dewar is of a unique thermal design to minimize its length, yet provide a low liquid helium boil-off rate (less than 14 L per day for the 275-channel configuration). The nominal volume is 85 L. With its associated gantry and *Patient-Support System*, the dewar can accommodate a continuous spectrum of subject orientations, ranging from fully supine to seated upright.

"Flux-locked-loop" SQUID control and digital-signal-processor (DSP) devices have been employed in VSM MedTech's implementation of the *control electronics*. By restricting the use of analogue components only to the SQUID preamplifier

and completing the feedback loop digitally, the transfer functions of different channels may be accurately matched. By incorporating a digital design, the electronic characteristics of each channel are identical and allow sampling across all channels to be highly synchronized. Both of these features are critical to the success of synthetic higher-order gradiometer noise cancellation and other sophisticated signal-processing techniques. Furthermore, by employing DSP devices, the electronic characteristics are governed by firmware coding, enabling enhanced flexibility and the future implementation of design refinements. With a 32-bit architecture for signal digitization (corresponding to a dynamic range in excess of 190 dB), complete resolution is maintained without the need for range switching. Since the SQUID sensors are processed digitally, all channels are sampled synchronously and possess well-matched transfer functions. All adjustable parameters required for the correct setting of each SQUID and "flux-lock-loop" (e.g., SQUID DC bias current, loop forward gain, demodulation delay, reverse gain, etc.) are controlled by digital circuitry. Each of these parameters is controllable from the acquisition workstation and can be set automatically through use of the acquisition-software interface. In this way, each SQUID channel is assured an optimal and stable operating status, without the need for retuning.

Data acquired from up to 128 EEG electrodes may be collected simultaneously with the MEG measurement. To minimize magnetic-field disturbances, which would interfere with the MEG recordings, the EEG electrodes are constructed of nonmagnetic materials having a low-conductivity character. In addition to the EEG, the system also accommodates up to eight channels for EOG and/or EMG measurements and a further 27 channels for monitoring various input and/or output signals. Data are acquired by the system-control electronics and transferred to a LINUX-based acquisition computer for display and later storage within a database.

An example of the performance of the 275-channel cortical CTF MEG™ System is provided in Figure 2.18 (b) with an MEG of a somatosensory-evoked field (DC to 300 Hz bandwidth, 628 averages and third-order gradiometer noise cancellation).

The *peripheral interface unit* (PIU) provides many functions not directly related to the SQUID- or EEG-sensing systems. These include coil drivers for head localization, external-signal inputs, external-signal outputs and triggering from external devices. Each coil-driver circuit receives a voltage waveform from an ADC channel unit and converts it into a current to drive a coil. This current is sensed with a series resistor, and the voltage across the resistor is fed back to a DAC channel unit for digitization and filtering. The current drivers can be used to drive the head-localization coils and/or user-supplied loads which may be connected to the external-output connectors on the front panel of the console.

A real-time processing cluster allows complex processing to proceed in real-time. This includes cross-talk correction, noise cancellation by formation of higher-order gradients, decimation (including filtering and resampling), user-selected filtering and continuous head localization (CHL). For the purpose of registering the subject's head relative to the MEG sensor array, three small coils are placed on the

Fig. 2.19. The CTF MEG™ System configuration for fetal MEG. The Patient Support System slides back to allow easy access to the MEG sensor array.

subject's head at anatomical landmarks (typically the nasion and pre-auricular points). Sinusoidal signals (at three separate frequencies) are applied to the coils, which each produce their own magnetic signal. The magnetic field from each of the three coils is simultaneously detected by the MEG system array and processed by an algorithm which accurately locates the position and orientation of each coil in three-dimensional space. Knowing the separate frequency signature of each of the coils, *a head-coordinate system* is then established and the MEG data registered with respect to this coordinate system. The accuracy of this method is better than 2 mm (Huonker et al., 1996; Vrba, 2000). A similar approach can be used for CHL, with the energizing frequencies continuously being above the MEG signal frequencies of interest.

Based on experience obtained with cortical MEG instrumentation, an alternative CTF MEG™ System configuration has been developed by VSM MedTech especially for fetal investigations (Robinson et al., 2001). In this design, an array of SQUID sensors is arranged for optimal coverage of the mother's anterior abdominal surface, from the perineum to the top of the uterus (in late gestation), as shown in Figure 2.19.

Primary-sensor flux-transformers are axial first-order gradiometers, with a 8 cm baseline. The dewar operates in a horizontal orientation, and has sufficient capacity for one-week operation between helium refills. A SQUID reference array of 29 channels is incorporated for the attenuation of environmental and vibrational noise. System white-noise levels are typically 4–7 $fT/\sqrt{Hz}$ above 1 Hz (Robinson et al., 2001).

An overview of VSM MedTech/CTF-systems, including the year of installation and location, is provided in Table 2.3.

Table 2.3. Installed base of CTF MEG™ systems for cortical and fetal MEG applications, including the year of installation and location.

Year	No. of channels	Affiliation	North America	Europe	Asia
1993	64	MEG cortical			Tsukuba
1996	143	MEG cortical		Vienna	
	64	MEG cortical			Osaka
	64	MEG cortical			Sakai
1997	151	MEG cortical		Amsterdam	
1998	151	MEG cortical		Tuebingen	
	151	MEG cortical		Paris	
	64	MEG cortical			Tokyo
1999	151	MEG cortical			Tokyo
	64	MEG cortical	Los Angeles		
	151	MEG cortical		Birmingham	
2000	64	MEG cortical	Toronto		
	151	MEG fetal	Little Rock		
2001	151	MEG cortical	Toronto		
2002	151	MEG cortical		Nijmegen	
	275	MEG cortical	Bethesda		
	151	MEG cortical	Kansas City		
	83	MEG fetal	Kansas City		
2003	275	MEG cortical	San Francisco		
	151	MEG cortical			Beijing
	143	MEG cortical		Athens	
2004	275	MEG cortical		Muenster	
	151	MEG cortical	Vancouver		
	275	MEG cortical	Albuquerque		
	275	MEG cortical		Lyon	
	275	MEG cortical		London	
2005	275	MEG cortical	Cincinnati		
	275	MEG cortical	Montreal		
	275	MEG cortical		Birmingham[a)]	
2006	275	MEG cortical	Montreal, MNI		
	151	MEG fetal		Tuebingen	
	275	MEG cortical	Philadelphia		
	275	MEG cortical			Chongqing
	275	MEG cortical		Hamburg	
	275	MEG cortical		Frankfurt	
	275	MEG cortical	Winston-Salem		
	275	MEG cortical		Cardiff	

[a)] Upgrade from a previous MEG system.

2.2.7.3
Elekta Neuromag®

The Low-Temperature Laboratory at the Helsinki University of Technology is pioneering the development of biomagnetic instrumentation. The first four-channel SQUID gradiometer was built in 1983 (Ilmoniemi et al., 1984), a seven-channel gradiometer in 1986 (Knuutila et al., 1987), and a 24-channel planar gradiometer in 1989 (Kajola et al., 1989; Ahonen et al., 1991). All of these systems were designed for and used in the Otaniemi magnetically shielded room (Kelhä, 1981). Based on this experience and knowledge, the company Neuromag Ltd. was established in Helsinki in 1989, and today is known as Elekta Neuromag®.

Elekta Neuromag® (www.elekta.com, www.neuromag.com) offers three multichannel systems: two helmet-shaped MEG-devices (306/204 channels and 144 channels, described by Knuutila et al., 1993), and one MCG system. All Neuromag MEG- and MCG-devices have the same basic components: multichannel SQUID-magnetometer/gradiometer sensors, gantry, patient support bed, head/chest position indicator, data acquisition unit, signal processor for continuous data and system controlling as well as data analysis software and a magnetically shielded room. They are based mainly on planar first-order gradiometers and magnetometers respectively (Laine et al., 1999), as shown in Figure 2.20 (a). This coil configuration combines the focal sensitivity of the planar gradiometers (measuring $\Delta B_z/\Delta x$ and $\Delta B_z/\Delta y$) of the magnetic field component B_z normal to the dewar surface and the widespread sensitivity of the magnetometers (measuring the normal component B_z). The shape of each of the two loops comprising a single planar gradiometer is a 2.68×1.00 cm^2 rectangle, with a baseline of 1.70 cm. The magnetometer coil shapes are 2.10×2.10 cm^2.

The noise density are for magnetometers: 3 $fT/\sqrt{Hz}$ (white noise) and for gradiometers 2.7 $fT/cm/\sqrt{Hz}$. The external disturbances sensed by the magnetometers are eliminated using a novel software-based technique with which magnetometers can be gradiometrized up to arbitrary order. The quantitative performance criteria of Elekta Neuromag® sensor array are explained in detail by Nenonen et al. (2004).

The lead fields (sensitivity patterns) of the two gradiometers and the magnetometer integrated on one sensor unit are illustrated in Figure 2.20 (b). The lead fields of the three channels in a sensor element are orthogonal to each other. This means that despite overlapping of the pick-up loops, the three channels of the sensor element convey orthogonal information: the signal in any one of the three channels cannot be predicted from the signals of the other two. The flux transformers are equipped with integrated RC-shunts to eliminate high-frequency interference. The geometrical accuracy of the planar gradiometers is outstanding owing to the photolithography on silicon technology employed in the manufacture (Fig. 2.20a). This, together with the relatively short baseline, results in excellent inherent immunity to external interference. The initial balance of the planar thin-film gradiometers is better than 10^{-3}.

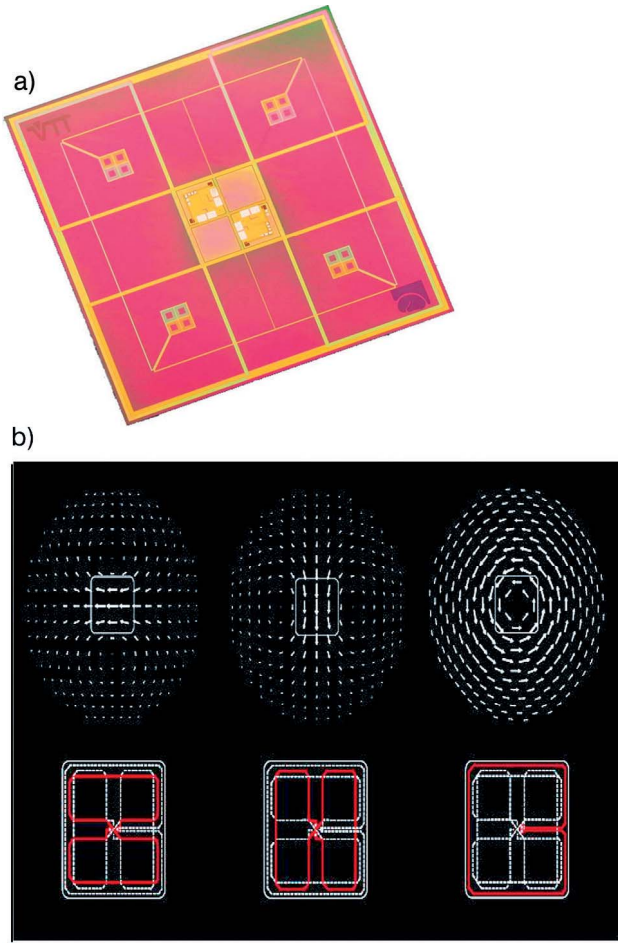

Fig. 2.20. (a) A single triple-sensor thin-film element manufactured on a silicon chip using a photolithographic technique.
(b) Schematic presentation of the lead fields of the pick-up coils at the triple sensor unit shown at the left.

The shape of the helmet is based on anatomical data (Ahonen et al., 1993). The helmet size accommodates 98% of population, its maximum dimensions being: length 22.2 cm, width 18.1 cm, depth 21.0 cm. The helmet consists of two coaxial tubes of composite structure with helmet-shaped shells at the lower ends. The bottom is broader in the occipital area than in the frontal area, which provides a better fit with the shape of the skull. The distance of the vacuum gap (sensor to outside surface of the dewar) is 17 mm.

The Elekta Neuromag® helmet-shaped MEG-device (306/204 channels) is shown in Figure 2.21. The up-and-down movement of the gantry can be operated by one

Fig. 2.21. Elekta Neuromag® helmet-shaped MEG-device (306/204 channels).

person. Changes between seated and supine measurement positions take less than 2 minutes, with no stabilization time required. For ease and clarity of operations all patient-related cables are connected to the side panels of the gantry. The bed and chair are on wheels so that the patient can be pulled out of the shielded room, for example in case of a clinical emergency. A separate chair insert to facilitate pediatric measurements is provided. This chair is equipped with a neck support and a removable table.

The integrated EEG system consists of 60 single-ended channels and four differential channels, enabling recordings of EEG, EOG, EMG and ECG signals. The EEG system includes a nonmagnetic EEG cap interface. Both the number of EEG channels and the number of channels supported by the EEG cap can be increased up to 128 channels. The Elekta Neuromag® 306-MEG helmet system offers high spatial sampling of the magnetic field (the field distribution is sampled by 510 coils at distinct locations directly above the cortex, and the coils are configured into 306 MEG channels, i.e., 204 planar gradiometers and 102 magnetometers), high dynamic range (up to 27 bits) and high sampling rate (10 kHz). This is provided with extensive software capabilities for data acquisition, data manipulation, source modeling, anatomic visualization, and DICOM 3.0 based image transfer and retrieval.

Digital signal processors (DSPs) are used to read out the signals from the SQUIDs, EEG channels, miscellaneous channels and trigger lines. A single common clock is used to synchronize the events. The DSPs also carry out filtering of the signals. Multiple parallel real-time computers are used to collect the data from the DSP units. Eventually, the parallel real-time computers are connected to the acquisition workstation via a high-speed switch.

The electronics of the MEG system incorporate 24-bit converters between the analogue and digital signal domains. These converters sample the sensor signals at a rate of 30 to 50 kHz, which is subsequently downsampled by the digital signal processors to rate chosen by the user (e.g., 600 Hz). This downsampling process increases the resolution at the small signal end of the dynamic range via averaging. With the rates given above, three more bits are added to the resolution, thus yielding in the majority of MEG-measurements a 27-bit effective resolution of the filtered output signal. Since computers work most efficiently with storage elements of multiples of eight bits, the 27-bit signal is stored as a 32-bit number. After removing the contributions of external magnetic noise sources, the remaining brain signal has a rather moderate dynamic range. Therefore, the user can select to store the noise-compensated signals with either 16-bit or 32-bit resolution. The latter approach naturally yields twice as large files as the former. The maximum sampling rate for all channels is 10 kHz. For all available sampling rates all channels are used. All channels, including MEG, EEG, trigger and analogue input channels are sampled simultaneously. It must be borne in mind that the highest frequencies studied so far with MEG have ranged up to 600–1000 Hz.

In order to measure the exact position of the head or the chest of the subject with respect to the dewar, three or four position-indicating coils are attached to the scalp or to the chest, respectively. The magnetic fields of the coils are measured with the magnetometer and the positions of the coils with respect to an anatomical frame of reference are obtained with a 3D digitizer type Polhemus Isotrak II (Ahonen et al., 1993). This information is the basis for integrating MEG/MCG results with, for example, MR images. The location of the head relative to the helmet is defined using four or five *head position indicator* (HPI) coils attached to the subject's head. The locations of the coils are, with respect to the anatomy, digitized prior to the measurement with the Polhemus Istorak system. The head position is continuously measured by means of these coils that are energized with high-frequency AC-currents of different frequencies above the measurement bandwidth. The coil positions are continuously calculated from the measured distribution of the magnetic field.

For the analysis of patient data, a movement compensation is very useful which consists of dynamic recording of the head position and a method that takes the recorded movement into account in the analysis. In Elekta Neuromag® software this is accomplished by decomposing the measured data with the Signal Space Separation method into a source model fixed to the head coordinate system, and the signals that would have been measured from a static subject are calculated (Taulu et al., 2005).

The co-registration of *functional MEG data* and *MR images* is carried out using MRI integration software module that is an integral part of the Elekta Neuromag® Software. The co-registration is based on three pieces of information (anatomical landmarks and the locations of the head position indicator coils, location of the head relative to the helmet, the digitized anatomical landmarks identified from MRI images). Anatomical landmarks – usually preauricular points and nasion – are identified and marked from orthogonal MRI slice sets.

The external noise cancellation for magnetometer channels is routinely performed using the *signal space projection* (SSP) method. In this method the noise cancellation is based on the signals from the MEG magnetometer array itself. No separate reference sensor system is required. During installation of the MEG system, the spatial interference patterns originating from external sources and penetrating the shielded room is determined from an ''empty-room'' recording made with the system itself. In all subsequent measurements, a noise cancellation factor exceeding 1000 (>60 dB) is obtained by ''projecting out'' these spatial interference patterns (directions in the signal space) from the measured data. The interference patterns are stable typically over several months, even years. The method introduces no bias to source localization, and does not add any noise to the signals. The SSP method can also be applied also to gradiometers to increase their inherently noise immunity even further. For details of SSP, see Uusitalo and Ilmoniemi (1997).

The *signal space separation* (SSS) method is a novel development which greatly increases the robustness of practical MEG measurements, as is more required especially in clinical work. The magnetometers can be gradiometrized up to arbitrary order by the SSS method, in which the biomagnetic and external interference signals are separated. The SSS method is based on the fundamental properties of magnetic fields (Maxwell's Equations), and on the accurate geometry and calibration of the device enables the separation of artifacts from signals of magnetic origin. Furthermore, magnetic signals from sources inside and outside of the sensor helmet can be differentiated. Consequently, a ''software magnetic shielding'' effect is achieved which rejects signals from sources outside of the helmet. The shielding factor is of the order of the calibration accuracy – that is, a 1‰ calibration accuracy leads to a shielding factor of about 1000. The shielding factor for even near-by external sources – such as the heart of a small child within about 10 cm from the nearest channels – is considerable. For a detailed description of the proprietary SSS method, the reader is referred to Taulu et al. (2005). It is possible to eliminate the interference due to ferromagnetic particles on the subject's head with this method, record neuromagnetic DC-phenomena, and identify and eliminate channel artifacts. The SSS method greatly increases the robustness of the MEG method by eliminating or greatly reducing the most common artifacts.

Somatosensory evoked fields (SEF) to median nerve stimulation (about 100 averages) in a healthy adult subject are represented in Figure 2.22 (a, upper trace). Isocontours of the corresponding magnetic-field component perpendicular to the head surface calculated on a triangulated scalp surface are shown in Figure 2.22 (a, lower trace) for two time points.

An example of records of brainstem auditory evoked fields (BAEF) is shown in Figure 2.22 (b) (Parkkonen and Mäkelä, 2002), in comparison to brainstem auditory evoked potentials (BAEP). In this case, the sources are so deep that the signals can be seen with a much better signal-to-noise ratio with magnetometers than with gradiometers. It should also be noted that the amplitude resolution of the Elekta Neuromag® data acquisition is quite sufficient to resolve the extremely low signal of amplitude below 5 fT.

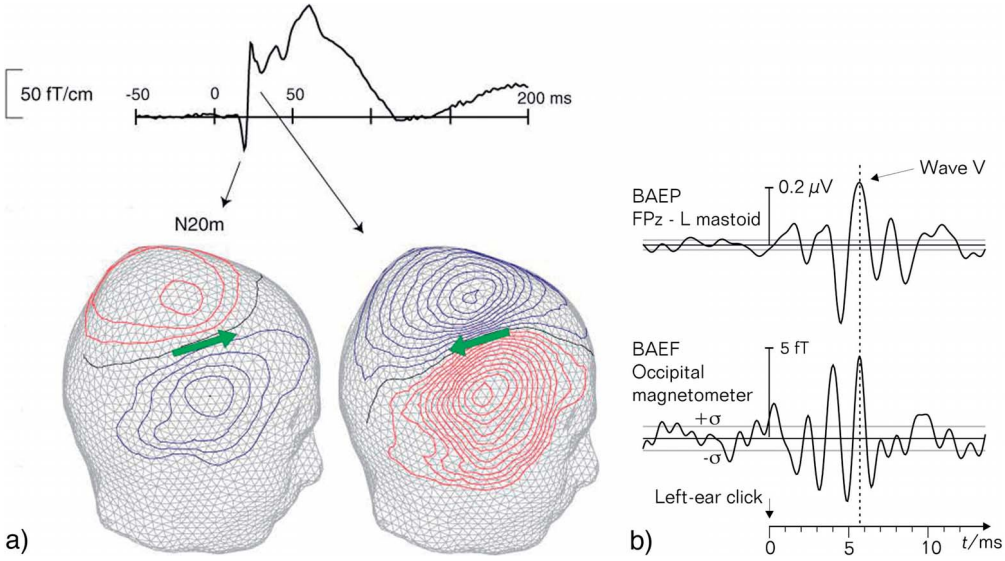

Fig. 2.22. (a) Somatosensory evoked field (upper trace) and isocontours (lower trace) after median nerve stimulation (100 averages) recorded by Elekta Neuromag® helmet-shaped MEG-device. (b) Brainstem auditory evoked field (BAEF; ca. 16 000 averaged epochs) recorded by Elekta Neuromag® helmet-shaped MEG-device and brainstem auditory evoked potential (BAEP) waveforms.

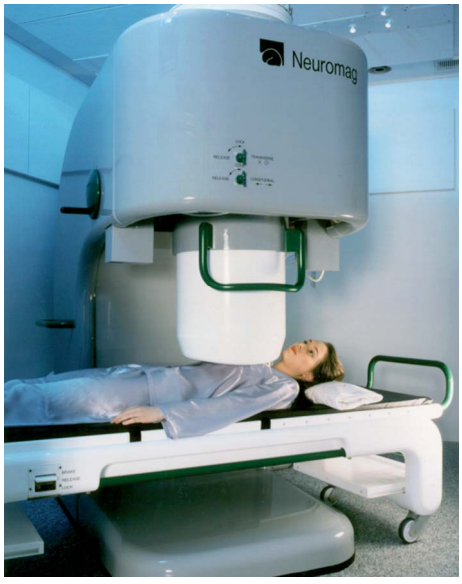

Fig. 2.23. 99-channel cardiomagnetometer prototype of Elekta Neuromag®.

Table 2.4. Installed Elekta Neuromag Systems including the year of installation and location.

Year	No. of channels	Affiliation	North America	Europe	Asia
1992	122	MEG helmet		Espoo	
1994	122	MEG helmet			Kyoto
	122	MEG helmet		Helsinki	
1995	122	MEG helmet			Osaka
	122	MEG helmet	Albuquerque		
	68	MCG		Helsinki	
	122	MEG helmet			Tokyo, NTT
	122	MEG helmet		Düsseldorf	
1996	122	MEG helmet		Heidelberg	
1997	122	MEG helmet	Salt Lake City		
	122	MEG helmet			Tokorozawa
1998	306	MEG helmet		Espoo[a)]	
	306	MEG helmet	Salt Lake City[a)]		
	122	MEG helmet			Sendai
	122	MEG helmet			Tokyo Univ.
1999	204	MEG helmet			Matsumoto
	204	MEG helmet			Tokyo Univ.[a)]
	306	MEG helmet			Sendai[a)]
	122	MEG helmet			Chiba TDC
	204	MEG helmet			Sapporo
	204	MEG helmet			Tokyo NCNP
2000	306	MEG helmet		Helsinki[a)]	
	204	MEG helmet			Niigata
	204	MEG helmet			Hirosaki
	204	MEG helmet			Akita
	204	MEG helmet			Hiroshima
	306	MEG helmet			Taipei
	99	MCG		Helsinki[a)]	
	306	MEG helmet	Charlestown		
2001	122	MEG helmet		Alexandroupoli	
	306	MEG helmet			Tokorozawa[a)]
	122	MEG helmet			Chiba, TD Univ.
	306	MEG helmet			Shijiazhuang
2002	204	MEG helmet			Komaki
	306	MEG helmet			Okazaki
	204	MEG helmet			Gunma
2003	306	MEG helmet			Kyoto[a)]
2004	101	MEG helmet, Experimental			Hokkaido

Table 2.4 *(continued)*

Year	No. of channels	Affiliation	North America	Europe	Asia
2005	306	MEG helmet			Yamagata
	306	MEG helmet			Seoul
	306	MEG helmet	San Diego		
	306	MEG helmet	Pittsburgh		

[a] Upgrade from a previous system.

The 99-channel cardiomagnetometer (Fig. 2.23) has the same sensor elements as the whole-head array. The sensor samples the magnetic field by means of pick-up loops at 165 distinct locations above the thorax arranged on a slightly curved spherical surface. Of these loops, 132 are coupled to form 66 planar gradiometers, organized in orthogonal pairs. The midpoint of each pair coincides with the location of a magnetometer loop. Altogether, 99 independent signals are thus provided as inputs for MCG data analysis. Noise suppression is carried out by software, utilizing either the SSP or SSS technique. The dewar has a cylindrically shaped lower tip with a diameter of 30 cm and radius of curvature of 79 cm. The distance from the liquid helium space to the outer surface of the dewar bottom is about 2.5 cm and the helium boil-off rate is about 6 L per day. Besides MCG, the system may also be applied in fetal MEG.

An overview of the Elekta Neuromag® systems, together with installation year and location, is provided in Table 2.4.

2.2.7.4 Advanced Technologies Biomagnetics (AtB) s.r.l.

The Italian company AtB (Advanced Technologies Biomagnetics) has developed MCG as well as MEG devices (www.atb-pro.com). The basic component of all magnetic sensors is a fully integrated planar SQUID magnetometer based on Niobium technology. The sensing area is a square of 8 mm side length. This SQUID element is the modular basis for a flexible construction of complex sensor systems, including arrays of triaxial vector magnetometers with an intrinsic noise level better than 7 $fT/\sqrt{Hz}$ at 10 Hz.

The noise cancellation strategy is based on a combination of cost-optimized shielded environment and real-time compensation (software gradiometers) using reference magnetometers measuring the environmental disturbances. The liquid helium dewars are built on the basis of monolithic structures of compound materials for maximization of safety and reliability; that is, it is composed of only one entire inner and one entire outer container made of fiberglass composite, which results in low-noise dewars. The distance at the dewar bottom [“warm” (300 K) to

"cold" (4.2 K)] is typically about 18 mm. The typical filling volume for MCG-dewars is 62 L, and the stationary evaporation rate is about 8 L per day. On this basis, the ARGOS family with several sensor array configurations has been developed, optimized for different applications as MCG, MEG or fMCG recordings. The systems operate in AtB-magnetically shielded rooms most with three layers of μ-metal and one rf shield.

The *ARGOS 50 MCG* is a planar biomagnetometer designed especially for magnetocardiography, and contains 77 SQUID magnetometers. The sensor array (lowest level) consists of 55 SQUID sensors recording B_z (i.e., the magnetic field component perpendicular to the chest and the Earth's surface, respectively). They are located in a hexagonal grid with a grid constant of 3.2 cm covering a circular planar surface with a diameter of 23.0 cm. Some 7.0 cm above these is the corresponding second level, with 19 magnetometers acting as compensation coils. The third level, located 14.0 cm above the first one, contains a triplet of magnetometers oriented in x-, y-, and z-directions. Software gradiometers (first-order gradiometers with 7.0-cm or 14.0-cm baseline or second-order gradiometers) can be used digitally to reduce the quasi-homogeneous ambient noise (Erné et al., 1999).

The multichannel-vector-magnetocardiograph *ARGOS 200* is a biomagnetometer specially designed for magnetocardiography and magnetoneurography (see Fig. 2.24a). The main idea of the ARGOS 200 is to form a triplet of SQUIDs to allow recording of the magnetic field vector (i.e., B_x, B_y and B_z). The triplets are distributed over four levels (Nowak et al., 2003). The lower level, the main measurement plane, is a planar sensor array consisting of 56 SQUID sensor triplets covering a circular planar surface with a diameter of 23.0 cm. The reference array consists of seven SQUID sensor triplets located in the second level in a plane which is positioned parallel to the measurement plane at a distance of 9.8 cm. The third or fourth level with one triplet, are located at distances of 19.6 cm and 25.4 cm, respectively, above the measurement plane. The center of the triplets in the third and fourth levels are located at the axis (measurement plane's position 0-0) of the insert. In total, 195 SQUID sensors are used. The position plot of a recorded vector MCG is shown in Figure 2.24 (b).

The *ARGOS 150* is a helmet-shaped system for magnetoencephalography. The sensor array consists of 165 SQUID sensors located in 165 independent measurement sites, with an inter-sensor separation less than 3.0 cm for appropriate spatial sampling.

The *ARGOS 500* is a helmet-shaped biovector magnetometer specially designed for magnetoencephalography (Pasquarelli et al., 2004a) (Fig. 2.25). The large vertical-oriented dewar is localized and fixed on the basement with a helmet-shaped cavity to accommodate the patient's head. The sensor array consists of 165 SQUID sensors triplets located in 165 independent measurement sites, with an inter-sensor separation of less than 3.0 cm (Pasquarelli et al., 2004b). The *ARGOS 500/PL* is a system derived from the ARGOS 500, but with standard, quasi-radial, nonvectorial sensor distribution. This device resembles the ARGOS 500.

The *bioelectrical amplifiers* are low-noise, high-impedance, differential-input biopreamplifiers, modularly expandable between 32 and 128 channels. The maximum

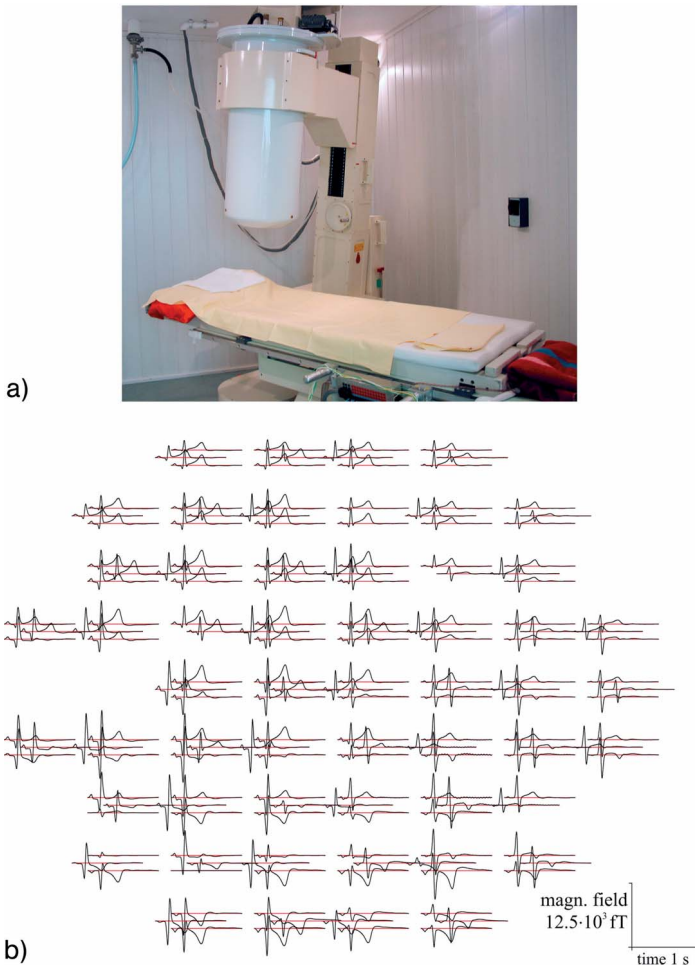

Fig. 2.24. (a) Multichannel vector-magnetocardiograph ARGOS 200. (b) Position plot of a vector-MCG-recording by ARGOS 200.

number of electrical channels usable simultaneously with the magnetic recordings depends on the chosen configuration of magnetic sensor and data acquisition system. The *data acquisition system* is modularly expandable until 644 channels. The resolution of conversion is better then 18 bits. A fixed sampling rate can be chosen either by 8.4 kHz for a maximum of 330 channels or alternatively by 4.2 kHz for a maximum of 660 channels. DC-coupled or AC-coupling at hardware level and acquisition bandpass is determined via digital filters.

An overview of AtB-ARGOS systems, together with installation year and location, is provided in Table 2.5.

Fig. 2.25. Argos 500 with patient bed inside a magnetically shielded room.

2.2.7.5 CardioMag Imaging™

CardioMag Imaging™ (CMI) (www.cardiomag.com) was incorporated in 1999. The company introduced a line of commercially available cardiac diagnostic devices called MagnetoCardioGraphs (e.g., a 9- or a 36-channel system) which record the electrical activity of the heart using SQUID-sensors with the capability of operating in unshielded environments. Therefore, a second-order gradiometer (diameter 2.0 cm) is the base antenna for these devices. An intrinsic noise level is obtained with 10 $fT/\sqrt{Hz}$ between 1 and 10 Hz, which is normally superimposed by the clinical environmental disturbances. A total balancing of the measuring channels is achieved with less than 10^{-4} with an additional Electronic Noise Suppression System using three background environment reference channels. The nine-channel device covers an area of 8.0×8.0 cm^2, and the 36-channel device an area of 20.0×20.0 cm^2. The measurement system is installed in a dewar with a capacity of 13.5 L for liquid helium. The helium boil-off rate is less than 2.5 L per day.

An installed nine-channel CMI-MagnetoCardioGraph is shown in Figure 2.26 (a) in a clinical environment (Chest Pain Unit).

Having received regulatory approvals such as FDA, UL, CE Mark, and GMP certifications, the CMI-systems are now being used to collect clinical data in accordance with a number of diagnostic protocols aimed at rapid, real-time cardiac functional testing. Patients undergo a safe and silent, resting 6- to 10-minute non-invasive test procedure, during which time a series of cardiac signals are displayed and subsequently analyzed to determine the existence or absence of heart disease (Brazdeikis et al., 2002; Brisinda et al., 2003).

Table 2.5. Installation year and location of AtB-ARGOS systems.

Year	No. of channels	Affiliation	Europe
1998	77	ARGOS 50	Chieti
1998–2004	77	ARGOS 50	Ulm
1999	165	ARGOS 150 (helmet)	Chieti
2003	195	ARGOS 200	Jena
2003–2004	495	ARGOS 500 (helmet)	Ulm
2005	150	ARGOS 500 (helmet)	Naples
	495	ARGOS 500/PL (helmet)	Avellino
	495	ARGOS 500/PL (helmet)	Chieti
	77	ARGOS 50	Hoyerswerda
2006	495	ARGOS 500 (helmet)	Roma

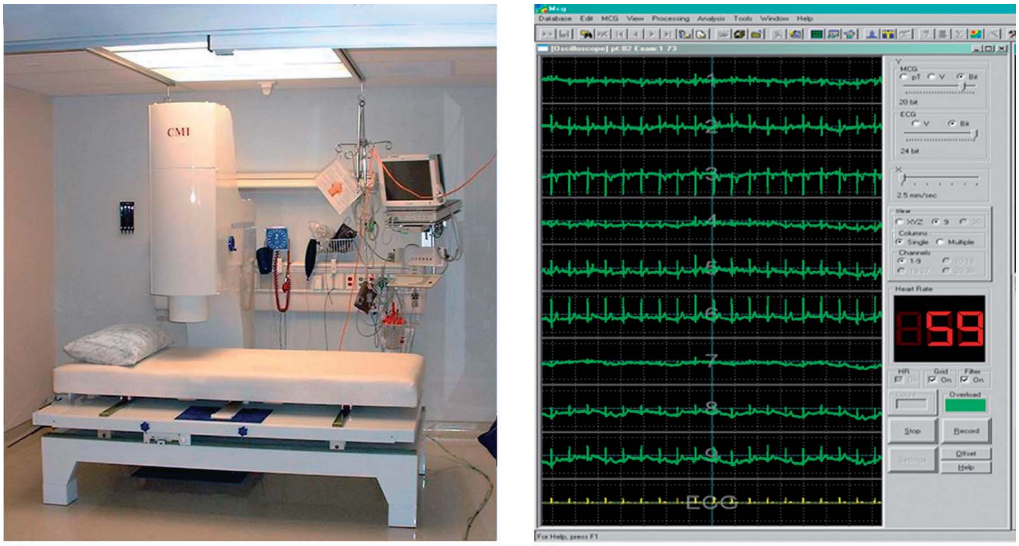

a) b)

Fig. 2.26. (a) CMI-2409 MagnetoCardioGraph installed in a Chest Pain Unit. (b) Real-time traces of nine MCG channels (upper traces) and one ECG channel (lowest traces) recorded by the CMI-2409 system.

Table 2.6. Installation year and location of the CMI-systems.

Year	No. of channels	Affiliation	North America	Europe	Asia
2002	9	CMI-2409	Baltimore		
2002	36	CMI-2436		Rome	
2002	9	CMI-2409		Hoyerswerda	
2003	9	CMI-2409	Los Angeles		
2003	9	CMI-2409	Rochester		
2003	9	CMI-2409			Tianjin
2005	9	CMI-2409			Shenzhen
2005	9	CMI-2409		Krakow	

Fourteen channels (nine MCG channels, three reference channels, one cardiac trigger channel, one accessory channel) with 24-bit ADC per channel with a 1000 Hz sampling rate (500–2000 Hz range) are available for data acquisition. For signal processing, analogue and digital filtering, low-pass and high-pass filtering, signal averaging and spectral noise analysis are available. Figure 2.26 (b) represents a real-time MCG and ECG recorded by the nine-channel CMI-MCG system in unshielded environment.

In addition to showing both magnetic and electric cardiac traces, the system also displays a series of animated magnetic field maps that dynamically display cardiac activity in the form of color contour maps. These two- and three-dimensional maps represent changes in current flow during an averaged cardiac cycle. Automated diagnostic algorithms that incorporate intelligent machine learning techniques may show promise for generalized heart-health scanning examinations.

An overview of CMI-MagnetoCardioGraphs-systems, together with installation year and location, is provided in Table 2.6.

2.2.7.6
Tristan Technologies, Inc.

Tristan Technologies was first created in 1991 by many people associated originally with several San Diego superconducting companies, including Biomagnetic Technologies (BTi) and S.H.E. Corporation. This company was subsequently sold to Conductus, Sunnyvale in 1993, and became its Instrument and Systems Division. This division in San Diego closed in July 1997, and the employees reformed Tristan Technologies (www.tristantech.com) in August 1997.

Tristan's strength is in the design and manufacture of laboratory and custom SQUID systems (Fagaly, 1999). Tristan's standard product line of SQUID instrumentation is available for scientific laboratory applications. Custom SQUID magnetometers supplied by Tristan include both liquid cryogen and cryocooled high-temperature SQUID magnetometer and gradiometer systems, liquid helium

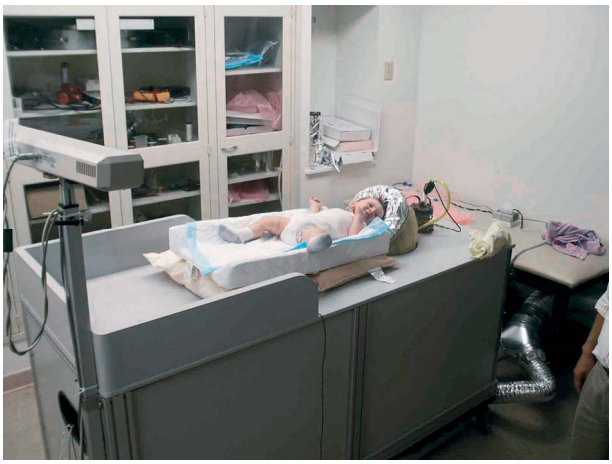

Fig. 2.27. BabySQUID® Neonatal Biomagnetometer. The magnetometer is located in the infant bed. Electronics and data acquisition system is located in the cart. The rectangular device at the end of the infant bed is the projector for the optical positioning system.

scanning SQUID microscopes with μm-resolution (the world's first magnetic microscope), liquid nitrogen SQUID microscopes for magneto-immunoassay measurements, and biomagnetometers for medical applications, which vary from single-channel devices to complex multi-channel systems.

The model 607 microSQUID™, which can be used for animal investigations, has seven sensors with 4 mm-diameter detection coils and four reference coils (B_x, B_y, B_z, and dB_z/dz). Research instruments for animal measurements have typically been low channel count systems with smaller detection coils. The higher spatial resolution required for animal measurements also requires closer spacing. The use of adjustable tail dewars that permit closer spacing between the sensor and room-temperature sources and coil-in-vacuum technology allow small-diameter (1–4 mm) detection coil arrays to be built, without having to use excessively thick dewar tail pieces. The noise amounts to 15–20 $fT/\sqrt{Hz}$. The coil to room-temperature distances were <2 mm.

The Model 637 is a fully integrated magnetic source imaging system with 37 channels that cover almost 500 cm^2, and can be used for magnetocardiography including fetal MCG, magnetoencephalography and magnetoenterography (measurement of the stomach and intestines).

The gutSQUID® is a 37-channel system for measuring the blockage of arterial blood flow (ischemia) in the gastrointestinal (GI) tract, which can lead to intestinal necrosis (Bradshaw et al., 1999). SQUID magnetometers permit the measurement of low-frequency oscillations (8–15 cycles per minute) related to electrical activity in the GI tract. This system is a vector system that records all three components of the magnetic vector (B_x, B_y, and B_z).

Nerve conduction involves rapid axonal spikes of duration on the order of 1 ms. Tristan's ultra-high-speed 73-channel model 661 spineSQUID™ system acquires data in excess of 100 000 samples per second on each channel, including reference channels. This permits tracking of axonal events, and allows the tracking of very rapid changes in nerve conduction.

Tristan's babySQUID® Neonatal Biomagnetometer is an MEG system specifically designed for detecting cortical function in the newborn (Fig. 2.27), and is built to operate without the need for magnetic shielding. The measurement cradle and its companion electronics cart are portable and can be wheeled in and out of elevators, obstetric suites, and neonate intensive care units. The system has 76 detection coils (diameter 6 mm) with a sensor coverage area of 300 cm^2. Its spatial resolution is four times greater than that of existing ''adult'' whole-head MEG sensors. An optical one-click 3D imaging system is used to track patient movements. The optical tracking and mapping system update movement at 30 Hz with 0.5-mm accuracy. The inherent system noise is about 15 $fT/\sqrt{Hz}$ at 1 Hz. The gap (300 K–4 K) is about 7 mm.

2.2.7.7
Philips Research, Hamburg

The Philips company has designed and manufactured a *twin-dewar biomagnetometer* system with 2×31 channels for operation inside a shielded room (e.g., AK 3b). This biomagnetometer is based on a modular technique; that is, every single channel can be optimized or replaced individually. The symmetrical first-order axial gradiometers have a diameter of 2.0 cm and a base length of 7 cm (Dössel et al., 1993). Both the pick-up coil and the compensation coil have two turns of niobium wire wound around a common fiber-reinforced epoxy cylinder. The imbalance of the gradiometers is less than 0.1%, and they are galvanically coupled to the SQUIDs. The field noise of the system is less than 10 $fT/\sqrt{Hz}$ at 1 Hz (Nowak and Huonker, 1996). Data are acquired by commercially available EEG amplifiers (SynAmps, Neuroscan).

The double-dewar construction allows measurements to be performed over both hemispheres of the head for magnetoencephalography, or over the chest for magnetocardiography (Fig. 2.28) and, of course, single-dewar (31-channels) investigations are also possible. In addition, 62 channels of the EEG/ECG can be recorded simultaneously.

The positions of the dewars in relation to each other and to the subject can be obtained by localizing up to 10 small magnetic markers (coil triplets). Each marker consists of three coils perpendicular to each other, thus giving independence from the orientation of the coil triplet (Fuchs and Dössel, 1992).

The investigations performed with the device described can be divided into two main groups: neuromagnetic (e.g., auditory and somatosensory-evoked responses, presurgical mapping, fetal MEG, spontaneous brain activity) and cardiomagnetic measurements. Magnetic Source Imaging (MSI) is used for both groups; this is based on biomagnetic measurement and MRI in order to localize the magnetic source using the markers described above.

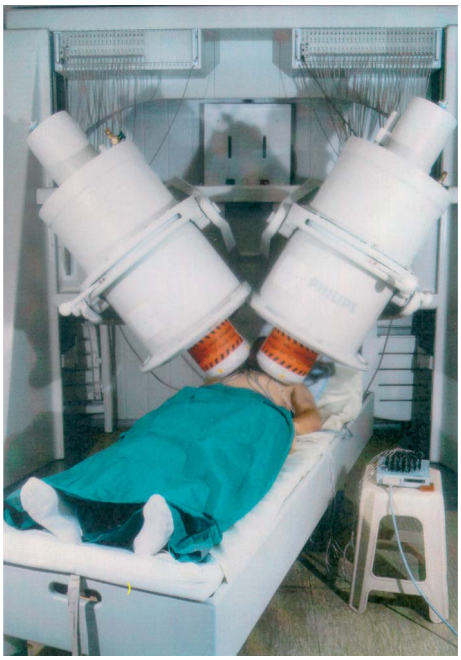

Fig. 2.28. 62-channel twin dewar biomagnetometer during MCG-recording (Philips).

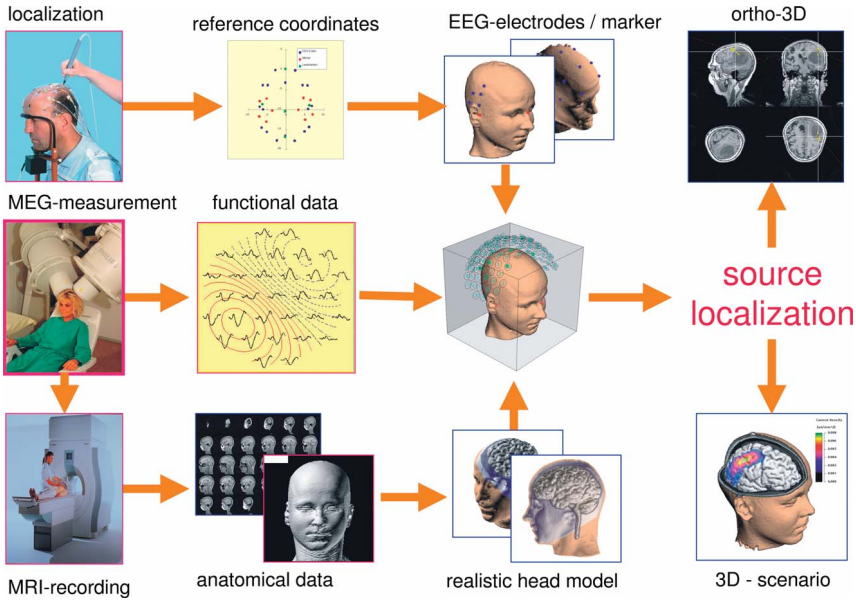

Fig. 2.29. Magnetic Source Imaging (MSI). (Material provided by R. Huonker).

A result of the MSI-procedure is demonstrated in Figure 2.29, using an auditory evoked response. The MEG recorded is shown on the middle right-hand side (averaged data, position plot, isomagnetic field map), and the MRI data on the middle left-hand side (one slice of the raw data, reconstructed MR-images of the head surfaces with markers). A pointset matching by coordinate transformation allows morphological information and the magnetic field pattern to be superimposed in a morphological coordinate system, as shown in the right part of Figure 2.29. With respect to the physiology of the source, different source models can be applied in order to perform MSI (Huonker et al., 1996).

The principle of localizing, for example an anterior infarction in cardiomagnetism, is based on the same procedure (Leder et al., 1998). In 1994, two of these double-dewar systems were installed in Germany (one in Jena and one in Hamburg).

2.2.8 Special Biomagnetic Measurement Devices

2.2.8.1 Micro-SQUID Systems

As the biomagnetic fields fall off as $1/r^2$ to $1/r^3$ with the distance r (source-detection coil), it may be advantageous to decrease the space between the pick-up coil and the outer bottom dewar in order to achieve a higher signal-to-noise ratio. This also provides higher spatial resolution (Wikswo, 1988; Wikswo et al., 1989). To address this need, BTi San Diego developed a closely spaced, four-channel micro-SQUID device with four axial asymmetric first-order gradiometers (Buchanan et al., 1989). A similar device was installed in Yoshio Okada's biomagnetic center in Albuquerque, inside a magnetically shielded room. This micro-SQUID device contains pick-up coils of 4.0 mm diameter, with a baseline of 16 mm and a channel separation of 6 mm. The magnetic field sensitivity is about 50 $fT/\sqrt{Hz}$. The spacing between the pick-up coils and outside surface of the dewar is, at 1.2 mm (Okada et al., 1992), uniquely achieved by mounting the pick-up coils in the vacuum space of the dewar. With this device, magnetic signals from, for example hippocampal slices of a guinea pig, can be investigated (Kyuhou and Okada, 1993; Okada and Xu, 1996; Okada et al., 1997).

This device can also be used to study a phenomenon called "spreading depression", which is believed to be the physiological basis for the aura in classic migraine (Okada et al., 1993). It has been also used to study the ability of MEG to localize cortical sources, by comparing the locations of the generators inferred from somatic evoked fields produced by the somatosensory cortex of the juvenile swine against the locations determined with electrocorticograms and depth recordings (Okada et al., 1996).

Moreover, high-spatial resolution SQUID magnetometers were developed with a pick-up coil diameter of 1.0 mm (Ono et al., 2004) and of 0.2 mm (Kobayashi and Uchikawa, 2003) for investigations with animals and nerves, respectively.

2.2.8.2 The Jena 16-Channel Micro-SQUID Device

Basic research studies require extremely high spatial resolution (small pick-up coils, minimal distance between source and pick-up coil) that covers an area of about 9 cm^2 with more than 10 channels. Based on experience in biomagnetic instrumentation in Jena (Albrecht et al., 1981, 1989; Nowak et al., 1991, 1995; Gießler et al., 1993), an ultra-high-spatial resolution 16-channel Micro-SQUID device was developed and manufactured. The pick-up coils were designed to be positioned in a rectangular 4×4 grid covering an area of 3.2×3.2 cm^2 with the shortest distance of 8.4 mm between neighbors. The diameter of the pick-up coils was 6.7 mm, and the first-order asymmetric gradiometers had an average base length of 3.0 cm. The gradiometer support was constructed from Macor and the gradiometers were Nb-wire wound. The balance was about 1%, and the system was installed inside a magnetically shielded room (Nowak et al., 1999).

The gradiometer assembly is shown in Figure 2.30 (a). Typical values of the flux density noise were about 22 $fT/\sqrt{Hz}$ at 1 Hz. A specially designed dewar was used (Quantum Magnetics, San Diego, USA), with a distance of about 3 mm between the inner dewar and outer dewar bottom. Epileptic spikes initiated by stereotactic intracortical penicillin injections in rabbits were investigated. A typical MEG-signal is shown in Figure 2.30 (b). The position plot of the 16 MEG-channels (bandwidth 0.1 to 70 Hz, time window of 1 s) is superimposed with isomagnetic lines (positive signals, solid line; negative signals, dashed line; signal differences between two isolines, 50 fT). The adapted software CURRY® (Philips, Hamburg, Germany) was used for signal analysis. Another example of a real-time 16-channel MEG recording of a dc-shift during cortical spreading depression in a rat is shown in Figure 2.30 (c). This equipment provides new possibilities necessary for the analysis of physiological as well as pathophysiological processes in the brain. Moreover, it enables the investigation of single-event analysis in the brain and avoids the loss of important information by data averaging. Furthermore, the high spatial resolution allows for the differentiation of neuronal activities that are only a few millimeters apart. This may provide new insights into the functional organization of neuronal functions during a great variety of physiological and pathophysiological events.

2.2.8.3 Planar Gradiometers

First- and second-order planar gradiometers with which $\Delta B_z/\Delta x$ or $\Delta B_z/\Delta y$ and $\Delta^2 Bz/\Delta x^2$ or $\Delta^2 B_z/\Delta y^2$ respectively can be recorded have been proposed and investigated by several groups (Ketchen et al., 1978; de Waal and Klapwijk, 1982; van Nieuwenhuyzen and de Waal, 1985). The advantage of planar gradiometers is that, due to thin-film technology, a high initial balance (better than 10^{-3}) can be achieved. A possible disadvantage from the practical and economical point of view is a limit in the length of the baseline (limit of the sensitivity to deep sources).

a)

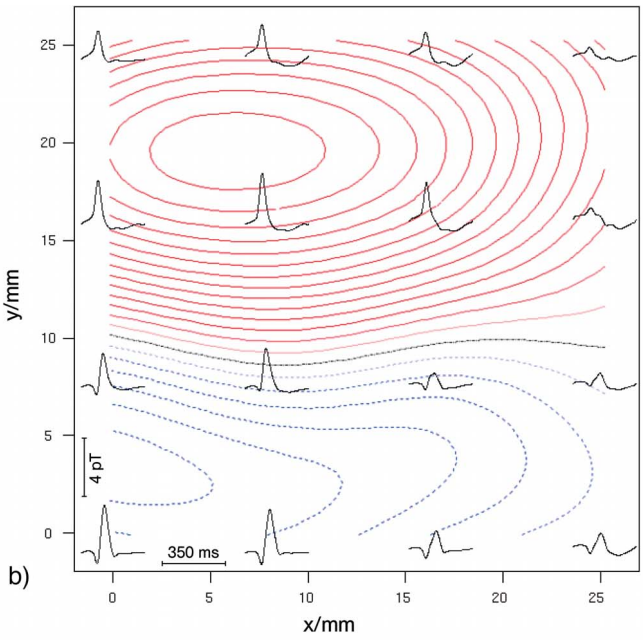

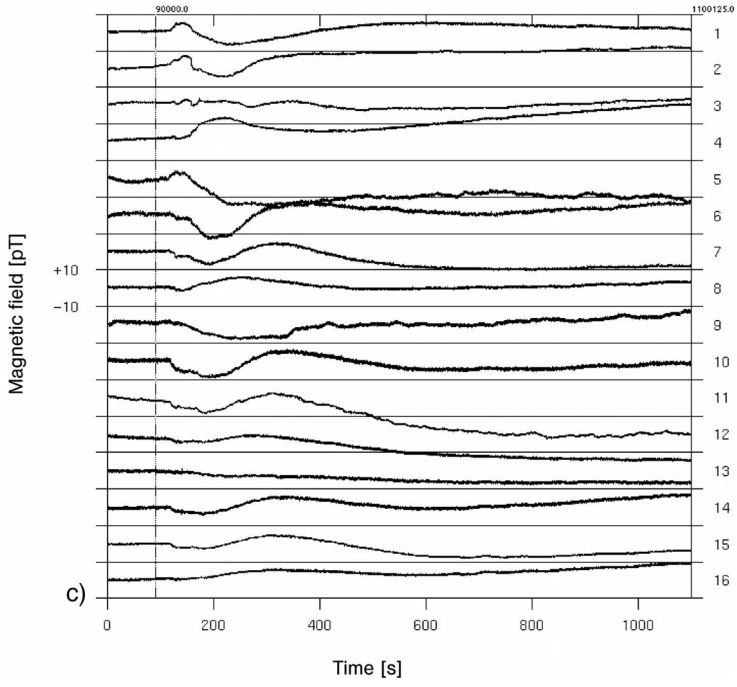

Fig. 2.30. (a) 16-channel gradiometer arrangement; lower part: 16 pick-up coils with five turns; upper part: four groups of compensation coils with one turn per pick-up coil. (b) MEG-recordings of epileptic spikes: position plot with isomagnetic lines (difference between two isomagnetic lines: 50 fT, averages: 100). (c) Real-time MEG-recordings of a dc-shift during cortical spreading depression in a rat.

A planar eight-channel tangential-field gradiometer system was proposed and realized by Josephs et al. in order to measure the magnetic field components $\Delta^2 B_x/\Delta z^2$ and $\Delta^2 B_y/\Delta z^2$. These authors used standard printed-circuit board (copper/epoxy) technology with the superconducting circuit formed by PbSn solder coating of lithographically prepared copper tracks. The rectangular coils are 1.25 cm wide and 1.55 cm, 3.1 cm and 1.55 cm long, with 2, −2, and 2 turns (Josephs et al., 1995). This system, with about 18 $fT/\sqrt{Hz}$ white noise, has an adequate noise performance level for many neuromagnetic investigations.

A first-order planar SQUID gradiometer system was fabricated and tested by Stolz et al. (2003) for biomagnetic applications with two pick-up loops (quadratic, 2 cm) and with a baseline of 4 cm. The intrinsic noise corresponds to a field resolution in one loop better than 3 $fT/\sqrt{Hz}$ white noise.

Planar gradiometers are applied in multichannel biomagnetic devices such as those developed by Neuromag, Helsinki (Kajola et al., 1989).

2.2.8.4
Japanese 256-Channel Device (SSL-Project)

In connection with the Japanese Superconducting-Sensor-Laboratory (SSL) Project, a 256-channel device was developed and realized for measurements inside magnetically shielded rooms. Today, this system is in operation at the Tokyo Denki University, in the magnetically shielded COSMOS room (Harakawa et al., 1996).

The 256-channel system consists of magnetometers using Drung-type SQUIDs (Uehara et al., 1993; Matsuda et al., 1995) mounted inside a dewar with a bottom formed to fit the human head (similar to the whole-head systems described above).

The helium consumption is about 9 L per day, and the dewar is automatically refilled every third day. The white noise of the system is 5 $fT/\sqrt{Hz}$. Other devices were also developed, such as the middle-scale SQUID system, in which 64 gradiometers are distributed over a measuring area of 17.5×17.5 cm^2 in a dewar with a flat bottom; this system can be used for both MCG and MEG recordings. Furthermore, a 16-channel system for MEG and a 32-channel system for MCG investigations have been constructed.

2.2.8.5
Vector-Magnetometers

More complete information about magnetic fields can be obtained by recording the magnetic field vector, for example with vector-magnetometers. The first vector MCG was recorded by Wikswo et al., who used a first-order gradiometer (baseline 15 cm), the axis of which was about 35° to the horizontal. Successive 120° rotations of the dewar around its vertical axis allowed sequential measurement of three orthogonal vector components (Wikswo et al., 1975).

The same idea was applied by Gießler, but instead using a well-balanced symmetrical second-order gradiometer, with a diameter of 3.0 cm and a baseline of 7.5 cm (Gießler et al., 1993). A more advanced 129-channel vector neuroimaging

system has been presented by Yoshida et al. (2000) in which the 129 channels represent 43 measuring points. Each of these consists of three first-order gradiometers wire-wound on the same cylindrical support. The corresponding three gradiometer coils are perpendicular to each other. The baseline is 5.0 cm, and each coil of the vector gradiometer has the same elliptical shape (large diameter 2.7 cm; short diameter 1.6 cm). The noise level is lower than 10 $fT/\sqrt{Hz}$ above 10 Hz (Yoshida et al., 2000). Recently a 304 SQUID Vector Magnetometer was designed and constructed by Schnabel et al. (2004).

Furthermore, the AtB system ARGOS 200 contains triaxial vector magnetometers (65 triplets with 195 SQUIDs) with an intrinsic noise level better than 7 $fT/\sqrt{Hz}$ at 10 Hz (see also Section 2.2.7.4).

2.2.8.6
Biomagnetic Devices with Cryocooler

Easy-handling systems based on cryocoolers can completely avoid the handling of liquid helium, as was demonstrated in 1981 (Sullivan et al., 1981). Moreover, Sata et al. have presented a 61-channel MEG system which can be cryocooled to maintain superconductivity (Sata et al., 1996). Here, the thin-film dc SQUIDs and pick-up coils are directly cooled by a Gifford-McMahon/Joule-Thomson cryocooler, without liquid helium, with the valve motor used to switch between high- and low-pressure helium gas being located outside the magnetically shielded room. The 61-channel system consists of first-order axial gradiometers (2.0 cm in diameter and with a 5.0 cm baseline) arranged radially on a spherical surface (12.5 cm radius). The noise from the cryocooler (about 15 pT) has a periodic characteristic which can be suppressed by signal processing. The white noise level of the system is in the range between 12 and 18 $fT/\sqrt{Hz}$ (Sata et al., 1996). The operation of dc SQUIDs on a two-stage GM-cryocooler with amagnetocaloric regenerator was also demonstrated in this group, achieving similar noise values (Fujimoto et al., 1993).

Low-noise cryocoolers operating on the pulse tube principle (Gerster et al., 1998) are being optimized to meet the requirements of HTS-SQUID magnetometers with resolutions in the order of 10 $fT/\sqrt{Hz}$.

2.2.9
High-Temperature Superconductivity

The term ''high-temperature superconductivity'' (HTS) refers to a new generation of superconductors, the development of which began in 1986 (Bednorz and Müller, 1986). Some of these oxide superconductors such as ''YBaCuO''-materials become superconductive at temperatures higher than 77 K, the temperature of liquid nitrogen. HTS-materials offer the possibility of substituting liquid nitrogen for liquid helium as a cooling medium. Liquid nitrogen is much easier to handle, much cheaper than liquid helium (about 1% of the cost), and is available in most of the hospitals. In addition, because liquid nitrogen has a high volume heat of evapora-

tion, the boil-off rate of the cryostats decreases and consequently the distance between the pick-up coils and the dewar outer bottom can be reduced significantly.

A $T_{c,\max}$ of 135 K was achieved using a $HgBa_2Ca_2Cu_3O_{8+x}$ HTS material (Buckel and Kleiner, 2004). One goal of these investigations was to improve the SQUID resolution (e.g., Tavrin et al., 1994; Cantor et al., 1995; Dantsker et al., 1995; Drung et al., 1996; Peiselt et al., 2003; Lee et al., 2004). Another goal was their application in biomagnetic instrumentation (e.g., Seidel et al., 1998; Zhang et al., 2000; Mizukami et al., 2003).

A hand-held, small-sized cryostat with integrated YBaCuO magnetometers was developed to record the magnetocardiogram (Schilling et al., 1996).

Burghoff et al. demonstrated the usefulness of HTS-SQUIDs for diagnostic applications when measuring the MCG within a shielded room (Burghoff et al., 1996). A thin-film planar HTS-SQUID gradiometer with bicrystal or step-edge Josephson junctions has been developed and applied for MCG recordings in an unshielded environment (Weidl et al., 1997).

Only a few types of multichannel biomagnetic instrumentation based on HTS-SQUIDs are known. Dilorio et al. presented a four-channel device with low-noise integrated HTS-SQUID magnetometers. This system had a magnetic field sensitivity of about 70 $fT/\sqrt{Hz}$ at 1 kHz and about 280 $fT/\sqrt{Hz}$ at 1 Hz (Dilorio et al., 1995), and could be used for both heart and brain investigations. A seven-channel system with packaged HTS-SQUIDs has been described by ter Brake et al. (1997), in which the averaged white-noise level of all seven channels was given with 120 $fT/\sqrt{Hz}$.

A modular nine-channel HTS-SQUID system for MCG measurements was developed for measurements in an unshielded environment. Galvanically coupled HTS-SQUID magnetometers with intrinsic white noise levels of about 70 $fT/\sqrt{Hz}$ were used. A noise level of about 1 $pT/\sqrt{Hz}$ was achieved in an unshielded environment using active noise compensation (David et al., 1996).

A 32-channel system was also developed with YBaCuO thin-film SQUIDs using step-edge Josephson junctions (Itozaki et al., 1996). The sensors were placed in an array of 6×6 except for the four corners, with a channel separation of 4 cm. A nitrogen dewar with a diameter of 40 cm and a height of about only 20 cm was developed for this purpose (Itozaki et al., 1996). The magnetic field resolution of the system was less than 1 $pT/\sqrt{Hz}$ at 10 Hz, and its value for MCG measurements was demonstrated in a shielded environment.

Tsukamoto et al. (2001) fabricated a highly balanced directly coupled $YBa_2Cu_3O_Y$ gradiometer which could be used in an unshielded environment and had a balance better than 10^{-3}. The noise density for this gradiometer was 300 $fT/cm/\sqrt{Hz}$ (>100 Hz) and 3 $pT/cm/\sqrt{Hz}$ (>1 Hz).

Until now, a serious limitation of the HTS technique in biomagnetic instrumentation has been the lack of mass production of low-noise HTS-SQUIDs, in addition to the fact that wires for the winding of gradiometers are unavailable. Welding the connection of two HTS-conductors also remains problematic. On the other hand, the progress which has been made in the development of low-noise HTS-SQUIDs with a white noise level below 10 $fT/\sqrt{Hz}$ is beyond doubt (Dantsker et al., 1995;

Drung et al., 1996). Indeed, the development of simple-to-operate biomagnetometers which can be used in a clinical environment is becoming increasingly realistic.

2.2.10 Perspectives

One advantages of biomagnetic measurement techniques is the contact-free recording of biomagnetic signals, and this is especially important in fetal MCG and fetal MEG (see Section 2.5) or MEG in the newborn (Pihko et al., 2004). Furthermore, this method is particularly suitable for repeated measurements, because it places no stress on the patient under investigation.

Moreover, the magnetic field has a high spatial and temporal resolution and provides additional information about the electric field (Haberkorn, 1996; Pflieger et al., 2000).

Today, several multichannel biomagnetometers with a white noise level below 5 $fT/\sqrt{Hz}$ (as described in Section 2.2.7) are available. As there is a tendency to separate magnetoencephalographic and magnetocardiographic measurement devices, special devices for these main fields of application (brain, heart and fetal investigations) have been developed as whole-head MEG systems and MCG systems, as well as slightly curved devices applicable to MEG, MCG, FMCG, FMEG, MGG, the study of stimulus propagation in the peripheral nervous system (Curio et al., 1995), and other biomagnetic investigations. Although more than 60 multichannel measurement devices have been installed worldwide, the distribution of these systems remains problematic due not only to their high costs but also to their lack of user friendliness, diagnostic power, and clinical acceptance. Although the use of HTS-SQUIDs (cooling temperature 77 K, using liquid nitrogen) rather than LTS-SQUIDs (cooling temperature 4.2 K, using liquid helium) would reduce operating costs and make the system more user-friendly, the noise parameters achieved with HTS-SQUIDs are not comparable with those of the LTS-SQUID multichannel systems. In fact, problems of noise – whether of environmental, thermal magnetic, dewar or biological origin – may in time limit the widespread distribution of these biomagnetic measurement devices.

The SQUID is the only magnetic field sensor with a high spatial resolution which is sufficiently sensitive to record biomagnetic fields in the range of fT, in comparison with optically pumped magnetometers, fiber-optic-based magnetic sensors, magnetoresistive magnetometers and flux gate magnetometers. Nevertheless, an optical pumping magnetometer has already been developed to map the magnetic field of the heart (Bison et al., 2003).

The number of channels required in biomagnetic measurement devices is often a compromise between the main application field of the system and economic factors. The devices described in Sections 2.2.7 and 2.2.8 are applicable to, and optimized for, most biomagnetic recordings with respect to the number of channels. One means of solving the problem of comparing magnetic signals measured with different multichannel devices was suggested by Burghoff, who transformed the

recorded signals of different devices (magnetometers, axial gradiometers, and planar gradiometers) into a reference system, and subsequently demonstrated its efficacy in the heart (Burghoff et al., 1997).

Perhaps the most promising application of biomagnetic measurement methods is that of magnetic source imaging (MSI) (see Fig. 2.29), which includes current imaging by means of morphologically constrained reconstructions (Fuchs et al., 1995). MSI represents a very powerful tool for the direct assessment of electrical sources within the human body (for overviews, see Nowak et al., 2002; Halgren et al., 2004). Moreover, it can – noninvasively – provide information about current distribution on the heart surface, providing the cardiologist with details of the exact location and temporal resolution of infarcts and other dysfunctions. Likewise, in neurology, psychiatry and neurophysiology, MSI can provide information on the location and temporal behavior of sources within the human brain for a wide variety of clinical and basic research questions. As a presurgical method in particular, it permits the possibility of reducing the discomfort of the patient, as well as healthcare expenditure, by minimizing the number of invasive investigations such as biopsies. The use of systems with 70 or more channels covering the region of interest (e.g., the heart or head) will allow investigations to be performed in a single step, thus opening a window to cognitive processes, for example. Such examinations can be conducted more rapidly than body surface potential mapping and EEG recordings due to their need for much less preparation time.

Clearly, when used in conjunction with advanced software, biomagnetism can be used as a diagnostic tool in a clinical context to localize electrically active sources with high spatial and temporal resolution complementary to electric field measurements.

Acknowledgments

The author thanks J. Bork (VAC), M. Burghoff, L. Trahms and A. Schnabel (PTB Berlin), G. Haight and J. Vrba (VSM MedTech), J. Nenonen (NEUROMAG), Y. Okada (University Albuquerque), K. Squire (4D NeuroImaging), as well as colleagues of the University of Jena, J. Haueisen, M. Liehr, S. Erné, B. Hilgenfeld, R. Huonker, F. Gießler, F. Schmiedel, U. Schulze, P. Seidel and M. Thürk, for their support.

References

Ahonen, A.I., Hämäläinen, M.S., Kajola, M.J., Knuutila, J.E.T., Lounasmaa, O.V., Simola, J.T., Tesche, C.D., and Vilkman, V.A. (1991). Multichannel SQUID systems for brain research. *IEEE Trans. Magn.*, **MAG-27**, 2786–2792.

Ahonen, A.I., Hämäläinen, M.S., Kajola, M.J., Knuutila, J.E.T., Laine, P.P., Lounasmaa, O.V., Parkkonen, L.T., Simola, J.T., and Tesche, C.D. (1993). 122-Channel squid instrument for investigating the magnetic signals from the human brain. *Phys. Scripta*, **T49**, 198–205.

Aittoniemi, K., Karp, P.J., Katila, T., Kuusela, M.L., and Varpula, T. (1978). On balancing superconducting gradiometric magnetometers. *J. Physique Coll.*, **39** (C6), 1223–1225.

Albrecht, G., Hilbert, A., Kirsch, G., Nowak, H., Vodel, W., and Zach, H.G. (1981). Application of dc thin-film SQUIDs and technique for biomagnetic measurements. *Cryogenics*, **21**, 607–608.

Albrecht, G., Burghoff, M., Gießler, F., Haberkorn, W., and Nowak, H. (1989). High resolution magnetocardiography, source localization and multichannel magnetometry. In: Williamson, S.J., Hoke, M., Stroink, G. and Kotani, M. (Eds.), *Advances in Biomagnetism*, Plenum Press, New York, pp. 349–352.

Bardeen, J., Cooper, L.N., and Schrieffer, J.R. (1957). Theory of superconductivity. *Phys. Rev.*, **108**, 1175–204.

Baule, G.M. (1965). Instrumentation for measuring the heart's magnetic field. *Trans. N. Y. Acad. Sci.*, **27** (ser. II), 689–700.

Baule, G.M. and McFee, R. (1963). Detection of the magnetic field of the heart. *Am. Heart J.*, **55**, 95–96.

Baum, E. and Bork, J. (1991). Systematic design of magnetic shields. *J. Magn. Magnetic Mater.*, **101**, 69–74.

Becker, W., Diekmann, V., Jürgens, R., and Kornhuber, C. (1993). First experiences with a multichannel software gradiometer recording normal and tangential components of MEG. *Physiol. Meas.*, **14** (A), 45–50.

Bednorz, J.G. and Müller, K.A. (1986). Possible high Tc superconductivity in the Ba-La-CuO-system. *Z. Phys.*, **64** (B), 189–193.

Benzel, E.C., Lewine, J.D., Buchholz, R.D., and Orrison, Jr., W.W. (1993). Magnetic source imaging: a review of the Magnes system of Biomagnetic Technologies Incorporated. *Neurosurgery*, **33** (2), 252–259.

Best, K.J. and Bork, J. (1989). Abschirmkabinen in medizinischer Diagnose und Halbleiter-Technologie. *ETZ*, **110** (16), 814–819.

Bison, G., Wynands, R., and Weis, A. (2003). A laser-pumped magnetometer for the mapping of human cardiomagnetic fields. *Appl. Phys. B*, **76**, 325–328.

Bork, J., Hahlbohm, H.-D., Klein, R., and Schnabel, A. (2001). The 8 layered magnetically shielded room of the PTB: Design and construction. In: Nenonen, J., Ilmoniemi, R.J., and Katila, T. (Eds.), *Biomag 2000: Proceedings of the 12th International Conference on Biomagnetism*, University of Technology, Helsinki, pp. 970–973.

Bradshaw, L.A., Ladipo, J.K., Staton, D.J., Wikswo, J.P., Jr., and Richards, W.O. (1999). The human vector magnetogastrogram and magnetoenterogram. *IEEE Transactions on Biomedical Engineering*, **46**, 959–970.

Brazdeikis, A., Taylor, A.A., Mahmarian, J.J., Xue, Y., and Chu, C.W. (2002). Comparison of magnetocardiograms acquired in unshielded clinical environment at rest, during and after exercise and in conjunction with myocardial perfusion imaging. In: Nowak, H., Haueisen, J., Giessler, F., and Huonker, R. (Eds.), *Biomag 2002: Proceedings of 13th International Conference on Biomagnetism*, VDE Verlag, Berlin, pp. 530–532.

Brisinda, D., Meloni, A.M., and Fenici, R. (2003). First 36-channel magnetocardiographic study of CAD patients in an unshielded laboratory for interventional and intensive cardiac care. *Lecture Notes in Computer Science*, **2674**, 122–131.

Buchanan, D.S., Crum, D.B., Crox, D., and Wikswo, Jr., J.P. (1989). Micro-SQUID: a close-space four channel magnetometer. In: Williamson, S.J., Hoke, M., Stroink, G., and Kotani, M. (Eds.), *Advances in Biomagnetism*, Plenum Press, New York, pp. 677–679.

Buckel, W. and Kleiner, R. (2004). *Superconductivity*. Wiley-VCH, Weinheim.

Burghoff, M., Trahms, L., Zhang, Y., Bousack, H., and Borgmann, M. (1996). Diagnostic application of high-temperature SQUIDs. *J. Clin. Eng.*, **21** (1), 62–66.

Burghoff, M., Steinhof, U., Haberkorn, W., and Koch, H. (1997) Comparability of Measurement Results Obtained with Multi-SQUID-Systems of Different Sensor Configurations. *IEEE Trans. Appl. Supercond.*, **7** (2), 3465–3468.

Burghoff, M., Schnabel, A., Drung, D., Thiel, F., Knappe-Grüneberg, S., Hartwig, S., Kosch, O., Trahms, L., and Koch, H. (2004). Discrimination of multiple sources using a SQUID vector

magnetometer. In: Halgren, E., Ahlfors, S., Hämäläinen, M., and Cohen, D. (Eds.), *BIOMAG 2004, Proceedings 14th International Conference on Biomagnetism*, Boston, pp. 99–100.

Cantor, R., Lee, L.P., Teepe, M., Vinetskiy, V., and Longo, J. (1995). Low-noise, single-layer $YBa_2Cu_3O_{7-x}$ DC SQUID magnetometers at 77 K. *IEEE Trans. Appl. Supercond.*, **AS-5**, 2927–2930.

Clarke, J. (1977). Superconducting Quantum Interference Devices for low frequency measurements. In: Schwartz, B.B. and Forner, S. (Eds.), *Superconductor Applications: SQUIDs and Machines*, Plenum Press, New York, pp. 67–124.

Clarke, J. and Braginski, A. (2004). *The SQUID Handbook: Fundamentals and Technology of SQUIDs and SQUID Systems*, Vol. 1, Wiley-VCH, Weinheim.

Cohen, D. (1967a). Magnetic fields around the torso: production by electrical activity of the human heart. *Science*, **156**, 652–654.

Cohen, D. (1967b). Shielded facilities for low-level magnetic measurements. *J. Appl. Phys.*, **38** (Suppl.), 1295–1296.

Cohen, D. (1968). Magnetoencephalography: Evidence of magnetic fields produced by alpha-rhythm currents. *Science*, **161**, 784–786.

Cohen, D. (1970). Large-volume conventional magnetic shields. *Revue de Physique Applique*, **5**, 53–58.

Cohen, D., Edelsack, E.A., and Zimmerman, J.E. (1970). Magnetocardiograms taken inside a shielded room with a superconducting point-contact magnetometer. *Appl. Phys. Letters*, **16**, 278–280.

Cohen, D., Schläpfer, U., Ahlfors, S., Hämäläinen, M., and Halgren, E. (2002). New Six-Layer Magnetically Shielded Room for MEG. In: Nowak, H., Haueisen, J., Giessler, F., and Huonker, R. (Eds.), *Biomag 2002: Proceedings of 13th International Conference on Biomagnetism*, VDE Verlag, Berlin, pp. 919–921.

Curio, G., Mackert, B.M., Burghoff, M., Kötitz, R., Drung, D., and Marx, P. (1995). Neuromagnetic correlates of evoked somatosensory activity travelling through the lumbosacral cauda equina and thoracic spinal cord in man. In: Baumgartner, C., Deecke, L., Stroink, G., and Williamson, S.J. (Eds.), *Biomagnetism: Fundamental Research and Clinical Applications*, Elsevier, IOS Press, Amsterdam, pp. 723–726.

Dantsker, E., Ludwig, F., Kleiner, R., Clarke, J., Teepe, M., Lee, L.P., McAlford, N., and Button, T. (1995). Addendum: low noise $YBa_2Cu_3O_{7-x}$-$SrTiO_3$-$YBa_2Cu_3O_{7-x}$ multilayers for improved superconducting magnetometers. *Appl. Phys. Lett.*, **67**, 725–726.

David, B., Grundler, D., Krey, S., Doormann, V., Eckart, R., Krumme, J.P., Rabe, G., and Dössel, O. (1996). High-Tc-SQUID magnetometers for biomagnetic measurements. *Supercond. Sci. Technol.*, **9**, A96–A99.

Dettmann, F., Richter, W., Albrecht, G., and Zahn, W. (1979). A monolithic thin film dc-SQUID. *Phys. Stat. Sol.*, **51** (a), 185–188.

de Waal, V.J. and Klapwijk, T.M. (1982). Compact integrated dc-SQUID gradiometer. *Appl. Phys. Lett.*, **41**, 669–671.

Dieckmann, V., Jürgens, R., Becker, W., Elias, H., Ludwig, W., and Vodel, W. (1996). RF-SQUID to DC-SQUID upgrade of a 28-channel magnetoencephalography (MEG) system. *Meas. Sci. Technol.*, **7**, 844–852.

Dilorio, M.S., Yang, K.Y., and Yoshizumi, S. (1995). Biomagnetic measurements using low-noise integrated SQUID magnetometers operating in liquid nitrogen. *Appl. Phys. Lett.*, **67** (13), 1926–1928.

Dössel, O., David, B., Fuchs, M., Krüger, J., Lüdeke, K.M., and Wischmann, H.A. (1993). A 31-channel SQUID system for biomagnetic imaging. *Appl. Superconductivity*, **1** (10–12), 1813–1825.

Drung, D. (1995). The PTB 83-SQUID system for biomagnetic applications in a clinic. *IEEE Trans. Appl. Supercond.*, **5** (2), 2112–2117.

Drung, D. (2002). High-performance DC SQUID read-out electronics. *Physica C*, **368**, 134–140.

Drung, D. (2003). High-T_c and low T_c dc-SQUID electronics. *Supercond. Sci. Technol.*, **16** (12), 1320–1336.

Drung, D. and Koch, H. (1993). An electronic second-order gradiometer for biomagnetic applications in clinical shielded rooms. *IEEE Trans. Appl. Supercond.*, **3**, 2594–2597.

Drung, D. and Koch, H. (1994). An integrated DC-SQUID magnetometer with variable additional positive feedback. *Supercond. Sci. Technol.*, **7**, 242–245.

Drung, D., Ludwig, F., Müller, W., Steinhoff, U., Trahms, L., Shen, Y.Q., Jensen, M.B., Vase, P., Holst, T., Freltoft, T., and Curio, G. (1996). Integrated Y $Ba_2Cu_3O_{7-x}$ magnetometer for biomagnetic measurements. *Appl. Phys. Lett.*, **68** (10), 1421–1423.

Erné, S.N., Pasquarelli, A., Kammrath, H., Della Penna, S., Torquati, K., Pizzella, V., Rossi, R., Granata, C., and Russo, M. (1999). ARGOS 55 – The New MCG System in Ulm. In: Yoshimoto, T., Kotani, M., Kuriki, S., Karibe, H., and Nakasato, N. (Eds.), *Recent Advances in Biomagnetism: Proceedings of the 11th International Conference on Biomagnetism*, Tohoku University Press, Sendai, pp. 27–30.

Fagaly, R.L. (1990). In: *Neuromagnetic Instrumentation*, Raven Press, New York, pp. 11–32.

Fagaly, R.L. (1999). SQUIDs: Instruments and Applications. In: Webster, J. (Ed.), *Encyclopedia of Electrical and Electronics Engineering*, volume 20, Wiley, New York, pp. 311–322.

Fife, A.A., Vrba, J., Robinson, S.E., Haid, G., Hoang, T., Kishi, D., Kubik, P.R., Lee, S., Loewen, R., McCubbin, J., McKay, J., McKenzie, D., Spear, P., Taylor, B., Tillotson, M., and Coppola, R. (2002). A 275 channel Whole-cortex MEG System. In: Nowak, H., Haueisen, J., Giessler, F., and Huonker, R. (Eds.), *Biomag 2002: Proceedings of 13th International Conference on Biomagnetism*, VDE Verlag, Berlin, pp. 912–914.

Foley, C.P., Keene, M.N., ter Brake H.J.M., and Vrba, J. (2004). In: Clarke, J. and Braginski, A. (Eds.), *The SQUID Handbook: Fundamentals and Technology of SQUIDs and SQUID Systems*, Vol. 1, Wiley-VCH, Weinheim, pp. 251–344.

Fuchs, M. and Dössel, O. (1992). On-line head position determination for MEG measurements. In: Hoke, M., Erné, S.N., Okada, Y.C., and Romani, G.L. (Eds.), *Advances in Biomagnetism '91*, Elsevier, Amsterdam, pp. 869–873.

Fuchs, M., Wagner, M., Wischmann, H.A., and Dössel, O. (1995). Cortical Current Imaging by Morphologically Constrained Reconstructions. In: Baumgartner, C., Deecke, L., Stroink, G., and Williamson, S.J. (Eds.), *Biomagnetism: Fundamental Research and Clinical Applications*, Elsevier Science, IOS Press, Amsterdam, pp. 320–325.

Fujimoto, S., Ogata, H., and Kado, S. (1993). Magnetic Noise produced by GM-Cryocoolers. *Cryocoolers*, **7**, 560–568.

Gerster, J., Kaiser, G., Reißig, L., Thürk, M., and Seidel, P. (1998). Low noise cold head of a four-valve pulse tube refrigerator. *Proceedings: Adv. Cryo. Eng.*, **43**, 2077–2084.

Gießler, F., Rissanen, A., and Malmivuo, J. (1993). A combined method for low-noise biomagnetic measurement systems. *Meas. Sci. Technol.*, **4**, 884–892.

Haberkorn, W. (1996). Biomagnetisches Vorwärtsproblem für zeitabhängige Quellen. *Biomedizinische Technik*, **41** (1), 288–289.

Hämäläinen, M., Hari, R., Ilmoniemi, R.J., Knuutila, J., and Lounasmaa O.V. (1993). Magnetoencephalography – theory, instrumentation, and applications to noninvasive studies of the working human brain. *Rev. Mod. Phys.*, **65** (2), 413–497.

Halgren, E., Ahlfors, S., Hämäläinen, M., and Cohen, D. (2004). *BIOMAG 2004, Proceedings 14th International Conference on Biomagnetism*, Boston.

Harakawa, K., Kajiwara, G., Kazami, K., Ogata, H., and Kado, H. (1996). Evaluation of High-Performance Magnetically Shielded Room for Biomagnetic Measurement. *IEEE Trans. Magn.*, **32** (6), 5252–5260.

Hilgenfeld, B., Strähmel, E., Nowak, H., and Haueisen, J. (2003). Active magnetic shielding for biomagnetic measurement using spatial gradient fields. *Phys. Meas.*, **24**, 661–669.

Hoenig, H.E., Daalmans, G., Folberth, W., Reichenberger, H., Schneider, S., and Seifert, H. (1989). Biomagnetic multichannel system with integrated SQUIDs and first-order gradiometers operating in a shielded room. *Cryogenics*, **29**, 809–813.

Hoenig, H.E., Daalmans, G.M., Bär, L., Bömmel, F., Paulus, A., Uhl, D., Weisse, H.J., Schneider, S., Seifert, H., Reichenberger, H., and Abraham-Fuchs, K. (1991). Multichannel DC SQUID sensor array for biomagnetic applications. *IEEE Trans. Appl. Supercond.*, **27** (2), 2777–2785.

Huonker, R., Nowak, H., Rzanny, R., and Rieke, K. (1996). Combined 3D-neuromagnetic source imaging and MRI-scans. In: Hashimoto, I., Okada, Y.C., and Ogawa, S. (Eds.), *Visualization of Information Processing in the Human Brain: Recent Advances in MEG and Functional MRI*, Elsevier Science, Amsterdam, *Electroenceph. Clin. Neurophysiol.*, **47** (Suppl.), 439–447.

Ilmoniemi, R.J., Hari, R., and Reinikainen, K. (1984). A four-channel SQUID magnetometer for brain research. *Electroenceph. Clin. Neurophysiol.*, **58**, 467–473.

Itozaki, H., Tanaka, S., Toyoda, H., Hirano, T., Haruta, Y., Nomura, M., Saijou, T., and Kado, H. (1996). A multi-channel high-Tc SQUID system and its application. *Supercond. Sci. Technol.*, **9**, A38–A41.

Jaycox, J.M. and Ketchen, M.B. (1981). Planar coupling scheme for ultra-low noise dc-SQUIDs. *IEEE Trans. Magn.*, **MAG-17** (1), 400–403.

Josephs, O., Fiaschi, K.A., Singh, K.D., and Swithenby, S.J. (1995). A Multichannel tangential-field gradiometer system. In: Baumgartner, C., Deecke, L., Stroink, G., and Williamson, S.J. (Eds.), *Biomagnetism: Fundamental Research and Clinical Applications*, Elsevier Science, IOS Press, Amsterdam, pp. 490–492.

Josephson, B.D. (1962). Possible new effects in superconductive tunneling. *Phys. Lett.*, **1**, 251–253.

Kajola, M., Ahlfors, S., Ehnholm, G.J., Hallström, J., Hämäläinen, M.S., Ilmoniemi, R.J., Kiviranta, M., Knuutila, J., Lounasmaa, O.V., Tesche, C.D., and Vilkman, V. (1989). A 24-channel magnetometer for brain research. In: Williamson, S.J., Hoke, M., Stroink, G., and Kotani, M. (Eds.), *Advances in Biomagnetism*, Plenum Press, New York, pp. 673–676.

Kandori, A., Miyashita, T., and Tsukada, K. (2000). Cancellation technique of external noise inside a magnetically shielded room used for biomagnetic measurements. *Rev. Sci. Instrum.*, **71** (5), 2184–2190.

Kelhä, O.V. (1981). Construction and performance of the Otaniemi magnetically shielded room. In: Erné, S.N., Hahlbohm, H.D., and Lübbig, H. (Eds.), *Biomagnetism*, Walter de Gruyter, Berlin, pp. 33–50.

Ketchen, M.B., Goubau, W.M., Clarke, J., and Donaldson, G.B. (1978). Superconducting thin-film gradiometer. *J. Appl. Phys.*, **49** (7), 4111–4116.

Kim, I.S., Yu, K.K., Lee, Y.H., Kim, K.W., and Park, Y.K. (2004). Performance of high-T_c dc SQUID magnetometers for use in a magnetically disturbed environment. *Phys. Stat. Sol. A*, **201** (8), 1969–1972.

Knuutila, J., Ahlfors, S., Ahonen, A., Hallström, J., Kajola, M., Lounasmaa, O.V., Vilkman, V., and Tesche, C. (1987). Large-area low-noise seven-channel dc SQUID magnetometer for brain research. *Rev. Sci. Instrum.*, **58**, 2145–2156.

Knuutila, J.E.T., Ahonen, A.I., Hämäläinen, M.S., Kajola, M.J., Laine, P.P., Lounasmaa, O.V., Parkkonen, L.T., Simola, J.T.A., and Tesche, C.D. (1993). A 122-channel whole-cortex SQUID system for measuring the brain's magnetic fields. *IEEE Trans. Magn.*, **29**, 3315–3320.

Kobayashi, K. and Uchikawa, Y. (2003). Development of a high spatial resolution SQUID magnetometer for biomagnetic research. *IEEE Trans. Magn.*, **39** (5), 3378–3380.

Koch, H., Cantor, R., Drung, D., Erné, S.N., Matthies, K.P., Peters, M., Ryhänen, T., Scheer, H. J., and Hahlbohm, H.D. (1991). A 37 channel dc SQUID magnetometer system. *IEEE Trans. Magn.*, **27** (2), 2793–2796.

Kyuhou, S. and Okada, Y.C. (1993). Detection of magnetic signals from isolated transverse CA1 hippocampal slice of the guinea pig. *J. Neurophysiol.*, **70**, 2665–2668.

Laine, P., Hämäläinen, M., and Ahonen, A. (1999). Combination of magnetometers and planar gradiometers in an MEG system. In: Yoshimoto, T., Kotani, M., Kuriki, S., Karibe, H., and Nakasato, N. (Eds.), *Recent Advances in Biomagnetism: Proceedings of the 11th International Conference on Biomagnetism*, Tohoku University Press, Sendai, pp. 47–50.

Leder, U., Pohl, H.P., Michaelsen, S., Fritschi, T., Huck, M., Eichhorn, J., Müller, S., and Nowak, H. (1998). Non-invasive biomagnetic imaging in coronary artery disease based on individual current density maps of the heart. *Int. J. Cardiol.*, **64**, 83–92.

Lee, S.G., Park, S.M., Kang, C.S., Yu, K.-K., Kim, I-S., and Park, Y.K. (2004). Fabrication

and magnetocardiography application of the second-order superconducting quantum interference device gradiometer made from a single-layer of $YBa_2Cu_3O_7$ film. *Appl. Phys. Lett.*, **84**, 568.

Mager, A. (1976). Large magnetic shields. *J. Magn. Magnetic Mater.*, **2**, 245–255.

Mager, A. (1981). A magnetically shielded room. In: Erné, S.N., Hahlbohm, H.D., and Lübbig, H. (Eds.), *Biomagnetism*, Walter de Gruyter, Berlin, pp. 51–78.

Matlashov, A., Zhuravlev, Y., Lipovich, A., Alexandrov, A., Mazaev, E., Slobodchikov, V., and Wazhiewski, O. (1989). Electronic noise suppression in multichannel neuromagnetic system. In: Williamson, S.J., Hoke, M., Stroink, G., and Kotani, M. (Eds.), *Advances in Biomagnetism*, Plenum Press, New York, pp. 725–728.

Matsuba, H., Shintomi, K., Yahara, A., Irisawa, D., Imai, K., Yoshida, H., and Seike, S. (1995). Superconducting shield enclosing a human body for biomagnetism measurement. In: Baumgartner, C., Deecke, L., Stroink, G., and Williamson, S.J. (Eds.), *Biomagnetism: Fundamental Research and Clinical Applications*, Elsevier Science, IOS Press, Amsterdam, pp. 483–489.

Matsuda, N., Takada, Y., Kazami, K., Uehara, G., and Kado, H. (1995). Design and fabrication of a multi-loop superconducting quantum interference device, a clover leaf SQUID. *Jpn. J. Appl. Phys.*, **34**, L27–L30.

Mizukami, A., Nishiura, H., Sakuta, K., and Kobayashi, T. (2003). High critical temperature SQUID magnetometer with feedforward active noise control system for magnetocardiographic measurement in unshielded environment. *Physica C*, **392–396**, 1411–1415.

Nenonen, J., Kajola, M., Simola, J., and Ahonen, A. (2004). Total information of multichannel MEG sensor arrays. In: Halgren, E., Ahlfors, S., Hämäläinen, M., and Cohen, D. (Eds.), *Biomag 2004: Proceedings of the 14th Int. Conf. on Biomagnetism*, Biomag 2004 Ltd., Boston, pp. 630–631.

Nowak, H. (1998). Biomagnetic Instrumentation. In: Andrä, W. and Nowak, H. (Eds.), *Magnetism in Medicine*, Wiley-VCH, Berlin, pp. 87–135.

Nowak H. and Huonker, R. (1996). Multikanalregistrierung für das Gehirnmagnetfeld. In: Ahlers, H. (Ed.), *Multisensorikpraxis*, Springer Verlag, Berlin, pp. 252–265.

Nowak, H., Gießler, F., and Huonker, R. (1991). Multichannel magnetography in unshielded environments. *Clin. Phys. Physiol. Meas.*, **12** (B), 5–11.

Nowak, H., Huonker, R., Gießler, F., Haueisen, J., Emmerich, E., and Eiselt, M. (1995). Messung kleinvolumiger Magnetfeldquellen. *Biomed. Techn.*, **40** (1), 359–360.

Nowak, H., Gießler, F., Eiselt, M., Huonker, R., Haueisen, J., and Röther, J. (1999). A16-channel SQUID Device for biomagnetic investigations of small objects. *Medical Engineering and Physics*, **21**, 563–568.

Nowak, H., Haueisen, J., Giessler, F., and Huonker, R. (2002). *Biomag 2002: Proceedings of 13th International Conference on Biomagnetism*, VDE Verlag, Berlin,

Nowak, H., Leder, U., Göring, M., Haueisen, J., Erné, S., and Trebeschi, A. (2003). Multichannel-vectormagnetocardiography: a new biomedical engineering approach. *Biomed. Techn.*, **44** (1), 368–369.

Ohta, H., Matsui, T., and Uchikawa, Y. (2004). Whole-head SQUID System in a Superconducting Magnetic Shield. In: Halgren, E., Ahlfors, S., Hämäläinen, M., and Cohen, D. (Eds.), *Biomag 2004: Proceedings of the 14th Int. Conf. on Biomagnetism*, Biomag 2004 Ltd., Boston, pp. 634–635.

Okada, Y.C. and Xu, C. (1996). Single-epoch neuromagnetic signals during epileptiform activities in guinea pig longitudinal CA3 slices. *Neurosci. Lett.*, **211**, 155–158.

Okada, Y.C., Kyuhou, S., Lähteenmäki, A., and Xu, C. (1992). A high-resolution system for magnetophysiology and its applications. In: Hoke, M., Erné, S.N., Okada, Y.C., and Romani, G.L. (Eds.), *Advances in Biomagnetism '91*, Elsevier, Amsterdam, pp. 375–383.

Okada, Y.C., Kyuhou, S., and Xu, C. (1993). *Tissue current associated with spreading depression inferred from magnetic field recordings*, Urban and Schwarzenberg, München, pp. 249–265.

Okada, Y.C., Papuashvili, N.S., and Xu, C. (1996). What can we learn from MEG studies of the somatosensory system of the swine? In: Hashimoto, I., Okada, Y.C., and Ogawa, S. (Eds.), Visualization of Information Processing in the Human Brain: Recent Advances in MEG and Functional MRI, Elsevier Science, Amsterdam, *Electroenceph. Clin. Neurophysiol.*, **47** (Suppl.), 35–46.

Okada, Y.C., Wu, J., and Kyuhou, S. (1997). Genesis of MEG signals in a mammalian CNS structure. *Electroenceph. Clin. Neurophysiol.*, **103**, 474–485.

Ono, Y., Ishiyama, A., Kasai, N., and Chinone, K. (2004). Development of biomagnetic measurement system for mice with high spatial resolution. *Appl. Phys. Lett.*, **85** (2), 332–334.

Overweg, J.A. and Walter-Peters, M.J. (1978). The design of a system of adjustable superconducting plates for balancing a gradiometer. *Cryogenics*, **189**, 529–534.

Parkkonen, L. and Mäkelä, J. (2002). MEG sees deep sources: Measuring and modelling brainstem auditory evoked fields. In: Nowak, H., Haueisen, J., Giessler, F., and Huonker, R. (Eds.), *Biomag 2002, Proc. 13th Int. Conf. on Biomagnetism*, VDE Verlag, Berlin, Offenbach, pp. 107–109.

Pasquarelli, A., De Melis, M., Marzetti, L., and Erné, S.N. (2004a). Calibration of a Vector-MEG Helmet System. In: Halgren, E., Ahlfors, S., Hämäläinen, M., and Cohen, D. (Eds.), *Biomag 2004: Proceedings of the 14th Int. Conf. on Biomagnetism*, Biomag 2004 Ltd., Boston, pp. 636–637.

Pasquarelli, A., Rossi, R., De Melis, M., Marzetti, L., Trebeschi, A., and Erné, S.N. (2004b). Argos 500: Operation of a Helmet Vector MEG. In: Halgren, E., Ahlfors, S., Hämäläinen, M., and Cohen, D. (Eds.), *Biomag 2004: Proceedings of the 14th International Conference on Biomagnetism*, Biomag 2004 Ltd., Boston, pp. 34–35.

Peiselt, K., Schmidl, F., Linzen, S., Anton, A.S., Hübner, U., and Seidel, P. (2003). High-Tc dc-SQUID gradiometers in flip-chip configuration. *Supercond. Sci. Technol.*, **16**, 1408–1412.

Pflieger, M.E., Simpson, G.V., Ahlfors, S.P., and Ilmoniemi, R.I. (2000). Super-additive information from simultaneous MEG/EEG data. In: Aine, C.J. Okada, Y.C., Stroink, G., Swithenby, S.J., and Wood, C.C. (Eds.), *Biomag 96: Proceedings of 10th International Conference on Biomagnetism*, Springer, New York, pp. 1154–1157.

Pihko, E., Lauronen, L., Wikström, H., Taulu, S., Nurminen, J., Kivitie-Kallio, S., et al. (2004). Somatosensory evoked potentials and magnetic fields elicited by tactile stimulation of the hand during active and quit sleep in newborns. *Clin. Neurophysiol.*, **115**, 448–455.

Platzek, D., Nowak, H., Gießler, F., Röther, J., and Eiselt, M. (1999). Active shielding to reduce low frequency disturbances in direct current near biomagnetic measurements. *Rev. Sci. Instrum.*, **70** (5), 2465–2470.

Resmer, F., Nowak, H., Gießler, F., and Haueisen, J. (2004). Development of an active magnetic screen to allow a biomagnetometer to be used in an unshielded environment. *Supercond. Sci. Technol.*, **17**, 1365–1371.

Robinson, S.E. (1989). Environmental noise cancellation for biomagnetic measurements. In: Williamson, S.J., Hoke, M., Stroink, G., and Kotani, M. (Eds.), *Advances in Biomagnetism*, Plenum Press, New York, pp. 721–724.

Robinson, S.E., Burbank, M.B., Fife, A.A., Haid, G., Kubik, P.R., Sekachev, I., Taylor, B., Tillotson, M., Vrba, J., Wong, G., Lowery, C., Eswaran, H., Wilson, D., Murphy, P., and Preißl, H. (2001). A biomagnetic instrumentation for human reproductive assessment. In: Nenonen, J., Ilmoniemi, R.J., and Katila, T. (Eds.), *Biomag 2000: Proceedings of the 12th International Conference on Biomagnetism*, University of Technology, Helsinki, pp. 919–922.

Safonov, Y.D., Provotorov, V.M., Lube, V.M., and Yakimenkov, L.J. (1967). Method of recording the magnetic field of the heart (magnetocardiography). *Bull. Exp. Biol. Med.*, **64** (7), 1022–1024.

Sata, K., Fujimoto, S., Fukui, N., Haraguchi, E., Kido, T., Nishiguchi, K., and Kang, Y.M. (1996). *Development of SQUID Based Systems Cooled by GM/JT Cryocoolers*, Elsevier Science, Oxford, pp. 1173–1176.

Schilling, M., Krey, S., and Scharnweber, R. (1996). Biomagnetic measurements with an integrated $YBa_2Cu_3O_7$ magnetometer in a hand-held cryostat. *Appl. Phys. Lett.*, **69** (18), 2749–2751.

Schnabel, A., Burghoff, M., Hartwig, S., Petsche, F., Steinhoff, U., Drung, D., and Koch, H. (2004). A Sensor Configuration for a 304 SQUID Vectot Magnetometer. In: Halgren, E., Ahlfors, S., Hämäläinen, M., and Cohen, D., *BIOMAG 2004, Proceedings 14th International Conference on Biomagnetism*, Boston, pp. 638–639.

Seidel, P., Weidl, R., Brabetz, S., Schmidl, F., Nowak, H., and Leder, U. (1998). Magnetocardiography with high-T-C gradiometers working in unshielded environments. *Appl. Supercond.*, (7–9), 309–316.

Seppä, H. (2001). Ultimate limitation of the SQUID magnetometer. In: Nenonen, J., Ilmoniemi, R.J., and Katila, T. (Eds.), *Biomag 2000: Proceedings of the 12th International Conference on Biomagnetism*, University of Technology, Helsinki, pp. 923–926.

Simola, J., Taulu, S., Parkkonen, L., and Kajola, M. (2004). Active shielding method for an MEG device. In: Halgren, E., Ahlfors, S., Hämäläinen, M., and Cohen, D., *BIOMAG 2004, Proceedings 14th International Conference on Biomagnetism*, Boston, p. 38.

Stolz, R., Zakosarenko, V., Bondarenko, N., Schulz, M., Fritzsch, L., Oukhanski, N., and Meyer, H.G. (2003). Integrated SQUID-gradiometer system for magneto-cardiography without magnetic shielding. *IEEE Trans. Appl. Supercond.*, **13** (2), 356–359.

Sullivan, D.B., Zimmerman, J.E., and Ives, J.T. (1981). Operation of a Practical SQUID Gradiometer in a Low-power Stirling Cryocooler. *NBS Special Publication*, **607**, 186–194.

Taulu, S., Kajola, M., and Simola, J. (2004). Suppression of interference and artifacts by the Signal Space Separation Method. *Brain Topography*, **16**, 269–275.

Taulu, S., Simola, J., and Kajola, M. (2005). Applications of the Signal Space Separation Method. *IEEE Transactions on Signal Processing*, **53** (9), 3359–3372.

Tavrin, Y., Zhang, Y., Wolf, W., and Braginski, A.I. (1994). A second-order SQUID gradiometer operating at 77 K. *Supercond. Sci. Technol.*, **7**, 265–268.

ter Brake, H.J.M., Fleuren, F.H., Ulfman, J.A., and Flokstra, J. (1986). Elimination of fluxtransformer crosstalk in multichannel SQUID magnetometers. *Cryogenics*, **26**, 667–670.

ter Brake, H.J.M., Dunajski, Z., Van der Mheen, W.A.G., and Flokstra, J. (1989). Electronic balancing of multichannel SQUID magnetometers. *J. Phys. E: Sci. Instr.*, **22**, 560–564.

ter Brake, H.J.M., Huonker, R., and Rogalla, H. (1993). New results in active noise compensation for magnetically shielded rooms. *Meas. Sci. Technol.*, **4**, 1370–1375.

ter Brake, H.J.M., Karunanithi, R., Holland, H.J., Flokstra, J., Veldhuis, D., Vargas, L., Hilgenkamp, J.W.M., Jaszczuk, W., Janssen, N., Roesthuis, F.J.G., and Rogalla, H. (1997). A seven channel high-Tc SQUID-based heart scanner. *Meas. Sci. Technol.*, **8**, 927–931.

Tsukamoto, A., Fukazawa, T., Takagi, K., Yokosawa, K., Suzuki, D., and Tsukada, K. (2001). Fabrication of highly balanced directly coupled $YBa_2Cu_3O_Y$ gradiometers and their noise properties in an unshielded environment. *Appl. Phys. Lett.*, **79**, 4405.

Uehara, G., Matsuda, N., Kazami, K., Takada, Y., Kado, H. (1993). Asymmetric bias injection technique for Drung-type superconducting quantum interference devices. *Jpn. J. Appl. Phys.*, **32**, L1735–L1738.

Uusitalo, M. and Ilmoniemi, R.J. (1997). Signal-space projection method for separating MEG and EEG into components. *Med. Biol. Eng. and Comput.*, **35**, 135–140.

van Nieuwenhuyzen, G.J. and de Waal, V.J. (1985). Second-order gradiometer and dc-SQUID integrated on a planar substrate. *Appl. Phys. Lett.*, **44** (4), 439–441.

Vodel, W. and Mäkiniemi, K. (1992). An ultra low noise dc-SQUID system for biomagnetic research. *Meas. Sci. Technol.*, **3**, 1155–1160.

Vrba, J. (2000). Multichannel SQUID biomagnetic systems. In: Weinstock, H. (Ed.), *Applications of Superconductivity, NATO ASI Series*, Kluwer Academic Publishers, Dordrecht-Boston-London, pp. 61–138.

Vrba, J. and Robinson, S.E. (2002). SQUID sensor array configurations. *Supercond. Sci. Techn.*, **15**, R51–R89.

Vrba, J., Fife, A.A., and Burbank, M.B. (1982). Spatial discrimination in SQUID gradiometers and third-order gradiometer performance. *Can. J. Phys.*, **60**, 1060–1073.

Vrba, J., Haid, G., Lee, S., Taylor, B., Fife, A.A., Kubik, P., McCubbin, J., and Burbank, M.B. (1991). Biomagnetometers for unshielded and well shielded environments. *Clin. Phys. Physiol. Mes.*, **12** (B), 81–86.

Vrba, J., Betts, K., Burbank, M.B., Cheung, T., Fife, A.A., Haid, G., Kubik, P.R., Lee, S., McCubbin, J., McKay, J., McKenzie, D., Spear, P., Taylor, B., Tillotson, M., Cheyne, D., and Weinberg, H. (1993). Whole cortex, 64 channel SQUID biomagnetic system. *IEEE Trans. Appl. Supercond.*, **3**, 1878–1882.

Vrba, J., Angus, V., Betts, K., Burbank, M.B., Cheung, T., Fife, A.A., Haid, G., Kubik, P.R., Lee, S., Ludwig, W., McCubbin, J., McKay, J., McKenzie, D., Robinson, S.E., Smith, M., Spear, P., Taylor, B., Tillotson, M., Cheyne, D., and Weinberg, H. (2000). 143-channel whole-cortex MEG system. In: Aine, C.J. Okada, Y.C., Stroink, G., Swithenby, S.J., and Wood, C.C. (Eds.), *Biomag 96: Proceedings of 10th International Conference on Biomagnetism*, Springer Verlag, New York, pp. 138–141.

Weidl, R., Brabetz, S., Schmidl, F., Klemm, F., Wunderlich, S., and Seidel, P. (1997). Heart monitoring with high-Tc dc SQUID gradiometers in an unshielded environment. *Supercond. Sci. Technol.*, **10**, 95–99.

Wikswo, Jr., J.P. (1988). High-resolution measurements of biomagnetic fields. *Advances in Cryogenic Engineering*, Plenum Press, New York, **33**, pp. 107–116.

Wikswo, J.P. (1995). SQUID magnetometers for biomagnetism and nondestructive testing: important questions and initial answer. *IEEE Trans. on Appl. Supercond.*, **5** (2), 74–120.

Wikswo, J.P. (2004). SQUIDs remain best tool for measuring brain's magnetic field. *Physics Today*, **57** (2), 15–17.

Wikswo, Jr., J.P., Malmivuo, J.A., Barry, W.H., Crawford, G.E., Fairbank, W.M., Giffard, R.P., Harrison, D.C., and Roy, R.H. (1975). Vector magnetocardiography – an improved technique for observation of electrical activity of the human heart. *Proc. San Diego Biomed. Symp.*, **14**, 359–367.

Wikswo, Jr., J.P., Friedman, R.N., Kilroy, A.W., van Egeraat, J.M., and Buchanan, D.S. (1989). Preliminary measurements with Micro-SQUID. In: Williamson, S.J., Hoke, M., Stroink, G., and Kotani, M. (Eds.), *Advances in Biomagnetism*, Plenum Press, New York, pp. 681–684.

Williamson, S.J. and Kaufman, L. (1981). Biomagnetism. *J. Magn. Magn. Mater.*, **22** (2), 129–202.

Williamson, S.J., Kaufman, L., and Brenner, D. (1977). Biomagnetism. In: Schwartz, B.B. and Forner, S. (Eds.), *Superconductor Applications: SQUIDs and Machines*, Plenum Press, New York, pp. 355–402.

Yoshida, Y., Arakawa, A., Kondo, Y., Kajihara, S., Tomita, S., Tomita, T., Takanashi, Y., and Matsuda, N. (2000). A 129-channel Vector Neuromagnetic Imaging System. In: Aine, C.J. Okada, Y.C., Stroink, G., Swithenby, S.J., and Wood, C.C. (Eds.), *Biomag 96: Proceedings of 10th International Conference on Biomagnetism*, Springer, New York, pp. 154–157.

Zhang, Y., Panaitov, G., Wang, S.G., Wolters, N., Otto, R., Schubert, J., Zander, W., Krause, H.-J., Soltner, H., Bousack, H., and Braginski, A.I. (2000). Second-order, high-temperature superconducting gradiometer for magneto-cardiography in unshielded environment, *Appl. Phys. Lett.*, **76**, 906.

Zimmerman, J.E. (1983). *Cryogenic*, Plenum Press, New York, pp. 43–67.

Zimmerman, J.E., Thiene, P., and Harding, J.T. (1970). Design and operation of stable rf-biased superconducting point-contact quantum devices, and a note on the properties of perfectly clean metal contacts. *J. Appl. Phys.*, **42**, 1572–1580.

2.3 Cardiomagnetism

Gerhard Stroink, Birgit Hailer, and Peter Van Leeuwen

2.3.1 Introduction

2.3.1.1 Historical Background

Cardiomagnetism refers to the detection, analysis and interpretation of the magnetic fields generated by the electrical activity of the heart. The peak value of the magnetic fields of the heart, measured near the chest, is more than a million times smaller than the Earth's magnetic field. Special techniques are required to measure such small fields, and a major technical breakthrough was made with the introduction, during the late 1960s, of the SQUID. This sensitive, superconducting magnetometer is now commonly used to detect cardiac magnetic fields. Further details regarding the different techniques required to measure these small biomagnetic fields are provided in Chapter 2.2.

The first magnetocardiograms (MCGs) measured with a SQUID were recorded by Cohen et al. in 1970 at MIT, inside a magnetically shielded room (Cohen et al., 1970). SQUID technology was also available at Helsinki University of Technology, and MCGs were routinely measured there during the 1970s (Saarinen et al., 1978). By placing the input coil of the SQUID at several locations over the chest area and comparing the magnetic field time traces with those of normal subjects, different pathologies could be detected. During the early 1980s, several research groups recorded MCGs by moving a single SQUID probe from point to point on a 7×8 grid in a plane parallel to the anterior torso. Utilizing the continuously recorded electrocardiogram (ECG), the MCG data were then analyzed to identify at each location the MCG signal strength at a particular time instance of the cardiac cycle. These MCG data points were then combined to produce a magnetic field map (MFM). By repeating this process for every time instant, sequential MFMs – typically 2 ms apart – were produced. The maps were then analyzed to characterize different patient groups (Nakaya et al., 1984; Stroink et al., 1985). Spatial features were also compared with those of electrocardiographic maps (body surface potential maps: BSPMs) of the same subject to determine the unique information content of

MFMs during the different cardiac time segments (Horacek and Stroink, 1981; Peters et al., 1983; MacAulay et al., 1985).

Obtaining MFMs was further simplified with the production of the first commercial multichannel systems with 37 SQUID channels that became available around 1990 (Schneider et al., 1990). State-of-the-art MCG instrumentation consists of about 60 to 150 SQUID sensors covering the whole anterior surface (see Section 2.2.7). Such systems are capable of measuring the MCG over the whole chest area, simultaneously, at the location of each SQUID channel. The fact that this method is truly noninvasive, and that no electrical leads are needed, ensures that detailed spatial-temporal information about the electrophysiology of the heart can be collected in a matter of minutes. The capacity of the multichannel system to measure many subjects over a short time period makes it ideal as a screening tool. A modern MCG system is shown in Figure 2.23. A more complete historical perspective of MCG measurements is provided by Stroink (1992) and Tavarozzi et al. (2002a).

In addition to the developments in instrumentation, recently developed mathematical techniques are now capable of combining the information from the MFMs with the detailed anatomical information as obtained, for instance, with magnetic resonance imaging (MRI), computed tomography (CT), or electron beam tomography (EBT). With such combinations of techniques it is possible to calculate, for example, the current distribution over the heart surface every 1 ms, and thus provide a dynamic picture of cardiac electrical activity during the heart cycle. This fusion of functional and anatomical information in order to visualize the cardiac activation sequence, noninvasively, greatly enhances the capabilities of the multichannel system as a research and clinical tool.

The first part of this section will describe, in general terms, the basic principles that determine the cardiac magnetic field patterns and how such patterns can be used to extract clinical information about heart function. In the second part, some of the clinical investigations in magnetocardiology, and how MCGs can assist in determining, for instance, risk factors for sudden cardiac death, will be summarized. Reviews on magnetocardiography have been produced by Siltanen (1989), Fenici et al. (1991), Nakaya and Mori (1992), and Tavarozzi et al. (2002b). Stroink et al. (1996) reviewed both magnetocardiographic and the closely related and complementary electrocardiographic body surface mapping. Some more fundamental aspects of cardiomagnetism can be found in the review by Hobbie (1997).

2.3.1.2 Electrophysiology

The rhythmic contractions of the human heart are triggered by the electrical activation of cardiac muscle cells. In the resting state, the cardiac cells are "polarized"; the interior of the cells has a negative potential relative to the exterior. In response to stimuli, ions move across the cell membrane, causing a rapid loss of the internal negative potential. After this short depolarization stage the cell repolarizes, restoring the internal potential of the cells to its original negative value. For cardiac cells

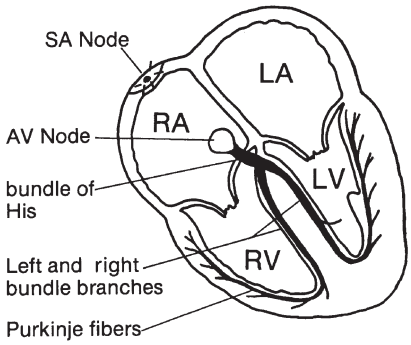

Fig. 2.31. Schematic representation of the heart, showing an activation wavefront that starts at the sinoatrial (SA) node in the right atrium (RA). After depolarizing the right and left atrium (LA), the wavefront propagates through the atrioventricular (AV) node, bundle of His, Left and Right bundle branches and Purkinje fibers to depolarize the left and right ventricles (LV and RV).

this repolarization stage lasts about 200–300 ms and prepares the cell for another excitation cycle. During the repolarization process the cells are refractory – that is, they are unable to respond to an additional stimulus.

The muscle cells of the heart form a *syncytium*; that is, they are so joined as to form a continuous medium enabling the electrical activity to spread from one cell to the next throughout the myocardium. In a normal, healthy heart this activation starts at the sinoatrial (SA) node, located in the upper part of the right atrium, and spreads over the atria (Fig. 2.31). After a short delay at the atrioventricular (AV) node, the wavefront propagates across the electrical insulating AV separation via the His Purkinje conduction system (consisting of the bundle of His, left and right bundle branches, and the Purkinje fibers), into the ventricles. During activation, a distinct, propagating boundary is formed between the already activated and the still-to-be-activated part of the myocardium. This depolarization wavefront is followed by the repolarization wavefront some time later. These wavefronts can be represented by many small current segments, more or less perpendicular to this wavefront (Fig. 2.32). These active current segments (primary currents) generate a passive current flow (volume currents) in the surrounding conductive thoracic tissues. Because of the resistivity of these tissues, voltage leads on the body surface will measure potential differences (Ohm's law) that can be recorded as the ECG. The magnetic fields generated by these primary and volume currents can be measured near the torso as MCGs.

The normal sequence of events described above, which serves to optimize cardiac output, can be disturbed in many ways. Different pathologies lead to a large variety of conduction abnormalities, represented by abnormal primary current distributions and volume currents, which show up as abnormal MCGs, ECGs, MFMs, and BSPMs. Some of these pathologies will be described in more detail in the second part of this section.

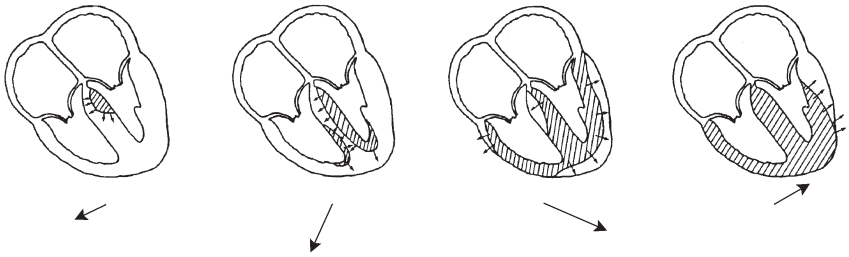

Fig. 2.32. A wavefront of depolarization (the boundary between shaded and nonshaded area) moving over the ventricles. This depolarization wavefront can be represented by a uniform dipole layer. The sum of all dipoles at a given moment results in the total current dipole vector, shown at the bottom of each frame. This equivalent dipole is part of a model that helps to visualize how this depolarization affects the potentials and magnetic fields observed on the torso.

2.3.2 Forward Solutions

2.3.2.1 Introduction

In the forward solution, the magnetic field or potential distributions at the body surface are calculated from the current distributions generated by the active cardiac muscle cells. These primary currents are directly related to the depolarization and repolarization processes within the myocardial cells. These processes vary to some extent from cell to cell throughout the myocardium, and will change dramatically when cells are damaged. The torso shape and the conductivities of the different torso compartments influence the volume currents flowing throughout the body in response to the primary currents. The accuracy with which the magnetic fields and potentials at the body surface are calculated depends on the approximations made in representing the cellular activities and the torso geometry. Thus, two models are required: (1) the source model, expressing cardiac activation in terms of current sources; and (2) a volume conductor model, defining the conductive medium in which the volume currents flow. Finally, it must be specified where the magnetic fields and potentials are to be measured in relation to the sources and the volume conductor, and which magnetic field component is desired. In what follows, some of the more common source and volume conductor models will be described. For more detail, the reviews of Stroink (1993) and Nenonen (1994), and the textbooks of Malmivuo and Plonsey (1995) or Gulrajani (1998), may be consulted.

2.3.2.2 Single Current Dipole in an Infinite Homogeneous Conductive Medium

As a first approximation, the active, distributed cardiac sources can be grouped into a single current dipole, representing the total ''vector of electrical activity'' or

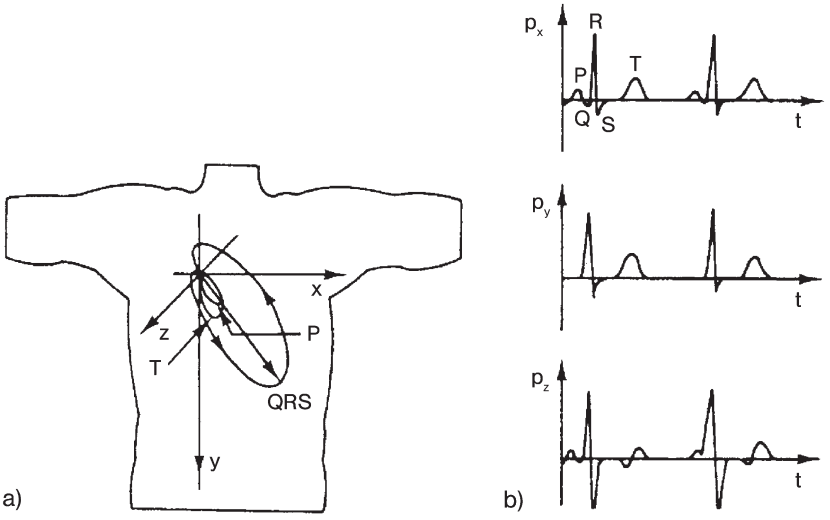

Fig. 2.33. (a) Locus of the total current dipole vector, **P**, during the cardiac cycle. (b) The x-, y-, z-components of the total dipole vector as a function of time resembling the ECG. (Adapted from Hobbie (1997), with permission.)

"heart vector" at a given moment. This total current dipole has been used extensively in vector cardiology to understand the relationship between cardiac function and the sign and magnitude of the different ECG complexes measured with the different ECG leads. It is clear that a single current dipole vector, **P**, which is the sum of the dipole moments of all cells active at the polarization wavefront, is an extremely simplified model of cardiac activity. Focusing on the current segments perpendicular to the action potential wavefronts, the direction and magnitude of **P**, can be estimated at any given moment. The way in which the depolarization wavefront moves over the ventricles is illustrated in Figure 2.32; below each frame is shown the total equivalent current dipole vector, **P**, for that moment. It is assumed that this macroscopic current dipole is located at the center of the heart. The direction and magnitude of this vector during the cardiac cycle for a normal heart is shown in Figure 2.33a. The x-axis points to the subject's left, the y-axis to the feet, and the z-axis from back to front. The small loop labeled P describes the trajectory of the equivalent current dipole during atrial depolarization; the loop QRS during ventricular depolarization. Ventricular repolarization is represented by loop T. The x-, y-, and z-components of this total dipole vector, **P**, are shown in Figure 2.33b.

It is this x-component that, to the first order, is represented by the ECG that measures the potential difference between the wrists. The magnetic field map (MFM) due to a current dipole pointing in the negative x-direction (shown as a thick arrow) located a distance, d, below and parallel to the displayed measuring plane,

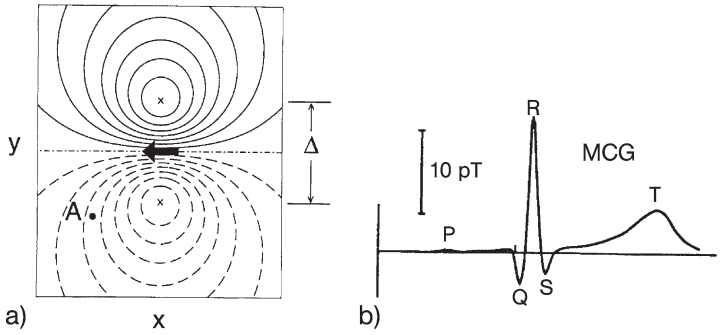

Fig. 2.34. (a) Magnetic field distribution of B_z in the x-y plane, due to a current dipole, **P** (heavy arrow), pointing in the negative x-direction, located a distance, *d*, below this plane. It is assumed that this dipole is located within an infinite or semi-infinite homogeneous conducting volume. Solid lines indicate that B_z is pointing into the plane; dotted lines that the field is pointing out of the plane. Δ is the distance between the extrema, whereas A is a point in the x-y measuring plane. (b) A magnetocardiogram (MCG) measured at A, when the current dipole, **P**, follows the locus of Fig. 2.33 (a) during a cardiac cycle.

is shown in Figure 2.34a. We first consider a dipole in an infinite conductive medium. The magnetic field due to the volume currents generated by a dipole in such a medium does not contribute to the magnetic field anywhere in space (Grynszpan and Geselowitz, 1973). Only the current dipole itself contributes to the measured magnetic field. The magnetic field of this dipole, acting like a current segment, in an infinite homogeneous medium is straightforward and is given by the Biot–Savart law. The magnetic field lines due to this current dipole follow circular paths in a plane perpendicular to the direction of this dipole. They intercept the measuring plane shown in Figure 2.34a such that the magnetic field lines emerge from the plane on one side of the dipole and point into this x-y plane at the other side. Their direction is determined by the right-hand rule. Also shown in the figure is the distribution of the magnitude of the magnetic field component B_z, in the plane. By convention, the magnetic field component pointing into the measuring plane is positive.

For B_z, the dipole's volume current contribution to the magnetic field is also zero for a semi-infinite conductor, as was verified experimentally by Cohen and Hosaka (1976) using a tank model. This semi-infinite volume conductor bounded by an insulator, such as air, is the simplest description resembling the torso geometry. The magnetic field map of B_z on this boundary plane due to the current dipole is identical to such a map if the plane were located in an infinite homogeneous volume. This simplifies visualizing B_z-maps. Alternatively, given such a magnetic field map (Fig. 2.34a), it is possible to determine all relevant information about this parallel dipole. The direction of the dipole is given by the direction of the zero-field line and the right-hand rule; the depth, *d*, of the dipole underneath the measuring plane is related to the distance between the extrema, Δ, according to: $d = \Delta/\sqrt{2}$.

To obtain a sense of the general features of the time trace of the cardiac magnetic field (the MCG) at a point A in the measuring plane, we can combine the field pattern described above with the position and magnitude of the equivalent current dipole in the x-y plane, as shown by the different loops in Figure 2.33a. When the equivalent current dipole, representing cardiac activity, rotates and changes in magnitude during the heart cycle, so will the MFM in the plane above it, and consequently, so will the magnetic field at point A in Figure 2.34a. A typical MCG is shown in Figure 2.34b; this shows features similar to the ECG (Fig. 2.33b), including a P wave due to atrial depolarization, a R wave during the QRS interval, resulting from ventricular depolarization, and the T wave due to the ventricular repolarization. The polarity and magnitude of the different complexes depend on where in the x-y plane the measurement is obtained.

Some general observations can be made which help in the interpretation of MFMs of the B_z component. These observations apply only for the unrealistic cardiac model of a single current dipole in an infinite or semi-infinite homogeneous conductive medium.

- No magnetic field is measured when the current dipole vector is perpendicular to the measuring plane. That is, only the component of the current dipole vector parallel to the measuring plane (the x-y plane) produces a magnetic field B_z.
- It follows that the magnitude of the extrema is directly proportional to the component of the current dipole vector parallel to the measuring plane, and that
- The resulting magnetic field map (MFM) is symmetric along the zero field contour line and has a dipolar character.
- No magnetic field is measured directly above the origin of the current dipole vector.
- The zero field contour line and the sign of the extrema determine the direction of the current dipole.
- The distance between the extrema determine the distance, d, of the dipole below the measuring plane.

These properties can be used as guidelines to interpret B_z-maps measured near the torso of subjects. They provide an estimate of the location and the strength of the heart vector component in the x-y plane during the heart cycle. Any deviation of the normal behavior of the heart vector during the heart cycle will result in abnormal magnetic field maps.

2.3.2.3 Current Dipole in a Realistic Torso

Inhomogeneities in the volume conductor, the body, surrounding the current dipole will influence the current flow and consequently the measured voltages and magnetic fields. The most important influence is the irregularly shaped outer boundary of the torso where the conductivity drops to zero. To model the effect of torso inhomogeneities on the magnetic fields of a current dipole, the dipole is

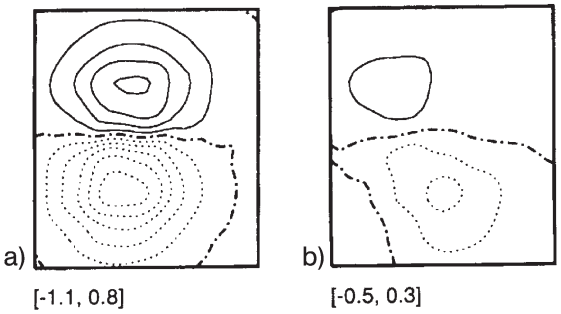

Fig. 2.35. The calculated magnetic field distribution B_z due to a current dipole in a realistic torso volume pointing in the negative x-direction (a) and the z-direction (b). The dipole is located at the interventricular septum. The dipole has a strength of 1 μAm; the torso has different conductivities for the blood-masses in the heart, the torso, and lungs. Conductivity outside the torso is zero. The numbers below the map give the extrema in pT. The measuring plane is near and parallel to the anterior torso, covering an area of 28 × 24 cm.

placed in a geometrically well-defined and accurate myocardium filled with blood and surrounded by lungs, all embedded in a simplified but realistically shaped torso. Each compartment has its characteristic uniform conductivity. The effect of the different regions with the different conductivities is taken into account by introducing secondary current sources, which are distributed over the interface between the regions. The magnetic field at a point near the torso is then the superposition of the magnetic field of the primary current source, representing cardiac activity, and the magnetic field of all the secondary current sources at the interfaces. No analytical method exists to calculate the magnetic field near such a piecewise homogeneous torso model. Numerical techniques, such as the Boundary Element Method (BEM) (Horacek, 1973; Peters et al., 1983; Purcell et al., 1988; Van Oosterom et al., 1990; Ferguson and Stroink, 1997) or the Finite Element Method (FEM) (Czapski et al., 1996), are required. Over the years, considerable efforts have been made by many research groups to enhance the accuracy and speed of such calculations (Gulrajani, 1998). Figure 2.35 shows the MFM calculated with the BEM for a realistic torso model with a current source located at the septum between the ventricles. This is approximately where the Q wave is generated. The maps demonstrate the effect of the torso boundary on B_z with the dipole oriented in the negative x-direction (Fig. 2.35a) and in the z-direction (Fig. 2.35b). In a realistic torso, the z-directed dipole shows a relatively small – but measurable – magnetic field, whereas in the semi-infinite volume conductor it does not have a magnetic field, B_z, in the measuring plane, as indicated previously.

Detailed studies with such torso models show that the influence of the volume conductor on the MFM is smallest when the dipole is laying in the x-y plane, that is parallel to the measuring plane, and is located near the anterior surface. MFMs of dipoles pointing perpendicular to the measuring plane (in the z-direction) are to a large extent determined by the details of the torso geometries. Of the three mag-

netic components, the B_z component of the magnetic field is the least effected by torso geometries (Hosaka et al., 1976; Purcell et al., 1988) and therefore reflects most directly the cardiac activity. It is the component most often measured in magnetocardiology. As with the ECG, the most accurate forward solutions are obtained using individualized torso models based on MRI or CT scans of a given subject (Van Oosterom and Huiskamp, 1992). However, most of the effects of different torso geometry on the observed maps features can be taken into account by using scaling factors applied to a standard torso (Nenonen et al., 1991a; Tan et al., 1992; Czapski et al., 1996).

2.3.2.4 Extended Source Models

Several earlier models related the surface ECG and MCG directly to the action potentials at the heart surface. Horacek (1973) simulated the normal MCG by using about 1800 current dipoles of time-varying orientation and amplitudes. These dipoles were located at the epicardial surface and activated in sequence according to experimentally measured activation sequences from isolated human hearts (Durrer et al., 1970). In the Miller–Geselowitz model, the heart consisted of 4000 time-varying dipole sources (Miller and Geselowitz, 1978) which were grouped together to provide a multiple dipole model of the heart. For the myocardium, these authors used the bidomain model in which the heart muscle is simplified by assuming that it consisted of two uniform regions, the intracellular space and the space between the cells, the interstitial space. Each domain was a passive conductor separated by the cell membrane, while each region had its own conductivity properties. The early forward model by Horacek, as well as the Miller–Geselowitz and Cuffin–Selvester models (Hosaka et al., 1976), all used a realistic outer torso. The results obtained were in fairly good agreement with actual measured ECGs and MCGs for normal ventricular activation and repolarization and for myocardial infarctions; a major achievement at that time. They also provided the mathematical tools for more elaborate models, directly based on action potentials at the cellular level. Van Oosterom and Huiskamp (1992) used the classical uniform double-layer model of cardiac activation to simulate ventricular depolarization. In this source model, the activation wavefront consisted of a surface of uniform current dipole density at the depolarization wavefront. Its location in time could be calculated from measured body surface potentials. Again, the calculated MCG during the QRS resemble measured the MCGs on the torso surface. This model was based on ECG subject data and since it appeared that ECG data could be used to predict the general features of MCG signals, it was suggested that MCG data did not contain substantial new information that could be obtained from the ECG (Van Oosterom et al., 1990). The development of magnetocardiology during the 1980s and early 1990s was hampered because the earlier theoretically models could not provide a clear answer to the uniqueness of the data content in MCG, not obtainable from ECG data. However, the above models ignored anisotropic electrical conductivity. Roth and Wikswo (1986), as well as Barach and Wikswo (1994), used the ani-

sotropic bidomain model to predict magnetic field patterns from source configurations that are electrically silent but produce characteristic magnetic fields. Such configurations drew considerable attention because they exemplify the unique information content of the MCG. The swirl in the muscle structure near the apex of the heart and the associated circular conductivity pattern is considered an example of a location where magnetic fields are emphasized. Murdick and Roth (2004) showed that models that do not include anisotropy can make incorrect predictions. Magnetic field patterns predicted by models that take into account the anisotropic conductivity in the intra- and extracellular spaces, have been measured with submillimeter resolution using a MicroSQUID (Staton et al., 1993; Fong et al., 2004).

To include anisotropic conduction, Hren et al. (1995) constructed a detailed model of the normal heart by filling an anatomically accurate myocardium with a cubic lattice of 0.125 mm^3 cells, each with a principal fiber direction assigned to it. The propagation of electrical excitation within this ventricular myocardium with anisotropic conductivity is based on realistic action potentials assigned to each cell. The next cell is activated when the transmembrane potential exceeds the threshold value. Conductivity along the fibers is about nine times larger than conductivity perpendicular to the fibers. At a later stage, a realistic ventricular conduction system was added (Simelius et al., 2001). This sophisticated heart model, when placed in a realistic torso, is used to calculate the magnetic field and potential maps at the torso surface when the endocardium or epicardium is stimulated at a particular location (Hren, 1996). Similarly, the model predicts the BSPM and MFM at the onset of ectopic beats or ventricular tachycardias (VT). Such potential and magnetic field maps are often unique for each site of onset of cardiac activity, and consequently map features can assist in locating this onset site. This site can then be ablated to inhibit the onset of potentially lethal arrhythmias. The calculated potential maps agree with those measured following endocardial pacing (Sippens-Groenewegen et al., 1993), thus validating this detailed model of cardiac activation. To date, few such pacing MFM, which could validate the magnetic maps predicted by this model, have been recorded (Fenici and Melillo, 1993; Moshage et al., 1996) (see also Section 2.3.9).

This detailed model was also used to calculate the potential and magnetic field maps that can be observed in patients with Wolff–Parkinson–White (WPW) syndrome. These patients have an accessory conductive pathway between the atria and the ventricles that allows the atrial activation to enter the ventricle somewhere along the AV ring, bypassing the AV node and therefore the normal conduction system. This extra pathway, together with the normal conduction system, results in a circuitous path that can cause arrhythmias, which may in turn lead to ventricular fibrillation and sudden cardiac death. Failing treatment with medication, this extra pathway can be ablated using a catheter under fluoroscopic guidance (this is discussed in more detail in the clinical studies using MFMs of WPW patients; see Section 2.3.9.2).

When this accessory pathway activates the ventricles prematurely, a BSPM and MFM characteristic for its location along the AV ring is observed near the end of the PR interval. Using computer models, Nenonen et al. (1991b) and Hren et al.

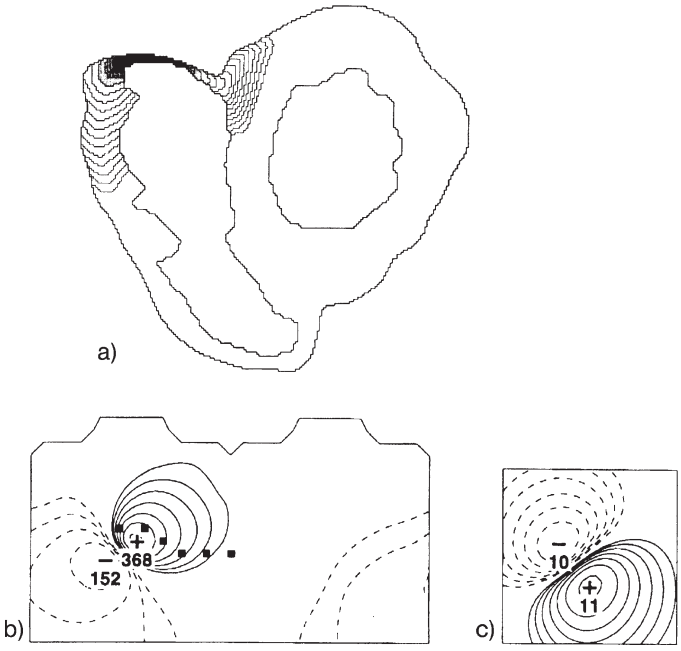

Fig. 2.36. (a) Isochromes of the simulated activation sequence started at a right posterior site on the atrioventricular ring. Isochrones are displayed at 2-ms intervals. (b) The potential map (V) at the body surface calculated at 20 ms after the onset of the activation sequence initiated at the right posterior preexcitation site (shown in (a)). The top border of the potential map represents the neck and shoulders, and the lower border the waist; the anterior chest is depicted on the left half of the map, with the left midaxillary line at the centre of the map. Precordial leads V1 through V6 are shown as black squares. The extrema are given in mV. (c) The magnetic map at the same time instance as (b). The map represents an area of 28 × 28 cm covering the anterior surface; the extrema are given in pT. (After Hren et al., 1998a).

(1998a,b) calculated both the magnetic and potential maps every 2 ms after onset of this abnormal ventricular pre-excitation at many sites. MFMs were calculated for 35 pre-excitation sites located along the AV ring. Example of such maps are shown in Figure 2.36. Overall, the maps agree well with those measured for the same pre-excitation sites in patients, thus validating this realistic model for this application. Some discrepancy can be explained by volume conductor effects and/or inconsistencies among maps reported by several authors for the same pre-excitation site. The calculated maps are useful in a clinical setting as they provide an "atlas" of MFMs, each characteristic for a particular location for the accessory pathway. As such, they assist the clinician in noninvasively locating the pre-excitation site before starting the otherwise lengthy ablation procedure. The MFM pattern recognition technique to locate accessory pathways and the accuracy that can be achieved has been discussed in detail by Hren et al. (1998a, 2001).

2.3.2.5
Summary

State-of-the-art simulations of body surface magnetic or potential maps (MFMs and BSPMs) are based on models of cardiac activation that use anisotropic propagation and modifiable action potentials assigned to cellular units of sub-millimeter resolution. These models, together with realistic torso models, are mathematically complex but have reached a stage where the calculated maps generated during the heart cycle closely resemble the measured magnetic and potential body surface maps of normal subjects. Such models are extremely useful for our understanding of the normal activation processes and to interpret measured maps that result from an abnormal activation sequence in an otherwise normal heart, such as that observed in endocardial pacing and in patients with WPW syndrome. Several models have also attempted to simulate magnetic maps for the ischemic and infarcted heart (e.g., Killmann et al., 1995). Although these maps mimic general features observed in the measured maps, it is more difficult to validate these models for more complex medical conditions.

2.3.3
Inverse Solutions

2.3.3.1
Introduction

In an inverse solution, the information contained in MFMs can be used to determine, mathematically, the location and strength of the electrophysiological sources that generate the map. The process involves calculating repeatedly, with the forward solution, the MFM for a particular source and volume model for the sensor configuration used in the measurements. This calculated map is then compared with the map measured. Source parameters (location, direction and magnitude) are readjusted in a systematic manner so that the best fit between observed and calculated maps is obtained. An inverse solution is not unique; that is, many different source combinations can result in the same observed MFM. Consequently, assumptions must be made about the nature and extent of the sources as well as the volume conductor to arrive at a well-defined, sensible inverse solution. These assumptions are based on our knowledge of the underlying physiology. As a first approximation, the cardiac activity can be represented by a single-current dipole embedded in an infinite or semi-infinite homogeneous conductive medium. The resulting equivalent current dipole (ECD) inverse solution can be considered a first-order estimate of the source parameters. This source model is adequate when estimating, for instance, the location of the initial activation of the ventricle via an accessory pathway in patients with WPW syndrome, or the onset of an ectopic beat originating from an arrhythmogenic region of the heart in patients suffering from periods of sustained ventricular tachycardia. However, for many cardiac patholo-

gies such a single-current dipole is inadequate to describe the often complicated underlying electrophysiological processes. More sophisticated source models assume that the electrical activity of the heart can be represented by a multipole series, a moving dipole, multiple dipoles, or multiple moving dipoles, including that of a dipole layer representing the action potential wavefront. With each of these source models several torso approximations can be used, for example a semi-infinite medium, a spherical homogeneous torso, or a realistically shaped torso with internal inhomogeneities representing the lungs and intraventricular blood masses, as discussed earlier. As a general rule the inverse solutions become more accurate, but also more unstable with increasing complexity of the source and volume models. Mathematical safeguards must be incorporated to ensure that the inverse solution converts to a single solution. When providing inverse solution results, some measure of confidence in that particular solution should be presented.

In a more advanced application of the inverse solution, one can solve for the potentials on the epicardial surface. This type of inverse solution was originally introduced by Barr and Spach (1978) and pursued in different form and presentation by different, mainly BSPM, research groups (e.g., Cuppen and Van Oosterom, 1984; Horacek and Clements, 1997; Oster and Rudy, 1997; Hren and Stroink, 2001). The advantage of this presentation is that the spread of the epicardial and endocardial action potential wavefronts can be measured directly during open-heart surgery or in animal models, and the inverse solution so validated. An accurate display of the propagation of the wavefront in time over the cardiac surfaces, obtained noninvasively, would be a powerful diagnostic tool in assessing cardiac function. Areas of abnormal conduction can then be identified. For example, determining noninvasively the location, size and electrical properties of the infarcted and surrounding ischemic region would be clinically extremely useful.

There is a large body of literature available on the techniques involved in the inverse problem. From a mathematical point of view, there are many similarities with such techniques applied to functional brain imaging based on EEG and MEG data (see Section 2.4). Although many of the basic concepts as it applies to MCG have been developed in the inverse solution for body surface potential maps (Oster and Rudy, 1997; Gulrajani, 1998), inverse solutions for cardiac MFMs contain special challenges and solutions. MFM inverse solutions techniques have been reviewed by Nenonen and Katila (1991), Nenonen (1994) and Stroink et al. (1996). Some recent advances in MFM source localization and imaging are described in more detail in the following section.

2.3.3.2 Model Data Using the Current Dipole as Source Model

Before using an inverse solution on patient data, inverse solutions must be validated with simulated data. For simulated "data", the MFMs are calculated from the forward solutions discussed earlier. In such an approach, all the source parameters are known and the effects of instrumentation noise, source and volume con-

ductor models as well as measuring parameters on the accuracy and stability of the inverse solution can be investigated.

Oostendorp and Van Oosterom (1989), Purcell et al. (1987) and Purcell and Stroink (1991) have all described an elegant inverse solution method using a current dipole in a realistically shaped homogeneous torso using the Boundary Element Method (BEM) (Ferguson and Stroink, 1997). This ''fast forward solution'' is now commonly used as part of any inverse solution. Using this BEM, Hren et al. (1996) calculated the MFMs due to a single-current dipole, located at many different locations in the realistic heart mass. Ten of these locations were distributed over the AV ring and mimic the accessory pathways found in patients suffering from WPW syndrome. The B_z values were calculated at 56 locations in a plane near the anterior surface covering the area typically measured with large multichannel systems. Moreover, to mimic realistic data, Gaussian noise of up to 10% of the peak values of the magnetic fields was added. Next, the inverse solution was applied to this realistic model data, using a variety of volume conductors.

It was found that substantial improvements in the accuracy of localization of the current dipole are achieved by using realistic torsos, as opposed to the infinite or semi-infinite homogeneous volume conductor. For deep sources, the average localization errors are over 2 cm for the infinite homogeneous torso, but less than 1 cm for the realistic torso model. Further improvements can be achieved by including the lungs and blood masses in the torso model. With this detailed model, on average the localization error is about 0.5 cm when the current dipole is oriented parallel to the measuring plane (in the x-y-plane) and located near the anterior surface. This is comparable to what can be achieved under identical circumstances when body surface potential data are used. The localization error is, on average, somewhat larger when using magnetic fields of z- (anterior-posterior) directed dipoles. This reflects the sensitivity of this component to details of the volume conductor model, as was pointed out earlier. Pesola et al. (2000) performed a systematic study on the many variations in the torso models that could influence the localization accuracy. The results of this study provided a detailed guide of the magnitude of the localization errors that could be expected when the geometry and topology of the torso compartments used in the BEM are not accurately known.

One weakness in these validation studies is that the forward as well as the inverse solution uses the same, rather simple source model – that of a current dipole. In a more realistic approach, it is possible to use as a source model in the forward solution the extensive computer model of the human ventricular myocardium described earlier (Leon and Horácek, 1991; Hren et al., 1998a). This features an anatomically accurate heart geometry, an intramural anisotropic structure, and an excitation process based on the interactions among the 1.7 million cells. This source model is situated in a realistic torso model and, as described earlier, was used to calculate the onset of ventricular activation near each of 35 accessory pathways that bridge the AV ring. By using this detailed cardiac model to calculate the ''data'' and the single-current dipole within a realistic torso in the inverse solution, the accuracy in locating the accessory pathway was found to vary for both magnetic

and potential maps when moving around the AV ring (Hren et al., 1998b). Assuming that the electrical properties of the volume conductor as well as the lead positions are known precisely, and no noise is present, the results show that MFM can locate the onset of pre-excitation, on average, with an accuracy of 0.7 ± 0.3 cm. Given these ideal circumstances this result is probably the best that can be expected for any inverse solution applied to real data. Starting with potential maps based on the same detailed cardiac model provides similar accuracies under these optimal conditions.

The model calculations suggest that if the cardiac event can be modeled with some confidence as a current dipole (such as the onset of arrhythmias) and realistic torso geometry and measuring conditions are used, then such an event can be located accurately. The uncertainty in determining the location with an inverse solution will be larger if poor signal-to-noise levels and uncertainties in the torso geometries and probe positions also need to be considered. The accuracy of 1 cm typically obtained in these model calculations is considered adequate for most clinical purposes, it being of sufficient accuracy to plan and thereby shorten ablation procedures.

2.3.3.3
Model Data Using Distributed Sources as Source Model: Imaging

Only when electrical activation is confined to a small area, such as during the onset of atrial and ventricular activity and for particular pathologies, is the current dipole source model a realistic representation of cardiac activation. In order to visualize, through an inverse solution, specific epicardial activity from BSPM or MCG data over a longer time interval, more complex source models are required (Shahidi et al., 1994; Oster et al., 1997). One particularly useful source model is the uniform double layer (UDL), which describes the activity of the heart during ventricular depolarization by the activation times at the ventricular epicardial and endocardial surfaces (Van Oosterom and Huiskamp, 1992). The strength of describing the inverse problem in terms of ventricular depolarization times is that this approach implicitly poses time constraints on the permissible solutions. These constraints, when based on reasonable physiological conditions, stabilize and enhance the accuracy of the inverse solution. Determining the time sequences as a goal in the inverse solution is less demanding for the inverse solution than calculating local values of the potential at the epicardium. Such time sequences provide an extremely valuable tool in assessing conduction abnormalities. Oostendorp et al. (1996) and Oostendorp and Pesola (2001) used this model to calculate from ECG and MCG data on the body surface, the activation sequence on the epicardial surface of the heart.

Cardiac activation can also be represented by a large number of current dipoles distributed over and constrained to lie on the cardiac surfaces. The task is then to determine which current dipoles must be active at a given moment to generate the observed magnetic field map on the body surface. This current density estimation (CDE) provides a powerful image of cardiac activity at a given moment, or as a se-

quence of cardiac activity when a time sequence of MFMs is so analyzed. The system of equations that connects the large amount of unknown current dipoles on the epicardium with the many measuring points on the body surface is underdetermined and has no unique solution, so that additional constraints are needed. New developments in mathematical techniques have improved such inverse solutions. In one class of solutions it is assumed that the total length of the vector that represents the best-fitting dipoles is minimized. This solution is termed the minimum norm estimate (MNE) (see e.g., Nenonen, 1994). Additional knowledge about the strength and location of the dipoles, based on physiology, as well as ''preconditioning'' the matrix involved in the calculations help to stabilize the solution, particularly for deep sources and noisy data (Ferguson and Stroink, 1995; Pesola and Nenonen, 2001).

The minimum norm method for MFMs has been explored for a variety of cardiac conditions (e.g., Killmann et al., 1995; Pesola et al., 1997; Leder et al., 1998). Pesola et al. (1997) used real MCG data, generated by placing a nonmagnetic catheter in the heart, to assess different regularization techniques to calculate the location of the catheter tip with MNE. Based on this assessment, these authors then calculated CDE maps on the epicardial surface for both simulation data and MFM data of patients with coronary artery disease (CAD) (Pesola et al., 1999a). CDE was found (potentially) to be a good method for localizing both myocardial ischemia in single-vessel CAD patients, as well as more complex chronic ischemia in three-vessel CAD patients. Leder et al. (1998) calculated CDE in two myocardial infarction (MI) patients and two healthy subjects. Low current densities were found for the MI patients in regions that corresponded to infarcted segments. The successes described above suggest that the minimum norm can provide a powerful method to image current densities and consequently cardiac activity on the epicardium.

In addition to high-quality MCG data, the imaging techniques described above require a detailed knowledge of the torso boundaries as well as the location of the epicardial surface and of the sensors in relation to the torso and heart. CAT and MRI are most commonly used to obtain such detailed anatomical information. Special care is required to link these anatomical imaging techniques with the MCG measurements (Dössel et al., 1995) so that the results of the inverse solution can be accurately superimposed on, for example, the image of the epicardial surface. The resulting fusion of functional information from the inverse solution with anatomical information provides a comprehensive picture to visualize cardiac activity, as will be shown in the clinical part of this section (see Section 2.3.9).

2.3.3.4 Summary

The localization of particular pathologies responsible for arrhythmias with a single-current dipole as source and the visualization of more extensive cardiac electrical activity with current density images or activation maps promise to be useful tools in the clinical environment. Requirements for success include the availability of powerful mathematical techniques that can be validated on model and patient

data. Much effort has been applied to both MFM and BSPM research fields focused on obtaining the necessary mathematical tools for cardiac imaging. Fortunately, the trend is clearly moving towards developing user-friendly software packages that translate MFMs into reliable, myocardial activation images containing diagnostically useful information.

Also needed are multichannel systems that can sample, within a very short time period, a large area near the torso. This is essential when mapping single or arrhythmic cardiac events, or when studying large patient groups. Finally, for accurate inverse solutions a detailed knowledge of the outer torso surface, the cardiac surfaces and, to a lesser degree, the boundaries of other major inner body compartments is needed. The technology needed to obtain this information, together with computer programs to apply the information to inverse solutions, is presently commercially available.

2.3.4 Validation

Model data obtained from a forward solution can validate the often complex inverse solution algorithms. In order to mimic measurements, noise and positioning errors are added. Although extremely useful and essential for the initial testing, theoretical studies can only test the theoretical limitations of inverse modeling. Inverse solutions also need to be validated with actual measurements on phantom models and subjects. Phantom studies involve detailed and accurate measurements on well-defined sources with characteristics that are fully understood. Validation on subjects is extremely important to demonstrate possible applications and the limits of the inverse approach under clinical conditions.

Some results on the localization accuracy of a single-current dipole in a plastic phantom model of the thorax containing a conductive solution have been reported. For example, Pesola et al. (1999b) used such a phantom model and digital torso representation to test the accuracy of locating artificial dipole sources immerged in this torso tank. Localization errors between 3 and 10 mm could be achieved, depending on the depth of the sources and the signal-to-noise ratio. In the analysis of these data, inaccuracies in positioning the dipole in the phantom model, as well as the accuracy in representing the digitized torso and the many ways in which the BEM can be applied, have also to be considered. Such phantom and similar tank studies confirm the localization accuracies obtained from purely theoretical model studies, as described in Section 2.3.3.2.

Both, Fenici et al. (1991) and Moshage et al. (1992) developed nonmagnetic catheters for phantom and patient studies. In a recent study, Fenici et al. (2003a) evaluated the accuracy of the three-dimensional source localization in an unshielded clinical laboratory, using a phantom model containing this nonmagnetic catheter. For their inverse solution they used a magnetic dipole in a semi-infinite space, the current dipole in a realistic torso, and the distributed currents source model. The results showed that with the current dipole model, on average, localization ac-

curacies of about 9 mm could be obtained, thereby confirming the results obtained earlier in a shielded room from a multicenter research effort (Pesola et al., 1999b). These authors concluded that such dipole localization is accurate enough to guarantee proper localization of cardiac dipolar sources in an unshielded clinical environment.

The activated catheter tip, when introduced intravenously into the heart, not only serves as a current dipole but also induces atrial or ventricular depolarization where the tip touches the endocardial surface. These experiments provide an excellent mechanism to verify, in a clinical setting, the validity of an inverse algorithm for a current dipole in a real torso, as well as testing the validity of the current dipole model for the onset of ventricular or atrial depolarization. Moreover, whereas inducing depolarization with a catheter in combination with measuring ECGs or BSPMs (known as "pace mapping") is commonly used in a clinical setting to locate and subsequently ablate the onset of arrhythmias, pace mapping with MFM is not yet fully explored.

In a detailed study the nonmagnetic, stimulating catheter was introduced into patients, and the MFMs (Fenici et al., 1999) and both MFMs and BSPMs (Pesola et al., 1999c) were measured. The location of the pacing catheter tip and stimulated depolarization was computed from the maps using a moving equivalent current dipole source in a patient-specific boundary element torso model. These data were analyzed with inverse solutions, with the current dipole as source and individual torsos as volume conductors, using BEM. The average MCG localization error was 7 ± 3 mm, whereas the average BSPM localization error was 25 ± 4 mm. These uncertainties include problems of individual patient positioning, electrode positions and in the required coordinate transfer between MCG/BSPM inverse solutions, and the anatomical X-ray and MR images. The better localization accuracy achieved for MFM was also confirmed in a separate series of pacing studies in an unshielded clinical environment by Fenici et al. (2003b).

The results described above, involving phantom models and cardiac pacing in patients, provide a sense of the accuracy that can be achieved, under real measuring conditions, in locating cardiac events that can be modeled with a single-current dipole. The accuracy achieved, consistently less than 1 cm for MFM, is sufficient for several clinical applications (as will be demonstrated in Section 2.3.9). More complex heart conditions must be represented by more elaborate source models.

As mentioned earlier, the uniform double layer (UDL) is a source model that describes the local activation time at the ventricle surface. Mainly developed at the University of Nijmegen (Huiskamp and Van Oosterom, 1988), the UDL has been validated in a number of studies. In one study most relevant to MCG, Oostendorp and Pesola (2001) used human data obtained from patients who underwent open-chest surgery in order to treat ventricular arrhythmia. The authors calculated the activation times from BSPMs, MFMs and combined MFM/BSPM data sets of four patients with myocardial infarction. Based on the MRI images, individual torso and heart shapes were constructed. The calculated ventricular activation times (see Fig. 2.37) based on the MCG, ECG and combined MCG/ECG data were then compared (validated) with the activation time of the epicardial potentials

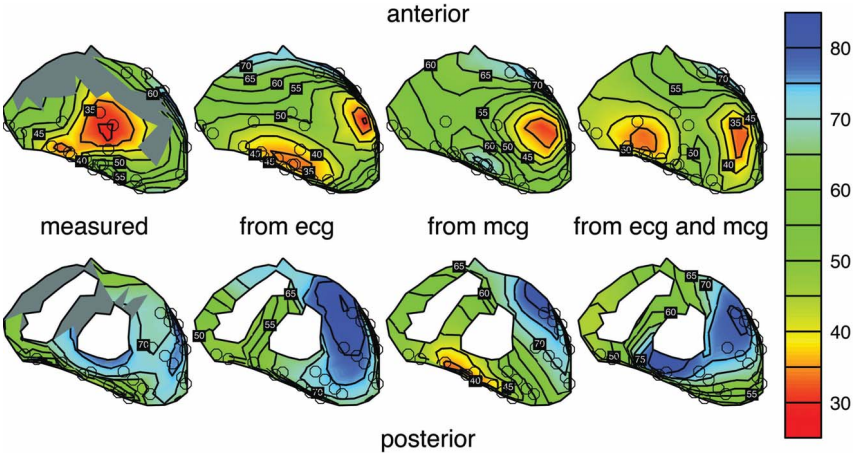

Fig. 2.37. Activation times for a patient who had suffered a myocardial infarction and underwent open-chest surgery in order to treat ventricular arrhythmias. Top row: anterior aspect; bottom row: posterior aspect. From left to right: measured activation times, activation times estimated from measured BSPMs, from measured MFMs, and from the combined data set. Isochrones are drawn at 5-ms intervals. The circles indicate the positions of the epicardial electrodes. (From Oostendorp and Pesola, 2001).

measured with 102 bipolar leads placed in a electrode sock system wrapped around the heart.

The results supported the suggestion that, for the combined data set, the estimated activation sequence corresponds better to the measured one than each of the separate data sets. It was concluded from a comparison between the calculated and measured activation maps that the UDL method correctly identifies most dominant features of the ventricular activation time patterns. In a subsequent analysis of some of these data, a further improved agreement was obtained (Oostendorp and Nenonen, 2003). The authors also pointed out that these findings should encourage the further development of MFM- and BSPM-based activation time imaging (see also Wach et al., 2001) to provide clinically useful techniques for the noninvasive localization of cardiac arrhythmic foci and many other pathologies causing abnormal myocardial activation.

Validation studies as described above are extremely valuable in gaining confidence in the somewhat involved inverse solution procedure. However, many more such studies will be required to base the clinical diagnosis of abnormalities in the heart's conduction sequence on the source images calculated from MFM and/or BSPM. Given the complexity of the heart's electrophysiological system and the many cardiac diseases originating from conduction abnormalities (or that might be apparent from such abnormalities), the ability to assess the electrical activity of the heart noninvasively will be of extreme value from human, clinical, and economic points of view.

2.3.5
Clinical Applications of Magnetocardiography

As magnetocardiography provides unique access to the electrophysiological processes of the heart, researchers have long considered its clinical application, and many investigations of the technique have been conducted in cardiac disease states. Here, a brief overview is provided of current experiences in the clinical application of MCG for cardiovascular disorders. Each subsection provides a brief description of the cardiac condition in question, followed by some pertinent published reports.

2.3.6
Ischemic Heart Disease

Ischemic heart disease (IHD) is the leading cause of death in adults in industrial countries, where the annual incidence is generally high. For diagnostic purposes, coronary angiography is the current ''gold standard'', but due to a combination of X-ray exposure, adverse side effects and high cost, the method is restricted to those patients with very high pre-test likelihood of IHD. Despite the development of novel noninvasive diagnostic tests, including new imaging technology, 12-lead ECG and echocardiography at rest and under stress remain the most common methods in routine clinical use. Although these are fast and simple diagnostic procedures, their predictive value remains limited. Hence, there is a need for cost-effective diagnostic procedures for IHD that are easy and quick to perform and which deliver a reliable basis for subsequent clinical action.

MCG provides a rapid, noninvasive means of registering cardiac electric activity. Concurrent with the dependable registration of cardiac magnetic fields, a variety of

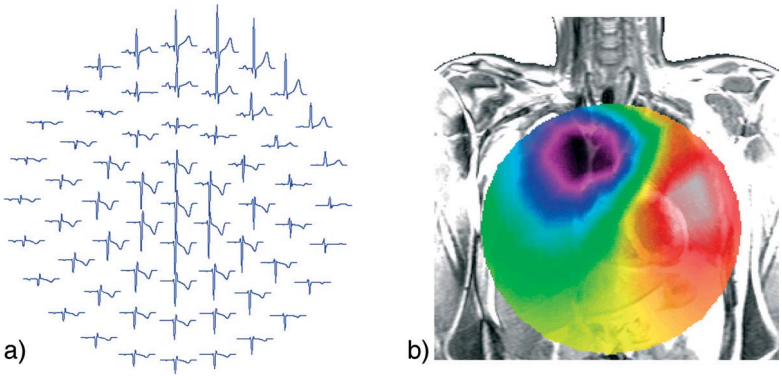

Fig. 2.38. Magnetocardiogram in a healthy subject.
(a) Signal-averaged traces from a 61-channel prethoracic acquisition.
(b) Magnetic field map at Q onset schematically superimposed on an MR image.

data analysis procedures have been developed to examine and quantify cardiac electrophysiological changes. Signal analysis, mapping techniques and the ability to study the three-dimensional localization of cardiac electrical activity have made MCG a potentially useful tool in the early evaluation of the presence and localization of changes related to myocardial ischemia, and have also permitted comparison to ECG procedures. The clinical potential of MCG in the context of IHD may be examined from several aspects:

- Prevention: the ability to identify persons at risk.
- Diagnosis: the early detection of patients with hemodynamically relevant stenoses of the coronary arteries with and without myocardial infarction (MI).
- Follow-up: the post-interventional study of patients and the identification of viable myocardium with the indication for further revascularization procedures.

In the following, an overview of the progress of cardiomagnetism made in the above areas will be outlined with regard to approaches for evaluating magnetic signals recorded from the heart. The different measures are based primarily on the morphology of the MCG signal, the time intervals which can be calculated from it, the reconstruction and analysis of magnetic field maps, and the estimation of current density and current source parameters (Fig. 2.38).

2.3.6.1 Analysis of MCG Signal Morphology

Myocardial ischemia induces changes in the electrophysiological properties of the myocardium, resulting in a decrease in resting membrane potential and conduction velocity, with a dispersion of the activation wavefront. Although in terms of field distribution MCG and ECG are complementary, the signal morphology is comparable for both methods. By performing the first single-channel MCG in a CAD patient after exercise testing, Saarinen et al. (1974) were able to show a depression of the ST segment in the MCG signal. They also found that the ratio of the ischemic ST segment depression to R wave amplitude after stress was even greater in the MCG than in the ECG. Cohen et al. (1983) described TQ baseline elevation and ST depression after a two-step exercise test of a patient with CAD, demonstrating the noninvasive measurement of injury currents.

When analyzing ST segment and T-wave amplitude after exercise in both MCG and BSPM in 24 CAD patients with specified ischemic regions and no previous myocardial scar, Hänninen et al. (2001) identified optimal MCG locations sensitive to ST depression and elevation as well as to the increase or decrease of the T-wave amplitude. These authors noted that the locations were dependent on the stenosed vessel region, that the T-wave changes could separate stenosed vessel regions as well as ST segment changes, and that the most informative sites were outside the 12-lead standard ECG. In a later study in 44 patients with ischemia documented by coronary angiography and exercise thallium scintigraphy, the same group was able to show a decrease in MCG ST amplitude, ST slope and T-wave amplitude under

exercise testing (Hänninen et al., 2002). The optimal sites for the measurement of these parameters were over the abdomen, but a reciprocal increase was found over the left parasternal area.

Using a nine-channel MCG system in an unshielded setting, Chen et al. (2004) analyzed MCG time traces and waveform morphology parameters in healthy subjects and 11 patients with documented exercise-induced ischemia. On the basis of ST- and T-wave signal amplitudes determined under resting and stress conditions, differences were found between the healthy subjects and patients, in particular post exercise. With regard to these differences, the T-wave amplitude over the upper left thorax was most effective, and changes persisted longer post exercise than changes in the ST segment.

Myocardial viability in CAD was evaluated by Morguet et al. (2004), who examined several time and area MCG parameters using a 49-channel system. In 15 patients with single-vessel disease whose myocardial viability was determined on the basis of single photon emission computed tomography (SPECT) as well as positron emission tomography (PET), the amplitudes of the R and T waves were identified as parameters with the highest selectivity in terms of myocardial viability.

Taken together, these results show that ischemia affects the MCG signal amplitudes, in particular during the ST segment and at T-wave apex. The location of these changes may also be associated with the affected vessels.

2.3.6.2 Determination of Time Intervals

Apart from quantifying changes in amplitude, the examination of signal morphology also permits the calculation of time intervals which describe the de- and repolarization activities of the myocardium. ECG-determined QT interval prolongation has been associated with an increased risk of malignant arrhythmias in patients after MI (Schwartz and Wolf, 1978). The predictive value could be improved by the calculation of QT dispersion (QTd), measured as the difference between the maximum and minimum QT duration in the 12-lead ECG. QTd is assumed to reflect inhomogeneity of ventricular repolarization in different regions of the myocardium. The fact that ventricular arrhythmias may be due not only to myocardial scar but also to ischemia indicates that the latter is an important factor influencing electrophysiological processes (Higham et al., 1995). Thus, it was consistent to seek further dependency between CAD and QT duration in the setting of acute coronary syndromes and stable angina.

With regard to the determination of QTd, MCG has an advantage over 12-lead ECG as generally more than 36 registration sites covering a large part of the precordial thorax are available for investigation; this permits a more detailed examination of the spatial aspects of QT duration disparity. Indeed, QTd has allowed better separation between CAD patients without MI and healthy subjects on the basis of multichannel MCG compared to 12-lead ECG (Hailer et al., 1999a,b; Shabalin et al., 2002; Van Leeuwen et al., 2003a). However, consideration of the spatial distribution of QTd improved its sensitivity in the detection of CAD. Increased QT variability

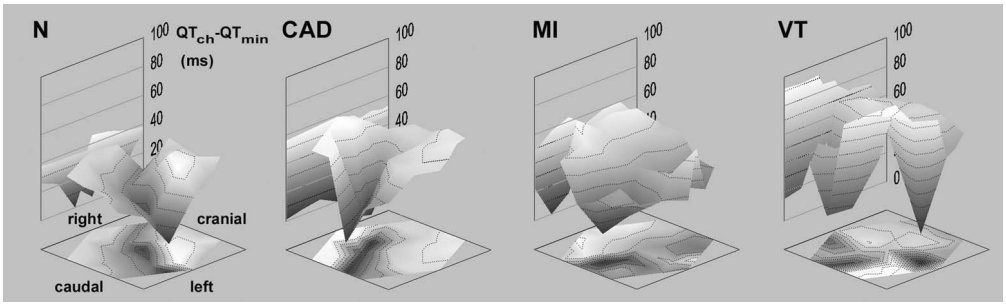

Fig. 2.39. Precordial spatial distribution of QT interval duration based on acquisitions using a 37-channel biomagnetometer in four subjects. Healthy subject (N), patient with coronary artery disease without myocardial infarction (CAD); post-MI patient without ventricular tachycardia (MI); and post-MI patient with ventricular tachycardia (VT). Isochron step = 20 ms; Z-axis: minimum QT value set to 0 ms, QTch = QT values for the channels. Note the progressively higher values, changes in local variability and changes in overall pattern in the patients. (From Van Leeuwen et al., 2003a, with permission).

between neighboring sites and an alteration in the global repolarization pattern compared to healthy subjects could be displayed in CAD patients not only under stress (Hailer et al., 1999a) but also in a resting condition (Hailer et al., 1999b; Van Leeuwen et al., 2003a) (Fig. 2.39).

The spatial patterns involved have been quantified using two smoothness indexes: SI, which quantifies the mean dispersion at each registration site; and SIn, which normalizes SI by taking the overall spatial dispersion pattern into account (Van Leeuwen et al., 1996). Local irregularity in QT duration as expressed by SI was increased in patients with CAD but no wall motion irregularity at rest, indicating more regional heterogeneity of repolarization in contrast to healthy subjects. Furthermore, SIn as a marker for the global pattern of QT dispersion was significantly higher in patients with CAD, which indicates a greater deviation from the pattern found in healthy subjects (Hailer et al., 1999b).

With regards to methodology, the manual determination of QT interval duration is cumbersome, particularly in multichannel measurements. The computed automatic calculation in MCG data has been shown to produce reliable results in several studies (Oikarinen et al., 1998; Smith et al., 2003; Van Leeuwen et al., 2003b). The effects of coverage area comparing precordial and prethoracic recordings have also been examined (Klein et al., 2002). Furthermore, the MCG-derived QTd has been shown to be robust with regard to rapid changes in autonomic tone, but it is affected by respiration and left ventricular loading (Haapalahti et al., 2000).

2.3.6.3
Parameters of the Magnetic Field

As described in Section 2.3.1.1, acquiring signals at defined multiple locations over a thoracic area permits the reconstruction of cardiac MFM. These maps can be

characterized by different measures, and some have been shown to be helpful in separating healthy subjects from patients with IHD, not only under stress but also in a resting condition.

MCG reveals independent, complementary information compared to body surface ECG (Lant et al., 1990; Hänninen et al., 2001). The magnetic field has been analyzed in various studies during the course of the cardiac cycle using different parameters for the quantification of MFM characteristics. One of the most common parameters used has been the MFM orientation. The rationale behind this choice is that ischemia-induced changes in the distribution of magnetic field strength over the precordial thorax will lead to a reorientation of the MFM. The concept has led to various approaches in its quantification in which the spatial distribution of the positive and negative field values, the maximum MFM gradient, or the characteristics of a calculated ECD have been used.

In the first approach, orientation is determined on the basis of the relative positions of two distinct points: one representing the positive field components; the other the negative. These points can be established on the basis of the positive and negative centers of gravity which take both the positions and magnetic field strength values at the registration sites into account. This approach has been examined by Hailer, Van Leeuwen and coworkers, who first attempted to discriminate between healthy subjects and patients who had suffered an acute MI. The course of MFM orientation during the QRS complex was very similar in healthy subjects, whereas those of all MI patients deviated from this course, notably at the R peak (Hailer et al., 2000). In a further study which included 42 CAD patients with and without prior MI, as well as 20 healthy subjects, the time course of orientation was examined over the QT interval (Van Leeuwen et al., 1999a). With a specificity of 90% for the control group, MI patients could be identified with a sensitivity of 85%, and CAD patients without prior MI and with normal resting ECG with a sensitivity of 68%. By examining the constituent X- and Y-axis components during the T wave in the same subject groups, no single component was found to be primarily responsible for the discriminatory power of orientation (Cremer et al., 1999). In further studies examining the influence of the prethoracic area of coverage, a higher sensitivity for CAD could be obtained by positioning sensors symmetrically over a precordial region than by simply including more registration sites which lie distally in the caudal and right-lateral directions (Van Leeuwen et al., 2003c). By applying this approach to a group of 40 patients with suspected CAD, it was found that MFM orientation deviated more clearly from control values in those patients in whom CAD was confirmed on the basis of coronary angiography (Van Leeuwen et al., 2004).

Analogous to the determination of MFM orientation on the basis of the positive and negative centers of gravity, the position of maximum and minimum field strength may be used. This approach, used by Park and Jung (2004) and Chen et al. (2004), registers discontinuities in the course of orientation resulting from the presence of relative extrema associated with MFM nondipolarity. When examining 86 patients with suspected CAD under resting conditions, Park and Jung found that the 53 patients with angiographically confirmed CAD and elevated

troponin levels demonstrated greater variation of MFM orientation during the ascending part of the T wave. By comparing 11 patients with ischemia to 51 healthy controls, Chen and coworkers showed that, in the interval up to T-wave peak, the post-exercise stability of MFM orientation was greater in the healthy subjects.

Spatial gradients may be measured or calculated at any point of the MFM, and this forms the basis of an alternative definition of field orientation, namely the direction of the maximum spatial gradient of the magnetic field. This approach has been studied by Hänninen, Takala and coworkers, who examined orientation in the ST segment and at T apex. Analogous to the development of the ST segment depression and T-wave inversion in ECG during exercise as a parameter for myocardial ischemia, these authors determined MFM orientation at rest and post exercise in 17 healthy subjects and in 27 patients with single-vessel disease (Hänninen et al., 2000). They were able to show alterations in the orientation of the field gradient both during the ST segment and at T-wave apex after exercise in the CAD group compared to the control group, whereby changes in ST segment orientation were most profound immediately after cessation of stress, but those in the T wave occurred later. In a second study, the same group included 44 CAD patients with and without MI, and compared the results of various MCG-determined ST segment and T-wave parameters (including orientation) to results obtained in 26 healthy controls (Hänninen et al., 2002) (see also Section 2.3.6.1). The magnetic field orientation at ST segment was found to perform equally well as the other ST parameters, and this parameter helped to explain statistically the presence of ischemia. The application of the gradient method was taken a step further by examining the heart rate dependency of orientation. In a study including 24 patients with single-vessel disease and 17 healthy controls, orientation was determined continuously for 10 minutes after cessation of exercise, and its relationship to heart rate investigated (Takala et al., 2002) (Fig. 2.40). On the basis of regression analysis, it was found that heart rate-adjusted MFM rotation over the ST segment and at T-wave apex improved the detection of ischemia caused by $\geq$75% stenosis of the coronary vessels.

Using the same approach, Fenici et al. (2002a) compared orientation at rest in 10 healthy subjects and 10 patients with single- or multivessel disease, collecting the data in an unshielded setting. An abnormal orientation was found in the patient group, particularly during the ST segment.

It is also possible to assess the orientation of cardiac electric activity on the basis of estimating the source parameters (this is described in Section 2.2.6.4). Overall, there appears to be a general agreement that ischemia may be documented by MFM orientation, though direct comparison or the pooling of the results of various studies is difficult due to differences in the approaches used.

Other aspects of the cardiac magnetic field investigated in the context of ischemia include the assessment of field strength and nondipolar content. For example, Tsukada et al. (2000) reported a reduction in both de- and repolarization field strength, based on isointegral QRS and ST-T values, in CAD patients with multivessel disease with and without MI compared to healthy subjects. Assessment of the reduction in the coherence of MFM structure is also possible on the basis of

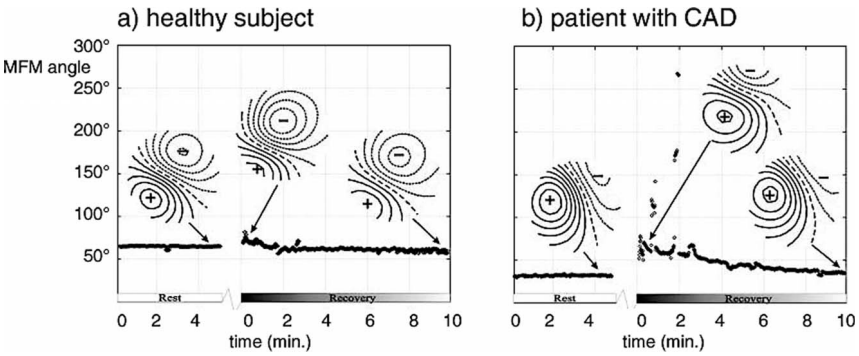

Fig. 2.40. Orientation of the T-wave magnetic field map of successive heart beats at rest and during the recovery from exercise plotted against time. (a) Healthy subject; (b) patient with coronary artery disease (CAD). At rest, the MFM angle has an approximately constant value. After exercise, the MFM angle is tilted more in the patient than in the control, and in the control the angle returns faster to the baseline value. The step between two isofield lines in the MFMs shown is 2 pT. (Adapted from Takala et al., 2002, with permission).

the examination of the dipolar and nondipolar content of the maps. The latter may be calculated using the Karhunen–Loeve transformation (KLT). In a study of 15 CAD patients with and without relevant stenosis of the coronary arteries, KLT was used to show that, under pharmacologically induced stress, the patient subgroups could be distinguished on the basis on the nondipolar content of their QRST isointegral maps (Van Leeuwen et al., 1999b). Furthermore, using KLT analysis Stroink et al. (1999) showed that the nondipolar content of MFM was significantly higher in a group of 30 post-MI patients with and without VT compared to a cohort of 76 healthy subjects.

Yamada and coworkers analyzed the tangential components of the cardiac magnetic field in 10 patients who had reversible myocardial ischemia and 10 patients with old MI, documented by scintigraphy, as well as in 10 healthy subjects. The integral values of the tangential components during QRS and JT intervals were calculated. In particular, their quotient showed clearly reduced values not only for the old MI patients but also in the patients with reversible ischemia when compared to the values for healthy subjects (Yamada et al., 2001).

2.3.6.4 Source Parameters

One of the major advantages of MCG over 12-lead ECG is the ability to study the three-dimensional localization of cardiac electrical activity. This makes MCG a potentially useful tool in the determination of source parameters to evaluate the presence and localization of changes in myocardial de- and repolarization. As described in Section 2.3.3.3, current density estimation (CDE) is one approach in the description of source parameters in order to identify differences between electrophysiolog-

ical properties in healthy subjects and patients in the state of myocardial ischemia. On the basis of a computer simulation study, Killmann et al. (1995) investigated the method of CDE to localize myocardial ischaemia. A computer model of the entire human heart was used to simulate the excitation and repolarization process in eight topographically different cases of myocardial ischemia. At the S point of the cardiac cycle, myocardial ischemia could be localized on the basis of the current density reconstruction method for the injury current, and the authors concluded that magnetocardiography might be a suitable method for the noninvasive diagnosis of ischemia in daily clinical routine.

In the field of chronic ischemia and myocardial viability, current densities for the endocardial surface of the left ventricle were calculated and applied to predefined myocardial geometry acquired from MR images (Leder et al., 1998). The areas corresponding to the infarcted segments of the heart defined by the clinical reference methods revealed markedly decreased regional current densities. CDE was also tested in the localization of ischemia in patients with single- and three-vessel disease under stress. Areas of low CDE amplitude were found to match with the scar regions, whereas a high CDE amplitude was found to correlate with areas of viable, ischemic cardiac tissue (Pesola et al., 1999a).

Using a high-resolution DC SQUID gradiometer, Uchida et al. (2001) studied changes of the current source distribution before and after coronary artery occlusion in seven rats on the basis of minimum norm estimation. The current distribution increased significantly at the ischemic area within the ST segment, whereas in the T wave the direction of the currents changed. These results supported the simulations of the infarction model by Killmann et al. (1995) and Czapski et al. (1996).

Clinically relevant results have also been obtained using a one-channel system in an unshielded setting. On the basis of CDE within the ST-T interval at rest, differences could be shown between normals and a group of 52 CAD patients (Hailer et al., 2003). The results were based on a classification system derived from quantification of the symmetries or asymmetries of the current density vector (CDV) maps in the phase of ventricular repolarization. During normal repolarization, the underlying electrical activity should be coordinated and the current distributions represented in the CDV maps should be primarily characterized by currents in a left- and downward direction. Disturbances in repolarization ought to affect the symmetry of the maps, and these asymmetries were quantified on the basis of the weighted sums of the directions of the vectors. Normal CDV maps were classified as 0 and with the classes 1–4 indicating an increasing deviation from the normal direction and from a dipolar pattern. The results confirmed the initial hypothesis: in healthy subjects most maps were classified as category 0, 1 or 2, whereas in CAD patients the categories 3 and 4 (i.e., the asymmetrical map patterns) prevailed. The same approach showed that, after successful coronary interventional therapy in CAD patients, the classification tended toward normal maps (Hailer et al., 2005a). Confirmation was provided by one of the largest MCG studies published to date, which examined 177 patients with angiographically documented CAD (stenoses $\geq 50\%$), 123 symptomatic patients without hemodynamically relevant stenosis, and 117 healthy subjects (Hailer et al., 2005b). Under resting condi-

tions, CAD patients could be identified on the basis of CDV map classification with a sensitivity of 73% and a specificity of 70%.

An alternative approach which makes no ECD assumptions is the visualization of magnetic field gradients as so-called pseudo current density maps (Kosch et al., 2001). Using this method, Sato and coworkers created vector arrow maps during ventricular de- and repolarization in 25 patients with IHD and in 25 healthy subjects (Sato et al., 2001). On that basis they were able to identify 88% of the patients with severe coronary lesions during repolarization. A further correlation could be found between certain map patterns (such as a rightward shift of current arrows, a multipolar pattern and a decreased time integral value) and various heart diseases, for example left ventricular overloading or prior MI. Kandori et al. (2001a) recorded 64-channel MCG in eight patients with angina and four healthy subjects, and analyzed the relationship between currents recorded before and after exercise test as well as after interventional therapy. These authors calculated the exercise-induced current for each channel as the ratio of current after exercise to that during rest. CAD patients displayed three distinct patterns in current ratio maps, depending on the affected coronary artery. After successful interventional therapy the pattern returned to that of healthy subjects.

Although single ECDs in a homogenous medium are not necessarily accurate enough for 3D localization of focal activity (see Section 2.3.3), their properties might nonetheless aid in the differentiation of ischemia. It has been shown that the orientation of ECDs calculated in a homogenous sphere model are similar in healthy subjects at selected times during the QT interval, and that the orientation in patients with CAD, with and without MI, deviated from the normal (sensitivity 80%, specificity 90%) (Van Leeuwen et al., 1999a). Particularly at T-wave apex, depending on infarct localization, the ECD rotated away from the normal direction in diverging directions.

2.3.6.5
Conclusion

A multitude of studies have been performed in the context of CAD, both in acute states as well as in the phase of chronic disorders with stable symptoms. In order to focus these efforts, the introduction of standardized procedures for data acquisition, processing and analysis is required. Consensus would allow prospective multicenter studies to be conducted in a sufficient number of patients, and the potential of MCG could be used to close the remaining gap in the noninvasive diagnosis of CAD.

2.3.7
Hypertensive Cardiovascular Disease

An elevated arterial pressure is probably the most important public health problem in developed countries and, with an incidence of 5.8%, is one of the main causes of

global mortality. Left ventricular hypertrophy (LVH) as a response to the increased afterload is a powerful independent risk factor for cardiovascular morbidity, stroke, heart failure, and even sudden cardiac death and other cardiovascular events. The prognosis is related to left ventricular mass, whereby the initial changes associated with cardiac remodeling may be difficult to detect as the left ventricular mass may not be altered at that stage. Although electrocardiography is a good predictor of future morbidity and mortality, it is a poor measure of left ventricular mass.

In clinical practice, echocardiography is the method of choice to evaluate cardiac structural or functional changes. However, a major disadvantage of the method relates to problems of reproducibility and its operator-intensive and operator-dependent characteristics. Cardiac MRI has demonstrated a fourfold greater reproducibility and accuracy when compared to echocardiography, but is expensive and not generally available. As cardiac electrical activity is still commonly recorded as a temporal spatially biplanar image on a surface electrocardiogram, there remains the need for a three-dimensional spatial and temporal image of the electric activity. Multichannel magnetocardiography could fulfill these criteria as it allows a spatial and temporal analysis of the cardiac activity, and is also operator-independent.

In early MCG research investigations on hypertensive disease, Fujino et al. (1984) described certain changes of the MCG signal that could be associated to left ventricular overloading. In a group of 95 patients, these authors found increases in the amplitude of the Q or S wave in the upper anterior part of the thorax, and of the R wave in the left lower part of the thorax, indicating increased leftward force due to left ventricular overloading. In examining 40 patients with essential hypertension, Nomura et al. (1988) found changes in T-wave patterns compared to the patterns in 50 healthy subjects. These changes included MFM shifts to the upper right and a change from dipolar to multipolar patterns which were also reflected in vector arrow maps. Furthermore, estimation of the direction (orientation) of the ECG and MCG vector at T maximum showed that the latter were altered in the patient group.

Beside these descriptive parameters of MCG changes due to hypertension, the hypothesis was tested that MCG can not only detect but also quantify the degree of LVH in patients with overload-induced myocardial alteration (Karvonen et al., 2002).

For that purpose, QRS and T-wave areas, as well as their difference, were calculated in 42 patients with hypertension and in 12 healthy subjects. Isointegrals were calculated for de- and repolarization, and the shift in MFM orientation between the QRS and T-wave integrals was determined. Concomitant with typical ECG changes, these authors found that the MCG measures were altered in pressure overload-induced hypertrophy, and that these measures correlated significantly to left ventricular mass. A more recent study (Comani et al., 2004) dealt with the same intention to evaluate the ability of MCG for the detection of early signs of left ventricular remodeling in patients with mild to moderate arterial hypertension. In contrast to the study of Karvonen and coworkers, these patients had a normal ventricular mass index but a high wall thickness ratio (as documented by echocardiography) and no signs of LVH on 12-lead ECG. A number of MCG parameters

were examined, including QRS and T isointegrals, the RS index (which correlates MFM between R and S), and the orientation of an ECD at R and T. Comparing the values in 25 male patients to those in a control group showed that, although a trend to different values was notable for a number of the measures, only the QRS integral values differed significantly. The authors noted, however, that they attempted to detect electrophysiological abnormalities induced by early left ventricular remodeling due to hypertension, and were of the opinion that MCG might play an overall role in the evaluation of this disease.

2.3.7.1 Conclusion

The potential of MCG in hypertensive disease is given by the ability of certain parameters to detect early signs of LVH (see also Section 2.3.8) and remodeling as an independent risk factor for cardiovascular morbidity and mortality.

2.3.8 Cardiomyopathy

The cardiomyopathies constitute a group of diseases in which the dominant feature is the direct involvement of the heart muscle itself. They are distinctive because they are not the result of pericardial, hypertensive, congenital, valvular, or ischemic diseases. A variety of schemes have been proposed for classifying the cardiomyopathies. Three basic types of functional impairment have been described: dilated cardiomyopathy (DCM); hypertrophic cardiomyopathy (HCM); and restrictive cardiomyopathy (RCM). In most cases the etiology is unknown or genetic, as in familiar hypertrophic cardiomyopathy. In DCM it is likely that the condition represents a final common pathway that is the end result of myocardial damage produced by a variety of cytotoxic, metabolic, immunological, familial, and infectious mechanisms.

The role of MCG is mainly the description and identification of certain risk factors, such as the probability of developing malignant arrhythmias. Selbig et al. (1999) evaluated the diagnostic potential of MCG for the identification of sudden cardiac death survivors and gene carriers in a genetically characterized HCM family. On the basis of a residual map score of the QRST integral, these authors were able to separate HCM patients from healthy family members, and concluded that the clinical value of MCG in this context might represent an alternative approach to identify borderline phenotypes at increased risk of sudden cardiac death as the first manifestation of HCM. The risk of malignant arrhythmias was also evaluated in patients with nonischemic DCM by Gödde et al. (2001), who analyzed spatiotemporal beat-to-beat variability using the ECD model. On the basis of a parameter termed "electrical T-wave circulation", the beat-to-beat variability of the tangential component of the current dipole vectors within the T wave was described and used to separate patients with DCM and CAD with a history of a malignant ar-

rhythmia. Again, the authors proposed that this parameter might be used to predict arrhythmic events in CAD and DCM patients.

In addition to the group of Mori (see Section 2.3.7), some of the first investigations into cardiomyopathies were conducted by Schmitz et al. (1990). These authors examined the coherence of MFM during the ST segment (on the basis of the RS score) in 10 patients with varying forms of cardiomyopathy, and found that RS scores to be substantially lower than those of 62 healthy volunteers, thus indicating the presence of advanced electrophysiological disturbances in cardiomyopathy patients. Kandori et al. (2001b) and coworkers examined eight patients with HCM, DCM and RCM and, on the basis of a combination of MCG parameters based on current vectors calculated during the ST segment and T wave, were able to distinguish them clearly from healthy subjects. The assessment of left ventricular mass in HCM is possible using the same parameters as for LVH in hypertensive disease (Takala et al., 2000; Karvonen et al., 2002). With regard to cardiomyopathies resulting from other myocardial diseases (mainly IHD), the value of multichannel MCG is described in the corresponding sections.

2.3.8.1 Conclusion

The role of MCG in cardiomyopathies is mainly related to the structural changes also seen in other myocardial changes due to, for example, ischemic, hypertensive, or valvular heart disease. The common clinical relevance of all these disorders is the increased risk of malignant arrhythmias. MCG might be of help in the risk stratification of these patients (see corresponding sections).

2.3.9 Cardiac Arrhythmias

The mechanisms responsible for cardiac arrhythmias are generally divided into categories of disorders of impulse formation, disorders of impulse conduction, or combinations of the two. Although a variety of tools is available, ranging from noninvasive procedures such as 12-lead ECG and 24-hour Holter monitoring to invasive strategies such as electrophysiological studies, there remains a need for noninvasive characterization of specific arrhythmias in order to determine the optimal therapeutic approach. The value of magnetocardiography in the field of arrhythmias is given by its ability to:

- identify and describe disorders of the electrophysiological properties of the myocardium that predispose it to arrhythmias, thus permitting the protection of these patients by specific therapeutic options such as the implantation of defibrillators or drug treatment; and
- localize the arrhythmic substrate prior to catheter ablation procedures.

The potential of MCG in the above scheme, in the context of disease etiology and therapy based on current experience, is described in the following sections.

2.3.9.1 Atrial Arrhythmias

Premature atrial complexes are among the most common causes of an irregular pulse. They can precipitate or presage the occurrence of sustained supraventricular tachyarrhythmias.

Atrial tachycardia has an atrial rate of generally 150 to 200 beats per minute, with a P-wave morphology different from that of the sinus P wave. It occurs most commonly in patients with significant structural heart disease. In case of catheter ablation, the localization of the origin of atrial tachycardias is indicated. Fenici et al. (1989) were among the first to report on the localization of the source of focal atrial tachycardia using MCG mapping. In contrast to ECG, where the origin of the arrhythmia was only classifiable in one of the four patients studied, MCG mapping provided reproducible three-dimensional localizations in all cases. Mäkijärvi et al. (1993a) and coworkers were also able to localize the onset of the P wave in a patient with focal atrial tachycardia, and the localization result was related to heart anatomy using MR images. Subsequent catheter mapping confirmed the high right atrial location of the focus. Technical improvement permitted the 3D localization of the position of an artificial dipole source generated at the tip of an amagnetic catheter by multichannel magnetocardiographic mapping (see Section 2.3.4). Atrial pacing and pacing-induced atrial arrhythmias could be visualized with a spatial resolution of 3–4 mm^2 using a system inside a shielded location (Fenici et al., 1996), though the accuracy was reduced to 10 mm^2 when the system was installed in an unshielded laboratory (Fenici et al., 2002b).

Atrial flutter is less common than atrial fibrillation, and is now recognized as a macro-reentrant atrial rhythm. Radiofrequency catheter ablation of typical flutter is highly effective at curing atrial fibrillation, and has a long-term success rate of 90–100% (Fischer et al., 1996). Although few reports have been made to date on MCG applications in atrial flutter, Yamada et al. (2003) examined seven patients with atrial flutter using animated MFM constructed from the tangential components. During atrial flutter, these MFM showed a circularly rotating pattern which was distinguishable from disorganized patterns occurring during atrial fibrillation.

Atrial fibrillation (AF) is characterized by wavelets propagating in different directions and causing disorganized atrial depolarizations without effective atrial contraction. Electrical activity of the atrium can be detected as small irregular baseline undulations of variable amplitude and morphology, at a rate of 350 to 600 beats per minute. The maintenance of sinus rhythm is a clinical challenge in order to avoid complications such as embolism or heart failure. Research investigations have focused on the role of trigger factors of AF and different techniques, including catheter ablation procedures in order to restore sinus rhythm.

As the studies of Yamada et al. (2003) have demonstrated, MCG offers the opportunity to evaluate the homogeneity of atrial excitation and refraction, especially in

patients with paroxysmal AF. Mäkijärvi et al. (1993a) analyzed the capability of MCG mapping in separating WPW patients with documented AF from those without AF. Patients with AF attacks were found to have more dispersed atrial depolarization distributions compared to patients without AF. The authors proposed the use of MCG in the clinical context for the identification of WPW patients at risk of AF and the need for ablation therapy in order to avoid a fast ventricular rate during AF. In comparing MCG parameters in healthy volunteers to those of AF patients after spontaneous or electrical conversion to sinus rhythm, Winklmaier et al. (1998) documented significantly longer P-wave duration and a lower homogeneity of the magnetic field distributions during the P wave, while no significant differences were found for ECG parameters. The inhomogeneity of atrial activity with paroxysmal AF was further confirmed in 26 patients by Stadnyuk et al. (2002), who performed MCG and echocardiography before and after transesophageal electrophysiological testing. In contrast to healthy subjects, the patient group revealed signs of inhomogeneity of atrial excitation, particularly after induction of paroxysmal AF.

2.3.9.2 Ventricular Pre-Excitation

Pre-excitation occurs when the atrial impulse activates the whole or some part of the ventricle earlier than would be expected if the impulse had traveled by way of the normal specialized conduction system only. This premature activation is caused by accessory AV pathways that are responsible for the most common variety of pre-excitation. Due to technological improvements, radiofrequency catheter ablation of the accessory pathway is increasingly advisable for patients with frequent symptomatic arrhythmias (Miles and Zipes, 2000). The role of MCG in this disorder could be the precise localization of the accessory pathway prior to ablation therapy in order to reduce X-ray exposure and to plan in detail the course of the electrophysiological procedure.

Katila et al. (1987) were among the first to develop a current multipole model with dipole and quadripole terms to localize the sources of bioelectrical activity in the human heart in the context of WPW syndrome. The same group continued this approach in a clinical setting, and combined magnetic mapping with 3D anatomical models reconstructed from MR imaging (Mäkijärvi et al., 1992). These authors were able to show that noninvasive MCG mapping could significantly contribute to the invasive catheter mapping for optimal pre-procedure localization of the pre-excitation site and AV accessory pathways in WPW syndrome. They tested different source models for optimal localization compared to invasive electrophysiological study or intraoperative mapping in a group of 15 WPW patients, with the best results (2–4 cm) being obtained using the magnetic dipole model. The same group further characterized different magnetocardiographic QRS and delta wave morphologies and corresponding map patterns for different pathway locations. A spatial difference of 1.8 cm on average was obtained by Weismüller et al. (1991) in a group of nine patients with WPW syndrome. On the basis of phantom studies and pacing in a number of patients requiring temporary ventricular stimu-

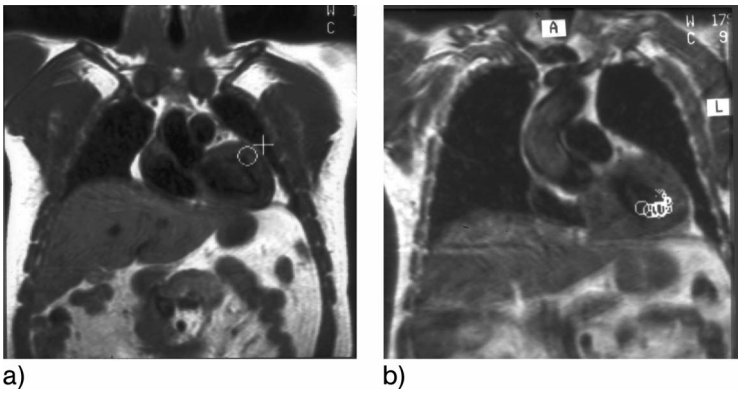

Fig. 2.41. Localized activity fused with anatomical data from MR images. (a) Localization of the accessory pathway in a patient with WPW syndrome (+, MCG localization; O, catheter localization). (b) Localization of the origin and propagation of VT in the left apex (circle diameter shows the relative dipole strength). (Images courtesy of W. Moshage).

lation, Moshage et al. (1996) demonstrated the spatial localization accuracy to be better than 1.5 cm for a dipole-to-dewar distance up to 15 cm (Fig. 2.41a). These authors also examined 32 patients with WPW syndrome, whereupon the MCG localization during the delta wave was in good agreement with, among other things, the topological findings from invasive mapping.

The clinical value of MCG was further evaluated by Fenici et al. (2003b), who tested its reliability in an unshielded electrophysiological catheterization laboratory. While ECG allowed a certain localization of the accessory pathway (defined as agreement among at least four of five different algorithms) in 68% of 28 patients with WPW syndrome, MCG permitted identification of the anatomical course in 89.3% of the patients and performed especially well in patients with posteroseptal pathways. Thus, the authors concluded that MCG might close the diagnostic gap in patients with paraseptal and multiple accessory pathways.

2.3.9.3 Ventricular Arrhythmias

Premature ventricular complexes occur in association with a variety of stimuli, and may precede VT or sudden cardiac death after MI. The diagnosis of VT is generally defined as the occurrence of a series of three or more consecutive, abnormally shaped premature ventricular complexes. Since the era of implanted defibrillators, ablation is generally used as an adjunct therapy to reduce the frequency of VT and defibrillator shocks.

The advent of multichannel MCG systems made the registration of spontaneous events easily possible, and in turn made the noninvasive localization of the arrhythmogenic area plausible, with the clinical advantage of reducing the time-

consuming process of endocardial mapping before catheter ablation. Moshage et al. (1991), using a 37-multichannel MCG system, were among the first to evaluate the magnetocardiographic localization in patients with premature ventricular contraction and VT. The localization results were assigned to anatomic structures by application of MR imaging (see Fig. 2.41b). Furthermore, a nonmagnetic, MR imaging-compatible pacing catheter was developed to verify MCG localization accuracy. Localization of the origin of VT, spontaneous premature ventricular complexes and also paced beats was possible with a high spatial accuracy and an error of a few millimeters in case of paced beats (Moshage et al., 1996).

Fenici and Melillo (1993), using a one-channel system, were the first to localize ventricular extrasystoles and sustained VT in several patients with cardiomyopathy or IHD, but with the disadvantage of long recording times and nonsimultaneous registration of the magnetic fields. In later studies, the magnetocardiographic localization of the VT focus was also proven by successful catheter ablation during the electrophysiological intervention with a difference of less than 10 mm (Oeff and Müller, 2000). In a more recent study, Agren et al. (2002) examined ventricular arrhythmias in 84 patients after surgical repair of tetralogy of Fallot, a cardiac disorder of nonischemic cardiomyopathy. Beside multichannel MCG registration, MRIs were performed for anatomic correlation. This combination of methods allowed a completely noninvasive localization of ventricular ectopic beats, mainly in the right ventricular outflow tract or the right ventricular free wall.

2.3.9.4 Risk Stratification for Malignant Arrhythmias After MI

Coronary heart disease and its consequences account for at least 80% of sudden cardiac deaths in Western cultures, and is therefore the major structural predisposing factor. Beside ischemia, myocardial scarring as a result of prior MI is one of the main pathophysiological reasons responsible for malignant arrhythmias. Although defibrillators represent a very effective treatment option, they are costly and involve invasive procedures; thus, reliable identification of patients who will benefit is essential. In recent years, a variety of different markers have been developed for noninvasive screening of high-risk patients. In the context of parameters based on electrophysiological processes, MCG represents an important independent approach as it contains unique information content not present in ECG.

Parallel to electrical late potentials arising from arrhythmogenic ventricular tissue, Mäkijärvi (1991) investigated the time domain of late fields in high-resolution MCG in the identification of patients with a history of VT after MI. When comparing 20 patients with and without VT after MI, these authors were able to detect abnormal late ventricular electric activity in the VT group. In the signal-processed QRS complexes of the latter group, QRS duration was longer, late field amplitudes were higher, and the duration of the late low-amplitude signal was longer compared to that in MI patients without VT. The sensitivity and specificity in identifying those patients were both 80%, while the positive and negative predictive values were 78% and 86%, respectively (Mäkijärvi et al., 1993b). Similar results were ob-

tained by Weismüller et al. (1993) in eight patients with ventricular late potentials in the signal-averaged ECG. The same group was also able to localize magnetic late ventricular activity by examining the site of origin of the last dipole map. In six of eight patients the origin was located within the border zone of the infarction.

Confirmation of the ability of MCG to identify a propensity to sustained VT in a larger number of patients was achieved by Korhonen et al. (2000) in 38 post-infarction patients with a history of VT, and in 62 without any history. Using late field measures comparable to those used in previous studies, these authors found that filtered QRS duration and RMS amplitude of the last 40 ms were significantly changed in the VT group. Furthermore, the sensitivity and specificity of MCG measures were higher than those obtainable with signal-averaged ECG, in contrast to earlier reports (Mäkijärvi, 1991). This difference was particularly clear in patients with severe left ventricular dysfunction. Beside delayed electrical activity, increased intra-QRS fragmentation seemed to correlate with regional inhomogeneous slow conduction as substrate for ventricular arrhythmias in post-MI patients (Oeff and Müller, 2000; Korhonen et al., 2001).

Korhonen et al. (2002) also showed that time domain and intra-QRS fragmentation parameters in MCG correlate with invasively registered electrograms. The study included 22 patients with old MI undergoing map-guided subendocardial resection to treat sustained VT. The correlations of intra-QRS fragmentation to the end of ventricular excitation were higher in comparison to time domain parameters, especially in the anterior infarct location. After the therapeutic intervention, MCG late fields and intra-QRS fragmentation reverted to more normal values, as an indicator for the association between delayed ventricular conduction as substrate for VT and the MCG arrhythmia risk parameters. In patients vulnerable to recurrent sustained VT, inhomogeneities during the repolarization process could also be identified on the basis of the trajectories of MFM minima and maxima (Stroink et al., 1999). Comparing the ST-T trajectory plots of 15 MI and 15 VT patients enabled their separation with an accuracy of 83%.

A further ECG parameter – QT interval prolongation – has been associated with an increased risk of ventricular fibrillation and sudden cardiac death in hereditary long QT syndrome (Jervell and Lange-Nielsen, 1957), as well as in patients after MI (Schwartz and Wolf, 1978). QT dispersion (QTd) has been proposed as a better non-invasive method for detecting the inhomogeneity of ventricular recovery times and delayed ventricular conduction which may increase the vulnerability to ventricular re-entry and sustained tachycardia (Pye et al., 1994). However, by taking only the two extreme values into account, QTd is very sensitive to outlier error, in particular because the determination of T_{end} is problematic. QTd is thus a simple, strictly temporal approach which does not take local heterogeneity of repolarization into consideration (see also Section 2.3.6.2).

Here also, the spatial precordial or prethoracic coverage of multichannel MCG registration offers advantages over conventional 12-lead ECG, not only because of the inherent possibility of accessing electrophysiological processes not available in ECG, but also because of the substantially higher number of registration sites and their spatial distribution. Oikarinen et al. (1998) compared various MCG QTd mea-

sures in 10 post-MI patients with a history of sustained VT, and in eight without history. The acquisition of MCG signals at 42 sites formed the basis for the calculation of these measures. The results showed significant differences between the patient groups for the dispersion of the QT_{end} interval and more clearly for QT_{apex}.

Not only did the data published by Hailer and coworkers agree with those of the Finish group, but they could also show that the consideration of spatial aspects of QT duration improved the capability of MCG to separate between patients after MI with and without VT (Hailer et al., 1998). Local and global spatial regularity was quantified using two smoothness indices, SI and SIn, which were previously described by Van Leeuwen et al. (1996) (see Section 2.3.6.2). These indexes were shown to permit statistically significant separation of the post-MI VT and nonVT groups not only with respect to the QT but also for the QT_{apex} and JT_{apex} intervals. In a further study including 31 post-MI patient without VT and 11 such patients with VT, Van Leeuwen et al. (2003a) found a sensitivity of 100% and a specificity of 77% with respect to the identification of VT patients on the basis of SIn.

2.3.9.5
Conclusion

In the era of new catheter mapping systems that allow rapid localization procedures prior to ablation therapy, the priority of MCG as a tool for noninvasive localization would seem to be low. The future role of MCG in the field of arrhythmias will mainly focus on the identification and description of electrophysiological properties disposing to certain arrhythmias such as AF or VT. The noninvasive early detection of these patients will not only help to prevent these arrhythmias but also restrict expensive therapeutic options to those patients with the highest benefit.

2.3.10
Clinical Conclusions

In the clinical setting, a variety of approaches implementing MCG have been explored in order to characterize different cardiac disorders. Their application in clinical routine will depend both on the accessibility of such approaches and on their capability to deliver diagnostic information.

With respect to rhythm disturbances, the picture is mixed. The noninvasive localization of the origin of arrhythmic activity using MCG has been superseded by the development of invasive strategies that allow fast and precise mapping procedures. On the other hand, the application of MCG in the identification of patients with an increased risk for malignant arrhythmias shows promise: late potentials, QRS fragmentation and QT interval distribution enable the analysis of both spatial and temporal signal characteristics. Also, the recent MCG studies performed in the context of AF are encouraging. In principle, MCG offers insights into pathophysiological mechanisms of the development of electrical disorders so that further research should be supported and continued.

The most promising application at present would seem to be in the context of CAD. With increasing numbers of patients with unspecified chest pain, there remains a need for noninvasive methods in order to facilitate clinical decision-making with respect to initiating other invasive, elaborate, and/or costly techniques. In CAD, numerous MCG reports have been published and the immediate goal must be to consolidate the diverse positive results through standardization of protocols and conduction of large-scale studies.

Other areas where the clinical potential of MCG has been demonstrated include hypertensive cardiovascular diseases and cardiomyopathies, and efforts must continue to help delineate the most fruitful approach here. Mention should also be made of applications in the area of prenatal MCG (see Chapter 2.5). Although the establishment of MCG in clinical routine has been less rapid than for other new technologies, the recent progress made – especially over the past few years – clearly indicates that this method may have a role to play.

References

Agren, P.L., Goranson, H., Jonsson, H., and Bergfeldt, L. (2002). Magnetocardiographic and magnetic resonance imaging for non-invasive localization of ventricular arrhythmia origin in a model of nonischemic cardiomyopathy. *PACE*, **25** (2), 161–166.

Barach, J.P. and Wikswo, J.P. (1994). Magnetic fields from stimulated cardiac action currents. *IEEE Trans. Biomed. Eng.*, **41** (10), 969.

Barr, R.C. and Spach, M.S. (1978). Inverse calculation of QRS-T epicardial potentials from body surface potential distributions for normal and ectopic beats in the intact dog. *Circ. Res.*, **42**, 661–675.

Chen, J., Thomson, P.D., Nolan, V., and Clarke, J. (2004). Age and sex dependent variations in the normal magnetocardiogram compared with changes associated with ischemia. *Ann. Biomed. Eng.*, **32** (8), 1088–1099.

Cohen, D. and Hosaka, H. (1976). Magnetic field produced by a current dipole. *J. Electrocardiol.*, **9**, 409–417.

Cohen, D., Edelsack, E.A., and Zimmerman, J.E. (1970). Magnetocardiograms taken inside a shielded room with a superconducting point-contact magnetometer. *Appl. Phys. Lett.*, **16**, 278–280.

Cohen, D., Savard, P., Rifkin, R.D., Lepeschkin, E., and Straiss, W.E. (1983). Magnetic measurement of S-T and T-Q segment shift in humans. Part II: exercise-induced S-T segment depression. *Circ. Res.*, **53**, 274–279.

Comani, S., Gallina, S., Lagatta, A., Orlandi, M., Morana, G., Luszio, S.D., Brisinda, D., De Caterina, R., Fenici, R., and Romani, G.L. (2004). Concentric remodeling detection by magnetocardiography in patients with recent onset arterial hypertension. *PACE*, **27** (6P1), 709–718.

Cremer, P., Van Leeuwen, P., Hailer, B., Lange, S., and Grönemeyer, D. (1999). Changes in magnetic field maps during repolarization in patients with coronary artery disease. *Med. Biol. Eng. Comput.*, **37** (2), 1480–1481.

Cuppen, J.J.M. and Van Oosterom, A. (1984). Model studies with the inversely calculated isochrones of ventricular depolarization. *IEEE-BME Trans. Biomed. Eng.*, **31**, 652–659.

Czapski, P., Ramon, C., Huntsman, L.L., Bardy, G.H., and Kim, Y. (1996). On the contribution of volume currents to the total magnetic field resulting from the heart excitation process: a simulation study. *IEEE Trans. Biomed. Eng.*, **BME-43** (1), 95–104.

Dössel, O., David, B., Fuchs, M., Krüger, J., and Wischmann, H.A. (1995). Simple test procedures for multichannel SQUID systems. In: Baumgartner, C., Deecke, L., Stroink, G., and Williamson, S.J. (Eds.), *Biomagnetism: Fundamental research and*

clinical applications. IOS Press, Amsterdam, pp. 515–520.

Durrer, D., Van Dam, R.T., Freud, G.E., Janse, M.J., Meijler, F.L., and Arzbaecher, R.C. (1970). Total excitation of the isolated human heart. *Circulation*, **41**, 899–912.

Fenici, R. and Melillo, G. (1993). Magnetocardiography: ventricular arrhythmias. *Eur. Heart. J*., **14** (Suppl. E), 53–60.

Fenici, R.R., Melillo, G., Capelli, A., Deluca, C., and Maselli, M. (1989). Atrial and ventricular tachycardias: invasive-validation and reproducibility of magnetocardiographic imaging. In: Williamson, S.J., Hoke, M., Stroink, G., and Kotani, M. (Eds.), *Advances in Biomagnetism*, Plenum, New York, pp. 441–449.

Fenici, R.R., Melillo, G., and Masselli, M. (1991). Clinical magnetocardiography: 10 years experience at the Catholic University. *Int. J. Cardiac Imag.*, **7**, 151–167.

Fenici, R., Fenici, P., and Van Bosheide, J. (1996). Amagnetic catheter for biomagnetically guided endocardial mapping and ablation of cardiac arrhythmias. In: Reichl, H. and Heuberger, A. (Eds.), *Micro System Technologies*, VDE-Verlag GmbH, Berlin, pp. 711–716.

Fenici, R., Nenonen, J., Pesola, K., Korhonen, P., Lötjönen, J., Mäkijärvi, M., Toivonen, L., Poutanen, V., Keto, P., and Katila, T. (1999). Nonfluoroscopic localization of an amagnetic stimulation catheter by multichannel magnetocardiography. *PACE*, **22**, 1210–1220.

Fenici, R., Brisinda, D., Nenonen, J., Mäkijarvi, M., and Fenici, P. (2002a). Study of ventricular repolarization in patients with myocardial ischemia, using unshielded multichannel Magnetocardiography. In: Nowak, H., Haueisen, J., Giessler, F., and Huonker, R. (Eds.), *Biomag 2002, Proceedings 13th International Conference on Biomagnetism*, VDE Verlag, Berlin, Offenbach, pp. 520–523.

Fenici, R., Brisinda, D., Nenonen, J., Mäkijarvi, M., and Fenici, P. (2002b). Multimodal integration of MAP recordings and MCG imaging in patients with paroxysmal atrial arrhythmias, using the MultiMAP amagnetic catheter. In: Nowak, H., Haueisen, J., Giessler, F., and Huonker, R. (Eds.), *Biomag 2002, Proceedings 13th International Conference on Biomagnetism*, VDE Verlag, Berlin, Offenbach, pp. 518–520.

Fenici, R., Brisinda, D., Nenonen, J., and Fenici, P. (2003a). Phantom validation of multichannel magnetocardiographic source localization. *PACE*, **26** (2), 426–430.

Fenici, R., Brisinda, D., Nenonen, J., and Fenici, P. (2003b). Noninvasive Study of ventricular preexcitation using multichannel magnetocardiography. *PACE*, **26** (2), 431–435.

Ferguson, A.S. and Stroink, G. (1995). Localization of epicardial sources using magnetic and potential maps. In: Baumgartner, C., Deecke, L., Stroink, G., and Williamson, S.J. (Eds.), *Biomagnetism: Fundamental research and clinical applications*. IOS Press, Amsterdam, pp. 641–646.

Ferguson, A.S. and Stroink, G. (1997). Factors affecting the accuracy of the boundary element method in the forward problem-I: Calculating surface potentials. *IEEE Trans. Biomed. Eng.*, **BME-44** (11), 1139–1155.

Fischer, B., Jais, P., Shah, D., Chouairi, S., Haissaguerre, M., Garrigues, S., Poquet, F., Gencel, L., Clementy, J., and Marcus, F.I. (1996). Radiofrequency catheter ablation of common atrial flutter in 200 patients. *J. Cardiovasc. Electrophysiol.*, **7**, 1225–1233.

Fong, L.E., Holzer, J.R., McBride, K., Lima, E.A., Baudenbacher, F., and Radparvar, M. (2004). High-resolution imaging of cardiac biomagnetic fields using a low-transition-temperature superconducting quantum interference device microscope. *Appl. Phys. Lett.* **84**, 3190–3192.

Fujino, K., Sumi, M., Saito, K., Murakami, M., Higuchi, T., Nakaya, Y., and Mori, H. (1984). Magnetocardiograms of patients with left ventricular overloading recorded with a second-derivate SQUID gradiometer. *J. Electrocardiol.*, **17**, 219–228.

Gödde, P., Czerski, K., Agrawal, R., Sancar, D., Robinson, D., Schultheiss, H.P., and Behrens, S. (2001). Assessment of risk for sudden cardiac death in patients with dilative cardiomyopathy and coronary artery disease by means of spatio-temporal turbulence analysis. In: Nenonen, J., Ilmoniemi, R.J., and Katila, T. (Eds.), *Biomag 2000, Proceedings 12th International Conference on Biomagnetism*, Helsinki Univ. Technology, Espoo, pp. 569–571.

Grynszpan, G. and Geselowitz, D.B. (1973). Model studies of the magnetocardiogram. *Biophys. J.*, **13**, 911–924.

Gulrajani, R.M. (1998). *Bioelectricity and Biomagnetism*. John Wiley & Sons, Inc., New York.

Haapalahti, P., Makijärvi, M., Korhonen, P., Takala, P., Montonen, J., Salorinne, Y., Oikarinen, L., Viitasalo, M., and Toivonen, L. (2000). Magnetocardiographic QT dispersion during cardiovascular autonomic function tests. *Basic Res. Cardiol.*, **95**, 424–430.

Hänninen, H., Takala, P., Mäkijärvi, M., Montonen, J., Korhonen, P., Oikarinen, L., Nenonen, J., Katila, T., and Toivonen, L. (2000). Detection of in exercise-induced myocardial ischemia by multichannel magnetocardiography in single vessel coronary artery disease. *Ann. Noninvasive Electrocardiol.*, **5**, 147–157.

Hänninen, H., Takala, P., Mäkijärvi, M., Montonen, J., Korhonen, P., Oikarinen, L., Simelius, K., Nenonen, J., Katila, T., and Toivonen, L. (2001). Recording locations in multichannel magnetocardiography and body surface potential mapping sensitive for regional exercise induced myocardial ischemia. *Basic Res. Cardiol.*, **96**, 405–414.

Hänninen, H., Takala, P., Korhonen, P., Oikarinen, L., Mäkijärvi, M., Nenonen, J., Katila, T., and Toivonen, L. (2002). Features of ST segment and T wave in exercise induced myocardial ischemia evaluated with multichannel magnetocardiography. *Ann. Med.*, **4**, 120–129.

Hailer, B., Van Leeuwen, P., Lange, S., Grönemeyer, D., and Wehr, M. (1998). Spatial dispersion of the magnetocardiographically determined QT interval and its components in the identification of patients at risk for arrhythmia after myocardial infarction. *Ann. Noninvasive Electrocardiol.*, **3**, 311–318.

Hailer, B., Van Leeuwen, P., Lange, S., and Wehr, M. (1999a). Spatial distribution of QT dispersion under stress in coronary artery disease. *J. Electrocardiol.*, **32**, 207–216.

Hailer, B., Van Leeuwen, P., Lange, S., Pilath, M., and Wehr, M. (1999b). Coronary artery disease may alter the spatial dispersion of QT interval at rest. *Ann. Noninvasive Electrocardiol.*, **4**, 267–273.

Hailer, B., Van Leeuwen, P., Donker, D., Rahn, N., Lange, S., and Wehr, M. (2000). Changes in magnetic field maps at QRS-onset after myocardial infarction. In: Aine, C.J., Okada, Y., Stroink, G., Swithenby, S.J., and Wood, C.C. (Eds.), *Biomag 96, Proceedings 10th International Conference on Biomagnetism*, Springer, New York, pp. 467–470.

Hailer, B., Chaikovsky, I., Auth-Eisernitz, S., Schäfer, H., Steinberg, F., and Gronemeyer, D.H. (2003). Magnetocardiography in coronary artery disease with a new system in an unshielded setting. *Clin. Cardiol.*, **26**, 465–471.

Hailer, B., Van Leeuwen, P., Chaikovsky, I., Auth-Eisernitz, S., Schäfer, H., and Grönemeyer, D. (2005a). The value of magnetocardiography in the course of coronary intervention. *Ann. Noninvasive Electrocardiol.*, **10** (2), 188–198.

Hailer, B., Chaikovsky, I., Auth-Eisernitz, S., Schäfer, H., and Van Leeuwen, P. (2005b). The value of magnetocardiography in patients with and without relevant stenoses of the coronary arteries using an unshielded system. *PACE*, **28** (1), 8–16.

Higham, P.D., Furniss, S.S., and Campbell, R.W.F. (1995). QT dispersion and components of the QT interval in ischaemia and infarction. *Br. Heart J.*, **73**, 32–36.

Hobbie, R.K. (1997). *Intermediate Physics for Medicine and Biology*, 3rd edition. Springer Verlag, Berlin.

Horacek, B.M. (1973). Digital model for studies in magnetography. *IEEE Trans. Magn.*, **MAG-6**, 346–347.

Horacek, B.M. and Stroink, G. (1981). Electrocardiogram and magnetocardiogram: independence testing. In: *Proceedings 34th Annual Conference of Engineering in Medicine and Biology*, Houston, Texas.

Horacek, B.M. and Clements, J.C. (1997). The inverse problem of electrocardiography: A solution in terms of single- and double-layer sources on the epicardial surface. *Math. Biosc.*, **144**, 119–145.

Hosaka, H., Cohen, D., Cuffin, N., and Horacek, B.M. (1976). The effect of the torso boundaries on the magnetocardiogram. *J. Electrocardiol.*, **9** (4), 418–425.

Hren, R. (1996). *A realistic model of the human ventricular myocardium: application to the*

study of ectopic activation. PhD Thesis, Dalhousie University.

Hren, R. and Stroink, G. (2001). Non-invasive characterization of multiple ventricular events using electrocardiographic imaging. *Med. Biol. Eng. Comput.*, **39**, 447–454.

Hren, R., Nenonen, J., MacInnes, P., and Horacek, B.M. (1995). Simulated activation from endocardial pacing sites in an anisotropic model of human ventricles. In: Murray, A. and Arzbaecher, R. (Eds.), *Computers in Cardiology*, IEEE Press, Piscataway, pp. 95–98.

Hren, R., Zhang, X., and Stroink, G. (1996). Comparison between electrocardiographic and magnetocardiographic inverse solutions using the boundary element method. *Med. Biol. Eng. Comput.*, **34** (2), 110–114.

Hren, R., Stroink, G., and Horacek, B.M. (1998a). Spatial resolution of body surface potential maps and magnetic field maps: a model study applied to the localization of ventricular preexcitation sites. *Med. Biol. Eng. Comput.*, **36**, 145–157.

Hren, R., Stroink, G., and Horacek, B.M. (1998b). Accuracy of the single current dipole inverse solution in localizing ventricular pre-excitation sites: a simulation study. *Med. Biol. Eng. Comput.*, **36**, 323–329.

Hren, R., Stroink, G., Jazbinsek, V., and Trontelj, Z. (2001). Localization of septal accessory pathways using simulated magnetic field maps as template. In: Nenonen, J., Ilmoniemi, R.J., and Katila, T. (Eds.), *Biomag 2000, Proceedings 12th International Conference on Biomagnetism*, Helsinki Univ. Technology, Espoo, pp. 851–853.

Huiskamp, G.J.M. and Van Oosterom, A. (1988). The depolarization sequence of the human heart surface computed from measured body surface potentials. *IEEE Trans. Biomed. Eng.*, **BME-35**, 1047–1058.

Jervell, A. and Lange-Nielsen, F. (1957). Congenital deaf-mutism, functional heart disease with prolongation of the Q-T interval and sudden death. *Am. Heart J.*, **54**, 59–68.

Kandori, A., Kanzaki, H., Miyatake, K., Hashimoto, S., Itoh, S., Tanaka, N., Miyashita, T., and Tsukada, K. (2001a). A method for detecting myocardial abnormality by using a current-ratio map calculated from an exercise-induced magnetocardiogram. *Med. Biol. Eng. Comput.*, **39**, 29–34.

Kandori, A., Kanzaki, H., Miyatake, K., Hashimoto, S., Itoh, S., Tanaka, N., Miyashita, T., and Tsukada, K. (2001b). A method for detecting myocardial abnormality by using a total current-vector calculated from ST-segment deviation of a magnetocardiogram signal. *Med. Biol. Eng. Comput.*, **39** (1), 21–28.

Karvonen, M., Oikarinen, L., Takala, P., Kaartinen, M., Rossinen, J., Hännine, H., Montonen, J., Nenonen, J., Mäkijärvi, I., Keto, P., Toivonen, L., Nieminen, M., and Katila, T. (2002). Magnetocardiographic indices of left ventricular hypertrophy. *J. Hypertension*, **20**, 2285–2292.

Katila, T., Maniewski, R., Mäkijärvi, M., Nenonen, J., and Siltanen, P. (1987). On the accuracy of source localisation in cardiac measurements. *Phys. Med. Biol.*, **32**, 125–131.

Killmann, R., Jaros, G.G., Wach, P., Graumann, R., Moshage, W., Renhardt, M., and Fleischmann, P. (1995). Localization of myocardial ischaemia from the magnetocardiogram using current density reconstruction method: computer simulation study. *Med. Biol. Eng. Comput.*, **33**, 643–651.

Klein, A., Van Leeuwen, P., Hailer, B., Lange, S., Lukat, M., Geue, D., and Grönemeyer, D. (2002). QT interval distribution in coronary artery disease determined in a large array biomagnetometer. In: Nowak, H., Haueisen, J., Giessler, F., and Huonker, R. (Eds.), *Biomag 2002, Proceedings 13th International Conference on Biomagnetism*, VDE Verlag, Berlin, Offenbach, pp. 557–559.

Korhonen, P., Montonen, J., Mäkijärvi, M., Katila, T., Nieminen, M.S., and Toivonen, L. (2000). Late fields of the magnetocardiographic QRS complex as indicators of propensity to sustained ventricular tachycardia after myocardial infarction. *J. Cardiovasc. Electrophysiol.*, **11**, 413–420.

Korhonen, P., Montonen, J., Endt, P., Mäkijärvi, M., Trahms, L., Katila, T., and Toivonen, L. (2001). Magnetocardiographic intra-QRS fragmentation analysis in the identification of patients with sustained

ventricular tachycardia after myocardial infarction. *PACE*, **24** (8), 1179–1186.

Korhonen, P., Pesola, K., Jarvinen, A., Mäkijärvi, M., Katila, T., and Toivonen, L. (2002). Relation of magnetocardiographic arrhythmia risk parameters to delayed ventricular conduction in postinfarction ventricular tachycardia. *PACE*, **25** (9), 1339–1345.

Kosch, O., Steinhoff, U., Jazbinšek, V., Trontelj, Z., and Trahms, L. (2001). Non-invasively measured cardiac magnetic field maps improve the estimation of the current distribution. *Comput. Cardiol.*, **28**, 286–289.

Lant, J., Stroink, G., ten Voorde, B., Horacek, B.M., and Montague, T. (1990). Complementary nature of electrocardiographic and magnetocardiographic data in patients with ischemic heart disease. *J. Electrocardiol.*, **23**, 315–322.

Leder, U., Pohl, H.P., Michaelsen, A., Fritschi, T., Huck, M., Eichhorn, J., Müller, S., and Nowak, H. (1998). Noninvasive biomagnetic imaging in coronary artery disease based on individual current density maps of the heart. *Int. J. Cardiol.*, **64**, 83–92.

Leon, L.J. and Horácek, B.M.J. (1991). A computer model of excitation and recovery in the anisotropic myocardium. *J. Electrocardiol.*, **24**, 1–15.

MacAulay, C.E., Stroink, G., and Horacek, B.M. (1985). In: Weinberg, H., Stroink, G., and Katila, T. (Eds.), *Biomagnetism: Applications and Theory, Signal analysis of magnetocardiograms to test their independence*, Pergamon Press, New York, pp. 115–120.

Mäkijärvi, M. (1991). Recording of abnormal late ventricular activity by high-resolution magnetocardiography. *Int. J. Cardiac Imag.*, **7**, 237–241.

Mäkijärvi, M., Nenonen, J., Leiniö, M., Montonen, J., Toivonen, L., Nieminen, M.S., Katila, T., and Siltanen, P. (1992). Localization of accessory pathways in Wolff-Parkinson-White syndrome by high-resolution magnetocardiographic mapping. *J. Electrocardiol.*, **25**, 143–155.

Mäkijärvi, M., Nenonen, J., Toivonen, L., Montonen, J., Katila, T., and Siltanen, P. (1993a). Magnetocardiography: supra ventricular arrhythmias and preexcitation syndromes. *Eur. Heart J.*, **14**, 46–52.

Mäkijärvi, M., Montonen, J., Toivonen, L., Siltanen, P., Nieminen, M.S., Leiniö, M., and Katila, T. (1993b). Identification of patients with ventricular tachycardia after myocardial infarction by high-resolution magnetocardiography and electrocardiography. *J. Electrocardiol.*, **26**, 117–123.

Malmivuo, J. and Plonsey, R. (1995). *Bioelectromagnetism*, Oxford University Press, New York.

Miles, W.M. and Zipes, D.P. (2000). Atrioventricular reentry and variants: Mechanisms, clinical features, and management. In: Zipes, D.P. and Jalife, J. (Eds.), *Cardiac Electrophysiology: From Cell to Bedside*. 3rd edition, W.B. Saunders, Philadelphia, pp. 638–655.

Miller, W.T. and Geselowitz, D.B. (1978). Simulation studies of the electrocardiogram. I. The normal heart. *Circ. Res.*, **43**, 301–315.

Morguet, A.J., Behrens, S., Kosch, O., Lange, C., Zabel, M., Selbig, D., Munz, D.L., Schultheiss, H.P., and Koch, H. (2004). Myocardial viability evaluation using magnetocardiography in patients with coronary artery disease. *Coronary Artery Dis.*, **15** (3), 155–162.

Moshage, W., Achenbach, S., Göhl, K., Weikl, A., Bachmann, K., Wegener, P., Schneider, S., and Hares, W. (1991). Biomagnetic localization of ventricular arrhythmias. *Radiology*, **187**, 685–692.

Moshage, W., Achenbach, S., Göhl, K., Härer, W., Schneider, S., and Bachmann, K. (1992). Magnetocardiography in combination with MRI: verification of localization accuracy with a nonmagnetic pacing catheter. In: Hoke, M., Erné, S.N., Okada, Y., and Romani, G. (Eds.), *Biomagnetism: Clinical Aspects*, Elsevier Science Publishers, Amsterdam, pp. 447–451.

Moshage, W., Achenbach, S., Göhl, K., and Bachmann, K. (1996). Evaluation of the non-invasive localization accuracy of cardiac arrhythmias attainable by multichannel magnetocardiography (MCG). *Int. J. Cardiac Imaging*, **12**, 47–59.

Murdick, R.A. and Roth, B.J. (2004). A comparative model of two mechanisms from which a magnetic field arises in the heart. *J. Appl. Phys.*, **95** (9), 5116–5121.

Nakaya, Y. and Mori, H. (1992). Magnetocardiography. *Clin. Phys. Physiol. Meas.*, **13** (3), 191–229.

Nakaya, Y., Sumi, M., Saito, K., Fujino, K., Murakami, M., and Mori, H. (1984). Analysis of current source of the heart using isomagnetic and vector arrow maps. *Jpn. Heart J.*, **25**, 701–711.

Nenonen, J.T. (1994). Solving the inverse problem in magnetocardiography. *IEEE Eng. Med. Biol. Mag.*, **13** (6), 487–496.

Nenonen, J. and Katila, T. (1991). Noninvasive functional localization by biomagnetic methods. *J. Clin. Eng.*, **16** (5), Part I, 423–434; Part II, ibid 495–503.

Nenonen, J., Purcell, C.J., Horacek, B.M., Stroink, G., and Katila, T. (1991a). Magnetocardiographic functional localization using a current dipole in a realistic torso. *IEEE Trans. Biomed. Eng.*, **38** (7), 658–664.

Nenonen, J., Edens, J.A., Leon, L.J., and Horacek, B.M. (1991b). Computer model of propagation excitation in the anisotropic human heart. In: Ripley, K. and Murray, A. (Eds.), *Computers in Cardiology*, IEEE Computer Society Press, Los Alamitos, pp. 217–220.

Nomura, M., Fulino, K., Katayama, M., Takeuchi, A., Fukuda, Y., Sumi, M., Murakami, M., Nakaya, Y., and Mori, H. (1988). Analysis of the T wave of the magnetocardiogram in patients with essential hypertension by means of isomagnetic and vector arrow maps. *J. Electrocardiol.*, **21**, 174–182.

Oeff, M. and Müller, H.P. (2000). Electrocardiographic and magnetocardiographic body surface mapping. *Herzschr. Elektrophysiol.*, **11**, 31–39.

Oikarinen, L., Paavola, M., Montonen, J., Viitasalo, M., Makijarvi, M., Toivonen, L., and Katila, T. (1998). Magnetocardiographic QT interval dispersion in postmyocardial infarction patients with sustained ventricular tachycardia: validation of automated QT measurements. *PACE*, **21**, 1934–1942.

Oostendorp, T.F. and Van Oosterom, A. (1989). Source parameter estimation in in-homogeneous volume conductors of arbitrary shape. *IEEE Trans. Biomed. Eng.*, **BME-36**, 382–391.

Oostendorp, T.F. and Pesola, K. (2001). Noninvasive determination of the activation sequence of the heart based on combined ECG and MCG measurements. In: Nenonen, J., Ilimoniemi, R.J., and Katila, T. (Eds.), *Biomag 2000, Proceedings 12th International Conference on Biomagnetism*, Helsinki Univ. Technology, Espoo, pp. 813–820.

Oostendorp, T.F. and Nenonen, J. (2003). Non-invasive estimation of the activation sequence of the heart in the presence of old myocardial infarctions: comparison to invasive patient data. *Int. J. Bioelectromagnetism*, **5** (1), 221–224.

Oostendorp, T., Nenonen, J., and Huiskamp, G. (1996). Comparison of inverse solution obtained from ECG and MCG data. IEEE BME Conference, Amsterdam, CD-rom.

Oster, H.S. and Rudy, Y. (1997). The use of temporal information in the regularization of the inverse problem in electrocardiology. *IEEE Trans. Biomed. Eng.*, **44**, 188–199.

Oster, H.S., Taccardi, B., Lux, R.L., Ershler, P.R., and Rudy, Y. (1997). Noninvasive electrocardiographic imaging: reconstruction of epicardial potentials, electrograms, and isochrones and localization of single and multiple electrocardiac events. *Circulation*, **96**, 1012–1024.

Park, J.W. and Jung, F. (2004). Qualitative and quantitative description of myocardial ischemia by means of magnetocardiography. *Biomed. Tech.*, **49** (10), 267–273.

Pesola, K. and Nenonen, J. (2001). Current density imaging on the epicardial surface of the heart. In: Nenonen, J., Ilimoniemi, R.J., and Katila, T. (Eds.), *Biomag 2000, Proceedings 12th International Conference on Biomagnetism*, Helsinki Univ. Technology, Espoo, pp. 835–838.

Pesola, K., Nenonen, J., Fenici, R., and Katila, T. (1997). Comparison of regularization methods when applied to epicardial minimum norm estimates. *Biomed. Tech.*, **42** (Suppl. 1), 273–276.

Pesola, K., Hanninen, H., Lauerma, K., Lötjönen, J., Mäkijärvi, M., Nenonen, J., Takala, P., Voipo-Pulkki, L.M., Toivonen, L., and Katila, T. (1999a). Current density estimation on the left ventricle epicardium: A potential method for ischemia localization. *Biomed. Tech.*, **44** (Suppl. 2), 143–146.

Pesola, K., Tenner, U., Nenonen, J., Endt, P., Brauer, H., Leder, U., and Katila, T. (1999b). Multichannel magnetocardio-

graphic measurements with a physical thorax phantom. *Med. Biol. Eng. Comp.*, **37**, 2–7.

Pesola, K., Nenonen, J., Fenici, R., Lötjönen, J., Mäkijärvi, M., Fenici, P., Korhonen, P., Lauerma, K., Valkonen, M., Toivonen, L., and Katila, T. (1999c). Bioelectromagnetic localization of a pacing catheter in the heart. *Phys. Med. Biol.* **44**, 2565–2578.

Pesola, K., Lötjönen, J., Nenonen, J., Magnin, I.E., Lauerma, K., Fenici, R., and Katila, T. (2000). The effect of geometric and topologic differences in boundary element models on magnetocardiographic localization accuracy. *IEEE Trans. Biomed. Eng.*, **BME-47** (9), 1237–1247.

Peters, M.J., Dunajski, Z., Heringa, A., and Van Dam, R. h. (1983). The mapping of the measured cardiac electric potential and magnetic field distribution. *Il Nuovo Cimento*, **2D** (2), 311–324.

Purcell, C.J. and Stroink, G. (1991). Moving dipole inverse solution using realistic torso models. *IEEE Trans. Biomed. Eng.*, **BME-38** (1), 82–84.

Purcell, C.J., Stroink, G., and Horacek, B.M. (1987). Towards a magnetic inverse solution. *Proceedings IEEE 9th International Conference of Engineering in Medicine and Biology Society*, pp. 214–215.

Purcell, C.J., Stroink, G., and Horacek, B.M. (1988). Effect of torso boundaries on electrical potential and magnetic field of a dipole. *IEEE Trans. Biomed. Eng.*, **BME-35** (9), 671–678.

Pye, M., Quinn, A.C., and Cobbe, S.M. (1994). QT interval dispersion: a non-invasive marker of susceptibility to arrhythmia in patients with sustained ventricular arrhythmias? *Br. Heart J.*, **71**, 511–514.

Roth, B.J. and Wikswo, Jr., J.P. (1986). A bidomain model for the extracellular potential and magnetic field of cardiac tissue. *IEEE Trans. Biomed. Eng.*, **BME-33**, 467–469.

Saarinen, M., Karp, P.J., Katila, T.E., and Siltanen, P. (1974). The magnetocardiogram in cardiac disorders. *Cardiovasc. Res.*, **8**, 820–834.

Saarinen, M., Siltanen, P., Karp, P.J., and Katila, T.E. (1978). The normal magnetocardiogram: I. Morphology. *Ann. Clin. Res.*, **10** (Suppl. 21), 1–43.

Sato, M., Terada, Y., Mitsui, T., Miyahita, T., Kandori, A., and Tsukada, K. (2001). Detection of myocardial ischemia by magnetocardiogram using 64-channel SQUID system. In: Nenonen, J., Ilmoniemi, R.J., and Katila, T. (Eds.), *Biomag 2000, Proceedings 12th International Conference on Biomagnetism*, Helsinki Univ. Technology, Espoo, pp. 523–526.

Schmitz, L., Brockmeier, K., Trahm, S.L., and Erne, A. (1990). Magnetocardiography in patients with cardiomyopathy and operated congenital heart disease. In: Williamson, S.J., Hoke, M., Stroink, G., and Kotani, M. (Eds.), *Advances in Biomagnetism*, Plenum Press, New York, pp. 453–456.

Schneider, S., Hoenig, E., Reichenberger, H., Abraham-Fuchs, K., Moshage, W., Oppelt, A., Stefan, H., Weikl, A., and Wirth, A. (1990). Multichannel biomagnetic system for study of electrical activity of the brain and heart. *Radiology*, **176**, 825.

Schwartz, P.J. and Wolf, S. (1978). QT interval prolongation as a predictor of sudden death in patients with myocardial infarction. *Circulation*, **57**, 1074–1077.

Selbig, D., Bode, M., Soltner, H., Ziegert, K., Halling, H., Bousack, H., Trahm, S.L., and Stellbrink, C. (1999). Magnetocardiographic evaluation of a genetically characterized family with hypertrophic cardiomyopathy. In: Yoshimoto, T., Kotani, M., Kuriki, S., Karibe, H., and Nakasato, N. (Eds.), *Recent Advances in Biomagnetism*, Tohoku University Press, Sendai, pp. 1063–1064.

Shabalin, A.V., Treti'akova, T.V., Kuznetsov, A.A., Motorin, S.V., and Golyshev, N.V. (2002). Comparative analysis of parameters of corrected and uncorrected QT-interval dispersion of magneto-, electrocardiography and isomagnetic maps in patients with ischemic heart disease. *Kardiologiia*, **42**, 20–23.

Shahidi, A.V., Vard, P., and Nadeau, R. (1994). Forward and inverse problems in electrocardiography: Modeling and recovery of epicardial potentials in humans. *IEEE Trans. Biomed. Eng.*, **41**, 249–256.

Siltanen, P. (1989). Magnetocardiography. In: MacFarlane, P.W. and Veitch Lawrie, T.D. (Eds.), *Comprehensive Electrocardiology*, Pergamon Press, New York, pp. 1405–1438.

Simelius, K., Nenonen, J., Hren, R., and Horacek, B.M. (2001). Electromagnetic extracardiac fields simulated with a bidomain propagation model. In: Nenonen, J., Ilimoniemi, R.J., and Katila, T. (Eds.), *Biomag 2000, Proceedings 12th International Conference on Biomagnetism*, Helsinki Univ. Technology, Espoo, pp. 847–850.

SippensGroenewegen, A., Spekhorst, H., van Hemel, N.M., Herre Kingma, J., Hauer, R.N.W., de Bakker, J.M.T., Grimbergen, C.A., Janse, M.J., and Dunning, A.J. (1993). Localization of the site of origin of postinfarction ventricular tachycardia by endocardial pace mapping. *Circulation*, **88** (5), 2290–2306.

Smith, F.E., Langley, P., Trahm, S.L., Steinhoff, U., Bourke, J.P., and Murray, A. (2003). Comparison of automatic repolarization measurement techniques in the normal magnetocardiogram. *PACE*, **26**, 2121–2126.

Stadnyuk, L., Kozlovsky, V., Budnyk, M., Sosnytsky, V., Minov, Y., Sutkovyy, P., and Nizhenkovsky, I. (2002). Magnetocardiographic and echocardiographic parameters after short induced paroxysm of atrial fibrillation. In: Nowak, H., Haueisen, J., Giessler, F., and Huonker, R. (Eds.), *Biomag 2002, Proceedings 13th International Conference on Biomagnetism*, VDE Verlag, Berlin Offenbach, pp. 596–598.

Staton, D.J., Friedman, R.N., and Wikswo, Jr., J.P. (1993). High resolution SQUID imaging of octupolar currents in anisotropic tissue. *IEEE Trans. Appl. Supercond.*, **3** (1), 1934–1936.

Stroink, G. (1992). Cardiomagnetism: a historical perspective. In: Hoke, M., Erné, S.N., Okada, Y., and Romani, G. (Eds.), *Biomagnetism: Clinical Aspects*, Elsevier Science Publishers, Amsterdam, pp. 399–404.

Stroink, G. (1993). Cardiomagnetic imaging. In: Zaret, B.L., Kaufman, L., Berson, A.S., and Dunn, R.A. (Eds.), *Frontiers in Cardiovascular Imaging*, R.A. Ven Press, New York, pp. 161–177.

Stroink, G., MacAuley, C., Montague, T.J., and Horacek, B.M. (1985). Normal and abnormal components in magnetocardiographic maps of a subject with myocardial infarction. *Med. Biol. Eng. Comp.*, **23** (Suppl. 1), 61–62.

Stroink, G., Lamothe, M.J.R., and Gardner, M.J. (1996). Magnetocardiographic and electrocardiographic mapping studies. In: Weinstock, H. (Ed.), *SQUID Sensors: Fundamentals, Fabrication and Applications*, NATO ASI Series, Kluwer, The Netherlands, pp. 413–444.

Stroink, G., Meeder, R.J.J., Elliott, P., Lant, J., and Gardner, M. (1999). Arrhythmia vulnerability assessment using magnetic field maps and body surface potential maps. *PACE*, **22**, 1718–1728.

Takala, P., Montonen, J., Aalto, T., Makijarvi, M., Nenonen, J., Yildirim, Y., Niemine, M.S., and Katila, T. (2000). Magnetocardiographic assessment of left ventricular hypertrophy: Correlation with echocardiography. In: Aine, C.J., Okada, Y., Stroink, G., Swithenby, S.J., and Wood, C.C. (Eds.), *Biomag 96, Proceedings 10th International Conference on Biomagnetism*, Springer, New York, pp. 558–561.

Takala, P., Hänninen, H., Montonen, J., Korhonen, P., Mäkijärvi, M., Nenonen, J., Oikarinen, L., Toivonen, L., and Katila, T. (2002). Heart rate adjustment of magnetic field map rotation in detection of myocardial ischemia in exercise magnetocardiography. *Basic Res. Cardiol.*, **97**, 88–96.

Tan, G.K., Bauer, F., Stroink, G., and Purcell, C.J. (1992). The effect of measuring conditions on MCG inverse solutions. *IEEE Trans. Biomed. Eng.*, **BME-39** (9), 921–927.

Tavarozzi, I., Comani, S., Del Gratta, C., Romani, G.L., Di Luzzo, S., Brisinda, D., Gallina, S., Zimarino, M., Fenici, R., and De Caterina, R. (2002a). Magnetocardiography: current status and perspectives. Part I: Physical principles and instrumentation. *Ital. Heart J.*, **3**, 75–85.

Tavarozzi, I., Comani, S., Del Gratta, C., Di Luzzo, S., Romani, G.L., Gallina, S., Zimarino, M., Brisinda, D., Fenici, R., and De Caterina, R. (2002b). Magnetocardiography: current status and perspectives. Part II: Clinical applications. *Ital. Heart J.*, **3**, 151–165.

Tsukada, K., Miyashita, T., Kandori, A., Mitsui, T., Terada, Y., Sato, M., Shiono, J., Horgome, H., Yamada, S., and Yamaguchi, I. (2000). An iso-integral mapping technique using magnetocardio-

gram and its possible use for diagnosis of ischemic heart disease. *Int. J. Cardiac Imaging*, **16**, 55–60.

Uchida, S., Goto, K., Tachikawa, A., Iramina, K., and Ueno, S. (2001). Measurement of high spatial resolution magnetocardiogram and source localization in rats with occlusion. In: Nenonen, J., Ilmoniemi, R.J., and Katila, T. (Eds.), *Biomag 2000, Proceedings 12th International Conference on Biomagnetism*, Helsinki Univ. Technology, Espoo, pp. 534–537.

Van Leeuwen, P., Hailer, B., and Wehr, M. (1996). Spatial distribution of QT-intervals: an alternative approach to QT dispersion. *PACE*, **19**, 1894–1899.

Van Leeuwen, P., Hailer, B., Lange, S., Donker, D., and Grönemeyer, D. (1999a). Spatial and temporal changes during the QT interval in the magnetic field of patients with coronary artery disease. *Biomed. Tech.*, **44**, 139–142.

Van Leeuwen, P., Stroink, G., Hailer, B., Lange, S., Adams, A., Lange, S., and Grönemeyer, D. (1999b). Rest and stress magnetocardiography in coronary artery disease. *Med. Biol. Eng. Comput.*, **37**, 1482–1483.

Van Leeuwen, P., Hailer, B., Lange, S., and Grönemeyer, D. (2003a). Spatial distribution of repolarization times in patients with coronary artery disease. *PACE*, **26**, 1706–1714.

Van Leeuwen, P., Geue, D., Poplutz, C., Klein, A., Lange, S., and Grönemeyer, D. (2003b). Reliability of automated determination of QRST times in ECG and MCG. *Biomed. Tech.*, **48** (suppl 1), 370–371.

Van Leeuwen, P., Klein, A., Matil, K., Geue, D., Poplutz, C., Lange, S., Hailer, B., and Grönemeyer, D. (2003c). Influence of area of coverage on cardiac magnetic field map orientation. *Biomed. Tech.*, **48** (suppl. 1), 238–239.

Van Leeuwen, P., Lange, S., Klein, A., Geue, D., Matil, K., Hailer, B., and Grönemeyer, D. (2004). Relationship between clinical and magnetocardiographic parameters in the context of coronary artery disease. In: Halgren, E., Ahlfors, S., Hämäläinen, M., and Cohen, D. (Eds.), *Biomag 2004, Proceedings 14th International Conference on Biomagnetism*, Biomag 2004 Ltd., Boston, pp. 413–414.

Van Oosterom, A. and Huiskamp, G.J. (1992). Torso modeling in electrocardiography. In: Hoke, M., Erne, S.N., Okada, Y.C., and Romani, G.L. (Eds.), *Biomagnetism, Clinical Aspects*, Elsevier Science Publishers, Amsterdam, pp. 405–415.

Van Oosterom, A., Oostendorp, T.F., Huiskamp, G., and Brake, H.J.M. (1990). The magnetocardiogram as derived from electrocardiographic data. *Circ. Res.*, **67**, 1503–1509.

Wach, P., Modre, R., Tilg, B., and Fischer, G. (2001). An iterative linearized optimization technique for non-linear ill-posed problems applied to cardiac activation time imaging. *Int. J. Comput. Maths. Elect. Electronic Eng.*, **20**, 676–688.

Weismüller, P., Abraham-Fuchs, K., Schneider, S., Richter, P., Kochs, M., Edrich, J., and Hombach, V. (1991). Biomagnetic noninvasive localisation of accessory pathways in WPW-Syndrome. *PACE*, **14**, 1961–1965.

Weismüller, P., Abraham-Fuchs, K., Killmann, R., Richter, P., Härer, W., Höher, M., Kochs, M., Eggeling, T., and Hombach, V. (1993). Magnetocardiography: three-dimensional localisation of the origin of ventricular late fields in the signal averaged magnetocardiogram in patients with ventricular late potentials. *Eur. Heart J.*, **14**, 61–68.

Winklmaier, M., Pohle, C., Achenbach, S., Kaltenhauser, M., Moshage, W., and Daniel, W.G. (1998). P wave analysis in MCG and ECG after conversion of atrial fibrillation. *Biomed. Tech.*, **43** (suppl. 1), 250–251.

Yamada, S., Tsukada, K., Miyashita, T., Watanabe, S., and Yamaguchi, I. (2001). Evaluating ventricular repolarization abnormalities in the at-rest phase in ischemic heart disease by using magnetocardiograms. *Biomed. Tech.*, **46** (suppl. 2), 47–49.

Yamada, S., Tsukada, K., Miyashita, T., Kuga, K., and Yamaguchi, I. (2003). Noninvasive, direct visualization of macroreentrant circuits by using magnetocardiograms: initiation and persistence of atrial flutter. *Europace*, **5** (4), 343–350.

2.4
Neuromagnetism

Thomas R. Knösche, Nobukazu Nakasato, Michael Eiselt, and Jens Haueisen

2.4.1
Introduction

The activity of the human brain involves a complex interplay of electrical, chemical, and mechanical processes, extending over both space and time. This vast diversity of phenomena carrying information on brain functions naturally leads to a great variety of possible means by which this information can be extracted. However, the application of such methods alone does not guarantee an understanding of how the brain functions. Only clever experimental design and sound theoretical reasoning can, together with reliable brain imaging, shed light onto the complex processes that make us think.

Brain imaging techniques are characterized by the brain process that they monitor, by their degree of invasiveness, and by their spatial and temporal resolutions. Methods relying on metabolic and hemodynamic changes in the brain tissue indirectly reflect neuronal activity, as for example positron emission tomography (PET) and functional magnetic resonance imaging (fMRI). These represent different degrees of invasiveness (radioactive substances, large magnetic fields), and good spatial and poor temporal resolution. A much more direct (and completely noninvasive) measure of the activity of nerve cells is delivered by electroencephalography (EEG). However, the EEG signals are modified considerably by the electrical properties of the head tissues. Moreover, the synchronous activity of large populations of cells is required to produce measurable extracranial signals. Consequently, EEG yields excellent time (fractions of a millisecond), but poor spatial resolution.

Magnetoencephalography (MEG) monitors the same electrical brain activity as EEG and shares many of its properties, but it is less disturbed by the complex conductivity profile of the head tissues, and this leads to a higher spatial reconstructability of the brain processes. Another typical trait of the technique in comparison to EEG is the different sensitivity profile, which largely excludes deep areas and those currents that flow perpendicular to the cranial surface. MEG relies on the extremely weak magnetic fields caused by neuronal electrical activity (see Section 2.4.2). Typically, signals of some hundreds of femtoteslas (10^{-15} Tesla) in size

must be separated from environmental noise, which are five to six orders of magnitude stronger, and this requires techniques such as gradiometer schemes and magnetically shielded chambers. For information on techniques used to measure neuromagnetic fields, the reader is referred to Section 2.2.

In this section, we first address the neurophysiological mechanisms that lead to the generation of EEG and MEG signals, after which the methodological framework for the extraction of the spatial and temporal properties of neural activity from the measured signals is introduced. In subsequent sections, the application of MEG to the investigation of primary somatosensory systems, as well as to higher cognitive functions, is described. Finally, some clinical applications of magnetoencephalography are presented.

2.4.2
The Generation of Magnetic Signals by the Brain

2.4.2.1
Introduction

The directed flow of charged elements gives rise to a magnetic field. In most physical entities this flow is represented by electrons, but in living systems selective ion movements form the basis of the magnetic field. Since different types of ions simultaneously take part in this flow, the resultant field is the sum of multiple small magnetic fields. The contribution of ions to the magnetic field brings some peculiarities. For example, positively and negatively charged ions moving in opposite directions generate the same magnetic field. The aim of this section is to characterize the current present in the brain which generates the magnetic field distant from the active tissues – that is, the field on the outside of the brain. This current can be described by modeling of the current dipole.

2.4.2.2
Technical Development and Limits of Detection

The detection of a magnetic field depends heavily on the improvement of available measuring sensors. In this regard, there are two main directions of development: (1) increasing the spatial resolution; and (2) increasing the sensitivity.

In living systems the elements causing magnetic fields (sources) are small and build up complex structures. Sensitivity and spatial resolution of the sensor systems cause limitations in detection. First, the distant fields of two sources, which are very near to each other but of opposite directions (current flow), usually cancel each other and may be not detected if sensor sensitivity is low. For example, the depolarization of dendritic regions near the soma causes currents directed to the apical parts of the dendrite and to the soma. Two current dipoles result with an opposite direction, forming a quadrupolar field. The field strength decreases rapidly with increasing distance between the sources and the sensor, and thus the field is

too weak to be detected on the outside of the brain. Second, the spatial pattern of activation and inhibition of cortical regions is complex, causing in turn complex magnetic fields. A precise description of these intricate fields is only possible with sensors that provide high spatial resolution. Recent developments (see Section 2.2) have moved the boundaries of detectable signals considerably, and today we are able to observe functions that only a few years ago were impossible to record.

Using a microSQUID, the synchronized activity of about 10 000 pyramidal cells can be detected, corresponding to an activated cerebral tissue volume as small as 1 mm^3 (Okada et al., 1997).

2.4.2.3
Electrophysiology of Brain Cells

Resting Membrane Potential

The ion concentrations of the intracellular and extracellular spaces differ. Within the extracellular space, concentrations of sodium, calcium and chloride ions are much higher than in the intracellular space. In contrast, the potassium concentration is highest in the intracellular space. This unequal distribution is maintained by the selective permeability of the plasma membrane, which in turn depends on the electric potential, the intracellular calcium concentration, and the action of neurotransmitters. During resting conditions the permeability of the plasma membrane permits potassium to leave the cell via ion channels formed by special proteins. This efflux causes negative potential within the cell and positive potential in the extracellular space. The radial symmetry of the transmembrane currents causes the magnetic fields to cancel each other. Moreover, the transmembrane currents are very weak at resting potential. Therefore, it can be assumed that the currents at resting membrane potential do not contribute to the external magnetic field.

Conduction and Transmission of Cellular Activity

Neuronal excitation is conducted over great distances with high velocity by action potentials. These are short-lasting and localized depolarizations of the plasma membrane caused by rapid changes in membrane conductivity and resulting in ion currents during depolarization, as well as during repolarization. The conduction velocity can be accelerated if the membrane resistance is increased, or if the membrane capacity is decreased. Myelinization of the axon fibers contributes to such an increase in conduction velocity. Two features are responsible for difficulties in detecting a magnetic field of action potentials. First, current dipoles at the region of the action potential generation are directed forward and backward, the result being a quadrupolar magnetic field. The amplitude of this field is much weaker at greater distances from the active tissue in comparison to a dipolar magnetic field. Second, because of the short duration of the action potential, temporal summation is limited. However, the chance for summation increases if neurons in a limited region are synchronously activated.

The transmission of excitation and inhibition from one cell to another occurs in the majority of cases by the release of neurotransmitters at synapses. To initiate the release of a transmitter, the action potentials must depolarize the presynaptic membrane. Although the generated magnetic fields are weak, recent findings indicate that MEG is capable of detecting these magnetic fields produced by the presynaptic thalamocortical axonal terminals if they are highly synchronized (Ikeda et al., 2002).

Long-lasting potentials are generated postsynaptically, and two fundamental types may be distinguished, namely excitatory and inhibitory. Excitation is mainly initiated by the neurotransmitter glutamate, the binding of which at the postsynaptic receptor induces a long-lasting increase in sodium or calcium ion influx. The type of ion entering the cell membrane depends on the activated receptor type; for example, AMPA-receptors are mainly permeable for sodium, and NMDA-receptors for calcium. The influx of sodium into the cell depolarizes the membrane as the number of negatively charged ions outside the cell increases in relation to the positively charged ions. As a consequence a current sink appears in the extracellular space, and this is accompanied by current sources distant from there (Mitzdorf, 1985). A capacitive current in the intracellular space is responsible for the spread of depolarization which is directed away from the region of excitation, for example from the apical dendrite to the soma. This depolarization influences the permeability of voltage-dependent ion channels. Here, specific potassium channels are of significance, since when they are activated a potassium ion efflux results and thus the resting membrane potential reoccurs. Some of these ion channels show an unequal distribution between parts of the neuron (Johnston et al., 2003). If ion channels are more frequent at the dendrites, a current source is established there, and a current sink is created near the soma. Thereby current dipoles appear, which are inversely directed to the current dipoles at the beginning of the excitation (Murakami et al., 2003). The generated magnetic field is inversely directed to that at the beginning of excitation.

The main neurotransmitter causing inhibitory postsynaptic potential is gamma-amino butyric acid (GABA). The action of $GABA_A$ receptors causes chloride channels to open, while the action of $GABA_B$ receptors opens potassium channels.

The functions of neurons are closely coupled with that of glia cells. As mentioned previously, the excitation of neurons causes an increase in extracellular potassium concentration. A significant amount of potassium is taken up by the glia cells, and thus the negative effects of high extracellular potassium concentration on consecutive neuronal activity are avoided. Hence, the glia cells act as a buffer to high levels of extracellular potassium (Gardner-Medwin, 1981). Since glia cells are coupled via gap junctions and build up an extended compartment, an ion movement across multiple cells is possible. This type of intracellular current may be important in the occurrence of a migraine, in focal epilepsy, and most likely after brain tissue injury caused by ischemia (stroke) or head trauma. Recent findings in animal investigations have suggested that this type of intracellular current might contribute to the appearance of slow magnetic field changes (Bowyer et al., 1999a,b).

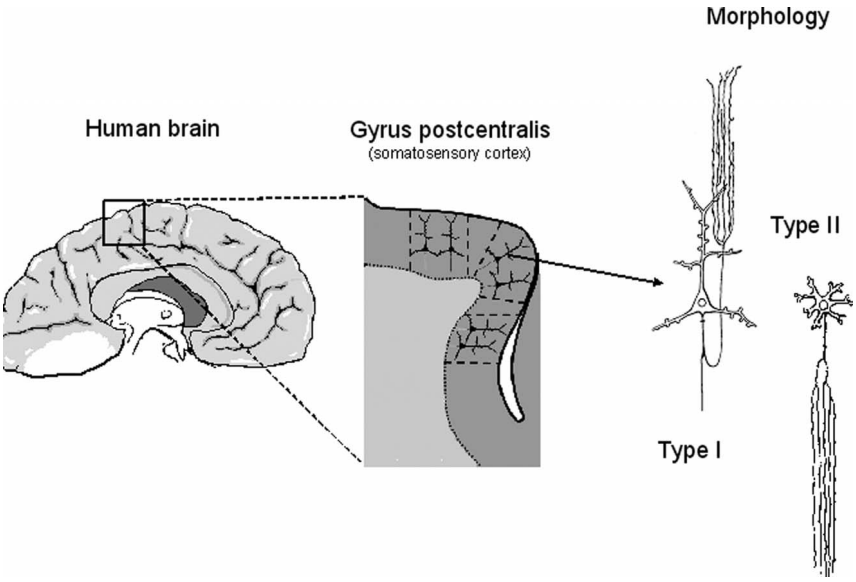

Fig. 2.42. Left: The human brain is gyrencephalic, characterized by gyri and sulci. Orientation of neurons changes with respect to the brain surface caused by the folding of the gray matter. The main axis of pyramidal cells is in some cases tangential and in some cases perpendicular to the surface. Right: Pyramidal cells are a good example of neurons with an open field structure (type I) generating magnetic fields detectable on the outside of the head. The type II cells have a closed field structure and are less likely candidates for generating magnetic fields on the outside of the head.

Excitatory Cells in the Brain

The shapes of neurons generally range between these two types:

- **Type I:** The ideal cell has a single dendrite and one long axon. This type is said to have an "open-field" configuration, because field potential changes spread throughout the conducting medium. When the current is axial, as would be the case for a cell having the open-field configuration, the associated magnetic field should be dipolar and thus could easily be detected if the cell axis is tangential to the brain surface. The pyramidal cell has in part an open-field configuration, made up by the main trunk of the apical dendrite and the axon (Fig. 2.42; Morphology, Type I). In part it has also a closed-field configuration, made up by the terminal branches of the apical and basal dendrites. Thus, depending on the spatial pattern of excitation, this cell type may be the primary contributor to the magnetic field recorded on the outside of the brain.
- **Type II:** At the other extreme is the cell of which the dendrites extend radially in all directions (Fig. 2.42; Morphology, Type II). This type is said to have a "closed-field" configuration, because field potential changes are limited to the length of

the dendrites. In a cell with a closed-field configuration with major activation of its dendrites, the current is radially symmetric (spherical symmetry). No magnetic field can be detected. The stellate cell may be considered the ideal neuron with a closed-field configuration. Brain regions consist of both major cell types in variable frequency. They are arranged in complex spatial patterns. As cell composition in the hippocampus is not very complex, examination provides evidence that type I cells are the major contributor to the magnetic field (Okada et al., 1997).

Other cortical regions are organized in layers and columns, with their main axes orthogonal to the cortical layers (Fig. 2.42; Gyrus postcentralis). The predominant organization of the cellular axis within a column is perpendicular to the cortical surface. Pyramidal neurons are found mainly in layers III and V. Since the pyramidal neurons are cells with an open-field configuration, it is expected that they mainly contribute to the magnetic field on the outside of the head and that the orientation of these cells is important for the magnetic field. The primary source of the magnetic field on the outside of the head is an ensemble of current dipoles within columns. Since multiple cells form a column-like structure, it seems reasonable to assume that multiple dipoles within a column exist. However, differentiation between these dipoles is not yet possible through measurement of the magnetic field on the outside of the head. Brain regions with a large number of open-field neurons are the major contributors to a magnetic field; however, recent results suggest that regions with fewer open-field neurons also contribute (Hashimoto et al., 1996). Thus, the transmission of somatosensory excitation to the cortex may generate a magnetic field which possibly correlates with excitation of the thalamic neurons.

In addition to the type of cell morphology, the orientation of the main cell axis in relation to the skull is of great importance for the magnetic field on the outside of the head. The magnetic field component radial to the skull is essentially due to the component of the primary current dipoles tangential to the skull.

2.4.2.4 Extracellular Space

It is difficult to estimate to what extent the extracellular current (the volume current) contributes to the magnetic field on the outside of the brain. This is in part due to the complexity of the extracellular space. If this space is of infinite dimension and of uniform conductivity, the extracellular currents are symmetric in such a way that the magnetic field generated by each extracellular current path is canceled by the magnetic field generated by other extracellular current elements. Deviation from these conditions may cause the magnetic field of extracellular currents to contribute to the magnetic field outside the head. However, mainly the intracellular current may be considered as the source of the magnetic field on the outside of the head related to brain activity.

Electromagnetic Tissue Properties

Most important is the tissue conductivity, which differs depending on the tissue type. The spread of extracellular currents caused by cellular electric activity is mainly confined to the inside of the skull. The brain tissue inside the skull may be compared to a compartment with similar conductivity within (gray matter ca. 0.3 S m^{-1}, white matter 0.14 S m^{-1}) surrounded by a compartment with high conductivity such as liquor (ca. 1.54 S m^{-1}). The symmetry of extracellular currents is distorted by these conductivity barriers. Tissue permeability can be considered constant in living tissue. Studies of the heads of piglets, which have a gyrencephalic brain similar to the human brain, show that the bone is of almost no importance in the distribution of the magnetic field. A detailed analysis provides evidence that only small changes in the magnetic field occur if the current dipole is located deep within the brain, causing weakening of the amplitude if the bone is removed (Okada et al., 1999).

Anisotropy

Each intracellular current is accompanied by an extracellular current. As mentioned above, extracellular current in a uniform conducting medium is distributed homogeneously over a large area. A more detailed analysis of tissue configuration provides evidence that the extracellular space is far from being uniform (Rice et al., 1993). For example, conductivity depends on the direction of the current, and thus there is anisotropy of conductivity. This is caused by the arrangement of myelinated and nonmyelinated neuronal fibers, reducing conductivity perpendicular to the fibers in contrast to conductivity parallel to the fibers. Likewise, conductivity in gray matter is influenced according to the parallel orientation of pyramidal cells, and apical dendrites collected into bundles perpendicular to the cortical surface. These structures cause a preferred direction of the extracellular ion current. Furthermore, the amount of anisotropy varies between cortical regions. For example, it is less significant in cortical regions with a high number of granular cells in comparison to the regions with many pyramidal cells. The influence of anisotropy on the magnetic field detected on the outside of the brain has been investigated extensively (Haueisen et al., 2002).

2.4.2.5 Pathophysiology

Damage of neuronal tissue, for example in the case of brain infarction, is accompanied by numerous changes causing magnetic fields.

Anoxic Depolarization

Anoxic depolarization results from a dramatic reduction in oxygen supply, such that the energetic cell metabolism is strongly reduced. This causes cessation of Na-K-ATPase and the cells depolarize. The depolarization triggers the opening of sodium channels, there following an influx of this ion and a near-simultaneous efflux of potassium.

These processes are the cause of magnetic field changes, and are in part reversible with resupply of oxygen and if the cells are not irreversibly damaged. These magnetic field shifts occur simultaneously with changes of the DC-electrocorticogram (Takanashi et al., 1991). Because the electric changes occur simultaneously over the whole cortex, it is supposed that differences in the amplitude of cell depolarization may cause ion movements responsible for the magnetic field measured on the outside of the brain.

Periinfarct Depolarization

Changes in the electric potential similar to those after a localized KCl application to the cortical surface can be detected after brain infarction. They propagate slowly over great distance and involve almost all cortical areas of one hemisphere; they are similar to spreading depression. Changes of long duration can be detected in the magnetic field – sometimes longer than minutes (Chen et al., 1992).

The causes and detailed mechanisms of these long-lasting depolarizations remain unclear. However, it has been shown that long-lasting increases in extracellular potassium concentrations, which are buffered in part by glia cells, simultaneously depolarize neurons. The depolarization does not involve all structures of the neurons simultaneously, and thus an intracellular current may result. A similar phenomenon appears to be the basis for the development of a migraine, which however does not result from cell damage (Bowyer et al., 2001).

Injury Currents

If the energy supply to cells decreases to below a critical threshold, then the cells are unable to ensure the integrity of the cell structure. Similarly to anoxic depolarization, this causes an influx of sodium and efflux of potassium, leading to a dramatic increase in the extracellular potassium concentration. Irrespective of whether this high extracellular potassium concentration initiates the depolarization of neighboring neurons, there is a strong potassium ion gradient within the extracellular space. A current emerges in the direction of this ion gradient. Since the current is equal in all directions the resulting magnetic fields cancel each other; however, if there is an asymmetry, the magnetic field can be measured on the outside of the tissue. This has been shown by elegant investigations of injuries in muscle and nerve tissues (Carbon et al., 2004). It seems possible that damage within the brain may also cause slow magnetic field changes.

2.4.2.6
Final Remarks

During recent years, knowledge of the complex mechanisms of magnetic field generation by the brain has improved dramatically. In fact, it may soon be possible to not only exactly localize active brain regions, but also to characterize the basic functional processes using MEG. However, the sensitivity and spatial resolution of sensors require further improvement, and more systematic investigations are needed of the relevance of cell functions in magnetic field generation on the outside of the brain.

2.4.3 Analysis of Neuromagnetic Fields

2.4.3.1 Signal Analysis

Electrophysiological brain signals as are employed in MEG or EEG reflect the superposition of the magnetic or electric fields caused by a great number of simultaneous intracranial processes. Some of these are not related to any apparent external event (such as the presentation of a stimulus or the execution of a movement), giving rise to *spontaneous* activity. Others are related (time-locked) to such events, causing *event-related* activity. Additionally, signals can be divided into *transient* (singular deflections) and *oscillatory* (repetitive deflections) activities. Spontaneous oscillatory activity was among the first recorded electrophysiological signals from the brain (Berger, 1929). Brain oscillations are divided according to their frequency into various bands, which are labeled with Greek letters following the history of their discovery (e.g., α, β, γ, δ, and θ waves), and cover the frequency range of about 2 to 100 Hz. [There are also very high frequencies (ca. 600 Hz) in MEG signals that are probably due to coherent volleys of action potentials; e.g., Curio et al., 1997.] Some of these rhythms seem to be associated with the inactivity (idling) of neuronal populations in primary cortical areas. MEG has contributed much to the localization of the sources of these oscillations. The α-rhythm (8–12 Hz) is most prominent over parietal and occipital parts of the skull, and is reduced by opening the eyes (the Berger effect) as well as by visual stimuli and visual imagery (see e.g., Klimesch, 1999). This is thought to reflect idling of the visual areas. The idling of the somatomotor cortex seems to be the cause of the μ-rhythm, which contains two frequency components, one around 10 Hz and another around 20 Hz. Both components differ in their exact origin and in the way they are suppressed by actual and planned movements (Pfurtscheller, 1989; Salmelin and Hari, 1994; Salmelin et al., 1995a). Finally, the τ-rhythm (8–12 Hz) probably reflects the idling of the auditory cortex (Hari and Salmelin, 1997).

Other brain rhythms do not seem to be associated to idling states, but rather to active processes in the brain. They include the frontal β-rhythm, the θ-rhythm and the γ-rhythm. The θ-waves (4–8 Hz) appear to originate from the hippocampus and reflect working memory processes (e.g., Klimesch, 1999). Oscillatory activity in the γ frequency band has received a great deal of attention in recent years. It seems that neuronal assemblies representing different parts of the same object bind together by synchronous firing in the γ frequency range, as has been shown in animal models (e.g., Gray et al., 1989) and in humans (e.g., Tallon-Baudry et al., 1996, 1997; Herrmann and Mecklinger, 2000). Hence, these oscillations most probably play a fundamental role in important cognitive faculties such as perception and memory. The above-mentioned fact that the so-called idling rhythms are suppressed by primary sensory or motor activity leads to the possibility of measuring cortical activity indirectly. Techniques such as event-related synchronization/desynchronization (Pfurtscheller and Aranibar, 1977), temporal spectral evolution

(Salmelin et al., 1995b), event-related spectral perturbation (Makeig, 1993), and task-related power increase/decrease (Gerloff et al., 1998) offer the possibility of measuring event-related activity without the need to define the precise time point of the event.

All of these methods involve a time-frequency transformation and then use the spectral power alone (without phase) for averaging. This has the effect that any small time jitter between the oscillatory event and the related external event (e.g., stimulus) would not lead to cancellation of the average signal. Such activity, which is grossly time-locked but not precisely phase-locked to the event, is called ''induced activity'', in contrast to ''evoked activity'', which is strictly phase-locked. Popular time-frequency transformations used for the analysis of brain signals include for example simple band pass filtering with subsequent rectification and smoothing (Pfurtscheller and Aranibar, 1977), the wavelet transform, and computation of the amplitude envelope using the Hilbert transform (Clochon et al., 1996; Knösche and Bastiaansen, 2002). In many cases, a spatial transformation is also used in order to more accurately reflect the spatial structure and the localizations of the underlying neuronal populations. This can involve relatively simple procedures working on the sensor space, such as the EEG surface Laplacian (Hjorth, 1975) and the MEG tangential derivative (Bastiaansen and Knösche, 2000), as well as more sophisticated techniques based on source reconstruction algorithms (see next section). In Figure 2.43 it is demonstrated how ipsilateral and contralateral motor activity due to self-paced finger movements can be dissociated by using the MEG tangential derivative in conjunction with event-related desynchronization/synchronization (ERD/ERS).

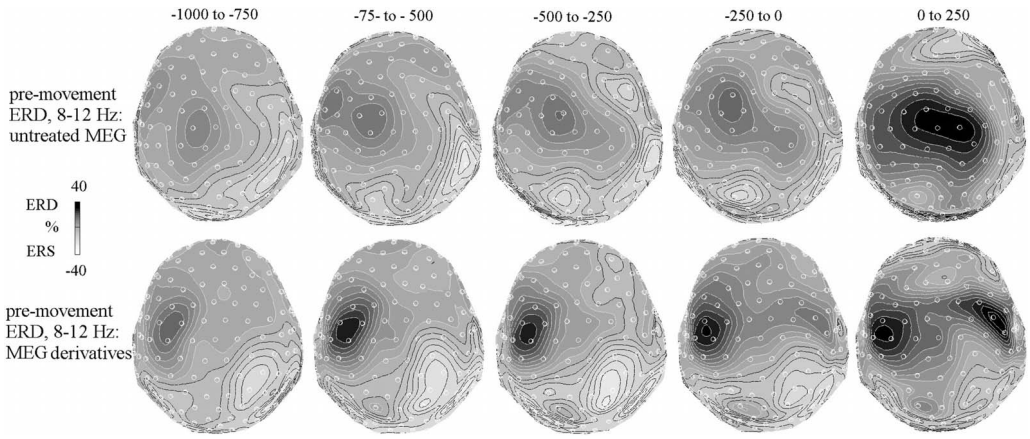

Fig. 2.43. Grand averages of pre-movement event-related desynchronization (ERD) in the 8- to 12-Hz frequency band, on untreated MEG and on MEG derivatives, elicited by self-paced finger movements. Dark: ERD (power decrease), light: ERS (power increase). (Adapted from Bastiaansen and Knösche, 2000).

The great complexity of the neural system with its many feedforward and feedback loops imposes a large degree of nonlinearity onto its behavior and the resulting brain signals. Hence, it has been proposed to employ mathematical tools based on chaos theory for the analysis of EEG and MEG signals (Elbert et al., 1994). Techniques relying on the largest *Lyapunov exponent* or the *fractal dimension* of a signal can be used to characterize the degree of complexity of the underlying brain system. Such methods are especially promising for the assessment of (especially pathological) brain states.

In brain science, transient changes in relation to externally observable events – so-called *event-related potentials* or *event-related fields* – are probably amongst the most widely used features of EEG and MEG. Since these signals are usually hidden in a stream of spontaneous activity with similar or larger amplitude, they are extracted by averaging techniques. For this purpose, the event is repeated many times and the signal is recorded during a fixed time window (epoch) around each event. Averaging the epochs tends to preserve the event-related signal, while at the same time it reduces the level of random background activity. The validity of the method relies on two main assumptions: (1) that the event-related signal is stationary, and (2) that the noise is random and completely uncorrelated to the event. Under these assumptions, the signal-to-noise ratio (variance of signal divided by variance of noise) improves by the square root of the number of epochs. In reality, both assumptions are not strictly true, leading to an imperfect extraction of the event-related signal.

Before averaging, it is advisable to improve the quality of the signal as much as possible. Artifacts, caused by electrical activity of the eyes, muscles or the heart, must be identified and either be removed (by rejecting the contaminated epochs) or corrected. Artifact correction procedures have been proposed based on dipole modeling (Berg and Scherg, 1994) and linear regression (Croft and Barry, 2000). However, since artifacts and signals cannot be assumed to be mutually orthogonal neither in the temporal nor in the spatial dimension, it is always likely that not only the artifact, but also the signal is affected by the correction procedure. Hence, such techniques should be used only if the number of epochs is inherently limited by the experiment and simple rejection of contaminated epochs would result in too few epochs for an acceptable signal-to-noise ratio. Temporal and spatial filtering techniques exploit the fact that the targeted event-related signals often contain (partially) different temporal and spatial frequencies from the spontaneous background activity. Digital temporal filters are usually employed to remove high-frequency noise as well as irrelevant slow drifts from the EEG or MEG signal. Spatial filters in the sensor space (not to be confused with spatial filters in the source space) normally suppress low spatial frequencies. For EEG, the surface Laplacian (Hjorth, 1975), based on the second derivative of the potential with respect to the scalp surface, provides such a filter. However, since high spatial frequencies are emphasized the method is quite sensitive to small errors (e.g., in electrode position) as well as to noise in the data, and requires a relatively large number of electrodes ($>$100; Junghöfer et al., 1997). For MEG measured with magnetometers or axial gradiometers, the tangential derivative (computed as the magnitude of the tangential

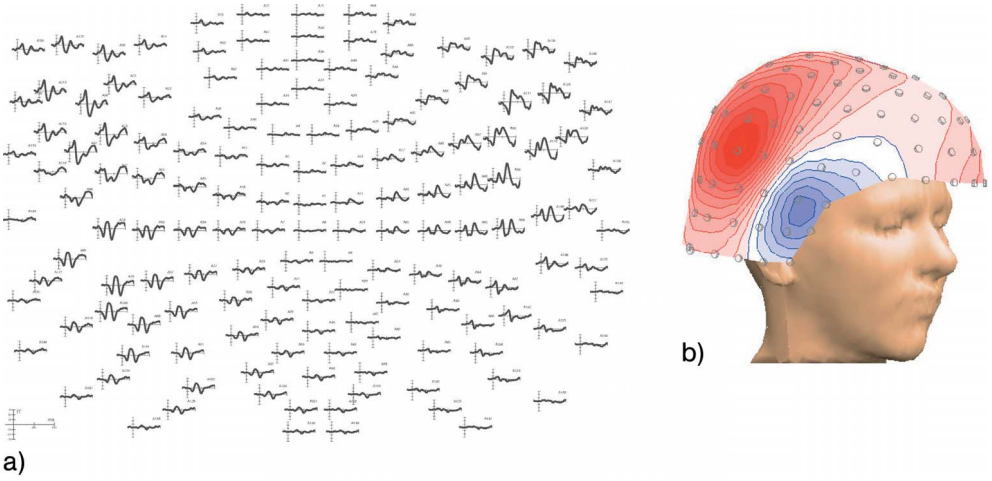

Fig. 2.44. Display of MEG data. (a) Time courses of the 148 channels of an auditory evoked field, arranged on the flattened geometry of the helmet-shaped sensor array of a MAGNES WHS-2500 magnetometer system (4D Neuroimaging, San Diego, CA, USA). (b) Three-dimensional color-contour map of a similar data set at the peak of the P2m component (210 ms after tone onset). Red denotes field lines directed away from the head surface.

gradient vector) produces a signal that has its maxima near the actual sources (Bastiaansen and Knösche, 2000).

Averaged EEG or MEG signals can be displayed as time courses and as maps. Time courses highlight the temporal evolvement of the signal at each sensor (Fig. 2.44a), while maps show the distribution of the signal over the scalp surface (EEG) or the sensor surface (MEG) at one particularly latency, usually by means of contour lines and color shading (Fig. 2.44b).

As noted previously, EEG or MEG signals typically represent the superposition of the effects of a number of brain processes, which we might call functional components. It is therefore an important goal of EEG/MEG analysis to disentangle these components. Ideally, a component forms a functional entity – that is, it reacts as a whole to relevant experimental manipulations. It should be characterized by a defined neuronal network (fixed topography) and a typical time course. Often, components are identified by visual inspection as positive- or negative-going waves in the signal that can be manipulated independently by experimental parameters. Here, the computation of difference signals between experimental conditions and the identification of peaks and zero-crossings plays an important role (see Fig. 2.45).

Typical decomposition algorithms used in EEG/MEG analysis aim at components, which are characterized by a spatial distribution (topography), which is invariant in time, and a time course, which is invariant in space (except for a scaling factor). Such components are suited to represent the activity of a particular neuro-

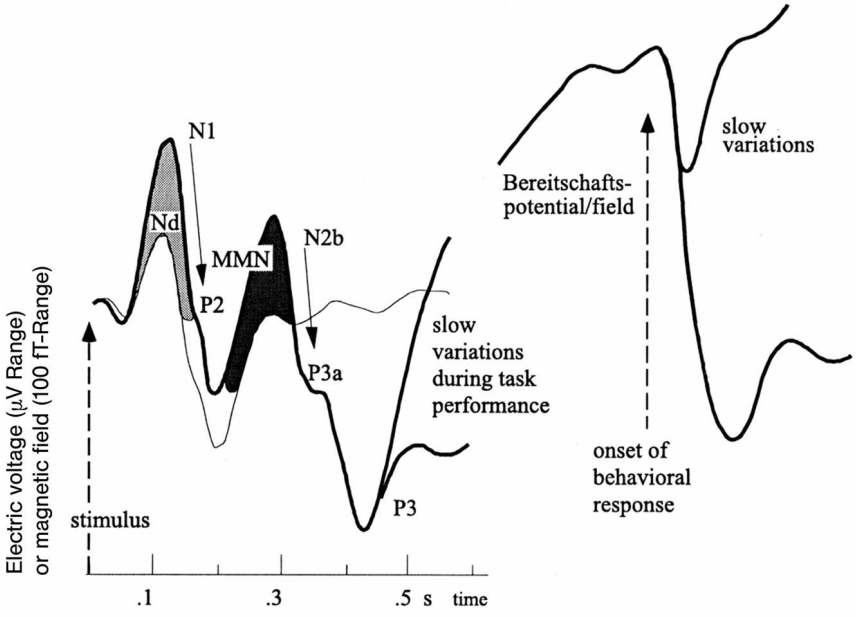

Fig. 2.45. Schematic categorization of endogenous components of event-related potentials/fields in response to a stimulus (left) and prior to a response (right). The Nd depends on attention processes; the MMN (mismatch negativity) appears, if some repetitive aspect of the stimulus is violated. Relevant stimuli that interrupt ongoing processing can give rise to a P300. Preparation for motor responses is reflected by slow fluctuations (Bereitschaftspotential/field).

nal network with varying activity in time. The definition of the actual decomposition requires additional constraints on the shape of or the mutual relationships between the topographies and/or the time courses. Such constraints can be imposed by model assumptions, for example in the spatio-temporal dipole model (Scherg and Berg, 1991), or by spatial or temporal templates extracted from other experiments or experimental conditions, where the respective component is (assumed to be) present in relative isolation. Principal component analysis (PCA) decomposes spatio-temporal data sets into mutually orthogonal components (e.g., Mosher et al., 1992). Alternatively, independent component analysis (ICA) uses statistical independence as criterion to separate functional components (e.g., Wübbeler et al., 2000).

2.4.3.2 Modeling and Source Reconstruction

It is clear that brain signals obtained with EEG and MEG contain information on the spatial distribution of the underlying generators throughout the brain, though this information is, as will be discussed below, incomplete. There is a great variety

of methods to extract this information by solving the so-called neuroelectromagnetic inverse problem. This problem can be split into two relatively independent sub-problems: the *forward problem*, and the actual *inverse problem*. The solution of the neuroelectromagnetic forward problem predicts the recorded EEG or MEG data, given a certain set of neuronal generators (sources) as well as certain physical properties of the surrounding head tissue and the measurement apparatus. The solution of the inverse problem is based on the forward solution and attempts to reconstruct the sources from the actually measured signals.

The solution of the forward problem requires a great deal of modeling. First, a model of the sources must be built. In reality, intracranial electrical activity is immensely complex and would need a virtually infinite number of parameters for a complete description. For mathematical treatment, especially with regard to the inverse problem, it is necessary to simplify this description and to reduce the number of free parameters. With few exceptions, all such models are based on a discretization into current dipoles, which one could call the atoms of source modeling. A current dipole adequately describes the current flow in a small volume element (''small'' as compared to the distance between sources and sensors) and is characterized by position (three parameters), direction (two angles) and strength (one parameter). Direction and strength are often combined to a three-dimensional moment vector. Typical strength values are around 20 nAm, accounting for about one million single postsynaptic potentials (Hämäläinen et al., 1993). A characteristic MEG pattern generated by a current dipole is shown in Figure 2.44. More complex source configurations can be described as a linear combination of many dipolar elements. Hence, it is sufficient to formulate solutions to the forward model for such a dipolar source. By increasing the number of dipolar elements, one can in principle reach any level of accuracy. It should, however, be mentioned that there are alternatives based on multipole expansions of the scalar electrical or the magnetic vector potential (e.g., Katila, 1983; Nolte and Curio, 2000). With the current dipole model as a basis, one can easily derive equations for the magnetic induction and the electric potential in an infinitely extended, isotropic, and homogeneous conductive medium from the set of Maxwell's Equations.

$$\vec{B}_{\infty}(\vec{r}) = \frac{\mu_0}{4\pi}\sum_{i=1}^{N}\frac{\vec{q}_i \times (\vec{r} - \vec{r}_{q_i})}{|\vec{r} - \vec{r}_{q_i}|^3} \qquad V_{\infty}(\vec{r}) = \frac{1}{4\pi\sigma}\sum_{i=1}^{N}\frac{\vec{q}_i \cdot (\vec{r} - \vec{r}_{q_i})}{|\vec{r} - \vec{r}_{q_i}|^3} \tag{2.10}$$

where B is magnetic induction, V is electrical potential, μ_0 is magnetic permeability (constant), σ is the conductivity of the medium, N is the number of dipoles, q_i is the moment of the i^{th} current dipole, r is the location of measurement, and r_{qi} the location of i^{th} dipole.

These equations form the basis for most solutions of the forward problem. We will now consider how to incorporate models for the measuring device and for the head tissue into these equations. The transformation from the electrical potential or the magnetic induction provided by Eqs. (2.10) to the actual output of the measurement device can normally be realized by simple calculations – that is, subtrac-

tion of potential at the reference electrode for EEG and integration over the coil surface, as well as subtraction according to gradiometer scheme for MEG. More elaborate modeling of the sensor properties is usually not necessary. The bulk of the efforts regarding the forward solution goes into modeling the tissues of the head, resulting in substantial alteration of the simple relationships described in Eqs. (2.10). The head can be seen as an inhomogeneous and anisotropic volume conductor surrounding the generators of EEG and MEG. This conductive medium makes the measurement of EEG only possible in the first place by providing the electrical connection between the active neurons and the head surface electrodes. However, how the primary currents related to neuronal activity translate into voltage drops between the electrodes depends upon the precise conductivity profile of the head in a complicated way. In particular, the low-conducting skull exercises a major influence. For MEG, the impact of the head tissue is smaller, since magnetic fields generated by the primary currents can be measured directly and undistorted by the sensors. However, these signals are overlaid by the magnetic fields caused by the Ohmic return currents. Hence, the three-dimensional distribution of current flow in the head must be modeled on the basis of Maxwell's Equations. Fortunately, one can assume quasi-stationarity – that is, the inductive and capacitive effects can be neglected (Plonsey and Heppner, 1967), thereby simplifying the matter substantially.

Head modeling crucially depends on two factors: (1) available information on the conductivity profile of the head; and (2) numerical techniques (as well as the necessary computer power) to use this information. The first factor is very often the limiting one: if, for example, there is no reliable information on the conductivity tensor at every point of the head, a sophisticated modeling technique, which could use this fine-grained information, is no better (or even worse) than a simple model assuming homogeneous conductivity.

Available techniques range from very simple to quite complex (for an overview, see e.g. Zanow, 1997). The actual choice depends on the accuracy requirements of the problem, the availability of anatomical information (e.g., individual MRI), certain practicability issues [e.g., the *finite element method* (FEM) is computationally very costly and cannot always be used], and modeling peculiarities (e.g., patients with holes in the skull or infants with open sutures). Generally, the modeling of MEG signals can be solely based on the interior of the skull, while for EEG the skull itself and the extracranial tissues must also be considered (Hämäläinen and Sarvas, 1987).

In a first approximation, one could consider the human head as a sphere. In this case, it is possible to formulate analytical solutions for the neuroelectromagnetic forward problem. For the magnetic case, the solution has been given by Sarvas (1987). Interestingly, it transpires that the radial conductivity profile – for example, the exact size of the brain – does not matter at all in this simple model. For the electrical case, a solution based on Legendre polynomials has been provided by de Munck (1989).

Currently, the simple sphere models are increasingly replaced by numerical models that are better capable of accounting for the actual shape of the main

inter-tissue boundaries within the head, such as scalp surface, inside and outside of the skull, and brain surface. Such models can be based on either standardized or individual heads. The most widespread technique is the *boundary element method* (BEM; Hämäläinen and Sarvas, 1987). Here, the head is divided into major compartments, each of which is assumed to be homogeneous and isotropic. The boundaries between the compartments are discretized into so-called boundary elements, mostly triangles. The conductivities of the compartments are set to approximate standard values. The shape information is usually won from magnetic resonance images). The BEM describes the head tissues by a piece-wise linear and isotropic model, thereby accounting for the major and most influential tissue features, such as the boundaries of the skull. For a complete description of the conductivity profile of the head, however, one would need a technique that can assign to every point in the head not only a scalar conductivity value, but also a conductivity tensor, which accounts for the direction-dependent properties of the material. The FEM is just such a technique (e.g., Buchner et al., 1997; Haueisen et al., 1997), but although it is very promising and will certainly dominate the future, there are still some problems that limit its applicability. The gravest one of these is the general lack of accurate conductivity information on a voxel basis. Diffusion-weighted MRI techniques (diffusion tensor imaging, DTI) seem to promise some remedy to this problem. This technique measures the direction-dependent water diffusivity, which is of course related to electrical conductivity. Attempts to derive a conductivity tensor from DTI data have been made (Tuch et al., 2001). A second obstacle for the more widespread use of FEM has been the relatively great computational effort. This especially limits its usefulness in the framework of the inverse solution, where the forward problem must normally be solved many times. Recently, techniques have been developed to speed up the method to such an extent that it becomes interesting for the solution of the inverse problem (Wolters et al., 2004). Finally, the correct representation of current sources in FEM models has turned out to be a substantial challenge (Schimpf et al., 2002).

The forward problem of neuroelectromagnetism has a unique solution. Provided that we know the three-dimensional distributions of source current density and conductivity (as tensors) with absolute precision, we also know the measured EEG and MEG. For the inverse problem, the situation is less favorable. For any given set of EEG or MEG measurements, there are an infinite number of possible source configurations that could have given rise to these signals, no matter how many sensors we use and how accurately we measure. So, which of these solutions should be preferred? The answer to this question is difficult and should rely on two fundamental principles of science – *Occam's razor* and *Bayes' law* on conditional probabilities. The law of Bayes allows incorporating additional knowledge, for example from other imaging modalities (e.g., fMRI) or from anatomical constraints, into the solution, thus reducing the degree of underdetermination of the inverse problem. Occam's razor, in contrast, is the preferred way to deal with the remaining uncertainty. It states, that from all equally probable solutions the simplest one should be preferred (William of Occam: *pluralitas non est ponenda sine necessitate* [complexity should not be assumed unnecessarily]; see Wildner,

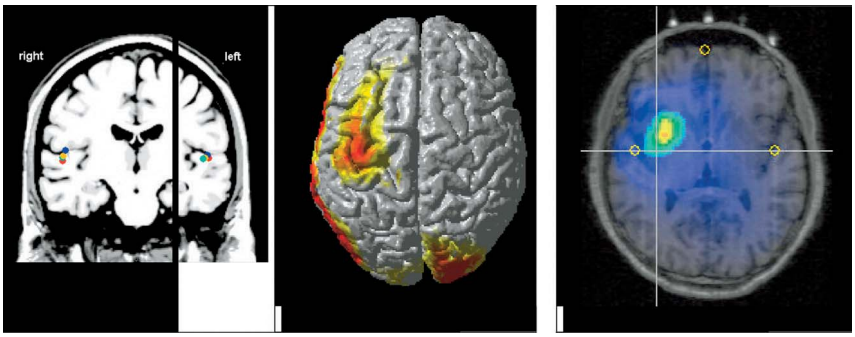

Fig. 2.46. Some examples for inverse solutions based on MEG and EEG data. Left: Source locations in the auditory cortex found by spatio-temporal dipole modeling of MEG data from an auditory mismatch paradigm (Knösche et al., 2002). Middle: MEG-based brain surface current density (BSCD) reconstructions of motor activity in musicians listening to piano music (Haueisen and Knösche, 2001). Right: Multiple signal classification (MUSIC) reconstruction based on an averaged epileptic spike in EEG (T.R. Knösche, unpublished data).

1999). In common terms, this principle forbids filling the white spots on the map with fantastic landscapes.

The techniques available to solve the *inverse problem* are both numerous and diverse (for some examples, see Fig. 2.46). The choice of a particular method depends for example on the nature of the expected results (e.g., few focal sources or extended widespread activity) and the availability of additional information (e.g., locations of activated areas from fMRI, shape of individual cortical sheet). In the following section we will discuss some families of inverse algorithms, especially with respect to their implicit assumptions, their possibilities to incorporate additional information, their stability in the presence of noise, and their particular suitedness for certain types of MEG activity. Comparative evaluations of different methods can be found elsewhere (e.g., Yao and Dewald, 2005; Stenbacka et al., 2002).

The spatio-temporal multiple dipole model (Scherg and Berg, 1991) is one of the most popular approaches. It is based on rather strong assumptions: the generators of the MEG or EEG are described by a small number of focal centers of activity, which remain active for some time. If these assumptions are physiologically adequate and if the signal-to-noise ratio is high, this model offers excellent data reduction: for example, the time courses of perhaps 148 MEG channels are reduced to the time courses, positions, and orientations of two or three current dipoles. There are three basic models for the temporal behavior of the dipole parameters. The *moving dipole model* imposes no constraints – the strengths, orientations, and positions are independent between different latencies. The *fixed dipole model* assumes that positions and orientations remain constant over the entire period of analysis, while only the strengths may change. This model is based on the notion that the neuronal populations, which are represented by the dipoles, do not move or rotate

after all. However, due to the limited spatial resolution, a dipole may represent several different generators with almost the same positions, but separate orientations (e.g., around a sulcus). This situation is accounted for by the *rotating dipole model*, which assumes stationary dipole positions, but time-variant orientations. The measured MEG or EEG values are linearly dependent upon the dipole strengths, but they depend nonlinearly on the positions (and, for the fixed model, also the orientations) of the dipoles. This leads to two nested optimization problems: for any given leadfield matrix L, the source strengths S can be determined from the measured values M by linear inverse techniques. The leadfield matrix L, in turn, depends on positions (and orientations) of the dipoles in a nonlinear manner [see Eqs. (2.10)]. This requires a nonlinear iterative search procedure (e.g., using the Simplex or the Marquardt algorithm), where each forward calculation involves the solution of the embedded linear problem.

$$M = L(\bar{r}) \cdot S \tag{2.11}$$

Here, M is the matrix containing measure values, with a row per channel and a column per time sample, S is the matrix containing source strength, with a row per dipole (or dipole direction for the rotating dipole model) and a column per time sample, and L is the lead field matrix, containing the forward solution for every combination of dipoles and measurement channels, depending on dipole positions r (and orientations for the fixed model).

An important problem associated with dipole solutions is that we must make a choice on the number of sources in advance. This is not trivial, since overmodeling (too many dipoles) may result in instable models, which are excessively influenced by noise. Information criteria are one way to achieve an optimal compromise between model complexity (number of dipoles) and data explanation (Knösche et al., 1998). The problem of noise distorting dipole solutions has been tackled by including the noise into the model (e.g., de Munck et al., 2002).

Additional knowledge, for example from fMRI experiments, can be imposed as constraints on the free dipole parameters. The limits and specific problems associated with the combination of MEG dipole fit and fMRI have been addressed (e.g., Fujimaki et al., 2002). The use of simultaneous recordings of EEG and MEG offers another potential possibility of narrowing the information gap in the inverse problem (e.g., Fuchs et al., 1998). Finally, it should be emphasized that the point-like nature of dipole fit solutions might pretend a degree of accuracy that is not real. Fuchs et al. (2004) provide methods to attach confidence volumes to the dipole positions, thus drawing a more realistic picture of the solution.

There are a number of possible reasons, why the spatio-temporal dipole model might not be appropriate. For example, the focality assumption could be violated to an intolerable extent, or the signal-to-noise ratio could be too low. This is often the case for brain activity associated with higher cognitive functions. In such cases, methods that reconstruct a distributed current source density distribution can be applied. They deliver blurred pictures of the brain activity throughout a certain region of interest, which can be for example the entire brain volume, the brain

surface, or the surface of the cortical sheet. They are usually based on the principle of linear estimation. The predefined region of interest is discretized into suitably small elements, each of which is characterized by a set of two or three current dipoles. The positions of these dipoles are fixed to the element center, while their orientations are chosen in such a way that they span the space of possible current flow directions. (In the simplest case, three orthogonal dipoles allow for all current directions. In other cases, only currents tangential to the brain surface (MEG) or those perpendicular to the cortical sheet might be allowed.) The strengths of all these dipoles relate linearly to the measured MEG (or EEG) values (see Eq. (2.11), with L being fixed). Since Eq. (2.11) is generally underdetermined – that is, there are more dipole strengths to reconstruct, than there are measured values – so-called minimum norm least squares (MNLS; Hämäläinen and Ilmoniemi, 1994) solutions are computed. These select, out of all possible solutions, the one with a minimum $L2$ norm of some linear transformation of the solution vector. (If not the $L2$ norm, but a different norm (e.g., $L1$) is minimized, the problem becomes nonlinear and no direct inversion can be formulated (see e.g., Fuchs et al., 1999). Such norms can often deliver a less blurred picture of the brain activity. It is, however, not clear, if this focalization yields any extra information.) The general form of the solution is:

$$S = WL^T(LWL^T)^+ \cdot M \tag{2.12}$$

where W is the weighting matrix, weights the column space of L; $(\cdot)^+$ denotes the regularized inverse.

There are several theoretical approaches that all lead in principle to the above result (all following the idea of Occam's razor):

1. The null space approach, requiring the projection of the solution onto the null space of L to be zero.
2. The minimum norm approach, selecting the solution with the shortest Euclidean norm.
3. The maximum likelihood approach, singling out the most likely of all possible solutions. A rigid formulation of the maximum likelihood approach based on the Bayesian formalism is the maximum a posteriori (MAP) estimator (Baillet and Garnero, 1997). It allows the convenient incorporation of any a priori knowledge.

The various realizations of the above algorithm differ in three ways:

a) the collection of dipoles the matrix L is based on,
b) the weighting matrix W,
c) the method to compute the inverse of the usually ill-posed matrix (LWL^T).

In this scheme, point (a) serves the a priori limitation the space of possible solutions, point (b) determines, how Occam's razor works (dealing with the informa-

tion deficit) and how additional information/assumptions are included, and point (c) is concerned with numerical stability and depends on the noise.

A very useful concept for the assessment of the properties of an inverse estimator is the resolution matrix R.

$$\hat{S} = E \cdot M = E \cdot L \cdot S = R \cdot S \tag{2.13}$$

This maps the hypothetical real source S to the solution $\hat{S}$ of the inverse estimator E [see Eq. (2.13)] – that is, each column of R contains the response of the estimator to a point source at the respective location. The ideal resolution matrix would be unity; the degree of deviation from this ideal quantifies the degree of blurring associated with the estimator. Hence, one obvious approach for constructing the inverse estimator is to minimize the deviation of the resolution matrix from unity (Backus and Gilbert, 1968; Grave de Peralta-Menendez and Gonzalez-Andino, 1998).

In the following, we will briefly present some of the most widespread variations of this general principle. A very informative treatment of the principal possibilities and limitations of the linear inverse is provided by Hauk (2004). Since there has been much debate on the best way to implement the linear inverse, it should be pointed out that each solution that is compatible with both the EEG/MEG data and all available constraints and additional information is equally valid, no matter whether we like the results or not. There is no way to further distinguish between "better" and "worse" solutions.

The brain surface current density (BSCD; Knösche et al., 1996; see Fig. 2.46) reconstructs a blurred picture of the brain activity, which is projected onto the brain surface. The method is robust and does not need any individual anatomical information. The depth information is sacrificed on purpose, because it is especially ill-determined by the data alone, if no plausible assumption on the shape of the sources (e.g., focality) is possible (see also Fuchs et al., 1999). Magnetic field tomography (MFT) is a technique based on MNLS estimates in three dimensions, where the typical bias towards superficial sources is countered by a suitable weighting function (Ioannides et al., 1995). Low-resolution electromagnetic tomography (LORETA; Pascual-Marqui et al., 1994; Fig. 2.46) is based on the minimization of the norm of the second spatial derivative of the solution, rather than of the solution itself. In this way, the solutions with the lowest spatial curvature are selected. Standardized low-resolution brain electromagnetic tomography (sLORETA) applies location-wise inverse weighting with the estimated variance to a classical MNLS solution (Pascual-Marqui, 2002; Wagner et al., 2004).

Another class of techniques comprises the so-called *scanning methods*, also referred to as *spatial filters* or *beamformers*. They are not true inverse algorithms, as they do not reconstruct the brain activity underlying a particular measurement as a whole (Vrba and Robinson, 2001). Instead, they consider each point or region in the brain separately and assess the plausibility of this point/region being a contributor to the measured activity. Instead of one possible generator distribution, which can explain the measured data, one obtains a collection of possible con-

tributors – that is, the description of an entire class of solutions. This allows the extraction of sensible information on the localization of the generators, even if true inverse methods fail. Scanning methods include for example the synthetic aperture magnetometry (SAM; Vrba and Robinson, 2001) and the multiple signal classification (MUSIC; Mosher et al., 1992).

2.4.4 The Investigation of the Primary Sensory and Motor Systems

2.4.4.1 Introduction

For a variety of reasons, primary sensory and motor systems were investigated long before the advent of magnetic recordings. Perhaps the most important motivation for such investigations has been the study of the normal function of these systems. Once information is available about the normal function, dysfunctions can be assessed much more easily and clinical applications devised (see Section 2.4.6). Moreover, the analysis of primary systems can yield important information for the investigation of higher cognitive functions. Even technical applications such as robotics might benefit from knowledge about the function of primary systems in man. One of the often-stated advantages of the primary systems as an object of investigation is that it has assumedly a simpler structure and is therefore easier to investigate than other systems. With the introduction of MEG, source localization gained much more importance in the analysis of primary systems, and many new aspects have been revealed through MEG studies.

2.4.4.2 Somatosensory System

Following the early somatosensory evoked field (SEF) studies (Brenner et al., 1978), numerous aspects have been investigated (for reviews, see Hari and Forss, 1999; Kakigi et al., 2000). Techniques to evoke somatosensory activity include electric, tactile, and laser stimulation, this being applied primarily to the skin, or alternatively inside the body, perhaps as electric tongue stimulation (Karhu et al., 1991). The most often-applied stimulation technique (also used in neurological diagnostics) is cutaneous electrical stimulation of peripheral nerves (e.g., the median nerve at the wrist); the measured spatial-temporal magnetic data from such an experiment is shown in Figure 2.47. One outstanding property of the first cortical component (N20) is that it is completely exogenous (it is not influenced by subjective factors such as attention), and it can therefore be used as a reference in more complex paradigms.

Source localization with the help of equivalent current dipoles shows that the activity in the contralateral primary somatosensory cortex SI arises mainly from Brodmann areas 3b and 1 (Wood et al., 1985), with a clear somatotopical represen-

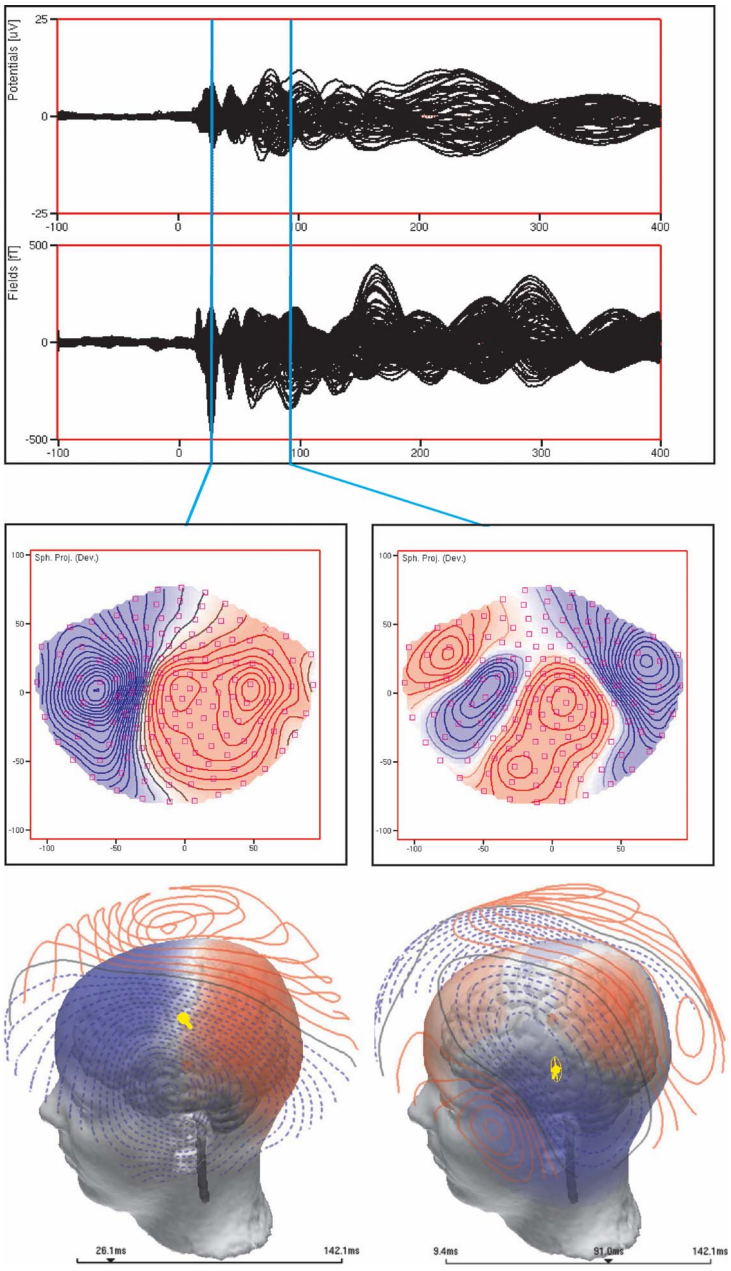

Fig. 2.47. Somatosensory evoked field (SEF) time traces of 148 channels (top), magnetic fields maps at 26.1 and 91 ms after stimulation (middle), and localized dipolar sources (in yellow, with confidence ellipsoids) in the primary (SI, left column) and secondary (SII, right column) somatosensory cortex and in a 3D view (bottom). (Material provided by R. Huonker).

tation of different body parts (Okada et al., 1984; Suk et al., 1991; Gallen et al., 1994). Further processing is undertaken in the bilaterally activated secondary somatosensory cortex SII, the posterior parietal cortex, central mesial cortex, and the frontal lobe (Mauguiere et al., 1997; Hari and Forss, 1999). An oscillatory brain activity with a mean frequency of ca. 650 Hz is overlaying the initial low-frequency (up to 250 Hz) cortical responses at latencies of 18 to 30 ms after stimulus (N20, P25) (Curio et al., 1994). Although the fast oscillatory activity is located in the same cortical areas (3b and 1), it is functionally different from the low-frequency components (e.g., Curio, 2000; Hashimoto, 2000; Haueisen et al., 2001).

2.4.4.3 Auditory System

Since the initial studies during in the late 1970s (Reite et al., 1978), auditory evoked fields (AEF) have been investigated intensively (for reviews, see Jacobson, 1994; Näätänen and Winkler, 1999; Yvert et al., 2001). The functional analysis of the tonotopy of the human auditory cortex was investigated at an early stage by Romani et al. (1982), and later by Pantev et al. (1988). Both groups used sine-wave tones of different frequencies as stimuli. Romani and colleagues analyzed the steady-state responses, whereas Pantev's group investigated the 100-ms component of the responses to tone-bursts of 500-ms duration. The corresponding source localization for the evoked magnetic fields showed the presumed tonotopic organization: for lower frequencies the equivalent current dipoles were found more superficially than for higher frequencies.

Auditory evoked components are commonly divided into early (ELC: up to 10 ms), middle (MLC: 10–70 ms), and long latency components (LLC: 70–250 ms). They can be evoked by clicks, tones, or tone bursts, as well as by compound sounds. While the ELCs are assumed to be generated in subcortical areas of auditory processing and thus less suitable for MEG investigations, the MLCs include subcortical and cortical sources (e.g., Heschel's gyri, supratemporal gyrus), and the LLCs are mainly generated in cortical regions. The localization in the primary auditory cortex for the N100 latency of a healthy volunteer is shown in Figure 2.48.

2.4.4.4 Visual System

The first magnetic field recordings after visual stimulation were reported as early as the mid-1970s (Brenner et al., 1975; Cohen, 1975). Stimulation techniques include pattern reversal (e.g., checker-board stimulation) or pattern on/off, single or multi-focal flashes, and more complex stimulation figures as well as moving stimuli. For the simple onset stimulations, it is assumed that the primary answers (latency 40–80 ms) are mainly generated in Brodmann area 17 (V1), while the secondary answers (latency 90–240 ms) involve also V2. Repetitive flash stimulation can lead to an entrainment of the alpha rhythm in MEG and EEG recordings. This effect (called photic driving) is important in the investigation of epileptic pa-

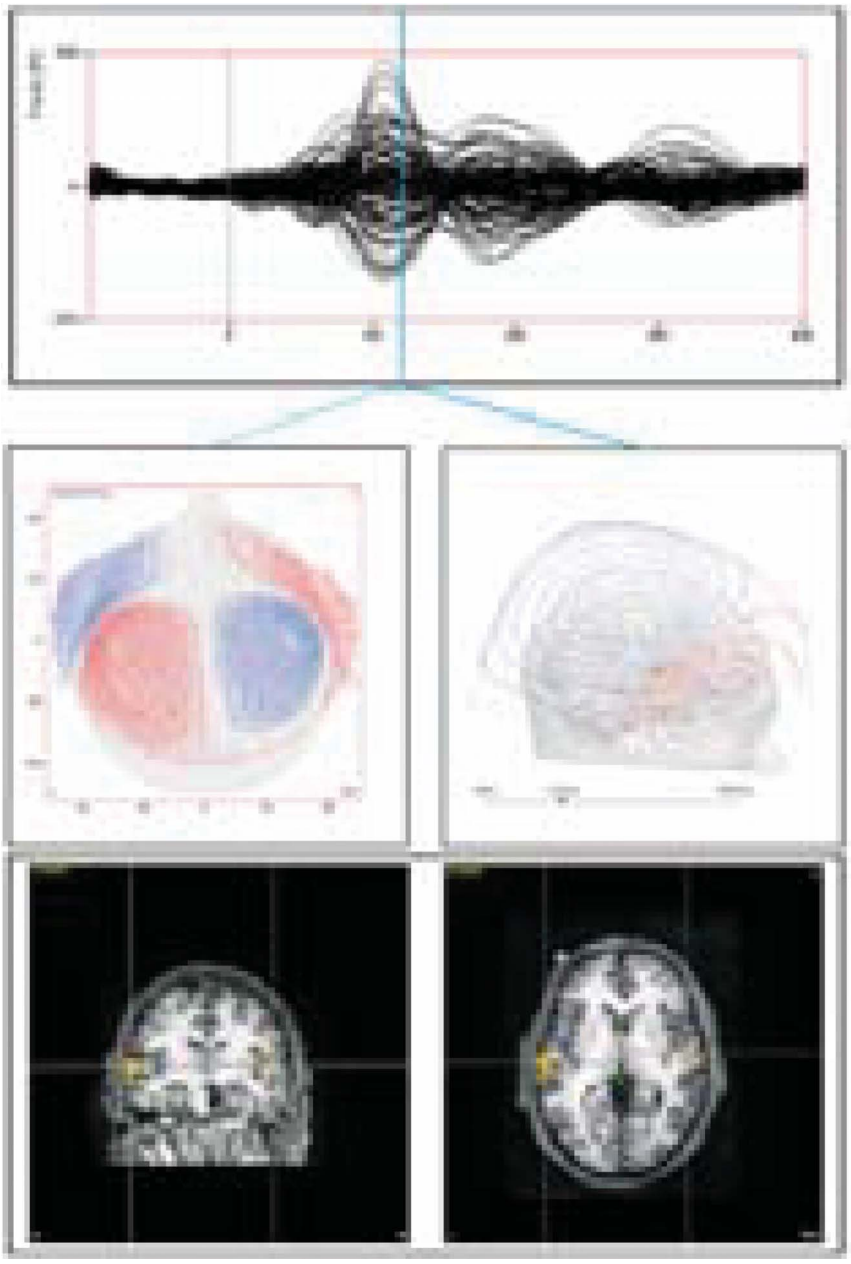

Fig. 2.48. Auditory evoked field time traces of 148 channels (top), magnetic field map at 122.2 ms after stimulation in spherical projection (middle left) and 3-D view (middle right), and localized dipolar sources (in yellow, with confidence ellipsoids) in the primary auditory cortex and in a coronal and axial MRI slice view (bottom). (Material provided by B. Maess and R. Huonker).

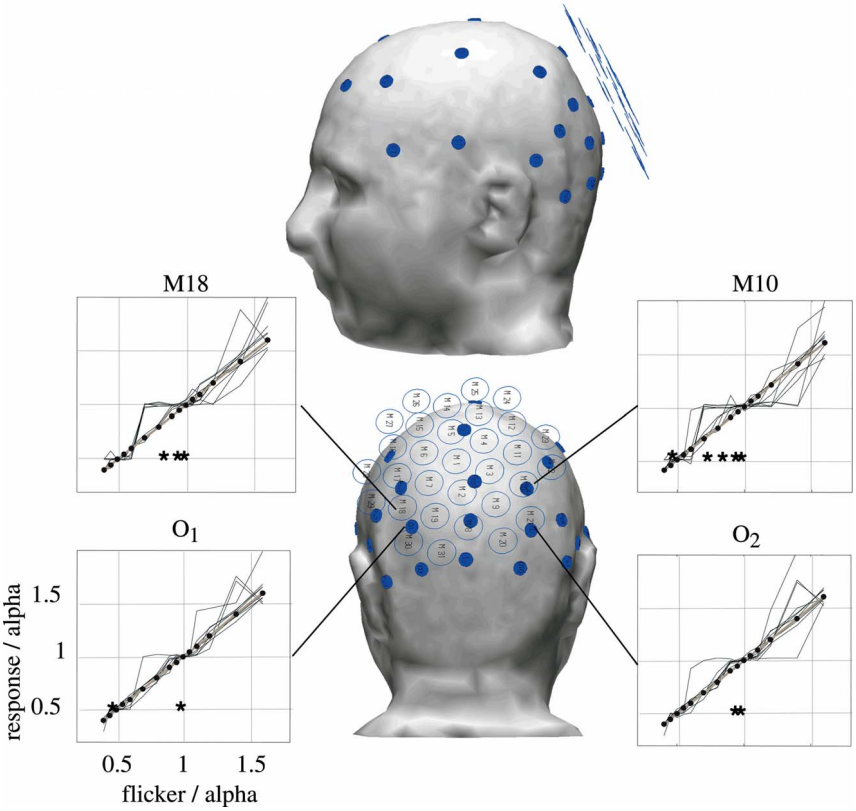

Fig. 2.49. Entrainment effects for two simultaneously recorded MEG (M18 and M10) and EEG (O_1 and O_2) channels. The positions of the electrodes (disks) and the pick-up coils (circles) are given in side view (top) and back view (bottom). The ratio of flicker to alpha at rest is plotted against response (max. peak of spectra) to alpha at rest producing horizontal lines in case of entrainment. A diagonal line would indicate no entrainment. The dots on the horizontal gray line denote the 15 performed stimulations (significance of entrainment effect: * $p \leq 0.05$). (Material from Schwab et al., 2006).

tients (for a recent review, see Parra et al., 2005), and the frequency entrainment was found to be more pronounced in MEG as compared to EEG (Schwab et al., 2006). The effect for 10 healthy volunteers is shown in Figure 2.49.

2.4.4.5 Olfactory and Gustatory System

Compared to the number of studies reporting on somatosensory, auditory, and visual evoked magnetic fields, the number of studies investigating the olfactory and gustatory system by means of magnetic recordings is very low. The first studies

were published only in the mid-1990s (olfactory: Kobal et al., 1995; gustatory: Murayama et al., 1996), but the interest in both fields has been growing (e.g., Hummel, 2000; Walla et al., 2002; Onoda et al., 2005).

2.4.4.6 Motor System

The first investigations on the movement-related magnetic field (Bereitschaftsfeld, movement-evoked fields) date back to the early 1980s (Deecke et al., 1982; Hari and Antervo, 1982; Okada et al., 1982; Weinberg et al., 1983). Paradigms include active and passive movements, self-paced and externally paced movements, whereby finger movements are a common choice of the investigators (Kristeva et al., 1991). Since the mid-1990s, one focus of interest has been the synchronization mechanisms involved in the control of movements both under normal conditions and in patients (for a review, see e.g. Schnitzler and Gross, 2005). Also of clinical interest are passive movements, which make the investigation of the sensory-motor system possible in patients, regardless of their degree of motor impairment. The spatio-temporal magnetic field data after passive movement of the fingers, together with typical source localization results, is shown in Figure 2.50. Activation started 27 ms after the onset of movement and remained for about 100 ms. Four activation maxima occurred within this time range: PM1 at 27 ms, PM2 at 46 ms, PM3 at 85 ms, and PM4 at 125 ms. Not all components were distinguishable in every subject partly due to overlapping effects, but PM3 was present in all subjects. Dipolar sources were located within 1 cm of the central sulcus for all four components (Lange et al., 2001).

2.4.4.7 Perspectives

Although a plethora of literature is already available on the normal function of the primary systems, it still seems that only a small fraction of all aspects of these functions has been revealed. Here, MEG provides the possibility to image brain activity on a millisecond time scale (e.g., Hari et al., 2000), and this permits the investigation of interactions within primary systems and with other systems (e.g., Haueisen and Knösche, 2001).

2.4.5 Neuromagnetic Fields and Brain Science: Cognitive Functions

The identification of brain networks underlying higher cognitive functions is a substantial challenge to any brain-imaging technique, due to the very high spatial and temporal complexity of these networks, and their great variability across experiments and individuals. Some of the most popular methods used in neuroscience, such as fMRI or PET, produce relatively precise – but almost static

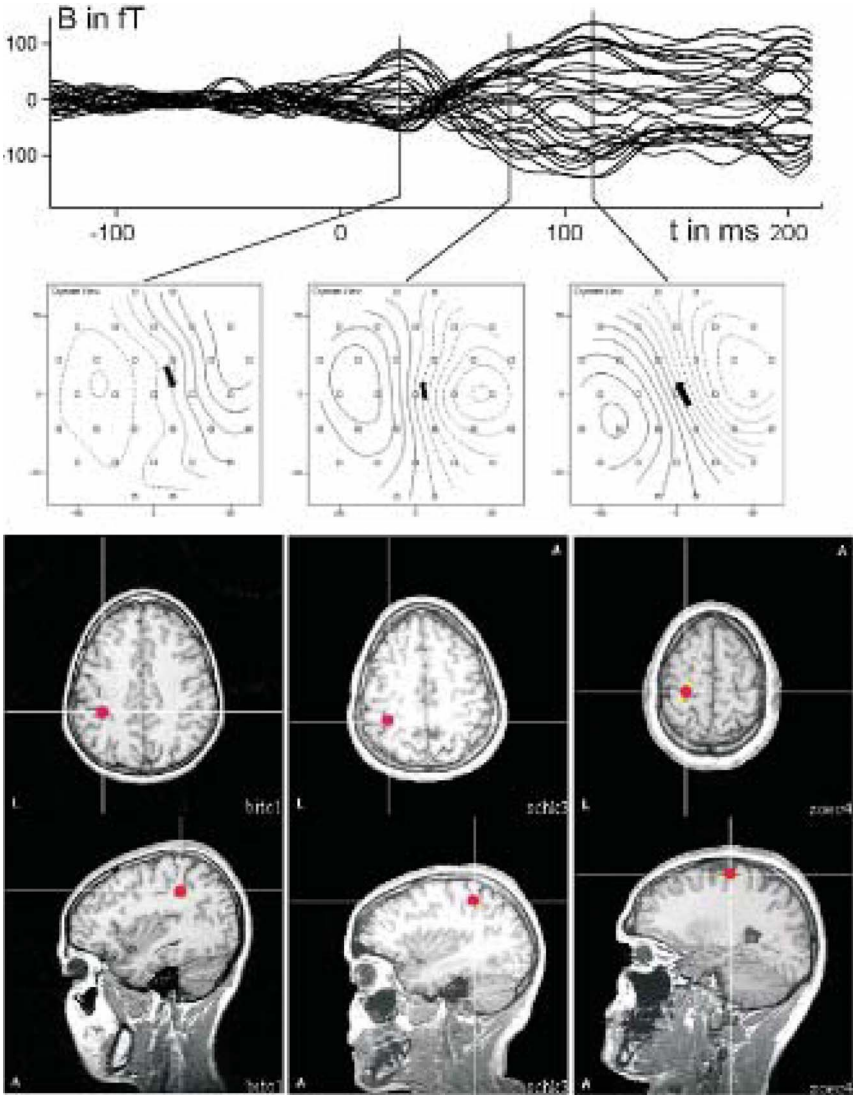

Fig. 2.50. Evoked fields after passive movement at t = 0: time traces of 31 channels (top), magnetic field maps measured over the contralateral somatosensory region for three components (middle) and, and localized dipolar sources (gray dots) close to the central sulcus visualized in a axial and saggital MRI slice view (bottom). (Material from Lange et al., 2001).

– pictures of the neural networks. Other techniques, such as EEG, yield a fine-grained reflection of temporal relationships, but only very limited spatial information. Magnetoencephalography, in combination with source localization methods (see Section 2.4.2), provides at least a partial remedy to this dilemma: while the

time resolution is (as with electroencephalography) only limited by the technical sampling rate, a spatial resolution of up to a few millimeters can be achieved under certain circumstances. In this section, we demonstrate how MEG can be used to reveal the spatio-temporal characteristics of the neural networks underlying higher cognitive functions. Here, we will focus exclusively on studies with normal subjects, while pathological cases will be discussed in Section 2.4.6. Due to space limitations, the following account is essentially incomplete, and some topics (e.g., decision-making, error-processing, and pain perception) were, by necessity, excluded. Other topics such as attention, memory, and emotion will be treated only briefly.

2.4.5.1

Brain Correlates of Cognition: Components and Localizations

Before describing how neuronal networks underlying higher cognitive function were revealed by MEG, will the main characteristic parameters of such networks will be briefly defined, and their significance to brain function illuminated.

An important concept in functional architecture of the brain has always been localization – that is, the idea that certain regions, areas, or cell populations are responsible for certain tasks. There is a great body of evidence, especially from the fMRI and PET investigations, that this is certainly a valid concept; one such example is the established role of the fusiform gyrus for the recognition of faces. On the other hand, the concept of (macroscopic) localization alone seems insufficient to describe the functional organization of the brain. For example, the objects, concepts, and events stored in memory seem to be defined by specific networks formed by many neuronal populations. The question to be asked is how these networks are defined, both permanently (e.g., for long-term memory) and transiently (e.g., for working memory or object representation during perception). Permanent networks could be realized by increased connectivity, for example by heightened synaptic strengths (Herrmann et al., 2004). The transient representation of objects and activation of memory contents could be achieved by synchronized oscillations (Singer, 2000). Hence, oscillation parameters such as *frequency*, *phase*, and *phase coupling* are relevant for the characterization of brain function. Finally, the *timing* of oscillatory as well as nonoscillatory events at the various locations is a crucial dimension for the understanding of functional networks. Note that, in most cases, it is possible to reveal only some aspects of these networks, and more universal models of cognitive processes can only be obtained from the integration of many different studies.

Magnetoencephalography can, in principle, yield information on all described aspects of functional networks. However, while timing and frequency can be resolved with great accuracy, the identification of location is less perfect. The combination with high spatial resolution methods (e.g., fMRI) provides some possibilities to improve this, but there are limitations (see Section 2.4.3.2 and Fujimaki et al., 2002). Additional anatomical and functional knowledge, both general and individual, can also improve the uniqueness and interpretability of functional networks extracted

from MEG data. In the following sections, examples are provided of how MEG has contributed to the identification of such neuronal networks.

2.4.5.2
Human Communication

Spoken Language

Speech is the principal means of information exchange between humans. Our ability to live together in society depends crucially upon the fast and accurate processing of speech signals (for a model of the processing of speech, see Friederici, 2002). MEG studies have made significant contributions to the revelation of brain processes in this model. Initial acoustic processing, as reflected by early waves in MEG and EEG (up to about 200 ms after stimulus onset), has been extensively studied by means of MEG (see Section 2.4.4). As highlighted by Näätänen et al. (2001), these early components already reflect a great deal of complex stimulus processing. For example, attention modulation of MEG responses has been observed as early as 20–40 ms after the onset of auditory stimuli (Hari et al., 1989). The identification and segregation of phoneme and voice information was found to be reflected by the magnetic mismatch negativity and localized in the planum temporale (BA42) by means of MEG dipole localization (Knösche et al., 2002).

The construction of syntactic phrase structures is reflected by a specific electrophysiological component, the *early left anterior negativity* (ELAN; Friederici et al., 1993) and its MEG equivalent (ELANm; Gross et al., 1998), peaking about 150 ms after the onset of a critical word. This process appears to involve Broca's area and its right hemisphere homologue as well as bilateral planum polare, as has been suggested by a number of MEG source localization studies on the perception of connected speech using *magnetic field tomography* (Gross et al., 1998), *brain surface current density mapping* (Knösche et al., 1999), and *dipole localization* (Friederici et al., 2000) (Fig. 2.51). Other MEG studies have identified contributions from the

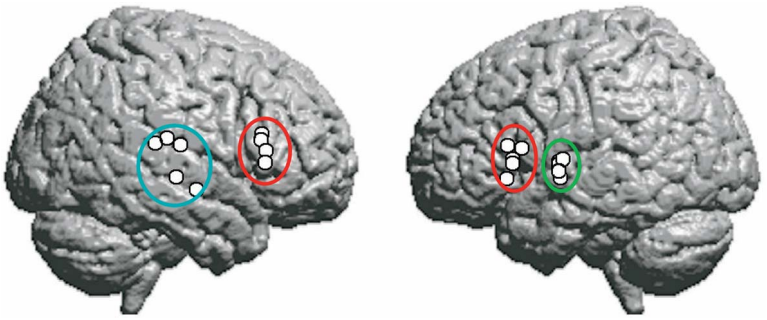

Fig. 2.51. Equivalent current dipole localizations of MEG activity related to syntactic violation in auditory speech. The dipoles cluster in left and right inferior frontal cortex (red circles), left planum polare (green circle), and in what possibly is right planum temporale (blue circle). (Data taken from Friederici et al., 2000).

superior temporal lobe to early syntactic processing (Kubota et al., 2003; Shtyrov et al., 2003). The N400, peaking around 300–600 ms after the onset of a critical word, is regarded as a correlate of lexical-semantic integration (Kutas and Hillyard, 1980). Several attempts to reveal its functional properties and neuronal substrate using MEG have been made, suggesting a network involving bilateral posterior superior temporal and inferior parietal lobe in both hemispheres (e.g., Helenius et al., 2002; Kujala et al., 2004).

In contrast to speech perception, speech production poses a greater challenge to the MEG investigator, as inevitable motor activity – both cerebral and muscular – is likely to contaminate the measurements. A number of picture naming studies have been performed, where the preparation phase before the actual utterance was investigated (Levelt et al., 1998; Maess et al., 2002). The activity of the auditory cortices during actual speech production was also targeted (e.g., Houde et al., 2002).

Written Language

Reading can be studied more easily on both word and sentence levels by using electrophysiological methods, as compared to connected speech. The material can be presented word by word at precisely defined latencies. MEG has been used to reveal the neural basis for the recognition of characters and words, as well as the processing of syntactic and semantic information. In a silent reading and naming task, Kober et al. (2001) could reliably localize several language-relevant areas including Broca's area, Wernicke s area, and superior temporal gyrus, thereby demonstrating the potential usefulness of MEG for presurgical planning. Synchronized oscillatory activity in the gamma band was associated to semantic processing by Braeutigam et al. (2001).

Most character-recognition studies are concerned with the perception of Chinese or Japanese letters, demonstrating activity in both dorsal and ventral visual pathways, as well as in superior temporal gyrus (Kuriki et al., 1996; Kamada et al., 1998). Assadollahi and Pulvermüller (2001) used MEG to show that nonphysical properties of words (e.g., word frequency) are processed in the occipital cortex very early (from 120 ms) after stimulus onset. On the sentence level, semantic processing of words has been investigated by manipulating the expectancy (congruity) of sentence-final words, eliciting the magnetic equivalent of the N400 (N400m), which was attributed to multiple active areas including Broca's area, Wernicke's area, and superior temporal gyrus (Helenius et al., 1998; Halgren et al., 2002). Other studies on semantic processing have addressed the functional meaning of the various subcomponents of the N400m (see Pylkkänen and Marantz, 2003).

Music

Music is a very old and uniquely human faculty. Though generally not directly linked to the exchange of information, it plays an important role in human communication as it expresses cultural and social identity as well as emotion and, to a certain extent, also semantic contents. The degree of similarity between music and speech has often been a matter of debate. There are fundamental parallels, but also

important differences. For discussions, see for example Neuhaus et al. (2006) and Koelsch et al. (2004).

The perception of pitch – perhaps the most important parameter of musical tones – has been studied with MEG by Patel and Balaban (2001), leading to two important conclusions:

- Pitch seems to be discriminated mainly in the right hemisphere. Zatorre et al. (2002) proposed that the left hemisphere is more specialized in the fine-grained processing of temporal aspects of auditory input, while the right hemisphere has a better pitch or frequency resolution. This leads to left/right hemisphere dominance for language/music processing.
- Perception of different pitches is reflected by different time courses, rather than spatial localization of the related brain activity.

The processing of harmonic relations, which play a principal role in musical structure, has been investigated through the brain's MEG response to harmonic violations. Kuriki et al. (2005) reported enhanced N100m and P200m components in response to key violations, which localize near the primary auditory cortex (for N100m), demonstrating quite early (and possibly automatic) detection of tonality mismatch within the auditory cortex. Other, somewhat later, markers for harmonic expectancy violations have been identified using EEG around 200 ms (Koelsch et al., 2000; *early right anterior negativity*, ERAN) and 350 ms (Patel et al., 1998; *right anterior temporal negativity*, RATN). The ERAN has been associated with generators in bilateral BA44 (Broca's area) by MEG source localization (Maess et al., 2001), suggesting that the role of Broca's area and its homologue in fast and automated syntax parsing might be less language-specific than previously thought. Besides the processing of tonality, also the processing of pitch contour, interval structure, and rhythm has been shown to take place at very early latencies using MEG (Fujioka et al., 2004; Vuust et al., 2005).

An important structural element in both speech and music is the subdivision of the auditory stream into phrases. Steinhauer et al. (1999) have identified an EEG marker for the perception of intonational phrase boundaries in speech (*closure positive shift*, CPS). A similar component was also found for phrase boundaries in music and attributed to a network of active areas in the limbic system using MEG source localization (Knösche et al., 2005; Neuhaus et al., 2006). This result is similar to Maess and colleagues' localization of the ERAN in Broca's area, in favor of a certain degree of overlap between neuronal networks underlying the perception of speech and music.

A number of MEG studies have dealt with short- and long-term plasticity of the functional organization of the somatomotor and auditory cortices as a result of musical training (e.g., Pantev et al., 1999). An enhanced coupling between auditory and motor systems was demonstrated by Haueisen and Knösche (2001). These authors used MEG to show that the hand area of the somatomotor cortex is involuntarily activated in pianists (but not in nonpianists) during the perception of well-trained piano music, without any actual or imagined movement.

Nonverbal Communication

Although language is certainly the principal means of human communication, there are a number of very important nonverbal communication modes, including behavior, facial expression, eye gaze, and gestures. The most basic way to obtain information about others' intentions is the observation of their actions (see also next section). For the recognition of actions, it is postulated that the observed action must be mapped onto the observer's internal representations of the same action. Such interaction between sensory and motor mechanisms is supported by the *mirror neuron system*, which was first identified in monkeys (Rizzolatti et al., 1996). Other aspects of nonverbal communication are more symbolic in nature. Eye gaze, facial expression, certain types of behavior, and gestures convey information on a person's attitude towards something or somebody as well as about his/her state of mind or intentions. Such signals are thought to be processed in the *social recognition system* (Allison et al., 2000). In an MEG study, Nakamura et al. (2004) reveal orchestrated multiple brain activity across different neuronal systems, including *object recognition system* (ventral occipito-temporal; see e.g. Ungeleider and Haxby, 1994), mirror neuron system, and social recognition system during the recognition of hand signs.

Several MEG studies have dealt with the recognition of facial expressions and eye gaze (Streit et al., 1999; Lewis et al., 2003; Ioannides et al., 2004; Kimura et al., 2004; Watanabe et al., 2005). The recognition of faces, including their emotional content, was mainly reflected by early activity ($<$200 ms) in the fusiform gyrus and the amygdala. The recognition of eye movements (gaze) was also found to take place very early (140–225 ms after stimulus onset) in the MT/V5 area at the occipito-temporal border.

2.4.5.3

Recognition of Objects: Perceptual Binding

Our sensory organs constantly receive information from the environment, for example the pitch, volume, timbre, and spatial location of sounds or the color and intensity of light at a certain angle of our visual field. One of the most fundamental questions in neuroscience is how the brain groups these sensory inputs together in order to form recognizable objects. This process is often referred to as *binding*. As a more in-depth treatment of this topic cannot be provided here, the interested reader is referred to reviews by Singer (2000) and Herrmann et al. (2004).

Synchronized oscillations, especially in the γ-range ($\sim$40 Hz; see Section 2.4.3.1), are thought to play a major role in the binding processes. MEG has made substantial contributions to the investigation of the role of such oscillations in both temporal and spatial binding. In the visual domain, paradigms using illusory figures (e.g., Kanizsa triangles) were used by a number of authors in order to demonstrate the role of synchronization in the γ-band for perceptual binding (Tallon-Baudry et al., 1997; Herrmann and Mecklinger, 2000). Others employed the coherent motion of stimuli (Sokolov et al., 1999). In the auditory domain, several studies identified γ-oscillations as a neurophysiological correlate for temporal binding and recog-

nition of auditory objects (Joliot et al., 1994; Palva et al., 2002). On the other hand, nonoscillatory magnetic brain responses have been investigated with regard to their significance for object recognition and feature binding (e.g., Okusa et al., 2000).

2.4.5.4 Actions: Planning, Execution, Perception, and Imagery

Motor actions are of fundamental importance for our survival in any environment. They need to be planned and controlled with speed and precision. Moreover, mental imagery of actions enables us to predict their possible outcome without actual movements. Finally, the perception and recognition of actions of others is an important prerequisite for our ability to predict their behavior and intentions.

Preparation, control, and execution of movements are very closely related. They involve transient, slow, and oscillatory magnetic activity in both primary sensorymotor (see Section 2.4.4) and higher cognitive areas. The role of magnetic μ-rhythms for the preparation and execution of movements was investigated by means of event-related spectral power changes (see Section 2.4.3.1; Feige et al., 1996; Salmelin and Sams, 2002). Distinct networks of coupled oscillators in the 8-Hz range were identified, for example, by Schnitzler et al. (2004). Slow magnetic fields in the preparatory phase before a movement (readiness field) have been discovered and their generators localized. A detailed picture of this was drawn by Pedersen et al. (1998), who combined the use of MEG and PET to identify a succession of different generators of the readiness field between 900 and 100 ms prior to the onset of voluntary finger movements: middle frontal gyrus, supplementary motor area, pre-motor cortex, and M1. The *contingent magnetic variation* (CMV), which is elicited during the anticipation of an action-relevant cue, has been attributed to a network comprising both action and perception related areas (Gomez et al., 2004).

Internal simulation of one's own actions and the recognition of another person's actions seem to be very closely related. The neural basis for such a close interaction between motor actions and the visual observation of the same actions has been identified as the mirror neuron system in both nonhuman and human primates by Rizzolatti and colleagues (e.g., Rizzolatti et al., 1996; Iacoboni et al., 1999). MEG has been used to identify such mirror neuron systems in humans for the perception of gestures (Nakamura et al., 2004), grasping movements (Rossi et al., 2002), mouth movements (Mottonen et al., 2005), tool use (Jarvelainen et al., 2004), and music (Haueisen and Knösche, 2001; Popescu et al., 2004). These systems seem to consist of a number of frontal, parietal and temporal areas, including bilateral inferior parietal and posterior superior temporal sites, as well as primary sensorymotor cortices. Similar networks were discovered to be active during the mere imagery (rather than observation) of actions (Lang et al., 1996; Schnitzler et al., 1997).

2.4.5.5 Attention

Attention is involved in virtually every cognitive task. It is the process of selectively allocating resources to a percept, a thought, or a task. Attention is limited and can

be divided. It lets the mind focus on relevant stimuli or tasks at the expense of irrelevant ones. We can concentrate on one voice in the cacophony of a cocktail party, on a single person in a large crowd, or on the actions that will be necessary to get the car moving as soon as the traffic light turns green.

One way to isolate the effects of attention in the auditory domain is the dichotic listening task, where one presents different stimuli to both ears and focuses the attention to one ear (e.g., by a suitable task). (For a review on auditory selective attention including all evidence, not only MEG, see Giard et al., 2000.) This paradigm was used in combination with an MEG-based dipole fit to localize the earliest attention modulated sources near the generators of the N100m in primary auditory cortex (see Section 2.4.4) with an activity latency of 100–150 ms post-stimulus onset (e.g., Fujiwara et al., 1998). Other authors have reported attention-modulated magnetic activity as early as 20 ms post stimulus in a similar paradigm, thus supporting the theory that attention regulates auditory input before or at the initial stages of cortical processing (Woldorff et al., 1993). In a series of pharmacological MEG studies, Kakhonen and colleagues (see e.g., Kahkonen and Ahveninen, 2002) investigated the role of different neurotransmitters (dopamine, serotonin) in auditory-selective attention.

Attention effects in the somatosensory domain (for a general review, see Johansen-Berg and Lloyd, 2000) could be located in the secondary somatosensory cortex (SII) at latencies around 55 ms, while there were no such effects in the primary somatosensory cortex (SI) (e.g., Hoechstetter et al., 2000).

Visual spatial attention was investigated by several research groups using MEG (e.g., Hopf et al., 2000). Modulating the attention to stimuli in one domain by distracters in another domain represents an alternative way in which to study attentional effects. Sokolov et al. (1999), for example, showed that γ-activity elicited by coherent motion of two bars (see also Section 2.4.5.3) was eliminated, if attention was captured by auditory distracters.

2.4.5.6 Memory

Just like attention, memory is a fundamental cognitive faculty. Whenever information from the past contributes to current cognitive processes, some kind of memory must be involved. Consequently, there are many different types of memory, which to discuss in detail would be beyond the scope of this text. According to its content, implicit (priming, skills, habits, etc.) and explicit (facts and events) memory can be distinguished; according to its time range, we know ultra-short (sensory, echoic, or iconic memory), short-, and long-term memory. The working memory comprises contents of short-term and long-term memory. Memory contents must be encoded, maintained, and retrieved. The vastness of the topic forces us to report selectively some aspects of memory that have been investigated with MEG.

Sensory memory is associated with the respective sensory domain (e.g., auditory, visual). In the auditory domain, it can be investigated by the auditory mismatch response (in EEG mismatch negativity, MMN; see e.g., Näätänen et al., 2001), which occurs at about 150 ms after the onset of a physically deviating stimulus and is not

bound to attention. MEG studies have contributed to the revelation of the neural substrate of this response, which lies in the supratemporal plane near the auditory cortex, for simple tones (Alho et al., 1993), words (Pulvermüller et al., 2001; Knösche et al., 2002), and music (Fujioka et al., 2004). McEvoy et al. (1997) discovered a cortical area sensitive to auditory sensory memory just anterior of the sources of the auditory N100m (see Section 2.4.4). Moreover, oscillatory neuromagnetic activity in the α, θ, and γ frequency bands was reported as a correlate of working memory (see e.g., Lutzenberger et al., 2002, for gamma-band activity during an audiospatial working memory task). Extensive MEG investigations have focused on the neural networks underlying various types of memory, including spatial working memory in the visual domain (e.g., Croize et al., 2004) and working memory for words (e.g., Breier et al., 1998).

2.4.5.7 Emotions

The role of emotions in human behavior can hardly be overestimated, with each and every one of our actions being influenced by emotions to some degree. Hence, it is no wonder that this has also become a topic for MEG research. One of the most important sources for emotions is the human face, and there have been a number of studies investigating the perception of emotional facial expressions, identifying activity in, for example the amygdala, inferior frontal cortex, temporal cortex, as well as midline occipital cortex (e.g., Streit et al., 1999; Halgren et al., 2000).

2.4.6 Clinical Applications

2.4.6.1 Introduction

Magnetoencephalography has clinical applications for the evaluation of normal and abnormal brain functions, and the localization of cortical sources. Currently, the localization of epileptic discharges and presurgical brain mapping represent the most common clinical applications (Nakasato and Yoshimoto, 2000; Knowlton and Shih, 2004; Wheless et al., 2004), while other diagnostic applications remain in the research stage. In this section, the current status of clinical MEG is reviewed in the order of simplicity of cortical source configuration, on which the source estimation accuracy of MEG depends so heavily.

2.4.6.2 Somatosensory Evoked Fields (SEFs)

The first cortical response of the SEFs can be assumed as a single cortical source concentrated in a small area along the central sulcus. Together with the excellent

reproducibility of the response, source estimation by a single dipole model can provide an accuracy of a few millimeters.

Localization of the Primary Sensory (SI) Cortex Facing the Central Sulcus

Identification of the central sulcus – the borderline between the frontal and parietal lobes – is the first step of functional brain mapping. The SI cortex is located in the posterior bank of the central sulcus facing the primary motor (MI) cortex of the opposite bank. The central sulcus may be recognized by the sulcal and gyral pattern on anatomic MR images (Ebeling et al., 1989; Berger et al., 1990; Sobel et al., 1993). However, anatomical identification of the central sulcus is not always possible in a patient with anatomical anomaly, structural lesions, or brain edema. SEF can provide critical information in such patients (Fig. 2.52). Identification of the central sulcus by SEFs due to electrical stimulation of the median nerve at the wrist is the most established clinical application of MEG (Sobel et al., 1993; Kawamura et al., 1996; Nakasato et al., 1996b; Inoue et al., 1999; Nakasato and Yoshimoto, 2000). The first cortical component of the median nerve SEF is called N20m, as the magnetic counterpart of the N20 of the *somatosensory evoked potentials* (SEPs). N20 is caused by a negative potential over the parietal scalp, with a peak latency of around 20 ms. The *equivalent current dipole* (ECD) of the N20m is localized on the middle part of the central sulcus, corresponding to the contralateral SI cortex of the hand (Fig. 2.52). Similarly, the first cortical component of the posterior tibial nerve at the ankle is termed P38m, as the magnetic counterpart of the P38 of the SEPs. P38 is caused by a positive potential over the vertex with a peak latency of around 38 ms. The ECD of the P38m is localized on the highest part of the central sulcus, corresponding to the contralateral foot SI cortex (Fig. 2.52) (Nakasato et al., 1996b). The first cortical component of the lip stimulation was identified as N15m (Nagamatsu et al., 2001), occurring earlier than the P20m, which previously had been believed to be the initial peak (Hoshiyama et al., 1996). The ECDs of N15m and P23m are localized on the lower part of the central sulcus, corresponding to the contralateral face SI cortex.

Somatotopic Organization of the Primary Somatosensory Cortex

Combination of multiple stimulation points is practically useful for the clinical application of SEFs. Identification of the central sulcus can be verified by multiple SEF sources, and the central sulcus can be anatomically traced on three-dimensional MR imaging (see Fig. 2.52) (Suk et al., 1991; Yang et al., 1993; Ohtomo et al., 1996). Knowledge of the somatotopic organization of the SI cortex is also important before presurgical decision-making, especially if maximum brain resection is required such as for malignant gliomas and medically intractable epilepsy (Nakasato et al., 1996b; Kumabe et al., 2000; Nakasato and Yoshimoto, 2000). Neurological deficits are minimum and transient after unilateral resection of the orofacial SI and MI areas, because the contralateral cortex can compensate for the loss of function. In contrast, resection of the hand SI or MI cortex causes permanent deficit of the skilled activity of the contralateral side. Noninvasive detection of SEFs can provide the critical information of somatotopy before surgery.

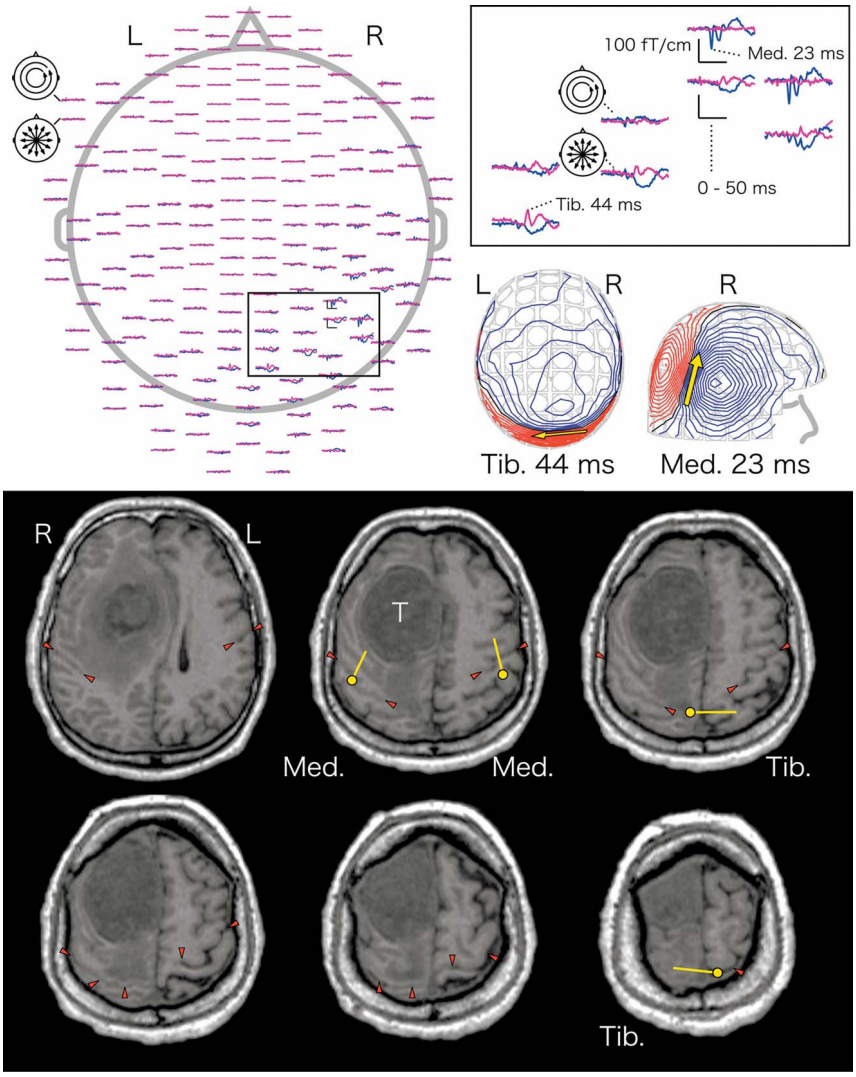

Fig. 2.52. Somatosensory evoked fields in a patient with a right frontal lobe tumor. Top left: The latitudinal and longitudinal derivatives of the magnetic field (upper and lower curves in each pair, respectively) for left median (blue) and posterior tibial (red) nerve stimulation are shown. Top right: Maximum signals of the first peak appeared over the lateral central area for the median nerve stimulus (N20m) and the medial central area for the posterior tibial nerve stimulus (P38m). Isofield maps indicate single dipole patterns. Bottom: Position (circles) and orientation (bars) of the equivalent current dipoles of the N20m and the P38m for bilateral stimuli superimposed on the magnetic resonance image. Note that the central sulcus (arrowheads) is shifted towards the posterior direction due to the mass effect of the tumor (T).

Abnormal SEFs in Neurological Diseases

SEFs can be used for the quantitative evaluation of abnormal SI function. Ishitobi et al. (2005) found that abnormal SI function could be demonstrated by SEFs in patients with unilateral polymicrogyria. Latencies of the median nerve N20m and the tibial nerve P38m were all within the normal range in both normal and dysplastic hemispheres. However, the amplitudes of the N20m and P38m in the dysplastic hemispheres were smaller in one patient and larger in two patients compared to the normal hemispheres. Orientation of the *equivalent current dipoles* (ECDs) of N20m and P38m was abnormal in the dysplastic hemisphere, although the somatotopic arrangement of the median and tibial nerve responses was normal. These findings suggest residual SI function with abnormal amplitude and orientation of neuronal current within the dysplastic cortex.

Iwasaki et al. (2001) measured SEFs for median nerve stimulus in patients with severe traumatic brain injury followed by persistent consciousness disturbance. Latency of the first peak (N20m) was longer, and those of the second (P30m) and third (N45m) peaks were shorter, in the patients compared to normal adults. Moreover, the ECD moments of N20m and P30m were smaller and those of N45m and P60m larger in patients than in normal adults. Most of these patients had large skull and/or brain defects due to primary damage and/or surgical procedures, such as decompressive craniectomy and hematoma evacuation. In contrast to the SEFs, amplitude evaluation of scalp SEPs is difficult in such patients, because of the inhomogeneous head conductivity.

2.4.6.3 Auditory Evoked Fields (AEFs)

The middle- to long-latency responses in the AEFs are generated from slightly larger cortical areas than the short-latency SEFs. Although the auditory cortex is located in the bilateral temporal lobes, reliable source estimation is still possible using a two-dipole model for whole-head data or a single-dipole model for hemispheric data.

Localization of Auditory Cortex in the Temporal Lobe

Bilateral auditory cortex responses are obtained by both monaural and binaural stimulus. *Auditory evoked potentials* (AEPs) show a single potential peak in the mid-frontal and mid-vertex areas due to overlaps of the bilateral signals. In contrast, the bilateral AEFs can be clearly separated (Nakasato et al., 1995; Kanno et al., 1996). The most prominent peak of the AEFs is N100m, the magnetic counterpart of the N100 in AEPs. The ECD of the N100m is localized on the upper surface of the bilateral posterior temporal lobes (Fig. 2.53). The source of the auditory field can be used as a useful landmark for surgical intervention in temporal lobe diseases, as it originates from the posterior part of the temporal plane adjacent to the posterior language area (Ohtomo et al., 2002).

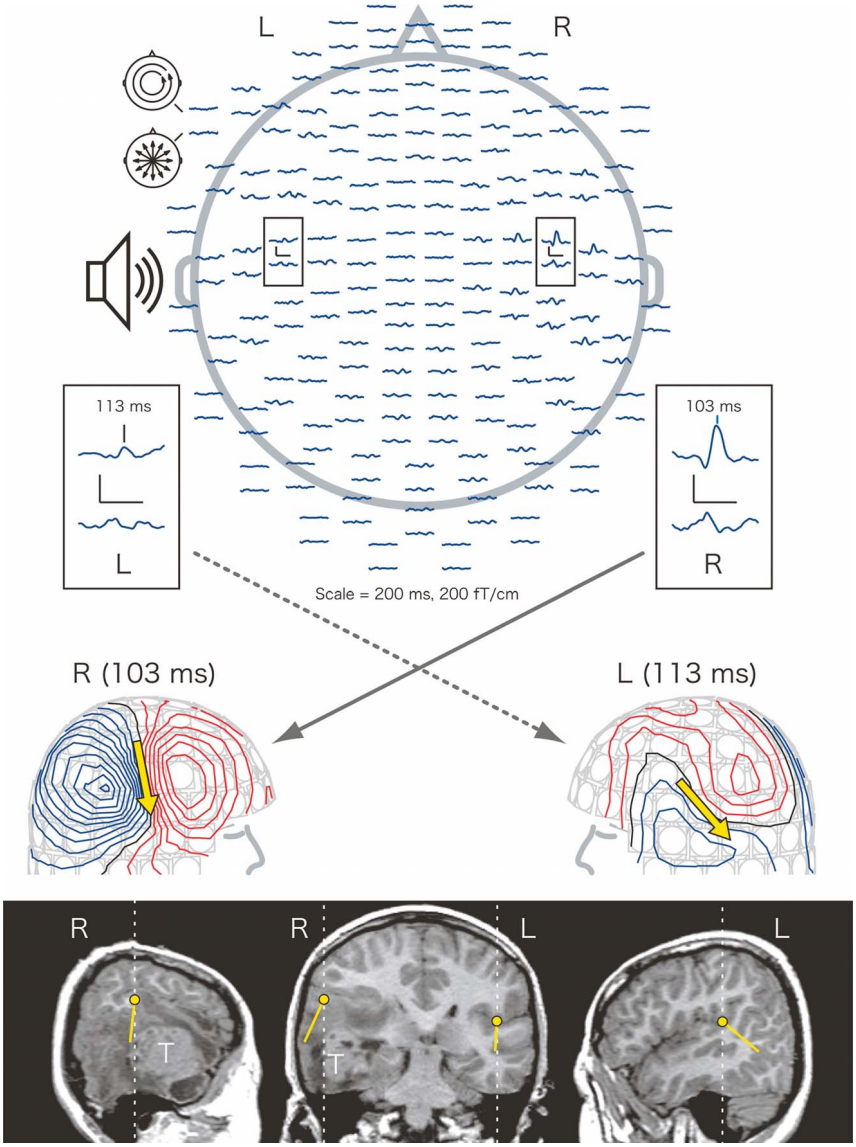

Fig. 2.53. Auditory evoked fields in a patient with a right temporal lobe tumor.
Top: Magnetic fields from −100 to 300 ms after the left ear stimulus with 2000-Hz tone burst are shown. Maximum signals appeared over the bilateral temporal area at a latency of around 100 ms (N100m). Middle: Isofield maps indicate single dipole patterns over the left and right temporal areas.
Bottom: Position (circles) and orientation (bars) of the equivalent current dipoles of the N100m superimposed on the magnetic resonance image. Note that the right auditory cortex is elevated upwards due to the mass effect of the tumor (T).

Abnormal AEFs in Neurological Diseases

Unilateral temporal lobe lesions may diminish the ipsilateral AEFs, although the patient may not complain of any hearing disturbance. Nakasato et al. (1997) evaluated N100m latency in 14 patients with temporal lobe tumors with no hearing disturbance. Before surgery, seven patients had normal N100m latency in both normal and lesion hemispheres, and MR imaging indicated no tumor invasion or edema in the posterior one-third of the superior temporal planes. In the other seven patients, the N100m latency was prolonged in the lesion hemisphere, and the posterior portion of the superior temporal plane was affected by the tumor or perifocal edema. Prolonged N100m latency recovered to the normal range after tumor removal in two of four patients investigated postoperatively. Functional evaluation of such specific cortical areas will become more important in the era of minimally invasive surgery.

2.4.6.4

Visually Evoked Magnetic Fields (VEFs)

VEFs are generated from the bilateral cortices if the full visual field is stimulated. Source estimation by a two-dipole model may be less reliable for full-field VEFs, because the distance between the bilateral visual cortices in the medial occipital lobes is less than that of the bilateral auditory cortices in the temporal lobes. Therefore, left or right hemi-field stimulus is usually used clinically, to evoke the unilateral response from the right or left occipital lobe, respectively, which can be accurately localized by a single-dipole model.

Localization of the Visual Cortex in the Occipital Lobe

Pattern reversal stimuli are one of the most reliable and reproducible stimuli for *visual evoked potentials* (VEPs) as well as for VEFs (Seki et al., 1996). Three major components – N75m, P100m, and N145m – are known to be located on the lateral bottom of the calcarine fissure contralateral to the stimulated visual hemi-field (Seki et al., 1996; Hatanaka et al., 1997, 1998; Shigeto et al., 1998) (Fig. 2.54). The separation of bilateral activities is much clearer for VEFs than for VEPs. The pattern reversal stimulus for the full visual field elicits a double-dipole pattern in the isofield map of P100m (Nakasato et al., 1996a; Seki et al., 1996), but only a single positive peak in the isopotential map of P100. Therefore, VEFs can be used to evaluate differences in amplitude and peak latency in bilateral responses. Stimulus of the full visual field is clinically useful because visual fixation cannot be so strict.

Abnormal VEFs in Neurological Diseases

Nakasato et al. (1996a) investigated the VEFs for full visual field stimuli by pattern reversal in patients with visual field deficits. Patients with homonymous hemianopsia due to unilateral occipital lesion showed only a single-dipole pattern of the P100m over the normal occipital area. Patients with bitemporal hemianopsia due to pituitary tumors had only a single-dipole pattern of the P100m over the occipital area ipsilateral to the stimulated eye. All P100m sources were located at the lateral

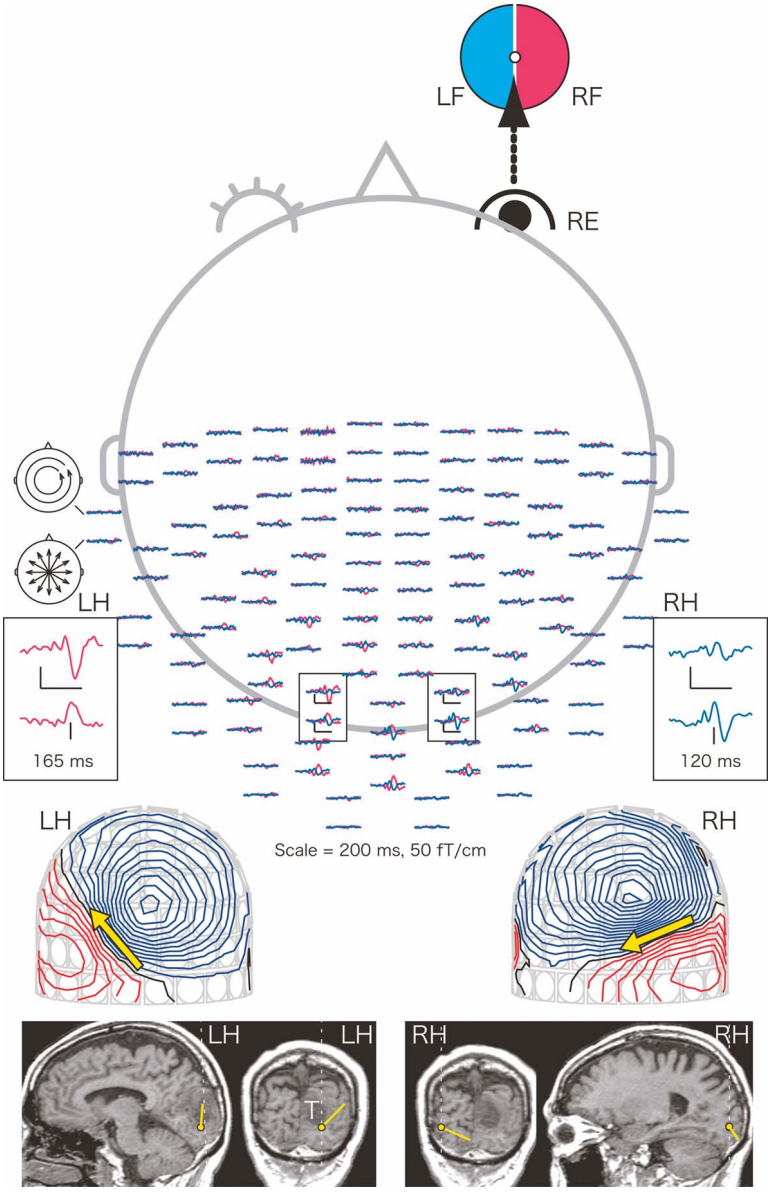

Fig. 2.54. Visually evoked fields for the pattern reversal stimulus in a patient with a left occipital lobe tumor. Top left: Magnetic fields from −100 to 300 ms with stimulation of the left and right visual fields (LF: blue line; RF: red line) are shown. Maximum signals appeared over the occipital area at a latency of around 120 ms (P100m) in the normal right hemisphere (RH) and around 165 ms in the lesion left hemisphere (LH). Middle: Isofield maps at the bilateral peaks indicate single-dipole patterns over the left and right occipital areas. Bottom: Position (circles) and orientation (bars) of the equivalent current dipoles of the bilateral peaks superimposed on the magnetic resonance image. Note that the left visual cortex is located just beneath the tumor (T).

end of the calcarine fissures, corresponding to the findings in normal subjects (Seki et al., 1996; Hatanaka et al., 1997). Kanno et al. (1997) found prolonged P100m latency of the pattern reversal VEFs only in the lesion hemisphere of patients with occipital meningioma. Recently, Inoue et al. (2004) reported that the combination of VEFs and three-dimensional anisotropic contrast MR imaging was useful to preserve visual function in a patient with an occipital lobe tumor.

2.4.6.5
Language-Related Fields (LRFs)

When language stimuli are presented acoustically or visually, early responses from the primary auditory and visual areas may be followed by late responses from the language areas (Simos et al., 1998; Papanicolaou et al., 1999; Suzuki et al., 2001; Halgren et al., 2002). Amplitude asymmetry of the late magnetic fields can predict the language-dominant hemisphere (Fig. 2.55). Although the single dipole model can be used for the averaged data of LRFs, source estimation accuracy can only be estimated at the laterality or lobar level, but not to an accuracy of a few millimeters. The LRFs are useful for surgical planning of epilepsy and brain tumors. The language-dominant hemisphere may be lateralized by task-dependent desynchronization of synchronized brain activity. Hirata et al. (2004) used synthetic aperture magnetometry to analyze MEG activity during a silent reading task in 20 consecutive preoperative neurosurgical patients. Beta (13–25 Hz) and gamma (25–50 Hz) band desynchronization was found in the inferior frontal gyrus or middle frontal gyrus in the unilateral hemisphere congruent with the results of the Wada test. For further information on the cognitive relevance of language-related fields, see also Section 2.4.5.2.

2.4.6.6
Spontaneous Brain Activity in Epilepsy

Interictal Epileptic Discharge

MEG studies of interictal epileptic discharge were first reported during the early 1980s (Barth et al., 1982; Modena et al., 1982), followed by landmark reports which emphasized the clinical utility of MEG for epilepsy (Rose et al., 1987; Sutherling et al., 1987; Stefan et al., 1990). Epilepsy is characterized by recurrent episodes of paroxysmal brain dysfunction due to sudden, disorderly, and excessive neuronal discharges.

Antiepileptic drugs are not completely effective in almost half of the patients. Thus, resection surgery may be indicated for patients with medically intractable localization-related epilepsy if the epileptic area is located outside the functionally eloquent area. Anatomical information, such as MR imaging, is useful to visualize the organic lesion in epilepsy patients. However, the epileptic focus may be located separately from any visible lesions, or even in the absence of abnormal findings. Scalp EEG is the most powerful tool to detect functional abnormality and demonstrate epileptic activity. As the localization accuracy of scalp EEG is not sufficiently

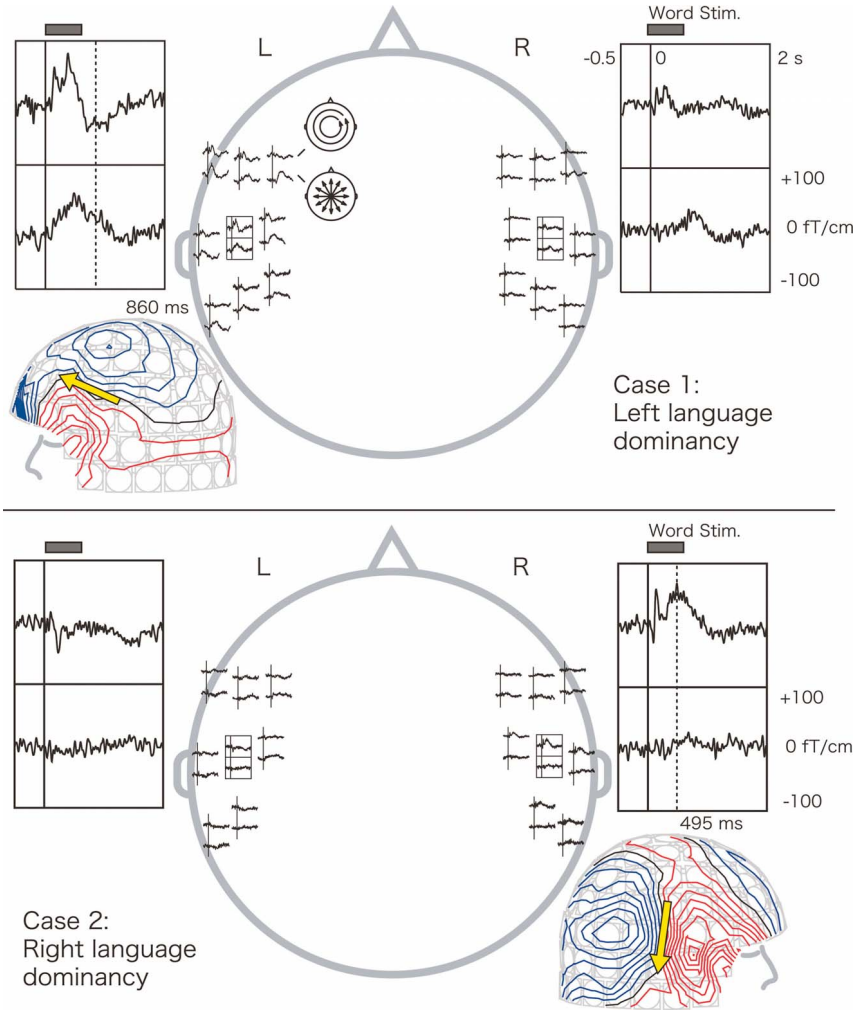

Fig. 2.55. Language-related magnetic fields in two patients with epilepsy in whom the Wada test and cortical stimulation confirmed left (Case 1, top) and right hemispheric (Case 1, lower) language dominancy, respectively. Maximum signals appeared at a latency of around 250 to 1250 ms, indicating significant asymmetry of the amplitude.

high for presurgical decision-making, intracranial EEG studies are often recommended. MEG provides a practical intermediate between scalp and intracranial EEG studies for the presurgical evaluation of epilepsy because MEG is noninvasive, as is scalp EEG. Moreover, MEG has a higher localization accuracy than scalp EEG though lower than intracranial EEG, and MEG may also detect abnormal discharges overlooked by scalp EEG.

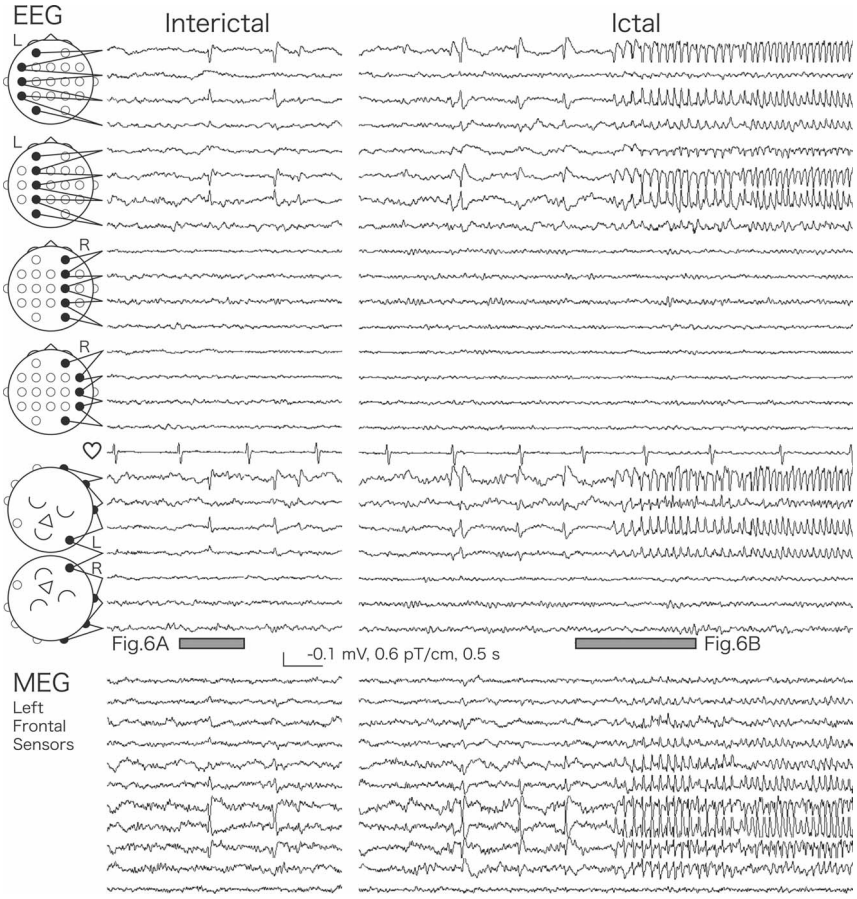

Fig. 2.56. Simultaneous EEG and MEG of interictal and ictal discharges in a patient with medically intractable epilepsy. Note concurrent peaks in both EEG and MEG for interictal solitary spikes as well as ictal spike bursts. Isofield map and source localization during periods of bars are shown in Figure 2.57.

The higher localization accuracy of MEG can directly detect neocortical epilepsy located in the convexity area. Localization of the interictal spike zone and functionally eloquent areas may allow resection surgery without invasive intracranial monitoring. Even in the presence of more complicated pathophysiology of epilepsy, MEG may encourage subsequent intracranial invasive EEG. Any skull defect is known to produce serious errors in source estimation based on scalp EEG, whereas MEG maintains its accuracy for patients with skull defects (Figs. 2.56 and 2.57).

Limbic epilepsy originates from deep foci such as the hippocampus or amygdala in mesial temporal lobe epilepsy. MEG and scalp EEG may not directly detect the primary activity in the deep mesial foci. MEG spike localization in the lateral neocortex probably demonstrates the secondary activity propagated from the mesial

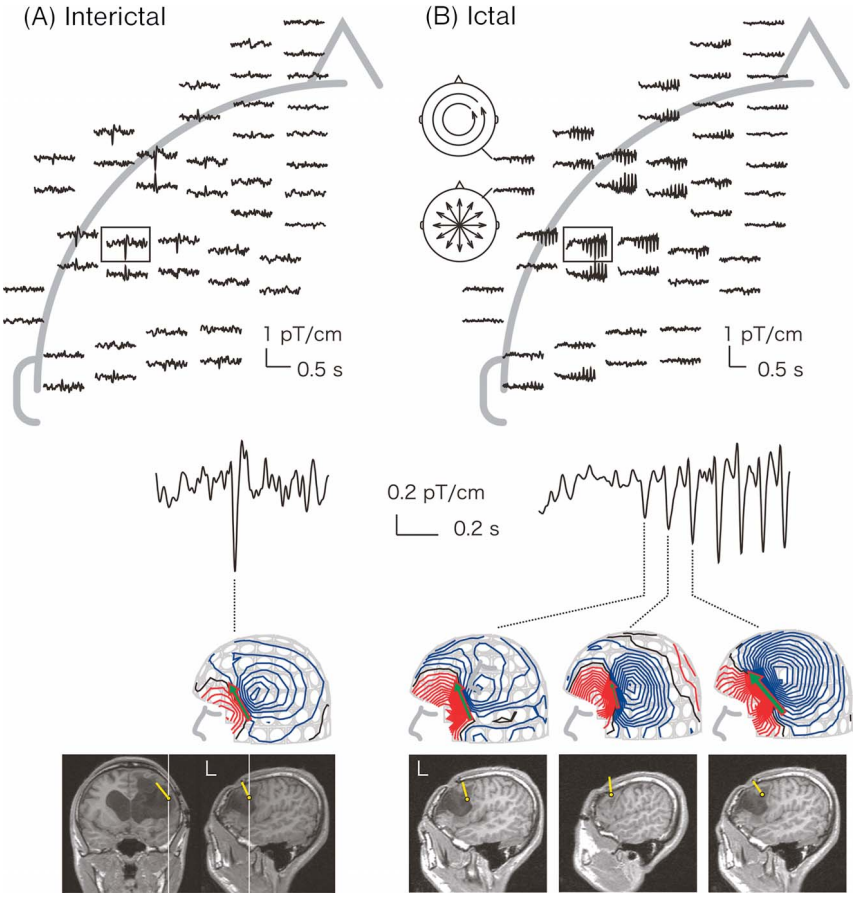

Fig. 2.57. Top: Waveform of the left fronto-temporal MEG sensors. Middle: The isofield maps. Bottom: The equivalent current dipoles of the interictal solitary spike and the ictal spike burst shown in Figure 2.56. This 23-year-old male patient underwent craniectomy surgery for resection of a left frontal lobe tumor at age 6 years. His medically intractable epilepsy consisted of simple partial seizures with aphasia and generalized seizures during sleep. Surgery was not indicated due to seizure onset from the left frontal language area.

structure. In patients with temporal lobe epilepsy without neocortical lesions, favorable seizure outcome can be expected after the standard anterior temporal lobectomy with amygdalohippocampectomy based on the localization of anterior-temporal (AT) spikes in MEG. In contrast, non-AT localization indicates either nonmedial temporal lobe epilepsy or spike propagation to the posterior and extra-temporal neocortex. Patients with non-AT spike localization should undergo intensive evaluations, such as intracranial EEG (Iwasaki et al., 2002).

The higher spatial resolution of MEG is especially useful in patients with bilaterally synchronized spikes. In patients with "secondary" bilateral synchronized

spikes, spatio-temporal analysis clearly demonstrates the primary spike zone in one hemisphere followed by the secondary spike zone in the contralateral hemisphere with a time lag of around 20 ms (Yu et al., 2004), which corresponds to the interhemispheric transfer time via the corpus callosum.

Ictal Epileptic Discharge

Although MEG is less suitable for long-term seizure monitoring than EEG, ictal activity is occasionally recorded during interictal study by chance (Figs. 2.56 and 2.57) (Iwasaki et al., 2003). Previous reports have confirmed that the ictal MEG localization was concordant with intracranial ictal localization (Eliashiv et al., 2002; Assaf et al., 2003).

Comparison with Scalp EEG

In theory, both radial and tangential currents to the scalp can be measured by EEG as well as by MEG due to the effect of inhomogeneous head conductivity. However, when considering the effects of noise, EEG is more sensitive for radial current than for tangential current, and vice versa for MEG. In practice, more epileptic discharges (i.e., spikes) are recognized by MEG without concurrent EEG discharges than discharges detected by both MEG and EEG or by EEG only (Lin et al., 2003; Park et al., 2004; Iwasaki et al., 2005). As the unique MEG spikes have smaller ECD moment than the concurrent EEG and MEG spikes, Park et al. (2004) speculated that scalp EEG overlooks small tangential spikes because it is far more influenced by background brain activity due to the effect of inhomogeneous head conductivity. Simultaneous observation of EEG and MEG also influences spike identification in each modality, and use of information from both modalities increases the sensitivity and specificity of spikes.

2.4.6.7

Spontaneous Brain Activity in Structural Brain Lesions and Ischemia

Normal spontaneous brain activity of EEG and MEG consists of various frequency bands. Alpha waves (8–13 Hz) are dominant in the occipital area when the subject is awake and relaxed with eyes closed. Beta waves with frequency greater than 13 Hz are seen during wakefulness and light sleep. Theta rhythm (4–7 Hz) and delta rhythm with frequency lower than 4 Hz are usually observed in the light and deep sleep stages. In addition, theta and delta waves may appear in various types of pathological conditions such as brain tumors and ischemia. The source of the spontaneous activity, both normal and abnormal, spreads over the bilateral cerebral cortices, so that separation of each generator is not easy in scalp EEG. The higher spatial resolution of MEG may help to highlight and localize abnormal slow waves (Vieth et al., 1992; Kamada et al., 1997; Qiao et al., 2003). Seki et al. (2005) revealed that some patients with stenotic lesions of the internal carotid artery system have upper theta band (6–8 Hz) activity originating from the temporo-parietal area of the lesion hemisphere. Neither MEG nor EEG detected this theta rhythm in age-matched elderly subjects who had no ischemic foci based on T2-weighted MR imaging or vascular stenosis based on MR angiography of the head and neck. Ab-

normal theta rhythm in the temporo-parietal area may indicate mild or subclinical abnormalities due to ischemia in the internal carotid artery system.

2.4.6.8
Perspectives

During the past two decades, new measurement systems of MEG have been the focus of intense competition, and the newer models must have more sensor channels, higher sampling rate, wider dynamic range, and more sophisticated noise cancellation systems. Today, interest is shifting from hardware to software, namely the source estimation algorithm. There is no unique solution for the electromagnetic inverse problem. Moreover, the target signal as well as background brain activity has multiple and extended current sources. For example, there is a need to measure small epileptic discharges with bigger background brain activity. As the averaging technique cannot be applied to spontaneous activity, the signal-to-noise ratio must be lower than that of the evoked magnetic fields. The problem that we face is how to establish the reliability level of the source estimation, and comparison with other modalities is essential for clinical research in order to validate the source estimation accuracy of MEG. In the near future, collaboration with clinical users will be more important in the development of algorithms for MEG source estimation.

References

Alho, K., Huotilainen, M., Tiitinen, H., Ilmoniemi, R.J., Knuutila, J., and Näätänen, R. (1993). Memory-related processing of complex sound patterns in human auditory-cortex – a MEG study. *NeuroReport*, **4**, 391–394.

Allison, T., Puce, A., and McCarthy, G. (2000). Social perception from visual cues: role of the STS region. *Trends Cogn. Sci.*, **4**, 267–278.

Assadollahi, R. and Pulvermüller, F. (2001). Neuromagnetic evidence for early access to cognitive representations. *Neuroreport*, **12**, 207–213.

Assaf, B.A., Karkar, K.M., Laxer, K.D., Garcia, P.A., Austin, E.J., Barbaro, N.M., and Aminoff, M.J. (2003). Ictal magnetoencephalography in temporal and extratemporal lobe epilepsy. *Epilepsia*, **44**, 1320–1327.

Backus, G.E. and Gilbert, J.F. (1968). The resolving power of gross earth data. *Geophys. J. Roy. Astron. Soc.*, **16**, 69–205.

Baillet, S. and Garnero, L. (1997). A Bayesian approach to introducing anatomo-functional priors in the EEG/MEG inverse problem. *IEEE Trans. Biomed. Eng.*, **44**, 374–385.

Barth, D.S., Sutherling, W., Engel, J. Jr., and Beatty, J. (1982). Neuromagnetic localization of epileptiform spike activity in the human brain. *Science*, **218**, 891–894.

Bastiaansen, M.C.M. and Knösche, T.R. (2000). Tangential derivative mapping of axial MEG Applied to event-related desynchronisation (ERD) research. *Clin. Neurophysiol.*, **111**, 1300–1305.

Berg, P. and Scherg, M. (1994). A multiple source approach to the correction of eye artifacts. *Electroencephalogr. Clin. Neurophysiol.*, **90**, 229–241.

Berger, H. (1929). Über das Elektrenkephalogramm des Menschen. *Arch. Psychiat. Nerven.*, **87**, 527–570.

Berger, M.D., Cohen, W.A., and Ojemann, G.A. (1990). Correlation of motor cortex brain mapping data with magnetic resonance imaging. *J. Neurosurg.*, **72**, 383–387.

Bowyer, S.M., Okada, Y.C., Papuashvili, N., Moran, J.E., Barkley, G.L., Welch, K.M., and Tepley, N. (1999a). Analysis of MEG signals of spreading cortical depression with propagation constrained to a rectangular cortical strip. I. Lissencephalic rabbit model. *Brain Res.*, **843**, 71–78.

Bowyer, S.M., Tepley, N., Papuashvili, N., Kato, S., Barkley, G.L., Welch, K.M., and Okada, Y.C. (1999b). Analysis of MEG signals of spreading cortical depression with propagation constrained to a rectangular cortical strip. II. Gyrencephalic swine model. *Brain Res.*, **843**, 79–86.

Bowyer, S.M., Aurora, K.S., Moran, J.E., Tepley, N., and Welch, K.M. (2001). Magnetoencephalographic fields from patients with spontaneous and induced migraine aura. *Ann. Neurol.*, **50**, 582–587.

Braeutigam, S., Bailey, A.J., and Swithenby, S.J. (2001). Phase-locked gamma band responses to semantic violation stimuli. *Cogn. Brain Res.*, **10**, 365–377.

Breier, J.I., Simos, P.G., Zouridakis, C., and Papanicolaou, A.C. (1998). Relative timing of neuronal activity in distinct temporal lobe areas during a recognition memory task for words. *J. Clin. Exp. Neuropsychol.*, **20**, 782–790.

Brenner, D., Williamson, S.J., and Kaufman, L. (1975). Visually evoked magnetic-fields of human brain. *Science*, **190** (4213), 480–482.

Brenner, D., Lipton, J., Kaufman, L., and Williamson, S.J. (1978). Somatically evoked magnetic fields of human brain. *Science*, **199** (4324), 81–83.

Buchner, H., Knoll, G., Fuchs, M., Rienacker, A., Beckmann, R., Wagner, M., Silny, J., and Pesch, J. (1997). Inverse localization of electric dipole current sources in finite element models of the human head. *Electroencephalogr. Clin. Neurophysiol.*, **102**, 267–278.

Carbon, M., Wübbeler, G., Mackert, B.M., Mackert, J., Ramsbacher, J., Trahms, L., Chen, Q., Chopp, M., Chen, H., and Tepley, N. (1992). Magnetoencephalography of focal cerebral ischemia in rats. *Stroke*, **23**, 1299–1303.

Chen, Q., Chopp, M., Chen, H., and Tepley, N. (1992). Magnetoencephalography of focal cerebral ischemia in rats. *Stroke*, **23**, 1299–1303.

Clochon, P., Fontbonne, J.M., Lebrun, N., and Etévenon, P. (1996). A new method for quantifying EEG event-related desynchronization: amplitude envelope analysis. *Electroencephalogr. Clin. Neurophysiol.*, **98**, 126–129.

Cohen, D. (1975). Measurements of magnetic-fields produced by human heart, brain, and lungs. *IEEE Trans. Magn.*, **MA11** (2), 694–700.

Croft, R.J. and Barry, R.J. (2000). EOG correction: Which regression should we use? *Psychophysiology*, **37**, 123–125.

Croize, A.C., Ragot, R., Garnero, L., Ducorps, A., Pelegrini-Issac, M., Dauchot, K., Benali, H., and Burnod, Y. (2004). Dynamics of parietofrontal networks underlying visuospatial short-term memory encoding. *Neuroimage*, **23**, 787–799.

Curio, G. (2000). Linking 600-Hz 'spikelike' EEC/MEG wavelets ('sigma-bursts') to cellular substrates – Concepts and caveats. *J. Clin. Neurophysiol.*, **17** (4), 377–396.

Curio, G. (2004). Non-invasive magnetic detection of human injury currents. *Clin. Neurophysiol.*, **115**, 1027–1032.

Curio, G., Mackert, B.M., Burghoff, M., Koetitz, R., Abrahamfuchs, K., and Harer, W. (1994). Localization of evoked neuromagnetic 600-Hz activity in the cerebral somatosensory system. *Electroencephalogr. Clin. Neurophysiol.*, **9** (6), 483–487.

Curio, G., Mackert, B.M., Burghoff, M., Neumann, J., Nolte, G., Scherg, M., and Marx, P. (1997). Somatotopic source arrangement of 600 Hz oscillatory magnetic fields at the human primary somatosensory hand cortex. *Neurosci. Lett.*, **234**, 131–134.

Deecke, L., Weinberg, H., and Brickett, P. (1982). Magnetic fields of the human brain accompanying voluntary movement. *Bereitschaftsmagnetfeld. Exp. Brain Res.*, **48** (1), 144–148.

de Munck, J.C. (1989). *A mathematical and physical interpretation of the electromagnetic field of the brain.* PhD thesis, University of Amsterdam, The Netherlands.

de Munck, J.C., Huizenga, H.M., Waldorp, L.J., and Heethaar, R.M. (2002). Estimating stationary dipoles from MEG/EEG data contaminated with spatially and temporally correlated background noise. *IEEE Trans. Sign. Process.*, **50**, 1565–1572.

Ebeling, U., Steinmetz, H., Huang, Y.X., and Kahn, T. (1989). Topography and identification of the inferior precental sulcus in MR imaging. *Am. J. Roentgenol.*, **153**, 1051–1056.

Elbert, T., Ray, W.J., Kowalik, Z.J., Skinner, J.E., Graf, K.E., and Birbaumer, M. (1994). Chaos and physiology – deterministic chaos in excitable cell assemblies. *Psychol. Rev.*, **74**, 1–47.

Eliashiv, D.S., Elsas, S.M., Squires, K., Fried, I., and Engel, J. Jr. (2002). Ictal magnetic source imaging as a localizing tool in partial epilepsy. *Neurology*, **59**, 1600–1610.

Feige, B., Kristeva-Feige, R., Rossi, S., Pizzella, V., and Rossini, P.M. (1996). Neuromagnetic study of movement-related changes in rhythmic brain activity. *Brain Res.*, **734**, 252–260.

Friederici, A.D. (2002). Towards a neural basis of auditory sentence processing. *Trends Cogn. Sci.*, **6**, 78–84.

Friederici, A.D., Pfeifer, E., and Hahne, A. (1993). Event-related brain potentials during natural speech processing: Effects of semantic, morphological and syntactic violations. *Cogn. Brain Res.*, **1**, 183–192.

Friederici, A.D., Wang, Y., Herrmann, C.S., Maess, B., and Oertel, U. (2000). Localization of early syntactic processes in frontal and temporal cortical areas: a magnetoencephalographic study. *Hum. Brain Mapp.*, **11**, 1–10.

Fuchs, M., Wagner, M., Wischmann, H.A., Köhler, T., Theissen, A., Drenckhahn, R., and Buchner, H. (1998). Improving source reconstructions by combining bioelectric and biomagnetic data. *Electroencephalogr. Clin. Neurophysiol.*, **107**, 93–111.

Fuchs, M., Wagner, M., Köhler, T., and Wischmann, H.A. (1999). Linear and nonlinear current density reconstructions. *J. Clin. Neurophysiol.*, **16**, 267–295.

Fuchs, M., Wagner, M., and Kastner, J. (2004). Confidence limits of dipole source reconstruction results. *Clin. Neurophysiol.*, **115**, 1442–1451.

Fujimaki, N., Hayakawa, T., Nielsen, M., Knösche, T.R., and Miyauchi, S. (2002). An fMRI-constrained MEG source analysis with procedures of dividing and grouping activation. *NeuroImage*, **17**, 324–343.

Fujioka, T., Trainor, L.J., Ross, B., Kakigi, R., and Pantev, C. (2004). Musical training enhances automatic encoding of melodic contour and interval structure. *J. Cogn. Neurosci.*, **16**, 1010–1021.

Fujiwara, N., Nagamine, T., Imai, M., Tanaka, T., and Shibasaki, H. (1998). Role of the primary auditory cortex in auditory selective attention studied by whole-head neuromagnetometer. *Cogn. Brain Res.*, **7**, 99–109.

Gallen, C.C., Schwartz, B., Rieke, K., Pantev, C., Sobel, D., Hirschkoff, E., and Bloom, F.E. (1994). Intrasubject reliability and validity of somatosensory source localization using a large array biomagnetometer. *Electroencephalogr. Clin. Neurophysiol.*, **90** (2), 145–156.

Gardner-Medwin, A.R. (1981). Possible roles of vertebrate neuroglia in potassium dynamics, spreading depression and migraine. *J. Exp. Biol.*, **95**, 111–127.

Gerloff, C., Richard, J., Hadley, J., Schulman, A.E., Honda, M., and Hallett, M. (1998). Functional coupling and regional activation of human cortical motor areas during simple, internally paced and externally paced finger movements. *Brain*, **121**, 1513–1531.

Giard, M.H., Fort, A., Mouchetant-Rostaing, Y., and Pernier, J. (2000). Neurophysiological mechanisms of auditory selective attention in humans. *Front. Biosci.*, **5**, D84–D94.

Gomez, C.M., Fernandez, A., Maestu, F., Amo, C., Gonzalez-Rosa, J.J., Vaquero, E., and Ortiz, T. (2004). Task-specific sensory and motor preparatory activation revealed by contingent magnetic variation. *Cogn. Brain Res.*, **21**, 59–68.

Grave de Peralta-Menendez, R.G. and Gonzales-Andino, S.L. (1998). A critical analysis of linear inverse solutions to the neuroelectromagnetic inverse problem. *IEEE Trans. Biomed. Eng.*, **45**, 440–448.

Gray, C.M., König, P., Engel, A.K., and Singer, W. (1989). Oscillatory responses in cat visual cortex exhibit inter-columnar synchronization which reflects global stimulus properties. *Nature*, **338**, 334–337.

Gross, J., Ioannides, A.A., Dammers, J., Maess, B., Friederici, A.D., and Müller-Gärtner, H.J. (1998). Magnetic field

tomography analysis of continuous speech. *Brain Topogr.*, **10**, 273–281.

Halgren, E., Raij, T., Marinkovic, K., Jousmaki, V., and Hari, R. (2000). Cognitive response profile of the human fusiform face area as determined by MEG. *Cereb. Cortex*, **10**, 69–81.

Halgren, E., Dhond, R.P., Christensen, N., Van Petten, C., Marinkovic, K., Lewine, J.D., and Dale, A.M. (2002). N400-like magnetoencephalography responses modulated by semantic context, word frequency, and lexical class in sentences. *NeuroImage*, **17**, 1101–1116.

Hämäläinen, M.S. and Sarvas, J. (1987). Feasibility of the homogeneous head model in the interpretation of neuromagnetic data. *Phys. Med. Biol.*, **32**, 91–97.

Hämäläinen, M.S. and Ilmoniemi, R.J. (1994). Interpreting magnetic fields of the brain: minimum norm estimates. *Med. Biol. Eng. Comput.*, **32**, 35–42.

Hämäläinen, M., Hari, R., Ilmoniemi, R.J., Knuutila, J., and Lounasmaa, O.V. (1993). Magnetoencephalography – theory, instrumentation, and applications to non-invasive studies of the working human brain. *Rev. Modern Physics*, **65**, 413–497.

Hari, R. and Antervo, A. (1982). Comparison of Magnetoencephalographic and Electroencephalographic Techniques in event-related response research – a brief survey. *Scand. J. Psychol.*, 170–174.

Hari, R. and Salmelin, R. (1997). Human cortical oscillations: A neuromagnetic view through the skull. *Trends Neurosci.*, **20**, 44–49.

Hari, R. and Forss, N. (1999). Magnetoencephalography in the study of human somatosensory cortical processing. *Philos. Trans. Roy. Soc. London. Ser. B, Biol. Sci.*, **354**, 1145–1154.

Hari, R., Hämäläinen, M., Kaukoranta, E., Makela, J., Joutsiniemi, S.L., and Tiihonen, J. (1989). Selective listening modifies activity of the human auditory-cortex. *Exp. Brain Res.*, **74**, 463–470.

Hari, R., Levanen, S., and Raij, T. (2000). Timing of human cortical functions during cognition: role of MEG. *Trends Cogn. Sci.*, **4** (12), 455–462.

Hashimoto, I. (2000). High-frequency oscillations of somatosensory evoked potentials and fields. *J. Clin. Neurophysiol.*, **17** (3), 309–320.

Hashimoto, I., Papuashvili, N., Xu, C., and Okada, Y.C. (1996). Neuronal activities from a deep subcortical structure can be detected magnetically outside the brain in the porcine preparation. *Neurosci. Lett.*, **206**, 25–28.

Hatanaka, K., Nakasato, N., Seki, K., Mizoi, K., and Yoshimoto, T. (1997). Striate cortical generators of the N75, P100 and N145 components localized by pattern reversal visual evoked magnetic fields. *Tohoku J. Exp. Med.*, **182**, 9–14.

Hatanaka, K., Nakasato, N., Kanno, A., Seki, K., Ohtomo, S., Fujiwara, S., and Yoshimoto, T. (1998). Integration of function of the primary visual cortex revealed by neuromagnetic analysis. In: Hashimoto, I. and Kakigi, R. (Eds), *Recent Advances in Human Neurophysiology.* Elsevier, Amsterdam, pp. 369–373.

Haueisen, J. and Knösche, T.R. (2001). Involuntary motor activation in pianists evoked by music perception. *J. Cogn. Neurosci.*, **13**, 786–792.

Haueisen, J., Ramon, C., Eiselt, M., Brauer, H., and Nowak, H. (1997). Influence of tissue resistivities on neuromagnetic fields and electric potentials studied with a finite element model of the head. *IEEE Trans. Biomed. Eng.*, **44**, 727–735.

Haueisen, J., Schack, B., Meier, T., Curio, G., and Okada, Y. (2001). Multiplicity in the high-frequency signals during the short-latency somatosensory evoked cortical activity in humans. *Clin. Neurophysiol.*, **112** (7), 1316–1325.

Haueisen, J., Tuch, D.S., Ramon, C., Schimpf, P.H., Wedeen, V.J., George, J.S., and Belliveau, J.W. (2002). The influence of brain tissue anisotropy on human EEG and MEG. *NeuroImage*, **15**, 159–166.

Hauk, O. (2004). Keep it simple: a case for using classical minimum norm estimation in the analysis of EEG and MEG data. *NeuroImage*, **21**, 1612–1621.

Helenius, P., Salmelin, R., Service, E., and Connolly, J.F. (1998). Distinct time courses of word and context comprehension in the left temporal cortex. *Brain*, **121** (6), 1133–1142.

Helenius, P., Salmelin, R., Service, E., Connolly, J.F., Leinonen, S., and Lyytinen, H. (2002). Cortical activation during spoken-word segmentation in nonreading-impaired and dyslexic adults. *J. Neurosci.*, **22**, 2936–2944.

Herrmann, C.S. and Mecklinger, A. (2000). Magnetoencephalographic responses to illusory figures: early evoked gamma is affected by processing of stimulus features. *Int. J. Psychophysiol.*, **38**, 265–281.

Herrmann, C.S., Munk, M.H.J., and Engel, A.K. (2004). Cognitive functions of gamma band activity: memory match and utilization. *Trends Cogn. Sci.*, **8**, 347–355.

Hirata, M., Kato, A., Taniguchi, M., Saitoh, Y., Ninomiya, H., Ihara, A., Kishima, H., Oshino, S., Baba, T., Yorifuji, S., and Yoshimine, T. (2004). Determination of language dominance with synthetic aperture magnetometry: comparison with the Wada test. *NeuroImage*, **23**, 46–53.

Hjorth, B. (1975). Online transformation of EEG scalp potentials into orthogonal source derivations. *Electroencephalogr. Clin. Neurophysiol.*, **39**, 526–530.

Hoechstetter, K., Rupp, A., Meinck, H.M., Weckesser, D., Bornfleth, H., Stippich, C., Berg, P., and Scherg, M. (2000). Magnetic source imaging of tactile input shows task-independent attention effects in SII. *Neuroreport*, **11**, 2461–2465.

Hopf, J.M., Luck, S.J., Girelli, M., Hagner, T., Mangun, G.R., Scheich, H., and Heinze, H.J. (2000). Neural sources of focused attention in visual search. *Cereb. Cortex*, **10**, 1233–1241.

Hoshiyama, M., Kakigi, R., Koyama, S., Kitamura, Y., Shimojo, M., and Watanabe S. (1996). Somatosensory evoked magnetic fields following stimulation of the lip in humans. *Electroencephalogr. Clin. Neurophysiol.*, **100**, 96–104.

Houde, J.F., Nagarajan, S.S., Sekihara, K., Merzenich, M.M. (2002). Modulation of the auditory cortex during speech: an MEG study. *J. Cogn. Neurosci.*, **14**, 1125–1138.

Hummel, T. (2000). Assessment of intranasal trigeminal function. *Int. J. Psychophysiol.*, **36** (2), 147–155.

Iacoboni, M., Woods, R.P., Brass, M., Bekkering, H., Mazziotta, J.C., and Rizzolatti, G. (1999). Cortical mechanisms of human imitation. *Science*, **286**, 2526–2528.

Ikeda, H., Leyba, L., Bartolo, A., Wang, Y., and Okada, Y.C. (2002). Synchronized spikes of thalamocortical axonal terminals and cortical neurons are detectable outside the pig brain with MEG. *J. Neurophysiol.*, **87**, 626–630.

Inoue, T., Shimizu, H., Nakasato, N., and Yoshimoto, T. (1999). Accuracy and limitation of functional magnetic resonance imaging for identification of the central sulcus: comparison with magnetoencephalography in patients with brain tumors. *NeuroImage*, **10**, 738–748.

Inoue, T., Fujimura, M., Kumabe, T., Nakasato, N., Higano, S., and Tominaga, T. (2004). Combined three-dimensional anisotropy contrast imaging and magnetoencephalography guidance to preserve visual function in a patient with an occipital lobe tumor. *Minim. Invasive Neurosurg.*, **7**, 249–252.

Ioannides, A.A., Liu, M.J., Liu, L.C., Bamidis, P.D., Hellstrand, E., and Stephan, K.M. (1995). Magnetic field tomography of cortical and deep processes: Examples of 'real-time mapping' of averaged and single trial MEG signals. *Int. J. Psychophysiol.*, **20**, 161–175.

Ioannides, A.A., Poghosyan, V., Dammers, J., and Streit, M. (2004). Real-time neural activity and connectivity in healthy individuals and schizophrenia patients. *NeuroImage*, **23**, 473–482.

Ishitobi, M., Nakasato, N., Yoshimoto, T., and Iinuma, K. (2005). Abnormal primary somatosensory function in unilateral polymicrogyria: an MEG study. *Brain Dev.*, **27**, 22–29.

Iwasaki, M., Nakasato, N., Kanno, A., Hatanaka, K., Nagamatsu, K., Nagamine, Y., and Yoshimoto, T. (2001). Somatosensory evoked fields in patients with comatose survivors after severe head injury. *Clin. Neurophysiol.*, **112**, 204–210.

Iwasaki, M., Nakasato, N., Shamoto, H., Nagamatsu, K., Kanno, A., Hatanaka, K., and Yoshimoto, T. (2002). Surgical implications of neuromagnetic spike localization in temporal lobe epilepsy. *Epilepsia*, **43**, 415–424.

Iwasaki, M., Nakasato, N., Shamoto, H., and Yoshimoto, T. (2003). Focal magnetoence-

phalographic spikes in the superior temporal plane undetected by scalp EEG. *J. Clin. Neurosci.*, **10**, 236–238.

Iwasaki, M., Pestana, E., Burgess, R.C., Luders, H.O., Shamoto, H., and Nakasato, N. (2005). Detection of epileptiform activity by human interpreters: blinded comparison between electroencephalography and magnetoencephalography. *Epilepsia*, **46**, 59–68.

Jacobson, G.P. (1994). Magnetoencephalographic studies of auditory-system function. *J. Clin. Neurophysiol.*, **11** (3), 343–364.

Jarvelainen, J., Schurmann, M., and Hari, R. (2004). Activation of the human primary motor cortex during observation of tool use. *NeuroImage*, **23**, 187–192.

Johansen-Berg, H. and Lloyd, D.M. (2000). The physiology and psychology of selective attention to touch. *Front. Biosci.*, **5**, D894–D904.

Johnston, D., Christie, B.R., Frick, A., Gray, R., Hoffman, D.A., Schexnayder, L.K., Watanabe, S., and Yuan, L.L. (2003). Active dendrites, potassium channels and synaptic plasticity. *Philos. Trans. R. Soc. Lond. B Biol Sci.*, **358**, 667–674.

Joliot, M., Ribary, U., and Llinás, R. (1994). Human oscillatory brain activity near 40 Hz coexists with cognitive temporal binding. *Proc. Natl. Acad. Sci. USA*, **91**, 11748–11751.

Junghöfer, M., Elbert, T., Leiderer, P., Berg, P., and Rockstroh, B. (1997). Mapping EEG-potentials on the surface of the brain: a strategy for uncovering cortical sources. *Brain Topogr.*, **9**, 203–217.

Kahkonen, S. and Ahveninen, J. (2002). Combination of magneto- and electroencephalography in studies of monoamine modulation on attention. *Methods Find. Exp. Clin. Pharmacol.*, **24**, 27–34.

Kakigi, R., Hoshiyama, M., Shimojo, M., Naka, D., Yamasaki, H., Watanabe, S., Xiang, J., Maeda, K., Lam, K., Itomi, K., and Nakamura, A. (2000). The somatosensory evoked magnetic fields. *Prog. Neurobiol.*, **61**, 495–523.

Kamada, K., Saguer, M., Moller, M., Wicklow, K., Katenhauser, M., Kober, H., and Vieth, J. (1997). Functional and metabolic analysis of cerebral ischemia using magnetoencephalography and proton magnetic resonance spectroscopy. *Ann. Neurol.*, **42**, 554–563.

Kamada, K., Kober, H., Saguer, M., Moller, M., Kaltenhauser, M., and Vieth, J. (1998). Responses to silent Kanji reading of the native Japanese and German in task subtraction magnetoencephalography. *Cogn. Brain Res.*, **7**, 89–98.

Kanno, A., Nakasato, N., Fujita, S., Seki, K., Kawamura, T., Ohtomo, S., Fujiwara, S., and Yoshimoto, T. (1996). Right hemispheric dominance in the auditory evoked magnetic fields for pure-tone stimuli. *Electroencephalogr. Clin. Neurophysiol.*, **47** (Suppl.), 129–132.

Kanno, A., Nakasato, N., Seki, K., Hatanaka, K., Mizoi, K., and Yoshimoto, T. (1997). Postoperative normalization of prolonged P100m latency in the visual evoked magnetic field in a patient with occipital meningioma. *No To Shinkei*, **49**, 373–376.

Karhu, J., Hari, R., Lu, S.T., Paetau, R., and Rif, J. (1991). Cerebral magnetic-fields to lingual stimulation. *Electroencephalogr. Clin. Neurophysiol.*, **80** (6), 459–468.

Katila, T.E. (1983). On the current multipole presentation of the primary current distribution. *Il Nuovo Cimento*, **2D**, 660–664.

Kawamura, T., Nakasato, N., Seki, K., Kanno, A., Fujita, S., Fujiwara, S., and Yoshimoto, T. (1996). Neuromagnetic evidence of pre- and post-central cortical sources of somatosensory evoked responses. *Electroencephalogr. Clin. Neurophysiol.*, **100**, 44–50.

Kimura, I., Kubota, M., Hirose, H., Yumoto, M., and Sakakihara, Y. (2004). Children are sensitive to averted eyes at the earliest stage of gaze processing. *NeuroReport*, **15**, 1345–1348.

Klimesch, W. (1999). EEG alpha and theta oscillations reflect cognitive and memory performance: a review and analysis. *Brain Res. Rev.*, **29**, 169–195.

Knösche, T.R. and Bastiaansen, M.C.M. (2002). On the time resolution of event-related desychronization: a simulation study. *Clin. Neurophysiol.*, **113**, 754–763.

Knösche, T.R., Praamstra, P., Stegeman, D., and Peters, M.J. (1996). Linear estimation discriminates midline source and motor cortex contribution to readiness potential, *Electroencephalogr. Clin. Neurophysiol.*, **99**, 183–190.

Knösche, T.R., Berends, E.M., Jagers, H.R.A., and Peters, M.J. (1998). Determining the number of independent sources of the EEG – a simulation study on information criteria. *Brain Topogr.*, **11**, 111–124.

Knösche, T.R., Maess, B., and Friederici, A.D. (1999). Processing of syntactic information monitored by brain surface current density mapping based on MEG. *Brain Topogr.*, **12**, 75–87.

Knösche, T.R., Lattner, S., Maess, B., Schauer, M., and Friederici, A.D. (2002). Early parallel processing of auditory word and voice information. *NeuroImage*, **17**, 1493–1503.

Knösche, T.R., Neuhaus, C., Haueisen, J., Alter, K., Maess, B., Witte, O.W., and Friederici, A.D. (2005). The perception of phrasing in music. *Hum. Brain Mapp.*, **24**, 259–273.

Knowlton, R.C. and Shih, J. (2004). Magnetoencephalography in epilepsy. *Epilepsia*, **45**, 61–71.

Kobal, G., Kettenmann, B., and Stefan, H. (1995). Olfactory event-related magnetic-fields – a new technique in localizing the neocortical olfactory areas. *Chemical Senses*, **20** (1), 164.

Kober, H., Moller, M., Nimsky, C., Vieth, J., Fahlbusch, R., and Ganslandt, O. (2001). New approach to localize speech relevant brain areas and hemispheric dominance using spatially filtered magnetoencephalography. *Hum. Brain Mapp.*, **14**, 236–250.

Koelsch, S., Gunter, T.C., Friederici, A.D., and Schroeger, E. (2000). Brain indices of music processing: 'Non-musicians' are musical. *J. Cogn. Neurosci.*, **12**, 520–541.

Koelsch, S., Kasper, E., Sammler, D., Schulze, K., Gunter, T., and Friederici, A.D. (2004). Music, language and meaning: brain signatures of semantic processing. *Nat. Neurosci.*, **7**, 302–305.

Kristeva, R., Cheyne, D., and Deecke, L. (1991). Neuromagnetic fields accompanying unilateral and bilateral voluntary movements – topography and analysis of cortical sources. *Electroencephalogr. Clin. Neurophysiol.*, **81** (4), 284–298.

Kubota, M., Ferrari, P., and Roberts, T.P.L. (2003). Magnetoencephalography detection of early syntactic processing in humans: comparison between L1 speakers and L2 learners in English. *Neurosci. Lett.*, **353**, 107–110.

Kujala, A., Alho, K., Service, E., Ilmoniemi, R.J., and Conolly, J.F. (2004). Activation in the anterior left auditory cortex associated with the phonological analysis of speech input: localization of the phonological mismatch negativity response with MEG. *Cogn. Brain Res.*, **21**, 106–113.

Kumabe, T., Nakasato, N., Inoue, T., and Yoshimoto, T. (2000). Primary thumb sensory cortex located at the lateral shoulder of the inverted omega-shape on the axial images of the central sulcus. *Neurol. Med. Chir. (Tokyo)*, **40**, 393–403.

Kuriki, S., Hirata, Y., Fujimaki, N., and Kobayashi, T. (1996). Magnetoencephalographic study on the cerebral neural activities related to the processing of visually presented characters. *Cogn. Brain Res.*, **4**, 185–199.

Kuriki, S., Isahai, N., and Ohtsuka, A. (2005). Spatiotemporal characteristics of the neural activities processing consonant/dissonant tones in melody. *Exp. Brain Res.*, **162**, 46–55.

Kutas, M. and Hillyard, S.A. (1980). Reading senseless sentences: Brain potentials reflecting semantic incongruity. *Science*, **207**, 203–205.

Lang, W.F., Cheyne, D., Hollinger, P., Gerschlager, W., and Lindinger, G. (1996). Electric and magnetic fields of the brain accompanying internal simulation of movement. *Cogn. Brain Res.*, **3**, 125–129.

Lange, R., Nowak, H., Haueisen, J., and Weiller, C. (2001). Passive finger movement evoked fields in magnetoencephalography. *Exp. Brain Res.*, **136**, 194–199.

Levelt, W.J.M., Praamstra, P., Meyer, A.S., Helenius, P., and Salmelin, R. (1998). An MEG study of picture naming. *J. Cogn. Neurosci.*, **10**, 553–567.

Lewis, S., Thoma, R.J., Lanoue, M.D., Miller, G.A., Heller, W., Edgar, C., Huang, M.X., Weisend, M.P., Irwin, J., Paulson, K., and Canive, J.M. (2003). Visual processing of facial affect. *NeuroReport*, **14**, 1841–1845.

Lin, Y.Y., Shih, Y.H., Hsieh, J.C., Yu, H.Y., Yiu, C.H., Wong, T.T., Yeh, T.C., Kwan, S.Y., Ho, L.T., Yen, D.J., Wu, Z.A., and Chang, M.S. (2003). Magnetoencephalographic yield of interictal spikes in temporal lobe epilepsy. Comparison with scalp EEG recordings. *NeuroImage*, **19**, 1115–1126.

Lutzenberger, W., Ripper, B., Busse, L., Birbaumer, N., and Kaiser, J. (2002). Dynamics of gamma-band activity during an audiospatial working memory task in humans. *J. Neurosci.*, **22**, 5630–5638.

Maess, B., Koelsch, S., Gunter, T.C., and Friederici, A.D. (2001). Musical syntax is processed in Broca's area: an MEG study. *Nat. Neurosci.*, **4**, 540–545.

Maess, B., Friederici, A.D., Damian, M., Meyer, A.S., and Levelt, W.J.M. (2002). Semantic category interference in overt picture naming: sharpening current density localization by PCA. *J. Cogn. Neurosci.*, **14**, 455–462.

Makeig, S. (1993). Auditory event-related dynamics of the EEG spectrum and effects of exposure to tones. *Electroencephalogr. Clin. Neurophysiol.*, **86**, 283–293.

Mauguiere, F., Merlet, I., Forss, N., Vanni, S., Jousmaki, V., Adeleine, P., and Hari, R. (1997). Activation of a distributed somatosensory cortical network in the human brain. A dipole modelling study of magnetic fields evoked by median nerve stimulation. 1. Location and activation timing of SEF sources. *Electroencephalogr. Clin. Neurophysiol.*, **104** (4), 281–289.

McEvoy, L., Levanen, S., and Loveless, N. (1997). Temporal characteristics of auditory sensory memory: Neuromagnetic evidence. *Psychophysiology*, **34**, 308–316.

Mitzdorf, U. (1985). Current source-density method and application in cat cerebral cortex: investigation of evoked potentials and EEG phenomena. *Physiol. Rev.*, **65**, 35–90.

Modena, I., Ricci, G.B., Barbanera, S., Leoni, R., Romani, G.L., and Carelli, P. (1982). Biomagnetic measurements of spontaneous brain activity in epileptic patients. *Electroencephalogr. Clin. Neurophysiol.*, **54**, 622–628.

Mosher, J.C., Lewis, P.S., and Leahy, R.M. (1992). Multiple dipole modelling and localization from spatio-temporal MEG data. *IEEE Trans. Biomed. Eng.*, **39**, 541–557.

Mottonen, R., Jarvelainen, J., Sams, M., and Hari, R. (2005). Viewing speech modulates activity in the left SI mouth cortex. *NeuroImage*, **24**, 731–737.

Murakami, S., Hirose, A., and Okada, Y.C. (2003). Contribution of ionic currents to magnetoencephalography (MEG) and electroencephalography (EEG) signals generated by guinea-pig CA3 slices. *J. Physiol.*, **553**, 975–985.

Murayama, N., Nakasato, N., Hatanaka, K., Fujita, S., Igasaki, T., Kanno, A., and Yoshimoto, T. (1996). Gustatory evoked magnetic fields in humans. *Neurosci. Lett.*, **210** (2), 121–123.

Näätänen, R. and Winkler, I. (1999). The concept of auditory stimulus representation in cognitive neuroscience. *Psychol. Bull.*, **125** (6), 826–859.

Näätänen, R., Tervaniemi, M., Sussman, E., Paavilainen, P., and Winkler, I. (2001). 'Primitive intelligence' in the auditory cortex. *Trends Neurosci.*, **24**, 283–288.

Nagamatsu, K., Nakasato, N., Hatanaka, K., Kanno, A., Iwasaki, M., and Yoshimoto, T. (2001). Neuromagnetic detection and localization of N15, the initial response to trigeminal stimulus. *NeuroReport*, **12**, 1–5.

Nakamura, A., Maess, B., Knösche, T.R., Gunter, T.C., Bach, P., and Friederici, A.D. (2004). Cooperation of different neuronal systems during hand sign recognition. *NeuroImage*, **23**, 25–34.

Nakasato, N. and Yoshimoto, T. (2000). Somatosensory, auditory and visual evoked magnetic fields in patients with brain diseases. *J. Clin. Neurophysiol.*, **17**, 201–211.

Nakasato, N., Fujita, S., Seki, K., Kawamura, T., Matani, A., Tamura, I., Fujiwara, S., and Yoshimoto, T. (1995). Functional localization of bilateral auditory cortices using an MRI-linked whole head magnetoencephalography (MEG) system. *Electroencephalogr. Clin. Neurophysiol.*, **94**, 183–190.

Nakasato, N., Seki, K., Fujita, S., Hatanaka, K., Kawamura, T., Ohtomo, S., Kanno, A., Ikeda, H., and Yoshimoto, T. (1996a). Clinical application of visual evoked fields using an MRI-linked whole head MEG system. *Front. Med. Biol. Eng.*, **7**, 275–283.

Nakasato, N., Seki, K., Kawamura, T., Ohtomo, S., Kanno, A., Fujita, S., Hatanaka, K., Fujiwara, S., Kayama, T., Takahashi, A., Jokura, H., Kumabe, T., Ikeda, H., Mizoi, K., and Yoshimoto, T. (1996b). Cortical mapping using an MRI-linked whole head MEG system and presurgical decision making. *Electroencephalogr. Clin. Neurophysiol. Suppl.*, **47**, 333–341.

Nakasato, N., Kumabe, T., Kanno, A., Ohtomo, S., Mizoi, K., and Yoshimoto, T. (1997). Neuromagnetic evaluation of cortical auditory function in patients with temporal lobe tumors. *J. Neurosurg.*, **86**, 610–618.

Neuhaus, C., Knösche, T.R., and Friederici, A.D. (2006). Effects of musical expertise and boundary markers on phrase perception in music. *J. Cogn. Neurosci.*, **18** (3), 472–493.

Nolte, G. and Curio, G. (2000). Current multipole expansion to estimate lateral extent of neuronal activity: A theoretical analysis. *IEEE Trans. Biomed. Eng.*, **47**, 1347–1355.

Ohtomo, S., Nakasato, N., Kawamura, T., Kanno, A., Seki, K., Fujita, S., Shimizu, H., Fujiwara, S., and Yoshimoto, T. (1996). Correspondence of anatomy and function in the human digit sensory cortex revealed by an MRI-linked whole head MEG system. *Electroencephalogr. Clin. Neurophysiol.*, **47** (Suppl.), 91–95.

Ohtomo, S., Nakasato, N., Kumabe, T., and Yoshimoto, T. (2002). Auditory evoked N100m as a possible landmark of posterior language cortex in patients with temporal lobe gliomas. In: Nowak, H., Haueisen, J., Giessler, F. and Huonker, R. (Eds.). *Proceedings of the 13th International Conference on Biomagnetism*, VDE Verlag, Berlin, pp. 95–97.

Okada, Y.C., Williamson, S.J., and Kaufman, L. (1982). Magnetic-field of the human sensorimotor cortex. *Int. J. Neurosci.*, **17** (1), 33–38.

Okada, Y.C., Tanenbaum, R., Williamson, S.J., and Kaufman, L. (1984). Somatotopic organization of the human somatosensory cortex revealed by neuromagnetic measurements. *Exp. Brain Res.*, **56** (2), 197–205.

Okada, Y.C., Wu, J., and Kyuhou, S. (1997). Genesis of MEG signals in a mammalian CNS structure. *Electroencephalogr. Clin. Neurophysiol.*, **103**, 474–485.

Okada, Y.C., Lähteenmäki, A., and Xu, C. (1999). Comparison of MEG and EEG on the basis of somatic evoked responses elicited by stimulation of the snout in the juvenile swine. *Clin. Neurophysiol.*, **110**, 214–229.

Okusa, T., Kakigi, R., and Osaka, N. (2000). Cortical activity related to cue-invariant shape perception in humans. *Neuroscience*, **98**, 615–624.

Onoda, K., Kobayakawa, T., Ikeda, M., Saito, S., and Kida, A. (2005). Laterality of human primary gustatory cortex studied by MEG. *Chemical Senses*, **30** (8), 657–666.

Palva, S., Palva, J.M., Shtyrov, Y., Kujala, T., Ilmoniemi, R.J., Kaila, K., and Näätänen, R. (2002). Distinct gamma-band evoked responses to speech and non-speech sounds in humans. *J. Neurosci.*, **22**, RC211.

Pantev, C., Hoke, M., Lehnertz, K., Lütkenhöner, B., Anogianakis, G., and Wittkowski, W. (1988). Tonotopic organization of the human auditory-cortex revealed by transient auditory evoked magnetic-fields. *Electroencephalogr. Clin. Neurophysiol.*, **69** (2), 160–170.

Pantev, C., Wollbrink, A., Roberts, L.E., Engelien, A., and Lütkenhöner, B. (1999). Short-term plasticity of the human auditory cortex. *Brain Res.*, **842**, 192–199.

Papanicolaou, A.C., Simos, P.G., Breier, J.I., Zouridakis, G., Willmore, L.J., Wheless, J.W., Constantinou, J.E., Maggio, W.W., and Gormley, W.B. (1999). Magnetoencephalographic mapping of the language-specific cortex. *J. Neurosurg.*, **90**, 85–93.

Park, H.M., Nakasato, N., Iwasaki, M., Shamoto, H., Tominaga, T., and Yoshimoto, T. (2004). Comparison of magnetoencephalographic spikes with and without concurrent electroencephalographic spikes in extratemporal epilepsy. *Tohoku J. Exp. Med.*, **203**, 165–174.

Parra, J., Kalitzin, S.N., and da Silva, F.H.L. (2005). Photosensitivity and visually induced seizures. *Curr. Opin. Neurol.*, **18** (2), 155–159.

Pascual-Marqui, R.D. (2002). Standardized low-resolution brain electromagnetic tomography (sLORETA): Technical details. *Methods Find. Exp. Clin. Pharmacol.*, **24** (Suppl. D), 5–12.

Pascual-Marqui, R.D., Michel, C.M., and Lehmann, D. (1994). Low resolution electromagnetic tomography – a new method for localizing electrical activity in the brain. *Int. J. Psychophysiol.*, **18**, 49–65.

Patel, A.D. and Balaban, E. (2001). Human pitch perception is reflected in the timing of stimulus-related cortical activity. *Nat. Neurosci.*, **4**, 839–844.

Patel, A.D., Gibson, E., Ratner, J., Besson, M., and Holcomb, P. (1998). Processing syntactic relations in language and music:

an event-related potential study. *J. Cogn. Neurosci.*, **10**, 717–733.

Pedersen, J.R., Johannsen, P., Bak, C.K., Kofoed, B., Saermark, K., and Gjedde, A. (1998). Origin of human motor readiness field linked to left middle frontal gyrus by MEG and PET. *NeuroImage*, **8**, 214–220.

Pfurtscheller, G. (1989). Functional topography during sensorimotor activation studied with event-related desynchronization mapping. *J. Clin. Neurophysiol.*, **6**, 75–84.

Pfurtscheller, G. and Aranibar, A. (1977). Event-related cortical desynchronization detected by power measurements of scalp EEG. *Electroencephalogr. Clin. Neurophysiol.*, **42**, 817–826.

Plonsey, R. and Heppner, D.B. (1967). Considerations of quasi-stationarity in electrophysiological systems. *Bull. Math. Biophysics*, **29**, 657–664.

Popescu, M., Otsuka, A., and Ioannides, A.A. (2004). Dynamics of brain activity in motor and frontal cortical areas during music listening: a magnetoencephalographic study. *NeuroImage*, **21**, 1622–1638.

Pulvermüller, F., Kujala, T., Shtyrov, Y., Simola, J., Tiitinen, H., Alku, P., Alho, K., Martinkauppi, S., Ilmoniemi, R.J., and Näätänen, R. (2001). Memory traces for words as revealed by the mismatch negativity. *NeuroImage*, **14**, 607–616.

Pylkkänen, L. and Marantz, A. (2003). Tracking the time course of word recognition with MEG. *Trends Cogn. Sci.*, **7**, 187–189.

Qiao, F., Kuroda, S., Kamada, K., Houkin, K., and Iwasaki, Y. (2003). Source localization of the re-build up phenomenon in pediatric moyamoya disease – a dipole distribution analysis using MEG and SPECT. *Childs Nerv. Syst.*, **19**, 760–764.

Reite, M., Edrich, J., Zimmerman, J.T., and Zimmerman, J.E. (1978). Human Magnetic Auditory Evoked Fields. *Electroencephalogr. Clin. Neurophysiol.*, **45** (1), 114–117.

Rice, M.E., Okada, Y.C., and Nicholson, C. (1993). Anisotropic and heterogeneous diffusion in the turtle cerebellum: implications for volume transmission. *J. Neurophysiol.*, **70**, 2035–2044.

Rizzolatti, G., Fadiga, L., Gallese, V., and Fogassi, L. (1996). Premotor cortex and the recognition of motor actions. *Cogn. Brain Res.*, **3**, 131–141.

Romani, G.L., Williamson, S.J., Kaufman, L., and Brenner, D. (1982). Characterization of the human auditory-cortex by the neuromagnetic method. *Exp. Brain Res.*, **47** (3), 381–393.

Rose, D.F., Sato, S., Smith, P.D., Porter, R.J., Theodore, W.H., Friauf, W., Bonner, R., and Jabbari, B. (1987). Localization of magnetic interictal discharges in temporal lobe epilepsy. *Ann. Neurol.*, **22**, 348–354.

Rossi, S., Tecchio, F., Pasqualetti, P., Ulivelli, M., Pizzella, V., Romani, G.L., Passero, S., Battistini, N., and Rossini, P.M. (2002). Somatosensory processing during movement observation in humans. *Clin. Neurophysiol.*, **113**, 16–24.

Salmelin, R. and Hari, R. (1994). Characterization of spontaneous MEG rhythms in healthy adults. *Electroencephalogr. Clin. Neurophysiol.*, **91**, 237–248.

Salmelin, R. and Sams, M. (2002). Motor cortex involvement during verbal versus non-verbal lip and tongue movements. *Hum. Brain Mapp.*, **16**, 81–91.

Salmelin, R., Hämäläinen, M., Kajola, M., and Hari, R. (1995a). Functional segregation of movement-related rhythmic activity in the human brain. *NeuroImage*, **2**, 237–243.

Salmelin, R., Forss, N., Knuutila, J., and Hari, R. (1995b). Bilateral activation of the human somatomotor cortex by distal hand movements. *Electroencephalogr. Clin. Neurophysiol.*, **95**, 444–452.

Sarvas, J. (1987). Basic mathematical and electromagnetic concepts of the biomagnetic inverse problem. *Phys. Med. Biol.*, **32**, 11–22.

Scherg, M. and Berg, P. (1991). Use of prior knowledge in brain electromagnetic source analysis. *Brain Topogr.*, **4**, 143–150.

Schimpf, P.H., Ramon, C., and Haueisen, J. (2002). Dipole models for the EEG and MEG. *IEEE Trans. Biomed. Eng.*, **49**, 409–418.

Schnitzler, A. and Gross, J. (2005). Normal and pathological oscillatory communication in the brain. *Nat. Rev. Neurosci.*, **6** (4), 285–296.

Schnitzler, A., Salenius, S., Salmelin, R., Jousmaki, V., and Hari, R. (1997). Involvement of primary motor cortex in motor imagery: A neuromagnetic study. *NeuroImage*, **6**, 201–208.

Schnitzler, A., Timmermann, L., and Gross, J. (2004). The role of large scale neural interactions for normal motor control and tremor disorders. *Neurol. Psychiatry Brain Res.*, **11**, 23–26.

Schwab, K., Ligges, C., Jungmann, T., Hilgenfeld, B., Haueisen, J., and Witte, H. (2006). Alpha entrainment in EEG and MEG recordings. *NeuroReport* (in press).

Seki, K., Nakasato, N., Fujita, S., Hatanaka, K., Kawamura, T., Kanno, A., and Yoshimoto, T. (1996). Neuromagnetic evidence that the P100 component of pattern reversal visual evoked response originates in the bottom of calcarine fissure. *Electroencephalogr. Clin. Neurophysiol.*, **100**, 436–442.

Seki, S., Nakasato, N., Ohtomo, S., Kanno, A., Shimizu, H., and Tominaga, T. (2005). Neuromagnetic measurement of unilateral temporo-parietal theta rhythm in patients with internal carotid artery occlusive disease. *NeuroImage*, **25**, 502–510.

Shigeto, H., Tobimatsu, S., Yamamoto, T., Kobayashi, T., and Kato, M. (1998). Visual evoked cortical magnetic responses to checkerboard pattern reversal stimulation: a study on the neural generators of N75, P100 and N145. *J. Neurol. Sci.*, **156**, 186–194.

Shtyrov, Y., Pulvermüller, F., Näätänen, R., and Ilmoniemi, R.J. (2003). Grammar processing outside the focus of attention: an MEG study. *J. Cogn. Neurosci.*, **15**, 1195–1206.

Simos, P.G., Breier, J.I., Zouridakis, G., and Papanicolaou, A.C. (1998). Assessment of functional cerebral laterality for language using magnetoencephalography. *J. Clin. Neurophysiol.*, **15**, 364–372.

Singer, W. (2000). Response synchronization: a universal coding strategy for definition of relation. In: Gazzaniga, M.S. (Ed.), *The New Cognitive Neuroscience*. The MIT Press, Cambridge, MA.

Sobel, D.F., Gallen, C.C., Schwartz, B.J., Waltz, T.A., Copeland, B., Yamada, S., Hirschkoff, E.C., and Bloom, F.E. (1993). Locating the central sulcus: comparison of MR anatomic and magnetoencephalographic functional method. *Am. J. Neuroradiol.*, **14**, 915–925.

Sokolov, A., Lutzenberger, W., Pavlova, M., Preissl, H., Braun, C., and Birbaumer, N. (1999). Gamma-band MEG activity to coherent motion depends on task-driven attention. *NeuroReport*, **10**, 1997–2000.

Stefan, H., Schneider, S., Abraham-Fuchs, K., Bauer, J., Feistel, H., Pawlik, G., Neubauer, U., Rohrlein, G., and Huk, W.J. (1990). Magnetic source localization in focal epilepsy. Multichannel magnetoencephalography correlated with magnetic resonance brain imaging. *Brain*, **113**, 1347–1359.

Steinhauer, K., Alter, K., and Friederici, A.D. (1999). Brain potentials indicate immediate use of prosodic cues in natural speech processing. *Nat. Neurosci.*, **2**, 191–196.

Stenbacka, L., Vanni, S., Uutela, K., and Hari, R. (2002). Comparison of minimum current estimate and dipole modeling in the analysis of simulated activity in the human visual cortices. *NeuroImage*, **16**, 936–943.

Streit, M., Ioannides, A.A., Liu, L., Wolwer, W., Dammers, J., Gross, J., Gaebel, W., and Müller-Gärtner, H.W. (1999). Neurophysiological correlates of the recognition of facial expressions of emotion as revealed by magnetoencephalography. *Cogn. Brain Res.*, **7**, 481–491.

Suk, J., Ribary, U., Cappell, J., Yamamoto, T., and Llinas, R. (1991). Anatomical localization revealed by MEG recordings of the human somatosensory system. *Electroencephalogr. Clin. Neurophysiol.*, **78**, 185–196.

Sutherling, W.W., Crandall, P.H., Engel, J., Jr., Darcey, T.M., Cahan, L.D., and Barth, D.S. (1987). The magnetic field of complex partial seizures agrees with intracranial localizations. *Ann. Neurol.*, **21**, 548–558.

Suzuki, K., Okuda, J., Otsuka, Y., Sugawara, A., Hatanaka, K., Nakasato, N., Kanno, A., Yoshimoto, T., Fujii, T., and Yamadori, A. (2001). Judging semantic and episodic incongruity – a magnetoencephalographic study. *NeuroReport*, **12**, 195–199.

Takanashi, Y., Chopp, M., Levine, S.R., Kim, J., Moran, J.E., Tepley, N., Chen, Q., Barkley, G.L., and Welch, K.M. (1991). Magnetic fields associated with anoxic depolarization in anesthetized rats. *Brain Res.*, **562**, 13–16.

Tallon-Baudry, C., Bertrand, O., Delpuech, C., and Pernier, J. (1996). Stimulus specificity of phase-locked and non-phase-locked 40 Hz visual responses in human. *J. Neurosci.*, **16**, 4240–4249.

Tallon-Baudry, C., Bertrand, O., Wienbruch, C., Ross, B., and Pantev, C. (1997). Combined EEG and MEG recordings of visual 40 Hz responses to illusory triangles in human. *NeuroReport*, **8**, 1103–1107.

Tuch, D.S., Wedeen, V.J., Dale, A.M., George, J.S., and Belliveau, J.W. (2001). Conductivity tensor mapping of the human brain using diffusion tensor MRI. *Proc. Natl. Acad. Sci. USA*, **98**, 11697–11701.

Ungerleider, L.G. and Haxby, J.V. (1994). 'What' and 'where' in the human brain. *Curr. Opin. Neurobiol.*, **4**, 157–165.

Vieth, J., Kober, H., Weise, E., Daun, A., Moeger, A., Friedrich, S., and Pongratz, H. (1992). Functional 3D localization of cerebrovascular accidents by magneto-encephalography (MEG). *Neurol. Res.*, **14**, 132–134.

Vrba, J. and Robinson, S.E. (2001). Signal processing in magnetoencephalography. *Methods*, **25**, 249–271.

Vuust, P., Pallesen, K.J., Bailey, C., van Zuijen, T.L., Gjedde, A., Roepstorff, A., and Ostergaard, L. (2005). To musicians, the message is in the meter – Pre-attentive neuronal responses to incongruent rhythm are left-lateralized in musicians. *NeuroImage*, **24**, 560–564.

Wagner, M., Fuchs, M., and Kastner, J. (2004). Evaluation of sLORETA in the presence of noise and multiple sources. *Brain Topogr.*, **16**, 277–280.

Walla, P., Hufnagl, B., Lehrner, J., Mayer, D., Lindinger, G., Deecke, L., and Lang, W. (2002). Evidence of conscious and subconscious olfactory information processing during word encoding: a magnetoencephalographic (MEG) study. *Cogn. Brain Res.*, **14** (3), 309–316.

Watanabe, S., Miki, K., and Kakigi, R. (2005). Mechanisms of face perception in humans: A magneto- and electro-encephalographic study. *Neuropathology*, **25**, 8–20.

Weinberg, H., Deecke, L., Brickett, P., and Boschert, J. (1983). Slow magnetic fields of the Brain preceding movements and speech. *Il Nuovo Cimento*, **2D** (2), 495–503.

Wheless, J.W., Castillo, E., Maggio, V., Kim, H.L., Breier, J.I., Simos, P.G., and Papanicolaou, A.C. (2004). Magnetoencephalography (MEG) and magnetic source imaging (MSI). *Neurologist*, **10**, 138–153.

Wildner, M. (1999). In memory of William of Occam. *Lancet*, **354**, 2172.

Woldorff, M.G., Gallen, C.C., Hampson, S.A., Hillyard, S.A., Pantev, C., Sobel, D., and Bloom, F.E. (1993). Modulation of early sensory processing in human auditory-cortex during auditory selective attention. *Proc. Natl. Acad. Sci. USA*, **90**, 8722–8726.

Wolters, C.H., Grasedyck, L., and Hackbusch, W. (2004). Efficient computation of lead field bases and influence matrix for the FEM-based EEG and MEG inverse problem. *Inverse Problems*, **20**, 1099–1116.

Wood, C.C., Cohen, D., Cuffin, B.N., Yarita, M., and Allison, T. (1985). Electrical sources in human somatosensory cortex – identification by combined magnetic and potential recordings. *Science*, **227** (4690), 1051–1053.

Wübbeler, G., Ziehe, A., Mackert, B.M., Müller, K.R., Trahms, L., and Curio, G. (2000). Independent component analysis of noninvasively recorded cortical magnetic DC-fields in humans. *IEEE Trans. Biomed. Eng.*, **47**, 594–599.

Yang, T.T., Gallen, C.C., Schwartz, B.J., and Bloom, F.E. (1993). Noninvasive somatosensory homunculus mapping in humans by using a large-array biomagnetometer. *Proc. Natl. Acad. Sci. USA*, **90**, 3098–3102.

Yao, J. and Dewald, J.P.A. (2005). Evaluation of different cortical source localization methods using simulated and experimental EEG data. *NeuroImage*, **25**, 369–382.

Yu, H.Y., Nakasato, N., Iwasaki, M., Shamoto, H., Nagamatsu, K., and Yoshimoto, T. (2004). Neuromagnetic separation of secondarily bilateral synchronized spike foci: report of three cases. *J. Clin. Neurosci.*, **11**, 644–648.

Yvert, B., Crouzeix, A., Bertrand, O., Seither-Preisler, A., and Pantev, C. (2001). Multiple supratemporal sources of magnetic and electric auditory evoked middle latency components in humans. *Cereb. Cortex*, **11** (5), 411–423.

Zanow, F. (1997). Realistically shaped models of the head and their application to EEG and MEG. PhD thesis, University of Twente, The Netherlands.

Zatorre, R.J., Belin, P., and Pehune, V.B. (2002). Structure and function in auditory cortex: music and speech. *Trends Cogn. Sci.*, **16**, 37–46.

2.5
Fetal Magnetography

Uwe Schneider and Ekkehard Schleussner

2.5.1
Fetal Magnetocardiography

2.5.1.1
General

Fetal magnetocardiography (fMCG), which was first described by Kariniemi et al. in 1974, provides the opportunity to derive the magnetic field that parallels the fetal cardiac activity cycle noninvasively and is detectable above the maternal abdomen. During the past 15 years, with the spread of available measurement systems worldwide, an increasing number of international publications and conference contributions have documented and pursued the clinical and scientific value of this technique. The major stronghold of this very elegant means of deriving a biological signal of exploitable strength from the fetus is the absolute noninvasiveness, since measurements are carried out entirely without delivering any form of energy to the precious unborn. The only unfortunate setback to use of the technique is the high cost of the equipment required (Peters et al., 2001). The aim of this section is to highlight the details of the current methods, and to compare and complement them with alternative means of monitoring fetal cardiac function. Prospects for the future development of the method are also discussed.

2.5.1.2
Fetal Cardiac Physiology

Rhythmic myocardial action and pump function can be observed on day 22 post conception (p.c.). Primarily, the myocardial cells generate the action potential which is transmitted via intercellular nexus (gap junctions). Differentiation of the conduction pathways follows the craniocaudal direction. Depolarization occurs within each region of the heart by a different rate, the highest rate constituting the pacemaker. Pacemaker function swaps from the so-called atrioventricular to the sinoatrial ring around the eighth week of gestational age (GA). Concurrently, accessory pathways are a transient physiological feature of the fetal heart, and these de-

generate from about 18 weeks GA onwards (Knierim and Mecking, 1983). At day 52 p.c. the ECG is formed by an atrial and a ventricular depolarization and repolarization. At 16 weeks, GA functional maturation of the conducting system can be appreciated (Shenker, 1979).

Sympathetic and parasympathetic nerve fibers were identified at days 42–44 p.c.; these form webs during the next 14 to 16 days. The fetal heart rate increases from around 125 beats per minute (bpm) to 175 bpm between six and nine weeks GA, and thereafter decreases to about 160 bpm by 14 weeks GA.

2.5.1.3 Methodical Approaches

The conventional multi-channel fMCG contains three entities of information concerning the fetal heart (Fig. 2.58). From the raw trace, the "rhythm strip", the train of QRS complexes usually is visible that allows an estimation to be made of the overall fetal heart rate, permits analysis of the beat-to-beat information, and provides an additional impression of QRS configuration or gross abnormalities suggestive of abnormal conduction. The P wave may be visible, but visibility of the T wave is highly unlikely from the raw trace (Menendez et al., 1997). The cardiac time intervals can be measured in the averaged signal (Fig. 2.58c). In addition, the array of a multichannel recording system facilitates spatial information on the magnetic field distribution (Fig. 2.58b) (Wakai et al., 1994).

Analysis of Cardiac Time Intervals (CTI)

The earliest successful fMCG was performed at 13 weeks' GA with signals in the order of noise (Dunjaiski and Peters, 1995). Below 20 weeks of GA, detection rates are low (Menendez et al., 1998). Within a well-established and standardized (see Section 2.5.1.4) experimental setting using an up-to-date multichannel system, the train of R peaks can reliably be derived from about 20 weeks onwards, with increasing amplitudes throughout the second half of the pregnancy (van Leeuwen et al., 2004a).

With regard to the majority of previously published studies, CTI are analyzed after averaging the P-QRS-T complex (Horigome et al., 2000; Kähler et al., 2002a; van Leeuwen et al., 2004b), with 15–20 averages being considered minimum (Quinn et al., 1994), and 100–400 averages practicable (Menendez et al., 1998).

In order to characterize their behavior in fMCG, the different components of the P-QRS-T complex should be categorized in two different ways:

- The P wave and QRS complex are the expression of the spread of excitation within the myocardium. The PQ segment is considered as the time of propagation via the AV node and the conducting system, while ST segment and T wave represent the repolarization time.
- Clinically, the P wave and PQ segment is sub-summarized in the PR interval. QRS complex, ST segment and T wave comprise the QT time, if corrected for heart rate QTc (Bazett's formula).

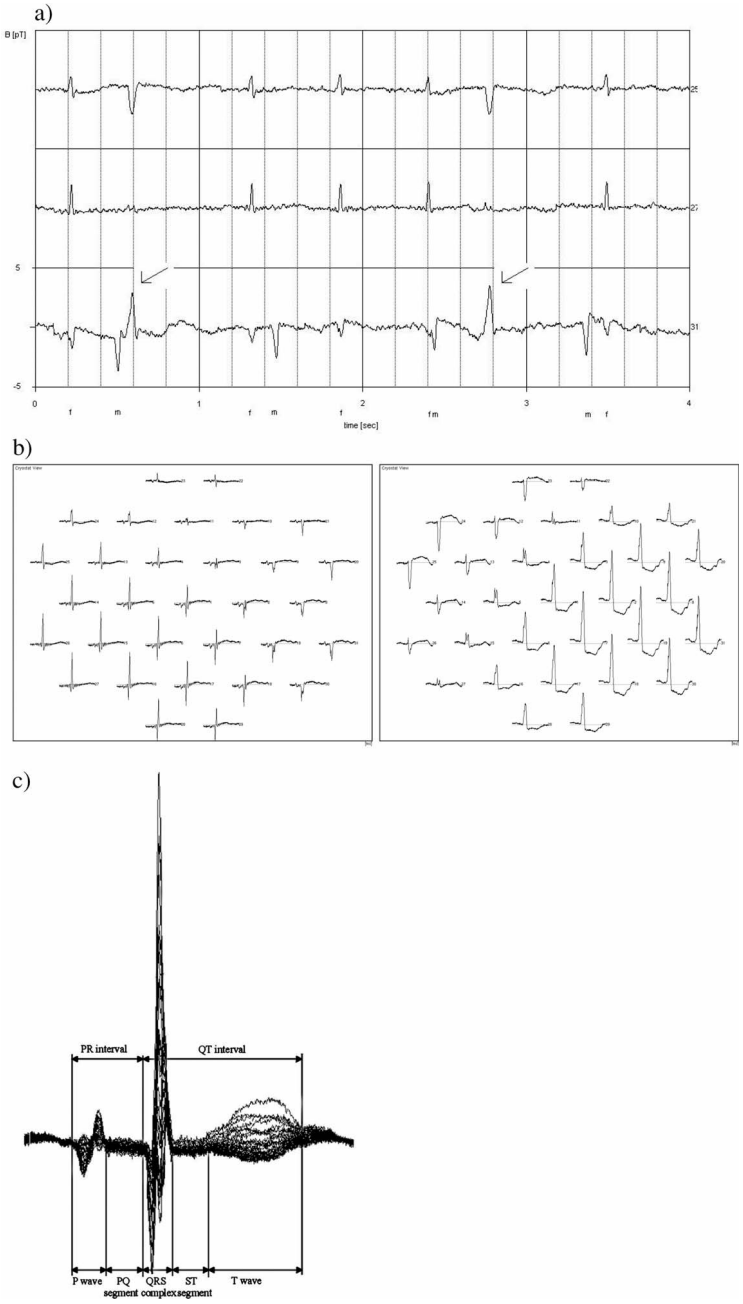

Fig. 2.58. (a) Raw trace of a single magnetic channel from a multichannel system showing maternal (m) and fetal (f) QRS complexes and a ventricular extrasystole (marked with an arrow). (b) 31-channel-array (Philips) showing the spatial distribution of the averaged PQRST complex and ventricular extrasystole. (c) Averaged fetal magnetocardiogram without additional filtering showing the cardiac time intervals according to the standards as described in Section 2.5.1.4. (Adapted from Grimm et al., 2003a).

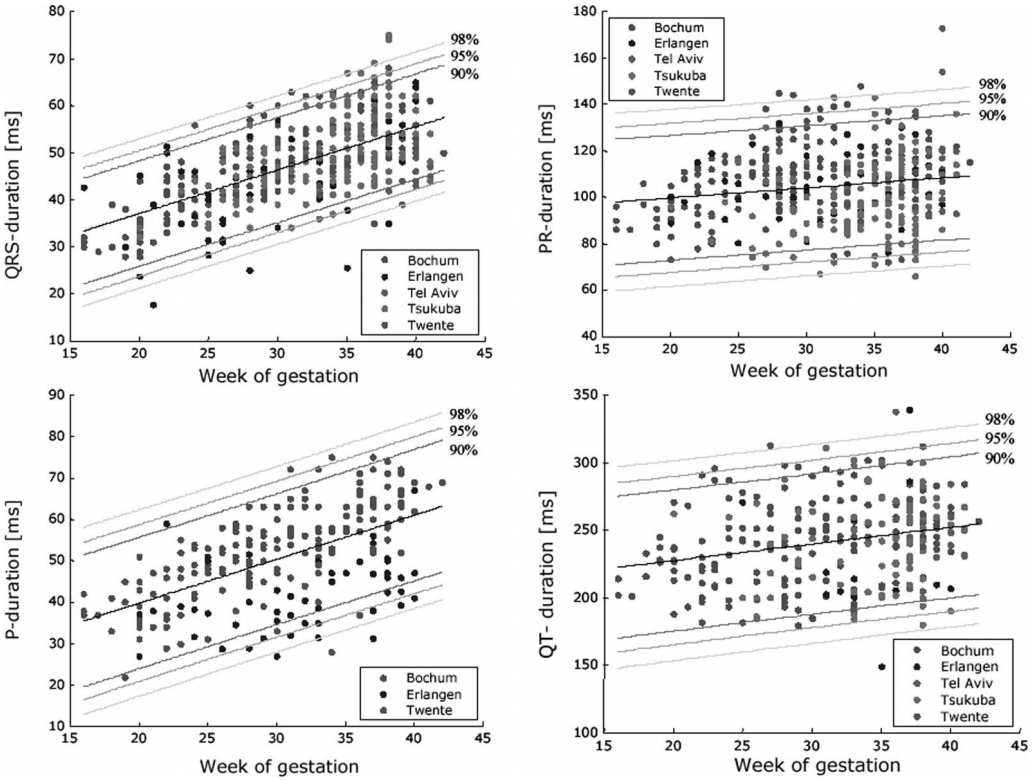

Fig. 2.59. Distribution of normal values obtained by pooling data from different centers into a database. (Image modified from Stinstra et al., 2002, with permission of the Royal College of Obstetricians and Gynaecologists).

The duration of the P wave significantly increases with advancing GA as an expression of the increase of atrial myocardial mass (for normal values, refer to Fig. 2.59). The P wave may be of variant shape or biphasic, and its beginning is difficult to determine (Leuthold et al., 1999). The durations of PR and the QT interval depend on the fetal heart rate (van Leeuwen et al., 2004b).

The QRS complex is the most prominent component in the fMCG signal, and its duration increases throughout the second half of gestation on average by a factor of 1.4 (Fig. 2.59). An observed difference between males and females beyond 30 weeks' GA is the likely expression of lower biometric data and birth weight in females towards term (van Leeuwen et al., 2004a). Detection of the QRS complex reaches 100% with current multichannel systems, and P-wave detection has been described as between 47% and 90+% during the early stages of pregnancy. The detection rates of the T wave are considerably lower, ranging from 22% (Quinn et al., 1994) to 90% (van Leeuwen et al., 2004a), and the unequivocal determination of its

beginning and end are more obscure. However, in cases of QT prolongation, QT interval determination has consistently been described as distinctive (see Section 2.5.1.6).

Van Leeuwen et al. (2004b) were able to show an increase of wave durations (P and QRS) with an increasing number of recording channels. The effect was more pronounced comparing one to seven channels rather than two different multichannel systems (39 versus 61 channels). These results confirmed the observations from a multi-center study comparing systems of varying channel numbers (Fig. 2.59). Seven channels is the recommended minimum for reliable CTI determination, especially prior to 30 weeks' GA. Interobserver variability is minimal for QRS onset and end and, expectedly, highest for T-wave determination.

Analysis of Fetal Heart Rate Variability

The variability in beat-to-beat intervals (normal-to-normal, NN-intervals) of the heart is the common terminus of a variety of neurovegetative and humoral regulatory processes that integrate numerous variables (Dalton et al., 1983). This creates an expression of complex interactions that has often been approached either by breaking these complex interactions down into linear algebra, or by modeling nonlinear, complex explanations in order to exploit their informational content.

International standards have been defined in adult cardiology to characterize heart rate variability (HRV), and these standards could be adapted in fMCG to the analysis of fetal heart rate variability (FHRV) (Grimm et al., 2003a). FHRV is altered both physiologically in association with advancing gestation and the development of neurovegetative behavioral states. Changes also occur in case of pathological intrauterine conditions related to restricted placental oxygen transmission (intrauterine growth restriction, fetal hypoxia, fetal acidosis) (Maulik et al., 1983; van Leeuwen et al., 1999b).

The results are technically influenced by the sample time and quality of the recording (the rate of missing beats). In the antenatal setting, FMCG has proved to be as adequate in the study of FHRV as was the fetal scalp electrode ECG intra partum (Kariniemi and Hukkinen, 1977).

The parameters of the time domain are the expression of the statistical distribution of NN-intervals and their beat-to-beat differences. They may be subcategorized into those expressing overall variability (i.e., standard deviation of normal-to-normal beats; SDNN) or particularly short-term variability (i.e., root mean square of successive differences; RMSSD). Van Leeuwen et al. (1999b) observed the known decrease in mean fetal heart rate and demonstrated an overall increase in the parameters of the time domain as an expression of increasing FHRV with advancing GA.

By applying fast Fourier transformation to the temporally modulated fetal heart rate trace, Wakai et al. (1993) and Hartmann et al. (1997) reported that almost all spectral power is contained below 0.2 Hz. With advancing GA, a decrease in the low-frequency (0.04–0.15 Hz)/high-frequency (0.15–0.4 Hz) ratio has been observed (Zhuravlev et al., 2002). Additionally, respiratory sinus arrhythmia is repre-

sented in the spectrum beyond 0.4 Hz as a developmental feature during the third trimester of gestation (see Fig. 2.60).

Van Leeuwen et al. (1999b) and Lange et al. (2001) focused on the approximate entropy in fMCG data as a complexity measure, and have described an overall decrease but diversion of signal predictability with GA.

Analysis of Signal Morphology

The analysis of signal appearance has previously been performed from a practical point of view. In order to visualize the whole of the cardiac complex, those parts that could be traced in the raw signal were averaged, and clearly allowances had therefore to be made on the acuity of the signal. Independent component analysis has been applied to fetal data both in order to separate different sources (i.e., in twins; Burghoff and van Leeuwen, 2004), and to study beat-to-beat variability of the CTI without averaging (Comani et al., 2004). Additional filtering must be applied. ICA involves an alternative mathematical manipulation of the original signal compared to standard signal averaging (Grimm, 2003; Comani, 2004). Therefore, correspondence to existing normal values has yet to be demonstrated.

2.5.1.4 Standards and International Reference Values

The effort to bring forward internationally applicable current performance standards for fMCG was triggered when a common database for the parameter was created at the University of Twente, The Netherlands (Stinstra et al., 2002). The results from 582 normal subjects were pooled, and although these confirmed the developmental changes of the CTI as described, they revealed systematic differences between various centers (see Fig. 2.59) (http://bct.tn.utwente.nl/database).

The standards are proposed with two intentions: (1) To achieve comparability of data obtained on different equipment or to attribute differences to technical specificities; and (2) to facilitate matters of discussing the differences and to help reviewers and scientists to asses the quality of presented results (Grimm et al., 2003a). The accompanying clinical data were subcategorized into three levels of priority according to their importance and availability. If ever available, ultrasound is recommended to localize the fetal heart immediately prior to investigation, especially if small-size devices are in use. Sturm et al. (2004) have reported an impressive improvement in detection, from 50 to 100%, simply by introducing ultrasound prior to fMCG recording with a multichannel system covering an area of 23 cm. The recording time should be a minimum of 2 minutes, and 5 minutes is required for analysis of the FHRV. The sampling rate for fMCG was generally suggested as 1000 Hz in order to achieve temporal acuity of 1 ms, and filters should be used as sparsely as possible, and declared. Determination of the CTI should be performed from the first to last event in any of the channels available after averaging of the PQRST complex, selectively where appropriate. An accompanying maternal ECG trace is recommended (http://www.biomag.uni-jena.de/fMCG).

2.5.1.5
Monitoring Fetal Cardiac Function: A Brief Comparison of Methods

Four methods are available to monitor fetal cardiac function during pregnancy: cardiotocography; echocardiography; direct intrapartual and transabdominal fetal ECG; and fMCG.

The most widespread method is *ultrasound-based cardio-(toco)-graphy* applying a 1.5-MHz Doppler ultrasound beam to detect periodic changes in fetal cardiac wall movements. The method is in wide use to assess fetal well-being according to semi-quantitative visual criteria, both during pregnancy from about 24 weeks' GA onwards and during labor, with high specificity. Due to poor temporal resolution and the need to perform auto-correlation for heart rate determination, the method lacks the temporal acuity for FHRV analysis (Peters et al., 2001).

Fetal ultrasound *echocardiography* is the recognized clinical specialist standard to diagnose both congenital heart defects (CHD) and fetal arrhythmia. The method delivers information on cardiac morphology and disturbances of the temporal sequence of cardiac action. The temporal resolution is crude, and no information on waveforms is retrievable. In addition, the method is restricted to highly specialized investigators and is remarkably influenced by fetal movement and position.

The *intrapartual fetal ECG* from a scalp electrode after rupture of the membranes is a recognized complementary tool to assess fetal distress, and analyses of T/QRS ratio and ST segment have been introduced into clinical practice (Johannson et al., 1992). Deriving the fetal ECG transabdominally is reasonably reliable between 22 and 27 weeks' GA (Lewis, 2003). The R peak can be distinguished from the noise and used for further signal processing. The method is free of risk for mother and fetus, and relatively easy to apply; it therefore qualifies for long-term ambulatory application. To date, two major constraints have prevented the method from becoming standard. First, the overlay from the maternal ECG is much more pronounced than for instance in fMCG due to the direct volume conduction of both signals. Second, from 27 to about 35 weeks' GA the fetal ECG, in contrast to the fMCG, is severely attenuated by the vernix caseosa, which has a conductivity of 10^{-5} to 10^{-6} S m^{-1} (comparative values: amniotic fluid ~1.5 S m^{-1}, soft tissue ~0.15 S m^{-1}) (Wakai et al., 2000; Stinstra and Peters, 2002).

2.5.1.6
Complementary Role in Clinical Diagnosis

Fetal Arrhythmia

The overall incidence of fetal arrhythmias has been determined at between 0.2 and 2%. Immaturity of the cardiac conducting system has been proposed as the major cause of those cases who remain uncomplicated although if, as usual, the case is identified by chance on cardiotocography or ultrasound examination, CHD, intrauterine infection, maternal systemic disease or maternal diabetes should be ruled out. A classification based on ultrasound has been suggested by Chaoui et al. (1991). In more than 70% of the cases an irregular rhythm occurs in the form of

supraventricular or ventricular extrasystoles, bigemini or trigemini (van Leeuwen et al., 1999a; Menendez et al., 2001). An underlying cause may be found in 1–2% of the cases, while 1–2% also progress to supraventricular re-entry tachycardia (re-entry SVT) that may lead to cardiac decompensation and nonimmunological fetal hydrops.

Paroxysmal SVT, atrial flutter (AF) and atrial fibrillation are associated with CHD in 7% of cases, and in particular with those presenting with atrial dilatation, such as atrial septal defect (ASD) or mitral valve regurgitation (Hosono et al., 2002a). SVT are subdivided into focal SVT and reentry SVT, the latter with involvement [i.e., Wolff–Parkinson–White (WPW) syndrome], or without involvement of the AV node (i.e., AF) (see also Section 2.5.1.2). Kandori et al. (2003) proposed a classification of WPW syndrome by estimating the position of the accessory pathway from the phase angle between the modeled single dipoles of the Δ-wave and the R peak. Differential diagnosis is important, since transplacental therapy is guided by the form of SVT: in the case of WPW syndrome flecainide is more likely to induce cardioversion than digoxin, which has in the past been the drug of first choice for a "trial of transplacental cardioversion" (Hosono et al., 2001; Kähler et al., 2001).

fMCG has proven viable for classifying fetal arrhythmias from the second trimester onwards. Interestingly, among a study group of 69 subjects with documented rhythm abnormalities on fMCG, 37 were previously classified as normal and in only eight cases had arrhythmia been suspected by other methods (van Leeuwen et al., 1999a). Several authors have reported apparent V-shaped decelerations in fetal heart rate prior to 25 weeks' GA due to sinus bradycardia, but this observed phenomenon has been attributed to physiological immaturity of the pacemaker.

Fetal bradycardia may hint at severe underlying disturbances. Several reports exist regarding the diagnosis of fetal QT prolongation along with an increased risk for ventricular tachycardia and sudden cardiac death at an early stage in life (Hamada et al., 1999; Hosono et al., 2002b; Schneider et al., 2005). Systemic maternal disease, and in particular those associated with Anti-Ro-autoantibodies, carry the particular risk to irreversibly damage the fetal cardiac conducting system (Wakai et al., 1998). fMCG monitoring provides an opportunity to exclude abnormalities of the AV conduction in such patients.

Congenital Heart Defects (CHDs)

CHDs are the domain of ultrasound diagnosis, and are described with an incidence of four to nine per 1000 births. On routine ultrasound scanning between 16 and 22 weeks' GA, between 25 and 60% of the major CHDs are identified when using the four-chamber view only (Tegnander et al., 1995). Detailed echocardiography is indicated in those cases where CHD is suspected. While postnatal ECG changes do not correspond to the severity of the malformation, the conductive system might be involved.

In the past, the description of fMCG changes in association with CHDs has remained occasional and restricted to case reports. The observed changes find their explanation in cardiac pathophysiology. Atrial septal defects (ASDs) were as-

sociated with a qualitative increase of P-wave amplitude (Kähler et al., 2002b). The functional stress to the right ventricle, as in ASD and hypoplastic left heart, was associated with an RsR' appearance and prolongation of the QRS complex suggestive of functional right bundle block (Quartero et al., 2002). On the other hand, an association of QRS prolongation in some cases combined with a prolonged P wave has been observed with right ventricular hypoplasia, atrioventricular septal defects and complex combined malformations. Malformation such as transposition of the great arteries may also show no apparent abnormality in P-QRS-T configuration of the fMCG. Horigome et al. (2001) applied the model of the approximation of a current dipole to the study of fetal cardiomegaly, and observed an increase in dipolar strength in the study group. Hosono et al. (2004) studied 14 fetuses with different cardiac malformations and observed prolongation of the QTc in half of these. Six of these seven fetuses died during the neonatal period, despite intensive neonatal and pediatric cardiology care. These authors suggested a prognostic value of QTc prolongation in the case of congenital cardiac malformation.

2.5.1.7 Clinical Research

Fetal MCG in Complicated Pregnancies

Fetal arrhythmia and CHD are of major clinical importance for the individual case, but their overall prevalence is low in comparison to the major issues in perinatal medicine. Two centers have applied fMCG to study intrauterine growth-restriction (IUGR) of fetuses in comparison to matched normals. In the group of normal subjects, both studies reproduced the increase in duration of the P wave and QRS complex with increasing GA. In the group of IUGR fetuses, both intervals were significantly shorter and, in contrast, did not correlate significantly with GA (van Leeuwen et al., 2001; Grimm et al., 2003b). Inconsistencies among these findings that eventually prevented discriminative group differences were attributed to variability in the levels of nutritional impairment and the needs and capabilities of the fetuses to counteract by compensatory mechanisms.

Modeling and Source Localization

The fetus in the uterus surrounded by vernix caseosa and amniotic fluid is, in a technical sense, a complex multicompartment system, that requires differential approaches for modeling. The appearance of the vernix caseosa at the start of the third trimester represents first, an increase in phospholipid concentration in the amniotic fluid around 32 weeks' GA, and a second, a turning point for cardiac source modeling (Stinstra and Peters, 2002). The conductivity of the vernix is frequency dependent on a high-pass filtering effect; its resistance rises by a factor of 20 between 1 kHz (10^{-5} S m^{-1}) and 10 Hz (10^{-7} S m^{-1}). Prior to 28 weeks, the currents are mainly contained within the amniotic fluid, but beyond 28 weeks the Z-component along the fetal axis is dominant in the maternal body surface potential. Depending on whether holes are considered in the vernix (the mouth and bottom of the fetus) or not, the signal attenuation by the vernix reaches a factor of 10

or 100. Therefore, the low-frequency regions of the fetal ECG are unlikely to be visualized (T wave). The influences of the volume conductor on the fMCG are not zero, but are considerably lower than those on the fECG. It has been suggested, that the fetal ECG from the maternal abdomen during the third trimester is best derived between the right lower and left upper quadrant when the fetus is in left cephalic presentation.

2.5.1.8 Perspectives

Derivation of the fMCG provides a signal that is reliably detectable before, or at the latest around 20 weeks of gestation. The unique signal quality qualifies the fMCG as the only applicable method to study cardiac electrophysiology in the fetus throughout the second half of pregnancy.

fMCG is noninvasive, generally easy to use, and is suggested for all cases where an ECG might be indicated. This usually involves transporting the pregnant woman to the fMCG unit, where facilities for acute obstetric intervention are often minimal. In situations where acute fetal compromise may be life-threatening and continuous obstetric observation is required, fMCG is not recommended.

To date, the only appreciable absolute clinical indication is the observation, or the apparent risk of fetal or perinatal compromise in association with suspected fetal arrhythmia. However, as the number of these clinical cases is rare, the use of this method is unlikely to propagate beyond a few centers. Nevertheless, only electrophysiological investigation will secure the correct diagnosis and hence guide therapeutic options.

The situation with regard to CHDs is less clear, as recently emerging data have suggested a prognostic value for repolarization disturbances. Since CHDs are directly related to cardiac function, an fMCG investigation is highly recommended. In order to enhance knowledge about fMCG under clinical conditions such as fetal arrhythmia or CHD, the results must be placed in context with postnatal findings from standard procedures such as neonatal ECG and echocardiography.

For major health issues in perinatal medicine, such as preterm labor, intrauterine growth restriction, placental dysfunction associated with pregnancy-induced hypertension, HELLP syndrome or pre-eclampsia, a particular therapeutic or prognostic value of fMCG has yet to be elaborated.

In an extension to the above-mentioned ''classical'' parameters of fMCG analysis, the signal contains a considerable additional amount of information yet to be explored (Fig. 2.60) (Wakai, 2004). The series of time instants that determine fetal heart actions is accompanied by information on trunk movements and breathing activity of the fetus. Both of these features are components of the ''biophysical profile'' and undergo a maturation process that parallels the maturation of vegetative regulation processes.

The applied systems range from single-channel, second-order gradiometer devices operated in an unshielded environment to multichannel gradiometer or magnetometer apparatus suspended in a magnetically shielded room. In order to re-

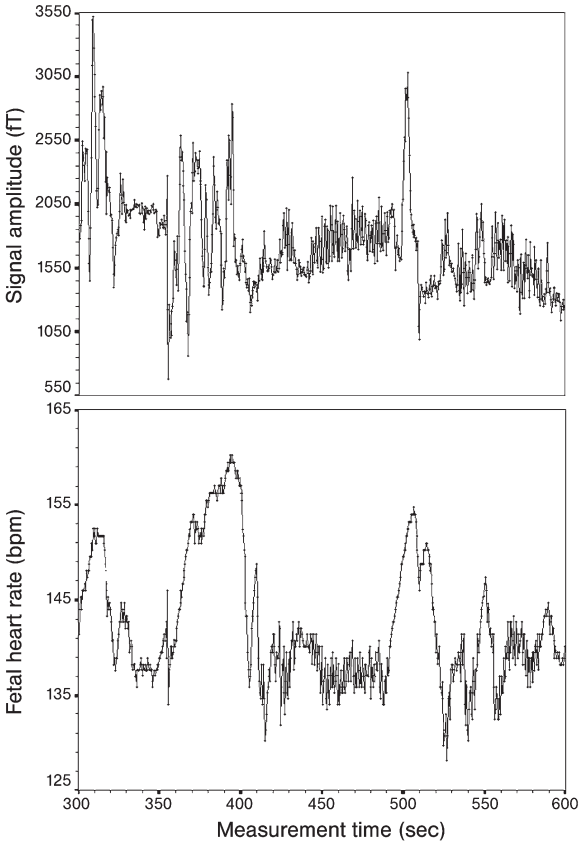

Fig. 2.60. Fetal actocardiogram showing fetal heart rate trace (lower graph) and amplitude of the matched QRS signals (upper graph). Amplitude variations indicate fetal body movements that are associated with heart rate accelerations. Note the small oscillation period of respiratory sinus arrhythmia. (Data with courtesy from R.T. Wakai, University of Wisconsin, Madison, USA).

solve the well-defined temporal properties of the signal for the analysis of heart rate variability or diagnosis of fetal arrhythmia, smaller systems offer great promise and may in the longer term even be cost-effective. The exploitation of spatial properties and the use of signal space projection or independent component analysis requires multiple channels which, unavoidably, involves magnetic shielding. Consequently, the use of these systems will be constrained within an experimental setting in the foreseeable future.

However, if current research can demonstrate the superiority of these systems over current clinical diagnostic procedures, it might lead to further use of these devices, with consequent reductions in cost, increases in procedure efficacy and automatization, handling by trained nonacademic staff, and overall to an exponential increase in clinical expertise.

2.5.2 Fetal Magnetoencephalography

2.5.2.1 General Aspects

Investigations into the development of the fetal brain are of the utmost scientific and clinical interest. Moreover, they are vitally important not only from a methodological standpoint but also with regard to their ethical consequences.

Ultrasound is the method of choice for assessing the morphological integrity of the fetal brain, as it is easy to use, relatively cheap and widely available. To date, MRI has been burdened with the questionable amounts of energy delivered to the fetus, and until recently was only used under strict experimental conditions or if clinical consequences permitted. Functional tests of the fetal brain's integrity are of a global character. More recently, functional MRI studies described increases in the metabolic activity of brain regions after activation by auditory stimuli (Hykin et al., 1999).

Although the concept of recording fetal cerebral activity by biomagnetic means dates back more than 20 years, very few reports have been made on fetal magnetoencephalography (fMEG). There is evidence that MEG and EEG are to some extent complementary in terms of the information they provide, notably with regard to the electrical isolation of the fetus by vernix and the diversity of multiple tissues of different electrical conductivity. EEG does not apply here.

The use of SQUID-based technology in a magnetically shielded room appears to be a prerequisite to recording fetal cerebral activity. To date, reports on spontaneous activity have remained anecdotal (Rose and Eswaran, 2004), and consequently the following section will focus on evoked responses recorded by fMEG.

The method carries the burden of a complex variety of influencing factors, all of which depend upon the signal-to-noise ratio as the central parameter for data quality (Schneider et al., 2001). For systematic analysis, these have been classified into three major categories:

- The strength of the cortical signal is an individual parameter that depends on stimulus physics.
- The major constraint to signal amplitude is the distance between sensor and source, and its stable position during the time when the necessary number of stimuli is applied for signal averaging.
- There is major biomagnetic activity from other surrounding tissues that overwhelms the expected biomagnetic fields from the fetal brain.

The practical factors influencing fMEG are summarized in Table 2.7.

Fetal and maternal cardiac activity that is unavoidably recorded coincidentally with the fMEG represents the major source of "noise" (Schneider et al., 2001). The amplitudes of the cardiac magnetic fields are in the order of 100-fold higher than the expected fetal cortical responses (Wakai et al., 1996; Lengle et al., 2001).

Table 2.7. Influencing factors on data quality in fetal magnetocardiography.

	Intervention impossible or (currently/generally) not acceptable	Conditions to be controlled in the session protocol	Specific post-recording reduction possible
Approximation sensor-source	Comfortable position of the pregnant woman	Gestational age (GA)	
	Anatomical limits of positioning the dewar	Distance from the dewar to the abdominal surface	
	Position of fetal head	Localization of the fetal head and the temporo-parietal cortex area in particular	
		Distance between fetal head and abdominal surface	
Spatial consistency	Fetal movements during recording session	Fetal resting phase	
	Sufficient averaging signal-to-noise ratio	Recording time	
Additional biomagnetic activity	Maternal breathing movements		Fetal heart signal
	Maternal abdominal wall muscle activity		Maternal heart signal
	Activity of the uterine smooth muscle		
Stimulus parameters	Parameters of stimulus transmission	Stimulus parameters	
		Adaptation processes	

Although the pioneering fMEG studies were performed without additional cardiac artifact reduction, more recently a variety of approaches have been applied to overcome the disturbances, including selective subtraction algorithms, signal space projection or adaptive beam-forming from multi-channel, high spatially resolving devices.

Smaller devices have been used on occasion to reduce the distance between sensor and source, but they do not provide the spatial resolution and positioning appears to be more difficult. No advantages to multichannel systems could be elaborated by one group (Schneider et al., 2005).

2.5.2.2
Development of Senses

Development of the Auditory System: A Brief Outline

The sensory modalities in humans mature in the sequence: tactile, vestibular, auditory, and visual. This sequence is comparable to that found in other vertebrates (Courchesne, 1990).

The hearing organ develops from the auditory placode of the ectoderm, beginning during the third week p.c. It forms the auditory pit, later the vesicle, that migrates into the deep, divides into the hearing and the vestibular organs of the inner ear from the fifth week p.c. onwards, and eventually finds contact with the first pharyngeal pouch and the first branchial groove that form the Eustachian tube and the external acoustic meatus (Peck, 1994). The development of receptor cells in the organ of Corti has been observed between the second and fifth gestational months from the base to the tip of the cochlea. During that time, a shift of the response to low frequencies occurs towards more apical receptor cells (Peck, 1994).

The developmental stages of the central hearing system are less clear. The ganglia of the cochlear nerve begin to develop during the fourth week p.c., their maturation paralleling that of the membranous labyrinth. The central auditory tract begins to develop far prior to the initiation of cochlear function. The gyration of the auditory cortex has been observed beginning in the second gestational month, and leading to the typical six-layer cortical appearance during the seventh month, at about the same time that the synapses are formed (Dooling et al., 1983). Myelinization begins at about 20 weeks, is still incomplete at term, and continues until the fourth year of life (Querleu et al., 1989; Peck, 1994).

Cortical auditory evoked responses (CAER) were described in a premature form from 23 (Rotteveel et al., 1987) and 25 (Pasman et al., 1991) developmental weeks onwards in very early preterm neonates. They are described as following a maturational sequence with increasing gestational age from an early stage via a transitional stage to a post-transitional stage in which a primary complex (Na-Pb/P1-N1) can be distinguished from a secondary complex (P2-N2- (P3, N3, P4) from around 34 weeks post menstruation (p.m.). The negative latency development with increasing conceptional age was directly correlated to the grade of myelinization and the length of the neurons (Eggermont, 1995). This correlation could be shown logarithmically for P1, P2 and N2 negative for age versus latency, and positive for age versus amplitude, up to the age of three years in auditory evoked potentials (AEPs) of the EEG.

In addition to stimuli resulting in time-locked auditory evoked responses, cerebral processing of deviant stimuli in a train of ''standards'' was observed to cause distinct electrophysiological differences in the response to both stimuli; this is referred to as mismatch negativity (MMN) (Näätänen, 1995).

MMN renders a few favorable characteristics for the application during the perinatal period. It has a magnetic counterpart referred to as MMNm, is an automatic response without requirement of a task, and is independent of the level of attention (Huotilainen et al., 2003). MMN was identified in newborns at term as well

as in preterm neonates as the earliest discriminative response to sound (Cheour et al., 1996). MMN in newborns is more pronounced using deviants in tone length rather than tone frequency, with the optimum stimulus onset asynchrony being described at about 800 ms (Cheour et al., 2002a,b).

The Visual System

The different parts that form the orbita originate from different source tissues: neuroectodermal (retina, iris, optic nerve); ectodermal (lens, cornea); and mesodermal. Photoreceptor cells differentiate and are synaptically linked from after 18 weeks (Baerts and Fetter, 1998). Myelinization of the optic nerve commences at between six and eight months, and of the posterior visual pathway just before term (Fielder et al., 1998).

The traveling external light to the uterus has been described as being even more attenuated than sound, a matter that has led to the impairment of profound studies about behavioral responses to light *in utero*. Prenatal responses to light were reported from 25 weeks onwards (Arabin et al., 1999).

Visual evoked potentials, however, were elicited from very early preterm neonates from 23 developmental weeks onwards. With increasing age the latency of the responses decrease, and its morphology becomes more complex, indicating visual pathway maturation (Fielder et al., 1998).

2.5.2.3 Applications of fMEG

Cortical Auditory Evoked Responses (CAER)

Successful fMEG applying CAER can be expected as early as at transition from the second to third trimester of gestation, when the central auditory pathways appear to be functioning (see Section 2.5.2.2). In fact, the earliest successful recording of a fetal CAER was described after 27 weeks' GA by Holst et al. (2005) and Schleussner and Schneider (2004). Other authors have described CAER from around 29 weeks' GA onwards. Mobility of the fetuses and a disadvantageous fetus-to-amniotic fluid ratio make earlier detection rather unlikely.

With their first single case report, Blum et al. (1985) pioneered the efforts on fMEG. The recordings were made with a single-channel device, and the positive detection of a N1 component at 140 ms was followed up in the newborn baby. In addition, in the neonate a second complex was detected between 250 and 350 ms of latency. Wakai et al. (1996) described an auditory evoked fetal component in four recordings from 14 subjects with latencies close to 200 ms. Detection rates increased with advancing methodical knowledge and repetitive recordings from the same fetuses (Eswaran et al., 2000, 2002a, 2005).

While initial reports described CAER amplitudes of 75 to 100 fT, more recent studies have shown in a larger number of recordings that the amplitudes must be expected in a much lower range. The low signal-to-noise ratio requires some type of positive signal reproduction (Lengle et al., 2001). By the early 2000s, the detection rates had reached beyond 50%, with the most prominent components of less

than 200 ms or between 200 and 300 ms. More recently, success rates of more than 90% were reported (Eswaran et al., 2005).

Mismatch Negativity (MMN)

The application of MMNm in fMEG represents the most recent approach, and has delivered promising results. Based on previous information from newborns, Huotilainen et al. (2003) performed a study in term neonates using an oddball paradigm with deviants in tone frequency: a standard of 500 Hz (with two upper harmonics at 1000 Hz and 1500 Hz and attenuation by 3 and 6 dB) was in 12% of cases replaced by a deviant of 750 Hz (1500 Hz, 2250 Hz). The protocol elicited a response to the standard with a mean latency of 208 $\pm$ 52 ms. The described latency relates to the 250-ms response described previously by Blum et al. (1985) and Lengle et al. (2001) in neonates, and the ''N2pm'' component as described by Schleussner and Schneider (2004a,b) in fetuses (see Section 2.5.2.4). The MMNm was observed in 11 of the 12 neonates. Modeling of an equivalent current dipole was possible in 10 out of 12 neonates with a mean latency of 247 $\pm$ 25 ms. The almost identical study paradigm was applied in two fetal studies by Huotilainen et al. (2005) and Draganova et al. (2005), based at two different fMEG centers with different technical setup and different cardiac artifact rejection procedures. Detection rates to the standard sound were seven of 17 fetuses (mean latency 230 ms, amplitude 13 fT) and 15 out of 25 fetal data sets (mean latency 260 ms, mean amplitude $<$10 fT), respectively. In summarizing the results of both studies, the MMNm could be found in more than 90% of those fetal data sets where a response to the standard tone was discernible. Mean latency of the MMN was described beyond 300 ms (307 $\pm$ 39 ms and 332 ms). Notably, the response amplitudes to the deviant stimulus were considerably higher than to the standards, reaching up to 30 fT in both studies.

Visual Evoked Cortical Responses

The primary approach to fetal cortical evoked responses in fMEG was auditory for the reasons mentioned previously (see Section 2.5.2.2). It was not until 2002 that the first report on visual evoked responses (VER) from the human fetus recorded by fMEG were reported by Eswaran et al. (2002b). In four out of 10 fetuses a discernible response could be elicited by a flash of 33 ms duration, 625 nm wavelength, 8800 lux and an inter-stimulus interval of 2 s and $\pm$250 ms of randomization. Latency of the responses was described between 180 and 350 ms. This pilot study was followed up by the same authors documenting VER from 28 weeks onwards, with latencies between 147 ms and 384 ms (see Fig. 2.61) (Eswaran et al., 2004, 2005). The average amplitude of the signals was 26 fT, and detection rates reached 68%.

2.5.2.4

Developmental Aspects of Fetal Evoked Responses

Single components at different latency ranges were described in the earlier reports on fMEG, and the interpretation tended to be inconsistent to some extent, though

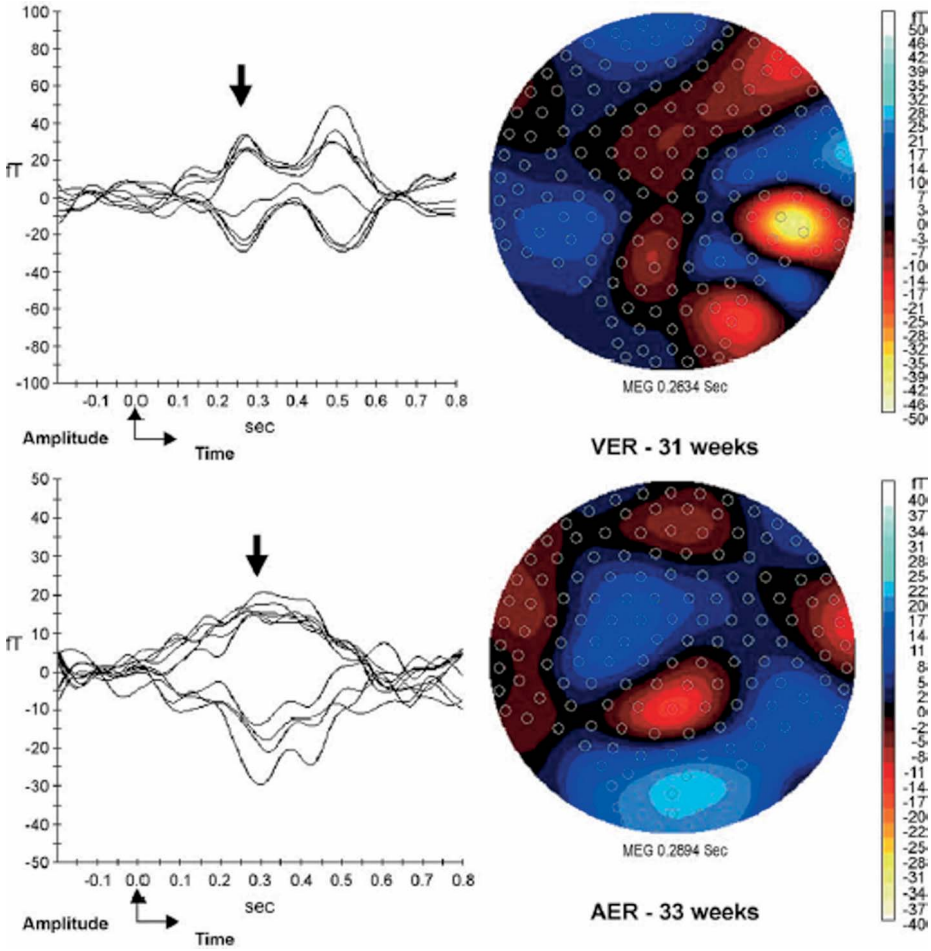

Fig. 2.61. Visual evoked response from a fetus at 31 weeks' gestation at a latency of 263.4 ms (top) and auditory evoked response from a fetus at 33 weeks' gestation at a latency of 289.4 ms (bottom). A color-coded map shows the location of the corresponding magnetic activity over the 151-sensor layout. (Reprinted from Eswaran et al., 2005, p. 60, Copyright ©2005, with permission from Elsevier).

with an increasing number of recordings the most likely detected components were round 200 ms and between 200 and 300 ms (Fig. 2.62) (Schleussner and Schneider, 2004). In a preliminary study conducted by the same authors, the component of less than 200 ms latency was found to occur with significantly lower latencies when derived from the right in comparison to the left cerebral hemisphere (Schleussner et al., 2004a). The first clinical study in the field investigated the acute effect of maternal steroid administration for fetal premature lung maturation on fetal CAER. Latency delay of auditory responses both in the mothers and the fe-

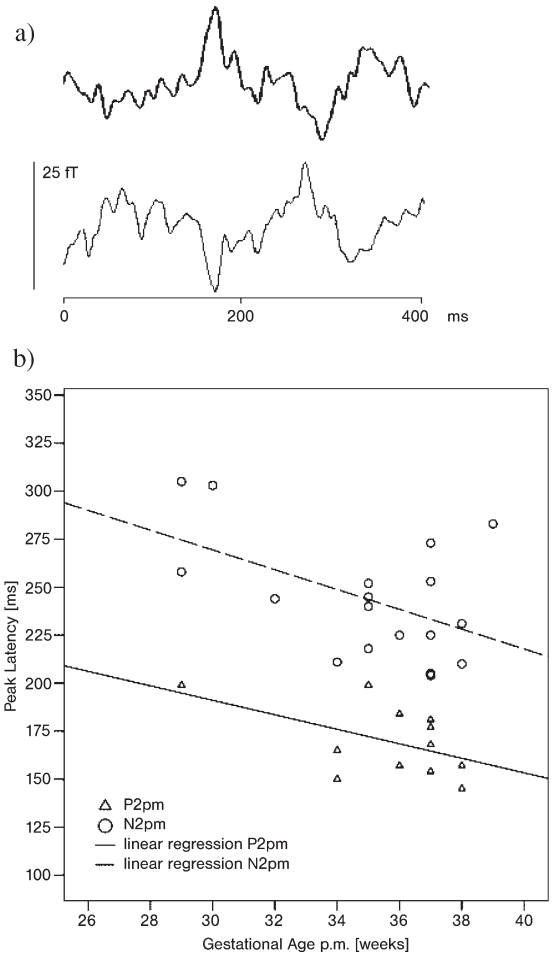

Fig. 2.62. (a) Cortical auditory evoked response from human fetal brain. Note the "P2pm – N2pm" complex with inverse polarity in two different channels of the 31-channel array (Philips™). (b) Latency development of the CAER components with gestational age with significant correlations ($r = -0.51$; $p = 0.022$ and $r = -0.43$; $p = 0.026$) (Schleussner and Schneider, 2004). Detection rates 23.1 (12 of 52 recordings) and 34.6% (18 of 52 recordings), respectively.

tuses was observed combined with an amplitude increase of the maternal N1 and P2 components of the AEP (Schleussner et al., 2004b).

2.5.2.5
Perspectives

In contrast to fMCG, fetal magnetoencephalography is burdened by low signal amplitudes that have led to difficulties in persuading the scientific community of

its benefits ever since its development over 20 years ago. However, even more than fMCG, fMEG serves as a window to the fetus that, if ongoing methodical problems can be overcome, will surely provide an unrivalled technique for use in fetal medicine.

References

Arabin, B., van Lingen, R., Baerts, W., and van Eijck, J. (1999). The development of senses. In: Chervenak, A.F. and Kurjak, A. (Eds.), *Fetal Medicine: the clinical care of the fetus as a patient*. Parthenon Publishers London, New York, pp. 171–180.

Baerts, W. and Fetter, W.P. (1998). Retinopathy of prematurity. In: Kurjak, A. (Ed.), *Textbook of perinatal medicine*. Parthenon London, New York, pp. 129–140.

Blum, T., Saling, E., and Bauer, R. (1985). First magnetoencephalographic recordings of the brain activity of the human fetus. *Br. J. Obstet. Gynaecol.*, **92**, 1224–1229.

Burghoff, M. and van Leeuwen, P. (2004). Separation of fetal and maternal magnetocardiographic signals in twin pregnancy using independent component analysis (ICA). In: Nowak, H., Haueisen, J., Giessler, F., and Huonker, R. (Eds.), *Biomag 2002, Proceedings 13th International Conference on Biomagnetism*, VDE Verlag, Berlin, Offenbach, pp. 311–312.

Chaoui, R., Bollmann, R., Hoffmann, H., and Göldner, B. (1991). Fetal echocardiography III: Fetal arrhythmias. *Zbl. Gynäkologie*, **113**, 1335–1350.

Cheour-Luhtanen, M., Alho, K., Sainio, K., Rinne, T., Reinikainen, K., Pohjavouri, M., Renlund, M., Aaltonen, O., Eerola, O., and Näätänen, R. (1996). The ontogenetically earliest discriminative response of the human brain. *Psychophysiology*, **33**, 478–481.

Cheour, M., Kushnerenko, E., Ceponiene, R., Fellman, V., and Näätänen, R. (2002a). Electric brain responses obtained from newborn infants to changes in duration in complex harmonic tones. *Dev. Neuropsychol.*, **22**, 471–479.

Cheour, M., Ceponiene, R., Leppänen, P., Alho, K., Kujala, T., Renlund, M., Fellman, V., and Näätänen, R. (2002b). The auditory sensory memory trace decays rapidly in newborns. *Scand. J. Psychol.*, **43**, 33–39.

Comani, S., Mantini, D., Pennesi, P., Lagatta, A., and Cancellieri, G. (2004). Independent component analysis: fetal signal reconstruction from magnetocardiographic recordings. *Comput. Methods. Programs. Biomed.*, **75**, 163–177.

Courchesne, E. (1990). Chronology of postnatal human brain development: event related potential, positron emission tomography, myelinogenesis and synaptogenesis studies. In: Rohrbaugh, J.W., Parasuraman, R., and Johnson, R.J. (Eds.), *Event-related brain potentials: basic issues and applications*. Oxford University Press, New York, pp. 210–241.

Dalton, K.J., Dawes, G.S., and Patrick, J.E. (1983). The autonomic nervous system and fetal heart rate variability. *Am. J. Obstet. Gynecol.*, **146**, 456–462.

Dooling, E.C., Chi, J.G., and Gilles, F.H. (1983). Telencephalic development: Changing gyral patterns. In: Gilles, F.H., Leviton, A., and Dooling, E.C. (Eds.), *The Developing Human Brain*. John Wright PSG Inc., Boston, pp. 94–104.

Draganova, R., Eswaran, H., Murphy, P., Huotilainen, M., Lowery, C., and Preissl, H. (2005). Sound frequency change detection in fetuses and newborns, a magnetoencephalographic study. *NeuroImage*, **28**, 354–361.

Dunjaiski, Z. and Peters, M. (1995). Development of the fetal magnetocardiogram from the 13th week of gestation onwards. In: Baumgartner, C., Deecke, L., Stroink, G., and Williamson, S.J. (Eds.), *Biomagnetism: Fundamental Research and Clinical Applications*, IOS Press, Amsterdam, pp. 704–708.

Eggermont, J.J. (1995). Evoked potentials as indicators of auditory development. *Int. J. Pediatr. Otorhinolaryngol.*, **32** (Suppl), 183–186.

Eswaran, H., Lowery, C.L., Robinson, S.E., Wilson, J.D., Cheyne, D., and McKenzie, D. (2000). Challenges of recording human fetal auditory-evoked response using magnetoencephalography. *J. Matern. Fetal Med.*, **9**, 303–307.

Eswaran, H., Preissl, H., Wilson, J.D., Murphy, P., Robinson, S.E., Rose, D., Vrba, J., and Lowery, C.L. (2002a). Short-term serial magnetoencephalography recordings of fetal auditory evoked responses. *Neurosci. Lett.*, **331**, 128–132.

Eswaran, H., Wilson, J., Preissl, H., Robinson, S., Vrba, J., Murphy, P., Rose, D., and Lowery, C. (2002b). Magneto-encephalographic recordings of visual evoked brain activity in the human fetus. *Lancet*, **360**, 779–780.

Eswaran, H., Lowery, C.L., Wilson, J.D., Murphy, P., and Preissl, H. (2004). Functional development of the visual system in human fetus using magnetoencephalography. *Exp. Neurol.*, **190** (Suppl. 1), S52–S58.

Eswaran, H., Lowery, C.L., Wilson, J.D., Murphy, P., and Preissl, H. (2005). Fetal magnetoencephalography – a multimodal approach. *Dev. Brain Res.*, **154**, 57–62.

Fielder, A.R., Moseley, M.J., and Ng, Y.K. (1998). The immature visual system and premature birth. In: Whitelaw, A. and Cooke, R.W.I. (Eds.), *The very immature infant less than 28 weeks gestation*. Churchill, Livingstone, London, New York, pp. 1094–1118.

Grimm, B., Haueisen, J., Huotilainen, M., Lange, S., van Leeuwen, P., Menendez, T., Peters, M.J., Schleussner, E., and Schneider, U. (2003a). Recommended standards for fetal magnetocardiography. *Pacing Clin. Electrophysiol.*, **26**, 2121–2126.

Grimm, B., Kähler, C., Schleussner, E., Schneider, U., Haueisen, J., and Seewald, H.J. (2003b). Influence of intrauterine growth restriction on cardiac time intervals evaluated by fetal magnetocardiography. *Early Hum. Dev.*, **74**, 1–11.

Hamada, H., Horigome, H., Asaka, M., Shigemitsu, S., Mitsui, T., Kubo, T., Kandori, A., and Tsukada, K. (1999). Prenatal diagnosis of long QT syndrome using fetal magnetocardiography. *Prenat. Diagn.*, **19**, 677–680.

Hartmann, M., van Leeuwen, P., and Gronemeyer, D. (1997). Fetal heart rate variability in pregnancy. Spectral analysis based on magnetocardiography. *Biomed. Tech.*, **42** (Suppl.), 61–62.

Holst, M., Eswaran, H., Lowery, C., Murphy, P., Norton, J., and Preissl, H. (2005). Development of auditory evoked fields in human fetuses and newborns: a longitudinal MEG study. *Clin. Neurophysiol.*, **116**, 1949–1455.

Horigome, H., Takahashi, M.I., Asaka, M., Shigemitsu, S., Kandori, A., and Tsukada, K. (2000). Magnetocardiographic determination of the developmental changes in PQ, QRS and QT intervals in the foetus. *Acta Paediatr.*, **89**, 64–67.

Horigome, H., Shiono, J., Shigemitsu, S., Asaka, M., Matsui, A., Kandori, A., Miyashita, T., and Tsukada, K. (2001). Detection of cardiac hypertrophy in the fetus by approximation of the current dipole using magnetocardiography. *Pediatr. Res.*, **50**, 242–245.

Hosono, T., Chiba, Y., Shinto, M., Kandori, A., and Tsukada, K. (2001). A fetal Wolff-Parkinson-White syndrome diagnosed prenatally by magnetocardiography. *Fetal Diagn. Ther.*, **16**, 215–217.

Hosono, T., Kanagawa, T., Chiba, Y., Neki, R., Kandori, A., and Tsukada, K. (2002a). Fetal atrial flutter recorded prenatally by magnetocardiography. *Fetal Diagn. Ther.*, **17**, 75–77.

Hosono, T., Kawamata, K., Chiba, Y., Kandori, A., and Tsukada, K. (2002b). Prenatal diagnosis of long QT syndrome using magnetocardiography: a case report and review of the literature. *Prenat. Diagn.*, **22**, 198–200.

Hosono, T., Kandori, A., Chiba, Y., Sugita, Y., Fujii, M., Suetake, A., Haruna, J., Kitajima, E., and Tsukada, K. (2004). Magnetocardiography in fetuses with congenital structural heart diseases. *BIOMAG 2004 – Proceedings of the 14th International Conference on Biomagnetism*, pp. 319–320.

Huotilainen, M., Kujala, A., Hotakainen, M., Shestakova, A., Kushnerenko, E., Parkkonen, L., Fellman, V., and Näätänen, R. (2003). Auditory magnetic responses of healthy newborns. *NeuroReport*, **14**, 1871–1875.

Huotilainen, M., Kujala, A., Hotakainen, M., Parkkonen, L., Taulu, S., Simola, J.,

Nenonen, J., Karjalainen, M., and Näätänen, R. (2005). Short-term memory functions of the human fetus recorded with magnetoencephalography. *NeuroReport*, **19**, 81–84.

Hykin, J., Moore, R., Duncan, K., Clare, S., Baker, P., Johnson, I., Bowtell, R., Mansfield, P., and Gowland, P. (1999). Fetal brain activity demonstrated by functional magnetic resonance imaging. *Lancet*, **354**, 645–646.

Johannson, R.B., Rice, C., Shokr, A., Doyle, M., Chenoy, R., and O'Brien, P.M.O. (1992). ST waveform analysis of the fetal electrocardiogram could reduce fetal blood sampling. *Br. J. Obstet. Gynaecol.*, **99**, 167–168.

Kähler, C., Schleussner, E., Schneider, U., and Seewald, H.J. (2001). Prenatal diagnosis of the Wolf-Parkinson-White-syndrome by fetal magnetocardiography. *Br. J. Obstet. Gynaecol.*, **108**, 335–336.

Kähler, C., Schleussner, E., Grimm, B., Schneider, A., Schneider, U., Nowak, H., and Seewald, H.J. (2002a). Fetal magnetocardiography: development of the fetal cardiac time intervals. *Prenat Diagn.*, **22**, 408–414.

Kähler, C., Schleussner, E., Grimm, B., Schneider, U., Haueisen, J., Vogt, L., and Seewald, H.J. (2002b). Fetal magnetocardiography in the investigation of congenital heart defects. *Early Hum. Dev.*, **69**, 65–75.

Kandori, A., Hosono, T., Chiba, Y., Shinto, M., Miyashita, S., Murakami, M., Miyashita, T., Ogata, K., and Tsukada, K. (2003). Classifying cases of fetal Wolff-Parkinson-White syndrome by estimating the accessory pathway from fetal magnetocardiograms. *Med. Biol. Eng. Comput.*, **41**, 33–39.

Kariniemi, V. and Hukkinen, K. (1977). Quantification of fetal heart rate variability by magnetocardiography and direct electrocardiography. *Am. J. Obstet. Gynecol.*, **128**, 526–530.

Kariniemi, V., Ahopelto, J., Karp, P.J., and Katila, T.E. (1974). The fetal magnetocardiogram. *J. Perinat. Med.*, **2**, 214–216.

Knierim, H.J. and Mecking, D. (1983). Anatomie und pathologische Anatomie des spezifischen Reizbildungs – und Erregungsleitungssystems sowie des kontraktilen Myokards. In: Lüderitz, B. (Ed.), *Herzrhythmusstörungen*, Springer Berlin, Heidelberg, New York.

Lange, S., van Leeuwen, P., Geue, D., and Grönemeyer, D. (2001). Parameterwahl zur Bestimmung der Approximierten Entropie (ApEn) bei Magnetokardiogaphischen fetalen RR-Zeitreihen. *Biomed. Tech.*, **46** (Suppl. 1), 260–261.

Lengle, J.M., Chen, M., and Wakai, R.T. (2001). Improved neuromagnetic detection of fetal and neonatal auditory evoked responses. *Clin. Neurophysiol.*, **112**, 785–792.

Leuthold, A., Wakai, R.T., and Martin, C.B. (1999). Noninvasive in utero assessment of PR and QRS intervals from the fetal magnetocardiogram. *Early Hum. Dev.*, **54**, 235–243.

Lewis, M.J. (2003). Review of electromagnetic source investigations of the fetal heart. *Med. Eng. Phys.*, **25**, 801–810.

Maulik, D., Saini, V., and Zigrossi, S.T. (1983). Clinical significance of short-term variability computed from heart-rate waveforms. *J. Perinat. Med.*, **11**, 243–248.

Menendez, T., Achenbach, S., Moshage, W., Flüg, M., Beinder, E., Kollert, A., Bittel, A., and Bachmann, K. (1997). Development of the fetal magnetocardiogram during pregnancy. *Biomed. Tech.*, **42** (Suppl. 1), 88–91.

Menendez, T., Achenbach, S., Moshage, W., Flug, M., Beinder, E., Kollert, A., Bittel, A., and Bachmann, K. (1998). Prenatal recording of fetal heart action with magnetocardiography. *Z. Kardiol.*, **87**, 111–118.

Menendez, T., Achenbach, S., Beinder, E., Hofbeck, M., Klinghammer, L., Singer, H., Moshage, W., and Daniel, W.G. (2001). Usefulness of magnetocardiography for the investigation of fetal arrhythmias. *Am. J. Cardiol.*, **88**, 334–336.

Näätänen, R. (1995). The Mismatch Negativity: A powerful tool for cognitive neuroscience. *Ear and Hearing* (Special issue: Mismatch Negativity as an index of Cortical Function), **16**, 6–18.

Pasman, J.W., Rotteveel, J.J., de Graaf, R., Maassen, B., and Notermans, S.L. (1991). Detectability of auditory evoked response components in preterm infants. *Early Hum. Dev.*, **26**, 129–141.

Peck, J.E. (1994). Development of hearing. Part II. Embryology. *J. Am. Acad. Audiol.*, **5**, 359–365.

Peters, M.J., Crowe, J., Pieri, J.F., Quartero, H., Hayes-Gill, B., James, D., Stinstra, J., and Shakespeare, S. (2001). Monitoring the fetal heart non-invasively: a review of methods. *J. Perinat. Med.*, **29**, 408–416.

Quartero, H.W., Stinstra, J.G., Golbach, E.G., Meijboom, E.J., and Peters, M.J. (2002). Clinical implications of fetal magnetocardiography. *Ultrasound Obstet. Gynecol.*, **20**, 142–153.

Querleu, D., Renard, X., Boutteville, C., and Crepin, G. (1989). Hearing in the human fetus? *Semin. Perinatol.*, **13**, 409–420.

Quinn, A., Weir, A., Shahani, U., Bain, R., Maas, P., and Donaldson, G. (1994). Antenatal fetal magnetocardiography: a new method for fetal surveillance? *Br. J. Obstet. Gynaecol.*, **101**, 866–870.

Rose, D.F. and Eswaran, H. (2004). Spontaneous neuronal activity in fetuses and newborns. *Exp. Neurol.*, **190** (Suppl. 1), S37–S43.

Rotteveel, J.J., de Graaf, R., Stegemann, D.F., Colon, E.J., and Visco, Y.M. (1987). The maturation of central auditory conduction in preterm infants until three months post term V. Auditory cortical responses (ACRs). *Hearing Res.*, **27**, 95–100.

Schleussner, E. and Schneider, U. (2004). Developmental changes of auditory evoked fields in fetuses. *Exp. Neurol.*, **190** (Suppl. 1), 59–64.

Schleussner, E., Schneider, U., Arnscheidt, C., Kähler, C., Haueisen, J., and Seewald, H.J. (2004a). Prenatal evidence of left-right asymmetries in auditory evoked responses using fetal magnetoencephalography. *Early Hum. Dev.*, **78**, 133–136.

Schleussner, E., Arnscheidt, C., Schneider, U., Haueisen, J., Schwab, K., and Schwab, M. (2004b). Effects of antenatal glucocorticoids on human fetal cortical function detected by fetal magnetoencephalography. *J. Soc. Gynecol. Invest.*, **11**, A69.

Schneider, U., Schleussner, E., Haueisen, J., Nowak, H., and Seewald, H.J. (2001). Signal analysis of auditory evoked cortical fields in fetal magnetoencephalography. *Brain Topogr.*, **14**, 69–80.

Schneider, U., Haueisen, J., Loeff, M., Bondarenko, N., and Schleussner, E. (2005). Prenatal diagnosis of a long QT syndrome by fetal magnetocardiography in an unshielded bedside environment. *Prenatal. Diagn.*, **25**, 704–708.

Shenker, L. (1979). Fetal cardiac arrhythmias. *Obstet. Gynecol. Surv.*, **34**, 561–572.

Stinstra, J.G. and Peters, M.J. (2002). The influence of fetoabdominal tissues on fetal ECGs and MCGs. *Arch. Physiol. Biochem.*, **110**, 165–176.

Stinstra, J., Golbach, E., van Leeuwen, P., Lange, S., Menendez, T., Moshage, W., Schleussner, E., Kaehler, C., Horigome, H., Shigemitsu, S., and Peters, M.J. (2002). Multicentre study of fetal cardiac time intervals using magnetocardiography. *Br. J. Obstet. Gynaecol.*, **109**, 1235–1243.

Sturm, R., Müller, H.P., Pasquarelli, A., Demelis, M., Erne, S.N., Terinde, R., and Lang, D. (2004). Multi-channel magnetocardiography for detecting beat morphology variations in fetal arrhythmias. *Prenat. Diagn.*, **24**, 1–9.

Tegnander, E., Eik-Nes, S.H., Johansen, O.J., and Linker, D.T. (1995). Prenatal detection of heart defects at the routine fetal examination at 18 weeks in a non-selected population. *Ultrasound Obstet. Gynecol.*, **5**, 372–380.

van Leeuwen, P., Hailer, B., Bader, W., Geissler, J., Trowitzsch, E., and Grönemeyer, D.H. (1999a). Magnetocardiography in the diagnosis of fetal arrhythmia. *Br. J. Obstet. Gynaecol.*, **106**, 1200–1208.

van Leeuwen, P., Lange, S., Bettermann, H., Grönemeyer, D., and Hatzmann, W. (1999b). Fetal heart rate variability and complexity in the course of pregnancy. *Early Hum. Dev.*, **54**, 259–269.

van Leeuwen, P., Lange, S., Hackmann, J., Klein, A., Hatzmann, W., and Grönemeyer, D. (2001). Assessment of intrauterine growth retardation by fetal magnetocardiography. In: Nenonen, J., Ilmoniemi, R.J., and Katila, T. (Eds.), *BIOMAG 2000, Proceedings 12th International Conference on Biomagnetism*, Helsinki Univ. Technology, Espoo, pp. 603–606.

van Leeuwen, P., Lange, S., Klein, A., Geue, D., and Grönemeyer, D.H. (2004a). Dependency of magnetocardiographically determined fetal cardiac time intervals on

gestational age, gender and postnatal biometrics in healthy pregnancies. *BMC Pregn. Childbirth*, **2**, 4/6.

van Leeuwen, P., Lange, S., Klein, A., Geue, D., Zhang, Y., Krause, H.J., and Grönemeyer, D. (2004b). Reproducibility and reliability of fetal cardiac time intervals using magnetocardiography. *Physiol. Meas.*, **25**, 539–552.

Wakai, R.T. (2004). Assessment of fetal neurodevelopment via fetal magnetocardiography. *Exp. Neurol.*, **190** (Suppl. 1), S65–S71.

Wakai, R.T., Wang, M., Pedron, S.L., Reid, D.L., and Martin, C.B., Jr. (1993). Spectral analysis of antepartum fetal heart rate variability from fetal magnetocardiogram recordings. *Early Hum. Dev.*, **35**, 15–24.

Wakai, R.T., Wang, M., and Martin, B. (1994). Spatiotemporal properties of the fetal magnetocardiogram. *Am. J. Obstet. Gynecol.*, **170**, 770–776.

Wakai, R.T., Leuthold, C., and Martin, C.B. (1996). Fetal auditory evoked responses detected by magnetoencephalography. *Am. J. Obstet. Gynecol.*, **174**, 1484–1486.

Wakai, R.T., Leuthold, A.C., and Martin, C.B. (1998). Atrial and ventricular fetal heart rate patterns in isolated congenital complete heart block detected by magnetocardiography. *Am. J. Obstet. Gynecol.*, **179**, 258–260.

Wakai, R.T., Lengle, J.M., and Leuthold, A.C. (2000). Transmission of electric and magnetic foetal signals in a case of ectopia cordis: the dominant role of the vernix caseosa. *Phys. Med. Biol.*, **45**, 1989–1995.

Zhuravlev, Y.E., Rassi, D., Mishin, A.A., and Emery, S.J. (2002). Dynamic analysis of beat-to-beat fetal heart rate variability recorded by SQUID magnetometer: quantification of sympatho-vagal balance. *Early Hum. Dev.*, **66**, 1–10.

3
Magnetic Resonance

3.1
Introduction

Werner A. Kaiser

Since its introduction into clinical practice during the early 1980s, magnetic resonance (MR) has undergone dramatic development and is currently the best and most precise imaging procedure used in medicine. Indeed, such progress has been continued with the development of exciting new applications for all fields of medicine. Although it was widely believed that the new millennium might slow the use of MR procedures, progress has continued during the past few years and appears very unlikely to halt in the foreseeable future.

New applications, such as data acquisition using parallel imaging techniques, new reconstruction algorithms and dramatic improvements in image reconstruction will form the basis of this progress. The use of local sensitivity profiles of receiver coils in parallel imaging techniques [sensitivity encoding (SENSE) and simultaneous acquisition of spatial harmonics (SMASH)] allows increased speed and/or spatial resolution. In addition, magnets of increasingly higher field strength are being used, with 3-Tesla units ready to enter clinical use, and 7-Tesla and higher units under investigation in the laboratory. Whole-body MR imaging that can be performed in minutes and with high spatial resolution, whole-body MR angiography, and the routine use of diffusion, perfusion or blood oxygen level-dependent (BOLD) techniques and MR spectroscopy are just some examples of this exciting progress.

In Section 3.2, Arnulf Oppelt—a pioneer of the first Siemens MR department—underlines and explains the physical principles of MR, as well as new developments in parallel imaging, diffusion imaging, and MR angiography.

Functional imaging represents a major tool for investigating the complex actions of the brain based on BOLD effects. Thus, in Section 3.3.2 Speck and colleagues explain the principle of the BOLD effect and outline the accompanying changes in vascular perfusion. BOLD effects are usually very small, and sophisticated data analysis, motion correction, statistical analysis and control of artifacts are necessary in order to guarantee reliable, reproducible results. Functional brain imaging is also important to understand the "normal" physiological and functional processes in the brain (i.e., the visual system, language system, interactions of different parts of the brain, emotional effects), and this may impact heavily pre-surgical planning

for the optimized therapy of brain tumors, thus preserving vital functions and ensuring a good quality of life. Together, these techniques can add the ''human touch'' to medical understanding.

Striking progress has also been made in cardiovascular imaging by utilizing new improvements in MR imaging (MRI). These new techniques and sequences, when combined, permit the acquisition of high-resolution images in a single heartbeat, providing new insights into cardiac morphology, function and perfusion, as well as vessel analysis. These advances are outlined by Li and Larson in Section 3.3.1. Today, segmented cine images, real-time cine images, myocardial tagging and routine perfusion and stress testing form part of the daily routine in the cardiology clinic. Indeed, the ability to predict the ''heart at risk'' allows the prospective selection of patients for subsequent interventional procedures. Likewise, the precise delineation of necrotic tissue after myocardial infarction, as well as differentiation between necrotic and viable tissues, may impact on the planning of stent placement and/or balloon angioplasty. Coronary MR angiography allows the reliable detection of any relevant narrowing in the proximal two-thirds of the coronary artery, and thus offers non-invasive, risk-free analysis of life-threatening stenoses. The future precise differentiation of the coronary wall and plaque analysis is also envisaged. Clearly, MR imaging of the heart represents the perfect example of a ''one-stop-shop'' modality where, in a single examination, all questions relating to cardiac morphology, function, perfusion and biochemistry can be answered.

Another major area of progress for MRI techniques has been the precise and early depiction of cerebral ischemia and stroke, and their differential diagnosis (see Section 3.3.3). Long-term improvements, ranging from the early studies of Stejskal and Tanner in the mid-1960s, through those of Le Bihan in the late 1980s, until the present day have culminated in the development of diffusion-weighted images, diffusion tensor images and apparent diffusion coefficient (ADC) maps that now form a fundamental part of routine brain investigations in ischemic patients. Perhaps the most important point is that these images provide very early proof of ischemia, with ADC values being reduced only minutes after a stroke, and long before T_2-weighted scans can demonstrate any pathological changes. Bearing in mind that, during the early stages of an ischemic attack, ''time is brain'', this information is vital. More recently, diffusion tensor imaging has also been shown to provide valuable information about cerebral fiber tracks, and has begun to emerge as an important tool for non-invasive brain analyses previously considered unachievable.

The fascinating progress of the past few years has encouraged the development of ultra-high field MRI (between 7 and 9.4 T), and these machines show great promise not only for improved and better depiction of brain tumors, multiple sclerosis, cerebral vascular disease, but also for the precise delineation of deep venous and arterial structures (see Section 3.3.4). Improvements in signal-to-noise ratios and chemical shift spectral dispersion should also lead to improved imaging and spectral analyses for the depiction of diseases. Unfortunately, the road towards these goals is littered with obstacles such as inhomogeneity artifacts, safety concerns and high costs, all of which must be overcome by the dedication and ingenu-

ity of research groups. Indeed, intensive investigations to overcome such problems, including gradient compensation, tailored radiofrequency (RF) pulses, active and passive shimming and post-processing, are currently under way.

Since the early development of *in-vivo* MR procedures, the area of MR spectroscopy (see Section 3.3.7) has been one of great expectation, largely because it permits the non-invasive detection and quantification of biomolecules *in vivo*. With continuous technical progress having been made during recent years, including the optimization of field strength and field homogeneity and the development of broadband RF systems to detect protons and other nuclei such as ^{13}C, ^{19}F and ^{31}P, combined with improved software for the rapid acquisition of MR spectroscopy (MRS) data, spectroscopy has now entered the clinical arena as a valuable, even indispensable, tool. The possibility of monitoring metabolite concentrations and developing metabolic maps each represent vital progress in the differential diagnosis of diseases. In this respect, the acquisition of proton spectra in the brain to determine levels of metabolites such as *N*-acetyl-L-aspartate, creatine, phosphocreatine, trimethylamines, myoinositol and amino acids, allows the loss of neuronal tissue to be monitored in cases of dementia, multiple sclerosis and brain tumors. It also allows tumors to be differentiated based on increased choline peaks, and for specific metabolic enzyme differences [e.g., guanidinoacetate methyltransferase (GAMT) deficiency] to be detected. The differentiation between ischemic regions based on increased lactate production by tumors and abscesses is only one example of new MRS applications, and in the future the use of external tests with specific isotopes carrying ^{13}C or ^{19}F nuclei will most likely become routine, as will the non-invasive measurement of intracellular pH. Ultimately, MRS will undoubtedly find broad clinical application, simply because it can provide vital additional information that is not available by imaging alone, and this will prove invaluable in the reliable diagnosis of brain, prostatic or breast cancers.

Another much-improved area of MR has been the development and implementation of interventional procedures, and these are now ready for routine application. Rapid pulse sequences, MR-compatible, trackable interventional devices and new designs of magnets now allow active image guidance and monitoring of interventional procedures, using the well-known advantages of MR imaging (soft tissue contrast, no X-ray, multiplanar capabilities, etc.). Interventional MR procedures will become routine not only for the biopsy and aspiration of tissues but also for percutaneous therapies, including laser therapy, cryotherapy, RF therapy, and the injection of alcohol or drugs into the liver, brain, heart and other regions of the human body. Likewise, the complete spectrum of endovascular interventional procedures will be applied under MR guidance and/or MR monitoring in the future, and an excellent overview and outlook into this exciting field is provided in Section 3.3.5.

MR mammography has undergone major development during the past 20 years, and today is used to detect small breast cancers, to differentiate between scar and tumor recurrence, and to demonstrate multifocal manifestations of breast lesions. However, many technical, biological and pathophysiological problems associated with breast cancer remain unresolved (see Section 3.3.6), and the high incidence

and mortality of breast cancer continues to represent an important challenge for medical science. In future, breast cancer detection will undoubtedly be improved by the use of MR mammography, with its associated advantages of soft tissue contrast, lack of radiation, imaging of thin slices, and use of tumor-specific features such as ''tumor angiogenesis''. Likewise, digital image processing, parallel imaging, motion correction, and diffusion-weighted imaging will improve diagnosis. An important application in this field will be the combined MR-guided imaging biopsy and interventional therapy of breast lesions conducted in a single, ambulant outpatient procedure, using either RF, cryotherapy, laser therapy or highly focused ultrasound. Further improvements in diagnosis might also be provided by using MR spectroscopy and molecular imaging.

Today, MR is involved in many different fields, including cardiac and neuro applications, interventional guidance, surgical planning or navigation, and diffusion and perfusion imaging, these benefits being due to the unique ability of MR to collect anatomical, functional, and biochemical data. Clearly, the future of MR techniques is exciting, with patients not only undergoing diagnosis but also receiving successful treatment in a minimally invasive manner to provide them with a better quality of life.

3.2
Physical Principles and Technology of Magnetic Resonance Imaging

Arnulf Oppelt

3.2.1
Historical Overview

Magnetic resonance imaging (MRI) was introduced to clinical routine during the early 1980s, since when its unparalleled soft tissue contrast, combined with high spatial resolution and its capability to generate images of slices in arbitrary orientation and even of entire volumes, has made it a preferred imaging modality in many diagnostic situations. Furthermore, the possibility of displaying blood vessels with and without contrast agent, to map brain functions, and to analyze metabolism is widely valued.

Magnetic resonance (MR) is the phenomenon according to which particles with an angular and a magnetic moment precess in a magnetic field, thereby absorbing or emitting electromagnetic energy. This effect is called electron spin resonance (ESR) for unpaired electrons in atoms, molecules and crystals, and nuclear magnetic resonance (NMR) for nuclei. ESR was discovered in 1944 by the Russian scientist Zavoiskij (1945), but until now has not yet gained any real significance for clinical or medical applications. NMR was observed independently in 1945 by Bloch et al. (1946a) at Stanford University, in California, and Purcell et al. (1946) in Cambridge, Massachusetts. The Nobel Prize for physics was awarded in 1952 to these two American groups.

The interaction of atoms and nuclei with magnetic fields has been investigated, however, for a much longer time. In 1897, the Dutch scientist Pieter Zeeman reported that the optical spectrum of sodium could be affected by a strong magnetic field (Zeeman, 1897); a classical interpretation of the so-called Zeeman effect was given by the Irish physicist Joseph Larmor (1897). Some 25 years later, Walter Gerlach and Otto Stern (1924) found that silver atoms could align themselves only parallel and antiparallel to an external magnetic field – one of the fundamental experiments in quantum physics proving the quantization of the angular momentum. In 1937, Isidor Rabi (1937) determined precisely the magnetic moment of nuclei by investigating the interaction of a gas beam of atoms in a homogeneous magnetic field with a radiofrequency (RF) magnetic field. In 1936, and again in 1942, Gorter

and Broer (1936, 1942) reported on the failure to detect NMR in solids due to the short relaxation times.

NMR has proved to be an invaluable tool in physics, chemistry and biology for studying the structure of matter. Richard Ernst at Eidgenössische Technische Hochschule, in Zürich was awarded the Nobel Prize for chemistry in 1991 for progress in developing the method and demonstrating its applications. In 2002, Kurt Wüthrich, also from ETH Zürich, was awarded with the Nobel Prize in chemistry for determining the three-dimensional (3D) structure of biomolecules in aqueous solution with NMR spectroscopy.

The first attempts to use NMR for medical purposes were made 10 years after its detection by Odeblad and Lindström (1955) of the Karolinska Hospital, Stockholm, who analyzed the line widths of protons in biological samples. Singer (1959) reported on blood flow measurements with NMR, while the effect of flow on the NMR signal had been observed earlier by Suryan (1951). Based on the observation that the relaxation times in tumorous tissue tend to be prolonged, in 1971 Damadian (1971) claimed that NMR could be used for the detection of cancer. However, it was not until 1973, when Paul Lauterbur (1973) described how magnetic field gradients could be employed to obtain images similar to those recently generated with X-ray computed tomography, that interest in NMR for clinical applications increased dramatically. Paul Lauterbur was rewarded with the Nobel Prize in medicine in 2003 together with Peter Mansfield, another pioneer in magnetic resonance imaging.

The limits placed on spatial resolution by the wavelength in the imaging process with waves are circumvented in MRI by superposing two fields. With aid of an RF-field in the MHz range and a locally variable static magnetic field, the sharp resonance absorption of magnetic nuclei in biological tissue is used to obtain the spatial distribution of the nuclear magnetization. Thus, even spatial dimensions on the order of a single biological cell, can be resolved (Aguayo et al., 1986). In particular, hydrogen atoms, which occur naturally in large numbers, allow medically meaningful images to be produced. It is however possible to detect magnetic nuclei other than protons, such as ^{13}C, ^{19}F, ^{23}Na, ^{31}P or even hyperpolarized ^{3}He or ^{119}Xe in biological tissue, which are either naturally abundant or administered externally. Nevertheless, the value of information thus gained does not approach that obtained through the resonance of hydrogen nuclei.

3.2.2
Basic Physical Principles of NMR

All atomic nuclei with an odd number of protons or neutrons – that is, approximately two-thirds of all stable atomic nuclei – possess an intrinsic angular momentum and a magnetic dipole moment, which is proportional to the angular momentum. As the angular momentum is quantized – a fact that is described by the nuclear spin – an atomic nucleus can only assume discrete energy states in

a magnetic field; for example, a proton with spin $I = \frac{1}{2}$ can only align parallel or antiparallel.

In matter, atomic nuclei do not occur singly but always as an ensemble. For example, 1 mm^3 water contains 6.7×10^{19} hydrogen nuclei. Population of the energy levels in an external magnetic field B_0 is described by Boltzmann statistics giving a surplus of nuclear magnetic moments aligned parallel to the magnetic field (for the same reason air density decreases with increasing height). With water in a magnetic field of 1 T at room temperature, this surplus amounts to 3.2×10^{-6} of the protons. Thus, a small but measurable macroscopic angular momentum J_V per unit volume results associated with the nuclear magnetization

$$M_0 = \gamma J_V = N_V \frac{I(I+1)\gamma^2\hbar^2 B_0}{3kT} \tag{3.1}$$

where γ is the gyromagnetic ratio (e.g., for the hydrogen nucleus $\gamma/2\pi = 42.577$ MHz/T); $\hbar$ is Planck's constant ($\hbar = 1.05510^{-34}$ Js); k is Boltzmann's constant ($k = 1.3810^{-23}$ Ws/K); I is nuclear spin (e.g., for the proton $I = \frac{1}{2}$); N_V is the number of nuclei per unit volume; and T is temperature.

The nuclear magnetization of a sample with hydrogen atoms or protons aligns itself parallel to an applied magnetic field B_0. However, if this parallel alignment is disturbed, for example by suddenly changing the direction of B_0, a torque acts on the magnetic moment of the sample. According to the law of conservation of angular momentum, this torque causes a temporal change of the angular momentum of the sample, resulting in a precession of the magnetization with the (circular) Larmor frequency

$$\omega_L = -\gamma B_0 \tag{3.2}$$

The rotation direction of the precessing nuclear magnetization depends on the sign of γ, for hydrogen nuclei, which are the most frequently occurring nuclei in nature, the gyromagnetic ratio is positive so that a clockwise rotation results. Protons yield a nuclear magnetic resonance frequency of 42.577 MHz in a magnetic field of 1 T. The precession can be detected by measuring the alternating voltage induced in a coil wound around the sample (Fig. 3.1).

In an NMR experiment, the precession of the nuclear magnetization is often stimulated by disturbing the alignment of the nuclear magnetization parallel to the B_0-field by a RF field B_1 having a frequency similar to the Larmor frequency. It is provided by a coil wound around the sample with its field axis orthogonal to the static magnetic field. Often, this coil is also used for signal detection. The linearly polarized RF-field in this coil can be thought of as the superposition of two circularly polarized fields rotating in opposite directions. Thus, there is always the same direction of rotation as the Larmor precession, and in this reference frame (the rotating frame) B_1 is constant. The resulting torque causes the nuclear magnetization to precess around the axis of the B_1-field in the rotating frame in the same way as around the B_0-field in the laboratory frame. The combined precession

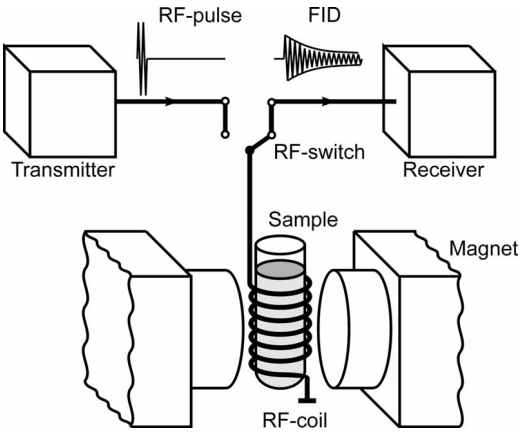

Fig. 3.1. Principle of the NMR experiment. The precession of nuclear spins in a magnetic field is detected with an induction coil after the equilibrium of the nuclear magnetization has been distorted with an RF-pulse.

movement around the basic static and the rotating RF-field causes the tip of the nuclear magnetization vector to execute a spiral path on the surface of a sphere (Fig. 3.2). The contrarotating RF-field, having twice the Larmor frequency in the rotating frame, acts as a perturbation and effectively averages out.

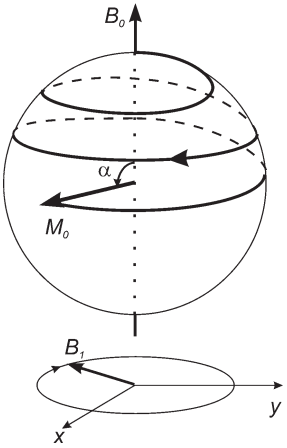

Fig. 3.2. Motion of the nuclear magnetization vector M_0 under the influence of a static magnetic field B_0 and a circularly polarized RF-field B_1 with Larmor frequency $-\gamma B_0$. The initial position of M_0 is parallel to B_0; after time t M_0 is oriented with an angle $\alpha = -\gamma B_1 t$ along the direction of B_0. (The direction of precession depends on whether the angular and the magnetic moment of the nuclei are parallel or antiparallel. For protons, a clockwise rotation follows).

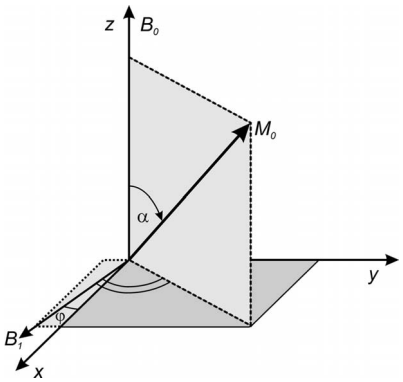

Fig. 3.3. Angular relations between a B_1 field acting on the nuclear magnetization M_0 in the rotating frame.

Under the influence of the B_1-field an angle α between the static magnetic field B_0 and the nuclear magnetic moment emerges, which is proportional to the duration t of the RF-field:

$$\alpha = -\gamma \int_0^t B_1(t)\, dt = -\gamma B_1 t \tag{3.3}$$

With a B_1-field that confines an angle φ with the x-axis of the rotating frame, the nuclear magnetization attains the components (Fig. 3.3)

$$M_x = -M_0 \sin\alpha \sin\varphi, \quad M_y = M_0 \sin\alpha \cos\varphi, \quad M_z = M_0 \cos\alpha \tag{3.4}$$

Switching off the RF-pulse after the nuclear magnetization is aligned orthogonally to the B_0-field ($\alpha = 90°$, hence a 90° pulse), induces the maximum signal in the sample coil.

3.2.3 The NMR Signal

Experience shows that the amplitude of the precessing nuclear magnetization decays with time, and the original state of equilibrium with the magnetization aligned parallel to the B_0-field is reestablished. This effect is described phenomenologically by two separate relaxation time constants, T_1 and T_2, in which the equilibrium states, M_0 and zero respectively, of the nuclear magnetization M_z parallel and $M_\perp$ perpendicular to B_0 are reached; T_1 is always $\geq T_2$. Longitudinal relaxation is associated with the dissipation of energy to the surroundings – that is, the lattice in which the nuclei are embedded – and is therefore also referred to as spin-lattice

relaxation. The sample heating due to this effect, however, is hardly measurable. Transverse relaxation is caused by interactions between the nuclear spins and thus often referred to as spin-spin relaxation. Since in the latter case the longitudinal component of the magnetization remains unchanged, the energy of the nuclear ensemble does not change; only the relationship of the phases between the individual spins is lost.

The behavior of the nuclear magnetization in an external magnetic field B_0 undergoing relaxation was described by Bloch et al. (1946b) by adding empirical terms to the classical law of motion conservation:

$$\frac{dM_\perp}{dt} = \gamma(\vec{M} \times \vec{B})_\perp - \frac{M_\perp}{T_2} \quad \text{and} \quad \frac{dM_z}{dt} = \gamma(\vec{M} \times \vec{B})_Z + \frac{(M_0 - M_z)}{T_1} \tag{3.5}$$

It follows from Bloch's equations (Eq. 3.5) that after a 90° pulse around the *x*-axis the transverse component of the nuclear magnetization is given in the rotating frame as

$$M_\perp(t) = iM_0 e^{-t/T_2} \tag{3.6}$$

(and $M_\perp(t)e^{i\omega_L t}$ in the laboratory frame respectively). The longitudinal component follows as

$$M_z(t) = M_0(1 - e^{-t/T_1}) \tag{3.7}$$

The *x*- and *y*-components of the transverse magnetization, which are combined here into the complex quantity $M_\perp = M_x + iM_y$ ($i = \sqrt{-1}$), can be measured with an induction coil and two phase-sensitive detectors in quadrature. The NMR signal is mixed with two local signals of Larmor frequency, one being in and the other being 90° out of phase; the mixing products represent M_x and M_y in the rotating frame. Alternatively, two induction coils oriented perpendicular to each other can be employed providing for a $\sqrt{2}$ times better signal-to-noise (S/N) ratio. The time course of the transverse magnetization after a 90° pulse is often called *free induction decay* (FID).

The frequency dependence of the transverse magnetization is given by Fourier transformation of the FID (Fig. 3.4). The imaginary part of the Fourier transformation describes the so-called absorption line

$$M_y(\omega) = M_0 \frac{T_2}{1 + (\omega - \omega_L)^2 {T_2}^2} \tag{3.8a}$$

and the real part the dispersion line

$$M_x(\omega) = M_0 \frac{-(\omega - \omega_L){T_2}^2}{1 + (\omega - \omega_L)^2 {T_2}^2} \tag{3.8b}$$

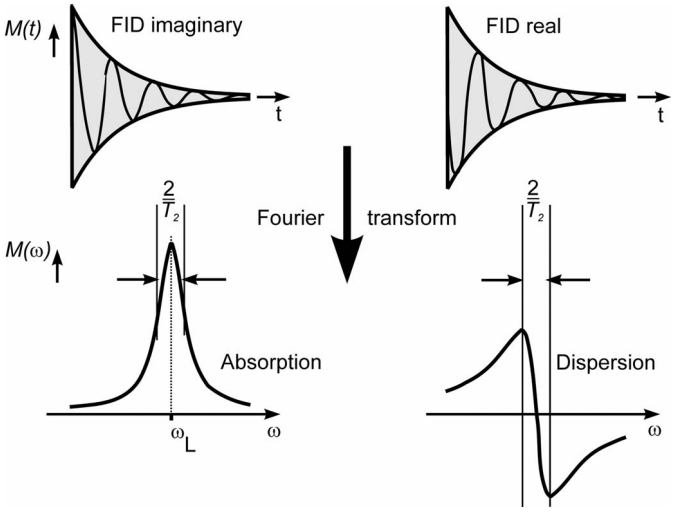

Fig. 3.4. Free induction decay (FID) after a 90° pulse with its Fourier transform, representing the NMR absorption and dispersion line.

Instead of taking the Fourier transformation of the FID, it is also possible to measure the absorption and dispersion directly by recording the change of resistance and inductance of the signal coil surrounding the sample as a function of frequency (or as a function of the B_0-field). Such continuous-wave (CW) methods, however, are much slower than pulse methods and are therefore hardly used anymore.

The full width at half maximum (FWHM) of the absorption and the distance between the extreme points of the dispersion line are given by the transversal relaxation time

$$\Delta\omega_{1/2} = \frac{2}{T_2} \tag{3.9}$$

Protons in distilled water exhibit a transversal relaxation time $T_2 \approx 1$ s. The measurement of T_2 through the free induction decay, however, is only possible in very homogenous magnetic fields. In practice, the B_0-field varies in space, resulting in different precession frequencies of the nuclear magnetization. Because of destructive interference a shortened FID is observed, resulting in an inhomogeneously broadened resonance line. The line shape depends on the spatial distribution ΔB_0 of the B_0-field over the entire sample. Reference is often made to an effective transversal relaxation time

$$\frac{1}{T_2{}^*} = \frac{1}{T_2} + \frac{\gamma \Delta B_0}{2} \tag{3.10}$$

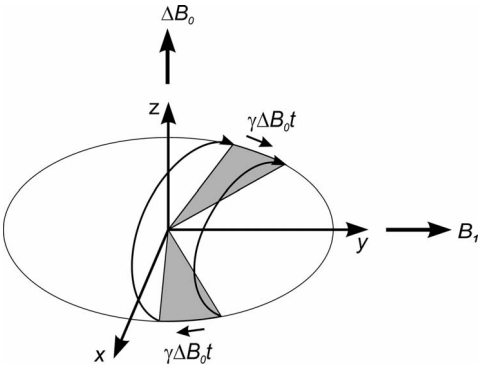

Fig. 3.5. The dephasing by an angle $\gamma\Delta B_0 t$ of transverse nuclear magnetization due to B_0-field inhomogeneities ΔB_0 is reversed with a 180° RF-pulse.

which, however, can only coarsely describe the effect of magnetic field inhomogeneities since the signal clearly no longer decays exponentially.

The signal loss in an inhomogeneous B_0-field can be recovered by means of a refocusing or 180° RF-pulse (Hahn, 1950). The diverging transverse magnetization after a 90° pulse due to B_0-field inhomogeneities converges again after a 180° pulse, since the 180° pulse reverses the order of the spins (Fig. 3.5). Thus, slowly precessing spins which have lagged behind now move ahead and realign themselves with the faster-precessing spins after a time according with the interval between the two RF-pulses. A spin echo is observed, the amplitude of which is determined by transverse relaxation.

In this context we will mention another type of echo, the so-called *stimulated echo*. When applying two 90° pulses instead of a 90°/180° pair, an echo also occurs, but only with half the amplitude resulting from using a 180° pulse. The other half of the magnetization is stored along the *z*-axis, thereby undergoing longitudinal relaxation. It can be tilted again into the transverse plane with a third 90° pulse, and manifests itself as a stimulated echo with a distance from the third 90° pulse corresponding to that of the first two 90° pulses (Fig. 3.6). The amplitude of the

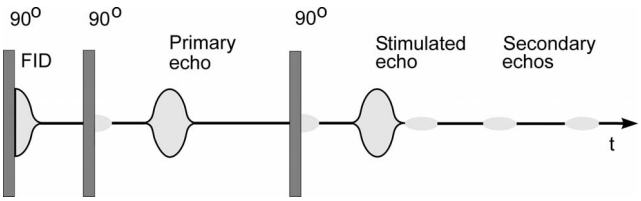

Fig. 3.6. Sequence with three 90° pulses, yielding a primary spin echo and a stimulated echo. In case of a deviation from the 90° condition additional secondary echoes appear.

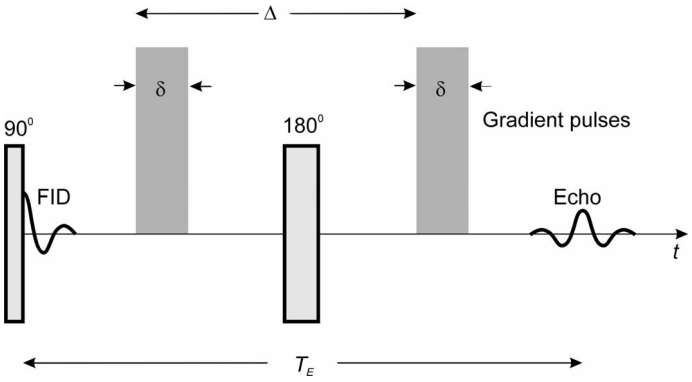

Fig. 3.7. Pulsed gradient spin echo (PGSE) sequence to obtain a diffusion-weighted NMR signal.

stimulated echo is determined by the longitudinal relaxation. At deviations from the exact 90° condition further echoes are observed that can be explained from interaction of the third RF-pulse with primary echo and with the FIDs from the first and second RF-pulse.

Relaxation is not the only mechanism which affects the amplitudes of the echoes. In particular, the molecules of liquids move stochastically (diffuse) during the time between excitation and observation of the echo from one position in the inhomogeneous B_0-field to another; in accordance with the field difference, the nuclei precess there with a different Larmor frequencies and thus no longer contribute fully to the echo amplitude (Carr and Purcell, 1954). The influence of spin diffusion can be enhanced by applying a strong magnetic field gradient pulse symmetrically before and after a refocusing RF-pulse (Stejskal and Tanner, 1965) (Fig. 3.7). In order not to lose too much signal due to transverse relaxation between the two gradient pulses, the refocusing 180° pulse can also be partitioned into two 90° pulses so that diffusion is probed with the stimulated echo. In magnetic resonance imaging, such types of experiments are of interest, because diffusion is strongly influenced by tissue microstructure. For example, anisotropic diffusion offers the possibility to obtain information about the fiber structure of a tissue. Diffusion depends on sample temperature and therefore may offer a possibility for a noninvasive measurement of temperature *in vivo*.

The gyromagnetic ratio determining the Larmor frequency of nuclei in the B_0-field is a fixed constant for each nuclear species. In NMR experiments with nuclei embedded in different molecules, however, slightly different resonance frequencies are observed. This effect is caused by the molecular electrons responsible for chemical bonding. These screen the external magnetic field, with the result that the atomic nucleus "sees" different magnetic fields (chemical shift) depending on the nature of the chemical bond.

Besides the chemical shift, a fine splitting of the magnetic resonance lines is also frequently observed. This is caused by the magnetic interaction (spin-spin

coupling) between the nuclei, which again acts indirectly via the valence electrons. Therefore, in chemistry molecular structure is often investigated with NMR spectroscopy.

3.2.4 Nuclear Relaxation

Within an ensemble of spins each single spin is exposed not only to the external magnetic field but also to the magnetic fields arising from the surrounding neighbor spins. As the neighbor spins may be aligned differently to the B_0-field (e.g., for $I = \frac{1}{2}$ parallel or antiparallel), these fields will differ from position to position. Therefore, a spread of Larmor frequencies results that corresponds to an NMR line width given by the quadratic average of all possible neighbor contributions:

$$\Delta\omega_0^2 = \left(\frac{2}{T_2}\right)^2 = \gamma^2 \langle b_z^2(r) \rangle = \gamma^2 \langle b_z^2(t) \rangle \tag{3.11}$$

One can assume that the quadratic average of all spatial field configurations $b_z(r)$ is the same as for all field configurations $b_z(t)$ evolving over time, a hypothesis termed *ergodic*. As the position of all spins is assumed to be fixed, $\Delta\omega_0$ is often called the *rigid lattice line width*. Compared to spins in a rigid lattice, mobile spins in fluids show a much narrower line width (or longer transversal relaxation time). This is a consequence of movement and collisions between the spins and water molecules, respectively.

The temporal behavior of fluctuating magnetic neighbor fields is described by the autocorrelation function

$$\langle b_z(t) b_z(t+\tau) \rangle = \lim_{T \to \infty} \frac{1}{T} \int_{-\infty}^{\infty} b_z(t) b_z(t+\tau)\, dt = \langle b_z^2(t) \rangle G(\tau) \tag{3.12}$$

Here, $G(\tau)$ indicates that the autocorrelation function normalized to $G(0) = 1$.

The spectral distribution of the fluctuating field is given by the Fourier transformation of the autocorrelation function (Fig. 3.8, upper part):

$$J(\omega) = \int_{-\infty}^{\infty} G(\tau) e^{-\omega t}\, d\tau \tag{3.13}$$

A magnetic field with spectral components that deviate only slightly from frequency zero exists over a long time (the *correlation time*). Motion between the spins causes rapidly changing neighbor fields with a distribution of spectral components over a much larger frequency range (short correlation time) than in a rigid lattice. Only the spectral components within the interval of the NMR line width $\Delta\omega$ have an influence on the NMR signal. So, the identity $G(0) = \frac{1}{2\pi} \int_{-\infty}^{\infty} J(\omega)\, d\omega = 1$ that

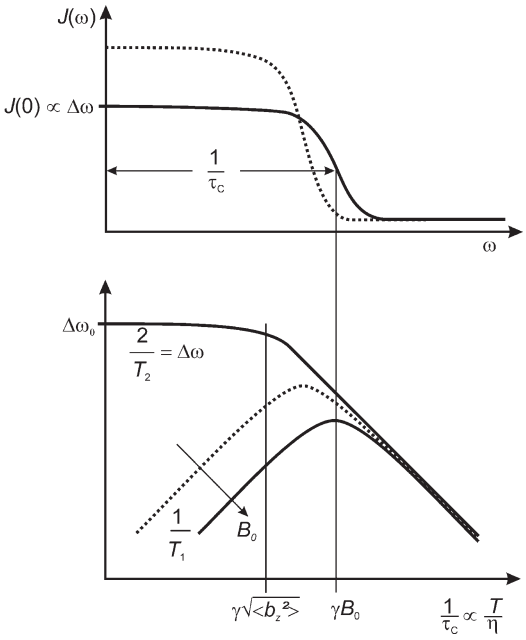

Fig. 3.8. The NMR relaxation rates $1/T_1$ and $1/T_2$ are determined by the spectral distribution $J(\omega)$ (upper plot). $J(\omega)$ describes the dependence of $1/T_1$ on the magnetic field B_0. $J(0)$ is a measure for the linewidth $\Delta\omega$, which depends on the width $1/\tau_C$ of $J(\omega)$ (lower plot). The correlation time τ_C is proportional to the ratio of viscosity η and temperature T in viscous fluids. $1/T_1$ reaches a maximum on τ_C, when $1/\tau_C = \gamma B_0$. (A logarithmic scale has been adopted in the schematics).

can be derived from Eq. (3.13) must be replaced with $\frac{1}{2\pi}\int_{-\Delta\omega}^{\Delta\omega} J(\omega)\, d\omega \approx J(0)\Delta\omega$, leading to the quadratic line width $\Delta\omega^2 \approx \Delta\omega_0^2 J(0)\Delta\omega$. It follows that at rapid spin fluctuations a narrowed NMR line width is observed:

$$\Delta\omega \approx \Delta\omega_0^2 J(0) \tag{3.14}$$

Given stochastic motion, one can assume an exponential decay for the auto-correlation function

$$G(\tau) = e^{-|\tau|/\tau_c} \tag{3.15}$$

with correlation time τ_c as the average time between two spin collisions.

From the Fourier transform of Eq. (3.15) the spectral density of the fluctuations follows as

$$J(\omega) = \frac{2\tau_c}{1 + \tau^2\omega^2} \tag{3.16}$$

so that the line width at rapid spin fluctuations results in

$$\Delta\omega = \frac{2}{T_2} = \omega_0^2 J(0) \approx 2\omega_0^2 \tau_C \quad \left(\tau_C \ll \frac{1}{\Delta\omega_0}\right) \tag{3.17}$$

An increase of the line width $\Delta\omega$ upon correlation time τ_c (or a decrease on collision frequency $1/\tau_C$) is yielded (Fig. 3.8, upper part). However, when the correlation time becomes comparable with the precession time of a spin in the rigid lattice field, $\Delta\omega$ is no longer determined by motions and approaches the rigid lattice line width $\Delta\omega_0$ (Fig. 3.8, lower part). It should also be mentioned that already the finite lifetime of the nuclear energy levels leads to an intrinsic line width $1/T_1$ in accordance with Heisenberg's uncertainty relationship. This term, therefore, must be added to Eq. (3.17), but it does not alter the general dependence of $\Delta\omega$ on the correlation time (see next section).

The longitudinal relaxation rate $1/T_1$ is a measure of the probability of transitions between the energy levels that a magnetic nucleus may assume in a static magnetic field B_0. Transitions are caused by magnetic RF-field components at Larmor frequency occurring during collisions between molecules that are perpendicular to the B_0-field. The frequency dependence of the transition rate again can be derived from the power spectrum $J(\omega)$ of the fluctuating field due to the molecular motion:

$$\frac{1}{T_1} = \gamma^2(\langle b_x^2\rangle + \langle b_y^2\rangle)J(\omega_L) \tag{3.18}$$

In water molecules the two protons are coupled via magnetic dipole–dipole interactions. Since the dipolar interaction depends on the mutual orientation of the spins, transitions between spin levels emerge when a water molecule tumbles. Random RF-fields causing relaxation occur with frequency components at Larmor frequency and twice the Larmor frequency. The magnetic field at $2\omega_L$ can be considered as having a circular polarized component that is constant in the reference frame rotating with ω_L. Thus, Eqs. (3.17) and (3.18) must be supplemented by a spectral density term with an argument $2\omega_L$. The general tendencies described persist, however.

$1/T_1$ passes through a maximum, when the correlation time is equal to the reciprocal of the Larmor frequency, $\tau_C = 1/\omega_L$ (Fig. 3.8, lower part). In pure water, $\tau_C \approx 3$ ps. The dependency of T_1, T_2 on τ_c has been verified by Bloembergen et al. (1948) with NMR measurements on viscous liquids, where the correlation time is a function of the ratio of viscosity over temperature. In 1981, Bloembergen received the Nobel Prize in physics for his contribution to the development of laser spectroscopy. The temperature dependence of T_1 of tissue can be used in magnetic resonance imaging as a means to follow noninvasively temperature changes, for example during thermal treatment.

In biological tissue the mechanism for relaxation is more complex than in viscous fluids. In general, mobile water and more immobile water molecules bound

to macromolecules exist in tissue. The two systems are coupled with each other by intermolecular dipole–dipole interaction, so that in addition to the direct spin-lattice relaxation an additional relaxation path between the more solid and the mobile protons exists (Bryant et al., 1991).

It is the wide range of relaxation times in biological tissue that makes NMR so interesting in medical diagnostics. T_1 is of the order of magnitude of several hundred milliseconds, while T_2 is in the range 30–100 ms. Displaying the nuclear magnetization of a biological object as a function of spatial coordinates (i.e., as an image), high contrast levels are produced and diseased areas can be visualized as a result of their different relaxation mechanisms.

Transfer of longitudinal magnetization from the bound water protons to the mobile water protons can be influenced externally. The FID of bound water decays so rapidly that it is normally not seen. However, when its broad resonance line is irradiated with a narrow bandwidth RF-pulse off-resonance from the narrow free water line, the two energy levels of the immobile protons reach an equal population without transverse magnetization being generated. Such an effect is called *saturation*. During collisions, saturation is transferred to the mobile water protons. After a subsequent 90° pulse, therefore, the intensity of the free water FID is reduced. Thus, in MRI magnetization transfer contrast (MTC) furnishes as the basis for another contrast option (Wolff and Balaban, 1989) besides relaxation, diffusion, and flow.

3.2.5 Signal-to-Noise Ratio

NMR in living beings, with the aim of obtaining biological or medical information, is only meaningful when the recorded nuclear magnetization can be correlated with the site of its origin. Before discussing methods of spatial resolution, however, we will define the fundamental restriction for such measurements. The signal induced by the precessing nuclear magnetization in the pick-up coil around the sample must compete with the noise generated by the thermal motion of the electrons in the coil and the Brownian molecular motion in the object under investigation – that is, the human body. When smaller volume elements (voxels) are to be resolved, a worse S/N ratio is observed, often requiring a longer time of measurement in order to average out the noise. Since the nuclear magnetization increases with the B_0-field, the S/N ratio improves with increasing Larmor frequency.

The voltage that is induced in the signal coil by the precessing magnetic moment of one voxel after a 90° pulse is given by

$$U_{\text{Signal}} = B_i \omega_L M_\perp \Delta v \tag{3.19}$$

where B_i is the geometry factor of the signal coil ("field per unit current"), Δv is the voxel volume, and $M_\perp \propto B_0/T$ is the transverse nuclear magnetization.

The noise voltage according to Nyquist is then:

$$U_{\text{Noise}} = \sqrt{\frac{2}{\pi} k(R_{\text{Coil}} T_{\text{Coil}} + R_{\text{Sample}} T_{\text{Sample}}) \Delta\omega} \tag{3.20}$$

where $\Delta\omega$ is the detection bandwidth for the signal; R_{Coil} is the resistance of signal coil without sample; R_{Sample} is the contribution of the sample to the resistance of the signal coil; T_{Coil} is the temperature of the signal coil; and T_{Sample} is the temperature of the sample.

Whilst with small samples of a few mm^3 (as are commonly investigated in the laboratory) the noise contribution $R_{\text{Coil}} T_{\text{Coil}}$ dominates, this is no longer true for samples as large as the human body. With a conductive sample, R_{Sample} can be accounted from the power absorption P_{Loss} in the sample caused by a (fictive) alternating current i in the coil (Hoult and Lauterbur, 1979):

$$R_{\text{Sample}} = \frac{P_{\text{Loss}}}{i^2} = \frac{1}{4} \sigma {B_i}^2 \omega^2 \int {r_\perp}^2 \, dv \tag{3.21}$$

where $r_\perp$ is the radius coordinate orthogonal to the field axis of the signal coil; σ is the electrical conductivity of the sample; and ω is the signal frequency (i.e., Larmor frequency).

Replacing the *field per unit current* B_i in Eq. (3.21) with a mean magnetic alternating field B_1 would give the power distributed in the sample by that flux density. Introducing the *filling factor* η, which is a measure of the ratio of the sample volume to the signal coil volume, and the *coil quality factor* Q, which gives the ratio of the energy stored in the coil to the energy loss per oscillation cycle, following a succession of steps omitted here then leads us to the relationship:

$$\frac{U_{\text{Signal}}}{U_{\text{Noise}}} = \alpha I(I+1) \gamma N_V \frac{\omega_L}{T_{\text{Sample}} \sqrt{\beta \frac{T_{\text{Coil}} V_{\text{Coil}}}{\eta Q \omega_L} + T_{\text{Sample}} \sigma \int {r_\perp}^2 \, dv}} \frac{\Delta v}{\sqrt{\Delta\omega}} \tag{3.22}$$

where I is the nuclear spin; N_V is the nuclear spin density; and α, β are constants of proportionality.

For small values of the "moment of inertia" $\int {r_\perp}^2 \, dv$ (i.e., small samples), and for small coil quality factors, the S/N ratio is proportional to $\omega^{3/2}$; for a high coil quality factor or a low coil temperature, it is directly proportional to the Larmor frequency (i.e., the B_0-field). B_0 is an important parameter in an NMR experiment, not only because of the S/N ratio but also because it determines the spectral resolution for distinguishing chemical compounds, and because the longitudinal relaxation times T_1 of biological tissue depend on this value.

Since the temperature cannot be lowered with living samples, once the NMR apparatus is set up (i.e., the magnet and antennae are chosen), the S/N ratio can still be influenced by the voxel size and bandwidth. Repeating the NMR experiment n times and adding the single signals together results in a S/N ratio improvement by

a factor of $\sqrt{n}$. However, since a reduction in spatial resolution is as undesirable as a longer time of measurement, these two choices are normally avoided.

The S/N ratio can be significantly improved applying small surface or local receiver coils. A local coil ''sees'' only a small part of the object under investigation that contributes with less noise (i.e., $\int r_{\perp}{}^2\, dv$ in Eq. 3.22).

3.2.6 Magnetic Resonance Imaging

In order to correlate the signal to its spatial origin, at least one of the two fields (i.e., the B_0- and B_1-fields) required for the NMR measurement must vary over space. If it were possible to generate a sharp maximum or minimum in space for these fields, one would obtain signals only from that region (Abe et al., 1974). However, along with the technical difficulties of generating sufficiently sharp field extrema, all information from the other regions of the object is not accessed.

For simplicity, we will restrict ourselves for the moment to a two-dimensional (2D) object. The utilization of the signal from the entire object rather than only from a single volume element (voxel) is achieved with the use of magnetic field gradients G, for which the NMR precession frequency (in the rotating frame) varies linearly along one direction in space:

$$\omega = -\gamma G r \tag{3.23}$$

The amplitude of the NMR signal as a function of frequency then corresponds to the sum of all spins along lines orthogonal to the direction of the magnetic field gradient (Lauterbur, 1973) – that is, the projection of the nuclear magnetization (Fig. 3.9):

$$P(r, \varphi) = \int M_{\perp}(x, y)\, ds \tag{3.24}$$

Normally the NMR signal is measured as a function of time rather than as a function of frequency; then, the projection can be obtained from the Fourier transformation of the time-dependent NMR signal.

Lauterbur's original suggestion was to collect a set of projections onto different gradient directions φ and to reconstruct an image of the nuclear magnetization with the same methods as used in X-ray computed tomography (Cormack, 1963, 1964; Hounsfield et al., 1973). It emerges, however, that a modification of this proposal by Kumar et al. (1975) offers greater flexibility and simpler image reconstruction, and this method is now used routinely in MRI.

The sample may be excited with a 90° pulse so that transverse nuclear magnetization $M_0(x, y)$ is generated. The phase of the magnetization is then made to vary along the y-direction with a gradient G_y switched on for a time T_y:

$$M_{\perp}(x, y, G_y T_y) = M_0(x, y) e^{-i\gamma G_y y T_y} \tag{3.25}$$

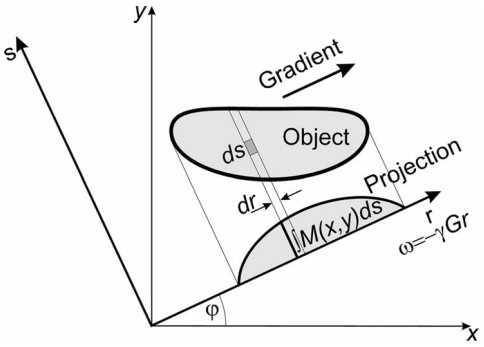

Fig. 3.9. The NMR signal amplitude as a function of frequency for a 2D-object in a linear magnetic field gradient, representing the line integral of the transverse magnetization (number of spins) along stripes orthogonal to the field gradient (projection).

A gradient in x-direction G_x is then applied and the NMR signal, which is the sum of magnetizations individually precessing at their locus, is recorded as a function of the time t (Fig. 3.10, upper part):

$$M_{\perp}(G_y, t) = \int\int dx\, dy [M_0(x, y) e^{-i\gamma G_y y T_y}] e^{-i\gamma G_x x t} \tag{3.26}$$

By repeating the encoding procedure with many different gradient strengths G_y, a 2D-set of signals as a function of G_y and the recording time t is obtained. As one can consider this signal set as an interferogram, it is usual to view it as being acquired in Fourier or k-space (Fig. 3.10, lower part) with spatial frequency coordinates

$$k_x(t) = -\gamma \int_0^t G_x(t)\, dt = -\gamma G_x t \quad \text{and} \quad k_y(t) = -\gamma \int_0^{T_y} G_y(t)\, dt = -\gamma T_y G_y \tag{3.27}$$

A 2D-Fourier transformation yields the distribution of the local transverse nuclear magnetization:

$$M_{\perp}(x, y) = \frac{1}{(2\pi)^2} \int_{-k_y^{\max}}^{k_y^{\max}} \int_{-k_x^{\max}}^{k_x^{\max}} M_{\perp}(k_x, k_y) e^{-i(k_x x + k_y y)}\, dk_x\, dk_y \tag{3.28}$$

The Fourier transformation of the amplitudes (real and imaginary part) along a line through the center of the Fourier space results in the projection (Eq. 3.24) of the investigated object onto the direction of this line; this is known as the *central slice theorem*.

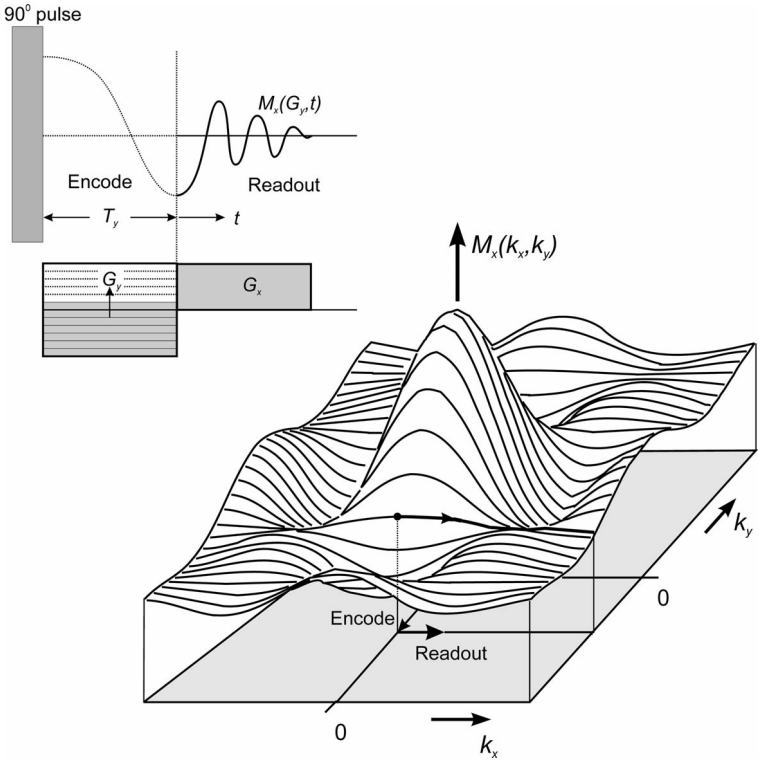

Fig. 3.10. Encoding the transverse nuclear magnetization with a gradient G_y and reading out the signal in a gradient G_x (upper part) is equivalent to scanning 2D-Fourier space (lower part): the nuclear magnetization is recorded along the spatial frequency direction k_x after preparation in k_y-direction (only the real part M_x is shown).

In imaging, an object is sampled with image elements (pixels) of size Δx, Δy, the size of which follows from the sampling theorem as

$$\Delta x,\, y = \frac{\pi}{k_{x,\,y}^{\max}} \tag{3.29a}$$

The spatial frequency interval must be chosen according to the size of the object (i.e., the field of view)

$$\Delta k_{x,\,y} = \frac{\pi}{x,\, y^{\max}} \tag{3.29b}$$

Hence, in order to image an object with diameter $2y^{\max}$ in y-direction (and of $2x^{\max}$ in x-direction, respectively) with the required spatial resolution Δy,

$N_y = 2y^{max}/\Delta y$ phase encoding steps are necessary, during which the gradient $-G_y{}^{max} \leq G_Y \leq G_y{}^{max}$ is stepped through, whereby each time $N_x = 2x^{max}/\Delta x$ samples must be taken of the NMR signal. Usually, N_y and N_x are chosen to be a power of two in order to employ the fast Fourier transform algorithm for image reconstruction (Cooley and Tukey, 1965).

Spatial resolution depends on the magnetic field gradient strength. In order to derive a condition for the gradient G_x in readout direction, we assume two spins separated by the distance d_x. In order to distinguish the two points, the frequency difference due to the gradient must be greater than that due to the natural line width and B_0-field inhomogeneities:

$$\gamma G_x d_x \geq \frac{2}{T_2} + \gamma \Delta B_0 \tag{3.30}$$

This condition is equivalent to $T_x < T_2^*$.

In order to display details separated by d, a pixel size of $d/2$ would be necessary. In MRI normally, much larger pixels (i.e., stronger gradients and shorter readout times) are used because of reasons of acquisition time and signal-to-noise.

An additional restriction for spatial resolution in MRI is given by self-diffusion. The phase variation over a pixel due to diffusion of the water molecules must be smaller than that already caused by the imaging gradients, leading to the constraint

$$d_{x,y} > \sqrt[3]{\frac{D}{\gamma G_{x,y}}} \tag{3.31}$$

where D is the diffusion coefficient (e.g., in tissue $D \approx 10^{-5}$ to 10^{-6} cm^{-2} s^{-1}). Although this restriction can be neglected in normal imaging experiments, it is of importance for MR microscopy.

The imaging principle described can be easily extended to three dimensions by adding and stepping through a gradient G_z during the encoding phase, though this requires a longer time of measurement. Since the information for the complete 3D-object is not always required, a 2D-object is often generated from the 3D-object by applying the gradient G_z during excitation with the RF-pulse (selective excitation). In this way, the spins are only excited in the slice where the precession frequency is identical with the pulse frequency.

3.2.7
Selective Excitation

Let us assume that the spin system with nuclear magnetization M_0 is exposed to a magnetic field gradient G_z and to a "long" amplitude-modulated RF-pulse $B_1(t)$ of duration $2T_z$. The RF-pulse tilts longitudinal magnetization around the x-axis into the transversal plane according to Eq. (3.4), where it precesses during the time $2T_z$

in the gradient G_z. The distribution of the transverse magnetization along the z-direction is approximately calculated in the rotating frame as

$$M_{\perp}(z, 2T_Z) = iM_0 \sin|\alpha(\omega)|e^{i\varphi(\omega)}e^{i\omega 2T_z}$$
$$\omega = -\gamma G_z z \tag{3.32}$$

The flip angle $|\alpha(\omega)|$ is determined by the spectral amplitude of the RF-pulse $B_1(t)$, as given by its Fourier transformation:

$$|\alpha(\omega)| = \left|\gamma \int B_1(t)e^{i\omega t}\, dt\right| \tag{3.33a}$$

and the azimuth $\varphi(\omega)$ of the axis around which the magnetization is tilted (Fig. 3.4) follows from:

$$\text{tg}\ \varphi(\omega) = \frac{\text{Im}(\alpha(\omega))}{\text{Re}(\alpha(\omega))} \tag{3.33b}$$

In order to obtain a rectangular distribution of the transverse magnetization along the slice thickness d at position z_0, the shape of the RF-pulse must be selected so as to give a rectangular frequency distribution with spectral width $\Delta\omega = \gamma G_Z d$ and a center frequency $\omega_0 = -\gamma G_z z_0$ (recalling that we are looking at the spins from the frame rotating with Larmor frequency ω_L, so that in the laboratory system a pulse with frequency $\omega_0 + \omega_L$ must be applied to the coil surrounding the sample). Since an RF-pulse with the shape of a sinc (i.e., $\frac{\sin \pi x}{\pi x}$)-function has such a rectangular spectrum, $B_1(t)$ is chosen to be a sinc-function modulated with the center frequency ω_0:

$$B_1(t) = B_1(T_z)\ \sin c\left(\frac{\Delta\omega}{2\pi}(t - T_z)\right)e^{i\omega_0(t-T_z)}$$
$$\Delta\omega = \gamma G_z d \tag{3.34}$$
$$\omega_0 = -\gamma G_z z_0$$
$$0 \le t \le 2T_z$$

where $2T_Z > 2\pi/\gamma G_z d$ is the pulse duration.

The sinc-pulse is restricted here to a duration of $2T_z$ in order to obtain a selective RF-pulse of finite length, and shifted by the interval T_z in order also to expose the spins to the signal part left of the pulse maximum; it should be adjusted to extend over several sinc oscillations in order to approximate a rectangular slice profile. With the phase of the RF-pulse chosen to be aligned along the x-axis in the rotating frame, for the transverse magnetization, it follows that

$$
\begin{aligned}
M_{\perp}(z, 2T_z) &= iM_0 \sin\left(\gamma \left| \int B_1(t) e^{i\omega t}\, dt \right|\right) e^{-iT_Z\omega} \\
&= iM_0 \sin \alpha_o \operatorname{rect}\left(\frac{z - z_0}{d}\right) e^{-i\gamma G_Z z T_Z} \qquad (3.35) \\
\operatorname{rect}(x) &= 1 \quad \text{for } -\frac{1}{2} < x < \frac{1}{2},\ \operatorname{rect}(x) = 0 \quad \text{for } |x| > \frac{1}{2} \\
\alpha_o &\approx 2\pi B_1(T_z)/G_z d
\end{aligned}
$$

An oscillating function of the transverse nuclear magnetization along the slice thickness then results (Fig. 3.11). The selective RF-pulse has flipped each spin in the slice addressed into the transverse plane, but in its own rotating frame. Since

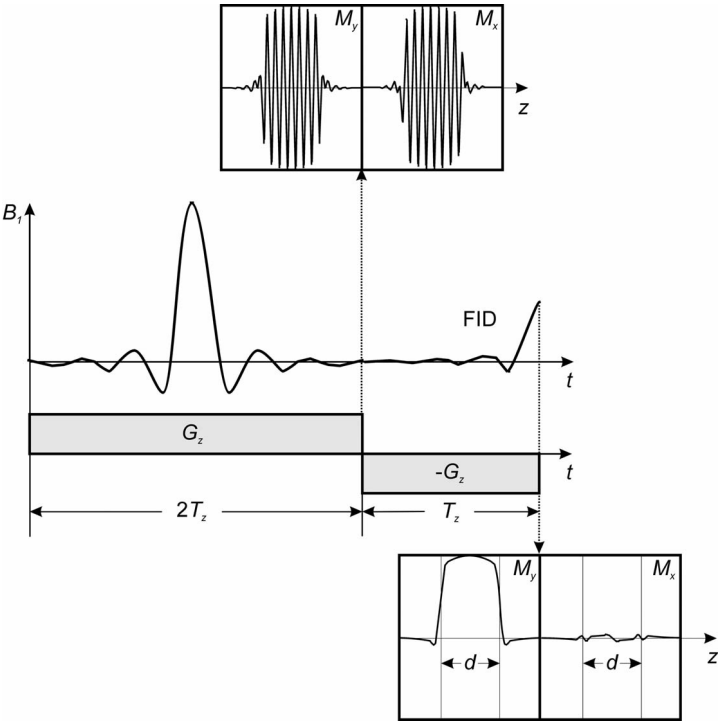

Fig. 3.11. *x*- and *y*-components of the transverse nuclear magnetization in the rotating frame after excitation with an RF-pulse of duration $2T_z$ in a magnetic field gradient G_z that is applied along the *z*-axis. The twisted transverse magnetization resulting immediately after the selective pulse realigns in a refocusing interval of duration T_z with a reversed gradient. The remaining oscillations at the edges of the refocused magnetization originate from the truncation of the sinc-pulse.

the resonance frequency changes over the slice width due to the applied gradient, the transverse nuclear magnetization is twisted in z-direction. The following free induction decay displays almost no signal, since the spiral-shaped nuclear magnetization cancels itself out. Reversing the polarity of the field gradient during a period T_z following the RF-pulse (Hoult, 1977) refocuses all those spins, resulting in a free induction decay corresponding to the full transverse magnetization in the excited slice (Fig. 3.11).

It should be mentioned that Eq. (3.32) is only an approximation, as Eq. (3.4) is only valid for those nuclei for which the frequency of the RF-pulse equals the Larmor frequency. Taking exactly into account the Bloch equations requires numerical methods. It can be seen that a residual nuclear magnetization $M_y(z)$ remains even after refocusing, which can be minimized, however, by tuning the refocusing interval and by modified RF-pulse shapes.

3.2.8 Partial Acquisition Techniques

As mentioned in Section 3.2.5, the S/N ratio of an NMR experiment can be improved by using a local receiver coil. In MRI, coil arrays are applied in order to augment the field of view. The signals from the single array elements are processed independently and eventually assembled to the final image. In order to reduce scan time without sacrificing on spatial resolution, the different spatial information contained in the sensitivity profiles $s_i(x, y)$ of the single coils can be used. As the MR signal of each coil is modulated with a spatially varying function

$$M_i(k_x, k_y) = \int s_i(x, y) M_\perp(x, y) e^{i(k_x x + k_y y)}\, dx\, dy \tag{3.36}$$

two different possibilities to improve the spatial resolution arise. SMASH (simultaneous acquisition of spatial harmonics; Sodickson and Manning, 1997) operates on the MR signals before, and SENSE (sensitivity encoding; Pruessmann et al., 1999) after image reconstruction. With SMASH, the single signals from the coil array are combined with weighting factors c_i chosen according to

$$\sum_{i=1}^{i_{\max}} c_i s_i(x, y) = e^{im\Delta k_y y}, \quad 1 \le m < i^{\max} \tag{3.37}$$

where c_i is the weighting factor for coil i; and $i^{\max}$ is the number of coil elements, giving

$$\sum_i c_i M_i(k_x, k_y) = \int M_\perp(x, y) e^{i(k_x x + (k_y + m\Delta k_y) y)}\, dx\, dy = M_\perp(k_x, k_y + m\Delta k_y) \tag{3.38}$$

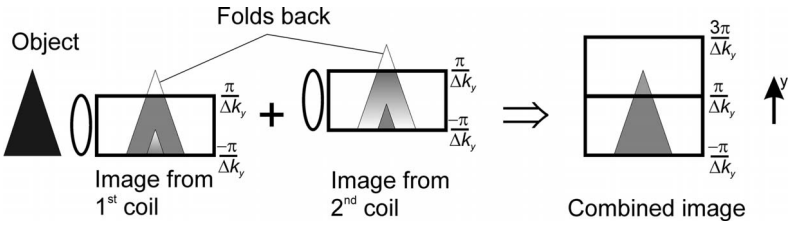

Fig. 3.12. Partial acquisition technique (PAT) for faster image acquisition. When every second Fourier line is left out, the field of view is reduced by a factor of two. Image parts outside the field of view fold back. When two images are acquired with different sensitivity profiles an undistorted image can be reconstructed.

Hence, up to $(i^{\max} - 1)$ additional phase encoding steps can be achieved for each gradient encoding step k_y, if the sensitivity profiles can be combined to form harmonically varying functions in space with a period $2\pi m / i^{\max} y^{\max}$. Vice versa, up to $(i^{\max} - 1)$ phase encoding steps can be saved without loss of spatial resolution, enabling a reduction in acquisition time by just this factor.

With the SENSE method an image is reconstructed from each single receiver coil. When less gradient phase-encoding steps are applied than are required due to the sampling theorem, the field of view is reduced and parts of the imaged object fold back (Fig. 3.12). Thus, accelerated data acquisition in parallel imaging requires unfolding in the image domain. The overfolded image parts with different intensity in every single coil image can be determined and removed by solving a system of linear equations containing the coil sensitivities as coefficients.

Partial acquisition techniques (PAT) such as SMASH and SENSE are based on the local sensitivity profiles of the receiving coils. Coil calibration, therefore, is a crucial part of image reconstruction. It has transpired that it is insufficient to work with a precalibrated, time-invariant set of coil sensitivity maps, and coil calibration must be performed for every image acquisition. One method is rapidly to scan a volume with reduced resolution immediately prior to the examination and to extract the coil profiles from it (this is the prescan method). Another possibility is to incorporate the acquisition of calibration data into each examination scan (the autocalibration method). Hereby, some of the Fourier lines to be reconstructed from the coil sensitivities are also measured directly by applying the necessary gradient steps. In this way, the weighting factors for combining the coil signals can be obtained without explicit knowledge of the coil sensitivities.

3.2.9
Pulse Sequence and Contrast

As has been shown, in order to obtain signals from which an image can be reconstructed the nuclear magnetization must be exposed to a sequence of RF and gradient pulses. Many modifications of these pulse sequences have been designed to

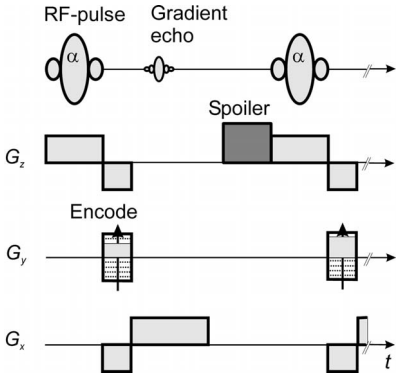

Fig. 3.13. Gradient echo sequence. For short repetition times (FLASH), the remaining transverse magnetization must be destroyed, for example with a spoiler gradient.

optimize the experiment with respect to special problems such as tissue contrast, display of flow, diffusion, susceptibility, or data acquisition time.

The simplest imaging sequence is the gradient echo sequence (Fig. 3.13). The nuclear magnetization of a slice is flipped by a selective RF-pulse (i.e., in the presence of the slice selecting gradient G_z) with flip angle α, into the transverse plane; reversing G_z for half the duration of the RF-pulse then compensates the phase variation of the transverse magnetization along the z-axis. During this time, the phase-encoding gradient G_y and a reversed gradient $-G_x$ are also applied. Subsequently, the signal is recorded in $+G_x$ for twice the duration of the reversed gradient. Due to the previous signal conditioning of the spin magnetization with $-G_x$, during signal readout both positive and negative spatial frequencies are recorded; signal maximum occurs when the phases that the spins have accumulated during the duration of $-G_z$ have been compensated. Consequently, this signal maximum is called a *gradient echo*. The pulse sequence is repeated with different phase-encoding gradients $-G_y^{\max} \leq G_y \leq G_y^{\max}$ until the Fourier space is filled with data. A 2D-Fourier transformation reconstructs the image of the transverse magnetization.

This pulse scheme can be rapidly repeated with a repetition time that is short with respect to the longitudinal relaxation time. The effective transverse magnetization is determined by the flip angle α and the longitudinal magnetization that reestablishes itself during the repetition interval T_R:

$$M_\perp(x, y) = M_0(x, y)\frac{(1 - e^{-T_R/T_1(x,y)})\sin\alpha}{1 - e^{-T_R/T_1(x,y)}\cos\alpha} \tag{3.39}$$

For a given repetition time and flip angle, the image intensity is determined by the local longitudinal relaxation time $T_1(x, y)$. Since at short repetition times with small flip angles a large signal can still be obtained, this pulse sequence is often

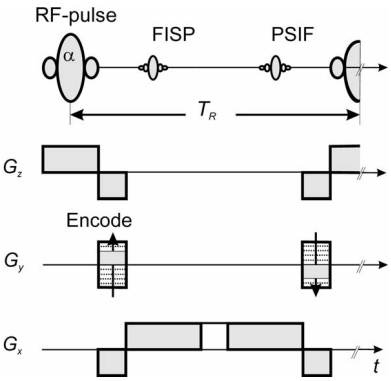

Fig. 3.14. DESS steady-state sequence employing a combination of FISP and PSIF.

referred to as FLASH (fast low angle shot; Haase et al., 1986). With FLASH imaging it is assumed that the phase memory of the transverse nuclear magnetization has been lost at the end of the repetition interval; since this is not true when the repetition interval is smaller than the transversal relaxation time, spoiling gradient pulses must be applied at the end of each interval in order to prevent the emergence of coherent image artifacts. An alternative is to add a stochastically varying jitter to the repetition interval.

In order to obtain an imaging sequence that actually uses the phase memory of the spins in order to yield a stronger signal at rapid repetition, and also to obtain information on the local transversal relaxation time, instead of applying a spoiler gradient the encoding gradient G_y can be reversed at the end of the repetition interval (Fig. 3.14). Thus, the spin phase before the RF-pulses is always the same, establishing a steady-state magnetization. Such a sequence is referred to as FISP (*fast imaging with steady precession*) or GRASS (*gradient recalled acquisition in the steady state*).

In steady-state sequences such as FISP or GRASS, the phase variation of the transverse magnetization is always the same between the RF-pulses. Without preparation gradients (i.e., the gradient pulses applied before the data are sampled) in *x*- and *z*-directions, one would observe a focused magnetization before and after the RF-pulse (Freeman and Hill, 1971). Graphically, one can consider the signal after the RF-pulse as an FID, and that before as one-half of an echo with an amplitude reduced by the factor e^{-2T_R/T_2} compared to the FID. In FISP, the steady-state FID is used to obtain an image, but the steady-state half-echo signal can also be used to obtain a FISP-like image with additional T_2 weighting (though this is not a strong effect at the short repetition times applied in steady-state sequences.) In this case the time course of the imaging sequence must be reversed, therefore, and is termed PSIF (Fig. 3.14). It is even possible to combine FISP and PSIF in a single sequence to give two images differing in T_2 contrast (DESS, *double echo in the steady state*). In very homogeneous B_0-fields and with very short repetition

times, it is also possible to set up a sequence that superposes the FISP and the PSIF signal to give a better S/N ratio. This sequence, originally proposed as FISP (Oppelt et al., 1986), is now termed "trueFISP".

The signal intensity of trueFISP is determined by the ratio T_1/T_2

$$M_{\perp}(x, y) \approx M_0(x, y) \frac{\sin \alpha}{1 + \frac{T_1(x, y)}{T_2(x, y)} + \left(1 - \frac{T_1(x, y)}{T_2(x, y)}\right) \cos \alpha} \tag{3.40}$$

for example, for fluids such as water, where $T_1 \approx T_2$, a signal equivalent to half of the maximum nuclear magnetization can be obtained using 90° pulses with rapid pulse repetition.

With gradient echo sequences, rapid image acquisition in less than 1 s is possible, but the contrast between different tissues is normally low. This can be enhanced by inverting the nuclear equilibrium magnetization using a 180° RF-pulse before the imaging sequence is started (Haase et al., 1989). Thus, during the fast imaging experiment the longitudinal magnetization undergoes relaxation back to its equilibrium state, producing image contrast with respect to tissues having different longitudinal relaxation times $T_1(x, y)$.

Because gradient echo sequences are so fast, they are very well-suited for 3D-data acquisition. Either the RF-pulses are applied nonselectively (i.e., without a slice selection gradient), or a very thick slice is excited. Spatial resolution is then achieved by successively encoding the nuclear magnetization with the gradients G_z and G_y in the y- and z-directions and reading out the signal in the gradient G_x. Since each volume element is repeatedly measured according to the number of phase-encoding steps, the S/N ratio is improved considerably. Image reconstruction is performed with a fast 3D-Fourier transformation, resulting in a block of images that can be displayed as slices through the three main coordinate axes. Image postprocessing also allows the display of images of arbitrary planes (multiplanar reformatting = MPR).

Gradient echo sequences require homogeneous B_0-fields in order to avoid signal loss due to dephasing of the transverse nuclear magnetization; the contrast with respect to tissues differing in T_2 is generally low. With so-called spin echo sequences utilizing an additional 180° pulse, there is greater flexibility with respect to the manipulation of image contrast, though generally at the expense of acquisition time. Spin echo sequences are also much more stable against inhomogeneities of the B_0-field, since inhomogeneities in the direction of the phase-encoding gradient have no effect.

In the standard spin echo imaging sequence, slice-selective 90° and 180° RF-pulses are used with phase-encoding gradients between them (Fig. 3.15); the echo signal is readout in the frequency-encoding (or projection) gradient. Two parameters are available for signal manipulation, the sequence repetition time T_R and the echo time T_E. The use of a long echo time allows transverse relaxation of the spin system before signal acquisition, whereas rapidly repeating the pulse sequence prevents longitudinal magnetization from being re-established. This effect is

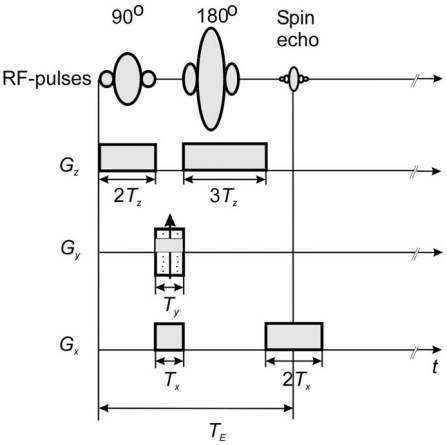

Fig. 3.15. Standard spin echo imaging sequence. The compensation of the twisted transversal magnetization caused by the selective 90° pulse is achieved here with the prolonged slice selecting gradient pulse after the selective 180° pulse.

called *saturation* (see also Section 3.2.4). The signal intensity in a pixel is given by

$$M_{\perp}(x, y) = M_0(x, y)(1 - e^{-T_R/T_1(x,y)})e^{-T_E/T_2(x,y)} \tag{3.41}$$

The repetition time and the echo time can be adjusted so that the image contrast due to different types of tissue is determined by either M_0, T_1 or T_2. Short values of T_E and T_R give T_1-weighted images, while a long T_E and a short T_R give spin density or M_0-weighted images, and long values of both T_E and T_R give T_2-weighted images. For imaging of the heart, no fixed T_R is chosen, but the sequence is triggered by the R-wave of the ECG.

Contrast between adjacent anatomic structures can be further enhanced by means of contrast agents. Since the addition of other magnetic moments increases magnetic interactions during the collisions between molecules in a fluid, a paramagnetic agent dispersed in the tissue accelerates the relaxation of excited spins, longitudinally as well as transversely. One commonly used contrast agent is Gd-DTPA (gadolinium diethylenetriaminepentaacetic acid) (Weinmann et al., 1984). When administered into the bloodstream, this contrast agent will accumulate at various levels in tissue due to the different microvascular structures.

The standard spin echo imaging sequence can be modified in several ways. At long repetition times, images of several different slices are acquired in no longer an acquisition time than for a single slice, when the different slices are addressed during the waiting interval. In order to obtain information on transverse relaxation, the NMR signal can be recovered several times by repeating the 180° pulses. Thus, several images are reconstructed with varying T_2 weighting for a single slice;

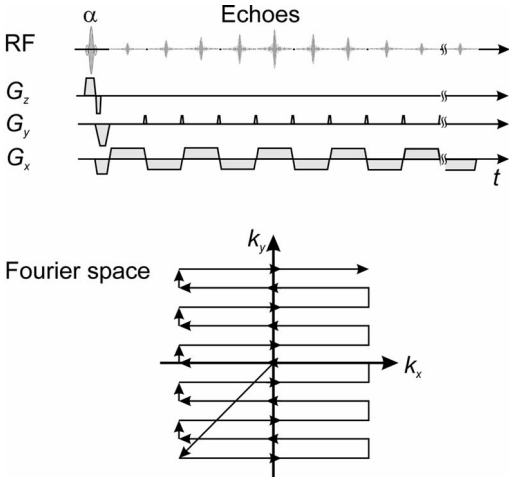

Fig. 3.16. Echo planar imaging (EPI) sequence employing a blipped phase encoding gradient (upper plot) and the according trajectory in Fourier space (lower plot).

the transversal relaxation time can be calculated in each pixel and even displayed as an image.

When each echo of a multi-echo sequence is encoded in the *y*-direction with a different gradient pulse, several lines in Fourier-space are recorded during one pulse sequence, significantly reducing the time of measurement (TSE = Turbo Spin Echo); it is even sufficient to scan only half of the Fourier space (HASTE = Half Fourier Acquired Single Shot Turbo Spin echo). When the 180° pulses are omitted and the polarity of the projection gradient is alternately reversed (Mansfield, 1977), a complete image can be acquired in less than 100 ms. Such a sequence (termed echo planar imaging; EPI) is the quickest way to obtain an MR image. Sir Peter Mansfield, the eminent NMR scientist and Nobel Prize winner in 2003, had proposed the principle as early as 1978, but it lasted until the 1990s that standard MR system hardware was capable of generating and switching the strong gradients required for execution. A pulse diagram together with the resulting trajectory in Fourier space is shown in Figure 3.16.

The sensitivity of gradient echo sequences (especially of echo planar imaging) to magnetic field inhomogeneities can be exploited to image effects in the human body which respond sensitively to changes in magnetic susceptibility. An example of this is perfusion of the human brain cortex, which varies according to certain actuating or perceptive tasks. If a certain region of the brain is activated (e.g., the visual cortex) when a subject under study sees light flashes, the local oxygen requirement increases. The circulatory system reacts by increasing the local blood supply even more than necessary. Consequently, the activation process results in an increased oxygen content of the venous blood flow. Oxygen is transported by hemoglobin that is confined to the red blood cells. Oxygenated hemoglobin (HbO_2)

is diamagnetic, while deoxygenated hemoglobin (Hb) is paramagnetic due to the presence of four unpaired electrons. These different magnetic susceptibilities lead to different signal intensities in susceptibility-sensitive (i.e. $T_2{}^*$-weighted sequences as EPI). Blood oxygen level-dependent (BOLD) contrast serves as the foundation of functional MRI (Ogawa et al., 1992).

3.2.10 Imaging of Flow

If the imaging object (or parts of it) move during image acquisition, then artifacts will occur, as a moving volume element acquires another phase in the applied gradient field than if it were resting. Image reconstruction then attributes the position of that voxel to other origins, giving rise to typical mirror images. With additional gradient pulses it is possible, however (at least partly) to compensate phase shifts due to movement. Those sequences are applied for images with less movement artifacts and especially, for imaging of flow.

Flow-related effects are used in *magnetic resonance angiography* (MRA), whereby vascular structures can be investigated without the use of contrast agents. Two effects are utilized, namely time of flight and phase changes.

By applying an imaging sequence with a rather large flip angle α at a short repetition time T_R, stationary tissue saturates, yielding only a minimal signal. The image intensity of nuclei flowing into the excited slice, however, is enhanced (Crooks et al., 1982). The increase in intensity is explained by the in-flow of nuclei into the imaged slice, which are not saturated from previous excitations. At gradient echo sequences signal intensity increases linearly with velocity until it reaches a plateau, at which all the spins within the excited slice are replaced after each RF-pulse (Fig. 3.17). For flow orthogonal to the imaging slice, the transit velocity v_t, at which no further signal increase is observed, amounts to $v_t = d/T_R$. For a given pulse repeti-

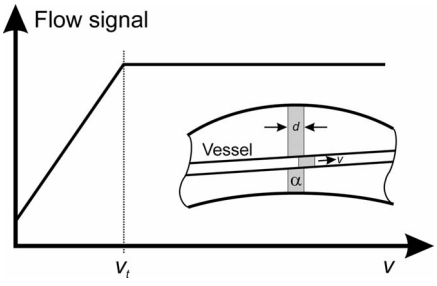

Fig. 3.17. Signal enhancement as a function of blood flow. The signal intensity of blood flowing with constant velocity v perpendicular to the imaging slice increases proportional to the flow velocity as more spins are replaced with unsaturated spins at higher velocities. Signal enhancement ends at the transit velocity v_t, when all spins within the slice are replaced during one T_R interval.

tion time T_R, total replenishment of spins occurs at lower transit velocities v_t for a thin slice d than a thick one (Wehrli, 1990).

Time of flight (TOF) effects can be utilized to create images that are similar in their appearance to those produced by X-ray angiography. With nonselective excitation pulses or pulses exciting a thick slice, a rapidly repeating 3D gradient echo sequence is set up, which produces a weak signal. Flow introduces fully relaxed spins to the imaged volume, giving rise to a stronger signal. In order to visualize the vascular structure, the method of *maximum intensity projection* (MIP) is often used (Koenig and Laub, 1988). In image postprocessing, the acquired 3D-image volume can be regarded as illuminated with parallel rays. Along each ray, the image element with the highest signal intensity is searched and displayed in the projection plane.

TOF MRA cannot be applied for the rapid imaging of large volumes as there is no reservoir of unsaturated spins left. In such cases, blood contrast agents containing for example Gd-chelates are administered intravenously. The bolus of blood with shortened T_1 produces a very strong signal so that it can be tracked with a rapid 3D-gradient echo sequence.

Phase-sensitive MRA makes use of the fact that moving spins acquire different transverse phases, according to their velocity in magnetic field gradients, than stationary spins. When the volume element is sufficiently small, so that it contains only spins with similar flow velocities, the flow can be quantitatively measured by analyzing the signal phase (*phase-contrast angiography*; Dumoulin et al., 1989). In comparison with TOF, phase-contrast angiography is well suited to slow flow velocities.

When, on the other hand, a volume element large enough to contain spins with a variety of velocities is chosen, this will give only a weak signal, because the individual contributions of the different spins cancel.

Given that the actual position $r(t)$ of a moving spin is

$$r(t) = r_0 + vt + \frac{1}{2}at^2 + \cdots \tag{3.42}$$

its phase angle ϕ follows from

$$\begin{aligned}\phi(t) &= \gamma \int_0^t G(t) r(t)\, dt \\ &= \gamma\left(r_0 \int_0^t G(t)\, dt + v \int_0^t tG(t)\, dt + \frac{a}{2}\int_0^t t^2 G(t)\, dt + \cdots \right)\end{aligned} \tag{3.43}$$

Thus, the phase of stationary spins is determined by the 0^{th} moment $\int G(t)\, dt$, the phase of spins with uniform velocity v by the 1^{st} moment $\int tG(t)\, dt$, and the phase of accelerated spins by the 2^{nd} moment $\int t^2 G(T)\, dt$ of the applied gradient sequence. A bipolar gradient has no influence on the phase of stationary spins, while in two bipolar gradient pulses back to back the phase of uniform flow is re-

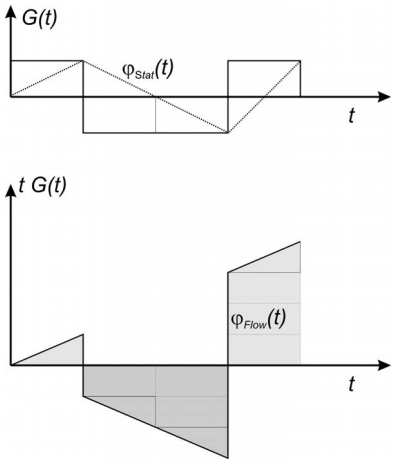

Fig. 3.18. Upper: Gradient pulses for phase and motion compensation and time dependence of the phase of stationary and moving spins. Applying a bipolar gradient pulse before the data readout phase minimizes the influence of uniform flow. Lower: Development of the phase of stationary and moving spins during the application of gradient pulses. The phase of stationary spins is proportional to the area (0^{th} order moment) under the gradient, the phase of uniformly flowing spins is proportional to the 1st order moment (the area under the function $tG(t)$). After a bipolar gradient stationary spins have no phase accumulated, while for the same effect at uniform flow two bipolar gradients are required.

stored. So, at least three gradient lobes are needed to have velocity compensation (this is also known as *first-order flow compensation*; Fig. 3.18). Higher-order motions, such as acceleration, are not refocused in first-order flow compensation and are best dealt with by using a short echo time. The subtraction of an image not being flow compensated from an image with flow compensation cancels out the signal from the stationary tissue, leaving only the vascular structure (Laub and Kaiser, 1988).

3.2.11 Diffusion Imaging

As outlined in Section 3.2.3, molecules in liquids or tissue move stochastically (diffuse) due to their thermal energy (Brownian motion). In a spin echo experiment with strong gradients before and after the refocusing RF-pulse (one 180° or two 90° pulses), therefore, spins accumulate different phases leading to destructive interference (see Fig. 3.7). In order to obtain a diffusion-weighted image, the spatial distribution of the magnetization during the echo can be measured with an echo planar (EPI) gradient readout sequence (Turner et al., 1990). The image formation part of the sequence is completely decoupled from the diffusion encoding part. In diffusion-weighted EPI (DW-EPI), the imaging ''readout''-module typically takes less than 0.1 s, thus ''freezing'' patient motion.

The diffusion-weighted signal obtained is given by:

$$M(\vec{q}, \Delta) = M_0 e^{-bD}$$
$$\vec{q} = \gamma \vec{G}_D \delta \tag{3.44}$$
$$b = q^2(\Delta - \delta/3)$$

where δ is the duration of the diffusion encoding gradient G_D; and Δ is the distance between the two diffusion-encoding gradient pulses.

Experiments have shown that diffusion in biological tissue (e.g., in fibers) is often not isotropic. Apparently in such materials, it is restricted differently in direction due to the microstructure. The quantity D in Eq. (3.44) can no longer be considered as a scalar, but is often characterized as the apparent diffusion tensor. In order to access anisotropic diffusion (e.g., in regions of brain white matter, where bundles of fibers run in parallel), at least six diffusion-encoding gradient directions must be applied (termed *diffusion tensor imaging* or DTI).

Diffusion-weighted (DW) imaging has emerged as an immediate, quick, and robust means of visualizing pathological processes such as acute brain ischemia. A high signal in DW images indicates restricted diffusion, which is associated with cell swelling (cytotoxic edema). DW-EPI is an important step in a comprehensive approach to diagnosing and treating acute stroke.

3.2.12 MR Spectroscopy

The tissues of the human body contain mostly water and fat, and consequently the signal displayed in magnetic resonance images derives principally from the hydrogen nuclei in these compounds. Because the chemical shift of fat differs from that of water, different slices are excited with a selective RF-pulse. Also, fat and water appear shifted with respect to each other in the direction of the readout gradient. Although these effects can be masked using stronger slice selection and readout gradients, this requires a greater RF-power and a larger bandwidth, in turn leading to an increase in thermal noise. Various pulse sequences have therefore been developed to obtain pure fat or pure water images. Such sequences are employed, when the strong signal of one compound obscures the weak signal of the other.

One possibility here is to suppress the fat or the water signal with a saturation pulse before beginning the actual imaging sequence. This employs a 90° pulse which has exactly the frequency of the undesired compound and subsequently dephases (spoils) the generated transverse magnetization with a strong gradient pulse. The imaging sequence that follows then acts only on the desired compound (Haase et al., 1985).

In some cases, pure fat and water images are generated using two pulse sequences with different readout delays. The difference is chosen so that the magnetization of fat and water is parallel in one case and antiparallel in the other case

(Dixon, 1986). Adding and subtracting the signals from the two sequences yields either a pure fat or a pure water image. The technique of identifying metabolites by employing echo times that generate defined in-phase or opposite-phase alignment of the transverse nuclear magnetization is called spectral editing. This approach can be used, for example, to separate lactate from lipid resonances in proton spectroscopy.

Of special interest here is the detection of metabolites, either by the NMR of hydrogen ^{1}H or of other nuclei, such as phosphorus ^{31}P. Due to the very low concentrations of metabolites, their NMR signal is much weaker than that of water and fat. In order to obtain a sufficient S/N ratio, it is therefore necessary to work with lower spatial resolution and longer acquisition times than with normal imaging.

Measuring chemical shifts requires a B_0-field with a high field flux density (>1 T) and very good homogeneity. Either the spectrum of a single volume element can be measured (*single voxel spectroscopy*) or the spatial distribution of spectra in the object can be acquired (*chemical shift imaging*). Furthermore, the slight temperature-dependence of the chemical shift of water (ca. -0.01 ppm K^{-1}) offers another possibility for temperature measurement with MRI (besides longitudinal relaxation and diffusion).

In the human brain, metabolites such as choline, glutamic acid and *N*-acetyl aspartate can be identified using proton spectroscopy. Likewise, alcohol consumed by the individual under investigation can also be detected. A B_0-field homogeneity necessary to resolve the chemical shifts of these compounds is usually not achievable over the entire sensitive volume of the RF-coils. A common procedure, therefore, is first to acquire a 2D or 3D-image and then to select the region from which the spectrum is to be obtained. This region is then excited with three selective RF-pulses. By observing the free induction decay (with all gradients switched off), the B_0-field is shimmed. The best magnetic field homogeneity is obtained in the selected volume when the area under the FID is a maximum.

Since the intensity of the water signal can be several orders of magnitude greater than that of the signals from metabolites, it must be suppressed, for example with a saturation pulse. The subsequent volume selection sequence – for example a selective 90° pulse with a gradient in the *x*-direction and two selective 90° or 180° pulses with a gradient in the *y*- and *z*-directions – then acts only on the metabolites, the spectral lines of which result from a Fourier transformation of the FID (Bottomley, 1987).

For diagnostic purposes, a quantitative determination of the concentration of the metabolites in the localization volume is desirable. However, due to the many unknown calibration factors, one is usually restricted to the analysis of relative peak heights. Among the disorders studied with ^{1}H-NMR spectroscopy are included tumors in adults and children, epilepsy, stroke, neurodegenerative diseases, psychiatric disorders, and inborn genetic disorders.

It has also been shown that complementing an MR imaging procedure with spectroscopy significantly increases the diagnostic value of prostate examination. Additional spatially and spectral selective saturation pulses suppress lipid contaminations. In healthy prostate tissue the signal of citrate with a chemical shift of 2.6

ppm dominates, while the signal of choline-containing compounds at 3.2 ppm is relatively low. Since these signal levels appear to be significantly altered in cancerous tissue, the choline over citrate signal ratio has been suggested as a pathologic marker.

The chemical shifts of ^{31}P lines are larger than those of protons, so that the field homogeneity requirements are less stringent. The reduced sensitivity of ^{31}P due to its small magnetic moment and natural abundance requires the S/N ratio to be improved by repeating the measurement several times; this permits the acquisition of a complete spectroscopic image, rather than a ^{31}P spectrum from only a single voxel.

In spectroscopic imaging, spatial resolution is achieved either solely by 3D-encoding or by selective excitation and 2D-encoding. The signal is observed as free induction decay in the absence of any gradients. A 3D or 4D-Fourier transformation results in a data set consisting of the voxels for the investigated region, with a spectrum for each voxel (Brown et al., 1982). In ^{31}P spectra from living tissue, adenosine triphosphate, phosphocreatine and inorganic phosphate can usually be recognized. Instead of viewing the spectrum in each single volume element, the spatial distribution of the single metabolites can also be displayed as an image. Phosphocreatine (PCr) serves as an energy store to provide adenosine triphosphate (ATP) by the action of creatinine kinase, and acts as a fuel for energy-consuming processes in cells (e.g., muscular activity). This leads to the formation of inorganic phosphate (P_i,), for which the chemical shift depends on the pH value of the surroundings, thereby permitting quantification of the intracellular pH value.

Although at first NMR spectroscopy in living beings appears attractive because it should permit immediate insight into cell metabolism, its clinical importance has remained limited until now. Compared to nuclear medicine, where radioactive tracers can be detected at very low concentrations, NMR is a very insensitive method. This restricts its application with regard to components other than fat and water to detecting volume elements that are several cm^3 in size, and to metabolites of limited biological or medical value.

In addition to ^{1}H and ^{31}P, other nuclei (e.g., ^{13}C and ^{23}Na) have been investigated *in vivo*, but have not yet proved to be of clinical importance. ^{19}F has been detected *in vivo* from drugs used to treat cancer, while hyperpolarized ^{3}He or ^{119}Xe have been investigated as gaseous contrast agents for imaging the lungs. Although *in vivo* NMR spectroscopy or imaging with nuclei other than hydrogen remains an interesting field of research, it has not yet achieved clinical importance, as for example imaging with hydrogen nuclei.

3.2.13 System Design Considerations

A magnetic resonance imaging system closely resembles the type of processor-based Fourier NMR spectrometers used routinely in analytical chemistry. However, the system is adapted to the size of a human patient, and the components and soft-

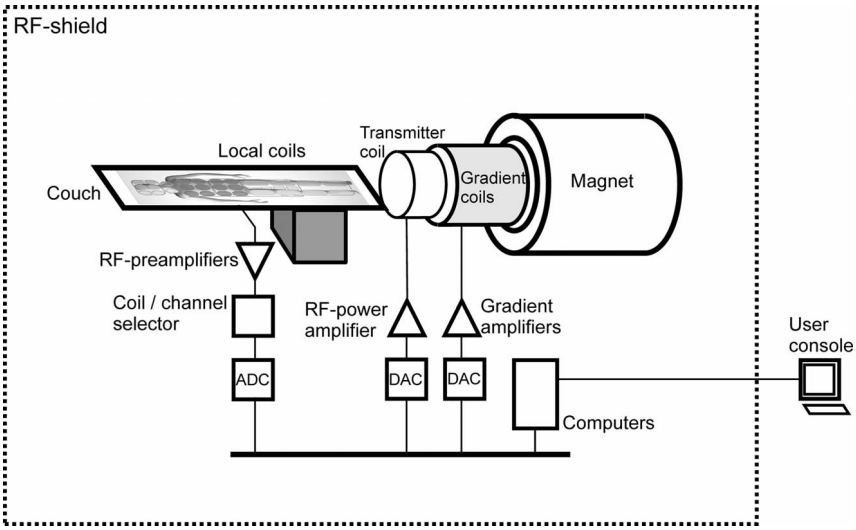

Fig. 3.19. Block diagram of an MRI system. ADC = analog-to-digital converter; DAC = digital-to-analog converter.

ware are structured to meet imaging requirements. A block diagram of an MR imager is shown in Figure 3.19. Of particular importance is the system or host computer, which controls all components of the system often applying digital processors themselves, and acts as the interface to the user. The software used must control the system, run the imaging sequences, perform image reconstruction and interact with the user, as well as perform archiving and increasing numbers of post-processing tasks.

The magnet is by far the most important (and expensive) component of the equipment. Although high magnetic fields are often employed in order to obtain a better S/N ratio, the use of fields above 1 T may encounter problems concerning the RF-field. RF-power absorption increases with the Larmor frequency squared (Eq. 3.21), and so must be restricted in order not to exceed a value according to the metabolic turnover of 1 W kg^{-1}. Furthermore, at Larmor frequencies above 60 MHz the penetration depth of the RF-field due to the skin effect can lead to shadowing in the image for large objects (Bottomley and Andrew, 1978). As the wavelength of the RF-field approaches dimensions in the human body, dielectric resonances can occur, causing image artifacts. In spite of these problems, the advantages of high magnetic fields with respect to S/N ratio and to enable good differentiation of metabolites prevail, such that 3 T magnets are currently on the verge of routine clinical use.

The gradient strength is another important factor which affects the performance of an MR imaging system. A minimum condition for gradient strength, namely to take into account the line broadening across one pixel, was mentioned previously (Eq. 3.30). In general, however, the gradient strength is chosen to be still larger, for

example in order to reduce signal decay during the encoding phase preceding the readout phase or to acquire several lines in Fourier space, as in TSE or EPI. Strong gradients are also necessary for sequences sensitive to flow, perfusion, or diffusion. The switching time for the gradients must always be as short as possible, since undesired signal decay occurs during switching intervals.

Switching the large currents of the gradients in the field of the magnet causes Lorentz forces that act on the gradient coils. As a consequence, the mechanical oscillations are excited, giving rise to acoustic noise that in fields of 1.5 T can easily exceed 100 dBA. Although constructive measures are applied and special pulse sequences designed for noise dampening, the wearing of ear protection by patients is mandatory in most cases in order to avoid damage to the hearing.

The gradient strength and switching time are ultimately limited by the electrophysiology of the patient, who will eventually experience stimulation of the peripheral nerves. During the early 20th century, the French physicist and physician Georges Weiss found that the threshold for electrical stimulation of nerves depended on the duration of the stimulating pulse (Weiss, 1901). According to the law of induction, an electric field can be generated with a time-varying magnetic field. By adopting Weiss' findings, the stimulation threshold of a train of magnetic field pulses dB/dt of duration τ can be estimated by the relationship:

$$\frac{dB}{dt}(\tau) = \dot{B}_{\mathrm{Rheo}}\left(1 + \frac{T_{\mathrm{Chron}}}{\tau}\right) \tag{3.45}$$

The so called rheobase $\dot{B}_{\mathrm{Rheo}}$ is the asymptotic threshold for $\tau \to \infty$. The influence of shorter pulses is described by the chronaxie T_{Chron}, which can be considered as the pulse length at which the actual threshold is twice the rheobase. As the induced electric field strength also depends on both object size and magnetic field distribution (at MRI, a gradient), the rheobase can vary. Test series with human volunteers indicate values of ca. 20 T s^{-1} for $\dot{B}_{\mathrm{Rheo}}$ and 370 µs for T_{Chron} (Schaefer et al., 2000), though these may show inter-individual differences. Reliable models (e.g., SAFE; stimulated approximation by filtering and evaluation; Hebrank and Gebhardt, 2000) have been developed that describe all dependencies of the stimulation threshold. These are implemented in clinical scanners so that nerve stimulation can be predicted. Nerve stimulations by switched magnetic field gradients, though painful, are harmless as they occur at much lower values than would cause any serious adverse effects, for example on the cardiac system (Budinger et al., 1991). Nevertheless they must be avoided during routine scans.

3.2.14 Magnets

Today, magnets with B_0-fields of up to 7 T with a bore designed for whole-body applications are used in research investigations. Such high magnetic fields are explored for high-resolution imaging and spectroscopy, including nuclei other

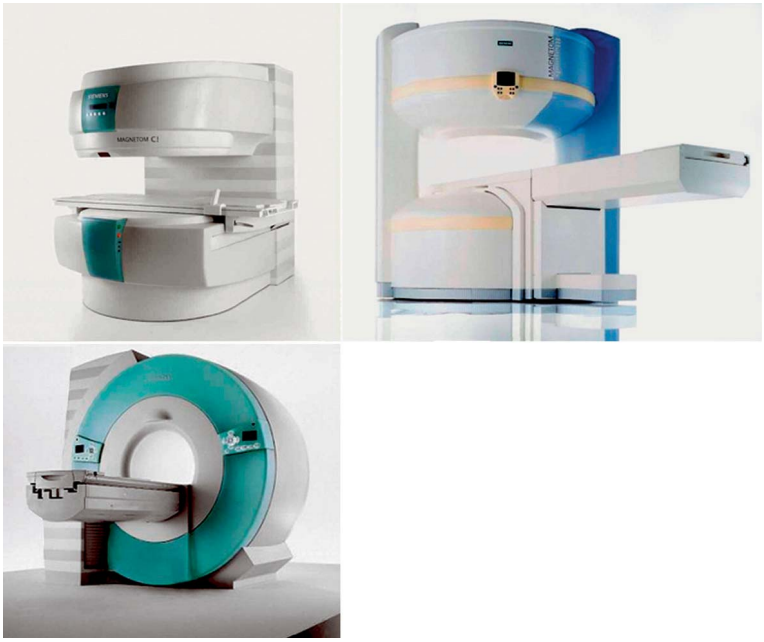

Fig. 3.20. Examples of MR imaging magnets (Siemens Medical Solutions). Upper left: Permanent 0.3-T magnet. Upper right: Superconducting open 1-T magnet. Lower: Superconducting 1.5-T magnet with a length of 1.20 m and an inner bore of 70 cm.

than protons (Barfuss et al., 1988). No severe biological effects are known to have been caused by static magnetic fields, other than some individuals who have reported nausea and a metallic taste when moving within the instrument. This effect, as well as a reduced mating rate in mice (Zimermann and Hentschel, 1987), is most probably due to eddy currents induced in conductive tissue.

B_0-fields between 0.2 and 1.5 T are applied routinely in the clinical situation, and are generated using different magnet designs (Fig. 3.20). Magnetic fields above 0.5 T in a volume suitable for patient investigations can only be obtained with superconducting magnets (supercons). Here, stringent design constraints must be considered, as superconductive wire is limited in its current-carrying capacity (superconductivity quenches at a critical magnetic field strength). One suitable material here is multifilament wire; this typically consists of 30 niobium-titanium strands each of 0.1 mm diameter, embedded in a copper matrix of approximate diameter 2 mm. The copper matrix must carry the current in case the superconducting filaments become resistive. These wires can carry currents of up to 500 A when cooled by liquid helium (4.2 K).

The desired flux density of the magnet then determines the number of windings on a core of given length. For an average bore diameter of 1 m at 1 T, this results

in a wire length of several tens of kilometers. The winding is divided into several subcoils, the number of turns of each being optimized in order to obtain the best magnetic field homogeneity. Without having to consider external interference or assembly tolerances, such a field would typically exhibit a variation of less than 5 ppm within a spherical volume of 50 cm. In practice, this figure is only on the order of several 100 ppm, making additional shimming procedures necessary.

In order to use wire with even higher critical current and/or to reduce the requirements for cooling, alloys other than NbTi have been investigated. Among currently available alloys, only Nb_3Sn can be operated at 10 K and allows conduction cooling, thereby avoiding the need for a liquid helium bath. However, this compound is brittle and difficult to process. In future, new high-temperature superconducting (HTSC) ceramic alloys may be used; these are able to carry more current than low-temperature superconductors at the temperature of liquid helium, but they are even more complicated to manufacture in sufficient length.

Cooling of the superconducting magnet coils can be achieved either by forcing a cooling agent, such as a liquefied gaseous mixture, through special cooling channels, or by placing the coils into a bath of liquid helium; the latter approach is by far the most common, but care must be taken to minimize evaporation of the expensive helium. Hence, the liquid helium vessel is suspended on thin fiberglass rods in a vacuum in order to minimize thermal convection. Thermal radiation is reduced by filling the vacuum space with many layers of superinsulating foils and the use of cooled radiation shields around the helium vessel. These shields or cooled by refrigeration. State-of-the-art technology also recondenses evaporating helium internally, allowing "zero boil off" systems.

Once charged, superconductive magnets keep their field permanently, thereby storing a considerable amount of energy. For a 1-T magnet with an inner bore of 1 m diameter, this energy is about 1.75 MJ. In case of an emergency, the magnet can be discharged rapidly by electrically heating the flux coil to above the critical temperature for superconductivity. The energy is then dissipated through resistors connected in parallel to the windings, thereby evaporating the liquid helium.

The fringe field of superconducting MR magnets presents a major source of risk, since in its gradient ferromagnetic parts are exposed to strong forces. On occasion, iron fragments may be accelerated into the magnet bore, causing major damage and even lethal accidents if persons are hit. When patients are close to a superconducting MRI magnet, their pacemakers can be influenced, hearing aids damaged, and credit cards erased. MR imaging magnets, therefore, must be placed in a controlled zone that is inaccessible to the public. In order to reduce the extension of the fringe field, superconducting coils with an oppositely directed current around the field coils (Mansfield and Chapman, 1986) are now employed. At such actively shielded magnets the dipole field vanishes almost entirely and only an octupole field remains, which decreases with the 5th power of distance.

B_0-fields below 0.5 T are generated with iron yoke magnets driven by permanent magnetic material such as NdFeB. The large amount of iron necessary leads to weights that can easily exceed that of a supercon by a factor of two. In order to form the flux return path (e.g., C-shaped), appropriately dedicated open magnet de-

signs are possible, and these lend themselves very well to investigations of adipose and claustrophobic patients (Fig. 3.20). Likewise, interventional procedures can be performed and children can be attended during the investigation.

3.2.15 Shimming

Due to the influence of the surroundings and to manufacturing inaccuracies, additional means are required to ensure the homogeneity of the magnet. Since a magnetic field in vacuum obeys the Laplace equation, its spatial distribution can be described with a spherical harmonic expansion:

$$B_0(r,\vartheta,\varphi) = \sum_{n=0}^{N} \sum_{m=0}^{M \le N} \left(\frac{r}{R}\right)^n P_n^m(\cos\vartheta)[A_n^m \cos m\varphi + B_n^m \sin m\varphi] \tag{3.46}$$

From a field measurement across the surface of a sphere with radius R, the coefficients of the expansion can be determined and the total magnetic field distribution within this sphere calculated.

In order to shim a supercon, current-carrying resistive windings are arranged on a cylindrical tube inside the magnet bore, and configured so that the field of each partial winding corresponds to one coefficient of the harmonic expansion (Figs. 3.21 and 3.22). The orthogonality of the spherical harmonics corresponds to

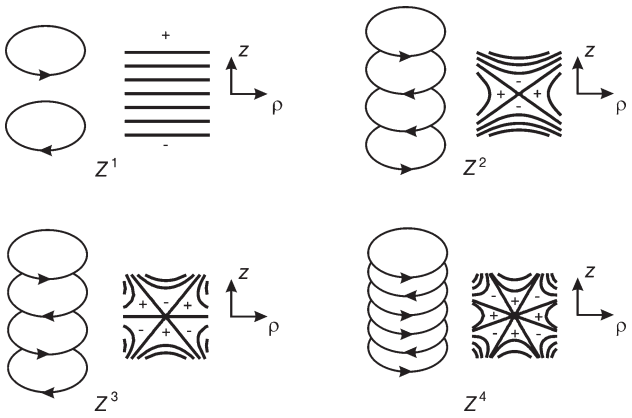

Fig. 3.21. Basic winding schemes for the zonal magnetic field terms used for shimming and the related field patterns (lines of constant flux density B_0). The configuration for Z^1 is basically also used to generate the magnetic field gradient G_z ($Z^n \cong P_n(\cos\vartheta, \rho^2 = x^2 + y^2)$).

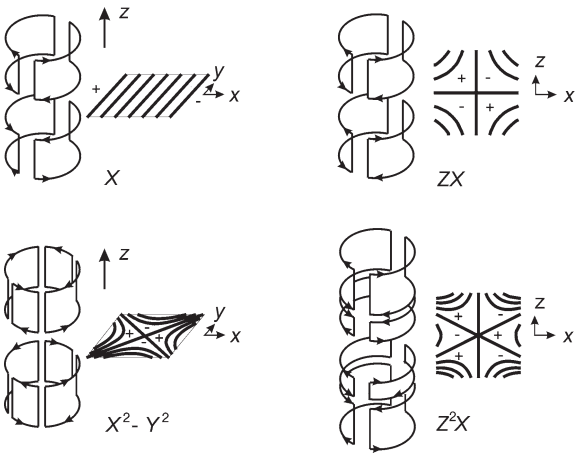

Fig. 3.22. Basic winding schemes for the tesseral field terms used for shimming ($X \cong P_{11} \cos \varphi$, $ZX \cong P_{21} \cos \varphi$, $X^2 - Y^2 \cong P_{22} \cos \varphi$, $Z^2X \cong P_{31} \cos \varphi$). The configuration for X is basically also used to generate the magnetic field gradients G_x and G_y, respectively.

coils, which are almost completely decoupled both from the superconducting coil and from each other. The higher the degree and order, the more complex the shim coil set becomes; typically, 12 coils are used for compensating zonal aberrations to the 4th degree and tesseral to the 2nd order.

Frequently, field inhomogeneities are compensated by mounting iron plates in the magnet bore, or outside the cryostat. For each standard plate position, one can determine the field expansion generated. In this case, however, the expansion contains more than one coefficient. At a field strength such as generated with supercons, the iron plates are magnetically saturated so that the effect of several plates gives rise to linear superpositioning. By varying the linear combination of the different field expansions, corresponding to various positions of the iron plates, the magnet can then be shimmed.

3.2.16 Gradient System

To improve the spatial resolution, reduce the measurement time, perform diffusion measurements and allow increasingly complex pulse sequences, fast-switching magnetic field gradients $\partial B_z/\partial x,\ y,\ z$ of high strength are required. However, as the magnetic field within the imaging volume has no vortexes (i.e., $\nabla \times \vec{B} = 0$), a gradient in the x- or y-direction of the B_0-field must also always lead to a gradient of a B_x or B_y component. These so-called Maxwell gradients can cause image distortions when working with weak magnetic fields.

In principle, gradient coils are designed with the same geometry as the first-order shimming coils. The dimensions of the windings, on the other hand, are adapted to much larger currents and to short switching times. As has been mentioned in Section 3.2.13, the pulsed current flowing through the gradient coils leads to mechanical vibrations, which translate into movements of the air molecules around the gradient coils, and in this way considerable noise is generated. The noise can be significantly amplified by the mechanical resonance of the coil system and acoustic resonance of the cavities between the windings. Possible countermeasures include a rigid construction with small sound-emitting surfaces, a design avoiding mechanical and acoustic resonance frequencies within the band of excitation, and acoustic insulation.

The switched gradient creates eddy currents in the conducting surfaces of the surrounding gradient coil, mainly in the cryo-shields of the superconducting magnets, which counteract the magnetic field changes. The effect of this is equivalent to a low-pass filtering of the time variation of the gradient shape, but in practice this can be compensated by appropriate high-pass filtering of the gradient driving pulse. However, since the eddy current distribution – especially in the radial direction – differs from the coil current distribution, the spatial dependence of the magnetic field due to the eddy currents can differ from that of the gradient coils. A spatial gradient field distortion varying in time then results, which cannot be compensated with a shaped driving pulse. This must be taken into consideration when designing the gradient coils. These effects can be minimized with the use of actively shielded gradient coils.

Gradient strengths up to 45 $mT\,m^{-1}$ (or even 72 $mT\,m^{1}$ when all three gradient axes are energized simultaneously) with a rise time of 50 μs m mT^{-1} are now in clinical use. In order to generate current pulses of suitable duration and amplitude, including eddy current compensation, special high-precision gradient power supplies with low ripple and noise are necessary. The switching of electric power of 1 MW within <0.5 ms is a formidable technical challenge.

3.2.17 RF-System

The transmitter and receiver coils (antennas), the provision of shaped RF-pulses for excitation of the magnetic resonance, and the detection of signals in phase and amplitude are implemented in the RF-system. Although in principle the same coil can be used for transmitting and receiving, the two tasks are mostly covered by separate coils. A large transmit coil provides for the best RF-field homogeneity, while the S/N ratio is optimized with local receiver coils.

As discussed in Section 3.2.2, the NMR phenomenon requires circularly polarized RF-fields. The RF-power required for spin excitation places limitations on image sequences in order not to generate excessive heat in the patient. A reduction of power absorption by a factor of 2 can be achieved using circularly rather than linearly polarized transmitter coils. Circularly polarized receiver coils lead to an improvement of the S/N ratio by a factor of $\sqrt{2}$.

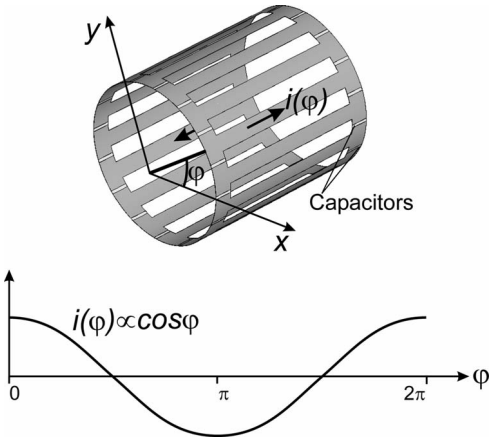

Fig. 3.23. Design principle of a bird cage resonator; the rods are connected by capacitors.

MR antennas make use of only the near field. With body antennas, the geometric dimensions are already comparable with the wavelength, especially at Larmor frequencies larger than 20 MHz. Therefore, coils with concentrated inductances can no longer be constructed, and resonators (so-called birdcages; Tropp, 1989) are used instead. These employ circularly arranged rods parallel to the B_0-field that are driven by currents with sinusoidally varying amplitudes along the circumference (Fig. 3.23).

For receiving, as mentioned above, much reliance is placed on local coils. These are, in the simplest case, single loops placed directly above the organ to be investigated, such that the direction of the RF-field is perpendicular to the coil surface. Two loops side-by-side but with opposite winding directions (a so-called butterfly) generate an RF-field parallel to the coil surface. With a combination of the two coil designs, the full circular RF-field of the precessing magnetization can be retrieved.

The decreasing signal with distance leads to an intensity variation in the MR-image, which can be compensated during image processing. The field of view can be increased without loss in sensitivity when several decoupled local coils are used, each with its own signal acquisition path (phased array; Roemer et al., 1990) (Fig. 3.24). In this way, several independent images are acquired at the same time, and these are combined into a single image in the system computer. For dedicated applications special coils are applied; an example is endo-cavitary investigations for imaging the prostate gland. For imaging of the extremities, flexible coils have been developed, with solenoids applied at the mamma.

The signal from the NMR detection coils are amplified in preamplifiers with a very low noise figure, and then demodulated. Today, mostly digital demodulators are employed to avoid stability problems. As the clock rates of current analog-to-digital converters (ADCs) cannot yet directly convert the RF-signals of high-field MR scanners, they are first mixed down from the Larmor frequency to an intermediate frequency by analog mixers. The intermediate frequency signals are then

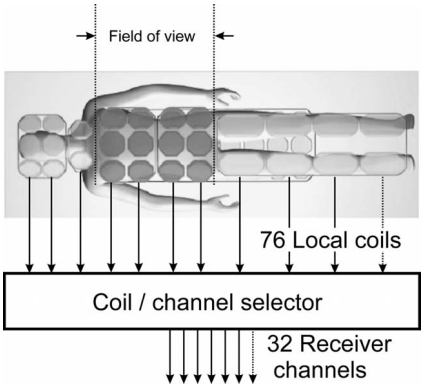

Fig. 3.24. Total imaging matrix (TIM) enabling whole-body imaging without patient repositioning. The field of view is selected with the table position and the coil channel selector. TIM is very well suited to partial acquisition techniques (PAT).

digitized and digitally multiplied with an in-phase and a 90° out-of-phase local sine wave to directly obtain the real and imaginary parts of the nuclear magnetization in the rotating frame. After suppressing frequency components above the Nyquist frequency with a low-pass filter, the signals are further processed in the system computer for image reconstruction.

A single side band modulator is used to generate the transmitter pulses. The amplitude and frequency of the required pulse in the rotating frame are provided by the MRI system computer as complex digital information. Real and imaginary parts are multiplied each with a digitally generated harmonic signal with a phase shift of 90°. The two modulated waves are added and mixed upwards to obtain the Larmor frequency in order to be fed to the RF-amplifier, which drives the transmitter coil.

At B_0-fields of 1.5 T, RF-pulse powers of up to 15 kW are required. For certain pulse sequences, the average power transmitted to the patient (*specific absorption rate*, SAR) would already exceed international safety standards (EN/IEC, 2002). Clinical MR imaging systems must therefore determine for each patient, which RF-power is needed for a certain pulse angle (e.g., a 90° pulse), so that pulse sequences leading to too-high an energy loading can be avoided. For example, at field strengths of 1.5 T the repetition time with spin echo sequences is no longer limited by the performance of the MR imaging system, but by the SAR.

MR imaging systems must be effectively shielded because, on the one hand, the transmit pulses could lead to external interference with communication systems, while on the other hand the pick-up of external RF-signals would severely interfere with the NMR signal and result in image distortions. A shielding factor greater than 100 dB is normally required, and consequently the magnet is usually installed in a room having walls covered with copper foil, while the electronics and operat-

ing console are outside. RF-shielded doors are used, and all connections leading into the magnet room are carefully filtered. Special RF-shielded windows allow the operating personnel to observe the patient during an examination. A communication link with television-monitoring and an intercom are also provided.

3.2.18 Conclusions

Since the early 1980s, when the first commercial instruments became available, clinical MR has expanded rapidly in terms of both medical applications and the number of units installed. Although initially considered to be an expensive method to create images of inferior quality, MRI has since established itself as a clinical diagnostic tool in previously inconceivable applications, and the potential of the method remains unexhausted. In fact, MRI has led to the first large-scale industrial application of superconductivity and has brought about a far greater public awareness of a physical phenomenon previously known only to a handful of scientists.

Until now, the growth and spectrum of applications of MR have exceeded all predictions. Today, a total analysis of the morphology and function of the heart, including the coronary arteries, seems realistic, while diffusion-weighted imaging can show infarcted regions in the brain and diffusion tensor imaging enables the display of nerve fiber bundles. The BOLD effect provides for an intrinsic contrast agent allowing functional imaging. Clearly, MRI is entering the domain of nuclear medicine (and is even competing with biomagnetism).

Current technological trends are directed to still faster acquisition times and better image quality. Since further increases in magnetic gradient strength are limited due to the stimulation of peripheral nerves, partial acquisition techniques such as SMASH, SENSE and their derivatives will lead to increasingly advanced RF-coil configurations. In modern MR scanners, up to 76 different coil elements can be combined with 32 independent RF-channels, allowing patients to be scanned from head to foot within a few minutes, simply by moving them through the magnet bore (Magnetom Flash, 2004). This offers the possibility of screening with MR for cancer or circulatory deficiencies. Moreover, image quality is increased by applying stronger magnetic fields. Indeed, 3-T magnets are today being introduced into clinical routine, while whole-body magnets of 7 T or more are the subject of intense research.

In order to allow better patient access, more open magnets are required. Although in the past this has been the domain of low-field systems with their limited image quality, short high-field magnets with a large inner bore are now available, the dimensions of which approach those of an X-ray CT scanner. An alternative design, though more complex and expensive, employs magnets with a vertical field that is generated by two superconducting coil systems (see Fig. 3.20).

Open magnets facilitate the use of MRI as an imaging modality during minimally invasive procedures, for example in stereotactic brain surgery, tumor abla-

tion, or vascular procedures. Dedicated nonmagnetic tools are required for this purpose. Though still at the research stage, interventional MR has shown great promise due to its high soft tissue contrast and the possibility of measuring tissue temperatures noninvasively.

References

Abe, Z., Tanaka, K., Hotta, K., and Imai, M. (1974). Noninvasive measurements of biological information with application of nuclear magnetic resonance. In: *Biological and Clinical Effects of Low Magnetic and Electric Fields*. Thomas Springfield, Illinois, pp. 295–317.

Aguayo, J.B., Blackband, S.J., Schoeniger, J., Mattingly, M.A., and Hintermann, M. (1986). Nuclear magnetic resonance imaging of a single cell. *Nature*, **232**, 190.

Barfuss, H., Fischer, H., Hentschel, D., Ladebeck, R., and Vetter, J. (1988). Whole body MR imaging and spectroscopy with a 4 T system. *Radiology*, **169**, 811.

Bloch, F.W., Hansen, W.W., and Packard, M. (1946a). Nuclear induction. *Phys. Rev. (L)*, **69**, 127.

Bloch, F., Hansen, W.W., and Packard, M. (1946b). The nuclear induction experiment. *Phys. Rev.*, **70**, 474.

Bloembergen, N., Purcell, E.M., and Pound, R.V. (1948). Relaxation effects in nuclear magnetic resonance absorption. *Phys. Rev.*, **73**, 679.

Bottomley, P.A. (1987). Spatial localization in NMR spectroscopy in vivo. *Ann. N. Y. Acad. Sci.*, **508**, 333.

Bottomley, P.A. and Andrew, E.R. (1978). RF magnetic field penetration, phase shift, and power dissipation in biological tissue: implications for NMR imaging. *Phys. Rev. Biol.*, **23**, 630.

Brown, T.R., Kincaid, B.M., and Ugurbil, K. (1982). NMR shift imaging in three dimensions. *Proc. Natl. Acad. Sci. USA*, **79**, 3523.

Bryant, R.G., Mendelson, D.A., and Lester, C.C. (1991). The magnetic field dependence of proton spin relaxation in tissue. *Magn. Reson. Med.*, **21**, 117.

Budinger, T.F., Fischer, H., Hentschel, D., Reinfelder, H.E., and Schmitt, F. (1991). Physiological effects of fast oscillating magnetic field gradients. *J. Comput. Assist. Tomogr.*, **15**, 909.

Carr, H.Y. and Purcell, E.M. (1954). Effects of diffusion on free precession in nuclear magnetic resonance experiments. *Phys. Rev.*, **94**, 630.

Cooley, J.W. and Tukey, J.W. (1965). An algorithm for machine calculation of complex Fourier series. *Math. Computation*, **19**, 297.

Cormack, A.M. (1963). Representation of a function by its line integrals, with some radiological applications, part 1. *J. Appl. Phys.*, **34**, 2722.

Cormack, A.M. (1964). Representation of a function by its line integrals, with some radiological applications, part 2. *J. Appl. Phys.*, **35**, 2908.

Crooks, L., Sheldon, P., Kaufmann, L., Rowan, W., and Millert, T. (1982). Quantification of obstruction in vessels by nuclear magnetic resonance (NMR). *IEEE Trans. Nucl. Sci.*, **NS-29**, 1181.

Damadian, R. (1971). Tumor detection by nuclear magnetic resonance. *Science*, **171**, 1151.

Dixon, W.T. (1986). Simple proton spectroscopic imaging. *Radiology*, **153**, 189.

Dumoulin, C.L., Souza, S.P., Walker, M.F., and Wagle, W. (1989). Three-dimensional phase contrast angiography. *Magn. Reson. Med.*, **9**, 139.

EN/IEC 60601-2-33, (2002). Particular requirements for the safety of magnetic resonance equipment for medical diagnosis.

Freeman, R. and Hill, H.D.W. (1971). Phase and intensity anomalies in Fourier transform NMR. *J. Magn. Reson.*, **4**, 366.

Gerlach, W. and Stern, O. (1924). Über die Richtungsquantelung im Magnetfeld. *Ann. Physik*, **74**, 673.

Gorter, C.J. (1936). Mißglückter Versuch zur Kerninduktion. *Physica*, **III**, 995.

Gorter, C.J. and Broer, L.F.J. (1942). Negative result of an attempt to observe nuclear magnetic resonance in solids. *Physica*, **IX**, 591.

Haase, A., Frahm, J., Hänicke, W., and Matthaei, D. (1985). ^{1}H NMR chemical shift selective (CHESS) imaging. *Phys. Med. Biol.*, **30**, 341.

Haase, A., Frahm, J., Matthaei, D., Hänicke, W., and Merboldt, K. (1986). FLASH imaging: rapid NMR imaging using low flip angle pulses. *J. Magn. Reson.*, **67**, 217.

Haase, A., Matthaei, D., Bartkowski, R., Dühmke, E., and Leibfritz, D. (1989). Inversion recovery snapshot FLASH MRI: fast dynamic T_1 contrast. *J. Comput. Assist. Tomogr.*, **13**, 1036.

Hahn, E. (1950). Spin echos. *Phys. Rev.*, **80**, 580.

Hebrank, F.X. and Gebhardt, M. (2000). SAFE model – a new method for predicting peripheral nerve stimulations in MRI. *Proc. Int. Soc. Magn. Reson. Med.*, **8**, 2007.

Hoult, D.I. (1977). Zeugmatography: a criticism of the concept of a selective pulse on the presence of a field gradient. *J. Magn. Reson.*, **26**, 165.

Hoult, D.I. and Lauterbur, P.C. (1979). The sensitivity of the Zeugmatographic experiment involving human samples. *J. Magn. Reson.*, **34**, 425.

Hounsfield, G.N., Ambrose, J., Perry, J., et al. (1973). Computerized transverse axial scanning (tomography), parts 1, 2. *Br. J. Radiol.*, **46**, 1016.

Koenig, H.A. and Laub, G.A. (1988). The processing and display of three-dimensional data in magnetic resonance imaging. *Electromedica*, **56**, 42.

Kumar, A., Welti, D., and Ernst, R. (1975). NMR Fourier Zeugmatography. *J. Magn. Reson.*, **18**, 69.

Laub, G.A. and Kaiser, W.A. (1988). MR angiography with gradient motion refocusing. *J. Comp. Assist. Tomogr.*, **12**, 377.

Larmor, J. (1896–1897). The influence of a magnetic field on radiation frequency. *Proc. Roy. Soc.*, **60**, 514.

Lauterbur, P.C. (1973). Image formation by induced local interactions: Examples employing nuclear magnetic resonance. *Nature*, **242**, 469.

Magnetom Flash 2 (2004). Siemens Medical Solutions, GP MR 66040 WS 120420.

Mansfield, P. (1977). Multi planar image formation using NMR spin echos. *J. Phys. C: Solid State Phys.*, **10**, L55.

Mansfield, P. and Chapman, B. (1986). Active screening of coils for static and time-dependent magnetic field generation in NMR imaging. *J. Phys. E: Sci. Instr.*, **19**, 540.

Odeblad, E. and Lindström, G. (1955). Some preliminary observations of proton magnetic resonance in biologic samples. *Acta Radiol.*, **43**, 469.

Ogawa, S., Tank, D.W., Menon, R., Ellermann, J.M., Kim, S.G., Merkle, H., and Ugurbil, K. (1992). Intrinsic signal changes accompanying sensory stimulation: functional brain mapping with magnetic resonance imaging. *Proc. Natl. Acad. Sci. USA*, **89**, 5951.

Oppelt, A., Graumann, R., Barfuß, H., Fischer, H., Hartl, W., and Schajor, W. (1986). FISP – eine neue schnelle Pulssequenz für die Kernspintomographie. *Electromedica*, **54**, 15.

Pruessmann, P., Weiger, M., Scheidegger, M.B., and Boesiger, P. (1999). SENSE: sensitivity encoding for fast MRI. *Magn. Reson. Med.*, **42**, 952–962.

Purcell, E.M., Torrey, H.C., and Pound, R.V. (1946). Resonance absorption by nuclear magnetic moments in a solid. *Phys. Rev. (L)*, **69**, 37.

Rabi, I.I. (1937). Space quantification in a gyrating magnetic field. *Phys. Rev.*, **51**, 652.

Roemer, P.B., Edelstein, W.A., Hayes, C.E., Souza, S.P., and Mueller, O.M. (1990). The NMR phased array. *Magn. Reson. Med.*, **16**, 192.

Schaefer, D.J., Bourland, J.D., and Nyenhuis, J.A. (2000). Review of patient safety in time-varying gradient fields. *J. Magn. Reson. Imaging*, **12**, 20–29.

Singer, J.R. (1959). Blood flow rates by nuclear magnetic resonance measurements. *Science*, **130**, 1652.

Sodickson, D.K. and Manning, W.J. (1997). Simultaneous acquisition of spatial harmonics (SMASH): Fast imaging with radiofrequency coil arrays. *Magn. Reson. Med.*, **38**, 591–603.

Stejskal, E.O. and Tanner, J.E. (1965). Spin diffusion measurements: spin echoes in the presence of a time dependent field gradient. *Chem. Phys.*, **42**, 288.

Suryan, G. (1951). Nuclear resonance in flowing liquids. *Proc. Indian Acad. Sci.*, Section **A33**, 107.

Tropp, J. (1989). The theory of the bird-cage resonator. *J. Magn. Reson.*, **82**, 51–62.

Turner, R., LeBihan, D., Maier, J., Vavrek, R., Hedges, L.K., and Pekar, J. (1990). Echo-planar imaging of intravoxel incoherent motion. *Radiology*, **177**, 407.

Wehrli, F.W. (1990). Time of flight effects in MR imaging of flow. *Magn. Reson. Med.*, **14**, 187.

Weinmann, H.J., Brasch, R.C., Press, W.R., and Wesbey, G.E. (1984). Characteristics of gadolinium-DTPA complex: A potential NMR contrast agent. *Am J. Roentgenol.*, **143**, 619.

Weiss, G. (1901). Sur la possibilite de rendre comparable entre eux les appareils servant a l'exitation electrique. *Arch. Ital. Biol.*, **35**, 413.

Wolff, S.D. and Balaban, R.S. (1989). Magnetization transfer contrast (MTC) and tissue water proton relaxation in vivo. *Magn. Reson. Med.*, **10**, 135.

Zavoiskij, E.K. (1945). Paramagnetic relaxation of liquid solutions for perpendicular fields (in Russian). *J. Phys. USSR*, **9**, 211.

Zeeman, P. (1897). On the influence of magnetism on the nature of light emitted by a substance. *Phil. Mag.* **43**, 226.

Zimmermann, B. and Hentschel, D. (1987). Wirkung eines statischen Magnetfeldes (3.5 T) auf das Reproduktionsverhalten von Mäusen, auf die embryonale und fetale Entwicklung und auf ausgewählte hämatologische Parameter. *Digitale Bilddiagnostik*, **7**, 155.

3.3
Modern Applications of MRI in Medical Sciences

3.3.1
New MRI Techniques for Cardiovascular Imaging

Debiao Li and Andrew C. Larson

3.3.1.1
Introduction

Although over 20 million cardiovascular imaging examinations are performed annually using X-ray angiography, echocardiography, or nuclear medicine, the rapidly evolving techniques of cardiovascular magnetic resonance imaging (CMRI) offer many advantages which may ultimately position MRI as the modality of choice for cardiovascular imaging. MRI offers a host of contrast mechanisms which can be readily adapted to delineate tissues and physiological phenomena of particular diagnostic importance. This flexibility has led to the promise of a "one-stop shop" comprehensive CMRI examination using only a single modality for diagnostic cardiovascular imaging (Pettigrew et al., 1999). In this section, CMRI techniques for the interrogation of cardiovascular morphology, cardiac function and flow, myocardial perfusion, myocardial viability, and coronary MR angiography will be described.

3.3.1.2
Cardiovascular Morphology

Static anatomical imaging of the cardiovascular system has been performed using spin echo-based MRI techniques for a number of years. With the introduction of multi-echo spin echo techniques – known as *turbo spin echo* (TSE) or *fast spin echo* (FSE) – the possibility of acquiring high-resolution images of the heart and blood vessels within a breath-hold (Simonetti et al., 1996), or even in a single heartbeat (Laub et al., 1995), have become a reality (Fig. 3.25). Signal from moving blood is typically suppressed using black blood inversion recovery preparation techniques. The primary application of black blood TSE is for morphological imaging of the

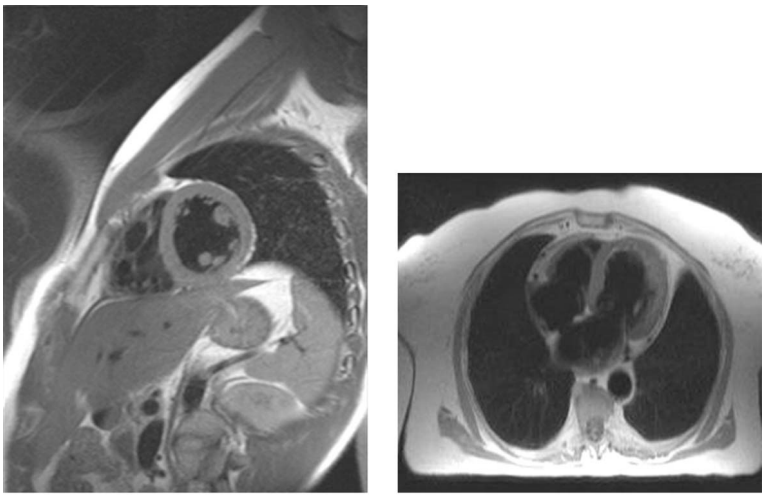

Fig. 3.25. Short-axis (a) and long-axis (b) black-blood cardiac images. Each complete image was acquired in about 300 ms, a sufficiently short acquisition duration to avoid most respiratory motion artifacts.

myocardium, valves (Arai et al., 1999), and thoracic blood vessels. More recently, high-resolution variations of black blood TSE have been applied to imaging of the vessel walls and atherosclerotic plaque in the aorta (Fayad et al., 2000a) and coronary arteries (Fayad et al., 2000b).

3.3.1.3
Cardiac Function and Flow

MR cineangiography (“cine”) involves acquiring a series of images depicting tissue position throughout the cardiac cycle, allowing not only an interrogation of cardiovascular morphology and motion but also an assessment of cardiac function (Atkinson and Edelman, 1991). MR cine techniques allow the measurement of myocardial mass, ejection fraction, and wall thickness. Cinematic viewing of these image series allows detection of hypokinetic or hyperkinetic wall motion abnormalities. MR flow imaging techniques allow the measurement of blood flow velocity for functional measurements and the detection of hemodynamic abnormalities.

Segmented Cine

MR cineangiography is generally performed with segmented acquisition strategies during a breath-hold using a steady-state free precession (SSFP) technique. Electrocardiographic triggering is generally required. Detection of the R wave triggers repeated acquisition of a *k*-space segment during each cardiac cycle. Imaging data is

synchronized by simply combining those segments acquired at the same cardiac phase to produce an image. Ideally, chosen cine acquisition parameters should allow reconstruction of 15 to 20 cardiac phases depending upon a patient's heart-rate.

Temporal resolution for cineangiography can be increased by using "sliding-window" echo-sharing techniques (Riederer et al., 1988). Rather than simply reconstructing images at the cardiac cycle positions of the acquired phases, intermediate images can be reconstructed by "sharing" sub-sets of the phase-encoding lines acquired during adjacent phases to reconstruct intermediate images and thereby provide a greater temporal resolution. The following set of imaging parameters are typical of those commonly utilized for SSFP segmented cine imaging with state-of-the art 1.5-T clinical scanners for an eight heartbeat breath-held acquisition: 6 mm slice thickness, 300×250 mm^2 field of view (FOV), repetition time (TR)/echo time (TE) = 3.0/1.5 ms, 60° flip-angle, 15 lines per segment, 256×120 matrix, 1.2×2.1 mm^2 in-plane voxel size.

For the assessment of myocardial function, cine image series are typically acquired in four-chamber, three-chamber, two-chamber, and short-axis orientations. Short-axis images are typically acquired as a stack of eight to ten parallel slices evenly spaced to cover the left ventricle from base to apex. Examples of these four imaging orientations are shown in Figure 3.26.

Real-Time Cine

Real-time (RT) cine imaging techniques can be utilized when either breath-holding or electrocardiographic (ECG) gating are not possible. For these techniques, *k*-space data for the reconstruction of each cardiac image are acquired within temporally distinct acquisition windows rather than multiple acquisition windows from multiple cardiac cycles. Real-time techniques inherently eliminate the issues associated with cardiac gating, but inevitably increase the difficulty of achieving a temporal resolution, spatial resolution, signal-to-noise ratio (SNR), and overall image quality sufficient for clinical utility.

The utilization of efficient acquisition strategies is critical for effective RT cineangiography. Recently, the most effective strategies for RT cine MRI involved the combination of SSFP pulse sequences with either the GRAPPA (Griswold et al., 2002) or TSENSE (Kellman et al., 2001) parallel imaging techniques. Whereas RT SSFP sequences alone can provide temporal resolution on the order of 55 ms with echo-sharing while achieving in-plane spatial resolution of 2.3×4.5 mm^2 (300×225 mm^2 FOV; TR/TE = 2.2/1.1 ms; 128×50 matrix), SSFP combined with parallel imaging techniques with up to fourfold acceleration can either increase the temporal resolution to 27.5 ms (with no echo-sharing) or alternatively increase the spatial resolution to 2.3×2.25 mm^2. Radial (Shankaranarayanan et al., 2001) and spiral (Kerr et al., 1997) *k*-space sampling techniques have also been shown to provide improved efficiency for RT cineangiography. The RT cine images in Figure 3.27 were acquired using GRAPPA SSFP with a factor-of-2 acceleration to provide a temporal resolution of 55 ms (without echo-sharing) with spatial resolution of $2.3 \times 3.8 \times 7.0$ mm^3.

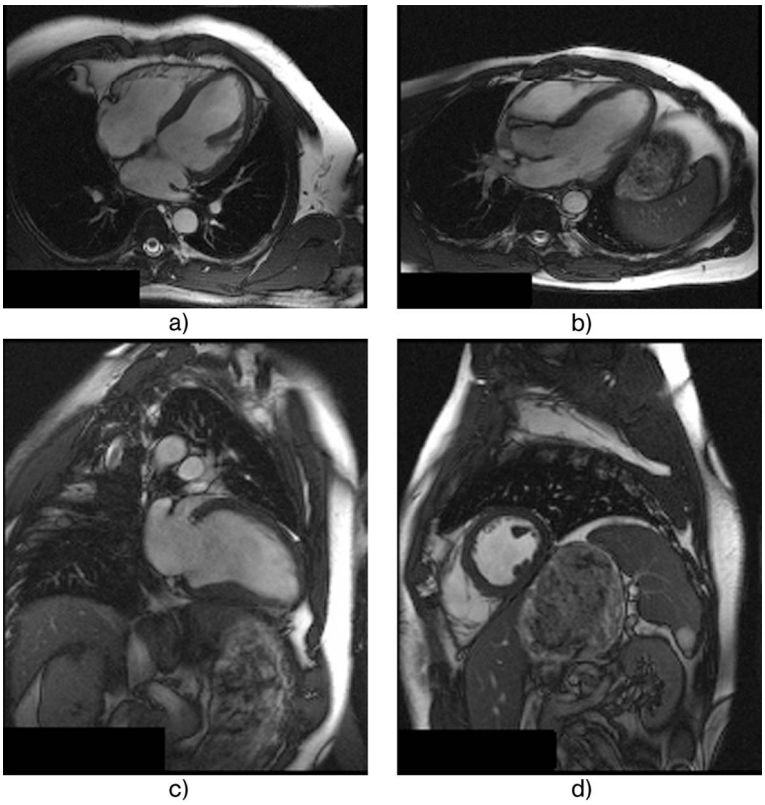

Fig. 3.26. Conventional imaging orientations for the assessment of cardiac function include (a) four-chamber, (b) three-chamber, (c) two-chamber, and (d) short-axis (typically base-to-apex stack, only mid-ventricle slice shown).

Myocardial Tagging

Myocardial tagging combined with cineangiography can permit tracking of discrete tissue points within the myocardium, and therefore more accurate evaluation of regional myocardial deformation (McVeigh and Zerhouni, 1991). Myocardial tagging is performed by saturating thin parallel sections of tissue early in the cardiac cycle, ideally immediately following ECG R-wave detection. The tags deform along with the myocardium during contraction and relaxation. The saturation tags are most commonly applied using spatial modulation of magnetization (SPAMM) techniques (Axel and Dougherty, 1989). Grid tags can be generated by the application of two sets of SPAMM tags in perpendicular orientations, as shown in the short-axis images in Figure 3.28 with 400×320 mm^2 FOV, 256×144 matrix, and 8 mm SPAM tag spacing. Tag spacing is generally limited to no less than 5 mm.

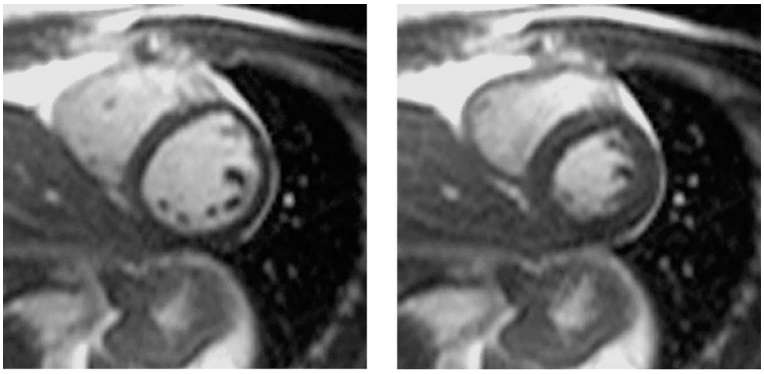

Fig. 3.27. Short-axis images at diastole (a) and systole (b)

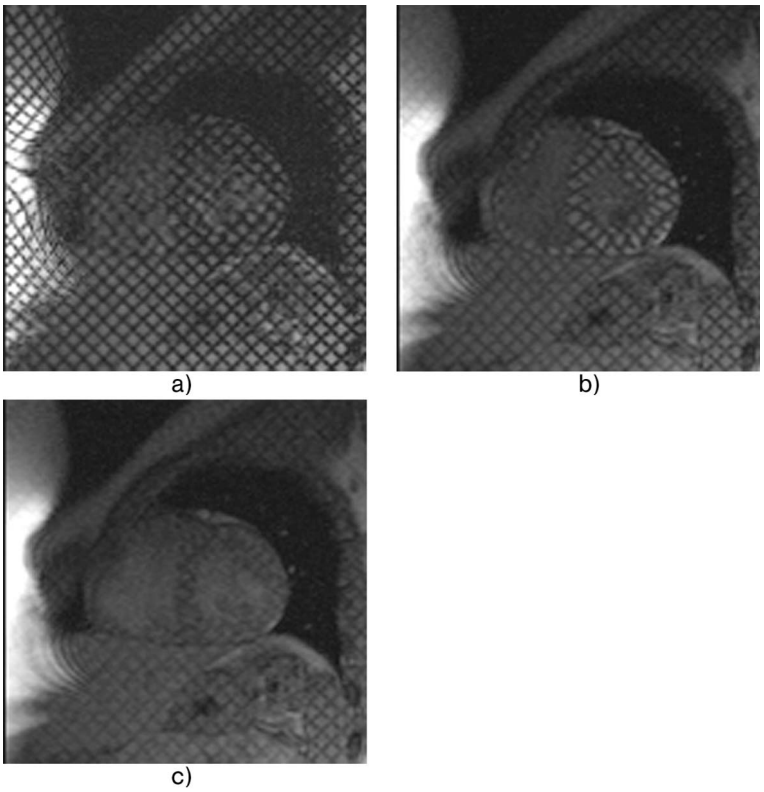

Fig. 3.28. SPAMM cardiac cine images in the mid short-axis orientation shortly after tag saturation following R-wave trigger (a), end-systole (b), and late diastole (c). Note the fading of tag lines during diastole resulting from T_1 relaxation.

Cinematic viewing of the resulting tagged image series can be very informative to trained observers when attempting to locate regions of myocardial wall motion abnormalities. Advanced image processing utilities also permit the automated tracking of these tag lines during myocardial contraction and relaxation, allowing quantitative measurement of the shortening and elongation of myocardium along with the computation of stress–strain relationships (Moore et al., 1999).

Flow

Spins moving parallel to a magnetic field gradient accumulate phase proportional to velocity and the first-order moment of the applied magnetic field gradients (Moran, 1982). While generally only magnitude images are reconstructed for most CMRI applications, the reconstruction of phase images can be very useful for the measurement of blood flow velocity (Axel and Morton, 1987). Assuming adequate velocity compensation along two spatial dimensions, the spins can be velocity encoded along the third dimension such that voxel phase in the resulting images corresponds to flow velocity along the axis of velocity encoding. The maximum flow velocity for which a given velocity encoding sequence can avoid aliasing is known as the ''VENC'' of the sequence.

Most MR velocity mapping techniques involve acquiring two cine image series, each synchronized with the cardiac cycle while reversing the polarity of the velocity encoding gradients between the two acquisitions. A single cine image series can then be generated by subtracting the phase of the negative polarity series from the phase of the positive polarity series. The intensity of the resulting images can then be converted to a velocity measurement based upon the known first-order gradient moment at TE. Measurements with opposite polarity-encoding gradients are necessary in order to eliminate phase artifacts unrelated to flow. Each set of two measurements will ultimately produce a single image series with velocity encoding in a single dimension. Acquisition of two additional data sets along each dimension is necessary in order to provide velocity information along all axes. The resulting velocity map images are displayed with gray-scale values such that dark pixels represent negative velocities (black = maximum negative velocity) whereas bright pixels represent positive velocities (white = maximum positive velocity), with gray mid-range pixels representative of static tissue. Examples of through-plane velocity-encoded images in a transverse slice orientation perpendicular to the great thoracic vessels are shown in Figure 3.29.

The most clinically relevant flow imaging orientations include cross-sections through the mitral valve, tricuspid valve, aorta, and pulmonary artery. While flow imaging techniques must use a sufficiently narrow slice thickness to avoid intravoxel dephasing effects, reduction of slice thickness is ultimately limited by the SNR.

Post-processing tools can be utilized to convert flow velocity measures (cm s^{-1}) to flow volume measures (mL s^{-1}) based on voxel size. Typically, a polygonal region-of-interest (ROI) is drawn encompassing the lumen of a vessel in order to generate a time curve representative of the mean flow volume within a particular vessel.

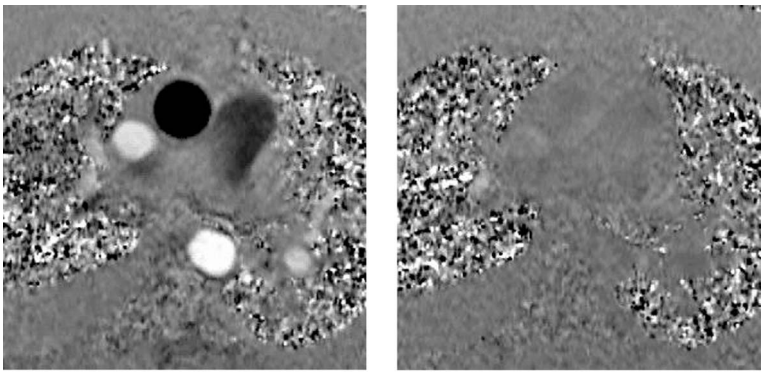

Fig. 3.29. (a) Systolic and (b) diastolic through-plane velocity-encoded images in a transverse slice orientation crossing the great thoracic vessels. Note the opposing directions of flow in the ascending and descending aorta during systole (a) and the expected relative lack of flow during diastases (b).

3.3.1.4 Perfusion

CMRI perfusion imaging techniques attempt to identify regions of restricted coronary artery blood flow resulting in reduced perfusion of the myocardial capillary beds. The only clinically validated CMRI perfusion measurement technique involves monitoring the first pass of gadolinium-based contrast agent into the myocardium (Manning et al., 1991). A delay in uptake of the contrast agent is an indication of a perfusion deficit potentially resulting from coronary artery occlusion.

First-pass contrast-enhanced perfusion imaging involves acquiring a series of single-shot images immediately following intravenous injection of Gd-DTPA in order to monitor myocardial uptake of the contrast agent. The contrast agent is administered by peripheral injection into the antecubital vein at injection rates from 3 to 5 mL s^{-1}, typically using a full dose of 0.1 mmol kg^{-1}. Single-shot images are acquired at multiple slice positions during each cardiac cycle, usually over a period of 30–40 s. Saturation recovery (SR) magnetization preparation is applied prior to the sampling of images at each slice position. Because Gd-DTPA is a T_1-shortening contrast agent, saturation enhances the conspicuity of tissue containing the contrast agent relative to the surrounding tissues. While SR techniques provide weaker T_1-weighting than competing inversion recovery (IR) preparation techniques, IR strategies are difficult to combine with a multislice acquisition and are quite sensitive to variations in cardiac cycle length. For these reasons, IR preparation approaches are less commonly utilized for first-pass perfusion imaging.

Perfusion defects are more readily detected under stress conditions. First-pass imaging is therefore commonly performed during pharmacological stimulation to artificially increase blood flow to the myocardium. Stimulation can generally be ac-

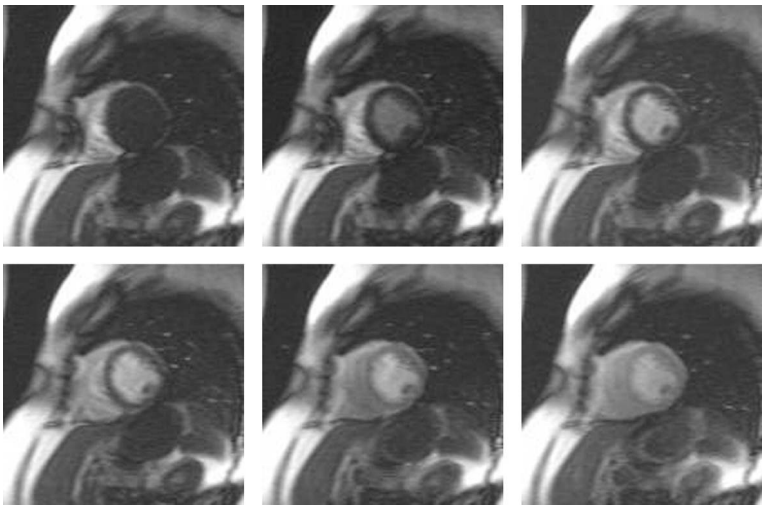

Fig. 3.30. Six consecutive images at a single short-axis slice position from a first-pass perfusion series acquired using the SR SSFP technique. Note that the contrast agent bolus first enters the right ventricle, then the left ventricle, before perfusing into the myocardium.

complished with dipyridamole or adenosine, causing dilation of the coronary arteries. Stenotic vessels are unable to respond to the same degree as normal vessels, giving rise to regional differences in myocardial blood flow.

Relatively long myocardium contrast agent wash-out times generally allow only a single first-pass measurement during an examination, and therefore adequate heart coverage must be achieved by the slice positions sampled during each heartbeat of the first-pass scan. Sufficient spatial resolution ($\sim 2 \times 2 \times 8$ mm^3) is necessary to detect clinically significant ischemic regions. However, the acquisition window for each single-shot image should not exceed ~120–150 ms in order to avoid artifacts at the left ventricular blood pool to endocardium interface caused by motion artifacts. Depending upon patient heart rate, a trade-off must be made between overall coverage and spatial resolution. With state-of-the-art hardware and software, typically three to five short-axis slices are sampled during each heartbeat. Ideally, a first-pass imaging sequence should result in images with signal intensity directly proportional to Gd-DTPA contrast agent concentration in order to allow accurate perfusion measurements.

The series of short-axis images in Figure 3.30 was acquired after 0.1 mmol kg^{-1} injection of Gd-DTPA using first-pass SR SSFP imaging with the following parameters: TR/TE = 2.2/1.1; 300×225 mm^2 FOV; 128×60 matrix; 8-mm slice thickness; TI = 60 ms.

Trained observers can qualitatively assess first-pass image series for the presence of perfusion deficits. Alternatively, specialized software can be used to extract infor-

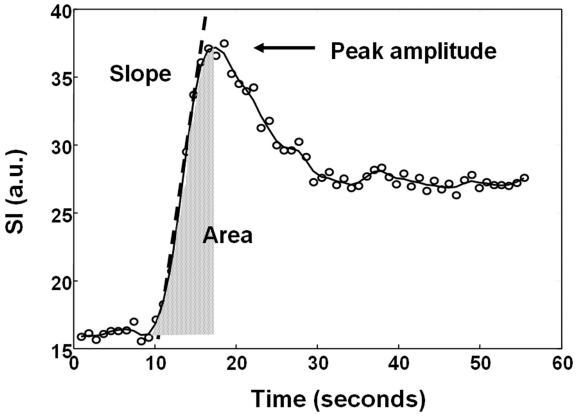

Fig. 3.31. First-pass time-intensity curve showing computation of the semi-quantitative perfusion measures of up-slope, peak signal, and area under up-slope.

mation from dynamic perfusion studies and present it in useful forms. Contours are drawn to segment the myocardium into localized regions. The mean signal within these regions are used to generate time-intensity curves which provide the semi-quantitative perfusion measures (Wilke et al., 1993) of up-slope, peak signal, and area under up-slope, as shown for a single example region in Figure 3.31. Regions with a perfusion deficit tend to exhibit a delayed up-slope and decreased maximum signal intensity relative to normally perfused myocardium. These measures can be compared to clinical indexes of normal versus abnormal perfusion. Fully quantitative assessments of myocardial perfusion are possible using first-pass MRI with excellent correlation to microsphere measures in animal models (Wilke et al., 1997). However, the complex strategies necessary for fully qualitative measurements are somewhat time consuming currently limiting clinical application.

3.3.1.5 Delayed-Enhancement Imaging

Differentiation between necrotic and stunned myocardium is critical when considering potential reperfusion therapies. Recently developed CMRI techniques are rapidly gaining acceptance as an important clinical tool for the assessment of myocardial viability. While T_2-weighted spin-echo imaging (Ratner et al., 1985), MR spectroscopic imaging (Yabe et al., 1995) as well as ^{23}Na (Kim et al., 1999) and ^{39}K (Parrish et al., 1997) MR imaging techniques have demonstrated utility for the *in-vivo* assessment of myocardial tissue viability, delayed-hyperenhancement strategies are the most commonly utilized MRI method for visualizing myocardial infarction in clinical practice (Kim et al., 2000). Injected Gd-DTPA contrast agents diffuse into the interstitial spaces of both infarcted and viable myocardial tissues.

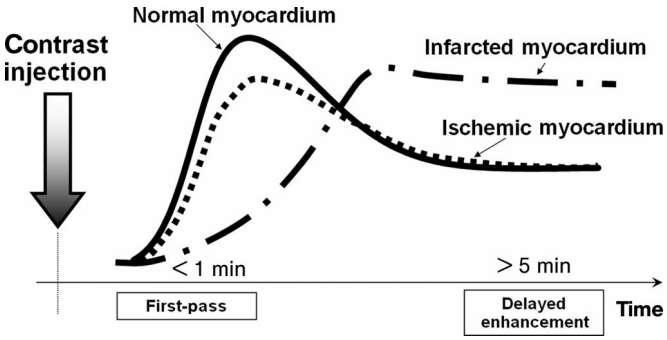

Fig. 3.32. Descriptive example of myocardial signal following Gd-DTPA contrast injection in normal, ischemic, and infarcted tissues. Combination of first-pass imaging with delayed-hyperenhancement imaging can allow discrimination between regions of infarction and ischemia.

After about 15–30 minutes the contrast agent is reabsorbed from viable myocardial tissues for excretion, but the reabsorption rate is significantly reduced in regions of acute or chronic myocardial necrosis. When imaged using T_1-weighted MRI, necrotic tissues appear as regions of high signal intensity. A descriptive example of myocardial signal in normal, ischemic, and infarcted myocardium is shown in Figure 3.32. A combination of first-pass imaging with delayed-hyperenhancement imaging can allow discrimination to be made between regions of myocardial ischemia and necrosis.

Segmented T_1-weighted FLASH sequences are most commonly utilized for delayed-hyperenhancement MRI (Simonetti et al., 2001). Inversion recovery magnetization preparation is applied to null viable myocardium prior to the acquisition of each segment of phase-encoding lines. Delayed-hyperenhancement images are acquired at 10–30 minutes after Gd-DTPA contrast injection. Often, a portion of the contrast dose is administered during a first-pass perfusion examination ($\sim$0.1 mmol kg^{-1}) with any final portion (additional $\sim$0.1 mmol kg^{-1}) being administered immediately following the first-pass examination.

Typical imaging parameters for a breath-held IR prepared FLASH acquisition for delayed-hyperenhancement MRI include: TI = 200–300 ms; 140 Hz per pixel BW; 138 $\times$ 256 matrix; 23 lines per segment; TR/TE = 8.0/4.0 ms, and flip-angle = 20–30° for an overall acquisition time of 12 heartbeats. Several images acquired with this type of acquisition scheme are shown in Figure 3.33 (note the high signal intensity of infarcted tissue regions relative to the normal myocardium).

3.3.1.6 Coronary MR Angiography

Despite the availability of various screening tests, including echocardiographic, radionuclide, and ultrasound approaches, a substantial minority of patients referred for coronary angiography have no significant coronary artery disease (Manning and

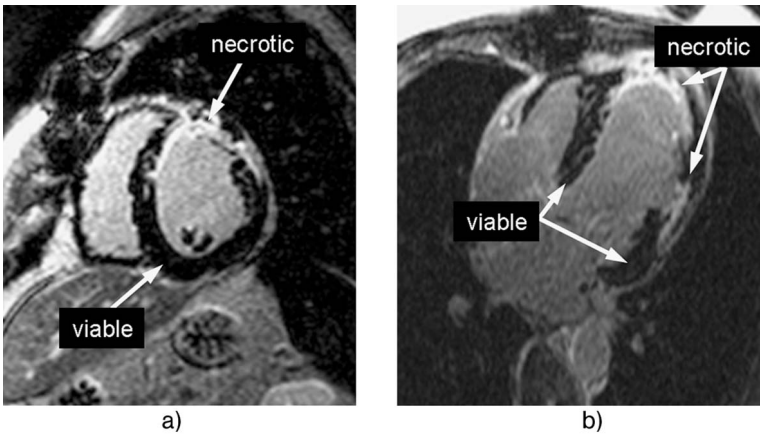

Fig. 3.33. Delayed-hyperenhancement images in (a) short-axis and (b) long-axis orientations, acquired using the IR FLASH technique. Note the high signal intensity of infarcted tissue regions relative to the nulled normal myocardium.

Edelman, 1993). There is a clear need for a noninvasive, cost-effective, and reliable method of directly detecting functionally significant coronary artery disease (defined as a reduction in the luminal diameter of at least 50%) in the high-prevalence population.

The MR techniques used to evaluate the vascular anatomy – collectively known as *magnetic resonance angiography* (MRA) – have become routine clinical tests in the head and neck, abdomen, and extremities. However, MRA of the coronary arteries is a more challenging task, and a number of factors have hindered its progress. These include the motion of the heart during cardiac and respiratory cycles, the highly tortuous course and small size of the coronary arteries, and the adjacency of coronary arteries to epicardial fatty tissues, atrial appendages, coronary veins, and major blood pools which have little natural image contrast with the coronary arteries. The spatial displacement of coronary arteries during each heartbeat and respiratory cycle is on the order of several centimeters. The proximal coronary arteries have calibers in the range of 2 to 4 mm, and rarely exceed 5 mm in normal humans (Hofman et al., 1995), while distal portions of the coronary arteries and branch vessels are of even smaller sizes. The major challenge has been to overcome the limitations of coronary artery motion during cardiac and respiratory cycles. In order to eliminate cardiac motion effects, ECG-triggering has been used to ensure that data are acquired during mid-diastole, whereas to eliminate respiratory motion effects, breath-holding or navigator-echo-guided respiratory gating and slice following has been used.

Basic Imaging Scheme

A variety of protocols have been used for coronary artery imaging. A common feature of most methods is the basic sequence structure and the need to determine

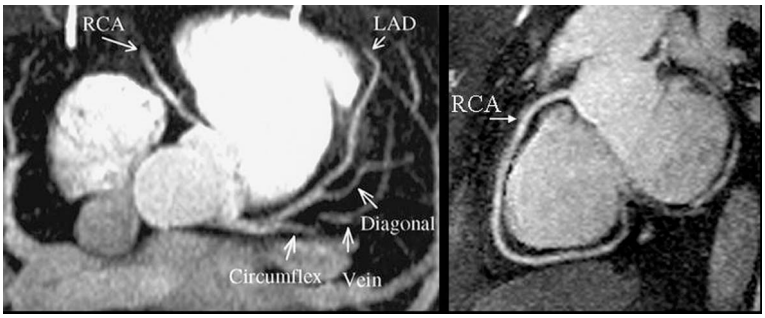

Fig. 3.34. Reformatting of post-contrast 3D breath-hold images. LAD = left anterior descending; RCA = right coronary artery. (Reproduced from Li et al., 2001, with permission).

optimal planes for imaging the coronary arteries. In this section, attention will be focused on two major coronary artery imaging approaches that have undergone preliminary clinical testing: volume-targeted breath-hold imaging; and free-breathing imaging with navigator-echo-based motion correction. The basic technique for coronary artery imaging is an ECG-triggered, segmented 3D approach. A certain delay time from the trigger signal is allowed to ensure that data are collected during mid-diastole. This effectively freezes the heart motion, provided that the heart returns to the same position for each heartbeat, and the data acquisition window is short compared to the duration of diastole.

Contrast-Enhanced FLASH (fast low angle shot)

In volume-targeted imaging, a breath-hold scan with a thin slab is acquired to cover a major coronary artery branch. Repeated scans are collected to cover different parts of the coronary artery system, including the left main (LM), left anterior descending (LAD), left circumflex (LCX), and right coronary artery (RCA).

For breath-hold coronary MRA, a short TR is required in order to acquire adequate spatial resolution within the limited imaging time. T_1-shortening contrast agents have been used to improve the SNR and contrast-to-noise ratio (CNR) of coronary MRA (Li et al., 2001). During each heartbeat, 25 or 31 in-plane phase-encoding steps were acquired depending on the heart rate of the subject. With a TR of 3.8 s, the data acquisition duration per heartbeat was 95 or 118 s, respectively. Three heartbeats were required to cover each k_x-k_y plane of the 3D k-space in an interleaved manner. Other imaging parameters included: TE = 1.9 ms; flip angle = 22°; in-plane resolution = (1.4–2.0) × (1.0–1.2) mm^2; slab thickness = 24–32 mm; number of partitions = 8; slice thickness = 3–4 mm; and imaging time = 24 heartbeats. An inversion recovery time (TI) of 250–300 ms was used to suppress myocardial tissue while allowing almost full recovery of the blood signal.

Two separate 20-mL contrast injections were administered, and each injection was followed by a targeted scan. The two scans covered the left and right coronary arteries, respectively. 3D images can be reformatted to provide a more complete view of the coronary arteries (Fig. 3.34).

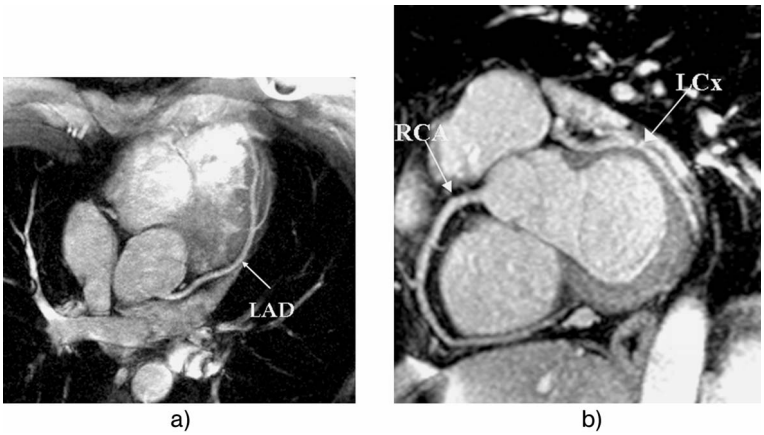

Fig. 3.35. Coronary artery images acquired with 3D breath-hold SSFP depicting (a) the left anterior descending artery (LAD) and (b) the right coronary artery (RCA) in healthy volunteers. LCx = left circumflex artery. (Reproduced from Deshpande et al., 2002, with permission).

3D Breath-hold Volume Targeted SSFP

Since the implementation of advanced MR imaging systems during late 1990s allowed the use of short TR (e.g., <4 ms) and improved static field homogeneity, SSFP has become the method of choice for cardiac cine imaging (Carr et al., 2001). In general, it can generate much higher SNR and CNR than FLASH with the same imaging time.

For coronary MRA, the basic SSFP sequence was modified to allow ECG-triggered data acquisition and fat saturation for coronary artery imaging (Deshpande et al., 2001). Examples of 3D breath-hold TrueFISP coronary images are shown in Figure 3.35. Imaging parameters were: TR/TE = 3.5/1.4 ms; flip angle = 70°; FOV = (180–250) × (380–400) mm^2; acquisition matrix size = (160–175) × 512; slab thickness = 18 mm; number of partitions = 6 (12 interpolated); in-plane resolution = (1.0–1.6) × (0.74–0.78) mm^2; scan time = 24–30 heartbeats during suspended inspiration. The MRI examinations were performed on a 1.5-T whole-body scanner with a high-performance gradient sub-system (maximum gradient strength 40 mT m^{-1}; maximum gradient slew rate 200 mT m^{-1} ms^{-1}).

Coronary Artery Imaging with Free Breathing and Real-Time Slice Correction

The major problem with breath-hold coronary artery imaging is the limited SNR and spatial resolution due to the constraint of imaging time. One method to alleviate this limitation is to acquire data during free breathing. The position shifts due to respiration during data acquisition of different parts of *k*-space are corrected by changing the slice position in real-time such that the entire *k*-space is acquired at the same slice position, despite the motion of coronary arteries during respiration (Oshinski et al., 1998). To obtain a reference of position shifts of coronary arteries

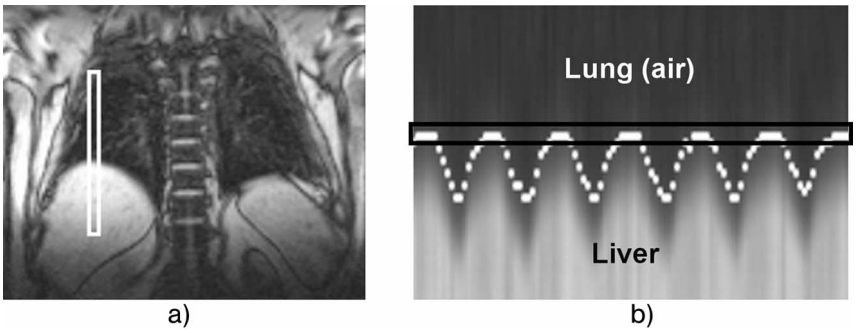

Fig. 3.36. Position of navigator echo excitation column (a) and series of navigator echo measurements over multiple respiratory cycles (b).

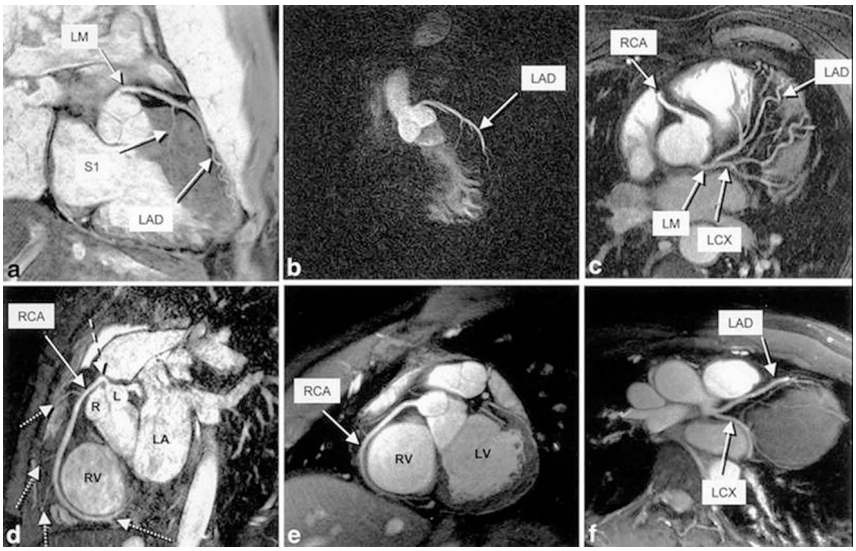

Fig 3.37. Reformatted images of 3D coronary MRA data acquired with real-time navigator technology during free breathing.
(a) A video-inverted black-blood coronary MRA is displayed adjacent to a spin-tagged acquisition of (b) the left coronary arterial system. (c) An RCA together with a left coronary arterial system, including the LM, LAD, LCX, and some smaller-caliber branching segments (using a T2Prep segmented *k*-space gradient-echo acquisition). (d) An anomalous RCA (dashed arrow) from the left coronary cusp (L) acquired with a T2Prep SSFP sequence is shown (R = right coronary cusp; RV = right ventricle; LA = left atrium).
(e, f) Right and left coronary arterial systems acquired with an interleaved spiral imaging sequence. (Reproduced from Etienne et al., 2002, with permission).

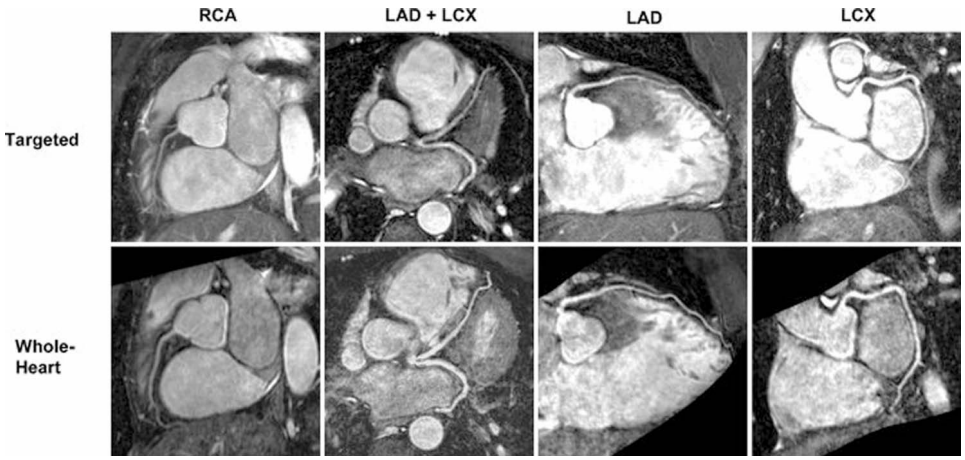

Fig. 3.38. The coronary arteries of a volunteer. Note that contrast to the background is improved, especially in the more distal segments of the LAD and LCX. In the LAD+LCX visualization of the whole-heart approach, the length of vessels is only partly shown, as vessels orthogonal to the visualization plane are poorly visualized in this type of reconstruction. This problem did not occur in the transverse-targeted volume, because the imaged volume did not cover the critical part of the vessels. Alternative orientations provided better visualization of the LAD and LCX in both approaches. (Reproduced from Weber et al., 2003, with permission).

during data acquisition, navigator echoes are collected along the cranial-caudal direction at the dome of the diaphragm (Fig. 3.36). Example coronary artery images using this technique are shown in Figure 3.37.

Whole-heart coronary MRA was implemented based on a free-breathing True-FISP technique with magnetization preparation and a SENSE factor of 2 (Weber et al., 2003). Example images are shown in Figure 3.38. Current limitations on the SNR and spatial resolution of coronary MRA at 1.5 T can be improved by imaging at higher field strengths (Stuber et al., 2003).

3.3.1.7
Coronary Artery Wall Imaging

The purpose of coronary MR angiography is to detect clinically significant lumen stenosis. Since acute ischemic coronary syndromes are often caused by the rupture of a mildly to moderately stenotic coronary artery plaque, leading to the formation of thrombi, it is important to detect the presence of vulnerable plaques before they cause serious consequences. Substantial progress has been made in using MRI to visualize arterial wall and assess plaque composition. While the early studies focused on the carotid arteries (Yuan et al., 2002a) and the aorta. more recently proton-density-weighted, T_1-weighted, and T_2-weighted images must be acquired for the accurate characterization of various plaque components (Rogers et al., 2000). Examples of a thin fibrous cap are shown in Figure 3.39. Recently, MRI

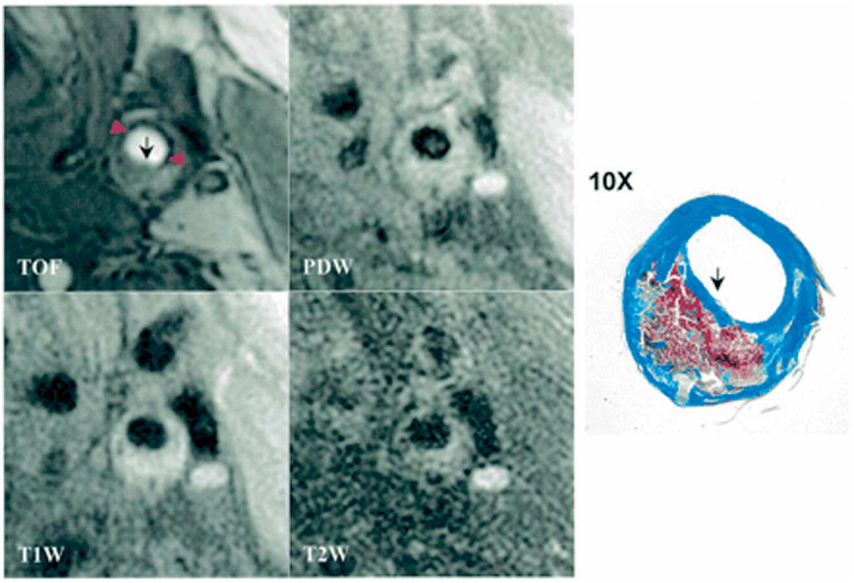

Fig. 3.39. Example of a thin intact fibrous cap as seen on MRI along with the corresponding matched histological cross-section. A distinct hypointense band (red arrowheads) is clearly visible on a segment of the luminal boundary of an atherosclerotic common carotid artery on the TOF image, but is missing on the surface of the bulk of the plaque (black arrow). PD-weighted (PDW), T_1-weighted (T1W), and T_2-weighted (T2W) images from the same location show a smooth surface, suggesting an absence of rupture. A Mallory's Trichrome-stained histology section of the area confirms the presence of a large necrotic core covered by a thin fibrous cap (arrow) (scale bar = 1 mm). (Reproduced from Yuan et al., 2002b, with permission).

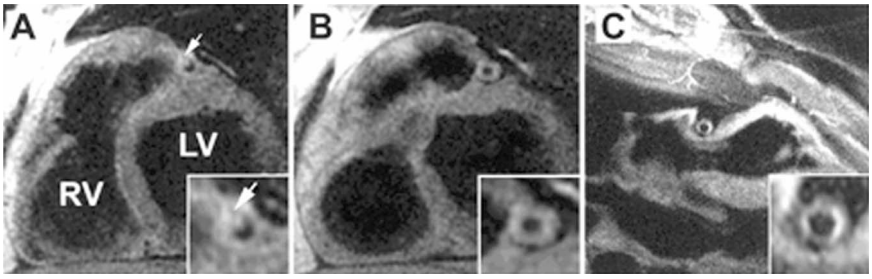

Fig. 3.40. *In-vivo* MR black-blood cross-sectional images of human coronary arteries, showing (A) a plaque, presumably with deposition of fat (arrow); (B) a concentric fibrotic lesion in the left anterior descending artery; and (C) an ectatic, but atherosclerotic, right coronary artery. LV = left ventricle; RV = right ventricle. (Reproduced from Fayad et al., 2000b, with permission).

has been used MRI to detect the presence of coronary plaques, though the major challenge is again to overcome cardiac and respiratory motion effects. The main technique for coronary artery wall imaging is the 2D ECG-triggered black-blood turbo-SE sequence. The groups of Fayad et al. (2000b) and Botnar et al. (2000) were first to demonstrate the feasibility of using MRI to visualize coronary artery wall and to detect coronary plaques, with breath-hold or navigator-echo being used to eliminate respiratory motion effects. The typical in-plane resolution was 0.5–1.0 mm, and the slice thickness was 2–5 mm. Some patient study examples are shown in Figure 3.40.

Most vessel wall imaging studies acquire cross-sectional images. A 3D technique utilizing local inversion and spiral data acquisition was used to obtain both cross-sectional and in-plane vessel wall images (Botnar et al., 2001), and achieved near-isotropic spatial resolution ($0.7 \times 0.7 \times 1.0\ mm^3$). The real-time respiratory gating and slice correction scheme with navigator echo was used.

References

Arai, A.E., Epstein, F.H., Bove, K.E., and Wolff, S.D. (1999). Visualization of aortic valve leaflets using black blood MRI. *J. Magn. Reson. Imaging*, **10**, 771–777.

Atkinson, D. and Edelman, R. (1991). Cineangiography of the heart in a single breath-hold with a segmented TurboFLASH sequence. *Radiology*, **178**, 357–360.

Axel, L. and Morton, D. (1987). MR flow imaging by velocity-compensated/uncompensated difference images. *J. Comput. Assist. Tomogr.*, **11**, 31–34.

Axel, L. and Dougherty, L. (1989). MR imaging of motion with spatial modulation of magnetization. *Radiology*, **171**, 841–849.

Botnar, R.M., Stuber, M., Kissinger, K., Kim, W., Spuentrup, E., and Manning, W.J. (2000). Noninvasive coronary vessel wall and plaque imaging with magnetic resonance imaging. *Circulation*, **102**, 2582–2587.

Botnar, R.M., Kim, W.Y., Bornert, P., Stuber, M., Spuentrup, E., and Manning, W.J. (2001). 3D coronary vessel wall imaging utilizing a local inversion technique with spiral image acquisition. *Magn. Reson. Med.*, **46**, 848–854.

Carr, J.C., Simonetti, O.P., Bundy, J., Li, D., Pereles, S., and Finn, J.P. (2001). Cine MR angiography of the heart with segmented true fast imaging with steady-state precession. *Radiology*, 2001, **219**, 828–834.

Deshpande, V., Shea, S., Laub, G., Simonetti, O.P., Finn, J.P., and Li, D. (2001). 3D Magnetization-prepared true-FISP: a new technique for imaging coronary arteries. *Magn. Reson. Med.*, **46**, 494–502.

Deshpande, V.S., Shea, S., Chung, Y.C., McCarthy, R.M., Finn, J.P., and Li, D. (2002). Improving spatial resolution of breath-hold 3D true-FISP imaging of coronary arteries using asymmetric sampling. *J. Magn. Reson. Imaging*, **15**, 473–478.

Etienne, A., Botnar, R.M., Van Muiswinkel, A.M., Boesiger, P., Manning, W.J., and Stuber, M. (2002). "Soap-Bubble" visualization and quantitative analysis of 3D coronary magnetic resonance angiograms. *Magn. Reson. Med.*, **48**, 658–666.

Fayad, Z.A., Nahar, T., Fallon, J.T., Goldman, M., Aguinaldo, J.G., Badimon, J.J., Shinnar, M., Chesebro, J.H., and Fuster, V. (2000a). In vivo magnetic resonance evaluation of atherosclerotic plaques in the human thoracic aorta: a comparison with transesophageal echocardiography. *Circulation*, **101**, 2503–2509.

Fayad, Z.A., Fuster, V., Fallon, J., Jayasundera, T., Worthley, S., Jayasun, T., Worthley, S., Helft, G., Aguinaldo,

J., Badimon, J., and Sharma, S. (2000b). Noninvasive in vivo human coronary artery lumen and wall imaging using black-blood magnetic resonance imaging. *Circulation*, **102**, 506–510.

Fayad, Z.A., Fuster, V., Nikolaou, K., and Becker, C. (2002). Computed tomography and magnetic resonance imaging for noninvasive coronary angiography and plaque imaging: current and potential future concepts. *Circulation*, **106**, 2026–2034.

Griswold, M.A., Jakob, P.M., Heidemann, R.M., Nittka, M., Jellus, V., Wang, J., Kiefer, B., and Haase, A. (2002). Generalized autocalibrating partially parallel acquisitions (GRAPPA). *Magn. Reson. Med.*, **47**, 1202–1210.

Hofman, M.B., Paschal, C.B., Li, D., Haacke, E.M., van Rossum, A.C., and Sprenger, M. (1995). MRI of coronary arteries: 2D breath-hold versus 3D respiratory gated acquisition. *J. Comput. Assist. Tomogr.*, **19**, 56–62.

Kellman, P., Epstein, F.H., and McVeigh, E.R. (2001). Adaptive sensitivity encoding incorporating temporal filtering (TSENSE). *Magn. Reson. Med.*, **45**, 846–852.

Kerr, A.B., Pauly, J.M., Hu, B.S., Li, K.C., Hardy, C.J., Meyer, C.H., Macovski, A., and Nishimura, D.G. (1997). Real-time interactive MRI on a conventional scanner. *Magn. Reson. Med.*, **38**, 355–367.

Kim, R.J., Judd, R.M., Chen, E.L., Fieno, D.S., Parrish, T.B., and Lima, J.A. (1999). Relationship of elevated 23Na magnetic resonance image intensity to infarct size after acute reperfused myocardial infarction. *Circulation*, **100**, 185–192.

Kim, R.J., Wu, E., Rafael, A., Chen, E., Parker, M., Simonetti, O.P., Klocke, F., Bonow, R., and Judd, R.M. (2000). The use of contrast-enhanced magnetic resonance imaging to identify reversible myocardial dysfunction. *N. Engl. J. Med.*, **343**, 1445–1453.

Laub, G., Simonetti, O.P., and Nitz, W. (1995). Single-shot imaging of the heart with HASTE. *Intl. Soc. Magn. Reson. Med.* 246 (abstract).

Li, D., Carr, J.C., Shea, S.M., Zheng, J., Deshpande, V.S., Wielopolski, P.A., and Finn, J.P. (2001). Coronary arteries: magnetization-prepared contrast-enhanced three-dimensional volume-targeted breath-hold MR angiography. *Radiology*, **219**, 270–277.

Manning, W.J. and Edelman, R.R. (1993). Magnetic resonance coronary angiography. *Magn. Reson. Q.*, **9**, 131–151.

Manning, W.J., Atkinson, D.J., Grossman, W., Paulin, S., and Edelman, R.R. (1991). First pass nuclear magnetic resonance imaging studies using gadolinium DTPA in patients with coronary artery disease. *Am. Coll. Cardiol.*, **18**, 959–965.

McVeigh, E.R. and Zerhouni, E.A. (1991). Noninvasive measurement of transmural gradients in myocardial strain with MR imaging, *Radiology*, **180**, 677–683.

Moore, C.C., McVeigh, E.R., and Zerhouni, E.A. (1999). Noninvasive measurement of three-dimensional myocardial deformation with tagged magnetic resonance imaging during graded local ischemia. *J. Cardiovasc. Magn. Reson.*, **1**, 207–222.

Moran, P.R. (1982). A flow velocity zeugmatographic interface for NMR imaging in humans, *Magn. Reson. Imaging*, **1**, 197–203.

Oshinski, J.N., Hofland, L., Dixon, W.T., and Pettigrew, R.I. (1998). Magnetic resonance coronary angiography using navigator echo gated real-time slice following. *Int. J. Card. Imaging*, **14**, 191–199.

Parrish, T.B., Fieno, D.S., Fitzgerald, S.W., and Judd, R.M. (1997). Theoretical basis for sodium and potassium MRI of the human heart at 1.5 T. *Magn. Reson. Med.*, **38**, 653–661.

Pettigrew, R.I., Oshinski, J.N., Chatzimavroudis, G., and Dixon, W.T. (1999). MRI techniques for cardiovascular imaging. *J. Magn. Reson. Imaging*, **10**, 590–601.

Ratner, A.V., Okada, R.D., Newell, J.B., and Pohost, G.M. (1985). The relationship between proton nuclear magnetic resonance relaxation parameters and myocardial perfusion with acute coronary arterial occlusion and reperfusion. *Circulation*, **71**, 823–828.

Riederer, S.J., Tasciyan, T., Lee, J.N., Wright, R.C., and Herfkens, R.J. (1988). MR fluoroscopy: technical feasibility. *Magn. Reson. Med.*, **8**, 1–15.

Rogers, W.J., Prichard, J.W., Hu, Y.L., Olson, P.R., Benckart, D.H., Kramer, C.M., Vido, D.A., and Reichek, N. (2000). Characterization of signal properties in atherosclerotic plaque components by intravascular MRI. *Arterioscler. Thromb. Vasc. Biol.*, **20**, 1824–1830.

Shankaranarayanan, A., Simonetti, O.P., Laub, G., Lewin, J.S., and Duerk, J.L. (2001). Segmented *k*-space and real-time cardiac cine MR imaging with radial trajectories. *Radiology*, **221**, 827–836.

Simonetti, O.P., Finn, J.P., White, R.D., Laub, G., and Henry, D.A. (1996). "Black blood" T2-weighted inversion-recovery MR imaging of the heart. *Radiology*, **199**, 49–57.

Simonetti, O.P., Kim, R.J., Fieno, D.S., Hillenbrand, H.B., Wu, E., Bundy, J.M., Finn, J.P., and Judd, R.M. (2001). An improved MR imaging technique for the visualization of myocardial infarction. *Radiology*, **218**, 215–223.

Stuber, M., Botnar, R.M., Fischer, S.E., Lamerichs, R., Smink, J., Harvey, P., and Manning, W.J. (2003). Preliminary report on in vivo coronary MRA at 3 Tesla in humans. *Magn. Reson. Med.*, **48**, 425–429.

Weber, O.M., Martin, A.J., and Higgins, C.B. (2003). Whole-heart steady-state free precession coronary artery magnetic resonance angiography. *Magn. Reson. Med.*, **50**, 1223–1228.

Wilke, N., Simm, C., Zhang, J., Ellermann, J., Ya, X., Merkle, H., Path, G., Ludemann, H., Bache, R., and Ugurbil, K. (1993). Contrast-enhanced first pass myocardial perfusion imaging: correlation between myocardial blood flow in dogs at rest and during hyperemia. *Magn. Reson. Med.*, **29**, 485–497.

Wilke, N., Jerosch-Herold, M., Wang, Y., Huang, Y., Christensen, B., Stillman, A., Ugurbil, K., McDonald, K., and Wilson, R. (1997). Myocardial perfusion reserve: assessment with multisection, quantitative, first-pass MR imaging. *Radiology*, **204**, 373–384.

Yabe, T., Mitsunami, K., Inubushi, T., and Kinoshita, M. (1995). Quantitative measurements of cardiac phosphorus metabolites in coronary artery disease by 31P magnetic resonance spectroscopy. *Circulation*, **92**, 15–23.

Yuan, C., Kerwin, W.S., Ferguson, M.S., Polissar, N., Zhang, S., Cai, J., and Hatsukami, T.S. (2002a). Contrast-enhanced high resolution MRI for atherosclerotic carotid artery tissue characterization. *J. Magn. Reson. Imaging*, **15**, 62–67.

Yuan, C., Zhang, S.X., Polissar, N.L., Echelard, D., Ortiz, G., Davis, J.W., Ellington, E., Ferguson, M.S., and Hatsukami, T.S. (2002b). Identification of fibrous cap rupture with magnetic resonance imaging is highly associated with recent transient ischemic attack or stroke. *Circulation*, **105**, 181–185.

3.3.2
Functional Magnetic Resonance Imaging (fMRI)

Oliver Speck, Axel Schreiber, Clemens Janz, and Jürgen Hennig

Since the early 1990s, when Ogawa and colleagues first introduced the concept of blood oxygenation level dependent (BOLD)-contrast (Ogawa et al., 1990), functional magnetic resonance imaging (fMRI) has found widespread interest and application in a vast number of neurocognitive and neurophysiological studies. While MR imaging of anatomical structures has long been established, this new MRI technique for localizing brain activity is currently under investigation for clinical applications. In the future, due to its easy integration into the clinical routine, fMRI will clearly become an important tool for neurologists, neuroradiologists, and neurosurgeons.

3.3.2.1
Physiological and Physical Basis

There is a close relationship between neuronal activity and cerebral perfusion in most situations: typically, at 4–6 s after neuronal activation the local cerebral blood flow rises by approximately 30%, and the blood volume by 7%, whereas the local cerebral metabolic rate of oxygen rises only by about 5% (Fox and Raichle, 1986). The increase in blood flow can be measured by employing flow-sensitive pulse sequences, or by the application of exogenous contrast agents (Belliveau et al., 1991).

Another more subtle mechanism of functional contrast is based on the different magnetic properties of deoxygenated (paramagnetic) and oxygenated (diamagnetic) hemoglobin. The paramagnetic deoxyhemoglobin distorts the local magnetic field on a microscopic scale, leading to a signal decrease in close range to vessels. The proton spins within a voxel experience a different magnetic field and thus have different Larmor frequencies. For this reason, they lose their phase coherence, and this results in a shortening of T_2 and T_2^* relaxation times (intravoxel dephasing). In 1990, Ogawa denoted this contrast mechanism by blood oxygenation level-dependent (BOLD) contrast, because the amount of deoxyhemoglobin depends on the oxygen saturation of the blood (Ogawa et al., 1990).

At rest, approximately 40% of the cortical blood volume is deoxygenated. The small rise in total oxygen extraction following neuronal activation is overcompensated by oxygen delivery due to the rise in blood flow (Fig. 3.41). Therefore, the level of deoxyhemoglobin is reduced to approximately 20–25%, and this reduction leads to a signal rise during neuronal activation.

At 150–300 ms after the onset of neuronal activation, localized oxygen delivery occurs, reducing the amount of oxyhemoglobin. Some 200–400 ms later, an increase in blood volume is observed, followed by an increase in the amount of oxyhemoglobin within the next 1000 ms (Frostig et al., 1990). Most fMRI experiments, however, are only designed for mapping brain activation and therefore only make

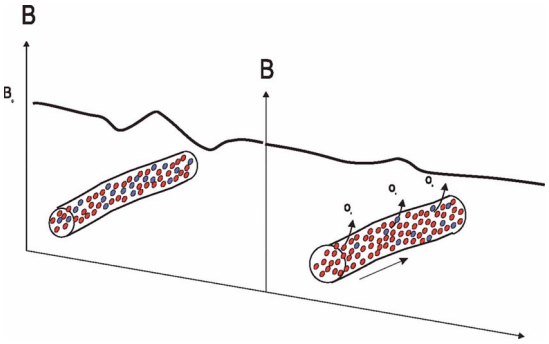

Fig. 3.41. Scheme of the BOLD contrast mechanism. The paramagnetic deoxyhemoglobin distorts the local magnetic field in the vicinity of vessels and capillaries. During rest (left), more cortical blood (red) is deoxygenated than during cortical activation (right), which leads to less perturbation of the magnetic field and hence to a signal rise.

use of the dominant signal rise. In this case, a blocked task paradigm is to be preferred to make use of the dominant positive BOLD-contrast.

Single trial experiments showed a tri-phasic signal time course after the onset of a brief visual stimulus. Within the first 2 s after onset of the stimulus, a small signal reduction is reported (Ernst and Hennig, 1994). Although this signal change coincides with the increase of the deoxygenation level, a direct relationship is not proven. During the second phase, which starts after 2–3 s and lasts for 7–10 s, a positive BOLD-effect can be observed. Finally, a BOLD undershoot occurs, which returns to baseline only after about 40 s. This undershoot can be attributed to either a metabolic or a nonmetabolic (increase of the blood volume) BOLD effect, and is currently the subject of much discussion (Janz et al., 1997; Buxton et al., 1998) (Fig. 3.42).

3.3.2.2 Methods for fMRI

The vast majority of fMRI examinations employs the BOLD-contrast, using techniques sensitive to local distortions in the magnetic field (susceptibility sensitive

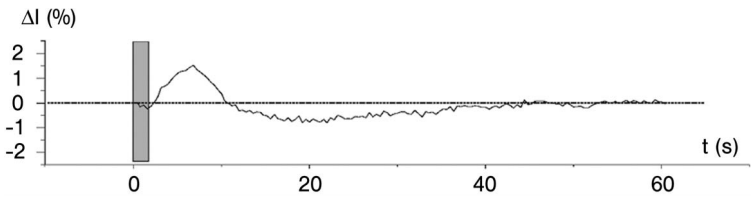

Fig. 3.42. Typical signal time-course within the visual cortex after a brief visual stimulus (gray bar).

techniques). These are T_2-weighted spin echo pulse sequences or $T_2{}^*$-weighted gradient echo pulse sequences, with the latter being preferred in most circumstances due to their higher sensitivity.

Echo planar imaging (EPI) (Mansfield and Maudsley, 1977), a very rapid gradient echo pulse sequence, requires very strong and fast gradient systems, which are now available on a broad basis in routine scanners. EPI allows the acquisition of one image in less than 100 ms. Hence, a whole-brain study can be performed in a few seconds. The high sensitivity of EPI to local magnetic field inhomogeneities also emerges as a disadvantage, as the magnetic field distortions due to susceptibility changes at borders between brain tissue and air (e.g., in the sphenoidal sinus) lead to severe image deformations or even signal loss, especially in the temporal brain and close to the skull base.

Other gradient echo techniques with long echo times (e.g., FLASH; Haase et al., 1986) do not impose severe demands on the gradient hardware. Gradient echo techniques also have many more benign imaging properties compared to EPI, and allow the achievement of spatial resolution well below 1 mm. Their main disadvantage is the long acquisition time of many seconds per slice. The possibility of performing whole-brain studies is therefore a distinct advantage of EPI for the clinical applications under discussion, and as a consequence EPI currently tends to be the ''workhorse'' of fMRI.

Techniques for fMRI using nonBOLD contrast mechanisms are mainly used in scientific studies. A variety of approaches has been proposed to measure activation-related changes in tissue perfusion, but all of these techniques – including FAIR (Kim, 1995) and EPISTAR (Edelman et al., 1994) – require direct observation of the MR signal from blood, and changes therein (Detre et al., 1992). Due to the small partial volume of blood with respect to the total tissue, such perfusion-based techniques show lower effects (1–2%) compared to BOLD techniques (typically 2–5%). Nevertheless, perfusion-based techniques offer at least potentially the advantage of being less complex than the BOLD approach. If perfusion measurement sequences with sufficient sensitivity could be developed, this approach would potentially lead to more stable and quantifiable results. One benefit of perfusion measurements is that they can be compared more easily with the existing positron emission tomography data, as PET also uses perfusion as a parameter for localization studies.

3.3.2.3 The fMRI Experiment

fMRI employs rapid imaging techniques that yield a low signal-to-noise ratio (SNR). The functional effects are of the order of the signal stability in the human brain (1.5 to 5% at 1.5 T), and therefore the functional effects cannot be recognized on a single volume. For this reason, an fMRI experiment acquires many volumes during at least two different experimental conditions. Usually, the effects are detected by an analysis of the corresponding voxel on all volumes. Therefore, it is necessary that the subject's brain remains in the same position during the entire

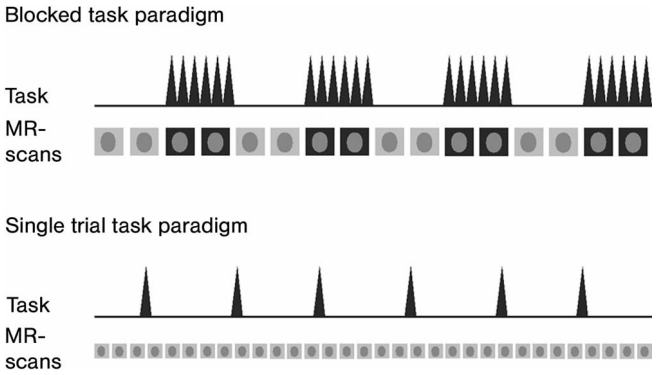

Fig. 3.43. Comparison of blocked and single trial task paradigms.

experiment. Details of data analysis and head motion correction are discussed in Section 3.3.2.4.

Task Paradigm

The simplest type of task paradigm is a blocked design that presents many trials of one category in immediate succession, such that blocks with different experimental conditions are alternated (e.g., task1, rest, task2, rest, . . .). However, with faster pulse sequences and modern scanners, single trial task paradigms become feasible. During a train of measurements single trials are presented with varying interstimulus intervals (Fig. 3.43). The time course of the MR signal during single trials is analyzed with respect to the stimulus timing and the cortical hemodynamic response to a single trial can then be estimated. This allows full advantage to be taken of the high temporal resolution of fMRI. These paradigms have been used for elucidation of the tri-phasic time course of the BOLD response to short visual stimuli (see Section 3.3.2.1). The major applications of single trial paradigms (also referred to as event-related fMRI) are cognitive tasks (Buckner et al., 1996).

The art of developing a paradigm can partly be derived from PET-paradigms but, as in PET studies, it is important to define an adequate baseline condition. Although in some cases rest is a sufficient condition in primary sensory or motor paradigms, it is important that care be taken. Cognitive tasks pose a more difficult problem, however. In general, fMRI allows for a wide range of task paradigms, and only a few constraints to the choice of paradigms are feasible with fMRI. It is important to note that only differential measures are taken, and therefore only the difference in cortical activation between conditions can be detected.

3.3.2.4 Data Analysis

For post-processing of fMRI, not only freeware but also commercial software packages are available, and modern MR systems generally possess integrated fMRI

processing systems within the operating console. Although fMRI experiments produce vast quantities of data (hundreds of megabytes per session), modern computer hardware is more than capable of processing the data in acceptable time.

Before any analysis of the voxel time course is conducted, the sequentially acquired functional volumes should be corrected for head motion, after which optional filtering in temporal and spatial domains can be carried out. The central point here is the statistical evaluation of signal changes due to the task or paradigm. If the statistical significance of the signal change exceeds an appropriate threshold, the corresponding voxel will be treated as activated. In order to interpret the data it is necessary to map the resulting activated areas to an anatomical image. Usually, T_1-weighted images are acquired for this purpose. Functional maps are constructed as pseudo-color overlays of the significant activation onto the corresponding T_1-weighted anatomical data.

In the case of a localization study, the results of investigations in a group of subjects must be matched. In order to map the activated areas onto a particular anatomical region of the cortex, these areas are registered to a standard atlas of the human brain (e.g., the Talairach atlas; Talairach and Tournoux, 1988), or onto the 3D data set of the individual brain. In this way the results of different studies of the same or distinct modalities can be compared (Apicella et al., 1989; Pellizari et al., 1989). A more sophisticated display method uses flat maps (Dale and Sereno, 1993; Carman et al., 1995), whereby the creased surface of the cortex is unfolded onto a flat 2D plane onto which the functional results are then mapped. This method is especially useful for visualizing a retinotopy when investigating the visual cortex.

Motion Correction

A functional investigation consists of a series of volumes which are acquired over periods lasting up to several minutes, and consequently small displacements of the subject's head during the measurements are unavoidable. In many cases the signal difference between two neighboring voxels is larger than the expected signal change due to the BOLD effect. If the intensities of neighboring voxels vary, for example by 10%, and the shift is about 0.5 mm (which would normally correspond to 25% of a single voxel), the intensity change would be 2.5%. This small displacement is comparable to the size of the BOLD effect, and could therefore mask it completely. In addition, stimulus-correlated movements of the subject may lead to false activation (see Fig. 3.44). Therefore, in order to conduct a statistical analysis it is essential that the head movements are not only detected but also corrected (Hajnal et al., 1994).

A variety of motion-correction algorithms have been developed (Woods et al., 1992; Friston et al., 1995), the majority of which are voxel-based matching algorithms, performed either iteratively or directly. Methods that register images by aligning specific landmarks are impractical for fMRI data sets, as trained personnel would have manually to identify the landmarks in each of hundreds of images.

In order to rate the quality of the matching of two volumes, a similarity measurement must be defined. Normally, the similarity of two volumes is maximized by an

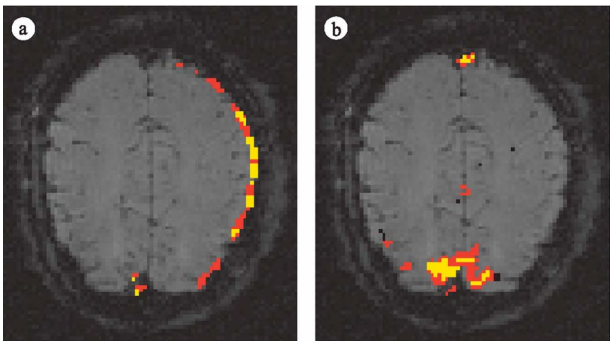

Fig. 3.44. Stimulus-correlated subject motion. (a) False-positive activation detected without motion correction. (b) True activation detected after motion correction (red and yellow color). The slice is acquired at a functional perfusion study with contrast agent during a visual stimulus and laid through the visual cortex.

optimization algorithm that varies the orientation of one of the two volumes. Standard registration methods are based either on the minimization of the variance of the voxel-wise ratio, least squares minimization, the maximization of the cross-correlation, or on the use of the minimum entropy method (MEM).

Statistical Analysis

The first and simplest analysis that was performed on functional data sets was a difference image. Here, all images during stimulation and all images at the rest phase are summed up, and subtraction of the two images yields the difference image. If the intensity of a voxel exceeds a given threshold, it will be treated as an activated voxel. However, because there is no evidence on the statistical significance of the results, statistical methods comparing the time course of each voxel with appropriate reference functions must be applied. These model-driven approaches rely on the correct choice of reference or model functions to describe the signal changes. Commonly, the paradigm timing is convolved with an empirical hemodynamic response function, which resembles the single event time course (see Fig. 3.42). The measured time course is then described as a linear combination of the model functions and a residual error term. Finally, statistical tests are applied (e.g., Student's *t*-test, z-score or ANOVA) to estimate the probability of the signal change being caused by the paradigm. In short, the amplitude of a paradigm-related signal change is compared to the unexplained noise in the data.

The determination of a statistical threshold for acceptance of an activation-related signal change is not trivial. In a common experiment, the matrix size of one slice is 128×128 voxels, so that one slice contains 16 384 voxels. If the threshold is too low, the possibility that a voxel is accidentally regarded as activated due to noise is very high, and this may lead to false activation outside the brain. On the other hand, if the threshold was chosen too high, a real activation could be re-

jected. Proper methods to correct the statistical threshold (e.g., simple Bonferoni correction) can adjust for the number of multiple tests performed within a data set.

In contrast to the model-driven analysis described above, data-driven analyses have been developed to obtain the BOLD-effect correlated signal changes in the data set. These approaches use no prior assumption on the BOLD time course; rather, the time courses of each voxel are categorized into different classes of similar courses. The aim of these data-driven methods is to obtain a group of voxel that represents the time course of the stimulus protocol. Methods proposed for this are cluster algorithms, for example the K-means algorithm (Ding et al., 1994), the Fuzzy C-means (Scarth et al., 1995), or an analysis based on a neuronal network using self-organizing maps (Fischer et al., 1997). Other data-driven methods utilize independent component analysis, principle component analysis, or factor analysis (McKeown et al., 2003).

Presentation

Once the activation is evaluated, the results must be presented in an appropriate manner, in order to allow an interpretation. Voxels with activation probabilities greater than an appropriate threshold are color-coded and used for the overlay. EPI images are not suitable for this purpose because they are very sensitive to susceptibility changes and imperfect shims, which leads to distortions and artifacts (Sumanaweera et al., 1994). Therefore, T_1-weighted images, acquired in the same session but with a better spatial resolution, higher contrast and more anatomical details, are preferred as background for the overlay. In order to combine the two different images, an elastic registration is necessary, as corresponding voxels may differ by a few millimeters due to distortion of the EPI images. Additionally, an inter-subject registration is indispensable for group analyses (Friston et al., 1991; Otte et al., 1997).

In the literature, cortical areas are often referred to in units of the Talairach bicommissural coordinate system, and consequently in order to compare the results it is necessary to match the images to the Talairach atlas (Collins et al., 1994). Here, an often-used attractive representation is a rendered 3D volume data set of the head, where the interesting regions are segmented and the activated voxels are drawn in the corresponding structures (Fig. 3.45b). Flat maps also provide a good overview of a cortical activation (Fig. 3.45a).

3.3.2.5 Current Results in fMRI

fMRI, as a noninvasive tool used in neuroimaging, yields high spatial resolution ($<$1 mm) and considerable temporal resolution ($<$0.5 s). During the first few years of its development, however, fMRI was validated by reproducing results from PET studies and by comparison between intraoperative electrical stimulation mapping and presurgical fMRI mapping in patients with intracerebral tumors (Puce, 1995; Yousry et al., 1995). To date, the field of fMRI has grown immensely, and currently over 5000 publications utilizing the procedure have been produced. In order to pro-

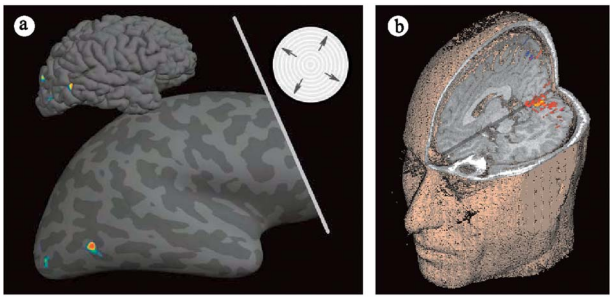

Fig. 3.45. (a) Flat map representation of the activation in the human motion-sensitive area V5/V5a during a visual motion perception (moving concentric rings, right above). (b) A rendered head volume during a visual stimulus.

vide an impression of the possibilities of fMRI, a small (albeit personal and by no means representative) selection of results is presented in the following section. When possible, reference to one of the countless reviews in the field is provided.

fMRI Resolution in the Visual Cortex

Studies on the tonotopy of the auditory cortex or on columnar organization of the visual cortex (e.g., ocular dominance; Menon et al., 1997) require very high-resolution functional imaging methods. The question of resolution in fMRI, however, is not only a technical issue; rather, it depends also on the physiology of the cortical blood supply. A rise in image resolution will not provide better functional resolution if the voxel size is already small in comparison with the cortical volume that has a jointly regulated blood supply.

In 1997, De Weerd and colleagues investigated the functional resolution of fMRI in the primary visual cortex (V1) of man with three elegant paradigms (De Weerd et al., 1997). The resolution in the polar direction was shown to be 22.5°.

In a second experiment, the extent of cortical activation at an eccentricity of 7.5° was observed experimentally to exceed the prediction from theoretical calculations based on the cortical magnification factor in humans (Sereno et al., 1995).

In a third experiment, a large patch of texture was presented. An eccentric square at 7.5° only showed a functional response for an extent larger than $6 \times 6°$. De Weerd et al. concluded that these results indicated a resolution for traditional fMRI experiments at 1.5 T of approximately 5 mm in the visual cortex (De Weerd et al., 1997). Of course, experiments with different design and stimuli may lead to different estimates of spatial resolution.

Nevertheless, a value of 5 mm was in concordance with results from another study conducted by Engel et al. (1997), and from optical imaging of the visual cortex by Malonek and Grinvald (1996). These authors showed that the area of hyperperfusion as a result of visual stimulation exceeded the area of increased oxygen extraction (the area of cortical activation) by 3–5 mm.

Functional Brain Mapping

Visual system As the stimulus-evoked change in the fMRI signal in the primary visual cortex was seen to be very large and robust, a number of methodological studies were instigated to investigate the visual cortex. For example, the first two fMRI studies using BOLD-contrast were conducted on the visual cortex (Kwong et al., 1992; Ogawa et al., 1992). Human vision is a complex neurocognitive brain function; hence, many aspects of the visual scene are analyzed separately and then combined to provide a uniform impression of the world. This multitude of aspects is represented on multiple cortical areas, and more than ten human cortical visual areas have now been differentiated (Engel et al., 1994; Sereno et al., 1995; O'Craven et al., 1997; for reviews, see Tootell et al., 1996; Wandell and Wade, 2003; Grill-Spector and Malach, 2004; and Kollias, 2004).

The display of the cortical representation of the visual field is termed *retinotopic mapping*. By using a visual stimulus that periodically varies either in polar angle or in its eccentricity, retinotopic maps can be generated with fMRI. In these maps, the cortical area that corresponds to a certain part of the visual field is encoded in color (Fig. 3.46).

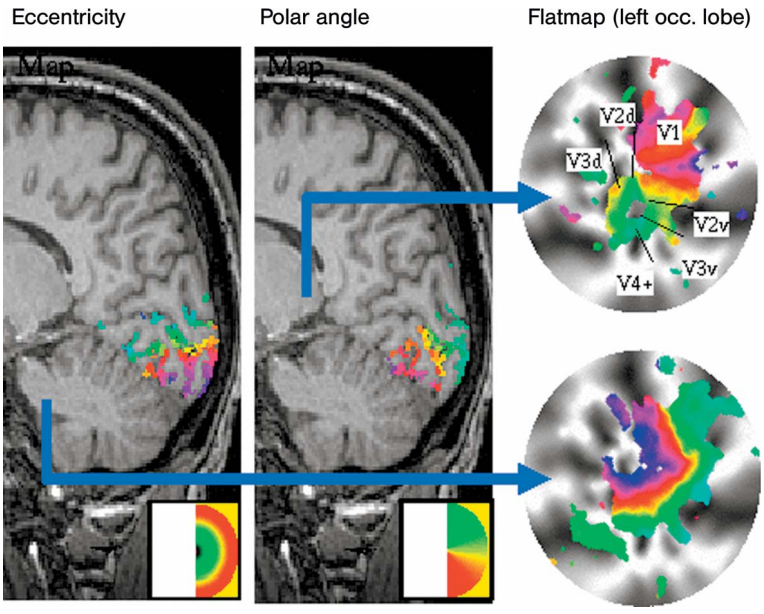

Fig. 3.46. Retinotopic maps of the visual cortex in a human subject. The visual field is encoded in the color shown and displayed as overlay on anatomical images or as cortical flat maps of the occipital lobe. (Illustration courtesy of M. Hoffmann, University of Magdeburg).

Attention The cerebellum was considered to be dedicated to motor control (there is much fMRI-based evidence for this; e.g. Ellermann et al., 1994; Nitschke et al., 1996). In 1997, Allen and colleagues reported the involvement of the cerebellum in cognitive neurobehavioral systems (Allen et al., 1997). These authors showed that attention and motor performance independently activated distinct cerebella regions. For the attention task, the subjects were presented with circles, squares, or triangles in red, green, or blue, and had to attend selectively to targets (squares or red shapes) within the visual dimension (form or color). In the motor task, the subjects were instructed repeatedly to execute a self-paced movement of the right hand in the absence of a visual stimulus. Two volumes of interest (VOI) within the cerebellum were defined and differentially analyzed. The *attention* VOI comprised the left posterior quadrangular lobule and the left superior semilunar lobule. The *motor* ROI included the right anterior vermis, the right central lobule and the right anterior quadrangular lobule. Activation in the attention VOI was tenfold greater during the attention task than during the motor task, whereas in contrast activation in the motor VOI was 2.5-fold greater during the motor task than during the attention task (Fig. 3.47).

Taken together, these results reflect a double dissociation between these two areas of the cerebellum with respect to their involvement in visual selective attention and movement. The authors suggested that the human cerebellum might

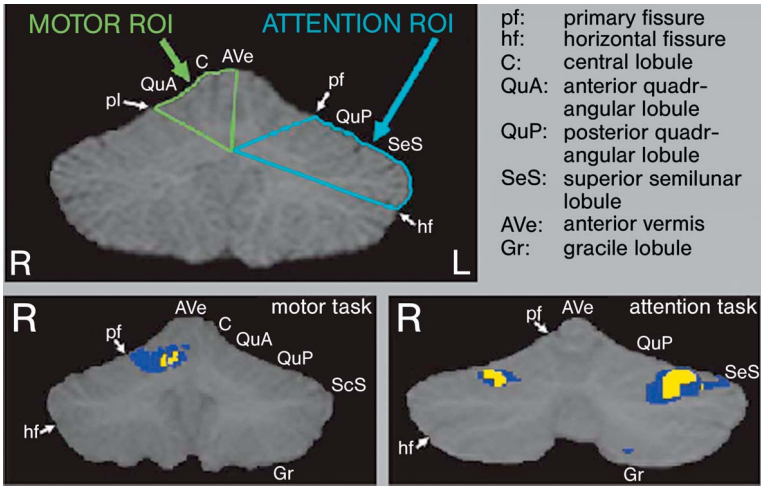

Fig. 3.47. Upper panel: Definition of volumes of interest (VOIs), shown on an anatomical MR image. Lower panel: Functional maps demonstrating the most common sites of activation across subjects overlaid on an average coronal anatomical image. Yellow: overlap of three or more subjects (out of six), blue: any two subjects. The motor activation hotspot lies 12 mm (= two slices) anterior to the attention hotspot. (Reprinted from Allen et al., 1997, © Copyright 1990, with permission from American Association for the Advancement of Science).

modulate attention and sensory responsiveness, as well as movements that reposition sensory receptors or track the trajectories of sensory information. The cerebellum seems not to be a device for motor control; rather, its prime function may be to learn to predict and prepare for imminent information acquisition, analysis or action.

Language This is a complex mental ability which includes sensomotor, mnestic and higher cognitive processes. Brain mapping studies can provide some hints as to which of the different theoretical concepts of language organization is realized in the cerebral cortex. The first suggestions were made by McCarthy et al. (1993) and Rueckert et al. (1994).

In 1997, Spreer presented a study comparing different stimulation paradigms for the localization of language-relevant cortical areas (Spreer et al., 1997); an example of a patient examination is shown in Figure 3.48. A language task that consisted of semantic decisions on simultaneously presented words was performed, while during the control condition decisions on the color of objects had to be made. The patient showed lateralized task-related cortical activation in the "classical" Broca (Brodman areas (BA) 44, 45) and Wernicke areas (BA 21, 22) on the left hemisphere.

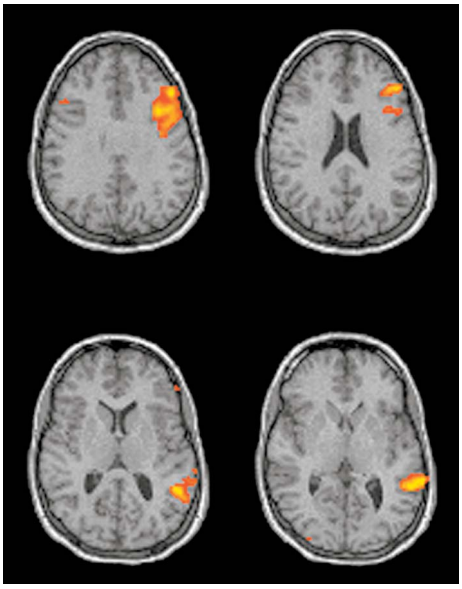

Fig. 3.48. Cortical areas activated during semantic decision-making (yellow to red color). Broca and Wernicke areas of the left hemisphere are the main areas for language processing and generation. (Illustration courtesy of J. Spreer, University of Freiburg).

Knowledge of language lateralization is important prior to epilepsy surgery. The possibility of replacing the invasive diagnostic procedure of the Wada test (intracarotid amobarbital test) with an fMRI measurement has been investigated (Desmond et al., 1995; Binder et al., 1996; Balsamo and Gaillard, 2002; Detre, 2004; Powell et al., 2004).

Presurgical mapping Several authors have proposed the introduction of fMRI into the preoperative evaluation of patients with intracranial tumors and vascular malformations, albeit for different reasons (e.g., Atlas et al., 1996; Steinmeier et al., 2002; Bogomolny et al., 2004; Keles and Bergerm, 2004; Vlieger et al., 2004). fMRI conducted in patients with lesions near eloquent cortical areas may help in the risk assessment, as well as assist in planning the surgical approach. In patients with displacement due to mass lesions it is sometimes difficult – or even impossible – to identify anatomical landmarks or eloquent cortical areas, which are thought to locate in the vicinity of the pathological focus. In the worst case the eloquent area lies within the pathologically altered tissue. Here, fMRI can fill the information void, though the intention to use such information in planning and executing surgical interventions pushes the method to its limits. Consequently it is essential that the fMRI-based data are very reliable and valid. Several methodological studies on fMRI functional localization (Jaeger et al., 1997; Yetkin et al., 1996) have shown a test-retest-reliability within the range of the physiological resolution of BOLD-contrast fMRI. The following example (Schreiber et al., 1997) describes a patient with a glioma (anaplastic ependymoma, WHO grade III) in the temporo-parieto-occipital region of the left hemisphere. With anatomical MRI, the central sulcus could not be identified on the left hemisphere, but two simple motor-paradigms (bilateral fist-clenching and pursing of the lips) (Fig. 3.49) showed that the distance between tumor and the sensory-motor cortex was sufficient to allow safe excision of the tumor. Postoperatively, the patient did not show any motor or sensory deficit.

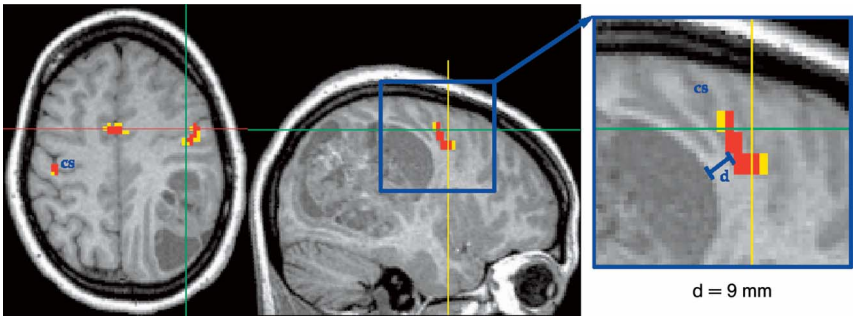

Fig. 3.49. 3D-dataset of the patient's brain cut in transverse and sagittal planes. The functional activation from the bilateral first clenching paradigm is superimposed in color onto the anatomic brain cuts.

3.3.2.6
Perspectives

Today, fMRI has evolved into a valuable tool in neurophysiologic research. Its temporal and spatial resolution allows mapping of the brain's localized but distributed functional networks, and it is completely noninvasive. Moreover, fMRI can replace the more expensive and invasive functional PET studies used to monitor regional cerebral blood flow.

In its ability to image processes on a time scale of a few seconds, fMRI has closed the gap in temporal resolution between PET and electrophysiological methods such as electroencephalography and magnetoencephalography. Furthermore, the partial overlap with PET in temporal and spatial resolution allows the use of the vast quantities of PET-based data not only as a cross-validation but also as a starting point for more sophisticated experiments, elucidating human neurophysiology on sub-second and millimeter scales. This intermodal fusion of fMRI and electrophysiological methods is possible due to their overlap, especially in single trial experiments.

Although as yet the theory of BOLD-contrast mechanisms is incomplete, our current knowledge is sufficient to develop safe and reliable clinical applications. Paradigms for the presurgical mapping of primary sensory and motor areas have been tested reliably. Likewise, those for mapping complex mental processes such as language have also been identified, the aim being to replace invasive diagnostic procedures in epilepsy, such as intracarotid amobarbital testing. Clearly, fMRI is ready to be established as an effective diagnostic tool in clinical routine.

References

Allen, G., Buxton, R.B., Wong, E.C., and Courchesne, E. (1997). Attentional activation of the cerebellum independent of motor involvement. *Science*, **275**, 1940–1943.

Apicella, A., Kippenhan, J.S., and Nagel, J.H. (1989). In Medical Imaging III: Imaging Processing. Fast multi-modality image matching. *SPIE*, **1092**, 252.

Atlas, S.W., Howard, R.S., Maldjian, J., Alsop, D., Detre, J.A., Listerud, J., D'Esposito, M., Judy, K.D., Zager, E., and Stecker, M. (1996). Functional magnetic resonance imaging of regional brain activity in patients with intracerebral gliomas: findings and implications for clinical management. *Neurosurgery*, **38**, 329–338.

Balsamo, L.M. and Gaillard, W.D. (2002). The utility of functional magnetic resonance imaging in epilepsy and language. *Curr. Neurol. Neurosci. Rep.*, **2** (2), 142–149.

Belliveau, J.W., Kennedy, D.N., McKinstry, R.C., Buchbinder, B.R., Weisskoff, R.M., Cohen, M.S., Vevea, J.M., Brady, T.J., and Rosen, B.R. (1991). Functional mapping of the human visual cortex by magnetic resonance imaging. *Science*, **254**, 716–719.

Binder, J.R., Swanson, S.J., Hammeke, T.A., Morris, G.L., Mueller, M., Fischer, W.M., Benbadis, S., Frost, J.A., Rao, S.M., and Haughton, V.M. (1996). Determination of language dominance using functional MRI: a comparison with the Wada test. *Neurology*, **46**, 978–984.

Bogomolny, D.L., Petrovich, N.M., Hou, B.L., Peck, K.K., Kim, M.J., and Holodny, A.I. (2004). Functional MRI in the brain tumor patient. *Top. Magn. Reson. Imaging*, **15** (5), 325–335.

Buckner, R.L., Bandettini, P.A., O'Craven, K.M., Savoy, R.L., Petersen, S.E., Raichle,

M.E., and Rosen, B.R. (1996). Detection of cortical activation during averaged single trials of a cognitive task using functional magnetic resonance imaging. *Proc. Nat. Acad. Sci. USA*, **93**, 14878–14883.

Buxton, R.B., Wong, E.C., and Frank, L.R. (1998). Dynamics of blood flow and oxygenation changes during brain activation: the balloon model. *Magn. Reson. Med.*, **39** (6), 855–864.

Carman, G.J., Drury, H.A., and van Essen, D.C. (1995). Computational methods for reconstructing and unfolding the cerebral cortex. *Cereb. Cortex*, **5**, 506.

Collins, D.L., Neelin, P., Peters, T.M., and Evans, A.C. (1994). Automatic 3D intersubject registration of MR volumetric data in standardized Talairach space. *J. Comput. Assist. Tomogr.*, **18**, 192.

Dale, A.M. and Sereno, M.I. (1993). Improved localization of cortical activity by combining EEG and MEG with MRI cortical surface reconstruction: A linear approach. *J. Cogn. Neurosci.*, **5**, 162–176.

De Weerd, P., Karni, A., Kastner, S., Ungerleider, L.G., and Jezzard, P. (1997). An investigation of fMRI resolution in the visual cortex. *NeuroImage*, **5** (4, part 2), 45.

Desmond, J.E., Sum, J.M., Wagner, A.D., Demb, J.B., Shear, P.K., Glover, G.H., Gabrieli, J.D., and Morell, M.J. (1995). Functional MRI measurement of language lateralization in Wada-tested patients. *Brain*, **118**, 1411–1419.

Detre, J.A. (2004). fMRI: applications in epilepsy. *Epilepsia*, **45** Suppl. 4, 26–31.

Detre, J.A., Leigh, J.S., Williams, D.S., and Koretsky, A.P. (1992). Perfusion imaging. *Magn. Reson. Med.*, **23**, 37–45.

Ding, X., Tkach, P., and Masaryk, T. (1994). Analysis of time-course functional MRI data with clustering method without use of reference signal. *Proceedings of the Society for Magnetic Resonance, Second Annual Meeting (San Francisco)*, 630 (Abstract).

Edelman, R.R., Siewert, B., Darby, D.G., Thangaraj, V., Nobre, A.C., Mesulam, M.M., and Warach, S. (1994). Qualitative mapping of cerebral blood flow and functional localization with echo-planar MR imaging and signal targeting with alternating radio frequency. *Radiology*, **192**, 513–520.

Ellermann, J.M., Flament, D., Kim, S.G., Fu, Q.G., Merkle, H., Ebner, T.J., and Ugurbil, K. (1994). Spatial patterns of functional activation of the cerebellum investigated using high field (4 T) MRI. *NMR Biomed.*, **7**, 63–68.

Engel, D.E., Rumelhard, S.A., Wandell, B.A., Lee, A.T., Glover, G.H., Chichilnisky, E.J., and Shadlen, M.N. (1994). fMRI of human visual cortex. *Nature*, **369**, 525.

Engel, S.A., Glover, G.H., and Wandell, B.A. (1997). Retinotopic organization in human visual cortex and the spatial precision of functional MRI. *Cereb. Cortex*, **7**, 181–192.

Ernst, T. and Hennig, J. (1994). Observation of a fast response in functional MR. *Magn. Reson. Med.*, **32**, 146–149.

Fischer, H., Büchert, M., and Hennig, E.J. (1997). Assessing the dynamics of fMRI data using selforganizing map clustering. In *Proceedings of the International Society for Magnetic Resonance in Medicine*, **3**, 1660.

Fox, P.T. and Raichle, M.E. (1986). Focal physiological uncoupling of cerebral blood flow and oxidative metabolism during somatosensory stimulation in human subjects. *Proc. Natl. Acad. Sci. USA*, **83**, 1140–1144.

Friston, K.J., Frith, C.D., Liddle, P.F., and Frackowiak, R.S.J. (1991). Plastic transformation of PET images. *J. Comput. Assist. Tomogr.*, **15**, 634.

Friston, K.J., Ashburner, J., Frith, C.D., Poline, J.-B., Heather, J.D., and Frackowiak, R.S.J. (1995). Spatial registration and normalization of images. *Hum. Brain Mapp.*, **2**, 165.

Frostig, R.D., Lieke, E.E., Ts'o, D.Y., and Grinvald, A. (1990). Cortical functional architecture and local coupling between neuronal activity and the microcirculation revealed by in vivo high-resolution optical imaging of intrinsic signals. *Proc. Natl. Acad. Sci. USA*, **87**, 6082–6086.

Grill-Spector, K. and Malach, R. (2004). The human visual cortex. *Annu. Rev. Neurosci.*, **27**, 649–677.

Haase, A., Frahm, J., Matthaei, D., Hänicke, W., and Merbboldt, K.D. (1986). FLASH imaging. Rapid NMR imaging using low flip angle pulses. *J. Magn. Reson.*, **67**, 258–266.

Hajnal, J.V., Myers, R., Oatridge, A., Schwieso, J.E., Young, I.R., and Bydder, G.M. (1994). Artifacts due to stimulus correlated motion in functional imaging of the brain. *Magn. Reson. Med.*, **31**, 283.

Jaeger, D., Schreiber, A., Scheremet, R., Mergner, T., and Hennig, J. (1997). Is fMRI reproducible? An EPI study using a motor paradigm. Magnetic Resonance Materials in *Physics, Biology, and Medicine, 14th Annual Meeting (Brussels)*, **5** (2. suppl.), 325 (abstract).

Janz, C., Speck, O., and Hennig, J. (1997). Time resolved measurements of brain activation after a short visual stimulus: New results on the physiological mechanisms of the cortical response. *NMR Biomed.*, **10**, 222–229.

Keles, G.E. and Bergerm, M.S. (2004). Advances in neurosurgical technique in the current management of brain tumors. *Semin. Oncol.*, **31** (5), 659–665.

Kim, S.G. (1995). Quantification of relative cerebral blood flow change by flow-sensitive alternating inversion recovery (FAIR) technique: application to functional mapping. *Magn. Reson. Med.*, **34**, 293–301.

Kollias, S.S. (2004). Investigations of the human visual system using functional magnetic resonance imaging (FMRI). *Eur. J. Radiol.*, **49** (1), 64–75.

Kwong, K.K., Belliveau, J.W., Chesler, D.A., Goldberg, I.E., Weisskoff, R.M., Poncelet, B.P., Kennedy, D.N., Hoppel, B.E., Cohen, M.S., and Turner, R. (1992). Dynamic magnetic resonance imaging of human brain activity during primary sensory stimulation. *Proc. Natl. Acad. Sci. USA*, **89**, 5675–5679.

Malonek, D. and Grinvald, A. (1996). Interactions between electrical activity and cortical microcirculation revealed by imaging spectroscopy: implications for functional brain mapping. *Science*, **272**, 551–554.

Mansfield, P. and Maudsley, A.A. (1977). Planar spin imaging by NMR. *J. Magn. Reson.*, **27**, 101–119.

McCarthy, G., Blamire, A.M., Rothman, D.L., Gruetter, R., and Shulman, R.G. (1993). Echo-planar magnetic resonance imaging studies of frontal cortex activation during word generation in humans. *Proc. Natl. Acad. Sci. USA*, **90**, 4952–4956.

McKeown, M.J., Hansen, L.K., and Sejnowsk, T.J. (2003). Independent component analysis of functional MRI: what is signal and what is noise? *Curr. Opin. Neurobiol.*, **13** (5), 620–629.

Menon, R.S., Ogawa, S., Strupp, J.P., and Ugurbil, K. (1997). Ocular dominance in human V1 demonstrated by functional magnetic resonance imaging. *J. Neurophysiol.*, **77**, 2780–2787.

Nitschke, M.F., Kleinschmidt, A., Wessel, K., and Frahm, J. (1996). Somatotopic motor representation in the human anterior cerebellum. A high-resolution functional MRI study. *Brain*, **119**, 1023–1029.

O'Craven, K.M., Rosen, B.R., Kwong, K.K., Treisman, A., and Savoy, R.L. (1997). Voluntary attention modulates fMRI activity in human MT-MST. *Neuron*, **18**, 591–598.

Ogawa, S., Lee, T.M., Nayak, A.S., and Glynn, P. (1990). Oxygenation-sensitive contrast in magnetic resonance image of rodent brain at high magnetic fields. *Magn. Reson. Med.*, **14**, 68–78.

Ogawa, S., Tank, D.W., Menon, R.S., Ellermann, J.M., Kim, S.G., Merkle, H., and Ugurbil, K. (1992). Intrinsic signal changes accompanying sensory stimulation: functional brain mapping with magnetic resonance imaging. *Proc. Natl. Acad. Sci. USA*, **89**, 5951–5955.

Otte, M., Schreiber, A., Büchert, M., Schmider, K., Hennig, J., Merger, T., and Lücking, C.H. (1997). *Proceedings of the International Society for Magnetic Resonance in Medicine, fifth Scientific Meeting (Vancouver)*, **3**, 2018 (abstract).

Pellizari, C.A., Chen, C.T.Y., Spelbring, D.R., Weichselbaum, R.R., and Chen, C.T. (1989). Accurate three-dimensional registration of CT, PET and/or MRI images of the brain. *J. Comput. Assist. Tomogr.*, **13**, 20.

Powell, H.W., Koepp, M.J., Richardson, M.P., Symms, M.R., Thompson, P.J., and Duncan, J.S. (2004). The application of functional MRI of memory in temporal lobe epilepsy: a clinical review. *Epilepsia*, **45** (7), 855–863.

Puce, A. (1995). Comparative assessment of sensorimotor function using functional magnetic resonance imaging and electrophysiological methods. *J. Clin. Neurophysiol.*, **12**, 450–459.

Rueckert, L., Appollonio, I., Grafman, J., Jezzard, P., Johnson, R.J., Le Bihan, D., and Turner, R. (1994). Magnetic resonance imaging functional activation of left frontal cortex during covert word production. *J. Neuroimag.*, **4**, 67–70.

Scarth, G., McIntry, M., Wowk, B., and Somorjai, R.L. (1995). *Proceedings of the Society for Magnetic Resonance, Third Annual Meeting (Nice)*, **1**, 238 (abstract).

Schreiber, A., Ziyeh, S., Hubbe, U., Spreer, J., Büchert, M., and Scheremet, R. (1997). *Proceedings of the International Society for Magnetic Resonance in Medicine, Fifth Scientific Meeting (Vancouver)*, **1**, 519 (abstract).

Sereno, M.I., Dale, A.M., Reppas, J.B., Kwong, K.K., Belliveau, J.W., Brady, T.J., Rosen, B.R., and Tootell, R.B. (1995). Borders of multiple visual areas in humans revealed by functional magnetic resonance imaging. *Science*, **268**, 889–893.

Spreer, J., Ziyeh, S., Hammen, A., and Wohlfahrt, R.A.S. (1997). Vergleich verschiedener Paradigmen für die funktionelle MRT zur Lokalisation sprachrelevanter Hirnregionen. *Aktuelle Neurologie*, **24** (31), 102 (abstract).

Steinmeier, R., Sobottka, S.B., Reiss, G., Bredow, J., Gerber, J., and Schackert, G. (2002). Surgery of low-grade gliomas near speech-eloquent regions: brainmapping versus preoperative functional imaging. *Onkologie*, **25** (6), 552–557.

Sumanaweera, T.S., Adler, J.R., Napel, S., and Glover, G.H. (1994). Characterization of spatial distortion in magnetic resonance imaging and its implications for stereotactic surgery. *Neurosurgery*, **35** (4), 696–703.

Talairach, J. and Tournoux, P. (1988). *Co-planar atlas of the Human brain: 3-dimensional proportional system: An approach to cerebral imaging*. Thieme Verlag, Stuttgart, New York.

Tootell, R.B., Dale, A.M., Sereno, M.I., and Malach, R. (1996). New images from human visual cortex. *Trends Neurosci.*, **19**, 481–489.

Vlieger, E.J., Majoie, C.B., Leenstra, S., and Den Heeten, G.J. (2004). Functional magnetic resonance imaging for neurosurgical planning in neurooncology. *Eur. Radiol.*, **14** (7), 1143–1153.

Wandell, B.A. and Wade, A. (2003). Functional imaging of the visual pathways. *Neurol. Clin.*, **21** (2), 417–443.

Woods, R.P., Cherry, S.R., and Mazziotta, J.C. (1992). Rapid automated algorithm for aligning and reslicing PET images. *J. Comput. Assist. Tomogr.*, **16**, 620.

Yetkin, F.Z., McAuliffe, T.L., Cox, R., and Haughton, V.M. (1996). Test-retest precision of functional MR in sensory and motor task activation. *Am. J. Neuroradiol.*, **17**, 95–98.

Yousry, T.A., Schmid, U.D., Schmidt, D., Heiss, D., Jassoy, A., Eisner, W., Reulen, H.J., and Reiser, M. (1995). Topography of the cortical motor hand area: Prospective detection with functional MR imaging and direct motor mapping at surgery. *Radiology*, **195**, 23–29.

3.3.3
New MRI Techniques for the Detection of Acute Cerebral Ischemia

Michael E. Moseley, Roland Bammer, and Joachim Röther

3.3.3.1
Introduction

During the past 15 years, diffusion- and perfusion-weighted MRI, which provide quantitative measures of the molecular motion and hemodynamics of cerebral perfusion in three-dimensional (3D) space, have evolved into two of the most powerful methods for mapping experimental as well as clinical cerebral ischemia.

Diffusion is the basis for one of the most useful contrast mechanisms in the imaging of stroke. Diffusion-weighted imaging (DWI) and more general methods, such as diffusion tensor imaging (DTI), have advanced from an experimental tool to a frequently used method for the clinical work-up of patients, and for a better understanding of the pathophysiology of cerebral diseases. In most scanning centers, diffusion-weighted MRI now belongs to the standard arsenal of MR pulse sequences. The impact that DWI has made for the early diagnosis of acute stroke requires it to be performed for every neuroimaging patient as a screening sequence for stroke in general. The possibility of diagnosing stroke within a reasonable window of opportunity to treat patients while brain tissue is still salvageable, and to triage patients with different etiology of a stroke, is of major importance for treatment decisions in critically ill patients.

Apparent diffusion coefficient (ADC) behavior derived from DWI can uniquely monitor the clinical evolution of tissue injury from acute ischemia to chronic infarction, and provides a rapid, noninvasive means for monitoring cellular energy failure, brain edema, and cellular necrosis. The hemodynamic patterns of tissue perfusion derived from perfusion-weighted imaging (PWI) delineate tissue with critical brain perfusion, and in combination with DWI may predict evolving ADC behavior and help classify ischemic lesions and predict their outcome. The mismatch of areas with reduced ADC and hypoperfusion – the so-called DWI/PWI mismatch – defines ''tissue-at-risk-of-infarction'' as viable and salvageable tissue, regardless of a restricted time window for stroke therapy.

This section provides an introduction and update into the clinical applications of DWI and PWI. Special emphasis is laid on more advanced diffusion and perfusion measurement techniques, such as motion correction and navigation, eddy current effects and corrections, as well as on the impact of parallel imaging on DWI and PWI. Much of the improvement in DWI and PWI image quality has occurred as a result of the quantum-leaps in scanner hardware and modern MR pulse sequences.

3.3.3.2 Evolution of DWI Changes in Stroke

DWI provides a technique for the mapping of proton contrast derived from the microvascular water environment (Le Bihan, 2003). In that way, the procedure is sensitive to the translation of water molecules over short distances (diffusion), and can detect ischemia-induced changes in water protons within minutes after an insult (Moseley et al., 1990a,b). During typical periods of observation ($\Delta = 40$ ms), these distances are on the order of 5 to 20 mμ. DWI utilizes a pair of magnetic field gradient pulses placed symmetrically around the 180° refocusing radiofrequency (RF) pulse to dephase and rephase stationary water protons (Stejskal and Tanner, 1965). Diffusive dephasing processes as occurs in the normal extracellular space results in a signal loss, whereas hindrances or slowing of extracellular diffusion leads to signal hyperintensity. Alteration in the time and amplitude of the gradient pulses (the b-value) alters the sensitivity of the image to diffusion with measurements at differing b-values. Incorporation of the matched pulsed gradient pair into an echo-planar imaging (EPI) sequence to measure the apparent diffusion coefficient (ADC) and to produce the ADC map is illustrated in Figure 3.50. A typical example is shown in Figure 3.51.

Images with rising b-values are the basis on which maps of the ADC are calculated (Le Bihan et al., 1992). The physiological background of the ADC was studied in many experimental investigations to show that it closely mirrors the metabolic state of the tissue, and is an indicator of cytotoxic cell edema. The ADC does not decrease until cerebral blood flow falls below a perfusion threshold of 15–20 mL per 100 g min^{-1} (Roberts et al., 1993; Hossmann, 1994). Hoehn-Berlage and colleagues combined DWI and multiparametrical mapping of ATP, pH, lactate and glucose to show that 2 h after focal ischemia an ADC decrease to 90% of baseline correlated with the area of tissue acidosis, whereas the area of ATP depletion corresponded with an ADC decrease to 70% (Hoehn-Berlage et al., 1995).

The evolution of cerebral ischemia to tissue infarction is characterized by a typical sequence of MRI signal changes. This scenario of ADC changes may be characterized as follows:

1. At very early time points following ischemia (minutes to hours), with regional perfusion lying below a threshold, ADC values are decreased in regions where T_2 values are still normal. A low ADC is considered to be an indicator of tissue in metabolic jeopardy, as successful reperfusion can re-establish the ADC to normal values, as seen in numerous animal studies. At these early time points, a low ADC would suggest membrane depolarization with water shift from the extra- to intracellular space (cytotoxic edema) (Moseley et al., 1990c; Röther et al., 1996). Without reperfusion, regions with low ADC will most likely go on to exhibit elevated T_2 values, and progress to necrosis unless the underlying perfusion deficit is corrected either on its own or with therapy.

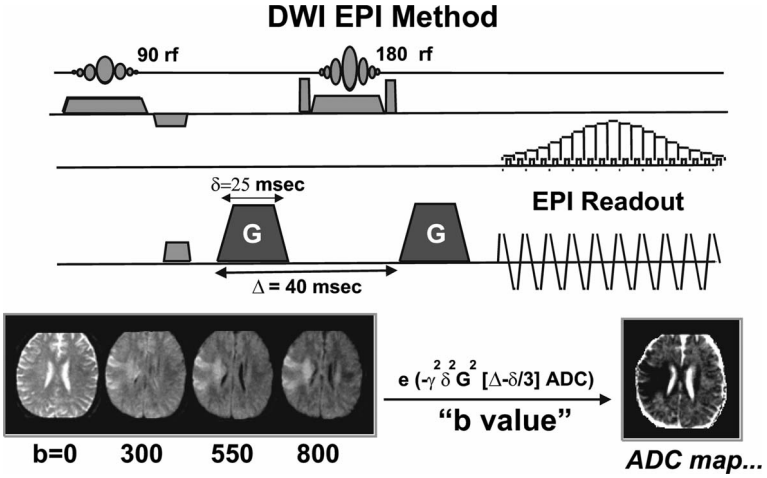

Fig. 3.50. The Stejskal–Tanner (ST) diffusion-weighted spin-echo echo-planar (EPI) MR pulse sequence timing diagram. The ST technique modifies any single- or multi-shot spin-echo sequence with a pair of diffusion-sensitizing gradient "pulses" of strength G ($mT \cdot m^{-1}$), duration δ and separation Δ. By changing the gradient pulse parameters, the amount of diffusion sensitivity can be controlled and the apparent diffusion coefficient (ADC) measured. This amount is often referred to as the *b*-value, where $b = \gamma^2\delta^2G^2(\Delta - \delta/3)$. To use this method in clinical stroke: (a) images with increasing diffusion weighting (over a range of *b*-values, 0–800 s mm^{-2}) are acquired sequentially; (b) after which the signal change due to diffusion is fitted to a single exponential of signal intensities against the *b*-value, the slope of the change being the ADC. (c) The resulting computed ADC map is composed of the slopes for all pixels in the original images. Note that differences in fast and slow diffusion rates (for example between CSF and gray matter) are best visualized at higher *b*-values, given sufficient SNR. The DWI "exam" must contain both a low and a series of higher *b*-values of at least 400–500 s mm^{-2} to visualize diffusion effects in stroke. As the *b*-value is increased, the ischemic lesion is made more conspicuous by virtue of the lower ADC of ischemic brain compared to faster proton apparent diffusion in normally perfused brain.

2. In the later stages (days), low ADC values are still seen in regions exhibiting elevated T_2 (Knight et al., 1994). This can occur when cytotoxic cellular swelling (within intact cells) exists in regions of increased water content. Comparison of T_2- and diffusion-weighted images shows a distinct difference in the regional hyperintensities. While elevated T_2 may be seen over a large diffuse region (reflecting distributions of extracellular vasogenic water), diffusion-weighted hyperintensity is confined to sharply defined areas of cytotoxically edematous tissue, since diffusional (ADC) slowing occurs on a cell-by-cell basis. This seemingly paradoxical occurrence in which both vasogenic and cytotoxic water exists, causes both T_2- and diffusion-weighted images to be hyperintense. Nonetheless, the diffusion-weighted image is a weighted average of how fast the bulk water signal diffuses; if the majority of the water is hindered or slowed, then the diffusion-weighted images will be hyperintense and the ADC will be lower than normal.

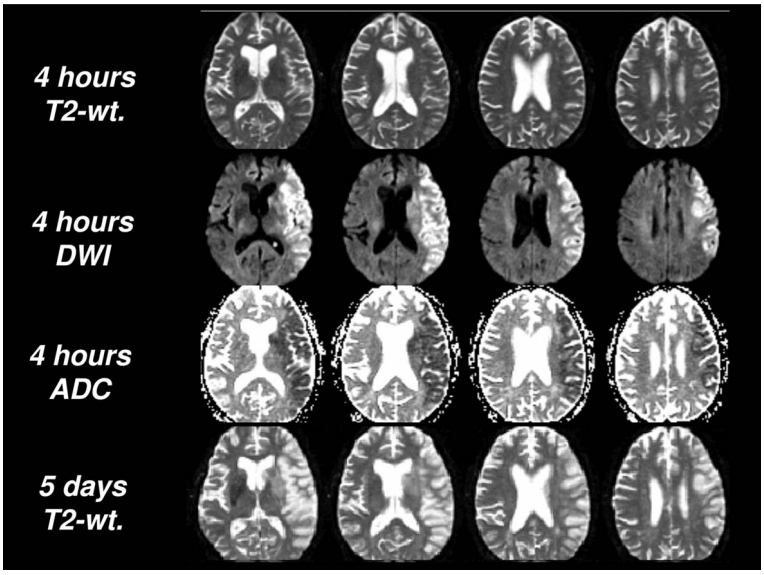

Fig. 3.51. A series of diffusion-weighted images of human brain at 4 h after onset of cerebral ischemia. EPI T_2-weighted (in which no diffusion-weighting is applied, $b = 0$), the corresponding diffusion-weighted images ($b = 881$ s mm^{-2}), and the calculated ADC maps for four slices of 16 images acquired from a patient at 4 h after onset of hemispheric aphasia. This is then compared to the T_2-weighted images acquired at 5 days. Note that the DWI depiction of lesion volume does not significantly decrease over the first 5 days, and is similar in volume to the corresponding relative cerebral blood volume maps (not shown).

3. In regions of complete infarction, both T_2 and ADC are observed to be higher than normal within similar regional distributions. The corresponding histopathology of these regions indicates cellular necrosis, in which cell lysis breaks down water diffusion barriers leading to an increase in ADC.

This situation can last for up to 10 days, until the ADC values return to "pseudonormal". However, as the diffusion-weighted images are also T_2-weighted, regional hyperintensity may be seen on DWI, even though the ADC is now above normal. This regional hyperintensity is of course due to the elevated T_2, and is not a sign of acute ischemia but rather of cerebral infarction. Because of this "T_2 shine through", every DWI examination must also include the ADC map, for these very reasons.

From the behavior of ADC and T_2 described above, the potential exists to determine the age of lesions, a clinical tool of enormous relevance in daily routine.

3.3.3.3 DWI in Clinical Practice

The detection of infarcted tissue and the delineation of hypoperfused tissue in a penumbral state that is at risk of infarction, is of paramount importance to guide the treatment of acute stroke. Computed tomography (CT) remains the most frequently applied image modality because of its broader availability. However, CT is mainly useful for the exclusion of intracerebral hemorrhage and rather insensitive for the detection of acute cerebral ischemia (Fiebach et al., 2002; Saur et al., 2003). CT detects net water increases, whereas DWI is sensitive to extra- to intracellular water shifts (Kucinski et al., 2002). Net water increases follow a slower time course (Schuier and Hossmann, 1980), while diffusion slowing is a process that occurs immediately after ischemic cell depolarization and is detected at about 60 s after cardiac arrest in a rat model (Huang et al., 1997; de Crespigny et al., 1999, 2001).

DWI in acute stroke has therefore become popular, since changes in proton self-diffusion are an early indicator of alterations in cellular homeostasis (Moseley et al., 1990a). Early experimental studies show, that DWI detects both the core and the penumbra of the evolving infarction, but is not able to differentiate between the two (Kohno et al., 1995). This is in line with further animal studies which showed that ischemic areas with ADC decreases may normalize, if the duration of the ischemia is not too long (Li et al., 2000), although ADC normalization does not necessarily indicate salvaged tissue (Neumann-Haefelin et al., 2000; Ringer et al., 2001).

Recent clinical studies have shown that ADC normalization occurs frequently in acute stroke patients with rapid recanalization, and that ischemic brain tissue with initially decreased ADC, especially within 3 h after stroke onset, may include ''tissue at risk'' (Fiehler et al., 2004). These observations of ADC normalizations have influenced the simplistic concept of the DWI/PWI mismatch as an indicator of irreversibly damaged tissue (DWI lesion) and the tissue-at-risk-of-infarction, the penumbral tissue. Additionally, the idea that the severity of the ADC decrease might be linearly linked to the likelihood of tissue recovery was refuted by studies which showed that even severely decreased ADC values may normalize in human stroke (Fiehler et al., 2002). Clearly, ADC normalization depends on the duration and severity of ischemia rather than the absolute value, as has been shown in previous experimental studies (Hoehn-Berlage et al., 1995; Kohno et al., 1995).

Although an ADC decrease in cerebral ischemia is not an absolute indicator of irreversible tissue damage, the DWI/PWI mismatch concept earns merit as an easy-to-apply method for the delineation of tissue-at-risk in acute ischemic stroke patients. Early detection of these alterations can dramatically impact treatment decisions and the therapeutic outcome for stroke victims (Lansberg et al., 2000; Thomalla et al., 2003). This is mainly because DWI is able to detect acute ischemic lesions within the ''window of opportunity'' for advanced stroke therapies, and promises to help reduce the extent and severity of ischemic damage in acute stroke victims (Röther, 2001; Röther et al., 2002). The clinical application has recently been described in a review of centers that routinely perform MRI screening of acute stroke patients before thrombolytic therapy (Hjort et al., 2005). An important

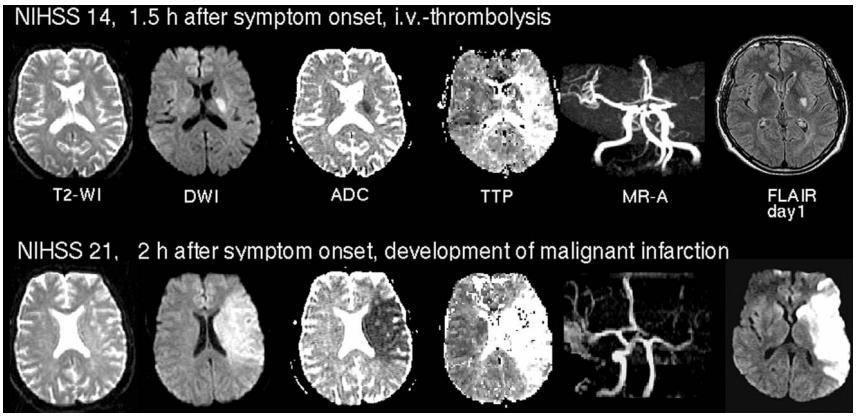

Fig. 3.52. Two acute stroke patients (upper and lower rows, respectively) with onset of symptoms as early as 1.5 and 2 h before MR imaging. Both patients show a normal T_2-weighted image, a diffusion slowing in DWI and ADC, a perfusion deficit in the territory of the middle cerebral artery (MCA), and a vessel occlusion in magnetic resonance angiography (MRA). While the first patient has a huge mismatch territory (PWI-DWI) and responds favorably to thrombolytic recanalization of the occluded MCA, the second patient shows a large diffusion lesion with negligible mismatch volume due to a carotid artery occlusion. The first patient recovered completely and had only a small striato-capsular infarction on follow-up MRI after 24 h, but the second patient developed malignant MCA infarction.

step towards the future application of MRI in acute stroke management is the use of the DWI/PWI mismatch concept to select patients in an extended time window at 3 to 9 h after stroke onset in order to apply a new thrombolytic agent (Hacke et al., 2005).

The selection of stroke patients eligible for thrombolysis in an extended time window, and in patients with unknown stroke onset, is an emerging application of stroke MRI (Schellinger et al., 2003). The combination of DWI, PWI and MR angiography (MRA) – termed "stroke MRI" – has developed towards a clinical tool that is utilized by many stroke centers to define "tissue at risk of infarction" where there is a high likelihood of surviving the ischemic insult in case of timely reperfusion. Two typical examples of stroke MRI in acute stroke patients are illustrated in Figure 3.52.

3.3.3.4 Improvements and Pulse Sequences for DWI and DTI

Much of the recent progress in DWI, DTI, and PWI has been due to "high-speed" imaging capabilities, and steady improvements within an overall theme that enhanced gradient strengths can be used to produce images in one or a few "shots" or echo-trains. Echo-planar and spiral imaging are two variations of such high-speed gradient-echo MRI techniques to be discussed, whereas spin-echo variations of high-speed imaging fall into the class of "fast spin-echo" MRI. High-speed MRI

suggests that images are acquired in a few seconds or less, providing the means to produce motion-free images or a series of rapidly acquired images. In addition to the improvements in gradients and pulse sequence design and implementation (Haselgrove and Moore, 1996; Bammer et al., 2003; Reese et al., 2003), the entire field of MR is today in the midst of a revolution where multiple RF coils can be used in various ''parallel imaging'' combinations to provide vast improvements in resolution, signal-to-noise ratio (SNR) and scan time, and all trade-offs imaginable. Together, hardware improvements and software pulse sequences are changing the face of MR techniques in stroke.

Beyond Routine DWI and DTI for Stroke

In addition to providing important clinical information, DWI, DTI and PWI have made valuable contributions in basic neuroscience and improved the understanding of pathophysiologic processes such as cerebral ischemia. Whereas DWI has largely limited itself to averaging out white matter directional effects, DTI enables investigation of the 3D orientation of major white matter fiber tracts and gross anatomic brain connectivity in a repeatable and nondestructive manner. It also offers, to some extent, a quantitative measure for not only the cognitive performance within individuals (Klingberg et al., 2000; Basser et al., 1994; Basser, 1995; Mori et al., 1999) but also the loss of structural coherence and eventually the alteration of myelin sheaths that may occur in diseases such as stroke (Verheul et al., 1994; Thomalla et al., 2004).

Diffusion Tensor Imaging

Although DTI has not yet been able to match the impact that DWI has had in stroke, it has proven to be a sensitive tool for detecting subtle abnormalities in the white matter of patients with diseases such as multiple sclerosis (Filippi et al., 2001; Bammer and Fazekas, 2002) or amyotropic lateral sclerosis (ALS) (Sach et al., 2004). DTI studies in the acute phase of stroke have shown that Wallerian degeneration of the axons of the pyramidal tract occurs as early as a few days after ischemic damage to the distant neuronal soma (Thomalla et al., 2004, 2005).

Despite DTI's sensitivity to white matter abnormalities shown in group comparisons, further investigations in this area are warranted to demonstrate its value for diagnosing individual patients. The anisotropic nature of water diffusion in white matter has led yet to another exciting modality that allows investigators to follow different fiber systems in white matter using a method to post-process DTI tensor maps. The method of ''tracking'' the preferred proton direction of displacement – ''fiber tracking'' – is based on orientational information garnered from DTI or more sophisticated methods, and promises to elucidate – at least at the gross morphological level – functional and anatomical connectivity in the brain. Fiber tracking rests on the observation that ADC values are higher along fiber tracts than across them, and that this is due to the highly directional diffusivity in nerve fibers. This property allows for mapping or ''tracking'' the preferred orientation of the tracts themselves (Fig. 3.53).

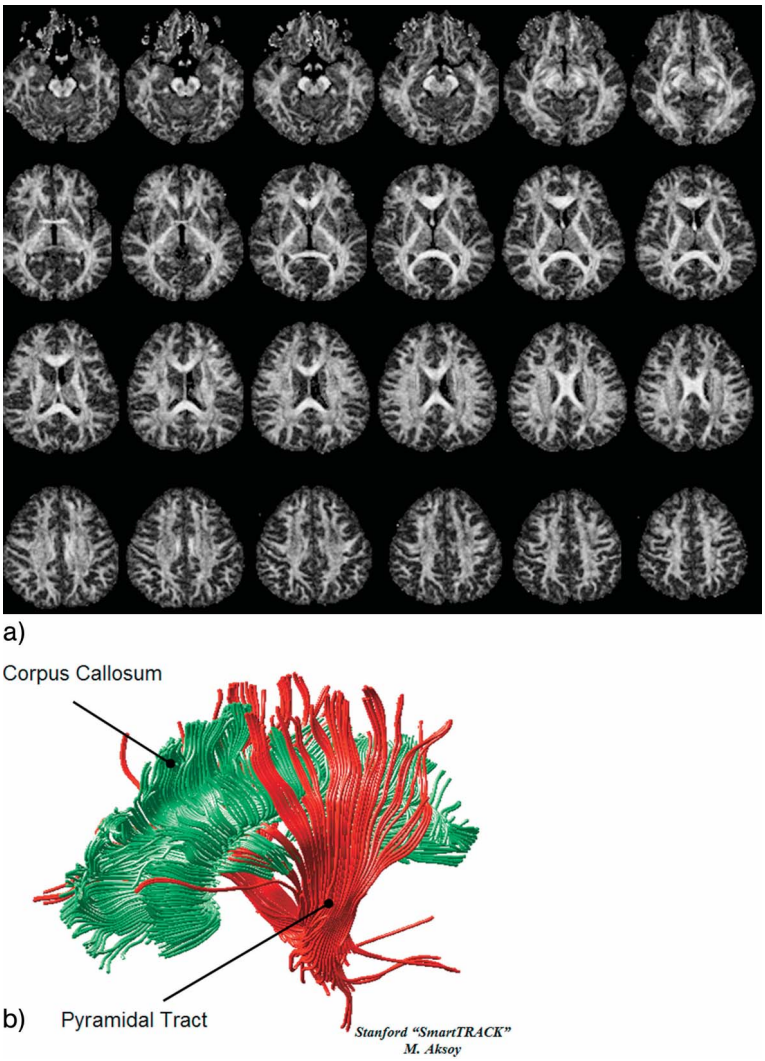

Fig. 3.53. (a) Fractional anisotropy (FA) maps from DTI examination (128 × 128; $b = 0$–1000 s mm^{-2}; six gradient directions, four averages, 12 min). The FA maps represent "anisotropic" diffusion along white matter (WM) tracts, and are quantitative measures of the white matter "integrity" and orientation. (b) The FA maps can then be processed to show the direction (tracks) of the WM tracts (fibers). The real value of DTI in stroke will largely be to better visualize WM defects and damage.

This new visualization angle opens a completely new arena of examinations, since it allows one to trace different fiber tracts multiple times and from various locations in a nondestructive fashion (Mori et al., 1999; Song et al., 2003).

It has long been assumed that the simple Gaussian model for diffusion can be inappropriate within a complex substrate such as human tissue. One way in which this model fails is in the presence of multiple fiber directions crossing or ''merging'' within a single imaging voxel. Application of the single Gaussian fiber diffusion tensor model should be reconsidered in that simple models break down in complex white matter structures. A novel approach to this problem has been to measure the diffusion coefficient at higher angular resolutions (Liu et al., 2002) in order to more accurately detect variations in diffusion along different directions. Reduction of the resulting 3D ADC representation into a set of orthogonal 3D functions (Frank, 2002) improves the visualization and comprehension of the underlying fiber structure. We have described a ''generalized diffusion tensor imaging'' (GDTI) method proposed to measure the higher-order statistics of a non-Gaussian diffusion process where a non-Gaussian diffusion process could be characterized by ''higher-order tensor'' (HOT) coefficients of the data (Liu et al., 2002) to better describe complex structures.

Another refinement in DWI stems from the demonstrated nonexponential attenuation of the echo amplitude with increasing *b*-values. In a study by Mulkern (Mulkern et al., 1999), performed on a clinical scanner for *b*-values up to 6000 s mm^{-2}, the signal decay from brain tissue *in vivo* showed nonmono-exponential behavior, and can be modeled by a multi-exponential function. It is the interpretation of the data that is of interest; some studies have attributed this behavior to compartmentation of water pools; others have suggested that restricted diffusion in one compartment can also lead to a nonmono-exponential behavior of the MR signal. In short, the physical significance of the parameters is still unclear and no consensus has been reached regarding the origins of the multi-component ADC, despite the potential value of understanding the complex movements of water in acute cerebral ischemia.

Measuring Diffusion in the Presence of Physiologic Motion

The greatest technical challenge associated with DWI has always been to overcome the effects of macroscopic motion, while retaining its sensitivity to the microscopic motion. To create diffusion-weighted contrast, DWI pulse sequences must be made sensitive to molecular motion on the order of several micrometers and because of this, are also extremely sensitive to bulk tissue motion. Even small (sub-millimeter) displacements during the diffusion-encoding phase will cause large phase changes in the resultant echo signal. Because bulk motion on this level is likely to be different during each echo acquisition, each echo will be perturbed differently from one excitation or view to the next. Higher resolutions using multi-shot sequences have not been used. For this reason, the most common form of data acquisition is still a single-shot readout type of sequence, in particular single-shot EPI (Mansfield, 1977; Turner et al., 1990). It has been the steady improvement in scanner gradients and hardware that has advanced DWI the most over the past decade, to

the extent that most state-of-the-art clinical scanners are easily capable of producing diffusion-weighted spin-echo EPI images of 128 × 128 resolutions in a single-shot with fair-to-good diagnostic quality.

DWI with Single-Shot EPI

An EPI pulse sequence samples all the data points necessary for reconstruction of an image after the application of a single RF excitation pulse (or a 90–180° RF-pulse combination for a spin-echo "SE-EPI" sequence), but at the cost that the maximum attainable spatial resolution of EPI can be markedly limited by T_2*-decay during the relatively long data acquisition. Worse perhaps, EPI has only a very small bandwidth per pixel along the phase-encoding "blipping" direction. Because of this, EPI is very susceptible to off-resonance effects, such as main field inhomogeneity, local susceptibility gradients, and chemical shift, all of which may lead to severe image degradation (note the typical SE-EPI DWI artifacts in the vicinity of air cavities).

To reduce these artifacts and to greatly improve the overall image quality, diffusion-weighted single-shot EPI (ssh-EPI) is routinely combined with recently introduced parallel imaging strategies (Sodickson and Manning, 1997; Griswold et al., 1999, 2000, 2002; Pruessmann et al., 1999; Bammer et al., 2001, 2002), such as SENSitivity Encoding (SENSE) (Pruessmann et al., 1999). SENSE is rapidly becoming a valuable complement to conventional encoding in MRI. It uses some of the spatial information contained in the individual elements of an RF coil array to more efficiently traverse *k*-space, and can "accelerate" virtually any conventional MRI technique without interfering with the numerous different contrast mechanisms used in MRI, such as diffusion weighting. SENSE can help to improve single-shot EPI and fast spin echo (FSE) scans by reducing artifacts, by improving spatial resolution, at some expense of SNR and FOV aliasing. In practical terms, the SENSE technique allows for an acceleration of the *k*-space traversal by the same number as there are component coils available.

The incorporation of parallel imaging schemes to improve the single-shot SE-EPI DWI sequence has greatly improved image quality in DWI (Fig. 3.54). The dramatic reduction of susceptibility and other artifacts by the use of multiple coils and SENSE-type strategies has in essence vastly rejuvenated DWI on all scanners and magnetic fields. Neuroimaging centers worldwide are currently active in incorporating various DWI parallel imaging "upgrades", and the resulting image improvements to routine DWI (and DTI) are significant.

DWI with FSE

Fast (or "Turbo") spin-echo imaging (FSE or TSE) has dramatically altered daily clinical practice as a fast and robust image readout strategy with negligible T_2* artifacts. Due to significant RF pulse specific absorption rate (SAR) constraints made worse by variable RF pulse flip angle distributions occurring during a long echo train, FSE has been a poor choice for DWI or DTI. One approach for diffusion-weighted FSE imaging has been the U-FLARE technique (Norris et al., 1992), which relies on the separation of different echo families so that they do not inter-

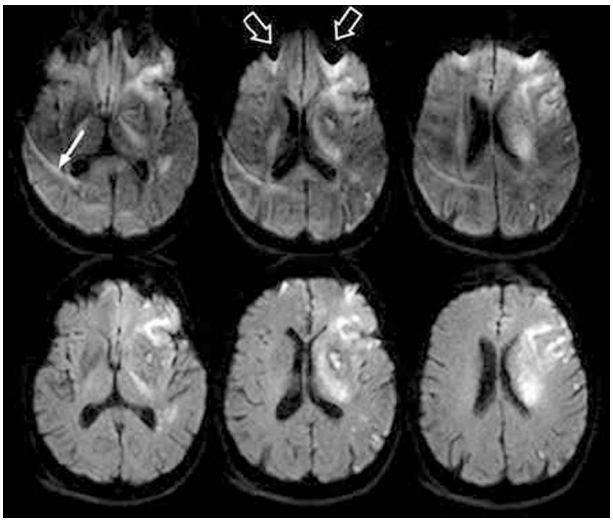

Fig. 3.54. Comparison of conventional single-shot EPI DWI (top) with the corresponding single-shot SENSE-DWI sequence (bottom) from three diffusion-weighted slices of 20 acquired from a suspected stroke with an accompanying subcortical hemorrhagic transformation. The $b = 1000$ s mm^{-2} images are shown. By means of the faster *k*-space traversal with SENSE (acceleration factor, $r = 2$), the chemical shift artifact can be strongly reduced (arrows). Moreover, magnetic susceptibility artifacts or artifacts from B_0-inhomogeneities can be also markedly diminished (open arrows). Note the improved conspicuity of the hemorrhagic lesion on the SENSE-DWI images.

fere. Le Roux and colleagues (Le Roux, 1998, 2000) presented a valid method for diffusion-weighted FSE-DWI which relies on an FSE employing a modified phase setting of the refocusing RF pulses. This approach has become the basis for the ''PROPELLER'' FSE-DWI method, a novel and effective FSE sequence for DWI described by Pipe et al. (2002).

The PROPELLER (Periodically Rotated Overlapping ParallEL Lines with Enhanced Reconstruction) method, which has inherent 2D navigator information in each FSE echo train, provides far greater immunity to geometric and T_2* distortions than that obtained with EPI sequences, while providing robust immunity to motion artifacts by collecting FSE trains in various frequency and phase directions in *k*-space, called ''blades''. Each blade passes through the center of frequency and phase space, which allows for a very good means of ''navigating'' each blade to any phase-inducing motional effects. In subsequent pluse repetition time (TRs) this blade is rotated, so that together the blades measure a circular region of *k*-space formed by their union. The basic idea of PROPELLER is that the blades can correct for inconsistencies prior to combining the data, so the primary inconsistency will be motion-caused phase differences. After data correction, the blades are combined to form the DWI image. Images from the commonly-used SE-EPI DWI sequence and the corresponding PROPELLER sequence for routine stroke DWI are compared in Figure 3.56.

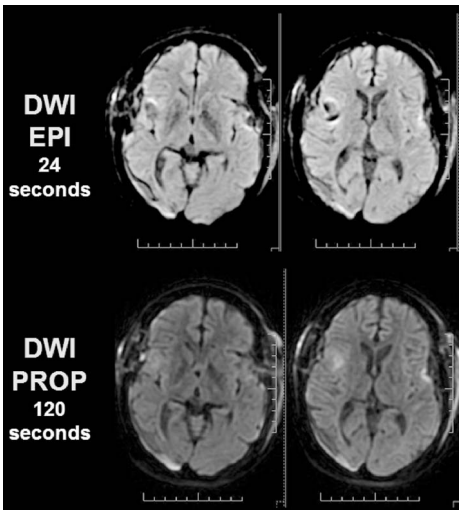

Fig. 3.55. Comparison of SE-EPI DWI and "Turbo-PROPELLER" DWI for imaging of stroke and hemorrhage. Shown are the SE-EPI DWI (128 × 128; $b = 1000$) diffusion-weighted images from four of 28 slices acquired in 24 s. Below are the corresponding Turbo-PROP images (128 × 128; ETL 16; $b = 1000$) from four of 18 slices acquired in 120 s. Single-shot SE-EPI DWI demonstrates significant susceptibility artifacts near air–tissue interfaces (top row). Typical signal pile up and loss as well as strong geometric distortions are apparent, obscuring tissue pathology through most slices (bottom row). Turbo-PROP PROPELLER DWI with identical acquisition matrix (128 × 128) demonstrates few artifacts and provides significantly better image quality. In this "Turbo" implementation of PROPELLER, five gradient echoes were acquired between each refocusing RF pulse to speed up the acquisition. The overall acquisition adds approximately 100 s to the scan time.

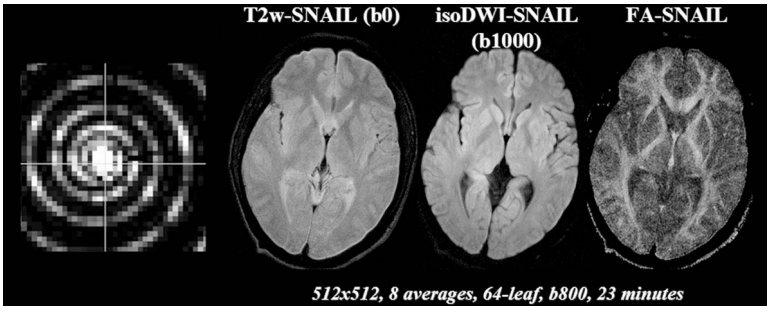

Fig. 3.56. Very high-resolution (512 × 512) DTI results acquired with a self-navigated variable-density spiral twice-refocused spin-echo (TRSE) sequence (SNAILS). (a) T2w-SNAIL image ($b = 0$). (b) Trace (isotropic average of x, y, and z) diffusion-weighted image. (c) FA map. Although the scan times are prohibitively long, this demonstrates the potential of self-navigated multi-shot DWI methods.

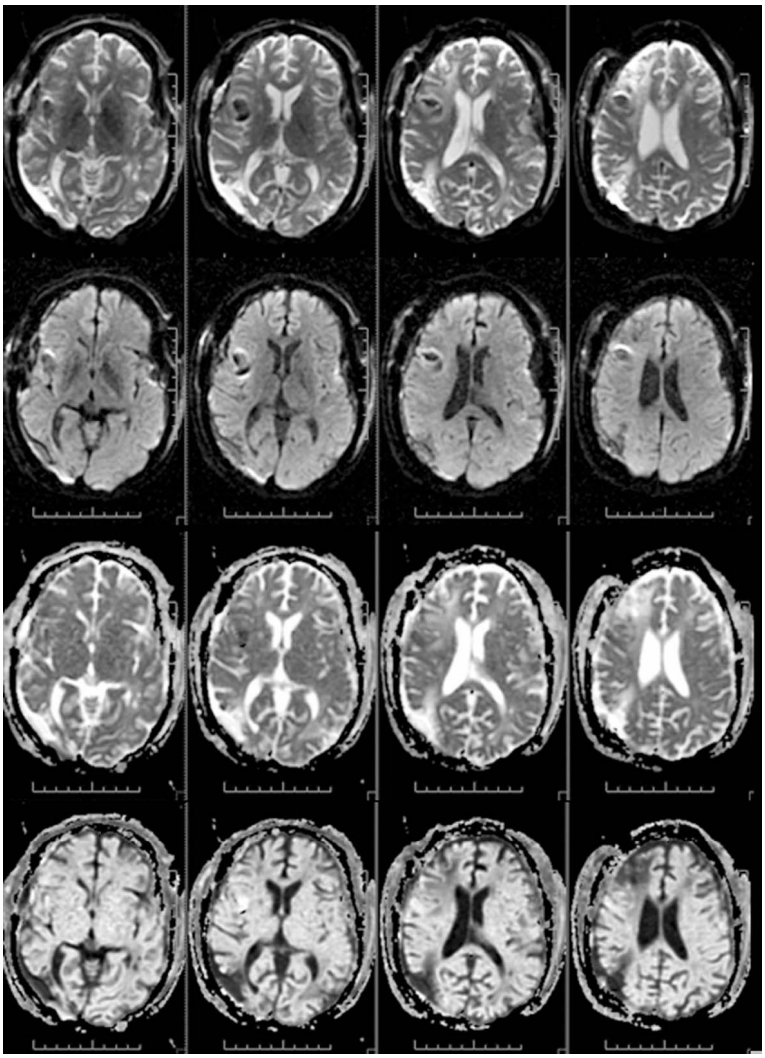

Fig. 3.57. (128 × 128, $b = 1000$) SE-EPI DWI single-shot 128 × 128 images from four (left to right) of 28 slices acquired in 24 s along the x-, y-, and z-gradient directions. The *b*0, DWI, trace ADC (''averaged'' along three axes to remove white matter anisotropy effects), and ADC ''expo'' images are shown from top to bottom at left. The ADC ''expo'' maps are processed to remove long ADC values such as CSF, which typically hides lower ADC values.

Diffusion-Weighted Spiral Imaging

Spiral scanning provides an alternative scheme to collect diffusion-weighted *k*-space data (Li et al., 1999; Bammer and Moseley, 2004; Liu et al., 2004). Spiral imaging has the potential advantages of being less demanding for the gradient systems by avoiding the need for rapid switching gradients, as is needed in EPI. Spiral

imaging is also relatively insensitive to flow artifacts and ghosting, since the center of *k*-space is collected at the start of the scan. Further, the center of *k*-space is redundantly sampled (''oversampled'') by the spiral trajectories, providing self-navigating capabilities (Fig. 3.57).

The widespread use of spiral scanning in routine clinical practice has been limited, however, by the lack of time-varying gradient-waveform capabilities and the lack of automated and rapid image reconstruction resources. Improvements of this technique are being achieved by means of variable density spiral scans, and this has led to a family of multishot spiral DWI pulse sequences which appear to provide most of the advantages inherent in the PROPELLER sequences, albeit with faster acquisitions (Bammer, 2004; Liu et al., 2004). One advantage of the spiral family for DWI and DTI is the ability of increasing the resolution of the images while retaining good motion suppression. The acquisition of very high-resolution (512×512) diffusion-weighted images for DWI or DTI is illustrated in Figure 3.56.

Which Diffusion MR Measure is Best for Stroke Imaging?

There exist a large number of variations of images that can be derived from the DWI or DTI examination. These are loosely described as: ''isotropic'' (the combined or averaged diffusion-weighted images acquired along the x-, y-, and z-gradient axes; the ADC maps acquired from the low and high *b*-value images; the ''trace'' images or ADC maps similar to the averaged x-, y-, and z-axis diffusion-weighted images; exponential ADC (''eADC'' or ADC ''Expo'') maps in which the large ADC values (primarily seen in cerebrospinal fluid) are suppressed; and the DTI-derived anisotropic maps of relative anisotropy ''RA'', fractional anisotropy ''FA''. Recent studies, seeking to sort the relative merits of these measures to visualize the presence and extent of acute clinical stroke, found that the average absolute percentage changes for the isotropic strategies were all above 38% (Harris et al., 2004).

The ADC maps had the most significant difference (−42.4%). The DTI-derived anisotropic images had no significant differences in acute stroke. The authors concluded that anisotropic maps do not consistently show changes during the first 6 h of ischemic stroke, and that averaged or isotropic diffusion-weighted or ADC images using DWI were more appropriate for detecting hyperacute stroke. It was noted, however, that anisotropic images may be useful to differentiate hyperacute stroke from acute and subacute stroke.

What is the Value of Adding Inversion Recovery Pulses to DWI?

The ADC derived from diffusion-weighted images has been used to differentiate reversible from irreversible ischemic injury. However, the ADC can be falsely elevated by partial volume averaging of cerebrospinal fluid (CSF) with parenchyma, which may limit the accuracy of this approach. IR sequences have been shown to help delineate low-ADC lesions by suppressing the hyperintense CSF signal from the ADC maps (Lansberg et al., 2001). Recent investigations were conducted to test whether the accuracy of differentiating reversible from irreversible ischemic injury could be improved by CSF suppression at image acquisition (Bykowski et al.,

2004). The results showed that CSF IR-prepared ADC (FLIPD) values more accurately depicted tissue fate compared to conventional ADC values in 16 patients, while CSF-suppressed ADC measurements gave a more accurate identification of reversible ischemic injury at the expense of SNR decreases at 1.5 T. More recently, another group (Simon et al., 2004) found that when SNR and contrast-to-noise-ratio (CNR) between ischemic and normal tissues were compared at higher fields of 3 T, the calculated ADC maps with and without the initial IR preparation were similarly assessed where the SNR and CNR were significantly lower for IR ADC value imaging than for conventional ADC values. The overall observation noted that ischemic tissue on IR DWI was significantly less conspicuous than on DWI, and that this potentially limited the clinical utility of this sequence at higher fields.

3.3.3.5 Functional DWI in Brain Mapping

The role of fMRI has become increasingly important in neuroimaging, for example in the presurgical mapping of gray matter (Hendler et al., 2003). Contrast mechanisms based on the blood oxygenation level, volume, and flow changes have been used to noninvasively detect brain activation secondary to the neuronal activity. Recently, several efforts have focused on alternative contrast mechanisms that may offer shorter temporal delays and more direct spatial localization in brain mapping. These include the detection of Lorentzian forces from neural activation from phase-sensitive images, the use of diffusion-weighting to sensitize the image to changes in incoherent displacements, and the mapping of small changes in the ADC from neural activity.

Phantom studies now suggest the possibility of detecting the destructive phase addition from the spatially incoherent, yet temporally synchronized, displacements caused by the Lorentz force experienced during electrical conduction within a strong magnetic field (Bellgowan et al., 2003).

Another approach has employed heavy diffusion weighting to remove the vascular signal and sensitize the minute and incoherent displacement in order to detect fast dynamic signal changes synchronized to a task (Li and Song, 2003). These authors observed fast functional signal changes consequent to the task activation by using a heavy diffusion-weighting protocol which possessed a different time course from the corresponding BOLD response and suggested an alternative origin different from the common BOLD signal sources. Li and Song concluded that the characteristics of the signal change suggested that it may be more directly linked to the neuronal activity temporally and spatially than the BOLD response. Song has recently expanded this approach to include the mapping of the diffusion tensor to detect synchronized fMRI signal changes during brain activation (Song et al., 2003).

Using fast-DWI, Le Bihan and colleagues observed changes in the apparent diffusion coefficient of water in the human brain visual cortex during activation by a flickering checkerboard task activation paradigm (Darquie et al., 2001). The ADC decrease was less than 1% but significant and reproducible, and closely followed the time course of the activation paradigm. The observed ADC findings were as-

cribed to a transient swelling of cortical cells that occurred with neural activation (Darquie et al., 2001).

These preliminary results from a variety of new imaging techniques suggest a new approach to the production of images of brain activation, with MRI from signals directly associated with neuronal activation rather than through changes in local blood flow. More importantly, the methods may in the near future provide noninvasive maps of the neural activation pathways in the central nervous system.

3.3.3.6
Conclusion and Future Outlook

In recent years, DWI has undergone rapid growth and development, such that the technique has escalated rapidly from an experimental tool to an established clinical methodology, the primary use of which has been in the evaluation of acute cerebral ischemia. Much like T_1- and T_2-relaxation, diffusivity can be thought of as an intrinsic tissue property. Thus, DWI may also be useful in imaging extracranial organs, such as the solid organs within the abdomen, or abnormalities in the musculoskeletal system. The ability to determine diffusion coefficients *in vivo* has great potential for furthering our understanding of normal and abnormal physiology, as well as for characterizing focal and diffuse disease within the human body. Historically, bulk physiologic motion has hampered the application of DWI to a wide variety of clinical questions. However, developments in MR hardware, pulse-sequences and computer science – all enhanced by the rapid evolution of parallel-imaging improvements – have led to a robust tool with reasonable image quality and outstanding diagnostic potential.

Acknowledgments

The authors (M.M., R.B.) acknowledge their support from the National Institutes of Health (1R01EB002771, 1R01NS35959), the Center of Advanced MR Technology at Stanford (P41RR09784), and the Lucas Foundation.

References

Bammer, R. (2004). Parallel Imaging: (Part II). *Top. Magn. Reson. Imaging*, **15** (4), 221.

Bammer, R. and Fazekas, F. (2002). Diffusion imaging in multiple sclerosis. *Neuroimaging Clin. N. Am.*, **12** (1), 71–106.

Bammer, R. and Moseley, M. (2004). Interleaved Dual-Echo Spiral-Out-Spiral-In DSC Imaging With Generalized SENSE. *Proceedings of the ISMRM, Kyoto*.

Bammer, R., Keeling, S.L., Augustin, M., Pruessmann, K.P., Wolf, R., Stollberger, R., Hartung, H.P., and Fazekas, F. (2001). Improved diffusion-weighted single-shot echo-planar imaging (EPI) in stroke using sensitivity encoding (SENSE). *Magn. Reson. Med.*, **46** (3), 548–554.

Bammer, R., Auer, M., Keeling, S.L., Augustin, M., Stables, L.A., Prokesch, R.W., Stollberger, R., Moseley, M.E., and Fazekas, F. (2002). Diffusion tensor imaging using single-shot SENSE-EPI. *Magn. Reson. Med.*, **48** (1), 128–136.

Bammer, R., Markl, M., Barnett, A., Acar, B., Alley, M.T., Pelc, N.J., Glover, G.H., and Moseley, M.E. (2003). Analysis and generalized correction of the effect of spatial gradient field distortions in diffusion-weighted imaging. *Magn. Reson. Med.*, **50** (3), 560–569.

Basser, P.J. (1995). Inferring microstructural features and the physiological state of tissues from diffusion-weighted images. *NMR Biomed.*, **8** (7-8), 333–344.

Basser, P.J., Mattiello, J., and LeBihan, D. (1994). Estimation of the effective self-diffusion tensor from the NMR spin echo. *J. Magn. Reson. B*, **103** (3), 247–254.

Bellgowan, P.S., Saad, Z.S., and Bandettini, P.A. (2003). Understanding neural system dynamics through task modulation and measurement of functional MRI amplitude, latency, and width. *Proc. Natl. Acad. Sci. USA*, **100** (3), 1415–1419.

Bykowski, J.L., Latour, L.L., and Warach, S. (2004). More accurate identification of reversible ischemic injury in human stroke by cerebrospinal fluid suppressed diffusion-weighted imaging. *Stroke*, **35** (5), 1100–1106.

Darquie, A., Poline, J.B., Poupon, C., Saint-Jalmes, H., and Le Bihan, D. (2001). Transient decrease in water diffusion observed in human occipital cortex during visual stimulation. *Proc. Natl. Acad. Sci. USA*, **98** (16), 9391–9395.

de Crespigny, A.J., Röther, J., Beaulieu, C., Moseley, M.E., and Hoehn, M. (1999). Rapid monitoring of diffusion, DC potential, and blood oxygenation changes during global ischemia. Effects of hypoglycemia, hyperglycemia, and TTX. *Stroke*, **30** (10), 2212–2222.

de Crespigny, A.J., Röther, J., Beaulieu, C., Neumann-Haefelin, T., and Moseley, M.E. (2001). Comparison of diffusion, blood oxygenation, and blood volume changes during global ischemia in rats. *Magn. Reson. Med.*, **45** (1), 10–16.

Fiebach, J.B., Schellinger, P.D., Jansen, O., Meyer, M., Wilde, P., Bender, J., Schramm, P., Juttler, E., Oehler, J., Hartmann, M., Hahnel, S., Knauth, M., Hacke, W., and Sartor, K. (2002). CT and diffusion-weighted MR imaging in randomized order: diffusion-weighted imaging results in higher accuracy and lower interrater variability in the diagnosis of hyperacute ischemic stroke. *Stroke*, **33** (9), 2206–2210.

Fiehler, J., Foth, M., Kucinski, T., Knab, R., von Bezold, M., Weiller, C., Zeumer, H., and Röther, J. (2002). Severe ADC decreases do not predict irreversible tissue damage in humans. *Stroke*, **33**, 79–86.

Fiehler, J., Knudsen, K., Kucinski, T., Kidwell, C.S., Alger, J.R., Thomalla, G., Eckert, B., Wittkugel, O., Weiller, C., Zeumer, H., and Röther, J. (2004). Predictors of apparent diffusion coefficient normalization in stroke patients. *Stroke*, **35** (2), 514–519.

Filippi, M., Cercignani, M., Inglese, M., Horsfield, M.A., and Comi, G. (2001). Diffusion tensor magnetic resonance imaging in multiple sclerosis. *Neurology*, **56** (3), 304–311.

Frank, L.R. (2002). Characterization of anisotropy in high angular resolution diffusion-weighted MRI. *Magn. Reson. Med.*, **47** (6), 1083–1099.

Griswold, M.A., Jakob, P.M., Chen, Q., Goldfarb, J.W., Manning, W.J., Edelman, R.R., and Sodickson, D.K. (1999). Resolution enhancement in single-shot imaging using simultaneous acquisition of spatial harmonics (SMASH). *Magn. Reson. Med.*, **41** (6), 1236–1245.

Griswold, M.A., Jakob, P.M., Nittka, M., Goldfarb, J.W., and Haase, A. (2000). Partially parallel imaging with localized sensitivities (PILS). *Magn. Reson. Med.*, **44** (4), 602–609.

Griswold, M.A., Jakob, P.M., Heidemann, R.M., Nittka, M., Jellus, V., Wang, J., Kiefer, B., and Haase, A. (2002). Generalized autocalibrating partially parallel acquisitions (GRAPPA). *Magn. Reson. Med.*, **47** (6), 1202–1210.

Hacke, W., Albers, G., Al-Rawi, Y., Bogousslavsky, J., Davalos, A., Eliasziw, M., Fischer, M., Furlan, A., Kaste, M., Lees, K.R., Soehngen, M., and Warach, S. (2005). The Desmoteplase in Acute Ischemic Stroke Trial (DIAS): a phase II MRI-based 9-hour window acute stroke thrombolysis trial with intravenous desmoteplase. *Stroke*, **36** (1), 66–73.

Harris, A.D., Pereira, R.S., Mitchell, J.R., Hill, M.D., Sevick, R.J., and Frayne, R. (2004). A comparison of images generated from diffusion-weighted and diffusion-

tensor imaging data in hyper-acute stroke. *J. Magn. Reson. Imaging*, **20** (2), 193–200.

Haselgrove, J.C. and Moore, J.R. (1996). Correction for distortion of echo-planar images used to calculate the apparent diffusion coefficient. *Magn. Reson. Med.*, **36** (6), 960–964.

Hendler, T., Pianka, P., Sigal, M., Kafri, M., Ben-Bashat, D., Constantini, S., Graif, M., Fried, I., and Assaf, Y. (2003). Delineating gray and white matter involvement in brain lesions: three-dimensional alignment of functional magnetic resonance and diffusion-tensor imaging. *J. Neurosurg.*, **99** (6), 1018–1027.

Hjort, N., Butcher, K., Davis, S.M., Kidwell, C.S., Koroshetz, W.J., Röther, J., Schellinger, P.D., Warach, S., and Ostergaard, L. (2005). Magnetic resonance imaging criteria for thrombolysis in acute cerebral infarct. *Stroke*, **36** (2), 388–397.

Hoehn-Berlage, M., Norris, D.G., Kohno, K., Mies, G., Leibfritz, D., and Hossmann, K.A. (1995). Evolution of regional changes in apparent diffusion coefficient during focal ischemia of rat brain: the relationship of quantitative diffusion NMR imaging to reduction in cerebral blood flow and metabolic disturbances. *J. Cereb. Blood Flow Metab.*, **15**, 1002–1011.

Hossmann, K.A. (1994). Viability thresholds and the penumbra of focal ischemia. *Ann. Neurol.*, **36**, 557–565.

Huang, N.C., Yongbi, M.N., and Helpern, J.A. (1997). The influence of preischemic hyperglycemia on acute changes in the apparent diffusion coefficient of brain water following global ischemia in rats. *Brain Res.*, **757** (1), 139–145.

Klingberg, T., Hedehus, M., Temple, E., Salz, T., Gabrieli, J.D., Moseley, M.E., and Poldrack, R.A. (2000). Microstructure of temporo-parietal white matter as a basis for reading ability: evidence from diffusion tensor magnetic resonance imaging. *Neuron*, **25** (2), 493–500.

Knight, R.A., Dereski, M.O., Helpern, J.A., Ordidge, R.J., and Chopp, M. (1994). Magnetic resonance imaging assessment of evolving focal cerebral ischemia. Comparison with histopathology in rats. *Stroke*, **25** (6), 1252–1262.

Kohno, K., Hoehn-Berlage, M., Mies, G., Back, T., and Hossmann, K.A. (1995). Relationship between diffusion-weighted MR images, cerebral blood flow, and energy state in experimental brain infarction. *Magn. Reson. Imaging*, **13** (1), 73–80.

Kucinski, T., Vaterlein, O., Glauche, V., Fiehler, J., Klotz, E., Eckert, B., Koch, C., Röther, J., and Zeumer, H. (2002). Correlation of apparent diffusion coefficient and computed tomography density in acute ischemic stroke. *Stroke*, **33** (7), 1786–1791.

Lansberg, M.G., Norbash, A.M., Marks, M.P., Tong, D.C., Moseley, M.E., and Albers, G.W. (2000). Advantages of adding diffusion-weighted magnetic resonance imaging to conventional magnetic resonance imaging for evaluating acute stroke. *Arch. Neurol.*, **57** (9), 1311–1316.

Lansberg, M.G., Thijs, V.N., O'Brien, M.W., Ali, J.O., de Crespigny, A.J., Tong, D.C., Moseley, M.E., and Albers, G.W. (2001). Evolution of apparent diffusion coefficient, diffusion-weighted, and t2-weighted signal intensity of acute stroke. *Am. J. Neuroradiol.*, **22** (4), 637–644.

Le Bihan, D. (2003). Looking into the functional architecture of the brain with diffusion MRI. *Nat. Rev. Neurosci.*, **4** (6), 469–480.

Le Bihan, D., Turner, R., Douek, P., and Patronas, N. (1992). Diffusion MR imaging: clinical applications. *Am. J. Roentgenol.*, **159** (3), 591–599.

Le Roux, P. (1998). Non CPMG fast spin-echo with full signal. *Annual Meeting of ISMRM*, 574.

Le Roux, P. (2000). Non-CPMG fast spin-echo in practice. *Annual Meeting of ISMRM*, 1530.

Li, F.H., Liu, K.F., Silva, M.D., Omae, T., Sotak, C.H., Fenstermacher, J.D., and Fisher, M. (2000). Transient and permanent resolution of ischemic lesions on diffusion-weighted imaging after brief periods of focal ischemia in rats: correlation with histopathology. *Stroke*, **31** (4), 946–954.

Li, T. and Song, A.W. (2003). Fast functional brain signal changes detected by diffusion weighted fMRI. *Magn. Reson. Imaging*, **21**, 829–833.

Li, T.Q., Takahashi, A.M., Hindmarsh, T., and Moseley, M.E. (1999). ADC mapping by means of a single-shot spiral MRI technique with application in acute cerebral

ischemia. *Magn. Reson. Med.*, **41** (1), 143–147.

Liu, C., Bammer, R., and Moseley, M.E. (2002). Multi-exponential analysis of gray and white matter structures in human brain. *10th Annual Meeting of ISMRM*.

Liu, C., Bammer, R., Kim, D.H., and Moseley, M.E. (2004). Self-navigated interleaved spiral (SNAILS): application to high-resolution diffusion tensor imaging. *Magn. Reson. Med.*, **52** (6), 1388–1396.

Mansfield, P. (1977). Multiplanar image formation using NMR spin-echoes. *J. Phys. Chem. Solid State Phys.*, **10**, L55–L58.

Mori, S., Crain, B.J., Chacko, V.P., and van Zijl, P.C. (1999). Three-dimensional tracking of axonal projections in the brain by magnetic resonance imaging. *Ann. Neurol.*, **45** (2), 265–269.

Moseley, M.E., Cohen, Y., Mintorovitch, J., Chileuitt, L., Shimizu, H., Kucharczyk, J., Wendland, M.F., and Weinstein, P.R. (1990a). Early detection of regional cerebral ischemia in cats: comparison of diffusion- and T2-weighted MRI and spectroscopy. *Magn. Reson. Med.*, **14** (2), 330–346.

Moseley, M.E., Kucharczyk, J., Mintorovitch, J., Cohen, Y., Kurhanewicz, J., Derugin, N., Asgari, H., and Norman, D. (1990b). Diffusion-weighted MR imaging of acute stroke: correlation with T2-weighted and magnetic susceptibility-enhanced MR imaging in cats. *Am. J. Neuroradiol.*, **11**, 423–429.

Moseley, M.E., Mintorovitch, J., Cohen, Y., Asgari, H.S., Derugin, N., Norman, D., and Kucharczyk, J. (1990c). Early detection of ischemic injury: comparison of spectroscopy, diffusion-, T2-, and magnetic susceptibility-weighted MRI in cats. *Acta Neurochir. Suppl. (Wien)*, **51**, 207–209.

Mulkern, R.V., Gudbjartsson, H., Westin, C.F., Zengingonul, H.P., Gartner, W., Guttmann, C.R., Robertson, R.L., Kyriakos, W., Schwartz, R., Holtzman, D., Jolesz, F.A., and Maier, S.E. (1999). Multi-component apparent diffusion coefficients in human brain. *NMR Biomed.*, **12** (1), 51–62.

Neumann-Haefelin, T., Kastrup, A., de Crespigny, A., Yenari, M.A., Ringer, T., Sun, G.H., and Moseley, M.E. (2000). Serial MRI after transient focal cerebral ischemia in rats: dynamics of tissue injury, blood-brain barrier damage, and edema formation. *Stroke*, **31** (8), 1965–1973.

Norris, D.G., Bornert, P., Reese, T., and Leibfritz, D. (1992). On the application of ultra-fast RARE experiments. *Magn. Reson. Med.*, **27** (1), 142–164.

Pipe, J.G., Farthing, V.G., and Forbes, K.P. (2002). Multishot diffusion-weighted FSE using PROPELLER MRI. *Magn. Reson. Med.*, **47** (1), 42–52.

Pruessmann, K.P., Weiger, M., Scheidegger, M.B., and Boesiger, P. (1999). SENSE: sensitivity encoding for fast MRI. *Magn. Reson. Med.*, **42** (5), 952–962.

Reese, T.G., Heid, O., Weisskoff, R.M., and Wedeen, V.J. (2003). Reduction of eddy-current-induced distortion in diffusion MRI using a twice-refocused spin echo. *Magn. Reson. Med.*, **49** (1), 177–182.

Ringer, T.M., Neumann-Haefelin, T., Sobel, R.A., Moseley, M.E., and Yenari, M.A. (2001). Reversal of early diffusion-weighted magnetic resonance imaging abnormalities does not necessarily reflect tissue salvage in experimental cerebral ischemia. *Stroke*, **32** (10), 2362–2369.

Roberts, T.P., Vexler, Z., Derugin, N., Moseley, M.E., and Kucharczyk, J. (1993). High-speed MR imaging of ischemic brain injury following stenosis of the middle cerebral artery. *J. Cereb. Blood Flow Metab.*, **13** (6), 940–946.

Röther, J. (2001). CT and MRI in the diagnosis of acute stroke and their role in thrombolysis. *Thromb. Res.*, **103** (Suppl 1), S125–S133.

Röther, J., de Crespigny, A.J., D'Arceuil, H., and Mosley, M.E. (1996). MR detection of cortical spreading depression immediately after focal ischemia in the rat. *J. Cereb. Blood Flow Metab.*, **16** (2), 214–220.

Röther, J., Schellinger, P.D., Gass, A., Siebler, M., Villringer, A., Fiebach, J.B., Fiehler, J., Jansen, O., Kucinski, T., Schoder, V., Szabo, K., Junge-Hulsing, G.J., Hennerici, M., Zeumer, H., Sartor, K., Weiller, C., and Hacke, W. (2002). Effect of intravenous thrombolysis on MRI parameters and functional outcome in acute stroke <6 hours. *Stroke*, **33** (10), 2438–2445.

Sach, M., Winkler, G., Glauche, V., Liepert, J., Heimbach, B., Koch, M.A., Buchel, C., and Weiller, C. (2004).

Diffusion tensor MRI of early upper motor neuron involvement in amyotrophic lateral sclerosis. *Brain*, **127** (2), 340–350.

Saur, D., Kucinski, T., Grzyska, U., Eckert, B., Eggers, C., Niesen, W., Schoder, V., Zeumer, H., Weiller, C., and Röther, J. (2003). Sensitivity and inter-rater agreement of CT and diffusion-weighted MR imaging in hyperacute stroke. *Am. J. Neuroradiol.*, **24** (5), 878–885.

Schellinger, P.D., Fiebach, J.B., and Hacke, W. (2003). Imaging-based decision making in thrombolytic therapy for ischemic stroke. Present status. *Stroke*, **34** (2), 575–583.

Schuier, F.J. and Hossmann, K.-A. (1980). Experimental brain infarcts in cats. II. Ischemic brain edema. *Stroke*, **11**, 593–601.

Simon, J.E., Czechowsky, D.K., Hill, M.D., Harris, A.D., Buchan, A.M., and Frayne, R. (2004). Fluid-attenuated inversion recovery preparation: not an improvement over conventional diffusion-weighted imaging at 3T in acute ischemic stroke. *Am. J. Neuroradiol.*, **25** (10), 1653–1658.

Sodickson, D.K. and Manning, W.J. (1997). Simultaneous acquisition of spatial harmonics (SMASH): fast imaging with radiofrequency coil arrays. *Magn. Reson. Med.*, **38** (4), 591–603.

Song, A.W., Harshbarger, T., Li, T., Kim, K.H., Ugurbil, K., Mori, S., and Kim, D.S. (2003). Functional activation using apparent diffusion coefficient-dependent contrast allows better spatial localization to the neuronal activity: evidence using diffusion tensor imaging and fiber tracking. *NeuroImage*, **20** (2), 955–961.

Stejskal, E. and Tanner, J. (1965). Use of spin echo in pulsed magnetic-field gradient to study anisotropic, restricted diffusion and flow. *J. Chem. Phys.*, **43**, 3579–3603.

Thomalla, G.J., Kucinski, T., Schoder, V., Fiehler, J., Knab, R., Zeumer, H., Weiller, C., and Röther, J. (2003). Prediction of malignant middle cerebral artery infarction by early perfusion- and diffusion-weighted magnetic resonance imaging. *Stroke*, **34** (8), 1892–1899.

Thomalla, G., Glauche, V., Koch, M.A., Beaulieu, C., Weiller, C., and Röther, J. (2004). Diffusion tensor imaging detects early Wallerian degeneration of the pyramidal tract after ischemic stroke. *NeuroImage*, **22** (4), 1767–1774.

Thomalla, G., Glauche, V., Weiller, C., and Röther, J. (2005). Time course of wallerian degeneration after ischaemic stroke revealed by diffusion tensor imaging. *J. Neurol. Neurosurg. Psychiatry*, **76** (2), 266–268.

Turner, R., Le Bihan, D., Maier, J., Vavrek, R., Hedges, L.K., and Pekar, J. (1990). Echo-planar imaging of intravoxel incoherent motion. *Radiology*, **177**, 407–414.

Verheul, H.B., Balazs, R., Berkelbach van der Sprenkel, J.W., Tulleken, C.A., Nicolay, K., Tamminga, K.S., and van Lookeren Campagne, M. (1994). Comparison of diffusion-weighted MRI with changes in cell volume in a rat model of brain injury. *NMR Biomed.*, **7**, 96–100. Erratum in: *NMR Biomed.* (1994) **7**, 374.

3.3.4
Clinical Applications at Ultrahigh Fields

Petra Schmalbrock and Donald W. Chakeres

3.3.4.1
Potential and Challenges with Ultrahigh Field MRI

Ultrahigh field MRI at 7–9.4 T in human-sized whole-body systems has become a new forefront of MRI. Following initial demonstrations of the feasibility at academic institutions (Robitaille et al., 2000; Ugurbil et al., 2003), the major MRI vendors have now embraced the potential of these systems, and embarked on the development of commercial ultrahigh field systems.

The principal advantage of increased magnetic field strength is that the signal-to-noise ratio (SNR) increases with increasing field strength, and that this SNR gain may, in turn, be used to either increase spatial or temporal resolution in proton MRI, or to significantly increase the sensitivity of MRI with other nuclei such as ^{13}C, ^{19}F, ^{23}Na, and ^{31}P (Lei et al., 2003). Furthermore, chemical shift spectral dispersion is increased, thus improving the detection of metabolites by allowing for better differentiation of spectral lines in MR spectroscopy. Finally, magnetic susceptibility effects from paramagnetic material increase with increasing field strength, and this provides advanced contrast mechanisms for naturally occurring paramagnetic material such as deoxyhemoglobin and tissue iron. Increased sensitivity to deoxyhemoglobin content presents a mechanism for improved depiction of venous vasculature (Reichenbach et al., 1998; Reichenbach and Haacke, 2001), and is the basis for *blood oxygen level dependent* (BOLD) neurofunctional MRI (Yacoub et al., 2003). Measurement of tissue iron may allow for noninvasive assessment of various conditions altering iron content in the brain, including normal aging and neurodegenerative diseases.

These potential advantages are offset not only by the increased cost for large high-field magnets, but by several fundamental physical conditions that presently pose serious challenges for ultrahigh field MRI, including artifacts from inhomogeneous B_0 and B_1 fields, different tissue relaxation times, and safety concerns.

Magnetic Susceptibility and B_0 Inhomogeneity

Susceptibility differences between diamagnetic tissue water and paramagnetic material cause local magnetic field changes. Such changes occur on a subvoxel spatial scale, for example with red blood cells (≈ 5 μm), ferritin (20 nm), and MRI contrast agents, and present an important contrast mechanism (see below). Conversely, susceptibility inhomogeneity on a spatial scale of several voxels (1–10 mm) near air/tissue interfaces produces severe image artifacts, including geometric distortions and signal loss. Susceptibility field inhomogeneity $\Delta B_0(x, y, z)$ can be described analytically for simple geometries, whether numerically modeled (Li et al., 1996; Truong et al., 2002), or experimentally measured (Spielman et al., 1998; Truong

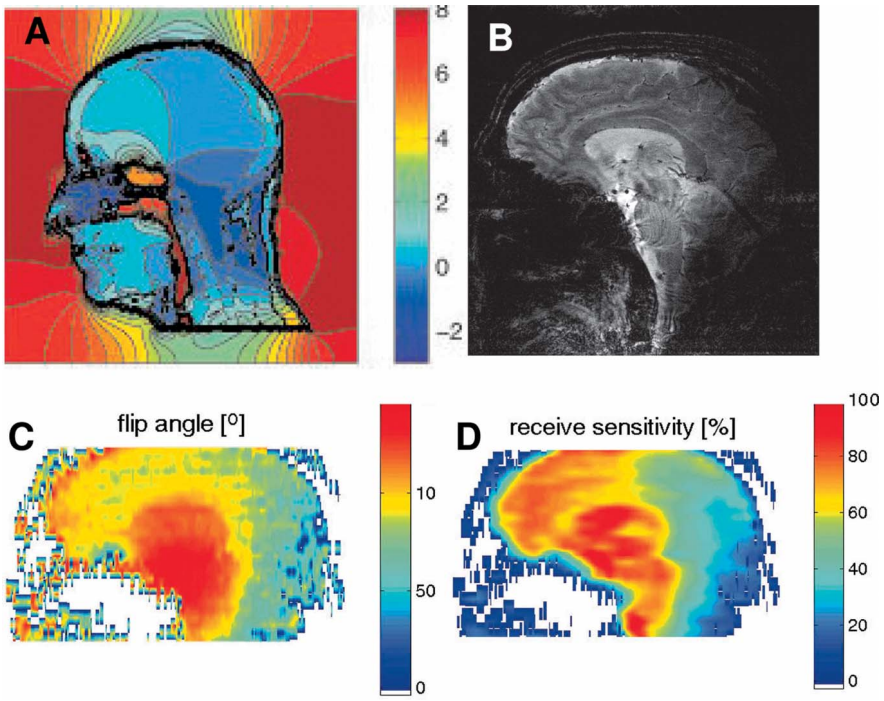

Fig. 3.58. (A) Numerically computed saggital susceptibility field map in human brain. (Truong et al., 2002). (B) Gradient echo image of the same subject using TR/TE 600 ms/ 12 ms, nominal flip 22.5°, FOV 18 cm, 1024 × 512, 2 mm slice thickness. (C) Matching flip angle map and (D) receive sensitivity map, computed from axial gradient echo images with nominal flip angles of 60°/120° using the relationship $S_{2\alpha}/S_{\alpha} = \sin 2\alpha/\sin \alpha = 2 \cos \alpha$. Note that in the ventricles, the receive sensitivity map is contaminated by proton density (Truong et al., 2006).

et al., 2006). For ultrahigh field MRI, B_0 inhomogeneity is especially problematic because field changes scale linearly with the magnetic field strength. For example, the numerical simulation in Figure 3.58A shows variability of 2 ppm near the sphenoid. Under typical image conditions, resultant image distortions are less then one pixel at 1.5 T and thus negligible, whereas they extend over several voxels at 8 T. Misregistration artifacts occur in both spin and gradient echoes in the frequency and slice encode direction. In addition, susceptibility inhomogeneity creates severe signal loss in gradient echo images, where the size of the signal void increases with increasing echo time and field strength. For example, areas of signal voids are seen near the sphenoid sinus with banding patterns extending up to the corpus callosum and in the cerebrospinal fluid (CSF) spaces anterior to the brainstem (Fig. 3.58B). Consequently, susceptibility artifact correction is of paramount importance for ultrahigh field MRI. Several approaches have been proposed for this purpose, including gradient compensation (Yang et al., 1998; Glover, 1999), tailored radiofrequency (RF) pulses (Cho and Ro, 1992; Stenger et al., 2002), active and pas-

sive shimming (Wilson et al., 2002), and post-processing (Irarrazabal et al., 1996; Kadah and Hu, 1998).

B_1 Inhomogeneity

Another fundamental challenge with ultrahigh field MRI arises from the fact that presently B_1 fields (i.e., radio waves > 300 MHz) with uniform amplitude are not easily achievable for human head or larger-sized samples. Intuitively, this may be understood as follows. The wavelength at 300–340 MHz in tissue is about 6 cm, which is smaller than the dimension of a human head. As a consequence, RF field distribution reflects complicated patterns of standing and propagating waves with local amplitude minima and maxima in three-dimensional space depending on the shape, orientation, dielectric, and conductive properties of the anatomic region to be imaged rather than on the design of the coil alone. Conversely, at lower field strengths, the wavelength is larger than anatomy and B_1 homogeneity can be achieved. High-field B_1 field distribution cannot be predicted intuitively, and several investigators (e.g., Chen et al., 1998; Ibrahim et al., 2001; Collins et al., 2002) have used numerical simulations to compute B_1 fields. The resultant complicated highly inhomogeneous patterns of RF intensity distribution are in agreement with experimentally measured maps. B_1 inhomogeneity leads to variable RF flip angles and receive sensitivity (Hoult, 2000; Ibrahim et al., 2005), thus adversely affecting image contrast, SNR and overall image quality (Fig. 3.58C,D).

It is evident that the problem of RF inhomogeneity needs to be addressed and solved in order to take full advantage of ultrahigh field MRI. This fundamental challenge remains yet to be solved, though a number of potential solutions have been proposed. Conventional RF coil design can address the problem only in part, because the RF distribution is dominated by the patient. Proposed solutions include use of shaped RF pulses, and multi-port excitation of TEM coils (Vaughan et al., 1994; Ibrahim et al., 2001). The latter concept may be extended by using multiple parallel transmit coils and RF amplifier chains. This approach alone – or in combination with multiple independent receive coils – may represent the most promising solution, and allow not only for improved RF and image homogeneity but also for faster imaging, analogous to existing receive coil parallel imaging methods (Sodickson and Manning, 1997; Pruessmann et al., 1999). For this, complicated and expensive hardware-software systems will be needed, but these are only now being conceptually explored and implemented.

Changes in Relaxation Times

A third fundamental challenge for ultrahigh field MRI arises from the fact that relaxation times change substantially compared to lower field strengths, thus significantly altering image appearance. Bottomley extrapolated data obtained at lower field strengths, and predicted increasing tissue T_1 relaxation times with increasing field strength, whereas T_2 relaxation times were predicted to remain approximately constant (Bottomley et al., 1984). Because of susceptibility effects, T_2^* relaxation times are expected to become significantly shorter at ultrahigh field MRI. Since all

Table 3.1. Relaxation time measurements at 8 T.

	PD[a)]	T_1 [ms]	T_2-multi[b)] [ms]	T_2 single[c)] [ms]	T_2* [ms]
Frontal WM	0.69	1300	74.5 ± 3.4 (n = 3)	39.0 ± 1.6 (n = 6)	20.5 (n = 1)
Motor GM	0.80	1800	74.3 ± 9.2 (n = 2)	37.5 ± 1.1 (n = 5)	20.3 (n = 1)
Frontal GM			71.4 (n = 1)	44.8 (n = 1)	

[a)] Proton densities are averages of values listed in Tofts (2003).
[b)] CPMG multi-echo sequence with 20-ms inter-echo time.
[c)] Single spin echo GESSE sequence (Yablonskiy and Haacke, 1997) with TE = 50 ms.

T_1 and T_2 relaxation time measurement methods are affected by flip angle variability, experimental measurements of relaxation times are complicated by B_1 inhomogeneity. Thus, preliminary T_1 and T_2 measurements at 8 T only used data from image regions where flip angles (measured as in Fig. 3.58) did not deviate more than 20° from the nominal 90°/180° (Table 3.1).

An important finding is that at 8 T multi-echo T_2 are almost twice as long as single echo T_2. The fundamental difference between single and multi spin echo sequences is that the signal decay observed with single echoes with long times between RF pulses is significantly affected by water molecule diffusion in magnetic field gradients (Hahn, 1950), whereas multi-echo Carr Purcell CP sequences using shorter times between successive 180° refocusing pulses are less affected (Carr and Purcell, 1954). That is, water protons acquire variable amounts of phase shift as they diffuse through magnetic field gradients produced by small-sized magnetic field perturbers. The phase spread among an ensemble of protons becomes larger for longer times between successive RF pulses and, as a consequence, Hahn and CP sequences have different signal decay constants T_2, if simple single exponential fitting is used to determine that decay constant (Ye et al., 1996; Bartha et al., 2002; Stefanovic et al., 2003). In tissue, deoxyhemoglobin in vessels, tissue iron stored in ferritin or MRI contrast agents produce local field variability on a spatial scale comparable to the water molecule diffusion length during the RF pulse interval – that is, in the 10 nm to 10 μm range. Effects from diffusion in locally variable fields are increased at higher field strength because field changes from small perturbers extend further. A number of theoretical models have been proposed to characterize this behavior (Kennan et al., 1994; Yablonskiy and Haacke, 1994; Weisskoff et al., 1994; Jensen et al., 2001; Kiselev and Novikov, 2002) and may ultimately be used to determine concentration and spatial distribution of paramagnetic tissue constituents. It should be noted that preliminary 8 T, CP-T_2s are comparable to low field values (e.g., Tofts, 2003). This is in line with early predictions by Bottomley, and may represent predominantly tissue water content and cellular architecture of the tissue.

In addition to the irreversible T_2 relaxation effects in spin echo sequences, local susceptibility field variability causes reversible dephasing effects in gradient echo sequences that are measured by T_2^* (with $1/T_2^* = 1/T_2 + 1/T_{2'}$ where $T_{2'}$ describes the reversible component). T_2^* values at 8 T that were measured with a modified gradient compensated sequence removing air/tissue susceptibility artifacts are listed in Table 3.1.

Safety Concerns

Last, but not least, there are additional safety concerns with ultrahigh field MRI, since the effects of ultrahigh magnetic field exposure have not yet been extensively studied, nor due to the higher exposure to RF energy. Initial studies have not identified any clear new safety hazards associated with ultrahigh field systems compared to clinical systems (Chakeres et al., 2003a,b; Chakeres and de Vocht 2004).

3.3.4.2

Image Characteristics in Normal Brain

Routine clinical MRI customarily uses three types of contrast, namely T_1, T_2, and proton density (PD) weighting, where images are acquired such that signal intensities predominantly reflect T_1, T_2, or PD. Familiarity with these common contrast patterns is the basis for standardized and reliable clinical diagnosis of MRI, and allows radiologists easily to identify and interpret signal changes due to pathology. The significantly longer T_1 and shorter T_2 at ≥ 7 T considerably alter image appearance and, for optimal utilization of ultrahigh field MRI, one needs to understand these changes in image contrast. In the following sections, calculated image contrast based on the parameters listed in Table 3.1 and image examples will be compared for gradient echo, spin echo, and inversion recovery sequences, and effects due to flip angle variability will be discussed.

T_1 and PD Gradient Echo (GE) Contrast

To illustrate the ultrahigh field contrast behavior, gradient echo contrast (for a spoiled, incoherent gradient echo sequence) was calculated first for short echo times (TE = 2 ms) to minimize the influence of T_2* effects such as not to contaminate T_1 or PD contrast. The calculated white matter/gray matter contrast (i.e., signal difference WM-GM) and gray matter/CSF contrast is shown in Figure 3.59. Weak T_1-weighting is achieved for certain TR/flip angle pairs (above the red line in Fig. 3.59A,B), though the signal difference is very small. Likewise, PD weighting results in appropriate TR/flip angle pairs (below the blue line in Fig. 3.59A,B). Comparative 2D-GE (Fig. 3.59C; TR/flip = 500/55°) and 3D-GE (Fig. 3.59D; TR/flip = 12/18°) images show weak T_1 contrasts – that is, the CSF is darkest, but gray and white matter are near isointense. A very high SNR (>100) is needed to produce a contrast-to-noise ratio (CNR) sufficient for tissue differentiation, and though SNR is high with ultrahigh field MRI, the reduced contrast diminishes the utility standard 2D-GE T_1- or PD weighted sequences. Because of the need for very short TR, 3D-GE sequences are further impaired by the long T_1.

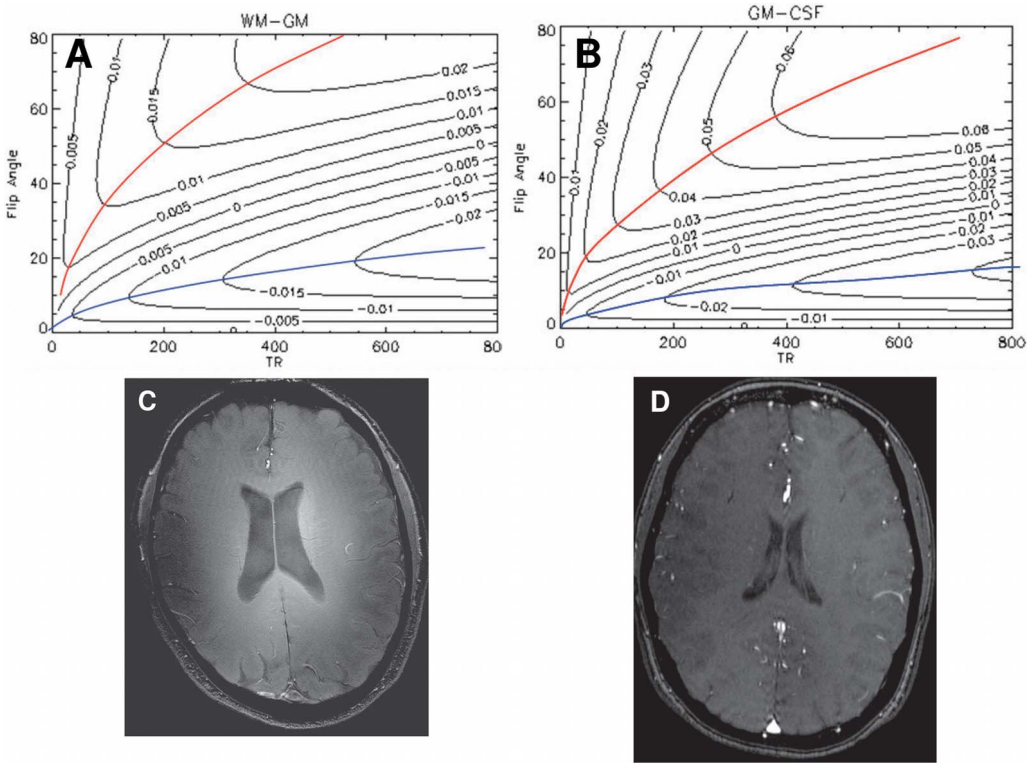

Fig. 3.59. Simulated contrast contour plots showing signal difference in TE = 2 ms incoherent GE images between white and gray matter (A), and gray matter and CSF (B) depending on TR and flip angle (calculated using Table 3.1 and PD, T_1, T_2, and T_2^* of 1.0, 4000 ms, 1000 ms and 100 ms for CSF). T_1 contrast is achieved above the red line, and PD contrast below the blue line. Also shown are comparative T_1-weighted 7-T images. (C) 2D-GE, TR/TE/flip = 500 ms/2 ms/55°, FOV 25 cm, 800 × 800 matrix, 4-mm slice. (D) 3D-GE, TR/TE/flip = 12 ms/3.5 ms/18°, FOV 24 cm, 512 × 384, 80 slices, 1.5 mm. Note that gray matter appears slightly brighter in the periphery of the 2D-GE image (C) because true flip angle in the peripheral regions is lower than the nominal flip angle, leading to contrast inversion. Arteries are bright in the 3D-GE image due to inflow enhancement, making this method suitable for MR angiography.

Susceptibility-Weighted Imaging (SWI)

The dramatic influence of TE on image contrast in ultrahigh field GE images is demonstrated in Figure 3.60. Contrast calculations show that with longer TE (≈ 10 ms), significant T_1-weighting is no longer achieved, but due to the much longer T_2^* for CSF compared to brain parenchyma, CSF yields highest signal for nearly all TR and flip angles. While overall contrast is not impressive, susceptibility-weighted images stand out by their superb depiction of small veins, which are seen as dark linear structures due to the very short T_2^* for deoxyhemoglobin. Studies in post-mortem specimens have shown that 8-T images with spatial

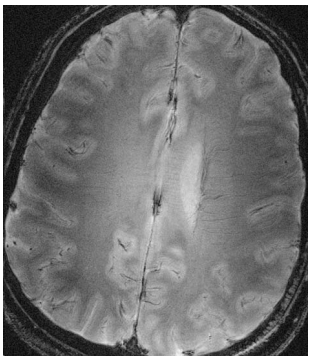

Fig. 3.60. Ultrahigh resolution 8 T BOLD venogram (TR/TE/flip angle 513 ms/10 ms/20°, FOV 20 cm, 1024 × 1024 matrix, 1-mm slice thickness). Note the exquisite depiction of leptomeningeal veins in this image region of the corpus callosum. The veins are dark in these images, while the overall image contrast is proton density-weighted.

resolutions of $0.25 \times 0.25 \times 2.0\ mm^3$ can depict vessels of less than 100 μm (Dashner et al., 2004). This contrast mechanism is analogous to the BOLD effect used in functional MRI (fMRI), and thus SWI has also been termed *BOLD venography*. While superb results are achieved with 2D-GE BOLD venography, thin-section 3D-GE BOLD venography at 8 T is inadequate because the GM and WM signal is low due to long T_1. This situation is different for 1.5 T or 3 T, where 3D-GE sequences can produce good BOLD venograms, albeit with extremely long scan times (Reichenbach et al., 1998). It was shown that phase rather than magnitude reconstruction can further improve susceptibility weighted images at 1.5 T and 3 T as well as at 8 T (Abduljalil et al., 2003). These images not only provide improved depiction of vasculature, but also exhibit better GM/WM contrast (see below).

Spin Echo Contrast

Spin echo (SE) images are profoundly impacted by RF inhomogeneity and the shift in relaxation times. In order to assess achievability for conventional T_1, T_2 and PD behavior in SE as a function of TR and for variable flip angle, several options were evaluated. Some analytical expression have been given to describe the dependence of SE images on the repetition time and excitation and refocusing flip angles; however, these apply only for long TR (Haacke et al., 1999), for fixed 90° excitation pulses and refocusing pulses with relatively small deviations (<20°) from 180° (Kingsley et al., 1998), or for multi-pulse equilibrium conditions (Hennig, 1988; Laurent et al., 2000). The simulations described here were obtained by numerically solving the iterative Bloch equations for a single echo SE sequence with α and 2α for the excitation and refocusing flip angles, respectively. Such calculations show complicated signal characteristics as a function of TR and α, that is not described by published analytic expressions. Examples for GM/WM contrast and GM/CSF contrast are shown in Figure 3.61. Conventional T_1 weighting is no longer achieved – that is, both the computations and images show that CSF has highest

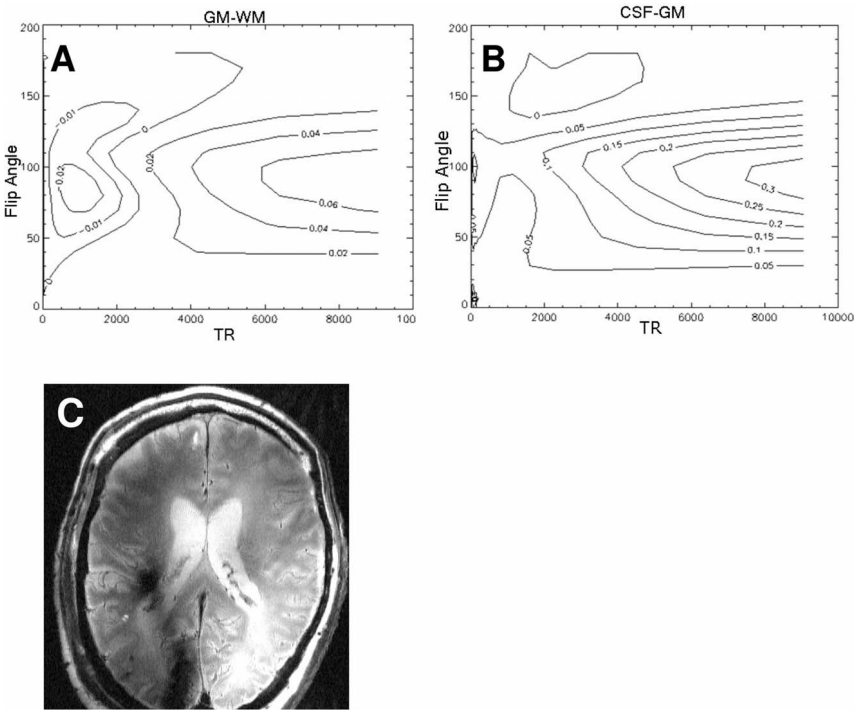

Fig. 3.61. Contour plots of gray matter/white matter (GM/WM) contrast (A) and gray matter/CSF contrast (B) computed by numerical solution of the iterative Bloch equations for single echo spin echo sequences with TE = 20 ms as a function of TR, α excitation angle and 2α refocusing angle. (C) For comparison, an 8-T spin echo image (TR/TE = 250 ms/20 ms) at a nominal flip angle $\alpha = 90°$ in the frontal area is shown. Very low flip angles and receive sensitivity create dark image regions on the lower left. GM/WM contrasts is variable as flip angles vary from about 150° in the center to 15° at the periphery.

signal irrespective of TR and flip angle, and contrast becomes highly variable and dependent on the local flip angle, especially for TR $< T_1$. For long TR, locally variable flip angles mostly result in signal scaling with overall conventional PD or T_2 contrast.

T_2 contrast also depends heavily on the type of SE (i.e., single versus multi-echo sequence), and also on the interpulse delay time because, as discussed above, water molecule diffusion in the magnetic fields of nm- to μm-sized perturbers leads to irreversible dephasing and thus different effective T_2 in different sequences. In addition, locally variable flip angles complicate the contrast behavior in T_2-weighted SE sequences. While adiabatic RF pulses could be used to remedy this problem, they will require prohibitively large RF, leading to excessive specific absorption rate (SAR) for human studies. Hennig showed that T_2-weighted fast spin echo (FSE) imaging with low SAR can be achieved by selecting optimized lower flip an-

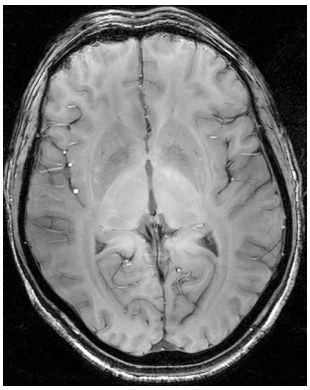

Fig. 3.62. T_1-weighted 3D magnetization prepared inversion recovery turbo gradient echo image acquired at 7 T (Philips, Achieva, Cleveland; TI = 1300 ms, TR/TE/flip angle = 14 ms/7 ms/8°, FOV 25 cm, 512 × 376, slice 3 mm). In these images with excellent T_1 contrast, arteries appear with high signal intensity due to time-of-flight enhancement, and veins are dark due to the BOLD effect.

gles (e.g., sequences such as TRAPS and Hyperecho; Hennig and Scheffler, 2001; Hennig et al., 2003). This approach is very promising for ultrahigh field MRI, but flip angle optimization will need to be adapted to the fact that excitation and refocusing pulses are locally variable.

Inversion Recovery Contrast

Standard inversion recovery-spin echo (IR-SE) or fast-spin echo (IR-FSE) are even more severely affected by RF inhomogeneity. Using simple slice-selective pulses leads to severe variability of image contrast across the image. Much more promising results are achieved with magnetization-prepared IR turbo gradient echo images (Fig. 3.62). Such sequences require only a few inversion pulses and can thus utilize adiabatic pulses for the inversion, followed by small flip angle image readout. In addition to excellent T_1 contrast, initial studies also show arterial in-flow enhancement and dark veins due to venous deoxyhemoglobin, which highlights the great promise of magnetization-prepared IR turbo gradient echo sequences.

3.3.4.3 Applications for Neuropathology

Brain Tumors

It is well known that the vascular bed in and near tumors, as well as tumor perfusion, are altered compared to the normal vasculature. Tumor vessels are frequently more tortuous, larger and more disorganized than vessels in normal brain, and angiogenesis is considered to be a marker for tumor aggressiveness in astrocytic neoplasms, specifically glioblastoma multiforme. Thus, the use of antiangiogenic drugs is being investigated for tumor treatment. Conversely, not only the delivery

of other drugs for tumor treatment but also radiation therapy rely on a good tumor blood supply. In any case, knowledge of tumor vascularity is crucial for successful therapeutic intervention. Accordingly, the histopathologic assessment of tumor vessels using endothelial cytology or staining techniques is being used to quantify angiogenesis, and has been shown to correlate to disease free-survival (Eberhard et al., 2000). The noninvasive assessment of tumor microvasculature is therefore of significant interest. Contrast-enhanced fast imaging has been used at standard clinical field strengths to indirectly evaluate the microvasculature of tumors by evaluating blood flow and volume parameters. Ultrahigh field SWI excels at depicting veins as small as 100 μm, and was used to study patients with brain tumors (Christoforidis et al., 2002, 2004). Studies comparing ultrahigh field BOLD venography with dynamic contrast-enhanced MRI at standard field strength, as well as studies correlating clinical outcome with 8-T MRI findings, are also under way.

Cerebrovascular Disease

Detailed assessment of microvasculature is also of interest in the assessment of cerebrovascular disease, and again ultrahigh field SWI shows great promise in this respect. Just as with standard clinical field strength MRI, subacute strokes are seen as sharply demarcated high signal areas at 8 T (Fig. 3.63). In addition, 8-T

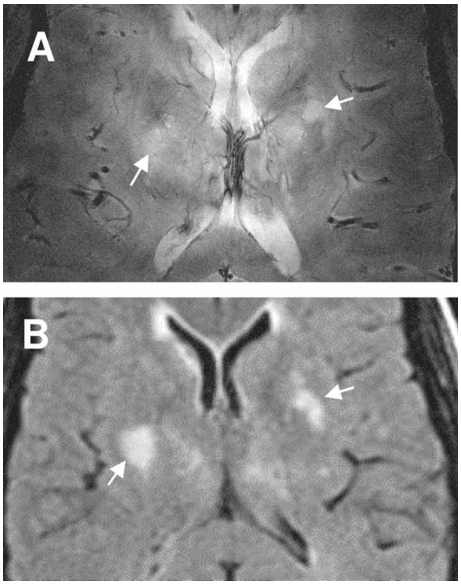

Fig. 3.63. (A) Axial 8 T susceptibility-weighted gradient echo image (TR/TE/flip = 700 ms/12 ms/22°, FOV 24 cm, 1024 × 1024 matrix, 2-mm slice thickness) compared to (B) 1.5 T FLAIR image. Multiple infarcts (white arrows) are seen as hyper-intensities on the FLAIR images and on the 8-T images. Small vessels surrounding the lesion are only delineated on the 8-T image.

SWI can depict subtle vascular abnormalities such as small cavernoma, hemorrhagic lesions, calcifications, and small lacunar infarcts (Novak et al., 2001, 2002; Chakeres et al., 2002), some of which were not seen at 1.5 T. This indicates that ultrahigh field MRI might play a significant role in the early assessment of factors that may precede stroke. To date, little is known of the relationship between known clinical risk factors or precursors such as hypertension or transient ischemic attacks, and underlying small (50–500 μm) vessel disease or silent microhemorrhagic lesions. Furthermore, ultrahigh field MRI may also play a role in the direct assessment of tissue oxygenation. Unfortunately, one potential limitation with ultrahigh field SWI is the greater sensitive to venous rather than to arterial disease. For the study of arterial disease at ≥ 7 T, the use of contrast agents may play an important role. Further studies are needed to assess the value of ultrahigh field SWI imaging in the evaluation of precursors for stroke, and the availability of user-friendly, standardized acquisition methods in a commercial ultrahigh field MRI system will be most helpful in this context.

Multiple Sclerosis

The higher spatial resolution achievable with ultrahigh field MRI is also of benefit for the assessment of multiple sclerosis (MS). At 8 T, demyelinating plaques are seen as high signal structures in both gradient and FSE images in typical locations, including the corpus callosum and periventricular regions system (Kangarlu et al., 2003). Beyond that, 8-T MRI excels at depicting the relationship between demyelinating lesions and deep venous structures. For example, so-called Dawson fingers – the central veins in the mid portions of plaques – were seen. Furthermore, direct visualization of gray matter MS lesions may be possible at high field. These initial studies show great promise, but many further investigations are required to fully exploit the potential advantages of ultrahigh field MRI for MS. In addition to high-resolution imaging, the assessment of MS with MR spectroscopy or diffusion-weighted imaging may be of interest.

Substantia Nigra and Parkinson's Disease

Idiopathic Parkinson's disease is associated with degeneration of the substantia nigra pars compacta, with selective loss of dopaminergic neurons. It is estimated that at least 60% of the dopaminergic neurons are lost before patients become symptomatic, preceded by 10 to 20 years of early disease progression. Calbindin D 28k immunohistochemical staining of the brainstem can differentiate the subanatomy of the substantia nigra (Damier et al., 1999), including five different regions termed *nigrosomes*. Parkinson's disease is characterized by severe focal loss of neurons in the nigrosomes, and progression of the clinical findings corresponds to focal cell loss in these specific regions.

Availability of a noninvasive imaging method to evaluate specific small subdivisions of the substantia nigra with great accuracy would be an essential biomarker in the assessment of Parkinson's disease. Preliminary 8-T phase images suggest that there is a close relationship between the low signal phase regions of the substantia nigra and the calbindin-staining regions. The substantia nigra demonstrated

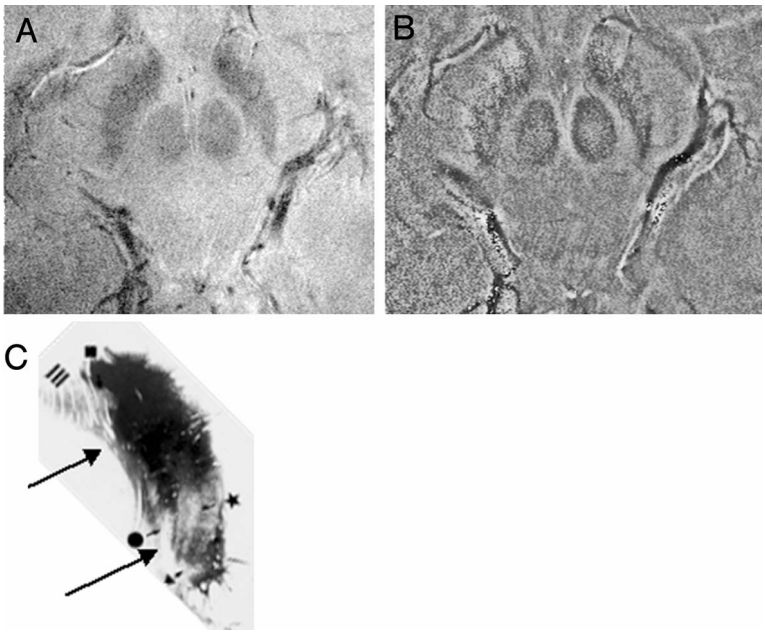

Fig. 3.64. Axial 8 T gradient echo magnitude (A) and phase (B) image human brainstem (TR/TE/flip angle 600 ms/12 ms/20°, FOV 18 cm, 1024 × 768, 2-mm slice thickness). Note that the margins of the substantia nigra appearing on the phase images are similar to the calbindin stains (C) with flame-like margins.

"flame" margins laterally on the phase images that correlated very well with calbindin staining (Fig. 3.64). Thus, ultrahigh field MRI may become an important new means of evaluating patients with Parkinson's disease.

Normal Aging and Alzheimer's Disease

It is well known that tissue iron content varies among different regions of the brain, and also changes with aging (Hallgren and Sourander, 1958). Paramagnetic tissue iron changes MRI relaxation times due to the diffusion of water molecules in the susceptibility field of the iron inclusions, and ultrahigh field MRI is particularly sensitive in this respect. Comparative contrast differences in T_2-weighted brain images of two subjects aged 27 years and 50 years at 1.5 T and 7 T are shown in Figure 3.65. For example, gray matter in the motorsensory cortex has a lower signal than adjacent white matter, and this difference is more pronounced in older than in younger subjects, whereas contrast is inverted in the frontal and temporal cortices. The signal is lowest in the globus pallidus, substantia nigra, red nuclei and caudate, all of which have much higher iron contents. Quantitative measurements of T_2-values exhibit a linear relationship to iron content computed from published values for iron content versus age. These initial studies suggest that ul-

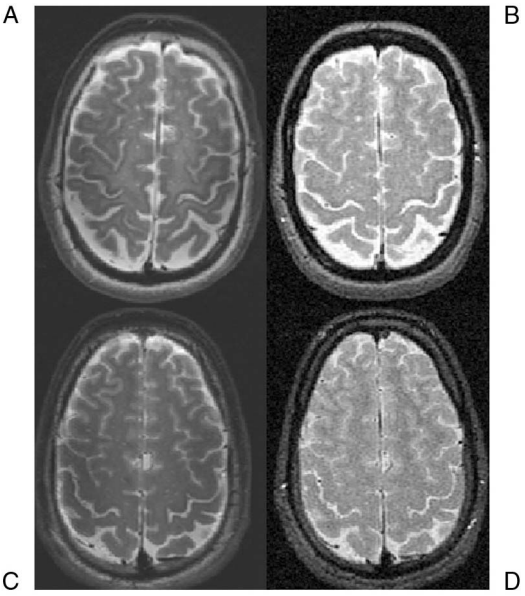

Fig. 3.65. Axial 1.5 T and 7 T T_2-weighted spin echo images of two healthy subjects aged 50 years (A, B) and 27 years (C, D). The 7-T images were acquired using a 7-T MRI (Philips, Cleveland, USA) and a single-echo spin-echo sequence with TR/TE 2000 ms/50 ms, FOV 24 cm, 256 × 192 matrix and 5-mm slice thickness; 1.5-T images used TE = 100 ms. Note the contrast inversion between frontal GM and WM and sensorimotor GM and WM that is especially pronounced in the older subject and at higher field strength.

trahigh field T_2-mapping may be more sensitive for assessing brain iron content than standard field strength MRI (Gelman et al., 1999; Georgiades et al., 2001; Zhou et al., 2001; Haacke et al., 2005), and thus is suited to the reliable quantification of iron in different regions of the brain and the assessment of aging.

Changes in brain iron content have also been associated with several neurodegenerative diseases, including Alzheimer's, Parkinson's and Huntington's disease. In Alzheimer's disease, oxidative stress has been implicated as one of the promoting factors, and is linked to brain iron content (Perry et al., 2000; Sayre et al., 2000); iron also appears to be associated with amyloid plaque (Smith et al., 1997). Because of this connection, several groups have attempted to measure brain iron with MRI as a biomarker for noninvasive assessment in Alzheimer's (Ordidge et al., 1994; Ogg et al., 1999; Bartzokis and Tishler, 2000; Schenck and Zimmerman, 2004). Ultrahigh field MRI should be significantly more sensitive than standard clinical field strength MRI, though further investigations in this area are clearly needed.

3.3.4.4 Conclusion and Outlook

Although ultrahigh field imaging offers great promise for a number of clinical applications, the hardware and software used will require careful design and modification compared to that of standard field strength MRI. For example, ultrahigh field MRI systems will require highly stable shims and gradients with minimal coupling between coils. Moreover, because susceptibility effects near air/tissue interfaces introduce severe B_0 inhomogeneity, more complex, higher-order shim coils will be needed, together with associated software to control these shims based on the magnetic field of individual acquisitions. Likewise, more complicated and expensive RF hardware, such as multiple transmitters with precise timing and phase control, will be needed for B_1 inhomogeneity correction. Again, additional software will be needed to control the multi-channel RF chain based on specific coil and head geometries.

Pulse sequences must be carefully designed and parameters adjusted, specifically for high-quality T_1-weighting, which is no longer achieved with simple gradient or spin echoes, but only with IR sequences. Overall, initial studies at 8 T showed that the most promising and successful image contrast behavior was related to tissue susceptibility effects. Due to the increased SNR at ultrahigh field strength, gradient echo images with in-plane resolution of 200–250 μm showed exquisite depiction of venous vasculature based on susceptibility effects from paramagnetic deoxyhemoglobin, providing very promising results for the imaging of brain tumors and cerebrovascular disease. Moderately T_2-weighted SE images may reflect paramagnetic tissue iron, while the advantages of ultrahigh field MRI for fMRI and MR spectroscopy has already been demonstrated (Ugurbil et al., 2003). Again, pulse sequences for spectroscopy and EPI sequences for fMRI must be optimized to provide satisfactory performance.

Finally, the early results obtained with a commercial 7-T MRI (Philips Achieva, Cleveland, USA) have shown great promise. For example, both time-of-flight and phase-contrast MR angiography were seen to be feasible at 7 T, with initial findings suggesting that vessel conspicuity is improved compared to lower field strength. Another highly promising sequence was that of the 3D IR magnetization-prepared fast gradient sequence, which combines excellent T_1 contrast with depiction of bright arteries with short TE (2–3 ms), and/or dark veins with long TE (7–12 ms). The use of these and many other MRI methods have yet to be fully explored over a wide range of clinical applications.

References

Abduljalil, A.M., Schmalbrock, P., Novak, V., and Chakeres, D.W. (2003). Enhanced gray and white matter contrast of phase susceptibility-weighted images in ultra-high field magnetic resonance imaging. *J. Magn. Reson. Imag.*, **18**, 284–290.

Bartzokis, G. and Tishler, T.A. (2000). MRI evaluation of basal ganglia ferritin iron and neurotoxicity in Alzheimer's and Huntington's disease. *Cell. Mol. Biol. (Noisy-le-grand)*, **46**, 821–833.

Bartha, R., Michaeli, S., Merkle, H., Adriany, G., Anderson, P.M., Chen, W., Ugurbil, K., and Garwood, M. (2002). In vivo $1H_2O$ T2+ measurement in the human occipital lobe at 4 T and 7 T by Carr Purcell MRI: detection of microscopic susceptibility contrast. *Magn. Reson. Med.*, **47**, 742–750.

Bottomley, P.A., Foster, T.H., Argensinger, R.E., and Pfeifer, L.M. (1984). A review of normal tissue hydrogen NMR relaxation times and relaxation mechanism from 1–100 MHz – Dependences on tissue type NMR frequency, temperature, species, excision and age. *Med. Phys.*, **11**, 425–448.

Carr, H.Y. and Purcell, E.M. (1954). Effects of diffusion on free precession in nuclear magnetic resonance experiments. *Phys. Rev.*, **94**, 630–638.

Chakeres, D.W. and de Vocht, F. (2004). Static magnetic field effects on human subjects related to magnetic resonance. *Prog. Biophys. Mol. Biol.*, **87**, 255–265.

Chakeres, D.W., Abduljalil, A.M., Novak, P., and Novak, V. (2002). Comparison of 1.5 and 8 Tesla high-resolution magnetic resonance imaging of lacunar infarcts. *J. Comput. Assist. Tomogr.*, **26**, 628–632.

Chakeres, D.W., Bornstein, R., and Kangarlu, A. (2003a). Randomized comparison of cognitive function in humans at 0 and 8 Tesla. *J. Magn. Reson. Imaging*, **18**, 342–345.

Chakeres, D.W., Kangarlu, A., Boudoulas, H., and Young, D. (2003b). Effect of up to 8 Tesla static magnetic field exposure on sequential human vital signs measurements. *J. Magn. Reson. Imaging*, **18**, 346–352.

Chen, J., Feng, Z., and Jin, J.M. (1998). Numerical simulation of SAR and B_1-field inhomogeneity of shielded RF coils loaded with the human head. *IEEE Trans. Biomed. Eng.*, **45**, 650–659.

Cho, Z.H. and Ro, Y.M. (1992). Reduction of susceptibility artifacts in gradient echo imaging. *Magn. Reson. Med.*, **23**, 193–200.

Christoforidis, G.A., Grecula, J.C., Newton, H.B., Kangarlu, A., Abduljalil, A.M., Schmalbrock, P., and Chakeres, D.W. (2002). Visualization of microvascularity within glioblastoma multiforme utilizing 8 Tesla high-resolution magnetic resonance imaging. *Am. J. Neuroradiol.*, **23**, 1553–1556.

Christoforidis, G.A., Kangarlu, A., Abduljalil, A.M., Schmalbrock, P., Chaudhury, A., Yates, A., and Chakeres, D.W. (2004). Susceptibility-based imaging of glioblastoma microvascularity at 8 T: Correlation of MR Imaging and post-mortem pathology. *Am. J. Neuroradiol.*, **25**, 756–760.

Collins, C.M., Yang, Q.X., Wang, J.H., Zhang, X., Liu, H., Michaeli, S., Zhu, X.H., Adriany, G., Vaughan, J.T., Merkle, H., Ugurbil, K., Smith, M.B., and Chen, W. (2002). Different excitation and reception distributions with a single loop transmit-receive surface coil near a head sized spherical phantom at 300 MHz. *Magn. Reson. Med.*, **47**, 1026–1028.

Damier, P., Hirsch, E.C., Agid, Y., and Graybiel, A.M. (1999). The substantia nigra of the human brain I. Nigrosomes and the nigral matrix, a compartmental organization based on calbindin D(28K) immunohistochemistry. *Brain*, **122**, 1421–1436.

Dashner, R., Kangarlu, K., Clark, D., RayChaudhury, A., and Chakeres, D. (2004). Limits of 8 Tesla magnetic resonance imaging spatial resolution of the deoxygenated cerebral microvasculature. *J. Magn. Reson. Imaging*, **19**, 303–307.

Eberhard, A., Kahlert, S., Goede, V., Hemmerlein, B., Plate, K.H., and Augustin, J.G. (2000). Heterogeneity for angiogenesis and blood vessel maturation in human tumors: implications for anti-angiogenic tumor therapies. *Cancer Res.*, **60**, 1388–1393.

Gelman, N., Gorell, J.M., Barker, P.B., Savage, R.M., Spickler, E.M., Windham, J.P., and Knight, R.A. (1999). MR imaging of human brain at 3.0 T: preliminary report on transverse relaxation rates and relation to estimated iron content. *Radiology*, **210**, 759–767.

Georgiades, C.S., Itoh, R., Golay, X., van Zijl, P.C.M., and Melhem, E.R. (2001). MR imaging of the human brain at 1.5 T: Regional variations in transverse relaxation rates in the cerebral cortex. *Am. J. Neuroradiol.*, **22**, 1732–1737.

Glover, G.H. (1999). 3D z-shim method for reduction of susceptibility effects in BOLD fMRI. *Magn. Reson. Med.*, 290–299.

Haacke, E.M., Brown, R.W., Thompson, M.R., and Venkatesan, R. (1999). *Magnetic Resonance Imaging: Physical Principles and Sequence Design*, Wiley.

Haacke, E.M., Cheng, N.Y.C., House, M.J., Liu, Q., Neelavalli, J., Ogg, R.J., Khan, A., Ayaz, M., Kirsch, W., and Obenaus, A. (2005). Imaging iron stores in the brain using magnetic resonance imaging. *Magn. Reson. Imaging*, **23**, 1–25.

Hahn, E.L. (1950). Spin echoes, *Phys. Rev.*, **4**, 580–594.

Hallgren, B. and Sourander, P. (1958). The effect of age on the non-haemin iron in the human brain. *J. Neurochem.*, **3**, 41–51.

Hennig, J. (1988). Multiecho imaging sequences with low refocusing flip angles. *J. Magn. Reson.*, **78**, 397–407.

Hennig, J. and Scheffler, K. (2001). Hyperechoes. *Magn. Reson. Med.*, **46**, 6–12.

Hennig, J., Weigel, M., and Scheffler, K. (2003). Multiecho sequences with variable refocusing flip angles: optimization of signal behavior using smooth transitions between pseudo steady states (TRAPS). *Magn. Reson. Med.*, **49**, 527–535.

Hoult, D.I. (2000). The principle of reciprocity in signal strength calculations – a mathematical guide. *Concepts Magn. Reson.*, **12**, 173–187.

Ibrahim, T.S., Lee, R., and Robitaille, P.M. (2001). Effects of RF coil excitation on field inhomogeneity at ultra high fields: a field optimized TEM resonator. *Magn. Reson. Imaging*, **19**, 1339–1347.

Ibrahim, T.S., Mitchell, C., Schmalbrock, P., Lee, R., and Chakeres, D.W. (2005). Electromagnetic perspective on the operation of RF coils at 1.5–11.7 Tesla. *Magn. Reson. Med.*, **54**, 683–690.

Irarrazabal, P., Meyer, C.M., Nishimura, D.G., and Macovski, A. (1996). Inhomogeneity correction using an estimated linear field map. *Magn. Reson. Med.*, **35**, 278–282.

Jensen, J.H., Chandra, R., and Yu, H. (2001). Quantitative model for the interecho time dependence of the CPMG relaxation rate in iron rich gray matter. *Magn. Reson. Med.*, **46**, 159–165.

Kadah, Y.M. and Hu, X. (1998). Algebraic reconstruction for magnetic resonance imaging under B0 inhomogeneity. *IEEE Trans Med Imaging*, **17**, 362–370.

Kangarlu, A., Rammohan, K.W., Bourekas, E.C., and Chakeres, D.W. (2003). In vivo microscopic imaging of multiple sclerosis with high field MRI. In: Filippi, M., Comi, G. (Eds.), *New Frontiers of MR-based techniques in Multiple sclerosis*. Springer.

Kennan, R.P., Zhong, J., and Gore, J.C. (1994). Intravascular susceptibility contrast mechanisms in tissue. *Magn. Reson. Med.*, **31**, 9–21.

Kingsley, P.B., Ogg, R.J., Reddick, W.E., and Stehen, R.G.: Correction of errors caused by imperfect inversion pulses in MR imaging measurements of T_1 relaxation times. *Magn. Reson. Imaging*, **16**, 1049–1055.

Kiselev, V.G. and Novikov, D.S. (2002). Transverse NMR relaxation as a probe of mesoscopic structure. *Phys. Rev. Lett.*, **89**, 27.

Laurent, W.M., Bonny, J.M., and Renou, J.P. (2000). Imaging of water and fat fractions, in high-field MRI with multiple slice chemical shift-selective inversion recovery. *Magn. Reson. Imaging*, **12**, 488–496.

Lei, H., Zhu, X.H., Zhang, X.L., Ugurbil, K., and Chen, W. (2003). In vivo P-31 magnetic resonance spectroscopy of the human brain at 7 T: an initial experience. *Magn. Reson. Med.*, **49**, 199–205.

Li, S., Dardzinski, B.J., Collins, C.M., and Yang, Q.X., Smith, M.B. (1996). Three dimensional mapping of the static magnetic field inside the human head. *Magn. Reson. Med.*, **36**, 705–714.

Novak, V., Kangarlu, A., Abduljalil, A.M., Novak, P., Slivka, A., Chakeres, D.W., and Robitaille, P.M. (2001). Ultrahigh field MRI at 8 T of subacute hemorrhagic Stroke. *J. Comput. Assist. Tomogr.*, **25**, 431–435.

Novak, V., Abduljalil, A., Chowdhary, A., Farrar, B., Braun, J.E., Novak, P., Slivka, A., and Chakeres, D. (2002). Impaired vasomotor reserve and 8 Tesla MRI in stroke. *Stroke*, **33**, 366–366.

Ogg, R.J., Langston, J.W., Haacke, E.M., Stehen, R.G., and Taylor, J.S. (1999). The correlation between phase shifts in gradient-echo MR images and regional brain iron concentration. *Magn. Reson. Imaging*, **17**, 1141–1148.

Ordidge, R.J., Gorell, J.M., Deniau, J.C., Knight, R.A., and Helpern, J.A. (1994). Assessment of relative brain iron concentrations using T_2-weighted and T_2^* weighted MRI at 3 T. *Magn. Reson. Med.*, **32**, 335–341.

Perry, G., Raina, A.K., Nunomura, A., Wataya, T., Sayre, L.M., and Smith, M.A. (2000). How important is oxidative damage? Lessons from Alzheimer's disease. *Free Radic. Biol. Med.*, **28**, 831–834.

Pruessmann, K.P., Weiger, M., Scheidegger, M.B., and Boesiger, P. (1999). SENSE: Sensitivity encoding for fast MRI. *Magn. Reson. Med.*, **42**, 952–962.

Reichenbach, J.R. and Haacke, E.M. (2001). High resolution BOLD venographic imaging: a window into brain function. *NMR Biomed.*, **14**, 453–467.

Reichenbach, J.R., Essig, M., Haacke, E.M., Lee, B.C., Przetak, C., Kaiser, W.A., and Schad, L.R. (1998). High-resolution venography of the brain using magnetic resonance imaging. *MAGMA*, **6**, 62–69.

Robitaille, P.M.L., Abduljalil, A.M., and Kangarlu, A. (2000). Ultrahigh resolution imaging of the human head at 8 Tesla, 2Kx2K for Y2K. *J. Comput. Assist. Tomogr.*, **24**, 2–8.

Sayre, L.M., Perry, G., Atwood, C.S., and Smith, M.A. (2000). The role of metals in neurodegenerative diseases. *Cell. Mol. Biol. (Noisy-le-grand)*, **46**, 731–741.

Schenck, J.F. and Zimmerman, E.A. (2004). High-field magnetic resonance imaging of brain iron: birth of a biomarker? *NMR Biomed.*, **17**, 433–445.

Smith, M.A., Harris, P.L.R., Sayre, L.M., and Perry, G. (1997). Iron accumulation in Alzheimer disease is a source of redox-generated free radicals. *Proc. Natl. Acad. Sci. USA*, **94**, 9866–9868.

Sodickson, D.K. and Manning, W.J. (1997). Simultaneous acquisition of spatial harmonics (SMASH): fast imaging with radiofrequency coil arrays. *Magn. Reson. Med.*, **38**, 591–603.

Spielman, D.M., Adalsteinson, E., and Lim, K.O. (1998). Quantitative assessment of improved inhomogeneity using higher order shims for spectroscopic imaging of the brain. *Magn. Reson. Med.*, **40**, 376–382.

Stenger, V.A., Boada, F.E., and Noll, D.C. (2002). Multishot 3D slice-select tailored RF pulses for MRI. *Magn. Reson. Med.*, **48**, 157–165.

Stefanovic, B., Sled, J.G., and Pike, G.B. (2003). Quantitative T2 in the occipital lobe: the role of the CPMG refocusing rate. *J. Magn. Reson. Imaging*, **18**, 302–309.

Tofts, P. (2003). *Quantitative MRI of the Brain*. Wiley.

Truong, T.K., Clymer, B.D., Chakeres, D.W., and Schmalbrock, P. (2002). Three-dimensional numerical simulations of susceptibility-induced magnetic field inhomogeneities in the human head at 8 Tesla. *Magn. Reson. Imaging*, **20**, 759–770.

Truong, T.K., Chakeres, D.W., and Schmalbrock, P. (2006). Effects of static and radiofrequency magnetic field inhomogeneity in ultra-high field magnetic resonance imaging. *Magn. Reson. Imag.*, **24**, 103–112.

Ugurbil, K., Adriany, G., Andersen, P., Chen, W., Garwood, M., Gruetter, R., Henry, P.G., Kim, S.G., Lieu, H., Tkac, I., Vaughan, T., Van De Moortele, P.F., Yacoub, E., and Zhu, X.H. (2003). Ultrahigh field magnetic resonance imaging and spectroscopy. *Magn. Reson. Med.*, **21**, 1263–1281.

Vaughan, J.T., Hetherington, H.P., Otu, J.O., Pan, J.W., and Pohost, G.M. (1994). High frequency volume coils for clinical NMR imaging and spectroscopy. *Magn. Reson. Med.*, **32**, 206–218.

Weisskoff, R.M., Zuo, C.S., Boxerman, J.L., and Rosen, B.R. (1994). Microscopic susceptibility variation and transverse relaxation theory and experiment. *Magn. Reson. Med.*, **31**, 601–610.

Wilson, J.L., Jenkinson, M., and Jezzard, P. (2002) Optimization of static field homogeneity in human brain using diamagnetic passive shims. *Magn. Reson. Med.*, **48**, 906–914.

Yablonskiy, D.A. and Haacke, E.M. (1994). Theory of NMR signal behavior in magnetically inhomogeneous tissues: the static dephasing regimen. *Magn. Reson. Med.*, **32**, 749–763.

Yablonskiy, D.A. and Haacke, E.M. (1997). An MRI method for measuring T_2 in the presence of static and RF magnetic field inhomogeneities. *Magn. Reson. Med.*, **37**, 872–876.

Yacoub, E., Duong, T.Q., Van de Moortele, P.F., Lindquist, M., Adriany, G., Kim, S.G., Ugurbil, K., and Hu, X. (2003). Spin-echo fMRI in humans using high spatial resolutions and high magnetic fields. *Magn. Reson. Med.*, **49**, 655–664.

Yang, Q.X., Williams, G.D., Demeure, R.J., Mosher, T.J., and Smith, M.B. (1998). Removal of local field gradient artifacts in T_2^*-weighted images at high fields by gradient-echo slice excitation profile imaging. *Magn. Reson. Med.*, **39**, 402–409.

Ye, F.Q., Martin, W.R.W., and Allen, P.S. (1996). Estimation for the iron concentration in excised gray matter by means of proton relaxation measurements. *Magn. Reson. Med.*, **35**, 285–289.

Zhou, J., Golay, X., van Zijl, P.C., Silvennoinen, M.J., Kauppinen, R., Pekar, J., and Kraut, M. (2001). Inverse T(2) contrast at 1.5 Tesla between gray matter and white matter in the occipital lobe of normal adult human brain. *Magn. Reson. Med.*, **46**, 401–406.

3.3.5
Interventional Magnetic Resonance Imaging: Concepts, Systems, and Applications

Clifford R. Weiss and Jonathan S. Lewin

3.3.5.1
Introduction

"*Primum non nocere* ... first, do no harm," is a central doctrine in the practice of medicine. This desire to help without hurting has driven medicine to develop minimally invasive methods of diagnosing and treating disease. It is not surprising, then, that over the past three decades medicine has evolved an increasing emphasis on image-guided intervention, traditionally using fluoroscopy, ultrasound, and computed tomography (CT). Most recently, however, radiologists' interventional skills and trends towards minimally invasive surgery have created a burgeoning interest in the use of magnetic resonance imaging (MRI) for guidance in interventional procedures.

To date, the range of MR-guided interventions has included biopsies, ablation procedures, cardiovascular applications, and intraoperative guidance in almost every organ system. The main advantages of using MRI to guide interventions (Lewin, 1999; Lewin et al., 2000) are as follows:

- *MR provides unparalleled soft tissue contrast and exquisite anatomic detail without the use of contrast*. This allows both for the identification of target lesions that are often not seen using other imaging modalities, and for the visualization of anatomy surrounding the target, which aids in preventing "collateral damage" during the procedure.
- *MR provides the unique ability to elicit different tissue characteristics during a procedure with the use of different pulse sequences*. More advanced functional information can also be obtained such as flow, perfusion, diffusion, as well as spectroscopic data. These functional capabilities can further aid in distinguishing pathology from anatomy, directing interventions towards the most promising locations, and determining the endpoint of an intervention.
- *MR provides multiplanar capabilities which allow for tracking of the interventional needle, probe or catheter, in any imaginable plane*. This allows for precise localization of the intervention and for extensive, "on the fly" (i.e., in real time) procedural customization.
- *MR provides the ability to continuously visualize vessels throughout the procedure without the need for intravenous contrast*. This is particularly useful with vascular interventions, although the conspicuity of vascular structures also helps to avoid serious complications during other interventional procedures.

- *MR provides the ability to perform interventions without the use of ionizing radiation.* This is of particular importance to younger patients who are imaged regularly, as well as to interventional radiologists/cardiologists and their staff who are exposed to radiation while performing numerous procedures each day.
- *MR provides the ability to monitor temperature changes in tissue during a procedure, which is of particular importance in thermal ablation procedures.*

Historically, relatively long imaging times, an inability to image the patient in real-time, and difficulty in patient access resulting from closed-bore superconducting cylindrical system designs, have combined to make MR an unlikely guidance modality for interventional procedures. More recently, many of these disadvantages have been overcome with newly designed system hardware, pulse sequence improvements, and user interface systems, which have allowed the development of rapid imaging on more open systems. The aim of this section is briefly to discuss the hardware and software improvements that have made interventional MRI a reality. In addition, the use of this technology for minimally invasive procedures and the technical issues specific to MR image-guidance will be described.

3.3.5.2 Imaging System Development

Advances in magnet and system design have accelerated progress in MR-guided intervention. Many different MR system configurations have been used to guide percutaneous procedures, and each of these systems has advantages and disadvantages for interventional imaging, there being a constant trade-off between signal-to-noise, access to the patient, useable field of view, and expense.

Understanding the role of different MR system designs in intervention requires a distinction to be made between image *guidance* and procedure *monitoring*. There are many procedures in which the information provided by MRI can be used to *monitor* a therapeutic intervention. MR has been used to monitor ablation procedures, in which thermal energy is deposited into a lesion and the resulting tissue changes are continuously or intermittently observed, and surgical interventions, in which the status of tumor resection or cyst aspiration may be intermittently examined. These forms of interventional MRI require much less modification to standard imaging systems because access to the patient is not necessarily required during the monitoring process. Consequently, both were performed in the early days of interventional MR on conventional cylindrical superconducting systems.

The use of MRI for interventional procedure *guidance* includes its use by radiologists during the manipulation of needles, electrodes, catheters, or laser fibers, and its application by surgeons to guide endoscopes, scalpels, or curettes. This form of intervention is more active and requires a significant departure from conventional diagnostic concepts and traditional imaging systems. The most basic form of this type of guidance can be provided from a retrospective data set through the use of frameless or frame-based stereotactic systems, though increasing emphasis has

been on the use of real-time or near-real-time guidance for interventional MRI procedures.

The factors contributing to high image quality in diagnostic MR include system field strength and the homogeneity and stability of the static and gradient magnetic fields. These factors are most obtainable by decreasing the ''openness'' of an imaging system. The optimal design of a magnet with regard to field homogeneity would be a complete sphere, without opening (Hinks et al., 1998). In contrast, the environment best suited to radiological or surgical intervention is one with maximum access to the patient, allowing complete freedom in interventional approach, and maintaining close proximity of monitoring and therapeutic devices. These attributes are in direct opposition to those facilitating image quality (Hinks et al., 1998). The use of MRI for the guidance of interventional procedures has required compromise between these opposing forces; this balance has been achieved through a number of different concepts and solutions, as described below.

Cylindrical Superconducting Systems

From an image quality point of view, cylindrical superconducting systems enjoy significant advantages, and because of this they have become the standard for image quality in the diagnostic arena. Until recently, this superior image quality has come with a price, namely severely limited access to and visualization/monitoring of patients during procedures. These limitations have traditionally allowed the successful performance of only certain procedures, primarily the monitoring of therapy and not procedure guidance. The excellent signal-to-noise ratio (SNR) achieved with these systems is well suited to temperature monitoring during radiofrequency (RF) and other thermal ablation procedures (Nour and Lewin, 2005b). Typically, however, the ablation probes have been inserted under CT guidance, or have used a neurosurgical stereotactic approach based on retrospective MR data.

One important area of research has been the development of MR methods for the guidance of angiographic procedures, with success performing intravascular procedures such as atrial septal puncture and directed myocardial injections of stem cells using only MR guidance (Arepally et al., 2005; Rickers et al., 2005). The relatively recent development of shorter-bore superconducting systems has allowed more access to the patient's groin. Several groups are investigating the use of this type of system for catheter-based intervention, with the radiologist controlling the procedure from the groin near the magnet aperture (Rickers et al., 2005; Wacker et al., 2005). Recently, small patient series have demonstrated that MR-guided cardiac and vascular interventions, including cardiac catheterization and lower-extremity angioplasty/stenting are safe and practical in patients (Razavi et al., 2003; Paetzel et al., 2004; Dick et al., 2005).

Numerous vendors have begun to produce hybrid XMR units that place MR and X-ray fluoroscopic equipment in close proximity (Fig. 3.66). These systems exploit the strengths of MRI (superb soft tissue resolution, tissue characterization, and multiplanar imaging) with the strengths of X-ray fluoroscopy (high-resolution real-time projection and extensive operator experience). The operator can easily al-

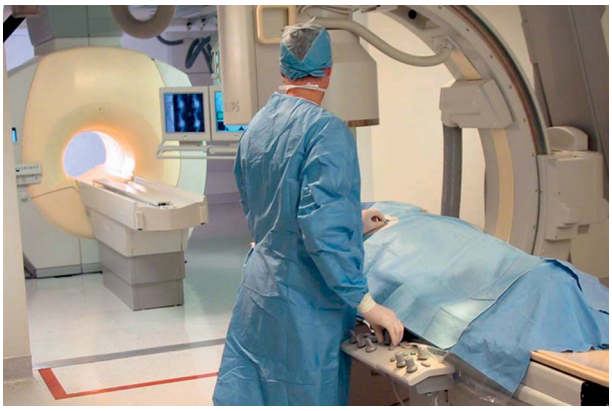

Fig. 3.66. Example of a suite for combined radiography and MRI studies, in this case, the UCSF Interventional XMR Suite (University of California, San Francisco). A patient can be moved rapidly and without repositioning on the patient table between the C-arm in the foreground (used for X-ray fluoroscopy) and the MR scanner in the background. The C-arm can be used for initial positioning of catheters, whereas the MR scanner is used for MR-guided procedures. Flat-panel displays suspended from the ceiling next to the bore of the MR magnet can be used for simultaneous display of MR and radiographic images for procedure guidance. (Courtesy of A. Martin, PhD, San Francisco, California; reprinted from Rickers et al., 2005, with permission from Elsevier).

ternate between the two modalities, without violating the sterile surgical field or re-zeroing the patient. XMR systems can also be used to monitor the effects of X-ray fluoroscopy-guided treatments such as angioplasty or atrial septal defect closures, by using MR to evaluate the site of intervention and the downstream organ system (e.g., kidney or myocardium) immediately following intervention.

In an attempt to provide more access to the patient without sacrificing high field image quality, vendors have begun producing cylindrical superconducting magnets with even shorter and wider bores. An excellent example of one such system is the 1.5 T Magnetom Espree by Siemens Medical Solutions. With a bore length of 1.25 m and a bore width of 70 cm, this system makes MR-guided interventions similar to procedures performed under CT guidance.

"Double Donut" Configuration

Another novel approach to obtaining access to a patient in a cylindrical system is exemplified in the "double donut" configuration of the Signa SP system (General Electric Health Care, Milwaukee, Wisconsin, USA) designed specifically for interventional applications. This design has taken the central segment out of a cylindrical system, thereby allowing patient access from the sides and top at the isocenter of the imaging system. This system has been used both to guide and to monitor a large number of surgical procedures and has been used in several published series of biopsies and aspirations.

Biplanar Magnet Designs

Another approach that has found widespread application for diagnostic MRI in the burgeoning "open MR" imaging market has been the use of a biplanar magnet design. With these magnets, the patient is positioned between flat magnetic poles, thereby leaving patient access from a range of side approaches. The biplanar concept has the advantage of a fairly homogeneous static magnetic field, but it is limited to lower field strength than cylindrical superconducting designs. The side access provided by these systems is analogous to that of C-arm fluoroscopy, and is amenable to needle- or catheter-directed procedures (Lewin, 1999).

3.3.5.3

Supplemental Technical Developments

There are several technical developments that are common to many of the magnet and system designs discussed above that have facilitated the guidance phase of interventional procedures. One development that has impacted the use of MR methods for procedure guidance has been the development of *fast MR pulse sequences* for use in interactive guidance during device placement. Currently, frame rates of between 10 and 20 frames per second can be achieved with millimeter resolution in all three axes. This combination of high speed and resolution has been achievable through the development of fast gradient-echo pulse sequences, modifications in *k*-space sampling and parallel imaging techniques (Blanco et al., 2005; Derakhshan and Duerk, 2005). In order to further increase the imaging speed in fluoroscopic application, strategies such as keyhole imaging update the central portion of *k*-space more frequently than the periphery, thereby preferentially updating the most prominent features in the acquired image. Other strategies include LoLo, reduced field of view imaging, segmented *k*-space, wavelet encoding, and non-Cartesian *k*-space sampling using spiral or radial trajectories. Parallel acquisition of image data using techniques such as SMASH and SENSE can reduce scan time by using the local spatial information that can be acquired from each coil within a phased array to reduce the number of phase-encoding steps without reducing in-plane resolution (Derakhshan and Duerk, 2005).

An innovation of significant benefit for MR-guided interventions has been the development of *trackable interventional devices*. Typically, these systems have interfaced an optically-linked 3D digitizer with the measurement control software of the MR imager. The 3D digitizer continuously relates spatial information to the measurement control software, which can then automatically adjust the scan plane orientation to visualize the interventional device (Rickers et al., 2005; Wacker et al., 2005).

Different visualization and tracking techniques have been developed for the flexible catheters used in cardiovascular interventional procedures (Wacker et al., 2005). Methods for catheter visualization can be roughly divided into three categories, namely passive, active, and semi-active. The difference is mainly based on whether the catheter functions as a receive antenna (active and semi-active), or

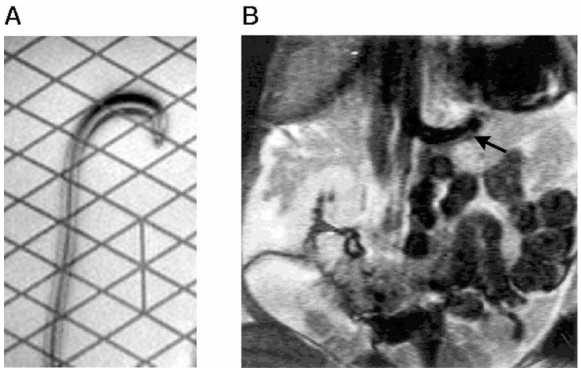

Fig. 3.67. Susceptibility artifact-based angiography catheter visualization. (A) MR image of a 5F C1-iron oxide containing a susceptibility artifact inducing angiographic catheter in a gel phantom. (B) True fast imaging with steady-state precession images acquired in a 0.2-T open magnet during insertion of the iron oxide-containing angiographic catheter (arrow) shown in (A). The catheter was advanced though the suprarenal aorta into the splenic artery. (Reprinted from Wacker et al., 2005, with permission from Elsevier).

whether its detection is based on a characteristic signature on images acquired with external coils (passive).

The passive approach relies on the field distortions or susceptibility artifacts that normally occur around the tips of standard catheters. These artifacts can be accentuated by impregnating the catheter with paramagnetic or ferromagnetic substances which then appear as areas of signal loss/distortion on the MR image (Fig. 3.67). Alternatively, filling a catheter with a contrast agent such as gadolinium will create bright signal spots on T_1-weighted images. The primary benefit of passive visualization is that there are very few concerns regarding RF heating. The major drawbacks are that susceptibility artifacts can be difficult to see, and that a passive catheter cannot be coupled directly to the MR system to supply real-time spatial coordinates for automated catheter tracking (Wacker et al., 2005).

The active approach to visualization incorporates a resonant circuit (microcoil) into the catheter tip, which is then coupled to a receive channel on the MR scanner. The position of the catheter can then be visualized based on the bright signal generated by the resonant circuit. The signal from the catheter can be reconstructed separately and superimposed on the background MRI image acquired with the surface coils (Figs. 3.68 and 3.69). Furthermore, actively tracked coils generate spatial coordinates for the catheter tip which allows for easy automated scan plane adjustment. The major concern with actively visualized catheters has been RF heating (Wacker et al., 2005).

Active devices without a wired connection to the scanner can also be constructed; these contain tuned resonant circuits that are inductively coupled to surface coils rather than being connected capacitively to the MR system (Quick et al., 2005).

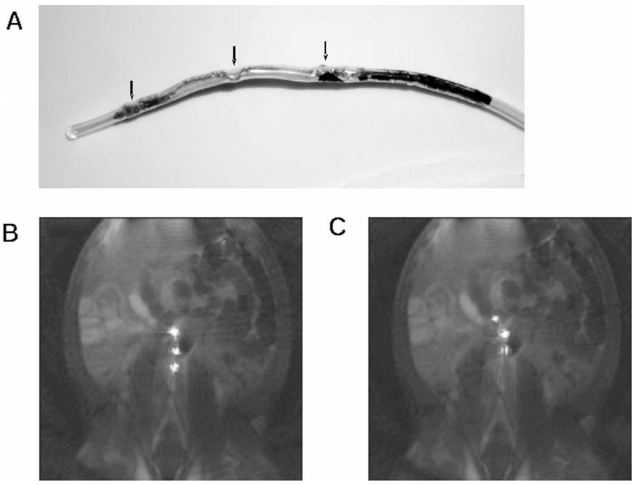

Fig. 3.68. Three-marker tracking coil. (A) Three geometrically separated micro-loops (arrows) are part of an active radiofrequency micro-antenna attached to the tip of a conventional angiographic catheter. (B, C) Images from a tracking experiment. The three-marker tracking coil is actively guided through the abdominal aorta (B) into the right renal artery (C) of a pig. (Reprinted from Wacker et al., 2005, with permission from Elsevier).

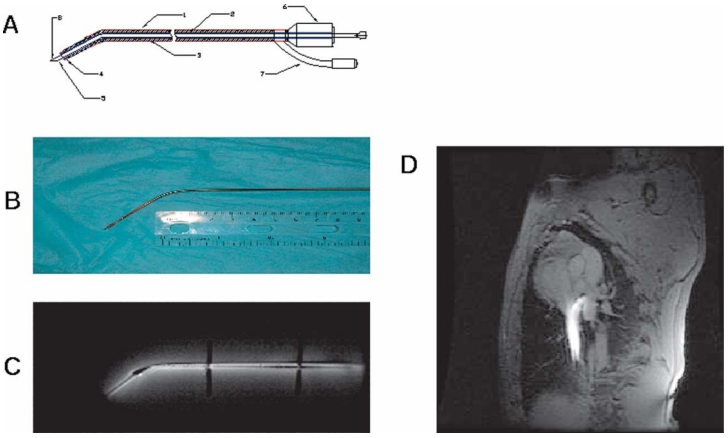

Fig. 3.69. Actively tracked intravascular needle system. (A) The needle is constructed from concentrically configured nitinol hypo-tubings arranged to form a loopless antenna, with RF circuitry that matches MR scanner. (B) Photograph of the intravascular needle antenna and (C) an image acquired by the needle in a saline phantom using an FGRE pulse sequence. (D) Image from an MR-guided atrial septal puncture experiment. The actively tracked needle has been guided into the right atrium of a pig. (Adapted from Arepally et al., 2005, with permission).

The resonant circuits provide local gain to the RF pulse and enhance the nearby signal. Because the catheter does not need to be connected to the MR system by long wires, the risk of MR heating is reduced, and catheter handling is facilitated. However, this lack of connection does not provide the MR system with the catheter's spatial coordinates, making automated image adjustment more difficult. If desired, this coil can be optically de-tuned over a fiber-optic link, so that the degree of signal intensity around the catheter tip can be controlled by the operator and the risk of RF heating can be reduced (Wong et al., 2000).

Another similar development, of particular importance to MR-guided cardiovascular interventions, has been the development of intravascular antennae. The designs generally include either wire loops or loopless antennae (Wacker et al., 2005). Loopless antennae are more compact, perform at any orientation, and demonstrate a lower sensitivity drop off than do the wire loop configurations. These antennae have been used for both transvascular and transesophageal vascular imaging (Shunk et al., 2001; Hofmann et al., 2005). When placed into a percutaneous biliary drainage tube, these antennae have even proven useful in assessing malignant biliary obstruction (Arepally and Weiss, 2005). Recent investigations have also shown that it is possible to design an expandable vascular stent to serve as an in-place intravascular antenna. This endovascular stent was designed to be a high-frequency resonator which can be inductively coupled to an external antenna and may prove useful in monitoring vessel patency after stenting (Kivelitz et al., 2003).

Interventional MR requires a more interactive approach than does diagnostic MR because the interventionalist must be able to see the device and its surroundings at all times during the procedure. Systems have been designed which provided automatic slice tracking by using the spatial coordinate information provided by an active catheter to perform automatic image plane adjustment. This keeps the catheter tip in view, without needing manual adjustment of the scan plane. Adaptive imaging systems combine active catheter tracking with automated control of various imaging parameters to switch automatically between rapid, real-time imaging during rapid catheter movement, and slower high spatial resolution scanning while the catheter remains stationary, without the need for manual adjustment. A number of user-interfaces have been developed to provide the operator with as much interactive control over scan and reconstruction algorithms as possible, along with visualization modes to allow for device manipulation in a 3D-rendered environment (Rickers et al., 2005; Wacker et al., 2005) (Fig. 3.70).

3.3.5.4 Specific Applications

When combined with the inherent benefits of MRI, the above-described technical developments have allowed for – and have been driven by – the development of a broad range of interventional MR applications. In broad terms these can be divided into MR-guided biopsies and percutaneous therapies, MR-guided cardiovascular and endovascular interventions, and intraoperative MRI. Intraoperative MRI is a well-established MR application, but is beyond the scope of this discussion.

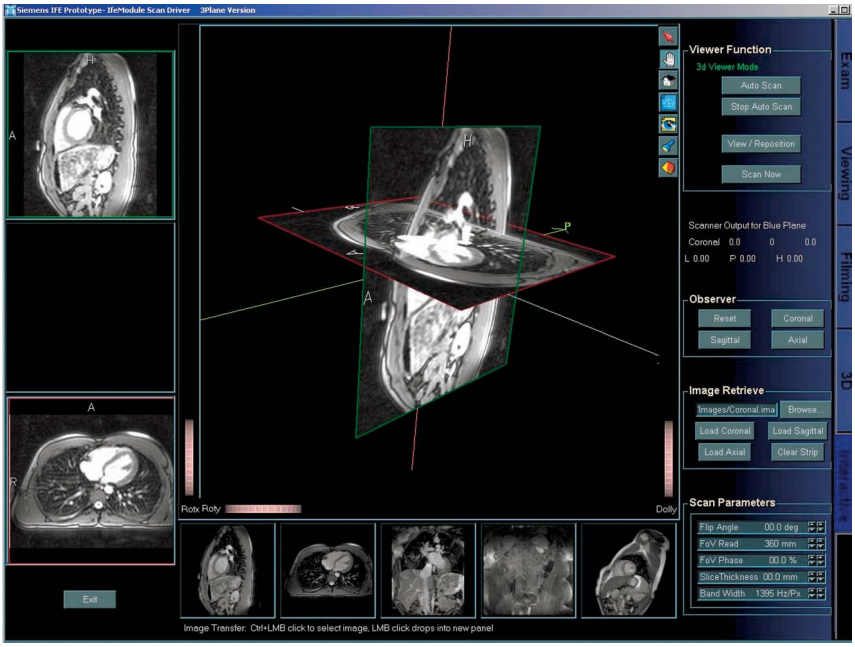

Fig. 3.70. Example of a user interface developed for real-time imaging and interactive scan control to facilitate MR-guided interventional procedures. In this screenshot, the interface is used to control the acquisition of images of the heart, including the standard short- and long-axis views, which are combined in the main viewing window to show the relative orientation of these two views, updated in real time. This system can be used to visualize cardiac motion while the image planes remain fixed or can be used for active slice manipulation so that slices can track catheter tip location. (Reprinted from Rickers et al., 2005, with permission from Elsevier).

Biopsy/Aspiration

One of the most straightforward interventional applications for a cross-sectional imaging modality is percutaneous biopsy and aspiration. The tissue contrast, spatial resolution, and multiplanar capabilities of MR have clear benefits for guidance of biopsy and aspiration applications, and this application was the first reported use of MRI to guide intervention. Unlike guidance by X-ray fluoroscopy and CT, there are a number of user-defined imaging parameters and needle trajectory decisions that can markedly alter device visibility – and therefore also the accuracy and safety – of MR-guided procedures. Safe clinical application of MR-guided techniques requires careful consideration of these factors during procedure planning and execution (Nour and Lewin, 2005a).

Depending upon the radiologist's preference, biopsies under MR image guidance can be performed using free-hand methods, frame-based stereotactic methods, or with frameless stereotactic systems. The simplest and most common technique is the free-hand technique, which is similar to the technique used in CT or

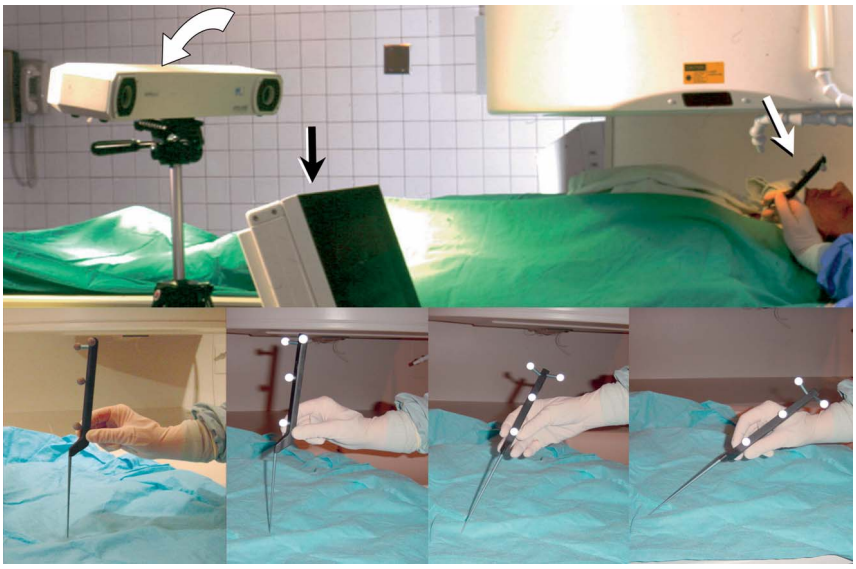

Fig. 3.71. Optical tracking system for MR-guided biopsy. A two-camera video sensor array (curved white arrow) detects the location and orientation of a handheld probe or needle guide (straight white arrow and lower row). The system automatically acquires continuous MR imaging based on the probe position and automatically updates a display of three images on a shielded liquid crystal display monitor adjacent to the scanner (straight black arrow). It is essential to maintain a clear line of sight between the camera system and the probe for this tracking mechanism to function. (Illustration courtesy of Siemens Medical Systems, Erlangen, Germany; reprinted from Nour and Lewin, 2005a, with permission from Elsevier).

ultrasound-guided biopsy (Lewin et al., 1998). Frame-based stereotactic methods use MR-compatible external stereotactic frames that enable calculation of target location based on Cartesian coordinates. Except for MR-guided breast biopsies, where frame-based stereotaxy is the mainstay, this method of guidance is rarely used for MR-guided biopsy. Frameless stereotaxy systems offer the accuracy of a measured stereotactic approach while allowing navigation in unlimited trajectories similar to free-hand techniques (Lewin et al., 1998) (Fig. 3.71).

Over the past two decades a number of investigators have described the use of MRI for guidance of biopsy and aspiration, and much of these early investigations were performed for the diagnosis of lesions in the head and neck (Lewin et al., 1998) (Fig. 3.72). The rapid acceptance of MR-guidance for head and neck biopsies is due, at least in part, to the striking advantages that MR-guidance provides for interventional procedures performed in areas of complex anatomy. The elimination of beam-hardening artifact inherent in CT has also supported the use of MR imaging for guidance of skull base and high cervical spine procedures (Lewin et al., 2000). Masses at the base of the neck, in particular those encroaching upon the brachial plexus, have also presented an excellent application, as has biopsy of retro-

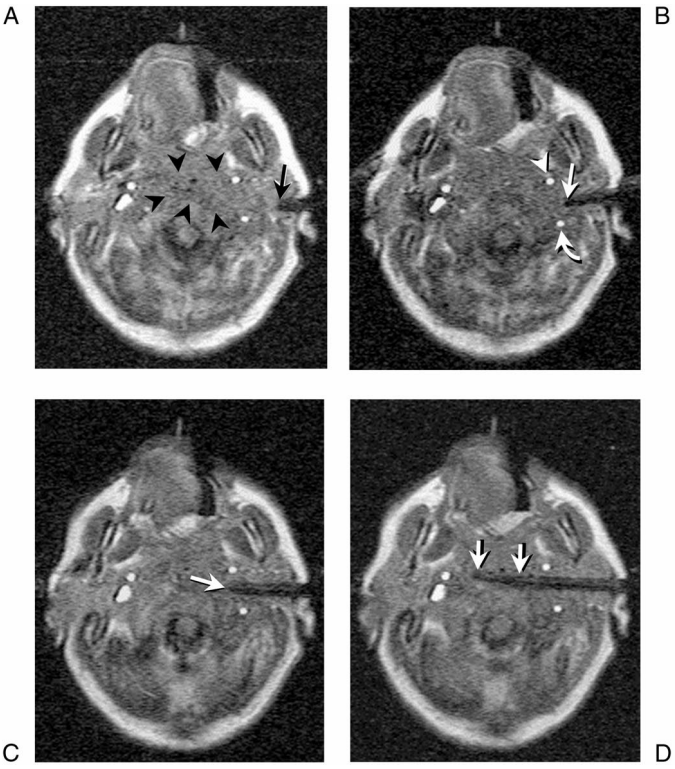

Fig. 3.72. Images obtained during guidance of needle biopsy of C1-2 vertebral and prevertebral mass. A previous attempt at surgical trans-oral biopsy had been unsuccessful. (A) Image early during insertion shows needle tip passing through the left parotid space (arrow). An ill-defined mass can be seen in the prevertebral space (arrowheads). (B) High vascular conspicuity resulting from 2D Fourier transform technique allows ready visualization of flow-related enhancement within the internal carotid (arrowhead) and vertebral (curved arrow) arteries. The needle tip (straight arrow) can be interactively directed to avoid these major vascular structures. The internal jugular vein is only visualized during portions of the respiratory cycle. While seen on the right, the vein was obstructed on the left in this patient. (C) The needle (arrow) is interactively redirected more anteriorly once safely beyond the internal carotid artery to allow deployment of the central stylet of the 18-gauge core-cutting needle. (D) After extending the central stylet of the side-notch cutting needle, the notch location can be visualized as an area of thinning of the distal needle tip (between arrows). Histology demonstrated chronic osteomyelitis and cellulitis, and the offending organism was successfully isolated. (Reprinted from Lewin, 1999, with permission).

pharyngeal and other masses within the deep head and neck spaces (Lewin, 1999; Lai et al., 2003).

The rationale behind MR-guided abdominal and pelvic biopsies is quite different from that in the head and neck. This is because minimally invasive, image-guided, body interventions have long been practiced using CT and ultrasound guidance

with great success. MRI-guided biopsies in the abdomen and pelvis provide the greatest advantages both in safety and in yield when the target lesions are not sufficiently visualized using these other modalities.

The ability to switch rapidly between combinations of T_1- and T_2-weighted tissue contrasts using rapid MR fluoroscopy sequences allows the interventionalist to maximize a lesion's visibility while inserting the biopsy device (Nour and Lewin, 2005a). Another indication for MR guidance in the abdomen is when multiplanar imaging will provide additional procedure safety due to the complex anatomic location of the target lesion, for example within the dome of the liver, in the subphrenic regions, in the pancreas, and in the adrenal glands. As in the neck, the high vascular conspicuity associated with gradient echo sequences also aids in obtaining a safer sampling of retroperitoneal lesions near the great vessels.

MR-guided prostate biopsy has been performed by a handful of groups via transrectal, transgluteal, and transperineal approaches, but at present is purely at the feasibility/developmental phase. However, the ability of T_2-weighted and spectroscopic imaging to detect early cancer holds great promise for the approximately 40% of prostate cancers that are not visible on ultrasound (Atalar and Menard, 2005).

Due to its unparalleled sensitivity, MR imaging is able to detect bone lesions not seen with other modalities. However, due to success rates of ultrasound- and CT-guided biopsy, the use of MRI to guide percutaneous diagnostic interventions in the musculoskeletal system has not gained the same level of popularity it has achieved elsewhere in the body. A number of feasibility studies have been conducted using MR to guide musculoskeletal aspirations, core biopsies, and transcortical trephine biopsies (Nour and Lewin, 2005a; Sequeiros and Carrino, 2005). The main benefit of MR-guided musculoskeletal biopsy again stems from its ability to target lesions that are poorly seen with other imaging modalities, and for lesions that are located in complex locations requiring a double oblique approach. Percutaneous sampling of lesions in the vicinity of nonferromagnetic hardware is another situation where MRI guidance may be of use in musculoskeletal biopsy due to the metal artifacts seen on CT or ultrasound.

A number of breast lesions are seen with MRI and MRI alone. MR is able to detect lesions which are mammographically, sonographically and clinically occult with a sensitivity that approaches 100%. However, the specificity of MRI of the breast is limited, ranging from 40 to 95% depending on patient selection and the imaging techniques used. Because of this discrepancy between sensitivity and specificity, MR-guided breast biopsy is necessary to evaluate the increasing number of indeterminate lesions detected only with MRI (van den Bosch and Daniel, 2005). The recent development MR-guided large-bore, vacuum-assisted core biopsy devices will make these techniques even more useful (van den Bosch and Daniel, 2005).

Percutaneous Therapies

One of the most rapidly developing areas in minimally invasive oncologic therapy is that of thermal ablation. The principle behind percutaneous thermal ablation

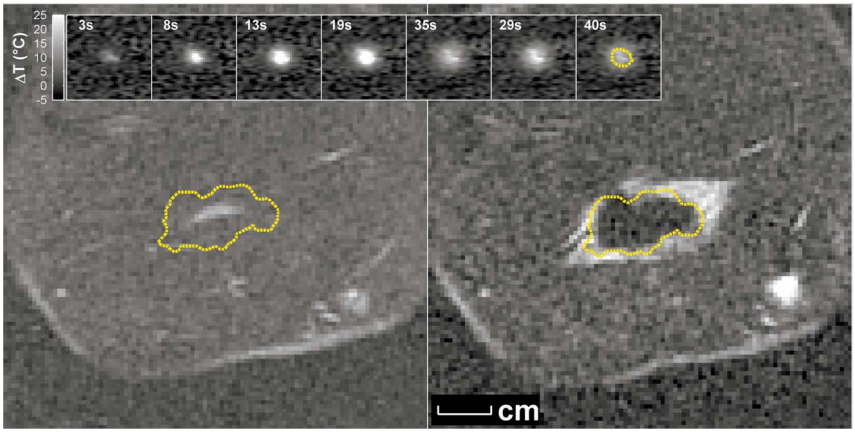

Fig. 3.73. Contrast-enhanced T_1-weighted images of an implanted VX2 tumor in rabbit thigh muscle acquired before (left) and after (right) focused ultrasound thermal ablation. The image on the right shows thermal dose contours superimposed, which agree superbly with the nonperfused area induced by the ablation – typically what has been found in animal studies. The inset shows a time series of temperature images of the focal heating during a 20-s sonication (imaging performed perpendicular to the direction of the ultrasound beam direction). This treatment was performed with an MR-guided focused ultrasound system that uses a phased-array transducer. (Reprinted from Jolesz et al., 2005, with permission from Elsevier).

procedures is very simple. A highly localized temperature change is achieved using RF, laser, microwave, focused ultrasound or cryotherapy to irreversibly damage target tissue while sparing the surrounding normal tissue. Most of the excitement surrounding MR-guided ablations is due to the ability of MRI to detect changes in signal directly related to tissue temperature change (MR thermometry), as well as to detect changes in tissue relaxation parameters that occurs as tissue undergoes necrosis (Nour and Lewin, 2005b). This results in an ability to predict regions of lethal tissue damage during the heating process temperature change and for depicting tissue damage, therefore providing real-time guidance for the deposition of RF energy (Fig. 3.73). With MR monitoring, the ablation zone size and shape can be altered during the procedure to maximize the therapeutic zone to include as much abnormal tissue as possible while minimizing collateral damage to surrounding tissues and anatomic structures. When other modalities, such as CT or ultrasound, are used to target and monitor therapy, real-time procedure tailoring is limited and residual tumor is often only seen on follow-up imaging, requiring multiple ablation sessions. Although still in the early stages of clinical trial, MR-guided ablations have been performed in the kidney and liver, with great success.

An additional use of MRI for percutaneous therapy is in the guidance and monitoring of direct intralesional drug injection. MR guidance has been especially helpful in the treatment of the insinuating malformations of the head and neck (Hayashi et al., 2003; Boll et al., 2004). The multiplanar imaging obtained with

MR allows the injection of alcohol or other sclerosing agents to be monitored during administration, to ensure filling of the entire targeted portion of the malformation, and to detect extravasation into local soft tissues or into draining veins.

Cardiovascular Interventions

Advances in scanner technology and pulse sequence design have made MR the "gold standard" for diagnosing cardiovascular disease. The development of fast, real-time MR imaging, trackable catheters and wires, of flexible user interfaces has catalyzed the development of MR-guided cardiovascular interventions (Rickers et al., 2005).

One of the areas of rapid development has been in the assessment and treatment of congenital heart disease in pediatric and adult patients (Razavi et al., 2003; Schulz et al., 2005). In fact, this is one of few areas where MR-guided cardiovascular interventions have already been transferred from animal models into clinical trials. One of the first clinical trials in MR-guided cardiovascular intervention was performed in a series of 16 patients with a variety of congenital heart diseases (Razavi et al., 2003). Using a hybrid XMR interventional suite and passive tracking carbon dioxide-filled balloon-tipped catheters, the investigators used a combination of X-ray fluoroscopy and MRI to advance and guide cardiac catheterization in 14 of these patients, and entered both right- and left-sided cardiac structures using MR guidance alone. Using this hybrid system, there was a fourfold reduction in median radiation dose to the patient when compared to a control population.

MR-guided therapeutic cardiac interventions are also being developed in animal models (Rickers et al., 2003b). These interventions include RF myocardial ablations, atrial septal puncture, atrial septal defect closure, and vascular dilatation procedures. Anatomically directed RF ablations have also been performed in the inferior vena cava, fossa ovalis and left atrium using a combination of a stereotactic catheter guidance system which combined real-time X-ray fluoroscopy with previously acquired 3D MR images (Dickfeld et al., 2004). With the development of balloon mitral valvuloplasty and RF catheter ablation of the pulmonary veins, there has been growing interest in the use of trans-septal catheterization of the left atrium, a procedure typically performed "blind" using secondary fluoroscopic markers. This has recently been performed under real-time MR guidance using an active MR intravascular needle system (Arepally et al., 2005) (Figs. 3.74 and 3.75).

A number of groups have successfully performed percutaneous atrial septal defect assessments and closures in animal models using real-time MR guidance and MR compatible closure devices (Rickers et al., 2003a, 2005). Furthermore, pulmonary artery stenoses and aortic coarctations have been dilated and stented, and prosthetic aortic and pulmonic valves have been placed under MR guidance (Rickers et al., 2003b, 2005) (Fig. 3.76).

One of the most exciting emerging applications within the field of MR-guided cardiac intervention is that of catheter-directed intramyocardial delivery of drugs, genes, or cells to ischemic or failing myocardium (Saeed et al., 2005). Directed delivery of therapies allow for the delivery of a highly concentrated dose to be deliv-

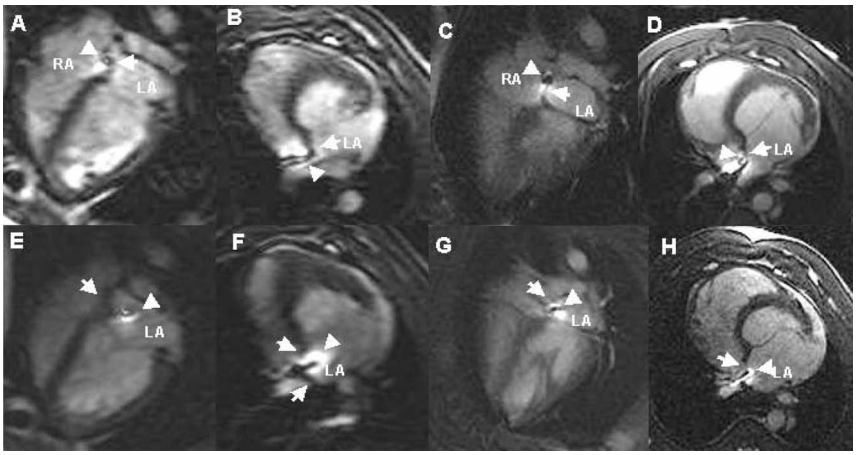

Fig. 3.74. Atrial septal puncture. (A–D) Visualization of the tip of the needle within the right atrium adjacent to and pressing on the fossa ovalis. (E–H) Active needle tip within the left atrium after having passed through the fossa ovalis. (A, C, E, G) are four-chamber views; (B, D, F, H) are axial views. Images (C, D, G, H) were acquired using a FIESTA sequence to verify the position accurately. Images (A, B, E, F) were acquired with a real-time sequence and used to guide the procedure. (Reprinted from Rickers et al., 2005, with permission).

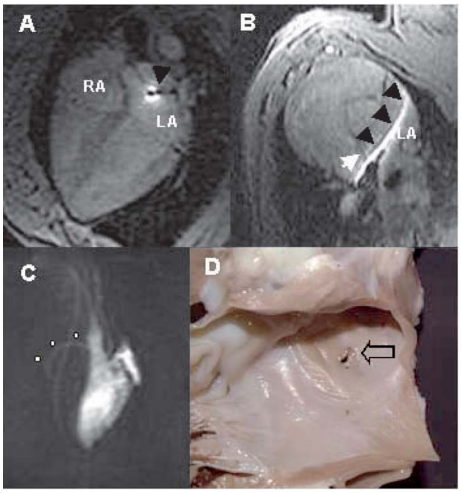

Fig. 3.75. Atrial septal puncture. Fast gradient echo images [four-chamber view (A), short-axis view (B)] demonstrate a wire that has been passed into the left atrium through the fossa ovalis. (C) Left ventriculogram obtained after injection of gadolinium through the septal puncture needle, which demonstrates the left atrium, left ventricle, aorta, and coronary arteries. Note that there is no filling of the right atria or ventricle. (D) Gross pathologic photo of the fossa ovalis viewed from the left atrium. The block arrow indicates the atrial septal punctures. RA = right atrium; LA = left atrium; small arrow = active needle tip; large arrow = fossa ovalis; black arrows = inactive wire; circles = right coronary artery. (Reprinted from Arepally et al., 2005, with permission).

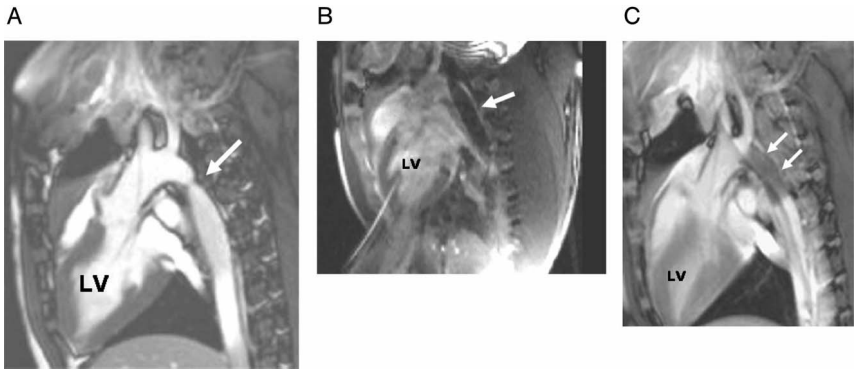

Fig. 3.76. MR-guided dilatation of aortic coarctation. (A) Sagittal view of the aortic arch and descending aorta obtained with a bright blood gradient echo cine sequence shows a severe coarctation of the aorta. A trigger catheter coming from the carotid artery was placed in the left ventricle (LV). Arrow shows coarctation of the aorta. (B) Dilatation of the coarctation was performed with an air-filled balloon under MR fluoroscopy with a true fast imaging with steady precession pulse sequence, with interactive control of scan plan by an assistant operator. The air-filled balloon (arrow) can be seen clearly as a dark structure in the lumen of the aorta, with excellent contrast against the bright blood. (C) The same view post dilatation and after placement of a nitinol stent (dark structure highlighted by two arrows). (Reprinted from Rickers et al., 2005, with permission from Elsevier).

ered specifically into areas of ischemia (Saeed et al., 2005). Catheter-directed local drug delivery requires the ability to perform accurate catheter guidance to the chosen injection site, ideally using an imaging modality which is able to distinguish between healthy, ischemic, infarcted or scarred myocardium, and which can monitor the effects of therapy. Cardiac MR is able to perform all of these tasks. A number of groups have already demonstrated the ability to perform MR-guided transendocardial injections in animal models using 1.5-T MR systems (Dick et al., 2003; Rickers et al., 2004, 2005; Saeed et al., 2004) (Fig. 3.77). These groups have been focusing on the therapeutic use of stem cells. This is probably due to the recent European clinical trials that demonstrated favorable effects on left ventricular function and remodeling in patients who received intracoronary injections of stem cells after acute myocardial infarction, and to the fact that stem cells can feasibly be labeled using (ultrasmall) superparamagnetic iron oxide particles. Moreover, these labeled stem cells can then be visualized and tracked using MR for weeks after injection (Rickers et al., 2005).

Endovascular Interventions

A wide range of MR-guided endovascular interventions has also been developed (Rickers et al., 2005; Wacker et al., 2005). MRI guidance for endovascular procedures offers several important advantages over conventional X-ray fluoroscopic guidance, including lack of iodinated contrast agents, the ability concurrently to detect blood vessels and three-dimensional anatomy, and the ability to detect

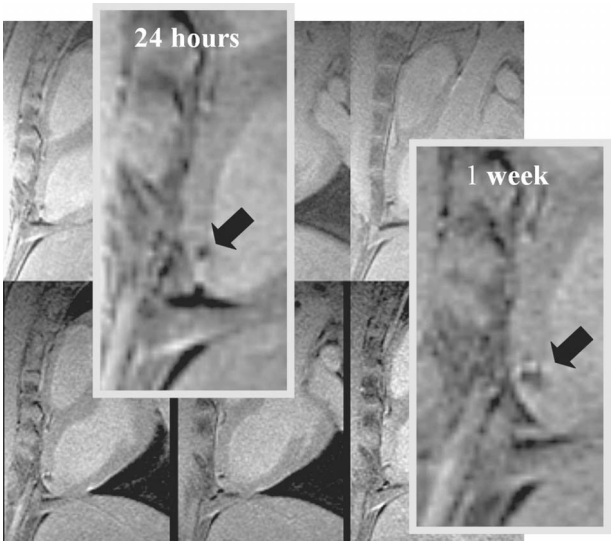

Fig. 3.77. Contiguous long-axis MR images acquired with a high-resolution, breath-hold ECG-gated fast gradient echo pulse sequence showing a hypointense lesion (arrows) caused by Feridex-PLL-labeled mesenchymal stem cells (MSCs) acquired within 24 h and 1 week of injection in a pig with a myocardial infarction. The inset to right shows a magnified view from a single long-axis image demonstrating expansion of lesion over 1 week and a change in the shape of the hypointense lesion from an ovoid shape to a shape with more irregular borders, suggesting migration of the MSCs. (Adapted from Kraitchman et al., 2003, with permission; reprinted from Rickers et al., 2005, with permission from Elsevier).

changes in end-organ function/perfusion at the time of an endovascular intervention (Omary et al., 2002). It is also feasible to monitor arterial wall injury after angioplasty/stenting using high-resolution MRI. Catheter-directed intra-arterial gadolinium-enhanced MR angiography has been performed in the aorta, carotid arteries, renal arteries, iliac arteries, and coronary arteries, predominantly in animal models, but also in small cohorts of human patients (Omary et al., 2002, 2005). Once a catheter has been placed for angiography, MR-guided endovascular interventions have been performed in animal models (Wacker et al., 2005). In humans, MRI-guided hemodialysis graft fistulography, transjugular intrahepatic portosystemic shunt (TIPS) creation, iliac, femoral and popliteal artery angioplasty/stent placement, and iliofemoral artery revascularization also have been performed (Dick et al., 2005; Kee et al., 2005).

One area where interventional MRI can be used to break new ground in image-guided intervention is in the creation of procedures that are impossible to perform using standard X-ray fluoroscopy due to inability to visualize soft tissue anatomy. For example, a novel device and MR fluoroscopy platform was recently devised to create an MR-guided invasive meso-caval shunt, essentially an anastomosis between the portal mesenteric venous system and the inferior vena cava (Weiss et al.,

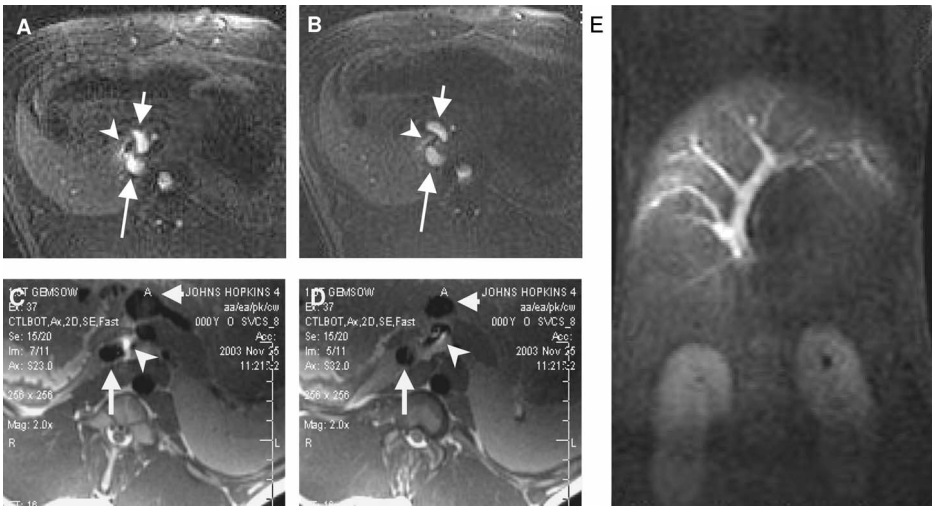

Fig. 3.78. MR-guided puncture of the superior mesenteric vein (SMV) from the inferior vena cava (IVC) with an intravascular needle. (A) Real-time SPGR sequence, axial view, where needle is advanced to the SMV. (B) As needle enters SMV, note the indentation of the needle upon the posterior wall of the SMV. (C, D) Confirmatory axial ECG-gated FSE sequence of the puncture. (C) Intravascular needle has punctured outside IVC. (D) Needle tip is in the SMV. Arrowhead = needle; long arrow = IVC; short arrow = SMV. (E) Confirmatory gadolinium portogram of the puncture using projection image. No contrast is seen within the IVC or within the abdominal parenchyma at any time.

2004) (Fig. 3.78). Mesocaval shunting is currently performed surgically because, when using X-ray fluoroscopy, it is impossible to visualize both the systemic and mesenteric circulation simultaneously in real time.

3.3.5.5 Conclusions and Outlook

The past two decades have witnessed significant technologic advancements in the field of MRI. These developments include more open, high-field MR systems, hybrid X-ray/OR/MR units, higher quality receiver chains, a variety of high-speed pulse sequences, instruments which are not only MR compatible, but which can be visualized and automatically tracked with MR, and new, robust user interface systems which give the interventionalist access to real-time multi-planar imaging and provide real-time control over pulse sequence and scan parameters. When combined with the benefits inherent to MRI, such as the lack of ionizing radiation, superior soft tissue contrast/anatomic detail, the ability to visualize vascular structures without exogenous contrast, and the ability to monitor therapeutic effects in real time, it is not surprising that the realm of possible MR-guided interventions has expanded – and continues rapidly to expand further.

There are a number of procedures which cannot be performed safely using other imaging modalities due to lack of tissue contrast and vascular conspicuity. It is these procedures, for which other imaging modalities are limited or open surgical intervention is the primary alternative, that provide the best area for application of MR-guided techniques. Of course, as the range of procedures that can potentially be guided by MR expands, and as data are gathered on the comparative clinical benefits of MR-guided and -monitored procedures, it is expected that the list of acceptable procedures will also expand.

The appropriate utilization of interventional MRI can result in a huge potential reduction in the costs associated with treating certain patients (Kucharczyk et al., 2001; Hall et al., 2003). For those patients in whom the use of MR image-guided biopsy, thermal ablation or chemical ablation can help to avoid open surgical procedures, there may be significant reductions in cost. This is in addition to the patient benefits resulting from reductions in morbidity, mortality, post-procedure discomfort, and the time required for recovery when open surgical procedures can be avoided. Such potential advantages of interventional MRI have provided the rationale for an increased interest in these techniques, and growing numbers of centers and radiology practices are now developing interventional or intraoperative MRI capabilities.

References

Arepally, A. and Weiss, C.R. (2005). Intrabiliary MR imaging. *Magn. Reson. Imaging Clin. N. Am.*, **13** (3), 481–489.

Arepally, A., Karmarkar, P.V., Weiss, C., Rodriguez, E.R., Lederman, R.J., and Atalar, E. (2005). Magnetic resonance image-guided trans-septal puncture in a swine heart. *J. Magn. Reson. Imaging*, **21** (4), 463–467.

Atalar, E. and Menard, C. (2005). MR-guided interventions for prostate cancer. *Magn. Reson. Imaging Clin. N. Am.*, **13** (3), 491–504.

Blanco, R.T., Ojala, R., Kariniemi, J., Perala, J., Niinimaki, J., and Tervonen, O. (2005). Interventional and intraoperative MRI at low field scanner – a review. *Eur. J. Radiol.*, **56** (2), 130–142.

Boll, D.T., Merkle, E.M., and Lewin, J.S. (2004). Low-flow vascular malformations: MR-guided percutaneous sclerotherapy in qualitative and quantitative assessment of therapy and outcome. *Radiology*, **233** (2), 376–384.

Derakhshan, J.J. and Duerk, J.L. (2005). Update to pulse sequences for interventional MR imaging. *Magn. Reson. Imaging Clin. N. Am.*, **13** (3), 415–429.

Dick, A.J., Guttman, M.A., Raman, V.K., Peters, D.C., Pessanha, B.S., Hill, J.M., Smith, S., Scott, G., McVeigh, E.R., and Lederman, R.J. (2003). Magnetic resonance fluoroscopy allows targeted delivery of mesenchymal stem cells to infarct borders in Swine. *Circulation*, **108** (23), 2899–2904.

Dick, A.J., Raman, V.K., Raval, A.N., Guttman, M.A., Thompson, R.B., Ozturk, C., Peters, D.C., Stine, A.M., Wright, V.J., Schenke, W.H., and Lederman, R.J. (2005). Invasive human magnetic resonance imaging: feasibility during revascularization in a combined XMR suite. *Catheter Cardiovasc. Interv.*, **64** (3), 265–274.

Dickfeld, T., Calkins, H., Zviman, M., Meininger, G., Lickfett, L., Roguin, A., Lardo, A.C., Berger, R., Halperin, H., and Solomon, S.B. (2004). Stereotactic magnetic resonance guidance for anatomically targeted ablations of the fossa ovalis and the left atrium. *J. Interv. Card. Electrophysiol.*, **11** (2), 105–115.

Hall, W.A., Kowalik, K., Liu, H., Truwit, C.L., and Kucharezyk, J. (2003). Costs and benefits of intraoperative MR-guided brain tumor resection. *Acta Neurochir. Suppl.*, **85**, 137–142.

Hayashi, N., Masumoto, T., Okubo, T., Abe, O., Kaji, N., Tokioka, K., Aoki, S., and Ohtomo, K. (2003). Hemangiomas in the face and extremities: MR-guided sclerotherapy-optimization with monitoring of signal intensity changes in vivo. *Radiology*, **226** (2), 567–572.

Hinks, R.S., Bronskill, M.J., Kucharczyk, W., Bernstein, M., Collick, B.D., and Henkelman, R.M. (1998). MR systems for image-guided therapy. *J. Magn. Reson. Imaging*, **8** (1), 19–25.

Hofmann, L.V., Liddell, R.P., Eng, J., Wasserman, B.A., Arepally, A., Lee, D.S., and Bluemke, D.A. (2005). Human peripheral arteries: feasibility of transvenous intravascular MR imaging of the arterial wall. *Radiology*, **235** (2), 617–622.

Jolesz, F.A., Hynynen, K., McDannold, N., and Tempany, C. (2005). MR imaging-controlled focused ultrasound ablation: a noninvasive image-guided surgery. *Magn. Reson. Imaging Clin. N. Am.*, **13** (3), 545–560.

Kee, S.T., Ganguly, A., Daniel, B.L., Wen, Z., Butts, K., Shimikawa, A., Pelc, N.J., Fahrig, R., and Dake, M.D. (2005). MR-guided transjugular intrahepatic portosystemic shunt creation with use of a hybrid radiography/MR system. *J. Vasc. Interv. Radiol.*, **16** (2 Pt 1), 227–234.

Kivelitz, D., Wagner, S., Schnorr, J., Wetzler, R., Busch, M., Melzer, A., Taupitz, M., and Hamm, B. (2003). A vascular stent as an active component for locally enhanced magnetic resonance imaging: initial in vivo imaging results after catheter-guided placement in rabbits. *Invest. Radiol.*, **38** (3), 147–152.

Kraitchman, D.L., Heldman, A.W., Atalar, E., et al. (2003). In vivo magnetic resonance imaging of mesenchymal stem cells in myocardial infarction. *Circulation*, **107**, 2292.

Kucharczyk, J., Hall, W.A., Broaddus, W.C., Gillies, G.T., and Truwit, C.L. (2001). Cost-efficacy of MR-guided neurointerventions. *Neuroimaging Clin. N. Am.*, **11** (4), 767–772, xii.

Lai, A., Maghami, E., Borges, A., Bonyadilou, S., Curran, J., Abemayor, E., and Lufkin, R. (2003). MRI-guided access to the retropharynx. *J. Magn. Reson. Imaging*, **17** (3), 317–322.

Lewin, J.S. (1999). Interventional MR imaging: concepts, systems, and applications in neuroradiology. *Am. J. Neuroradiol.*, **20** (5), 735–748.

Lewin, J.S., Petersilge, C.A., Hatem, S.F., Duerk, J.L., Lenz, G., Ciampitt, M.E., Williams, M.L., Kaczynski, K.R., Lanzieri, C.F., Wise, A.L., and Haaga, J.R. (1998). Interactive MR imaging-guided biopsy and aspiration with a modified clinical C-arm system. *Am. J. Roentgenol.*, **170** (6), 1593–1601.

Lewin, J.S., Nour, S.G., and Duerk, J.L. (2000). Magnetic resonance image-guided biopsy and aspiration. *Top Magn. Reson. Imaging*, **11** (3), 173–183.

Nour, S.G. and Lewin, J.S. (2005a). Percutaneous biopsy from blinded to MR guided: an update on current techniques and applications. *Magn. Reson. Imaging Clin. N. Am.*, **13** (3), 441–464.

Nour, S.G. and Lewin, J.S. (2005b). Radiofrequency thermal ablation: the role of MR imaging in guiding and monitoring tumor therapy. *Magn. Reson. Imaging Clin. N. Am.*, **13** (3), 561–581.

Omary, R.A., Green, J., Finn, J.P., and Li, D. (2002). Catheter-directed gadolinium-enhanced MR angiography. *Radiol. Clin. North Am.*, **40** (4), 953–963.

Omary, R.A., Schirf, B.E., Green, J.D., Kanwar, Y.S., Shea, S.M., Carroll, T.J., Carr, J., and Li, D. (2005). Catheter-directed MR angiography and cross-sectional imaging for the assessment of renal artery stenosis. *J. Vasc. Interv. Radiol.*, **16** (2 Pt 1), 255–260.

Paetzel, C., Zorger, N., Bachthaler, M., Volk, M., Seitz, J., Herold, T., Feuerbach, S., Lenhart, M., and Nitz, W.R. (2004). Feasibility of MR-guided angioplasty of femoral artery stenoses using real-time imaging and intraarterial contrast-enhanced MR angiography. *Röfo*, **176** (9), 1232–1236.

Quick, H.H., Zenge, M.O., Kuehl, H., Kaiser, G., Aker, S., Massing, S., Bosk, S., and Ladd, M.E. (2005). Interventional magnetic resonance angiography with no

strings attached: wireless active catheter visualization. *Magn. Reson. Med.*, **53** (2), 446–455.

Razavi, R., Hill, D.L., Keevil, S.F., Miquel, M.E., Muthurangu, V., Hegde, S., Rhode, K., Barnett, M., van Vaals, J., Hawkes, D.J., and Baker, E. (2003). Cardiac catheterisation guided by MRI in children and adults with congenital heart disease. *Lancet*, **362** (9399), 1877–1882.

Rickers, C., Jerosch-Herold, M., Hu, X., Murthy, N., Wang, X., Kong, H., Seethamraju, R.T., Weil, J., and Wilke, N.M. (2003a). Magnetic resonance image-guided transcatheter closure of atrial septal defects. *Circulation*, **107** (1), 132–138.

Rickers, C., Seethamraju, R.T., Jerosch-Herold, M., and Wilke, N.M. (2003b). Magnetic resonance imaging guided cardiovascular interventions in congenital heart diseases. *J. Interv. Cardiol.*, **16** (2), 143–147.

Rickers, C., Gallegos, R., Seethamraju, R.T., Wang, X., Swingen, C., Jayaswal, A., Rahrmann, E.P., Kastenberg, Z.J., Clarkson, C.E., Bianco, R., O'Brian, T., Verfaillie, C., Bolman, R.M., Wilke, N., and Jerosch-Herold, M. (2004). Applications of magnetic resonance imaging for cardiac stem cell therapy. *J. Interv. Cardiol.*, **17** (1), 37–46.

Rickers, C., Kraitchman, D., Fischer, G., Kramer, H.H., Wilke, N., and Jerosch-Herold, M. (2005). Cardiovascular interventional MR imaging: a new road for therapy and repair in the heart. *Magn. Reson. Imaging Clin. N. Am.*, **13** (3), 465–479.

Saeed, M., Lee, R., Martin, A., Weber, O., Krombach, G.A., Schalla, S., Lee, M., Saloner, D., and Higgins, C.B. (2004). Transendocardial delivery of extracellular myocardial markers by using combination X-ray/MR fluoroscopic guidance: feasibility study in dogs. *Radiology*, **231** (3), 689–696.

Saeed, M., Saloner, D., Weber, O., Martin, A., Henk, C., and Higgins, C. (2005). MRI in guiding and assessing intramyocardial therapy. *Eur. Radiol.*, **15** (5), 851–863.

Schulz, T., Trobs, R.B., Schneider, J.P., Hirsch, W., Puccini, S., Schmidt, F., and Kahn, T. (2005). Pediatric MR-guided interventions. *Eur. J. Radiol.*, **53** (1), 57–66.

Sequeiros, R.B. and Carrino, J.A. (2005). Musculoskeletal interventional MR imaging. *Magn. Reson. Imaging Clin. N. Am.*, **13** (3), 519–532.

Shunk, K.A., Garot, J., Atalar, E., and Lima, J.A. (2001). Transesophageal magnetic resonance imaging of the aortic arch and descending thoracic aorta in patients with aortic atherosclerosis. *J. Am. Coll. Cardiol.*, **37** (8), 2031–2035.

van den Bosch, M.A.A.J. and Daniel, B.L. (2005). MR-guided interventions of the breast. *Magn. Reson. Imaging Clin. N. Am.*, **13** (3), 505–517.

Wacker, F.K., Hillenbrand, C.M., Duerk, J.L., and Lewin, J.S. (2005). MR-guided endovascular interventions: device visualization, tracking, navigation, clinical applications, and safety aspects. *Magn. Reson. Imaging Clin. N. Am.*, **13** (3), 431–439.

Weiss, C.R., Karmarkar, P.V., Arepally, A., and Atalar, E. (2004). Real time MR-guided meso-caval puncture: towards the development of a percutaneous MR-guided meso-caval shunt. *12th Scientific Meeting of International Society of Magnetic Resonance in Medicine, Kyoto, Japan*.

Wong, E.Y., Zhang, Q., Duerk, J.L., Lewin, J.S., and Wendt, M. (2000). An optical system for wireless detuning of parallel resonant circuits. *J. Magn. Reson. Imaging*, **12** (4), 632–638.

3.3.6 New Approaches in Diagnostic and Therapeutic MR Mammography*

Werner A. Kaiser, Stefan O.R. Pfleiderer, Karl-Heinz Herrmann, and Jürgen R. Reichenbach

3.3.6.1 Introduction

Breast cancer is a major health problem, and represents the most common cancer worldwide in women. In Germany, it is estimated that 47 500 new breast cancer cases are identified each year (Giersiepen et al., 2005), while in North America one in eight women will develop breast cancer during her lifetime (Gordon et al., 2004). Currently, X-ray mammography is the primary imaging technique for early detection and diagnosis of breast lesions. However, the rate of missed lesions may be as high as 10–30% (Mushlin et al., 1998).

Due to its inherent high contrast in imaging soft tissue, magnetic resonance imaging (MRI) quickly became relevant in diagnostic imaging and tumor detection in the female breast. The first *in-vivo* data were presented during the early 1980s (Ross et al., 1982; El Yousef et al., 1983), but failed to gain broad clinical acceptance due to the poor spatial resolution and low signal-to-noise ratio (SNR).

It was the combination of rapid 2D gradient-echo (GRE) imaging with a dedicated breast coil coupled with the bolus injection of gadolinium dimeglumine that created the technique of dynamic MR mammography (MRM) (Kaiser and Zeitler, 1989). This technique showed high sensitivity for breast tumor malignancy, and the advancement of tissue delineation with contrast-enhanced dynamic MRI, as demonstrated by Kaiser and Zeitler (1989) and Heywang et al. (1989), substantially increased the available information in breast diagnostics.

Since that time impressive progress has been made in MRM, with steadily increasing diagnostic benefits (Padhani et al., 2005). Today, MRI of the breast is considered the most sensitive technique currently available for imaging breast cancer, even in comparison to state-of-the-art mammography and ultrasound. Sensitivities between 95% and 100% have been reported for the detection of invasive breast cancers (Fischer et al., 1999; Aichinger et al., 2002), and an absence of malignant findings with MRM is highly indicative that the woman's breast is free of cancer. MRM is extraordinarily useful to determine disease extent, for example multifocality or multicentricity, which helps to decide whether the patient is a candidate for breast-conserving therapy, and to exclude contralateral lesions. MRM is also able to differentiate scar from recurrent cancer, to identify primary cancer in young high-risk patients, and to evaluate tumor response to neoadjuvant chemotherapy. The technique has the unique ability to detect and visualize breast cancers with

* A list of abbreviations and acronyms is provided at the end of this section.

sizes as small as 3 mm. Despite this remarkable progress, however, the specificity to differentiate between benign and malignant findings is still largely varying (Bluemke et al., 2004).

Chances of survival are distinctly improved when breast cancer is diagnosed and treated at an early stage. For breast cancer therapy surgical tumor excision is a common procedure, but may impair breast volume and generate scars as well as cause physiological and psychological stress for the patients. Therefore, the development and application of alternative therapeutic strategies is of growing significance. One of the main therapeutic research areas involves the elimination of tumors by local deposition of energy or by applying therapeutic cold. Various MR-guided techniques are available, such as laser application, cryotherapy, highly focused ultrasound or application of radiofrequency (RF) currents (Mumtaz et al., 1996; Hynynen et al., 2001; Morin et al., 2004; Zippel and Papa, 2005).

3.3.6.2 Diagnostic MR Mammography

The basis of the high sensitivity of contrast enhanced MRM is tumor angiogenesis that accompanies a majority of breast cancers, even in their early stages (Weidner et al., 1991). Neoangiogenesis appears to be a reliable sign of breast tumors with sizes as small as 3 mm in diameter, as tumors need increased blood supply for nourishment and removal of metabolic waste material in order to maintain their uncontrolled growth. These tumor vessels often show higher permeability and leakage into the interstitial space, and the contrast agent will accumulate there faster than in healthy tissue.

Standard Protocol

Currently, dynamic contrast enhanced T_1-weighted imaging is considered as state-of-the-art procedure in breast cancer diagnostics, and is performed on clinical whole-body MR scanners with field strengths between 1.0 T and 3.0 T using dedicated phased-array breast coils (Hylton, 2005). Although a standardized, obligatory imaging protocol still does not exist, there is nevertheless some established consensus within the international community of radiologists on the minimal requirements to perform MRM. This includes the recommendation that imaging should be performed during the second week of the menstrual cycle in premenopausal women, and that 2D or 3D techniques should be used, including T_1-weighted, RF-spoiled, gradient-echo, and T_2-weighted sequences (spin-echo, turbo-spin-echo or inversion recovery). A minimum matrix of 256×256 is suggested. Slice thickness should be less than 4 mm, and echo times selected to avoid water/fat phase opposition.

Contrast Enhancement

For contrast enhancement a bolus of a nonspecific, chelated paramagnetic contrast medium (CM), such as Gd-DTPA, is administered intravenously. For the dynamic acquisition, one pre-contrast scan followed by post-contrast scans covering at least

6 min are performed with a temporal resolution of 60–90 s to monitor the signal time behavior of cancerous tissue in the presence of a paramagnetic contrast medium.

The uptake of the contrast agent in the tumor tissue can be observed as a signal increase due to shortened T_1 relaxation times of the tissue. Both high temporal and high spatial resolution are desired to resolve the kinetics of the time-signal behavior and to identify lesion boundaries and small breast lesions, respectively (Du et al., 2002).

Image Postprocessing

To facilitate detection of suspicious, enhancing areas due to the presence of the contrast agent, subtraction images are usually computed between each of the post-contrast scans and the pre-contrast scan (Fig. 3.79). Further image post-processing includes maximum intensity projections (MIP) of the subtracted images from the first and/or second acquisitions (Fig. 3.80). By using regions-of-interest (ROI), positioned within the suspicious foci (Figs. 3.81 and 3.82) on the original acquired images, the dynamic signal behavior is analyzed by calculating intensity over time plots (Sardanelli et al., 2003).

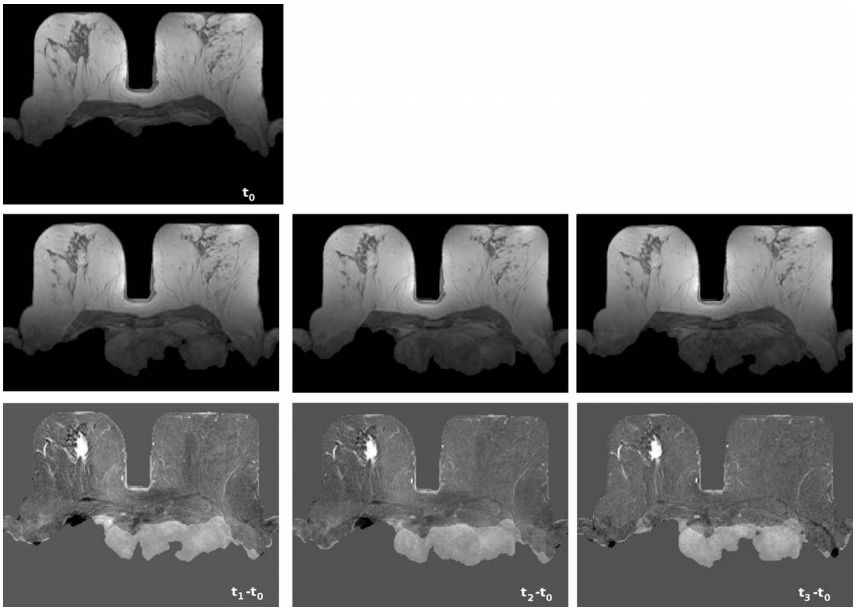

Fig. 3.79. A 60-year-old patient with an invasive ductal cancer in the center of the right breast. The upper row shows the native scan (t_0) and three contrast-enhanced scans ($t_1 \ldots t_3$). The lower row shows the corresponding subtracted images with the strongly enhancing lesion.

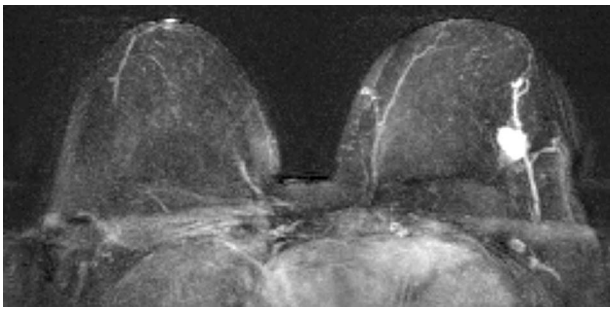

Fig. 3.80. The maximum intensity projection of the subtracted images reveals an increased vascularization of the malignant tumor located in the left breast.

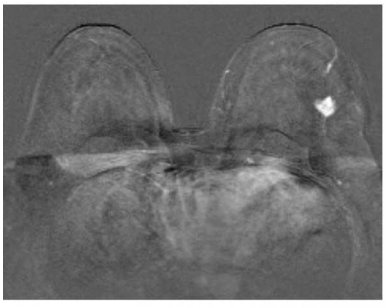

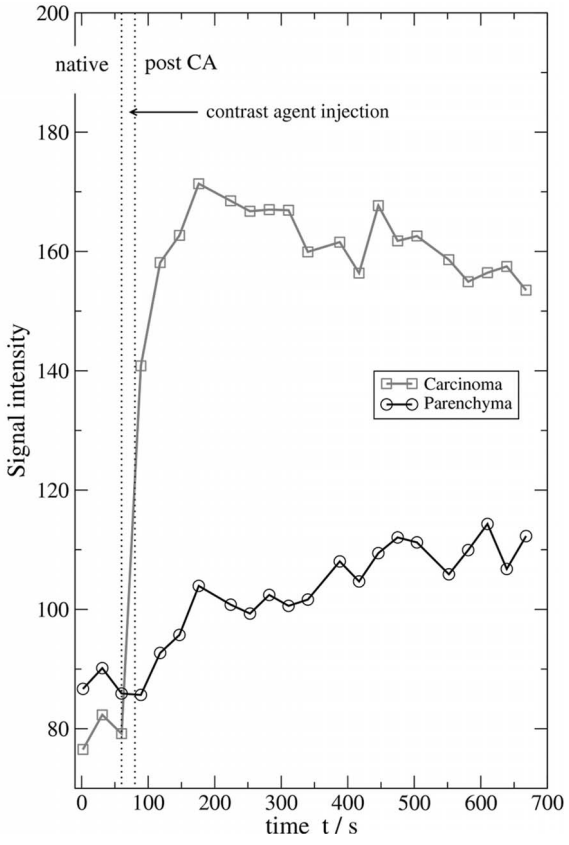

Fig. 3.81. Signal intensity-time curve for a malignant tumor. Note the strong, rapid enhancement followed by a plateau and washout of signal intensity at longer times. CA = contrast agent.

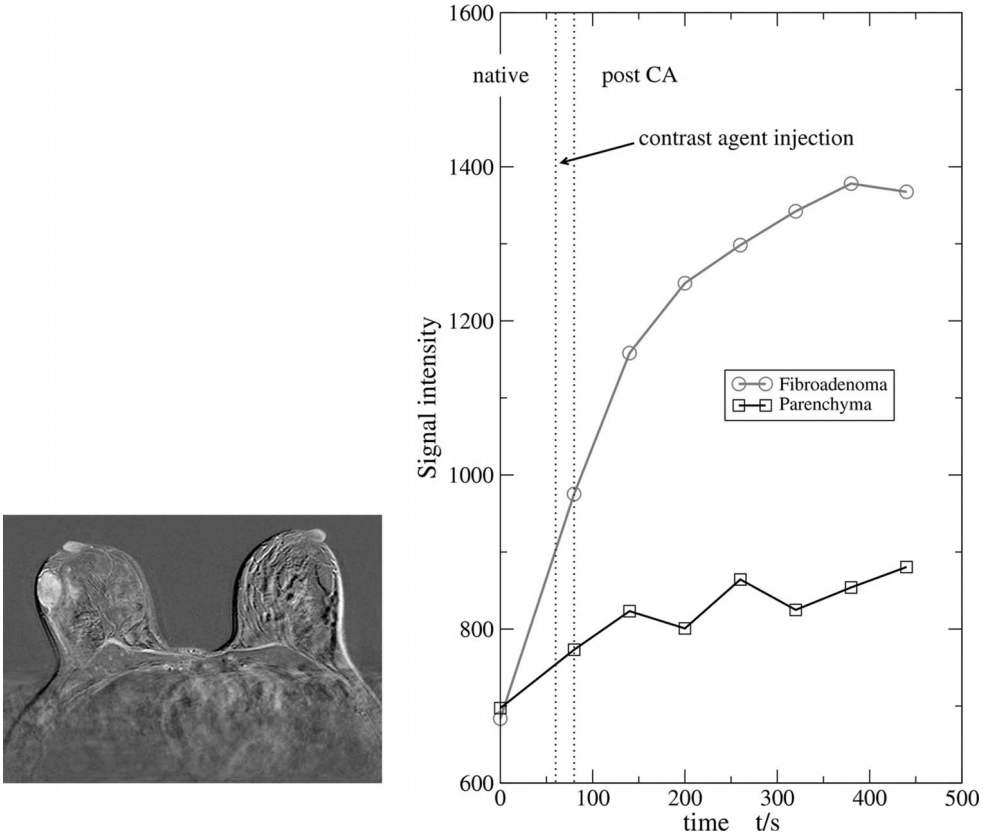

Fig. 3.82. Patient with a myxoid fibroadenoma in the right breast. Note the relatively slow, steady signal enhancement, which is indicative for a benign lesion. CA = contrast agent.

3.3.6.3
Current Limits and Disadvantages

Sensitivity and Specificity

What is generally considered an advantage may turn into a disadvantage, because breast MRI can be too sensitive and can pick up normal tissue, which, in turn, leads to additional examinations and negative biopsies. Therefore, correct image interpretation requires highly experienced and trained readers who achieve high sensitivities and specificities by taking additional morphologic and dynamic criteria into account (Fischer et al., 2005). Another disadvantage is that breast MRI is not able to detect certain types of very small calcifications, which may be an early indication of cancer.

Hormonal Influence

Several reports have described hormonal influences and associated alterations of the contrast enhancement kinetics in dynamic MRM. During the second half of

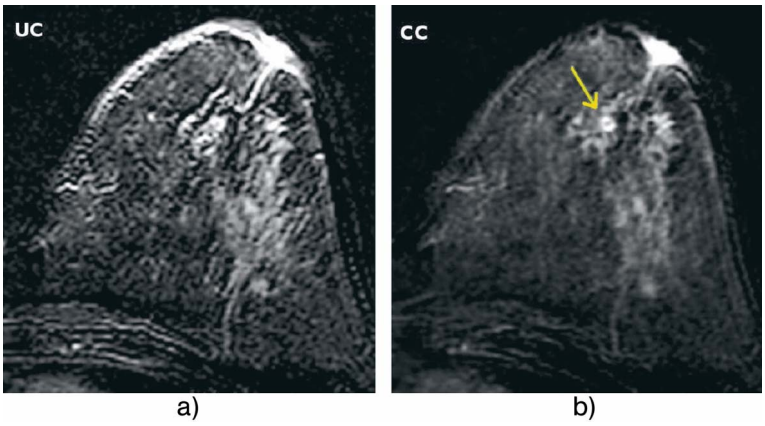

Fig. 3.83. Subtraction images of a dynamic MR data set. (a) In the motion-corrupted image the lesion is difficult to detect among all the artifacts. (b) In the corrected image the lesion is clearly visible (arrow).

the menstrual cycle generally higher contrast media uptake takes place in fibrocystic formations (Rieber et al., 1999) and normal breast parenchyma (Müller-Schimpfle et al., 1997). Other authors have reported volume changes of the breast during the menstrual cycle, or alterations of tissue composition during hormone replacement therapy (HRT) (Hussain et al., 1999; Reichenbach et al., 1999). While hormonal influence on CM uptake is certainly a factor to watch for, it has been shown that these effects were reproducible and reversible and did not affect the diagnostic quality of MRM (Pfleiderer et al., 2004).

Patient Motion

For the analysis of dynamic data it is essential that the patient's position does not change during the complete acquisition. However, this requirement is often not met and can affect the interpretation of the images or make an accurate diagnosis even impossible (Fig. 3.83). One of the problems of correcting breast data is that breast tissue deforms in a nonrigid manner and does not contain unambiguously corresponding internal landmarks. There exist several different approaches for matching MR data of the breast (Sivaramakrishna, 2005). However, many degrees of freedom are required to perform nonrigid elastic transformations, which make the registration problem challenging and computationally burdensome.

3.3.6.4 New Approaches to Diagnostic MR Mammography

As stated above, both high temporal and high spatial resolution are desired in dynamic MRM. Optimal spatial resolution is necessary for identifying small lesions and providing anatomic detail. Temporal resolution is essential for evaluating the

local time characteristics of contrast enhancement. Improving spatial resolution, however, will always be at the expense of temporal resolution and, in most cases, *vice versa*.

New Sequence Techniques

Several approaches have been taken to tackle this problem. Earlier concepts to increase scan speed included echo-planar imaging (EPI) (Hulka et al., 1995) or keyhole imaging (Bishop et al., 1997), but these failed to gain clinical acceptance due to their inherent sensitivity towards motion artifacts or unusual lesion contrast enhancement kinetics.

Dynamic 2D spiral MR imaging has been proposed to acquire data through the whole breast every 7.8 s (Daniel et al., 1998). This technique – like other fast, non-Cartesian *k*-space-trajectory MRI – requires water-selective excitation; this is critical, since without it off-resonance effects between fat and water result in substantial imaging artifacts, noise, and blurring. More recently, the technique was extended to 3D with significantly less off-resonance blurring and spiral artifacts (Yen et al., 2000).

Partial Parallel Imaging

Scan speed can be significantly increased by employing parallel imaging techniques (Sodickson and Manning, 1997; Pruessmann et al., 1999; Griswold et al., 2002). The increase in speed is achieved by undersampling *k*-space which reduces the field of view (FOV) and causes aliasing from regions where the object extends outside the reduced FOV. This aliasing is eliminated by using an array of receive coils with individual coil sensitivities to combine the aliased images from all coils in such a way that the aliasing is suppressed. All major vendors of MR systems have developed parallel imaging techniques and dubbed them with different acronyms, including ASSET, iPAT, and SENSE.

One drawback of parallel imaging is the lower SNR compared to conventional imaging because of reduced scan time, and also because the removal of the aliasing can magnify noise. The multiple channels on modern scanners enable higher-order parallel imaging methods that allow simultaneous bilateral acquisition of the breasts with the potential for providing both superior image quality and high temporal resolution at the same time (Friedman et al., 2005).

Imaging at higher field strengths (>1.5 T) with parallel techniques will be even more useful because the acquisition time can be shortened by exploiting the gain in SNR with a simultaneous reduction in specific absorption rate (SAR) due to the reduced number of phase-encoding steps. Recently, a 3D, fat-suppressed gradient-recalled echo (GRE) volumetric interpolated breath-hold examination (VIBE) was applied in combination with the parallel acquisition technique for single breath-hold evaluation of the breast (Tozaki and Fukuda, 2005).

Diffusion-Weighted Imaging

Diffusion-weighted imaging (DWI) has been used by several groups to differentiate between malignant and benign lesions (Guo et al., 2002; Sinha et al., 2002). DWI

provides a noninvasive means to quantify the apparent diffusion of water in tissues and the interstitial microenvironment, and may prove valuable to monitor cancer growth as well as response to treatment. Preliminary studies show that the apparent diffusion coefficient (ADC) is an indicator of cell density, and that benign pathologic and normal breast tissues have a larger ADC than malignant tumors. These results suggest that the measurement of extracellular water content could provide additional information that may further increase specificity. On the other hand, the clinical applicability of DWI in breast MRI has been limited so far due to the existence of gross physiologic motion and image distortion due to susceptibility effects.

Improving Specificity

Since the main issue of breast MRI is specificity, much effort has been made to improve the differentiation between benign and malignant breast lesions. One approach is to link kinetic and morphologic information, either by combining low- and high-resolution 3D-gradient echo sequences (Vomweg et al., 2004), or to create comprehensive extended scores for the evaluation (Fischer et al., 1999, 2005). Combining different existing MR techniques (Huang et al., 2004) or developing new and more sophisticated MRI techniques, such as echo-planar spectroscopic (EPS) imaging with high spectral and spatial resolutions (Du et al., 2002), might also help to improve specificity. Issues, such as morphologic patterns of enhancing lesions, internal architecture of lesions as well as temporal signal enhancement all represent important information, and are used as diagnostic criteria. With improved spatial resolution, typical lesion configurations (e.g., nodular, sharp margins, oval, round, speculated, unsharp, segmental, linear or attached to the pectoral muscle) may be better identified and used for differentiation.

Postprocessing

A new simple technique has been introduced recently for expanding the routine imaging protocol in dynamic MRM by using an interleaved 3D, dual-echo, gradient-echo sequence that allows the simultaneous acquisition of opposed-phase (OP) and in-phase (IP) magnitude and phase images during contrast agent administration with sufficiently high spatial and temporal resolutions (Reichenbach et al., 2005).

The underlying hypothesis is that the combined information from IP and OP dynamic images may improve the characterization of breast lesions. In particular, combining IP and OP images within a single sequence makes it possible to overcome the problems associated with partial volume effects, and to highlight enhanced tumor regions that are embedded in the surrounding fat, while still preserving the typical contrast enhancement features observed with conventional 3D in-phase scans. As illustrated in Figure 3.84, if subtraction is performed between two post-CM data sets acquired under IP and OP conditions, a huge gain in signal difference can be obtained. This holds true in particular for lesions with small volume fractions. This subtraction between two contrast-enhanced data sets has been dubbed *SIPOP* (*S*ubtraction between *I*n-*P*hase and *O*pposed-*P*hase) to differentiate

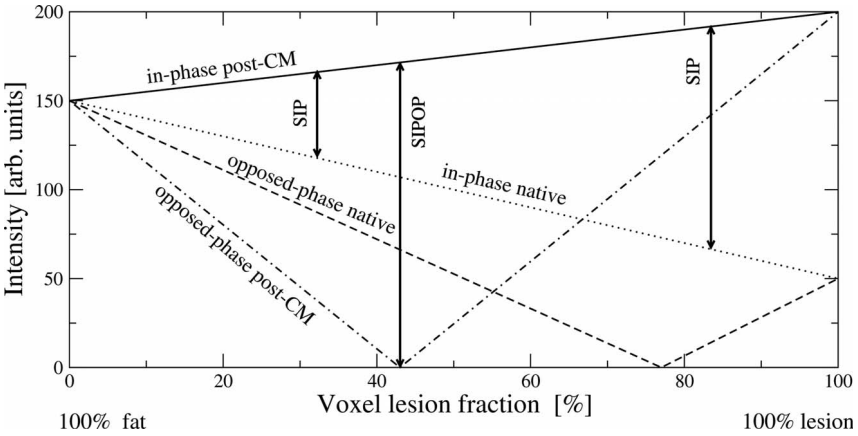

Fig. 3.84. MR-signal behavior for a two-compartment model (fat, water) before and after administration of a contrast medium (CM) as a function of lesion volume fraction for in-phase (dotted and solid line) and opposed-phase (dash-dotted and dashed line) imaging conditions. A signal ratio between fat and water of 3:1 and an initial (pre-CM) signal amplitude of 50 a.u. (arbitrary units) in a voxel containing only tumor was assumed. Contrast enhancement (post-CM) of the lesion was assumed to reach a maximum intensity of 200 a.u. For the opposed-phase condition the signal behavior is more complicated, leading to complete signal cancellation for certain values of the volume fraction f.

it from the conventional subtraction of native from contrast-enhanced IP images (*SIP*). A typical clinical example is shown in Figure 3.85.

3.3.6.5 Minimally Invasive Procedures: Biopsy and Therapy

MR-Guided Breast Biopsy

For quite some time one major limitation has been that biopsy was not possible for a lesion detected only by MRI, unless this lesion was also identified on a mammogram or directed ultrasound. Breast biopsies of suspicious lesions were thus commonly performed by open surgery. Only recently have image-guided large core or vacuum-assisted breast biopsy techniques been introduced, and these are now entering clinical routine.

Using stereotactic or MR-guided hookwire marking prior to surgery improves the success of tissue sampling (Veltman et al., 2005). However, to perform MR-guided interventions requires MR-compatible instruments. Tools, such as biopsy or therapy needles, cannulas, or trocars, should produce no image distortions or extended susceptibility artifacts that may obscure the target. Hence, the development of new inert, biocompatible materials with susceptibilities more closely matched to human tissue is important (Reichenbach et al., 2000). MR-guided minimally invasive procedures for the breast also require special coil equipment which

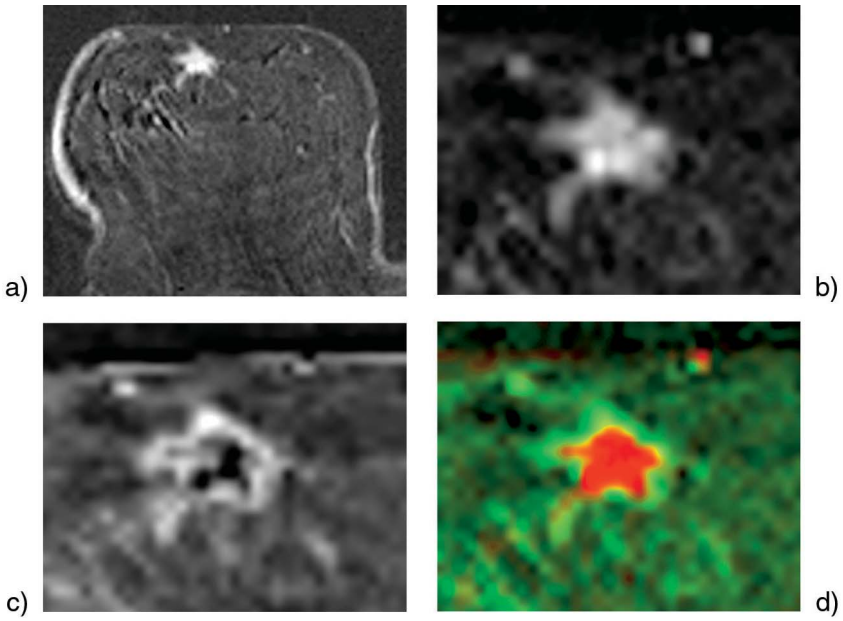

Fig. 3.85. A 62-year-old patient with an invasive lobular carcinoma of the right breast (a), an enlarged part of the lesion in the SIP image (b), in the SIPOP (subtraction of opposed-phase from in-phase) image (c) and in the colored overlay image (red: SIP, green: SIPOP) (d).

allows diagnostic imaging followed by subsequent tissue sampling in a single patient session (Pfleiderer et al., 2003).

Although MR-guided breast biopsies are now established procedures, they still require a two-step or even three-step approach. First, the lesion is detected and diagnosed by conventional MRM, after which the biopsy is performed outside the scanner tunnel before the patient is finally brought back into the magnet for control imaging. Clearly, a more ideal scenario would be to perform diagnostic imaging, MR-guided biopsy, and possibly even minimally invasive therapeutic procedures during the same session, without the need to relocate the patient. The problem, however, is that most clinical systems with field strengths of 1.0 T or higher have a closed magnet design which restricts direct patient access during image-guided intervention.

Thus, the availability of a device which allows biopsies to be performed within the magnet bore without having to move the patients would be beneficial by reducing the risk of involuntary patient motion, minimizing the risk of mispositioning due to repeated table movements, and shortening the examination time.

Recently, a prototype of such a robotic system, called ROBITOM (*Ro*botic system for *B*iopsy and *I*nterventional *T*herapy *o*f *M*ammary lesions) has been introduced (Kaiser et al., 2000). First clinical experiences with ROBITOM I and the second,

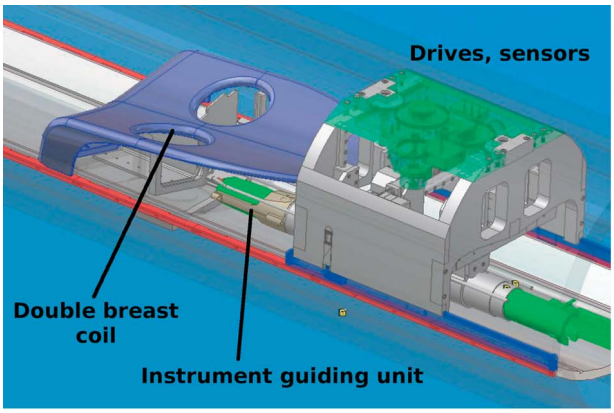

a)

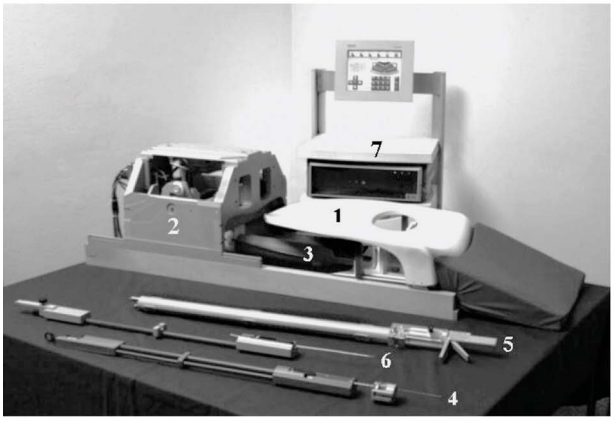

b)

Fig. 3.86. Schematic drawing (a) and photograph (b) of ROBITOM II with an interventional breast coil (1). A plastic rack (2) houses the piezo motors and sensors for positioning the extension arm along the *x*- and *y*-axis (3). This arm can be equipped with an instrument adapter for a scalpel and syringe for local anesthesia (4). The latter tool is replaced by the high-velocity gun (5) to insert the coaxial needle. The instrument adapter is then loaded with the biopsy-gun (6) (Magnum, Bard, Covington, USA) for taking the biopsy. The remote control (7) of the system is located outside the magnet bore within the fringe field of the scanner (<100 mT).

improved version, ROBITOM II (Pfleiderer et al., 2005a) have already been reported (Figs. 3.86 and 3.87).

3.3.6.6
MRI-Guided Percutaneous Minimally Invasive Therapy of Breast Lesions

Triggered by the National Cancer Institute, which published a statement in 1991 favoring breast-conservation therapy (BCT) as the preferred surgical treatment of early-stage breast cancer (NIH Consensus Conference, 1991), radical mastectomy

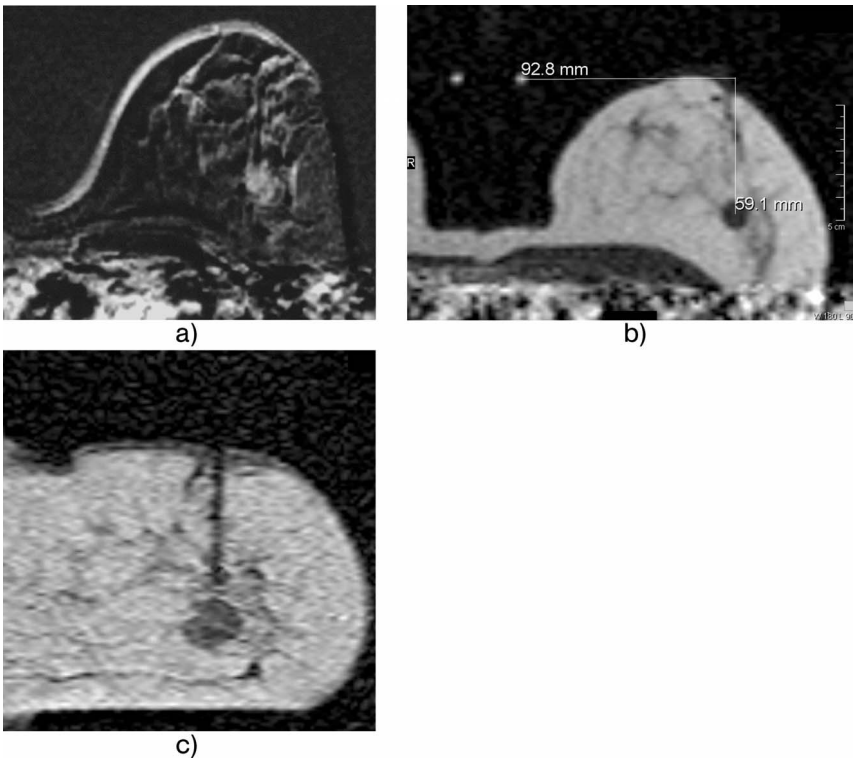

Fig. 3.87. (a) The contrast-enhancing lesion in the upper lateral quadrant of the left breast of a 46-year-old patient is identified on the subtracted transverse image of the dynamic series. (b) The spatial relationship between the lesion and the two oil markers was determined by the built-in scanner software (white lines). (c) After insertion, the trocar is centrally located with its tip in front of the suspicious lesion, as seen on the coronal 3D gradient echo image. The histology of the biopsy revealed an invasive ductal cancer which was confirmed after surgical excision.

has since then been slowly replaced by BCT. Based on 20-year follow-ups comparing BCT with radical mastectomy (Fisher et al., 2002; Veronesi et al., 2002), no improved outcome was indicated for radical mastectomy. Even for larger tumors radical therapeutic procedures are becoming less important, although it appears that BCT still tends to be underutilized in the U.S. (Morrow et al., 2001).

An increasing number of studies has been published meanwhile using percutaneous minimally invasive methods for treatment, such as interstitial laser therapy (ILT), radiofrequency ablation (RFA) (Burak et al., 2003), or high-intensive focused ultrasound (HIFU) (Hynynen et al., 2001).

All of these procedures deposit thermal energy to destroy the malignant tumor cells. RFA has been carried out using ultrasound as the monitoring imaging modality, whereas HIFU and ILT have mainly been performed under MR-guidance. Several studies demonstrate high success rates (>70% total tumor destruction) for

ILT (Dowlatshahi et al., 2002). With RFA treatment, the published rates for fully cured patients vary from 64% to 95% (Hayashi et al., 2003; Fornage et al., 2004) depending on the original diagnosis (focal, nonfocal). Complete tumor destruction after HIFU of breast cancer has been reported in two of nine (22%) patients (Gianfelice et al., 2003).

A different approach destroys tumor tissue by freezing. Cryotherapy can be applied percutaneously for the treatment of early breast cancer (Morin et al., 2004), and seems most effective with focal breast cancer of 15 mm diameter or less (Pfleiderer et al., 2005b). For tumors larger than 16 mm, patients still showed viable invasive residues after treatment (Pfleiderer et al., 2002). Similar findings have been reported by other authors, independent of the chosen minimally invasive method, thus indicating effective treatment only in early-stage T1 breast cancers (Roubidoux et al., 2004). MRI appears promising for the effective monitoring of cryotherapeutic interventions as frozen tissue is easily identified on the images. In contrast, ultrasound can only delineate the surface of the iceball facing the transducer due to acoustic shadowing of the tissue behind the iceball. Ultrasound may also underestimate the true microscopic extent of the tumor (Malich et al., 2001), which may then result in an undertreatment of breast lesions.

Ultimately, the combination of robot-assisted targeting and MR-guided intervention, as has been realized with ROBITOM, may prove to be the method of choice for exact delineation and ablation monitoring in the therapy of breast cancer. This concept of closely integrating imaging and minimally invasive treatment may lead to a one-stop-shop scenario, enabling diagnostic imaging, MR-guided breast biopsy and percutaneous minimally invasive therapy within one single patient session.

3.3.6.7 New Perspectives

Recent research has led to the identification of proteins in tumors that prove suitable as therapeutic targets, thus opening new avenues for the treatment of breast cancer (Schnitt, 2001). Imaging technologies – including MRI – continue to advance, and many powerful new methods for *in-vivo* cellular and molecular imaging are emerging. Multimodal methods that combine anatomic imaging with functional measurements may provide imaging assays that can be used noninvasively to assess the effects of treatment dynamically and over the whole tumor. Combined MR measurements of tumor vascularity, water diffusion, and chemical shift imaging of metabolic concentrations could add specificity, whereas recent advances in the understanding of molecular and genetic alterations underlying breast cancer development and progression, together with the development of new chemotherapeutic agents, may lead to novel therapeutic strategies (Sauer et al., 2002).

Tumor-targeted contrast agents for MRI may improve the specificity of breast MRI substantially. It is well known that malignant tumors express angiogenetic factors, such as the vascular endothelial growth factor (VEGF) or basic fibroblast growth factor (bFGF) which induce neoangiogenesis (Folkman and Klagsbrun, 1987). Without these growth factors, tumors would be limited to the size of a few

millimeters. Tumor vessels are very different from normal vessels; they may be tortuous, and have a higher permeability and leakiness which allows larger proteins to traverse the vessel walls.

One possible important pathological target for refined tumor diagnosis and prognosis is the Her-2/neu protein. This protein is a member of the epidermal growth factor (EGF) receptor family, and is known to be overexpressed in 25–35% of breast tumors (Kim et al., 2001). The receptor is expressed at the membrane surface, which makes it accessible to high-affinity binding of specific probes, such as optical (Hilger et al., 2004) or superparamagnetic nanoparticle probes. High-affinity anti-Her-2/neu antibodies have been coupled directly (Funovics et al., 2004) or via ligand molecules such as the streptavidin-biotin system (Artemov et al., 2003) to relatively small magnetic nanoparticles (SPIO; particle diameter ca. 50 nm). Although labeled cells could be successfully imaged *in vitro*, the availability of *in-vivo* data is so far still limited.

The use of biologically functionalized probes in imaging is a rapidly growing research field that will represent the next step towards a complete and integrated functional characterization of different pathologies, including tumors, arthritis, and inflammations. Multimodal approaches (NIR, MRI, PET, fluorescence marker, etc.) are especially promising. Specific magnetic nanoparticles will play an important role as potent MR signal contrast amplifiers for target detection, although the clinical viability, the biocompatibility of these particles and the involved metabolic processes still have to be investigated.

3.3.6.8 Conclusion

MRI of the breast is a powerful and versatile tool that will improve the ability to screen and treat women with breast cancer, and also provide insight that will catalyze changes in management. With the added information that this imaging modality provides, clinicians can better diagnose and even treat breast disease. Meanwhile, investigations continue into the optimization of MRI protocols and the development of new technologies. Further improvements and advancements are sure to result in an expanded role for MRI in breast imaging and therapy.

Abbreviations/Acronyms

2D	Two-dimensional
3D	Three-dimensional
ADC	Apparent diffusion coefficient
ASSET	Array spatial sensitivity encoding technique
bFGF	Basic fibroblast growth factor
BCT	Breast conservation therapy
CM	Contrast medium
DWI	Diffusion-weighted imaging

EPI	Echo planar imaging
EPS	Echo planar spectroscopy
FOV	Field of view
GRE	Gradient echo
HIFU	High intensive focused ultrasound
ILT	Interstitial laser therapy
iPAT	Integrated parallel acquisition techniques
IP	In-phase
MIP	Maximum intensity projection
MR	Magnetic resonance
MRI	Magnetic resonance imaging
MRM	Magnetic resonance mammography
NIR	Near-infrared
OP	Opposed-phase
PET	Positron emission tomography
RF	Radiofrequency
RFA	Radiofrequency ablation
ROBITOM	Robotic system for biopsy and interventional therapy of mammary lesions
ROI	Region of interest
SAR	Specific absorption rate
SENSE	Sensitivity encoding
SIP	Subtraction of in-phase
SIPOP	Subtraction between in-phase and opposed-phase
SPIO	Small paramagnetic iron oxide
SNR	Signal-to-noise ratio
VEGF	Vascular endothelial growth factor
VIBE	Volumetric interpolated breath-hold examination

References

Aichinger, U., Schulz-Wendtland, R., Kramer, S., Lell, M., and Bautz, W. (2002). Scar or recurrence – comparison of MRI and color-coded ultrasound with echo signal amplifiers. *Rofo Fortschr. Geb. Röntgenstr. Neuen Bildgeb. Verfahr.*, **174**, 395–401.

Artemov, D., Mori, N., Ravi, R., and Bhujwalla, Z.M. (2003). Magnetic resonance molecular imaging of the HER-2/neu receptor. *Cancer Res.*, **63**, 2723–2727.

Bishop, J.E., Santyr, G.E., Kelcz, F., and Plewes, D.B. (1997). Limitations of the keyhole technique for quantitative dynamic contrast-enhanced breast MRI. *J. Magn. Reson. Imaging*, **7**, 716–723.

Bluemke, D.A., Gatsonis, C.A., Chen, M.H., DeAngelis, G.A., DeBruhl, N., Harms, S., Heywang-Kobrunner, S.H., Hylton, N., Kuhl, C.K., Lehman, C., Pisano, E.D., Causer, P., Schnitt, S.J., Smazal, S.F., Stelling, C.B., Weatherall, P.T., and Schnall, M.D. (2004). Magnetic resonance imaging of the breast prior to biopsy. *JAMA*, **292**, 2735–2742.

Burak, W.E., Jr., Agnese, D.M., Povoski, S.P., Yanssens, T.L., Bloom, K.J., Wakely, P.E., and Spigos, D.G. (2003). Radiofrequency ablation of invasive breast carcinoma followed by delayed surgical excision. *Cancer*, **98**, 1369–1376.

Daniel, B.L., Yen, Y.F., Glover, G.H., Ikeda, D.M., Birdwell, R.L., Sawyer-Glover, A.M., Black, J.W., Plevritis, S.K., Jeffrey, S.S., and Herfkens, R.J. (1998). Breast disease: dynamic spiral MR imaging. *Radiology*, **209**, 499–509.

Dowlatshahi, K., Francescatti, D.S., and Bloom, K.J. (2002). Laser therapy for small breast cancers. *Am. J. Surg.*, **184**, 359–363.

Du, W., Du, Y.P., Bick, U., Fan, X., MacEneaney, P.M., Zamora, M.A., Medved, M., and Karczmar, G.S. (2002). Breast MR imaging with high spectral and spatial resolutions: preliminary experience. *Radiology*, **224**, 577–585.

El Yousef, S.J., Alfidi, R.J., Duchesneau, R.H., Hubay, C.A., Haaga, J.R., Bryan, P.J., LiPuma, J.P., and Ament, A.E. (1983). Initial experience with nuclear magnetic resonance (NMR) imaging of the human breast. *J. Comput. Assist. Tomogr.*, **7**, 215–218.

Fischer, D.R., Wurdinger, S., Boettcher, J., Malich, A., and Kaiser, W.A. (2005). Further signs in the evaluation of magnetic resonance mammography: a retrospective study. *Invest. Radiol.*, **40**, 430–435.

Fischer, U., Kopka, L., and Grabbe, E. (1999). Breast carcinoma: effect of preoperative contrast-enhanced MR imaging on the therapeutic approach. *Radiology*, **213**, 881–888.

Fisher, B., Anderson S., Bryant, J., Margolese, R.G., Deutsch, M., Fisher, E.R., Jeong, J.H., and Wolmark, N. (2002). Twenty year follow-up of a randomized trial comparing total mastectomy, lumpectomy, and lumpectomy plus irradiation for the treatment of invasive breast cancer. *N. Engl. J. Med.*, **347**, 1233–1241.

Folkman, J. and Klagsbrun, M. (1987). Angiogenic factors. *Science*, **235**, 442–447.

Fornage, B.D., Sneige, N., Ross, M.I., Mirza, A.N., Kuerer, H.M., Edeiken, B.S., Ames, F.C., Newman, L.A., Babiera, G.V., and Singletary, S.E. (2004). Small ($\leq$ 2 cm) breast cancer treated with ultrasound-guided radiofrequency ablation: Feasibility study. *Radiology*, **231**, 215–224.

Friedman, P.D., Swaminathan, S.V., and Smith, R. (2005). SENSE imaging of the breast. *Am. J. Roentgenol.*, **184**, 448.

Funovics, M.A., Kapeller, B., Hoeller, C., Su, H.S., Kunstfeld, R., Puig, S., and Macfelda, K. (2004). MR imaging of the her2/neu and 9.2.27 tumor antigens using immunospecific contrast agents. *Magn. Reson. Imaging*, **22**, 843–850.

Gianfelice, D., Khiat, A., Amara, M., Belblidia, A., and Boulanger, Y. (2003). MR imaging-guided focused US ablation of breast cancer: histopathologic assessment of effectiveness – initial experience. *Radiology*, **227**, 849–855.

Giersiepen, K., Heitmann, C., Janhsen, K., and Lange, C. (2005). Brustkrebs in *Gesundheitsberichterstattung des Bundes (Heft 25)*, Robert Koch-Institut (Ed.), Oktoberdruck, Berlin, 1–23.

Gordon, R., Wirth, M., Schellenberg, J., and Sivaramakrishna, R. (2004). Workshop on Alternatives to Mammography, Winnipeg, (http://www.win.trlabs.ca/wam/index.html).

Griswold, M.A., Jakob, P.M., Heidemann, R.M., Nittka, M., Jellus, V., Wang, J., Kiefer, B., and Haase, A. (2002). Generalized autocalibrating partially parallel acquisitions (GRAPPA). *Magn. Reson. Med.*, **47**, 1202–1210.

Guo, Y., Cai, Y.Q., Cai, Z.L., Gao, Y.G., An, N.Y., Ma, L., Mahankali, S., and Gao, J.H. (2002). Differentiation of clinically benign and malignant breast lesions using diffusion-weighted imaging. *J. Magn. Reson. Imaging*, **16**, 172–178.

Hayashi, A.H., Silver, S.F., van der Westhuizen, N.G., Donald, J.C., Parker, C., Fraser, S., Ross, A.C., and Olivotto, I.A. (2003). Treatment of invasive breast carcinoma with ultrasound-guided radiofrequency ablation. *Am. J. Surg.* **185**, 429–435.

Heywang, S.H., Wolf, A., Pruss, E., Hilbertz, T., Eiermann, W., and Permanetter, W. (1989). MR imaging of the breast with Gd-DTPA: use and limitations. *Radiology*, **171**, 95–103.

Hilger, I., Leistner, Y., Berndt, A., Fritsche, C., Haas, K.M., Kosmehl, H., and Kaiser, W.A. (2004). Near-infrared fluorescence imaging of HER-2 protein over-expression in tumour cells. *Eur. Radiol.*, **14**, 1124–1129.

Huang, W., Fisher, P.R., Dulaimy, K., Tudorica, L.A., O'Hea, B., and Button, T.M. (2004). Detection of breast malignancy: diagnostic MR protocol

for improved specificity. *Radiology*, **232**, 585–591.

Hulka, C.A., Smith, B.L., Sgroi, D.C., Tan, L., Edmister, W.B., Semple, J.P., Campbell, T., Kopans, D.B., Brady, T.J., and Weisskoff, R.M. (1995). Benign and malignant breast lesions: differentiation with echo-planar MR imaging. *Radiology*, **197**, 33–38.

Hussain, Z., Roberts, N., Whitehouse, G.H., Garcia-Finana, M., and Percy, D. (1999). Estimation of breast volume and its variation during the menstrual cycle using MRI and stereology. *Br. J. Radiol.*, **72**, 236–245.

Hylton, N. (2005). Magnetic resonance imaging of the breast: opportunities to improve breast cancer management. *J. Clin. Oncol.*, **23**, 1678–1684.

Hynynen, K., Pomeroy, O., Smith, D.N., Huber, P.E., McDannold, N.J., Kettenbach, J., Baum, J., Singer, S., and Jolesz, F.A. (2001). MR imaging-guided focused ultrasound surgery of fibroadenomas in the breast: a feasibility study. *Radiology*, **219**, 176–185.

Kaiser, W.A. and Zeitler, E. (1989). MR imaging of the breast: fast imaging sequences with and without Gd-DTPA. Preliminary observations. *Radiology*, **170**, 681–686.

Kaiser, W.A., Fischer, H., Vagner, J., and Selig, M. (2000). Robotic system for biopsy and therapy of breast lesions in a high-field whole-body magnetic resonance tomography unit. *Invest. Radiol.*, **35**, 513–519.

Kim, Y.S., Konoplev, S.N., Montemurro, F., Hoy, E., Smith, T.L., Rondón, G., Champlin, R.E., Sahin, A.A., and Ueno, N.T. (2001). HER-2/neu overexpression as a poor prognostic factor for patients with metastatic breast cancer undergoing high-dose chemotherapy with autologous stem cell transplantation. *Clin. Cancer Res.*, **7**, 4008–4012.

Malich, A., Boehm, T., Facius, M., Freesmeyer, M., Fleck, M., Anderson, R., and Kaiser, W.A. (2001). Differentiation of mammographically suspicious lesions: evaluation of breast ultrasound, MRI mammography and electrical impedance scanning as adjunctive technologies in breast cancer detection. *Clin. Radiol.*, **56**, 278–283.

Morin, J., Traore, A., Dionne, G., Dumont, M., Fouquette, B., Dufour, M., Cloutier, S., and Moisan, C. (2004). Magnetic resonance-guided percutaneous cryosurgery of breast carcinoma: technique and early clinical results. *Can. J. Surg.*, **47**, 347–351.

Morrow, M., Scott, S.K., Menck, H.R., Mustoe, T.A., and Winchester, D.P. (2001). Factors influencing the use of breast reconstruction postmastectomy: a National Cancer Database study. *J. Am. Coll. Surg.*, **192**, 1–8.

Müller-Schimpfle, M., Ohmenhausen, K., Stoll, P., Dietz, K., and Claussen, C.D. (1997). Menstrual cycle and age. Influence on parenchymal contrast medium enhancement in MR imaging of the breast. *Radiology*, **203**, 145–149.

Mumtaz, H., Hall-Craggs, M.A., Wotherspoon, A., Paley, M., Buonaccorsi, G., Amin, Z., Wilkinson, I., Kissin, M.W., Davidson, T.I., Taylor, I., and Bown, S.G. (1996). Laser therapy for breast cancer: MR imaging and histopathologic correlation. *Radiology*, **200**, 651–658.

Mushlin, A.I., Kouides, R.W., and Shapiro, D.E. (1998). Estimating the accuracy of screening mammography: a meta-analysis. *Am. J. Prev. Med.*, **14**, 143–153.

Padhani, A.R., Ah-See, M.L., and Makris, A. (2005). MRI in the detection and management of breast cancer. *Expert Rev. Anticancer Ther.*, **5**, 239–252.

Pfleiderer, S.O.R., Freesmeyer, M.G., Marx, C., Kühne-Heid, R., Schneider, A., and Kaiser, W.A. (2002). Cryotherapy of breast cancer under ultrasound guidance: initial results and limitations. *Eur. Radiol.*, **12**, 3009–3014.

Pfleiderer, S.O.R., Reichenbach, J.R., Azhari, T., Marx, C., Wurdinger, S., and Kaiser, W.A. (2003). Dedicated double breast coil for magnetic resonance mammography imaging, biopsy, and preoperative localization. *Invest. Radiol.*, **38**, 1–8.

Pfleiderer, S.O.R., Sachse, S., Sauner, D., Marx, C., Malich, A., Wurdinger, S., and Kaiser, W.A. (2004). Changes in magnetic resonance mammography due to hormone replacement therapy. *Breast Cancer Res.*, **6**, R232–R238.

Pfleiderer, S.O.R., Marx, C., Vagner, J., Franke, R.P., Reichenbach, J.R., and Kaiser, W.A. (2005a). Magnetic resonance-guided large-core breast biopsy inside a 1.5-T magnetic resonance scanner using an automatic system: in vitro experiments and preliminary clinical experience in four patients. *Invest. Radiol.*, **40**, 458–463.

Pfleiderer, S.O.R., Marx, C., Camara, O., Gajda, M., and Kaiser, W.A. (2005b). Ultrasound-guided percutaneous cryotherapy of small ($\leq$ 15 mm) breast cancers. *Invest. Radiol.*, **40**, 472–477.

Pruessmann, K.P., Weiger, M., Scheidegger, M.B., and Boesiger, P. (1999). SENSE: sensitivity encoding for fast MRI. *Magn. Reson. Med.*, **42**, 952–962.

Reichenbach, J.R., Przetak, C., Klinger, G., and Kaiser, W.A. (1999). Assessment of breast tissue changes on hormonal replacement therapy using MRI. A pilot study. *J. Comput. Assist. Tomogr.*, **23**, 407–413.

Reichenbach, J.R., Wurdinger, S., Pfleiderer, S.O., and Kaiser, W.A. (2000). Comparison of artifacts produced from carbon fiber and titanium alloy needles at 1.5 T MR imaging. *J. Magn. Reson. Imaging*, **11**, 69–74.

Reichenbach, J.R., Hopfe, J., Rauscher, A., Wurdinger, S., and Kaiser, W.A. (2005). Subtraction of in-phase and opposed-phase images in dynamic MR mammography. *J. Magn. Reson. Imaging*, **21**, 565–575.

Rieber, A., Nüssle, K., Merckle, E., Kreienberg, R., Tomczak, R., and Brambs, H.J. (1999). MR mammography. influence of menstrual cycle on the dynamic contrast enhancement of fibrocystic disease. *Eur. Radiol.*, **9**, 1107–1112.

Ross, R.J., Thompson, J.S., Kim, K., and Bailey, R.A. (1982). Nuclear magnetic resonance imaging and evaluation of human breast tissue: preliminary clinical trials. *Radiology*, **143**, 195–205.

Roubidoux, M.A., Sabel, M.S., Bailey, J.E., Kleer, C.G., Klein, K.A., and Helvie, M.A. (2004). Small (<2.0 cm) breast cancers: Mammographic and US findings at US-guided cryoablation – initial experience. *Radiology*, **233**, 857–867.

Sardanelli, F., Iozzelli, A., and Fausto, A. (2003). MR imaging of the breast: indications, established technique, and new directions. *Eur. Radiol.*, **13** (Suppl. 3), N28–N36.

Sauer, G., Deissler, H., Kurzeder, C., and Kreienberg, R. (2002). New molecular targets of breast cancer therapy. *Strahlenther. Onkol.*, **178**, 123–133.

Schnitt, S.J. (2001). Breast cancer in the 21st century: new opportunities and new challenges. *Mod. Pathol.*, **14**, 213–218.

Sinha, S., Lucas-Quesada, F.A., Sinha, U., DeBruhl, N., and Bassett, L.W. (2002). In vivo diffusion-weighted MRI of the breast: potential for lesion characterization. *J. Magn. Reson. Imaging*, **15**, 693–704.

Sivaramakrishna, R. (2005). 3D breast image registration – a review. *Technol. Cancer Res. Treat.*, **4** (1), 39–48.

Sodickson, D.K. and Manning W.J. (1997). Simultaneous acquisition of spatial harmonics (SMASH): fast imaging with radiofrequency coil arrays. *Magn. Reson. Med.*, **38**, 591–603.

Tozaki, M. and Fukuda, K. (2005). Supine MR mammography using VIBE with parallel acquisition technique for the planning of breast-conserving surgery: Clinical feasibility. *Breast*, 15 (1), 137–140.

Veltman, J., Boetes, C., Wobbes, T., Blickman, J.G., and Barentsz, J.O. (2005). Magnetic resonance-guided biopsies and localizations of the breast: initial experiences using an open breast coil and compatible intervention device. *Invest. Radiol.*, **40**, 379–384.

Veronesi, U., Cascinalli, N., Mariani, L., Greco, M., Saccozzi, R., Luini, A., Aguilar, M., and Marubini, E. (2002). Twenty-year follow-up of a randomized study comparing breast conservation surgery with radical mastectomy for early breast cancer. *N. Engl. J. Med.*, **347**, 1227–1232.

Vomweg, T.W., Teifke, A., Kunz, R.P., Hintze, C., Hlawatsch, A., Kern, A., Kreitner, K.F., and Thelen, M. (2004). Combination of low and high resolution sequences in two orientations for dynamic contrast-enhanced MRI of the breast: more than a compromise. *Eur. Radiol.*, **14**, 1732–1742.

Weidner, N., Semple J.P., Elch, W.R., and Folkman, J. (1991). Tumor angiogenesis and metastasis-correlation in invasive breast carcinoma. *N. Engl. J. Med.*, **324**, 1–8.

Yen, Y.F., Han, K.F., Daniel, B.L., Heiss, S., Birdwell, R.L., Herfkens, R.J., Sawyer-Glover, A.M., and Glover, G.H. (2000). Dynamic breast MRI with spiral trajectories: 3D versus 2D. *J. Magn. Reson. Imaging*, **11**, 351–359.

Zippel, D.B. and Papa, M.Z. (2005). The use of MR imaging guided focused ultrasound in breast cancer patients; a preliminary phase one study and review. *Breast Cancer*, **12**, 32–38.

3.3.7 MR Spectroscopy

Peter Bachert

3.3.7.1 Introduction

While conventional MR imaging (MRI) yields morphological and functional information, high-resolution nuclear magnetic resonance spectroscopy (NMRS or MRS) provides a window into the metabolism of tissue and organs. This means that certain biomolecules – essentially compounds of high mobility and low molecular mass – can be detected and quantified with respect to their concentration and metabolic turnover. The measurement technique is noninvasive and applicable to living tissue (*in vivo*) without risk of damage (if safety standards of radiofrequency energy deposition are obeyed). Presently, with these properties MRS is unique among the whole available technology.

The term ''high-resolution'' refers to studies of intramolecular spins in liquids where the rapid Brownian tumbling motion averages to zero the dipole-dipole interaction between pairs of nuclear spins. As a consequence, chemical shifts and scalar spin-spin couplings are resolved in strong magnetic fields (magnetic induction B_0). High-resolution is possible in spectra obtained from living tissue, particularly in localized proton (^{1}H) MRS of the human brain at $B_0 = 1.5$ T (Frahm et al., 1989) where linewidths of a few Hz are obtained routinely in whole-body tomographs.

Major clinical applications of MRS are studies of the energy metabolism of diseased muscle, of the neurochemistry of non-neoplastic diseases of the brain, and of tumor biochemistry. The latter is particularly important, because prognosis and response to chemo- and/or radiotherapy of a tumor disease are determined – in general terms – by tumor-biological factors. A large number of *in-vivo* MRS studies (clinical and animal studies) during the past 20 years have shown changes in MR spectra during tumor therapy that preceded changes in tumor morphology (Negendank, 1992).

3.3.7.2 High-Resolution Nuclear Magnetic Resonance Spectroscopy *In Vivo*

The substrate of MRS is microscopic magnetic fields that are modified by the interaction of the electron cloud of the molecule, which carries the nuclear spin, with the external static magnetic field B_0. This important physical effect is called ''chemical shift'', since chemical structure determines the change of the local magnetic field (B_{loc}) and hence of the resonance frequency (ω). The fundamental relationship reads:

$$\omega = \gamma B_{\text{loc}} = \gamma(1-\sigma)B_0 = \omega_0 - \gamma\sigma B_0 \tag{3.47}$$

where σ is a quantity that measures chemical shift, ω_0 is the Larmor frequency of the spin without shielding of the external field, and γ is the gyromagnetic ratio of the nucleus. In the case of ^{1}H: $\gamma = 2\pi \times 42.57$ MHz T^{-1}. Chemical shifts are of the order of 10^{-6} (ppm) of the resonance frequency. For example, the frequency shift of ^{1}H at $B_0 = 1.5$ T is about $10^{-6} \times \omega_0 = 63.9$ Hz.

Spin-Spin Couplings

Equation (3.47) is the solution of the eigenvalue problem of the Zeeman Hamiltonian, which is linear in the spin operator. Fine structure in MR spectra is explained by scalar and dipolar couplings, which are bilinear in the spin operators. High-resolution MR spectra often show line broadenings and multiplet splittings owing to the scalar coupling between two nuclear spins. This interaction, also called *J*-coupling, is mediated by the electron cloud of the molecule and is hence a pure intramolecular effect. The notation is explained by the structure of the Hamilton operator that describes this interaction. In its simplest form, it is the scalar product of the spin operators of the two nuclei times the coupling constant J: $J(\vec{\hat{\mathbf{I}}}_1 \cdot \vec{\hat{\mathbf{I}}}_2)$. For a pair of directly bound ^{13}C and ^{1}H nuclei, for example, scalar line splittings in ^{13}C MR spectra are of the order of $J_{\text{CH}} \sim 120$–180 Hz. If there are two or three bonds in between, the coupling strength reduces significantly.

The other spin-spin interaction, the dipole-dipole coupling, is effective through empty space and therefore can involve spins in the same or in different molecules. The dipolar coupling strength depends heavily on spatial distance (which is utilized for structure analysis of macromolecules with NMR). In liquid phase it is averaged to zero, as mentioned above. Without isotropic averaging the dipolar coupling would produce excessive broadening of resonance lines, making high-resolution MRS impossible. However, the interaction cannot be neglected completely. It provides relaxation pathways for excited spins in heteronuclear double-resonance experiments enabling signal enhancements of rare spins (nuclear Overhauser effect, NOE). Moreover, small line splittings of a few Hz were discovered in ^{1}H MR spectra of human leg muscle at 1.5 T which were attributed to non-vanishing residual dipolar interaction (Kreis and Boesch, 1994).

The complete nuclear spin Hamilton operator finally includes the quadrupolar coupling term which is quadratic in the spin operators. This interaction occurs in nuclei with spin $\mathrm{I} > \frac{1}{2}$. These are less important for *in-vivo* MRS; hence only spin $-\frac{1}{2}$ nuclei will be considered in the following.

Sensitivity

Since the frequency resolution of MRS is extraordinary, the effects of weak magnetic fields within molecules on microscopic magnetic moments can be detected. Nuclear magnetic moments are extremely small (e.g., the dipole moment of the proton: $\mu_{\text{p}} \sim 10^{-27}$ *J* T^{-1}), and so are the released energies (ΔE) when nuclear spins change their states in a magnetic field. The energy of the photon emitted

during an ^{1}H-spin flip in a field $B_0 = 1.5$ T is $\Delta E = 4.2 \times 10^{-26}$ $J = 2.6 \times 10^{-7}$ eV. The comparison, for example, with the energy of the single quanta detected in positron emission tomography (PET), $E_\gamma = 5.11 \times 10^5$ eV, shows that an astronomically large number of photons must be collected to obtain an MR signal. The low sensitivity (= signal-to-noise ratio, SNR) is the major limitation of MRS.

Technically, SNR is proportional to the first data point (= signal intensity I) of the acquired free induction decay (FID) or spin-echo. The measured quantity is the voltage $U_{\mathrm{ind}}(t)$ induced by the precessing transverse magnetization M_{transv} in the radiofrequency antenna (RF coil). $U_{\mathrm{ind}}(t)$ is proportional to the time derivative of M_{transv}, which depends on the number n of spins within the sensitive volume V of the coil, on γ, and B_0 (with exponent $\alpha \cong 2$):

$$\frac{\mathrm{d}M(t)_{\mathrm{transv}}}{dt} \propto \frac{\mathrm{n}}{V}\gamma^3 I(I+1)B_0^{\alpha} \tag{3.48}$$

The sensitivity increases when the experiment is repeated (SNR $\propto \sqrt{nex}$, *nex* = number of excitations) and when more spins are excited. MRS therefore requires long measurement times ($\sim$ min), large voxel sizes ($\sim$ cm^3), and high concentrations ($\sim$ mM) of the metabolites in the tissue (orders of magnitude valid for *in-vivo* MRS at 1.5 T). The threshold of metabolite concentrations is about $c_{\mathrm{min}} \sim 0.1$ mM $= 10^{-4}$ M $= 100$ nmol (g wet tissue)$^{-1}$.

Technical Prerequisites

The MRS examination is time-consuming, not only because of the requirement of large *nex*. A number of adjustment procedures of the measurement system must be performed before starting acquisition of spectra. These include positioning and tuning of the RF antenna, MRI to localize the region of interest and define the voxel, optimization of B_0-homogeneity (measures that increase homogeneity of magnetic fields are called "shim"), switch of the RF system from ^{1}H to X nucleus frequency (if necessary), and adjustment of RF pulses (e.g., for water signal suppression in ^{1}H MRS).

In order to obtain tissue-specific biochemical information by MRS in human subjects, techniques that permit spatial localization are mandatory. Progress in this field over the past 20 years has led to the following now widely employed methods:

- Planar coils (loop diameter of a few cm) to obtain signals from tissue near the surface of the human body (surface coils).
- Single-voxel spectroscopy (SVS) with STEAM (stimulated echo acquisition mode; Frahm et al., 1989) or PRESS (point-resolved spectroscopy), consisting of a series of 90°-90°-90° (STEAM) or 90°-180°-180° RF pulses (PRESS) with simultaneous orthogonal gradients in combination with coils with high B_1-homogeneity (e.g., volume resonators: head coil).
- Spectroscopic imaging (SI) with two or three phase-encoding gradients, but no frequency-encoding gradient (2D or 3D SI; Brown et al., 1982; Maudsley et al.,

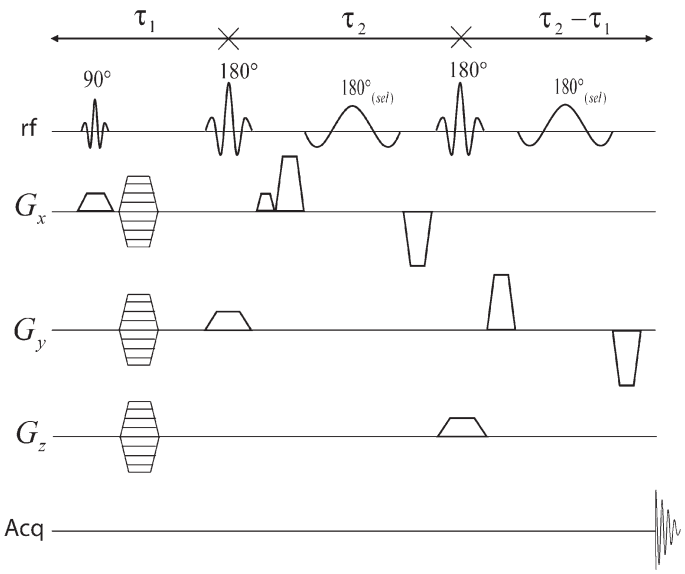

Fig. 3.88. Example of a high-performance pulse sequence for three-dimensional proton spectroscopic imaging (3D ^{1}H SI) developed for examinations of the human prostate (Scheenen et al., 2004). Double spin-echo sequence (PRESS) with three slice-selective radiofrequency (rf) pulses (90°-180°-180°) to generate an Hahn spin-echo from spins within the PRESS box and two frequency-selective inversion pulses ($180°_{(sel)}$) for water and lipid signal suppression (τ_i = time delays, G_j = gradients in three spatial directions, Acq = signal acquisition). The sequence starts with an outer volume suppression (OVS) module (not drawn).

1983) (Fig. 3.88) or echo-planar spectroscopic imaging (EPSI; Posse et al., 1995) where an oscillating gradient is applied during signal detection; at 1.5 T SI is essentially applicable to ^{1}H (voxel size: 1 cm^3), while ^{31}P permits only limited spatial resolution (voxel size: ca. 30 cm^3).

High-resolution MRS requires technical equipment beyond that of conventional MRI:

- high B_0 (the stronger the field, the larger the signal);
- high B_0-homogeneity (mandatory for acquisition of spectra with narrow resonance lines);
- broadband RF system including specific coils for detection of ^{1}H and different X nuclei (X = ^{13}C, ^{19}F, ^{31}P, etc.); the implementation of a second RF channel is useful, because it enables double-resonance techniques, for example ^{1}H-decoupling for X signal enhancement (NOE) and collapse of scalar-coupled multiplets to singlets in the spectrum of the X nucleus (Heerschap et al., 1989; Luyten et al., 1989; Bachert et al., 1992; Ende and Bachert, 1993; Gonen et al., 1997).

Finally, software is needed for the different processes of adjustment of the measurement system, the control of the sequence of RF and gradient pulses during the measurement, and the post-processing of acquired signals. Display and quantitative evaluation of MRS data includes:

- zero-filling and apodization of the FID or echo signal;
- Fourier transformation;
- phase and baseline correction;
- fit of resonance lines and calculation of peak areas (= signal intensity I), line positions, and line widths;
- determination of metabolite concentrations (absolute quantification); and
- calculation of metabolic maps from SI data.

Nuclei for *In-Vivo* MRS

The low sensitivity implies that, *in vivo*, MRS mainly uses spin probes that occur with high natural abundance (n.a.) in biological tissue. The most important endogenous magnetically active nuclei are ^{1}H and phosphorus (^{31}P). Carbon and oxygen are abundant in tissue, but the common isotopes (^{12}C, ^{16}O) possess nuclear spin $I = 0$ and thus are invisible for MRS. The rare carbon isotope ^{13}C ($I = \frac{1}{2}$, n.a. = 1.1%) is difficult to detect in tissue metabolites except in fatty acids (Heerschap et al., 1989; Ende and Bachert, 1993), while ^{17}O is very rare (n.a. $= 3.7 \times 10^{-4}$) and a quadrupolar nucleus ($I = 5/2$) with poor sensitivity.

Enriched compounds have also been used. By this means, MRS allows the disposition kinetics of administered drugs to be monitored by detecting the signal of a spinlabel in the compound and its subsequent metabolites. In some studies, for example of the flux through the tricarboxylic acid (TCA) cycle (animal studies) or of glucose consumption in the human brain (Beckmann et al., 1991), compounds labeled with ^{13}C were employed. Particularly useful as spin labels are nuclei with physiological concentrations below the detection limit of *in-vivo* MRS, but sufficient sensitivity owing to the high administered dose of the tracer, such as fluorine (^{19}F, I $= \frac{1}{2}$, n.a. = 100%) (Wolf et al., 1987).

At this point it is helpful to discuss the metabolic information that spectra of the nuclei ^{1}H, ^{13}C, ^{19}F, and ^{31}P can provide, and then to describe some applications of MRS to studies conducted in healthy volunteers and patients. The properties of those nuclei that are relevant for *in-vivo* MRS are listed in Table 3.2.

3.3.7.3

Metabolic Information and Clinical Application: *In-Vivo* ^{1}H MRS

The proton has the largest γ and hence the highest Larmor frequency $\omega_0 = \gamma B_0$ of all magnetic nuclei (if the radioactive isotope ^{3}H is ignored). It is also the most abundant nucleus in living tissue, with large amounts in water and fatty acids (lipids). ^{1}H therefore yields the most intense *in-vivo* MR signal (the second intense signal is that of ^{23}Na in free sodium ions). To resolve the metabolite signals, which

Table 3.2. Properties of important nuclei of *in-vivo* MRS (spin $\frac{1}{2}$).

Nucleus	LARMOR frequency at $B_0 = 1.5$ T [MHz]	Natural abundance [%]	Relative sensitivity	Sensitivity *in vivo*[a)]
^{1}H	63.9	99.98	1	1
^{13}C	16.1	1.11	1.76×10^{-4}	2.66×10^{-5}
^{19}F	60.1	100	0.83	–
^{31}P	25.9	100	6.63×10^{-2}	2.32×10^{-4}

[a)] If all nuclei were detectable by MRS. Endogenous fluorine (^{19}F) mainly in solid structures (teeth, bones) and hence invisible for magnetic resonance.

are at least 10^4 to 10^5 times smaller than the tissue water resonance, the dominant signals must be suppressed selectively.

Localized ^{1}H MRS (Frahm et al., 1989) has created a new window into brain metabolism (''living neurochemistry''; Danielsen and Ross, 1999). In the cerebral parenchyma, physiological motion and susceptibility effects are small, and this favors high spectral resolution. Moreover, as healthy brain tissue contains no free fatty acids in MRS-detectable amounts, there is no interference of interesting peaks in the aliphatic ^{1}H spectral region and only water-signal suppression is needed. A quite large number of resonances assigned to protons in small cerebral metabolites are well resolved at $B_0 = 1.5$ T. A localized (SVS) ^{1}H MR spectrum obtained with echo time $T_E = 30$ ms from the brain of a healthy volunteer is shown in Figure 3.89. There are characteristic resonances assigned to protons in the following metabolites:

- *N*-acetyl-*L*-aspartate (NAA; functional groups detectable by MRS: -C**H**$_3$, chemical shift: $\delta = 2.01$ ppm, and -C**H**$_2$-, $\delta = 2.60$ ppm [relative to the tetramethylsilane singlet at $\delta = 0$])
- Creatine and phosphocreatine (Cr, PCr [both compounds are indistinguishable by ^{1}H MRS]; >N–C**H**$_3$, $\delta = 3.03$ ppm, and -C**H**$_2$-, $\delta = 3.93$ ppm).
- Trimethylamines (free choline and choline-containing compounds, Cho; -N$^+$≡(C**H**$_3$)$_3$, $\delta = 3.22$ ppm).
- *myo*-Inositol (mI; C_4-, C_6-protons, $\delta = 3.56$ ppm).
- Amino acids (e.g., aspartate, Glx [glutamate and glutamine]).

Metabolite concentrations in normal human brain tissue were determined *in vivo* by means of localized ^{1}H MRS. Ranges of values as published in the literature are listed in Table 3.3. Metabolic changes in the tissue are reflected in pronounced effects in *in-vivo* ^{1}H MR spectra, as illustrated by the following examples:

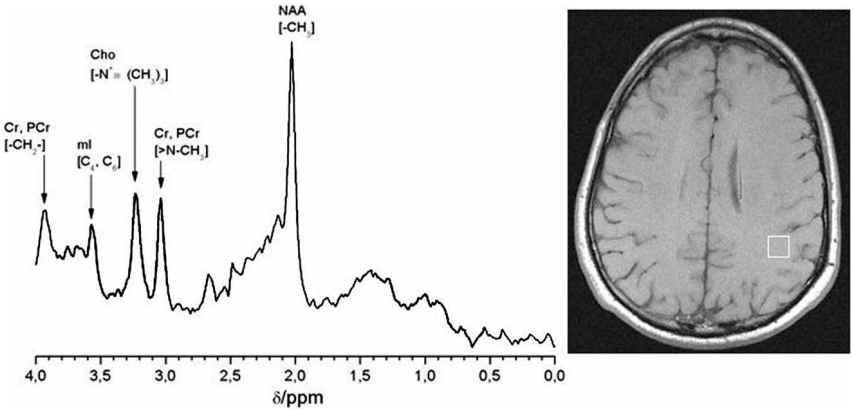

Fig. 3.89. Single-voxel ^{1}H MRS of the brain of a healthy volunteer (male, age 25 years). Double spin-echo sequence (PRESS) with water-signal suppression and measurement parameters: $T_R = 1500$ ms, $T_E = 30$ ms, *nex* = 256, measurement time = 6.4 min, voxel size = $15 \times 15 \times 15$ mm^3 (indicated in the transverse MR image), $B_0 = 1.5$ T; antenna system: head-imaging coil. Assignment of resolved resonances to molecular groups in the following metabolites: *N*-acetyl-*L*-aspartate (NAA, characteristic neurometabolite), creatines (Cr, PCr), cholines (Cho), and *myo*-inositol (mI). Chemical shifts δ (in ppm = 10^{-6}) are given relative to the frequency position of tetramethylsilane (TMS, $\delta = 0$).

- Loss of neuronal tissue, for example in dementia, multiple sclerosis, and brain tumors, proceeds with a reduction of NAA intensity (Fig. 3.90).
- ^{1}H MR spectra of tumors generally show enhanced Cho intensities (Figs. 3.90 and 3.91). The increase of Cho proceeds with tumor malignancy and proliferation.
- In spectra from regions with insufficient oxygen supply (hypoxic tissue) the characteristic signal of lactate can arise.

Table 3.3. Absolute concentrations (c) of metabolites of low molecular mass in normal human brain tissue as measured by localized ^{1}H MRS *in vivo* (ranges of values as published in the literature).

Metabolite(s)	Abbreviation	Chemical shift δ [ppm][a)]	c [mM]
N-acetyl-*L*-aspartate	NAA	2.01 [-CH_3]	8.0–17.0
Creatine, phosphocreatine	Cr, PCr	3.03 [>N–CH_3]	4.7–11.6
Cholines	Cho	3.22 [$-N^+\equiv(CH_3)_3$]	0.9–5.6
Myo-inositol	mI	3.56 [C_4-, C_6-protons]	3.3–8.1

[a)] Chemical shift reference: tetramethylsilane TMS ($\delta = 0$).

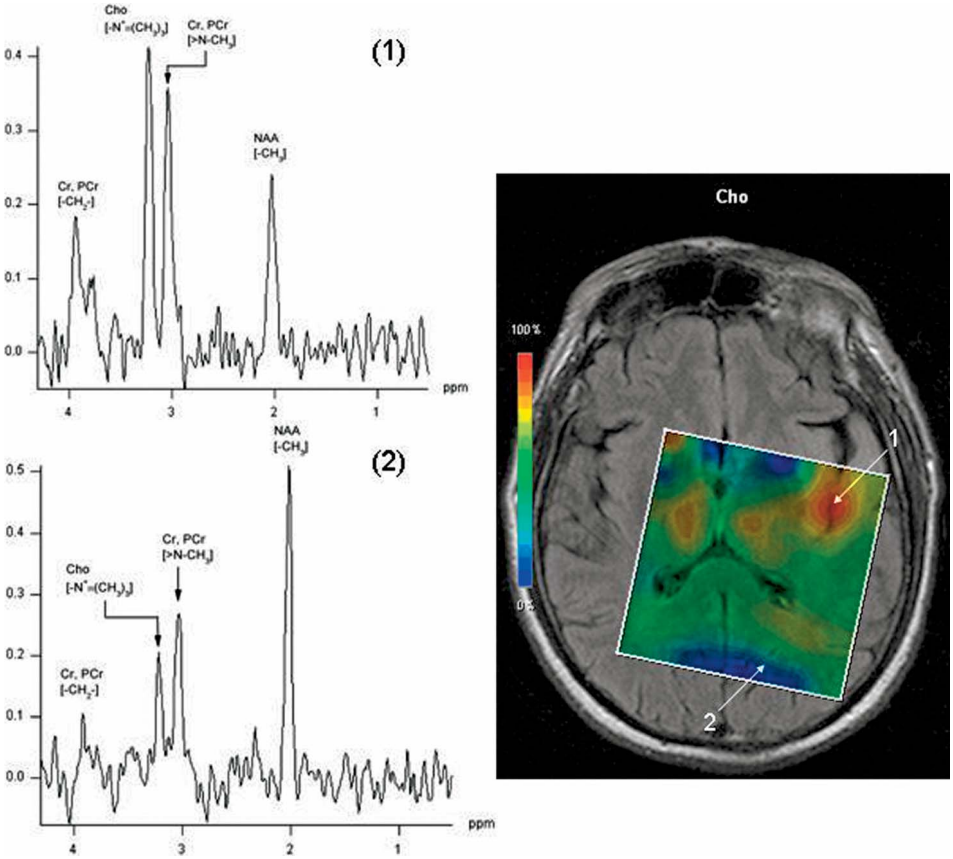

Fig. 3.90. Clinical study with proton spectroscopic imaging: spectrum from a patient (male, age 52 years) with brain tumor (astrocytoma). 2D ^{1}H SI with double spin-echo excitation (PRESS) and measurement parameters: $T_R = 2000$ ms, $T_E = 135$ ms, 16×16 phase-encoding gradient steps, *nex* = 2, measurement time = 6.2 min (weighted *k*-space acquisition), $B_0 = 1.5$ T; antenna system: head-imaging coil. Transverse MR image (right) with superimposed spectroscopic image of color-coded signal intensity (integrated peak area) of Cho (I_{Cho}); (1) spectrum from a voxel in the tumor region; (2) spectrum from a voxel in healthy brain tissue. Enhanced Cho and reduced NAA signals are observed in the tumor. Peak assignments, see Figure 3.89.

- Guanidinoacetate methyltransferase (GAMT) deficiency, the first creatine biosynthesis disorder detected in man, was discovered in 1994 in a child by means of cranial MRS. The MR spectra of brain (Fig. 3.92) and muscle of these patients are characterized by a strong decrease of the creatine (^{1}H) and phosphocreatine (^{31}P) resonances and the appearance of new signals assigned to guanidinoacetate (Gua; ^{1}H, $\delta = 3.8$ ppm) and guanidinoacetate phosphate (^{31}P, $\delta = 1$ ppm) (Stöckler et al., 1994).

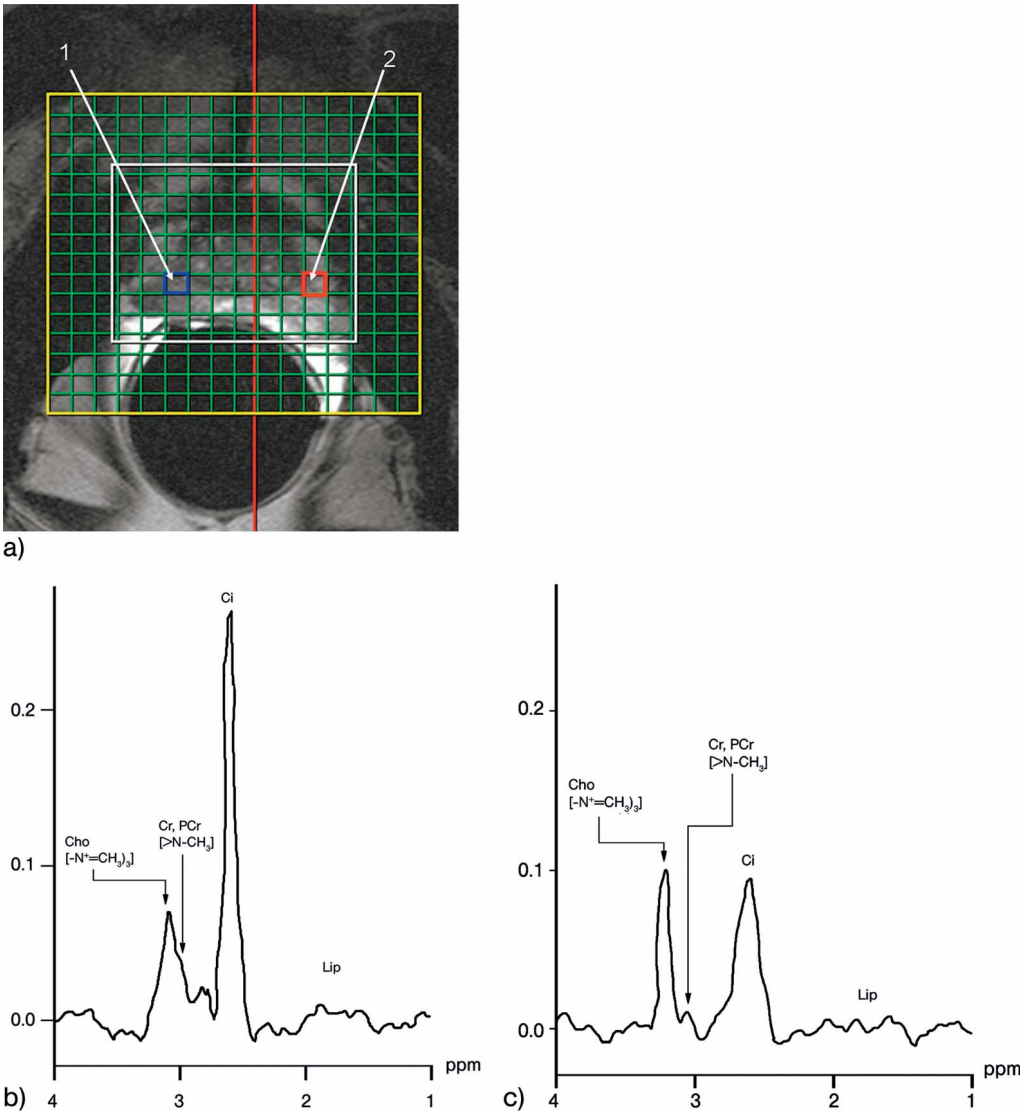

Fig. 3.91. Clinical study with proton spectroscopic imaging: spectra from the prostate of a patient (age 62 years) with adenocarcinoma in the right lobe of the prostate (hypointense area on the left in the transverse MR image [a]). 3D ^{1}H SI (pulse sequence in Fig. 3.88) with double spin-echo excitation (PRESS) and measurement parameters: $T_R = 650$ ms, $T_E = 120$ ms, measurement time = 10.3 min, voxel size = $(6\ \text{mm})^3$ (indicated in (a)), $B_0 = 1.5$ T; antenna system: endorectal coil. (a) Transverse localizer image showing region of excited spins (PRESS box, white); (b) spectrum from voxel 2 (red) in healthy prostatic tissue; (c) spectrum from voxel 1 (blue) in the tumor region. Enhanced Cho and reduced Ci signal are observed in the tumor tissue. Assignment of resolved resonances to molecular groups in the following metabolites: citrate (Ci; $\delta = 2.6$ ppm), creatines (Cr, PCr; $\delta = 3.0$ ppm), cholines (Cho; $\delta = 3.2$ ppm). Lipid signals (Lip) are efficiently suppressed by the pulse sequence. Chemical shifts δ (in ppm = 10^{-6}) are given relative to the frequency position of tetramethylsilane (TMS, $\delta = 0$).

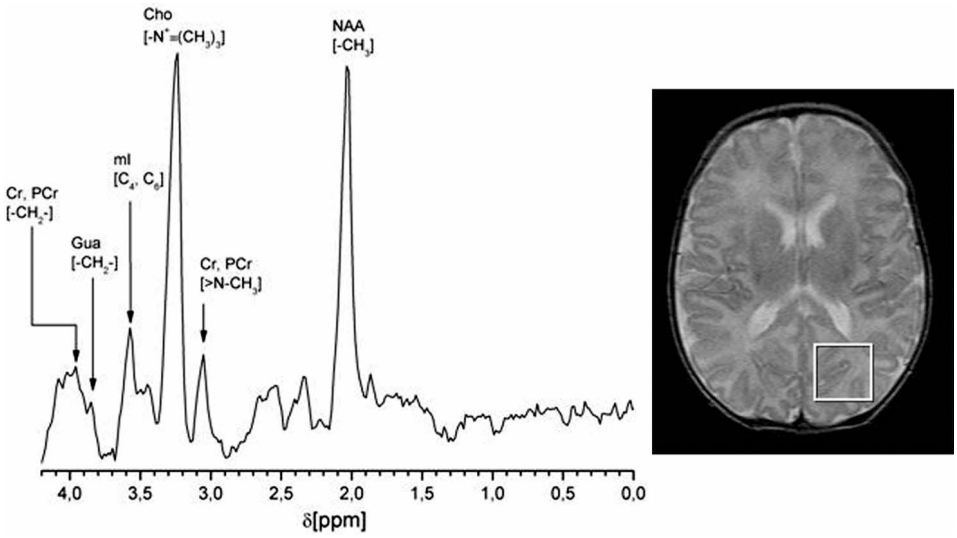

Fig. 3.92. Clinical study with single-voxel ^{1}H MRS: spectrum from the brain of a patient (female, age 1 month) with creatine deficiency syndrome. The disturbed biosynthesis of creatine is caused by deficiency of hepatic GAMT (*S*-adenosylmethionine:guanidinoacetate *N*-methyltransferase [EC 2.1.1.2]) and is reflected in the reduced peak intensity at $\delta = 3.0$ ppm in the ^{1}H MR spectrum. When creatine synthesis is blocked, guanidinoacetate (Gua) is expected to accumulate (tentative assignment of methylene proton signal of elevated Gua at $\delta = 3.8$ ppm). The enhanced choline (Cho) signal at $\delta = 3.2$ ppm is explained by the high phospholipid turnover in the developing brain of the child. Double spin-echo sequence (PRESS) with measurement parameters: $T_R = 1500$ ms, $T_E = 135$ ms, *nex* = 256, measurement time = 6.4 min, voxel size = $20 \times 20 \times 20$ mm^3 (indicated in the transverse MR image), $B_0 = 1.5$ T; antenna system: head-imaging coil. Peak assignments, see Fig. 3.89.

The most prominent resonance of *in-vivo* ^{1}H MR spectra of the normal brain is assigned to NAA. NAA is mainly found in neurons and therefore the NAA signal detected by means of *in-vivo* ^{1}H MRS is considered as a "neuronal marker". Interestingly, the physiological role of NAA in brain function is still not completely understood. NAA is also considered as an "osmolyte" (osmotically active intracellular metabolite, as are Cr, PCr, and Cho) and molecular water pump (Baslow, 2001). A decrease of NAA signal intensity (I_{NAA}) is observed in those neurological diseases, which proceed with loss of neurons and/or axons, for example glial tumors (Fig. 3.90) (Preul et al., 1998), ischemic stroke (Saunders, 2000), dementia (Ross et al., 1998), multiple sclerosis (Arnold et al., 2000), and temporal lobe epilepsy (Ende et al., 1997). ^{1}H MRS is an appropriate diagnostic modality for Canavan's disease (Grodd et al., 1990), a spongy white matter degeneration characterized by the loss of aspartoacylase activity and subsequent strong increase of NAA concentration.

The ^{1}H chemical shifts of creatine (Cr) and phosphocreatine (PCr) are the same, because the phosphate group in the PCr molecule is too far away to influence the

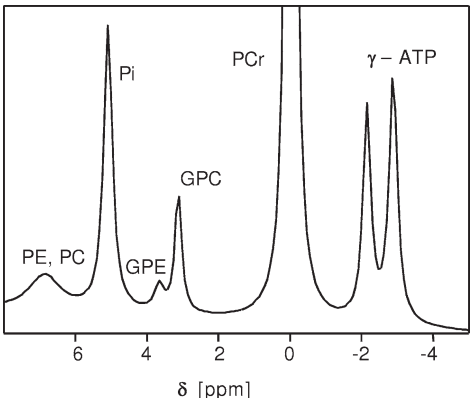

Fig. 3.93. Section of the *fit* of a ^{1}H-decoupled (WALTZ-8) *in-vivo* ^{31}P MR spectrum (B_0 = 1.5 T) of the calf muscle of a healthy volunteer. In the phosphodiester (PDE) resonance band the signals of the phospholipid-degradation products glycerophosphorylcholine (GPC) and glycerophosphorylethanolamine (GPE) are resolved owing to heteronuclear spin decoupling. The signals of the phospholipid-precursors phosphocholine (PC) and phosphoethanolamine (PE) (unresolved in this measurement) resonate in the phosphomonoester (PME) region. The frequency difference between inorganic phosphate (P_i) and phosphocreatine (PCr) resonances is a measure of intracellular pH. ATP = adenosine 5′-triphosphate. Chemical shifts δ (in ppm = 10^{-6}) are given relative to the frequency position of PCr ($\delta = 0$).

CH_3 and CH_2 protons of the creatine residue to a measurable amount. Therefore, the relative signal contribution of each compound to the *in-vivo* resonance is unclear. The $>N-CH_3$ resonance (actually a triplet) centered at $\delta = 3.03$ ppm is sometimes used for normalization or in intensity ratios such as I_{NAA}/I_{Cr}; however, it overlaps partially with the Cho peak and its intensity can vary considerably, for example in ischemic or neoplastic brain tissue (Saunders, 2000).

The major amount of choline is bound in membranes of the cells (as phosphatidylcholine). Signals of membrane phospholipids have never been resolved in *in-vivo* MR spectra. This is explained by restricted mobility which makes $T_2{}^*$ short and thus resonances very broad. The *in-vivo* ^{1}H resonance called "Cho" actually comprises trimethylamine proton signals of different compounds. The major contribution is attributed to phosphocholine (PC) and glycerophosphorylcholine (GPC). In *in-vivo* ^{31}P MRS the resonances of PC and GPC can be resolved by means of ^{1}H-decoupling techniques (Fig. 3.93) (Lyuten et al., 1989; Bachert et al., 1992). Presently, the true composition of the choline pool in healthy brain tissue and in brain tumors is not completely known. Considering the eminent value of this metabolite group for tumor diagnostics with MRS, further research investigations – particularly at higher B_0-values – are clearly needed.

Proton MRS studies of the brain revealed enhanced Cho signal intensities (I_{Cho}) in tumors (Fig. 3.90) and in demyelinating and inflammatory diseases (Danielsen and Ross, 1999; Arnold et al., 2000). In clinical ^{1}H MRS studies of patients with

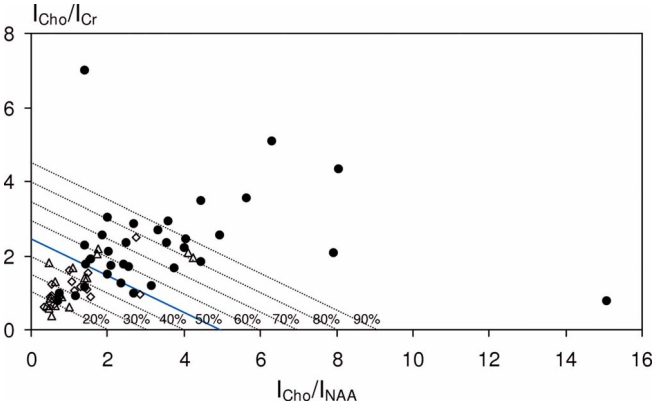

Fig. 3.94. Clinical study with single-voxel ^{1}H MRS (double spin-echo sequence [PRESS] with $T_R = 1500$ ms, $T_E = 135$ ms, *nex* = 200–300, $B_0 = 1.5$ T; antenna system: head-imaging coil). Monitoring stereotactic radiotherapy of patients ($n = 56$) with brain tumors ($n = 67$ lesions) (Schlemmer et al., 2001). Intensity ratios I_{Cho}/I_{Cr} versus I_{Cho}/I_{NAA} of lesions classified as progressive tumor (●, $n = 34$), radiation injury (△, $n = 17$), and stable disease (◇, $n = 15$). Analysis of I_{Cho}/I_{Cr} and I_{Cho}/I_{NAA} data yield correct retrospective classification as neoplastic and non-neoplastic in 82% and 81% of the lesions, respectively. Parallel lines (. . . . . .) obtained from linear discriminant analysis (LDA) yield the individual probability (in %) for progressive tumor.

brain tumors before, during, and after radiotherapy, the signal intensity ratios I_{Cho}/I_{Cr} and I_{Cho}/I_{NAA} were found to be useful spectral parameters for the differentiation of progressive tumor and radiation injury (Fig. 3.94) (Schlemmer et al., 2001). An enhanced I_{Cho} is also found in other tumor entities, particularly in prostate (Fig. 3.91 and Table 3.4) (Scheidler et al., 1999) and breast cancer (Sijens et al., 1988; Yeung et al., 2001).

The sugar-like compound *myo*-inositol (mI) is considered as an osmolyte and astrocyte marker (being localized almost exclusively in astrocytes). A detailed biochemical explanation of changes of the mI peak in *in-vivo* ^{1}H MR spectra is diffi-

Table 3.4. Diagnostic interpretation of spectral parameter R of *in-vivo* 3D ^{1}H SI of the human prostate (healthy, diseased) according to Scheidler et al., 1999.

$R = (I_{Cho} + I_{Cr})/I_{Ci}$[a)]	Diagnosis
$R < 0.75$	Normal tissue
$R > 0.75$ plus decrease of $I_{Ci}/I_{Ci,\,normal}$ by factor of 2	Possible cancer
$R > 0.86$	Definite cancer

[a)] I = intensity (integrated peak area) of corresponding resonance.

cult, because mI resides in the center of complex metabolic processes and the resonance also comprises the signal of *myo*-inositol monophosphate, *scyllo*-inositol, and glycine. Changes of the mI resonance have been observed in patients with brain tumors (Castillo et al., 2000), Alzheimer's disease (Shonk et al., 1995; Ross et al., 1998), hepatic encephalopathy (Kreis et al., 1990), or diabetes mellitus (Kreis and Ross, 1992).

Under pathological conditions, lactate (Lac), the final product of anaerobic glycolysis, can be detected by *in-vivo* ^{1}H MRS (Behar et al., 1984). The Lac resonance at $\delta = 1.33$ ppm is a scalar-coupled doublet (line splitting: $J_{HH} \cong 7$ Hz) from the β-methyl protons. Its phase is inverted with respect to the singlets when the spectrum is acquired with echo time $T_E = 1/J_{HH} = 135$ ms. The Lac signal indicates insufficient oxygen supply and may therefore appear in ischemia or tumor or in the case of interference of oxidative phosphorylation. The presence of the Lac resonance in the spectrum means that hypoxia is severe and extended regions in the tissue are affected.

If free fatty acids (triacylglycerides, lipids) are present, the Lac signal cannot be detected with conventional techniques. Lipid resonances (chemical shifts: $\delta \sim 0.9$–2.4 ppm and $\delta \sim 5.5$ ppm) are intense in many regions, except in healthy brain tissue. The strongest peak originates from methylene protons of fatty acids chains ($\delta = 1.40$ ppm), as many nuclei contribute. In muscle tissue, signals of intra- and extramyocellular lipids can sometimes be discriminated at $B_0 = 1.5$ T.

Besides brain and muscle studies, *in-vivo* ^{1}H MRS of the prostate has evolved into a promising diagnostic modality. Technically, the examination is more difficult than MRS of the brain: B_0 inhomogeneity is worse, in addition to water, intense lipid signal must also be suppressed, and the signal is poor unless an endorectal coil is employed.

In prostatic gland tissue an extraordinary large amount of citrate (Ci) is produced, secreted, and stored. Citrate plays a central role in the Krebs cycle (also termed the "citric acid cycle"). Because of its rapid metabolism, Ci is normally not detectable by *in-vivo* MRS. In the prostate, however, the enzymatic reaction Ci → *cis*-aconitate → iso-Ci is inhibited by Zn^{2+} ions, whereby no significant aconitase activation by Fe^{2+} can take place. The equilibrium is strongly shifted to the left, and oxidation of Ci in the cycle is diminished. As a consequence, the metabolite accumulates and gains a three- to fourfold higher concentration than in other tissues. Thus, the prostate is the only organ in the human body that shows Ci resonances in *in-vivo* MR spectra. For reasons of chirality, the two detectable methylene groups form an $(AB)_2$ spin system which yields in high field a multiplet of four lines (Schick et al., 1993), while *in vivo* often only one broad resonance (centered at $\delta = 2.6$ ppm) is observed. The results of an examination (3D ^{1}H SI with endorectal coil) of a patient with prostate cancer are shown in Figure 3.91. The localized spectra exhibit resonances of Ci, Cr, and Cho (the peaks of Cr and Cho often cannot be separated; Fig. 3.91b). In the tumor region I_{Cho} is increased and I_{Ci} decreased (Fig. 3.91c) compared to the spectra of normal prostatic tissue (Fig. 3.91b). The intensity ratio $R = (I_{Cho} + I_{Cr})/I_{Ci}$ was proposed as a diagnostic parameter for prostate cancer (Table 3.4) (Scheidler et al., 1999).

3.3.7.4
Metabolic Information and Clinical Application: *In-Vivo* ^{13}C MRS

The magnetically active, rare carbon isotope ^{13}C has a fourfold smaller γ than ^{1}H, and a relative sensitivity of 1.76×10^{-4} (compared to 1.00 of ^{1}H, calculated for the case that the samples contain the same number of nuclei; Table 3.2). ^{13}C spectra are characterized by a large chemical-shift range (ca. 220 ppm) and strongly scalar-coupled multiplets. ^{1}H-decoupling is required to remove these multiplet splittings. *In-vivo* ^{13}C MR spectra obtained at natural abundance are dominated by resonances of lipids (typically 13 resonances upon decoupling), while signals of other compounds, such as amino acids, Cr, Cho, glycogen, and ethanolamine are difficult to detect at 1.5 T (Ende and Bachert, 1993). ^{13}C MRS is superior to ^{1}H MRS with regard to the resolution of fatty acid signals and determination of lipid content in the tissue, but its implementation at whole-body MR scanners is expensive (broadband RF, coils, second RF channel). In studies with humans both the endogenous isotope in natural abundance and labeled compounds after administration have been detected (Heerschap et al., 1989; Shulman et al., 1990; Beckmann et al., 1991; Ende and Bachert, 1993). There are also some applications for oncology (Halliday et al., 1988; Bachert et al., 1992).

3.3.7.5
Metabolic Information and Clinical Application: *In-Vivo* ^{19}F MRS

The fluorine isotope ^{19}F has the second largest γ of all stable magnetic nuclei. The sensitivity is $(\gamma_F/\gamma_H)^3 = 83\%$ of that of ^{1}H if the sample contains the same number of nuclei (see Table 3.2). Fluorine is a trace element in biological tissue: its physiological concentration is less than 10^{-6} M, and thus below the detection limit of *in-vivo* MRS. ^{19}F is mainly immobilized in solid structures; its average fraction in the solid phase of teeth and bones is about 2×10^{-4}.

Since endogenous mobile metabolites do not contain fluorine in sufficient concentrations to be detected by ^{19}F MRS, signals must be derived from fluorine-containing compounds that are administered exogenously. A number of chemotherapeutic drugs and neuroleptics contain fluorine, and when ^{19}F MRS is applied their resonances can be observed without interfering background signals. Thus, fluorine has favorable properties for the study of metabolism and disposition kinetics *in vivo* (Bachert, 1998).

Wolf and coworkers pioneered ^{19}F MRS in humans (Wolf et al., 1987). Using a 1.5-T whole-body scanner, these authors performed the first ^{19}F MRS examinations of patients undergoing chemotherapy with 5-fluorouracil (5-FU) and demonstrated the detection of this fluoropyrimidine and its major catabolite (α-fluoro-β-alanine; FBAL). These investigations also represented the first noninvasive MRS study of drugs in human patients. Studies of the individual disposition kinetics of 5-FU are of interest in oncology (Figs. 3.95 and 3.96), and have been conducted by several groups (Semmler et al., 1990; Gonen et al., 1997; Schlemmer et al., 1994, 1999). In the liver and in tumors, 5-FU is converted into different metabolites,

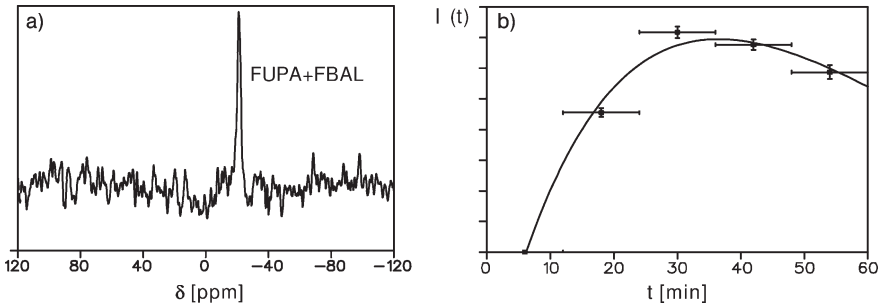

Fig. 3.95. Clinical study with ^{19}F MRS. Monitoring drug disposition kinetics in a tumor patient during chemotherapy with 5-fluorouracil (5-FU). 2D ^{19}F SI examination of the liver of a patient following intravenous infusion of 5-FU. Measurement parameters: $T_R = 60$ ms, $N \times N = 8 \times 8$, *nex* = 200, FOV = 50×50 cm^2, $B_0 = 1.5$ T, antenna system: planar surface coil of 18 cm diameter. (a) Localized ^{19}F MR spectrum from a voxel of size $6.25 \times 6.25 \times 4$ cm^3. The total signal of FUPA+FBAL (α-fluoro-β-ureidopropanoic acid+α-fluoro-β-alanine; Table 3.5) is resolved with SNR ~6:1. (b) *In-vivo* ^{19}F MR signal-time curve $I(t)$ of FUPA+FBAL detected in the same voxel. The horizontal bars represent the measurement time of 12.8 min (= $T_R\ N^2$ *nex*) (Bachert, 1998).

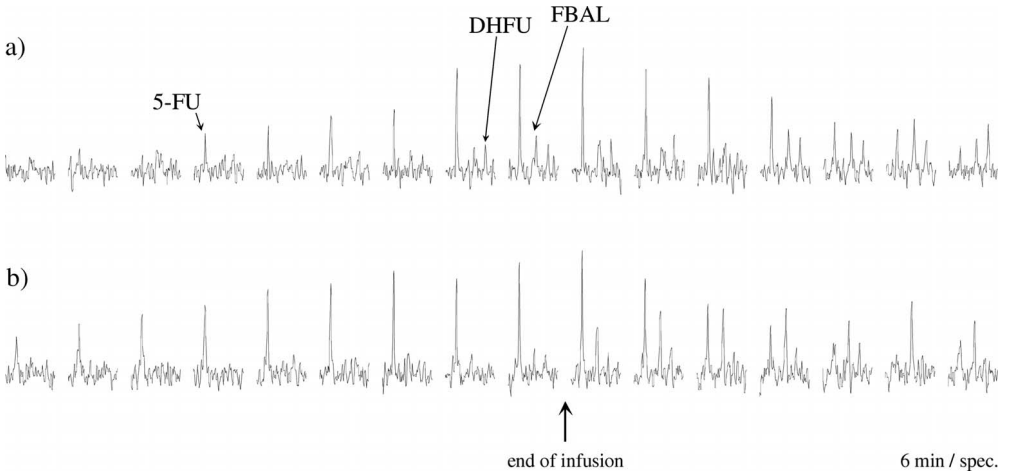

Fig. 3.96. Clinical study with ^{19}F MRS (Schlemmer et al., 1999). Monitoring disposition kinetics in a patient with squamous cell carcinoma (SCC) stage IV during chemotherapy with 5-fluorouracil (5-FU). ^{19}F MRS examination with a surface coil of 5 cm diameter positioned on the tumor. Measurement parameters: $T_R = 38$ ms, *nex* = 9300, measurement time = 5.9 min, $B_0 = 1.5$ T. (a) Series of 5.9-min spectra obtained during the period of 96 min after administration of 1000 mg 5-FU (m^2 body surface)$^{-1}$ at day 1 of week 1 of combined radiotherapy/[5-FU+carboplatin]chemotherapy. The resonances of 5-FU, 5,6-dihydro-5-fluorouracil (DHFU), and α-fluoro-β-alanine (FBAL) are resolved (Table 3.5). (b) Series of spectra obtained in the second examination of the same patient, at day 1 of week 5 (after 43.5 Gy). Quantitative evaluation of the spectra showed a significant increase of intratumoral levels of 5-FU and FBAL (the same finding in all patients [$n = 13$] of the study) which could explain the higher response rate of radiochemotherapy versus 5-FU monotherapy.

Table 3.5. Assignments and chemical shifts of resonances resolved in ^{19}F MR spectra ($B_0 = 1.5$ T) obtained in human patients during 5-fluorouracil chemotherapy.

Drug, metabolite(s)	Abbreviation	Chemical shift δ [ppm][a)]	Reference
5,6-Dihydro-5-fluorouracil	DHFU	−126	Schlemmer et al. (1994)
α-Fluoro-β-alanine	FBAL	−113	Wolf et al. (1987)
α-Fluoro-β-ureidopropanoic acid	FUPA	−111	Gonen et al. (1997)
5-Fluorouracil	5-FU	−94	Wolf et al. (1987)
5-Fluorouracil-nucleosides and -nucleotides	5-FUranuc	−89	Semmler et al. (1990)

[a)] Chemical shift reference: trifluoroacetic acid ($\delta = 0$).

which are identified easily because of the large fluorine chemical shifts. ^{19}F MR resonances that could be observed at $B_0 = 1.5$ T in patients receiving 5-FU chemotherapy are listed in Table 3.5.

In addition to 5-FU, other fluorinated compounds have been detected in studies in humans, for example halothane (Menon et al., 1993). Applications of ^{19}F MRS are of particular interest in psychiatry (Bartels and Albert, 1995).

3.3.7.6 Metabolic Information and Clinical Application: *In-Vivo* ^{31}P MRS

The abundance of the phosphorus isotope ^{31}P in biological tissue is sufficient for detection with *in-vivo* MRS. Since phosphorylation is one of the most important processes in biochemistry, the metabolic window of *in-vivo* ^{31}P MRS is remarkable, opening to intracellular carriers of energy, synthesis and degradation products of membrane phospholipids, and intracellular pH.

Scalar-coupled multiplets are removed by means of ^{31}P-[^{1}H] double resonance. The resulting proton-decoupled *in-vivo* ^{31}P MR spectrum (Fig. 3.93) shows resolved peaks of free phosphate (inorganic phosphate P_i; $\delta \sim 4$–5 ppm) and phosphate residues bound to the following metabolites:

- Adenosine 5′-triphosphate (ATP; with a characteristic resonance structure: β-ATP doublet-of-doublets [apparent triplet] with center at $\delta = -16.0$ ppm; α-ATP doublet, $\delta = -7.6$ ppm; γ-ATP doublet, $\delta = -2.4$ ppm).
- Phosphocreatine (PCr, singlet, $\delta = 0$ ppm, internal ^{31}P-chemical-shift reference).
- Glycerophosphorylcholine (GPC, $\delta = 2.9$ ppm) and glycerophosphorylethanolamine (GPE, $\delta = 3.5$ ppm) in the phosphodiester resonance band (PDE, $\delta \sim 2$–3 ppm).

- Phosphocholine (PC, $\delta = 6.5$ ppm) and phosphoethanolamine (PE, $\delta = 7.1$ ppm) in the phosphomonoester resonance band (PME, $\delta \sim 5$–7 ppm).

ATP and PCr are fundamental compounds of the energy metabolism of the living cell. ATP is the most important molecular carrier of chemical energy in all organisms. Its resonance, preferably of β-ATP, can be used for the normalization of ^{31}P MR signal intensities, since the living system always tries to keep the ATP concentration at constant levels. PCr behaves as a buffer of ATP and is a temporary intracellular storage form of energy.

PDE and PME signals are intense in the spectra of brain, liver, and tumor tissue. They form resonance bands of an unknown number of components. Broadband ^{1}H-decoupling resolves four peaks in this region (Luyten et al., 1989), which are assigned to intermediates (GPC, GPE, PC, PE) of membrane phospholipid turnover (Daly et al., 1987). Enhanced PME intensities are often observed in proliferating tumors. This is consistent both with the signal contribution of phosphocholine (PC) to this peak and the enhanced Cho signal in ^{1}H MR spectra of tumors. Again, this suggests an *in-vivo* resonance, in this case PME, as a noninvasive marker for therapy monitoring (Negendank, 1992).

As mentioned in the context of the Cho signal of ^{1}H MRS, phospholipids cannot be detected. Only a broad unresolved hump in the PME-PDE region of 1.5 T ^{31}P MR spectra of brain and liver is attributed to these compounds. There is speculation about the assignment of this background to other phosphoesters, nucleic acids, and phospholipids with transient high mobility, but the problem at present remains unsolved.

3.3.7.7 Application of MRS in Diagnostics and Clinical Research: Conclusions and Perspectives

MRS examinations have been performed in most organs of the human body, including the brain, cervical spinal cord, mamma, heart muscle, liver, kidney, prostate, testicle, skeletal muscle, and bone marrow. In some regions localization is difficult, or susceptibilities and physiological motion impair spectral quality (e.g., in the cervical spinal cord, lung, heart, kidney, prostate, and lumbar vertebra).

The purpose of the examination with MRS in diagnostic and clinical research is to obtain information on the metabolism of diseased cells. A large number of clinical problems have been addressed in MRS studies with patients. Mainly ^{1}H MRS was applied, but to a lesser extent also ^{31}P MRS. Examples of the application of MRS to studies of non-neoplastic diseases of the brain include multiple sclerosis (MS), Alzheimer's disease and other dementias, Parkinson's disease, amyotrophic lateral sclerosis (ALS), epilepsy, schizophrenia and other psychiatric disorders, anorexia nervosa, chronic alcoholism, ethyltoxic brain damage, cerebrovascular disorders, hepatic encephalopathy (HE), HIV infection (AIDS), asphyxia in newborns, near-drowning syndrome, and inherited disorders such as Canavan's disease, Huntington's disease, and creatine deficiency syndrome.

With regard to non-neoplastic diseases outside the brain, MRS has focused on studies of skeletal muscle (e.g., mitochondrial myopathies, McArdle syndrome, Melas syndrome, exercise intolerance in patients with cardiac failure, peripheral vascular disease), heart muscle (cardiovascular disorders, cardiac dysfunctions, interference of energy metabolism, heart transplants), and liver (e.g., liver pathologies, alcoholic liver disease, and liver function testing).

The main target of the clinical application of MRS is diagnosis and intra-therapy monitoring of tumors and suspicious lesions, the main purpose being to detect metabolic changes during tumor growth and treatment. Although MRS does not permit the accurate differential diagnostics of suspected lesions, changes in relative signal intensities yield information on malignancy and eventually tumor activity and proliferation.

The first MRS studies of tumors in human patients were conducted with ^{31}P in extremity tumors. The objectives were possible ^{31}P characteristics of these malignancies, tumor heterogeneity, response to therapy (early versus late changes in tumor spectra), the predictive value of the ^{31}P MR spectrum before treatment and of early spectral changes observed shortly thereafter, pretreatment pH and PCr signal intensity or early PME signal decrease as predictors of percent necrosis at resection, early P_i signal decrease as predictor of tumor shrinkage.

The largest experience exists with localized ^{1}H MRS of human brain tumors. The technique is well-developed and easily applicable in patients, particularly as the same hardware (high-quality head coil) as is used for MRI can be employed, and attainable spectral quality (SNR, frequency resolution) is optimum. Besides the differentiation of malignant lesions from degenerative or inborn alterations of cerebral parenchyma, the monitoring of radiation therapy of glial tumors has turned out to be an important application of MRS. As a sign of enhanced proliferative activity, primary and other tumors of the brain show an increased membrane turnover beyond the level encountered in inflammatory processes or augmented cell necrosis. As its direct marker, the ^{1}H resonance of mobile cholines (Cho) in the cells is of central importance. Clinical studies have shown that this signal yields valuable information on the malignancy of a glial tumor – despite the at least 4000-times larger voxels of MRS compared to MRI (this number for 1 cm^3 of ^{1}H SI at 1.5 T versus 0.25 mm^3 of $^{1}H_2O$-MRI). Similar to the case of intracellular pH via ^{31}P MRS, the ''averaging'' of signal contributions from heterogeneous tissue appears to induce a positive effect on biochemical evidence. Meanwhile, clinical studies have also demonstrated the value of the Cho ^{1}H resonance as a marker of malignant processes in the breast and prostate.

Several research groups have employed the correlation between Cho intensity and proliferative activity of cells successfully to discriminate radiation injury and progressive tumor. Moreover, the intensity ratios I_{Cho}/I_{Cr} and I_{Cho}/I_{NAA} not only reflect proliferative tumor activity but also indicate the probability of therapy failure. In healthy brain tissue, single-voxel ^{1}H MRS ($T_E = 135$ ms) yields the ratios $I_{Cho}/I_{Cr} \cong 1$ and $I_{Cho}/I_{NAA} \cong 0.5$, with high constancy. When these values increase significantly in a glial tumor after radiotherapy, there is a high probability of progressive disease.

So, what are the perspectives for MRS? A core of applications of MRS to the studies of tumors and non-neoplastic diseases in patients, which presently are at the research level, will reach broad clinical use. MRS in humans will certainly profit from higher B_0 in whole-body scanners, since at present instruments up to $B_0 = 8$ T are in operation. Sensitivity and spatial resolution will increase, other rare nuclei will be available, and the metabolic window will expand. Spectroscopic imaging with voxel sizes of a few mm^3 not only with ^1H, but also with ^{31}P or enriched ^{13}C in administered compounds for example, may attain the potential as the key molecular imaging tool. In the future, MRS may play an important role in genomics and proteomics, as it creates a noninvasive window onto the information flow from genome to proteins to small metabolites, rendering such studies possible even in humans.

References

Arnold, D.L., de Stefano, N., Narayanan, S., and Matthews, P.M. (2000). Proton MR spectroscopy in multiple sclerosis. *Neuroimaging Clin. N. Am.*, **10**, 789–798.

Bachert, P. (1998). Pharmacokinetics using fluorine NMR *in vivo*. *Prog. Nucl. Magn. Reson. Spec.*, **33**, 1–56.

Bachert, P., Bellemann, M., Layer, G., Koch, T., Semmler, W., and Lorenz, W.J. (1992). *In vivo* ^1H, ^{31}P-{^1H} and ^{13}C-{^1H} magnetic resonance spectroscopy of malignant histiocytoma and skeletal muscle tissue in man. *NMR Biomed.*, **5**, 161–170.

Bartels, M. and Albert, K. (1995). Detection of psychoactive drugs using ^{19}F MR spectroscopy. *J. Neural. Transm. Gen. Sect.*, **99**, 1–6.

Baslow, M.H. (2001). Functions of *N*-acetyl-*L*-aspartate and *N*-acetyl-aspartylglutamate in the vertebrate brain: Role in glial cell-specific signaling. *J. Neurochem.*, **75**, 453–459.

Beckmann, N., Turkalj, I., Seelig, J., and Keller, U. (1991). ^{13}C NMR for the assessment of human brain glucose metabolism *in vivo*. *Biochemistry*, **30**, 6362–6366.

Behar, K.L., Rothman, D.L., Shulman, R.G., Petroff, O.A.C., and Prichard, J.W. (1984). Detection of cerebral lactate *in vivo* during hypoxemia by ^1H NMR at relatively low field strengths (1.9 T). *Proc. Natl. Acad. Sci. USA*, **81**, 2517–2519.

Brown, T.R., Kincaid, B.M., and Ugurbil, K. (1982). NMR chemical shift imaging in three dimensions. *Proc. Natl. Acad. Sci. USA*, **79**, 3523–3526.

Castillo, M., Smith, J.K., and Kwock, L. (2000). Correlation of *myo*-inositol levels and grading of cerebral astrocytomas. *Am. J. Neuroradiol.*, **21**, 1645–1649.

Daly, P.F., Lyon, R.C., Faustino, P.J., and Cohen, J.S. (1987). Phospholipid metabolism in cancer cells monitored by ^{31}P NMR spectroscopy. *J. Biol. Chem.*, **262**, 14875–14878.

Danielsen, E.R. and Ross, B.D. (1999). *Magnetic resonance spectroscopy diagnosis of neurological diseases*. Marcel Dekker, Inc., New York, Basel.

Ende, G. and Bachert, P. (1993). Dynamic ^{13}C–^1H nuclear polarization of lipid methylene resonances applied to broadband proton-decoupled *in vivo* ^{13}C MR spectroscopy of human breast and calf tissue. *Magn. Reson. Med.*, **30**, 415–423.

Ende, G.R., Laxer, K.D., Knowlton, R.C., Matson, G.B., Schuff, N., Fein, G., and Weiner, M.W. (1997). Temporal lobe epilepsy: Bilateral hippocampal metabolite changes revealed at proton MR spectroscopic imaging. *Radiology*, **202**, 809–817.

Frahm, J., Bruhn, H., Gyngell, M.L., Merboldt, K.-D., Hänicke, W., and Sauter, R. (1989). Localized high-resolution proton NMR spectroscopy using stimulated echoes: Initial applications to human brain *in vivo*. *Magn. Reson. Med.*, **9**, 79–93.

Gonen, O., Murphy-Boesch, J., Li, C.-W., Padavic-Schaller, K., Negendank, W.G., and Brown, T.R. (1997). Simultaneous 3D NMR spectroscopy of proton-decoupled fluorine and phosphorus in human liver during 5-fluorouracil chemotherapy. *Magn. Reson. Med.*, **37**, 164–169.

Grodd, W., Krägeloh-Mann, I., Petersen, D., Trefz, F.K., and Harzer, K. (1990). *In vivo* assessment of *N*-acetylaspartate in brain in spongy degeneration (Canavan's disease) by proton spectroscopy. *Lancet*, **336**, 437–438.

Halliday, K.R., Fenoglio-Preiser, C., and Sillerud, L.O. (1988). Differentiation of human tumors from nonmalignant tissue by natural-abundance ^{13}C NMR spectroscopy. *Magn. Reson. Med.*, **7**, 384–411.

Heerschap, A., Luyten, P.R., van der Heyden, J.I., Oosterwaal, L.J.M.P., and den Hollander, J.A. (1989). Broadband proton decoupled natural abundance ^{13}C NMR spectroscopy of humans at 1.5 T. *NMR Biomed.*, **2**, 124–132.

Kreis, R. and Ross, B.D. (1992). Cerebral metabolic disturbances in patients with subacute and chronic diabetes mellitus: detection with proton MR spectroscopy. *Radiology*, **184**, 123–130.

Kreis, R. and Boesch, C. (1994). Liquid-crystal-like structures of human muscle demonstrated by in vivo observation of direct coupling in localized proton magnetic resonance spectroscopy. *J. Magn. Reson.*, **B 104**, 189–192.

Kreis, R., Farrow, N.A., and Ross, B.D. (1990). Diagnosis of hepatic encephalopathy by proton magnetic resonance spectroscopy. *Lancet*, **336**, 635–636.

Luyten, P.R., Bruntink, G., Sloff, F.M., Vermeulen, J.W.A.H., van der Heijden, J.I., den Hollander, J.A., and Heerschap, A. (1989). Broadband proton decoupling in human ^{31}P NMR spectroscopy. *NMR Biomed.*, **1**, 177–183.

Maudsley, A.A., Hilal, S.K., Perman, W.H., and Simon, H.E. (1983). Spatially resolved high-resolution spectroscopy by "four-dimensional" NMR. *J. Magn. Reson.*, **51**, 147–152.

Menon, D.K., Lockwood, G.G., Peden, C.J., Cox, I.J., Sargentoni, J., Bell, J.D., Coutts, G.A., and Whitwam, J.G. (1993). *In vivo* fluorine-19 magnetic resonance spectroscopy of cerebral halothane in postoperative patients: Preliminary results. *Magn. Reson. Med.*, **30**, 680–684.

Negendank, W. (1992). Studies of human tumors by MRS: A review. *NMR Biomed.*, **5**, 303–324.

Posse, S., Tedeschi, G., Risinger, R., Ogg, R., and Le Bihan, D. (1995). High speed ^{1}H spectroscopic imaging in human brain by echo planar spatial-spectral encoding. *Magn. Reson. Med.*, **33**, 34–40.

Preul, M.C., Caramanos, Z., Leblanc, R., Villemure, J.G., and Arnold, D.L. (1998). Using pattern analysis of *in vivo* proton MRSI data to improve the diagnosis and surgical management of patients with brain tumors. *NMR Biomed.*, **11**, 192–200.

Ross, B.D., Blüml, S., Cowan, R., Danielsen, E., Farrow, N., and Tan, J. (1998). *In vivo* MR spectroscopy of human dementia. *Neuroimaging Clin. N. Am.*, **8**, 809–822.

Saunders, D.E. (2000). MR spectroscopy in stroke. *Br. Med. Bull.*, **56**, 334–345.

Scheenen, T.W.J., Klomp, D.W.J., Röll, S.A., Fütterer, J.J., Barentsz, J.O., and Heerschap, A. (2004). Fast acquisition-weighted three-dimensional proton MR spectroscopic imaging of the human prostate. *Magn. Reson. Med.*, **52**, 80–88.

Scheidler, J., Hricak, H., Vigneron, D.B., Yu, K.K., Sokolov, D.L., Huang, L.R., Zaloudek, C.J., Nelson, S.J., Carrol, P.R., and Kurhanewicz, J. (1999). Prostate cancer: Localization with three-dimensional proton MR spectroscopic imaging – clinicopathologic study. *Radiology*, **213**, 473–480.

Schick, F., Bongers, H., Kurz, S., Jung, W.I., Pfeffer, M., and Lutz, O. (1993). Localized proton MR spectroscopy of citrate *in vitro* and of the human prostate *in vivo* at 1.5 T. *Magn. Reson. Med.*, **29**, 38–43.

Schlemmer, H.-P., Bachert, P., Semmler, W., Hohenberger, P., Schlag, P., Lorenz, W.J., and van Kaick, G. (1994). Drug monitoring of 5-fluorouracil: *In vivo* ^{19}F NMR study during 5-FU chemotherapy in patients with metastases of colorectal adenocarcinoma. *Magn. Reson. Imaging*, **12**, 497–511.

Schlemmer, H.-P., Becker, M., Bachert, P., Dietz, A., Rudat, V., Vanselow, B., Wollensack, P., Zuna, I., Knopp, M.,

Weidauer, H., Wannenmacher, M., and van Kaick, G. (1999). Alterations of intratumoral pharmacokinetics of 5-fluorouracil in head and neck carcinoma during simultaneous radiochemotherapy. *Cancer Res.*, **59**, 2363–2369.

Schlemmer, H.-P., Bachert, P., Herfarth, K.K., Zuna, I., Debus, J., and van Kaick, G. (2001). Proton MR spectroscopic evaluation of suspicious brain lesions after stereotactic radiotherapy. *Am. J. Neuroradiol.*, **22**, 1316–1324.

Semmler, W., Bachert, P., Gückel, F., Ermark, F., Schlag, P., Lorenz, W.J., and van Kaick, G. (1990). Real-time follow-up of 5-fluorouracil metabolism in the liver of tumor patients by means of F-19 MR spectroscopy. *Radiology*, **174**, 141–145.

Shonk, T.K., Moats, R.A., Gifford, P., Michaelis, T., Mandigo, J.C., Izumi, J., and Ross, B.D. (1995). Probable Alzheimer disease: Diagnosis with proton MR spectroscopy. *Radiology*, **195**, 65–72.

Shulman, G.I., Rothman, D.L., Jue, T., Stein, P., DeFronzo, R.A., and Shulman, R.G. (1990). Quantitation of muscle glycogen synthesis in normal subjects and subjects with non-insulin-dependent diabetes by ^{13}C nuclear magnetic resonance spectroscopy. *N. Engl. J. Med.*, **322**, 223–228.

Sijens, P.E., Wijrdeman, H.K., Moerland, M.A., Bakker, C.J.G., Vermeulen, J.W.A.H., and Luyten, P.R. (1988). Human breast cancer *in vivo*: H-1 and P-31 MR spectroscopy at 1.5 T. *Radiology*, **169**, 615–620.

Stöckler, S., Holzbach, U., Hanefeld, F., Marquardt, I., Helms, G., and Requart, M. (1994). Creatine deficiency in the brain: A new, treatable inborn error of metabolism. *Pediatr. Res.*, **36**, 409–413.

Wolf, W., Albright, M.J., Silver, M.S., Weber, H., Reichardt, U., and Sauer, R. (1987). Fluorine-19 NMR spectroscopic studies of the metabolism of 5-fluorouracil in the liver of patients undergoing chemotherapy. *Magn. Reson. Imaging*, **5**, 165–169.

Yeung, D.K., Cheung, H.S., and Tse, G.M. (2001). Human breast lesions: Characterization with contrast-enhanced in vivo proton MR spectroscopy – initial results. *Radiology*, **220**, 40–46.

4
Magnetic Substances and Externally Applied Fields

4.1
Introduction

Wilfried Andrä

Magnetic substances and externally applied magnetic fields are used in medicine for many different applications, both in diagnosis (magnetic markers, relaxometry, susceptometry) and therapy (drug delivery, cell separation, cancer treatment). A somewhat arbitrary selection of these applications will be covered in this chapter. Although interesting, many topics such as relaxometry, magnetic detoxification of blood, and magnetic pelvic floor therapy had to be omitted due to reasons of limited space. Others, including magnetic guidance of catheters, magnetic particle retention in stents, magnetically modulated microprobes, and magnetic particle imaging, among others, will be described briefly in Section 4.9.

There are many economically very lucrative – but scientifically unproven – applications of magnetism in medicine. These applications are concerned mainly with the action of electromagnetic fields on animals and humans. Unfortunately, only one aspect of this interesting field – the possible health risk associated with field exposure – is discussed in Section 1.4 of this book.

The application of electromagnetic fields as a therapeutic means is another interesting aspect of this area of study, but it would utilize far too much space in this book. Consequently, the interested reader is referred to critical reviews by Glaser (2004a,b), which provide much more detail on this topic and examine scientifically well-founded studies as well as reports which may be categorized as more or less dubious, or even purely esoteric.

Another example of suspect applications of magnetic fields for medical purposes is the widespread utilization of permanent magnets as parts of jewelry or in bandages, plasters, mattresses, etc. Many of these applications are extolled as being helpful in almost every disease. To this day, however, neither any scientific theory of the physical mode of action nor any definite proof of any positive therapeutic effect as gauged by statistical studies has been found (Wasiak and Anderson, 2001; Barret, 2003). Nevertheless, the sales of magnetic items by many companies are astonishingly high, with one recent report from 1999 estimating these to be about 5 billion dollars per year (Weintraub, 1999).

Another example of an economically lucrative – but scientifically unproven – application of magnetism in medicine is the so-called pulsed electromagnetic fields

(PEMF). The amplitudes of these applied magnetic fields are usually smaller than the strength of the Earth's field, and for this reason such fields are unable to cause any measurable heating effect which might be seen as a measure of physically related action. Indeed, an analysis of 37 clinical orthopedic studies including a total of 3379 patients who received PEMF therapy, was unable to confirm any assumed positive influence (Schmidt-Rohlfing et al., 2000).

PEMF, orthopedic applications and similar topics are not described in this chapter, and interested readers are referred to a recent book by Rosch and Markov (2004).

References

Barrett, S. (2003). Magnet therapy. *http://quackwatch.org/04ConsumerEducation/QA/Magnet.html*.

Glaser, R. (2004a). Elektro-Magneto-Therapie: Situation und Perspektiven. *News Letters der FGF*, **2004** (1), 16–25.

Glaser, R. (2004b). Elektrische und magnetische Felder in Diagnostik und Therapie. Ein Gebiet zwischen Scharlatanerie und wissenschaftlichem Fortschritt. *Skeptiker*, **17** (4), 136–143.

Rosch, P.J. and Markov, M.S. (2004). *Bioelectromagnetic Medicine*. Marcel Dekker, Inc. New York/Basel.

Schmidt-Rohlfing, B., Silny, J., and Niethard, F.U. (2000). Pulsierende elektromagnetische Felder in der Behandlung von Verletzungen und Erkrankungen der Bewegungsorgane – Eine Übersicht und Metaanalyse. *Z. Orthop.*, **138**, 379–389.

Wasiak, J. and Anderson, J.N. (2001). Do magnets alleviate chronic low-back pain? *Med. J. Australia*, **174**, 659.

Weintraub, M. (1999). Magnetic biostimulation in painful peripheral neuropathology: a novel intervention – a randomized, double-placebo crossover study. *Am. J. Pain Manage.*, **9**, 8–17.

4.2
Magnetic Monitoring as a Diagnostic Method for Investigating Motility in the Human Digestive System

Hendryk Richert, Olaf Kosch, and Peter Görnert

4.2.1
Introduction

The human digestive system, particularly the small intestine, is a difficult region to access with established investigative methods. Using different methods such as X-radiography, magnetic resonance imaging (MRI) or computed tomography (CT), it is easy to visualize the morphology of the gastrointestinal (GI) tract. Unfortunately, motility cannot be investigated satisfactorily with any of these established methods as they either deal with ionizing radiation (X-ray and scintigraphy) or they are too slow to register movements.

A relatively new investigative method uses a small capsule camera which yields information about the inner surface of the small intestine (Lewis and Swain, 2002). This camera supplies a picture every 500 ms for approximately 6 h, and using this instrument it is possible to identify abnormalities of the surface, especially internal bleeding. The main disadvantage of this method is that it requires a 6-h video evaluation session. A second disadvantage is that the exact position of the camera – and therefore the recorded abnormalities – cannot be determined. Therefore, there is a vital need for a method which is able to investigate the digestive motility and then to provide both the nature and the location of abnormalities.

Magnetic monitoring might be that method. Here, the patient simply swallows a small magnetic marker, which then moves on its natural path through the human digestive system as a small piece of indigestible material. During the total period of investigation the marker is tracked magnetically without using any electromagnetic radiation. Magnetic monitoring has been used successfully for several years, with investigations first being conducted at centers where biomagnetic signal sensing equipment, such as Superconducting Quantum Interference Device (SQUID) was available (Weitschies et al., 1994). These SQUID sensors (see also Section 2.2) allow the detection of extremely weak magnetic signals, but they must be cooled with liquid helium or nitrogen. Parallel to the SQUID activities, prototype systems based on fluxgate and magnetoresistive sensors have been developed. These can be used under room temperature conditions and provide exact information about the human GI tract (Andrä et al., 2000; Richert, 2003).

Magnetic monitoring is based on the evaluation of the stray field which is generated by a magnetic marker and can be measured with appropriate magnetic field sensors. The evaluation on a PC delivers both the three-dimensional position and orientation of the marker. Magnetic monitoring can be used for investigations of human digestive motility as well as for the evaluation of medicaments dissolving and absorbing processes inside the GI tract (Weitschies et al., 2001a,b).

4.2.2 Conventional Investigation Methods of the Human GI Tract

Currently, several methods for GI tract investigations are in use. These methods are utilized for chronic inflammatory (morbus Crohn) and functional GI tract diseases. Although most of these methods allow visualization of the geometry of the GI tract, they are not suitable for studying its motility.

Visualization with *X-rays* (Abrahamsson et al., 1988) is an inexpensive and often used method to achieve images of the entire human body, including the GI tract. Nevertheless, this method should not be used for functional investigations (more than one image) because of the ionizing effects of the X-rays. The same must be considered with *scintigraphic methods* (Siegel et al., 1992). Those methods which do not cause harmful side effects include *magnetic resonance imaging* (MRI) (Christmann et al., 1997), *sonography* (Amend et al., 1995), breath H_2*-test* (Rubinoff et al., 1989), *metal detectors* (Ewe et al., 1991), *inductive measurement* of soft magnetic tracers (Frei et al., 1970; Forsman, 1998), *telemetric capsules* (Lambert et al., 1991), *capsule camera* (Costamagna et al., 2002; Lewis and Swain, 2002), *electrogastrography* (EGG) (Pfaffenbach et al., 1998), and *magnetic monitoring* of permanent magnetic markers (Basile et al., 1992; Forsman, 1994; Weitschies et al., 1997, 2001b; Nomura et al., 2000; Ferreira and Carneiro, 2002). Some advantages and disadvantages of these systems are as follows:

- MRI is a complex method, which is not suitable for long-term and repetitive measurements. Furthermore, this method is not fast enough to measure GI tract motility as this requires measurements to be made every few seconds. Nevertheless, MRI is an excellent method for visualization of the entire GI system (Christmann et al., 1997).
- Sonographic investigations are used to estimate total transit times (Amend et al., 1995), though exact measurements are difficult due to the fact that ultrasound cannot pass through the air inside the GI tract.
- The accuracy of metal detectors dramatically decreases as the distances increase between the metal capsule and measurement system.
- Inductive measurements are used to investigate stomach emptying by following the signal of a soft magnetic "porridge" (Forsman, 1998), but investigation inside the small intestine is not possible because the porridge diffuses unpredictably.

- The capsule camera, which was introduced in 2002, provides an interesting option for GI tract investigation. These cameras, which transmit images for up to 8 h (Costamagna, 2002; Lewis and Swain, 2002), have a diameter of 11 mm and a length of 26 mm, and are approved for use inside the small intestine. The position of the camera can be localized by triangulation of the three strongest signals obtained by antennas fixed on the body of the patient. The resulting accuracy is approximately ± 3 cm (www.GivenImaging.com, 2004). The PC program of this system automatically recognizes and alerts when internal bleeding is present, but searching for pathological tissue requires manual evaluation of the entire recorded video. One drawback of this system is that the rather complex and expensive capsule is not re-useable. Another is that the intestine must be completely emptied if the camera is to work properly. The capsule camera is very useful for finding pathologic tissue and bleedings, but a complex functional diagnostic of the entire GI tract is not possible.
- EGG investigations provide information about electric pacemaker signals of the stomach and sections of the small intestine. It has been reported that changes in the pacemaker frequency of the stomach occur when certain diseases are present (Pfaffenbach et al., 1998). Unfortunately, other electrical activities – for example, from the heart, small intestine and muscular system – interact with the electrical potentials of the stomach so that sophisticated filters must be used to identify the relevant signals. These filters are necessary, but might cause the loss of important information. SQUID sensors can directly measure the electrical activities of the stomach and small intestine (Richards et al., 1996; Allos et al., 1997; Bradshaw et al., 1997a,b, 1999; Seidel et al., 1999). Compared to EGG measurements, SQUID measurements produce more detailed and therefore additionally characteristic frequencies (Comani et al., 1992; Turnbull et al., 1999). The main disadvantage of the SQUID systems is the need for cooling with liquid helium.

4.2.3 Magnetic Markers

Magnetic markers move through the GI system as indigestible material. Any occurring motility pattern inside the GI system influences their time-dependent local position and orientation. It is possible to measure all of these movements directly, and to do so without complex filters. Furthermore, modern magnetic materials such as NdFeB and SmCo provide a high magnetic moment. The increased magnetic field signal allows the use of fluxgate, magnetoresistive or Hall sensors, which function in a magnetically unshielded environment and do not require cooling. Using such sensor systems, investigations of the human digestive system can be readily accomplished with minimum expense at any hospital. Within the past few years, prototype systems have been developed by several groups (Andrä et al., 2000; Richert, 2003), though in each case the same mathematical background for marker localization has been used, irrespective of the sensor principle.

4.2.3.1 Inverse Monitoring

Inverse monitoring is based on the evaluation of the quasi-static magnetic field, which is being generated by a permanent magnetic marker. The position estimation is an inverse problem with six independent degrees of freedom. Knowledge of the magnetic moment of the marker, which is usually constant during transport through the GI tract, reduces the problem to five degrees of freedom, but inversion is maintained. The magnetic field must be measured by an arrangement of several magnetic field sensors, the minimum number of sensors being determined by the degrees of freedom. Disturbing magnetic fields, a high level of accuracy and large measurement volume increase the number of required sensors. Systems in use today generally contain more than 20 sensors. If possible, vectorial estimation of the magnetic field should be the preferred method as it provides greater accuracy and a larger measurement volume than a one-axis system. Most of the older SQUID systems are one-axis systems, and are therefore limited in their ability to estimate the position of the magnetic marker.

The solution of the inverse problem can be found through different approaches, though the results differ in accuracy, velocity, and interfering electromagnetic field compensation. Good choices are nonlinear optimization routines such as the Marquardt-Levenberg method or generic algorithms. One-step procedures such as neural networks have not been successfully implemented. In order to determine the actual position and orientation of the magnetic marker, all expected sensor signals must be calculated. The optimization algorithm minimizes the differences between measured and simulated magnetic field strengths by varying the position and orientation of the simulated magnetic marker using a quality function. This quality function indicates the accuracy of the solution.

4.2.3.2 Theoretical Background

The well-known description of the magnetic field of the magnetic dipole (see Chapter 1, Eq. 1.34) can also be written as:

$$\mathbf{H}(\mathbf{r}_i, \boldsymbol{\mu}) = \frac{1}{4\pi}\left(-\frac{\boldsymbol{\mu}}{r^3} + \frac{3 \cdot (\boldsymbol{\mu} \cdot (\mathbf{r}_i - \mathbf{R})) \cdot (\mathbf{r}_i - \mathbf{R})}{r^5}\right) \tag{4.1}$$

Knowledge of the magnetic dipole moment $\boldsymbol{\mu}$ and the position $\mathbf{R}$ of the dipole reveals the magnetic field at any point $\mathbf{r}_i$ in surrounding space that is generated by the magnetic dipole. It should be noted that Eq. (4.1) is an equation for a magnetic dipole field. For a magnetic marker field which is usually not an ideal dipole field (the exception is an homogeneously magnetized sphere), distances of at least ten times the maximum length of the magnetic marker provide acceptable results. The position of a magnetic marker, its degrees of freedom and the sensor positions, are shown schematically in Figure 4.1.

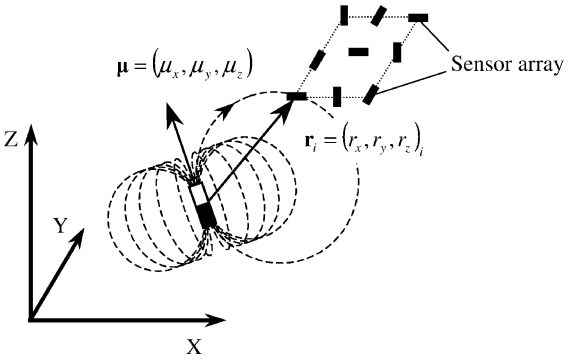

Fig. 4.1. Magnetic field of a magnetic dipole in three-dimensional space. The dipole-generated magnetic field can be calculated at any spatial position.

The marker is described by six degrees of freedom; three for its location in space (r_X, r_Y, r_Z) and three for the dipole moment of the marker (μ_x, μ_y, μ_z). The magnetic field generated by the magnetic marker can be accurately calculated only if all these values are known. The location of a magnetic marker cannot be directly calculated from a known magnetic field configuration around the marker. This inverse problem can only be solved by using a nonlinear optimization algorithm (Press et al., 1988).

For all utilized sensors, the induced magnetic field of a simulated marker at every sensor destination must be calculated and compared to the measured magnetic field values. All squared differences of simulated and measured magnetic field strengths are summarized to the quality-function:

$$Q = \sum_{i=1}^{n} [\mathbf{H}_i^{\text{meas}} - \mathbf{H}(\mathbf{r}_i - \mathbf{R}, \boldsymbol{\mu})^{\text{sim}}]^2 \tag{4.2}$$

This function must be minimized by variation of the position, orientation and – if not constant – the magnetic moment of the magnetic marker: $Q(\mathbf{r}, \boldsymbol{\mu}) \rightarrow \text{Min}$.

4.2.3.3 Forward Monitoring

For the forward monitoring (Andrä et al., 2000) a special case can be used where the axis of the magnetic dipole is aligned to one axis of the Cartesian coordinate system. Then, Eq. (4.1) simplifies to:

$$H_X = \frac{\mu}{4\pi} \frac{3zx}{s^5}, \quad H_Y = \frac{\mu}{4\pi} \frac{3zy}{s^5}, \quad H_Z = \frac{\mu}{4\pi} \frac{3z^2 - s^2}{s^5}, \quad \text{with } s^2 = x^2 + y^2 + z^2 \tag{4.3}$$

These equations can be easily solved in one step. Because of this alignment of the marker to only one axis of the coordinate system, there is no information about the capsule orientation. Therefore, the forward monitoring reveals only the three-dimensional position of the capsule but not its orientation.

4.2.4
Magnetic Monitoring Systems

4.2.4.1
Magnetic Monitoring with Three Magnetic Sensors

At the Jena Institute of Physical High Technology (IPHT), and currently also at the Jena University of Applied Sciences, a method has been developed that is based on the forward monitoring (Andrä et al., 2005). Such a system is shown in Figure 4.2. With only one three-axis magnetoresistive sensor (Honeywell Ltd.) above the capsule, the magnetic stray field generated by the magnetic marker can be measured and the position readily calculated. Due to the fact that the magnetic marker must be aligned with a strong magnetic field (10-times the Earth's magnetic field) produced by an electric coil, the sensor must be magnetically shielded using a smaller so-called compensation coil. During the entire measurement period the sensor is automatically positioned above the capsule position.

The magnetic capsule consists of a spherical magnetic marker, a polyethylene bearing, and a nondissolving shell. The capsule has a length of approx. 20 mm, a diameter of 7 mm, and a density of $\rho = 1.2$ g cm^{-3}. The magnetic moment

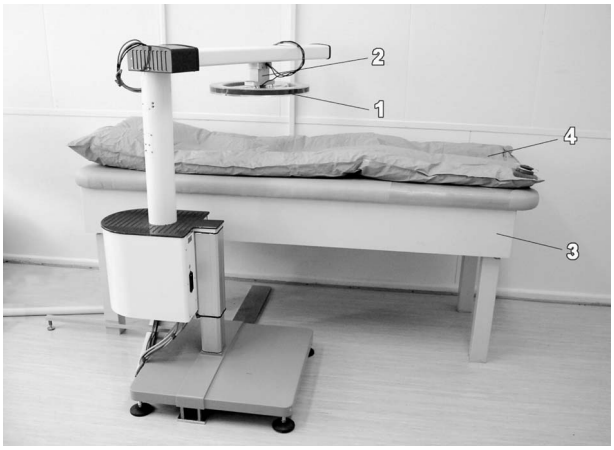

Fig. 4.2. Forward measurement system with automatically positioned AMR-sensor (University of Applied Science, Jena). (1) Main coil; (2) AMR-sensor; (3) nonmagnetic bed; (4) mattress.

of the capsule is in the range of 0.05 Am^2. A measurement is made in several steps. First, the marker must be aligned to the outer field H_{ext}. After shut off of the outer field, a first measurement is taken, after which the marker is rotated in the opposite direction again by the outer field. After shut off of this field a second measurement is taken. Using the difference signal from both measurements, the position of the marker can be calculated. By using difference signals the influence of interfering, slowly changing magnetic fields is ruled out. Averaging several measurements reduces the influence of high-frequency electromagnetic interferences, such that the accuracy of the system is in the range of a few millimeters. Measurement cycles of less than 1 s are possible, and magnetic shielding is unnecessary. For these reasons, the system is stable even against low frequencies from interfering electromagnetic fields. The main disadvantages are: (1) the complicated mechanical set-up of the measurement system (attributable to the moving sensor and coil); and (2) the complex set-up of the magnetic capsule with the rotatable magnetic marker. Because this method delivers only the position but not the orientation of the magnetic marker, not all motility patterns can be observed. The measurement range depends on the magnetic marker moment. For this system, the maximum distance between sensor and marker should not exceed 30 cm.

4.2.4.2
Magnetic Marker Monitoring Using Biomagnetic SQUID Measurement System

The method of magnetic marker monitoring with a biomagnetic SQUID measurement system (SQUID-MMM) allows the transport of solid drug forms with high spatiotemporal resolution to be tracked (Weitschies et al., 1991, 2005). Measurement systems with SQUIDs and a flat dewar bottom are suited to monitor magnetized solid drug forms in the GI tract. The sensitivity of SQUID measurement allows operators to track both the path and the disintegration of the magnetically labeled pharmaceutical dosage form via the decreasing magnetic moment. Only 1–2% micro particle magnetite (known as black food color E172 (Fe_3O_4)) is added during preparation of the dosage forms (capsules or tablets) and subsequently magnetized in a 2-T electromagnet. At the German Physikalisch-Technische Bundesanstalt (PTB), the SQUID-MMM measurements are performed using the 83-SQUID system (Fig. 4.3) inside a magnetically shielded room, AK3b (Drung, 1995).

The outputs of the 83-SQUIDs are electronically combined to 63 gradiometer channels (first order) and used in the localization procedure: 49 B_z gradiometer channels vertically and 14 gradiometer channels horizontally. As distance from the measurement head increases, the degree of location error increases; for example, at 25 cm the location is certain within 8 mm, but at 15 cm the location is certain within 2 mm. The magnetic moment can be calculated with a less than 6% error rate at up to 15 cm distance, and a less than 15% error rate at up to 25 cm distance (Weitschies et al., 2001a).

The SQUID-MMM is improved by online localization and online field visualization. After ingestion of the tablet, the online localization provides the actual position of the tablet in the human body relative to the sensor system. In order to

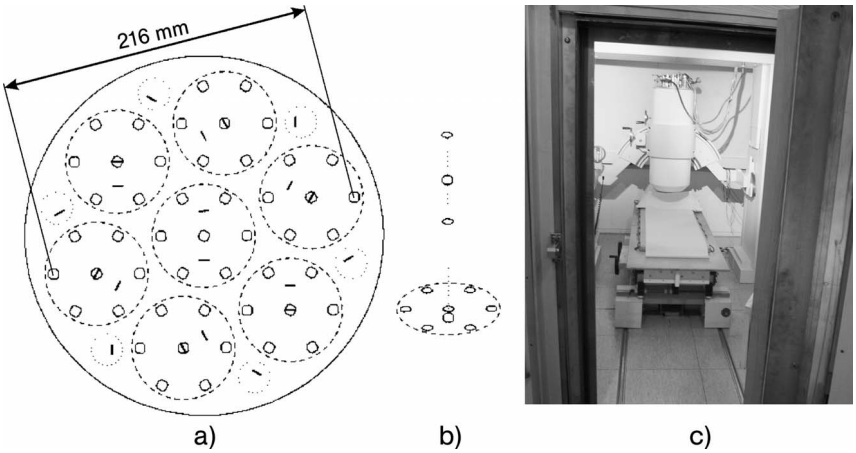

Fig. 4.3. PTB 83-SQUID system. (a) SQUID configuration (top view); (b) one out of seven modules (side view); (c) system inside the shielded room.

maintain an optimal signal-to-noise ratio, this information can be used to minimize the distance between the sensor system and the tablet (Kosch et al., 2004). Further filtering of the cardiac activity improves the measurement data. The SQUID-MMM is applicable for both medical and pharmaceutical investigations.

4.2.4.3
Magnetic Monitoring with Multiple AMR-Sensors

The MAGMA System (magnetic markers) was developed at INNOVENT in Jena (Richert et al., 2004). The working principle is inverse monitoring, and the magnetic field is measured with AMR sensors (anisotropic magnetoresistive sensors; Sensitec GmbH). The magnetic capsule consists of a single NdFeB magnet coated with high molecular-weight polyethylene.

A magnetic capsule has a volume of about 0.5 cm^3, a density of approx. 2 g cm^{-3}, and a magnetic moment of 0.08 Am^2.

A configuration of 48 sensors within two planes ensures the best spatial localization of the magnetic marker. The sensors are aligned in a hexagonal structure and all three Cartesian components of the magnetic field are measured. The measuring range is approx. $40 \times 40 \times 40$ cm^3. The measurement system is illustrated in Figure 4.4.

The position estimation of the marker is established by an evolutional algorithm-based, nonlinear optimization strategy. The use of this estimation algorithm calculates the position and orientation of the magnetic capsule in real-time, with a sampling rate of approximately one per second. The accuracy of the system is in the range of ± 2 mm in position and $\pm 1^\circ$ in orientation. Owing to real-time calculations, the motility patterns are immediately accessible.

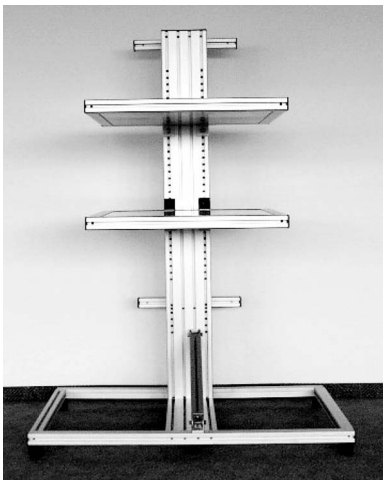

Fig. 4.4. Set-up of the MAGMA system for clinical investigations. The two planes contain 48 AMR sensors.

For the second generation of MAGMA-systems (currently under clinical investigation) the sampling rate could be increased to 50 Hz. At this rate, every motility pattern can be recorded, including those rapid patterns which take place inside the esophagus while swallowing.

4.2.4.4 Comparison of the Measuring Methods

All described systems deliver information about the motility conditions inside the human GI tract. The measurements are carried out with no negative impact on the patients, and the motility of the GI tract is recorded directly. The individual properties of the different systems provide a range of advantages for different applications (see Table 4.1).

A SQUID system requires the lowest quantities of magnetic marker material, and therefore the effects on the GI system are minimal. It provides all spatial and rotatory degrees of freedom and, if necessary, the magnetic moment of the magnetic marker. The sensors, however, require cryogenic cooling and most systems must be magnetically shielded.

Compared to this, both AMR systems can be used in magnetically unshielded environments. Forward monitoring uses a special case that greatly simplifies the calculation of the marker position but eliminates marker orientation information. The MAGMA system provides all degrees of freedom and can be used in a normal clinical environment.

Due to the required cooling costs, an investigation with a SQUID system is the most expensive. While the forward monitoring system needs only three magnetic

Table 4.1. Comparison of different monitoring systems.

System	Measurement range [T]	Notice	Information content	Used for
SQUID MMM	10^{-15}	Cooling with liquid N_2 or He, magnetic shielding or excellent gradiometer necessary	Position (R_x, R_y, R_z) Orientation (μ_x, μ_y, μ_z)	Magnetic monitoring for diagnostic purposes; visualization of drug disintegration
Forward monitoring	10^{-9}	Mechanical sensor positioning, no magnetic shielding, no cooling	Position (R_x, R_y, R_z)	Magnetic monitoring for diagnostic purposes
MAGMA	10^{-9}	No magnetic shielding, no cooling	Position (R_x, R_y, R_z) Orientation (μ_x, μ_y, μ_z)	Magnetic monitoring for diagnostic purposes

field sensors, the mechanical sensor positioning and the capsule are both fairly complex. The MAGMA system functions with at least six and up to 48 AMR sensors, and the magnetic capsule has a simple geometry.

4.2.4.5 Information Content of Magnetic Monitoring Investigations

Numerous investigations, for example with the MAGMA system, determined that magnetic monitoring is extremely beneficial for the accurate reconstruction of the magnetic marker path through the GI system. All MAGMA investigations were performed for a minimum of 4 h. Within the investigation period, the marker has generally passed the esophagus, the stomach, and parts of the small intestine, though in some exceptional cases the marker did not leave the stomach during the investigation period. The investigations were focused on local transit times and characteristic motility patterns.

A typical 4-h passage of a magnetic marker through the esophagus, stomach and small intestine is shown in Figure 4.5. Within a few seconds after swallowing, the magnetically marked capsule travels through the esophagus and into the stomach, where it remains for a certain time depending on individual parameters (ranging from several minutes to several hours). The capsule itself is too large to leave the stomach immediately, and can only pass the pylorus by the so-called ''housekeeper'' function.

Passage through the duodenum can easily be plotted as a large arc with a typical high-velocity peak. Beginning from the jejunum the small intestine is not fixed, but the position of the marker inside the intestine could be described as the cov-

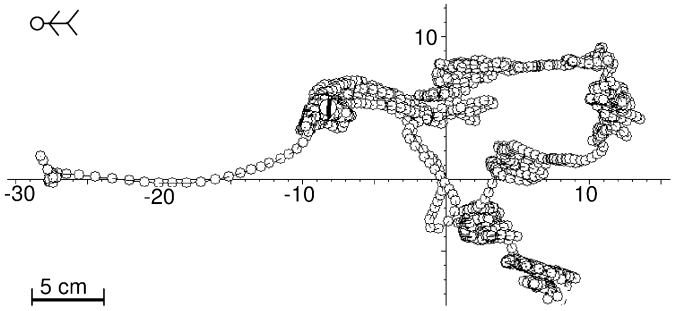

Fig. 4.5. Marker passage through the gastrointestinal tract of a patient over a period of 4 h.

ered path (Richert, 2003). Any movement of the patient, including coughing, breathing and shifting in reference to the measurement system, makes it complicated to classify the individual segments.

Nevertheless, measurement of the covered path provides an estimate of local transport velocities. The relationship between the covered path of a magnetic capsule exactly 120 min after entry into the duodenum and the individual body mass index (BMI; body weight/body height^2) for different patients is shown in Figure 4.6. The healthy control group reveals a linear dependency with modest dispersion, but for patient groups with diagnosed diseases no such dependency could be identified.

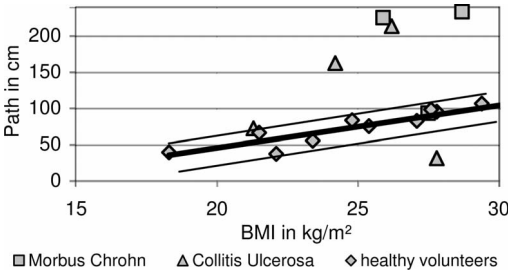

Fig. 4.6. Relationship between the covered path of the marker 120 min after entry into the duodenum and the individual body mass index (BMI) of several patients. Patients with diagnosed disease show a significantly different behavior than the healthy control group.

4.2.4.6 Motility Pattern of the GI System

All motility patterns of the GI system can easily be identified through investigation of magnetic marker movements, with different information being extracted by ex-

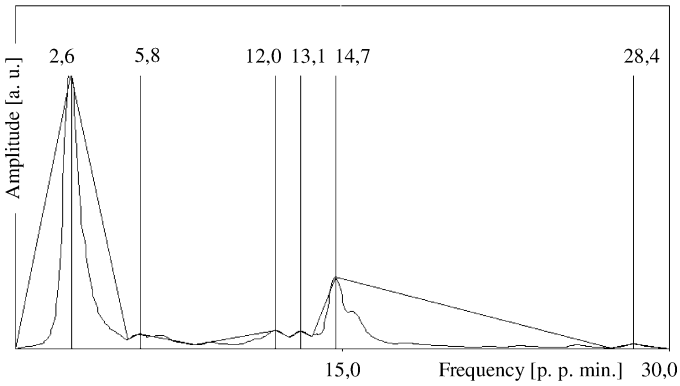

Fig. 4.7. Frequency spectra of the stomach with dominating frequency of 2.6 min^{-1}.

amining the spatial movement and rotation. Although the spatial movement reveals path length, local velocity and local transit times, this information can be masked by the patient's breathing, coughing, and shifting. A better way to calculate the dominating frequency might be an analysis of the marker rotation.

The frequency analyses of marker rotation over periods of approximately 10 min for a healthy volunteer are shown in Figures 4.7 to 4.10.

The stomach frequency spectrum is shown in Figure 4.7. The dominating frequency for this volunteer lies at exactly 2.6 min^{-1}, while the next peak lies at 14.7 min^{-1} and can be ascribed to the breathing of the volunteer. The dominating frequency of approximately three per minute is well known, and can be conclusively verified with the magnetic monitoring method.

Passage through the duodenum is characterized by a different frequency spectrum (see Fig. 4.8). The strongest frequency lies at 6.4 min^{-1}, but the well-known frequencies of 10 min^{-1} and 12 min^{-1} can also be identified (here exactly at

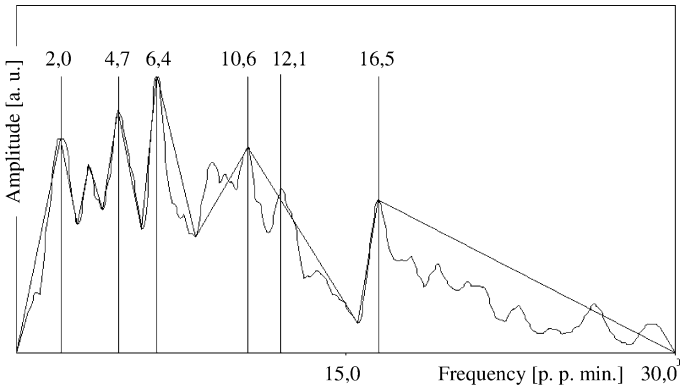

Fig. 4.8. Frequency spectra of the duodenum, showing the well-known, but here nondominant, frequency of 12 min^{-1}.

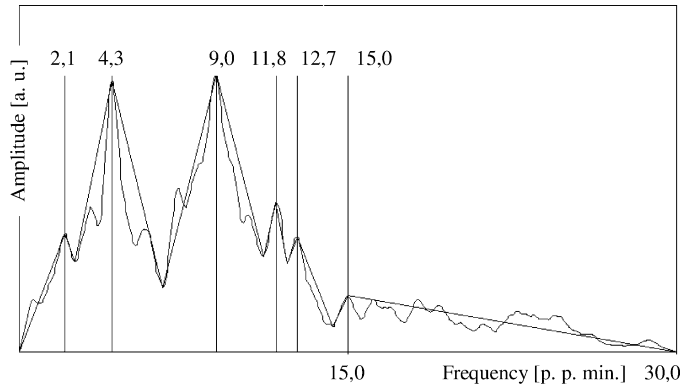

Fig. 4.9. Frequency spectra of the ileum with dominating frequencies of 4.3 min^{-1} and 9.0 min^{-1}.

10.6 min^{-1} and 12.1 min^{-1}). The breath signal changes to 16.5 min^{-1}, but is still rather strong.

For the remaining small intestine the frequency of approximately 10 min^{-1} is the strongest (Figs. 4.9 and 4.10). For the investigated volunteers the frequency changes slightly between 9 min^{-1} and 11 min^{-1} during the transport, depending on the local pacemakers. The substantial reduction in breath signal can be ascribed to the distance from the lung. The interpretation of the remaining frequencies and their changes due to diseases should be investigated in future studies.

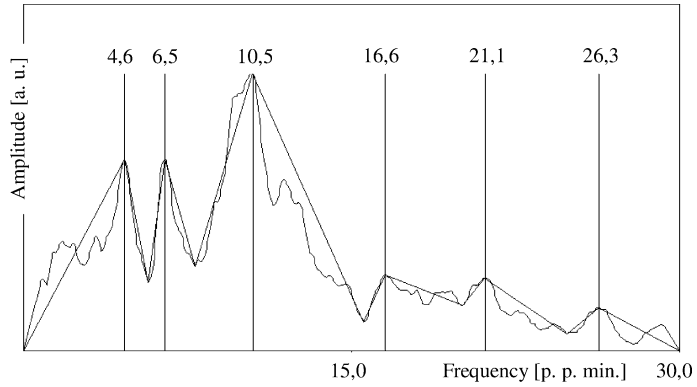

Fig. 4.10. Frequency spectra of the jejunum with dominating frequency of 10.5 min^{-1}.

4.2.4.7
Absorption Processes Inside the GI Tract

The disintegration of a magnetized tablet in the GI tract, as assessed by SQUID-MMM, is shown in Figure 4.11. Erosion of the tablet begins immediately after in-

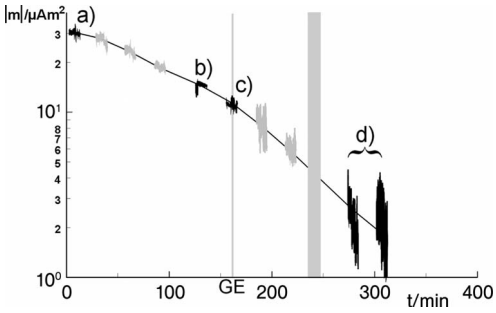

Fig. 4.11. Decay of the magnetic moment of the magnetically marked tablet during its path through the GI tract (semi-logarithmic plot). Data sets (a) to (d) are related to the locations displayed in Fig. 4.12 (a) to (d). GE refers to the instant of gastric emptying, as derived from Fig. 4.12(c).

gestion, but after approximately 160 min the erosion rate changes as a result of gastric emptying.

These data can be connected to the path of the dosage form through the GI tract (Fig. 4.12). During the first four measurement intervals the tablet remains in the proximal stomach, showing only minimal mobility. However, during the fifth recording interval (Fig. 4.12b), the tablet moves to the distal stomach, from where it is emptied into the small intestine (Fig. 4.12c). During the final two intervals (Fig. 4.12d), the tablet is located in the colon.

4.2.5 Conclusion and Outlook

Magnetic monitoring has been developed within the past few years and, for some applications such as the investigation of dissolution processes it is already in regular use. A large number of investigations of human GI tract motility have demonstrated the potential of magnetic monitoring based on the fact that the method does not use ionizing radiation and has no other harmful affects. Moreover, the informational content obtained with regard to local motility patterns exceeds that of any other currently available investigational method for the human intestine.

The correlation of local velocities, and especially the unique motility patterns of specific known diseases, might lead to an earlier diagnosis of functional diseases of the human digestive system. Indeed, initial correlations between local velocity and BMI have already established that there are significant differences between healthy volunteers and patients with different diseases.

The specific properties of the described magnetic monitoring systems (SQUID, and forward or inverse AMR) are highly complementary. While investigations of

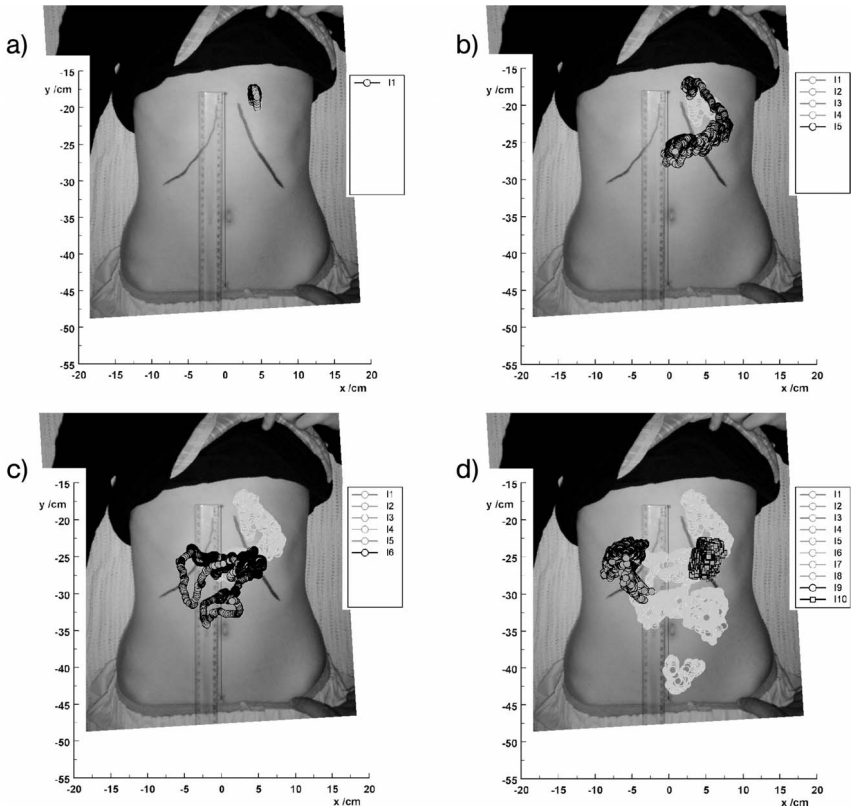

Fig. 4.12. Path of the magnetically marked dosage form through the GI tract of a volunteer in the fasted state. Intervals of 10-min duration are displayed while the marked dosage form moves through the fundus (a), antrum (b), duodenum (c), and transverse colon (d).

GI tract motility in normal clinical environments are possible with AMR sensor systems, dissolution processes to help understand absorption can be investigated with SQUID systems. Nonetheless, while much effort is required to reduce electromagnetic interference, the system has extremely high sensitivity.

In all cases magnetic monitoring investigations are noninvasive and the patient need swallow only a small magnetic pill. Consequently, the acceptance of this method is expected to be very high. However, before magnetic monitoring can be used widely for diagnostic purposes, important correlations between motility patterns and specific GI tract diseases must be established. To date, the data obtained have revealed some interesting relationships and will, undoubtedly, provide much more information in future.

Acknowledgments

The authors thank PD Dr. med. Eitner and Dr. med. Hocke for performing the multiple magnetic monitoring experiments, Prof. Andrä for support and fruitful discussions, and Sensitec GmbH for the development of the sensor array used in the MAGMA-system.

References

Abrahamsson, H., Antov, S., and Bosaeus, I. (1988). Gastrointestinal and colonic segmental transit time evaluated by a single abdominal x-ray in healthy subjects and constipated patients. *Scand. J. Gastroenterol.*, **23** (suppl. 152), 72–80.

Allos, S.H., Staton, D.J., Bradshaw, L.A., Halter, S., Wikswo, J.P., and Richards, W.O. (1997). Superconducting interference device magnetometer for diagnosis of ischemia caused by mesenteric venous thrombosis. *World J. Surg.*, **21**, 173–178.

Amend, M., Jakobeit, C., and Greiner, L. (1995). Akustisches Verhalten ingestierbarer Fremdkörper in vivo – zur Sonographie der gastrointestinalen Motilität. *Verdauungskrankheiten*, **13**, 21.

Andrä, W., Danan, H., Kirmße, H., Kramer, H., Saupe, P., Schmieg, R., and Bellemann, M.E. (2000). A novel method for real-time magnetic marker monitoring in the gastrointestinal tract. *Phys. Med. Biol.*, **45**, 3081–3093.

Andrä, W., Danan, H., Eitner, K., Hocke, M., Kramer, H.-H., Parusel, H., Saupe, P., Werner, C., and Bellemann, M.E. (2005). A novel method for examination of bowel motility. *Medical Physics*, **32** (9), 2942–2944.

Basile, M., Neri, M., Carriero, A., Casciardi, S., Comani, S., Del Gratta, C., Di Donato, L., Di Luzio, S., Macri, M.A., Pasquarelli, A., Pizella, V., and Romani, G.L. (1992). Measurement of segmental transit through the gut in man. *Dig. Dis. Sci.*, **37** (10), 1537–1543.

Bradshaw, L.A., Wells, R., Paul, S., Richards, W.O., and Wikswo, J.P. (1997a). Noninvasive measurement of gastric propagation using a SQUID magnetometer. *Proceedings of the 19th Annual International Conference of the IEEE Engineering in Medicine and Biology Society*, **6**, 2392–2393.

Bradshaw, L.A., Allos, S.H., Wikswo, J.P., and Richards, W.O. (1997b). Correlation and comparison of magnetic and electric detection of small intestine electrical activity. *Am. J. Physiol.* **272** (*Gastrointest. Liver Physiol.* **35**), G1159–G1167.

Bradshaw, L.A., Ladipo, J.K., Staton, D.J., and Wikswo, J.P. (1999). The human vector magnetogastrogram and magnetoenterogram. *IEEE Trans. Biomed. Eng.*, **46** (8), 959–970.

Christmann, V., Rosenberg, J., Seega, J., and Lehr, C.M. (1997). Simultaneous in vivo visualization and localization of solid oral dosage forms in rat gastrointestinal tract by MRI. *Pharmaceutical research*, **14** (8), 1066–1072.

Comani, S., Basile, M., Casiardi, S., Del Gatta, C., Di Luzio, S., Erné, S.N., Neri, M., Peresson, M., and Romani, G.L. (1992). Extracorporeal direct magnetic measurement of gastric activity. In: Hoke, M. (Ed.), *Biomagnetism: Clinical Aspects*. Elsevier Science, pp. 639–642.

Costamagna, G., Shah, S.K., Riccioni, M.E., Foschia, F., Mutignani, M., Perri, V., Vecchioli, A., Brizi, M.G., Picciocchi, A., and Marano, P. (2002). A prospective trial comparing small bowel radiographs and video capsule endoscopy for suspected small bowel diseases. *Gastroenterology*, **123** (4), 999–1005.

Drung, D. (1995). The PTB 83-SQUID system for biomagnetic applications in a clinic. *IEEE Trans. on Appl. Superconductivity*, **5** (2), 2112–2117.

Ewe, K., Press, A.G., Bollen, S., and Schuhn, I. (1991). Gastric emptying of indigestible tablets in relation to composition and time of ingestion of meals studied by metal detector. *Dig. Dis. Sci.*, **36** (2), 146–152.

Ferreira, A. and Carneiro, A. (2002). Detection of the gastrocolic reflex using a three axis fluxgate. In: Nowak, H., Haueisen, J., Giessler, F., and Huonker, R. (Eds.), *Biomag 2002: Proceedings of 13th International Conference on Biomagnetism*, VDE Verlag, Berlin, pp. 1096–1098.

Forsman, M. (1994). Measurement of gastrointestinal transit using fluxgate magnetometers. *Physics Med. Biol.*, **39** (a), 62.

Forsman, M. (1998). In: Andrä, W. and Nowak, H. (Eds.), *Magnetism in Medicine*, Wiley VCH, Berlin, Weinheim, New York, Brisbane, Singapore, Toronto, pp. 430–442.

Frei, E.H., Benmair, Y., Yerashalmi, Y., and Dreyfuss, F. (1970). Measurements of emptying of the stomach with a magnetic tracer. *IEEE Trans. Magn.*, **6**, 348–349.

Given Imaging: http://www.givenimaging.com.

Kosch, O., Weitschies, W., and Trahms, L. (2004). On-line localization of magnetic markers for clinical applications and drug delivery studies. In: Halgren, E., Ahlfors, S., Hämäläinen, M., and Cohen, D. (Eds.), *Biomag 2004: Proceedings 14th International Conference on Biomagnetism*, Biomag 2004 Ltd., Boston, pp. 261–262.

Lambert, A., Vaxman, F., Crenner, F., Wittmann, T., and Grenier, J.F. (1991). Autonomous telemetric capsule to explore the small bowel. *Med. Biol. Eng. Computing*, **29** (2), 191–196.

Lewis, B. and Swain, P. (2002). Capsule endoscopy in the evaluation of patients with suspected small intestinal bleeding. *Gastrointest. Endosc.*, **56** (3), 349–353.

Nomura, M., Saijyo, T., Haruta, Y., Itozaky, H., Toyada, H., Nakaya, Y., Ito, S., and Ado, H. (2000). Biomagnetic measurements of gastric mechanical motility using a high temperature SQUID imaging. In: Aine, C., Okada, Y., Stroink, G., Swithenby, S., and Wood, C. (Eds.), *Advances in Biomagnetism Research*, Springer Verlag, pp. 624–627.

Pfaffenbach, B., Adamek, R.J., and Lux, G. (1998). Stellenwert der Elektrogastrographie in der gastroenterologischen Funktionsdiagnostik. *Deutsche med. Wochenschrift*, **123**, 855–860.

Press, W.H., Teukolsky, S.A., Vetterling, W.T., and Flannery, B.P. (1988). *Numerical recipes in C*. Cambridge University Press.

Richards, W.O., Bradshaw, L.A., Staton, D.J., Garrard, C.L., Liu, F., Buchanan, S., and Wikswo, J.P. (1996). Magnetoenterography (MENG): noninvasive measurement of bioelectric activity in human small intestine. *Dig. Dis. Sci.*, **41**, 2293–2301.

Richert, H. (2003). *Entwicklung eines magnetischen 3-D-Monitoringsystems am Beispiel der nichtinvasiven Untersuchung des menschlichen Gastro-Intestinal-Traktes*. Dissertation, FSU Jena.

Richert, H., Wangemann, S., Surzhenko, O., Heinrich, J., Eitner, K., Hocke, M., and Görnert, P. (2004). Magnetisches Monitoring des menschlichen Magen-Darm-Traktes. *Biomedizinische Technik*, **49**, 718–719.

Rubinoff, M.J., Piccione, P.R., and Holt, P.R. (1989). Clonidine prolongs human small intestine transit time: use of the lactulose-breath hydrogen test. *Am. J. Gastroenterol.*, **84** (4), 372–374.

Seidel, S.A., Bradshaw, L.A., Ladipo, J.K., Wikswo, J.P., and Richards, W.O. (1999). Noninvasive detection of ischemic bowel. *J. Vasc. Surg.* **30** (2), 309–319.

Siegel, J.A., Urbain, J.L., Adler, L.P., Charkes, N.D., Maurer, A.H., Krevsky, B., Knight, L.C., Fisher, R.S., and Malmud, L.S. (1992). Biphasic nature of gastric emptying. *Gut*, **29** (1), 85–89.

Turnbull, G.K., Ritcey, S.P., Stroink, G., Brands, B., and van Leeuwen, P. (1999). Spatial and temporal variations in the magnetic fields produced by human gastrointestinal activity. *Med. Biol. Eng. Comput.* **37** (5), 549–554.

Weitschies, W., Wedemeyer, J., Stehr, R., and Trahms, L. (1991). Magnetically marked pharmaceutical dosage forms to monitor gastrointestinal transit by biomagnetic measurements. *Pharmac. Phamacol. Lett.*, **1**, 45–48.

Weitschies, W., Weyemeyer, R., and Trahms, L. (1994). Magnetic markers as a noninvasive tool to monitor gastrointestinal transit. *IEEE Trans Biomed. Eng.*, **41**, 192.

Weitschies, W., Kötitz, R., Cordini, D., and Trahms, L. (1997). High-resolution monitoring the gastrointestinal transit of a magnetically marked capsule. *J. Pharm. Sci.*, **86** (11), 1218.

Weitschies, W., Grützmann, R., Hartmann, V., and Breitkreutz, J. (2001a). Determina-

tion of the disintegration behaviour of magnetically marked tablets. *Eur. J. Pharm. Biopharm.*, **52**, 221–226.

Weitschies, W., Karaus, M., Cordini, D., Trahms, L., Breitkreutz, J., and Semmler, W. (2001b). Magnetic marker monitoring of disintegrating capsules. *Eur. J. Pharm. Sci.*, **13**, 411–416.

Weitschies, W., Kosch, O., Mönnikes, H., and Trahms, L. (2005). Magnetic marker monitoring: An application of biomagnetic measurement instrumentation and principles for the determination of the gastrointestinal behaviour of magnetically marked solid dosage forms. *Adv. Drug Deliv. Rev*, **57** (8), 1210–1222.

4.3
Remote-Controlled Drug Delivery in the Gastrointestinal Tract

Wilfried Andrä and Christoph Werner

4.3.1
Introduction

Site-specific drug delivery in the gastrointestinal tract has for many years been a challenge in the field of biopharmaceutics. Site-specific drug delivery can guarantee a safe and reproducible treatment of diseases in defined local positions, and may also avoid overdosing and corresponding adverse side effects as much as possible. In addition to these therapeutic goals, it would also be possible to investigate the site dependence of drug absorption along the digestive tract.

There are two main approaches to achieving targeted drug release to specific regions: (1) physiologically triggered release; and (2) remote controlled drug targeting (RCDT).

The first approach – physiologically triggered drug release – is already standard practice, as can be seen from the fact that about 10% of all oral drug formulations are retarded-release formulations. As an example there are four different methods of physiologically triggered drug release available for colon-specific drug targeting (Leopold 2001): pH-controlled; time-controlled; enzyme-controlled; and pressure-controlled drug targeting. All of these methods, however, suffer from ill-defined triggering parameters which may vary considerably from individual to individual, and also depend on a patient's state of health.

In an effort to overcome the weaknesses of physiologically triggered release, the RCDT method has been developed and tested for almost 100 years. In this context, the use of magnetic fields to initiate drug release remotely can be suggested due to their unique ability to penetrate tissue easily, at least at low frequencies. Therefore, most trials which have been conducted to develop a RCDT method are based on magnetic principles. A selection of the known approaches is presented in the following paragraphs. These approaches are suitable for the:

- investigation of site-specific absorption of different agents along the digestive tract (site-specific absorption); and
- administration of drugs to predetermined sites in the gut (drug targeting).

4.3.2
Physical Principles Used or Proposed for Remote Controlled Release

Although the demand for RCDT is often emphasized in the medical and pharmaceutical literature, the routine use of this technique has not yet been achieved on a large scale. Only one of the known capsule types has achieved a state of industrial production and commercial distribution – the InteliSite® capsule (Casper et al., 1992a,b). Numerous other capsule devices have been designed and published, as described elsewhere (for reviews, see Gröning, 1997; Gardner et al., 1997; Wilding et al., 2000; Danco, 2002; Wilding and Prior, 2003). The best descriptions of capsule types have been provided by Wilding and Prior (2003). In this section, only those capsules that are restricted to constructions utilizing magnetic materials or fields are reviewed.

4.3.2.1
Capsules Designed for Drug Release Under the Guiding or Withholding Influence of a Magnetic Field

Remarkably, the first attempt to deliver drugs to defined locations in the gastrointestinal (GI) tract was described in a patent specification in 1913 (Briede, 1913). This approach to RCDT was embodied by a capsule at least partly consisting of iron as a container for radioactive substances (Fig. 4.13A). The capsule was designed to be guided inside the digestive tract or kept at defined positions for the time needed to apply a certain dose of radiation.

This interesting concept of magnetic guiding or fixing was developed further by Werner and Gröning (1995) and Gröning and Berntgen (1996), who combined the Heidelberg capsule (Steinberg et al., 1965), or an osmotically controlled depot tablet with a permanent magnet (Kuhlmann, 2001). The system, consisting of a Heidelberg capsule and a piece of a NdFeB permanent magnet which could be attracted by a second permanent magnet placed on the abdomen of the volunteer, is shown in Figure 4.13C. The force between the two magnets was sufficiently high

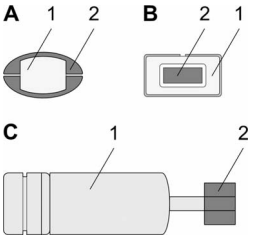

Fig. 4.13. Sketches of capsules designed for magnetic guidance and fixing according to (A) Briede (1913); (B) Gröning et al. (1996); (C) Gröning and Berntgen (1996). Approximately the same scale is used for the three examples. The agent container is denoted by (1), the magnetic part of the capsule by (2).

to considerably delay the residence time of the capsule in the stomach. In another study, Gröning et al. (1996) showed that a small permanent magnet incorporated in an osmotically controlled depot tablet (Fig. 4.13B) could be used to lengthen the residence time of the capsule in the upper region of the GI tract.

Some other examples of capsules designed for magnetic guidance or fixation can be found in the invention descriptions provided by Shioda et al. (1980), Nakago (1987), and Neusel (1996).

4.3.2.2
Capsules Using Mechanical Forces of Magnetic Fields to Open a Container

The attracting and repulsing forces between pieces of magnetic material are very often used in technical equipment. Use of this concept was, of course, also attempted in capsule construction. An interesting example was described by Danco (2002), who used a so-called Reed switch to close an electric circuit, thereby starting the output of gas from a hydrogen gassing cell and pressing the agent out of the container (Fig. 4.14A). A similar switch was used by Lambert et al. (1991), Gröning and Weyel (1993) and Vaxman et al. (1995) to trigger the release of drugs from a fairly sophisticated "autonomous telemetric capsule" (Fig. 4.14E). This special construction is described in more detail in Section 4.3.3.1.

Magnetic forces were also used in the patent of Merrill (1972) to open and close a contact between the medicament and a drug-permeable wall. Furthermore, Sinaiko (1994) used such forces to actuate a latch, thereby closing an opening after taking a sample of the gastric fluid.

In principle, the construction developed by Richert (2004) is also based on the forces between magnetic parts of the capsule (Fig. 4.14B). In this case, the initially acting attractive force between soft magnetic and permanent magnetic parts is switched off in the course of demagnetization by an alternating magnetic field with decreasing amplitude. In this way, the capsule parts are moved apart and the enclosed agent is released (Richert et al., 2004, 2005).

4.3.2.3
Capsule Operation Triggered by an Alternating (AC) Magnetic Field

Alternating (AC) magnetic fields with frequencies of less than about 100 kHz penetrate the tissue of the human body almost without any attenuation. This fact is often used to transmit signals or even energy to capsules inside the patient. Many different attempts have been made to utilize the transmitted AC field for remote controlled drug release. Unfortunately, however, some descriptions of capsules – especially those given in patent specifications – do not provide information on how the signal is used to trigger the drug delivery and are, therefore, not described here.

Magnetically Heated Memory Metals

Several types of capsules contain elastic parts of so-called memory metal (e.g., nickel-titanium alloy) which is, in the as-swallowed state, in a nonequilibrium state

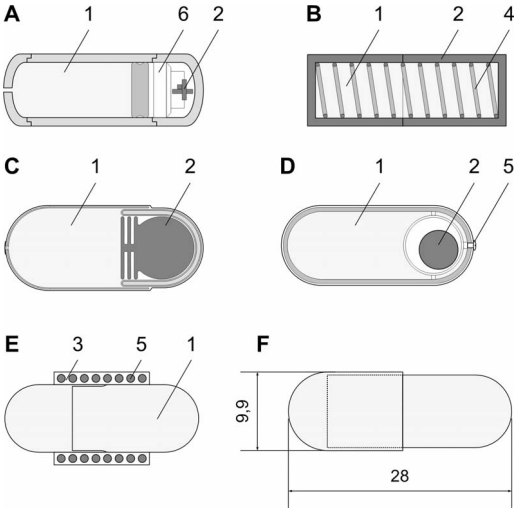

Fig. 4.14. Sketches (approximately true to scale) of capsules already tested *in vitro* according to (A) Danco (2002); (B) Richert (2004); (C) Dutz et al. (2005); (D) Andrä et al. (2004); (E) Andrä et al. (2002). For comparison, a hard gelatin capsule of the standard size 000 is plotted (F) and dimensions given in mm. Numbers denote: (1) the agent container; (2) the magnetic part; (3) the eddy current part; (4) the spring; (5) the fuse; and (6) a hydrogen gassing cell.

and, after heating, in a relaxed state with changed shape. The heating is provided by eddy currents in an AC field (Sekiguchi, 1982), or by an electric current flowing from a power supply integrated in the capsule and switched on by a transmitted signal (Honda et al., 1984), such as an ultrasound pulse (Kambara et al., 1985). The InteliSite® capsule (see Section 4.3.3.1) also utilizes memory metal, but the heating current is generated by the inductive voltage of a three-dimensional array of receiving coils (Casper et al., 1992a,b).

Melting of Solid Substances by Eddy Current Heating

Eddy current heating is a common means of transforming the energy of AC magnetic fields into heat, and this principle is utilized in several capsule constructions. One of the first successful approaches to RCDT was published by Eriksen et al. (1961) (see Section 4.3.3.1). Eriksen used the eddy current heating of a metal tube which in turn causes the melting of wax. The low melting point of Wood's metal was utilized by Hemmati (1968), who reported on the remote controlled drug release from a capsule (see Section 4.3.3.1) in a similar manner as described by Eriksen. An even simpler releasing mechanism was proposed by Minakawa and Henmi (1992), who designed a capsule coated by a thermosensitive polymer cover with low melting point. The heating energy was delivered by an alternating magnetic field, presumably via eddy currents in wire filament embedded in the polymer. In the design of Andrä et al. (2002), a belt consisting of wax and a copper

coil held two capsule parts together until the wax was melted by the eddy current heating of the copper (Fig. 4.14E).

Melting of a Fuse Thread

The above-described melting mechanisms function by taking the energy immediately out of the alternating magnetic field. There are several alternative solutions which make use either of the voltage induced in a properly tuned circuit or an integrated power source and drive a current through a wire, thereby heating a fuse thread until it breaks by melting. The former variant was published as patents by Hugemann and Schuster (1982, 1984), used in a revised form by Staib et al. (1986) (Fig. 4.15F), and more recently utilized by Houzego et al. (2001). Different embodiments of the latter kind were already reported by Hosoya et al. (1980) and by Schentag and D'Andrea (1994). In order to push the agent out of the capsule, Hugemann and Schuster, Houzego et al. (Fig. 4.15D) and Hosoya all made use of a spring relaxed by the melting thread. Schentag and D'Andrea took advantage of the expansion of a gas which is produced as soon as two reactants initially separated by a stretched diaphragm before being relaxed by the melting fuse come into contact (similar to the action of sherbet, the effervescent powder used in drinks).

Heating by Magnetic Hysteresis Losses

The heating of a capsule component that triggers a releasing mechanism is also possible without the application of electrical currents. The first proposal using this method was published by Andrä and Wendt (2000). The essential idea was to heat a mixture of wax and a magnetic oxide powder by the magnetic losses of the powder in an AC magnetic field, thereby melting the wax and breaking up a belt which held together two parts of the capsule shell. A similar construction was reported by Andrä et al. (2002) who used, in addition to eddy current heating, hysteresis losses as heating source. Dutz et al. (2003, 2005) and Andrä et al. (2006) developed this method further by using the heat generated in the magnetic powder to evaporate a low-boiling liquid which then inflated an expandable bag (Fig. 4.14C).

4.3.2.4

Application of Rotating Magnetic Fields

In addition to the application of alternating magnetic fields explained above, rotating magnetic fields are also utilized. Yokoi et al. (2003) described a mechanism inside a medical capsule which consisted of a screw with a permanent magnet magnetized perpendicular to its axis. An extracorporeal rotating magnetic field could then rotate the screw. In this way, a hole could be opened which let out the agent from a container. Moreover, in this invention the rotating field was used to perform several other functions, including moving a screw-shaped capsule through the gut. Quite another application of rotating fields was reported by Knauft et al. (2004). These authors used the torque exerted by the magnetic field on a permanent magnetic sphere that can move freely inside the capsule to turn the sphere with rather high frequencies (up to 500 Hz) and thereby to heat the bearing liquid (Fig. 4.14D).

The temperature increase, in turn, releases the agent by an opening mechanism, such as the melting of a temperature-sensitive stopper (Andrä et al., 2004).

4.3.3 Discussion and Outlook

4.3.3.1 Capsules already Used for Animal and Human Studies

Clearly, while numerous different attempts have been made to realize the goal of remote-controlled drug release in the GI tract, most of them are basically only ideas, conceptions or proposals which have never reached a state of practical significance. Several capsule types have been evaluated *in vitro*, and these may be suitable for further stages of development. However, to date only a few constructions have been used in studies with animals or volunteers, and these are described in more detail in the following section (see Table 4.2).

Studies Using Melting Materials

Some 45 years ago, Eriksen et al. (1961) described both a capsule and the extracorporeal equipment for its operation suitable for remote-controlled drug release. This report was a perfect example of a scientific paper which contained not only the detailed technical description of the system but also the results of its application for a study of site-dependent absorption of drugs in the gut. In the context of this book, the interesting technical data are partly provided in the caption of Figure 4.15C. Further interesting points concern the generation of the AC magnetic field provided by a so-called radiofrequency bombarder unit (frequency 500 kHz; power 2.5 kW) designed for technical induction heating and a special coil (internal diameter ca. 35 cm) which was sufficiently large for a dog or even a human to be placed in its opening. Estimations showed that heat absorption (by eddy currents in the metallic shell of the capsule) inside a dog amounted to ca. 0.2 W, which caused the melting of a wax seal (melting point 52 °C), at which time a metallic spring was released. The capsule position was detected by measuring the length of a thread fixed onto, and swallowed with, the capsule. A calibration was performed by means of fluoroscopic observation of radio-opaque silver rings connected to the thread. Eriksen et al. utilized the equipment to study the site-dependence of salicylate absorption in two dogs. A further study was performed by Lin et al. (1964) concerning the local absorption of other agents in five dogs.

Some seven years later, the details of a similar approach (Fig. 4.15A) were published by Hemmati (1968), clearly without knowledge of Eriksen's investigations. Wood's metal (melting point 47 °C) was used instead of wax as the melting material. The AC field was also provided by a commercial generator (frequency 1.5 MHz) and a ring-shaped coil with a sufficiently large internal diameter to take a man in its horizontally oriented opening. The capsule position and drug release were controlled by X-ray examination. Hemmati, probably for the first time, per-

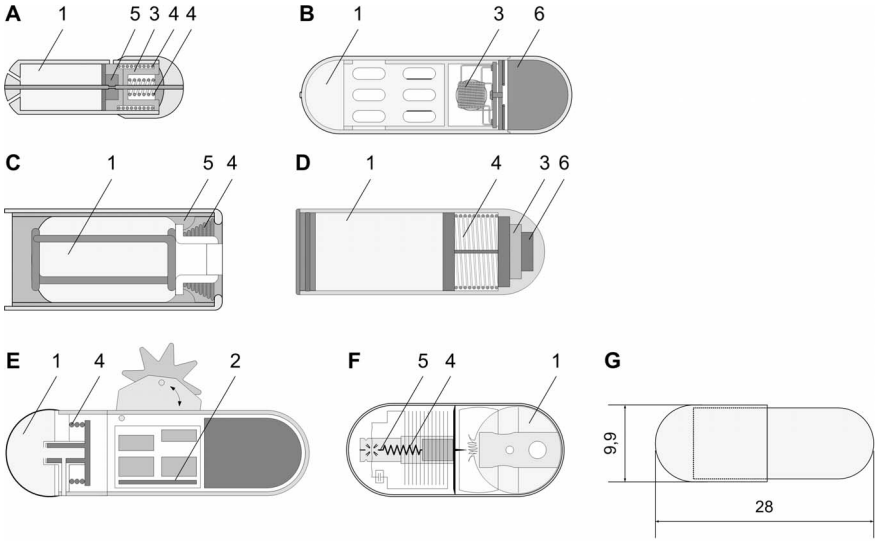

Fig. 4.15. Sketches (approximately true to scale) of capsules used for studies with animals and man according to (A) Hemmati (1968); (B) Casper et al. (1992); (C) Eriksen et al. (1961); (D) Houzego et al. (1999); (E) Lambert et al. (1995); (F) Hugemann and Schuster (1981). For comparison, a hard gelatin capsule of the standard size 000 is plotted. Numbers denote: (1) the agent container; (2) the magnetic part; (3) the eddy current or the heating part; (4) the spring; (5) the fuse; and (6) the radiotracer port.

formed a human study (in 40 volunteers) and investigated the local absorption of iron. Hemmati confirmed the result of earlier investigations that iron absorption takes place in the duodenum and the upper part of the jejunum.

High-Frequency (HF) Capsule

The next step of development was realized with the high-frequency (HF) capsule (Hugemann and Schuster, 1982). In contrast to the former two constructions, the capsule consisted mainly of nonmetallic substances. A ring-shaped coil in front of the examined person was driven by a HF current (27 MHz) which excited a tuned circuit inside the capsule to heat a thin wire. Here, the melting substance was a nylon thread and the output of the agent was initiated by piercing a latex balloon (Fig. 4.15F). During the following years, more than two dozen human studies with more than 200 examinations were carried out investigating the local absorption of numerous agents in different regions of the gut (e.g., Staib and Fuhr, 1995).

The Cogwheel Capsule

Quite another type of capsule construction was reported by a group in Strasbourg (Lambert et al., 1991; Vaxman et al., 1995). As shown in Figure 4.15E, the outstanding feature is a swivel-mounted cogwheel (diameter 10 mm) which acts as a

mileage indicator by counting the number of turns caused by its rotation along the intestinal wall. As a consequence, only the covered distance along the gut can be measured and not the capsule position in the human body. The advantage of this approach, as compared to the foregoing constructions, is the relatively small power needed to activate the releasing mechanism. This was realized by a magnetic switch which was probably operated by static magnetic fields as small as 800 A m^{-1} (e.g., Danco, 2002), or even by an extracorporeal permanent magnet. On the other hand, a lithium battery was integrated as power source which restricted the operation time to about one day. More than 130 investigations have been performed in humans, with 50 patients also being examined. Initially used as a distance meter in the gut, the capsule can also be utilized to release agents with a volume of about 1 mL.

The InteliSite® Capsule

One year after the report of the cogwheel capsule a new construction was published (Casper et al., 1992a,b). At present, this is the only capsule type available commercially, and is marketed as the InteliSite® capsule (Innovative Devices, Raleigh, North Carolina, USA). The main features of this capsule are shown in Figure 4.15B. In contrast to the "cogwheel-capsule", the InteliSite® does not require a battery; rather, it uses the voltage induced by an AC magnetic field (frequency 6.78 MHz) in a three-dimensional array of receiving coils that drives a current through a resistor of the corresponding circuit. Elements of memory metal in thermal contact with the resistor are heated ($\geq$ 40 °C), which in turn causes two concentric sleeves to rotate against each other in such a way that a series of openings becomes coincident and leaves the agent out of a container (volume 0.8 mL). Compared to the above-described capsules, one important difference is in the method of detecting the capsule position. The InteliSite uses a radionuclide (e.g., ^{99m}Tc) enclosed in a specially sealed capsule volume and detected by means of gamma scintigraphy. During the past decade the InteliSite® capsule has been utilized by several pharmaceutical laboratories; typical applications are described by Phitavala et al. (1998), Parr et al. (1999), and Clear et al. (2001). The number of studies performed with this capsule type, however, is not known, mainly due to the fact that most of these investigations are likely not yet published.

The Enterion™ Capsule

The most recent state of development is represented by a capsule type published for the first time by Houzego et al. (2001) and known as the "Enterion™ capsule" (Fig. 4.15D). A detailed description of this capsule is provided by Wilding et al. (2000), including a first report on the pharmacokinetic data obtained. As in the case of InteliSite®, the position is determined by using the radiation of a radionuclide contained in a special port inside the capsule, and detected by means of gamma scintigraphy. One important advantage over the InteliSite® is in the lower frequency (1.8 MHz) of the triggering AC magnetic field, which results in a smaller energy absorption by the tissue and consequently a greater reliability of activation in deeper body regions. The simpler construction of the Enterion™ is a reason for both a clearly smaller percentage of failures during operation, as well as

Table 4.2. Features of the capsule types shown in Figure 4.15.

Features	Type of capsule					
	Eriksen	**Hemmati**	**Lambert et al.**	**RF-capsule**	**InteliSite®**	**Enterion™**
Mechanism[a)]	Eddy current	Eddy current	Magnetic switch	Fuse thread	Memory metal	Fuse filament
Frequency[b)] (MHz)	0.5	1.5	0 (?)	27	6.78	1.8
Agent volume (mL)	0.4	0.3	1.0	0.8	0.8	1.0
Agent release[c)]	Active	Active	Active	Passive	Passive	Active
Detection method	Swallowed thread	X-ray	Mileage indicator	X-ray	Scintigraphy	Scintigraphy
Examinations	≥7 (dogs)	40	>130	>200	?	>950

[a)] For detailed descriptions, see the text.
[b)] Frequency of the AC magnetic field triggering the release mechanism.
[c)] "Active" indicates that the agent is pushed out of the capsule; "passive" describes release without additional pressure.

a greater volume (1.0 mL) of transported agents. In a recent communication by the company producing Enterion™, the number of studies was stated as greater than 35, and the number of swallowed capsules as over 950 (www.pharmprofiles, 2004).

4.3.3.2 Outlook

The development of RCDT systems clearly shows how problems such as a small volume of the agent container, sophisticated construction, exposure to X-ray radiation, and low reliability are being addressed and overcome in a step-by-step fashion. Today, investigations of site-specific absorption can be performed in a near-perfect manner. However, examinations with these engineered capsules are rather expensive, with a typical capsule costing about US$ 1000, and the method used to determine the capsule position in the body (scintigraphy) adding further to the cost. Moreover, only skilled personnel are able to carry out the investigations, which must be approved by an independent ethics committee. The number and location of hospitals capable of complying with these conditions is currently restricted.

One serious obstacle in the path of any improvement in this situation is the current methods available to detect the actual capsule position. The presently utilized

radiotracer method should be replaced by another which operates without ionizing radiation. Such a possibility exists if the recently developed method of magnetic marker monitoring (see Section 4.2) were to be combined with remote-controlled drug release.

In order to solve the second of the problems listed above – namely drug targeting – the RCDT system must be developed to a state where not only the costs are drastically reduced but also the application is much easier. Only then would this approach be suitable for drug targeting in hospitals of the middle range, and ultimately in the doctors' practices. However, taking into account the progress made during the past few years, there is a realistic chance that even this ambitious goal will be reached.

Acknowledgments

The authors thank Werner Lehmann for providing much of the cited literature, and Lydia Cartar and Urs Häfeli for their critical reading of the manuscript.

References

Andrä, W. and Wendt, M. (2000). Marker für eine Darm-Diagnostik und Darm-Therapie. *German Patent*, DE 197 45 890 C1.

Andrä, W., Bierlich, J., Danan, H., and Bellemann, M.E. (2002). Remote controlled drug release in the alimentary tract by local power deposition in alternating magnetic fields. *Biomed. Tech.*, **47** (Suppl. 1), 736–737.

Andrä, W., Bellemann, M.E., Danan, H., and Schmieg, R. (2004). Anordnung zur ferngesteuerten Freisetzung von Wirkstoffen. *German Patent*, DE 103 10 825 B3.

Andrä, W., Bellemann, M.E., Danan, H., Dutz, S., Liebisch, S., and Schmieg, R. (2006). *International Patent Application*, WO 2006/005287 A2.

Briede, O. (1913). Packung für Heilmittel, insbesondere radioaktive Substanzen. *German Patent*, 281869.

Casper, R.A., McCartney, M.L., Jochem, W.J., and Parr, A.F. (1992a). Medical capsule device actuated by radio-frequency (RF) signal. *US Patent*, 5,167,626.

Casper, R.A., McCartney, M.L., Jochem, W.J., and Parr, A.F. (1992b). Medical capsule device actuated by radio-frequency (RF) signal. *US Patent*, 5,170,801.

Clear, N.J., Milton, A., Humphrey, M., Henry, B.T., Wulff, M., Nichols, D.J., Anziano, R.J., and Wilding, I. (2001). Evaluation of the InteliSite capsule to deliver theophylline and frusemide tablets to the small intestine and colon. *Eur. J. Pharm. Sci.*, **13**, 374–384.

Danco, I. (2002). *Entwicklung von neuen Konzepten und Darreichungsformen zur Freisetzung von Wirkstoffen im Dickdarm (Colon-Targeting)*. Thesis, **18**, IPT-Verlag Münster.

Dutz, S., Andrä, W., Bierlich, J., Danan, H., Liebisch, S., and Bellemann, M.E. (2003). New in-vitro results of remote controlled drug release in the gastrointestinal tract. *Biomed. Tech.*, **48** (Suppl. 1), 206–207.

Dutz, S., Andrä, W., Danan, H., Leopold, C.S., Werner, C., Steinke, F., and Bellemann, M.E. (2005). Remote controlled drug delivery to the gastrointestinal tract: investigation of release profiles. *Biomed. Tech.*, **50** (Suppl. 1), 601–602.

Eriksen, S.P., Swintowsky, J.V., Serfass, E.J., Lin, T.H., Abrams, J., and Sturtevant, F.M. (1961). Equipment and methodology for relating gastrointestinal absorption to site of drug release. *J. Pharm. Sci.*, **50**, 151–156.

Gardner, D., Casper, R., Leith, F., and Wilding, I. (1997). Noninvasive method-

ology for assessing regional drug absorption from the gastrointestinal tract. *Pharm. Tech. Europe*, **21**, 82–89.

Gröning, R. (1997). Computer-controlled drug release from small-sized dosage forms. *J. Controlled Release*, **48**, 185–193.

Gröning, R. and Weyel, S. (1993). Electronically controlled release of drugs from capsules. *Eur. J. Pharm. Biopharm.*, **39**, 102–104.

Gröning, R. and Berntgen, M. (1996). Estimation of the gastric residence time of magnetic dosage forms using the Heidelberg capsule. *Pharmazie*, **51**, 328–331.

Gröning, R., Werner, M., Berntgen, M., and Georgarakis, M. (1996). Peroral controlled release dosage forms with internal magnets and extracorporal magnetic guidance – Investigations into the renal elimination of riboflavin. *Eur. J. Pharm. Biopharm.*, **42**, 25–28.

Hemmati, A. (1968). Die Bestimmung des Resorptionsortes von Eisen im Intestinalkanal mit einer fergesteuerten Darmkapsel. *Dtsch. Med. Wochenschr.*, **93**, 1468–1472.

Honda, M., Matsui, K., Kohri, K., Misawa, K., and Kambara, K. (1984). Medical capsule device. *US Patent*, 4,439,197.

Hosoya, T., Tanaka, F., and Nogichi, K. (1980). Capsule for medical use. *US Patent*, 4,239,040.

Houzego, P.J., Westland, D.J., Morgan, P.N., Wilding, I.R., and Hirst, P.H. (2001). An ingestible device. *International Patent Application* WO 01/45789 A2.

Hugemann, B. and Schuster, O. (1982). Vorrichtung zur Freisetzung von Substanzen an definierten Orten des Verdauungstraktes. *German Patent*, DE 29 28 477 C3.

Hugemann, B. and Schuster, O. (1984). Device for the release of substances at defined locations in the alimentary tract. *US Patent*, 4,425,117.

Kambara, K., Misawa, K., Honda, M., Matsui, K., and Kohri, K. (1985). Medical capsule device. *US Patent*, 4,507,115.

Knauft, S., Andrä, W., Werner, C., and Bellemann, M.E. (2004). Remote controlled release of agents by friction losses of a rotating permanent magnetic sphere in a viscous medium. *Biomed. Tech.*, **49** (Suppl. 2), 724–725.

Kuhlmann, E. (2001). *Entwicklung neuer magnetgesteuerter Depotarzneiformen mit verlängerter Magenverweilzeit*. Thesis **7**, IPT-Verlag Münster.

Lambert, A., Vaxman, F., Crenner, F., Wittmann, T., and Grenier, J.F. (1991). Autonomous telemetric capsule to explore the small bowel. *Med. Biol. Eng. Comput.*, **29**, 191–196.

Leopold, C.S. (2001). A practical approach in the design of colon-specific drug delivery systems. In: Molema, G. and Meijer, D.K.F. (Eds.), *Drug Targeting: Organ-Specific Strategies*, Wiley-VCH, Weinheim, pp. 157–170.

Liebisch, S., Andrä, W., Danan, H., Dutz, S., and Bellemann, M.E. (2004). Remote controlled release of agents by hysteresis losses of magnetic powders in alternating magnetic fields. *Biomed. Tech.*, **49** (Suppl. 2), 716–717.

Lin, T.H., Guarini, J.R., Eriksen, S.P., and Swintosky, J.V. (1964). Effect of site on the absorption of trimepazine-S^{35} and penicillin G in dogs. *J. Pharm. Sci.*, **53**, 1357–1359.

Merrill, E.W. (1972). Magnetically operated capsule for administering drugs. *US Patent*, 3,659,600.

Minakawa, S. and Henmi, H. (1992). Thermoelement for treatment of cancer. *European Patent Application*, 0 543 498 A1.

Nakago, G. (1987). Magnetic-force leadable capsule. *Japanese Patent*, 62161721 A.

Neusel, R. (1996). Verfahren und Anordnung zur Ansammlung und/oder Festhaltung von Wirkstoffen mittels magnetischer Kraft im lebenden Körper oder in äußeren Umwegleitungen. *German Patent*, DE 195 01 714 A1.

Parr, A.F., Sandefer, E.P., Wissel, P., McCartney, M., McClain, C., Ryo, U.Y., and Digenis, G.A. (1999). Evaluation of the feasibility and use of a prototype remote drug delivery capsule (RDDC) for non-invasive regional drug absorption studies in the GI tract of man and beagle dog. *Pharm. Res.*, **16**, 266–271.

Phitavala, Y.K., Heizer, W.D., Parr, A.F., O'Connor-Semmes, R.L., and Brouwer, K.L.R. (1998). Use of the InteliSite® capsule to study ranitidine absorption from various sites within the human intestinal tract. *Pharm. Res.*, **15**, 1869–1875.

Richert, H. (2004). Vorrichtung und Verfahren zum Freisetzen oder zur Entnahme von Substanzen an bzw. von unzugänglichen Stellen. *German Patent Application*, DE 103 02 614 A1.

Richert, H., Surzhenko, O., Wangemann, S., Hocke, M., and Görnert, P. (2004). Magnetische Kapselöffnung zur gezielten Wirkstofffreisetzung. *Biomed. Tech.*, **49** (Suppl. 2), 160–161.

Richert, H., Surzhenko, O., Wangemann, S., Heinrich, J., and Görnert, P. (2005). Development of a magnetic capsule as a release system for future applications in the human GI tract. *J. Magnet. Magnet. Mater.*, **293**, 497–500.

Schentag, J.J. and D'Andrea, D.T. (1994). Telemetry capsule and process. *US Patent*, 5,279,607.

Sekiguchi, Y. (1982). Capsule. *Japanese Patent*, 58135808 A.

Shioda, M., Ishita, K., and Kubo, T. (1980). Magnetic drug. *Japanese Patent*, 55011554 A.

Sinaiko, R.J. (1994). Externally controlled intestinal content sampler. *US Patent*, 5,316,015.

Staib, A. and Fuhr, U. (1995). Drug absorption differences along the gastrointestinal tract in man: detection and relevance for the development of new drug formulations. *Eur. J. Clin. Pharmacol.*, **12**, 34–56.

Staib, A.H., Loew, D., Harder, S., Graul, E.H., and Pfab, R. (1986). Measurement of theophylline absorption from different regions of the gastrointestinal tract using a remote controlled drug delivery device. *Eur. J. Clin. Pharmacol.*, **30**, 691–697.

Steinberg, W.H., Mina, F.A., Pick, P.G., and Frey, G.H. (1965). Heidelberg capsule I. In vitro evaluation of a new instrument for measuring intragastric pH. *J. Pharm. Sci.*, **54**, 772–776.

Vaxman, F., Lambert, A., Wittmann, T., and Grenier, J.F. (1995). The intestinal capsule: a new way of investigating the small intestine. *Ann. Chir.*, **49**, 180–186.

Werner, M. and Gröning, R. (1994). Magnetische Depotarzneimittel für die perorale Applikation mit verbesserter Resorption der Wirkstoffe. *German Patent Application*, DE 44 06 139 A1.

Wilding, I.R. and Prior, D.V. (2003). Remote controlled capsules in human drug absorption (HDA) studies. *Crit. Rev. Ther. Drug Carrier Syst.*, **20**, 405–431.

Wilding, I., Hirst, P., and Connor, A. (2000). Development of a new engineering-based capsule for human drug absorption studies. *Pharm. Sci. Technol. Today*, **3**, 385–392.

www.pharmprofiles.co.uk/faqhda.htm, 18.02.2004.

Yokoi, T., Mizuno, H., Uchiyama, A., Matsui, Y., and Okada, H. (2003). Capsule type medical treatment device. *Japanese Patent*, 2003325438 A.

4.4
Magnetic Stimulation

Shoogo Ueno and Minoru Fujiki

4.4.1
Introduction

Magnetic nerve stimulation, which has been studied for over a century, was first reported for the human brain by Barker et al. (1985). Since that time, significant advances have continued to be made, and today magnetic nerve stimulation is used widely both in neurophysiological studies and for clinical diagnoses. Recently, a method of focal and vectorial stimulation of the human brain was developed. This section provides an overview of the early attempts at, and more recent developments in, transcranial magnetic stimulation (TMS), together with details of the present status of the technique. After introducing the historical, technical and physiological principles and basic mechanisms of the method, a representative case of the use of TMS is described. There then follows a discussion of how human cortical function can be modified by magnetic stimulation, and how this might be used therapeutically in neurological disorders.

4.4.2
History

4.4.2.1
History of Magnetic Stimulation

During the past century, several investigational groups have studied the magnetic stimulation of excitable tissue (D'Arsonval, 1896; Bickford and Fremming, 1965; Irwin et al., 1970; Oberg, 1973; Ueno et al., 1978, 1984, 1986; Cohen, 1985).

In 1970, Maass and Asa proposed a transformer type of stimulation, in which a nerve bundle was threaded through a core as the secondary winding. These authors showed that the flux change in the core could be used to excite nerves. Later, Oberg (1973) proposed an air gap type of stimulation, in which a bundle of nerves was exposed to alternating magnetic fields. These studies demonstrated experimentally that induced eddy currents in the membrane tissues could be expected

to stimulate nerves, though the underlying nerve-excitation processes from magnetic stimulation were not understood (Ueno et al., 1978).

A number of experiments were carried out to measure action potentials of lobster giant axons under time-varying magnetic fields (Ueno et al., 1981, 1986). The axon membrane was excited by galvanic stimulation, and the action potential recorded intercellularly with microelectrodes. During propagation of the action potential along the axon, alternating or pulsed magnetic fields were applied across the middle of the axon to study whether magnetic fields have any effect on parameters such as the conduction velocity and refractory period of the nerve fiber and the amplitude, duration and shape of action potentials.

The results obtained from the lobster experiments suggested that nerve excitation by magnetic field influence are mediated via the induction of eddy current in the tissue surrounding the nerve. The induced current density depends on geometrical factors as well as the resistivity of the tissue in which the current flows. For nerve excitation, the microscopic eddy currents that flow inside the microstructures of the axon membrane are not very important. More important are the macroscopic eddy currents that flow along the nerve axon and in the tissues surrounding the nerve, as they contribute to the depolarization of the membrane.

After the study of single nerve axons, a new type of magnetic nerve stimulation was proposed (Ueno et al., 1984). An insulated magnetic core was implanted in the body with a nerve bundle positioned on the core aperture. The nerve could be stimulated by the eddy currents that flowed in the body fluids around the core when the magnetic flux in the core was changed. No interlinkage existed between the core and the nerves, and therefore this was deemed to be a good method for verifying that the nervous system responds to time-varying magnetic fields via eddy currents induced in the body.

4.4.2.2
The Beginnings of Magnetic Brain Stimulation

Magnetic stimulation of the human brain was first reported by Barker and colleagues during the mid-1980s (Barker et al., 1985, 1986, 1987). Parameters of muscular potentials, such as conduction velocity, latency and amplitude, were studied by several groups by recording the electromyographic (EMG) responses to stimulation of the motor cortex (Hess et al., 1986; Day et al., 1987; Mills et al., 1992; Rothwell et al., 1987; Rothwell, 1994; Amassian et al., 1989, 1992; Reilly, 1989; Cohen et al., 1990; Maccabee et al., 1990, 1993; Olney et al., 1990; Roth and Basser, 1990; Basser and Roth, 1991; Grandori and Ravazzanu, 1991; Esselle and Stuchly, 1992; Nilsson et al., 1992; Nagarajan and Durand, 1993). In these studies, current pulses were passed through a single coil placed outside the head; eddy currents induced in the head by pulsed magnetic fields stimulated the brain. With this method, broad areas of the brain were stimulated simultaneously. A method of localized magnetic stimulation of the human cortex was also developed by Ueno and colleagues (Ueno et al., 1988, 1990a,b).

The aim was to concentrate induced eddy currents in the vicinity of a target using a pair of opposing pulsed magnetic fields produced by a figure-of-eight coil. Using this method, specific areas of the motor cortex of the human were stimulated within a 5-mm resolution (Ueno et al., 1989a,b). Since the concentrated eddy currents beneath the intersection of the figure-of-eight coil flow in a direction parallel to the tangent of both circular coils, vectorial stimulation can be achieved. The neural fibers can be excited easily when stimulated by the eddy currents that flow parallel to the nerve fibers.

Exploiting this principle, functional maps related to the hand and foot areas were obtained (Ueno et al., 1989c, 1990a,b). It was observed that an optimal direction of stimulating currents for neural excitation exists in each functional area in the cortex. It was also observed that functional maps of the cortex vary with the orientation of the stimulating current. In order to explain the mechanism responsible for producing this anisotropic response to brain stimulation, a model of neural excitation elicited by magnetic stimulation was developed (Ueno et al., 1991). Moreover, a model was developed to examine how the threshold for nerve excitation changes with depth and length of nerve fibers and the bending angle of the axon (Hyodo and Ueno, 1996).

4.4.3
Principle of Transcranial Magnetic Stimulation

4.4.3.1
Vectorial and Localized Magnetic Stimulation: A Computer Simulation Study

Figures 4.16A and B illustrate the principle of localized stimulation of the brain (Ueno et al., 1988). The basic idea is to concentrate induced eddy currents in the

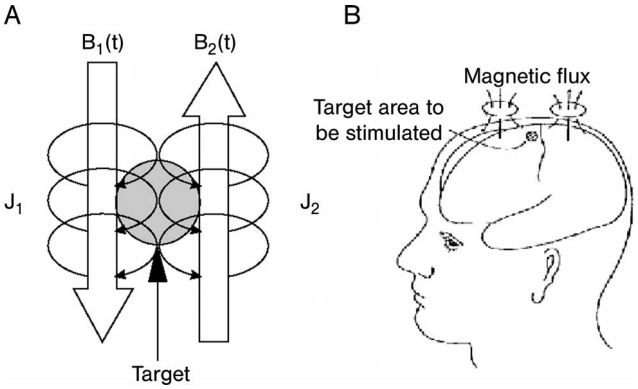

Fig. 4.16. (A) Principle of localized stimulation. Magnetic fields B1(t) and B2(t) are applied in opposite directions close to the target area. (B) A pair of coils is placed outside the head so that the magnetic fields enter the head in opposite directions around the target.

target area by a pair of time-varying magnetic fields. A pair of coils is positioned outside the head so that the time-varying magnetic fields, B1(t) and B2(t), enter the head in opposite directions close to the target. The induced eddy currents, J1 and J2, are expected to flow together. This convergence of eddy currents acts to raise the current densities in the target area, where depolarization of neural tissues can be caused.

This method is a different application of the same principle that was previously proposed to heat brain tumors (Ueno et al., 1985, 1987). To calculate the distributions of eddy currents, the human head is modeled by a quasi-spherical conductor of a dimension 12.0 units in diameter with a uniform conductivity. In fact, one unit corresponds to about 1 cm. The surface of the sphere is made up of 58 planes (see Fig. 4.17A), divided into 5504 small elements of a tetrahedron. The distribution of eddy currents in the conductor can be calculated using a finite element method. Distributions of eddy currents in a cross-section of the X–Y plane produced by a pair of one-turn coils are shown in Figures 4.17B and C. The coils are positioned at a distance of 1.0 unit from the surface.

A pair of coils of a dimension 2.0 units in diameter is positioned outside the head at $X = 0.0$, $Y = +2.0$ or -2.0, and $Z = 6.0$ units. These coils generate magnetic

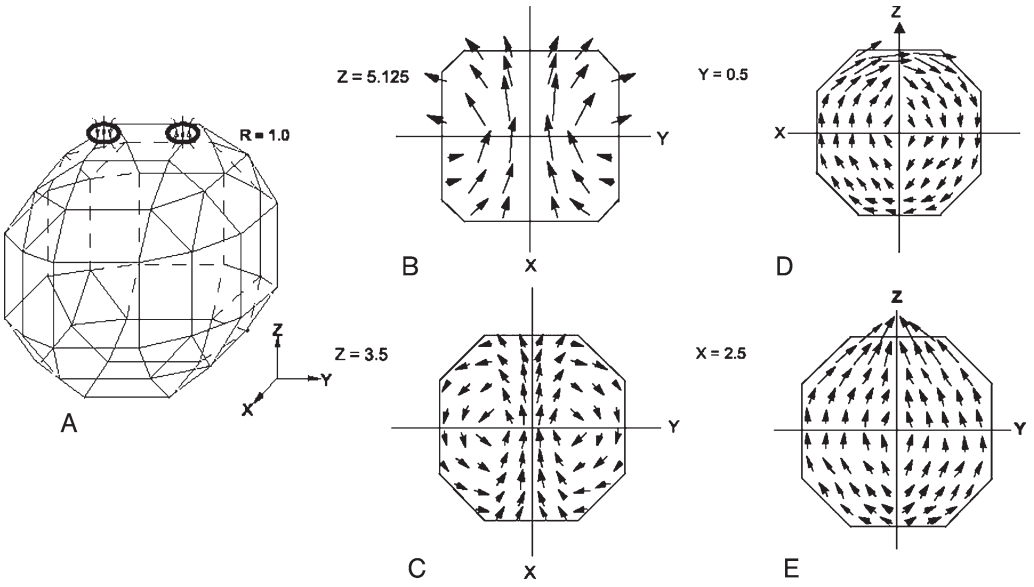

Fig. 4.17. Computer simulation study for induced eddy current. (A) A quasi-spherical volume conductor and paired-coil configuration. (B,C) Distributions of eddy currents flowing in a cross section of the X–Y plane produced by a pair of one-turn coils. (D,E) Distributions of eddy currents in a cross-section of (D) the X–Z plane and (E) the Y–Z plane as produced by a pair of one-turn coils.

fields in opposite directions when the currents are applied to the coils in opposite directions.

The calculated results are shown in Figures 4.17B and C and d,e. Figure 4.17B and C shows/current distributions induced in cross-sections at Z = 5.125 and 3.5 units. The current vectors form two vortices which flow together at the target between coils, so that eddy currents are concentrated in the target area. Figure 4.17D and E shows current distributions induced in an X–Z cross-section at Y = 0.5 units, and a Y–Z cross-section at X = 2.5 units. The current density decreases with the increase in depth from the surface. Clearly, the current density is higher at the target near the surface of the head.

The effect of distance between coils on the current density induced at the target was investigated. For simplicity, a cubical model of dimension 10.0 units on a side with a uniform conductivity is used for this study, as shown in Figure 4.18A. A pair of coils of dimension 2.0 units in diameter is positioned at X = 0.0, Y = +2.0 or −2.0, and Z = 6.0 units. Spatial distributions of eddy currents induced in an X–Y cross-section at Z = 4.5 units are shown in Figure 4.18B. The eddy currents flow together along the X-axis. Let us calculate the amplitude of eddy current densities on the Y-axis in Figure 4.18B, assuming that the resistivity = 1/sigma = 3 ohm·m, we obtain a current amplitude in the one-turn coils of $I = 1.0$ kA, frequency $f = 1.0$ kHz, and 1 unit = 0.01 m.

The results are shown in Figure 4.18C. The eddy current density at the target between the two coils, marked with a hatched pattern, generates a peak that is two- to three-fold higher than that of the current densities at nontarget regions. The ratio of the peak value at the target to the values at the nontargets increases with a decrease in the distance between the coils, with the ratio being highest when the coil distance is zero.

Current distributions in a three-dimensional head model are shown in Figure 4.19 (Sekino and Ueno, 2004). A three-dimensional human head model obtained from the Brooks Air Force Laboratory (Texas, USA) was used, and the numbers of nodes and elements were 81 192 and 74 369, respectively. A figure-of-eight coil consisted of a pair of circular coils with a diameter of 75 mm (see Fig. 4.19A). TMS was applied with a biphasic waveform with a pulse width of 240 μs. Calculations were performed using commercial software (PHOTO-Series developed by PHOTON Co., Ltd.) based on the finite element method.

The current distributions in TMS are shown in Figures 4.19B–D. The brain surface under the intersection of the coil exhibited high current density values, with a maximum current density within the brain of 82 A m^{-2}. Because the model had a homogeneous magnetic permeability, the magnetic fields were not disturbed by tissues, and efficiently induced eddy currents in the brain. The scalp under the coil exhibited the maximum current density of 158 A m^{-2}. The magnetic field generated by the coil attenuated with an increase of distance from the coil. The eddy current density exhibited higher values on the surface and gradually decreased with depth from the surface. Current densities at the center of the brain were below 10 A m^{-2}. Coils with smaller diameters induced more localized eddy currents and exhibited more significant attenuation in deep regions.

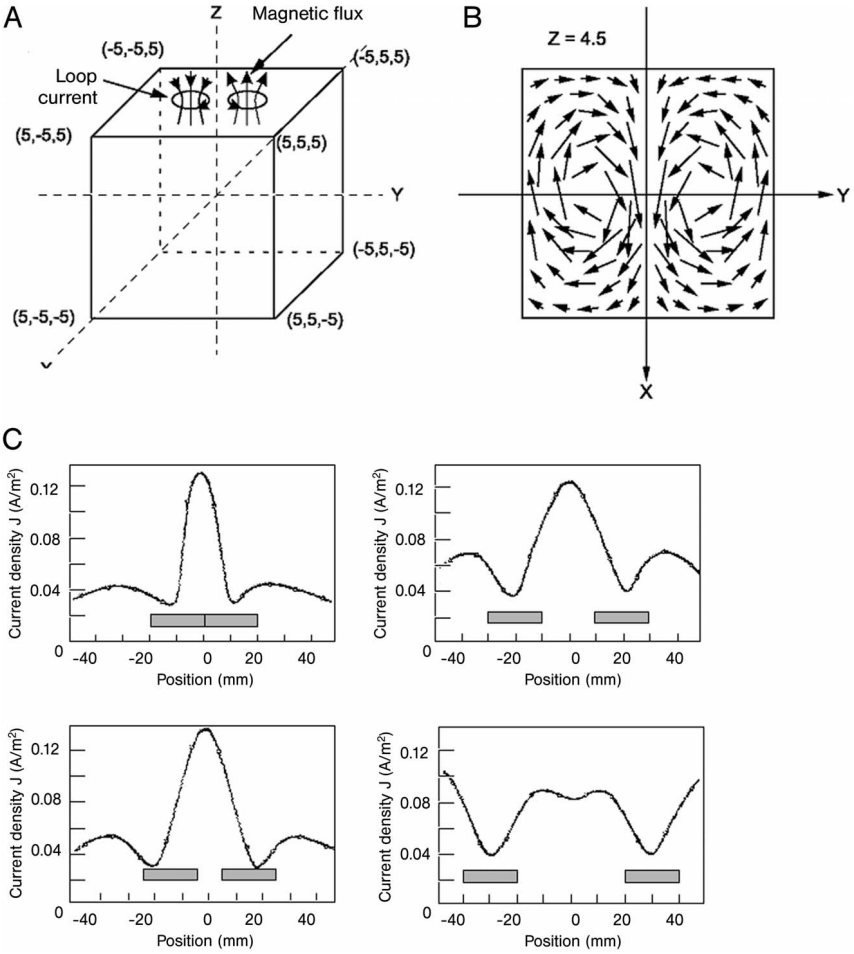

Fig. 4.18. (A) Cubical model and paired coil configuration. (B) Distributions of eddy currents in a cross-section of the X–Y plane produced by a pair of one-turn coils. Coils are positioned at a distance of 1.0 unit from the surface. (C) Changes of current density with the distance between coils.

4.4.3.2

Physiological Principle

The magnetic field in TMS is generated by passing a sub-millisecond high-current pulse through an insulated coil held above the scalp (Barker et al., 1985, 1986, 1987). The magnetically induced current (also termed the "eddy current") flows in the opposite direction with respect to the current in the coil. The induced eddy current – not the magnetic field itself – can depolarize neurons under the coil edge (not at the center of the coil) since the eddy current strength is maximal under the

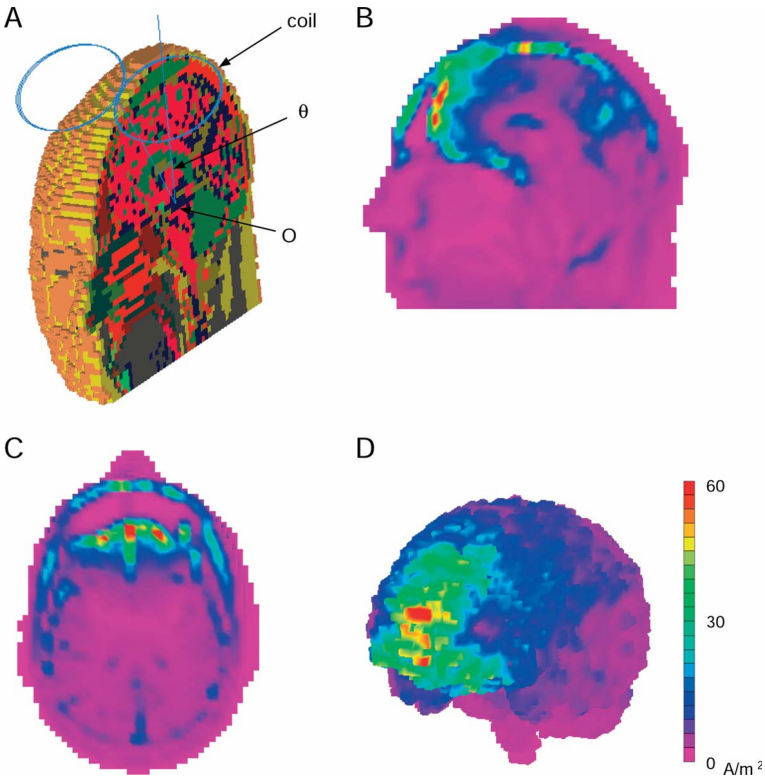

Fig. 4.19. (A) Numerical model of TMS to the human head. (B–D) Current distributions in TMS represented in sagittal and transversal slices, and the brain surface.

coil windings. The figure-of-eight coil provides focal stimuli at the center of the connection of the two coils (Amassian et al., 1989), where the currents of the two windings of the coil flow in the same direction. Electrical stimulation directly activates pyramidal neurons that cause direct (D) and followed by indirect (I) waves in the spinal dissenting volleys (Amassian et al., 1989). TMS is believed preferentially to stimulate interneurons which cause activation of motor neurons (Rothwell et al., 1987; Rothwell, 1994).

4.4.3.3 Functional Mapping of the Human Motor Cortex

Two types of coils are generally used: the round coil stimulates the perimeter of a large circular area, while the figure-of-eight coil has a more focused activation pattern. However, the single round coil is still useful for screening purposes or intraoperative monitoring (Fig. 4.20).

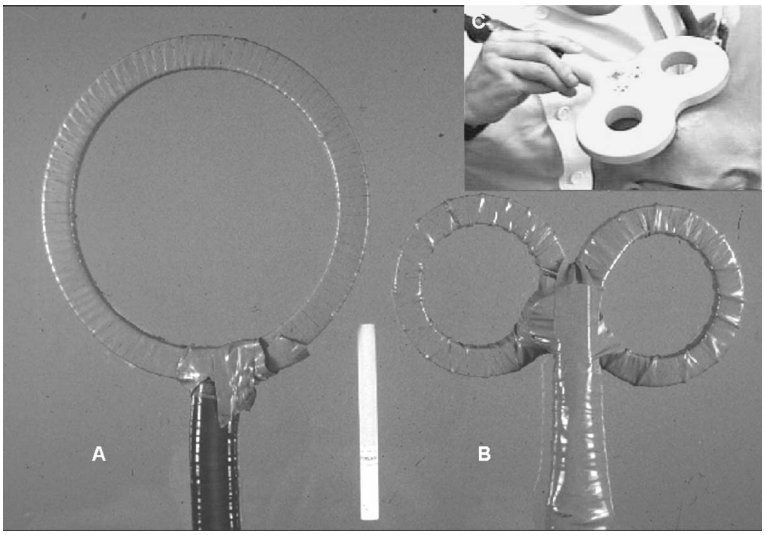

Fig. 4.20. Comparison of single round coil (A) and figure-of-eight-coil (B). (C) Illustrative clinical use for preoperative functional mapping.

TMS with a focal figure-of-eight coil can reveal the functional organization of the motor cortices. Traditionally, stimuli are applied at various scalp positions using a latitude/longitude-based coordinate system referenced to Cz in the 10–20 international system at the vertex while the amplitude of motor evoked potentials (MEPs) evoked in contralateral muscles is measured (Amassian et al., 1989; Ueno et al., 1989a,b,c, 1990a,b). This provides a ''map'' of sites on the scalp from which responses can be obtained in each target muscle (Fig. 4.21A).

The important parameters of such maps are the locations evoking the maximal responses, stimulus intensities, stimulus current directions and the degree of the voluntary target muscle contraction. The locations eliciting the maximal response of leg muscles and from proximal to distal muscles of the upper extremity usually line up in a medial to lateral direction along the central sulcus, suggesting that they provide a good estimate of the site of the most excitable region of the underlying corticospinal projection (Fig. 4.21D). The stimulus intensity is important because the weaker the intensity of the TMS stimulus, the smaller the area of the cortex where the induced current exceeds the activation threshold. Even with relatively weak stimulus intensities, however, TMS is considerably less focal than stimulation via electrodes placed on the cortical surface.

The clearest and most robust activation of hand muscles is obtained by induced eddy current direction perpendicular to the central sulcus; parallel with the initial part of the underlying corticospinal fiber projection (Fig. 4.21B). The excitability of the corticospinal projection is remarkably increased when the target muscle is under contraction (Fig. 4.21C). There is much variability in motor cortex excitability

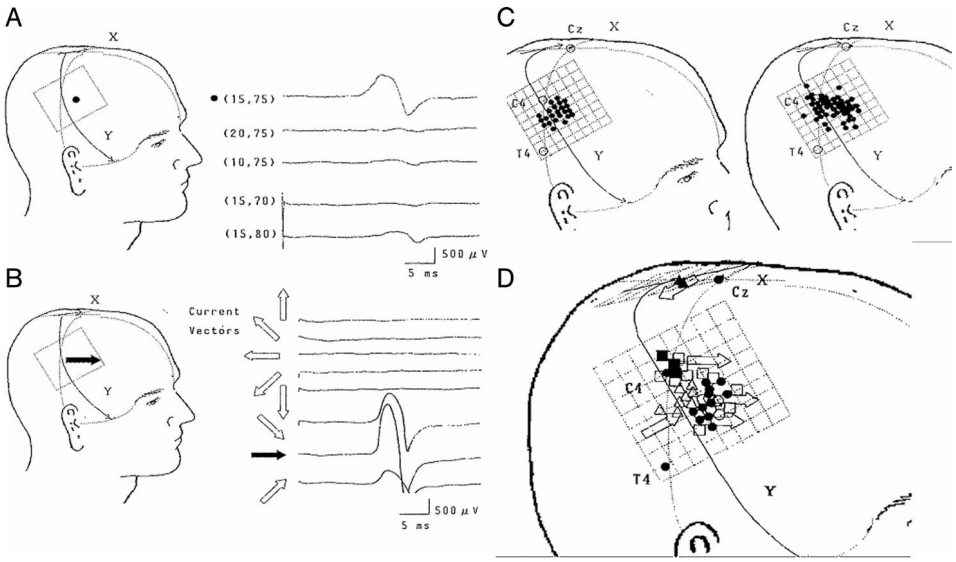

Fig. 4.21. Basic mechanisms of TMS for motor cortical mapping. (A) Stimulus resolution. Definite target abductor pollicis brevis (APB) muscle motor evoked potentials (MEP) was obtained after magnetic stimulation of the target point at $x = 15$ mm, $y = 75$ mm, whereas a marked reduction of the amplitude or no response was obtained by stimulation of points 5 mm anterior, posterior, lateral and medial to the target point. (B) Optimal current directions in order to evoke MEP from the APB muscle in one subject. The highest-amplitude MEP was obtained by currents in the posterior to anterior (P–A) direction. (C) Functional maps for the APB muscle with 5% (left) and 10% (right) of the maximal voluntary contraction of the muscle. During the contraction, the target muscles could be influenced from remarkably enlarged cortical areas. (D) Functional distribution of the six target muscles in the motor cortex at suprathreshold TMS intensity. The optimal current directions for each target muscle are shown by the white arrows. The excited areas for the five hand muscles were spatially overlapping. ● abductor pollicis brevis (APB); ○ first dorsalis interosseus (FDI); △ abductor digiti minimi (ADM); □ brachioradial (BR); ■ biceps brachii (BB); ▲ tibialis anterior (TA).

among the patients when the muscle is relaxed. Voluntary contraction presumably normalizes the levels of excitability in connected/adjacent neuronal populations so that differences between subjects caused by subthreshold levels of excitability are reduced.

Some studies that demonstrate changes in the MEP map area during contraction (Ueno et al., 1989a,b,c) probably reflect changes in the moment-to-moment cortical functional connectivity, as well as in the sensory feedback and in direct spinal activation. With a high grade of muscle contraction, the excitability is much higher and the motor area capable of causing muscle contraction much larger than at rest. It is not only cortical excitability that must be defined: the area of MEP maps also depends on the excitability of spinal mechanisms. In this regard, it is important to seek the location evoking maximal response of the target muscle under the correct conditions. It is important to use an optimal intensity (ca. 120% of the rest-

ing motor threshold; variable for each application), optimal stimulus current direction (P–A direction for hand muscles), and well-controlled muscle contraction. Again, this procedure promises to become much faster and more reliable with the direct navigation and visualization of the induced activating electric field within the brain.

4.4.3.4
Inhibition–Excitation Balance

Studies of cortical functions can also be carried out with TMS by using other measures. For example, the intracortical inhibitory and facilitatory interneuronal effect of conditioning subthreshold stimuli can be studied by using two connected or isolated stimulators (Ugawa, 1999). The preceded first subthreshold stimulus interferes with the second test stimulus, with various inter-stimulus intervals. The effect is dependent on the inter-stimulus interval causing inhibition and facilitation (Fig. 4.22). Ziemann et al. (1995, 1996a,b) have used centrally acting drugs to show that the initial period of inhibition (with 2–5 ms of inter-stimulus interval) is caused by gamma-aminobutyric acid (GABA), probably due to activity in the $GABA_A$ system.

TMS is capable of interfering with the normal pattern of neuronal activity during perception, motor execution, or higher-level cognitive processes. The recent development of rapid-rate magnetic stimulation (repetitive TMS; rTMS) has made it possible to perform noninvasive repetitive brain stimulation for neurophysiological investigations of disorders such as epilepsy, which have a direct influence on the excitation–inhibition balance.

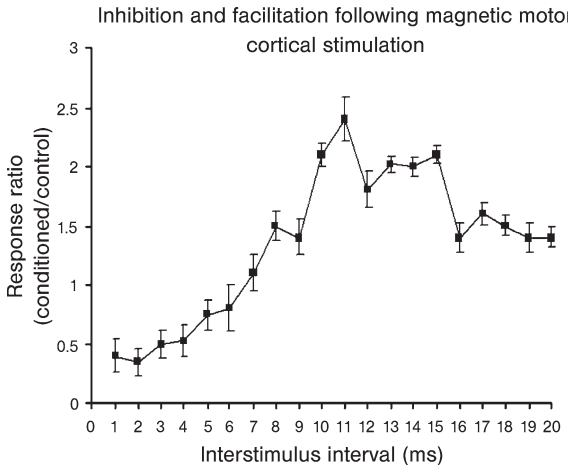

Fig. 4.22. Motor evoked potential changes in different conditioning stimuli–test stimuli inter stimulus intervals (ISIs). Intracortical inhibition in early ISIs and intracortical facilitation in late ISIs are useful for evaluation of the neural networks.

4.4.4
Clinical and Preclinical Application of TMS

4.4.4.1
Targeting Method

Recent advances in navigated brain stimulation (NBS) stereotactic TMS devices will allow noninvasive mapping of the spatial and temporal representation of any brain activity that reacts to magnetic stimuli (Krings et al., 1997, 2001a,b), including sensory, motor, language, and cognitive functions (Fig. 4.23). Stereotactic TMS coil positioning and real-time visualization of the stimulating electromagnetic field on individual magnetic resonance imaging (MRI) allow precise replicability of stimulation parameters as well as accurate dose definition (Ilmoniemi et al., 1999; Ruohonen and Ilmoniemi, 1999; Gugino et al., 2001). Frameless NBS allows the precise determination of a stimulation target (pink dot) from other imaging modalities or according to anatomical landmarks (Fig. 4.23).

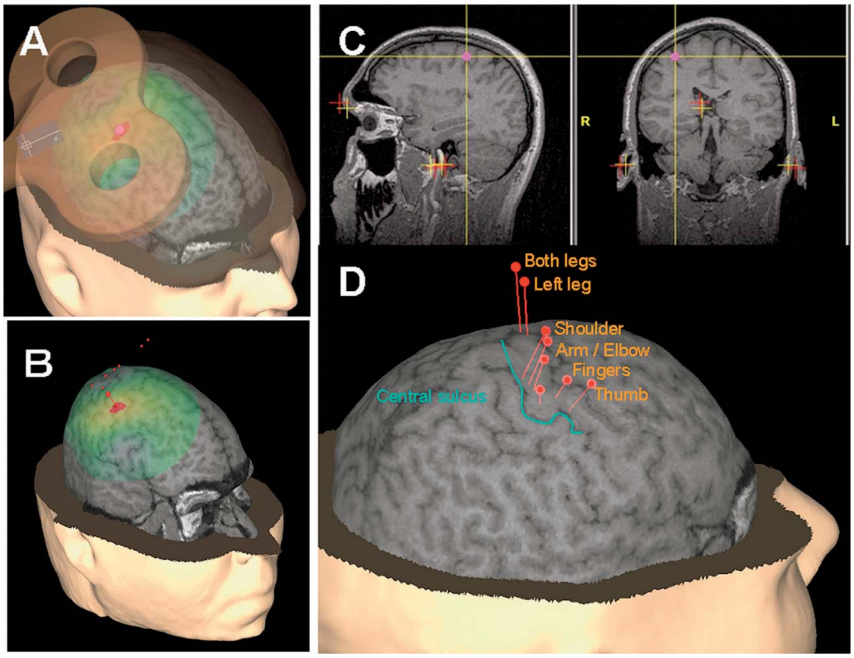

Fig. 4.23. Representative demonstration of navigated brain stimulation (NBS) for human brain mapping. (A,B) The stimulation area is reached by utilizing on-line, interactive interface which guides the stimulation coil to the target. The maximum electric field induced in the brain is visualized (red area) and the strength of the field, ''dose'' in the target determined. (C) NBS allows precise determination of a stimulation target (pink dot) from other imaging modalities or according to anatomical landmarks. (D) Reliable map of motor areas can be reached by recording the muscle responses to stimulation.

4.4.4.2
Representative Neurosurgical Case

A right-handed, 36-year-old man suffered from incomplete left hemiparesis manual muscle test (MMT) scoring 2 on the upper extremities, caused by a metastatic urachal carcinoma of the right premotor area, adjacent to the precentral gyrus. MRI indicated an irregular high and low mixed intensity mass at right frontal premotor area (Fig. 4.24A). The motor strip was identified by preoperative MRI, functional MRI (fMRI) and TMS results that were integrated on the navigation system (Fig. 4.24B). Distribution of the tumor margin and the motor cortex (both fMRI and TMS) can be drawn on the patient's scalp using the navigation system (Fig. 4.24C,D). Skin incision, craniotomy and operative approaches were considered from these results so as to avoid motor deterioration.

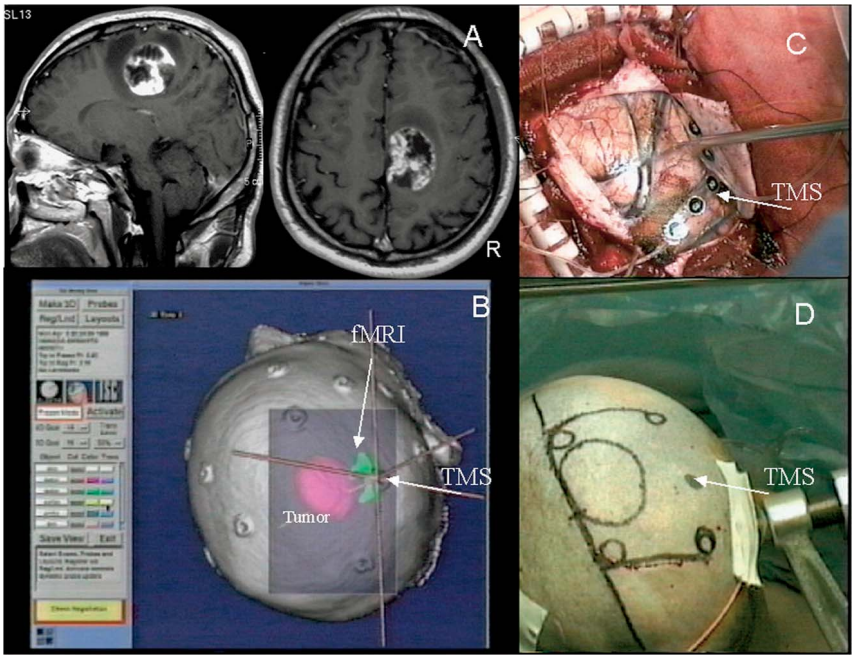

Fig. 4.24. Representative neurosurgical use of TMS in a case with metastatic brain tumor. (A) Magnetic resonance imaging (MRI) showed irregular high and low mixed intensity lesion at a right frontal premotor subcortical region. (B) Identified motor cortex by TMS (round landmark indicated under the cursor) and functional MRI (fMRI) (green area; activated by mimicking the movement elicited by TMS) were integrated on the 3D-MRI scalp position using the Navigation System. (C) Identification of the motor cortex and tumor localization after dural opening is quickly performed with the help of the Viewing Wand system, which memorizes the locations obtained from integrated MRI, fMRI and TMS data. (D) Drawing of the motor cortex and tumor margin on the patient's scalp helps easy, fast and safe surgical planning. Note that the reconstructed preoperative 3-D view (B) is totally reflected in the real scalp in the operation room.

4.4.4.3
Cellular–Molecular Level

A major and possibly very important future field of studies is the application of TMS in order to obtain therapeutic effects in neurological disorders. A number of animal studies on the basic mechanisms of rTMS-induced alterations of neurotrophic factors or gene expression and changes in plasticity have been conducted (Wang et al., 1996; Fujiki and Steward, 1997; Keck et al., 2000a,b, 2001, 2002; Lisanby and Belmaker, 2000; Muller et al., 2000; Ogiue-Ikeda et al., 2003).

There is strong evidence that gene expression such as the immediate early gene (Ji et al., 1998), astrocyte specific glial fibrillary acidic protein (GFAP) messenger ribonucleic acid (mRNA) (Fujiki and Steward, 1997) and brain-derived neurotrophic factor (Muller et al., 2000) are altered in response to rTMS (Fig. 4.25). This indicates that the measurable effects of TMS reach the cellular and molecular levels (Fig. 4.26). The most promising hypothesis is that induced neuroprotective or trophic factors may protect neurons from hypoxic insult (Fujiki et al., 2003).

Long-duration rTMS modulates the monoamine neurotransmitter system in content and turnover (Lisanby and Belmaker, 2000), and may also induce sprouting of mossy fibers in the hippocampus.

Increased dopaminergic neurotransmission may contribute to the beneficial effects of rTMS in the treatment of affective disorders and Parkinson's disease. The results of these studies provide strong evidence that noninvasive TMS can strongly modulate gene expression in neurons and astrocytes (Fujiki and Steward, 1997; Fu-

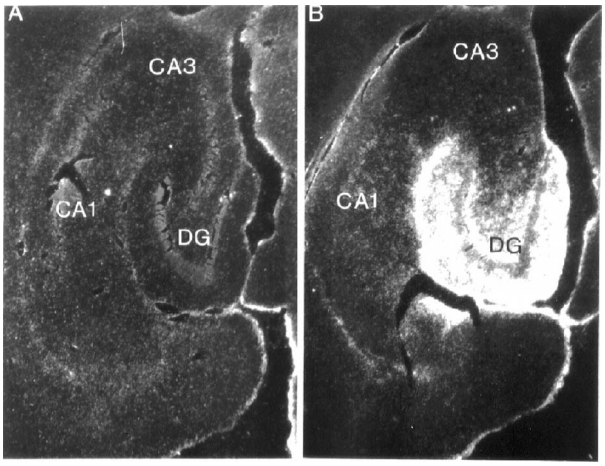

Fig. 4.25. Increases in glial fibrillary acidic protein (GFAP) messenger ribonucleic acid (mRNA) following rTMS (25 Hz) as revealed by in-situ hybridization (emulsion-coated slides). Dark-field photographs of autoradiograms illustrating the levels of GFAP mRNA in a control mouse (A) and in an animal killed 1 day following rTMS (25 Hz for 10 s) (B). DG = dentate gyrus; CA1 and CA3 indicate the respective zones in the hippocampus.

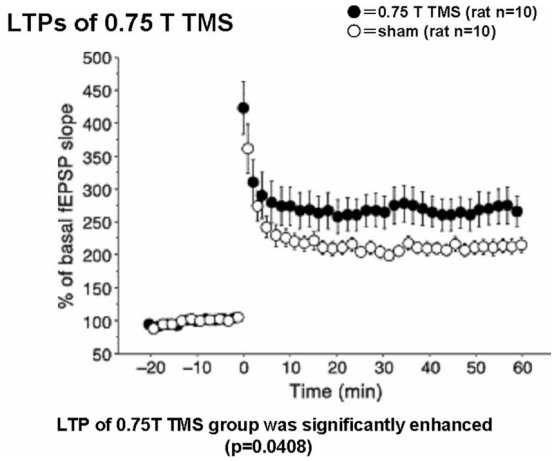

Fig. 4.26. Long-term potentiations (LTPs) of 0.75 T-stimulated and sham control groups. LTPs were observed in both the stimulated and sham control groups. The maintenance phase of the LTP of the stimulated group (260 ± 26%) (black circles) was significantly enhanced compared with the sham control group (212 ± 10%) (white circles) ($p = 0.0408$). Each circle represents the average of six successive responses (for 2 min) (10 rats per group). The error bar indicates 1 S.E.

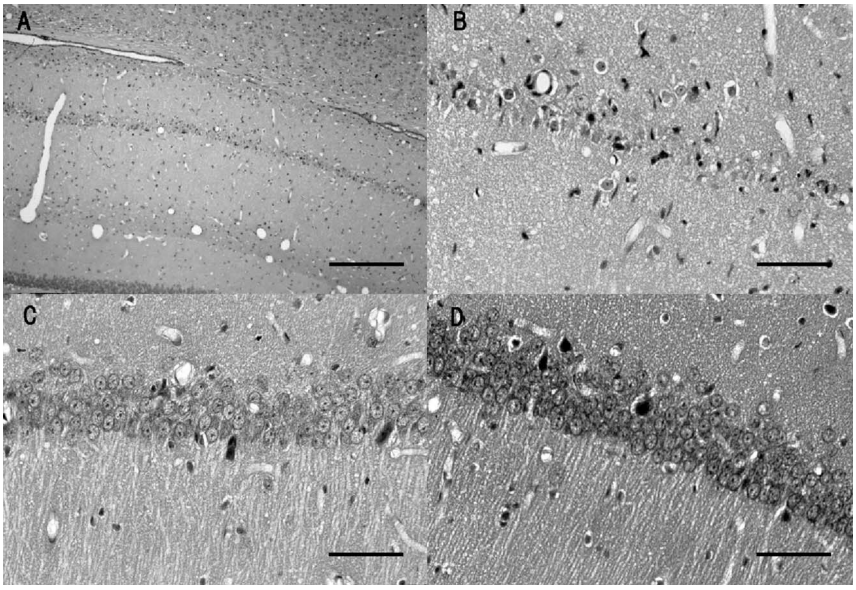

Fig. 4.27. Photomicrograph indicating neuronal density in the CA1 region of the hippocampus in an animal 7 days after BCCO ischemia (A,B), and in an animal with rTMS preconditioning 2 days before BCCO (D). Note the prominent cell loss in CA1 in the animal subjected to ischemia-only, and the relative absence of neuron loss in the animal that had received rTMS preconditioning. (C) Cell density in a sham-operated case. Scale bars: (A) = 200 μm; (B,D) = 50 μm; (C) = 100 μm.

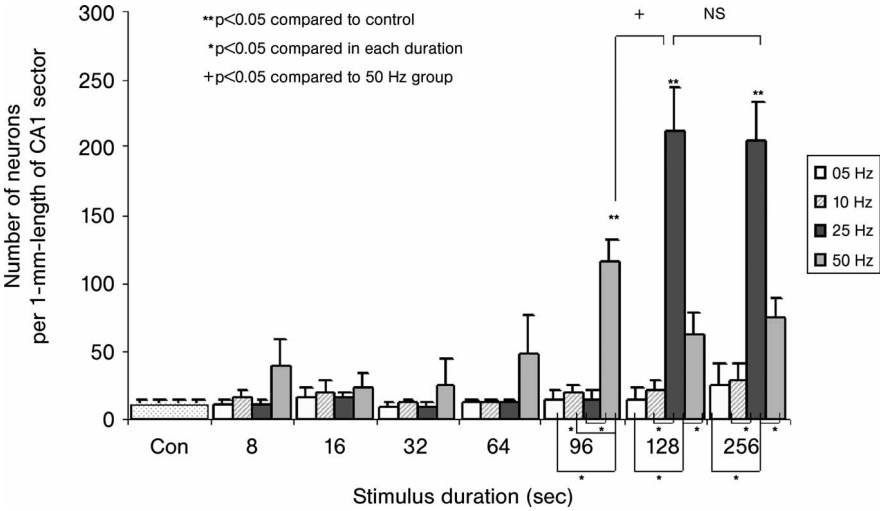

Fig. 4.28. Quantitative evaluation obtained from several combinations of stimulus condition. Neuronal density per 1-mm length of the CA1 sector, evaluated 7 days after BCCO after different combinations of stimulation. rTMS was reduced cell loss when delivered at frequencies of 25 and 50 Hz. Note that stimulation at 25 Hz for 128 s (3200 pulses) was more effective than stimulation at 50 Hz for 64 s (3200 pulses) or 128 s (6400 pulses). Stimulation at 50 Hz is less effective, even at the same number of pulses (for 64 s) or same or longer duration (for 128 or 256 s).

jiki et al., 2003; Ji et al., 1998; Muller et al., 2000). Thus, TMS – which originally was used simply as a means of assessing the function of descending motor tracts noninvasively – may ultimately be used as a means of modulating gene expression and inducing restorative plasticity or tolerance against injury in the brain (Fujiki et al., 2003) (Figs. 4.27 and 4.28).

Acknowledgments

The authors thank Drs. Risto Ilmoniemi and Jari Karhu, Helsinki University, Nexstim. Co. Ltd. for their cooperation in these studies. The studies were supported in part by grants from the Ministry of Education, Science and Culture in Japan, and the New Energy and Industrial Technology Development Organization.

References

Amassian, V.E., Cracco, R.Q., and Maccabee, P.J. (1989). Focal stimulation of the human cerebral cortex with the magnetic coil: a comparison with electrical stimulation. *Electroencephalogr. Clin. Neurophysiol.*, **74**, 401–416.

Amassian, V.E., Cracco, R.Q., Maccabee, P.J., and Cracco, J.B. (1992). Cerebello-frontal cortical projections in humans studied with the magnetic coil. *Electroencephalogr. Clin. Neurophysiol.*, **85**, 265–272.

Barker, A.T., Jalinous, R., and Freeston, I.L. (1985). Non-invasive magnetic stimulation of human motor cortex. *Lancet*, **i** (8437), 1106–1107.

Barker, A.T., Freeston, I.L., Jalinous, R., and Jarratt, J.A. (1986). Clinical evaluation of conduction time measurements in central motor pathways using magnetic stimulation of the human brain. *Lancet*, **i** (8493), 1325–1326.

Barker, A.T., Freeston, I.L., Jalinous, R., and Jarratt, J.A. (1987). Magnetic stimulation of the human brain and central nervous system: an introduction and results of an initial clinical evaluation. *Neurosurgery*, **20** (1), 100–109.

Basser, P.J. and Roth, B.J. (1991). Stimulation of a myelinated nerve axon by electromagnetic induction. *Med. Biol. Eng. Comput.*, **29**, 261–268.

Bickford, R.G. and Fremming, B.D. (1965). Neuronal stimulation by pulsed magnetic fields in animals and man. *Dig. 6th International Conference Medical Electrical Biological Engineering*, 112.

Cohen, D. (1985). Feasibility of a magnetic stimulator for the brain. In: Weinberg, H., Stroink, G., and Katila, T. (Eds.), *Biomagnetism: Applications and Theory*, Pergamon Press, pp. 466–470.

Cohen, M.S., Weisskoff, R.M., Rzedzian, R.R., and Kantor, H.L. (1990). Sensory stimulation by time-varying magnetic fields. *Magn. Reson. Med.*, **14** (3), 409–414.

Day, B.L., Thompson, P.D., Dick, J.P., Nakashima, K., and Marsdes, C.D. (1987). Different sites of action of electrical and magnetic stimulation of the human brain. *Neurosci. Lett.*, **75**, 101–106.

D'Arsonval, A. (1896). Dispotifs pour la mesure des courants alternatifs des toutes frequencies. *C.R. Acad. Sci.*, **48**, 450–451.

Esselle, K.P. and Stuchly, M.A. (1992). Neural stimulation with magnetic fields: analysis of induced electric fields. *IEEE Trans. Biomed. Eng.*, **BME-39**, 693–700.

Fujiki, M. and Steward, O. (1997). High frequency transcranial magnetic stimulation mimics the effects of ECS in upregulating astroglial gene expression in the murine CNS. *Mol. Brain. Res.*, **44**, 301–308.

Fujiki, M., Kobayashi, H., Abe, T., and Kamida, T. (2003). Repetitive transcranial magnetic stimulation for protection against delayed neuronal death induced by transient ischemia. *J. Neurosurg.*, **99**, 1063–1069.

Grandori, F. and Ravazzani, P. (1991). Magnetic stimulation of the motor cortex: Theoretical considerations. *IEEE Trans. Biomed. Eng.*, **38** (2), 180–191.

Gugino, L.D., Romero, J.R., Aglio, L., Titone, D., Ramirez, M., Pascual-Leone, A., Grimson, E., Weisenfeld, N., Kikinis, R., and Shenton, M.E. (2001). Transcranial magnetic stimulation coregistered with MRI: a comparison of a guided versus blind stimulation technique and its effect on evoked compound muscle action potentials. *Clin. Neurophysiol.*, **112** (10), 1781–1792.

Hess, C.W., Mills, K.R., and Murray, N.M. (1986). Measurement of central motor conduction in multiple sclerosis by magnetic brain stimulation. *Lancet*, **ii** (8503), 355–358.

Hyodo, A. and Ueno, S. (1996). Nerve excitation model for localized magnetic stimulation of finite neuronal structures. *IEEE Trans. Magn.*, **32** (5), 5112.

Ilmoniemi, R.J., Ruohonen, J., and Karhu, J. (1999). Transcranial magnetic stimulation – a new tool for functional imaging of the brain. *Crit. Rev. Biomed. Eng.*, **27**, 241–284.

Irwin, D.D., Rush, S., Evering, R., Lepeschkin, E., Montgomery, D.B., and Weggel, R.J. (1970). Stimulation of cardiac muscle by a time-varying magnetic field. *IEEE Trans. Magn.*, **MAG-6**, 321–322.

Ji, R.R., Schlaepfer, T.E., Aizenman, C.D., Epstein, C.M., Qiu, D., Huang, J.C., and Rupp, F. (1998). Repetitive transcranial magnetic stimulation activates specific regions in rat brain. *Proc. Natl. Acad. Sci. USA*, **95**, 15635–15640.

Keck, M.E., Engelmann, M., Muller, M.B., Henniger, M.S., Hermann, B., Rupprecht, R., Neumann, I.D., Toschi, N., Landgraf, R., and Post, A. (2000a). Repetitive transcranial magnetic stimulation induces active coping strategies and attenuates the neuroendocrine stress response in rats. *J. Psychiatr. Res.*, **34**, 265–276.

Keck, M.E., Sillaber, I., Ebner, K., Welt, T., Toschi, N., Kaehler, S.T., Singewald, N., Philippu, A., Elbel, G.K., Wotjak, C.T., Holsboer, F., Landgraf, R., and Engelmann, M. (2000b). Acute transcranial

magnetic stimulation of frontal brain regions selectively modulates the release of vasopressin, biogenic amines and amino acids in the rat brain. *Eur. J. Neurosci.*, **12**, 3713–3720.

Keck, M.E., Welt, T., Post, A., Muller, M.B., Toschi, N., Wigger, A., Landgraf, R., Holsboer, F., and Engelmann, M. (2001). Neuroendocrine and behavioral effects of repetitive transcranial magnetic stimulation in a psychopathological animal model are suggestive of antidepressant-like effects. *Neuropsychopharmacology*, **24**, 337–349.

Keck, M.E., Welt, T., Muller, M.B., Erhardt, A., Ohl, F., Toschi, N., Holsboer, F., and Sillaber, I. (2002). Repetitive transcranial magnetic stimulation increases the release of dopamine in the mesolimbic and mesostriatal system. *Neuropharmacology*, **43**, 101–109.

Krings, T., Buchbinder, B.R., Butler, W.E., Chiappa, K.H., Jiang, H.J., Rosen, B.R., and Cosgrove, G.R. (1997). Stereotactic transcranial magnetic stimulation: correlation with direct electrical cortical stimulation. *Neurosurgery*, **41**, 1319–1325.

Krings, T., Foltys, H., Reinges, M.H., Kemeny, S., Rohde, V., Spetzger, U., Gilsbach, J.M., and Thron, A. (2001a). Navigated transcranial magnetic stimulation for presurgical planning-correlation with functional MRI. *Minim. Invasive Neurosurg.*, **44**, 234–239.

Krings, T., Chiappa, K.H., Foltys, H., Reinges, M.H., Cosgrove, G.R., and Thron, A. (2001b). Introducing navigated transcranial magnetic stimulation as a refined brain mapping methodology. *Neurosurg. Rev.*, **24**, 171–179.

Lisanby, S.H. and Belmaker, R.H. (2000). Animal models of the mechanisms of action of repetitive transcranial magnetic stimulation (RTMS): comparisons with electroconvulsive shock (ECS). *Depress. Anxiety*, **12**, 178–187.

Maass, J.A. and Asa, M.M. (1970). Contactless nerve stimulation and signal detection by inductive transfer. *IEEE Trans. Magnetics*, **MAG-6**, 322–326.

Mills, K.R., Boniface, S.J., and Schubert, M. (1992). Magnetic brain stimulation with a double coil: the importance of coil orientation. *EEG Clin. Neurophysiol.*, **85**, 17–21.

Maccabee, P.J., Eberle, L., Amassian, V.E., Cracco, R.Q., Rudell, A., and Jayachandra, M. (1990). Spatial distribution of the electrical field induced in volume by round and figure '8' magnetic coils: relevance to activation of sensory nerve fibers. *Electroencephalogr. Clin. Neurophysiol.*, **76**, 131–141.

Maccabee, P.J., Amassian, V.E., Eberle, L.P., and Cracco, R.Q. (1993). Magnetic stimulation of straight and bent amphibian and mammalian peripheral nerve in vitro. *J. Physiol.*, **460**, 201–219.

Muller, M.B., Toschi, N., Kresse, A.E., Post, A., and Keck, M.E. (2000). Long-term repetitive transcranial magnetic stimulation increases the expression of brain-derived neurotrophic factor and cholecystokinin mRNA, but not neuropeptide tyrosine mRNA in specific areas of rat brain. *Neuropsychopharmacology*, **23**, 205–215.

Nagarajan, S.S. and Durand, D.M. (1993). Effects of induced electric fields on finite neuronal structures: a simulation study. *IEEE Trans. Biomed. Eng.*, **40**, 1175–1187.

Nilsson, J., Panizza, M., Roth, B.J., Basser, P.J., Cohen, L.G., Caruso, G., and Hallett, M. (1992). Determining the site of stimulation during magnetic stimulation of a peripheral nerve. *Electroencephalogr. Clin. Neurophysiol.*, **85**, 253–264.

Oberg, P.A. (1973). Magnetic stimulation of nerve tissue. *Med. Biol. Eng.*, **11**, 55–64.

Olney, R.K., So, Y.T., Goodin, D.S., and Aminoff, M.J. (1990). A comparison of magnetic and electrical stimulation of peripheral nerves. *Muscle Nerve*, **13**, 957–963.

Ogiue-Ikeda, M., Kawato, S., and Ueno, S. (2003). The effect of repetitive transcranial magnetic stimulation on long-term potentiation in rat hippocampus depends on stimulus intensity. *Brain Res.*, **993**, 222–226.

Reilly, J.P. (1989). Peripheral nerve stimulation by induced electrical currents: exposure to time-varying magnetic fields. *Med. Biol. Eng. Comput.*, **27**, 101.

Roth, B.J. and Basser, P.J. (1990). A model of stimulation of a nerve fiber by electromagnetic induction. *IEEE Trans. Biomed. Eng.*, **37** (6), 588–597.

Rothwell, J.C. (1994). Motor cortical stimulation in man. In: Ueno, S. (Ed.),

Biomagnetic Stimulation, Plenum Press, New York, London, pp. 49–57.

Rothwell, J.C., Day, B.L., Thompson, P.D., Dick, J.P.R., and Marsden, C.D. (1987). Some experiences of techniques for stimulation of the human cerebral motor cortex through the scalp. *Neurosurgery*, **20** (1), 156–163.

Ruohonen, J. and Ilmoniemi, R.J. (1999). Modeling of the stimulating field generation in TMS. *Electroencephalogr. Clin. Neurophysiol.*, **51** (Suppl.), 30–40.

Sekino, M. and Ueno, S. (2004). FEM-based determination of optimum current distribution in transcranial magnetic stimulation as an alternative to electroconvulsive therapy. *IEEE Trans. Magn.*, **40** (4), 2167–2169.

Ueno, S., Matsumoto, S., Harada, K., and Oomura, Y. (1978). Capacitative stimulatory effect in magnetic stimulation of nerve tissue. *IEEE Trans. Magn.*, **MAG-14**, 958–960.

Ueno, S., Lovsund, P., and Oberg, P.A. (1981). On the effect of alternating magnetic fields on action potential in lobster giant axon. *Proceedings of the 5th Nordic Meeting on Med. and Biol. Eng.*, Linkoping, Sweden, pp. 262–264.

Ueno, S., Harada, K., Ji, C., and Oomura, Y. (1984). Magnetic nerve stimulation without interlinkage between nerve and magnetic flux. *IEEE Trans. Magn.*, **MAG-20**, 1660–1662.

Ueno, S., Tashiro, T., Kamise, S., Oosako, T., and Harada, K. (1985). A paired-coil configuration for localized hyperthermia of deep tissues. *Digests of Intermagnetic Conference*, St. Paul, Minnesota, p. 3.

Ueno, S., Lovsund, P., and Oberg, P.A. (1986). Effects of time-varying magnetic fields on action potential in lobster giant axon. *Med. Biol. Eng. Comput.*, **24**, 521–526.

Ueno, S., Tashiro, T., Kamise, S., and Harada, K. (1987). Localized hyperthermia by means of a pair-coil configuration: calculation of current distributions in cubical model. *IEEE Trans. Magn.*, **MAG-23**, 2437–2439.

Ueno, S., Tashiro, T., and Harada, K. (1988). Localized stimulation of neural tissues in the brain by means of paired configuration of time-varying magnetic fields. *J. Appl. Phys.*, **64**, 5862–5864.

Ueno, S., Matsuda, T., Fujiki, M., and Hori, S. (1989a). Localized stimulation of the human motor cortex by means of a pair of opposing magnetic fields. *Digests of Intermagnetic Conference*, Washington D.C., p. 10.

Ueno, S., Matsuda, T., and Fujiki, M. (1989b). Localized stimulation of the human cortex by opposing magnetic fields. In: Williamson, J.S., Hoke, M., Stroink, G., and Kotani, M. (Eds.), *Advances in Biomagnetism*, Plenum Press, New York, London, pp. 529–532.

Ueno, S., Matsuda, T., and Fujiki, M. (1989c). Localized stimulation of the human brain by opposing pulsed magnetic fields. *Memoirs of the Faculty of Engineering – Kyushu University*, **49**, 161–173.

Ueno, S., Matsuda, T., and Fujiki, M. (1990a). Functional mapping of the human motor cortex obtained by focal and vectorial magnetic stimulation of the brain. *IEEE Trans. Magn.*, **26** (5), 1539–1544.

Ueno, S., Matsuda, T., and Hiwaki, O. (1990b). Localized stimulation of the human brain and spinal cord by a pair of opposing pulsed magnetic fields. *J. Appl. Phys.*, **66**, 5838–5840.

Ueno, S., Matsuda, T., and Hiwaki, O. (1991). Estimation of structures of neural fibers in the human brain by vectorial magnetic stimulation. *IEEE Trans. Magn.*, **27** (6), 5387–5389.

Ugawa, Y. (1999). Magnetic cerebellar stimulation. *Electroencephalogr. Clin Neurophysiol.*, **49** (Suppl.), 222–225.

Wang, H., Wang, X., and Scheich, H. (1996). LTD and LTP induced by transcranial magnetic stimulation in auditory cortex. *NeuroReport*, **7**, 521–525.

Ziemann, U., Lonnecker, S., and Paulus, W. (1995). Inhibition of human motor cortex by ethanol. A transcranial magnetic stimulation study. *Brain*, **118**, 1437–1446.

Ziemann, U., Lonnecker, S., Steinhoff, B.J., and Paulus, W. (1996a). The effect of lorazepam on the motor cortical excitability in man. *Exp. Brain Res.*, **109**, 127–135.

Ziemann, U., Lonnecker, S., Steinhoff, B.J., and Paulus, W. (1996b). Effects of antiepileptic drugs on motor cortex excitability in humans: a transcranial magnetic stimulation study. *Ann. Neurol.*, **40**, 367–378.

4.5
Liver Iron Susceptometry*

Roland Fischer and David Farrell

4.5.1
Introduction

Noninvasive iron measurements are attracting increased interest (Brittenham and Badman, 2003). One factor in this development is the recent progress in molecular biology that has led to the detection of different gene mutations in genetic hemochromatosis (Feder et al., 1996; Roetto and Camaschella, 2005). In secondary iron overload, as in thalassemia, interest has also been fueled by new developments in oral iron chelators (deferiprone, deferasirox), and by the realization that cardiomyopathy is the main cause of mortality in long-term survivors (Borgna-Pignatti et al., 2004).

A strong stimulus has also come from advances in measurement techniques. Liver iron susceptometry using SQUID biomagnetometers has been refined to the point that it offers a routine clinical method for the diagnosis and monitoring of iron overload. However, due to its cost and the technical expertise required, the method is only available to patients in a few centers worldwide. Reflecting the need to make iron assessment more generally available, less complex susceptibility-based methods are emerging as attractive alternatives to traditional SQUID techniques, and developments in magnetic resonance imaging (MRI) offer a further measurement capability.

This section outlines the current state of the field, with an emphasis placed on recent developments.

4.5.2
Iron Metabolism and Iron Overload

Iron plays an essential role in biological systems. Under normal circumstances, iron absorption (normal: 1–2 mg per day) is adjusted to physiological needs, but in iron-deficiency anemia, for example, it is significantly increased (maximum:

* A list of abbreviations and acronyms is provided at the end of this chapter.

5 mg per day). By contrast, the body has no natural means to increase iron elimination. Thus, increased iron absorption – as in primary hemochromatosis (PH), or by catabolized red blood cells from multiple blood transfusions (200–250 mg iron per unit) in secondary hemochromatosis (SH) – leads to iron accumulation. When improperly sequestered, iron can catalyze a variety of cytotoxic reactions, causing damage in a wide range of tissues and organs.

One of the most frequent inherited forms of PH is caused by the C282Y and H63D mutations of the hemochromatosis gene *HFE-1* on chromosome 6 (Feder et al., 1996). This condition is characterized by an up-regulated iron absorption with consecutive storage of iron mainly in the liver, by a global gene prevalence of about 6% in populations of Caucasian origin (Merryweather-Clarke et al., 1997) with 0.5% affected homozygotes in Northern Europeans, and by a highly variable phenotypic expression. Besides the *HFE-1* gene related hemochromatosis, there are other genetic forms (HFE types 2–4) more prevalent in Southern Europe (Roetto and Camaschella, 2005) and in populations of African origin (Gordeuk et al., 2003). Beyond initial blood parameter tests (serum iron, transferrin saturation, ferritin) and genotyping, the definitive test for the diagnosis of PH is the quantitative assessment of liver iron either by biopsy or noninvasive methods (Nielsen et al., 2003a).

The most important mechanisms for SH are blood transfusion and increased iron absorption in response to ineffective erythropoiesis in anemias (Heinrich et al., 1973). Among these anemias, thalassemia (Italy has 7000 and India has 10 000 such newborns per year) and sickle cell disease are prevalent in the ''malaria belt'' (Mediterranean countries, Africa, Asia) and in descendants of these populations worldwide. However, patients suffering from myelodysplastic syndrome or rare anemias (e.g., Diamond–Blackfan) are also affected by iron overload. In the thalassemias, iron overload is manifested at an early age (~2 years). With the introduction of iron chelation therapy, the assessment of iron stores has become important for long-term survival (Gabutti and Piga, 1996), for the adjustment of chelation treatment, and for the reduction of toxic side effects from excess iron (diabetes, cirrhosis, hyperthyroidism, and cardiac disease) or from excess chelation dosage (growth delay, bone deformities, sensorial impairment) (Pippard, 1994). Iron overload monitoring has been performed hitherto using serum ferritin, which can often be misleading, and by annual liver biopsies. It should be noted that iron reduction in response to chelation may differ in the liver and the heart (Anderson et al., 2002). Hence, establishing a low liver iron concentration (LIC) may not be sufficient to prevent patients from accumulating iron in the heart or other organs (pancreas, pituitary gland).

Iron overload as a ''silent killer'' affects patients with PH usually at older age (>40 years), while patients with SH may develop serious diseases already in childhood. Among the outcomes of SH are diabetes, liver fibrosis and cirrhosis, impotence, heart failure, hepatocellular carcinoma and pulmonary hypertension. Even the possibility that iron accumulation in the brain plays a role in Parkinson's and Alzheimer's diseases has been suggested. Iron toxicity is caused by free iron catalyzing the formation of free radicals, which are normally trapped by antioxidants.

However, in iron overload the capacity of the iron transport protein (transferrin) can become saturated with the consecutive appearance of free iron in the cells, which can be measured as non-transferrin-bound iron in the serum or plasma (Hershko et al., 1998). Toxicity from iron overload can be prevented by early diagnosis, blood donation and/or phlebotomy treatment in PH, or by continuous and reliable monitoring of liver and heart iron and effective chelation treatment in SH (Porter, 2005).

4.5.3 Technical Developments of Biomagnetic Liver Susceptometry (BLS)

Since the liver is the main iron storage organ, knowledge of the liver iron concentration allows the total body iron stores to be estimated (Fischer et al., 1999; Angelucci et al., 2000). The rationale for using *in-vivo* magnetic susceptibility measurements to measure liver iron stores was first described by Bauman and Harris (1967). Since the studies of Farrell and Brittenham (Farrell et al., 1980; Brittenham et al., 1982), a sustained effort has been made to refine the technique with respect to calibration, reproducibility, sensitivity, and subtracting thorax contributions from the signal (Bastuscheck and Williamson, 1985; Fischer et al., 1989; Paulson et al., 1991; Hartmann et al., 1992; Sosnitsky et al., 2000).

4.5.3.1 DC-Field Low-T_C SQUID Biosusceptometer

The *Hamburg biosusceptometer* (Biomagnetic Technologies Inc., San Diego, USA) was installed in a low ambient magnetic noise hospital area at the University Medical Center Hamburg-Eppendorf (Germany). It was the prototype of a commercially available SQUID biosusceptometer (Paulson et al., 1991), and has been in continuous routine clinical operation since 1989 with no major technical failure. In contrast to recent systems at Turin and Oakland (see below), it contains a sensor assembly with two symmetrical second-order gradiometer sensors ($r = 1.4$ cm and 3.4 cm) coupled to rf-SQUIDs, a 20-L dewar for liquid helium cooling (boil-off rate 3 L per day), a water bellows coupling membrane with a diameter of 25 cm, and a workstation (HP320; Hewlett Packard) for process control, data acquisition and analysis, with a data sampling rate of 100 Hz in eight data channels (Fischer, 1998). A *system sensitivity* equivalent to 20 μg Fe cm^{-3} was measured by ferric chloride solutions within a cylindrical water phantom at a depth of 15 mm (Paulson et al., 1991).

The design of the SQUID biosusceptometers at Turin and Oakland (Ferritometer®, Model 5700; Tristan Technologies, San Diego, USA) incorporated the experience accumulated at Hamburg, but placed additional emphasis on operation by members of the regular clinical staff (Starr et al., 2001; Fung et al., 2004) and on a better capability to perform measurement in children. Due to the higher environmental magnetic noise in both locations, active noise cancellation by a

Fig. 4.29. SQUID biosusceptometer at the Children's Hospital and Research Center at Oakland. An 11-year-old girl, covered by the waterbag, lies under the dewar tail before a 10-s vertical scan.

three-axis fluxgate magnetometer (MAG-03; Bartington Instruments Ltd., Oxford, UK) was employed (see Section 4.5.7).

The systems at Turin and Oakland comprise (Figs. 4.29 and 4.30):

- Two second-order gradiometers ($r = 1.4$ cm and 2.5 cm) and one planar gradiometer ($r_i/r_a = 1.9/2.8$), optimized for far- and near-field sensitivity, coupled to niobium dc-SQUIDs (maximum sensitivity 9 nT V^{-1}) inside a fiberglass dewar tail of 10 cm diameter.
- A 35-L dewar (boil-off rate < 3.5 L per day), allowing for a weekly liquid helium filling schedule.
- A microcomputer-controlled water reference system consisting of a latex coupling membrane glued to rubber bellows (diameter 20 cm) of low magnetic signature, water pressure feedback and integrated heating (30 °C).
- A lightweight aluminum-framed patient bed and table tops of honeycomb structure, which allows easier rolling over the floor.
- Process control by PC (handheld control, water pressure control, patient bed motion, position location), data acquisition (100 kHz National Instruments DAC cards: PCI-6023E and PCI-6031E), and online analysis under LabWindows CVI (National Instruments).

4.5.3.2
AC-Field SQUID Biosusceptometer

Instead of using localized, inhomogeneous magnetizing dc-fields, Bastuscheck and Williamson (1985) used a SQUID biomagnetometer in the uniform ac-field of large Helmholtz coils for liver iron measurements. This approach was later improved by a rigid instrumental setup with an almost field-free zone at the gradiometer coil's center (Sosnitsky et al., 2000).

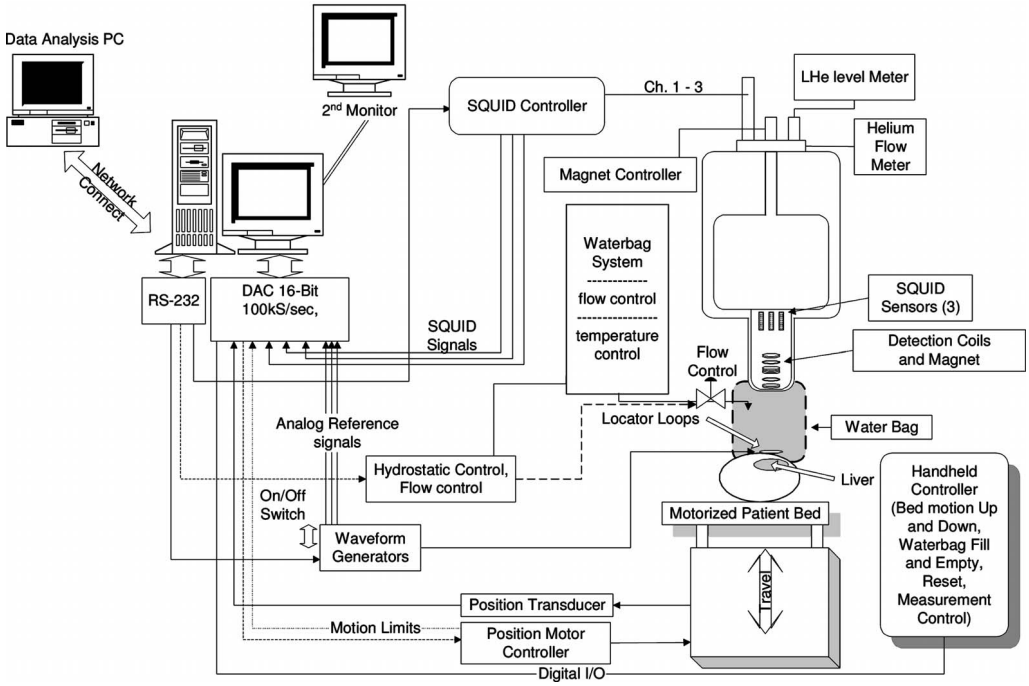

Fig. 4.30. System schematic of the Turin-Oakland SQUID biosusceptometers (Ferritometer®, Model 5700; Tristan Technologies, San Diego, USA).

The biomagnetism group of Sao Paulo (Carneiro et al., 2003) utilized one of the classic single-channel rf-SQUID biomagnetometers with a second-order gradiometer in an ac-field (114 μT, 7.7 Hz) of large rectangular coils (3×2 m), leading to a relatively low-cost and high-sensitivity instrument for noninvasive LIC determination. A water bag with an open surface compensates for the subject's irregular thorax shape in order to allow vertical body scans in the free air space above the liver position on a pneumatic bed. The *in-vivo* sensitivity was in the range of LIC of subjects with normal iron stores. First measurements in 34 subjects with normal iron stores (100–500 μg g^{-1} liver) and 20 patients with β-thalassemia major (750–5800 μg g^{-1} liver) revealed a clear separation between these two groups.

As biosusceptometers have only a poor spatial resolution, the inter-individual diamagnetic contribution of the thorax tissue limits the *in-vivo* sensitivity, especially in obese patients with large skin–liver distances. The biomagnetism group of Chieti employed large concentric coil pairs (diameter $D = 2.45$ m) and smaller pairs ($D = 1.41$ m) which were generating a homogeneous ac-field combined with a gradient field at 10 Hz. A seven-channel second-order SQUID gradiometer sensor is to be operated inside an rf-shielded room (Della Penna et al., 2003).

4.5.3.3 Room-Temperature Biosusceptometer

The prototype of a room-temperature-based susceptometer using a copper coil sensor in an ac-field (570 Hz) was developed by Quantum Magnetics Inc. (QM), San Diego, USA (Kumar et al., 2002). Coaxial field coils in a first-order and sensor coils in a second-order gradiometer configurations had a mean diameter of 7 cm and baselines of 9 and 11 cm, respectively. The temperature drift of the sensor was overcome by oscillating the whole sensor assembly with respect to the uniform water-coupling interface on the subject. A blind comparison between the SQUID biosusceptometer in New York (Brittenham et al., 1982) and QM's susceptometer resulted in a coefficient of determination $R^2 = 0.96$ in eight patients with thalassemia. Based on the design of the room-temperature susceptometer and its simplified manner of operation, an inexpensive and user-friendly biosusceptometer for clinical use may be expected.

A total-body ac-susceptometer with a wide aperture (>30 cm) between pick-up coil and field coil was recently developed for liver iron susceptometry at the University of Genova, Italy (Marinelli et al., 2005). In a first-order gradiometer configuration, concentric ac-field coils (diameters $d_1 = 14$ cm and $d_2 = 40$ cm, 234 Hz and 195 Hz, baseline $b = 8$ cm) are positioned in the center between detector coils ($d_1 = 16.1$ cm and $d_2 = 40.1$ cm, $b = 88$ cm). In a prone position, subjects are transversally scanned ($\pm$20 cm) between pick-up and field coil set. A database of 68 subjects with normal iron stores is utilized to calculate an individual background signal from anthropometric data. In a first blinded comparison with 30 thalassemia patients, LIC measurements were correlated with results obtained with the low T_C-SQUID biosusceptometer at Turin ($R^2 = 0.6$). A refinement of the methodology with current uncertainty of 500 μg g^{-1} liver is in progress.

A high-frequency (28 kHz) magnetic excitation field coil is used in a low-cost magnetic induction system (Casanas et al., 2004). At a distance of 0.32 to 0.37 m, a planar gradiometer receiver registers the electromagnetic signal from the excitation coil and from the magnetic perturbation by an object or subject caused by eddy currents. The real and imaginary parts of this perturbation reflect the magnetic susceptibility, the electric permittivity and conductivity. First measurements in humans showed a stronger contribution from the permittivity than from the susceptibility, which made discrimination between iron overloaded patients and subjects with normal iron stores difficult.

4.5.3.4 High-T_C Biosusceptometer

The main impediments to a wider clinical application of liver iron susceptometry have been instrumental cost, operational complexity, and the serious spatial resolution issue mentioned above. The latter makes it difficult to compensate for thorax susceptibility variations in patients with substantial liver depths (>25 mm), no

matter what particular coil design is employed. A novel susceptometer based on high-Tc superconductivity that addresses all these issues has been designed, built and tested on human subjects (D.E. Farrell, C.J. Allen, J.H. Tripp and G.M. Brittenham, personal communication). The instrument is based on the same physical principles as the Ferritometer®, but with the following modifications:

- A permanent (neodymium boron iron) magnet is employed instead of a superconducting coil, and the SQUIDs are replaced by magnetoresistive sensors.
- The superconducting flux transformers are fabricated from high-T_C material (yttrium barium copper oxide) and so require only liquid nitrogen as a cryogen.
- Five (magnetometer) measurement channels are employed, three for noise correction and two for separately registering signals from the liver, thorax overlay and contributions from the lung.

While retaining the well-understood advantages of superconductivity, this new design dispenses with most of the expensive ferritometer components (SQUIDs, large support gantry, computer-controlled bed), and could be manufactured for approximately one-fifth of the cost of that instrument. It is simple to use, as the patient remains fixed during a measurement while the susceptometer is scanned back and forward in a horizontal plane at 0.25 Hz. A complete measurement takes about 1 minute once the patient is in position. *In-vitro* measurements on liver phantoms with an equivalent iron concentration of 5000 μg g^{-1} at a depth of 20 mm have a typical standard deviation of 20 μg g^{-1}, or less than 0.5%. Repeated (day-to-day) measurements on normal subjects with this liver depth have a typical standard deviation of 50 μg g^{-1}. Furthermore, the instrument's lateral spatial resolution permits a fundamentally new approach to correcting for thorax susceptibility variations. The new method has been tested on a group of normal subjects ($n = 10$) with liver depths varying from 16 to 35 mm. After correcting for thorax variations, the result was 360 ± 120 μg g^{-1} liver, in accordance with the expectation for a group of subjects with normal iron stores. Further tests are planned on normal subjects, and on patients with biopsy-established iron concentrations.

4.5.4
Physical and Biochemical Basics

In-vivo liver iron susceptometry (and also MRI) exploits the strong paramagnetic response to an external magnetic field of hemosiderin and ferritin storage iron in competition with the diamagnetic response of other biologically relevant tissue (water, fat, skin, muscle). Ferromagnetic material is found only in pacemakers, dental braces, or inhaled ferromagnetic dust from welding. The magnetic flux change is usually induced by moving the patient or the susceptometer relative to each other within a fixed magnetic dc- or ac-field. The total magnetic flux change in an organ depends on the external field strength, the detector distance, the organ

geometry, and its magnetic volume susceptibility in the three-dimensional sensitivity space. The magnetic volume susceptibility of the liver ($\Delta\chi = \chi_{liver} - \chi_{ref}$), which is assumed to be homogeneous in the field of measurement, is measured relative to a reference medium (χ_{ref}, ref = air or water) by the induction of currents in the detector coils (gradiometers) due to a change of tissue magnetization. With knowledge of the specific magnetic volume susceptibility of the ferritin iron complex (χ_{Ftn}) [SI $g_{tissue}\ g_{Fe}^{-1}$], one can calculate the tissue iron concentration LIC [$g_{Fe} \cdot cm^{-3}$ or $g_{Fe}\ g_{tissue}^{-1}$] (Eq. 4.4):

$$LIC = \Delta\chi/\chi_{Ftn} \tag{4.4}$$

In iron overload, 60–80% of total liver iron consists of hemosiderin iron, while ferritin and hemoglobin iron are mainly present in normal iron stores. A hemoglobin iron contribution of 50–100 μg g^{-1} liver from the blood content of liver tissue must be taken into account in susceptometric measurements in subjects with normal iron stores (Fischer et al., 1989). The magnetic susceptibility of ferritin iron has been measured by different authors in different species (Michaelis et al., 1943; Schoffa, 1965; Shoden and Sturgeon, 1960; Bauman and Harris, 1967), and a reasonable mean value of the volume susceptibility for human liver ferritin iron seems to be $\chi_{Ftn} = 1600 \times 10^{-6}$ [SI] (Williamson and Kaufman, 1981) versus $\chi_{ref} = \chi_{water} = -9.032 \times 10^{-6}$ [SI]. (According to the international rules, SI units are used in the present text and denoted by the symbol [SI]). From the physicochemical similarity of the hemosiderin and ferritin molecular subunits, and from the agreement between magnetic and chemical determinations of iron concentrations in rat and human liver samples, one could assume that for their magnetic susceptibilities $\chi_{Ftn} \approx \chi_{Hsn}$. However, as magnetic measurements on hemosiderin samples are scarce (Shoden and Sturgeon, 1960; Allen et al., 2000), especially at room temperature, hypothetical differences between the magnetic susceptibility of hemosiderin and ferritin have not yet been ruled out. These differences may have even more impact on MRI measurements than on susceptometry (Vymazal et al., 2000). Using the Weidemann relationship (Fischer, 1998), which relates mass fractions m and magnetic volume susceptibilities χ, Eq. (4.4) can be split into the contributions from ferritin (Ftn), hemosiderin (Hsn), heme (Hem) iron compounds, and liver tissue (tiss) and reference media (ref) with $\chi_{Ftn} \approx \chi_{Hem}$:

$$\begin{aligned}\Delta\chi/\chi_{Ftn} = {} & m_{Ftn}/m_{liver} + (m_{Hsn}/m_{liver}) \cdot (\chi_{Hsn}/\chi_{Ftn}) + m_{Hem}/m_{liver} \\ & + (\chi_{tiss} - \chi_{ref})/\chi_{Ftn}\end{aligned} \tag{4.5}$$

Using the approximation $\chi_{Hsn}/\chi_{Ftn} \to 1$ in Eq. (4.5), the *in-vivo* susceptometric LIC_{BLS} values (Eq. 4.4) can then be linearly related with *in-vitro* wet weight nonheme iron concentrations from liver biopsy samples LIC_{biop}, represented by the first two terms, and with the last two terms as a small off-set. However, with $\chi_{Hsn}/\chi_{Ftn} \leq 1$, LIC by BLS will show a nonlinear relationship or larger scattering with LIC_{biop} at higher LIC values.

4.5.5 Magnetostatic Principles

The magnetic flux Φ_d linking a set of detector coils can be calculated from the scalar product of the applied magnetic field vector $\mathbf{B}_f(r)$ and the "lead field" vector $\mathbf{B}_d(r)$, which would be generated if a reciprocal unit current I_d is passed through the detector coils (Farrell et al., 1980; Tripp, 1983). This leads to the *Reciprocity Theorem of Susceptometry* for a magnetized object at distance $\mathbf{r}$ in Eq. (4.6). The principal value of this result in the present context is that it reduces the number of integrations required to calculate the performance of any set of field and detector coils.

$$\Phi_d(r) = (\mu_o I_d)^{-1} \int \chi(r)(\mathbf{B}_f \cdot \mathbf{B}_d) d^3\mathbf{r} \tag{4.6}$$

In *first-order approximation*, the diamagnetic susceptibility of tissue above the liver (skin, muscle, ribs, fat) is assumed to be equal to that of the reference medium (χ_{ref}) occupying the coupling interface, so that its contribution can be neglected. In this approximation, the magnetized liver moves in a magnetically homogeneous (water) space. From the reciprocity theorem of susceptometry, a linear equation (4.7) is derived for estimating the relative magnetic volume susceptibility $\Delta\chi_{liver} = \chi_{liver} - \chi_{ref}$ of the liver from measurement of the SQUID output signal $V(z)$ and the distance z.

$$V(z) = V_o + C\Delta\chi_{liver} \int (\mathbf{B}_f \cdot \mathbf{B}_d) d^3\mathbf{r} + \Delta V_{sys}(z) \tag{4.7}$$

After subtraction of the system background $\Delta V_{sys}(z)$ caused by the locator loop and the water-coupling interface, and with known calibration constant C, the SQUID voltages $V(z)$ can be correlated with magnetic flux integrals $\Phi(z) = \int (\mathbf{B}_f \cdot \mathbf{B}_d) d^3\mathbf{r}$ at distances z. The resulting linear regression coefficient $\Delta\chi_{liv}$ indicates the relative magnetic liver iron susceptibility, and the offset parameter (intercept) V_o is found by extrapolation to a patient at infinity (Paulson et al., 1989).

Flux integrals have been calculated for plane, hemispherical, cylindrical, and ellipsoidal objects of different radii, lengths or axes with a dynamically enlarged voxel structure for increasing $\rho(x, y)$- and z-coordinates. The magnetic flux densities $B(\rho, z)$ in the integrand are parameterized for a single circular loop of radius r and unit current I with complete elliptic integrals (Farrell et al., 1983). The integrand $\mathbf{B}_f \cdot \mathbf{B}_d$ is then calculated at five equidistant points in $\rho(x, y)$, z and the integral is calculated by a Newton–Cotes interpolation of fourth order. The flux integrals at increasing detector–object distances are fitted by polynomials of the fifth and sixth degree, and the coefficients are tabulated.

From sonographic imaging at the optimum measurement position, the anterior liver contour can be approximated by an ellipsoid. For a typical ellipsoid, with axes

7 cm, 6 cm, and 3.5 cm, 90% and 89% of the registered magnetic flux change is generated by the anterior half in the small and large detector coils of the Hamburg biosusceptometer, respectively. This represents a sensing region of ~300 cm^3 and thereby, the deeper and more complex liver regions (large vessels, kidney) are of secondary significance. Due to the strongly localized magnetic sensitivity, the effects of paramagnetic neighboring organs (lungs, intestine) can be neglected, at least for optimum measurement positions.

In *second-order approximation*, SQUID output voltages, $V(z)$, are analyzed as linear functions of flux integrals, $\Phi(z) = \int \mathbf{B}_f \cdot \mathbf{B}_d d^3\mathbf{r}$, for the overlying thorax tissue, Φ_{thorax}, and the liver (spleen), Φ_{liver}, as shown in Eq. (4.8).

$$V(z_{ll}) = C\{\Delta\chi_{thorax} \cdot \Phi_{thorax}(z_{ll}) + \Delta\chi_{liver} \cdot \Phi_{liver}(z_{ll} + z_{liver})\} + \Delta V_{sys} + V_o + O(z_{ll}) \quad (4.8)$$

The detector–skin distance z_{ll} is measured simultaneously during the bed movement by the AC-driven locator loop. From Eq. (4.8), shape information of the body geometry (Φ_{thorax}) can be derived by subtracting measurements versus water from measurements versus air reference ($\Delta\chi_{thorax} = 9.4 \times 10^{-6}$ [SI]). A multiple linear regression analysis of the voltage data results in magnetic volume susceptibilities for liver $\Delta\chi_{liver}$ and thorax $\Delta\chi_{thorax}$, relative to the reference medium (water) for both detector channels (Fischer et al., 1989, 2002).

4.5.6 Calibration and Validation

For biomagnetic liver susceptometry, no *calibration* by biopsy data is necessary. The calibration constant C in Eq. (4.7) can be derived from a physical measurement of *any* object with well-defined geometry and known magnetic susceptibility. For example, measurement of an infinite water half-space ($r \geq 25$ cm), offers a fast, reproducible and precise method (Starr et al., 2001). This avoids any uncertainties in geometry, system background, and magnetic contamination. After analyzing the data according to Eq. (4.7), the slope must represent the difference between the magnetic volume susceptibilities of water and air $\Delta\chi = \chi_{water} - \chi_{air} = -9.396 \times 10^{-6}$ [SI], corresponding to -5873 μg_{Fe} cm^{-3} (Paulson et al., 1989), and finally resulting in the instrumental calibration constant, C.

The *validation* (or verification) of liver iron concentrations determined by BLS has been accomplished by chemical determination of total or nonheme iron by atomic absorption spectroscopy in wet-weight (ww) liver biopsy samples (sample size > 5 mg_{ww}) in the range of LIC = 500–12 000 μg g^{-1} liver (Brittenham et al., 1982; Brittenham, 1988). In patients with hemochromatosis, LICs < 5000 μg $g_{ww}{}^{-1}$ were determined, with a goodness of fit of ${\chi_\nu}^2 = 0.99$ (Fischer et al., 1992). Beyond this concentration significant discrepancies were observed. Without a more precise knowledge of the magnetic susceptibility of hemosiderin iron, it cannot be ruled

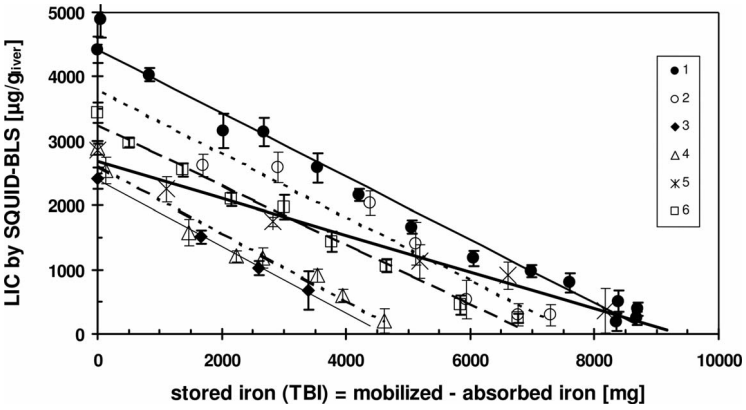

Fig. 4.31. Follow-up of phlebotomy treatment (mobilized iron minus absorbed food iron) by biomagnetic liver susceptometry (SQUID-BLS) in six patients with primary hemochromatosis (patient no. 5 has a larger liver volume).

out that this is caused by deviations of magnetic properties from ferritin iron. However, it is also possible that biopsy sampling errors and inhomogeneous iron distributions give rise to the discrepancies (Ambu et al., 1995; Villeneuve et al., 1996), especially at high LICs where fibrosis and cirrhosis are present. Although, *in-vivo* iron assessment methods (BLS, MRI) are wet-weight methods *per se*, liver iron quantification is often performed on dry-weight lyophilized, fresh tissue, or paraffin-embedded biopsy samples. However, these quantification methods are not standardized and the respective wet-to-dry weight conversion factors vary considerably (Butensky et al., 2005; Fischer et al., 2005).

Validation of the BLS method can also be demonstrated by monitoring patients with primary hemochromatosis (PH) during phlebotomy therapy (Fig. 4.31), similar to the study performed by Angelucci et al. (2000) in iron-overload patients after bone marrow transplantation. Each phlebotomy of 500 mL blood, mobilizes 250 mg of storage iron. In 26 patients with PH and an initial LIC of 760 to 4420 µg g^{-1} liver, the LIC did correlate linearly with mobilized storage iron taking into account also absorbed iron from food ($R^2 = 0.90–0.99$), with a mean LIC decrease of 410 $\pm$ 180 µg g^{-1} liver per g mobilized storage iron.

In a round-robin test with 20 thalassemia and sickle cell disease patients, and 10 subjects with normal iron stores, the low-T_C SQUID biosusceptometers at Hamburg, Turin, and Oakland were compared (LIC: normal up to 8000 µg g^{-1} liver). Liver iron assessment was performed at all three sites within one month under a standardized protocol (BLS-SOP, 2004). Prediction of LIC at Turin and Oakland in comparison with Hamburg revealed coefficients of determination between sites of $R^2 = 0.97$, resulting in intersite standard deviations of 247 and 326 µg g^{-1} liver, respectively (Fung et al., 2005).

4.5.7
Magnetic Background and Noise Problems

The detected signal is produced either by moving the patient in the magnetic field or by moving the sensor with respect to the patient. In the low-T_C systems (see Section 4.5.3), the main *system background* contributions, composed of the locator loop, the water-coupling membrane, and the patient bed, must be subtracted as function of distance from the data (BLS-SOP, 2004). This system background limits the sensitivity in the normal LIC range and makes the interpretation of details of the curvature fit difficult. In the case of systems with no patient movement as QM's room-temperature and the high-T_C biosusceptometer (see Section 4.5.3.4), a lower system background may be expected.

The three low-T_C systems installed in clinical settings are subjected to very different *environmental magnetic noise* in the measurement frequency range (dc to 5 Hz). The Hamburg biosusceptometer system, when located in a remote part of the hospital area, is almost unaffected by external noise ($<10^{-12}$ T/$\sqrt{\text{Hz}}$), while the system in Oakland, which is located close to a heavily frequented avenue, is subjected to low-frequency magnetic fields from car traffic ($\leq 10^{-6}$ T/$\sqrt{\text{Hz}}$), although both systems apply second-order gradiometers balanced better than 10^{-3}. After applying active electronic noise cancellation by a fluxgate, the environmental noise can be reduced to less than 10^{-9} T/$\sqrt{\text{Hz}}$ (Fung et al., 2004). One of the great advantages of the biomagnetic technique is its open architecture which, for example, allows measurements to be made in small children while in reassuringly close contact with their parents. Any type of shielded room would sacrifice this advantage, but noise cancellation by active shielding may be required in current and future systems at sites exposed to high environmental magnetic noise.

Besides system background and environmental magnetic noise, realistic *in-vivo* measurements suffer from poor spatial resolution in current biosusceptometer designs, and this results in inaccurate magnetic susceptibilities of the anterior thorax tissue and the liver (see Eq. 4.8). The *anterior thorax tissue contribution* can simulate falsely high LIC values up to 4000 μg g^{-1} liver in obese subjects. If the gradiometer configuration and/or magnetic noise does not allow for the simultaneous analysis of both $\Delta\chi_{\text{liver}}$ and $\Delta\chi_{\text{thorax}}$ from the curvature of the acquired data, then the approximate thorax tissue susceptibility must be derived from the body mass index (Fischer et al., 2002). Additionally, the skin–liver distance can be assessed sonographically only with an average uncertainty of ± 0.5 mm. Therefore, the overall uncertainty in realistic patient measurements is between 50 and 300 μg g^{-1} liver. In many of the relatively young and slim patients with thalassemia, the thorax tissue background is insignificant. Moreover, the enlarged organs (hepato- and/or splenomegaly) in these patients allow easy positioning, and also measurement of the spleen. Paramagnetic lung contributions around small-sized organs such as spleens in normal subjects may cause relatively large magnetic volume susceptibility effects in the range of 1000 μg g^{-1} due to the lower lung density.

The most common interference from *artificial metallic objects* arises from ferromagnetic dental braces (Engelhardt et al., 2004). For small magnetic perturbations varying slowly with distance, the error term $O(z_{\parallel})$ in Eq. (4.8) may be used for subtraction. Minor magnetic perturbations can also be caused by vascular access ports, surgical clips, and metallic body implants.

4.5.8 Alternative Methods

Magnetic resonance imaging has made significant recent advances in the measurement of iron overload (Jensen et al., 2001; Gandon et al., 2004; St. Pierre et al., 2005; Wood et al., 2005). In MRI, hydrogen nuclei in the liver interact with local fields generated by paramagnetic hemosiderin and ferritin iron atoms, while in BLS, the magnetic moment of the latter is measured directly. The nuclear phenomena involved in MRI are physically complex with the exception of the susceptometric approach used by Wang et al. (1999). In this approach, a small frequency shift $\Delta\nu$ in the nuclear resonance frequency ν_o, is observed across a regular plane boundary between two tissue compartments whose susceptibilities differ by $\Delta\chi$ and whose angle between the normal to the plane boundary and the static magnetic field is θ_N, as indicated in Eq. (4.9).

$$\Delta\nu/\nu_o = 4\pi/3(1 - 3\cos^2\theta_N)\Delta\chi \tag{4.9}$$

Wang et al. have shown how this direct approach can be used to make accurate *in-vivo* susceptibility measurements of liver tissue (Chu et al., 2004). However, the method is difficult to apply and the LIC values are restricted to the vicinity of blood vessels, which must be used as the reference compartment. Consequently, published MRI studies have relied on nuclear spin relaxation phenomena of hydrogen nuclei diffusing in the vicinity of paramagnetic iron centers. Although no à priori spin relaxation theory exists, empirical studies have revealed correlations between various relaxation time measures and iron concentration.

The standard method to emerge from these studies is the single spin-echo transverse relaxation rate (R_2) mapping (Clark and St. Pierre, 2000). A direct comparison between R_2-MRI and BLS in 23 patients with LIC between 270 and 10 350 $\mu g\ g^{-1}$ liver yielded a good linear correlation, with $R^2 = 0.86$ (Carneiro et al., 2005).

Gradient-recalled echo methods have been widely used for probing cardiac iron (Anderson et al., 2001; Westwood et al., 2003; Wood et al., 2004). With the short echo times ($T_E < 3$ ms) now available, these methods provide a more sensitive measure of the relatively low iron concentration in the heart (100–2000 $\mu g\ g_{ww}^{-1}$), albeit at the expense of greater sensitivity to artifacts from lung and liver interfaces. Finally, a recent effort has been made to distinguish different contributions to the complex nuclear relaxation process. This is aimed at differentiating between small-sized (ferritin) and cluster-sized (hemosiderin) iron molecules in liver and heart tissue (Tang et al., 2005).

4.5.9 Medical Applications

4.5.9.1 Measurement Procedures

In most systems, patients are positioned in the supine position on the bed with the body rotated 30–45° so that the right liver lobe is positioned directly beneath the sensor (see Fig. 4.29). The optimum liver position is found by bedside sonographic imaging under laser alignment. The procedure and its principles have been described elsewhere (Brittenham et al., 1982, 2001; Fischer, 1998; Sheth, 2003; BLS-SOP, 2004). A complete measurement involves sonography (skin–liver distance, right liver lobe geometry) and biosusceptometry (four to seven vertical scans) and takes about 30 minutes to complete. An online analysis is performed of each scan, in most cases yielding LICs that differ by less than 10% from final (offline) analysis of the complete dataset.

The Ferritometers® at Turin and Oakland are CE-marked (risk class I), while the biosusceptometer at Hamburg was approved in 2004 by German health authorities as an alternative noninvasive method replacing quantitative liver biopsy. At the time of writing, low-T_C SQUID-BLS has been used for iron assessment in more than 9000 patients (Cleveland/NY 1600; Hamburg 2400; Turin 4700; Oakland 600), with a broad range of age (from 2 to 80 years) and body weight (10 to 100 kg). As indicated in the following summary, the principal uses have been for diagnosing patients suspected of primary hemochromatosis and for monitoring iron overload during chelation treatment in patients with β-thalassemia major and other hemoglobinopathies (Nielsen et al., 2002).

4.5.9.2 Primary Hemochromatosis

BLS has been performed in more than 600 patients suspected of PH, with more than 1600 measurements having been made (Engelhardt et al., 2000). LICs > 1000 $\mu g\ g^{-1}$ liver were detected in 30% of these patients. BLS is successful in identifying those patients really afflicted by the disease (Nielsen et al., 2003a). Due to the benign noninvasive character of the measurement, the diagnosis for PH can be made at early stage before the onset of irreversible damage, even in young children (Nielsen et al., 2005). Monitoring phlebotomy therapy in patients with PH is especially useful for those with severe iron overload in their first period of total iron depletion (Nielsen et al., 2003b). BLS has verified that iron stores decline linearly with the iron removed by phlebotomy (Fischer et al., 1992). Moreover, total body iron stores were calculated from the mobilized storage iron in patients under phlebotomy treatment. A liver iron fraction of $88 \pm 11\%$ was derived in the range of 2500 to 4000 $\mu g\ g^{-1}$ liver from the corresponding BLS and liver volume measurements (see Fig. 4.31).

4.5.9.3 Iron-Deficiency Anemia

Measurement of iron stores in patients with iron deficiency anemia is not possible with present-day instrumentation. However, precision BLS measurements may be used to study the relative change of iron stores in patients and normal subjects. For example, in a study with nine long-distance runners, a significant therapy effect from 100 mg oral iron per day over three months was observed (Nachtigall et al., 1996). In children (aged 10–18 years) and adults (aged 18–64 years) with normal iron stores, LIC values have been measured by BLS in the range of 77 to 368 and 93 to 481 μg g^{-1} liver, respectively (Nielsen et al., 2002).

4.5.9.4 Secondary Hemochromatosis

Application of BLS in patients with secondary hemochromatosis is of major importance, as these patients must be monitored regularly (annually to biennially) in order to avoid long-term toxicity from iron overload or inadequate chelator dosing. The routinely used laboratory parameter, serum ferritin, has been shown to be a poor indicator for iron overload monitoring in thalassemia and sickle cell disease in comparison to BLS (Brittenham et al., 1993; Fischer et al., 1999). The ratio between iron accumulation from blood transfusions and total chelator intake was shown to correlate with LIC, and a LIC value > 4500 μg g^{-1} liver indicated a high risk for developing complications and for death (Brittenham et al., 1994). Moreover, compliance with actual chelation treatment was shown to be highly correlated with LIC (Fischer et al., 2000).

4.5.9.5 Long-Term Iron Chelation

The long-term efficacy of treatment with any iron chelator can be assessed by annual measurements of LIC and liver volume, with additional spleen iron and volume measurements in case of enlarged organs. The potential of BLS for this purpose has been demonstrated for the subcutaneously infused chelator desferrioxamine and the oral chelator deferiprone (or L1) (Nielsen et al., 1995; Olivieri et al., 1995; Brittenham et al., 1998; Töndury et al., 1998; Del Vecchio et al., 2000; Fischer et al., 2003; Meo et al., 2005). For chelators excreting iron predominantly via the fecal pathway – as the novel oral chelator Deferasirox, or ICL670 – only BLS or MRI can be used for practical long-term efficacy assessment (Piga et al., 2006). Because of the dominating impact of iron influx from red blood cell transfusion on the efficacy of any iron chelator, these rates must be accurately estimated (Fischer et al., 2003, 2005).

In the follow-up of ex-thalassemic patients after bone marrow transplantation, biosusceptometry offers a useful tool for the management of chelation treatment

and monitoring iron redistribution effects (Fischer et al., 1997). Since class I patients with LIC < 2000 μg g_{ww}^{-1} have the best chance of survival (Lucarelli et al., 1995), BLS can also provide a valuable guide to adjusting chelation treatment prior to transplantation.

4.5.9.6 Future Applications

Future applications may especially address patients with relatively low ferritin levels as nontransfused thalassemia intermedia patients (Nielsen et al., 2000) and patients with myelodysplastic syndrome, where chelation treatment has been disregarded with respect to age and the cumbersome perfusion treatment with desferrioxamine, but may be resumed with novel oral chelators.

4.5.10 Summary and Outlook

At the time of publication of the first edition of this book, traditional BLS using low-T_C SQUIDS was the only available noninvasive routine method for the accurate assessment of body iron stores. By contrast, as reviewed herein, iron assessment is now undergoing rapid development, and several advanced but significantly less expensive susceptibility-based methods are emerging as attractive alternatives to traditional BLS. Moreover, developments in MRI also promise to provide an additional measurement modality. In our judgment, if the strong promise of even just one of the many new susceptibility-based methods can be realized in practice, the technique will offer strong advantages over any MRI-based method in terms of accuracy, cost, access, convenience and last – but not least – patient preference.

Finally, due to its clinical importance, heart iron assessment provides a natural focus for future susceptometry investigations. On account of the relatively low iron concentrations involved, and interfering signals from neighboring organs, the assessment of heart iron presents a technical challenge. Nonetheless, we believe that detection of levels of ~500 μg g_{ww}^{-1} (corresponding to a critical T_2* of ~10 ms) will eventually be within reach.

Acknowledgments

The authors acknowledge useful discussions with Rainer Engelhardt.

Abbreviations

BLS	biomagnetic liver susceptometry
HFE	hemochromatosis gene
LIC	liver iron concentration
MRI	magnetic resonance imaging
PH	primary (hereditary) hemochromatosis
SH	secondary hemochromatosis
SQUID	superconducting quantum interference device

References

Allen, P.D., St. Pierre, T.G., Chuanusorn, W., Strom, V., and Rao, K.V. (2000). Low-frequency low-field magnetic susceptibility of ferritin and hemosiderin. *Biochim. Biophys. Acta*, **1500**, 186–196.

Ambu, R., Crisponi, G., Sciot, R., VanEyken, P., Parodo, G., Iannelli, S., Marongiu, F., Silvagni, R., Nurchi, V., Costa, V., Faa, G., and Desmet, V.J. (1995). Uneven hepatic iron and phosphorous distribution in beta-thalassemia. *J. Hepatol.*, **23**, 544–549.

Anderson, L.J., Holden, S., Davis, B., Prescott, E., Charrier, C.C., Bunce, N.H., Firmin, D.N., Wonke, B., Porter, J., Walker, J.M., and Pennell, D.J. (2001). Cardiovascular T2-star (T2*) magnetic resonance for the early diagnosis of myocardial iron overload. *Eur. Heart J.*, **22**, 2171–2179.

Anderson, L., Wonke, B., Prescott, E., Holden, S., Walker, J., and Pennell, D. (2002). Comparison of effects of oral deferiprone and subcutaneous desferrioxamine on myocardial iron concentrations and ventricular function in beta-thalassaemia. *Lancet*, **360**, 516–520.

Angelucci, E., Brittenham, G.M., McLaren, C.E., Ripalti, M., Baronciani, D., Giardini, C., Galimberti, M., Polchi, P., and Lucarelli, G. (2000). Hepatic iron concentration and total body iron store in thalassemia major. *N. Engl. J. Med.*, **343**, 327–331.

Bastuscheck, C.M. and Williamson, S.J. (1985). Technique for measuring the ac susceptibility of portions of the human body or other large objects. *J. Appl. Phys.*, **58**, 3896–3906.

Bauman, J.H. and Harris, J.W. (1967). Estimation of hepatic iron stores by in vivo measurement of magnetic susceptibility. *J. Lab. Clin. Med.*, **70**, 246–257.

BLS-SOP (2004). Liver Iron Susceptometry with the SQUID Biomagnetometers at Hamburg Biosusceptometer (UKE), Torino Centro SQUID (TOR), Oakland Ferritometer (CHO). Hamburg-Torino-Oakland, 1–20.

Borgna-Pignatti, C., Rugolotto, S., De Stefano, P., Zao, H., Cappellini, M.D., Del Vecchio, G.C., Romeo, M.A., Forni, G.L., Gamberini, M.R., Ghilardi, R., Piga, A., and Cnaan, A. (2004). Survival and complications in patients with thalassemia major treated with transfusion and deferoxamine. *Haematologica*, **89**, 1187–1193.

Brittenham, G.M. (1988). Noninvasive methods for the early detection of hereditary hemo-chromatosis. *Ann. N. Y. Acad. Sci.*, **526**, 199–208.

Brittenham, G.M. and Badman, D.G. (2003). Noninvasive measurement of iron: report of an NIDDK workshop. *Blood*, **101**, 15–19.

Brittenham, G.M., Farrell, D.E., Harris, J.W., Feldmann, E.S., Danish, E.H., Muir, W.A., Tripp, J.H., and Bellon, E.M. (1982). Magnetic susceptibility measurement of human iron stores. *N. Engl. J. Med.*, **307**, 1671–1675.

Brittenham, G.M., Cohen, A.R., McLaren, C.E., Martin, M.B., Griffith, P.M., Nienhuis, A.W., Young, N.S., Allen, C.J., Farrell, D.E., and Harris, J.W. (1993). Hepatic iron stores and plasma ferritin concentration in patients with sickle cell anemia and thalassemia major. *Am. J. Hematol.*, **42**, 81–85.

Brittenham, G.M., Griffith, P.M., Nienhuis, A.W., McLaren, C.E., Young, N.S., Tucker, E.E., Allen, C.J., Farrell, D.E., and Harris, J.W. (1994). Efficacy of deferoxamine in preventing complications of iron overload in patients with thalassemia major. *N. Engl. J. Med.*, **331**, 567–573.

Brittenham, G.M., Taylor, C.M., Angelucci, E., and Olivieri, N.F. (1998). Long-term evaluation of the efficiency of iron chelation in thalassemia major with balance studies using hepatic iron concentration to determine body iron stores. *Blood*, **92** (Suppl. 1), 38b.

Brittenham, G.M., Sheth, S., Allen, C.J., and Farrell, D.E. (2001). Noninvasive methods for quantitative assessment of transfusional iron overload in sickle cell disease. *Semin. Hematol.*, **38** (Suppl. 1), 37–56.

Butensky, E., Fischer, R., Hudes, M., Schumacher, L., Williams, R., Moyer, T.P., Vichinsky, E., and Harmatz, P. (2005). Variability in hepatic iron concentration in percutaneous needle biopsy specimens from patients with transfusional hemosiderosis. *Am. J. Clin. Pathol.*, **123**, 146–152.

Carneiro, A.A., Fernandes, J.P., Zago, M.A., Vovas, D.T., Angulo, I.L., and Baffa, O. (2003). An alternating current superconductor susceptometric system to evaluate liver iron overload. *Rev. Sci. Instrum.*, **74**, 3098–3103.

Carneiro, A.A., Fernandes, J.P., De Araujo, D.B., Elias, J., Jr., Martinelli, A.L., Covas, D.T., Zago, M.A., Angulo, I.L., St. Pierre, T.G., and Baffa, O. (2005). Liver iron concentration evaluated by two magnetic methods: magnetic resonance imaging and magnetic susceptometry. *Magn. Reson. Med.*, **54**, 122–128.

Casanas, R., Scharfetter, H., Altes, A., Remacha, A., Sarda, P., Sierra, J., Merwa, R., Hollaus, K., and Rosell, J. (2004). Measurement of liver iron overload by magnetic induction using a planar gradiometer: preliminary human results. *Physiol. Meas.*, **25**, 315–323.

Chu, L., Cohen, A.R., Muthupillai, R., Chung, T., and Wang, Z.J. (2004). MRI measurement of hepatic magnetic susceptibility – phantom validation and normal subject studies. *Magn. Reson. Med.*, **52**, 1318–1327.

Clark, P.R. and St. Pierre, T.G. (2000). Quantitative mapping of transverse relaxivity (1/T2) in hepatic iron overload: a single spin-echo imaging methodology. *Magn. Reson. Imag.*, **18**, 431–438.

Della Penna, S., Del Gratta, C., Cianflone, F., Erné, S.N., Granata, C., Pentiricci, A., Pizella, V., Russo, M., and Romani, G.L. (2003). An ac magnetizing field biosusceptometer using a SQUID based sensor with additional compensation module. *IEEE Trans. Appl. Superconductivity*, **13**, 348–351.

Del Vecchio, G.C., Crollo, E., Schettini, F., Fischer, R., and De Mattia, D. (2000). Factors influencing effectiveness of deferiprone in a thalassaemia major clinical setting. *Acta Haematol.*, **104**, 99–102.

Engelhardt, R., Fischer, R., Nielsen, P., and Gabbe, E.E. (2000). Iron quantification by non-invasive biomagnetic organ susceptometry. In: Aine, C.J., Okada, Y., Stroink, G., Swithenby, S.J., and Wood, C.C. (Eds.), *BIOMAG96: Proceedings of the 10th International Conference on Biomagnetism*, Springer, New York, pp. 647–650.

Engelhardt, R., Fung, E.B., Kelly, P., Biehl, T.R., Pakbaz, Z., Nielsen, P., Harmatz, P., and Fischer, R. (2004). Interaction of artificial metallic objects with biosusceptometric measurements. *Neurol. Clin. Neurophysiol.*, **32**, 1–4.

Farrell, D.E., Tripp, J.H., Zanzucchi, P.E., Harris, J.W., Brittenham, G.M., and Muir, W.A. (1980). Magnetic measurement of human iron stores. *IEEE Trans. Magnetics*, **16**, 818–823.

Farrell, D.E., Tripp, J.H., Brittenham, G.M., Danish, E.H., Harris, J.W., and Tracht, A.E. (1983). A clinical system for accurate assessment of tissue iron concentration. *Nuovo Cimento*, **2D**, 582–593.

Feder, J.N., Gnirke, A., Thomas, W., et al. (1996). A novel MHC class I-like gene is mutated in patients with hereditary haemochromatosis. *Nat. Genet.*, **13**, 399–408.

Fischer, R. (1998). Liver iron susceptometry. In: Andrae, W. and Nowak, H. (Eds.), *Magnetism in Medicine – a Handbook*, Wiley-VCH, Berlin, pp. 286–301.

Fischer, R., Eich, E., Engelhardt, R., Heinrich, H.C., Kessler, M., and Nielsen, P. (1989). The calibration problem in liver iron susceptometry. In: Williamson, S.J.,

Hoke, M., Stroink, G., and Kotani, M. (Eds.), *Advances in Biomagnetism*, Plenum, New York, pp. 501–504.

Fischer, R., Engelhardt, R., Nielsen, P., Gabbe, E.E., Heinrich, H.C., Schmiegel, W.H., and Wurbs, D. (1992). Liver iron quantification in the diagnosis and therapy control of iron overload patients. In: Hoke, M., Erné, S.N., Okada, Y.C., and Romani, G.L. (Eds.), *Advances in Biomagnetism '91*, Elsevier, Amsterdam, pp. 585–588.

Fischer, R., Nielsen, P., Dürken, M., Engelhardt, R., Garofalo, F., Gamberini, M.R., Zander, A., Janka, G.E., Gabbe, E.E., and Piga, A. (1997). The method of biomagnetic liver susceptometry in the follow-up of thalassemic patients after BMT. *Bone Marrow Transpl.*, **19** (Suppl. 2), 136–138.

Fischer, R., Tiemann, C.D., Engelhardt, R., Nielsen, P., Dürken, M., Gabbe, E.E., and Janka, G.E. (1999). Assessment of iron stores in children with transfusion siderosis by biomagnetic liver susceptometry. *Am. J. Hematol.*, **60**, 289–299.

Fischer, R., Piga, A., Tricta, F., Nielsen, P., Engelhardt, R., Garofalo, F., Di Piama, A., and Vullo, C. (2000). Iron quantification by non-invasive biomagnetic organ susceptometry. In: Aine, C.J., Okada, Y., Stroink, G., Swithenby, S.J., and Wood, C.C. (Eds.), *BIOMAG96: Proceedings of the 10th International Conference on Biomagnetism*, Springer, New York, pp. 651–654.

Fischer, R., Engelhardt, R., and Nielsen, P. (2002). The influence of thorax tissue in biomagnetic liver susceptometry (BLS). In: Nowak, H., Haueisen, J., Giessler, F., and Huonker, R. (Eds.), *Biomag 2002: Proceedings of 13th International Conference on Biomagnetism*, VDE Verlag, Berlin, pp. 1063–1065.

Fischer, R., Longo, F., Nielsen, P., Engelhardt, R., Hider, R.C., and Piga, A. (2003). Monitoring long-term efficacy of iron chelation therapy by deferiprone and desferrioxamine in patients with β-thalassaemia major: application of SQUID biomagnetic liver susceptometry. *Br. J. Haematol.*, **121**, 918–948.

Fischer, R., Piga, A., Harmatz, P., and Nielsen, P. (2005). Monitoring long-term efficacy of iron chelation treatment with biomagnetic liver susceptometry. *Ann. N. Y. Acad. Sci.*, **1054**, 350–357.

Fung, E.B., Fischer, R., Fagaly, R.L., Pakbaz, Z., Vichinsky, E., Starr, T.N., Ewing, T., Paulson, D.N., Hassenzahl, W.V., and Harmatz, P. (2004). The new SQUID biosusceptometer at Oakland: first year of experience. *Neurol. Clin. Neurophysiol.*, **5**, 1–4.

Fung, E.B., Longo, F., Fischer, R., Engelhardt, R., Pakbaz, Z., Opitz, H., Fagaly, R.L., Nick, H.P., Nielsen, P., Vichinsky, E., Piga, A., and Harmatz, P. (2005). Comparison of liver iron concentration measured by the SQUID biosusceptometers at Hamburg, Torino, and Oakland in patients with thalassemia and sickle cell disease. *Blood*, **106** (11), 3721.

Gabutti, V. and Piga, A. (1996). Results of long-term iron chelating therapy. *Acta Haematol.*, **95**, 26–36.

Gandon, Y., Olivie, D., Guyader, D., Aube, C., Oberti, F., Sebille, V., and Deugnier, Y. (2004). Non-invasive assessment of hepatic iron stores by MRI. *Lancet*, **363** (9406), 357–362.

Gordeuk, V.R., Caleffi, A., Corradini, E., Ferrara, F., Jones, R.A., Castro, O., Onyekwere, O., Kittles, R., Pignatti, E., Montosi, G., Garuti, C., Gangaidzo, I.T., Gomo, Z.A., Moyo, V.M., Rouault, T.A., MacPhail, P., and Pietrangelo, A. (2003). Iron overload in Africans and African-Americans and a common mutation in the SCL40A1 (ferroportin 1) gene. *Blood Cells Mol. Dis.*, **31**, 299–304.

Hartmann, W., Schneider, L., Wirth, A., Dördelmann, M., Zinser, D., Elias, H., Languth, W., Ludwig, L., and Kleihauer, E. (1992). Liver susceptometry for the follow up of transfusional iron overload. In: Hoke, M., Erné, S.N., Okada, Y.C., and Romani, G.L. (Eds.), *Advances in Biomagnetism '91*, Elsevier, Amsterdam, pp. 585–588.

Heinrich, H.C., Gabbe, E.E., Oppitz, K.H., Whang, D.H., Bender-Götze, C., Schäfer, K.H., Schröter, W., and Pfau, A. (1973). Absorption of inorganic and food iron in children with heterozygous and homozygous β-thalassemia. *Z. Kinderheilk.*, **115**, 1–22.

Hershko, C., Link, G., and Cabantchik, J. (1998). Pathophysiology of iron overload. *Ann. N. Y. Acad. Sci.*, **850**, 191–201.

Jensen, P.D., Jensen, F.T., Christensen, T., Heickendorff, L., Jensen, L.G., and Ellegaard, J. (2001). Indirect evidence for

the potential ability of magnetic resonance imaging to evaluate the myocardial iron content in patients with transfusional iron overload. *MAGMA*, **12**, 153–166.

Kumar, S., Avrin, W.F., Hecht, D., Trammel III, H.S., Perry, A.R., Freeman, W.N., and McManus, T. (2002). A room-temperature susceptometer to measure liver iron: susceptometer design and performance. In: Nowak, H., Haueisen, J., Giessler, F., and Huonker, R. (Eds.), *Biomag 2002: Proceedings of 13th International Conference on Biomagnetism*, VDE Verlag, Berlin, pp. 1066–1068.

Lucarelli, G., Giardini, C., and Baronciani, D. (1995). Bone marrow transplantation in thalassemia. *Semin. Hematol.*, **32**, 297–303.

Marinelli, M., Gianesin, B., Lavagetto, A., Lamagna, M., Oliveri, E., Terenzani, L., and Forni, G.L. (2005). Preliminary results of full body iron overload measurement by a magnetic susceptometer. *Blood*, **106** (11), 3714.

Meo, A., Ruggeri, A., La Rosa, M.A., Zanghi, L., Kordes, U., and Fischer, R. (2005). Long-term treatment with deferiprone in a L1 veteran. *Eur. J. Haematol.*, **74**, 523–525.

Merryweather-Clarke, A.T., Pointon, J.J., Shearman, J.D., and Robson, K.J. (1997). Global prevalence of putative haemochromatosis mutations. *J. Med. Genet.*, **34**, 275–278.

Michaelis, L., Coryell, C.D., and Granick, S. (1943). Ferritin III: the magnetic properties of ferritin and some other colloidal ferric compounds. *J. Biol. Chem.*, **148**, 463–480.

Nachtigall, D., Nielsen, P., Fischer, R., Engelhardt, R., and Gabbe, E.E. (1996). *Int. J. Sports Med.*, **17**, 473–479.

Nielsen, P., Fischer, R., Engelhardt, R., Tondury, P., Gabbe, E.E., and Janka, G.E. (1995). Liver iron stores in patients with secondary haemosiderosis under iron chelation therapy with deferoxamine or deferiprone. *Br. J. Haematol.*, **91**, 827–833.

Nielsen, P., Engelhardt, R., Duerken, M., Janka, G.E., and Fischer, R. (2000). Using SQUID biomagnetic liver susceptometry in the treatment of thalassemia and other iron loading diseases. *Transfus. Sci.*, **23**, 257–258.

Nielsen, P., Kordes, U., Fischer, R., Engelhardt, R., and Janka, G.E. (2002). SQUID-Biosuszeptometrie bei Eisenüberladungskrankheiten in der Haematologie. *Klin. Paediatr.* **214**, 218–222.

Nielsen, P., Fischer, R., Engelhardt, R., and Düllmann, J. (2003a). Diagnosis of hereditary haemochromatosis using non-invasive methods. *Transfus. Med. Hemother.*, **30**, 27–36.

Nielsen, P., Fischer, R., Buggisch, P., and Janka, G.E. (2003b). Effective treatment of hereditary haemochromatosis with desferrioxamine in selected cases. *Br. J. Haematol.*, **123**, 952–953.

Nielsen, P., Fischer, R., Engelhardt, R., and Janka-Schaub, G.E. (2005). Monitoring of liver iron in children with HFE-related hereditary haemochromatosis. *BioIron 2005: First Congress International Bioiron Society*, Prague, P235 (abstract).

Olivieri, N.F., Brittenham, G.M., Matsui, D., Berkovitch, M., Blendis, L.M., Cameron, R.G., McClelland, R.A., Liu, P.P., Templeton, D.M., and Koren, G. (1995). Iron-chelation therapy with oral deferiprone in patients with thalassemia major. *N. Engl. J. Med.*, **332**, 918–922.

Paulson, D.N., Engelhardt, R., Fischer, R., and Heinrich, H.C. (1989). The Hamburg Biosusceptometer for liver iron quantification. In: Williamson, S.J., Hoke, M., Stroink, G., and Kotani, M. (Eds.), *Advances in Biomagnetism*, Plenum, New York, pp. 497–500.

Paulson, D.N., Fagaly, R.L., Toussaint, R.M., and Fischer, R. (1991). Biomagnetic susceptometer with SQUID instrumentation. *IEEE Trans. Magnetics*, **27**, 3249–3252.

Piga, A., Galanello, R., Forni, G.L., Cappelini, M.D., Origa, R., Zappu, A., Guido, D., Bordone, E., Lavagetto, A., Zanaboni, L., Sechaud, R., Latham, N., Ford, J.M., Opitz, H., and Alberti, D. (2006). Randomized phase II trial of deferasirox (Exjade, ICL670), a once-daily orally-administered iron chelator, in comparison to deferoxamine in thalassemia patients with transfusional iron overload. *Haematologica*, **91**, 52–59.

Pippard, M.J. (1994). In: Brock, J.H., Halliday, J.W., Pippard, M.J., and Powell, L.W. (Eds.), *Iron Metabolism in Health and Disease*, Saunders, London, pp. 271–309.

Porter, J.B. (2005). Monitoring and treatment of iron overload: state of the art and new approaches. *Semin. Hematol.*, **42** (2), S14–S18.

Roetto, A. and Camaschella, C. (2005). New insights into iron homeostasis through the study of non-HFE hereditary haemochromatosis. *Best. Pract. Res. Clin. Haematol.*, **18**, 235–250.

Schoffa, G. (1965). Der Antiferromagnetismus des Ferritins bei Messungen der magnetischen Suszeptibilität im Temperaturbereich von 4.2 bis 300 °K. *Z. Naturforsch.*, **20** (b), 167–172.

Sheth, S.S. (2003). SQUID biosusceptometry in the measurement of hepatic iron. *Pediatr. Radiol.*, **33**, 373–377.

Shoden, A. and Sturgeon, P. (1960). Hemosiderin – a physico-chemical study. *Acta Haematol.*, **23**, 376–392.

Sosnitsky, V.N., Budnik, N.N., Minov, Y.D., Sutkovoj, P.I., and Vojtovich, I.D. (2000). System for magnetic susceptibility investigations of human blood and liver. In: Aine, C.J., Okada, Y., Stroink, G., Swithenby, S.J., and Wood, C.C. (Eds.), *BIOMAG96: Proceedings of the 10th International Conference on Biomagnetism*, Springer, New York, pp. 683–686.

Starr, T.N., Fischer, R., Ewing, T., Longo, F., Engelhardt, R., Trevisiol, E., Fagaly, R.L., Paulson, D.N., and Piga, A. (2001). A new generation SQUID biosusceptometer. In: Nenonen, J., Ilmoniemi, R.J., and Katila, T. (Eds), *Biomag 2000: Proceedings of the 12th International Conference on Biomagnetism*, University of Technology, Helsinki, pp. 986–989.

St. Pierre, T.G., Clark, P.R., Chuanusorn, W., Fleming, A.J., Jeffrey, G.P., Olynyk, J.K., Pootrakul, P., Robins, E., and Lindeman, R. (2005). Noninvasive measurement and imaging of liver iron concentrations using proton magnetic resonance. *Blood*, **105**, 855–861.

Tang, H., Jensen, J.H., Sheth, S., Swaminathan, S., Azabagic, A., Tosti, C., Brittenham, G.M., and Brown, T.R. (2005). MR measurement of ferritin and hemosiderin in patients with iron overload. *Proc. Intl. Soc. Mag. Med.*, **13**, 1880.

Töndury, P., Zimmermann, A., Nielsen, P., and Hirt, A. (1998). Liver iron and fibrosis during long-term treatment with deferiprone in Swiss thalassaemic patients. *Br. J. Haematol.*, **101**, 413–415.

Tripp, J.H. (1983). Physical concepts and mathematical models. In: Williamson, S.J., Romani, G.L., Kaufman, L., and Modena, I. (Eds.), *Biomagnetism: an Inter-disciplinary Approach*, Plenum Press, New York, pp. 101–139.

Villeneuve, J.P., Bilodeau, M., Lepage, R., Coté, J., and Lefebvre, M. (1996). Variability in hepatic iron concentration measurement from needle-biopsy specimens. *J. Hepatol.*, **25**, 172–177.

Vymazal, J., Urgosik, D., and Bulte, J.W. (2000). Differentiation between hemosiderin- and ferritin-bound brain iron using nuclear magnetic resonance and magnetic resonance imaging. *Cell. Mol. Biol.*, **46**, 835–842.

Wang, Z.J., Li, S., and Haselgrove, J.C. (1999). Magnetic resonance imaging measurement of volume magnetic susceptibility using a boundary condition. *J. Magn. Reson.*, **140**, 477–481.

Williamson, S.J. and Kaufman, L. (1981). Biomagnetism. *J. Magn. Magn. Mat.*, **22**, 129–202.

Westwood, M., Anderson, L.J., Firmin, D.N., Gatehouse, P.D., Charrier, C.C., Wonke, B., and Pennell, D.J. (2003). A single breath-hold multiecho T2* cardiovascular magnetic resonance technique for diagnosis of myocardial iron overload. *J. Mag. Reson. Imag.*, **18**, 33–39.

Wood, J.C., Tyszka, J.M., Carson, S., Nelson, M.D., and Coates, T.D. (2004). Myocardial iron loading in transfusion-dependent thalassemia and sickle cell disease. *Blood*, **103**, 1934–1936.

Wood, J.C., Enriquez, C., Ghugre, N., Tyzka, J.M., Carson, S., Nelson, M.D., and Coates, T.D. (2005). MRI R2 and R2* mapping accurately estimates hepatic iron concentration in transfusion-dependent thalassemia and sickle cell disease patients. *Blood*, **106**, 1460–1465.

4.6
Magnetic Hyperthermia and Thermoablation

Rudolf Hergt and Wilfried Andrä

4.6.1
Introduction

The healing power of heat has been known for a very long time, and used to cure a variety of different diseases. A new concept appeared however when heat treatment was recognized as a new and promising form of cancer therapy aside from the well-known methods of surgery, chemotherapy, and irradiation. O'Brien and Mekkaoui (1993) noted that, more than a century ago, Busch (1866) found cancer growth to be stopped at temperatures higher than about 42 °C, whereas normal cells could tolerate even higher temperatures (Gordon et al., 1979). At present, there is a wide spectrum of different methods of hyperthermia available. In addition to whole-body hyperthermia, where the systemic temperature must be carefully controlled at, for example 41.8 ºC (Robins et al., 1997), there are different ways of local intracorporeal heat generation, including capacitive or inductive coupling of radiofrequency (RF) fields, microwave radiation, ultrasound, perfusion therapy, interstitial laser photocoagulation and heat administered by external contact. A recent review provides the present clinical state of the art on hyperthermia in oncology (Falk and Issels, 2001).

There is in fact no strict borderline between tolerable and mortal temperatures, both on the systemic and cellular levels. Accordingly, there is a range of temperature elevation which is considered to be therapeutically useful. With increasing temperature different mechanisms of cell damage occur, and hence two therapy modalities may be differentiated:

- Treatments at temperatures of 42–45 °C for up to few hours – commonly denoted as *hyperthermia* – require combination with assisting other toxic agents (mostly irradiation or chemotherapy) for the reliable damage of tumor cells.
- In contrast, *thermoablation* is conceived as a therapy modality which aims at the thermal killing of all tumor cells. Therefore, temperatures in excess of at least 50 °C are generated in the tumor region for exposure times as short as a few minutes.

It should be pointed out that the curing chances of thermoablation in comparison to hyperthermia are generally rated as "controversial" in the literature. While Hilger et al. (2001) suggested magnetic thermoablation by heating magnetic particles at 55 °C for several minutes as a modality for the treatment of breast cancer, Jordan et al. (1997a) proposed that "... thermoablation is mostly undesired because of the critical systemic side effects and further clinical complications." Likewise, Moroz et al. (2002) referred to the risk of a shock syndrome due to a sudden release of large amounts of necrotic tumor material and major inflammatory response.

From the beginning, two essential problems have been identified:

- The generation of increased temperatures only within the target region, including a certain fringe area of the healthy tissue but leaving all other regions unaffected.
- Temperature control within, as well as outside, the target region.

Until now, neither problem has been solved satisfactorily.

Almost 50 years ago, Gilchrist and colleagues raised the hope of solving at least the first of the two above-mentioned problems by the application of magnetic principles (Gilchrist et al., 1957). By injecting a magnetic nanoparticle suspension into tumor tissue, the heat generated in an external alternating magnetic field may be concentrated mainly onto the particle-containing tissue portion. Later, suggestions for an automatic limitation of the temperature were made, again on the basis of magnetic means (e.g., Rand et al., 1985; Brezovich, 1988). Recently, the current status of magnetically mediated hyperthermia was critically reviewed by Moroz et al. (2002), who concluded that, to date, progress has been somewhat slow, but that the final success may be realized during the next decade. With regards to clinical applications, the so-called interstitial implant hyperthermia is clearly the most advanced technique (Moroz et al., 2002). In the case of magnetic particle hyperthermia, the initiation of the first clinical trials to prove feasibility and tolerability was reported recently (Gneveckow et al., 2005).

This section mainly describes the magnetically mediated heating via losses in small magnetic particles exposed to alternating magnetic fields. It is focused on the underlying principles of particle magnetism in order to provide an understanding of physical and technical limitations of this therapy method. Known results from literature are summarized mainly from a physical point of view, and a comparison with recent biomedical results is presented.

4.6.2
Physical Principles of Magnetic Particle Heating

Heating of magnetic substances in an external alternating magnetic field may be related to several physical mechanisms. The main magnetic loss process is associ-

ated with hysteresis occurring during reversal of the magnetization (see Sections 4.6.2.1 and 4.6.2.2). With decreasing particle size, the energetic barriers for magnetization reversal also decrease, and finally match thermal energy. In these so-called "superparamagnetic particles", losses follow special laws (see Section 4.6.2.3). Since an alternating magnetic field induces eddy currents in the tissue, the inductive RF method sometimes is also referred to as *magnetic hyperthermia*. This effect of eddy currents (see Section 4.6.2.4) is undesirable in magnetic particle hyperthermia as it is present in tumor tissue as well as in the surrounding healthy tissue. Eddy current-induced heating of small magnetic particles is negligible in comparison to the purely magnetic heating. Insofar, the term "inductive heating" – which is often used for magnetic particle heating in the biomedical literature – is misleading.

In systems of magnetic particles the energy is absorbed from an alternating (or rotating) magnetic field and is transformed into heat via at least one of the following mechanisms:

- Reversal of magnetization inside a magnetic particle.
- Rotation of the magnetic particle in a fluid suspension relative to the surroundings.

In order to compare different particle types, the amount of heat produced during one cycle of the alternating field is related to the mass of particles. The latter can be determined much more easily than volume; hence this relationship is denoted as the *specific magnetic loss energy*, W. The corresponding specific loss power, L (given in W g^{-1} of a specific material) is obtained by multiplying W with the frequency ν of the alternating field:

$$L(\nu) = W(\nu) \cdot \nu \tag{4.10}$$

taking into account that the losses W may also depend on the frequency and amplitude of the alternating field. Accordingly, these parameters of measurement must be specified in order to characterize the material.

4.6.2.1
Losses during Magnetization Reversal within the Particles

The magnetization reversal is usually described by the well-known hysteresis loop which is considered in Section 1.2 (see Fig. 1.21) from a physical viewpoint. Here, we treat the topic with respect to practical applications and define the specific magnetic losses as the area enclosed by the two branches (for increasing and decreasing field strength H) of the specific magnetization M/ρ as function of the field strength H

$$W_{\text{hys}} = \frac{\mu_0}{\rho} \cdot \oint M_H(H)\, dH \tag{4.11}$$

where $\mu_0 = 4\pi \times 10^{-7}$ Vs $(\mathrm{Am})^{-1}$ is the vacuum permeability, and ρ is the mass density of the magnetic material. M_H is the component of the magnetization parallel to the magnetic field. The variation of the magnetization M with the magnetic field strength H is a complicated process (see Section 1.2) which may considerably differ for different particle types. There are, however, some theoretical models, for example the magnetization reversal of so-called single-domain particles with uniaxial magnetic anisotropy treated by Stoner and Wohlfarth (1948), as well as several cases of a more complicated behavior which are described in terms of the micromagnetic theory (Shtrikman and Treves, 1963). However, the experimental confirmation of these theoretical models remains open, mainly due to the fact that the objects are very small. Only recently were modern methods of electron microscopy seen to offer possibilities for the direct depiction of processes of magnetization reversal in individual particles with diameters of less than 100 nm (Dunin-Borkowski et al., 2001). This range is of special interest because it is near to the theoretically expected transition from the multidomain state to the state where magnetic domain walls are not existing (Fabian et al., 1996). For further information, the reader is referred to the analysis provided by Hubert and Schäfer (1998). In Figure 4.32, experimental hysteresis loops of different magnetic iron oxide particles (e.g., a typical chemically precipitated sample m6.3, a sample BASF1 of acicular particles for recording applications and magnetosomes synthesized by bacteria) are compared with a theoretical loop of so-called Stoner–Wohlfarth particles. The dependence of hysteresis loss on field amplitude is shown in Figure 4.33 for the samples of Figure 4.32 in comparison to the theoretical Stoner–Wohlfarth curve. There are considerable deviations between the experimental results and theory.

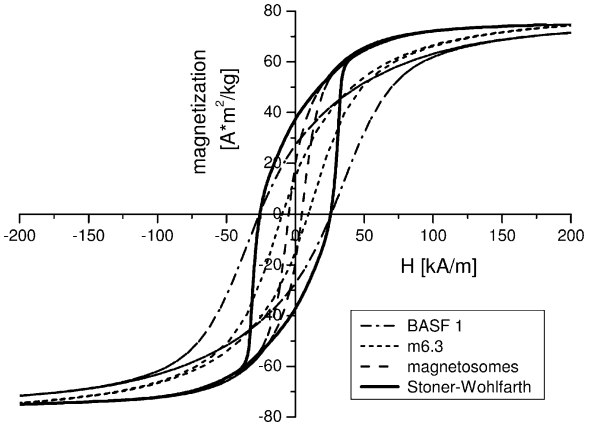

Fig. 4.32. Hysteresis loops of the specific magnetization as a function of the magnetic field for a chemically precipitated sample (m6.3; Dutz et al., 2005), a sample of commercial magnetic recording particles (BASF1), and magnetosomes (Hergt et al., 2005) in comparison with the loop of randomly oriented Stoner–Wohlfarth (S-W) particles. The S–W coercivity is adjusted to that of BASF1.

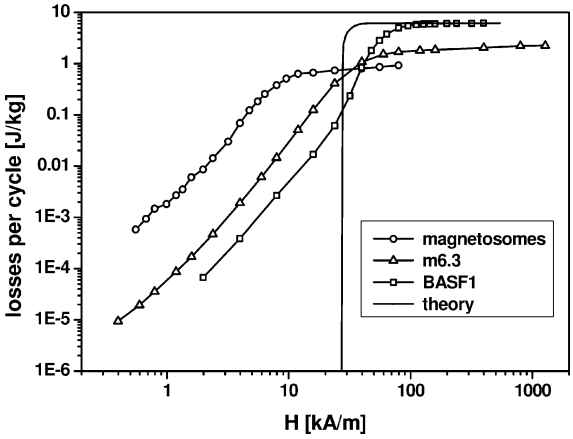

Fig. 4.33. Dependence of hysteresis losses per cycle on field amplitude for the samples shown in Figure 4.32.

Above a critical size domain walls exist in magnetic particles. If the motion of those walls is hindered by pinning centers, so-called Rayleigh losses occur for small amplitudes of the alternating magnetic field. Their dependence on the amplitude $H_{\max}$ was explained by Néel (1942, 1943) resulting in the formula:

$$W_{\text{hys}} = C_R \cdot (H_{\max})^3 \tag{4.12}$$

where C_R is determined by properties of the specific material. It may differ by orders of magnitude for different materials, as may be deduced from Figure 4.33.

From the practical point of view, large losses ought to be achieved with minimum effort – that is, with field amplitudes as low as possible. For low field amplitudes ($H < 10$ kA m^{-1}) the different curves in Figure 4.33 are almost in agreement with Eq. (4.12), while for greater amplitudes there are considerable deviations and none of the known theoretical predictions is met. The highest specific losses at low amplitudes are found for iron-oxide particles (mean diameter ≈ 35 nm) synthesized by magnetotactic bacteria (Hergt et al., 2005) (also shown in Fig. 4.33). Their size is near to that theoretically predicted for the transition of single-domain particles of magnetite (Fe_3O_4) from the low remanence (curling-) state to the high remanence (flower-) state (Fabian et al., 1996).

4.6.2.2 Losses Caused by Rotational Motion of Particles

In the preceding paragraph the ferromagnetic objects are assumed to remain fixed with respect to the surrounding medium. If, however, this medium is a liquid, the alternating magnetic field may also cause oscillating or rotating motions of the par-

ticles. In cases where the field amplitude does not exceed a certain critical value, magnetization of the particles remains essentially unaffected and the particle reacts as permanent magnet with a certain mass of inertia giving rise to losses caused by friction in the surrounding liquid. To illustrate this, the stationary rotation (frequency ν) of a sphere (mass m, density ρ) in a liquid (viscosity η) forced by a rotating magnetic field may be investigated. According to the theory of viscous friction (Landau and Lifshitz, 1978), the losses per cycle related to the mass of the sphere will be:

$$W_{\text{rot}} = 24 \cdot \pi^2 \cdot \eta \cdot \nu/\rho \tag{4.13}$$

Interestingly, these specific losses depend neither on the size of the sphere nor on the field amplitude, provided that the amplitude is sufficiently strong to overcome the torque exerted by the viscous friction. The required minimum field amplitude is given by:

$$H_{\min} = 12 \cdot \pi \cdot \eta \cdot \nu/(\mu_0 \cdot M_R) \tag{4.13a}$$

where M_R is the remanent magnetization of the rotating sphere. Introducing the viscosity of water ($\eta = 10^{-3}$ Pa·s) and a frequency of 70 kHz, the minimum field for magnetite (Fe_3O_4) assuming $M_R \approx 2.3 \times 10^5$ A m^{-1} evaluates as $H_{\min} \approx 10$ kA m^{-1}. Then, according to Eq. (4.13), the losses related to the mass of the sphere achieve $W_{\text{rot}} \approx 3$ J kg^{-1}. Rotational losses in rotating fields of 5 kA m^{-1} at 500 Hz were investigated by Knauft et al. (2004), using macroscopic spheres of NdFeB in silicone oil. Since the losses described by Eq. (4.13) are independent of the size of the sample, small particles in an aqueous liquid may also exhibit rotational losses, provided that they are in a suspended state and not immobilized by sticking on solid tissue elements.

4.6.2.3
Thermal Relaxation Effects in Magnetic Nanoparticles

Heating of magnetic particles in an alternating magnetic field may be understood in terms of several types of energetic barriers which must be overcome for reversal of the magnetic moments. With decreasing particle size, these barriers decrease and the probability of jumps of the spontaneous magnetization due to thermal activation processes increases. Accordingly, relaxation effects may be observed if the measurement frequency is smaller than the characteristic relaxation frequency of the particle system. The latter one may be understood in the frame of a model of two energy levels which are separated by an energy barrier being proportional to the anisotropy energy KV (V particle volume). Then, the so-called Neél relaxation time of the system is determined by the ratio of anisotropy energy KV to thermal energy kT (Néel, 1949):

$$\tau_N = \tau_o \exp[\text{KV}/(\text{kT})] \quad (\tau_o \sim 10^{-9} \text{ s}) \tag{4.14}$$

A critical grain volume V_c may be defined by $\tau_N(V_c) = \tau_m$ (τ_m characteristic time of measurement). For a measuring frequency of 300 kHz and a magnetic anisotropy energy density of 10^4 J m^{-3} (for magnetite particles of ellipsoidal shape with an aspect ratio of 1.4), the critical diameter is about 20 nm. The relaxation effects cause vanishing of the remanent magnetization, coercivity as well as hysteresis losses below the critical size. This transition to superparamagnetism occurs in a narrow frequency range. As a consequence, particles, which show superparamagnetic behavior in loop measurements at 50 Hz may give full hysteresis losses at 500 kHz. Losses in the ''superparamagnetic'' regime also lead to heating of the particle ensemble, and may be used for hyperthermia. The loss power density for a magnetic material in an alternating field of small amplitude H and frequency ν is given in linear approximation by (e.g., Landau and Lifschitz, 1960):

$$\mathrm{P}(\nu, H) = \mu_o \pi \chi''(\nu) \mathrm{H}^2 \nu \tag{4.15}$$

where $\chi''(\nu)$ is the imaginary part of susceptibility given in the simplest approximation (see e.g. Bertotti, 1998) by (M_S saturation magnetization)

$$\chi''(\nu) = \chi_o \phi/(1+\phi^2), \quad \phi = \nu\tau_N \quad \chi_o = \mu_o {M_S}^2 V/(\mathrm{kT}) \tag{4.16}$$

According to these equations, at low frequencies ($\phi \ll 1$) – that is, in the superparamagnetic regime – losses increase with the square of frequency, while for $\phi \gg 1$ losses saturate at $\mathrm{P} = \mu_o \pi \mathrm{H}^2 \chi_o/\tau_N$ – that is, the losses become independent of frequency. At the transition between these two regimes, the spectrum of the imaginary part of the susceptibility has a peak which is related via Eq. (4.14) to the mean particle size. The very strong size dependence of the relaxation time according to this equation leads to a very sharp maximum of the loss power density in dependence on particle size (cf. Fig. 2 of Hergt et al., 2002). Therefore, one may expect a remarkable output of heating power only for careful adjustment of field parameters (frequency and amplitude H) in accordance with particle properties (size and anisotropy). Otherwise, power density remains orders of magnitude too low. Moreover, one may expect for commonly observed log-normal size distributions of commercial particles that the majority of particles do not meet the condition $\phi = 1$ and deliver only negligible contribution to the specific heating power of the magnetic fluid. The same reasoning refers to the anisotropy, which appears besides particle volume in Eq. (4.14). In addition to the crystal anisotropy, small deviations from isometrical shapes lead to remarkable shape anisotropy, the variance of which may also result in a wide spread of relaxation times. The effect of size distribution on loss power density was elucidated by Rosensweig (2002). Clearly, preparation conditions must be optimized with respect to as far as possible homogeneity of the particle ensemble. For example, Hergt et al. (2004a) have reported on maghemite particles which, due to a special preparation technique, have a narrow size distribution resulting in a specific loss power of 600 W g^{-1} (at 11 kA m^{-1}

and 400 kHz) in comparison with values below 100 W g^{-1} for particles prepared by common chemical precipitation.

In addition to the discussed Neél losses which are caused by the reversal of magnetic moments inside the particles, a further loss type may arise due to particle rotation in the case of liquid suspensions of magnetic particles. This effect becomes essential if the magnetic moment direction is strongly coupled to the particle itself, for example by a large value of the magnetic anisotropy, combined with easy particle rotation due to a low viscosity η of the suspension medium. For spherical particles with the hydrodynamic radius r_h (which due to, for example, particle coating may be essentially larger than the radius of the magnetic particle core), the so-called Brownian relaxation time is given by

$$\tau_B = 4\pi\eta {r_h}^3/(\mathrm{kT}) \tag{4.17}$$

This expression was first derived by Debye (1929) for rotational polarization of molecules. The loss power density is given for Brown relaxation again by Eqs. (4.15) and (4.16), taking Eq. (4.17) as relaxation time. The dependence of loss power density on size is different from the case of Néel relaxation. It increases monotonously with particle size up to a saturation value for $\phi \gg 1$, as shown in the review of Hergt et al. (2002). For magnetite in water at a field amplitude of 8 kA m^{-1}, saturation may be estimated to be in the order of 100 W g^{-1}. The useful frequency is given according to the condition $\phi \gg 1$ by the mean particle size (e.g., $\nu = 10$ kHz for 40-nm hydrodynamic diameter).

In the general case, if both Néel and Brown relaxation are present, the effective relaxation time is

$$\tau_{\mathrm{eff}} = \tau_N \tau_B/(\tau_N + \tau_B) \tag{4.18}$$

The importance of Brown relaxation may be well illustrated by the measured susceptibility spectra shown in Figure 4.34 (Hergt et al., 2004a). By comparing the experimental points determined for the fluid suspension with the data of the same particles immobilized in gel, the effect of Brown relaxation becomes clear. The low-frequency peak of χ'' for the liquid suspension represents Brown losses. After immobilization, there is a remarkable reduction of χ'' near the Brown relaxation peak. Consequently, a considerable reduction in specific heating power may be expected when particles circulating in blood become attached to tumor cells or enter the cell plasma. However, the results of Figure 4.34 show that this detrimental effect may be avoided by choosing a suitable frequency of the external magnetic field well above the Brown peak. The experimental data points may be approximated satisfactorily (solid and dashed lines) by combining the above-described Eqs. (4.14) to (4.18) with the experimental size distribution determined by electron microscopy (for details, see Hergt et al., 2004a). The loss power density calculated by Eq. (4.15) is confirmed by calorimetric measurements which give a specific loss power of 600 W g^{-1} in a field of 400 kHz and 11 kA m^{-1}.

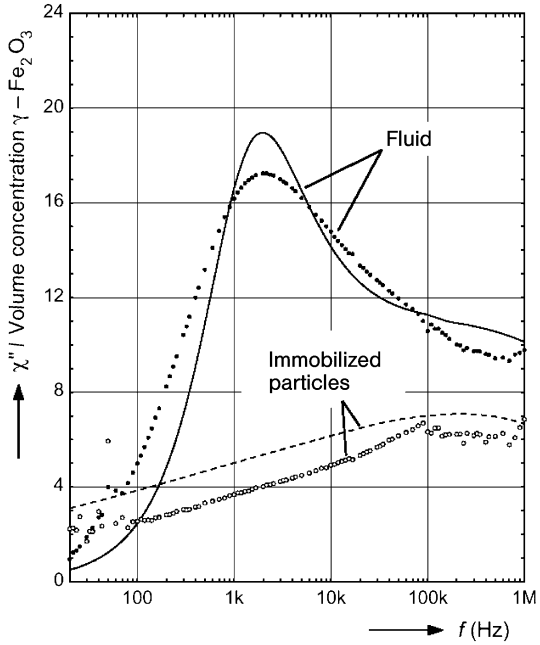

Fig. 4.34. Imaginary part of the specific susceptibility χ'' as function of the frequency. Experimental results (dots) are plotted of an aqueous maghemite ferrofluid and of the same particles immobilized in gel in comparison with calculated spectra (solid and dashed lines). (Reprinted from Hergt et al., 2004a, with permission from Elsevier).

4.6.2.4
Eddy Current Effects

The generation of eddy currents is a consequence of the law of induction (see Eq. (1.8) in Section 1.2), and is not restricted to magnetic materials. This process, however, provides an essential heating effect only in electrically conducting materials of macroscopic size. In particular, the high electrical conductivity of metals yields considerable currents in a closed circuit surrounding an alternating magnetic flux. The corresponding method of hyperthermia using implanted, electrically conducting seeds is described in detail by Brezovich (1988). Unfortunately, eddy current hyperthermia is a highly invasive method, because the implanted parts (preferably needle-shaped cylinders) typically have a diameter of 1 mm and must be arranged in arrays covering the whole region of the tumor. This drawback may be why the so-called "thermoseeds" were not widely accepted in the clinical scenario. In small oxide particles, eddy current losses cannot contribute any comparable heating effect because the heating power decreases with decreasing diameter of the conducting material.

As mentioned above, eddy currents are also induced in the tissue, but the specific electrical conductivity is much less than that of a metal (typically $\sigma_{\text{tissue}} \approx 0.6$

$(\Omega m)^{-1}$ as compared to $\sigma_{copper} \approx 6 \times 10^7\ (\Omega m)^{-1}$). On the other hand, the diameter of the region exposed to the alternating field may be relatively large. In the case of whole-body treatments, a diameter of approximately 30 cm may be assumed. For this situation, Brezovich (1988) found that a "... test person had a sensation of warmth, but was able to withstand the treatment for more than one hour without major discomfort" if the product $H \cdot \nu$ was below

$$(H \cdot \nu)_{crit} = 4.85 \times 10^8\ A/(m \cdot s) \tag{4.19}$$

Depending on the diameter of the exposed body region, on the duration of treatment, and on the seriousness of the illness, this critical product may be exceeded. However, it should be borne in mind that the specific loss power L_{edd} of tissue increases with the square of $(H \cdot \nu)$. As the results of an earlier study (Borrelli et al., 1984) exhibit deviations from Eq. (4.19), further detailed investigations are desirable.

4.6.3 Physical-Technical Implementation of the Therapy

4.6.3.1 Demand of Specific Heating Power

The demand of specific heating power of magnetic particles for hyperthermia is determined, first, by the temperature elevation needed to damage the cancer cells, and second by the concentration of magnetic particles in the tissue selected for therapy. Temperature elevations considered to be therapeutically useful vary between a few K for hyperthermia up to about 15 K for thermoablation. The temperature elevation in tumor tissue is a result of the balance of the two competing processes of heat generation within the magnetic nanoparticles and heat depletion into surrounding tissue mainly due to heat conduction. Accordingly, the intratumoral particle concentration needed for a defined temperature increase may be estimated for a given specific heating power of the magnetic material by solving the heat conductivity problem as given by Andrä et al. (1999). The so-called "bioheat equation" (Sonnenschein, 1986), which takes into account heat depletion due to blood perfusion, must be regarded only when there are large vessels in the immediate neighborhood of the tumor, or if the heating power is very low. In this situation, the physiological vasodilatation in normal tissue may be overcompensated in tumor tissue under hyperthermic conditions (Vaupel et al., 1986). For thermoablation – that is, a temperature elevation of 15 K at the tumor border – Figure 4.35 shows the dependence of the required heating power on the radius of an approximately spherical tumor for three values of particle concentration supplied in the tumor tissue. While a concentration of more than 0.1 g magnetite per cm^3 tumor tissue rarely may be practicable (for example by direct injection), concentrations for antibody-mediated particle targeting may be expected to be below

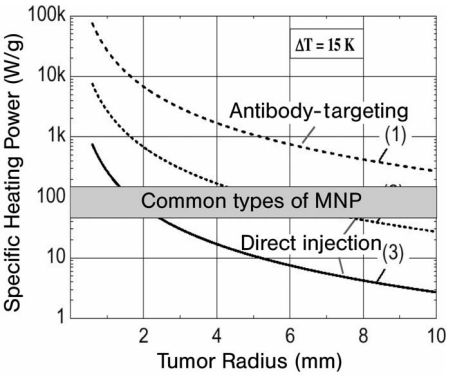

Fig. 4.35. Power demand of magnetic nanoparticles used for thermoablation in dependence on tumor radius for three different particle concentrations in tumor tissue: (1) 0.001 g cm^{-3}; (2) 0.01 g cm^{-3}; (3) 0.1 g cm^{-3}.

0.001 g cm^{-3}. Between both limits (curves (1) and (3) in Fig. 4.35) the heating power is altered by two orders of magnitude. Importantly, there is a rapid increase in the demand for specific heating power with decreasing tumor size. By considering common values of specific heating power reported in the literature (<100 W g^{-1} iron oxide), combined with presently preferred concentrations of about 10 mg cm^{-3} (curve (2) in Fig. 4.35), it can be seen that the diameter of the heated tissue region must not be less than 1 cm, even if the tumor is considerably smaller. In the case of antibody targeting, the low concentration of magnetic material transported into the tumor region demands a considerable increase in specific heating power, as may also be deduced from Figure 4.35. For presently available particle types and target concentrations, a useful effect of antibody targeting may be expected only for large tumors in the diameter range of some centimeters. Moreover, the data show clearly that a significant temperature increase for isolated tumor cells which took up magnetic particles cannot be expected. As stated previously by Rabin (2002), thermal effects at the cellular level are negligible as far as there is no macroscopic heating of cells in tissue linkage. Thus, there is no reason to differentiate extracellular macroscopic heating from ''intracellular hyperthermia'', as claimed repeatedly by Jordan et al. (1997a, 1999) and others (e.g., Bacri et al., 1997). In particular, there are no reasons for the damage of cell membranes by adsorbed magnetic nanoparticles caused by an external alternating magnetic field without macroscopic heating, which was assumed by Neuberger et al. (2005).

It should be pointed out that the scenario discussed here is the ''best case''. In practice, the tumor shape deviates considerably from spherical, and homogeneous filling of the tumor tissue with magnetic particles rarely will be achievable. Moreover, there may be an additional cooling effect by convection in blood vessels. Consequently, in practice the demand for heating power may considerably exceed the above-given estimations.

4.6.3.2
Parameters of the Alternating Magnetic Field

Clearly, the specific heating power delivered by magnetic particles depends on the AC-field parameters applied for tumor heating. The general tendency is that the higher both field amplitude and frequency, the more heating power may be generated in particles. However, in practice technical and economical as well as biomedical restrictions seriously limit any simultaneous increase of frequency and amplitude. In order to avoid excessive eddy current heating of healthy tissue, the product of field amplitude H and frequency ν should not exceed a critical value discussed in Section 4.6.2.4 (Eq. 4.19). Which favorable combination of AC-field amplitude and frequency is chosen depends heavily on the type of particles provided for the therapy. For particles with mean size in the superparamagnetic regime, losses increase with frequency according to Eq. (4.15), taking into account the particular frequency dependence of the imaginary part of the susceptibility (Eq. 4.16). In contrast, the dependence of hysteresis losses on frequency is linear for ferromagnetic particles. The dependence of magnetic losses on field amplitude obeys a square law for superparamagnetic particles (cf. Eq. 4.15) compared to a third-order power law for larger ferromagnetic particles in the Rayleigh regime (Eq. 4.12). As a consequence, for particles with hysteresis losses within the validity range of the Rayleigh regime, the field amplitude should be favored against frequency in the limiting product of Eq. 4.19 (e.g., reducing ν by a factor of 0.5 and simultaneously doubling H may gain a factor of four in specific heating power). Clearly, it makes no sense to increase the field in the saturation range of losses.

Besides the biological limitation given by Eq. (4.19), technical-economic reasons also determine the choice of amplitude–frequency pairing for therapy. Commonly, the alternating magnetic field to be used to heat magnetic nanoparticles is generated by means of coils driven by alternating current generators of fixed frequency. Hilger et al. (2005) have favored a frequency of about 400 kHz and amplitudes of about 10 kA m^{-1} in a number of experimental investigations with animals, tissue samples, and cell assemblies. For the first commercially developed equipment used to treat human patients, a frequency of 100 kHz and a field amplitude up to 18 kA m^{-1} was reported (Gneveckow et al., 2004). These authors used a coil with ferrite core and a C-shaped yoke, with a relatively large aperture height of up to 300 mm.

4.6.3.3
Optimization of the Magnetic Material

It follows from the above discussions, that there are biological, technical, and economic reasons for increasing the specific loss power (SLP) of magnetic nanoparticles. For biomedical applications, the vast number of known magnetic materials is strongly restricted by the demand of biocompatibility (e.g., nontoxicity, sufficient chemical stability in the bio-environment, appropriate circulation time in blood, harmless biodegradability). Few investigations have been conducted with iron par-

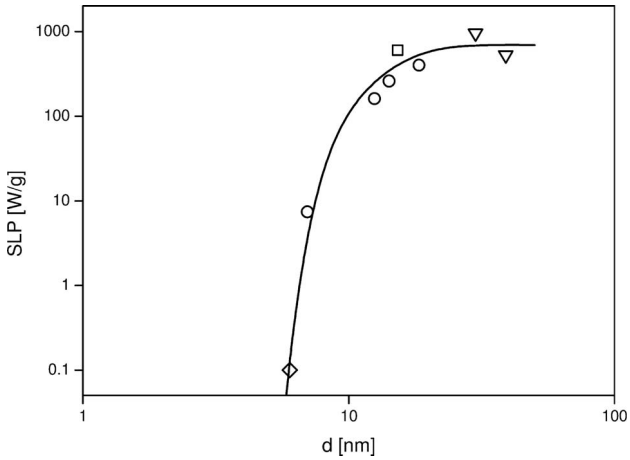

Fig. 4.36. Specific loss power (at ca. 400 kHz, 10 kA m^{-1}) depending upon mean particle core diameter for magnetic nanoparticles (Hergt et al., 1998 ◇; 2004a □; 2004b ○; 2005 ▽).

ticles, spinel ferrites and magnetic alloys; rather, the majority of investigations have concentrated on magnetic iron oxides Fe_3O_4 (magnetite) and γ-Fe_2O_3 (maghemite) that are well tolerated by the human body. Iron concentrations causing a dangerous acidosis in humans are reported to exceed 200 mg kg^{-1} body weight (Crotti, 1971), which is far beyond common diagnostic or therapeutic concentrations. At present, a variety of approved types of magnetic iron oxide particles for specific contrast enhancement in nuclear magnetic resonance imaging (MRI) are available commercially (for a review, see Taupitz et al., 2003). However, these relatively small superparamagnetic particles suffer from small SLP.

Magnetic iron oxide particles, though chemically well defined, may differ considerably with regard to their magnetic properties. In particular, the SLP depends heavily on the particle morphology and structure. Above all, the mean particle diameter is crucial for a high SLP (see Section 4.6.2). The experimentally determined dependence of SLP (field amplitude ca. 10 kA m^{-1}, frequency ca. 400 kHz) on mean particle diameter for different superparamagnetic particles (Hergt et al., 1998, 2004a,b, 2005) is illustrated graphically in Figure 4.36. Whilst a rapid increase in SLP with increasing diameter was found, it was clear that for multidomain particles this trend is reversed, as may be deduced from the experimental data of Heider et al. (1987) for magnetite particles with mean diameter > 50 nm. Clearly, a maximum of SLP for particles between multidomain and superparamagnetic size range is expected (Hergt et al., 1998), though the position and height of that maximum are as yet unclear.

The experimental data of Figure 4.36 show that the commonly used, very small, superparamagnetic particles (e.g., core diameter 3.3 nm; Jordan et al., 1993) are not the optimum choice for large heating power. A very large value of SLP of almost 1 kW g^{-1} at an AC-field amplitude of 10 kA m^{-1} and a frequency of 410 kHz was found by Hergt et al. (2005) for bacterial magnetosomes having a mean diameter of about 35 nm. However, at present the technical preparation of stable suspensions of magnetic particles with those dimensions are faced with difficulties.

In addition to mean particle diameter, particle size distribution also has a major effect on SLP value (see Section 4.6.2.3). Quantitatively, this effect was demonstrated by the calculations of Rosensweig (2002), but for experimental confirmation a high-SLP fraction was obtained from a commercial ferrofluid by magnetic fractionation (Hergt et al., 2004b). Moreover, a large SLP of 600 W g^{-1} (at 410 kHz and 11 kA m^{-1}) was found for magnetite particles which, due to a special preparation procedure, showed a rather narrow normal size distribution rather than the commonly observed log-normal distribution (Hergt et al. 2004a).

Effective magnetic anisotropy is also important for magnetic losses. The intrinsic magnetic anisotropy related to the crystal lattice is relatively small for cubic iron oxides (in the order of some kJ m^{-3}; McCurrie, 1994). However, it may be exceeded considerably by the magnetic shape anisotropy even for relatively small deviations of particle shape from a sphere (in the order of 10%). The strong influence of shape anisotropy on hysteresis losses is seen, for example, in Figures 4.32 and 4.33 for acicular particles developed for magnetic recording. Magnetic anisotropy may also be considerably influenced by the particle coating (Berkowitz et al., 1975) needed to stabilize the suspension, as well as for coupling of functional groups. The coating may also influence the SLP if there is a contribution of Brown relaxation losses, though these arise preferably in the region of middle frequencies (<50 kHz, cf. Fig. 4.34) (see Section 4.6.2.3).

A compilation of published data of SLP from several groups was provided in Table 1 of the first edition (Andrä, 1998).

It is extremely questionable whether SLP may exceed the order of magnitude of 10 kW g^{-1} for useful field parameters (see Section 4.6.3.2). According to the data of Figure 4.35, the minimum tumor size treatable by magnetic particle thermoablation would be essentially reduced by intratumoral injection of particles with SLP = 1 kW g^{-1}. However, for particle supply by antibody targeting, treatment would be limited to above about 1 cm tumor diameter for a tissue concentration of 1 mg cm^{-3}. It is questionable whether such a concentration might actually be achieved with antibody-functionalized magnetic particles.

The above discussion demonstrates that a good knowledge of structural and magnetic properties of the magnetic nanoparticles is a compulsory precondition for designing valuable particle systems with large SLP for hyperthermia or thermoablation. Many methods are available for magnetic nanoparticle preparation, and a discussion of procedures is beyond the scope of this book. However, the interested reader might refer to the recent review of Tartaj et al. (2003).

4.6.4
Biomedical Status of Magnetic Particle Hyperthermia

4.6.4.1
Studies with Animals and Cell Cultures

Studies in Animals

Magnetic particle hyperthermia (MPH) was first suggested by Gilchrist et al. (1957), who performed experiments on dogs with the aim of destroying metastases in the lymph nodes. In those early basic investigations, not only relevant biomedical problems but also questions of particle magnetism and suitable technical implementation were taken into account. Subsequently, many experiments were conducted in a variety of mammal species, including mice, rats, rabbits, dogs, and pigs. The most important results have been reviewed by Moroz et al. (2002). In summary, most previous investigations showed that temperature elevations sufficient for tumor degradation may be realized in animal experiments under tolerable systemic loads. Commonly, damage to the tumor cells is proved by histological evaluation of the treated tissue. Although many questions related to MPH have been clarified in animal experiments, extrapolation to the treatment of humans has been restricted, mainly because the small-sized equipment had been developed for use in animals. Moreover, the curative value of MPH had not been satisfactorily demonstrated. Post-treatment survival with statistically profound determination of surviving fractions was considered only in a few experiments. For example, Luderer et al. (1983) reported only 12% of treated adenocarcinoma-bearing mice to survive at 100 days post treatment. Later, Jordan et al. (1997b), using C3H mammary carcinoma-bearing mice, reported 44% of animals to be alive and to have minimal or no further tumor growth at 60 days after MPH treatment. A logistic regression analysis of tumor volumes reflected the critical problem of homogeneity of the intra-tumoral magnetic particle distribution. The best result, reported by Yanase et al. (1998a), identified 87.5% of rats with no tumor regrowth within three months. Using magnetite cationic liposomes, the same group reported the induction of antitumor immunity by MPH (Yanase et al., 1998b), while Le et al. (2001) achieved successful tumor control using antibody fragment-coated magnetoliposomes. Since the 1980s, and in parallel to the various animal experiments, many patents related to MPH have been registered, the most comprehensive of which were those of Rand et al. (1985) and Handy et al. (2003).

Studies in Cell Culture

Research studies into MPH were also flanked by many *in-vitro* experiments using cell cultures. The main purpose of these experiments was to test the biocompatibility of coated magnetic iron oxides and to investigate any interactions of magnetic nanoparticles with different cell species in aqueous suspension. The coatings mainly included dextran, carboxydextran, citrate, polyethleneglycol, or starch. The toxicity of various coatings was studied by Häfeli and Pauer (1999). Chan et al. (1993), when comparing survival fractions of A549 human lung adenocarcinoma

cells after heating by water bath or by MPH, concluded that cancer cell damage was due to purely thermal effects. This finding was in accordance with the theoretical investigations of Rabin (2002), which considered the principal laws of heat transfer, and contradicted the often-cited opinion (e.g., Jordan 1997a, 1999) that "intracellular hyperthermia" is a particularly effective means of causing cell damage. One very important means of achieving effective tumor cell damage by MPH is to ensure a sufficiently high concentration of nanoparticles in the tumor tissue, irrespective of the position of the nanoparticles on the cellular level (see Section 4.6.3.1). In the case of systemic application of particles this concentration depends on the targeting efficiency – that is, the degree of retention of particles in or on tumor cells (e.g., by endocytosis or adsorption on cell membranes).

Differences in the cellular uptake of magnetic nanoparticles by different cell types, as well as of particle coatings, were demonstrated *in vitro* by several authors (e.g., Jordan et al., 1999). Suzuki et al. (1995) achieved a highly specific cellular uptake by coupling tumor-specific monoclonal antibodies onto the polyethylene glycol coating of magnetite particles. After incubation with BM314 cells, 90 pg magnetite per tumor cell was detected, which was fourfold that of unlabelled control cells. Much more highly specific antibody labeling is required, however, to achieve magnetic particle enrichment in tumor tissue cells using only MPH. Although some problems associated with nanoparticle–living cell interaction were solved by *in-vitro* experimentation, care must be taken when validating reports of temperature elevations in cell suspensions as a result of MPH. Reported temperature elevations are often measured under good thermal isolation of the samples, which is not representative for the real situation in the body. These experiments are conclusive only if the heat capacity of the experimental arrangement is well known, and when the specific heating power of the particles used may subsequently be calculated (Hiergeist et al., 1999).

In summary, whilst both animal and cell culture studies have identified certain essential preconditions for successful MPH, a number of unresolved risk factors have delayed initiation of the first human clinical trials with this technique.

4.6.4.2 Application to Human Patients

Although, in 1957, Gilchrist was highly optimistic with regard to the ultimate application of MPH to humans, almost 50 years passed before the first clinical trials were initiated. Provided that the correct particles are available, the primary problem in human studies is to deliver the particles to the tumor. This may be achieved in two main ways (only the first of which is currently under practical consideration):

- By injecting the particle suspension directly into the tumor, or into blood vessels that supply the tumor.
- By using a relatively targeted delivery to the tumor, either by labeling the magnetic particles with tumor-specific antibodies, or by particle guidance using inhomogeneous magnetic fields.

The key problem with this new therapy – of which Jordan and colleagues were well aware during the mid-1990s (Jordan et al., 1997b) – is to provide an adequate particle supply to the tumor tissue. Since the temperature elevation caused by an external alternating magnetic field is confined to tissue regions containing magnetic particles in sufficient concentration (see discussion in Section 4.6.3.1), the tissue distribution of the applied particle suspension should – in the ideal case – exactly fit the tumor shape. A number of serious practical difficulties have arisen in attempting to achieve this goal, however. Initially, the particle distribution must be monitored after injection using suitable diagnostic means such as sonography, radiography, or MRI (cf. Hilger et al., 2002). Then, knowing the spatial distribution and SLP of the magnetic particles, it is possible – using the above-described physical principles (see Section 4.6.3.1) – to calculate the temperature increase. Heating may be controlled by adjusting the field amplitude and duration of the field exposure, while the local temperature increase is measured online using, for example, optical fiber sensors introduced into the tumor tissue. The correct matching of an infiltrative growing tumor (e.g., as often occurs with glioblastoma) by injecting a suitable magnetic nanoparticle suspension seems impossible, however. Relying on high-resolution imaging of the tumor shape, the physician must fill the tumor tissue with particles but with limited involvement of healthy tissue. The problem is that, even for a globular, well-bounded tumor, homogeneous injection is difficult as tissue inhomogeneity causes the suspension to spread irregularly from the tumor into the normal tissue, which has a softer texture than the tumor. In an effort to avoid such spread, Jordan et al. (1997b) recommended the use of a very slow infiltration and/or repeated multi-site injections, though the latter approach carries the danger of needle track implantation or local tumor spread, as noted by Moroz et al. (2002). In view of these problems, it is perhaps remarkable that the first human trials have already commenced, and a technically advanced hyperthermia and thermoablation system for clinical application has recently been developed by Gneveckow et al. (2004). As a result, clinical trials on the feasibility and tolerability of magnetic particle hyperthermia are currently under way at the Bundeswehrkrankenhaus, Berlin (Gneveckow et al., 2005).

In an effort to improve the site specificity of MPH, the suggestion was made to label the magnetic particles with target-specific ligands (e.g., antibodies) (Handy et al., 2003). However, at the time of writing only preliminary results are known, and these are restricted to *in-vitro* experiments with cell cultures (Suzuki et al., 1995) or to *in-vivo* studies using intra-tumoral injection (Shinkai et al., 1999; Le et al., 2001). The targeting efficiency – that is, the concentration enhancement at the tumor site compared to the magnetic particle content of the inner organs – was not satisfactorily investigated till now for remote (e.g., intravenous) particle application. In fact, the expected concentrations are so low that the achievement of a useful heating effect would require considerable enhancement of the specific heating power of the magnetic nanoparticles (see Section 4.6.3.1).

The enrichment of magnetic nanoparticles in a target region of the body by applying external magnetic fields has been shown, in principle, by several groups. Unfortunately, the method is hampered by the fact that when using extracorporeal

magnets the center of attraction for the particles cannot be positioned within the body. Furthermore, as magnetic attraction is proportional to the magnetic moment of the particles, there is insufficient targeting for superparamagnetic particles. On the other hand, for larger single domain particles there is the tendency towards agglomeration and the added hazard of unintended embolization. In this respect, the method has been investigated for arterial embolization hyperthermia (for a review, see Moroz et al., 2002).

In summary, provided that some serious practical problems of controlled particle delivery can be resolved, MPH appears to offer a promising approach to highly selective cancer therapy.

Acknowledgments

The authors thank Dipl.-Ing. S. Dutz for help in preparing the figures.

References

Andrä, W. (1998). Magnetic hyperthermia. In: Andrä, W. and Nowak, H. (Eds.), *Magnetism in Medicine*, Wiley-VCH, Berlin, pp. 455–470.

Andrä, W., d'Ambly, C.G., Hergt, R., Hilger, I., and Kaiser, W.A. (1999). Temperature distribution as function of time around a small spherical heat source of local magnetic hyperthermia, *J. Mag. Mag. Mater.*, **194**, 197–203.

Bacri, J.C., Da Silva, M.d.F., Perzynski, R., Pons, J.N., Roger, J., Sabolovic, D., and Halbreich, A. (1997). Use of magnetic nanoparticles for thermolysis of cells in a ferrofluid. In: Häfeli, U. (Ed.), *Scientific and Clinical Applications of Magnetic Carriers*, Plenum Press, pp. 597–606.

Berkowitz, A.E., Lahut, J.A., Jacobs, I.S., Levinson, L.M., and Forester, D.W. (1975). Spin pinning at ferrite-organic interfaces. *Phys. Rev. Lett.* **34**, 594.

Bertotti, G. (1998). *Hysteresis in Magnetism*, Academic Press.

Borelli, N.F., Luderer, A.A., and Panzarino, J.N. (1984). Hysteresis heating for the treatment of tumours, *Phys. Med. Biol.*, **29**, 487.

Brezovich, I.A. (1988). Low frequency hyperthermia. *Medical Physics Monograph*, **16**, 82.

Busch, C.J. (1866). Einfluss heftiger Erysipeln auf organisierte Neubildungen. In: Andrä, C.J. (Ed.), *Verhandlungen des naturhistorischen Vereines der preussischen Rheinlande und Westphalens*, Max Cohen and Sohn, Bonn, pp. 28–33.

Chan, D.C.F., Kirpotin, D.B., and Bunn, P.A. (1993). Synthesis and evaluation of colloidal magnetic iron oxides for the site specific rf-induced hyperthermia of cancer. *J. Mag. Mag. Mater.*, **122**, 374–378.

Crotti, J.J. (1971). Acute iron poisoning in children. *Clin. Toxicol.*, **4**, 615.

Debye, P. (1929). *Polar Molecules*. Dover Publications, New York.

Dunin-Borkowski, R.E., McCartney, M.R., Pósfai, M., Frankel, R.B., Bazylinski, D.A., and Buseck, P.R. (2001). Off-axis electron holography of magnetotactic bacteria: magnetic microstructure of strains MV-1 and MS-1. *Eur. J. Mineral.*, **13**, 671.

Dutz, S., Hergt, R., Mürbe, J., Müller, R., Zeisberger, M., Andrä, W., Töpfer, J., and Bellemann, M.E. (2006). Hysteresis losses of magnetic nanoparticle powders in the single domain size range. *J. Magn. Magn. Mater.* (accepted for publication).

Fabian, K., Kirchner, A., Williams, W., Heider, F., Leibl, T., and Hubert, A. (1996). Three-dimensional micromagnetic

calculations for magnetite using FFT. *Geophys. J. Intern.*, **124**, 89.

Falk, M.H. and Issels, R.D. (2001). Hyperthermia in oncology. *Int. J. Hyperthermia*, **17**, 1.

Gilchrist, R.K., Medal, R., Shorey, W.D., Hanselman, R.C., Parrot, J.C., and Taylor, C.B. (1957). Selective inductive heating of lymph nodes. *Ann. Surg.*, **146**, 596.

Gneveckow, U., Jordan, A., Scholz, R., Brüß, V., Waldöfner, N., Ricke, J., Feussner, A., Hildebrandt, B., Rau, B., and Wust, P. (2004). Description and characterization of the novel hyperthermia- and thermoablation-system MFH®300F for clinical magnetic fluid hyperthermia. *Med. Phys.*, **31**, 1444–1451.

Gneveckow, U., Jordan, A., Scholz, R., Eckelt, L., Maier-Hauff, K., Johannsen, M., and Wust, P. (2005). Magnetic force nanotherapy: with nanoparticles against cancer. experiences from three clinical trials. *Biomed. Techn.*, **50**, 92–93.

Gordon, R.T., Hines, J.R., and Gordon, D. (1979). Intracellular hyperthermia: a biophysical approach to cancer treatment via intracellular temperature and biophysical alterations. *Medical Hypotheses*, **5**, 83.

Häfeli, U. and Pauer, G.J. (1999). In vitro and in vivo toxicity of magnetic microspheres. *J. Magn. Magn. Mater.*, **194**, 76.

Handy, E.S., Ivkov, R., Ellis-Busby, D., Foreman, A., Braunhut, S.J., Gwost, D.U., and Ardman, B. (2003). Thermotherapy via targeted delivery of nanoscale magnetic particles. *US Patent Appl. Publ.* US2003/0032995.

Heider, F., Dunlop, D.J., and Sugiura, N. (1987). Magnetic properties of hydrothermally recrystallized magnetite crystals. *Science*, **236**, 1287–1290.

Hergt, R., Andrä, W., d'Ambly, C.G., Hilger, I., Kaiser, W.A., Richter, U., and Schmidt, H.G. (1998). Physical limits of hyperthermia using magnetite fine particles. *IEEE Trans. Magn.*, **34**, 3745.

Hergt, R., Hiergeist, R., Hilger, I., and Kaiser, W.A. (2002). Magnetic nanoparticles for thermoablation. *Recent Res. Devel. Mater. Sci.*, **3**, 723.

Hergt, R., Hiergeist, R., Hilger, I., Kaiser, W.A., Lapatnikov, Y., Margel, S., and Richter, U. (2004a). Maghemite nanoparticles with very high AC-losses for application in RF-magnetic hyperthermia. *J. Magn. Magn. Mater.*, **270**, 345.

Hergt, R., Hiergeist, R., Zeisberger, M., Glöckl, G., Weitschies, W., Ramirez, L.P., Hilger, I., and Kaiser, W.A. (2004b). Enhancement of AC-losses of magnetic nanoparticles for heating applications. *J. Magn. Magn. Mater.*, **280**, 358.

Hergt, R., Hiergeist, R., Zeisberger, M., Schüler, D., Heyen, U., Hilger, I., and Kaiser, W.A. (2005). Magnetic properties of bacterial magnetosomes as potential diagnostic and therapeutic tools. *J. Magn. Magn. Mater.*, **293**, 80.

Hiergeist, R., Andrä, W., Buske, N., Hergt, R., Hilger, I., Richter, U., and Kaiser, W.A. (1999). Application of magnetite ferrofluids for hyperthermia. *J. Magn. Magn. Mater.* **201**, 420.

Hilger, I., Andrä, W., Hergt, R., Hiergeist, R., Schubert, H., and Kaiser, W.A. (2001). Electromagnetic heating of breast tumours in interventional radiology: In vitro and in vivo studies in human cadavers and mice. *Radiology*, **218**, 570.

Hilger, I., Hofmann, F., Reichenbach, J.R., Bergemann, C., Hiergeist, R., Andrä, W., Hergt, R., and Kaiser, W.A. (2002). Bildgebende Darstellung von Magnetite in vitro. *Fortschr. Röntgenstr.* **174**, 101–103.

Hilger, I., Hergt, R., and Kaiser, W.A. (2005). Use of magnetic nanoparticle heating in the treatment of breast cancer. *IEE Proc. Nanobiotechnol.*, **152**, 33–39.

Hubert, A. and Schäfer, R. (1998). *Magnetic Domains*. Springer, Berlin-Heidelberg-New York.

Jordan, A., Wust, P., Fähling, H., John, W., Hinz, A., and Felix, R. (1993). Inductive heating of ferrimagnetic particles and magnetic fluids. *Int. J. Hyperthermia*, **9**, 51–68.

Jordan, A., Wust, P., Scholz, R., Fähling, H., Krause, J., and Felix, R. (1997a). Magnetic Fluid Hyperthermia. In: Häfeli, U. (Ed.), *Scientific and Clinical Applications of Magnetic Carriers*, Plenum Press, pp. 569–595.

Jordan, A., Scholz, R., Wust, P., Fähling, H., Krause, J., Wlodarczyk, W., Sander, B., Vogl, T., and Felix, R. (1997b). Effects of magnetic fluid hyperthermia on C3H mammary carcinoma in vivo. *Int. J. Hyperthermia*, **13**, 587.

Jordan, A., Scholz, R., Wust, P., Schirra, H., Schiestel, T., Schmidt, H., and Felix, R. (1999). Endocytosis of dextran and silan-coated magnetite nanoparticles and the effect of intracellular hyperthermia on human mammary carcinoma cells in vitro. *J. Magn. Magn. Mater.*, **194**, 185–196.

Knauft, S., Andrä, W., Werner, C., and Bellemann, M.E. (2004). Remote controlled release of agents by friction losses of a rotating permanent magnetic sphere in a viscous medium. *Biomed. Techn.*, **49** (Suppl. 2), 724.

Landau, L.D. and Lifshitz, E.M. (1960). *Electrodynamics of Continuous Media*, Pergamon Press London.

Landau, L.D. and Lifshitz, E.M. (1978). *Lehrbuch der theoretischen Physik*, Bd. 6, Berlin: Akademie-Verlag.

Le, B., Shinkai, M., Kitade, T., Honda, H., Yoshida, J., Wakabayashi, T., and Kobayashi, T. (2001). Preparation of tumour specific magnetoliposomes and their application for hyperthermia. *J. Chem. Eng. Jap.*, **34**, 66–72.

Luderer, A., Borrelli, N.F., Panzarino, J.N., Mansfield, G.R., Hess, D.M., Brown, J.L., and Barnett, E.H. (1983). Glass-ceramic-mediated, magnetic-field-induced localized hyperthermia: response of a murine mammary carcinoma. *Radiation Res.*, **94**, 190.

McCurrie, R.A. (1994). *Ferromagnetic Materials*, Academic Press, London.

Moroz, P., Jones, S.K., and Gray, B.N. (2002). Magnetically mediated hyperthermia: current status and future directions. *Int. J. Hyperthermia*, **18**, 267.

Neuberger, T., Schöpf, B., Hofmann, H., Hofmann, M., and Rechenberg, B. (2005). Superparamagnetic nanoparticles for biomedical applications. *J. Magn. Magn. Mater.*, **293**, 483.

Néel, L. (1942). Théorie des lois d'aimantation de Lord Rayleigh: Les déplacements d'un paroi isolée. *Cah. Phys.*, **12**, 1.

Néel, L. (1943). Théorie des lois d'aimantation de Lord Rayleigh: Multiple domaines et champ coercitif. *Cah. Phys.*, **13**, 18.

Néel, L. (1949). Influence des fluctuations thermiques a l'aimantation des particules ferromagnétiques. *C. R. Acad. Sci.*, **228**, 664.

O'Brien, K.T. and Mekkaoui, A.M. (1993). Numerical simulation of thermal fields occurring in the treatment of malignant tumors by local hyperthermia. *J. Biomechanical Eng.*, **115**, 247.

Rabin, Y. (2002). Is intracellular hyperthermia superior to extracelluar hyperthermia in the thermal sense? *Int. J. Hyperthermia*, **18**, 194–199.

Rand, R.W., Snow, H.D., Elliott, D.G., and Haskins, G.M. (1985). Induction heating method for use in causing necrosis of neoplasm. *US Patent* 4, **545**, 368.

Robins, H.I., Rushin, D., Kutz, M., Tutsch, K.D., Tiggelaar, C.L., Paul, D., Spriggs, D., Kraemer, C., Gillis, W., Feierabend, C., Arzoomanian, R.Z., Longo, W., Alberti, D., D'Oleire, F., Qu, R., Wilding, G., and Stewart, J.A. (1997). Phase I clinical trial of melphalan and 41.8 °C whole-body hyperthermia in cancer patients. *J. Clin. Oncol.*, **15**, 158.

Rosensweig, R.E. (2002). Heating magnetic fluid with alternating magnetic field. *J. Magn. Magn. Mater.*, **252**, 370.

Shinkai, M., Yanase, M., Suzuki, M., Honda, H., Wakabayashi, T., Yoshida, J., and Kobayashi, T. (1999). Intracellular hyperthermia for cancer using magnetite cationic liposomes. *J. Magn. Magn. Mater.*, **194**, 176–184.

Sonnenschein, R. (1986). Temperaturfeldberechnungen zur Hyperthermiebehandlung bei ausgewählten Tumoren. In: Streffer, C., Herbst, M., and Schwabe, H. (Eds.), *Lokale Hyperthermie*, Deutscher Ärzte-Verlag, Köln.

Stoner, E.C. and Wohlfarth, E.P. (1948). A mechanism of magnetic hysteresis in heterogeneous alloys. *Phil. Trans. Roy. Soc.*, **A240**, 599.

Shtrikman, S. and Treves, D. (1963). Micromagnetics. In: Rado, G.T. and Suhl, H. (Eds.), *Magnetism*, *Volume III*, Academic Press, New York, London, pp. 395–414.

Suzuki, M., Shinkai, M., Kamihira, M., and Kobayashi, T. (1995). Preparation and characteristics of magnetite labelled antibody with the use of polyethylene glycol derivatives. *Biotechnol. Appl. Biochem.*, **21**, 1179.

Tartaj, P., del Puerto-Morales, M., Veintemillas-Verdaguer, S., Gonzalez-Carreno, T., and Serna, C.J. (2003). The preparation of magnetic nanoparticles for applications in biomedicine. *J. Phys. D: Appl. Phys.*, **36**, R182–R197.

Taupitz, M., Schmitz, S., and Hamm, B. (2003). Superparamagnetische Eisenoxidpartikel: Aktueller Stand und zukünftige Entwicklungen. *Fortschr. Röntgenstr.*, **175**, 752.

Vaupel, P., Kallinowski, F., and Kluge, M. (1986). Pathophysiologische Aspekte der Hyperthermiewirkung in malignen Tumoren: Durchblutungsänderungen in Xenotransplantaten menschlicher Mammakarzinome. In: Streffer, C., Herbst, M., and Schwabe, H. (Eds.), *Lokale Hyperthermie*, Deutscher Ärzte-Verlag, Köln.

Yanase, M., Shinkai, M., Honda, H., Wakabayashi, T., Yoshida, J., and Kobayashi, T. (1998a). Intracellular hyperthermia for cancer using magnetite cationic liposomes: an in vivo study. *Jpn. J. Cancer Res.*, **89**, 463–469.

Yanase, M., Shinkai, M., Honda, H., Wakabayashi, T., Yoshida, J., and Kobayashi, T. (1998b). Antitumour immunity induction by intracellular hyperthermia using magnetite cationic liposomes. *Jpn. J. Cancer Res.*, **89**, 775–782.

4.7
Magnetic Cell Separation for Research and Clinical Applications*

Michael Apel, Uwe A.O. Heinlein, Stefan Miltenyi, Jürgen Schmitz, and John D.M. Campbell

4.7.1
Introduction

Magnetic cell sorting has become a standard method for cell separation in many different fields. Numerous publications have demonstrated its use, from the laboratory bench to the clinic; from small to large scale; from abundant cells to rare cells with complex phenotypes; and from human and mouse cells to many other species. The isolation of almost any cell type is possible from complex cell mixtures, such as peripheral blood, hematopoietic tissue (spleen, lymph nodes, thymus, bone marrow, etc.), nonhematopoietic tissue (solid tumors, epidermis, dermis, liver, thyroid gland, muscle, connective tissue, etc.) or cultured cells (Molday and MacKenzie, 1982; Miltenyi et al., 1990; Kato and Radbruch, 1993; Radbruch et al., 1994; Kantor et al., 1997; McNiece et al., 1997; Miltenyi and Schmitz, 1999).

In this section we focus on the clinical applications of magnetic cell sorting with MACS® Technology. We will first introduce the MACS concept and thereafter present the most important clinical applications in the field of cellular therapy:

- Stem cell enrichment for graft engineering
- Natural killer cells for tumor therapy
- T cell subsets in transplantation
- Enrichment of antigen-specific T cells for immune therapy
- Dendritic cells and cellular vaccination strategies
- Stem cells in cardiac repair

For further information on related technologies, the reader is referred to recent publications (for a review, see Ugelstad et al., 1998).

* A list of abbreviations and acronyms is provided at the end of this section.

4.7.2 MACS® Technology

4.7.2.1 The Concept

The variety of magnetic cell separation systems currently available differs principally in two features: (1) the composition and size of the magnetic particles used for cell labeling; and (2) the mode of magnetic separation. The MACS system is characterized by the use of nano-sized super-paramagnetic particles (ca. 50 nm in diameter), unique separation columns and MACS separators – the instruments where the separation process takes place (Miltenyi et al., 1990; Kantor et al., 1997; Miltenyi and Schmitz, 1999). Magnetic cell separation using the MACS system is performed in three steps as outlined in Figure 4.37:

- *Magnetic labeling*: The cell preparation and labeling methods are similar to those used in flow cytometry. Individual cells of a cell suspension are immunomagnetically labeled using MicroBeads which typically are directly covalently conjugated to a monoclonal antibody (mAb) or ligand specific for a certain cell type.
- *Magnetic separation*: Thereafter, the cell suspension is passed through the separation column that contains a ferromagnetic matrix and is placed in a MACS separator. The separator contains a strong permanent magnet creating a high-gradient magnetic field on the magnetizable column matrix. Labeled target cells are retained in the column via magnetic forces, whereas unlabeled cells flow through. By simply rinsing the column with buffer, the entire untouched cell fraction is obtained.
- *Elution of the labeled cell fraction*: After removing the column from the magnetic field of the MACS separator, the retained labeled cells can easily be eluted with buffer. The entire procedure can be performed in less than 30 minutes, and both cell fractions – magnetically labeled and untouched cells – are ready for further use, such as flow cytometry, molecular biology, cell culture, transfer into animals, or clinical cellular therapy.

4.7.2.2 Magnetic Separation Strategies

Magnetic cell selection is a very simple but flexible technique, and in planning isolation only two basic strategies require to be considered: *positive selection* or *depletion*. The optimal separation strategy depends on the frequency of target cells in the cell sample, their phenotype compared with the other cells in the sample, the availability of reagents, and a full consideration of how the target cells are to be used, including any restrictions with respect to purity, yield, and activation status.

Positive selection means that the desired target cells are magnetically labeled and isolated directly as the positive cell fraction (Fig. 4.37). It is the most direct and spe-

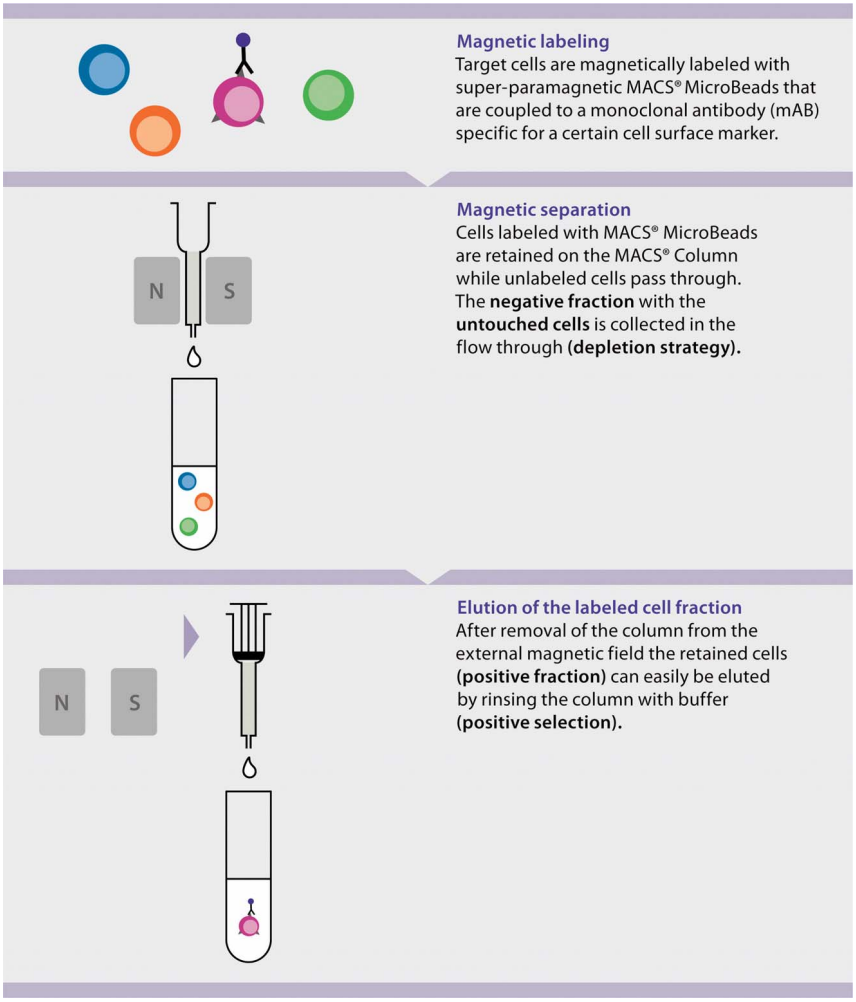

Fig. 4.37. The principle of high-gradient magnetic cell sorting. Both fractions, magnetically labeled and unlabeled, can be recovered and used in further experiments.

cific way to isolate the target cells from a heterogeneous cell suspension, and requires one or more cell surface markers which are specific for the target cells. Positive selection is particularly well-suited for the isolation of *rare cells*, such as hematopoietic stem cells, from complex cell mixtures such as blood cells (e.g., see Fig. 4.43; enrichment of $CD34^+$ or $CD133^+$ stem cells).

Both fractions – labeled and unlabeled – can be recovered and used. Depending on the cell type, on the target surface molecules used upon magnetic labeling, and on the labeling moiety of the MicroBeads [monoclonal antibody (mAb) or ligand],

Table 4.3. Comparison of positive selection and depletion.

Positive selection should be considered for:	A depletion strategy should be considered:
• Best purity, especially for enrichment of rare cells • Best recovery • Fast procedure	• For the removal of unwanted cells • If no specific antibody is available for target cells • If binding of antibody to target cells is not desired • For the subsequent isolation of a cell subset by means of positive selection (e.g., see Fig. 4.44: multiparameter magnetic cell sorting)

the functional status of the cells can be influenced. This is a problem inherent to labeling with antibodies (Ab) or ligands that recognize and crosslink cell-surface receptors and thus may induce or suppress signal transduction. Labeling with Ab-conjugated MicroBeads has no additive effect compared to labeling with an unconjugated crosslinking Ab.

Depletion means that the unwanted cells are magnetically labeled and eliminated from the cell mixture, and the nonmagnetic, untouched fraction contains the cells of interest (Fig. 4.37). Additionally, potential effects on the functional status of cells are minimized. A single depletion procedure can remove up to 99.99% of the magnetically labeled cells, leaving a highly pure fraction of unlabeled cells.

In particular, this strategy may be advantageous if functional studies such as T cell activation studies or gene expression profiling will be performed with the target cells. If the desired target cells are heterogeneous, or do not have a well-defined phenotype, removing well-characterized cells by depletion is an efficient way to isolate the target cell population. Commonly used examples of depletion approaches include: the selective elimination of fibroblasts which often overgrow other cells from primary tissue cultures; the enrichment of fetal erythroblasts from maternal blood by leukocyte depletion; the enrichment of nonhematopoietic tumor cells from blood and bone marrow of cancer patients by leukocyte depletion; and the depletion of T cells from allogeneic stem cell grafts. Which separation strategy is favorable in which experimental setting is listed in Table 4.3.

4.7.2.3 Magnetic Labeling Strategies and Reagents

Direct labeling provides the most rapid means of magnetic labeling. When a mAb specific for a certain cell surface antigen can be directly coupled to the MicroBeads, *only one labeling step* is required (Fig. 4.38).

Direct labeling minimizes the number of washing steps and thereby prevents cell loss. For many human, mouse, rat and nonhuman primate cell surface markers, antibody-conjugated MicroBeads are available as one-step reagents.

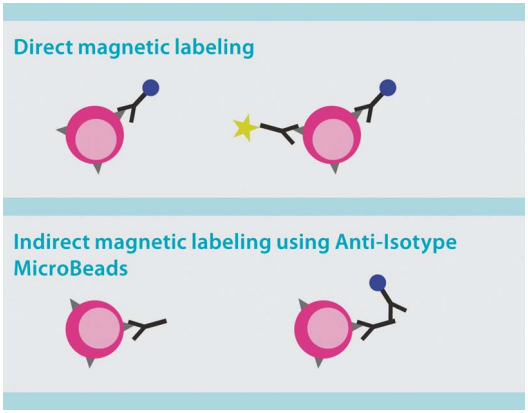

Fig. 4.38. Principles of magnetic labeling with superparamagnetic MicroBeads. Direct labeling: one-step magnetic labeling, where a cell-surface antigen-specific mAb is directly conjugated to the MicroBeads. Indirect labeling (anti-immunoglobulin): two-step magnetic labeling. In the given example, anti-isotype MicroBeads are illustrated. Cells are labeled at first with a cell-surface antigen-specific Ab and subsequently with anti-immunoglobulin Ab-conjugated MicroBeads.

Indirect labeling (Fig. 4.38) is performed when no direct MicroBeads are available, when a panel of antibodies (Ab) directed against multiple cell surface antigens is used, or when two-step magnetic labeling is significantly more efficient compared to one-step labeling – for example, with weakly expressed antigens, or Ab of low affinity.

Cells are labeled with a primary antibody that is unconjugated, biotinylated, or fluorochrome-conjugated. In a second step, three different indirect magnetic labeling methods can be used:

1. Anti-immunoglobulin Ab-conjugated MicroBeads, to detect unlabeled primary Ab.
2. Streptavidin-conjugated MicroBeads or anti-biotin Ab-conjugated MicroBeads, to detect biotinylated primary Ab.
3. Anti-fluorochrome Ab-conjugated MicroBeads (e.g. anti-FITC Ab-conjugated MicroBeads) to detect fluorochrome-labeled primary Ab.

4.7.2.4 Superparamagnetic MicroBeads

MACS MicroBeads are superparamagnetic particles made from an iron oxide core and a dextran coating (Fig. 4.39). They are nano-sized, ranging from 20 to 150 nm in diameter, and form colloidal solutions – that is, they remain dispersed (Kantor et al., 1997; Miltenyi et al., 1990). *Superparamagnetism* means that in a magnetic field the iron oxide cores magnetize strongly like ferromagnetic material, but when

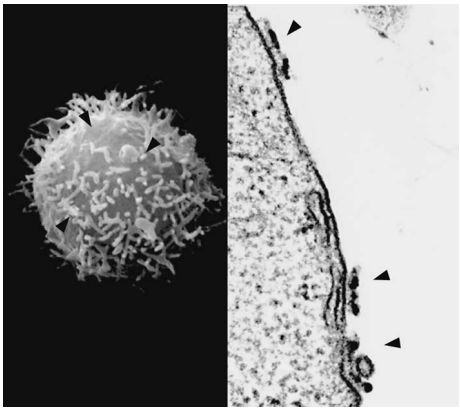

Fig. 4.39. Scanning (left) and transmission (right) electron micrographs of a $CD8^+$ T cell, isolated by MACS Technology using CD8 Ab-conjugated superparamagnetic MicroBeads (illustration courtesy of Prof. Groscurth, Zurich, Switzerland). Some superparamagnetic MicroBeads are marked with arrowheads; these are about 50 nm in diameter, form colloidal solutions, and are biodegradable. Their small size enables fast kinetics of the MicroBead-cell reaction and minimizes unspecific binding. Thus, enrichment of cells of more than 10 000-fold is possible from frequencies below one cell in 10^8 cells.

removed from the magnetic field the particles do not retain any residual magnetism. The dextran coating of the MicroBeads permits chemical conjugation of biomolecules. Numerous highly specific mAb, fluorochromes, oligonucleotides and various other moieties have all been covalently linked to MicroBeads, thereby transferring additional biochemical and physical properties to them (Miltenyi et al., 1990; Kato et al., 1993).

The nano-sized iron-dextran particles confer several unique features on MACS Technology. The MicroBeads are *biodegradable*, and do not alter cell function. Effects on the functional status of cells by magnetic labeling with the MicroBeads are primarily dependent on the target cell-surface antigen and on the degree of crosslinking by mAb or ligands conjugated to the MicroBeads, but not on the MicroBeads themselves. Cells labeled with MicroBeads have been used for numerous functional *in-vitro* assays, experimental transfers into animals, and therapeutic transplantations in humans.

4.7.2.5 Column Technology and Research Separators

As the MicroBeads are extremely small, the amount of magnetizable material bound to cells is very low. Therefore, specific devices are required to generate a high-gradient magnetic field powerful enough to retain the labeled cells. MACS Technology uses high-gradient magnetic cell separation units consisting of a strong permanent magnet (0.4–1 Tesla) and a separation column with a matrix of ferromagnetic steel wool or iron spheres (Fig. 4.40).

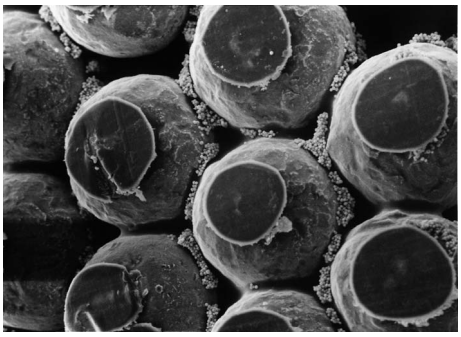

Fig. 4.40. Matrix of a MACS column. The matrix consists either of ferromagnetic steel wool or of iron spheres, as shown. To avoid corrosion and potential damage to the cells through direct contact with the matrix material, the ferromagnetic column matrix is coated with a thin biocompatible plastic polymer layer.

When the columns are placed in between the poles of the magnet of the MACS Separator, high magnetic gradients up to some 10^4 T m^{-1} are generated in the vicinity of the ferromagnetic matrix. The magnetic force is then sufficient to retain the target cells labeled with a very small number of MicroBeads. Once the column is removed from the magnet, the column matrix rapidly demagnetizes and the cells which were retained can be eluted easily and completely by simply rinsing the column with buffer.

MACS columns for research use are available in various sizes (Fig. 4.41) for rapid (5–30 min) processing of different amounts of cells. In fact, up to 2×10^{10} cells, containing up to 10^9 target cells, can be routinely handled. This is in striking contrast to fluorescence-activated cell sorting (FACS), where cells are sorted one after the other, limiting the sorting speed to about 5000 cells per second (i.e., 10^8 cells in 6 h).

4.7.2.6
CliniMACS® Plus Instrument, and Accessories

The CliniMACS is an automated cell-selection device, based on MACS technology. It enables the operator to perform large-scale magnetic cell selection in a closed and sterile system (Fig. 4.42).

The use of clinical-grade isolation or depletion of cells has grown dramatically over the past few years, and this is now a standard technique established in many cellular therapy centers. The CliniMACS is an extremely flexible system for separating cells labeled with clinical-grade MicroBeads. Cells are processed and labeled using standard clean-room techniques in a closed-bag system. The processed cells are then attached to a tubing set, and processed using the pre-set programs of the CliniMACS instrument. The target cells are recovered in a transfer pack or cell culture bag, after which they are ready for downstream processing, once again using a closed system.

a)

c)

b)

Fig. 4.41. Separation hardware. Various MACS separators and columns are available that are each individually designed for specific applications. (a) The MidiMACS separator is the instrument of choice for separation of up to 10^8 labeled cells and up to 2×10^9 total cells in combination with LS columns. (b) Enlarged view of the central separation unit of all MACS separators: the permanent magnet with a MACS column. For different applications a variety of further MACS columns is available. (c) The autoMACS is an automated benchtop magnetic cell sorter for high cell numbers or multiple samples. It is capable of sorting up to 10^6 cells per second from samples of up to 4×10^9 cells.

Fig. 4.42. (a) The CliniMACS® Plus Instrument. This is an automated cell selection system for clinical-scale magnetic enrichment of target cells or for depletion of unwanted cells in a closed and sterile system. For separation, a single-use tubing set, including a separation column, is attached to the CliniMACS instrument. The cell preparation bag, containing the labeled cells, is then connected to the tubing set. After starting the selection program, the system automatically applies the cell sample to the separation column, performs a series of washing steps, and finally elutes the purified target cells. The CliniMACS system has received CE approval for clinical use in Europe and many other countries for the selection of $CD34^+$, $CD133^+$, $CD14^+$, $CD3^+$, $CD19^+$, $CD56^+$ cells from human peripheral blood and bone marrow. In the United States, CliniMACS products are available for use in clinical trials under an approved IDE (Investigational Device Exemption) or IND (Investigational New Drug application). (b) CliniMACS buffer. (c) Transfer bag.

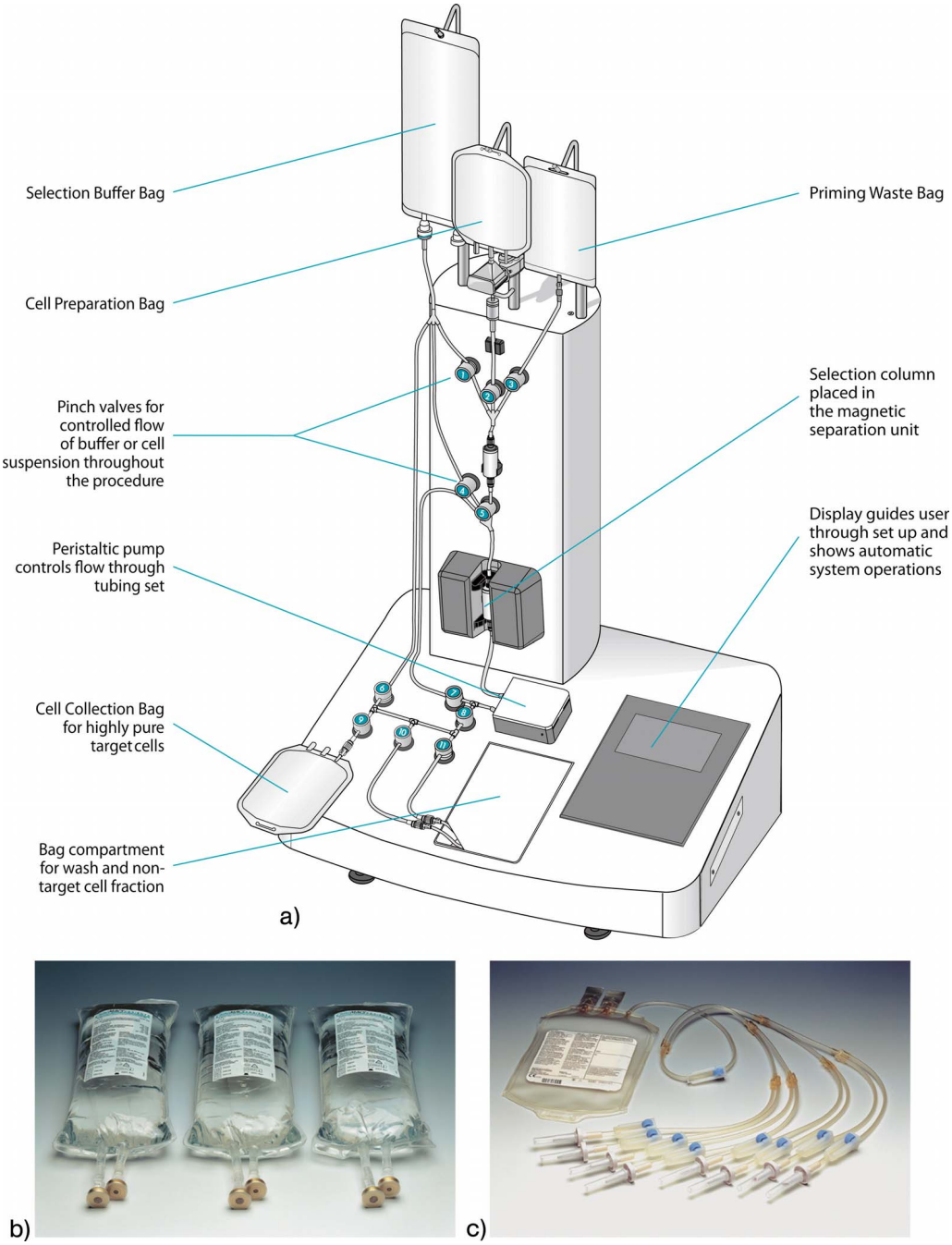

Fig. 4.42. (legend see page 578)

4.7.3
Magnetic Cell Sorting for Clinical Applications

In this section we will discuss the specific applications for the CliniMACS cell selection system being used and developed in the clinic today.

4.7.3.1
Stem Cell Enrichment for Graft Engineering in Hematological Disorders

Hematopoietic stem cell transplant is currently the only curative therapy available in a broad range of *hematological malignancies*, and is also now a standard treatment for other hematological disorders. Stem cell transplants can be carried out using bone marrow, or leukapheresis collections from donors who have been treated with granulocyte-colony stimulating factor (G-CSF) to mobilize stem cells into the peripheral blood. Successful stem cell transplantation depends on both the replacement of diseased stem cells and the establishment of the donor immune system in the recipient in order to maintain graft integrity and to eradicate residual diseased marrow. One danger inherent to the transplantation of allogeneic stem cells is *Graft versus Host Disease* (GVHD). The risk of developing GVHD increases dramatically with the use of matched unrelated (MUD) or haploidentical donors. Donor T cells in the graft mediate GVHD, and controlling the numbers of these cells in grafts is essential for preventing GVHD. Additionally, B cells from the donor may carry *Epstein–Barr virus* (EBV), which can lead to serious post-transplantation complications such as lymphoproliferative disease. Magnetic sorting using the CliniMACS Plus instrument now forms the basis of several different graft engineering approaches aimed at minimizing GVHD and post-transplantation infection. The most important of these approaches will be highlighted in the following sections.

CD34

Enrichment of stem cells using CD34 CliniMACS reagent and the CliniMACS device has been the mainstay of graft manipulation strategies for several years. By selecting the donor stem cells using CD34, an excellent passive depletion of T cells and B cells of between four and five orders of magnitude can regularly be achieved. Thus, selection of CD34 cells with the CliniMACS instrument produces a product of highly purified stem cells whilst removing cells that can cause GVHD or EBV infection (for an example of CD34 selection, see Fig. 4.43).

The application of selected $CD34^+$ cells in transplantation regimes depends on the disease being treated. Transplantation of $CD34^+$ cells alone – inherently preventing GVHD and EBV infection – leads to a profound leucopoenia. Also, immune effector cells may be required to aid engraftment, and to protect against infection until the transplanted immune system begins to function. Therefore, a number of disease-specific strategies have been devised to combine the safety of a pure stem cell transplant, coupled to a controlled add-back of immune effector cells.

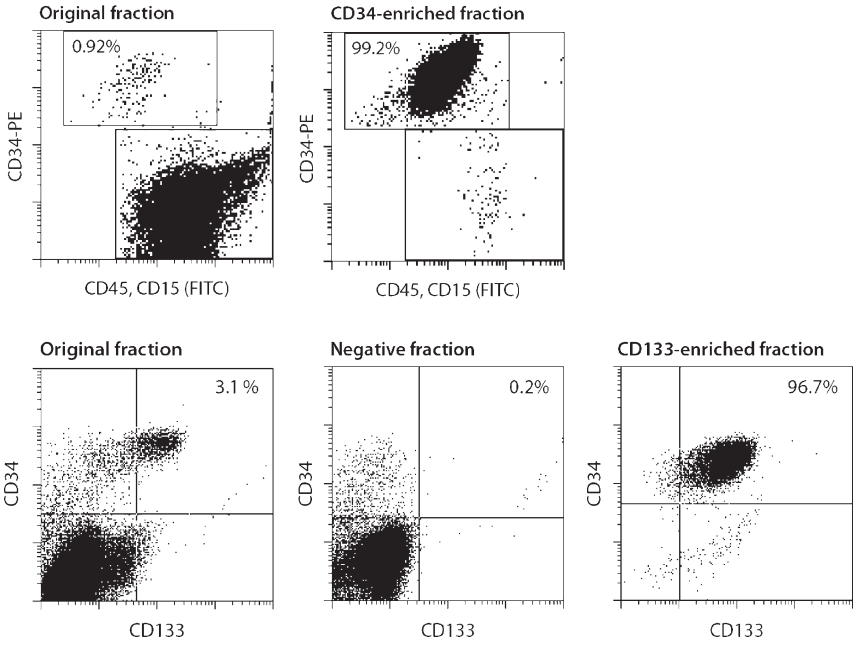

Fig. 4.43. Flow cytometry dot plots showing isolation of stem cells by positive selection according to CD34 and CD133 with the CliniMACS Plus instrument. Mononuclear cells are harvested by standard methods from peripheral blood, cord blood, bone marrow, fetal liver, or leukapheresis. For separation with a CliniMACS instrument, hematopoietic stem and progenitor cells are directly magnetically labeled using MACS MicroBeads specific for CD34 (upper) or CD133 (lower). After enrichment, 99.2% respectively 96.7% pure stem cell fractions are obtained starting from frequencies of 0.92% and 3.1%. The dot plots show the lymphocytes stained with fluorescent antibodies against the indicated CD markers before and after separation. The x- and y-axes indicate the fluorescence intensity on a logarithmic scale. Each dot corresponds to one cell. Detailed information on flow cytometry is reviewed in Gòttlinger et al. (1999).

Autoimmunity and Autologous Transplants for Malignancy Stem cell transplantation is designed for the physician to provide extremely powerful chemotherapy and to eradicate either diseased hematopoetic tissue (malignant or nonmalignant) or solid tumors. The immune system is then "rescued" from this myelo-depleting or -ablating treatment through stem cell transplantation. In the autoimmune setting, stem cells are required from an allogeneic donor in order to replace diseased stem cells, but large numbers of immune effectors are not required to fight an underlying malignancy. In these cases, transplantation of $CD34^+$ cells alone selected with a CliniMACS Plus instrument has been shown to be effective in treating a variety of autoimmune disorders/inborn errors (Gaipa et al., 2003; Lang et al., 2003), even when the donor and recipient were not a complete match. Thus, CD34 selection allows the stem cells to be replaced without the danger of GVHD.

Exactly the opposite situation is true in autologous transplantations for malignancy – there is no danger from self-T cells causing GVHD, but tumor cells can be contained in the nonstem cell fraction of the bone marrow or leukapheresis harvest. Appropriately selected CD34 cells enable the replacement of stem cells killed by chemotherapy, while very efficiently depleting tumor cells from the graft – this is termed ''tumor purging''. This approach has been shown to be beneficial in diseases such as neuroblastoma or lymphoma (Flohr et al., 2002; Handgretinger et al., 2002).

Allogeneic and Haploidentical Transplants One advantage of the CliniMACS system is that the unwanted cell fraction is also retained in a sterile enclosed system after separation, so these cells can be available for downstream processing. This is important in allogeneic and haploidentical transplantation, where graded doses of CD34-negative cells, particularly T cells, may be required to maintain graft integrity and fight underlying malignancy.

Numerous studies have now reported very successful transplant outcomes in a range of malignancies where GVHD has been extremely well controlled, often without immunosuppressive drug treatment, by transplanting purified $CD34^+$ cells and adding back low doses of T cells as required. Malignancies treated thus far include both chronic and acute leukemias in adults as well as pediatric tumors, even with haploidentical donors (three from six HLA alleles mismatched) (Lang et al., 2003; Benesch et al., 2004; Bethge et al., 2004; Aversa et al., 2005).

CD133 is a marker expressed on a subset of human stem cells. CD133 stains 35–70% of $CD34^+$ cells, and also a subset of $CD34^-$ stem cells (de Wynter et al., 1998) (Fig. 4.43). When transplanted into NOD/SCID mice, $CD133^+CD34^-$ cells rapidly induce myeloid and lymphoid engraftment, suggesting that these cells are potent hematopoetic progenitors (Kuci et al., 2003). $CD133^+$ cells are also the only cells capable of generating megakaryocyte colony-forming units (CFU-MK) *in vitro* (Charrier et al., 2002), again showing the importance of this cell type in hematopoiesis.

Early studies with $CD133^+$ cell transplants have now begun, with encouraging results. Several centers have reported improved platelet engraftment compared to historical controls, when transplants are supported with $CD133^+$ cells. Transplants of $CD133^+$ cells alone have been shown to induce rapid and stable *hematopoetic engraftment* (Lang et al., 2003, 2004; Bornhauser et al., 2005).

Depletion of $CD3^+$ and $CD19^+$ Cells As discussed for CD34 above, the transplantation of stem cells alone is not always an option in hematological malignancy, and often complex add-back of T cells or other immune effector cells is required to ensure the best engraftment and repopulation of the immune system. The CliniMACS CD3 and CD19 magnetic depletion system has been developed in order to produce a straightforward way to deplete unwanted T and B cells, whilst leaving the innate immune system cells in the graft intact. The CD3 and CD19 reagents are available separately so that the depletion can be tailored to any specific require-

ments. In particular, grafts depleted of CD3/CD19 cells contain numbers of stem cells comparable to grafts selected for CD34, but contain large numbers of natural killer (NK) cells, whilst maintaining good T cell depletion (Preijers et al., 2004). Preservation of the NK fraction in particular is of interest, as NK cells have been recently shown to potentially aid durable engraftment and mediate anti-tumor effects in certain transplantation settings (see Section 4.7.3.2).

Stem cells in leukapheresis products depleted of CD3/CD19 cells have been shown to be efficient as hematopoetic progenitors (Barfield et al., 2003), and early reports suggest that the products can be effective and safe in the haploidentical transplant setting. Thus, this very new approach has the potential to remove unwanted T and B cells from grafts, while maintaining stem cell potency, and potentially improving the transplant outcome through the effects of NK cells contained in the graft.

4.7.3.2
NK Cells: CD56 and CD3

It has long been known that NK cells are capable of eradicating certain susceptible tumor cells [e.g., acute myeloid leukemia (AML) cells; Lowdell, 2003]. However, attempts at cytokine-activated NK cell therapy during the 1980s and 1990s were largely ineffective. Recent advances in NK receptor biology has led to a far better understanding of these cells (Roigas et al., 1998; Hayakawa et al., 2002). Interest in NK therapy has recently been reignited with the discovery that mismatches in NK receptors between donor and recipient can have a major influence over transplantation outcome. In particular, mismatches in the killer inhibitory receptor (KIR) family between donor and recipient have been found to greatly influence the outcome of transplant in AML (Ruggeri et al., 2002; Giebel et al., 2003).

In order to harness the potential of $CD56^+$ NK cells for exciting new therapies, the CliniMACS CD56 reagent has been developed. This is used in conjunction with the CD3 reagent to first deplete T cells, and then enrich $CD56^+$ NK cells (see Fig. 4.44). (If NKT cells are required, then the CD3 depletion step can be omitted, although the exact impact of $CD3^+CD56^+$ cells on GVHD is unknown.) $CD3^-CD56^+$ cells isolated with this two-step procedure are now been used in early clinical trials, and results will be available shortly.

4.7.3.3
T Cell Subset Graft Engineering Strategies

As discussed above, although many graft manipulation strategies are based on T cell removal, strategic add-back of T cells is often required for a successful transplant outcome. T cells are essential in fighting infection and the eradication of residual tumor cells. Until recently, T cell add-back was often carried out by simply calculating the T cell content of unmanipulated donor material, and adding this back at a set rate of T cells per kg. New developments in clinical magnetic cell sorting mean that it is now possible to manipulate and isolate specific T cell subsets

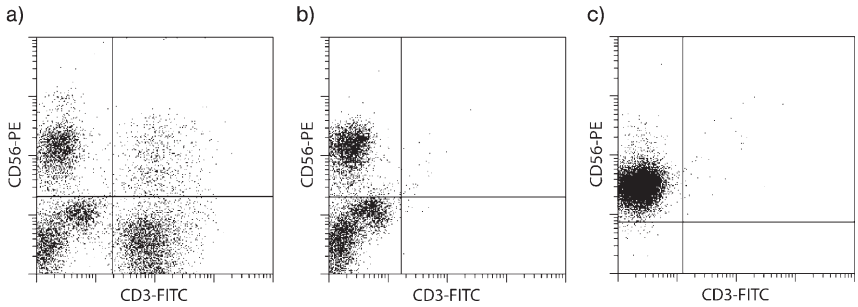

Fig. 4.44. Strategy to isolate natural killer (NK) cells for immunotherapy in two sequential steps (multiparameter magnetic cell sorting). (a) Before separation, (b) after CD3 depletion, (c) after CD3 depletion and CD56 selection. The dot plots demonstrate the enrichment of $CD56^+$ NK cells. $CD3^+$ T cells are first removed by depletion with CD3 CliniMACS reagent. The nonretained cells from the first separation are again magnetically labeled with CD56 and enriched on a second column.

for add-back to patients, and even possible to isolate T cells of known specificity from the donor to mount a response against infections in the recipient. All of these approaches mean that it is becoming increasingly possible to control GVHD but to retain the positive power of donor T cells.

Cytotoxic T Cells (CD8)

Initially carried out using rabbit complement, the depletion of $CD8^+$ T cells has been examined as a route to reduce GVHD after transplant for almost 15 years. Initially focusing on depletion of the graft, it was found that GVHD was significantly reduced where $CD8^+$ cells were removed before transplant of otherwise whole bone marrow (Champlin et al., 1990; Nimer et al., 1994). More recently, CD8 depletion has been applied to *donor lymphocyte infusion* (DLI) treatment, which is increasingly used after stem cell transplant (some CD34 selected) to "push" engraftment and eradicate tumor cells. DLI can commonly be performed months after the initial stem cell transplantation. In small studies, results with $CD8^+$ cell-depleted DLI have been very encouraging, with very significant reductions in the incidence of GVHD reported compared with the use of unmanipulated DLI (Baron et al., 2002; Soiffer et al., 2002). In particular, $CD8^+$ cell-depleted DLI may be of benefit in *chronic myeloid leukemia* (CML) and *multiple myeloma* (MM), where anti-tumor responses are seen in some patients but without accompanying GVHD (Bellucci et al., 2002). The depletion of $CD8^+$ cells is now possible using the CliniMACS Plus instrument, giving excellent CD8 depletion rates. Trials incorporating $CD8^+$ cell-depleted DLI are currently under way.

$CD25^+$ T Cells

CD25 is the low-affinity interleukin (IL)-2 receptor (alpha-chain), and is significant in two ways for the manipulation of T cells. First, it is expressed by recently activated T cells; second, it is expressed constitutively by regulatory T cells. Using the

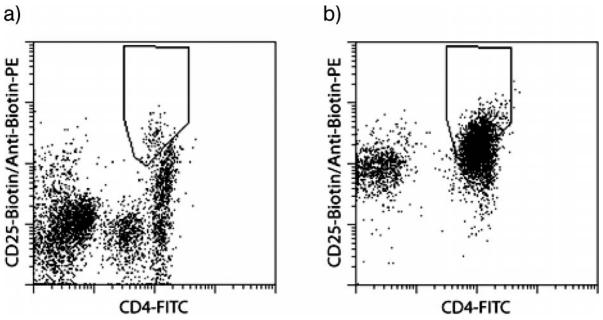

Fig. 4.45. Regulatory T cells ($CD25^+$); (a) before separation, (b) after separation. The dot plots illustrate the enrichment of $CD25^+$ T cells using CliniMACS CD25 MicroBeads and the CliniMACS instrument. The CliniMACS CD25 reagent is suitable for depletion of $CD25^+$ activated regulatory T cells or alloreactive $CD25^+$ T cells from peripheral blood specimen or also *in-vitro* cultures (data not shown). Analysis of the content of $CD25hiCD4^+$ regulatory T cells: For flow-cytometric analysis a specific electronic window is defined. Regulatory T cells have been described as $CD4^+$ T cells, which highly express CD25. The expression of CD4 is slightly reduced as compared to conventional $CD4^+$ T helper cells.

CliniMACS CD25 immunomagnetic depletion system, $CD25^+$ cells of both types can efficiently be removed from stem cell grafts (Fig. 4.45).

The induced expression of CD25 after T cell activation can be used to remove donor T cells which become activated in response to recipient cells. Carried out by culturing donor transplant material cells with recipient antigen-presenting cells (APC) before transplant, this ''allodepletion'' strategy has already been tested using anti-CD25 immunotoxins (Fehse et al., 2000; Solomon et al., 2002). The transplantation of stem cell collections depleted of $CD25^+$ cells has been found to reduce the incidence of GVHD in the high-risk haploidentical transplant setting. Trials using CliniMACS depletion of $CD25^+$ alloreactive cells are ongoing.

Recently, the $CD25^+$ regulatory T cell phenotype has been characterized in depth (Jonuleit et al., 2002). $CD25^+$ cells positively isolated with the CliniMACS Plus instrument are highly enriched for regulatory cells and have the potential to be used therapeutically, for example, to induce tolerance in a patient suffering from GVHD (Hoffmann et al., 2006). Alternatively, $CD25^+$ regulatory cells could be depleted from the blood of cancer patients to enable easier generation of cancer-specific T cells (Powell et al., 2005).

4.7.3.4
Antigen-Specific T Cells: Cytokine Capture System

An extremely powerful way to examine T cell-mediated immune responses, in vaccination, transplantation or disease studies, is to determine the ability of T cells to respond to a specific antigen by the production of effector cytokines such as interferon-gamma (IFN-γ). For the first time, a system has been developed to use

this powerful technique as a method to isolate functional Ag-specific T cells for immune therapy. The Cytokine Secretion Assay [in clinical format, the Cytokine Capture System (IFN-γ) (CCS)] is an innovative method for analyzing and enriching live cytokine-secreting cells (Manz et al., 1995; for a review, see Campbell, 2003). In this assay, a cytokine affinity matrix is built on the cell plasma membrane, which traps IFN-γ produced by the cell in response to specific stimuli. The specifically bound cytokine is then detected, and the cells enriched on the CliniMACS Plus instrument using Anti-IFN-γ MicroBeads. This system allows enrichment of specific T cells from extremely low precursor frequencies. The isolated T cells can either be used directly for therapy or expanded further *in vitro* (Feuchtinger et al., 2004, 2005; Rauser et al., 2004; Beck et al., 2005; Hammer et al., 2005).

Carrying out the CCS requires the following steps for cytokine secretion assay (Fig. 4.46):

- The T cells are stimulated with a specific antigen.
- A cytokine-specific Catch Reagent is attached to the cell surface of all cells. This is composed of the IFN-γ-specific ''catch'' antibody conjugated with a CD45-specific monoclonal antibody. This ensures that all leukocytes are evenly labeled with the Catch Reagent.
- The cells are incubated for 30–45 min at 37 °C to allow IFN-γ secretion. The secreted cytokine binds to the cytokine-specific Catch Reagent on the secreting cells.
- Bound IFN-γ is then labeled with a second IFN-γ-specific ''enrichment'' antibody conjugated to superparamagnetic particles for enrichment by the CliniMACS Plus instrument. The efficiency of labeling and separation is controlled by staining with anti-IFN-γ-phycoerythrin (an example is given in Fig. 4.47).

The first clinical applications of these techniques are in the treatment of viral infection during stem cell transplantation, where it has already been shown that donor-antigen-specific T cells may be effective in controlling viruses such as cytomegalovirus (CMV) (Riddell et al., 1992; Peggs et al., 2003; Rauser et al., 2004). Previously, cells were prepared by repeated stimulation of T cells with Ag; this was a long-term process (>2 months) that often generated lines with narrow specificity (Riddell et al., 1992). CMV-specific T cells isolated by CCS retain the effector-memory phenotype characteristic of these cells, and expand extremely well *in vitro*, so that sufficient cells for vaccination can be established within 10–14 days (Rauser et al., 2004). Thus, the CCS method can save months of work to produce a potentially more potent T cell product for anti-viral therapy, and these cells are now being used in early clinical trials. Other researchers are also using the CCS to isolate tumor-specific T cells, even at very low precursor frequencies, and this is another exciting possibility for the application of the CCS in the future.

4.7.3.5
Dendritic Cells (DCs): CD14-derived DCs, BDCA-1, BDCA-4

Dendritic cells are the most efficient APC of the immune system. DCs are present at low levels in most tissues, acting as sentinels that patrol the boundaries against

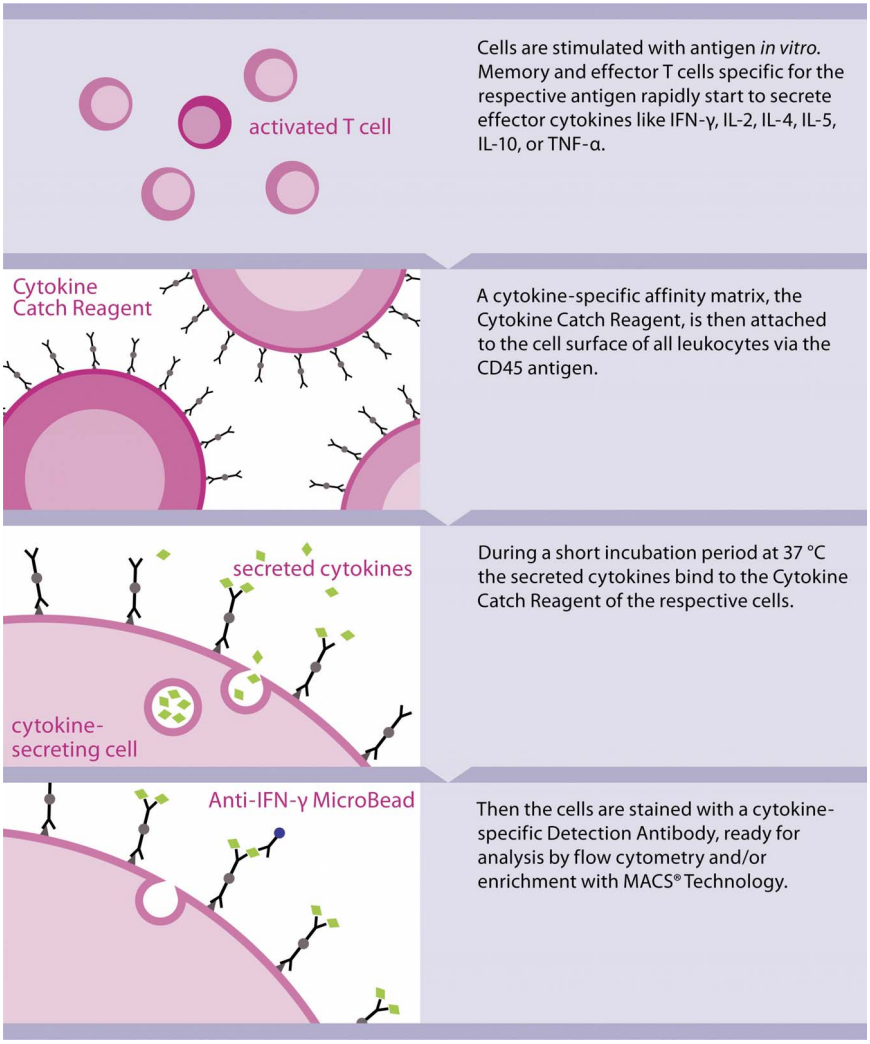

Fig. 4.46. Schematic representation of the Cytokine Secretion Assay. The system enables enrichment of cytokine-secreting cells. In a clinical format, the Cytokine Capture System is designed to enrich antigen-specific T cells for immune therapy.

foreign enemies, such as infectious agents (Banchereau, 1997). The potent antigen-presenting ability of DCs is currently of great interest in the clinical manipulation of immune responses. *Vaccination with DCs*, particularly in cancer and viral-induced disease, may lead to the establishment of Ag-specific immune responses in the patient, which ultimately may eliminate the pathogen or tumor.

Until recently, DCs for therapy have been generated in large numbers from precursor cells, such as $CD34^+$ cells or $CD14^+$ monocytes (Pickl et al., 1996; Thurner

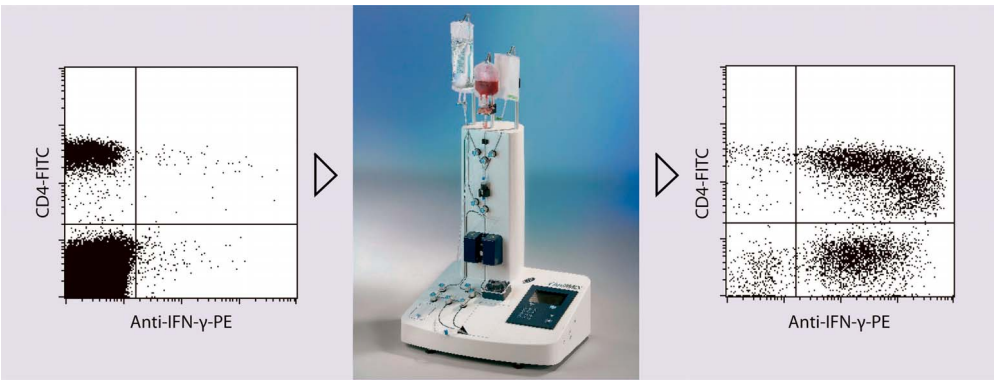

Fig. 4.47. Typical enrichment of IFN-γ producing CMV-specific T cells using the CCS. IFN-γ producing CMV-specific T cells are enriched from $<$0.3% to $>$90% of the T cell population after CliniMACS enrichment.

et al., 1999; see Fig. 4.48). Using *CD14 selection on the CliniMACS* Plus instrument, it is possible to isolate very large numbers of precursors for the generation of monocyte-derived DCs (Mo-DCs) for therapy. Mo-DCs are analogous to DCs of myeloid origin (mDCs), and have already been successfully used in early clinical trials. In these trials, monocytes are isolated using CliniMACS CD14 sorting, and are cultivated in GM-CSF and IL-4 to produce DCs. This results in large numbers of DCs for vaccinating patients against a variety of antigens, from both infectious diseases and tumors (Carlsson et al., 2003; Mazzolini et al., 2005).

In humans, DCs have been identified which develop from at least two different progenitor cell types: these are DCs of myeloid origin (mDC, or DC1), and DCs of plasmacytoid origin (pDC, or DC2) (Dzionek et al., 2000, 2002). There is also heterogeneity within each DC group. The mDC and pDC subsets react to differing maturation signals, produce different cytokines in response to stimulus, and may orchestrate the immune response in different ways. DCs are present in relatively small numbers in the bloodstream ($<$1% of mononuclear cells) (Fay, 1998) and, until recently, no suitable specific markers were available to isolate these cells. We have generated novel reagents to isolate blood DCs for therapy, using the antibodies blood dendritic cell antigen (BDCA)-1 (CD1c) and BDCA-4 to isolate mDC and pDC, respectively. This means that, for the first time, the potent Ag-presenting abilities of natural DCs can be exploited for clinical use, and the specific functions of mDCs and pDCs (Ito et al., 1999; Cella et al., 1999, 2000; Fong et al., 2001) can be investigated in clinical trials. In order to isolate mDCs, the leukapheresis product is first depleted of $CD19^+$ cells (some of which are $CD1c^+$), followed by positive selection with BDCA-1 (CD1c) MicroBeads. For pDCs, cells are directly isolated using anti-BDCA-4 MicroBeads, and the purity determined by staining with Anti-BDCA-2 and CD123 (Fig. 4.48).

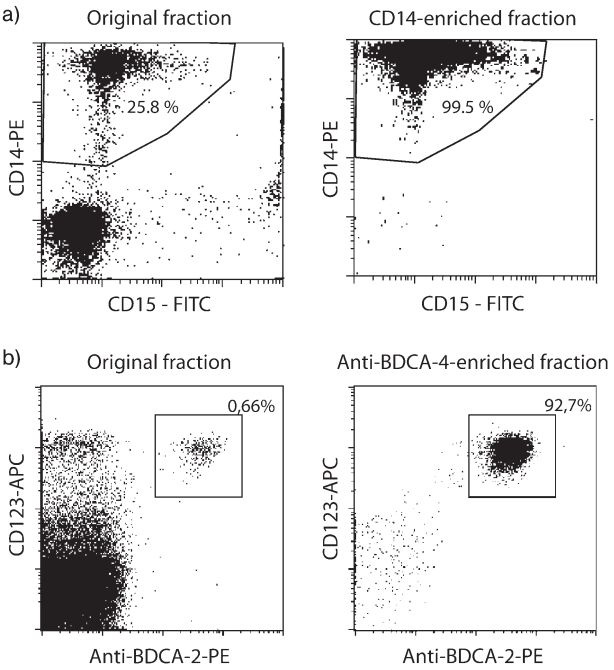

Fig. 4.48. Different strategies for enrichment of DC and DC precursors. (a) The dot plots show that pure $CD14^+$ cells can be selected using the CliniMACS instrument for the subsequent generation of monocyte-derived dendritic cells (MoDC). (b) BDCA-4 selection results in a highly purified population of $CD123^+$ $BDCA\text{-}2^+$ plasmacytoid dendritic cells (pDC).

4.7.3.6

Into the Future: Cardiac Regeneration Using $CD133^+$ Stem Cells

Finally, in this discussion of magnetic sorting for clinical applications, mention must be made of the extremely exciting emerging field of tissue repair using hematopoetic stem cells. Heart disease, particularly *ischemic heart disease* remains the number one cause of death in the industrialized world. During the past few years, it has become clear that the transplantation of stem cells, whether of hematopoetic or nonhematopoietic origin, has the capacity to restore function in ischemic heart tissue (Orlic et al., 2001; Burt et al., 2003; Leinwand, 2003; Stamm et al., 2003).

One challenge in this expanding field is the rapid isolation of appropriate stem cells for transplantation in a clinically acceptable manner, as many of the stem cells produced experimentally are very difficult to make into a clinical cell product. Magnetic sorting using the CliniMACS Plus instrument and CD133 CliniMACS reagent has provided a solution to both the clinical-grade handling of cells and isolation of a stem cell population with genuine potential for tissue repair.

$CD133^+$ cells are stem cells with a more primitive phenotype than $CD34^+$ cells (de Wynter et al., 1998; Kuci et al., 1998). $CD133^+$ cells selected by MACS technology can differentiate into cells of a mesenchymal phenotype, that can be subsequently induced to differentiate into cells of a variety of different tissue types (Tondreau et al., 2005). This multipotency of $CD133^+$ cells is now being exploited in new protocols to treat heart disease where $CD133^+$ cells are introduced to ischaemic tissues during standard cardiac surgery (Stamm et al., 2003; Ghodsizad et al., 2004). The CliniMACS Plus instrument can simply be used in the operating theater to start isolating bone marrow $CD133^+$ cells at the initiation of surgery. The cells are then ready for injection by the end of the normal period of surgery (Ghodsizad et al., 2004). Although these are early trials, certainly when combined with coronary artery bypass grafting, injection of $CD133^+$ cells has been shown to improve left ventricular function and infarct tissue perfusion (Stamm et al., 2003; Ghodsizad et al., 2004). Several Phase II controlled trials have been initiated based on these early successes and, to date, data from these studies supports that of the first trials.

$CD133^+$ cells selected with the CliniMACS Plus instrument therefore represent an exciting new direction for the magnetic sorting of stem cells – the ability to reconstitute not only hematopoetic tissue but also other organs of the body. In addition to cardiac repair, where a large number of trials are now being initiated, the first results have also been reported that $CD133^+$ cell treatment may help in regenerating liver tissue (am Esch et al., 2005). Thus, the multipotent $CD133^+$ stem cell, selected with the CliniMACS Plus instrument, may together form the basis for a wide range of new therapies in the future where immunomagnetic selection means that many tissues in the body can be rebuilt.

Abbreviations/Acronyms

Ab	antibody
Ag	antigen
AML	acute myeloid leukemia
APC	antigen-presenting cell
BDCA	blood dendritic cell antigen
CCS	cytokine capture system
CD	cluster of differentiation
CFU-MK	megakaryocyte colony-forming units
CML	chronic myeloid leukemia
CMV	cytomegalovirus
DCs	dendritic cells
DLI	donor lymphocyte infusion
EBV	Epstein–Barr virus
FACS	fluorescence-activated cell sorting
FITC	fluorescein isothiocyanate
G-CSF	granulocyte-colony-stimulating factor

GM-CSF	granulocyte-macrophage colony-stimulating factor
GVHD	graft versus host disease
HLA	human leukocyte antigen
IFN	interferon
IL	interleukin
KIR	killer inhibitory receptor
mAb	monoclonal antibody
mDC	DC of myeloid origin
MM	multiple myeloma
Mo-DC	monocyte-derived dendritic cell
MUD	matched unrelated
NK cell	natural killer cell
NOD	nonobese diabetes
pDC	plasmacytoid dendritic cell
PE	R-phycoerythrin
SCID	severe combined immunodeficiency

References

am Esch, J.S., Knoefel, W.T., Klein, M., Ghodsizad, A., Fuerst, G., Poll, L.W., Piechaczek, Ch., Burchardt, E., Feifel, N., Stoldt, V., Stockschlader, M., Stoecklein, N., Tustas, R.Y., Eisenberger, C.F., Peiper, M., Haussinger, D., and Hosch, S.B. (2005). Portal application of autologous CD133+ bone marrow cells to the liver: a novel concept to support hepatic regeneration. *Stem Cells*, **23**, 463–470.

Aversa, F., Terenzi, A., Tabilio, A., Falzetti, F., Carotti, A., Ballanti, S., Felicini, R., Falcinelli, F., Velardi, A., Ruggeri, L., Aloisi, T., Saab, J.P., Santucci, A., Perruccio, K., Martelli, M.P., Mecucci, C., Reisner, Y., and Martelli, M.F. (2005). Full haplotype-mismatched hematopoietic stem-cell transplantation: a Phase II study in patients with acute leukemia at high risk of relapse. *J. Clin. Oncol.*, **23** (15), 3447–3454.

Banchereau, J. (1997). Dendritic cells: therapeutic potentials. *Transfus. Sci.*, **18**, 313–326.

Barfield, R.C., Otto, M., Houston, J., Holladay, M., Geiger, T., Martin, J., Leimig, T., Gordon, P., Chen, X., and Handgretinger, R. (2003). A one-step large-scale method for T- and B-cell depletion of mobilized PBSC for allogeneic transplantation. *Cytotherapy*, **6**, 1–6.

Baron, F., Siquet, J., Schaaf-Lafontaine, N., Baudoux, E., Hermanne, J.P., Fillet, G., and Beguin, Y. (2002). Pre-emptive immunotherapy with CD8-depleted donor lymphocytes after CD34-selected allogeneic peripheral blood stem cell transplantation. *Haematologica*, **87**, 78–88.

Beck, O., Topp, M.S., Koehl, U., Roilides, E., Simitsopoulou, M., Hanisch, M., Sarfati, J., Latge, J.P., Klingebiel, T., Einsele, H., and Lehrnbecher, T. (2005). Generation of highly-purified and functionally active human TH1-cells against *Aspergillus fumigatus*. *Blood*, **107** (5), 1182–1193.

Bellucci, R., Alyea, E.P., Weller, E., Chillemi, A., Hochberg, E., Wu, C.J., Canning, C., Schlossman, R., Soiffer, R.J., Anderson, K.C., and Ritz, J. (2002). Immunologic effects of prophylactic donor lymphocyte infusion after allogeneic marrow transplantation for multiple myeloma. *Blood*, **99**, 4610–4617.

Benesch, M., Urban, C., Sykora, K.W., Schwinger, W., Zintl, F., Lackner, H., Lang, P., and Handgretinger, R. (2004). Transplantation of highly purified $CD34^+$ progenitor cells from alternative donors in children with refractory severe aplastic anaemia. *Br. J. Haematol.*, **125**, 58–63.

Bethge, W.A., Faul, C., Handgretinger, R., Lang, P., Kanz, L., and Einsele, H. (2004). Haploidentical allogeneic haematopoietic cell transplantation with CD34 selected stem cells for the treatment of haematologic malignancies: high survival and low incidence of GVHD (abstract). *Bone Marrow Transplant.*, **33** (Suppl. 1), 339.

Bornhauser, M., Eger, L., Oelschlaegel, U., Auffermann-Gretzinger, S., Kiani, A., Schetelig, J., Illmer, T., Schaich, M., Corbeil, D., Thiede, C., and Ehninger, G. (2005). Rapid reconstitution of dendritic cells after allogeneic transplantation of $CD133^+$ selected hematopoietic stem cells. *Leukemia*, **19**, 161–165.

Burt, R., Pearce, W., Luo, K., Oyama, Y., Davidson, C., Beohar, N., and Gheorghiade, M. (2003). Hematopoietic stem cell transplantation for cardiac and peripheral vascular disease. *Bone Marrow Transplant.*, **32** (Suppl. 1), 29–31.

Campbell, J.D.M. (2003). Detection and enrichment of antigen-specific $CD4^+$ and $CD8^+$ T cells based on cytokine secretion. *Methods*, **31**, 150–159.

Carlsson, B., Cheng, W.S., Totterman, T.H., and Essand, M. (2003). Ex-vivo stimulation of cytomegalovirus (CMV)-specific T cells using CMV pp65-modified dendritic cells as stimulators. *Br. J. Haematol.*, **121**, 428–438.

Cella, M., Jarrossay, D., Facchetti, F., Alebardi, O., Nakajima, H., Lanzavecchia, A., and Colonna, M. (1999). Plasmacytoid monocytes migrate to inflamed lymph nodes and produce large amounts of type I interferon. *Nat. Med.*, **5**, 919–923.

Cella, M., Facchetti, F., Lanzavecchia, A., and Colonna, M. (2000). Plasmacytoid dendritic cells activated by influenza virus and CD40L drive a potent TH1 polarization. *Nat. Immunol.*, **1**, 305–310.

Champlin, R., Ho, W., Gajewski, J., Feig, S., Burnison, M., Holley, G., Greenberg, P., Lee, K., Schmid, I., and Giorgi, J. (1990). Selective depletion of $CD8^+$ T lymphocytes for prevention of graft-versus-host disease after allogeneic bone marrow transplantation. *Blood*, **76**, 418–423.

Charrier, S., Boiret, N., Fouassier, M., Berger, J., Rapatel, C., Pigeon, P., Mareynat, G., Bonhomme, J., Camilleri, L., and Berger, M.G. (2002). Normal human bone marrow $CD34^+CD133^+$ cells contain primitive cells able to produce different categories of colony-forming unit megakaryocytes *in vitro*. *Exp. Hematol.*, **30**, 1051–1060.

de Wynter, E.A., Buck, D., Hart, C., Heywood, R., Coutinho, L.H., Clayton, A., Rafferty, J.A., Burt, D., Guenechea, G., Bueren, J.A., Gagen, D., Fairbairn, L.J., Lord, B.I., and Testa, N.G. (1998). $CD34^+AC133^+$ cells isolated from cord blood are highly enriched in long-term culture-initiating cells, NOD/SCID-repopulating cells and dendritic cell progenitors. *Stem Cells*, **16**, 387–396.

Dzionek, A., Fuchs, A., Schmidt, P., Cremer, S., Zysk, M., Miltenyi, S., Buck, D.W., and Schmitz, J. (2000). BDCA-2, BDCA-3, and BDCA-4: three markers for distinct subsets of dendritic cells in human peripheral blood. *J. Immunol.*, **165**, 6037–6046.

Dzionek, A., Inagaki, Y., Okawa, K., Nagafune, J., Rock, J., Sohma, Y., Winkels, G., Zysk, M., Yamaguchi, Y., and Schmitz, J. (2002). Plasmacytoid dendritic cells: from specific surface markers to specific cellular functions. *Hum. Immunol.*, **63**, 1133–1148.

Fay, J. (1998). Dendritic cells in the treatment of cancer. *Baylor Univ. Med. Cent. Proc.*, **11**, 217–219.

Fehse, B., Frerk, O., Goldmann, M., Bulduk, M., and Zander, A.R. (2000). Efficient depletion of alloreactive donor T lymphocytes based on expression of two activation-induced antigens (CD25 and CD69). *Br. J. Haematol.*, **10**, 644–651.

Feuchtinger, T.F., Lang, P., Hamprecht, K., Schumm, M., Greil, J., Jahn, G., Niethammer, D., and Einsele, H. (2004). Isolation and expansion of human adenovirus-specific CD4+ and CD8+ T cells according to IFN-gamma secretion for adjuvant immunotherapy. *Exp. Hematol.*, **32** (3), 282–289.

Feuchtinger, T.F., Matthes-Martin, S., Richard, C., Lion, T., Hamprecht, K., Peters, C., Schumm, M., Beck, R., Niethammer, D., Handgretinger, R., and Lang, P. (2005). Adoptive transfer of adenovirus specific T-cells in children with systemic adenovirus infection after allogeneic stem cell transplantation. *Blood* (ASH Annual Meeting Abstracts), **106**, 80.

Flohr, T., Hess, G., Kolbe, K., Gamm, H., Nolte, H., Stanislawski, T., Huber, C., and Derigs, H.G. (2002). Rituximab *in vivo* purging is safe and effective in combination with CD34-positive selected autologous stem cell transplantation for salvage therapy in B-NHL. *Bone Marrow Transplant.*, **29**, 769–775.

Fong, L., Hou, Y., Rivas, A., Benike, C., Yuen, A., Fisher, G.A., Davis, M.M., and Engleman, E.G. (2001). Altered peptide ligand vaccination with Flt3 ligand expanded dendritic cells for tumor immunotherapy. *Proc. Natl. Acad. Sci. USA*, **98**, 8809–8814.

Gaipa, G., Dassi, M., Perseghin, P., Venturi, N., Corti, P., Bonanomi, S., Balduzzi, A., Longoni, D., Uderzo, C., Biondi, A., Masera, G., Parini, R., Bertagnolio, B., Uziel, G., Peters, C., and Rovelli, A. (2003). Allogeneic bone marrow stem cell transplantation following $CD34^+$ immunomagnetic enrichment in patients with inherited metabolic storage diseases. *Bone Marrow Transplant.*, **31**, 857–860.

Ghodsizad, A., Klein, H.M., Borowski, A., Stoldt, V., Feifel, N., Voelkel, T., Piechaczek, Ch., Burchardt, E., Stockschlader, M., and Gams, E. (2004). Intraoperative isolation and processing of BM-derived stem cells. *Cytotherapy*, **6**, 523–526.

Giebel, S., Locatelli, F., Lamparelli, T., Velardi, A., Davies, S., Frumento, G., Maccario, R., Bonetti, F., Wojnar, J., Martinetti, M., Frassoni, F., Giorgiani, G., Bacigalupo, A., and Holowiecki, J. (2003). Survival advantage with KIR ligand incompatibility in hematopoietic stem cell transplantation from unrelated donors. *Blood*, **102**, 814–819.

Göttlinger, C., Mechtold, B., and Radbruch, A. (1999). Operation of a flow cytometer. In: Radbruch, A. (Ed.), *Flow Cytometry and Cell Sorting*, 2nd edn., Springer-Verlag, Berlin Heidelberg, pp. 3–25.

Hammer, M.H., Meyer, S., Brestrich, G., Moosmann, A., Kern, F., Tesfa, L., Babel, N., Mittenzweig, A., Rooney, C.M., Hammerschmidt, W., Volk, H.D., and Reinke, P. (2005). HLA type-independent generation of antigen-specific T cells for adoptive immunotherapy. *Eur. J. Immunol.*, **35** (7), 2250–2258.

Handgretinger, R., Lang, P., Ihm, K., Schumm, M., Geiselhart, A., Koscielniak, E., Hero, B., Klingebiel, T., and Niethammer D. (2002). Isolation and transplantation of highly purified autologous peripheral $CD34^+$ progenitor cells: purging efficacy, hematopoietic reconstitution and long-term outcome in children with high-risk neuroblastoma. *Bone Marrow Transplant.*, **29**, 731–736.

Hayakawa, Y., Kelly, J.M., Westwood, J.A., Darcy, P.K., Diefenbach, A., Raulet, D., and Smyth, M.J. (2002). Tumor rejection mediated by NKG2D receptor-ligand interaction is dependent upon perforin. *J. Immunol.*, **169**, 5377–5381.

Hoffmann, P., Boeld, T.J., Eder, R., Albrecht, J., Doser, K., Piseshka, B., Dada, A., Niemand, C., Assenmacher, M., Orsó, E., Andreesen, R., Holler, E., and Edinger, M. (2006). Isolation of CD4+CD25+ regulatory T cells for clinical trials. *Biol. Blood Marrow Transplant.*, **12** (3), 267–274.

Ito, T., Inaba, M., Inaba, K., Toki, J., Sogo, S., Iguchi, T., Adachi, Y., Yamaguchi, K., Amakawa, R., Valladeau, J., Saeland, S., Fukuhara, S., and Ikehara, S. (1999). A $CD1a^+/CD11c^+$ subset of human blood dendritic cells is a direct precursor of Langerhans cells. *J. Immunol.*, **163**, 1409–1419.

Jonuleit, H., Schmitt, E., Kakirman, H., Stassen, M., Knop, J., and Enk, A.H. (2002). Infectious tolerance: human $CD25^+$ regulatory T cells convey suppressor activity to conventional $CD4^+$ T helper cells. *J. Exp. Med.*, **196**, 255–260.

Kantor, A.B., Gibbons, I., Miltenyi, S., and Schmitz, J. (1997). Magnetic cell sorting with colloidal superparamagnetic particles. In: Recktenwald, D. and Radbruch, A. (Eds.), *Cell Separation Methods and Applications*, Marcel Dekker Inc., New York, Basel, Hong Kong.

Kato, K. and Radbruch, A. (1993). Isolation and characterization of $CD34^+$ hematopoietic stem cells from human peripheral blood by high gradient magnetic cell sorting. *Cytometry*, **14**, 384–392.

Kuci, S., Taylor, G., Neu, S., Schumm, M., Niethammer, D., and Handgretinger, R.

(1998). Phenotypic and functional characterization of mobilized peripheral blood CD34+ cells coexpressing different levels of c-Kit. *Leuk. Res.*, **22**, 355–363.

Kuci, S., Wessels, J.T., Buhring, H.J., Schilbach, K., Schumm, M., Seitz, G., Loffler, J., Bader, P., Schlegel, P.G., Niethammer, D., and Handgretinger, R. (2003). Identification of a novel class of human adherent CD34$^-$ stem cells that give rise to SCID-repopulating cells. *Blood*, **101**, 869–876.

Lang, P., Klingebiel, T., Bader, P., Greil, J., Schumm, M., Schlegel, P.G., Eyrich, M., Mueller-Weihrich, S., Niethammer, D., and Handgretinger, R. (2003). Transplantation of highly purified peripheral-blood CD34$^+$ progenitor cells from related and unrelated donors in children with nonmalignant diseases. *Bone Marrow Transplant.*, **33**, 25–32.

Lang, P., Bader, P., Schumm, M., Feuchtinger, T., Einsele, H., Fuhrer, M., Weinstock, C., Handgretinger, R., Kuci, S., Martin, D., Niethammer, D., and Greil, J. (2004). Transplantation of a combination of CD133$^+$ and CD34$^+$ selected progenitor cells from alternative donors. *Br. J. Haematol.*, **124**, 72–79.

Leinwand, L.A. (2003). Hope for a broken heart? *Cell*, **114**, 658–659.

Lowdell, M.W. (2003). Natural killer cells in haematopoietic stem cell transplantation. *Transfus. Med.*, **13**, 399–404.

Manz, R., Assenmacher, M., Pfluger, E., Miltenyi, S., and Radbruch, A. (1995). Analysis and sorting of live cells according to secreted molecules, relocated to a cell-surface affinity matrix. *Proc. Natl. Acad. Sci. USA*, **92**, 1921–1925.

Mazzolini, G., Alfaro, C., Sangro, B., Feijoo, E., Ruiz, J., Benito, A., Tirapu, I., Arina, A., Sola, J., Herraiz, M., Lucena, F., Olague, C., Subtil, J., Quiroga, J., Herrero, I., Sadaba, B., Bendandi, M., Qian, C., Prieto, J., and Melero, I. (2005). Intratumoral injection of dendritic cells engineered to secrete interleukin-12 by recombinant adenovirus in patients with metastatic gastrointestinal carcinomas. *J. Clin. Oncol.*, **23**, 999–1010.

McNiece, I., Briddell, R., Stoney, G., Kern, B., Zilm, K., Recktenwald, D., and Miltenyi, S. (1997). Large-scale isolation of CD34$^+$ cells using the Amgen cell selection device results in high levels of purity and recovery. *J. Hematother.*, **6**, 5–11.

Miltenyi, S. and Schmitz, J. (1999). High gradient magnetic cell sorting. In: Radbruch, A. (Ed.), *Flow Cytometry and Cell Sorting*, 2nd edn., Springer-Verlag, Berlin, Heidelberg, pp. 218–247.

Miltenyi, S., Müller, W., Weichel, W., and Radbruch, A. (1990). High gradient magnetic cell separation with MACS. *Cytometry*, **11**, 231–238.

Molday, R.S. and MacKenzie, D. (1982). Immunospecific ferromagnetic iron-dextran reagents for the labeling and magnetic separation of cells. *J. Immunol. Methods*, **52**, 353–367.

Nimer, S.D., Giorgi, J., Gajewski, J.L., Ku, N., Schiller, G.J., Lee, K., Territo, M., Ho, W., Feig, S., and Selch, M. (1994). Selective depletion of CD8$^+$ cells for prevention of graft-versus-host disease after bone marrow transplantation. A randomized controlled trial. *Transplantation*, **57**, 82–87.

Orlic, D., Kajstura, J., Chimenti, S., Jakoniuk, I., Anderson, S.M., Li, B., Pickel, J., McKay, R., Nadal-Ginard, B., Bodine, D.M., Leri, A., and Anversa, P. (2001). Bone marrow cells regenerate infarcted myocardium. *Nature*, **410**, 701–705.

Peggs, K.S., Verfuerth, S., Pizzey, A., Khan, N., Guiver, M., Moss, P.A., and Mackinnon, S. (2003). Adoptive cellular therapy for early cytomegalovirus infection after allogeneic stem-cell transplantation with virus-specific T-cell lines. *Lancet*, **362**, 1375–1377.

Pickl, W.F., Majdic, O., Kohl, P., Stockl, J., Riedl, E., Scheinecker, C., Bello-Fernandez, C., and Knapp, W. (1996). Molecular and functional characteristics of dendritic cells generated from highly purified CD14$^+$ peripheral blood monocytes. *J. Immunol.*, **157**, 3850–3859.

Powell, D.J., Parker, L.L., and Rosenberg, S.A. (2005). Large-scale depletion of CD25+ regulatory T cells from patient leukapheresis samples. *J. Immunother.*, **28** (4), 403–411.

Radbruch, A., Mechtold, B., Thiel, A., Miltenyi, S., and Pflüger, E. (1994). High gradient magnetic cell sorting. *Methods Cell Biol.*, **42**, 387–403.

Preijers, F.W., Schattenberg, A., Ruijs, C., and Trilsbeek, C. (2004). Bone marrow transplantation after processing by gradients and negative immunomagnetic T- and B-cell selection to prevent GvHD without loss of engraftment potential (abstract). *Bone Marrow Transplant.*, **33** (Suppl. 1), 93.

Rauser, G., Einsele, H., Sinzger, C., Wernet, D., Kuntz, G., Assenmacher, M., Campbell, J.D.M., and Topp, M.S. (2004). Rapid generation of combined CMV-specific $CD4^+$ and $CD8^+$ T cell lines for adoptive transfer into recipients of allogeneic stem cell transplantations. *Blood*, **103**, 3565–3572.

Riddell, S.R., Watanabe, K.S., Goodrich, J.M., Li, C.R., Agha, M.E., and Greenberg, P.D. (1992). Restoration of viral immunity in immunodeficient humans by the adoptive transfer of T cell clones. *Science*, **257**, 238–241.

Roigas, J., Wallen, E.S., Loening, S.A., and Moseley, P.L. (1998). Heat shock protein (HSP72) surface expression enhances the lysis of a human renal cell carcinoma by IL-2 stimulated NK cells. *Adv. Exp. Med. Biol.*, **451**, 225–229.

Ruggeri, L., Capanni, M., Urbani, E., Perruccio, K., Shlomchik, W.D., Tosti, A., Posati, S., Rogaia, D., Frassoni, F., Aversa, F., Martelli, M.F., and Velardi, A. (2002). Effectiveness of donor natural killer cell alloreactivity in mismatched hematopoietic transplantations. *Science*, **295**, 2097–2100.

Soiffer, R.J., Alyea, E.P., Hochberg, E., Wu, C., Canning, C., Parikh, B., Zahrieh, D., Webb, I., Antin, J., and Ritz, J. (2002). Randomized trial of $CD8^+$ T cell depletion in the prevention of graft-versus-host disease associated with donor lymphocyte infusion. *Biol. Blood Marrow Transplant.*, **8**, 625–632.

Solomon, S.R., Tran, T., Carter, C.S., Donnelly, S., Hensel, N., Schindler, J., Bahceci, E., Ghetie, V., Michalek, J., Mavroudis, D., Read, E.J., Vitetta, E.S., and Barrett, A.J. (2002). Optimized clinical-scale culture conditions for *ex vivo* selective depletion of host-reactive donor lymphocytes: a strategy for GVHD prophylaxis in allogeneic PBSC transplantation. *Cytotherapy*, **4**, 395–406.

Stamm, C., Westphal, B., Kleine, H.D., Petzsch, M., Kittner, C., Klinge, H., Schumichen, C., Nienaber, C.A., Freund, M., and Steinhoff, G. (2003). Autologous bone-marrow stem-cell transplantation for myocardial regeneration. *Lancet*, **361**, 45–46.

Thurner, B., Röder, C., Dieckmann, D., Heuer, M., Kruse, M., Glaser, A., Keikavoussi, P., Kämpgen, E., Bender, A., and Schuler, G. (1999). Generation of large numbers of fully mature and stable dendritic cells from leukapheresis products for clinical application. *J. Immunol. Methods*, **223**, 1–15.

Tondreau, T., Meuleman, N., Delforge, A., Dejeneffe, M., Leroy, R., Massy, M., Mortier, C., Bron, D., and Lagneaux, L. (2005). Mesenchymal stem cells derive from CD133 positive cells in mobilized peripheral blood and cord blood: proliferation, Oct-4 expression and plasticity. *Stem Cells*, **23** (8), 1105–1112.

Ugelstad, J., Prestvik, W.S., Stenstad, P., Kilaas, L., and Kvalheim, G. (1998). Selective cell separation with monosized magnetizable polymer beads. In: Andrä, W. and Nowak, H. (Eds.), *Magnetism in Medicine*, Wiley-VCH, Berlin, pp. 473–490.

4.8
Magnetic Drug Targeting

Christoph Alexiou and Roland Jurgons

4.8.1
Background and History of Magnetic Drug Targeting

Targeted drug delivery is a continuing challenge in medicine. During the past 20 years, many different approaches for targeted drug delivery systems have been developed, the aim being to increase drug concentrations in the respective tissue compartments (Collins, 1984; Gupta, 1990; Gupta and Hung, 1990a,b; Torchilin, 2000; see also Section 4.3). Drug delivery systems can be either passive – based on specific properties of pathological tissues and specific characteristics of targeted organs (Arap et al., 2002); or active – often magnetically directed and based on various carrier systems (Zacharski et al., 2002). *Monoclonal antibodies* for thrombolysis (Haber, 1994), drug-containing *tumor-specific antibodies* or drug-loaded pH-sensitive thermosensitive *liposomes*, respectively (Yatvin et al., 1980; Torchilin et al., 1993), can be used in the treatment of cancer (Sachdeva, 1998; Leveugle et al., 2000). Furthermore, *magnetoliposomes* can be used for local hyperthermia (Shinkai et al., 1994).

Magnetic drug targeting is a drug delivery system, in which the medication and a suitable magnetic active component (e.g., Fe_3O_4) is transported by means of a stable pharmaceutical microcarrier system. This coupled substance is injected intravascularly and concentrated under the influence of an external magnetic field towards a desired location of the body (Kato et al., 1980, 1981; Gupta and Hung, 1994).

Historically, the concept of injecting magnetic fluid compounds began during the 1960s, and the procedure was subsequently developed in order to occlude cerebral and renal aneurysms (Alksne et al., 1966; Hilal et al., 1974). The technique incorporating medications and magnetic particles into a carrier sphere developed as a result of attempts to irreversibly aggregate magnetic particles in the presence of an external magnetic field, which resulted in this case in vascular thrombosis. This allowed the further development of magnetic drug targeting. Among these target-directed drug administrations, focus has been centered on a type of active drug targeting in which the magnetic particles – along with their transported substances – are held in position by an external magnetic field at the target region, thus pre-

venting their flow with the bloodstream. One prerequisite for the efficacy of this system is to reach the microcirculation of the target-directed area and to release the active ingredient on a cellular or subcellular level (Widder et al., 1978, 1979). In the field of oncology, controlled release of the magnetic coupled cytostatic agent at cellular or subcellular levels permits the minimization of toxicity in normal tissue and endothelial cells. This contrasts with the adverse side effects often seen following systemic administration of chemotherapeutic agents. The fact that the tumor vessels show an increased microvascular macromolecular permeability also facilitates extravasation of the carrier ingredient, and subsequent release of the medication (Gerlowski and Jain, 1986). Two important requirements of magnetic drug targeting are first, that sufficient perfusion of the target-directed area occurs, and second that there is good accessibility of the external magnetic field.

A variety of magnetic cytostatic agents have been developed in the field of oncology. During the early stages of this procedure the ability to directly couple cytostatic agents with magnetic particles had not been developed, and consequently both components had to be incorporated into diverse carrier microspheres (Widder et al., 1978, 1983; Morris et al., 1984; Gupta and Hung, 1994). Widder employed large denatured albumin molecules as carrier substances, in which the cytostatic agent doxorubicin, as well as magnetic particles were stored. Following intra-arterial injection into the tail artery of rats, these microspheres were selectively fixed in 3-cm proximally positioned Yoshida sarcomas with a permanent magnet. Over 80% of the animals demonstrated tumor remission following this type of selective cytostatic administration.

During the 1970s, Kramer (1974) and Rahman et al. (1974) each used a similar application and administered the cytostatic agents daunorubicin, mercaptopurine and actinomycin bound to magnetic microspheres. However, enzymatic and mechanical damage of the carrier microspheres often occurred in the organism, such that the magnetic influence of transporting substances was lost. At this time, it was impossible to couple the cytostatic agent directly to the magnetic particle, and consequently both components were incorporated into separate albumin microspheres. As a result, the therapeutic efficacy was dependent upon the intact and constant bond of both substances to the outer protein layer. The albumin spheres utilized ranged in size from 1 to 7 μm, and this led to a reduction in intravascular availability due to rapid phagocytosis of the particles via the macrophage-monocyte system. Injectible preparations of this particle size may also cause dangerous emboli. Since the maximum incorporation of albumin microspheres onto the Fe_3O_4 particles was 20%, the particles' magnetic ability was often inadequate (Gupta and Hung, 1994). Moreover, as the direct coupling of cytostatic agent and magnetic particles as a physiological unit was not possible, no further developments were made in this field.

In 1996, Bergemann – for the first time – was able to demonstrate the direct chemical bonding of cytostatic agents with ferrofluids, as a physiological unit (German patent application no. 19624426.9) , thereby resolving the problem of unstable carrier microspheres. The single magnetic particles were covered by starch polymers, and the pharmaceutical in turn was bound ionically to the particles. These

ferrofluids were investigated by Lübbe et al. (1996a,b) in a series of studies performed on mice and rats, followed by Phase I and II studies in 14 patients suffering from a variety of malignant tumors. The ferrofluids were administered intravenously, and demonstrated minimal low toxicity. Kuznetsov et al. (1997) subsequently conducted animal studies using disperse particles consisting of a ferromagnetic core composed of iron or its oxides and attached to a carbon structure or coated with carbon. The particle sizes ranged from 0.01 to 1 μm, and they were combined with antibiotic solutions (anti-cancer drugs). Under the influence of an external permanent magnetic field, the particles could be concentrated in a respective body compartment (i.e., the tumor), where the bound drug was released. In clinical trials conducted in several Russian clinics and in more than 100 patients with different types of tumor, the particles led in most cases either to a full recovery or to an improvement of the patients' condition (Kuznetsov et al., 1997).

4.8.2 Regional Chemotherapies for Cancer Treatment

Chemotherapeutic agents have been used for cancer therapy for almost 50 years, and today more than 50 such compounds are in frequent use. These cytostatic agents impact upon the genetic system of cells, interfering with metabolic pathways or destroying cellular structures, and this results in a suppression of tumor cell proliferation. Cytostatic agents are classified according to their mechanism of action into several groups:

- Alkylating substances (e.g., cyclophosphamide, ifosfamid, busulfan, mitoxantrone) react with active groups in the cell and the DNA. Reaction with alkylating drugs results in incorrect doubling of the DNA during cell division and, therefore to mutation, cytotoxicity, and cell death.
- Antimetabolites (e.g., 5-fluorouracil, methotrexate) inhibit the cell cycle phase specifically by blocking the pre-stage of nucleic acid synthesis during S phase.
- Suppressors of mitosis (e.g., vindesin, vinblastin) inhibit cell division phase specifically by damaging the spindle apparatus.
- Antineoplastic antibiotics (e.g., adriamycin, bleomycin) suppress DNA-dependent RNA synthesis.
- Other agents (e.g., dacarbacin, cisplatin, paclitaxel) act by different (in part nonclarified) mechanisms.

Unfortunately, cytostatic agents cannot discriminate between tumor and healthy tissues, and consequently chemotherapy also impairs healthy (especially growth-intensive) cells and united cell structures. This results in cellular toxic effects on the bone marrow, gastrointestinal tract and germ cells that may be mutagenic, teratogenic, and/or cancerogenic. The risk of second tumors induced by chemotherapy has been estimated at up to 3% (Neglia et al., 2001). These second tumors are caused by long-term therapy with high cytostatic dosages, predominantly with

Table 4.4. Different regional chemotherapies in cancer treatment.

1. Intratumoral therapy

2. Intracavital therapy
   - liquor-cerebrospinal cavity
   - intrapleural
   - intrapericardial
   - intraperitoneal
   - intravesical
   - intravaginal

3. Intra-arterial infusion
   - *A. hepatica* (primary and secondary tumors of the liver)
   - *A. mammaria interna* (mammarian cancer)
   - *A. carotis interna* (brain tumors)
   - *A. carotis externa* (head and neck tumors)
   - *A. iliaca interna* (pelvic tumors, soft tissue tumors)
   - *A. bronchiales* (pulmonary carcinomas)
   - *A. femoralis*, *A. axillaris* (sarcomas of extremities)

4. Intraportal infusion
   - *V. portae* (secondary tumors of the liver)

5. Regional perfusion
   - perfusion of extremities (soft tissue tumors, malignant melanoma)
   - perfusion of the liver (primary and secondary tumors of the liver)

6. Chemoembolization
   - liver, kidney

alkylating drugs. Regular systemic chemotherapy is limited due to the toxic effects on healthy tissue (Poste and Kirsh, 1983), and due to the correlation between applied dose and cytotoxic effects on tumor cells, it is necessary to utilize several locoregional application modes (Table 4.4). Local chemotherapy is aimed at concentrating the chemotherapeutic agent in the tumor region, thereby reducing negative side effects in healthy tissues.

4.8.3 Current Applications of Magnetic Drug Targeting

Recent advances in nanofabrication techniques have introduced a wide array of highly sophisticated biomedical applications for magnetic nanoparticles. These dif-

ferent applications are used both *in vitro* and *in vivo* (Lübbe et al., 2000, 2001), depending on the relationship between the size, shape and composition of magnetic nanoparticles, as well as the magnetic fields and biological systems.

4.8.3.1 *In-Vitro* Studies

Magnetically targetable carriers (MTC™) were formulated by Allen et al. (1997) as an alloy of iron and activated carbon in the size range of 0.5 to 2 μm and bound to paclitaxel, a promising antitumor agent for head and neck cancer. This MTC™-paclitaxel compound released 38% of the adsorbed drug in sera over 24 h. In addition, these carrier complexes could be retained in a magnetic field at capillary (0.2 cm s^{-1}) to arteriole (28 cm s^{-1}) flow rates, and the cytotoxicity of paclitaxel *in vitro* was not affected by the presence or absence of magnetic field retention of a specific MTC™ over the tumor cells.

Another example of the *in-vitro* application of magnetic nanoparticles is that of Magnetofection™. Gene vectors bound to magnetic nanoparticles are used to transfect cells *in vitro* after which, under the influence of an external magnetic field (NE-Fe-B-permanent magnet), the cells show an increasing transfection (Scherer et al., 2002).

4.8.3.2 *In-Vivo* Studies

Magnetically targeted carriers, a suspension of 0.5 to 5.0 μm-diameter magnetically active, carbon-coated iron particles which allow the subsequent binding of doxorubicin molecules through a reversible process of adsorption (MTC-Dox, FerX®; San Diego, CA, USA), were used to treat hepatocellular carcinomas (Rudge et al., 2001). Between April 2001 and June 2002, four patients received several intra-arterial injections (hepatic artery) of MTC-Dox while a portable external magnetic field (permanent magnet) was focused onto the tumor region. Intraprocedural magnetic resonance imaging after each dose showed increasing areas of signal intensity loss owing to a magnetic susceptibility artifact caused by iron. One patient had a substantial reduction in tumor size, while the others showed a stable tumor size during the observation period of 5 to 17 months (Wilson et al., 2004). Some necrosis of the liver corresponding to embolization after treatment was described (Goodwin et al., 2001), and recently (April, 2004) a global multi-center Phase II/III study using MTC-Dox was abruptly halted because the trial's clinical endpoints could not be met with statistical significance using the product as currently manufactured.

Among current preclinical studies, magnetic nanoparticles (100-nm diameter, Chemicell®; Berlin, Germany), ionically bound to mitoxantrone (Novantrone®; Lederle, Wyeth-Pharma, Germany) were injected into the tumor-supplying artery of tumor-bearing rabbits (VX2 squamous cell carcinoma, medial portion of the hind limb) and a very strong external magnetic field (1.7 T) was focused onto this area (Alexiou et al., 2000, 2001, 2003) (Fig. 4.49).

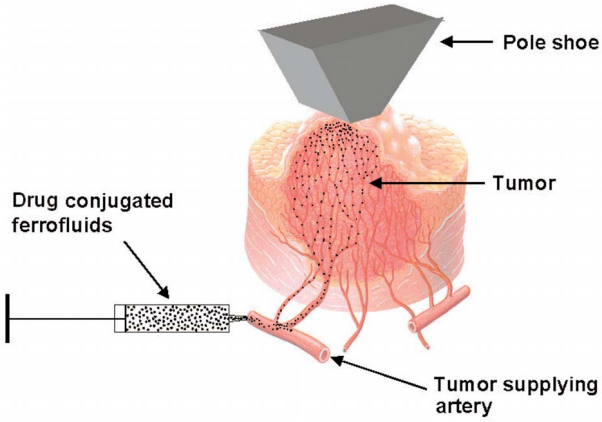

Fig. 4.49. Schematic of the principle of magnetic drug targeting.

With this form of drug delivery, total remissions could be achieved by using only 20% and 50% of the regular systemic chemotherapeutic dosages, without negative side effects (Alexiou et al., 2000, 2001, 2002). Tissue samples removed for histology immediately after magnetic drug targeting demonstrated the distribution of ferrofluids in the tumor tissue and the surrounding connective and muscle tissue *in vivo* (Fig. 4.50). Studies using ^{59}Fe-radiolabeled ferrofluids showed concentrations after magnetic targeting to be 33.6-fold higher in the tumor and 235.5-fold higher in the peritumoral area compared to those in controls (without external magnetic field) (Alexiou et al., 2003). When using intra-arterial magnetic drug targeting, with only 20% and 50% of the normal systemic mitoxantrone dose (10 mg m^{-2} body surface area, intravenous), drug levels in the region of the tumor were 74-fold those identi-

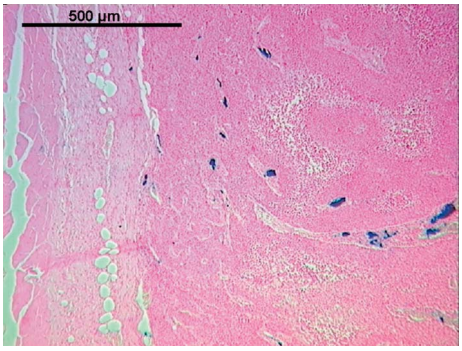

Fig. 4.50. Histological cross-section of a rabbit VX2-squamous cell carcinoma after treatment with intra-arterial magnetic drug targeting. Ferrofluids are visible as blue (dark) pigment in the vessel (staining: Prussian blue).

fied after systemic administration (Alexiou et al., 2003). Histological examination (using electron microscopy) showed that the nanoparticles had reached the intracellular space of cancer cells after magnetic drug targeting, and that the mechanism of uptake was endocytosis (Alexiou et al., 2005, 2006).

Magnetoliposomes are colloidal particles that consist of a magnetic core covered by a lipid layer. They are recognized as useful drug delivery carriers due to their controllable size and membrane properties, their large capacity for carrying various agents, and their biocompatibility (Viroonchatapan et al., 1995). Nobuto et al. (2004) examined the efficiency of systemic chemotherapy with small magnetoliposomes containing doxorubicin and an externally applied electromagnetic field (0.4 T) in osteosarcoma-bearing hamsters, and achieved a suppression of primary tumor growth for at least two weeks.

Magnetic targeting can also be used to deliver therapeutic radioisotopes (Häfeli, 2001). Different radioisotopes can be used to treat over different ranges, depending on their nature; for example, the β-emitter ^{90}Y will irradiate up to a range of 12 mm in tissue. Experiments in mice showed that intraperitoneally injected radioactive-based magnetic microspheres were concentrated near a subcutaneous tumor in the belly area with a small magnet above. The dose-dependent irradiation from the ^{90}Y magnetic microsphere resulted in complete disappearance of $>$50% of the tumors (Häfeli et al., 1997).

4.8.4 Outlook

For *in-vivo* applications, a wide range of nanoparticle characteristics such as component material, size and coating can influence biocompatibility and biodistribution (Storm et al., 1995; Torchilin and Trubetskoy, 1995). Nanoparticles must be sufficiently small so as not to occlude the capillary system and cause embolization, yet large enough to be attracted by an external magnetic field. Previously, there was shown to be a correlation between the attraction of the magnetic particles and the applied magnetic field strength (Alexiou et al., 2002). Furthermore, nanoparticles of $>$100 nm in diameter were cleared more efficiently by cells of the mononuclear phagocyte system than were smaller particles (Storm et al., 1995). For the application of nanoparticles bound to anticancer agents in human patients, the basic precondition is that particle suspensions follow the regulatory requirements of national and international pharmacopoeia.

References

Alexiou, C., Arnold, W., Klein, R., Parak, F., Hulin, P., Bergemann, C., Erhardt, W., Wagenpfeil, S., and Lübbe, A.S. (2000). Locoregional cancer treatment with magnetic drug targeting. *Cancer Res.*, **60**, 6641–6648.

Alexiou, C., Arnold, W., Hulin, P., Klein, R., Renz, H., Parak, F.G., Bergemann, C., and Lübbe, A.S. (2001). Magnetic mitoxantrone nanoparticle detection by histology, x-ray and MRI after magnetic drug targeting. *J. Magn. Magn. Mater.*, **225**, 187–193.

Alexiou, C., Schmidt, A., Hulin, P., Klein, R., Bergemann, C., and Arnold, W. (2002). Magnetic drug targeting: biodistribution and dependency on magnetic field strength. *J. Magn. Magn. Mater.*, **252**, 363–366.

Alexiou, C., Jurgons, R., Schmid, R., Bergemann, C., Henke, J., Erhardt, W., Huenges, E., and Parak, F.G. (2003). Magnetic drug targeting – Biodistribution of the magnetic carrier and the chemotherapeutic agent mitoxantron after locoregional cancer treatment. *J. Drug Target.*, **11**, 139–149.

Alexiou, C., Jurgons, R., Schmid, R.J., Hilpert, A., Bergemann, C., Parak, F.G., and Iro, H. (2005). In vitro and in vivo investigations of targeted chemotherapy with magnetic nanoparticles. *J. Magn. Magn. Mater.*, **293**, 389–393.

Alexiou, C., Schmid, R.J., Jurgons, R., Kremer, M., Wanner, G., Bergemann, C., Huenges, E., Nawroth, T., and Parak, F.G. (2006). Targeting cancer cells: magnetic nanoparticles as drug carriers. *Eur. Biophys. J.*, **35**, 446–450.

Alksne, J.F., Fingerhut, A., and Rand, R. (1966). Magnetically controlled metallic thrombosis of intracranial aneurysms. *Surgery*, **60**, 212–218.

Allen, L.M., Kent, J., Wolfe, C., Ficco, C., and Johnson, J. (1997). MTC™: a magnetically targetable drug carrier for paclitaxel. In: Häfeli, U., Schütt, W., Teller, J., and Zborowski, M. (Eds.), *Scientific and Clinical Applications of Magnetic Carriers*, Plenum Press, New York, London, pp. 481–494.

Arap, W., Haedicke, W., Bernasconie, M., Kain, R., Rajotte, D., Krajewski, S., Ellerby, H.M., Bredesen, D.E., Pasqualini, R., and Ruoslathi, E. (2002). Targeting the prostate for destruction through a vascular address. *Proc. Natl. Acad. Sci. USA*, **99**, 1527–1531.

Collins, J.M. (1984). Pharmacological rationale for regional drug delivery. *J. Clin. Oncol.*, **2**, 498–505.

Gerlowski, L.E. and Jain, R.K. (1986). Microvascular permeability of normal and neoplastic tissues. *Microvasc. Res.*, **31**, 288–299.

Goodwin, S.C., Bittner, C.A., Peterson, C.L., and Wong, G. (2001). Single dose toxicity study of hepatic intra-arterial infusion of doxorubicin coupled to a novel magnetically targeted drug carrier. *Toxicol. Sci.*, **60**, 177–183.

Gupta, P.K. (1990). Drug targeting in chemotherapy: a clinical perspective. *J. Pharm. Sci.*, **79**, 949–962.

Gupta, P.K. and Hung, C.T. (1990a). Comparative disposition of adriamycin delivered via magnetic albumin microspheres in presence and absence of magnetic fields in rats. *Life Sci.*, **46**, 471–484.

Gupta, P.K. and Hung, C.T. (1990b). Targeted delivery of low dose doxorubicin hydrochloride administered via magnetic albumin microspheres in rats. *J. Microencap.*, **7**, 85–92.

Gupta, P.K. and Hung, C.T. (1994). Magnetically controlled targeted chemotherapy. In: Willmott, N. and Daly, J. (Eds.), *Microspheres and Regional Cancer Therapy*, CRC Press, Boca Raton, Florida, pp. 71–116.

Haber, E. (1994). Antibody targeting as a strategy in thrombolysis. In: Kaw, B.A., Narula, J., and Strauss, H.W. (Eds.), *Monoclonal antibodies in cardiovascular diseases*, Lea & Febiger, Malvern, pp. 187–197.

Häfeli, U.O. (2001). Radioactive magnetic microspheres In: Arshady, R. (Ed.), *Microspheres, Microcapsules and Liposomes: Magneto- and Radio-Pharmaceuticals*, **3**, Citus Books, London, pp. 559–584.

Häfeli, U.O., Pauer, G.J., Roberts, W.K., Humm, J.L., and Macklis, R.M. (1997). Magnetically targeted microspheres for intracavitary and intraspinal ^{90}Y radiotherapy. In: Häfeli, U., Schütt, W., Teller, J., and Zborowski, M. (Eds.), *Scientific and Clinical Applications of Magnetic Carriers*, Plenum Press, New York, London, pp. 501–516.

Hilal, S.K., Michelsen, W.J., Driller, J., and Leonard, E. (1974). Magnetically guided devices for vascular exploration and treatment. *Radiology*, **113**, 529–534.

Kato, T., Nemoto, R., Mori, H., Unno, K., Goto, A., and Homma, M. (1980). An approach to magnetically controlled cancer chemotherapy. *J. Jap. Soc. Cancer Ther.*, **15**, 876–880.

Kato, T., Nemoto, R., Mori, H., Abe, R., Unno, K., Goto, A., Murota, H., Harada, M., Kawamura, K., and Homma, M. (1981). An approach to magnetically controlled cancer chemotherapy. *J. Jap. Soc. Cancer Ther.*, **16**, 1351–1357.

Kramer, P.A. (1974). Albumin microspheres vehicles for archiving specificity in drug delivery. *J. Pharm. Sci.*, **63**, 1646–1647.

Kuznetsov, A., Harutyunyan, A.R., Dobrinski, E.K., Filippov, V.I., Malenkov, A.G., Vanin, A.F., and Kuznetsov, O.A. (1997). Ferro-carbon particles: Preparation and clinical applications. In: Häfeli, U., Schütt, W., Teller, J., and Zborowski, M. (Eds.), *Scientific and Clinical Applications of Magnetic Carriers*, Plenum Press, New York, London, pp. 379–389.

Leveugle, B., Mann, D., Madiyalakan, R., and Noujaim, A.A. (2000). Therapeutic antibodies for prostate cancer. *IDrugs*, **3**, 1191–1198.

Lübbe, A.S., Bergemann, C., Huhnt, W., Fricke, T., Riess, H., Brock, J.W., and Huhn, D. (1996a). Preclinical experiences with magnetic drug targeting: tolerance and efficacy. *Cancer Res.*, **56**, 4694–4701.

Lübbe, A.S., Bergemann, C., Riess, H., Schriever, F., Reichardt, P., Possinger, K., Matthias, M., Dorken, B., Herrmann, F., Gurtler, R., Hohenberger, P., Haas, N., Sohr, R., Sander, B., Lemke, A.J., Ohlendorf, D., Huhnt, W., and Huhn, D. (1996b). Clinical experiences with magnetic drug targeting: a Phase I study with 4′-epidoxorubicin in 14 patients with advanced solid tumors. *Cancer Res.*, **56**, 4686–4693.

Lübbe, A.S., Bergemann, C., and Alexiou, C. (2000). Magnetically-controlled drug targeting for cancer treatment. *Recent Res. Devel. Cancer*, **2**, 183–191.

Lübbe, A.S., Alexiou, C., and Bergemann, C. (2001). Clinical applications of magnetic drug targeting. *J. Surg. Res.*, **95**, 200–206.

Morris, R.M., Poore, G.A., Howard, D.P., and Sefranka, J.A. (1984). Selective targeting of magnetic albumin microspheres containing low-dose doxorubicin: total remission in yoshida-bearing rats. In: Davis, S.S., Illum, L., McVie, J.G., and Tomlinson, E. (Eds.), *Microspheres and Drug Therapy. Pharmaceutical, immunological and medical aspects*, Elsevier, New York, pp. 439–440.

Neglia, J.P., Friedmann, D.L., and Yasui, Y. (2001). Second malignant neoplasms in five-year survivors of childhood cancer: childhood cancer survivor study. *J. Natl. Cancer. Inst.*, **93**, 618–629.

Nobuto, H., Sugita, T., Kubo, T., Shimose, S., Yasunaga, Y., Murakami, T., and Ochi, M. (2004). Evaluation of systemic chemotherapy with magnetic liposomal doxorubicin and a dipole external electromagnet. *Int. J. Cancer*, **109**, 627–635.

Poste, G. and Kirsh, R. (1983). Site specific (targeted) drug delivery in cancer therapy. *Biotechnol.*, **10**, 869–885.

Rahman, Y., Cerny, E.A., Tallaksen, S.L., Wright, B.J., Nance, S.O., and Thompson, J.F. (1974). Liposomes-encapsulated actinomycin D: potential in cancer chemotherapy. *Proc. Soc. Exp. Biol. Med.*, **146**, 1173–1176.

Rudge, S., Peterson, C., Vessely, C., Koda, J., Stevens, S., and Catterall, L. (2001). Adsorption and desorption of chemotherapeutic drugs from magnetically targeted carrier (MTC). *J. Control. Release*, **74**, 335–340.

Sachdeva, M.S. (1998). Drug targeting systems for cancer therapy. *Expert. Opin. Investig. Drugs*, **7**, 1849–1864.

Scherer, F., Anton, M., Schillinger, U., Henke, J., Bergemann, C., Kruger, A., Gänsbacher, B., and Plank, C. (2002). Magnetofection enhancing and targeting gene delivery by magnetic force in vitro and in vivo. *Gene Ther.*, **9**, 102–109.

Shinkai, M., Suzuki, M., Iijima, S., and Kobayashi, T. (1994). Antibody-conjugated magnetoliposomes for targeting cancer cells and their application in hyperthermia *Biotechnol Appl. Biochem.*, **21**, 125–137.

Storm, G., Belliot, S.O., Daemen, T., and Lasic, D.D. (1995). Surface modification of nanoparticles to oppose uptake by the mononuclear phagocyte system. *Adv. Drug Deliv. Rev.*, **17**, 31–48.

Torchilin, V.P. (2000). Drug targeting. *Eur. J. Pharm. Sci.*, **11**, 81–91.

Torchilin, V.P. and Trubetskoy, V.S. (1995). Which polymer can make nanoparticulated drug carriers long circulating? *Adv. Drug Deliv. Rev.*, **16**, 141–155.

Torchilin, V.P., Zhou, F., and Huang, L. (1993). pH-sensitive liposomes. *Liposome Res.*, **3**, 201–205.

Viroonchatapan, E., Ueno, M., Sato, H., Adachi, I., Nagae, H., Tazawa, K., and Horikoshi, I. (1995). Preparation and characterization of dextran magnetite-incorporated thermosensitive liposomes: an on-line flow system for quantifying magnetic responsiveness. *Pharm. Res.*, **12**, 1176–1183.

Widder, K.J., Senyei, A.E., and Scarpelli, D.G. (1978). Magnetic microspheres: a model system for site specific drug delivery in vivo. *Proc. Soc. Exp. Biol. Med.*, **158**, 141–146.

Widder, K.J., Senyei, A.E., and Ranney, D.F. (1979). Magnetically responsive microspheres and other carriers for the biophysical targeting of antitumor agents. In: Gavattini, S., Goldin, A., Howking, F., Kopin, I.J., and Schnitzer, R.J. (Eds.), *Advances in Pharmacology and Chemotherapy*, Academic Press, New York, pp. 213–239.

Widder, K.J., Morris, R.M., Poore, G.A., Howard, D.P., and Senyei, A.E. (1983). Selective targeting of magnetic albumin microspheres containing low-dose doxorubicin: total remission in yoshida sarcoma bearing rats. *Eur. J. Cancer Clin. Oncol.*, **19**, 135–139.

Wilson, M.W., Kerlan, R.K., Fidelman, N.A., Venook, A.P., La Berge, J.M., Koda, J., and Gordon, R.L. (2004). Hepatocellular carcinoma: regional therapy with a magnetic targeted carrier bound to doxorubicin in a dual MR imaging/conventional angiography suite – initial experience with four patients. *Radiology*, **230**, 287–293.

Yatvin, M.B., Kreutz, W., Horwitz, B.A., and Shinitzky, M. (1980). pH-sensitive liposomes: possible clinical implications. *Science*, **210**, 1253–1255.

Zacharski, L.R., Ornstein, D.L., Gabazza, E.C., D'Alessandro-Gabazza, C.N., Brugarolas, A., and Schneider, J. (2002). Treatment of malignancy by activation of the plasminogen system., *Semin. Thromb. Hemost.*, **28**, 5–18.

4.9
New Fields of Application

Wilfried Andrä and Urs Häfeli

4.9.1
Introduction

Magnetism and its application in many scientific fields continues to be a hot topic, appearing not only in the medical applications described in the present book, but also in articles published in almost every single issue of top-rated journals, including *Nature* and *Science*. In the following section, we highlight a necessarily restricted and somewhat arbitrary selection of new fields of applications that have come to our attention during the past couple of years. Many of these concern the use and application of magnetic particles which, in combination with applied magnetic fields, can be used for many different analytical, diagnostic, and therapeutic applications. Such applications are also discussed in a bi-annual meeting, the International Conference on the "Scientific and Clinical Applications of Magnetic Carriers", which aims at bringing together developers and users of magnetic particle-based techniques (for more information: http://www.magneticmicrosphere.com). Following the 2004 meeting, the conference proceedings were published in the form of 107 full-size, peer-reviewed papers in a special issue of the *Journal of Magnetism and Magnetic Materials* (Vol. 293, 2005). In addition to the many articles dealing with particle preparation and their medical and biological aspects, new techniques covering the analytical and magnetic separation field were also described. Some of these will be discussed in the following sections.

4.9.2
Magnetic Particle Imaging (MPI)

The imaging of body parts, organs and tissues in humans is highly useful for medical diagnosis. Numerous imaging techniques have been developed to allow for the examination of regions not accessible to the naked eye. X-radiography remains the most often utilized of these techniques, but is also the one associated with the

highest risk of side effects. About 35 years ago, a much safer option was offered through the application of magnetism introduced in the form of magnetic resonance imaging (MRI). This method, first described by Lauterbur (1973), causes selected volume parts inside the body to respond to an alternating (AC) field, allowing the signal from these parts to be separated from those of the surroundings. The separation is realized by applying an inhomogeneous magnetic field that resonates with the frequency of nuclear magnetic resonance specifically in the selected region. Using a special three-dimensional scanning procedure, the selected region is moved across the examined body volume and the total picture reconstructed from the magnetic resonance signal (see Section 3.2). Lauterbur, in his original report, did not restrict the method to magnetic resonance but instead more generally described "... image formation by induced local interactions".

A novel application of this general idea was recently proposed by Gleich (2003). The method, as described by Gleich and Weizenecker (2005) and Trabesinger (2005), is termed "magnetic particle imaging" (MPI). The idea is to highlight a small region within a larger surrounding volume by marking it with magnetic particles. Magnetic particles show a strongly nonlinear magnetization dependence (see Section 4.6); this is in contrast to the magnetization of tissue, which exhibits a magnetization proportional to the magnetic field up to very high field strengths. The particle magnetization as a function of the magnetic field may coarsely be subdivided into three different sections: (1) a high-strength positive field; (2) a high-strength negative field, for which the magnetization is almost constant (saturation); and (3) a restricted field region near zero for which the magnetization changes steeply. Only the small selection field range near zero is moved by a special scanning procedure across the examined volume. There are two variants of MPI. In the first variant, an AC magnetic field with small amplitude (modulation field) is superimposed on the slowly moving selection field; this causes the particle magnetization to respond with the harmonics of the modulation frequency. This mode of operation is similar to that used with flux-gate magnetometers (see Section 1.3.3). The second variant uses a strong selection field that is moved with high speed across the examined volume, thereby switching the magnetization of all particles in the selected small region. In both variants the actual position of the selection field must be known and, at the same time, the responding stray field of the particles must be detected by suitable means, such as by detection coils carefully compensated with respect to the externally applied fields.

Gleich and Weizenecker (2005) demonstrated the general operability of magnetic particle imaging using an array of small drill-holes (diameter ≈ 0.5 mm) filled with an undiluted, commercially available MRI contrast agent (Resovist®; Schering AG, Berlin, Germany). Using the contrast agent containing magnetic oxide particles with a magnetic core well below 100 nm, the holes could be clearly resolved.

For medical application of MPI, the regions of interest must be marked selectively. This can be achieved, for example, using methods of drug targeting (see Section 4.8), including the labeling of magnetic carriers (see Section 4.7) and the guiding of labeled magnetic particles to the corresponding sites.

4.9.3
Magnetically Modulated Optical Nanoprobes

Usually, magnetic nanospheres or microspheres do not appear as individual particles but rather act as a collection of them. Recently, however, individual particles sized in the micrometer range and smaller were marked and observed by means of a simple but interesting method. The trick was to cover one side of the spherical magnetic particles with a metal cap, thereby breaking the spherical symmetry with respect to optical properties such as reflectance and fluorescence. Then, when the particles were turned by a rotating magnetic field, individual particles could be observed by optical microscopy. They appeared as blinking stars and could thus be differentiated from the background. This method has been described in a series of papers, starting with an overall description of these so-called magnetically modulated optical nanoprobes (MagMOONs) (Anker et al., 2005), and followed by applications in microrheology (Behrend et al., 2005) and pH sensing (McNaughton et al., 2005; Roberts et al., 2005).

The preparation of MagMOONs started from polymer and silica nanospheres and microspheres that were modified by incorporating magnetic ''nanocrumbs'', such as particles consisting of Ba-ferrite or chromium dioxide. For fluoroscopic investigations a fluorescent substance was also added. The crucial preparation step was the coating of one side of each sphere with a cap of aluminum or gold. When these capped magnetic spheres were suspended in a liquid they behaved like a compass and were able to be oriented by a magnetic field (Behrend et al., 2005). In such a rotating magnetic field the MagMOONs experience a torque proportional to the vector product of the magnetic field strength and the magnetic moment of the particle. According to the equation of motion, the spheres show rotational motion determined by the driving torque and different kinds of friction depending on the rotational speed and the viscosity of the surrounding liquid. By shining light at the particles, it was possible to examine a blinking response from reflected light as a function of the frequency, and the viscosity of the liquid could be measured on a microscopic scale (Behrend et al., 2005).

The second demonstrated use of MagMOONs was as probes to measure the pH value of the surrounding liquid. They do this by sensing the alterations of the fluorescence spectra emitted from special agents, such as carboxynaphthofluorescein and ETH 5350, in response to the pH value (McNaughton et al., 2005). By applying suitable chemical labeling, MagMOONs have the potential to be chemical sensors for a broad range of agents (Anker et al., 2005; McNaughton et al., 2005; Roberts et al., 2005).

4.9.4
Magnetic Guidance

The term ''magnetic guidance'' is primarily applied to the motion of objects assisted by a magnetic field towards a target inside the human body. In most cases,

the magnetic field acts by means of the force exerted by its gradient on a magnetic moment (see Section 1.2.2.4). In terms of a coarse estimation, this force is proportional to the volume of the guided magnetic object. For spherical objects with a radius R, the force is proportional to R^3, while the opposing force caused by friction is only proportional to R^2. Therefore, the larger the object, the more the friction forces can be surpassed by the magnetic force. In the case of soft magnetic objects, the magnetic force points in the direction of increasing field strength. As a consequence, a target located inside the human body requires a maximum field inside the body. According to Earnshaw's theorem of magnetostatics, however, it is not possible to generate a maximum field inside a body using extracorporeal coils or permanent magnets (McCaig and Clegg, 1987). This fact should be borne in mind, especially when magnetic particles need to be concentrated at a region deep inside the human body.

4.9.4.1
Small Particles Guided by Extracorporeally Generated Field Gradients

Attracting magnetic forces on macroscopic objects, especially at the body surface or near to the pointed poles of permanent magnets, can be very strong. This had already been demonstrated in 600 BC through the extraction of bulk iron pieces from the eye (see Section 1.1.3). Since then, most applications of magnetic forces have dealt with macroscopic parts such as catheters and other devices as are used in stereotactic neurosurgery (see Section 1.1.5). Recently, however, an increasing number of investigations have been carried out with very small objects such as superparamagnetic particles. These objects are of particular interest due to their ability to act as carriers for drug targeting (see Section 4.8). In order to mathematically model particle deposition in deeper target regions, a theoretical study was recently performed which considered not only the influence of Stokes drag and magnetic forces on the particles, but also the interactions and collisions between moving red blood cells in the bloodstream (Grief and Richardson, 2005). These interactions cause a diffusive motion much greater than standard Brownian diffusion. The authors came to the same conclusion as McCaig and Clegg (see above), namely, that it is impossible to target regions inside the body using externally applied magnetic fields. Nevertheless, numerous publications have reported results obtained with magnetic nanoparticles which could be concentrated or retained from clearance by high-gradient magnetic fields. Recent reviews of this field are provided by Neuberger et al. (2005) and Schillinger et al. (2005). Unfortunately, in most of the reported investigations, only minimal information can be found about the quantitative parameters of the magnetic field and its spatial distribution. One of the exceptions is a recent report (Xu et al., 2005) that describes the geometry of a permanent magnet with one pyramid-shaped pole. Furthermore, field parameters are provided in detail and particle retention of ferrofluids was shown as a function of the flow speed at different distances from the pole tip.

4.9.4.2 Field Gradients Generated by Magnetic Implants

One interesting way of overcoming the problem of establishing a field maximum inside the human body is through the implantation of magnetizable objects of suitable geometry. The basic problem of collecting magnetic particles at the surface of magnetized wires was first discussed some three decades ago. At that time, it was shown that a wire magnetized across its axis generates a strongly inhomogeneous magnetic field near its surface, attracting particles even against strong hydrodynamic forces (Friedlaender et al., 1978). Recently, different systems of transdermal implants for the retention of magnetic particles transported inside an artery were modeled by Avilés et al. (2005). These authors concluded that an implanted ferromagnetic wire magnetized by an extracorporeal permanent magnet is a promising tool for the intra-arterial retention of magnetic particles. The same group further modeled the ability of magnetizable intravascular stents to concentrate magnetic particles at defined positions in arteries near the stent wires (Chen et al., 2005). This group was particularly interested in particles destined for intravascular transport, which must be smaller than a few micrometers in order to avoid thrombosis or embolization. The results of both investigations showed that single particles of this size cannot be concentrated or retained against the hydrodynamic forces of blood flow with velocities above 5 cm s^{-1} by practicable magnetic field strengths ($\mu_0 H \leq 1$ T). It is, however, well known that under the influence of a magnetic field, agglomeration of magnetic particles does occur and clusters do form. These clusters are then amenable to magnetic guiding. The findings of another group (Yellen et al., 2005) showed experimental evidence that particles as small as 0.4 μm could be captured by a copper mesh electroplated with a cobalt-nickel alloy in a flow chamber with velocities of 5 cm s^{-1}. Unfortunately, the optical resolution of the corresponding microscopic photographs does not allow for the single particles to be distinguished from the particle agglomerates.

Another aspect of magnetic targeting – the concentration of magnetic particles in a tumor – was modeled by Rotariu and Strachan (2005). Blood flow velocities in the arterioles and capillaries of tumors are much lower than in arteries, and the chance to capture particles as small as 1 μm is thus much higher, especially after the implantation of needle-shaped magnets.

The partly contradictory results of the above-mentioned modeling papers show that further investigations are needed in order to come to a final decision on the feasibility of magnetic targeting deep in the body. The possible risks due to embolization by magnetic agglomerates must also be further examined and investigated in animal models.

4.9.4.3 Magnetic Devices Moved by Alternating or Rotating Magnetic Fields

The magnetic guidance of objects through the vascular system or the tissue is hindered by friction forces. The action of a magnetic field gradient on a magnetic mo-

ment is often too weak to overcome these opposing forces. It is, however, possible to excite the movements of a magnetic vehicle by externally applied alternating or rotating magnetic fields, thereby drastically reducing the frictional resistance and even actively pushing the object ahead. A well-known example is the so-called para-operational device (POD) described by Frei et al. (1966). The main propulsion principle of PODs consists of vibrating movements of a permanent magnet exposed to both a strong static and a weak alternating magnetic field and assisted by suitable tails attached to the device. The resulting motion is similar to the swimming of a tadpole. Interestingly, rotating PODs were also described in Frei et al.'s publication.

Although several studies have been carried out using PODs, this interesting device failed to reach clinical acceptance. The basic idea of rotating objects, however, was recently taken up again by Ishiyama et al. (2001, 2002). These authors performed *in-vitro* studies with screw-shaped objects containing a permanent magnet magnetized perpendicular to the screw axis. When these vehicles were exposed to a rotating magnetic field, they were able to move along their axis through media with a wide range of Reynolds numbers. Dutz et al. (2004) recently published similar investigations, as did McNaughton et al. (2005), who used screw-shaped vehicles as fluorescent sensors. Compared with already established gradient-based magnetic navigation systems (see for example Fig. 1.8 in Section 1.1.5), the required electric power for these types of rotating vehicles is orders of magnitudes smaller. Therefore, the further development of this guidance principle may be a promising alternative for different medical applications.

References

Anker, J.N., Behrend, C.J., Huang, H., and Kopelman, R. (2005). Magnetically-modulated optical nanoprobes (MagMOONs) and systems. *J. Mag. Mag. Mater.*, **293**, 655–662.

Avilés, M.O., Ebner, A.D., Chen, H., Rosengart, A.J., Kaminski, M.D., and Ritter, J.A. (2005). Theoretical analysis of a transdermal ferromagnetic implant for retention of magnetic drug carrier particles. *J. Mag. Mag. Mater.*, **293**, 605–615.

Behrend, C.J., Anker, J.N., McNaughton, B.H., and Kopelman, R. (2005). Microrheology with modulated optical nanoprobes (MOONs). *J. Mag. Mag. Mater.*, **295**, 663–670.

Chen, H., Ebner, A.D., Kaminski, M.D., Rosengart, A.J., and Ritter, J.A. (2005). Analysis of magnetic drug carrier particle capture by a magnetizable intravascular stent – 2: Parametric study with multi-wire two-dimensional model. *J. Mag. Mag. Mater.*, **293**, 616–632.

Dutz, S., Andrä, W., Richert, H., and Bellemann, M.E. (2004). Design and evaluation of methods for the controlled movement of magnetic markers in viscous media and biomaterials. *Biomed. Techn.*, **49** (Suppl. 2), 722–723.

Frei, E.H., Drirller, J., Neufeld, H.N., Barr, I., Bleiden, L., and Askenazy, H.M. (1966). The POD and its applications. *Med. Res. Eng.*, **5**, 11–18.

Friedlaender, F.J., Takayasu, M., Rettig, J.B., and Kentzer, C.P. (1978). Particle flow and collection process in single wire HGMS studies. *IEEE Trans. Magn.*, **MAG-14**, 1158–1164.

Gleich, B. (2003). Verfahren zur Ermittlung der räumlichen Verteilung magnetischer Partikel. German patent application DE 101 51 778 A1.

Gleich, B. and Weizenecker, J. (2005). Tomographic imaging using the nonlinear response of magnetic particles. *Nature*, **435**, 1214–1217.

Grief, A.D. and Richardson, G. (2005). Mathematical modelling of magnetically targeted drug delivery. *J. Mag. Mag. Mater.*, **293**, 455–463.

Ichiyama, K., Sendoh, M., Yamazaki, A., Inoue, M., and Arai, K.I. (2001). Swimming of magnetic micro-machines under a very wide-range of Reynolds number conditions. *IEEE Trans. Magn.*, **MAG-37**, 2868–2870.

Ishiyama, K., Sendoh, M., and Arai, K.I. (2002). Magnetic micromachines for medical applications. *J. Mag. Mag. Mater.*, **242–245**, 41–46.

Lauterbur, P.C. (1973). Image formation by induced local interactions: Examples employing nuclear magnetic resonance. *Nature*, **242**, 190–191.

McCaig, M. and Clegg, A.G. (1987). *Permanent Magnets*. Pentech Press, London.

McNaughton, B.H., Anker, J.N., and Kopelman, R. (2005). Magnetic microdrill as a modulated fluorescent pH sensor. *J. Mag. Mag. Mater.*, **293**, 696–701.

Neuberger, T., Schöpf, B., Hofmann, H., Hofmann, M., and von Rechenberg, B. (2005). Superparamagnetic nanoparticles for biomedical applications: possibilities and limitations of a new drug delivery system. *J. Mag. Mag. Mater.*, **293**, 483–96.

Roberts, T.G., Anker, J.N., and Kopelman, R. (2005). Magnetically modulated optical nanoprobes (MagMOONs) for detection and measurement of biologically important ions against the natural background fluorescence of intracellular environments. *J. Mag. Mag. Mater.*, **293**, 715–724.

Rotariu, O. and Strachan, N.J.C. (2005). Modelling magnetic carrier particle targeting in the tumor microvasculature for cancer treatment. *J. Mag. Mag. Mater.*, **293**, 639–641.

Schillinger, U., Brill, T., Rudolph, C., Huth, S., Gerstin, S., Krötz, F., Hirschberger, J., Bergemann, C., and Plank, C. (2005). Advances in magnetofection: magnetically guided nucleic acid delivery. *J. Mag. Mag. Mater.*, **293**, 501–508.

Trabesinger, A. (2005). Particular magnetic insights. *Nature*, **435**, 1173–74.

Xu, H., Song, T., Bao, X., and Hu, L. (2005). Site-directed research of magnetic nanoparticles in magnetic drug targeting. *J. Mag. Mag. Mater.*, **293**, 514–519.

Yellen, B.B., Forbes, Z.G., Halverson, D.S., Fridman, G., Barbee, K.A., Chorny, M., Levy, R., and Friedman, G. (2005). Targeted drug delivery to magnetic implants for therapeutic applications. *J. Mag. Mag. Mater.*, **293**, 647–654.

5
Conclusions and Perspectives

Jens Haueisen

This second edition of *Magnetism in Medicine* includes a large number of changes when compared to the First Edition. In many aspects it should be seen rather as a new book than simply a new edition – a point which reflects, at least in part, the highly dynamic nature of magnetism in medicine, with so many new developments and applications over the past few years. As in the First Edition, one of the main emphases in this book is the integration of basic science and clinical research. In such a highly interdisciplinary field, where physicists, engineers and clinicians must work in unison in order to achieve their research goals, everybody should be able to understand the others' disciplines in some depth. Clinicians need to know about the technology they are using, the physicists and engineers need to know about the various clinical aspects, whilst all members of the team require a good basic knowledge of the physiological and pathophysiological mechanisms involved. The successful development of new diagnostic and therapeutic approaches is possible only in such an environment.

Biomagnetic SQUID-based recording technology, which measures the extremely weak magnetic fields produced by living systems, has developed continuously over the past few years, with increasing numbers of channels per system (currently up to 500). Vectorial measurements (recording all three components of the magnetic field at approximately one site) represent one new and promising direction in this field, while another promising sector lays in the development of optical magnetometers. Although the first biomagnetic measurements with optical magnetometers date back to the early 1990s, recent developments have shown that these devices offer very interesting prospects for biomagnetic imaging.

Magnetic source imaging (MSI), which involves the reconstruction of brain activity based on biomagnetic recordings, individual anatomical information, and forward and inverse procedures, has become established as a standard tool in both basic and clinical research. However, it has also stimulated developments in other fields, such as source imaging based on electric potential measurements. The unique nature and strength of bioelectromagnetic measurements – and consequently of MSI – is to provide images of brain or heart activity on a millisecond time scale, allowing the analysis of information transfer mediated by cortical oscil-

lations or the noninvasive imaging of activation sequences in the heart. In terms of reimbursement for clinical applications of MSI (epilepsy and presurgical mapping), this is currently available in the USA and Japan, and possibly available in Europe in the not-too-distant future.

Another future clinical application based on biomagnetic measurements is that of diagnosis and monitoring of fetal arrhythmias. Indeed, the unique signal quality qualifies fetal magnetocardiography (fMCG) as the only valid method for studying fetal cardiac electrophysiology during late pregnancy. Moreover, as the method is noninvasive and easy to apply, its use is proposed in all cases where an ECG might be indicated, promoted by the availability of low-cost, bed-side recording systems. Fetal magnetoencephalography (fMEG), on the other hand, is currently much further from clinical application, mainly because it monitors an extremely weak signal that cannot be obtained in all recording sessions. Nonetheless, fMEG represents a new ''window'' to the fetal brain.

Many developments have occurred in magnetic resonance imaging (MRI) since the first edition of this book was published. In high-field areas, for example, 7 and 9.4-Tesla systems have been developed and are currently undergoing evaluation, while at the other end of the spectrum low-field MRI using SQUIDs has resulted in completely new diagnostic devices by combining MRI and MEG. Newly introduced parallel imaging (multiple recording channels) has already resulted in fewer artifacts and shorter recording times. Remarkable progress has also been made in areas such as whole-body MRI and MR angiography, routine applications of diffusion, perfusion or BOLD-techniques, in addition to MR-spectroscopy (MRS).

Today, MRS represents a most valuable clinical tool, due mainly to the rapid availability of data. For example, determining metabolite concentrations are vital when diagnosing many diseases, with proton spectra of the brain being used to monitor levels of *N*-acetyl-aspartate, creatine, phosphocreatine, trimethylamines, *myo*-inositol and amino acids associated with neuronal tissue loss in dementia and other brain diseases. In this respect, metabolic changes in the brain can be mapped using functional magnetic resonance spectroscopy (fMRS) imaging techniques, while multimodal imaging using electromagnetic, metabolic, and hemodynamic activity will increase our understanding of brain function and provide new means of experimental validation in neuroscience.

Perhaps the most striking steps forward, however, have been made in cardiovascular imaging, with improved MRI. Today, by combining new techniques and sequences – including the acquisition of high-resolution images in a single heartbeat – new insights are available in cardiac morphology, function, perfusion, and vessel analysis.

As with the above-described areas of magnetism in medicine, the magnetic stimulation of excitable tissue has been developed and is now widely used in neuroscience research and clinical diagnosis. Here, new methods for focal and vectorial stimulation have been introduced with transcranial magnetic stimulation (TMS) which, when combined with electric source imaging and stereotactic multi-channel TMS, will accelerate interest in this area. In addition, new applications of TMS –

including the modulation of gene expression and induction of restorative plasticity or tolerance against brain injury – should reach clinical practice in the near future.

The use of magnetic particles in a variety of forms and sizes for diagnostic and therapeutic approaches represents yet another major domain of innovation. The ability to concentrate magnetic nanoparticles in a target region of the body by applying an external magnetic field has been demonstrated in principle, and has opened the door to magnetic particle hyperthermia and associated highly selective cancer therapy.

In conclusion, the elegance, noninvasive nature and other advantages of magnetic procedures in medicine – combined with the need to solve many current research problems – will ensure that this highly technological field retains its dynamic state over the years to come.

Index

Related Titles

J. Clarke, A. I. Braginski (Eds.)

The SQUID Handbook

Volume I: Fundamentals and Technology of SQUIDs and SQUID Systems

2004
ISBN-13: 978-3-527-40229-8
ISBN-10: 3-527-40229-2

J. Clarke, A. I. Braginski (Eds.)

The SQUID Handbook

Volume II: Applications of SQUIDs and SQUID Systems

2004
ISBN-13: 978-3-527-40408-7
ISBN-10: 3-527-40408-2

W. R. Hendee, E. R. Ritenour

Medical Imaging Physics

2002
ISBN-13: 978-0-471-38226-3
ISBN-10: 0-471-38226-4

W. R. Hendee (Ed.)

Biomedical Uses of Radiation

1999
ISBN-13: 978-3-527-29668-2
ISBN-10: 3-527-29668-9